STRUCTURE-RELATED INTRINSIC ELECTRICAL STATES AND FIRING PATTERNS OF NEURONS WITH ACTIVE DENDRITES

EDITED BY: Sergey M. Korogod
PUBLISHED IN: Frontiers in Cellular Neuroscience and
Frontiers in Computational Neuroscience

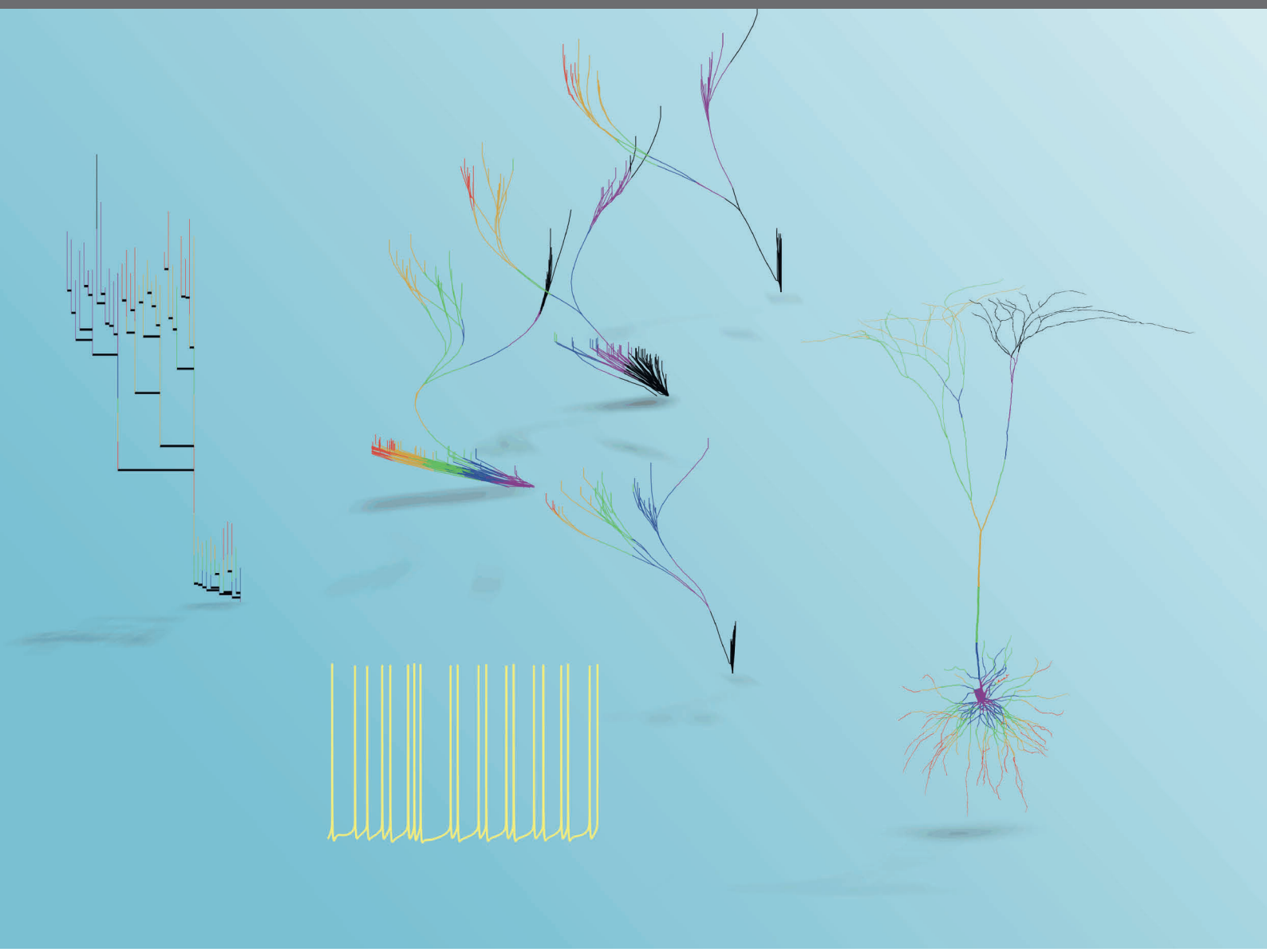

frontiers Research Topics

frontiers

ISSN 1664-8714
ISBN 978-2-88945-608-6
DOI 10.3389/978-2-88945-608-6

About Frontiers

Frontiers is more than just an open-access publisher of scholarly articles: it is a pioneering approach to the world of academia, radically improving the way scholarly research is managed. The grand vision of Frontiers is a world where all people have an equal opportunity to seek, share and generate knowledge. Frontiers provides immediate and permanent online open access to all its publications, but this alone is not enough to realize our grand goals.

Frontiers Journal Series

The Frontiers Journal Series is a multi-tier and interdisciplinary set of open-access, online journals, promising a paradigm shift from the current review, selection and dissemination processes in academic publishing. All Frontiers journals are driven by researchers for researchers; therefore, they constitute a service to the scholarly community. At the same time, the Frontiers Journal Series operates on a revolutionary invention, the tiered publishing system, initially addressing specific communities of scholars, and gradually climbing up to broader public understanding, thus serving the interests of the lay society, too.

Dedication to Quality

Each Frontiers article is a landmark of the highest quality, thanks to genuinely collaborative interactions between authors and review editors, who include some of the world's best academicians. Research must be certified by peers before entering a stream of knowledge that may eventually reach the public - and shape society; therefore, Frontiers only applies the most rigorous and unbiased reviews.
Frontiers revolutionizes research publishing by freely delivering the most outstanding research, evaluated with no bias from both the academic and social point of view. By applying the most advanced information technologies, Frontiers is catapulting scholarly publishing into a new generation.

What are Frontiers Research Topics?

Frontiers Research Topics are very popular trademarks of the Frontiers Journals Series: they are collections of at least ten articles, all centered on a particular subject. With their unique mix of varied contributions from Original Research to Review Articles, Frontiers Research Topics unify the most influential researchers, the latest key findings and historical advances in a hot research area! Find out more on how to host your own Frontiers Research Topic or contribute to one as an author by contacting the Frontiers Editorial Office: researchtopics@frontiersin.org

STRUCTURE-RELATED INTRINSIC ELECTRICAL STATES AND FIRING PATTERNS OF NEURONS WITH ACTIVE DENDRITES

Topic Editor:
Sergey M. Korogod, Bogomoletz Institute of Physiology, National Academy of Sciences of Ukraine, Ukraine

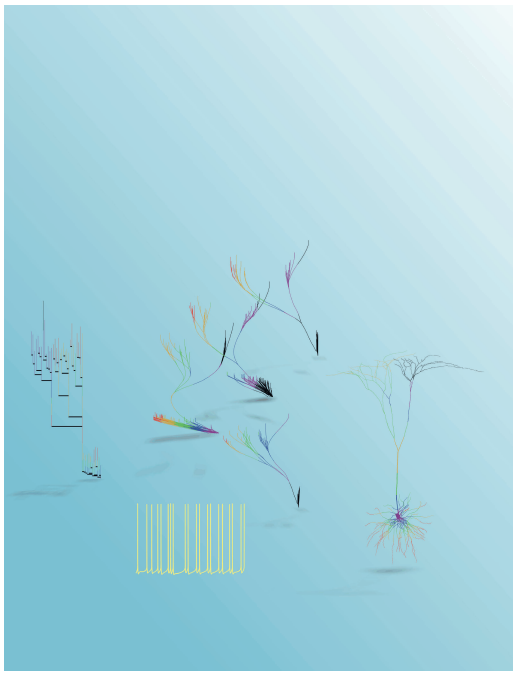

Snapshots of color-coded membrane potentials in function of path distance from soma mapped on the dendrogram and 3D image of modeled pyramidal neuron generating complex intrinsic pattern of action potentials.
Image: "Dancing dendrites" by Sergey M. Korogod.

Activity of the multi-functional networked neurons depends on their intrinsic states and bears both cell- and network-defined features. Firing patterns of a neuron are conventionally attributed to spatial-temporal organization of inputs received from the network-mates via synapses, in vast majority dendritic. This attribution reflects widespread views of the within-cell job sharing, such that the main function of the dendrites is to receive signals and deliver them to the axo-somatic trigger zone, which actually generates the output pattern. However, these views are now revisited due to finding of active, non-linear properties of the dendritic membrane in neurons of practically all explored types. Like soma and axon, the dendrites with active membrane are able to generate self-maintained, propagating depolarizations and thus share intrinsic pattern-forming role with the trigger zone. Unlike the trigger zone, the dendrites have complex geometry, which is subject to developmental, activity-dependent, or neurodegenerative changes. Structural features of the arborization

inevitably impact on electrical states and cooperative behavior of its constituting parts at different levels of organization, from sub-trees and branches to voltage- and ligand-gated ion channels populating the dendritic membrane. More than two decades of experimental and computer simulation studies have brought numerous phenomenological demonstrations of influence of the dendritic structure on neuronal firing patterns. A necessary step forward is to comprehend these findings and build a firm theoretical basis, including quantitative relationships between geometrical and electrical characteristics determining intrinsic activity of neurons.

The articles in this eBook represent progress achieved in a broad circle of laboratories studied various aspects of structure and function of the neuronal dendrites. The authors elucidate new details of dendritic mechanisms underlying intrinsic activity patterns in neurons and highlight important questions that remain open in this important domain of cellular and computational neuroscience.

Citation: Korogod, S. M., ed (2018). Structure-Related Intrinsic Electrical States and Firing Patterns of Neurons With Active Dendrites. Lausanne: Frontiers Media.
doi: 10.3389/978-2-88945-608-6

Table of Contents

SECTION 4

FUNCTIONAL COMPARTMENTALIZATION OF DENDRITES AND SOMATO-DENDRITIC COUPLING

SECTION 5

TOOLS FOR STUDIES OF DENDRITIC AND AXONAL PROCESSES

SECTION 6

FINE TEMPORAL STRUCTURE OF FIRING PATTERNS

frontiers in Cellular Neuroscience

EDITORIAL
published: 22 August 2018
doi: 10.3389/fncel.2018.00229

Editorial: Structure-Related Intrinsic Electrical States and Firing Patterns of Neurons With Active Dendrites

*Sergey M. Korogod**

Department of Molecular Biophysics, O. O. Bogomoletz Institute of Physiology, National Academy of Sciences of Ukraine, Kiev, Ukraine

Keywords: dendrites, voltage-gated conductances, excitability, intrinsic firing patterns, synaptic and dendritic integration, electric coupling, computer modeling

Editorial on the Research Topic

Structure-Related Intrinsic Electrical States and Firing Patterns of Neurons With Active Dendrites

Activity of neurons embedded in networks is an inseparable composition of intrinsic and evoked processes. Prevalence of either component depends on the neuron's function (e.g., signal pacemaker vs. transmitter) and state (e.g., low vs. high depolarization states). Complex firing patterns of a neuron are conventionally attributed to complex spatial-temporal organization of inputs received from the network-mates via synapses, in vast majority dendritic. However, these views require revisiting with account of active properties of the dendrites. Structural features of the arborization inevitably impact on electrical states of its constituting parts at different levels of organization, from branches and sub-trees to ion channels. This Research Topic aimed at bringing together contributions of researches from different domains and gaining deeper insight into the nature of neuronal intrinsic firing patterns. Being cross-listed in Frontiers in Cellular Neuroscience and Frontiers in Computational Neuroscience, it contains 22 articles (14 and 8 in the respective journal specialties, respectively) including 14 original research articles, 4 reviews; 1 mini review, 1 methods, and 2 hypothesis and theory articles.

OPEN ACCESS

Edited and reviewed by:
Christian Hansel,
University of Chicago, United States

***Correspondence:**
Sergey M. Korogod
isabroad@gmail.com

Received: *19 June 2018*
Accepted: *16 July 2018*
Published: *22 August 2018*

Citation:
Korogod SM (2018) Editorial: Structure-Related Intrinsic Electrical States and Firing Patterns of Neurons With Active Dendrites. Front. Cell. Neurosci. 12:229. doi: 10.3389/fncel.2018.00229

HISTORICAL PERSPECTIVES OF STUDIES OF STRUCTURE-RELATED INTRINSIC NEURONAL ACTIVITY

Llinás who pioneered in discovery of active membrane properties of neuronal dendrites and putting forward the notion the intrinsic activity of neurons, provides a historical perspective of studies, which flagged beginning of modification of the reflex viewpoint of brain function, as the global neuroscience paradigm, toward one, in which sensory input modulates rather than dictates brain function. The author explains how unique firing signatures of different type neurons are related to their specific sets of voltage-gated ion channels, dendritic in particular, and notes that complex intrinsic properties allow neurons to function either as relay systems, or as oscillators and/or resonators.

Bower describes his view of the history, achievements and merits of the first "community model," a Purkinje neuron model with detailed morphology and appropriate active conductances of the dendrites. The author emphasizes on importance of using such models for testing, interpreting, and predicting experimental data rather than for demonstrating the plausibility of a particular idea and illustrates implementations of this approach in their "community model" of Purkinje cell.

DENDRITIC ORIGINS OF FIRING PATTERNS IN NEURONS

Alford and Alpert review dendritic mechanisms of synaptic integration in neurons forming the spinal central pattern generator in lamprey. These mechanisms transform an unpatterned glutamatergic input into a patterned, rhythmic output that is a feature of the spinal network. Dendritic origin of the intrinsic oscillatory activity is defined by the interplay of Ca^{2+} entry through NMDA-type glutamatergic channels with contribution from voltage-gated Ca^{2+} channels and outward current through Ca^{2+}-sensitive K^{+} channels producing in-phase oscillations of intracellular Ca^{2+} and the membrane potential in the dendrites.

Magnani et al. address specific oscillatory and firing properties of stellate cells in layer II of the medial entorhinal cortex. Using the quadratic sinusoidal analysis the authors compare characteristics of subthreshold membrane potential oscillations and supra-threshold firing of action potentials (APs) generated in response to multi-sinusoidal current stimulation. The quadratic responses were likely dominated by the dendrites and contained frequencies that were not present in the input signal and the characteristics of the subthreshold oscillations at resonance frequencies near the threshold were similar to those of the supra-threshold spike trains.

Based on the analysis of somatic and dendritic plateau properties observed in spiny neurons of amygdala, striatum, and cortex Oikonomou et al. describe their hypothesis stating that the somatic voltage upstates are determined by dendritic plateau potentials. This view is supported in experiments using voltage-sensitive dye imaging, which reported rising of the somatic plateau after the onset of the dendritic voltage transient and collapsing with the breakdown of the dendritic plateau depolarization. It is hypothesized that dendritic plateau potentials underlay detection and transformation of coherent network activity into a ubiquitous neuronal upstate.

Psarrou et al. investigated the effects of the basal dendrites morphology on the firing behavior on models of reconstructed pyramidal neurons in layer V of rat prefrontal cortex. Earlier studies revealed in these cells characteristic firing patterns: regular spiking (RS), intrinsic bursting (IB), and repetitive oscillatory bursting. Variation of dendritic geometry and distribution of ion conductances allowed the authors to derive pattern-predictive structural characteristics. The RS- or IB-generating cells were best discriminated by the total length, volume, and branch number, regardless of the distribution of conductances in basal trees.

Tran-Van-Minh et al. review the biophysical determinants of linear, sublinear, and supralinear effects of multiple co-activated synapses contacting active neuronal dendrites. The authors highlight the interplay of dendritic morphology and channels, spiking threshold and distribution of synaptic inputs. Sublinear relations are favored by the combination of thin dendritic diameter and low expression of voltage-gated channels, whereas thick dendrites expressing voltage-gated channels of inward current favor supralinear relations, from boosting synaptic depolarization to regenerative dendritic spikes.

FIRING PATTERNS IN NORMALLY DEVELOPING AND DEGENERATING NEURONS

The geometry, expression and properties of membrane ion channel of neuronal dendrites are subject to changes during normal development and neurodegenerative disease. Some of these aspects are addressed in the following contributions.

Durand et al. explored mouse lumbar motoneurons in isolated spinal cord at a postnatal age of P3-P9 just before mice weigh-bear and walk. The authors characterized the reconstructed dendritic geometry and firing patterns evoked by somatically applied depolarizing currents, particularly of triangular ascending-descending time course (ramps). A transient type pattern was firing during the ascending phase of the current. It was observed in about 40% of cells between P3 and P5 and tended to disappear with age. Linear and clockwise hysteresis firing patterns dominated at P6–P7 age. Prolonged sustained and counterclockwise hysteresis (mature) firing patterns emerged at P8–P9 age and likely were related to maturation of dendritic L-type Ca^{2+} channels. Hence, it is P8–P9 age, when the electrical properties of mouse motoneurons rapidly change to provide the mature motor behaviors.

Dhupia et al. on a model of reconstructed CA1 pyramidal neuron studied the role of geometry of atrophied dendrites in electrical responsiveness of the dendritic tree with distributed hyperpolarization-activated h-channels. The atrophy was mimicked by pruning outer branches. Based on analysis of responses evoked by sinusoidal currents of constant amplitude and linearly increasing frequency, the authors conclude that, in the presence of an h-channel gradient, atrophied neurons respond to incoming inputs and transfer signals across the dendritic tree more efficiently, have significantly diminished spatial gradients of input resistance and local/transfer impedance than those in unpruned cell.

FUNCTIONAL COMPARTMENTALIZATION OF DENDRITES AND SOMATO-DENDRITIC COUPLING

Firing patterns of spinal motoneurons containing channels of persistent inward current (PIC) in the dendritic membrane were explored by Kim and Heckman on a two-compartment model. The authors analyzed model responses to application of triangular current depending on the somato-dendritic electrical coupling, dendritic location and activation of PIC conductances. A variation of PIC activation parameters mimicking neuromodulatory effects of brain stem systems led to narrowing the structure-dependent coupling resistance range, in which the model generated nonlinear (hysteretic) firing patterns. Outside the range, the firing mode became linear irrespectively of PIC location. It is concluded that neuromodulation by the

brainstem systems may play a role in switching the motoneurons between linear and non-linear firing modes.

Manuel et al. investigated a two-compartment model of lumbar motoneuron expressing L-type Ca^{2+} conductance and Ca^{2+} -sensitive K^{+} conductance responsible for afterhyperpolarization (AHP) and having a strong electrical coupling of the somatic and dendritic compartments. The cells with different somato-denritic distribution of those conductances were stimulated by triangular ramp currents to determine conditions for a counterclockwise hysteresis of firing frequency-to-current relation associated with the motoneuron bistability. This occurred when L-type conductance in proximal dendrite or soma was co-expressed with and counterbalanced by the AHP conductance. The authors conclude that for the motoneuron firing pattern the dynamical interaction between the L-type and AHP currents is as fundamental as the segregation of the L-type current in dendrites.

Simões-de-Souza et al. developed computational models of three classes of the olfactory bulb granule cells with distinct distributions of spines along their active reconstructed dendrites and investigated how each class integrate synaptic inputs. The classes were defined by the regions, to which their dendrites were confined: the whole external plexiform layer for class I, and lower or upper 1/2 to 1/3 of this layer for class II or III, respectively. Independently of the location of the stimuli and the dendritic tree morphology, the AP always originated in the terminal dendrites and required different quantities of spines to be activated in each dendritic region. The authors conclude that these model predictions might have important computational implications in the context of functioning of olfactory bulb circuits.

Yang et al. studied response properties of CA1 pyramidal neurons in acute brain slices employing the 3D digital holographic photolysis to uncage glutamate at multiple dendritic sites. The somatic responses were integrated supra-linearly or sub-linearly if the stimulation sites were, respectively, clustered on a single dendrite or distributed across multiple dendrites. Such difference was observed for oblique and basal dendrites, but not for the tuft dendrites responding linearly to both types of stimulation. Multi-branch integration occurring at oblique and basal dendrites allows somatic AP firing to follow the driving stimuli over a significantly wider frequency range than in case of single branch integration. However, multi-branch integration requires greater input strength to drive the somatic APs. These data show that integration of such driving signals in a single dendrite is fundamentally different from that in multiple dendrites.

In a study on models of reconstructed CA1 pyramidal cells, Ferrante and Ascoli analyzed how synaptically evoked spiking in these neurons exhibiting higher or lower excitability is regulated by different feedforward inhibition (FFI) GABAergic pathways. The pathways mediated by fast-spiking, perisomatic-targeting basket cells and regular-spiking, dendritic-targeting bistratified cells were stimulated separately or jointly at different strengths. Bistratified interneurons affected low-, but not high-excitable pyramidal cells; whereas basket cells affected both pyramidal cell types similarly. Selective FFI produced by bistratified and basket cells alone modulated respectively, threshold and gain of pyramidal cell firing. Simultaneous FFI via both pathways acting synergistically enlarged the dynamic range of response. The authors conclude that their results provide experimentally testable hypotheses of the differential function of those interneurons.

Iannella and Launey used a biophysically detailed model of a reconstructed neocortical layer 2/3 pyramidal cell to investigate the effect of changes in parameters of the spike timing-dependent plasticity (STDP) of dendritic synapses on the formation of the so-called "dendritic mosaic" composed of clusters of synapses with similar efficacies. The mosaic formation depended on the balance between potentiation and depression, mean presynaptic firing rate and, crucially, the dendritic morphology. Any imbalance led to degradation of such cluster organization. The authors suggest that, synaptic plasticity favors the formation of clustered efficacy engrams.

TOOLS FOR STUDIES OF DENDRITIC AND AXONAL PROCESSES

Du et al. describe an approach to the reduction of models of neurons possessing weakly excitable large dendritic trees and the strongly excitable small spike initiation zone. It is illustrated on an example of the lobula giant movement detector neuron of the locust. An initial 879-compartment model was transformed by decoupling its branches, reducing separately active and quasi-active branches, re-coupling these two reduced components into a resulting model. The latter being faster retained the full integrative qualities of the original two-order larger model as follows from close similarity of these two models responses to similar stimuli.

Slice preparations are common in electrophysiological studies of neurons and identification of their processes as axon or dendrites in the ongoing experiment is not trivial. Petersen et al. describe a new method allowing reliable identification of axon initial segment (IS) and dendrites by timing of averaged somatic spike and local field potential (LFP) recorded near a targeted neurite. Informative is the timing of the negative LFP event relative to the spike threshold calculated as the first positive peak on the third derivative of the LFP: the event starting before or after reaching the somatic spike threshold indicated location of the LFP electrode near axon IS or dendrite origin, respectively.

Biophysical properties of synaptic receptor channels are important for determining of both efficacy of synaptic transmission and activation of dendritic voltage-gated channels underlying active properties of dendrites. Stepanyuk et al. describe a new method using a maximum likelihood approach to non-stationary fluctuation analysis that allows to estimate a number of synaptic transmission parameters from a small set of postsynaptic current recordings. The method is illustrated on examples of processing of simulated macroscopic synaptic currents, from which the pre-defined parameters of synaptic receptor channels were accurately retrieved.

Singh and Zald describe a new form of dendrite-to-soma transfer function employing separation of slow and fast components of the dendritic electrical events. On an example of analysis of postsynaptic signal transfer along dendrites possessing non-linear NMDA-type conductance, the authors show that their linear "hook" function, being a computational cost-efficient alternative to sigmoid transfer functions, correctly reproduces saturation and linear behaviors for large and small inputs, respectively.

FINE TEMPORAL STRUCTURE OF FIRING PATTERNS

Mrówczyński et al. in their mini-review discuss occurrence and functional significance of the doublets of the APs frequently observed at the onset of contractions of mammalian motor units during recruitment to strong or fast movements. The authors draw attention to the duration of the AHP, which follows the APs, results from activation of corresponding potassium conductance and significantly influences firing rate in both slow and fast motoneurons.

Mlinar et al. examined spiking activity in a large number of genetically identified serotonergic neurons of the dorsal raphe nucleus (DRN) in slices. They found wide homogeneous distribution of firing rates suggesting that, in terms of intrinsic firing properties, the DRN serotonergic neurons represent a single cellular population. The majority of neurons exhibited regular, pacemaker-like activity with the spiking regularity proportional to the firing rate. In a small subset of neurons, the firing rate exhibited low frequency oscillations. The observed transitions between regular and oscillatory firing suggested that the oscillatory firing mode is an alternative to regular firing in serotonergic neurons.

Cho et al. explored fine temporal structure of firing APs evoked in nociceptive cutaneous C-fibers by application of noxious chemical stimuli and related the firing patterns with pain behavior. They extracted groups of three consecutive spikes (spikelets) and analyzed their duration and within-group inter-spike intervals. The analysis revealed substance-specific patterns: continuous firing for KCl, single or multiple bursts for capsaicin, and repeated short bursts (chattering) for GABA. The authors suggested that information about the agonist chemicals may be encoded by C-afferents in specific temporal patterns, which, via different temporal summation of postsynaptic responses, may influence the pain sensation.

AUTHOR CONTRIBUTIONS

The author confirms being the sole contributor of this work and approved it for publication.

Conflict of Interest Statement: The author declares that the research was conducted in the absence of any commercial or financial relationships that could be construed as a potential conflict of interest.

frontiers in
CELLULAR NEUROSCIENCE

REVIEW ARTICLE
published: 04 November 2014
doi: 10.3389/fncel.2014.00320

Intrinsic electrical properties of mammalian neurons and CNS function: a historical perspective

Rodolfo R. Llinás*

Department of Neuroscience and Physiology, New York University School of Medicine, New York, NY, USA

Edited by:
Sergey M. Korogod, National Academy of Sciences of Ukraine, Ukraine

Reviewed by:
Alexej Verkhratsky, University of Manchester, UK
Sergey M. Korogod, National Academy of Sciences of Ukraine, Ukraine

****Correspondence:***
Rodolfo R. Llinás, Department of Neuroscience and Physiology, New York University School of Medicine, 550 First Ave., New York, NY 10016, USA
e-mail: llinar01@med.nyu.edu

This brief review summarizes work done in mammalian neuroscience concerning the intrinsic electrophysiological properties of four neuronal types; Cerebellar Purkinje cells, inferior olivary cells, thalamic cells, and some cortical interneurons. It is a personal perspective addressing an interesting time in neuroscience when the reflex view of brain function, as the paradigm to understand global neuroscience, began to be modified toward one in which sensory input modulates rather than dictates brain function. The perspective of the paper is not a comprehensive description of the intrinsic electrical properties of all nerve cells but rather addresses a set of cell types that provide indicative examples of mechanisms that modulate brain function.

Keywords: oscillations, voltage-gated ion channels, oscillatory phase reset, mammalian neurons, oscillatory resonance

INTRODUCTION

That the function of the nervous system is ultimately to be defined as the product of interacting networks woven by nerve cells has been the central dogma of neuroscience for almost a century. Fundamental to this view has been the realization that nerve cells are truly individual elements. Indeed, while the variety of forms that nerve cells may display was described in elegant detail by the work of brilliant morphologists of the turn of the century, their most significant contribution was the proposal of the neuron doctrine (cf. Ramón y Cajal, 1904).

On the other hand, from a physiological point of view the neuron doctrine was considered for a long time to signify a unity of excitability, where the variance among the different neurons related to their shape and connectivity, but not to their individual electrophysiological properties. Thus, following the discovery of excitatory and inhibitory synaptic potentials, it was assumed that the necessary and sufficient functional coinage for the expression of functionality in nerve nets had been defined. Over the past 30 years, however, another fundamental issue has arisen with respect to the physiological properties of nerve cells—that of their intrinsic electroresponsive properties. This concept may be stated simply: "Neuronal types are not interchangeable." That is, a neuron of a given type (e.g., a thalamic cell) cannot be functionally replaced by one of another type (e.g., an inferior olivary cell), even if their synaptic connectivity and the type of neurotransmitter outputs are identical. (The difference is that the intrinsic electrophysiological properties of thalamic cells are extraordinarily different from those of inferior olivary neurons).

This being the case, the intrinsic electrophysiological signature of nerve cells becomes a central theme in neuronal function. Indeed, when such elements interconnect, the dynamics of the resulting neuronal networks are governed not only by the flow of synaptic current, but also by the intrinsic properties of the neurons partaking in such circuits. Likewise, the electrical activity observed in a network is not only related to the excitatory and inhibitory interactions among neurons but also to their inherent or intrinsic electrical activity (Llinás and Hess, 1976; Llinás, 1988).

The term "intrinsic electrical properties" has been used to encompass both passive and active membrane characteristics (for example, see van Lunteren and Dick, 1992). In this review it is used in a more restricted sense to designate those active membrane properties that endow a cell with the ability to shape incoming stimuli and indeed to fire or maintain subthreshold oscillations in the absence of synaptic input. That is, these cells are capable of more than the classical input-output relationship of increasing their firing frequency with stimulus strength or action of neuromodulators (see Binder et al., 1993, for motoneurons). Due to the presence of bursting, neurons with such usual properties were first recognized in systems concerned with rhythmic activity such as breathing, swallowing and chewing. Indeed, the rhythmic firing of hypoglossal neurons was reported as early as 1973 (Lund and Dellow, 1973). However, the contribution of intrinsic electrical properties of hypoglossal motoneurons to such periodicity was not recognized, but rather thought to arise from the action of excitatory and inhibitory synaptic inputs, the presence of gap junctions, and input from a central pattern generator. It was not until much later that the role of the intrinsic electrical properties of the neurons themselves was recognized (see Ramirez and Richter, 1996, for a review of respiratory neurons). In fact, when hippocampal neurons were observed to fire spontaneously when inhibitory input was blocked, the authors concluded "It remains to be determined whether neural properties and connectivity found to

be important in this hippocampal rhythm may also play a role in the generation of other rhythmic activities in the mammalian CNS" (Wong et al., 1984). Such spontaneous rhythmicity had been reported for the inferior olive (IO) *in vivo* as early as 1968 (Armstrong et al., 1968). That they were indeed intrinsic to the IO cell was shown in 1986 (Llinás and Yarom, 1986).

Below, some examples are given from our work that illustrate different intrinsic electrical properties in mammalian central neurons. Very surprising, the role of intrinsic activity in the generation of motricity, initially proposed by Graham-Brown (1911), was forgotten for more than halve a century.

INTRINSIC ELECTRICAL PROPERTIES OF SPECIFIC CELL TYPES

CEREBELLAR PURKINJE CELLS

The question of intrinsic electroresponsive properties in vertebrate CNS neurons was first encountered in the detailed study of cerebellar Purkinje cells (Llinás and Hess, 1976; Llinás and Sugimori, 1980a,b). These studies demonstrated that Purkinje cells have intricate firing properties and that the dendritic and somatic membranes each have markedly different voltage-dependent conductances that are supported by different types of ionic channels, which combine to give these cells their unique firing signature. At the somatic level, in addition to the Na^+ and K^+ conductances that generate the fast action potential, a voltage-dependent, persistent, or very slowly inactivating Na^+ conductance [$g_{Na(p)}$ (p for persistent)] was also initially encountered in these neurons (Llinás and Sugimori, 1980a). This latter conductance generates a slow, tetrodotoxin (TTX)-sensitive depolarizing response, which, once activated generates prolonged plateau potentials that may last for tens to hundreds of milliseconds (presently known as an "up state").

This gNa(p) has also been described in cortical (Connors et al., 1982; Stafstrom et al., 1982) and thalamic (Jahnsen and Llinás, 1984a,b) neurons. The dendrites of Purkinje cells, by contrast, do not support voltage-gated Na^+ conductances, but rather voltage-gated Ca^{2+} conductances that generate dendritic Ca^{2+}-dependent spikes and/or plateau potentials (Llinás and Hess, 1976; Llinás and Sugimori, 1980a,b) and are supported by a calcium channel named the P channel (for Purkinje cell). These different membrane conductances and their distribution over the somato-dendritic plasmalemmal membrane endow Purkinje cells with intricate electroresponsive properties, including intrinsic transmembrane voltage oscillations. Such activity can be evoked by direct current injection or by extracellular iontophoretic application of an excitatory transmitter such as glutamic acid at the dendritic level (**Figure 1**).

The characteristics of somatic and dendritic electroresponsiveness to dendritic glutamate application have been studied using double impalement of Purkinje cells in cerebellar slices. Recordings made during one such experiment in which glutamic acid was applied to the distal dendritic tree are shown in **Figure 1**. The schematic to the left shows the approximate location of the dendritic and somatic recording electrodes and the iontophoretic glutamate electrode. The trace in B illustrates the main features of dendritic electroresponsiveness. There are two types of Ca^{2+}-dependent responses: maintained all-or-none depolarizing plateau responses and slow-rising spikes. The plateau responses have constant amplitude, may last for hundreds of milliseconds, are accompanied by a large conductance increase, and are usually not seen in the soma. On the other hand, the Ca^{2+}-dependent spikes in the dendrites are large and are usually elicited in prolonged bursts (**Figure 1B**), which influence somatic electroresponsiveness. As shown in **Figure 1C**, they may be recorded in the soma as slow changes in the membrane potential that trigger increases in the firing frequency of the fast, sodium-dependent somatic action potentials. In turn, the somatic action potentials can be observed in the dendrites below the mid-dendritic level as small, fast-rising depolarization.

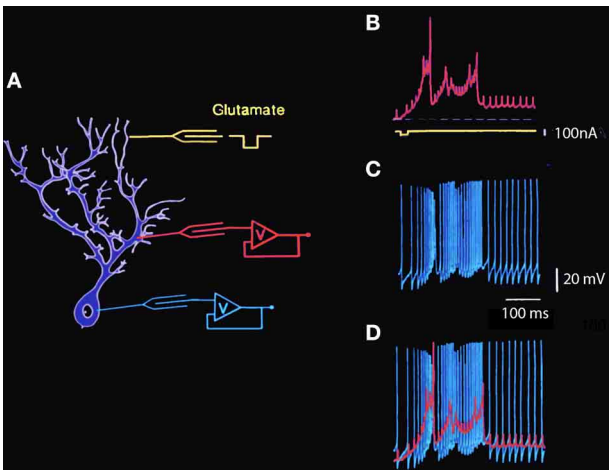

FIGURE 1 | Simultaneous intracellular recording from Guinea pig cerebellar Purkinje cell dendrite and soma *in vitro*. **(A)** Diagram of intracellular recording sites at somatic and dendritic levels and the location of the extracellular glutamic acid iontophoretic application site. **(B)** Intradendritic recording. The large amplitude wide action potentials are Ca-dependent while the smaller fast action potentials represent the passive invasion of the somatic action potentials into the dendritic tree. Note the presence of a sustained plateau depolarization at the dendritic level following the spiking phase of the dendritic response. **(C)** Simultaneous intrasomatic recording showing fast somatic Na-dependent action potentials. Note that each of the large somatic spikes is seen at dendritic level with a short delay and that the calcium dependent dendritic spikes generate high frequency spiking as somatic level. **(D)** Superposition of dendritic (red) and somatic (blue) spikes to illustrate the temporal relationship between somatic and dendritic spikes and plateau amplitudes (Llinás and Sugimori, 1980a,b. This example is unpublished).

The ionic basis for Purkinje cell firing was examined by studying the response to depolarizing pulses in the absence of Ca currents and in the absence of Na currents (**Figure 2**). Addition of Co to the bath blocked the calcium conductance. Direct depolarization elicited fast somatic spikes on a slow depolarizing ramp bringing the membrane to a plateau potential. When the amplitude of the depolarizing pulse was increased the depolarizing ramp occurred earlier (**Figure 2B**, arrows) without changing the spike threshold or plateau level (**Figure 2B**). Pharmacological block of the fast sodium channel by addition of TTX to the bath changed the firing pattern as shown in **Figure 2D**. The fast somatic spikes were blocked while the slow dendritic spike burst and afterdepolarization (**Figure 2D**, arrow) remained (compare **Figure 2C** and **Figure 2**D).

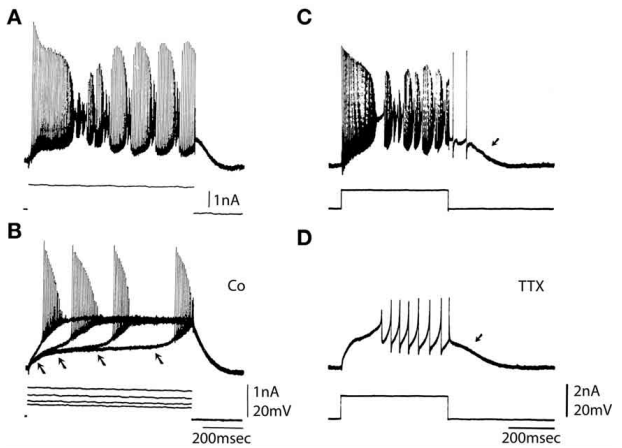

FIGURE 2 | Ionic basis for Purkinje somatic recordings. (A) Activity elicited from Purkinje cell soma by direct depolarization. Note fast spikes and underlying slower depolarizations. **(B)** After blocking the calcium conductance by addition of Co to the bath direct depolarization elicited fast spikes. Note that with increased depolarization spike onset moved to the left (arrows), but the plateau level of spike threshold did not change. **(C)** Repetitive response to somatic depolarization. **(D)** Block of sodium channels with TTX reveals underlying slow spikes and afterdepolarization (arrow). (From Llinás and Sugimori, 1980a.).

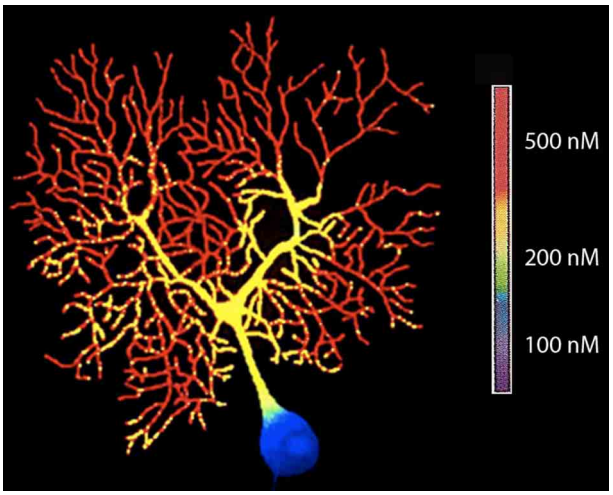

FIGURE 3 | High-resolution fluorescent image of a dendritic calcium spike in a Purkinje cell filled with fura-2 by microinjection (380-nm excitation). (From Tank et al., 1988.).

These experiments have provided valuable information relating to the ionic basis of the electrical responsiveness of the soma and dendritic trees and allowed the determination of electrotonic length and some of the active membrane properties of Purkinje cells in general. Yet, they do not provide a direct demonstration of the spatio-temporal distribution of electroresponsiveness over the entire soma dendritic membrane. This requires the use of techniques such as ion-sensitive dyes.

The spatial distribution of ionic channels over the plasmalemmal membrane and the associated compartmentalization of both the physiological and the cell biological properties are critical issues in the characterization of central neuronal function. For example, the precise distribution of specific channels with respect to the locus of synaptic input may address not only electrical integrative properties but also the precision with which different compartments may be addressed biochemically. Indeed, the spatial distribution of second messenger systems activated by $[Ca^{2+}]_i$ (Hemmings et al., 1986) will be determined by the distribution of calcium channels.

An early experiment of this type was carried out 26 years ago by Tank et al. (1988). In these experiment Fura II signals were used to determine $[Ca^{2+}]_i$ in Purkinje cells (Tank et al., 1988). Fura II was injected ionophoretically into the cell and a quantitative evaluation of changes in $[Ca^{2+}]_i$ was made using the fluorescence ration at 340/380 nM as seen in **Figure 3**.

The results agreed with the hypotheses of the dendritic segregation of Ca^{2+} conductances that was suggested by early electrophysiological experiments (Llinás and Hess, 1976; Llinás and Sugimori, 1980a,b). They also allow a general mapping of the location of voltage-gated Ca2+ channels as inferred from the specific regions of the neuron, where $[Ca^{2+}]_i$ demonstrate transients lasting 5–15 ms.

With respect to the functional significance of the results, these findings indicated that the Ca^{2+}-dependent plateau potentials are a dendritic boosting mechanism for the synaptic current generated in Purkinje cell dendrites leading to a high-frequency burst of sodium spikes at the soma and axon. This provides a mechanism for spatial and temporal summation of inhibition at the cerebellar nuclear neurons. Other possibilities to be considered relate to role in increased intracellular calcium in the modulation of cell biological mechanisms and the modification of long-term cell biological properties.

The next approach in Purkinje cells was to carry out direct single channel recordings (**Figure 4**) at both the somatic and dendritic levels (Usowicz et al., 1992). The location of channels on dendrites made it clear that, given the dendritic surface to volume factor relationship, calcium dye imaging would be more effectively implemented at dendritic level. On the other hand, it was also clear that the final calcium concentration change at the cytosolic level would be larger and probably longer lasting at the dendritic than at the somatic level.

In short then, the evidence was clear that Purkinje cells have complex intrinsic properties from the merging of dendritic and somatic conductances giving these cells a unique electrophysiological signature.

INFERIOR OLIVARY CELLS AND REBOUND CALCIUM SPIKES

Cells of the inferior olivary nucleus have also been shown to have dendritic and somatic conductances underlying an intrinsic electrophysiological profile. Indeed, *in vitro* experiments using brainstem slices (Llinás and Yarom, 1981, 1986) first demonstrated that IO neurons have a set of voltage-gated ionic conductances that give these cells intrinsic oscillatory properties (**Figure 5**). Thus, the firing of IO cells is characterized by an initial fast-rising action potential (a somatic sodium spike), which is prolonged to 10–15 ms by an afterdepolarization (a Ca^{2+}-dependent dendritic spike).

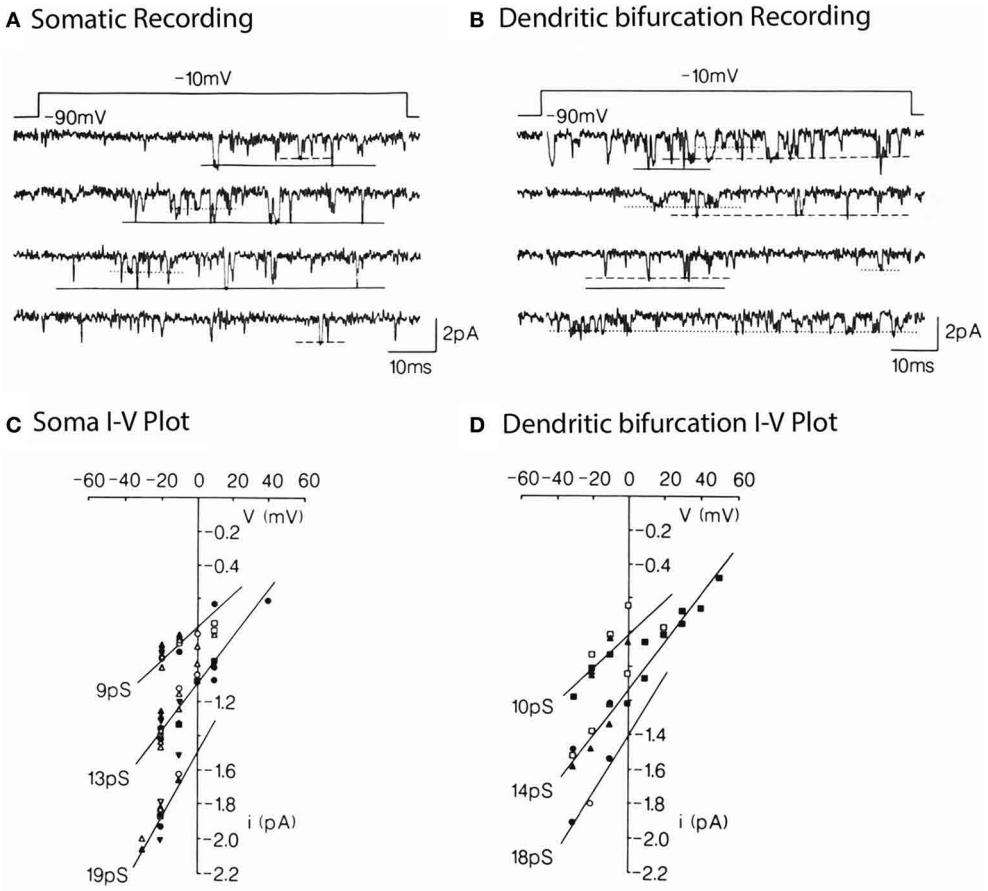

FIGURE 4 | Multiple conductance of Ca^{2+} channels in the somata and dendrites of cerebellar Purkinje cells. (A) Single Ca^{2+} channel currents carried by 110 mM Ba^{2+} in a somatic patch, evoked by voltage step jumps (≈70 ms) applied once every 5 s. Three opening levels are indicated by solid, dashed, and dotted lines. **(B)** Currents in a dendritic patch. Same conditions as in **(A)**. Voltage dependence **(C,D)** for the currents levels illustrated in **(A,B)**. Pooled data for 8 somatic and 5 dendritic patches. The indicated conductances are the slope of the lines through the dots (from Usowicz et al., 1992).

The abrupt long-lasting afterhyperpolarization (AHP) following the plateau afterdepolarization totally silences the spike-generating activity. This hyperpolarization is typically terminated by a sharp, active rebound response (**Figure 5A**, arrow), which arises when the membrane potential is negative to the resting level. This rebound response is due to the activation of a somatic Ca^{2+}-dependent action potential and results from a second voltage-dependent Ca^{2+} conductance, which is inactive at the resting membrane potential (−65 mV). Membrane hyperpolarization deinactivates this conductance, and, as the membrane potential returns to baseline, a "low threshold" Ca^{2+}-dependent spike is generated (Llinás and Yarom, 1981). The rebound potential can be modulated by small changes in the resting membrane potential such that a full Na^{+} spike, which, in turn, can set forth the whole sequence of events once again, is activated. In this way, the cell will fire at a frequency determined largely by the characteristics of the AHP (**Figure 5B**).

A direct demonstration of time course and amplitude of the "low threshold" transient calcium current [ICA (T)], encountered in this neuron (Llinás and Yarom, 1981) is shown in **Figure 6**, following a voltage clamp study of IO neuronal calcium currents.

The low threshold, transient calcium current is a powerful modulator of IO rhythmicity and is responsible for IO membrane potential oscillations. IO neuron oscillations can occur at two distinct frequencies, as determined by examining the firing properties of spontaneous bursts of spikes. A set of such events is shown in **Figure 7**.

It is evident, given the above, that individual IO cells can oscillate with two main limit cycles, one near 10 Hz (9–12 HZ) and the other near 4 HZ (3–6 HZ). Oscillation at the higher frequency seems to be governed by the resting potential of the neuron. Thus, when the cell is depolarized, its excitability would be dominated by the dendritic conductances and fire near 4 Hz. However, when the cell is hyperpolarized, its output is dependent on somatic conductances and will fire near 10 Hz.

Beyond its intrinsic oscillatory behavior, one of the most unexpected and novel properties of the dynamics of IO neurons was their phase-reset ability. Thus, synaptic input large enough to activate action potentials also produces a phase reset of the

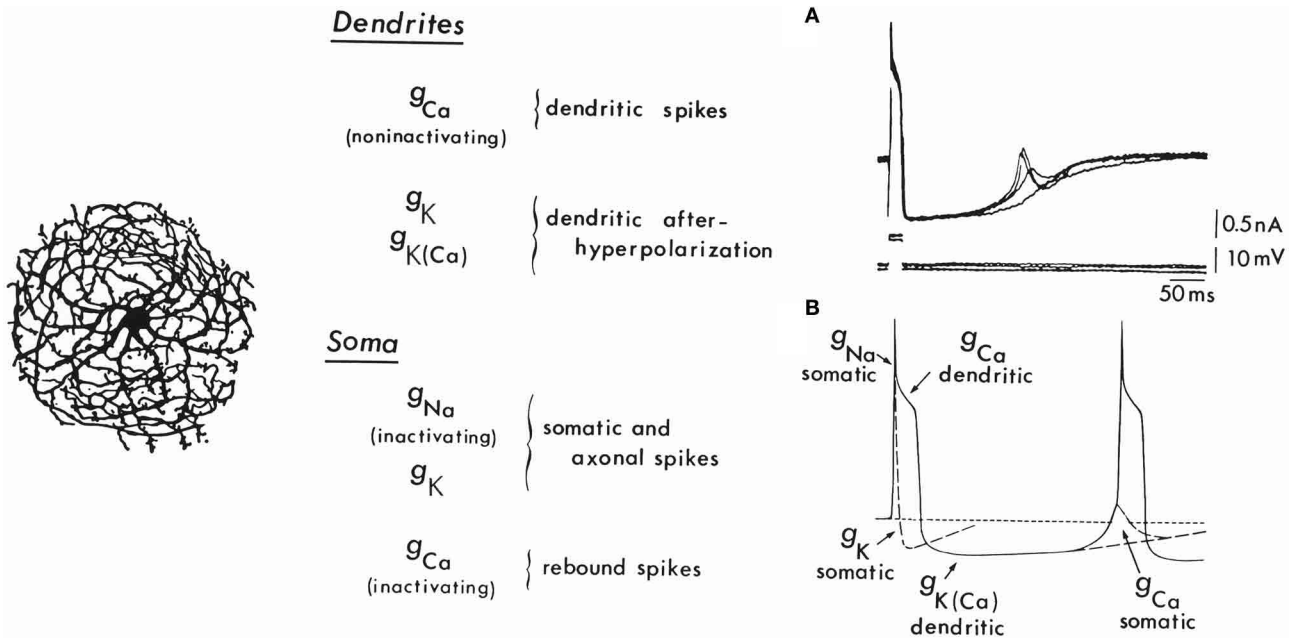

FIGURE 5 | Ionic conductances and the mechanism for oscillation in inferior olivary cells. Left: Drawing of an inferior olivary cell by Ramón y Cajal. **Center:** Table giving the distribution of ionic conductances in somatic and dendritic regions. At the soma a set of conductances (g_{Na} and g_k) generating fast action potentials may be observed. In addition, a strongly inactivated Ca^{2+} conductance is present, which produces rebound spikes, as seen in **(B)** [$g_{Ca\,(somatic)}$]. Also recorded at the soma is a large Ca^{2+}-dependent dendritic spike [$g_{Ca\,(dendtritic)}$] that generates the afterdepolarization and the powerful, long-lasting afterhypolarization, which is produced by a Ca^{2+}-dependent K+ conductance [$g_{K\ (Ca)}$]. In addition, a voltage-dependent K^+ conductance (g_K) seems to be present in the dendrites. **Right A:** Rebound spikes in the inferior olivary neuron (arrow) following blockage of the Na spike with tetrodotoxin (TTX). **Right B:** Summary of the ionic conductances that generate single-cell oscillations in neurons of the inferior olive.

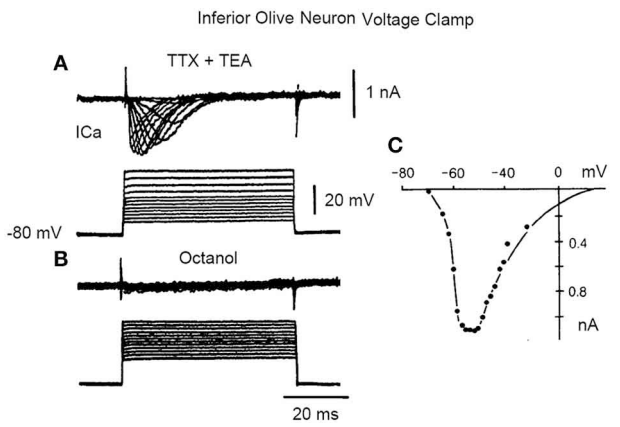

FIGURE 6 | Inward current in inferior olive cell after block of sodium and potassium currents with TTX and TEA, respectively. (A) A set of transmembrane square voltage camp steps of increasing amplitude generated a rapidly inactivating, transient, Ca current (Ica). **(B)** This current is blocked by addition of octanol. **(C)** Plot of the current voltage relation in **(A)**. (From Llinás and Yarom in Llinás et al., 1989).

oscillatory rhythm that is independent of the phase point at which the stimulus arrived. As shown in **Figure 8A**, a stimulus large enough to generate a spike discharge is immediately followed by a rapid return of the membrane potential oscillatory behavior. If the spike-activating stimulus is repeated, as in **Figure 8B**, it becomes apparent that the resultant oscillatory phase reset is the same regardless of the moment in time when the stimulus was delivered.

These oscillatory membrane potential properties can also be demonstrated to have interesting dynamic properties. Analysis of the oscillatory dynamics such as shown in **Figures 8A,B** demonstrated that IO cells have attractor properties as reconstructed from a time series analysis that has a structure close to a limit cycle with a regular periodic trajectory (Makarenko and Llinas, 1998). Average mutual information and false near neighbor methods were calculated and are shown in **Figures 8C,D**.

To reconstruct the attractor and Lyapunov exponents were derived and the results demonstrate zero, positive and negative exponents values indicating that the system displays low-dimensional chaotic dynamics, that actually explain the phase rest properties of their oscillation, as shown in **Figure 8B**. The application of this modeling to IO dynamics shown that the subthreshold oscillations support low dimensional chaotic dynamics and that IO electronic coupling leads to rapidly generated complex functional states without increasing the dimensionality of the system (Makarenko and Llinas, 1998).

Thus, in addition to uniform membrane potential oscillatory properties, because of their dynamics IO neurons have the unique ability to reset their oscillatory phase when activated (Leznik et al., 2002; Lefler et al., 2013). This reset property has been found to be functionally very significant as it allows a rapid reset of motricity when dominated by the somatic conductances and fire

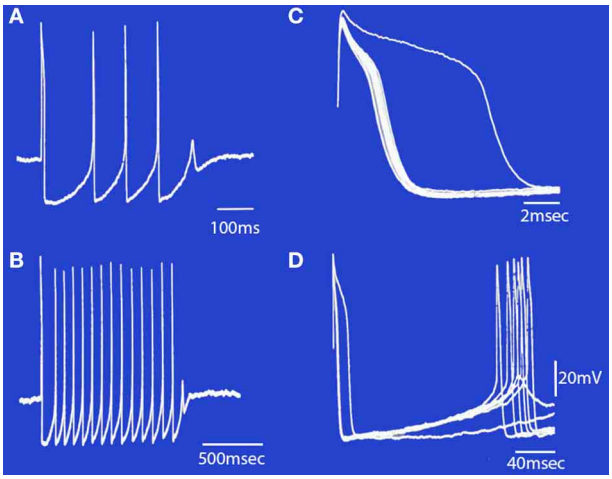

FIGURE 7 | Spontaneous bursts of spikes recorded intracellularly from an IO neuron displayed at different sweep speeds. (A) The neuron fired four action potentials and a fifth subthreshold response that corresponds to a subthreshold somatic Ca^{2+}-dependent spike. **(B)** A longer burst of spikes is shown at a slower sweep speed. Note that the first interspike interval in the burst was longer than the rest. **(C)** The rising phase of the action potentials in **(B)** are superimposed to illustrate the change in after-depolarization duration during the train. Note that the first action potential (which arises from the resting membrane potential level) has the longest after-depolarization. The other spikes in the train became progressively shorter until failure of spike generation occurred and the burst terminated. **(D)** The same set of records as in **(B)**, showing the duration of the after-hyperpolarization and the rebound somatic Ca^{2+}-dependent spikes. (Modified from Llinás and Yarom, 1986).

near 10 Hz—the basic rhythmicity of motor control in vertebrates (Vallbo and Wessberg, 1993; Lang et al., 2006). It has also been shown to be essential in the rapid reorganization of motricity following motor stumbling, even under robotic control (Porras and Llinás, 2014).

At the cerebellar level the functional significance of the oscillatory properties illustrated in **Figure 8** is an increased probability of Purkinje cell complex spike activation relating to rapid recovery of motor execution following stumbling, or other unpredicted motor events. Ultimately, then IO oscillatory activity is required for proper motor execution, as demonstrated by the total ataxia that follows T type calcium channels knockout (Choi et al., 2010).

THALAMIC CELLS

Thalamic neurons also have complex intrinsic properties that allow them to function either as relay systems, or as oscillators and/or resonators. That these two modes are intrinsic to the cells and are controlled by their membrane potential has been studied both *in vitro* (Llinás and Jahnsen, 1982; Jahnsen and Llinás, 1984a,b; Hirsch et al., 1985; McCormick and Prince, 1986, 1987; Crunelli et al., 1987; Wilcox et al., 1988) and *in vivo* (Deschenes et al., 1984; cf. Steriade and Llinás, 1988) The basic electrophysiological phenomenology observed in these cells is shown in **Figure 9**.

From a slightly depolarized membrane potential, the outward current injection elicited a subthreshold depolarization (**Figure 9A**, second trace). When the current pulse was delivered from a more depolarized potential, regular, tonic firing was elicited as shown in the top trace of **Figure 9A**. Thus, at

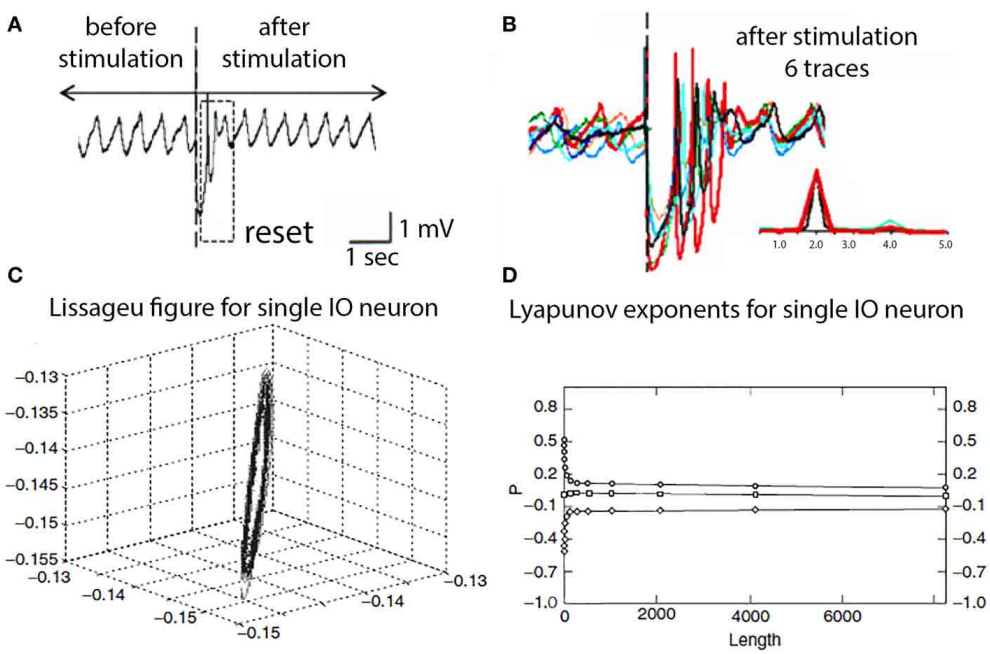

FIGURE 8 | IO oscillatory properties following spike activation. (A) One extracellular stimulus briefly interrupted the spontaneous oscillation. **(B)** Superimposition of six traces demonstrating the reset oscillatory phase is the same regardless at which point of the intrinsic oscillation the stimulus was delivered. Inset, power spectra for traces. (Leznik et al., 2002). **(C)** Lissageu figure obtained from the analysis of an IO neuron oscillation. The regularity of the figure shows that the IO attractor has a regular, periodic trajectory. **(D)** Calculated Lyapunov exponents indicative of low-dimensional chaotic dynamics.

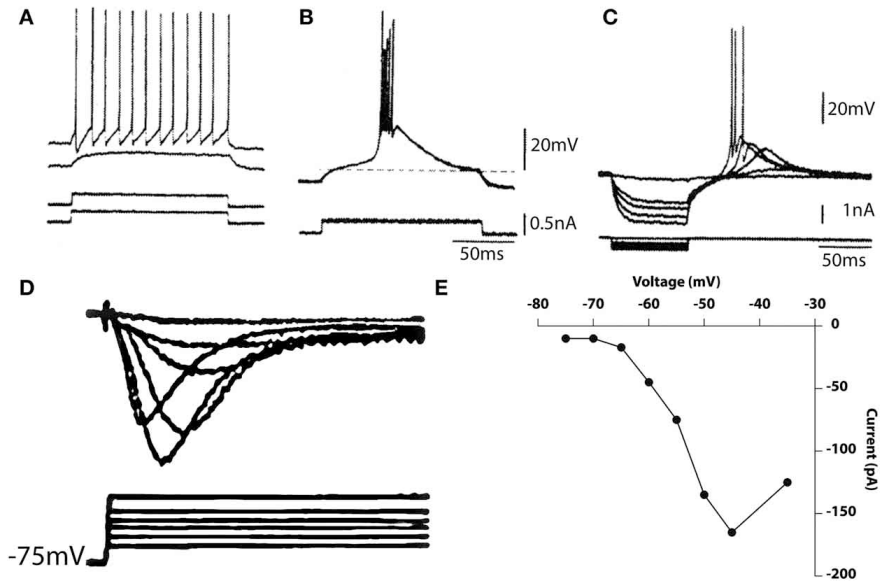

FIGURE 9 | Electrophysiological properties of thalamic cells recorded *in vitro*. **(A,B)** Depolarizing current pulses (bottom traces) elicited no response when delivered from the resting potential, tonic firing when delivered from a depolarized potential **(A)** and a burst response when delivered from a hyperpolarized level **(B)**. **(C)** Rebound response seen after hyperpolarizing pulses. **(D,E)** Calcium currents elicited by membrane depolarization from a hyperpolarized potential **(D)** and current–voltage relationship **(E)**. (Geijo-Barrientos and Llinás, unpublished observations).

or near the resting potential, tonic firing is elicited by membrane depolarization. Accordingly, the response to an excitatory synaptic input would be a single excitatory postsynaptic potential (EPSP) that may trigger single spikes. A very different response was elicited when a similar current pulse was delivered from a hyperpolarized level as in **Figure 9B**. Under these conditions, the same outward current pulse showed in A, triggered an all-or-none burst of spikes. The uniformity of the waveform of the burst is demonstrated by the fact that several traces are superimposed in **Figure 9B**. The response comprises two distinct parts, a low-threshold spike (LTS), a slowly rising and falling triangular-like potential, and a rapid succession of fast spokes. As in the IO, the LTS is due to activation of a Ca^{2+} conductance that is deinactivated by membrane hyperpolarization. The amplitude of the low-threshold response is related to the membrane potential before its generation. This is shown in **Figure 9C** where a series of hyperpolarizing pulses of increasing amplitude was delivered from a slightly hyperpolarized membrane level.

The rate of rise and amplitude of the rebound response elicited at the current break increased with progressively larger hyperpolarizing pulses. At the two highest levels, the rebound potential reached the firing threshold for Na^{+} -dependent spikes. The deinactivation of the low-threshold Ca^{2+}-dependent spike is also time-dependent; hyperpolarizing pulses of increasing duration produce graded deinactivation (Jahnsen and Llinás, 1984a), and complete recovery of the LTS occurs after a refractory period of 170–200 ms. Another characteristic of thalamic neurons, the presence of an A-like potassium current, may also be seen in **Figure 9C** as a longer time course to repolarization. Deinactivation of this conductance is responsible for the delay in the return of the potential to the holding potential at the end of the current injection.

A direct demonstration of the low threshold calcium conductance can best be described by the results from thalamic neuron voltage clamping. Such results are illustrated in **Figures 9D,E**. Indeed, the time course of the calcium inactivating T current is clearly demonstrable from a holding potential of 75 mV following Na and K conductance block by TTX and TEA respectively. The activation property of this current is shown in graph **Figure 9E**.

In addition to these voltage dependent conductances, thalamic neurons can modify their synaptic properties depending on membrane potential in a quite remarkable fashion. These properties are often not taken into account when considering their effects on arousal. Thus, fast reversible synaptic plasticity occurs in the thalamus by changes in postsynaptic membrane potential, independently of presynaptic volley size, and is rapidly reversible. It represents one of the few examples of rapid postsynaptically dependent synaptic plasticity as illustrated in **Figure 10**.

Three mechanisms are involved in this synaptic facilitation; (1) presynaptic short-term facilitation, (2) frequency–dependent activation of NMDA receptors, and (3) amplification of EPSP amplitude by intrinsic high-threshold conductances (Pedroarena and Llinás, 2001).

The significance of such finding resides in the fact that the thalamocortical system can quickly select functional states relating to gamma band allowing cognitive attractors to be continuously modulated by the combination of recurrent thalamocortical activity and the sensory input from the external world.

THALAMIC 40 Hz OSCILLATIONS

In addition to the now well-known thalamic currents responsible for the wake-sleep cycle (Steriade and Llinás, 1988), *in vitro* studies indicate that, in addition to the low frequency and alpha

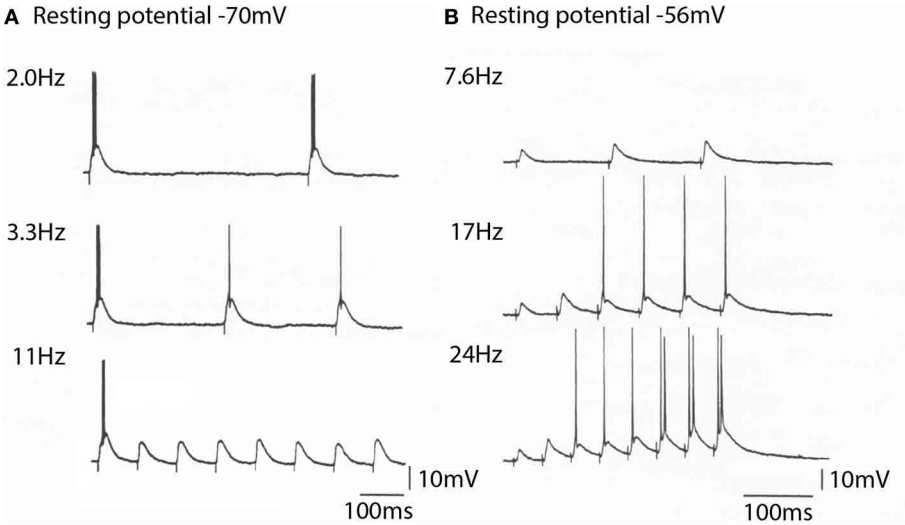

FIGURE 10 | The spike generation properties and EPSP amplitude generated by a thalamic neurons to cortico-thalamic volleys is membrane potential depend. (A) At −70 mV the thalamic cell generated spikes at frequencies bellow 10 Hz. Note that the EPSPs generated are all of the same amplitude (bottom trace). **(B)** At a resting potential of −56 mV the EPSP amplitude for the same cortical volley was initially smaller, but increased in amplitude with stimulus frequency. It could follow high frequency stimulation and produce rapid neuronal spike firing. (From Pedroarena and Llinás, 2001.).

rhythms, a gamma band rhythm is also present in thalamic neurons. This is particularly clear at dendritic levels and is supported by P/Q type calcium channels (Pedroarena and Llinás, 1997) and is essential in the generation of cognitive functions (Llinás et al., 2007). Indeed depolarization by direct current injection elicits well defined high frequency at potentials of −46 and −43 mV (**Figure 11A**) and the oscillations that can reach threshold for spike initiation at −40 mV (**Figure 11B**). These high frequency oscillations were blocked by P/Q channel blocker SFtx (Llinás et al., 1989; Mintz et al., 1992; cf Nimmrich and Gross, 2012).

The relationship of dendritic spikes and gamma oscillations was examined in a mathematical model of thalamocortical relay cells (Rhodes and Llinás, 2005). The model incorporated the generation of somatic spikes, low threshold rebound spike bursts, and fast somatic oscillations near threshold. In the distal dendrites the model neuron generated both isolated high-threshold calcium spikes and low threshold calcium spikes that did not require a high dendritic density of calcium channels. Somatic depolarization elicited firing in a dendrite (**Figure 11C**, red electrode; **Figure 11D**, red traces) that leads to subthreshold oscillations in the some (**Figure 11D**, white trace). When somatic depolarization ended, arrows in **Figure 11C**, dendritic spiking stopped. A similar pattern was seen when the location of the dendritic electrode was moved (blue and green in **Figures 11C,D**). The period of firing in the distal dendrites controlled the somatic oscillation frequency.

The gamma oscillations are generated in the dendrites as shown by dye imaging studies such as shown in **Figure 11E** where fluorescence of the calcium-specific dye flura 2 is restricted to the dendrites (Pedroarena and Llinás, 1997).

In thalamo-cortical slices, where the reciprocal connectivity is intact, thalamic stimulation results in the recurrent activity of the thalamocortical loop (**Figure 11F**). It is interesting to note that the high frequency cortical return excitation is mostly restricted to the dendritic thalamic compartment (**Figure 11E**). From the above it has been concluded that this dendritic conductance are not only related to oscillatory gamma band activity, but are essential in the generation of brain gamma band activity and of cognitive functions, as was demonstrated in mice genetically modified to delete P/Q type channels (Cav 2.1 null mice) (Llinás et al., 2007).

In all then, six ionic conductances have been described in thalamic neurons, in addition to those that underlie the axosomatic action potential as summarized in **Figure 12**.

(1) A voltage-dependent persistent, or very slowly inactivating somatic, Na^+ conductance, [$g_{Na(Ip)}$] This conductance generates a slow rebound depolarization in thalamic cells and plays a role in the genesis of the 10-Hz oscillation **Figure 10** (Jahnsen and Llinás, 1984b).

(2) A Ca^{2+}-dependent potassium somatic conductance, [$\mathbf{g}_{K(Ca)}$] which underlies the AHP. This conductance was demonstrated *in vitro* by the marked reduction of the AHP, after application of Ca^{2+} channel blockers (Jahnsen and Llinás, 1984b). The AHP amplitude is about 12 mV and can be reversed by inward current injection (Deschenes et al., 1984; Jahnsen and Llinás, 1984b).

(3) A fast, transient somatic potassium conductance ($\mathbf{g}_{IA}$), responsible for the slow return to baseline following hyperpolarization (Jahnsen and Llinás, 1984b; Kita and Kitai, 1986), which can prevent the abrupt recovery of neurons from a hyperpolarized condition. In fact, the duration of the hyperpolarization that generates the rebound response is aided by the presence of the transient K+ current.

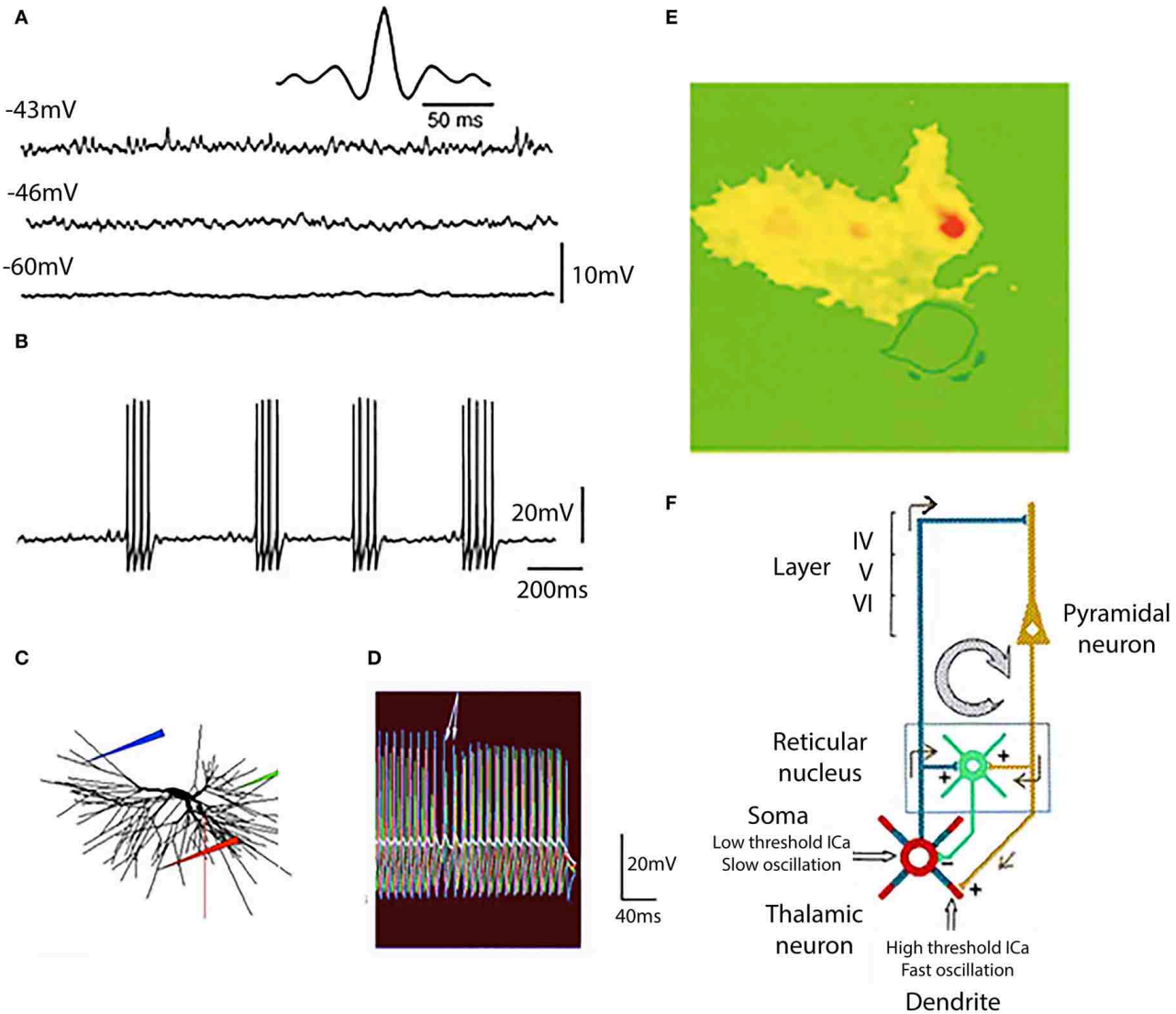

FIGURE 11 | Generation of gamma band oscillation by thalamic dendrites. (A) Three different levels of membrane potential are accompanied by a rapid membrane potential oscillation with clear gamma band frequency at −46 and −43 mV. This is demonstrated by the dominant frequency at 37.5 Hz at −43 mV as shown in the auto-correlogram (insert). **(B)** At a membrane potential of −40 mV action potentials were generated at the peak of each oscillatory wavelet and so the subthreshold oscillatory membrane properties are transformed into gamma band spike frequency projected via thalamocortical axons on to the cortical mantle. **(C,D)** The mechanism for this gamma band oscillation was of dendritic origin was tested with a computer model. **(E)** Direct demonstration that the gamma oscillations are mostly dendritic and carried by calcium ions was accomplished using calcium specific fura 2 fluorescence imaging. The cell was depolarized to the level that elicited fast firing calcium entry was restricted to the dendritic tree (yellow and red) **(F)**. Diagram of the oscillatory properties of thalamic neurons and the recurrent inhibition at somatic level via the thalamic nucleus reticular nucleus. [**(A,B,E,F)** from Pedroarena and Llinás, 1997; **(C,D)** from Rhodes and Llinás, 2005.].

(4) A low-threshold, rebound, somatic Ca^{2+} conductance [$g_{Ca(T)}$]. This conductance is inactive at the resting potential and deinactivates with hyperpolarization.
(5) A high-threshold, dendritic Ca^{2+} conductance [$G_{Ca(P/Q)}$]. This conductance triggers all-or-none depolarizing responses followed by activation of a Ca-gated K conductance.
(6) A somatic h-type potassium channel.

In contrast to the IO, the high threshold Ca^{2+} conductance is not strong in thalamic cells. Because of this difference, the dendritic Ca^{2+}-dependent spike does not dominate the firing of the thalamic neuron, allowing it a wider range of firing properties that that in IO neurons. The amplitude of the dendritic Ca^{2+} channels current in thalamic dendrites is smaller than that in inferior olivary neuron.

The six conductances combine to give thalamic neurons their unique oscillatory properties, as diagramed in **Figure 12**. At membrane potentials positive to −55 mV, fast action potentials are generated (red traces). At membrane levels near −55 mV, two types of firing are seen (black traces). In one case, the

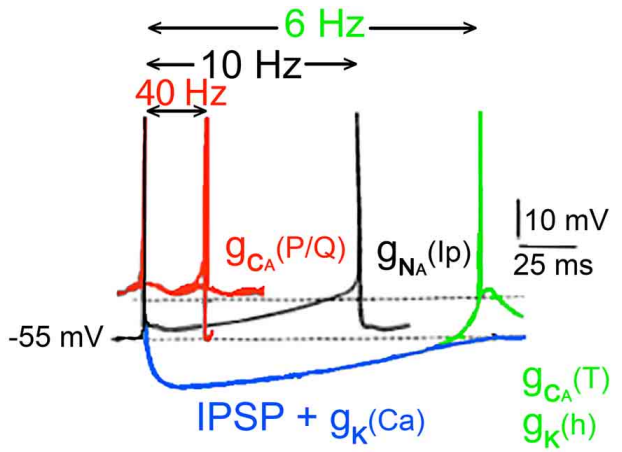

FIGURE 12 | Conducances underlying the oscillatory properties of thalamic neurons. In black, usual Na^+ dependent spike is followed by an after hyperpolarization generated by the classical voltage-sensitive K^+ conductance. Depending on membrane potential, this event can be followed by a persistent sodium current [($g_{Na(Ip)}$) black spikes]. Following an inhibitory synaptic potential a hyperpolarization dependant deinactivation of type a $g_{Ca(T)}$conductance, and the simultaneous inactivation of the potassium conductance $g_{K(Ih)}$ together generate a rebound response (green). The membrane potential is brought back to the threshold for the fast spike by the slow potassium conductance. In addition to the 10-Hz oscillations, slower oscillations (about 6 Hz) can occur by the rebound excitation (blue trace) following hyperpolarization of the cell [g_K (Ca)] and inhibitory postsynaptic potentials (IPSPs). Such hyperpolarization deinactivates the low-threshold Ca^{2+} conductance generating a rebound low threshold spike, which triggers the process once again activating potassium conductance (Ih). (Jahnsen and Llinás, 1984b,c; McCormick and Prince, 1986).

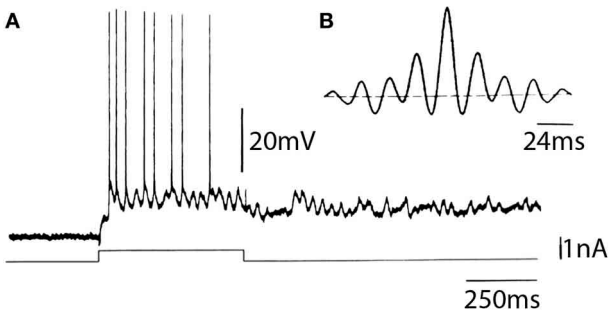

FIGURE 13 | *In vitro* intracellular recording from a sparsely spinous neuron of the fourth layer of the frontal cortex of guinea pig. (A) Characteristic response obtained in the cell following direct depolarization, consisting of sustained subthreshold oscillatory activity on which single spikes can be observed. **(B)** Autocorrelogram of the intrinsic oscillatory frequency indicated a 42 Hz intrinsic oscillation (Llinás et al., 1991).

fast sodium-dependent spike is followed by an AHP, due to an increase in both the classical voltage-activated potassium conductance (g_K) and by a Ca^{2+}-activated K^+ conductance [$g_{K\ (Ca)}$] that generates an AHP lasting for 70 ms or so, allowing the cell to fire at a frequency near 10 Hz. The response can be further augmented as a rebound from the inhibitory postsynaptic potential (IPSP) in blue.

Thalamic cell firing is basically produced by a slow depolarization of the cell produced by the activation of the persistent Na+ conductance [$g_{Na(IP)}$], which can serve as a continuous depolarizing drive once it is activated. Once the [$g_{Na(IP)}$] takes over it depolarizes the cell until another spike is generated and the process repeats itself, with a 10-Hz rhythmicity. If, on the other hand, the hyperpolarizing potassium conductances are combined with an A potassium current and/or IPSPs, the neurons are hyperpolarized sufficiently to deinactivate the low-threshold Ca^{2+} conductance [$g_{Na(Ip)}$] and to inactivate a potassium conductance (Ih) resulting in an oscillatory responses at frequencies near 6 Hz. Thus, their intrinsic properties allow thalamic neurons to display a versatility whereby they switch between tonic and phasic responses as diagrammed in **Figure 12**.

The point to be emphasized here is not the difference between these two groups of cells but rather the fact that they both have intrinsic properties that give them distinctive firing characteristics. From the above, it follows that the nervous system is constantly in action and that the patterns of activity arising from the sensory inputs and from the corollary discharge of motor outputs, are but a small modulatory component of the overall activity of the brain. Beyond these conductances, the thalamic neuron oscillatory patterns can also be generated via synaptic activation as elegantly demonstrated *in vitro* studies by Sohal et al. (2006).

CORTICAL NEURONS

The electrophysiology of cortical neurons has been extensively studied (Yuste et al., 2005) and the morphology-related intrinsic firing patterns in simulated neocortical pyramidal cells has been examined as well (Korogod and Tyc-Dumont, 2009). In this summary I will touch briefly on neuronal aspects of cortical neurons that relate very specifically to 40 Hz activation in relation to the intrinsic properties of a particular type of interneuron, the sparsely spinous neurons of the fourth cortical layer.

From an *in vitro* point of view, our research in the cerebral cortex of the guinea pig points to the existence of neurons in the fourth layer that have intrinsic subthreshold electroresponsive properties that endow these cells with a 30- to 45-Hz membrane potential oscillation (Llinás et al., 1991). These cells, which are often silent after penetration, demonstrate oscillation on direct membrane depolarization. On occasion, the cells may also show spontaneous oscillations at that frequency. When this occurs, further depolarization produced by direct current injection will generate a spike at the peak of the depolarizing phase of each oscillation. In other recordings in similar neurons, it was also found that a voltage-dependent persistent sodium conductance may underlie the generation of 40-Hz oscillation, which, in that case, outlasts the duration of the depolarizing pulse.

Examples of such recordings are shown in **Figure 13A**. Autocorrelation analysis of this response (**Figure 13B**) demonstrates that the frequency of oscillation of this cell was 42-Hz.

Following intracellular staining, these fourth-layer neurons were recognized as the sparsely spinous neurons that have been described by anatomists as being GABAergic and as having axons that ascend to the third layer and descend to the fifth layer in the cortex (Peters and Saint-Maie, 1984).

As opposed to the oscillations observed in the IO and thalamus, the oscillation of these fourth-layer inhibitory interneurons appears to be generated by a voltage-dependent sodium conductance followed by a potassium conductance, probably of the voltage- or Na^+-dependent variety. The sodium dependence of this oscillation was demonstrated by the addition of TTX to the bath, which blocked the oscillations generated by direct stimulation as well as those spontaneously generated. The subthreshold oscillations were, in fact, the first to disappear, followed by the blockage of the all-or-none fast spikes.

Other examples of similar types of oscillations, but with a lower frequency, have been observed in the giant stellate cells of the entorhinal cortex (Alonso and Llinás, 1992) as well as in the neurons of the nucleus parabrachialis in the brainstem (Leonard and Llinás, 1990). In contrast to the 40-Hz oscillations displayed by the cortical neurons, the latter two cell types oscillate at a frequency of 6–12 Hz, i.e., in the range of the theta and low alpha rhythms. The point of interest here is that similar current may generate different oscillatory frequencies, depending on the kinetics of the voltage-dependent conductances. Equally significant is the fact that oscillations at a similar frequency may have different ionic bases in different types of cells. This is probably related to secondary events that oscillation may ultimately regulate. Thus, as some cell oscillations may be a form of communication, in others, the hippocampus for example, oscillation may serve to trigger secondary changes such as long-term potentiation (Larson and Lynch, 1986). These latter require the activation of Ca^{2+}-dependent second messengers, in which case Ca^{2+} -based oscillation would be a significant parameter (Llinás and Steriade, 2006).

In vivo cortical studies that have taken a broader perspective than that provided by single cell *in vitro* electrophysiology have demonstrated in the cat, that high-frequency activity occurs in motor areas 4y, 6aB and in the posterior parietal associative area 5a during motionless focused attention (Bouyer et al., 1987). These recordings were obtained from the surface of the cortex, as well as from depth field analyses. With respect to the visual cortex, it was demonstrated (Gray et al., 1989) that, following specific visual input, a 40-Hz oscillation may be observed as a field potential envelope, and as single units in the overall envelope. This 40-Hz oscillation appears to be present only when the given cortical area is activated by an optimal physiological stimulus.

The question of the role of the intrinsic electrical properties of neurons in the overall function of the CNS must be defined, then, at the cell ensemble level. Perhaps one of the most interesting issues concerning global brain function relates to the rediscovery in recent years of 40-Hz oscillation, which may be observed in the cortex under certain conditions. In fact, 40-Hz oscillations have been observed in the cortex under certain conditions. For example, there are 40-Hz oscillations during physiological stimulation of the visual (Gray et al., 1989) or auditory cortex (Galambos et al., 1981; Spydell et al., 1985; Mäkelä and Hari, 1987; Johnson et al., 1988). In its absence, as occurs when P type calcium channels are (Ca 3.1) are deleted, there is a total lack of cognitive function. Such oscillations have also been recorded during intensive attention states such as occur when a predator is stalking its prey (Bouyer et al., 1987), or in humans, during the state of elevated attention prior to the execution of complicated tasks (Sheer, 1984). Similar activity as measured from the scalp by electric and magnetic means in humans appears to be well correlated with cognitive tasks and seems to be altered under pathological conditions (Ribary et al., 1989, 1991).

The issue here is that the oscillatory events may be used in intercellular communication as well as in the modulation of the intracellular milieu. From the point of view of 40-Hz oscillations, the oscillation in the GABAergic neurons may, in fact, be the origin of the macroscopic 40-Hz observed in the cortex. Indeed, since these cells receive direct synaptic input from thalamic neurons, and since they relay inhibition to pyramidal cells at a 40-Hz frequency, this will, in turn, produce a resonance activation of the pyramidal cells at a frequency of 40 Hz. The question of interest, then, is the mechanism by which such oscillations may become sufficiently synchronous to generate macroscopic events. Our own view on this matter is illustrated in **Figure 14**.

Thalamic input via projection neurons reaches the neurons of the fourth layer of the cortex that generate 40-Hz oscillation. These cells, which are GABAergic, can generate a 40-Hz IPSP on pyramidal neurons and allow them to fire at 40-Hz as a rebound from abrupt inhibition. Pyramidal cells, in turn, activate, via collaterals, the thalamic projection neurons as well as the neurons of the reticular thalamus and the interneurons at the thalamus itself. The direct excitatory input at 40-Hz to the projection

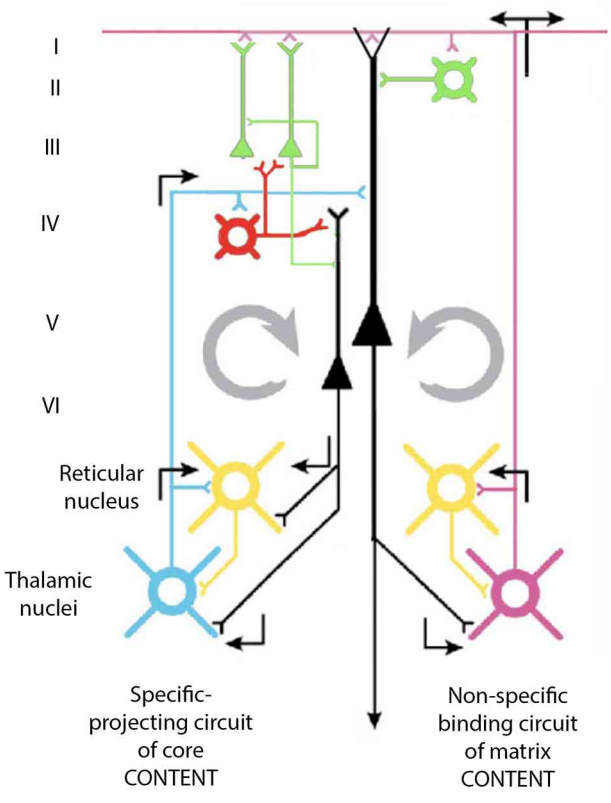

FIGURE 14 | Diagram of the proposed cortico-thalamo-cortical reverberating circuit, which may underlie 40-Hz oscillation at the cortex. See text.

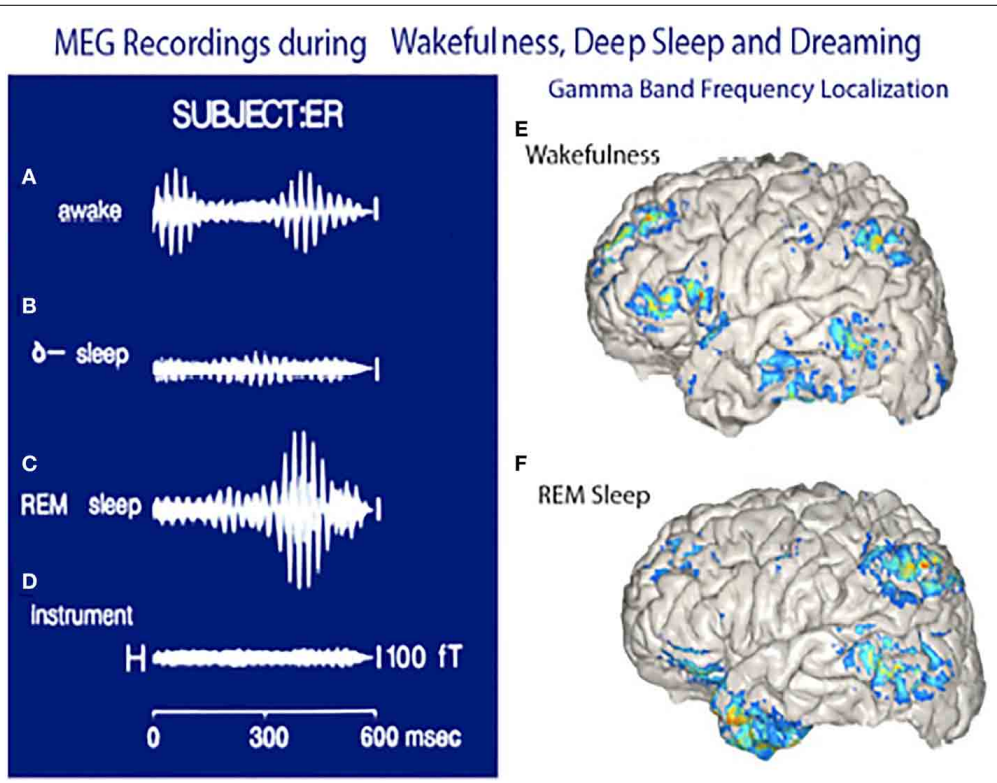

FIGURE 15 | Magnetoencephalographic (MEG) recordings in three functional states. (A) Magnetic recording demonstrating gamma band activity following a sensory stimulus in awake subject. **(B)** Recordings from same subject during deep, dreamless sleep. **(C)** Gamma band activity while dreaming. **(D)** Instrument noise in the absence of a subject. **(E)** Localization of gamma band activity in an awake subject note frontal and parietal and temporal association lobe activity. **(F)** Localization of gamma band activity recorded when the subject was dreaming. Note the lack of frontal lobe activity and the powerful activation of the temporal pole. (Llinás and Ribary, 1993 and unpublished observations.).

thalamic cells, as well as their disynaptic inhibition via the reticularis and intrathalamic GABAergic neurons, contributes to the thalamic oscillations at 40-Hz. This thalamic oscillation is then signaled back to the cortex, establishing a large resonant oscillation between the thalamus and the cortex, which can recruit sufficient elements to generate the synchronicity observed at both intracellular and extracellular levels in the cortex and thalamus.

According to this view, the inhibitory neurons that contact pyramidal cells directly may force them in combination to a synchronous excitatory input to rebound oscillation. These cells will then generate, via their descending axons, 40-Hz excitation of cells in the nucleus reticularis thalami (NRT), the intrinsic inhibitory neurons in the thalamus, and the projection thalamic neurons themselves.

Since the NRT cells are inhibitory (cf. Steriade and Llinás, 1988) they would further increase the resonance property of the thalamocortical system by their own driven 40-Hz input back through the fourth-layer interneurons. In this manner, a cortico-thalamo-cortical resonance even may actually be the basis of this 40-Hz rhythm recorded at the cortical level.

While Gray et al. (1989) have not recorded oscillation in the thalamus at 40-Hz, other investigators (Fuster et al., 1965) had, in fact, published intracellular recordings from geniculate neurons following light stimulation demonstrating clear 40-Hz activity. This indicates that activity at such frequencies is not a cortical phenomenon exclusively but may also be seen at the thalamic level.

The MEG recordings shown in **Figure 15** suggest that mostly somatosensory and visual auditory association cortices are active as well as the anterior temporal pole (amygdala) are the main players during dreaming while the frontal lobe remains only sparsely active (**Figure 15F**). Similar findings have been reported using MEG by Ioannides et al. (2004).

The functional significant of 40-Hz oscillation in the thalamocortical system becomes particularly interesting when one considers that it may serve as the basis for the temporal correlation of events that must be considered as a single perceptual or motor entity, the so called conjunction principle. This temporal superposition, in fact, may be at the very core of global brain function. Indeed, it may actually be observed using magnetic recording in humans, where 40-Hz activity can be demonstrated to be organized quite widely, demonstrating a phase shift from the front of the brain onto the back with a sweep speed in the rostro-caudal direction of about 5–10 ms (Ribary et al., 1989, 1991). This phase shift suggests that, via the activation of the NRT, a conjunctional type of activity may be generated at the thalamus, which allows thalamocortical resonance in a global, organized manner. This, in its most simplified form,

could serve to scan the brain front to back 200 times a second. Such scanning would be viewed as the basis for the generation of unitary perceptual entities out of many sensory and motor vector components, which represent the details of the perceived world.

Ultimately, we are then faced with a system that addresses the external world, not as a slumbering machine to be awoken by the entry of sensory information, but rather as a continuously humming brain willing to internalize and incorporate into its intimate activity an image of the external world, but always in the context of its own existence and its own intrinsic electrical activity. Most fundamental, however, is the fact that the system is not merely a computational entity, but rather that issues are substrate dependent (neurons) and, moreover, that ionic events such as the presence of P/Q calcium channel activity are actually crucial to its ultimate function. From a more global perspective it is the dialog between the incoming information arising, in mammals, from the dorsal thalamus that provides the content in our everyday cognitive activity, and the nonspecific system that provides context (i.e., the attention), that we give to such inputs (Llinás et al., 1994).

REFERENCES

Alonso, A., and Llinás, R. (1992). The electrophysiology of the mammillary complex *in vitro*. II. Medial mammillary neurons. *J. Neurophysiol.* 68, 1321–1331.

Armstrong, D. M., Eccles, J. C., Harvey, R. J., and Matthews, P. B. (1968). Responses in the dorsal accessory olive of the cat to stimulation of hind limb afferents. *J. Physiol. (Lond.)* 194, 125–145.

Binder, M. D., Heckman, C. J., and Powers, R. K. (1993). How different afferent inputs control motoneuron discharge and the output of the motoneuron pool. *Curr. Opin. Neurobiol.* 3, 1028–1034. doi: 10.1016/0959-4388(93)90177-Z

Bouyer, J. J., Montaron, M. F., Vahnée, J. M., Albert, M. P., and Rougeul, A. (1987). Anatomical localization of cortical beta rhythms in cat. *Neuroscience* 22, 863–869. doi: 10.1016/0306-4522(87)92965-4

Choi, S. W., Yu, E., Kim, D., Urbano, F. J., Makarenko, V., Shin, H. S. et al. (2010). Subthreshold membrane potential oscillations in inferior olive neurons are dynamically regulated by P/Q and T-type calcium channels: a study in mutant mice. *J. Physiol. (Lond.)* 588, 3031–3043. doi: 10.1113/jphysiol.2009.184705

Connors, B. W., Gutnik, M. K., and Prince, D. A. (1982). Electrophysiological properties of neocortical neurons *in vitro*. *J. Neurophysiol.* 48, 1302–1320.

Crunelli, V., Kelly, J. S., Leresche, N., and Pirchio, M. (1987). On the excitatory postsynaptic potential evoked by stimulation of the optic tract in the rat lateral geniculate nucleus. *J. Physiol. (Lond.)* 390, 243–256.

Deschenes, M., Paradis, M., Roy, J. P., and Steriade, M. (1984). Electrophysiology of neurons of lateral thalamic nuclei in cat, resting properties and burst discharges. *J. Neurophysiol.* 51, 1196–1219.

Fuster, J. M., Herz, A., and Creutzfeldt, O. D. (1965). Analysis of cell-discharge in spontaneous and optically modulated activity in the visual system. *Arch. Ital. Biol.* 103, 159–177.

Galambos, R., Makeig, S., and Talmachoff, P. J. (1981). A 40-Hz auditory potential recorded from the human scalp. *Proc. Natl. Acad. Sci. U.S.A.* 78, 2643–2647. doi: 10.1073/pnas.78.4.2643

Graham-Brown, T. (1911). The intrinsic factors in the act of progression is animals. *Proc. R. Soc. Lond. B Biol. Sci.* 84, 308–319. doi: 10.1098/rspb.1911.0077

Gray, C. M., Konig, P., Engel, A. K., and Singer, W. (1989). Oscillatory responses in cat visual cortex exhibit inter-columnar synchronization which reflects global stimulus properties. *Nature* 338, 334–337. doi: 10.1038/338334a0

Hemmings, H. C. Jr., Nairn, A. C., and Greengard, P. (1986). Protein kinases and phosphoproteins in the nervous system. *Res. Publ.* 64, 47–69.

Hirsch, J. C., Burnod, Y., and Korn, H. (1985). Dorsolateral geniculate neurons *in vitro*: reduced postsynaptic excitability following repetitive activation of the optic tract. *Neurosci. Lett.* 58, 151–156. doi: 10.1016/0304-3940(85)90345-3

Ioannides, A. A., Corsi-Cabrera, M., Fenwuck, P. B. C., Rio, Y., Laskaris, N. A., Khurshudyan, A., et al. (2004). MEG tomography of human cortex and brainstem in activity in waking and REM sleep saccades. *Cereb. Cortex* 14, 52–72. doi: 10.1093/cercor/bhg091

Jahnsen, H., and Llinás, R. (1984a). Ionic basis for the electroresponsiveness and oscillatory properties of guinea-pig thalamic neurons *in-vitro*. *J. Physiol. (Lond.)* 349, 227–248.

Jahnsen, H., and Llinás, R. (1984b). Electrophysiological properties of guinea-pig thalamic neurons: an *in-vitro* study. *J. Physiol. (Lond.)* 349, 205–226.

Jahnsen, H., and Llinás, R. (1984c). Voltage-dependent burst-to-tonic switching of thalamic cell activity: an *in vitro* study. *Arch. Ital. Biol.* 122, 73–82.

Johnson, B. W., Weinberg, H., Ribary, U., and Cheyne, D. O. (1988). Topographic distribution of the 40-Hz auditory evoked-related potential in normal and aged subjects. *Brain Topogr.* 1, 117–124. doi: 10.1007/BF01129176

Kita, H., and Kitai, S. T. (1986). Electrophysiology of rat thalamocortical relay neurons: an *in vivo* intracellular study. *Brain Res.* 371, 80–89. doi: 10.1016/0006-8993(86)90812-7

Korogod, S. M., and Tyc-Dumont, S. (2009). *Electrical Dynamics of Dendritic Space*. Cambridge, UK: Cambridge University Press. doi: 10.1017/CBO9780511691584

Lang, E. J., Sugihara, I., and Llinás, R. (2006). Olivocerebellar modulation of motor cortex ability to generate vibrissal movements. *J. Physiol.* 571, 101–120. doi: 10.1113/jphysiol.2005.102764

Larson, J., and Lynch, G. (1986). Induction of synaptic potentiation in hippocampus by patterned stimulation involves two events. *Science* 232, 985–988. doi: 10.1126/science.3704635

Lefler, Y., Torben-Nielsen, B., and Yarom, Y. (2013). Oscillatory activity, phase differences, and phase resetting in the inferior olivary nucleus. *Front. sys. neurosci.* 7, 22. doi: 10.3389/fnsys.2013.00022

Leonard, C., and Llinás, R. (1990). "Electrophysiology of mammalian pedunculopontine and laterodorsal tegmental neurons *in vitro*: implications for the control of REM sleep," in *Brain Cholinergic Systems*, eds M. Steriade and D. Biesold (New York, NY: Oxford University Press), 205–223.

Leznik, E., Makarenko, V., and Llinás, R. (2002). Electrotonically mediated oscillatory patterns in neuronal ensembles: an *in vitro* voltage-dependent dye-imaging study in the inferior olive. *J. Neurosci.* 22, 2804–2815.

Llinás, R. (1988). The intrinsic electrophysiological properties of mammalian neurons: a new insight into CNS function. *Science* 242, 1654–1664. doi: 10.1126/science.3059497

Llinás, R., Choi, S., Urbano, F. J., and Shin, H. S. (2007). Gamma band deficiency and abnormal thalamocortical activity in P/Q-type channel mutant mice. *Proc. Natl. Acad. Sci. U.S.A.* 104, 17819–17824. doi: 10.1073/pnas.0707945104

Llinás, R., Grace, A. A., and Yarom, Y. (1991). *In vitro* neurons in mammalian cortical layer 4 exhibit intrinsic oscillatory activity in the 10 to 50 Hz frequency range. *Proc. Natl. Acad. Sci. U.S.A.* 88, 897–901. doi: 10.1073/pnas.88.3.897

Llinás, R., and Hess, R. (1976). Tetrodotoxin-resistant dendritic spikes in avian Purkinje cells. *Proc. Natl. Acad. Sci. U.S.A.* 73, 2520–2523. doi: 10.1073/pnas.73.7.2520

Llinás, R., and Jahnsen, H. (1982). Electrophysiology of mammalian thalamic neurons *in vitro*. *Nature* 297, 406–408. doi: 10.1038/297406a0

Llinás, R., and Ribary, U. (1993). Coherent 40-Hz oscillation characterizes dream state in humans. *Proc. Natl. Acad. Sci. U.S.A.* 90, 2078–2081. doi: 10.1073/pnas.90.5.2078

Llinás, R., Ribary, U., Joliot, M., and Wang, X. J. (1994). "Content and context in temporal thalamocortical binding," in *Temporal Coding in the Brain*, eds G. Buzaki, R. Llinás, W. Singer, A. Berthoz, and Y. Christen (Berlin; Heidelberg: Springer-Verlag), 251–272.

Llinás, R., and Sugimori, M. (1980a). Electrophysiological properties of *in vitro* Purkinje cell dendrites in mammalian cerebellar slices. *J. Physiol. (Lond.)* 305, 197–213.

Llinás, R., and Sugimori, M. (1980b). Electrophysiological properties of *in vitro* Purkinje cell somata in mammalian cerebellar slices. *J. Physiol. (Lond.)* 305, 171–195.

Llinás, R., Sugimori, M., and Cherksey, B. (1989). Voltage dependent calcium conductances in mammalian neuron. The P channel. In calcium channels: structure and function *Ann. N. Y. Acad. Sci.* 560, 103–111. doi: 10.1111/j.1749-6632.1989.tb24084.x

Llinás, R., and Yarom, J. (1981). Properties and distribution of ionic conductances generating electroresponsiveness of mammalian inferior olivary neurons *in vitro*. *J. Physiol. (Lond.)* 315, 569–584.

Llinás, R., and Yarom, Y. (1986). Oscillatory properties of guinea-pig inferior olivary neurones and their pharmacological modulation: an *in vitro* study. *J. Physiol*. 376, 163–182.

Llinás, R. R., and Steriade, M. (2006). Bursting of thalamic neurons and states of vigilance. *J. Neurophysiol.* 95, 3297–3308. doi: 10.1152/jn.00166.2006

Lund, J. P., and Dellow, P. G. (1973). Rhythmical masticatory activity of hypoglossal motoneurons responding to an oral stimulus. *Exp. Neurol.* 40, 243–246. doi: 10.1016/0014-4886(73)90139-8

Makarenko, V., and Llinas, R. (1998). Experimentally determined chaotic phase synchronization in a neuronal system. *Proc. Natl. Acad. Sci. U.S.A*. 95, 15747–15752. doi: 10.1073/pnas.95.26.15747

Mäkelä, J. P., and Hari, R. (1987). Evidence for cortical origin of the 40-Hz auditory evoked response in man. *Electroencephalogr. Clin. Neurophysiol.* 66, 539–546. doi: 10.1016/0013-4694(87)90101-5

McCormick, D. A., and Prince, D. A. (1986). ACh induces burst firing in thalamic reticular neurons by activating at K+ conductance. *Nature* 319, 402–405. doi: 10.1038/319402a0

McCormick, D. A., and Prince, D. A. (1987). Actions of acetylcholine in guinea-pig and cat medial and lateral geniculate nuclei. *J. Physiol. (Lond.)* 392, 147–165.

Mintz, I. M., Adams, M. E., and Bean, B. P. (1992). P-type calcium cannels in rat central and peripheral neurons. *Neuron* 9, 85–95. doi: 10.1016/0896-6273(92)90223-Z

Nimmrich, V., and Gross, G. (2012). P/Q-type calcium channel modulators *Br. J. Pharmacol.* 167, 741–759. doi: 10.1111/j.1476-5381.2012.02069.x

Pedroarena, C., and Llinás, R. (1997). Dendritic calcium conductances generate high frequency oscillation in thalamocortical neurons. *Proc. Natl. Acad. Sci. U.S.A*. 94, 724–728. doi: 10.1073/pnas.94.2.724

Pedroarena, C., and Llinás, R. (2001). Interactions of synaptic and intrinsic electroresponsiveness determine corticothalamic activation dynamics. *Thalamus Relat. Syst.* 1, 3–14. doi: 10.1017/S1472928801000073

Peters, A., and Saint-Maie, R. L. (1984). "Smooth and sparcely spinous nonpyramidal cells forming local axonal plexus," in *Cerebral Cortex*, Vol. 1, eds A. Peters and E. G. Jones (New York, NY: Plenum Press), 419–445.

Porras, A., and Llinás, R. (2014). Bio-inspired coupled oscillatory phase reset control system applied to movement in an underwater vehicle. *Robot. Auton. Syst.* 62, 257–266. doi: 10.1016/j.robot.2013.09.007

Ramirez, J. M., and Richter, D. W. (1996). The neuronal mechanisms of respiratory rhythm generation. *Curr. Opin. Neurobiol.* 6, 817–825. doi: 10.1016/S0959-4388(96)80033-X

Ramón y Cajal, S. (1904). *Histoligie de Systeme Nerveux de L'homme et des Vertebrates*. Madrid: Instituto Ramón y Cajal.

Ribary, U., Llinás, R., Kluger, A., Suk, J., and Ferris, S. H. (1989). Neuropathological dynamics of magnetic, auditory steady-state responses in Alzheimer's disease,' in *Advances in Biomagnetism*, ed S. J. Williamson (New York, NY: Springer), 311–315.

Ribary, U., Ioannides, A. A., Singh, K. D., Hasson, R., and Llinás, R. (1991). Magnetic field tomography (MFT) of coherent thalamo-cortical 40-Hz oscillation in humans. *Proc. Natl. Acad. Sci. U.S.A*. 88, 11037–11041. doi: 10.1073/pnas.88.24.11037

Rhodes, P. A., and Llinás, R. R. (2005). A model of thalamocortical relay cells. *J. Physiol*. 565, 765–7781. doi: 10.1113/jphysiol.2004.070888

Sheer, D. (1984). "Focused arousal, 40-Hz EEG and dysfunction," in *Self Regulation of the Brain and Behavior*, eds T. H. Elbert, B. Rockstroh, W. Lutzenberger, and N. Birbaumer (Berlin: Springer-Verlag), 64–84. doi: 10.1007/978-3-642-69379-3_6

Sohal, V. S., Pangratz-Fuehrer, S., Rudolph, U., and Huguenard, J. R. (2006). Intrinsic and synaptic dynamics interact to generate emergent patterns of rhythmic bursting in cortical neurons. *J. Neurosci*. 26, 4247–4255. doi: 10.1523/JNEUROSCI.3812-05.2006

Spydell, J. D., Pattee, G., and Goldie, W. D. (1985). The 40-Hz auditory event related potential: normal values and effects of lesions. *Electroencephalogr. Clin. Neurophysiol.* 62, 193–202. doi: 10.1016/0168-5597(85)90014-0

Steriade, M., and Llinás, R. (1988). The functional states of the thalamus and the associated neuronal interplay. *Physiol. Rev.* 68, 649–742.

Stafstrom, C. E., Schwindt, P. C., and Crill, W. E. (1982). Negative slope conductance due to a persistent subthreshold sodium current in cat neocortical neurons *in vitro*. *Brain Res.* 236, 221–226. doi: 10.1016/0006-8993(82)90050-6

Tank, D. W., Sugimori, M., Connor, J. A., and Llinás, R. (1988). Spatially resolved calcium dynamics of mammalian Purkinje cells in cerebellar slice. *Science* 242, 773–777. doi: 10.1126/science.2847315

Usowicz, M. M., Sugimori, M., Cherksey, B., and Llinás, R. P. (1992). Type calcium channels in the soma and dentrites of adult Cerebellar Purkinje Cells. *Neuron* 9, 1185–1199. doi: 10.1016/0896-6273(92)90076-P

Vallbo, A. B., and Wessberg, J. (1993). Organization of motor output in slow finger movements in man. *J. Physiol.* 469, 673–691.

van Lunteren, E., and Dick, T. E. (1992). Intrinsic properties of pharyngeal and diaphragmatic respiratory motoneurons and muscles. *J. Appl. Physiol. (1985)* 73, 787–800.

Wilcox, K. C., Gutnick, M. J., and Christoph, G. R. (1988). Electrophysiological properties of neurons in the lateral habendula nucleus, an *in vitro* study. *J. Neurophysiol.* 59, 212–225.

Wong, R. K., Miles, R., and Traub, R. D. (1984). Local circuit interactions in synchronization of cortical neurones. *J. Exp. Biol.* 112, 169–178.

Yuste, R., MacLean, J. N., Smith, J., and Lansner, A. (2005). The cortex as a central pattern generator. *Nat. Rev. Neurosci*. 6, 477–483. doi: 10.1038/nrn1686

Conflict of Interest Statement: The author declares that the research was conducted in the absence of any commercial or financial relationships that could be construed as a potential conflict of interest.

Received: 27 July 2014; paper pending published: 22 August 2014; accepted: 23 September 2014; published online: 04 November 2014.

*Citation: Llinás RR (2014) Intrinsic electrical properties of mammalian neurons and CNS function: a historical perspective. Front. Cell. Neurosci. **8**:320. doi: 10.3389/fncel.2014.00320*

This article was submitted to the journal Frontiers in Cellular Neuroscience.

frontiers in Computational Neuroscience

REVIEW
published: 20 October 2015
doi: 10.3389/fncom.2015.00129

The 40-year history of modeling active dendrites in cerebellar Purkinje cells: emergence of the first single cell "community model"

James M. Bower *

Numedeon, Inc., Ashland, OR, USA

The subject of the effects of the active properties of the Purkinje cell dendrite on neuronal function has been an active subject of study for more than 40 years. Somewhat unusually, some of these investigations, from the outset have involved an interacting combination of experimental and model-based techniques. This article recounts that 40-year history, and the view of the functional significance of the active properties of the Purkinje cell dendrite that has emerged. It specifically considers the emergence from these efforts of what is arguably the first single cell "community" model in neuroscience. The article also considers the implications of the development of this model for future studies of the complex properties of neuronal dendrites.

Keywords: Purkinje cells, modeling, cerebellum, cerebellar, dendrite, active conductnaces, history

OPEN ACCESS

Edited by:
Sergey M. Korogod, International Center for Molecular Physiology, National Academy of Sciences of Ukraine, Ukraine

Reviewed by:
Benjamin Torben-Nielsen, University of Hertfordshire, UK
Fahad Sultan, University Tübingen, Germany

***Correspondence:**
James M. Bower
jim@numedeon.com

Received: *14 November 2014*
Accepted: *02 October 2015*
Published: *20 October 2015*

Citation:
Bower JM (2015) The 40-year history of modeling active dendrites in cerebellar Purkinje cells: emergence of the first single cell "community model". Front. Comput. Neurosci. 9:129. doi: 10.3389/fncom.2015.00129

INTRODUCTION

Analysis of the complex behavior of the mammalian cerebellar Purkinje cell has contributed significantly to our understanding of the role and function of active electrical properties in central nervous system dendrites. Further, as reviewed in this article, the study of the active properties of the dendrites of this neuron is unusual for neuroscience in the extent to which it has involved an interaction between "realistic" biophysically accurate computer models and laboratory-based experiments. Accordingly, in addition to considering the possible functional significance of the active dendritic properties of the mammalian Purkinje cell, this article also recounts in some detail the evolution of the models on which that analysis is based. Ideally, this history should serve as a model for the analysis of all aspects of the functional organization of nervous systems.

It turns out that the co-dependence between modeling and experimental studies of Purkinje cells was established at the earliest stages of study of this neuron's complex electrical behavior. This early interaction between models and experiments was induced by a claim made by Llinas et al. (1968) based on experimental results, that Purkinje cell dendrites were electrically active. That claim, based on experimentally obtained time delays in shock induced field potentials recorded at different depths of the alligator cerebellum, was immediately challenged by Calvin and Hellerstein (1969) who, citing Rall's (1964) pioneering cable modeling results, suggested that such delays were likely a simple consequence of passive dendritic current conduction alone. In defending their interpretation, Llinas and colleagues asserted in return that models based on volume conductors rather than cable models were a more appropriate basis for the analysis of extracellular field potentials. A few months later, Zucker (1969) entered the debate by actually performing calculations comparing both types of models, concluding that neither approach, in its classical form, could resolve the issue.

However, Zucker pointed out that similarities in simulated field potential results recently obtained from the more active cable theory models for mitral cells developed by Rall and Shepherd (1968) likely supported Llinas' original interpretation. In response, Calvin suggested that Zucker's model had too many free parameters, and defended his own argument as based on "*the simplest possible model consistent with our objective (to demonstrate that a) commonplace explanation for conduction velocities was as good as the more esoteric*" (Calvin, 1969, p. 637). It took 10 more years and the development of experimental brain slice procedures and the application of intracellular recording techniques for Llinas and Sugimori (1980a) to provide conclusive experimental evidence that Purkinje cell dendrites are in fact electrically active.

It is important to point out that while references to computational modeling was at the heart of this very early controversy, no effort was actually made by any of the discussants to actually build a model of the Purkinje cell dendrite (Calvin and Hellerstein, 1969). Instead, the first model of a Purkinje cell dendrite was published by Pellionisz and Szentagothai as the last of a series of early cerebellar network modeling studies (Pellionisz, 1970; Pellionisz and Szentágothai, 1973, 1974). As shown in **Figure 1**, in that model, the complex Purkinje cell dendrite was represented by only four branches in which synaptic influences were calculated independently, using a simple algebraic summation. On reaching threshold, each branch independently generated dendritic spikes which were then simply summed at the soma. Comparing results of network simulations using these four branch Purkinje cells to previous results with no dendritic structure these authors concluded that: "*the simulation experiments are giving quite strong hints in favor of the importance of dendritic geometry*" (Pellionisz and Szentágothai, 1974, p. 28).

Perhaps reflecting the influence of the original debate between Llinas and Calvin and Hallerstein in the 1960's, Llinas and Nicholson (1976) published the first true compartmental model of the Purkinje cell dendrite to specifically test new speculations on cerebellar physiology based on field potential recordings. In this case, the experiments involved climbing fiber-evoked responses in cat cerebellar cortex. As shown in **Figure 2**, while their compartmental model included conductances represented with Hodgkin Huxley model parameters (Hodgkin and Huxley, 1952), the model included only three dendritic compartments whose active properties were limited to the synapses.

One year later, as shown in **Figure 3**, Llinas now working with Pellionisz, published the first compartmental Purkinje cell model with more a more complex dendritic tree (Pellionisz and Llinás, 1977). Using as a base a previously published compartmental model of a spinal motorneuron (Dodge and Cooley, 1973), the new Purkinje cell model consisted of 62 compartments with the soma and initial segment incorporating Hodgkin Huxley channels (Hodgkin and Huxley, 1952). With this model the authors sought, for the first time, to use the model to replicate actual experimental responses of frog Purkinje cells including: (1) the rapid "antidromic" decrement in action potential amplitude in the dendrite following somatic current injection (Llinas et al., 1969b; Freeman and Nicholson, 1975); (2) the orthodromic activation of Purkinje cells following parallel fiber stimulation (Eccles et al., 1966a); and (3) the spike burst resulting from climbing fiber synaptic input (Eccles et al., 1966b, 1967). While the authors' state explicitly in their article that compartmental modeling is an essential technique to: "*(handle) a partially or totally active dendritic tree*" (Pellionisz and Llinás, 1977,

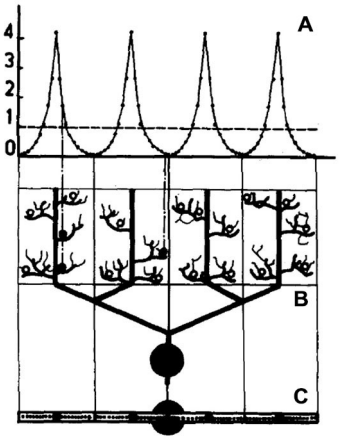

FIGURE 1 | Schematic representation of a model Purkinje cell model simulated in Pellionisz and Szentágothai (1974). The dendritic tree is divided into four non-overlapping synaptic territories meant to represent the main Purkinje cell dendritic branches. **(A)** shows the distribution of parallel fiber synapses on each dendritic branch, **(B)** is the modeled Purkinje cell viewed in a parasagittal plane and **(C)** is the Purkinje cell viewed from the top. The fine structure within each branch in this figure is only for illustrative purposes and did not influence the summation of synaptic inputs. Reproduced with permission from Pellionisz and Szentágothai (1974).

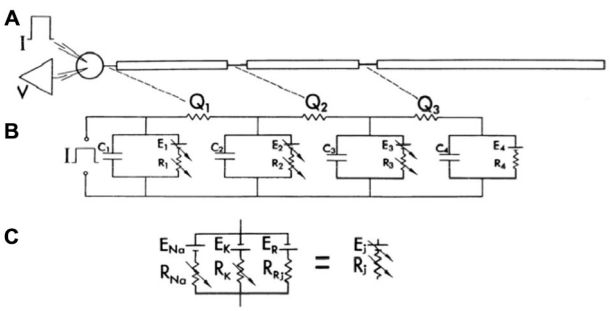

FIGURE 2 | The first published compartmental model of a Purkinje cell, consisting of a soma and three dendritic compartments. As shown in **(A)**, the model consisted of a soma and three dendritic compartments, with only the soma and the first two dendritic compartments receiving synaptic input. **(B)** Represents the electrical diagram representing the model. Compartments are separated by a resistance Qi. Potential across the soma and the first two dendritic compartments is represented by a variable battery (Ej) and a variable resistor (Rj) to simulate synaptic input in parallel with the membrane capacitance (Cj). The last compartment (4), had a constant resting emf. **(C)** Further describes the electrical variable battery and resistance. Further explanation for the structure of the model can be obtained from the original manuscript. The model was used in conjunction with experimental data to support the hypothesis that the climbing fiber made multiple synaptic inputs on the proximal Purkinje cell dendrite. Reproduced with permission from Llinas and Nicholson (1976).

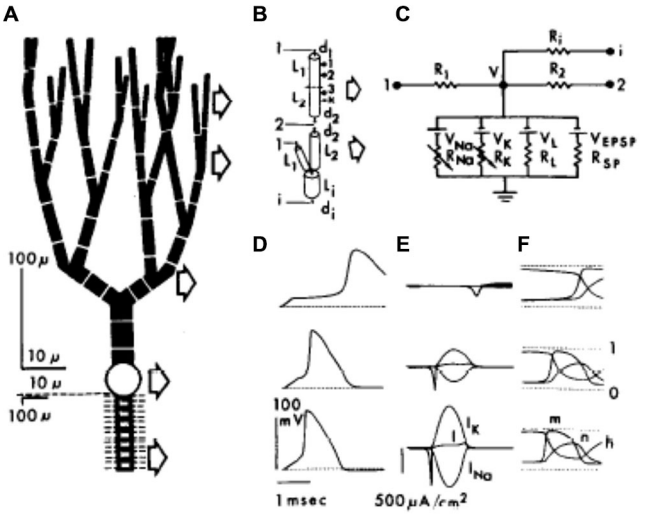

FIGURE 3 | The first full compartmental model of the Purkinje cell dendritic tree represented by 62 dendritic compartments (A), with each of the compartments (B) simulating ionic conductances using an equivalent electrical circuit (C). (D–F) show the responses of three different compartments after a simulated somatic current injection (dendritic branch point, upper row; soma middle row; node of Ranvier, lower row). Reproduced with permission from Pellionisz and Llinás (1977).

pg. 37) the model they reported still included no active voltage dependent dendritic conductances.

DEDUCING FUNCTION FROM STRUCTURE

In their original justification for building the first more realistic Purkinje cell model, Llinas and Pellionisz explicitly state that: "*Rigorous mathematical models of the electrical activity of central neurons (are) a powerful tool to test and interpret experimental data*" (Pellionisz and Llinás, 1977, p. 37). However, the model they actually published was clearly built to demonstrate the plausibility of dendritic mechanisms the authors had previously inferred from physiological results. In reviewing the cerebellar (and generally the neuroscience) modeling literature, this type of "demonstration model" is still the most common, with most published models specifically built to demonstrate the plausibility of one prior interpretation or another. Accordingly, these models are not intent on testing or interpreting experimental data, but instead on demonstrating the plausibility of a particular idea.

As described in the rest of this article, models can, and in the case of the cerebellar Purkinje cell have, instead been used to reveal unexpected and new interpretations of experiment and function. These models however, have been built first and foremost on anatomical structure and to replicate basic physiological responses, making as few functional assumptions as possible. As also demonstrated in the following history, models of this sort are also more likely to result in the kind of model sharing by multiple investigators in multiple laboratories which in principle can lead to cooperation, accelerating progress and understanding.

The first published Purkinje cell model that explicitly set out to deduce function from structure, without assuming the function to begin with was published by Shelton (1985) using, for the first time, an actual anatomical dendritic reconstruction of a real Purkinje cell (**Figure 4**). While structurally realistic, this model, like the earlier Purkinje cell models, did not include active dendritic properties, an omission justified by the authors assertion that: "*the part of the dendritic tree of the Purkinje cell which is thought to be essentially passive forms a very large fraction of the total membrane surface area of the cell*" (Shelton, 1985, p. 111), although the author later notes that dendritic passivity is an assumption of the model, rather than a conclusion. Instead the model was used to provide a description of the expected passive electrical properties of the Purkinje cell given the morphology of its dendrite. This was accomplished by tuning the model to replicate experimentally observed differences in dendritic and somatic input conductances. It should be noted that while this model was built on an actual anatomical reconstruction of a rat Purkinje cell, for technical reasons the only physiological data available was from Guinea Pigs. Accordingly the author

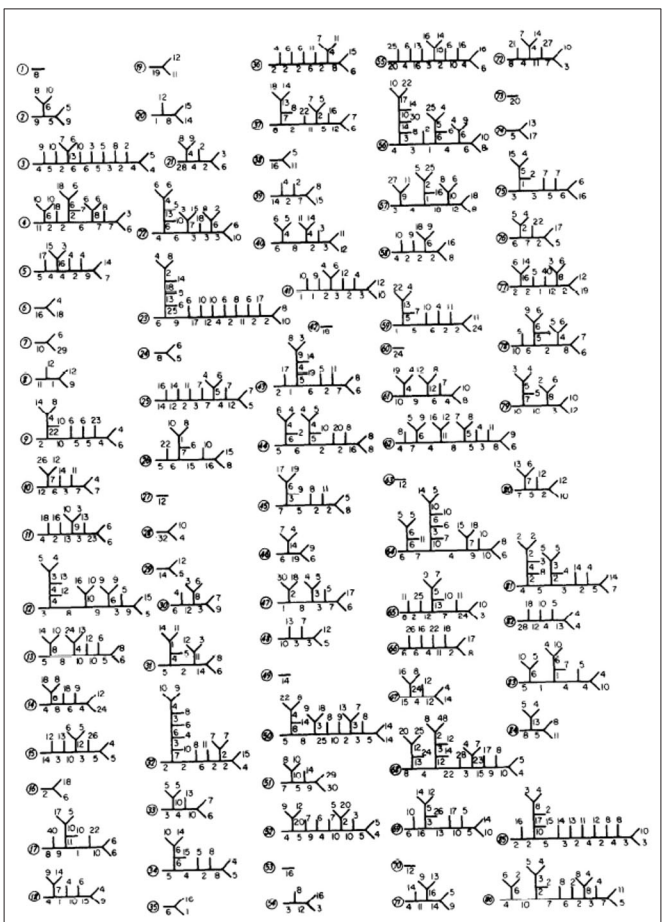

FIGURE 4 | From Shelton (1985) showing details of each of the modeled Purkinje spiny dendritic branches. Used with permission from Shelton (1985).

"stretched" the rat dendrite to better resemble a Guinea Pig Purkinje cell. In regard to the possible active properties of the Purkinje cell dendrite, Shelton's explicitly stated that his exploration of the passive properties of the dendrite should "*form the substrate for extensions which would treat more complex properties*" (Shelton, 1985, p. 111).

Reflecting Shelton's original intent, the next realistic model of the cerebellar Purkinje cell was published by Rapp et al. (1994, p. 114) explicitly as "*an essential step—a skeleton—for constructing biologically more realistic models of PC dendrites*". These authors, who based their model on Guinea Pig morphology, also explicitly tested Shelton's speculated on the possible influence of active synaptic conductances on passive membrane properties by applying the first synaptic inputs to the dendrite (Rapp et al., 1992). The Rapp et al. modeling publications also, for the first time, included new experimental data obtained by the author's specifically to parameterize the model, while also considered in some detail the application of newly developed parameter estimation methods for large compartmental models (Holmes and Rall, 1992). Rapp et al. (1994) also tested their results using different reconstructed dendritic morphologies. Harkening back to the original controversy about the appropriate form of modeling to explore dendritic function, these authors also explicitly compared compartmental modeling results to analytical cable model solutions pioneered by Rall (1964), Calvin and Hellerstein (1969), Zucker (1969) and Segev et al. (1985). In publishing their model, Rapp et al. (1994, p. 114) however, explicitly stated, once again, that it was now essential that Purkinje cell models, "*incorporate a variety of non-linear voltage- and ligand-gated channels that we know exist in the Purkinje cell dendrite*".

Returning to the community model sub-theme for this article, in addition to being the first Purkinje cell model (and one of the first in neuroscience) to be based on an actual anatomically reconstructed dendrite, the Shelton model was also the first Purkinje cell model whose components were reused by other modelers (Bush and Sejnowski, 1991; Genet et al., 2010; Blum and Wang, 1990; Brown et al., 2011), in each case adding active dendritic properties to the model. However, once again, in each modeling study, the intent was to demonstrate a previous idea about the functional significance of this property.

While Shelton's model was the first realistic Purkinje cell model, and was used by others to build new models, these versions of the Shelton models have not generated further versions. Likely this is due in part to the fact that these models were intended to demonstrate, rather than discover function, but also because the models were not written in a form easily transmitted to others. Instead, it is the original Rapp et al. (1992, 1994) Purkinje cell model (**Figure 5**) that lead to the model that has emerged as "*among the most successful, cited, and re-used/updated in computational neuroscience*" (Ascoli, 2007, p. 156). It is clear from the history that my laboratory played a critical role, first by translating the Rapp model into GENESIS, the general purpose simulator also built in my laboratory (Bower and Beeman, 1995, 2007) and second, because by adding a full set of active conductances to the model, independent of a set of underlying functional assumptions or objectives. This second feature of our modeling efforts I think is especially important, because it means that other investigators don't have to "buy" our interpretations or assumptions about function.

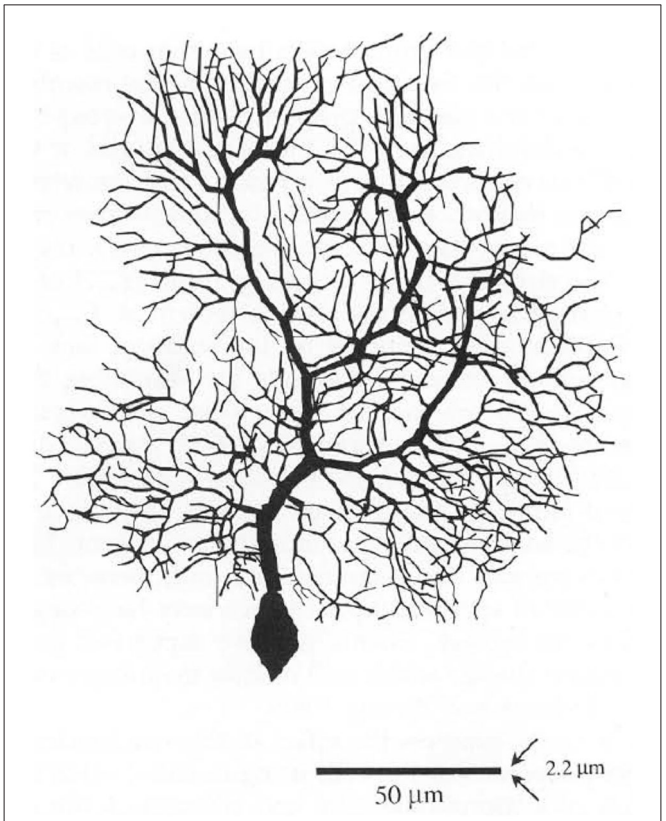

FIGURE 5 | The original Rapp et al Purkinje cell model, reconstructed from a Guinea Pig. Reproduced with permission from Rapp et al. (1992).

After obtaining a copy of the model from Rapp and colleagues even before their final article was published (De Schutter et al., 1993; Jaeger et al., 1993), we used GENESIS to included 10 active conductances differentially distributed in the soma and dendrite, parametrized on data from a wide range of *in vitro* voltage clamp experiments. The initial model-based results of the consequences of active dendritic processes for the basic physiological responses of recorded Purkinje cells were published in a series of three articles published in De Schutter and Bower (1994a,b,c). The first of these articles De Schutter and Bower (1994a) explicitly extended the work of Shelton (1985) and Rapp et al. (1992, 1994) with an analysis of the electrical structure of the Purkinje cell dendrite now including active voltage dependent conductances (**Figure 6**). The second article De Schutter and Bower (1994b) explored dendritic responses to climbing fiber input extending the study of the model to understand the possible influence of background excitatory synaptic inputs again first explored by Rapp et al. (1992, 1994) but now also including inhibitory synapses. The third article considered for the first time the response of an active Purkinje cell dendrite to the type of synaptic activity expected to result from stimulus driven input (De Schutter and Bower, 1994c). As the first neuronal model to use concurrent supercomputers (De Schutter and

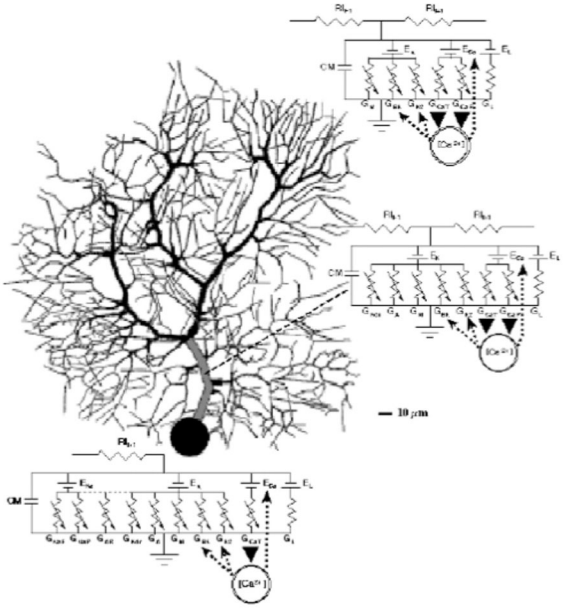

FIGURE 6 | Schematic description of the De Schutter and Bower Purkinje cell model with equivalent circuit diagrams for the modeled ionic conductance included in each section of the cell. Reproduced with permission from De Schutter (1999).

Bower, 1992), these simulations involved a much more extensive test of parameter space than previously possible, demonstrating that modeled responses were quite robust to changes in its primary parameters. Importantly for the reuse of this model by others, the use of the GENESIS simulation system specifically developed for sharing realistic neurobiological models (Bower and Beeman, 1995) made the Purkinje cell model one of the first if not the first published online (De Schutter, 1994). Again, availability of the model to anyone—its construction within a modeling platform, and I believe its focus on physiological rather than functional interpretations has led this model to be one of the first, if not the first community model in neuroscience.

EMERGENCE OF A COMMUNITY PURKINJE CELL MODEL

The articles by Rapp et al. (1992, 1994) and De Schutter and Bower (1994a,b,c) have collectively been cited more than 500 times, with the first description of the active Purkinje cell model De Schutter and Bower (1994a) responsible for almost half those citations. Importantly, the model, we now refer to as the "R-DB model", has formed the basis for considerable subsequent work from my own students both within my laboratory (Jaeger et al., 1996; Baldi et al., 1998; Sultan and Bower, 1998; Jaeger and Bower, 1999; Mocanu et al., 2000; Santamaria et al., 2002, 2007; Santamaria and Bower, 2004; Lu et al., 2005, 2009; Cornelis et al., 2010) and within their own independent laboratories and research (Staub et al., 1994; De Schutter, 1998; Vos et al., 1999; Howell et al., 2000; Steuber and De Schutter, 2001, 2002; Gauck and Jaeger, 2003; Solinas et al., 2003, 2006; Kreiner and Jaeger, 2004; Koekkoek et al., 2005; Santamaria et al., 2006, 2011; Shin and De Schutter, 2006; Shin et al., 2007; Steuber et al., 2007; Achard and De Schutter, 2008; De Schutter and Steuber, 2009; Anwar et al., 2012, 2013, 2014; Coop et al., 2010; Tahon et al., 2011; Cao et al., 2012; Couto et al., 2015). Perhaps more importantly the R-DB model has become a true "community model" as it is now being used by a growing number of authors as a base for further modeling work outside its laboratories of origin (Coop and Reeke, 2001; Mandelblat et al., 2001; Miyasho et al., 2001; Roth and Häusser, 2001; Chono et al., 2003; Khaliq et al., 2003; Steuber and Willshaw, 2004; Ogasawara et al., 2007; Yamazaki and Tanaka, 2007; Kulagina et al., 2008; Traub et al., 2008; Brown et al., 2011; Brown and Loew, 2012; Forrest et al., 2012; Forrest, 2015; Masoli et al., 2015). Several of these modeling efforts have now started their own lineage sequences, with, for example, the adaptation of the original R-DB Model by Miyasho et al. (2001), being further extended by Chono et al. (2003), Kulagina et al. (2008), and Brown et al. (2011). Importantly, the model has also been translated from the original GENESIS files to multiple other modeling platforms. As described in this next section, much of that modeling work has been focused on replicating and understanding the complex responses of Purkinje cells resulting from the active properties of its dendrite.

One of the first uses of the R-DB Model outside of my own laboratory's lineage, explicitly tested the model's ability to replicate PC responses obtained from new *in vitro* experimental studies using ion channel blockers (Miyasho et al., 2001). Using dendritic morphology from the rat (Shelton, 1985) parameterized with data from the R-DB Model, Miyasho et al. (2001) modified channel descriptions and conductance densities to reproduce the repetitive Ca^{2+} spike firing they had found experimentally after the application of TTX *in vitro*. Importantly, these authors also refined the kinetics of the K^+ delayed rectifier current, applying a new mechanism for calculating intracellular Ca^{2+} concentration while also changing the Ca^{2+} sensitivity of the calcium-activated dendritic K^+ conductance. With these changes, the model was extended to replicate physiological responses including: (1) characteristic Ca^{2+} dendritic spikes in the presence of TTX; (2) repetitive Ca^{2+} spiking patterns resulting from the presence of TTX; (3) the lack of Ca^{2+} spikes found after application of a P-type Ca^{2+} channel blocker; (4) the slow onset of the Ca^{2+} spikes in response to a depolorizing current steps; and (5) the marked shortening of the Ca^{2+} spike onset seen in the presence of 4-AP. Two years later, Chono et al. (2003) further refined the Miyasho et al. (2001) model by adding new channel descriptions as well as refinements in the conductance values for the simulated Ca^{2+} and Ca^{2+} dependent K^+ channels. These enhancements have since been incorporated into Purkinje cell modeling efforts by other groups (Traub et al., 2008; Brown et al., 2011).

Having extended the ability of the R-DB Model to replicate physiological data obtained under new pharmacological conditions, Miyasho et al. (2001) then explored the possible contribution to dendritic calcium spike generation of two low threshold dendritic calcium related conductances they had recently discovered in their own experimental studies (Watanabe et al., 1998). Adding Ni^{2+} sensitive Ca^{2+} channels to the

dendrites, these authors demonstrated that the model could now replicate the longer onset Ca^{2+} spikes found in the presence of Ni^{2+}.

This is the kind of cumulative refinement and advancement that can best, or perhaps can only take place with community models. However, equally important to changes in the structure of a community model, is the use of that model to explore new forms of behavior or perform new forms of analysis not considered by the original model's authors. To this end, several authors have used the R-DB Model in a reduced from to more closely examine neuronal dynamics (Mandelblat et al., 2001; Fernandez et al., 2007). In a series of publications, Brown et al. (2011) adapted the original R-DB Model to explore how mechanisms at the subcellular (biochemical) levels could be linked to somatic output (Rapp et al., 1992; Brown et al., 2011; Brown and Loew, 2012). While building a new model in Fortran, Traub et al. (2008) never-the-less extended R-DB Model parameters to explore the possible role of gap junctions between the initial axon segments of Purkinje cells in cerebellar cortical oscillations. To do so, he reduced overall dendritic complexity while maintaining a "realistic" path from the distal dendrite to the soma (see **Figure 7**).

The R-DB Model is also now being used in the context of both subcellular and network level scales. Sub-cellularly, the model has been used as a base to consider the effects of molecular or biophysical mechanisms on Purkinje cell function (Holmes and Rall, 1992; Brown et al., 2011; Brown and Loew, 2012), and to provide a larger context for studies of subcellular modeling of calcium diffusion (Santamaria et al., 2006, 2011; Anwar et al., 2012) as well as biophysical mechanisms of synaptic plasticity (Vladimirescu et al., 1981; Antunes and De Schutter, 2012; De Schutter, 2013). The model has also been used to build network level simulations in reduced (Yuen et al., 1995; Coop and Reeke, 2001; Sarro, 2004), and full form (Howell et al., 2000; Solinas et al., 2003; Santamaria et al., 2007).

The R-DB model has also been applied to new analytical studies, including, for example, questions involving the information processing potential of dendrites (Coop et al., 2010) as well as possible spike coding strategies (Jaeger and Bower, 1999; Steuber and De Schutter, 2001, 2002; De Schutter and Steuber, 2009). Efforts have also been made to link the structure of the R-DB Model to the kind of analysis involved in the field of artificial neural networks (Steuber and De Schutter, 2001; Sarro, 2004).

Finally, the R-DB Model is being used as a base for assessing modeling technology itself, including parameter estimation techniques (Van Geit et al., 2007) and the relationship between parameter variations and modeling results (Achard and De Schutter, 2008).

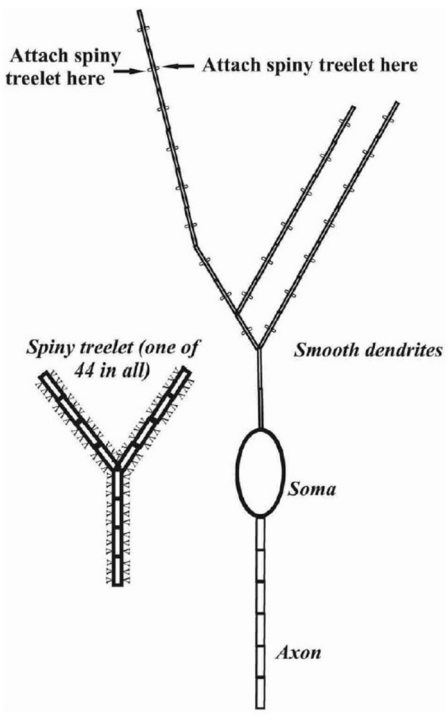

FIGURE 7 | Schematic representation of the cerebellar Purkinje cell model in Traub et al. (2008). Reflecting the focus of the study on putative gap junctions between the initial axon segments of Purkinje cells, this axonal region was represented by six compartments while the dendrite was reduced to 553 compartments with a particular emphasis on the spiny branchlets. Used with permission from Traub et al. (2008).

UNDERSTANDING PURKINJE CELL RESPONSES TO DIFFERENT TYPES OF INPUT

Having established the community status of the R-DB model, the remainder of this article will consider what has been learned as a result of the use of the model. While general reuse and improvement are important, ultimately the utility of any model, whether used by the community or not, is its ability to generate and truly test hypothesis regarding function (De Schutter, 1999). This is also the most complex and challenging application for any model, especially given the tendency of all scientists to want to see what they want to see. Accordingly especially important, in my view, is a clear establishment of community standards for model performance. In this regard, the next section is organized around a set of Purkinje cell behaviors actually identified by Pellionisz and Llinás, (1977, p. 42) as necessary for, "*any Purkinje cell model which claims to be adequate*". As described in subsequent sections of this article, all of these behaviors turn out to depend on the active properties of the Purkinje cell dendrite, and replicating and understanding these core response properties has provided the basis for further analysis of the functional significance of active dendritic processes.

Antidromic Spike Activation of the Purkinje Cell Dendrite

Perhaps the most straightforward characteristic Purkinje cell response, identified by Pellionisz and Llinas, is the fact that action potentials generated in the Purkinje cell soma do not propagate into its dendrite (**Figure 8**). At the time of the first Purkinje

cell modeling studies, this lack of antidromic dendritic invasion had already been predicted based on field potential recordings (Llinas et al., 1969b; Freeman and Nicholson, 1975), although the phenomenon was not directly observed experimentally until much later (Llinas and Sugimori, 1980b). In the early passive models, the lack of back propagation was attributed to the relative surface area of the cell dendrite compared to its soma (Pellionisz and Llinás, 1977; Rapp et al., 1994). This explanation was further elaborated in another passive modeling study using parameters obtained from the R-DB Model (although with different dendritic morphology) as due to a large cumulative impedance mismatch resulting from the high branching density of the Purkinje cell dendrite (Roth and Häusser, 2001). With respect to active dendritic mechanisms the models have shown that the very low Na^+ channel density in Purkinje cell dendrites provides no mechanism to overcome these morphological effects (De Schutter, 1999; Kitamura and Häusser, 2011) a result also reported in models of other types of mammalian neurons (Vetter et al., 2001).

Responses to Somatic Current Injection

It has been known since intracellular recordings were first made in Purkinje cells, that their response to current injection is complex (Llinas and Sugimori, 1980b). The modeling results shown in **Figure 8** were obtained from a passive Purkinje cell dendritic model after current injection in the soma. In fact, as shown in **Figure 9**, current injection in a real Purkinje cell (and the active R-DB model), produces a much more complex pattern of somatic and dendritic activity (Gähwiler and Llano, 1989; Hirano and Hagiwara, 1989; Kaneda et al., 1990; Regan, 1991; Wang et al., 1991; Lev-Ram et al., 1992). In part for this reason, although not explicitly a part of the original Pellionisz and Llinás (1977) standard for Purkinje cell models, the ability to replicate the results of *in vitro* current injection studies has become the defacto standard for testing and tuning active Purkinje cell models (Bush and Sejnowski, 1991; De Schutter and Bower, 1994b; Coop and Reeke, 2001; Mandelblat et al., 2001; Miyasho et al., 2001; Forrest et al., 2012).

While a full description of the mechanisms responsible for these *in vitro* response patterns is beyond the scope of this article, the general result from modeling studies is that this behavior of the Purkinje cell is a function of a complex interaction between all its biophysical and anatomical properties (De Schutter, 1999). This conclusion is somewhat in contrast with the more typical analysis from experimental studies which usually associate different features of the *in vitro* response properties to specific kinds of afferent input (Gähwiler and Llano, 1989; Hirano and Hagiwara, 1989; Kaneda et al., 1990; Regan, 1991; Wang et al., 1991; Lev-Ram et al., 1992; Miyasho et al., 2001), i.e., fast events associated with somatic action potential generation; the somewhat slower Ca^{2+} related dendritic bursting behavior assumed to be related to climbing fiber inputs; and longer time course events assumed to be influenced by granule cell related synaptic inputs (Traub et al., 2008; Brown et al., 2011; Isope et al., 2012; Kitamura and Kano, 2012). The models clearly show that these responses are actually related to the entire structure of the Purkinje cell and the interaction between its different afferent inputs. Bursting responses to climbing fiber inputs, for example, are also dependent on the level of background granule cell synaptic input.

It turns out that this co-dependence discovered in the models sheds new light on the importance of the experimental conditions under which Purkinje cells are studied. For example, it has actually been known for many years that the spontaneous behavior of Purkinje cells *in vitro* is quite different from

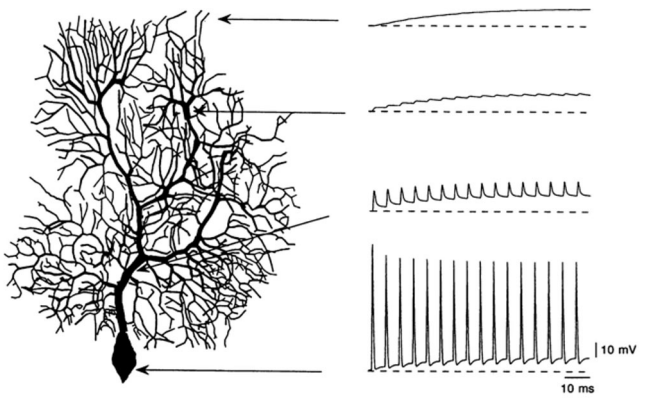

FIGURE 8 | Simulation of the lack of antidromic action potential dendritic invasion in a modeled Purkinje cell following simulated current injection in the soma. Used with permission from Rapp et al. (1994).

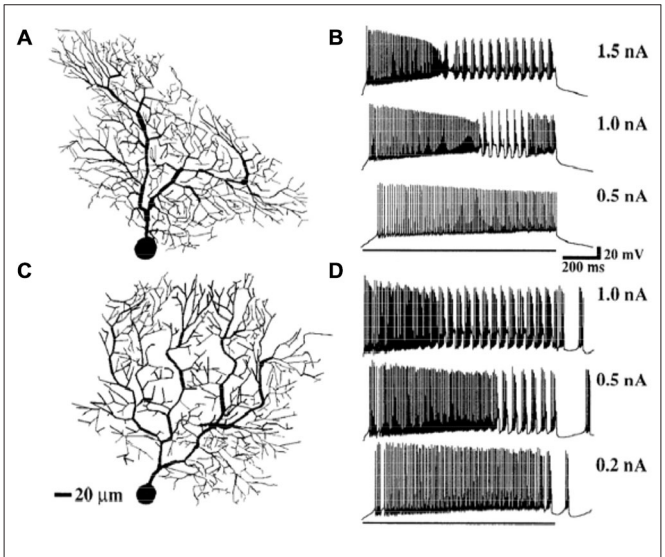

FIGURE 9 | Simulation of somatic responses to three different amplitude synaptic current injections in two models with different dendritic morphologies. Model **(A)** produced responses **(C)**, Model **(B)**, responses **(D)**. The results specifically replicate the typical rapid spiking to bursting pattern seen *in vivo* in response to somatic current injection. Given that identical amounts of current are injected, and each model has the same electrical parameters, the variations in response properties are due to the different morphologies of the modeled cells. Reproduced with permission from De Schutter and Bower (1994a).

the spontaneous behavior of Purkinje cell *in vivo* (Llinas and Sugimori, 1980b). As shown in the modeling results of **Figure 10A**, *in vitro* behavior consists of relatively rapid (usually >100 Hz) action potentials, interrupted periodically by spontaneous dendritic calcium spikes. In contrast, as simulated in **Figure 10C**, Purkinje cells *in vivo* generate spontaneous action potentials at lower frequencies (usually <80 Hz) that are quite irregular. Dendritic Ca^{2+} spikes are also believed to only appear *in vivo* in response to climbing fiber inputs (Llinas and Nicholson, 1976) whereas *in vitro* they occur spontaneously. Understanding how the response properties of the cell changes *in vitro* is important given how much of the study of the active properties of neurons has been done using this technique. What modeling results have suggested is that it is the lack of background synaptic input in what is essentially a deafferented brain slice preparation that is reasonable for differences in *in vivo* and *in vitro* behavior (Jaeger et al., 1996). Perhaps particularly important in Purkinje cells which are known to receive 150,000 excitatory parallel fiber inputs. However, when provided with background excitatory input alone, the R-DB Model produced a pattern of output that resembled neither the *in vitro* nor *in vivo* conditions (**Figure 10B**; De Schutter, 1999). Instead, replication of *in vivo* patterns required spontaneous input from both excitatory and inhibitory synaptic inputs (**Figure 10C**). Accordingly, the models predict both in single cell (Jaeger et al., 1996; Watanabe et al., 1998) and network form (Howell et al., 2000) that normal Purkinje cell behavior likely depends on current from constant background synaptic inputs, interacting with the active Ca^{2+} and K^{+} dependent channels in the dendrite and soma (De Schutter, 1998). Experimental studies specifically designed to test these modeling predictions are consistent with this interpretation (Jaeger and Bower, 1999; Kreiner and Jaeger, 2004). Realistic models have therefore provided an essential tool to relate *in vitro* response properties to the natural *in vivo* behavior of Purkinje cells especially challenging given the complexity of this cells active dendritic properties.

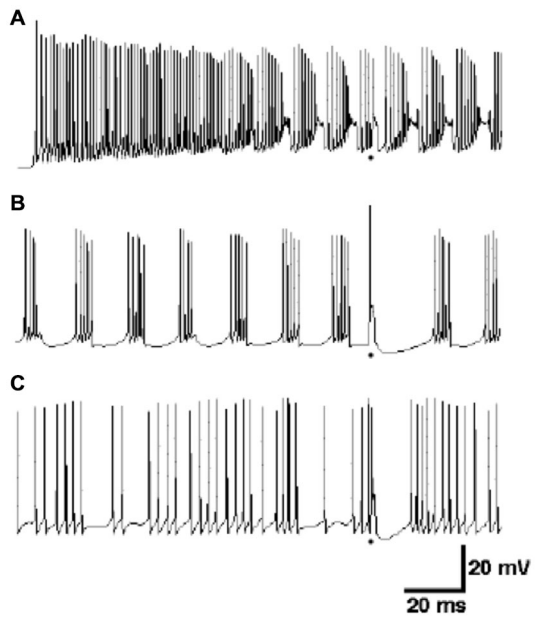

FIGURE 10 | Comparison of responses of the R-DB Model in the absence of background synaptic input to the dendrite (A), in the presence of only excitatory synaptic input (B) and both excitatory and inhibitory input (C). As described in the text, the firing pattern in **(A)** resembles Purkinje cell activity recorded *in vitro*, while **(C)** resembles *in vivo* activity. Figure used with permission from De Schutter (1999).

Purkinje Cell Responses to Climbing Fiber Activation

The fact that the Purkinje cell responds to climbing fiber activation *in vivo* with a burst of action potentials has been known for many years (Eccles et al., 1966b). In fact as already noted, the first compartmental Purkinje cell model was specifically constructed to test this experimentally derived prediction (Llinas and Hillman, 1969) that this response behavior was a consequence of the multiple synaptic contacts distributed over the Purkinje cell dendrite by a single climbing fiber (Llinas and Nicholson, 1976), with subsequent modeling focused on the actual biophysical mechanisms responsible for producing the "oscillatory wavelets" or "spike burst" characteristic (see **Figure 11F**) of climbing fiber responses (Pellionisz and Llinás, 1977). At the time, these authors concluded that the different peaks in the somatic burst response were generated by repetitive firing of the initial segment of the axon rather than by an active dendritic mechanism as had been previously proposed (Eccles et al., 1966b).

Neither Shelton (1985) nor Rapp et al. (1992, 1994) attempted to replicate Purkinje cell responses to climbing fiber activation, however, this was an important component of the initial analysis of the active dendritic and somatic model of De Schutter and Bower (1994b). In fact, after tuning model parameters to replicate responses to somatic current injection data, the ability of the model to generate climbing fiber burst responses without further tuning parameters was the first indication of the model's likely realism (see **Figure 11**). As already described, the model predicted that the correct *in vivo* form of the climbing fiber response was dependent on background patterns of excitatory and inhibitory synaptic input. However, analysis of the model also predicted that the dendritic response was dependent on the activation of P type Ca^{2+} channels in both the cells smooth and the spiny dendrites, with the duration of the dendrite spike being regulated by Ca^{2+} activated K^{+} conductances. The modeling results also suggested that the biphasic reversal potential of the climbing fiber induced EPSP, with an early portion reversing before the later portion (i.e., the climbing fibers "duel reversal potential") previously shown experimentally (Llinas and Hillman, 1969) and attributed solely to the spatial distribution of climbing fiber synapses (Llinas and Nicholson, 1976) was also likely dependent on the details of the active properties of the Purkinje cell dendrite. Further, an unexpected but important prediction of the model was that climbing fiber activation resulted in substantial increases in intracellular calcium not only in the smooth dendrites,

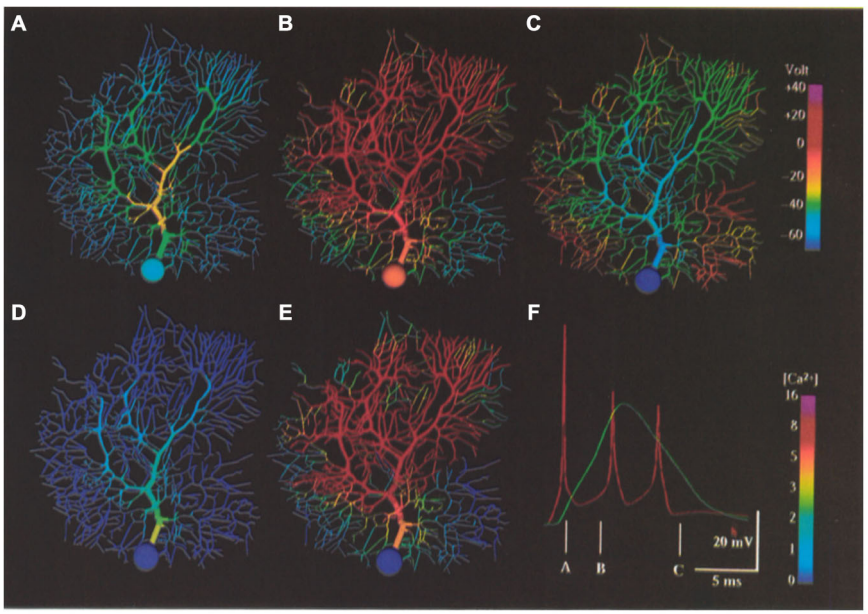

FIGURE 11 | False color representation of membrane potential and Ca^{2+} concentration during simulation of a climbing fiber input. (A) Membrane potential 1.4 ms after beginning of the resulting complex spike. **(B)** Membrane potential 4.0 ms after beginning of complex spike. **(C)** Membrane potential 10.0 ms after beginning of a complex spike (after the last somatic action potential). **(D,E)** Submembrane Ca'+ concentration at same times as **(A,B)**, respectively. **(F)** Complex spike as it appears in the soma (red) and distal dendrite (green) at the same times represented by **(A–C)** as indicated. Note the non-linear [Ca'+] scales. Figure used with permission from De Schutter and Bower (1994a).

where climbing fiber synapses actually terminate, but also in the smallest spiny dendritic branches receiving granule cell synaptic inputs (Gundappa-Sulur et al., 1999; Lu et al., 2009) again showing the interrelatedness of the anatomical and physiological components of the dendrite. The involvement of the entire dendrite in the climbing fiber event was simultaneously shown experimentally (Konnerth et al., 1992; Miyakawa et al., 1992). The model also predicted that inhomogeneity in local levels of calcium activation in the dendrite did not depend on a non-uniform distribution of Ca^{2+} channels as had previously been proposed Tank et al. (1988) and Llinas and Sugimori (1992). Instead the pattern of calcium response was a consequence of the non-uniform geometry of the Purkinje cell dendrite, and likely varied from Purkinje cell to Purkinje cell. Thus, unlike Rapp et al. (1994), who reported little effect of individual dendritic variations on cellular passive properties, the active model suggested that differences in individual Purkinje cell morphologies might, in fact have important functional significance.

Replication of the Simple Spike Firing of Purkinje Cells

The final, and it turns out most difficult standard for Purkinje cell modeling proposed by Pellionisz and Llinás (1977) was the ability to replicate simple spike firing in response to granule cell (parallel fiber) input. This is, of course, mor difficult because, in principle, understanding the important features of this behavior is likely linked directly to questions of neuronal coding, which we really know about nothing about. Never-the-less, it is the attempt to replicate this behavior of the Purkinje cell with the R-DB Model has produced the most interesting and provocative structural and functional predictions resulting in several new hypotheses regarding the cell's overall function and in fact the function of the cerebellum itself (Bower, 2002). The following sections will consider several examples.

The Natural Function of the Purkinje Cell Dendrite Depends on the Presence of Background Synaptic Inputs

As already described, one important prediction of the R-DB Model is that the natural behavior of the Purkinje cell dendrite depends on the presence of continuous excitatory and inhibitory synaptic input from the granule cell pathway. Again, while background excitatory granule cell (parallel fiber) synaptic activity had been anticipated for some time to influence ongoing Purkinje cell firing (Llinas et al., 1969a), in order to get realistic patterns of spiking out of the active Purkinje cell model it was necessary to also add background inhibitory synaptic inputs (De Schutter and Bower, 1994a). These modeling efforts resulted in several predictions. First the model predicted that Purkinje cell behavior was dependent on the ability of the soma, itself, to spontaneously generate action potentials. This ability has now been demonstrated experimentally (Pugh and Raman, 2009), and has recently also been further studied using a model derived from the R-DB line (Forrest et al., 2012). Second, as shown in **Figure 12**, the model predicted

that the large intrinsic voltage gated currents and not the relatively smaller currents associated with synaptic activation most influenced ongoing somatic spiking (Jaeger et al., 1996; De Schutter, 1998; Jaeger and Bower, 1999). In fact, the model predicted that the Purkinje cell dendrite is actually dominantly a current sink rather than a source, making the behavior of the Purkinje cell very different from that of a traditional integrate and fire neuron (see below). Further, the model suggested that background spontaneous parallel fiber inputs had much less of an effect on the actual timing of Purkinje cell spikes than did inhibitory synaptic input (Jaeger et al., 1996). While a full description of the dendritic dynamics underlying this behavior is beyond the scope of this chapter (for more details, see De Schutter and Bower, 1994b,c; Jaeger et al., 1996; De Schutter, 1999; Jaeger and Bower, 1999), experimental (Jaeger and Bower, 1999; Womack and Khodakhah, 2002a,b, 2004; Womack et al., 2004; Santamaria et al., 2007) and subsequent R-DB Model related studies (Howell et al., 2000; Miyasho et al., 2001; Coop et al., 2010; Brown et al., 2011; Forrest et al., 2012) have supported these unexpected but model-predicted interactions between the Purkinje cell dendrite and soma.

"Dendritic Democracy" and the Influence of Distal Synaptic Inputs

The influence of excitatory synaptic input in such a large dendrite has been a central issue for Purkinje cell modeling for many years. In fact, the publication by Llinas et al. (1968) that sparked the first consideration of modeling in Purkinje cells (Calvin and Hellerstein, 1969; Calvin, 1969; Zucker, 1969) started by posing the following fundamental question: "*In studying the anatomy of the Purkinje cell, one wonders how the distal region of (these large) dendrites can act upon the soma and axon . . .*" (Llinas et al., 1968, p. 1132). That article went on to identify two possibilities: *(i) by direct electrotonic spread from the distal dendrite to the soma, or (ii) by the initiation of action potentials or local responses which can be conducted either in an all- or-none manner or in a decremental fashion down to the axon.*" (Llinas et al., 1968, p. 1132). Considering this question was also a primary objective of the modeling efforts of both Shelton (1985) and Rapp et al. (1992, 1994), who both predicted, based on their passive models, that the Purkinje cell dendrite was actually electrotonically compact and therefore that distal synaptic inputs, in principle should have an influence on the soma similar to those more proximal. Shelton specifically describes the functional significance of the high passive dendritic input resistance as "*a specialization which optimizes the dendrites for signaling (the soma) with minimum (synaptic) attenuation*" (Shelton, 1985, p. 127). This apparent characteristic of the passive electrical properties of the Purkinje cell dendrite has been described as promoting "dendritic democracy" so that: "*somatic EPSP amplitude is only weakly dependent on synaptic location on Purkinje cell spiny branchlets*" (Roth and Häusser, 2001, p. 469).

In the description of the behavior of their passive models, Llinas et al. (1968), Pellionisz and Llinás (1977), Shelton (1985) and Rapp et al. (1994) all mentioned that this baseline "dendritic democracy" likely only applied to the passive electrical properties of the dendrite, and was therefore likely to change with the addition of active conductances. Shelton (1985, p. 128), specifically predicted that the addition of synaptic conductances would likely "*swamp*" the passive membrane conductivity significantly extending the electrotonic length of

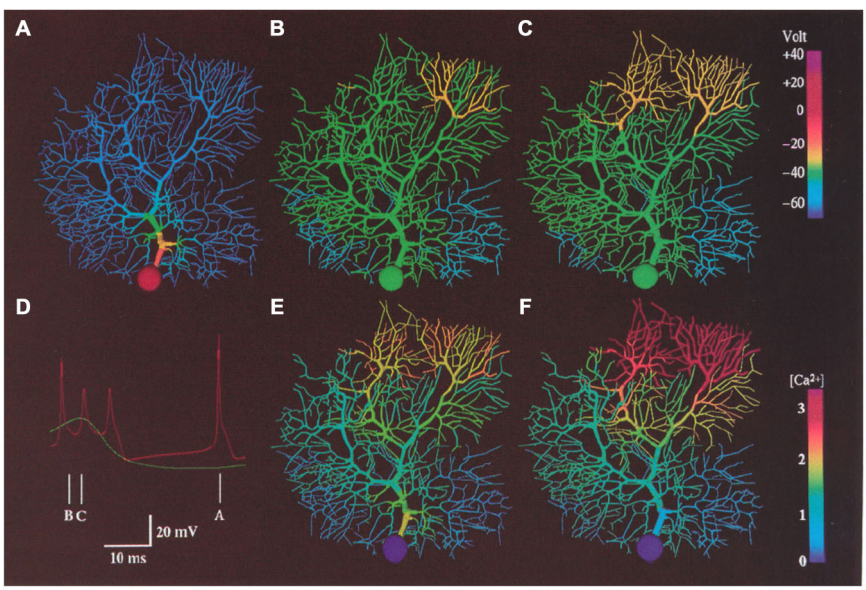

FIGURE 12 | False color representation of membrane potential and Ca^{2+} concentration during a 2.0 nA current injection in the soma of the modeled Purkinje cell. Simulated membrane potential is shown during a somatic action potential **(A)**, at the beginning of a dendritic spike **(B)** and 1.6 ms later **(C)**. **(D)** shows predicted somatic (red) and dendritic (Green) membrane potential at the times indicated. **(E,F)** indicated submembrane Ca^{2+} concentration at the same time as **(B,C)** respectively. Reproduced with permission from De Schutter and Bower (1994b).

the dendrite. Actual simulations by Rapp et al. (1992, 1994) again using a passive model, supported Shelton's speculation, predicting that individual parallel fiber synapses "*essentially loose their functional meaning (in the presence of large amounts of background synaptic input) and only activation of a large number of parallel fibers will significantly displace the membrane potential*" (Rapp et al., 1992, p. 530).

In fact, in our active dendritic models adding both synaptic conductances as well as the large voltage dependent dendritic Ca^{2+} related membrane conductances did further extend the electrotonic length of the dendrite (De Schutter and Bower, 1994b) a modeling result subsequently confirmed experimentally (Staub et al., 1994; Ascoli, 2007). However, as described in the third article in the series (De Schutter and Bower, 1994c), the addition of dendritic voltage dependent Ca^{2+} membrane conductances revealed a new and unexpected biophysical mechanism in which synchronously activated granule cell inputs induced a sub-threshold Ca^{2+} dependent amplification mechanism that restored "democracy" to the dendrite even in the presence of ongoing background synaptic input (**Figure 13**). While Llinas had suggested the general possibility that active membrane properties could facilitate the influence of synapses on the soma, and Shelton (1985, p. 128), specifically speculated that "*active dendritic spikes or active graded potentials may act as a booster mechanism to overcome the electrotonic lengthening of the dendrite due to synaptic activation*", the specific mechanism that emerged from the R-DB Model was unexpected. Instead of being dependent on a dendritic calcium spiking mechanism as previously assumed (Pellionisz and Szentágothai, 1974), the mechanism involved activation of a sub-spiking threshold calcium event (**Figure 13**). As a result, in these simulations, a small number of synchronously activated granule cell synaptic inputs produced a similar level of depolarization in the soma regardless of where they were located on the dendrite, a form of "dendritic democracy" that turned out to be dependent and reflect the actual temporal pattern of synaptic input. Further, and importantly, while generating a somatic spike in the passive dendritic models required the activation of large numbers of excitatory synapses (Llinas and Sugimori, 1980b; Rapp et al., 1992, 1994), the active model predicted that somatic spike generation due to synchronously activated synaptic input required an order of magnitude fewer active synapses (De Schutter and Bower, 1994c). This prediction was subsequently confirmed experimentally (Isope and Barbour, 2002). The model has also predicted a similar amplification effect on synchronized inhibitory inputs (Solinas et al., 2006).

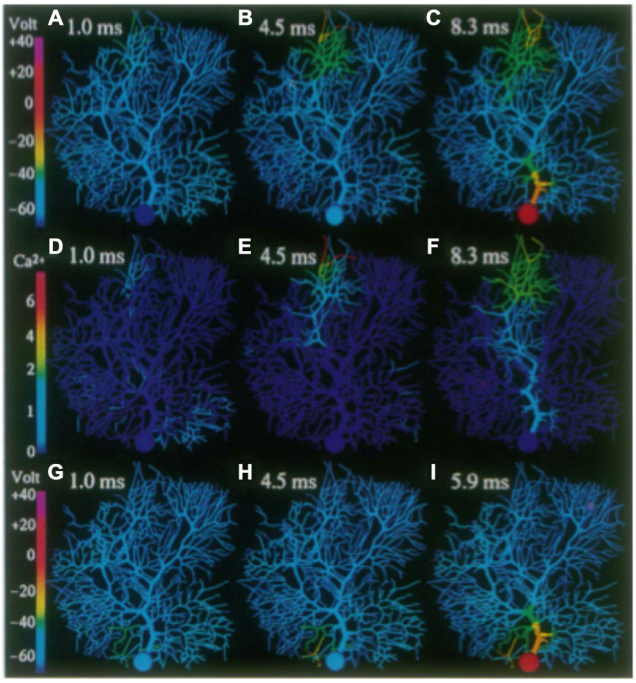

FIGURE 13 | False color images of the response of the R-DB Model to a synchronous synaptic input on a distal (A–F) and proximal (G-I) branchlet. Membrane potential in **(A–C)** and **(G–I)**. **(D–F)** Submembrane Ca^{2+} concentrations corresponding to activity in **(A–C)**. Reproduced with permission from De Schutter and Bower (1994c).

Purkinje Cells are Tuned to Operate in Context of Activity in the Overall Cerebellar Cortical Network

Another very general but critically important insight gained from the models is that understanding neuronal function requires that a neurons physiological properties be considered in the context of the network in which they are embedded, and in particular in the context of the temporal and spatial patterns of afferent information converging on that cell as a consequence of network structure. While this might at first seem completely obvious, by embedding the R-DB Model within realistic network simulations, very specific new predictions were obtained on this relationship (Santamaria et al., 2007). As with single cell modeling, it is our view that for models to generate new predictions (rather than simply demonstrate pre-conceived functional notions) network level modeling must also be tested against a clearly defined set of physiological behaviors, preferably not yet well understood (Bower, 1990). To be able to interpret the significance of the active properties of the Purkinje cell dendrite with respect to network organization, it will be necessary to first consider these network level physiological behaviors.

As it turns out the original motivation for cerebellar modeling in my laboratory was to investigate an unexpected and counterintuitive pattern of Purkinje cell responses to peripheral sensory stimuli (see **Figure 14**) observed *in vivo* (Bower and Woolston, 1983). Specifically, the spatial extent of Purkinje cell responses to peripheral stimuli was found to be far more restricted than was expected from the organization of cerebellar cortical circuitry and in particular the considerable anatomical spread of the parallel fibers within cerebellar cortex (Eccles et al., 1967, 1971; Bell and Grimm, 1969; Bower and Woolston, 1983). Results consistent or directly supporting this finding have now been reported in numerous subsequent experiments (Kolb et al., 1997; Cohen and Yarom, 1998; Lu et al., 2005; Holtzman et al., 2006; Heck et al., 2007; Rokni et al., 2008; de Solages et al., 2008; Brown

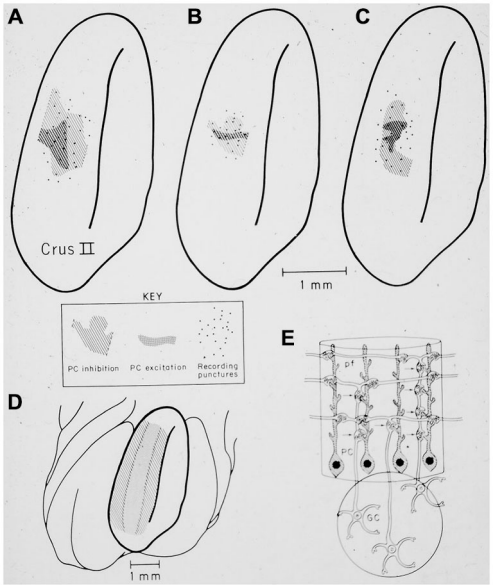

FIGURE 14 | (A–C) show the restricted spatial pattern of excitatory (dark stippling) and inhibitory (light hatching) Purkinje cell responses following peripheral stimulation in three experiments. The stimulus activated only granule cells beneath the region of excitatory PC responses. **(D)** shows the expected pattern of activation if parallel fibers drove Purkinje cell responses. **(E)** Original drawing from Llinas (1982) illustrating the hypothesis that synapses associated with the ascending segment of the granule cell axon drove the excitatory Purkinje cell responses. Reprinted with permission from Bower and Woolston (1983).

and Ariel, 2009; Walter et al., 2009; Dizon and Khodakhah, 2011).

In the original experimental studies published in the early 1980's, the restricted extent of Purkinje cells activated by peripheral stimuli was interpreted in the most obvious way by suggesting that parallel fibers were simply less influential on Purkinje cell output than had previously been assumed (Bower et al., 1980; Bower and Woolston, 1983). However, it was not clear why responding Purkinje cells were only found over regions of active granule cell layer. In Llinas (1982) suggested that this experimental result (Bower et al., 1980; Bower and Woolston, 1983) could be explained if Purkinje cells were driven by synchronous input from synapses made by granule cells as they ascend through the molecular layer past the Purkinje cell dendrite (Mugnaini, 1972), but not by more asynchronous parallel fiber inputs (Llinas, 1982). Llinas, however, attributed this effect simply to the reduced synchrony of parallel fiber inputs.

When considered now in the context of the R-DB Modeling results, this explanation seemed perfectly consistent with the relative lack of direct influence of background parallel inputs on Purkinje cell spiking, combined with the amplification mechanism for synchronize excitatory inputs (De Schutter and Bower, 1994c). Accordingly it was fully expected that the R-DB Model, once placed in a network context, would confirm Llinas speculation, that the effect simply had to do with the timing of the different synaptic inputs. It was surprising therefore, that even the most desynchronized pattern of parallel fibers, still induced the dendritic boosting mechanism driving somatic output (Santamaria et al., 2007). Resolving this difference between experimental data and modeling results required the introduction of feed-forward inhibitory synaptic inputs to the network model (Santamaria et al., 2007; Walter et al., 2009).

The modeling efforts intended to replicate the restricted pattern of Purkinje cell activation to afferent input (Bower and Woolston, 1983), have perhaps most fundamentally changed how we think of cerebellar cortical processing (Bower, 2010). While most previous theories of cerebellar function have focused on the parallel fiber system as the primary driver of Purkinje cell somatic firing (Braitenberg, 1967; Marr, 1969; Albus, 1971; Pellionisz and Szentágothai, 1974; Medina and Mauk, 2000; Vetter et al., 2001; Heck and Sultan, 2002; Ito, 2006; Kitamura and Kano, 2012), model analysis suggests that it is actually the synapses associated with the ascending segment of the granule cell axon, firing nearly synchronously and not the parallel fibers, which influence spike timing in the soma (De Schutter and Bower, 1994c). Further, the model has also predicted that ongoing somatic spiking activity is not directly influenced by synaptic input, but instead is mediated through the large active conductances in the soma and dendrite. In this view, the synchronous ascending input simply modifies the timing of action potentials that would have been generated anyway (Santamaria and Bower, 2004).

As just briefly described, perhaps one of the more important consequences of the modeling effort has been to clarify and make quite clear predictions regarding different functional roles of the parallel fibers and the ascending segment synapses of the same granule cell axon (Bower, 1997c). While parallel fiber inputs modulates the overall state of the dendrite, it is the ascending segment inputs that more closely drive output. Interestingly, this functional difference turns out to actually be manifest in the fine physical structure of the Purkinje cell dendrite itself. As shown in **Figure 15**, anatomical studies have demonstrated that the synapses associated with the ascending granule cell axon segments are found only on the distal regions of the dendrite (Gundappa-Sulur et al., 1999; Lu et al., 2009), where our network models predict that these synapses will be synchronously active in response to afferent mossy fiber stimuli (Santamaria et al., 2007). Our single cell models predict that the active properties of the dendrite mediate a boosting mechanism allowing this distant input to influence somatic spiking (De Schutter and Bower, 1994c). Anatomical studies have also shown that parallel fiber synapses are found primarily on the more proximal spiny dendrites (Gundappa-Sulur et al., 1999; Lu et al., 2009), where both the network (Santamaria et al., 2007) and single cell (Jaeger et al., 1996) models suggest they interact with feed forward inhibition to regulate the activation state of the large dendritic voltage dependent Ca^{2+} and Ca^{2+} activated K^{+} conductances. This places parallel fibers in a position to influence or modulate, the response of the dendrite to the synchronous ascending segment synapses. The models predict that this modulation by the parallel fibers and molecular layer inhibition is mediated through their control of the membrane voltage in the dendrite, and thus the state of activation of the large

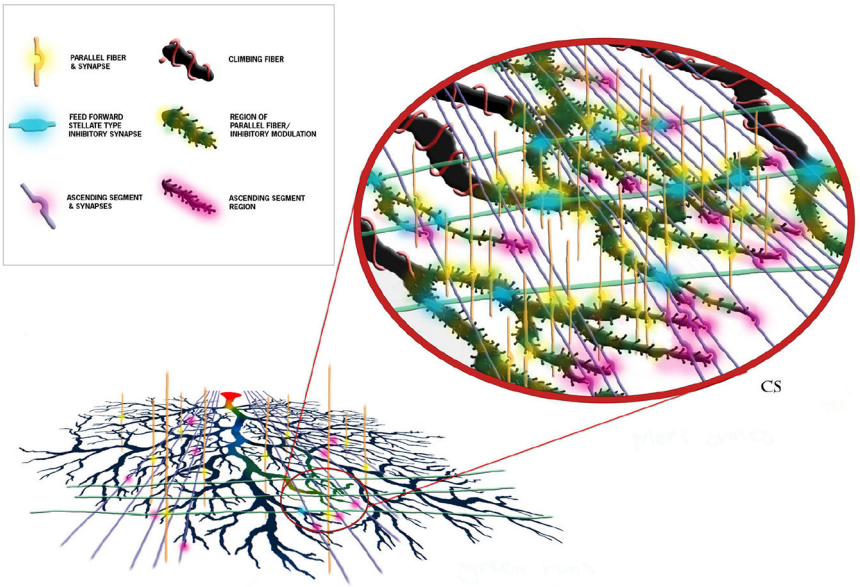

FIGURE 15 | Schematic representation of the proposed synaptic and functional structure of cerebellar Purkinje cells. Each element and region is color coded as shown in the figure legend. The diagram demonstrates that the influence of ascending segment synapses must traverse regions of the spiny dendrite influenced by parallel fibers and molecular layer inhibitory interneurons. This is predicted to form the anatomical basis for parallel fiber modulation. Reproduced with permission Bower and Bower (2013).

dendritic voltage dependent conductances. Thus the same active voltage dependent dendritic conductances are responsible for mediating the amplification mechanism for distal synchronous ascending segment inputs as well as the spiking behavior of the soma in general (Bower, 2010). As an aside, these results also suggest that climbing fiber activation resets these modulatory mechanisms (Bower, 1997b), a role consistent with another original prediction of the R-DB Model, that calcium influx from climbing fiber activation would spread to the distal most regions of the dendrite (De Schutter and Bower, 1994b). In this way, the use of anatomically and physiologically realistic models has resulted in predictions that, in effect, merge the anatomical and physiological properties of this cell. In my view, this is what is meant by exploring structure function relationships. Importantly again, the models were not built with these relationships in mind, they came out of running the models.

IMPLICATIONS AND THE IMPORTANCE OF COMMUNITY MODELS

In summary, while it was first suggested more than 40 years ago that the active properties of the Purkinje cell dendrite significantly influence the computation performed by this neuron, it has taken 40 years of combined modeling and experimental work to reach the beginning of an understanding about this relationship. Further, that emerging understanding suggests that much of our intuition over the last 40 years has been largely wrong. Changes in thinking about the physiological structure of the Purkinje cell dendrite has, in turn, driven, at least in our laboratory, a fundamental reconsideration regarding the function of the cerebellum as a whole (Bower, 1997a,b; Bower et al., 2012; for context for in the overall field see: Manto et al., 2012).

While general speculations on this subject can still be found in many experimental papers, the combination of realistic modeling and experimental studies described here has specifically revealed that Purkinje cell responses to granule cell-related excitatory and inhibitory synaptic inputs are quite different from the parallel fiber dominant, integrate and fire type cellular dynamics assumed by the most current theories of cerebellar function (Braitenberg, 1967; Marr, 1969; Albus, 1971; Pellionisz and Szentágothai, 1974; Medina and Mauk, 2000; Vetter et al., 2001; Heck and Sultan, 2002; Ito, 2006; Hong and Optican, 2008; Kitamura and Kano, 2012). In fact, while the 500+ references in the literature for the R-DB Model is very high compared to almost all models of its kind, in the last 20 years, there have actually been over 10,000 Purkinje cell experimental papers published, almost none of reference models of any kind. It is also completely standard, 40 years after Purkinje cell modeling started, for review articles on Purkinje cell function to make no mention what-so-ever of these modeling efforts or their results (e.g., from the last 2 years; Gallian and De Zeeuw, 2014; Grasselli and Hansel, 2014; Jörntell, 2014; Lewis and Raman, 2014; Voogd, 2014; Cerminara et al., 2015; Cheron et al., 2015; Dar, 2015; Louis, 2015; Tada et al., 2015). In fact, even review articles on subjects as central to the modeling as the active properties of the Purkinje cell dendrite can quite remarkably be published with hardly any mention of modeling results (Kitamura and Kano, 2012). Yet, many of the issues raised in those reviews, as well as the experimental papers they are based on raise issues that modelers have been investigating for years and many that have been resolved years ago.

How then are we to proceed in an organized way to understand function at any level, from the cerebellum itself down to the voltage dependent conductances in the Purkinje cell dendrite. This article is an example of how such study can proceed if based on realistic models shared by a community. Yet most published models are still designed to demonstrate a preexisting functional idea. In this regard, it is a remarkable fact that Pellionisz and Llinas first proposed more than 25 years ago a standard of "adequacy" for representing Purkinje cells (Pellionisz and Llinás, 1977). Yet most published models of Purkinje cells and certainly almost all published network models make no attempts what-so-ever to demonstrate that their Purkinje cells behave like actual Purkinje cells (Blum et al., 1993; Buonomano and Mauk, 1994; Yuen et al., 1995; Barto et al., 1999; Chauvet and Chauvet, 1999; Medina and Mauk, 2000; Spoelstra et al., 2000; Kistler and De Zeeuw, 2002; Brunel et al., 2004; Mauk and Ohyama, 2004; Yamazaki and Tanaka, 2007; Carrillo et al., 2008; Kulagina et al., 2008; de Gruijl et al., 2009; Abrams et al., 2010; Dean et al., 2010; Ohyama et al., 2010; Dean and Porrill, 2011; Li et al., 2012; Yamazaki and Nagao, 2012). It is entirely unclear what the value of a model is if the properties of its neurons, in this case a neuron with important active dendritic conductances, bears little resemblance to its actual physiological properties. Philosophers of science have long recognized the distinction between observation-based story telling and quantitative model-based analysis (Kuhn, 1962). In my view, models that misrepresent the actual physical properties of their neurons, including in this case usually neglecting the active properties of their dendrites, are essentially an extension of the story telling tradition. It is also worth noting that many of the models referenced above concern, perhaps, issues that many consider to be more directly related to cerebellar function, aging, learning, ataxia, effects of alcohol abuse, etc. These are clearly of interest to the cerebellar community, especially with the pressure for so-called translational science. In my view, a real understanding of these kinds of issues will absolutely depend on the continued construction and further elaboration of the level of realistic model described here, best done as part of a community. However, given the current state of the model, I see no reason why questions involving synaptic plasticity, pharmacological effects on specific ion channels, and even, possibly the kinds of aberrant behavior seen in Purkinje cells in some conditions of ataxia, can't begin to be studied with a model of this type.

This in fact, is perhaps the most important reason that over the next 20 years it will be critical for the computational neuroscience community to adopt and build community models (Bower and Bower, 2013). If we are all simply working on our own disconnected individual models, we have little chance of establishing the kind of tested and accepted underlying quantitative framework that is likely essential for real scientific progress. By committing to the use of community models we also establish a common structure that can be presented to the larger neuroscience community, not as just another model, but as a model that has been built, tested, verified and accepted by multiple researchers. Why shouldn't these models, then find their way into graduate training programs, or neuroscience textbooks? Why shouldn't such a model be used as a standard against which other models are tested? As long as modelers fail to cooperate, they will likely continue to be largely ignored, not only be experimentalists, but also by their fellow modelers. It is only through the cooperative building and testing of models that an underlying quantitative infrastructure will begin to be constructed for neuroscience. In my view, the last 40 years demonstrates that it is only through that kind of infrastructure that we will ever understand complex phenomena, like, for example, the functional implications of active neuronal processes.

REFERENCES

Abrams, Z. R., Warrier, A., Trauner, D., and Zhang, X. (2010). A signal processing analysis of purkinje cells *in vitro*. *Front. Neural Circuits* 4:13. doi: 10.3389/fncir.2010.00013

Achard, P., and De Schutter, E. (2008). Calcium, synaptic plasticity and intrinsic homeostasis in Purkinje neuron models. *Front. Comput. Neurosci.* 2:8. doi: 10.3389/neuro.10.008.2008

Albus, J. S. (1971). A theory of cerebellar function. *Math. Biosci.* 10, 25–61. doi: 10.1016/0025-5564(71)90051-4

Antunes, G., and De Schutter, E. (2012). A stochastic signaling network mediates the probabilistic induction of cerebellar long-term depression. *J. Neurosci.* 32, 9288–9300. doi: 10.1523/jneurosci.5976-11.2012

Anwar, H., Hepburn, I., Nedelescu, H., Chen, W., and De Schutter, E. (2013). Stocastic calcium mechanisms cause dendritic calcium spike variability. *J. Neurosci.* 40, 15848–15867. doi: 10.1523/JNEUROSCI.1722-13.2013

Anwar, H., Hong, S., and Schutter, E. (2012). Controlling Ca^{2+}-activated K+ channels with models of Ca^{2+} buffering in Purkinje cells. *Cerebellum* 11, 681–693. doi: 10.1007/s12311-010-0224-3

Anwar, H., Roome, C. J., Nedelescu, H., Chen, W., Kuhn, B., and De Schutter, E. (2014). Dendritic diameters affect the spatial variability of intracellular calcium dynamics in computer models. *Front. Cell. Neurosci.* 8:168. doi: 10.3389/fncel.2014.00168

Ascoli, G. A. (2007). Successes and rewards in sharing digital reconstructions of neuronal morphology. *Neuroinformatics* 5, 154–160. doi: 10.1007/s12021-007-0010-7

Baldi, P., Vanier, M. C., and Bower, J. M. (1998). On the use of Bayesian methods for evaluating compartmental neural models. *J. Comput. Neurosci.* 5, 285–314. doi: 10.1023/A:1008887028637

Barto, A. G., Fagg, A. H., Sitkoff, N., and Houk, J. C. (1999). A cerebellar model of timing and prediction in the control of reaching. *Neural Comput.* 11, 565–594. doi: 10.1162/089976699300016575

Bell, C. C., and Grimm, R. J. (1969). Discharge properties of Purkinje cells recorded on single and double microelectrodes. *J. Neurophysiol.* 32, 1044–1055.

Blum, E. K., Khademi, P. M., and Thompson, R. F. (1993). "Model and simulation of a simplified cerebellar neural network for classical conditioning of the rabbit eyeblink response," in *Proceedings of Analysis and Modeling of Neural Systems, Vol. 2* (Boston: Kluwer Academic).

Blum, E. K., and Wang, X. (1990). "Design for Purkinje cells," in *Analysis and Modeling of Neural Systems*, ed. A. F. H. Eeck (Boston: Kluwer Academic Press), 123–129.

Bower, J. M. (1990). "Reverse engineering the nervous system: an anatomical, physiological and computer based approach," in *An Introduction to Neural and Electronic Networks*, eds S. Zornetzer, J. Davis, and C. Lau (New York: Academic Press), 3–24.

Bower, J. M. (1997a). Is the cerebellum sensory for motor's sake, of motor for sensory's sake: the view from the whiskers of a rat? *Prog. Brain Res.* 114, 463–496.

Bower, J. M. (1997b). "The cerebellum and the control of sensory data aquisition," in *International Review of Neurobiology* Vol 41, *The Cerebellum and Cognition. International Review of Neurobiology*, ed. J. Schmahmann (San Diego, CA: Academic Press), 489–513.

Bower, J. M. (1997c). What do parallel fibers do? commentary on "The detection and generation of sequences as a key to cerebellar function: Experiments and Theory" by: Valentino Braitenberg, Detlef Heck, and Fahad Sultan. *Behav. Brain Sci.* 20:247.

Bower, J. M. (2002). The organization of cerebellar cortical circuitry revisited: implications for function. *Ann. N Y Acad. Sci.* 978, 135–155. doi: 10.1111/j.1749-6632.2002.tb07562.x

Bower, J. M. (2010). Model-founded explorations of the roles of molecular layer inhibition in regulating purkinje cell responses in cerebellar cortex: more trouble for the beam hypothesis. *Front. Cell. Neurosci.* 4:27. doi: 10.3389/fncel.2010.00027

Bower, J. M. (2012). "The computational structure of the cerebellar molecular layer," in *Handbook of Cerebellum and Cerebellar Disorders*, eds M. Manto, D. L. Gruol, J. D. Schmahmann, N. Koibuchi, and F. Rossi (Berlin: Springer), 1359–1380.

Bower, J. M. (2013). "The Purkinje cell as a community model in neuroscience," in *20 Years of Computational Neuroscience*, ed. J. M. Bower (Berlin: Springer), 103–140.

Bower, J. M., and Beeman, D. (1995). *The Book of GENESIS.* New York: Springer-Verlag.

Bower, J. M., and Beeman, D. (2007). Constructing realistic neural simulations with GENESIS. *Methods Mol. Biol.* 401, 103–125. doi: 10.1007/978-1-59745-520-6_7

Bower, J. M., and Woolston, D. C. (1983). Congruence of spatial organization of tactile projections to granule cell and Purkinje cell layers of cerebellar hemispheres of the albino rat: vertical organization of cerebellar cortex. *J. Neurophysiol.* 49, 745–766.

Bower, J. M., Woolston, D. C., and Gibson, J. M. (1980). Congruence of spatial patterns of receptive field projections to Purkinje cell and granule cell layers in the cerebellar hemispheres of the rat. *Soc. Neurosci. Abstr.* 6, 511.

Braitenberg, V. (1967). Is the cerebellar cortex a biological clock in the millisecond range? *Prog. Brain Res.* 25, 334–346. doi: 10.1016/s0079-6123(08)60971-1

Brown, M. E., and Ariel, M. (2009). Topography and response timing of intact cerebellum stained with absorbance voltage-sensitive dye. *J. Neurophysiol.* 101, 474–490. doi: 10.1152/jn.90766.2008

Brown, S.-A., and Loew, L. M. (2012). Computational analysis of calcium signaling and membrane electrophysiology in cerebellar Purkinje neurons associated with ataxia. *BMC Syst. Biol.* 6:70. doi: 10.1186/1752-0509-6-70

Brown, S.-A., Moraru, I. I., Schaff, J. C., and Loew, L. M. (2011). Virtual NEURON: a strategy for merged biochemical and electrophysiological modeling. *J. Comput. Neurosci.* 31, 385–400. doi: 10.1007/s10827-011-0317-0

Brunel, N., Hakim, V., Isope, P., Nadal, J. P., and Barbour, B. (2004). Optimal information storage and the distribution of synaptic weights: perceptron versus Purkinje cell. *Neuron* 43, 745–757. doi: 10.1016/s0896-6273(04)00528-8

Buonomano, D. V., and Mauk, M. D. (1994). Neural-network model of the cerebellum: temporal discrimination and the timing of motor-responses. *Neural Comput.* 6, 38–55. doi: 10.1162/neco.1994.6.1.38

Bush, P. C., and Sejnowski, T. J. (1991). Simulations of a reconstructed cerebellar Purkinje cell based on simplified channel kinetics. *Neural Comput.* 3, 321–332. doi: 10.1162/neco.1991.3.3.321

Calvin, W. H. (1969). Dendritic spikes revisited. *Science* 166, 637–638. doi: 10.1126/science.166.3905.637

Calvin, W. H., and Hellerstein, D. (1969). Dendritic spikes versus cable properties. *Science* 163, 96–97. doi: 10.1126/science.163.3862.96

Cao, Y., Maran, S. K., Dhamala, M., Jaeger, D., and Heck, D. H. (2012). Behavior-related pauses in simple-spike activity of mouse Purkinje cells are linked to spike rate modulation. *J. Neurosci.* 32, 8678–8685. doi: 10.1523/jneurosci.4969-11.2012

Carrillo, R. R., Ros, E., Boucheny, C., and Coenen, O. J. M. D. (2008). A real-time spiking cerebellum model for learning robot control. *Biosystems* 94, 18–27. doi: 10.1016/j.biosystems.2008.05.008

Cerminara, N. L., Lang, E. J., Sillitoe, R. V., and Apps, R. (2015). Redefining the cerebellar cortex as an assembly of non-uniform Purkinje cell microcircuits. *Nat. Rev. Neurosci.* 16, 79–93. doi: 10.1038/nrn3886

Chauvet, P., and Chauvet, G. A. (1999). Purkinje local circuits with delays: mathematical conditions of stability for learning and retrieval. *Neural Netw.* 12, 59–77. doi: 10.1016/s0893-6080(98)00106-3

Cheron, G., Márquez-Ruiz, J., and Dan, B. (2015). Oscillations, timing, plasticity and learning in the cerebellum. *Cerebellum* doi: 10.1007/s12311-015-0665-9 [Epub ahead of print].

Chono, K., Takagi, H., Koyma, S., Suzuki, H., and Ito, E. (2003). A cell model study of calcium influx mechanism regulated by calcium-dependent potassium channels in Purkinje cell dendrites. *J. Neurosci. Methods* 129, 115–127. doi: 10.1016/s0165-0270(03)00194-8

Cohen, D., and Yarom, Y. (1998). Patches of synchronized activity in the cerebellar cortex evoked by mossy-fiber stimulation: questioning the role of parallel fibers. *Proc. Natl. Acad. Sci. U S A* 95, 15032–15036. doi: 10.1073/pnas.95.25.15032

Coop, A. D., Cornelis, H., and Santamaria, F. (2010). Dendritic excitability modulates dendritic information processing in a Purkinje cell model. *Front. Comput. Neurosci.* 4:6. doi: 10.3389/fncom.2010.00006

Coop, A. D., and Reeke, G. N. J. (2001). The composite neuron: a realistic one-compartment Purkinje cell model suitable for large-scale neuronal network simulations. *J. Comput. Neurosci.* 10, 173–186. doi: 10.1023/A:1011269014373

Cornelis, H., Coop, A. D., Rodriquez, M., Beeman, D., and Bower, J. M. (2010). "Using models to collaborate, communicate and publish: an introduction to GENESIS 3.0 and the future of computational neurobiology," in *Proceedings of CNS 2010*.

Couto, J., Linaro, D., De Schutter, E., and Giugliano, M. (2015). On the firing rate dependency of the phase response curve of rat Purkinje neurons *in vitro*. *PLoS Comput. Biol.* 11:e1004112. doi: 10.1371/journal.pcbi.1004112

Dar, M. S. (2015). Ethanol-induced cerebellar ataxia: cellular and molecular mechanisms. *Cerebellum* 14, 447–465. doi: 10.1007/s12311-014-0638-4

Dean, P., and Porrill, J. (2011). Evaluating the adaptive-filter model of the cerebellum. *J. Physiol.* 589, 3459–3470. doi: 10.1113/jphysiol.2010.201574

Dean, P., Porrill, J., Ekerot, C.-F., and Jörntell, H. (2010). The cerebellar microcircuit as an adaptive filter: experimental and computational evidence. *Nat. Rev. Neurosci.* 11, 30–43. doi: 10.1038/nrn2756

de Gruijl, J. R., van der Smagt, P., and De Zeeuw, C. I. (2009). Anticipatory grip force control using a cerebellar model. *Neuroscience* 162, 777–786. doi: 10.1016/j.neuroscience.2009.02.041

De Schutter, E. (1994). Modelling the cerebellar Purkinje cell: experiments in computo. *Prog. Brain Res.* 102, 427–441. doi: 10.1016/s0079-6123(08)60557-9

De Schutter, E. (1998). Dendritic voltage and calcium-gated channels amplify the variability of postsynaptic responses in a Purkinje cell model. *J. Neurophysiol.* 80, 504–519.

De Schutter, E. (1999). Using realistic models to study synaptic integration in cerebellar Purkinje cells. *Rev. Neurosci.* 10, 233–245. doi: 10.1515/revneuro.1999.10.3-4.233

De Schutter, E. (2013). The importance of stochastic signaling processes in the induction of long-term synaptic plasticity. *Neural. Netw.* 47, 3–10. doi: 10.1016/j.neunet.2012.11.015

De Schutter, E., and Bower, J. M. (1992). "Purkinje neuron simulation on the Intel Touchstone Delta with GENESIS," in *Proceedings of the Grand Challenge Computing Fair*, eds T. Mihaly and P. Messina (Pasadena, CA: CCSF Publishing), 268–279.

De Schutter, E., and Bower, J. M. (1994a). An active membrane model of the cerebellar Purkinje cell. I. Simulation of current clamps in slice. *J. Neurophysiol.* 71, 375–400.

De Schutter, E., and Bower, J. M. (1994b). An active membrane model of the cerebellar Purkinje cell II. Simulation of synaptic responses. *J. Neurophysiol.* 71, 401–419. doi: 10.1115/1.802953.paper47

De Schutter, E., and Bower, J. M. (1994c). Simulated responses of cerebellar Purkinje cells are independent of the dendritic location of granule cell synaptic inputs. *Proc. Natl. Acad. Sci. U S A* 91, 4736–4740. doi: 10.1073/pnas.91.11.4736

De Schutter, E., and Bower, J. M. (1993). "Integration of synchronous and asynchronous synaptic inputs in a detailed compartmental model of the cerebellar Purkinje cell," in *Computation and Neural Systems 1992*, eds J. M. Bower and F. Eeckman (Boston, MA: Kluwer Press), 355–362.

De Schutter, E., and Steuber, V. (2009). Patterns and pauses in Purkinje cell simple spike trains: experiments, modeling and theory. *Neuroscience* 162, 816–826. doi: 10.1016/j.neuroscience.2009.02.040

de Solages, C., Szapiro, G., Brunel, N., Hakim, V., Isope, P., Buisseret, P., et al. (2008). High-frequency organization and synchrony of activity in the purkinje cell layer of the cerebellum. *Neuron* 58, 775–788. doi: 10.1016/j.neuron.2008.05.008

Dizon, M. J., and Khodakhah, K. (2011). The role of interneurons in shaping Purkinje cell responses in the cerebellar cortex. *J. Neurosci.* 31, 10463–10473. doi: 10.1523/jneurosci.1350-11.2011

Dodge, F. A., and Cooley, J. W. (1973). Action potential of the motorneuron. *IBM J. Res. Dev.* 17, 219–229. doi: 10.1147/rd.173.0219

Eccles, J. C., Faber, D. S., Murphy, J. T., Sabah, N. H., and Taborikova, H. (1971). Investigation on integration of mossy fiber inputs to Purkyne cells in the anterior lobe. *Exp. Brain Res.* 13, 54–77. doi: 10.1007/bf00236430

Eccles, J. C., Ito, M., and Szentagothai, J. (1967). *The Cerebellum as a Neuronal Machine.* Berlin: Springer.

Eccles, J. C., Llins, R., and Sasaki, K. (1966a). Parallel fibre stimulation and the responses induced thereby in the Purkinje cells of the cerebellum. *Exp. Brain Res.* 1, 17–39. doi: 10.1007/bf00235207

Eccles, J. C., Llinás, R., and Sasaki, K. (1966b). The excitatory synaptic action of climbing fibres on the Purkinje cells of the cerebellum. *J. Physiol.* 182, 268–296. doi: 10.1113/jphysiol.1966.sp007824

Fernandez, F. R., Engbers, J. D. T., and Turner, R. W. (2007). Firing dynamics of cerebellar Purkinje cells. *J. Neurophysiol.* 98, 278–294. doi: 10.3410/f.1086747.539661

Forrest, M. D. (2015). Simulation of alcohol action upon a detailed Purkinje cell neuron model and a simplier surrogate model that runs >400 times faster. *BMC Neuroscience* 16:27. doi: 10.1186/s12868-015-0162-6

Forrest, M. D., Wall, M. J., Press, D. A., and Feng, J. (2012). The sodium-potassium pump controls the intrinsic firing of the cerebellar Purkinje neuron. *PLoS One* 7:e51169. doi: 10.1371/journal.pone.0051169

Freeman, J. A., and Nicholson, C. (1975). Experimental optimization of current source-density technique for anuran cerebellum. *J. Neurophysiol.* 38, 369–382. doi: 10.1016/0006-8993(75)90494-1

Gähwiler, B. H., and Llano, I. (1989). Sodium and potassium conductances in somatic membranes of rat Purkinje cells from organotypic cerebellar cultures. *J. Physiol.* 417, 105–122. doi: 10.1113/jphysiol.1989.sp017793

Gallian, E., and De Zeeuw, C. I. (2014). Questioning the cerebellar doctrine. *Prog. Brain Res.* 210, 59–77. doi: 10.1016/B978-0-444-63356-9.00003-0

Gauck, V., and Jaeger, D. (2003). The contribution of NMDA and AMPA conductances to the control of spiking in neurons of the deep cerebellar nuclei. *J. Neurosci.* 23, 8109–8118.

Genet, S., Sabarly, L., Guigon, E., Berry, H., and Delord, B. (2010). Dendritic signals command firing dynamics in a mathematical model of cerebellar Purkinje cells. *Biophys. J.* 99, 427–436. doi: 10.1016/j.bpj.2010.04.056

Grasselli, G., and Hansel, C. (2014). Cerebellar long-term potentiation: cellular mechanisms and role in learning. *Int. Rev. Neurobiol.* 117, 39–51. doi: 10.1016/b978-0-12-420247-4.00003-8

Gundappa-Sulur, G., De Schutter, E., and Bower, J. M. (1999). Ascending granule cell axon: an important component of cerebellar cortical circuitry. *J. comp. Neurol.* 408, 580–596. doi: 10.1002/(sici)1096-9861(19990614)408:4<580::aid-cne11>3.0.co;2-o

Heck, D., and Sultan, F. (2002). Cerebellar structure and function: making sense of parallel fibers. *Hum. Mov. Sci.* 21, 411–421. doi: 10.1016/S0167-9457(02)00123-9

Heck, D. H., Thach, W. T., and Keating, J. G. (2007). On-beam synchrony in the cerebellum as the mechanism for the timing and coordination of movement. *Proc. Natl. Acad. Sci. U S A* 104, 7658–7663. doi: 10.1073/pnas.0609966104

Hirano, T., and Hagiwara, S. (1989). Kinetics and distribution of voltage-gated Ca, Na and K channels on the somata of rat cerebellar Purkinje cells. *Pflugers Arch.* 413, 463–469. doi: 10.1007/bf00594174

Hodgkin, A. L., and Huxley, A. F. (1952). A quantitative description of membrane current and its application to conduction and excitation in nerve. *J. Physiol.* 117, 500–544. doi: 10.1113/jphysiol.1952.sp004764

Holmes, W. R., and Rall, W. (1992). Electrotonic length estimates in neurons with dendritic tapering or somatic shunt. *J. Neurophysiol.* 68, 1421–1437.

Holtzman, T., Rajapaksa, T., Mostofi, A., and Edgley, S. A. (2006). Different responses of rat cerebellar Purkinje cells and Golgi cells evoked by widespread convergent sensory inputs. *J. Physiol.* 574, 491–507. doi: 10.1113/jphysiol.2006.108282

Hong, S., and Optican, L. M. (2008). Interaction between Purkinje cells and inhibitory interneurons may create adjustable output waveforms to generate timed cerebellar output. *PLoS One* 3:e2770. doi: 10.1371/journal.pone.0002770

Howell, F. W., Dyhrfjeld-Johnsen, J., Maex, R., Goddard, N., and De Schutter, E. (2000). A large scale model of the cerebellar cortex using PGENESIS. *Neurocomputing* 32–33, 1041–1046. doi: 10.1016/s0925-2312(00)00277-0

Isope, P., and Barbour, B. (2002). Properties of unitary granule cell-->Purkinje cell synapses in adult rat cerebellar slices. *J. Neurosci.* 22, 9668–9678.

Isope, P., Hildebrand, M. E., and Snutch, T. P. (2012). Contributions of T-type voltage-gated calcium channels to postsynaptic calcium signaling within Purkinje neurons. *Cerebellum* 11, 651–665. doi: 10.1007/s12311-010-0195-4

Ito, M. (2006). Cerebellar circuitry as a neuronal machine. *Prog. Neurobiol.* 78, 272–303. doi: 10.1016/j.pneurobio.2006.02.006

Jaeger, D., and Bower, J. M. (1999). Synaptic control of spiking in cerebellar Purkinje cells: dynamic current clamp based on model conductances. *J. Neurosci.* 19, 6090–6101. doi: 10.1007/978-0-387-89279-5_3

Jaeger, D., De Schutter, E., and Bower, J. M. (1993). "Prolonged activation following brief synaptic input in the cerebellar Purkinje cell: intracellular recording and compartmental modeling," in *Computation and Neural Systems 1992*, eds J. M. Bower and F. Eeckman (Boston, MA: Kluwer Press), 343–348.

Jaeger, D., De Schutter, E., and Bower, J. M. (1996). The role of synaptic and voltage-gated currents in the control of Purkinje cell spiking: a modeling study. *J. Neurosci.* 17, 91–106.

Jörntell, H. (2014). Cerebellar synaptic plasticity and the credit assignment problem. *Cerebellum* doi: 10.1007/s12311-014-0623-y [Epub ahead of print].

Kaneda, M., Wakamori, M., Ito, C., and Akaike, N. (1990). Low-threshold calcium current in isolated Purkinje cell bodies of rat cerebellum. *J. Neurophysiol.* 63, 1046–1051.

Khaliq, Z. M., Gouwens, N. W., and Raman, I. M. (2003). The contribution of resurgent sodium current to high-frequency firing in Purkinje neurons: an experimental and modeling study. *J. Neurosci.* 23, 4899–4912.

Kistler, W. M., and De Zeeuw, C. I. (2002). Dynamical working memory and timed responses: the role of reverberating loops in the olivo-cerebellar system. *Neural Comput.* 14, 2597–2626. doi: 10.1162/089976602760407991

Kitamura, K., and Häusser, M. (2011). Dendritic calcium signaling triggered by spontaneous and sensory-evoked climbing fiber input to cerebellar Purkinje cells *in vivo*. *J. Neurosci.* 31, 10847–10858. doi: 10.1523/JNEUROSCI.2525-10.2011

Kitamura, K., and Kano, M. (2012). Dendritic calcium signaling in cerebellar Purkinje cell. *Neural Netw.* 47, 11–17. doi: 10.1016/j.neunet.2012.08.001

Koekkoek, S. K. E., Yamaguchi, K., Milojkovic, B. A., Dortland, B. R., Ruigrok, T. J. H., Maex, R., et al. (2005). Deletion of FMR1 in Purkinje cells enhances parallel fiber LTD, enlarges spines and attenuates cerebellar eyelid conditioning in Fragile X syndrome. *Neuron* 47, 339–352. doi: 10.1016/j.neuron.2005.07.005

Kolb, F. P., Arnold, G., Lerch, R., Straka, H., and Buttner-Ennever, J. (1997). Spatial distribution of field potential profiles in the cat cerebellar cortex evoked by peripheral and central inputs. *Neuroscience* 81, 1155–1181. doi: 10.1016/s0306-4522(97)00255-8

Konnerth, A., Dreessen, J., and Augustine, G. J. (1992). Brief dendritic calcium signals initiate long-lasting synaptic depression in cerebellar Purkinje cells. *Proc. Natl. Acad. Sci. U S A* 89, 7051–7055. doi: 10.1073/pnas.89.15.7051

Kreiner, L., and Jaeger, D. (2004). Synaptic shunting by a baseline of synaptic conductances modulates responses to inhibitory input volleys in cerebellar Purkinje cells. *Cerebellum* 3, 112–125. doi: 10.1080/14734220410031990

Kuhn, T. (1962). *The Structure of Scientific Revolutions.* 4 Edn. Chicago, IL: University Press.

Kulagina, I. B., Korogod, S. M., Horcholle-Bossavitt, G., Batini, C., and Tyc-Dumont, S. (2008). Phase relationships between calcium and voltage oscillations in different dendrites of purkinje neurons. *Neurophysiol* 40, 404–411. doi: 10.1007/s11062-009-9066-3

Lev-Ram, V., Miyakawa, H., Lasser-Ross, N., and Ross, W. N. (1992). Calcium transients in cerebellar Purkinje neurons evoked by intracellelular stimulation. *J. Neurophysiol.* 68, 1167–1177.

Lewis, A. H., and Raman, I. M. (2014). Resurgent current of voltage gated Na(+) channels. *J. Physiol.* 592, 4825–4838. doi: 10.1113/jphysiol.2014.277582

Li, W.-K., Hausknecht, M. J., Stone, P., and Mauk, M. D. (2012). Using a million cell simulation of the cerebellum: network scaling and task generality. *Neural Netw.* 47, 95–102. doi: 10.1016/j.neunet.2012.11.005

Llinas, R. (1982). "General discussion: radial connectivity in the cerebellar cortex: a novel view regarding the functional organization of the molecular layer," in *The Cerebellum: New Vistas, (Exp. Brain Res. Suppl. Vol. 6)*, eds S. L. Palay and V. Chan-Palay (New York: Springer Verlag), 189–194.

Llinas, R., Bloedel, J. R., and Hillman, D. E. (1969a). Functional characterization of neuronal circuitry of frog cerebellar cortex. *J. Neurophysiol.* 32, 847–870.

Llinas, R., Bloedel, J. R., and Roberts, W. (1969b). Antidromic invasion of Purkinje cells in frog cerebellum. *J. Neurophysiol.* 32, 881–891.

Llinas, R., and Hillman, D. E. (1969). "Physiological and morphological organization of cerebellar circuits in various vertebrates," in *Neurobiology of Cerebellar Evolution and Development*, ed. R. Llinas (Chicago, IL: American Medical Association), 43–76.

Llinas, R., Nicholson, C., Freeman, J. A., and Hillman, D. E. (1968). Dendritic spikes and their inhibition in alligator purkinje cells. *Science* 163, 1132–1135. doi: 10.1126/science.160.3832.1132

Llinas, R., and Nicholson, C. (1976). Reversal properties of climbing fiber potential in cat Purkinje cells: an example of a distributed synapse. *J. Neurophysiol.* 39, 311–323.

Llinas, R., and Sugimori, M. (1980a). Electrophysiological properties of *in vitro* Purkinje cell dendrites in mammalian cerebellar slices. *J. Physiol.* 305, 197–213. doi: 10.1113/jphysiol.1980.sp013358

Llinas, R., and Sugimori, M. (1980b). Electrophysiological properties of *in vitro* Purkinje cell somata in mammalian cerebellar slices. *J. Physiol.* 305, 171–195. doi: 10.1113/jphysiol.1980.sp013357

Llinas, R., and Sugimori, M. (1992). "The electrophysiology of the cerebellar Purkinje cell revisited," in *The Cerebellum Revisited*, eds R. Llinas and C. Sotelo (New York: Springer Verlag), 167–181.

Louis, E. D. (2015). Essential tremor: a common disorder of purkinje neurons. *Neurscientist* doi: 10.1177/1073858415590351 [Epub ahead of print].

Lu, H., Esquivel, A. V., and Bower, J. M. (2009). 3D electron microscopic reconstruction of segments of rat cerebellar purkinje cell dendrites receiving ascending and parallel fiber granule cell synaptic inputs. *J. Comp. Neurol.* 514, 583–594. doi: 10.1002/cne.22041

Lu, H., Hartmann, M. J., and Bower, J. M. (2005). Correlations between purkinje cell single-unit activity and simultaneously recorded field potentials in the immediately underlying granule cell layer. *J. Neurophysiol.* 94, 1849–1860. doi: 10.1152/jn.01275.2004

Mandelblat, Y., Etzion, Y., Grossman, Y., and Golomb, D. (2001). Period doubling of calcium spike firing in a model of a Purkinje cell dendrite. *J. Comp. Neurosci.* 11, 43–62. doi: 10.1023/A:1011252730249

Manto, M., Bower, J. M., Conforto, A. B., Delgado-García, J. M., da Guarda, S. N. F., Gerwig, M., et al. (2012). Consensus paper: roles of the cerebellum in motor control–the diversity of ideas on cerebellar involvement in movement. *Cerebellum* 11, 457–487. doi: 10.1007/s12311-011-0331-9

Marr, D. (1969). A theory of cerebellar cortex. *J. Physiol.* 202, 437–471. doi: 10.1113/jphysiol.1969.sp008820

Masoli, S., Solinas, S., and D'Angelo, E. (2015). Action potential processing in a detailed Purkinje cell model reveals a critical role for axonal compartmentalization. *Front. Cell. Neurosci.* 9:47. doi: 10.3389/fncel.2015.00047

Mauk, M. D., and Ohyama, T. (2004). Extinction as new learning versus unlearning: considerations from a computer simulation of the cerebellum. *Learn Mem.* 11, 566–571. doi: 10.1101/lm.83504

Medina, J. F., and Mauk, M. D. (2000). Computer simulation of cerebellar information processing. *Nat. Neurosci.* 3, 1205–1211. doi: 10.1038/81486

Miyakawa, H., Lev-Ram, V., Lasser-Ross, N., and Ross, W. N. (1992). Calcium transients evoked by climbing fiber and parallel fiber synaptic inputs in guinea pig cerebellar Purkinje neurons. *J. Neurophysiol.* 68, 1178–1189.

Miyasho, T., Takagi, H., Suzuki, H., Watanabe, S., Inoue, M., Kudo, Y., et al. (2001). Low-threshold potassium channels and a low-threshold calcium channel regulate Ca^{2+} spike firing in the dendrites of cerebellar Purkinje neurons: a modeling study. *Brain Res.* 891, 106–115. doi: 10.1016/s0006-8993(00)03206-6

Mocanu, O. D., Oliver, J., Santamaria, F., and Bower, J. M. (2000). Branching point effects on the passive properties of the cerebellar granule cell axon. *Neurocomputing* 32, 207–212. doi: 10.1016/s0925-2312(00)00165-x

Mugnaini, E. (1972). "The histology and cytology of the cerebellar cortex," in *The Comparitive Anatomy and Histology of the Cerebellum: The Human Cerebellum, Cerebellar Connections and Cerebellar Cortex*, eds O. Larsell and J. Jansen (Minneapolis: University of Minnesota Press), 201–262.

Ogasawara, H., Doi, T., Doya, K., and Kawato, M. (2007). Nitric oxide regulates input specificity of long-term depression and context dependence of cerebellar learning. *PLoS Comput. Biol.* 3:e179. doi: 10.1371/journal.pcbi.0020179

Ohyama, T., Voicu, H., Kalmbach, B., and Mauk, M. D. (2010). A decrementing form of plasticity apparent in cerebellar learning. *J. Neurosci.* 30, 16993–17003. doi: 10.1523/JNEUROSCI.2455-10.2010

Pellionisz, A. (1970). Computer simulation of the pattern transfer of large cerebellar neuronal fields. *Acta Biochim. Biophys. Acad. Sci. Hung.* 5, 71–79.

Pellionisz, A., and Llinás, R. (1977). A computer model of cerebellar Purkinje cells. *Neuroscience* 2, 37–48. doi: 10.1016/0306-4522(77)90066-5

Pellionisz, A., and Szentágothai, J. (1973). Dynamic single unit simulation of a realistic cerebellar network model. *Brain Res.* 49, 83–99. doi: 10.1016/0006-8993(73)90403-4

Pellionisz, A., and Szentágothai, J. (1974). Dynamic single unit simulation of a realistic cerebellar network model. II. Purkinje cell activity within the basic circuit and modified by inhibitory systems. *Brain Res.* 68, 19–40. doi: 10.1016/0006-8993(74)90531-9

Pugh, J. R., and Raman, I. M. (2009). Nothing can be coincidence: synaptic inhibition and plasticity in the cerebellar nuclei. *Trends Neurosci.* 32, 170–177. doi: 10.1016/j.tins.2008.12.001

Rall, W. (1964). "Theoretical significance of dendritic trees for neuronal input-output relations," in *Neural Theory and Modeling*, ed. R. Reiss (Stanford, CA: Stanford University Press), 73–97.

Rall, W., and Shepherd, G. M. (1968). Theoretical reconstruction of field potentials and dendrodendritic synaptic interactions in olfactory bulb. *J. Neurophysiol.* 31, 884–915.

Rapp, M., Segev, I., and Yarom, Y. (1994). Physiology, morphology and detailed passive models of guinea-pig cerebellar Purkinje cells. *J. Physiol.* 474, 101–118. doi: 10.1113/jphysiol.1994.sp020006

Rapp, M., Yarom, Y., and Segev, I. (1992). The impact of parallel fiber background activity on the cable properties of cerebellar Purkinje cells. *Neural Comput.* 4, 518–533. doi: 10.1162/neco.1992.4.4.518

Regan, L. J. (1991). Voltage-dependent calcium currents in Purkinje cells from rat cerebellar vermis. *J. Neurosci.* 11, 2259–2269.

Rokni, D., Llinas, R., and Yarom, Y. (2008). Stars and stripes in the cerebellar cortex: a voltage sensitive dye study. *Front. Syst. Neurosci.* 1:1. doi: 10.3389/neuro.06.001.2007

Roth, A., and Häusser, M. (2001). Compartmental models of rat cerebellar Purkinje cells based on simultaneous somatic and dendritic patch-clamp recordings. *J. Physiol.* 535, 445–472. doi: 10.1111/j.1469-7793.2001.00445.x

Santamaria, F., and Bower, J. M. (2004). Background synaptic activity modulates the response of a modeled Purkinje cell to paired afferent input. *J. Neurophyiol.* 93, 237–250. doi: 10.1152/jn.00458.2004

Santamaria, F., Jaeger, D., De Schutter, E., and Bower, J. M. (2002). Modulatory effects of parallel fiber and molecular layer interneuron synaptic activity on purkinje cell responses to ascending segment input: a modeling study. *J. Comput. Neurosci.* 13, 217–235. doi: 10.1023/A:1020266315730

Santamaria, F., Tripp, P. G., and Bower, J. M. (2007). Feedforward inhibition controls the spread of granule cell-induced Purkinje cell activity in the cerebellar cortex. *J. Neurophysiol.* 97, 248–263. doi: 10.1152/jn.01098.2005

Santamaria, F., Wils, S., De Schutter, E., and Augustine, G. J. (2006). Anomalous diffusion in Purkinje cell dendrites caused by spines. *Neuron* 52, 635–648. doi: 10.1016/j.neuron.2006.10.025

Santamaria, F., Wils, S., De Schutter, E., and Augustine, G. J. (2011). The diffusional properties of dendrites depend on the density of dendritic spines. *Eur. J. Neurosci.* 34, 561–568. doi: 10.1111/j.1460-9568.2011.07785.x

Sarro, L. M. (2004). Characterization of dendrites as nonlinear computation devices. *Neurocomputing* 58–60, 581–586. doi: 10.1016/j.neucom.2004.01.098

Segev, I., Fleshman, J. W., Miller, J. P., and Bunow, B. (1985). Modeling the electrical behavior of anatomically complex neurons using a network analysis program: passive membrane. *Biol. Cybern.* 53, 27–40. doi: 10.1007/bf00355688

Shelton, D. P. (1985). Membrane resistivity estimated for the Purkinje neuron by means of a passive computer model. *Neuroscience* 14, 111–131. doi: 10.1016/0306-4522(85)90168-x

Shin, S. L., and De Schutter, E. (2006). Dynamic synchronization of Purkinje cell simple spikes. *J. Neurophysiol.* 96, 3485–3491. doi: 10.1152/jn.00570.2006

Shin, S.-L., Hoebeek, F. E., Schonewille, M., De Zeeuw, C. I., Aertsen, A., and De Schutter, E. (2007). Regular patterns in cerebellar Purkinje cell simple spike trains. *PLoS One* 2:e485. doi: 10.1371/journal.pone.0000485

Solinas, S., Maex, R., and De Schutter, E. (2003). Synchronization of Purkinje cell pairs along the parallel fiber axis: a model. *Neurocomputing* 52–54, 97–102. doi: 10.1016/s0925-2312(02)00846-9

Solinas, S. M. G., Maex, R., and Schutter, E. (2006). Dendritic amplification of inhibitory postsynaptic potentials in a model Purkinje cell. *Eur. J. Neurosci.* 23, 1207–1218. doi: 10.1111/j.1460-9568.2005.04564.x

Spoelstra, J., Schweighofer, N., and Arbib, M. A. (2000). Cerebellar learning of accurate predictive control for fast-reaching movements. *Biol. Cybern.* 82, 321–333. doi: 10.1007/s004220050586

Staub, C., De Schutter, E., and Knöpfel, T. (1994). Voltage-imaging and simulation of effects of voltage- and agonist-activated conductances on soma-dendritic voltage coupling in cerebellar Purkinje cells. *J. Comput. Neurosci.* 1, 301–311. doi: 10.1007/bf00961878

Steuber, V., and De Schutter, E. (2001). Long-term depression and recognition of parallel fibre patterns in a multi-compartmental model of a cerebellar Purkinje cell. *Neurocomputing* 38–40, 383–388. doi: 10.1016/s0925-2312(01)00458-1

Steuber, V., and De Schutter, E. (2002). Rank order decoding of temporal parallel fibre input patterns in a complex Purkinje cell model. *Neurocomputing* 44–46, 183–188. doi: 10.1016/s0925-2312(02)00388-0

Steuber, V., Mittmann, W., Hoebeek, F. E., Silver, R. A., De Zeeuw, C. I., Häusser, M., et al. (2007). Cerebellar LTD and pattern recognition by Purkinje cells. *Neuron* 54, 121–136. doi: 10.1016/j.neuron.2007.03.015

Steuber, V., and Willshaw, D. (2004). A biophysical model of synaptic delay learning and temporal pattern recognition in a cerebellar Purkinje cell. *J. Comput. Neurosci.* 17, 149–164. doi: 10.1023/b:jcns.0000037678.26155.b5

Sultan, F., and Bower, J. M. (1998). Quantitative Golgi study of the rat cerebellar molecular layer interneurons using principal component analysis. *J. Comp. Neurol.* 393, 353–373. doi: 10.1002/(sici)1096-9861(19980413)393:3<353::aid-cne7>3.0.co;2-0

Tada, M., Nishizawa, M., and Onodera, O. (2015). Redefining cerebellar atazia in degenerative ataxias: lessons from recent research on cerebellar systems. *J. Neurol. Neurosurg. Psychiatry* 86, 922–928. doi: 10.1136/jnnp-2013-307225

Tahon, K., Wijnants, M., De Schutter, E., and Maex, R. (2011). Current source density correlates of cerebellar Golgi and Purkinje cell responses to tactile input. *J. Neurophysiol.* 105, 1327–1341. doi: 10.1152/jn.00317.2010

Tank, D. W., Sugimori, M., Connor, J. A., and Llinás, R. R. (1988). Spatially resolved calcium dynamics of mammalian Purkinje cells in cerebellar slice. *Science* 242, 773–777. doi: 10.1126/science.2847315

Traub, R. D., Middleton, S. J., Knöpfel, T., and Whittington, M. A. (2008). Model of very fast (>75 Hz) network oscillations generated by electrical coupling between the proximal axons of cerebellar Purkinje cells. *Eur. J. Neurosci.* 28, 1603–1616. doi: 10.1111/j.1460-9568.2008.06477.x

Van Geit, W., Achard, P., and De Schutter, E. (2007). Neurofitter: a parameter tuning package for a wide range of electrophysiological neuron models. *Front. Neuroinform.* 1:1. doi: 10.3389/neuro.11.001.2007

Vetter, P., Roth, A., and Häusser, M. (2001). Propagation of action potentials in dendrites depends on dendritic morphology. *J. Neurophysiol.* 85, 926–937.

Vladimirescu, A., Zhang, K., Newton, A. R., Pederson, D. O., and Sangiovani-Vincentelli, A. (1981). *SPICE.* Berkeley California: University of California.

Voogd, J. (2014). What we do not know about cerebellar systems neuroscience. *Front. Syst. Neurosci.* 8:227. doi: 10.3389/fnsys.2014.00227

Vos, B. P., Maex, R., Volny-Luraghi, A., and De Schutter, E. (1999). Parallel fibers synchronize spontaneous activity in cerebellar Golgi cells. *J. Neurosci.* 19:RC6.

Walter, J. T., Dizon, M.-J., and Khodakhah, K. (2009). The functional equivalence of ascending and parallel fiber inputs in cerebellar computation. *J. Neurosci* 29, 8462–8473. doi: 10.1523/jneurosci.5718-08.2009

Wang, Y., Strahlendorf, J. C., and Strahlendorf, H. K. (1991). A transient voltage-dependent outward potassium current in mammalian cerbellar Purkinje cells. *Brain Res.* 567, 153–158. doi: 10.1016/0006-8993(91)91449-b

Watanabe, S., Takagi, H., Miyasho, T., Inoue, M., Kirino, Y., Kudo, Y., et al. (1998). Differential roles of two types of voltage-gated Ca^{2+} channels in the dendrites of rat cerebellar Purkinje neurons. *Brain Res.* 791, 43–55. doi: 10.1016/s0006-8993(98)00048-1

Womack, M. D., Chevez, C., and Khodakhah, K. (2004). Calcium-activated potassium channels are selectively coupled to P/Q-type calcium channels in cerebellar Purkinje neurons. *J. Neurosci* 24, 8818–8822. doi: 10.1523/jneurosci.2915-04.2004

Womack, M. D., and Khodakhah, K. (2002a). Characterization of large conductance Ca^{2+}-activated K+ channels in cerebellar Purkinje neurons. *Eur. J. Neurosci.* 16, 1214–1222. doi: 10.1046/j.1460-9568.2002.02171.x

Womack, M., and Khodakhah, K. (2002b). Active contribution of dendrites to the tonic and trimodal patterns of activity in cerebellar Purkinje neurons. *J. Neurosci.* 22, 10603–10612.

Womack, M. D., and Khodakhah, K. (2004). Dendritic control of spontaneous bursting in cerebellar Purkinje cells. *J. Neurosci.* 24, 3511–3521. doi: 10.1523/jneurosci.0290-04.2004

Yamazaki, T., and Nagao, S. (2012). A computational mechanism for unified gain and timing control in the cerebellum. *PLoS One* 7:e33319. doi: 10.1371/journal.pone.0033319

Yamazaki, T., and Tanaka, S. (2007). A spiking network model for passage-of-time representation in the cerebellum. *Eur. J. Neurosci.* 26, 2279–2292. doi: 10.1111/j.1460-9568.2007.05837.x

Yuen, G. L., Hockberger, P. E., and Houk, J. C. (1995). Bistability in cerebellar Purkinje cell dendrites modelled with high-threshold calcium and delayed-rectifier potassium channels. *Biol. Cybern.* 73, 375–388. doi: 10.1007/bf00199473

Zucker, R. S. (1969). Field potentials generated by dendritic spikes and synaptic potentials. *Science* 165, 409–413. doi: 10.1126/science.165.3891.409

Conflict of Interest Statement: The author declares that the research was conducted in the absence of any commercial or financial relationships that could be construed as a potential conflict of interest.

frontiers in
CELLULAR NEUROSCIENCE

ORIGINAL RESEARCH ARTICLE
published: 19 August 2014
doi: 10.3389/fncel.2014.00239

Nonlinear properties of medial entorhinal cortex neurons reveal frequency selectivity during multi-sinusoidal stimulation

Christophe Magnani [1], ***Michael N. Economo*** [2], ***John A. White*** [2] ***and Lee E. Moore*** [1]*

[1] *CNRS UMR 8257, Université Paris Descartes, Paris, France*
[2] *Department of Bioengineering, Brain Institute, University of Utah, Salt Lake City, UT, USA*

Edited by:
Sergey M. Korogod, National Academy of Sciences of Ukraine, Ukraine

Reviewed by:
Michael E. Hasselmo, Boston University, USA
Annalisa Scimemi, SUNY Albany, USA

***Correspondence:**
Lee E. Moore, CNRS UMR 8257, Université Paris Descartes, 45 rue des Saints-Pères, 75270 Paris Cedex 06, France
e-mail: lee.e.moore@gmail.com

The neurons in layer II of the medial entorhinal cortex are part of the grid cell network involved in the representation of space. Many of these neurons are likely to be stellate cells with specific oscillatory and firing properties important for their function. A fundamental understanding of the nonlinear basis of these oscillatory properties is critical for the development of theories of grid cell firing. In order to evaluate the behavior of stellate neurons, measurements of their quadratic responses were used to estimate a second order Volterra kernel. This paper uses an operator theory, termed quadratic sinusoidal analysis (QSA), which quantitatively determines that the quadratic response accounts for a major part of the nonlinearity observed at membrane potential levels characteristic of normal synaptic events. Practically, neurons were probed with multi-sinusoidal stimulations to determine a Hermitian operator that captures the quadratic function in the frequency domain. We have shown that the frequency content of the stimulation plays an important role in the characteristics of the nonlinear response, which can distort the linear response as well. Stimulations with enhanced low frequency amplitudes evoked a different nonlinear response than broadband profiles. The nonlinear analysis was also applied to spike frequencies and it was shown that the nonlinear response of subthreshold membrane potential at resonance frequencies near the threshold is similar to the nonlinear response of spike trains.

Keywords: entorhinal cortex, stellate neurons, grid cells, quadratic sinusoidal analysis, frequency domain, nonlinear oscillations, resonance

1. INTRODUCTION

The stellate cells in layer II of the medial entorhinal cortex have long been noted for their oscillatory character (Erchova et al., 2004) consisting of membrane potential oscillations (MPOs) and resonance properties (Engel et al., 2008; Giocomo and Hasselmo, 2008; Pastoll et al., 2012; Shay et al., 2012). More recently, it has been suggested that these cells participate in the grid-like firing fields with regard to an animals position in space. In intact animals, grid cells have increased activity at particular locations representing a hexagonal grid. It is unclear how stellate cells along with pyramidal neurons participate in the grid cell networks (Burgalossi and Brecht, 2014; Ray et al., 2014). It has been proposed that nonlinear stochastic current fluctuations from ion channels, rather than an internal periodic oscillator, is responsible for this behavior (Erchova et al., 2004; Dodson et al., 2011). These neurons project to the hippocampus and are implicated in the activity of place cells that encode a single location. Thus, it is of some interest to understand in detail the nonlinear properties of stellate cells and how these are utilized in neural networks that compute spatial position.

Quantitative information about the linear and quadratic behaviors can be obtained from a current clamp of the soma, which provides a basis to understand the just threshold behavior of these neurons in a particular neural network. We have used multi-sinusoidal stimulations to elicit stellate neuronal quadratic responses in the frequency domain, which are then encoded into a matrix representing a Hermitian operator. The underlying theory, termed quadratic sinusoidal analysis (QSA), was published by Magnani and Moore (2011) for voltage clamped neurons and in this paper, is applied to current clamp. The QSA not only quantitatively characterizes experimental data from stellate cells, but it also provides an evaluation of the corresponding conductance based models.

The method of frequency probing used here is based on a practical measurement technique, namely harmonic probing on Volterra kernels (Victor and Shapley, 1980; Boyd et al., 1983). Multi-sinusoidal stimulations enable nonlinear measurements of the neuronal response at harmonics $2f_i$ and interactive frequencies $|f_i \pm f_j|$. These measurements constitute the coefficients of the QSA matrix, which represents an operator as an algebraic object similar to a Volterra kernel rather than just an array of numbers. It provides a precise signature of the nonlinear voltage dependent conductances and their particular representation on the dendritic and somatic membranes.

Importantly, these studies show in detail how quadratic properties of neurons are dependent on the frequency content of the

stimulation and demonstrate that the nonlinear behavior accurately describes membrane potential responses at the level of normal synaptic activity (1–5 mV).

2. MATERIALS AND METHODS

2.1. TISSUE PREPARATION

All experimental protocols were approved by the Boston University and University of Utah Institutional Animal Care and Use Committees. Horizontal sections of entorhinal cortex were prepared from 14- to 28 d-old LongEvans rats. All chemicals were obtained from Sigma (St. Louis, MO) unless otherwise noted. After anesthetization with isoflurane and euthanasia, brains were removed and immersed in 0°C artificial CSF (ACSF) consisting of the following (in mM): 125 NaCl, 25 $NaHCO_3$, 25 D-glucose, 2 KCl, 2 $CaCl_2$, 1.25 NaH_2PO_4, 1 $MgCl_2$, and buffered to pH 7.4 with 95/5% O_2/CO_2. Horizontal slices were cut to a thickness of 400 μm (Vibratome 1000+; Vibratome, St. Louis, MO). Slices were incubated in a 32°C bubbled ACSF for 30 min before being cooled to room temperature (20°C). After the incubation period, slices were moved to the stage of an infrared, differential interference contrast-equipped microscope (Axioscope 2+; Zeiss, Oberkochen, Germany). All recordings were conducted between 32 and 34°C. Solutions and preparation were identical to those described in Fernandez and White (2008).

2.2. ELECTROPHYSIOLOGY

Electrodes were drawn on a horizontal puller (P97; Sutter Instruments, Novato, CA) and filled with an intracellular solution consisting of the following (in mM): 120 K-gluconate, 20 KCl, 10 HEPES, 7 diTrisPhCr, 4 Na_2ATP, 2 $MgCl_2$, 0.3 Tris-GTP, and 0.2 EGTA, buffered to pH 7.3 with KOH. Final electrode resistances were between 3 and 4 MΩ, with a range of measured access values between 4 and 12 MΩ. All recordings were taken from the medial entorhinal cortex (MEC). Stellate cells were identified as neurons within layer II of the MEC exhibiting a large sag profile in response to hyperpolarizing current and having a peak between 2 and 7 Hz in their subthreshold impedance spectrum. Electrophysiological recordings were performed with a current-clamp amplifier MultiClamp 700A; Molecular Devices, Union City, CA), and data were acquired using custom software developed in MATLAB 2014 (MathWorks, Natick, MA) using the data acquisition toolbox. All additional details of the electrophysiological measurements are given in Fernandez et al. (2013).

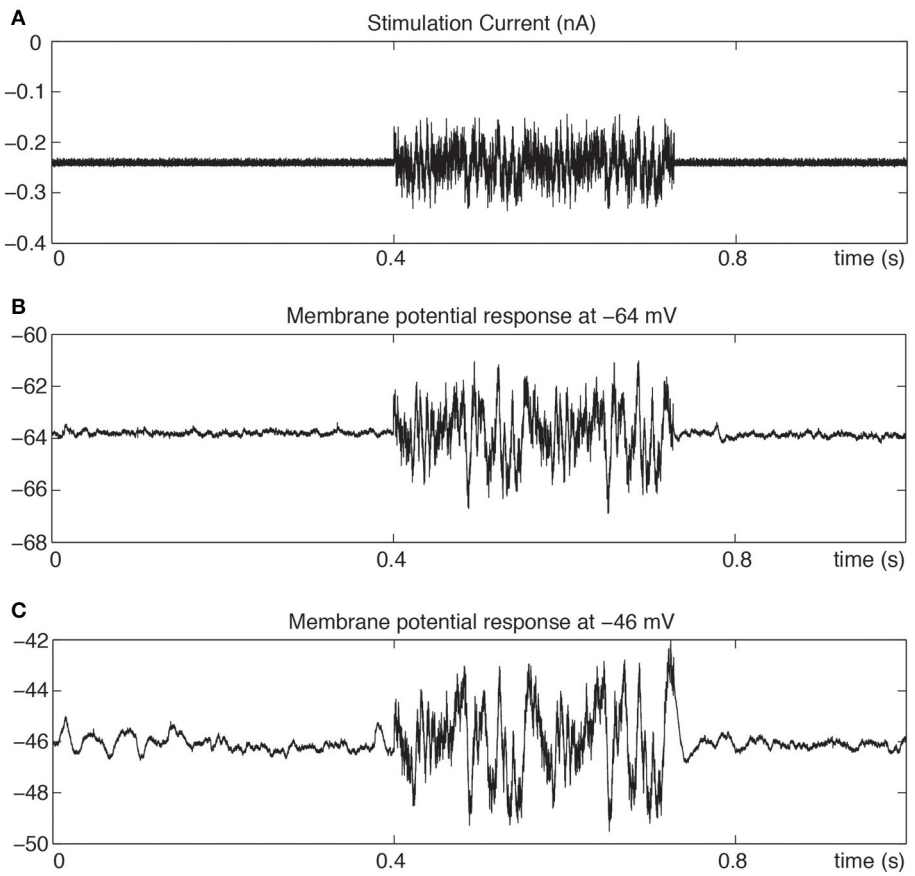

FIGURE 1 | Membrane potential response to multi-sinusoidal current stimulation with holding current adjusted to give −64 and −46 mV average membrane potentials. (A) Stimulation current with range of frequencies from 0.2 Hz to 2 kHz. **(B)** Membrane potential response at −64 mV. **(C)** Membrane potential response at −46 mV with spontaneous oscillations preceding the stimulation.

2.3. THEORETICAL SIMULATIONS

The simulations were done by implementing Hodgkin-Huxley type conductance based models in MATHEMATICA 8 and 9 (Wolfram Research, Champaign, IL, USA). The parameter estimation methods for all models is identical to that used for experiments on prepositus hypoglossi neurons in Idoux et al. (2008). The model structure consists of a soma and eight dendritic compartments with uniform distributions for three voltage dependant ionic conductances : persistent sodium g_{NaP}, potassium g_K and hyperpolarization activated conductance g_H. In particular, since action potentials are not being simulated, the total sodium conductance is treated as one non-inactivating conductance g_{NaP}. The gating variables are considered without power functions. Thus, the nonlinear behavior is essentially due to rate constants rather than power functions. Statistics were done with the PairedZTest of the Hypothesis Testing package of MATHEMATICA.

2.4. QSA THEORY

Linear systems are completely characterized by the linear superposition principle, which means that the response to a linear superposition of sine waves is a linear superposition of sine waves with the same frequencies but different amplitudes and phases. In contrast, the response of a nonlinear system can have frequencies not present in the stimulation. More precisely, if a multi-sinusoidal stimulation has frequencies f_i and f_j then the linear response will have frequencies f_i and f_j whereas the quadratic response will have additional harmonics $2f_i, 2f_j$ and interactive frequencies $|f_i \pm f_j|$. There also exist higher order interactions, such as $f_i + f_j + f_k$, however the neurons studied in this paper mainly manifest quadratic nonlinearities. In particular, multi-sinusoidal stimulations require small amplitudes such that only linear and quadratic responses are significant, although the amplitudes must be large enough to overcome the background noise.

A major obstruction to experimental measurements of nonlinear responses is due to frequency overlaps. This means that two (or more) input frequencies can generate the same output frequency. For example, the input frequencies 1, 2, 3, 4 (in Hz) generate ambiguous output frequencies such as $3 - 1 = 4 - 2$ (in Hz). A solution consists of choosing carefully the input frequencies without overlap up to the second order, higher orders being assumed negligible. An algorithm was written by Magnani and Moore (2011) to generate nonoverlapping frequencies.

The Fourier transform applied to a multi-sinusoidal current stimulation $I(t)$ generates Fourier coefficients at input frequencies f_i. The Fourier transform applied to the membrane potential $V(t)$ generates Fourier coefficients at input frequencies f_i as well as at harmonics $2f_i$ and interactive frequencies $|f_i \pm f_j|$. In linear analysis, the Fourier coefficients of $I(t)$ and $V(t)$ can be used to compute the linear transfer function (impedance) $Z[f_k] = V[f_k]/I[f_k]$. Following Magnani and Moore (2011), we compute

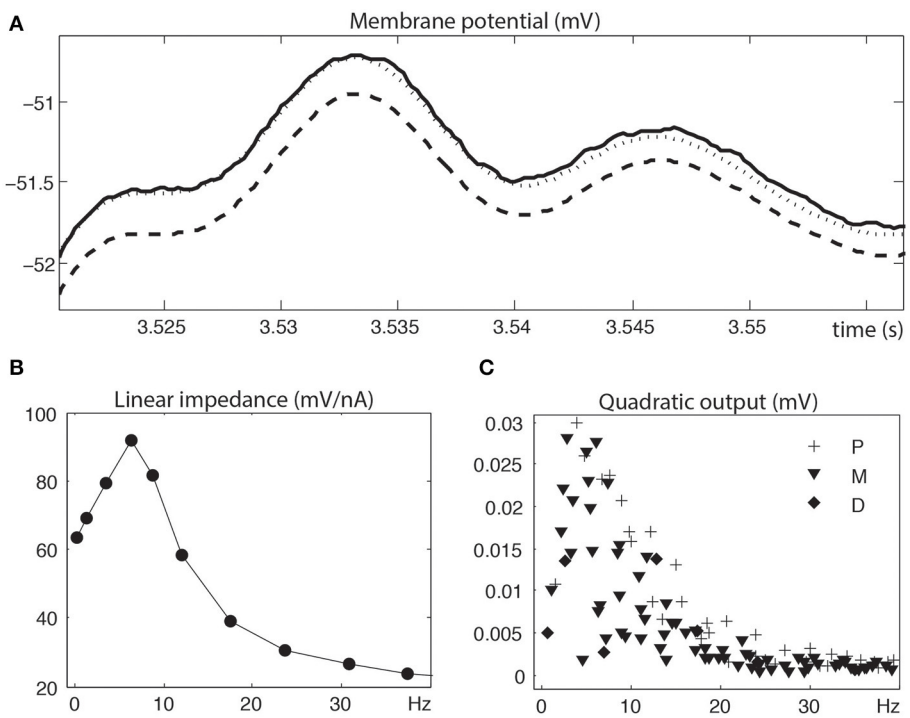

FIGURE 2 | Linear and quadratic analyses of a depolarized stellate neuron. (A) Zoomed measured membrane potential (solid), linear reconstruction (dashed) and linear + quadratic reconstruction (dotted). **(B)** Linear impedance at input frequencies (circle symbol at f_i). **(C)** Quadratic output at harmonics (diamond symbol at $2f_i$), interactive sums (plus symbol at $f_i + f_j$) and interactive differences (inverted triangle symbol at $|f_i - f_j|$). The linear and quadratic analyses were truncated at 40 Hz in order to better illustrate the larger responses at the lower frequencies. Stimulation frequencies are 0.3, 1.3, 3.5, 6.4, 8.7, 12.1, 17.5, 23.7, 30.8, 37.4, 42, 51.3, 60.2, 74.9, 85.9 (in Hz).

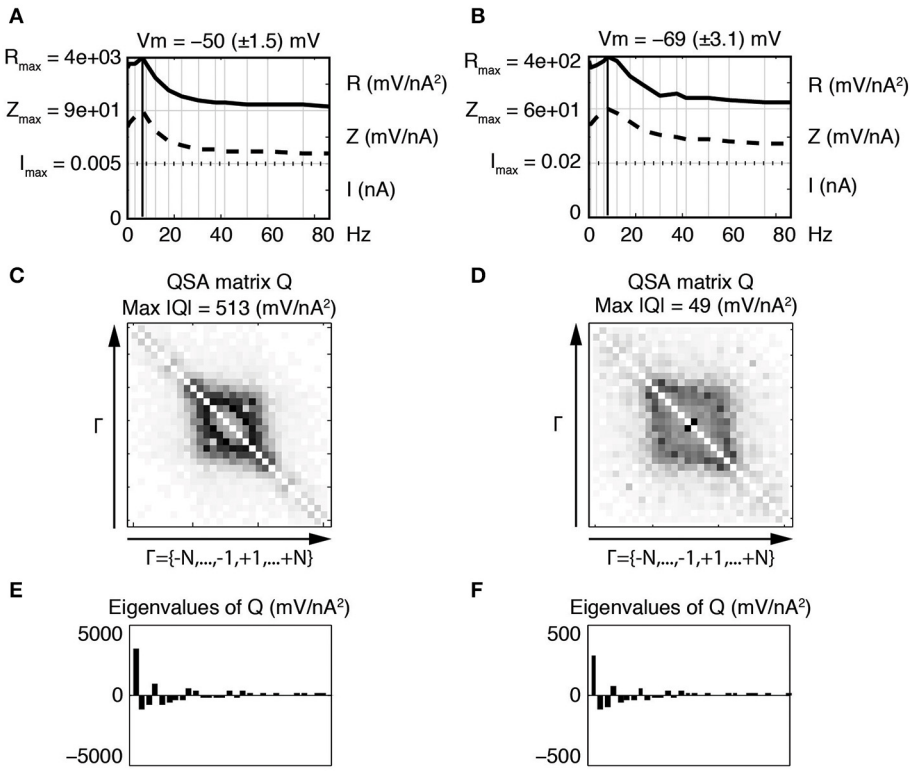

FIGURE 3 | Effect of the membrane potential level on linear and quadratic responses of a stellate neuron at −50 mV (left column) and −69 mV (right column). The standard deviation (STD) is indicated in parenthesis. The frequencies are indexed as f_k where $k \in \Gamma = \{-N, \ldots, -1, +1, \ldots, +N\}$ and $N = 15$ denotes the number of stimulation frequencies. **(A,B)** Juxtaposed plots with respect to the input frequencies, namely the amplitudes of current stimulation I, linear impedance Z, and R function. A vertical bold line indicates the resonance frequency, which is $f_4 = 6.4$ Hz for **(A)** and $f_5 = 8.7$ Hz for **(B)**. The amplitude for each plot ranges from zero to the indicated maximum. Each maximum coincides with zero for the next juxtaposed plot. **(C,D)** Amplitudes of the coefficients of the QSA matrix Q, where the darkest rectangle represents the maximum value given by Max$|Q|$ in the subtitle. Each matrix is indexed by Γ ordered from negative to positive numbers in the direction of the arrows. For example, column f_6 and row f_{-3} represents the frequency interaction $f_6 - f_3 = 12.1 - 3.5 = 8.6$ Hz. **(E,F)** Eigenvalues of the QSA matrix ordered by decreasing amplitudes. Stimulation frequencies are 0.3, 1.3, 3.5, 6.4, 8.7, 12.1, 17.5, 23.7, 30.8, 37.4, 42, 51.3, 60.2, 74.9, 85.9 (in Hz).

the quadratic transfer function

$$B_{ij} = \gamma_{ij} \frac{V[f_i + f_j]}{I[f_i]I[f_j]} \tag{1}$$

where $\gamma_{ii} = 1$ and $\gamma_{ij} = 1/2$ for $i \neq j$. The combinations $f_i + f_j$ include all sums and differences between $|f_i|$ and $|f_j|$ when considering both positive and negative frequencies. The frequencies f_k are indexed over the ordered set of integers $\Gamma = \{-N, \ldots, -1, +1, \ldots, +N\}$.

Importantly, Magnani and Moore (2011) have shown that the complex matrix B can be turned into a Hermitian matrix Q, termed the QSA matrix, by row flipping of the coefficients $Q_{i,j} = B_{-i,j}$. Although a Hermitian matrix has complex coefficients, its eigenvalues are real numbers, which are much easier to interpret physically as amplitudes in mV/nA^2. In this way, the quadratic part of the membrane potential can be expressed as an algebraic formula

$$V_2(t) = I_t^* Q I_t$$

where I_t is a time dependent vector encoding the multi-sinusoidal stimulation.

The quadratic response can be reduced to a sum of squares through eigenanalysis of Q

$$V_2(t) = \sum_{i \in \Gamma} d_i |w_i|^2$$

where d_i are eigenvalues (mV/nA^2) and $|w_i|^2$ are stimulation components (nA^2) obtained from a linear transformation (Magnani and Moore, 2011). In this way, the quadratic neuronal function can be interpreted as a set of quadratic filters where eigenvalues are amplitudes. When an eigenvalue is dominant and others are small, the quadratic neuronal function is approximately a simple square.

Bode plots are useful to represent amplitude with respect to frequency. The QSA matrix can be represented in this way by summing the amplitude components of each column. However, unlike eigenanalysis, this induces information loss. The R summation function (mV/nA^2) is defined by

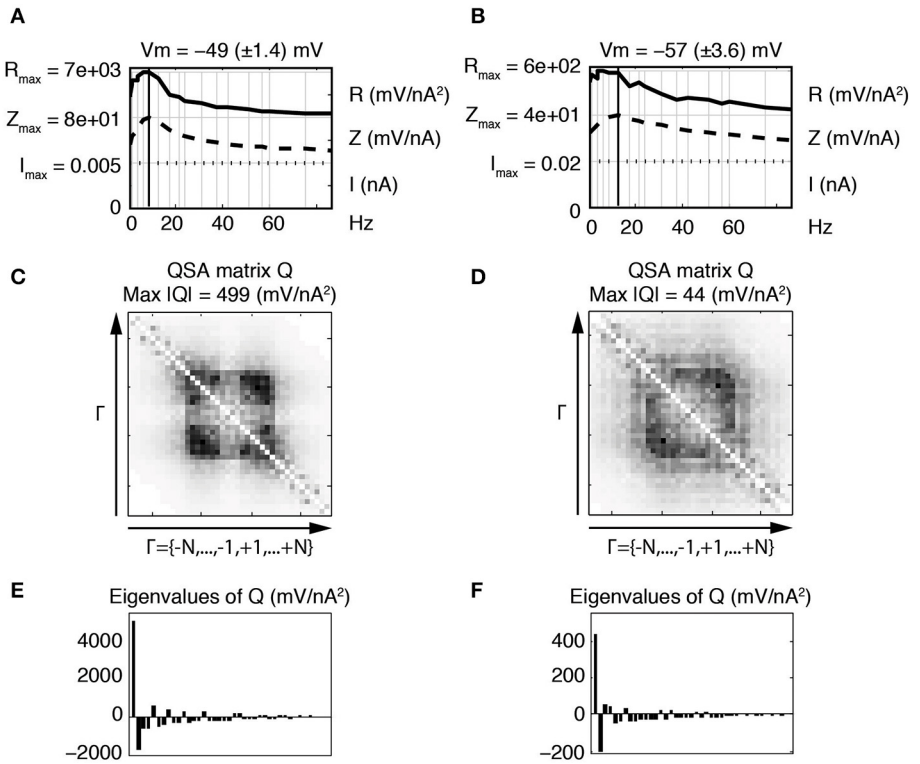

FIGURE 4 | Effect of the membrane potential level on linear and quadratic responses of stellate neuronal model simulations at −49 mV (left column) and −57 mV (right column). (A,B) Juxtaposed plots with respect to the input frequencies, namely the amplitudes of current stimulation I, linear impedance Z, and R function. The resonance frequencies are respectively $f_8 = 8.7$ Hz **(A)** and $f_9 = 12.1$ Hz **(B)**. **(C,D)** Amplitudes of the coefficients of the QSA matrix Q with the maximum value given by Max$|Q|$. **(E,F)** Eigenvalues of the QSA matrix. The model parameter values (in units based on mV and nA) are as follows : membrane capacitance $C_{soma} = 0.0000542$, maximal conductances $g_{leak} = 0.0005$, $g_K = 0.023$, $g_{NaP} = 0.0024$ and $g_H = 0.014$; the reversal potentials $V_{leak} = -55$, $V_K = -87$, $V_{NaP} = 77$ and $V_H = -43$. The functions α_n, β_n, α_m, β_m, α_h, β_h depend on the variable V and their description is given by Idoux et al. (2008) : $v_n = -35$, $s_n = 0.045$, $t_n = 0.7543$, $v_m = -38$, $s_m = 0.06$, $t_m = 0.000150$, $v_h = -51.65$, $s_h = -0.06$ and $t_h = 0.05$. Finally, the electronic length is $e_{length} = 0.50$ and the ratio of the dendritic area to the soma area is $A_{ratio} = 4.5$. Stimulation frequencies are 0.3, 0.4, 1.3, 1.5, 3.5, 4.0, 6.4, 8.7, 12.1, 17.5, 21.6, 23.7, 30.8, 37.4, 42.0, 51.3, 56.9, 60.2, 74.9, 85.9 Hz (in Hz).

$$R_j = \sum_{i \in \Gamma} |Q_{ij}| \tag{2}$$

Alternatively, a modified function R' with units homogenous to a linear transfer function (mV/nA) is defined by

$$R'_j = \sum_{i \in \Gamma} |Q_{ij}| \cdot |I_i| \tag{3}$$

Intuitively, the R and R' functions evaluate the sum of the amplitudes at all frequencies for which they interact.

Figure 1 illustrates the membrane potential response of a stellate neuron to a multi-sinusoidal current stimulation at two membrane potential levels. Membrane potential oscillations (MPOs) are clearly observed before and after the stimulation at the depolarized level. Also, the response shows larger oscillations during the depolarization. This neuron has a strong resonance in the same frequency range as the MPO's (Schreiber et al., 2004; Engel et al., 2008; Yoshida et al., 2011).

Figure 2 illustrates the linear and quadratic analyses of a depolarized stellate neuron. **Figure 2A** compares the measured membrane potential in the time domain to the linear reconstruction and linear + quadratic reconstruction. Clearly, for these signal levels, linear analysis is insufficient and quadratic analysis is required to capture the nonlinear neuronal behavior. **Figures 2B,C** show the linear impedance (mV/nA) and the quadratic output (mV) in the frequency domain. The Fourier components of the linear impedance occur at the stimulation frequencies, whereas those of the quadratic output occur at second order harmonics and interactive frequencies. Clearly, the quadratic output shows a strong overlap with the linear resonance frequencies.

The QSA theory applied to neurons does not rely on any assumption about their morphology or ion channel distribution. In particular, the complexity of Hodgkin-Huxley based multicompartmental models with their computational overhead is avoided. QSA analyses were done with MATLAB on both model simulations and experimental data, allowing precise comparisons of the quadratic responses.

3. RESULTS

3.1. EFFECT OF MEMBRANE POTENTIAL

Figure 3 illustrates the linear and quadratic responses of a stellate neuron for two membrane potentials −50 and −69 mV (left and right columns respectively). The stimulation frequencies were identical to those of **Figure 2** and are indexed as f_k where $k \in \Gamma = \{-15, \ldots, -1, +1, \ldots, +15\}$. The upper panels **Figures 3A,B** represent a juxtaposition of the amplitudes for the stimulations I, linear impedances Z, and R functions with respect to the input frequencies. The R functions are plotted as Bode plots in the same way as the impedances although the ordinate units are different. The maximum of each R function is close to the impedance resonance frequency. Statistics were calculated for a group of six stellate neurons. The maximum amplitude of the QSA matrix increased from 275 to 715 mV/nA^2 ($p = 0.0004$) for a membrane potential change of +7 mV in the range −65 to −48 mV.

As explained in previous publications (Magnani and Moore, 2011; Magnani et al., 2013), the QSA matrix provides a complete description of the quadratic response as ratios between output and input coefficients (Equation 1). In contrast, the coded points in **Figure 2C** show the quadratic measurements of the output without showing the frequency interactions (f_i, f_j). The QSA matrix was constructed from the Fourier coefficients of the data, then decomposed by eigenanalysis to compute its eigenvalues. Each cell of the QSA matrix represents the amplitude of the voltage response at two interactive frequencies divided by the amplitude of the current at these two frequencies (Equation 1). The matrix plots have many symmetries, which reflect particular algebraic properties of the underlying neural operator. The matrix plot is indexed by the set Γ ordered from negative to positive numbers in the direction of the arrows, that is to say $f_{-15}, \ldots, f_{-1}, f_{+1}, \ldots, f_{+15}$. Each cell at abscissa f_i and ordinate f_j encodes the ratio between the membrane potential at $f_i + f_j$ and the current at f_i and f_j. In particular, the white diagonal encodes interactions $f_i + f_{-i} = 0$, thus the DC is set to zero. The other diagonal $f_i + f_i$ encodes the harmonics $2f_i$. In **Figures 3C,D**, the QSA amplitudes appear concentrated at lower frequencies near the center of the matrix, which is consistent with the maximum of the R function.

The impedance and resonance frequency are much less dependent on the membrane potential than the QSA matrix and R function. This suggests that the quadratic neuronal function especially encodes nonlinear voltage dependent ionic conductances. The effect of the membrane potential on stellate neurons is pronounced for all nonlinearities, namely the amplitudes of the QSA coefficients, the eigenvalues and the R functions.

In this and all subsequent figures, the R function (mV/nA^2) is juxtaposed on the linear impedance (mV/nA), which in turn is juxtaposed on the stimulation amplitude Fourier spectrum (nA). Although the R function is a non reversible reduction of the QSA matrix, it provides a practical way to compare the linear and quadratic behaviors at input frequencies. It can be observed, in **Figures 3A,B**, that the R function has a resonance frequency range comparable (but not identical) to the linear case.

At −50 mV (**Figure 3**, left column), the QSA matrix gives more detail on frequency interactions showing enhanced amplitudes in the centered square delimited by $|f_{\pm 4}| = 6.4$ Hz, namely those that involve the resonance frequencies. At the more hyperpolarized membrane potential −69 mV (**Figure 3**, right column), the QSA matrix shows lower amplitudes. However, there is a peak for the harmonics of the lowest input frequency $2f_1 = 0.6$ Hz. Moreover, the quadratic response is enhanced around the centered square delimited by the slightly higher resonance frequency $f_5 = 8.7$ Hz. Thus, the shift in frequency of the nonlinear responses with membrane potential level is similar to the voltage dependence of the linear resonance frequencies (Shay et al., 2012).

The eigenanalysis of the QSA matrix reveals that the nonlinear function is concentrated in a single dominant eigenvalue. This suggests that the neuronal processing consists of a single nonlinear-linear unit as opposed to a parallel combination of several units (see Magnani and Moore, 2011). Dominant eigenvalues are frequently observed, however there are generally multiple significant eigenvalues. **Figure 4** illustrates that a simplified model of stellate neurons is able to capture the nonlinear behavior described by experiments of **Figure 3**.

3.2. LINEAR DISTORTIONS

Previous experiments by Haas and White (2002) suggested that the Fourier responses of stellate neurons to multiple frequencies were dependent on the frequency content of the stimulation, and furthermore these responses were different from that obtained when using single sine waves. We have explored this issue in more detail by comparing the responses of stellate neurons to stimulations containing many frequencies vs. QSA stimulations containing nonoverlapping frequencies. The presumed linear responses in the mV range to many frequencies show marked distortions compared to almost no distortions using nonoverlapping frequencies. The term, distortions, is used here to describe an irregular function with larger variations than generally seen in our linear impedance functions.

Figures 5A,C,E (left column) illustrates distortions in the frequency responses from stellate neurons due to nonlinear responses at overlapping frequencies. The upper trace (A) shows a marked distortion at −53 mV of linear responses stimulated with a very large number of frequencies near threshold. The middle trace (C) shows a significant reduction in the distortion of the linear response for a more hyperpolarized membrane potential with the same number of overlapping frequencies. Finally, the bottom trace (E) shows an almost undistorted linear response using nonoverlapping frequencies (up to the second order) despite a greater membrane potential STD.

Clearly, stimulations with overlapping frequencies generate interactive frequencies that overlap the input frequencies and thereby cause a distortion in the linear response. These effects naturally increase with the number and amplitudes of the particular frequencies. Similarly, **Figures 5B,D,F** (right column) illustrates similar distortions from a neuronal model. The upper panel (B), near threshold, shows that the linear response is significantly distorted due to the presence of nonlinear interactive frequencies for potential excursions in the mV range. The middle panel (D) shows less but distinct distortions at a lower STD and a more hyperpolarized membrane potential, which is consistent with the experimental results (left middle panel). The bottom panel

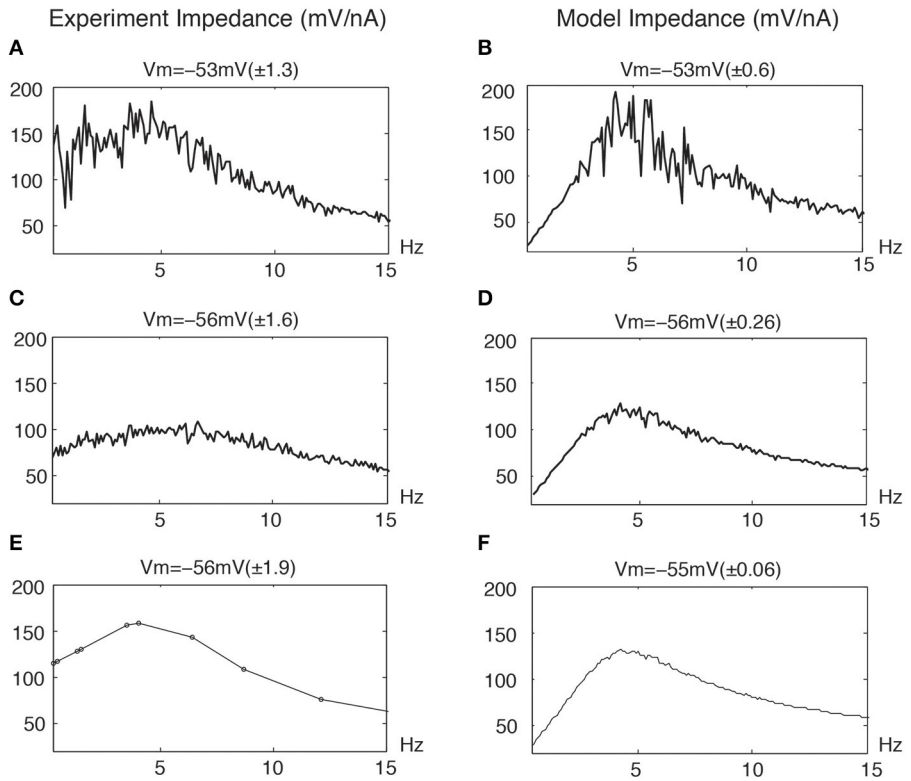

FIGURE 5 | Distortion of linear impedance (mV/nA) by the stimulation profiles for experimental data and model simulations. The average membrane potential V_m is given along with STD values of membrane potential. The standard deviations are given in parenthesis. **(A,C)** Experimental data : the same overlapping frequencies in 0.3 − 1000 Hz with 0.1 Hz intervals. **(E)** Experimental data : the nonoverlapping frequencies are the same as **Figure 4**. **(B,D,F)** Model simulations : the same overlapping frequencies in 0.3 − 500 Hz with 0.1 Hz intervals. The model parameters are given in **Figure 7**.

(F) shows an almost undistorted linear response with the same overlapping frequencies for a still lower STD membrane potential.

Generally, if the output amplitude STD using many overlapping frequencies is less than 0.5 mV, then the linear responses have minimal distortion. Undistorted linear responses can be obtained with fewer nonoverlapping frequencies for much higher STD membrane potential responses, typically up to 4 mV. Thus, a larger number of overlapping frequencies evoking responses in the mV range induce significantly more nonlinear effects than fewer nonoverlapping frequencies. Nonstationary signals, such as the chirp or the zap, are not optimal for linear analysis since their Fourier components distribute over all frequencies and dramatically generate frequency overlaps. Nevertheless, linear analysis is still possible for small stimulation amplitudes (Erchova et al., 2004; Schreiber et al., 2004).

3.3. LOW PASS STIMULATION FILTERING

The above results suggest that the effect of the frequency content of the stimulation on the true nonlinear response should be distinguished from the linear distortions. Experiments were done with a low pass filtered stimulation using nonoverlapping frequencies in which the high frequency amplitudes are reduced. Nonoverlapping frequencies assure that the linear responses are not distorted in order to accurately measure the nonlinear behavior. Since stellate neurons have resonance frequencies around 10 Hz or lower, it would not be surprising that these frequencies compared to high frequencies would have the largest amplitude responses and thus can easily evoke the nonlinear behavior.

The nonlinear responses induced by differently filtered Gaussian white noise inputs are likely to be stimulation dependent. This not only leads to nonlinear frequency interactions dependent on the frequency content of the stimulation, but linear analysis can also be altered since Fourier components at individual input frequencies would be contaminated by nonlinearities. Surprisingly these effects can occur at relatively small amplitudes of membrane potential responses, namely in the mV range. Thus, empirically, responses of neurons at their stimulating frequencies can be dependent on the frequency content of the stimulation, although a true linear response is not.

Figure 6 shows that the nonlinear responses of a stellate neuron to various low pass filtered stimulations are remarkably different despite identical linear behaviors. The cutoff frequencies are not the same between left and right columns, showing that the increase of high frequency interactions are related to high frequency filtering. Statistics were calculated for a group of three stellate neurons comparing the effect of the two low pass stimulation filters. The maximum amplitude of the QSA matrix increased from 1229 to 4204 mV/nA^2 ($p = 0.019$) for a membrane potential change of −60 to −55 mV.

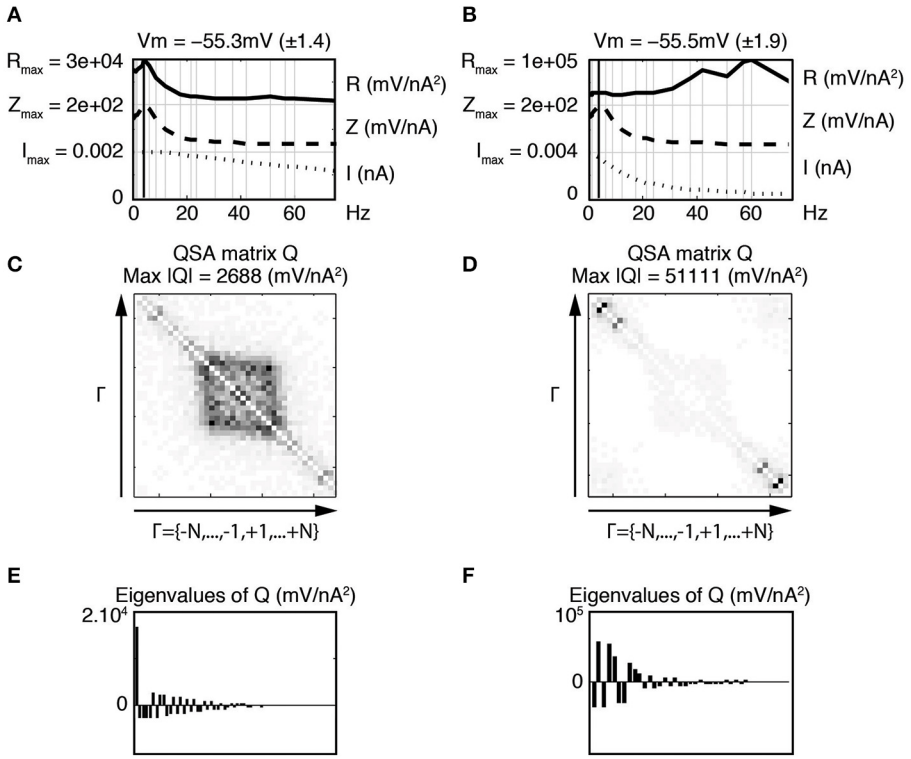

FIGURE 6 | Effect of stimulation profile on stellate neurons. Left column **(A,C,E)** Weakly low pass filtered stimulation *I* in dotted lines. Right column **(B,D,F)** Strongly low pass filtered stimulation *I* in dotted lines. The resonance of the impedance (*Z*) is $f_6 = 4.0$ Hz for both stimulations **(A,B)**. The attenuation of high frequencies in the stimulation of the second column induces enhanced quadratic responses as indicated by the *R* functions in the top row **(A,B)** as well as the QSA matrix **(C,D)** and eigenvalues **(E,F)**. The stimulation frequencies are the same as in **Figure 4**.

The coefficients of the QSA matrix are defined as the ratios between an interactive output and the product of the corresponding inputs for each pair of input frequencies. Thus, although the amplitudes of the high frequency responses decrease when the stimulation is filtered, the above ratio tends to increase. Therefore, the quadratic function appears sensitive to the frequency content of the stimulation even for membrane potential responses in the mV range.

Increases in the *R* functions at high frequencies are clearly observed, however the QSA matrix gives more detail about the interactive frequencies. The QSA matrix of the left column shows peak amplitudes for the harmonics of input frequencies near the linear resonance frequency, such as $2f_6 = 8$ Hz. Moreover, there are significant interactive differences between high input frequencies such as $f_{19} - f_{18} = 14.7$ Hz. The QSA matrix of the right column shows greatly enhanced high frequency interactions in response to the high frequency filtered stimulation. Although the lower frequency interactions near the resonance are not apparent, their amplitudes are similar as can be seen from the *R* functions. The complexity of these responses is also reflected through eigenanalysis that turns a single dominant eigenvalue to multiple eigenvalues when the stimulation is filtered. **Figure 7** illustrates similar results for model simulations. It will be shown below that the increases of the responses at interactions between high frequencies are quite sensitive to the relative amplitude ratio of the low vs. high frequency stimulation content.

The stimulation dependence of the nonlinear response is a good example of the dramatic difference between linear and nonlinear behaviors even at small signal amplitudes. Linear responses are independent of stimulation amplitude for all frequencies. However, we have shown that interactive differences between high frequencies are not proportional to the stimulation amplitude when sufficiently low pass filtered. The quadratic transfer function is defined as the ratio between an interactive output and the product of two inputs. When the enhanced interaction corresponds to a difference between high frequencies, the ratio tends to be maximized because the numerator reflects a significant nonlinear response and the denominator is small due to the low pass filtering.

3.4. BAND PASS STIMULATION FILTERING

The above results demonstrate that the frequency content of the stimulation plays an important role in the nature of the nonlinear response, but generally has minimal effects on the linear behavior if the membrane potential responses are less than 0.5 mV. In order to determine if nonlinear responses have limiting small signal responses that are independent of the content of the stimulation, model simulations were done by applying a Gaussian-like window to the stimulation in the frequency domain. In this way, the

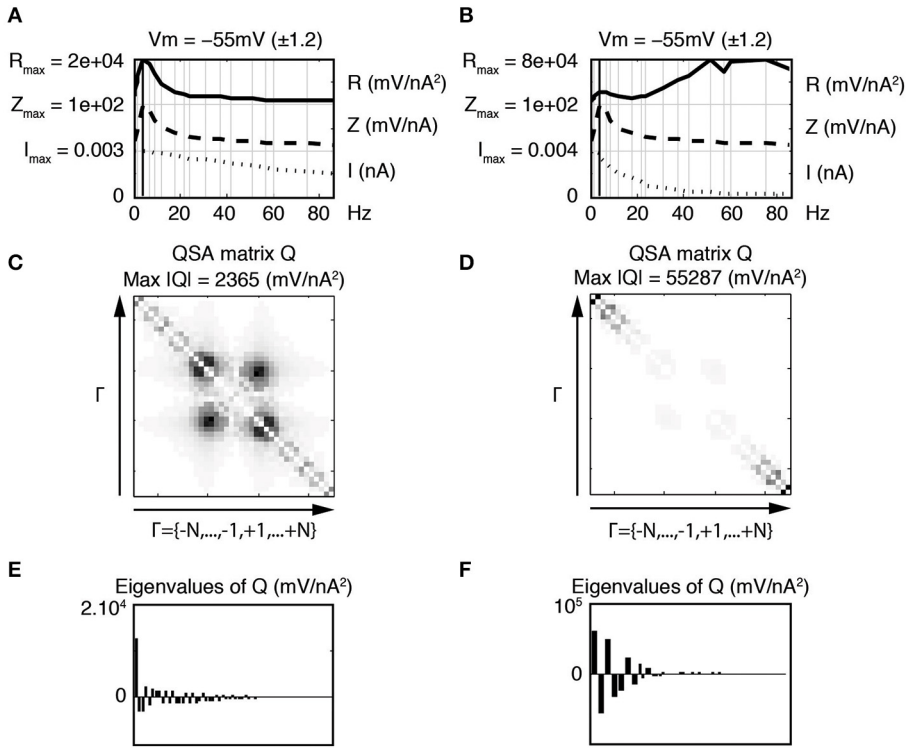

FIGURE 7 | Effect of stimulation profile on stellate neuronal model simulations. Left column **(A,C,E)** Weakly low pass filtered stimulation I in dotted lines. Right column **(B,D,F)** Strongly low pass filtered stimulation I in dotted lines. The resonance of the impedance (Z) is $f_6 = 4.0$ Hz for both stimulations **(A,B)**. The attenuation of high frequencies in the stimulation of the second column induces enhanced quadratic responses as indicated by the R functions in the top row **(A,B)** as well as the QSA matrix **(C,D)** and eigenvalues **(E,F)**. The stimulation frequencies are the same as in **Figure 4**. The parameter values (in units based on mV and nA) are as follows : membrane capacitance $C_{soma} = 0.0000542$, maximal conductances $g_{leak} = 0.0005$, $g_K = 0.0627$, $g_{NaP} = 0.0065$ and $g_H = 0.002926$; the reversal potentials $V_{leak} = -55$, $V_K = -87$, $V_{NaP} = 77$ and $V_H = -43$. The functions α_n, β_n, α_m, β_m, α_h, β_h depend on the variable V and their description is similar to those published by Idoux et al. (2008) : $v_n = -38$, $s_n = 0.035$, $t_n = 0.75$, $v_m = -38.76$, $s_m = 0.046$, $t_m = 0.000150$, $v_h = -51.65$, $s_h = -0.01$ and $t_h = 0.5567$. Finally, the electronic length is $e_{length} = 0.50$ and the ratio of the dendritic area to the soma area is $A_{ratio} = 4.5$.

stimulation shows a peak amplitude at a specific frequency (like a resonance).

Figure 8 illustrates that, in contrast to the linear impedance, if the stimulation peak is at a low frequency (panel A, near the resonance), then the maximum of the QSA matrix is much greater than for a stimulation peak at a higher frequency (lower row, beyond the resonance). Both stimulations evoke potential responses in the mV range and have identical linear impedances.

Discrete peaks can also be observed for the QSA matrix in **Figures 8B,D**. The panel B shows discrete peaks close to the harmonics of $f_4 = 1.5$ Hz as well as high frequency interactions in the corners. The panel D also shows discrete peaks clustered around harmonic frequencies of $f_7 = 6.4$ Hz and $f_8 = 8.7$ Hz. In summary, Gaussian-like window applied near the resonance (panel A) evokes output frequencies before and after $f_8 = 8.7$ Hz. Gaussian-like window applied after the resonance (panel C) leads to output frequencies that are near the resonance. Therefore, nonlinear responses involve a different frequency range compared to the linear resonance frequency.

Figure 9 illustrates that the quadratic response to very small stimulations is almost independent of the frequency content. In particular, both linear and quadratic functions are nearly identical for flat stimulation vs. low peak stimulation, as well as higher peak stimulation (not shown). Thus, the enhanced corners for low peak stimulation almost disappear if the membrane potential responses have STD values of 0.1 mV or less. In particular, the QSA matrix has a remarkable sensitivity to stimulations with low frequency content, especially near the resonance of the neuron. Indeed, **Figure 9A** shows a larger R function for such nonuniform stimulation profile.

From a mathematical point of view, the limit value of the QSA matrix for very small stimulations is consistent with local analysis and represents a quadratic transfer function as a Volterra kernel. For larger stimulations, the quadratic response becomes dependent on the stimulation and the ratio (Equation 1) cannot be interpreted as a transfer function. However, the nonlinear output is still a quadratic signal without higher order frequency contamination (Magnani and Moore, 2011). In fact, larger low peak stimulations evoke the low frequency range near the resonance, in which interactions $|f_i - f_j|$ corresponding to the enhanced corners are generated. Such an interpretation is supported by the enhanced output amplitudes of the interactive

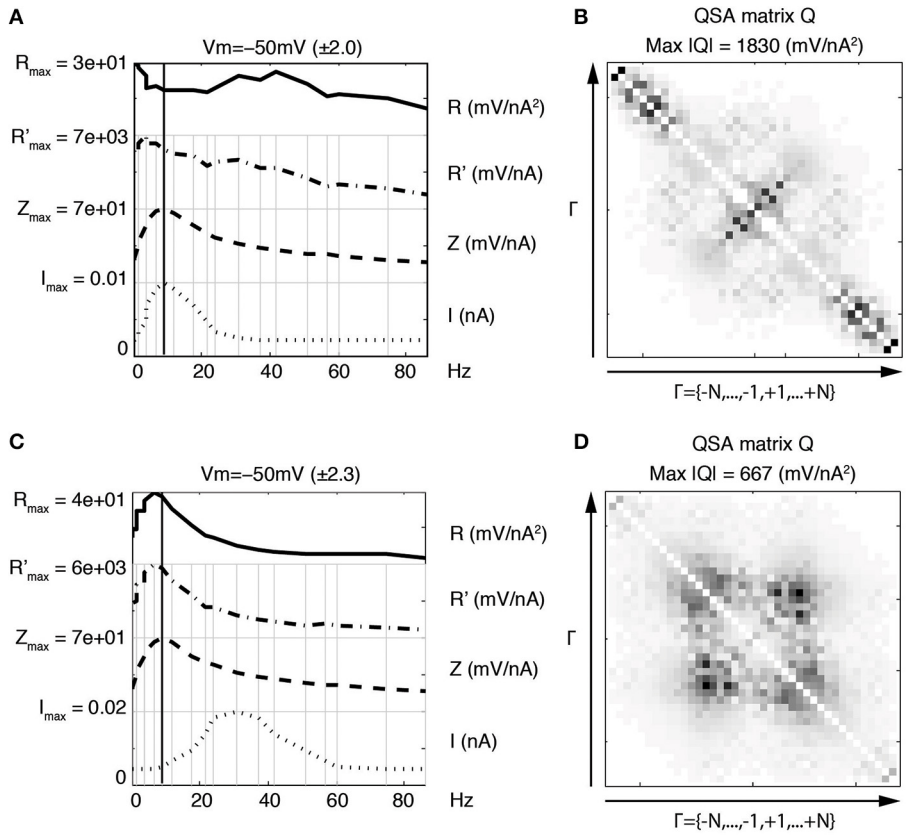

FIGURE 8 | Nonlinear effects of a Gaussian-like window applied to the stimulation Fourier components. Upper row **(A,B)** Gaussian-like window applied to the stimulation Fourier components near the resonance $f_8 = 8.7$ Hz. This induces enhanced frequency interactions between input frequencies near the resonance. Lower row **(C,D)** Gaussian-like window applied to the stimulation Fourier components three fold above the resonance $f_8 = 8.7$ Hz. The QSA matrix appears much smaller than for a stimulation peak near the resonance.

difference frequencies in **Figure 2C** (inverted triangles). This may increase the quadratic response at these interactions, relative to the stimulation.

These nonlinear effects are present at the usual membrane potential excursions in the mV range and appear amplified for stimulations tuned to the preferred frequency response of a particular neuron. Interestingly, other constant stimulation profiles (not represented) lead to quadratic functions independent of stimulation amplitudes for membrane potential responses up to a few mV. For stimulation profiles with enhanced low frequencies, this independence of stimulation amplitude occurs only for a tenfold lower response amplitude (10–100 microvolts), which again emphasizes the sensitivity of the nonlinear responses to the frequency content of the stimulation.

These results are consistent with experimental data of **Figure 6** showing that low frequency stimulation leads to an enhancement of high frequency interactions for both QSA matrix and *R* function. **Figure 8** indicates that high frequency interactions elicited by low frequency stimulation can nearly disappear if the stimulation peak is shifted to higher intermediate frequencies. In both cases, the linear responses remains identical despite major differences in the nonlinear behavior.

3.5. DENDRITIC STIMULATION

Since cable properties of dendrites induce a signal filtering, the marked effect of the stimulation content on the nonlinear response could play a role in how dendrites process signal inputs. It can be expected that distal vs. proximal synaptic inputs to single neurons would lead to different responses in the soma. **Figure 10** illustrates such effects with model simulations. It compares the soma potential response to a current stimulation in the soma (left column) vs. a stimulation of the most distal dendritic compartment (right column). In both cases, the stimulation profile is flat but the represented current *I* is not the stimulation but the computed current flowing across the soma membrane.

In order to compare the two approaches, a somatic impedance was calculated by determining the ratio of the soma potential and the current flowing across the soma membrane, rather than the total injected current typically used for either point or transfer impedances. This procedure determines just the impedance of the somatic compartment in isolation, which is nearly independent of the stimulation profile, as shown in **Figure 10**. At smaller stimulations, the two impedances converge to identical functions. Thus, this approach can be used to analyze the effect of dendritic filtering of the injected current from the dendrite on the nonlinear responses of just the soma.

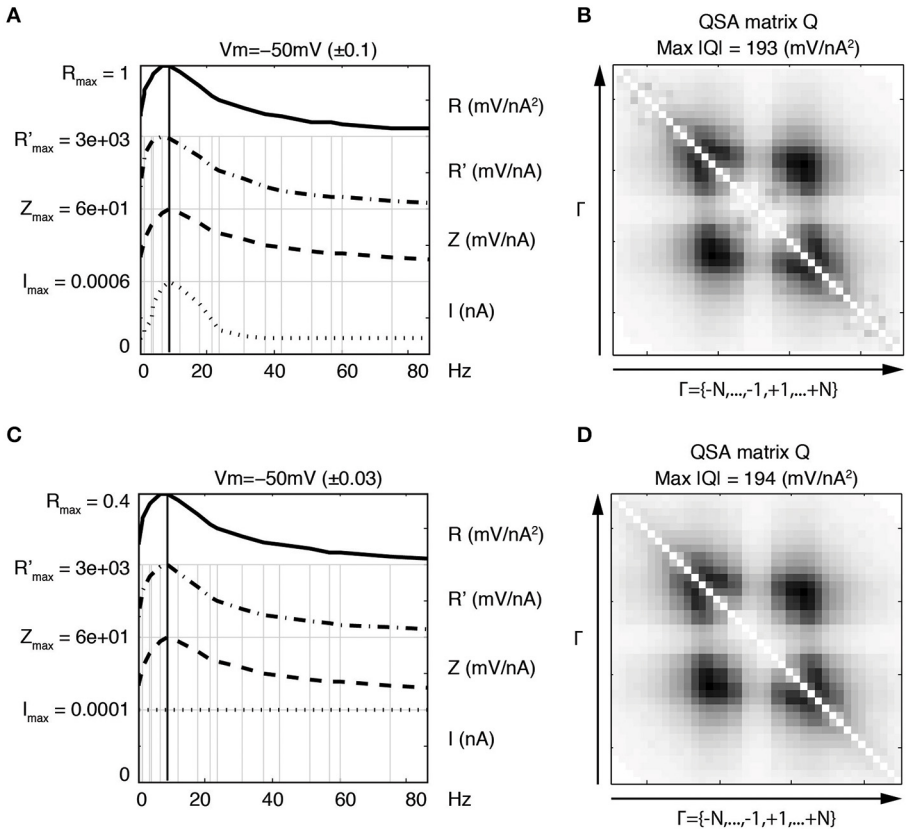

FIGURE 9 | Equivalence of nonlinear responses for different stimulation profiles at very small amplitudes. Upper row **(A,B)** Gaussian-like window applied to the stimulation Fourier components. Lower row **(C,D)** constant amplitude stimulation profile. The linear and nonlinear responses are nearly the same, however the maximum of the *R* function is about two fold higher for the Gaussian-like stimulation.

In general, the computed impedance for the somatic compartment is higher than the impedance of the soma plus the dendrite. This occurs because the impedance of a single somatic compartment is greater than the soma with attached dendritic compartments (not shown). More precisely, a significant portion of the injected current passes down the dendrite leaving a smaller current for the soma, which has a minimum value near the resonance frequency, at which the impedance is by definition maximal. Thus the smaller somatic current with the same soma potential gives a greater impedance. The total injected current would be the sum of the somatic current and remaining current flowing down the dendrite.

When a flat stimulation is injected at the end dendritic compartment (**Figure 10B**), the somatic current has a minimum near the resonance frequency and the somatic impedance is nearly the same to that determined with somatic stimulation. The simulations show that the nonlinear responses (QSA matrix, *R* function) are greater for the distal stimulation (right column) due to the dendritic filtering, which can be seen to be a Gaussian-like peak around 15 Hz.

When stimulating the end dendritic compartment, the other compartments significantly reduce the high frequency content of the current reaching the soma (**Figure 10**, right column). This current increases from a minimum at the resonant frequency to a maximal value and then progressively decreases with frequency as would be expected from dendritic filtering. These effects are the consequence of the progressive filtering of the membrane potential by each dendritic compartment toward the soma. Each individual dendritic compartment shows similar scaled linear behavior, which is dependent on the potential in each compartment as determined by the cable structure including the voltage dependent channels.

The QSA matrix for the dendritic stimulation shows enhanced corners that are similar to those observed for filtered stimulations applied to the soma in **Figures 6**, **8**. However, the dominating responses at the intermediate harmonics and interactive difference frequencies are comparable for both somatic and dendritic stimulations. Decreasing the stimulation amplitudes leads to the same limit functions for impedances and QSA matrices (not shown) as found for the Gaussian-like stimulations of **Figure 9**.

Figure 10D also shows peaks for the QSA matrix at harmonics and high frequency interactions (around $2f_6 = 8.0$ Hz and $f_{20} - f_{19} = 11$ Hz). These are similar to those observed for the Gaussian-like window of **Figure 8**, which has peaks clustered around harmonic frequencies of $f_7 = 6.4$ Hz and $f_8 = 8.7$ Hz.

Thus, the dendritic filtering is simulated by a Gaussian-like stimulation applied to the soma, which is related to the effect of a filtered stimulation applied to the soma as in **Figures 6**, **7**. In

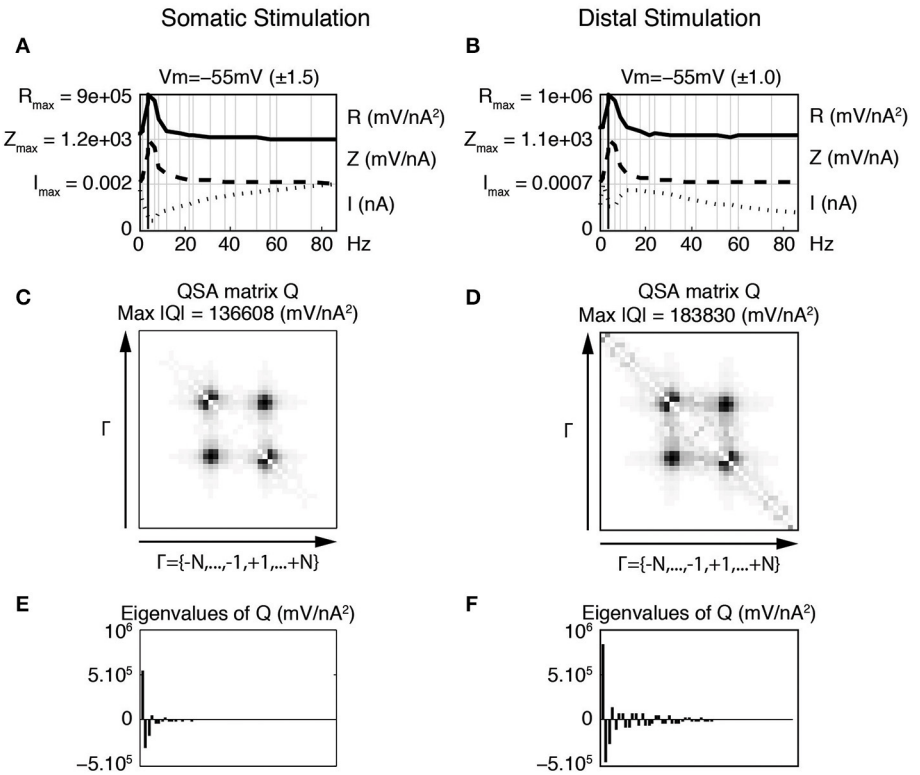

FIGURE 10 | Effect of distal vs. proximal flat stimulation on somatic nonlinearities. The linear and quadratic functions were calculated using only the current passing across the soma membrane, as opposed to the total injected current. Thus, the analyses apply to the soma independent of the location of the stimulating electrode. Left column **(A,C,E)** Responses to the flat stimulation of the somatic compartment. Right column **(B,D,F)** Responses to the flat stimulation applied at the most distal compartment. **(A,B)** Juxtaposed plots with respect to the input frequencies, namely the amplitudes of current stimulation *I*, linear impedance *Z*, and *R* function. The resonance of the impedance is $f_6 = 4.0$ Hz for both stimulations. **(C,D)** Amplitudes of the coefficients of the QSA matrix *Q* with the maximum value given by Max|*Q*|. **(E,F)** Eigenvalues of the QSA matrix. All parameters of the model neuron are the same as in **Figure 7**.

summary, these results support the fact that the enhancement of low frequency amplitudes increases nonlinear responses.

Increasing the electronic length leads to somatic current profiles similar to the filtered stimulations of **Figures 6**, **7** and QSA matrices that are quite similar. From a physiological point of view, these nonlinear effects due to filtering are very much dependent on the precise dendritic location of the stimulation and appear to be present at all input amplitudes. However, these nonlinearities are not significant until the soma potential responses are in the mV range where they also contribute to a distortion of the linear behavior if the frequency content of the stimulation is overlapping. Clearly, higher order nonlinearities are also generated with very large stimulations.

3.6. SPIKE FREQUENCY MODULATION

The subthreshold nonlinear responses are markedly dependent of the membrane potential and essentially reach their maximum values just below the threshold. This would suggest that the nonlinear behavior at just below the threshold membrane potential could provide a reasonable estimation of the suprathreshold action potential response. In order to directly determine suprathreshold responses, a QSA analysis was done on action potential responses using three or four stimulation frequencies near the resonance, namely 0.3, 1.3, and 3.5, or 4, 6.4, 8.7, and 12.1 Hz, the latter encompassing the resonance range of frequencies. Both linear and quadratic analyses were done using a Fourier analysis of unit spike events constructed from their peak values, which extracts the expected low frequency responses.

Figure 11A shows modulated action potential responses to a multi-sinsuoidal stimulation containing three frequencies (0.3, 1.3, and 3.5 Hz) that are all below the resonance. The underlying traces show the linear and quadratic membrane potential reconstructions for just these frequencies, which are sufficiently low to minimize the contamination of the Fourier transform by the shape of action potentials. **Figure 11B** represents linear and quadratic analyses of the membrane potential for the same neuron stimulated just below threshold. Since there are few frequencies, the superimposed reconstructed linear and quadratic responses have slight differences (**Figure 11A**, dashed linear vs. dotted quadratic lines). However, the quadratic responses remain significant (Magnani and Moore, 2011) to encode fundamental nonlinear properties of the neuron that cannot be predicted by linear analysis. The linear impedance shows three rising values that precede the usual resonance of stellate neurons. The

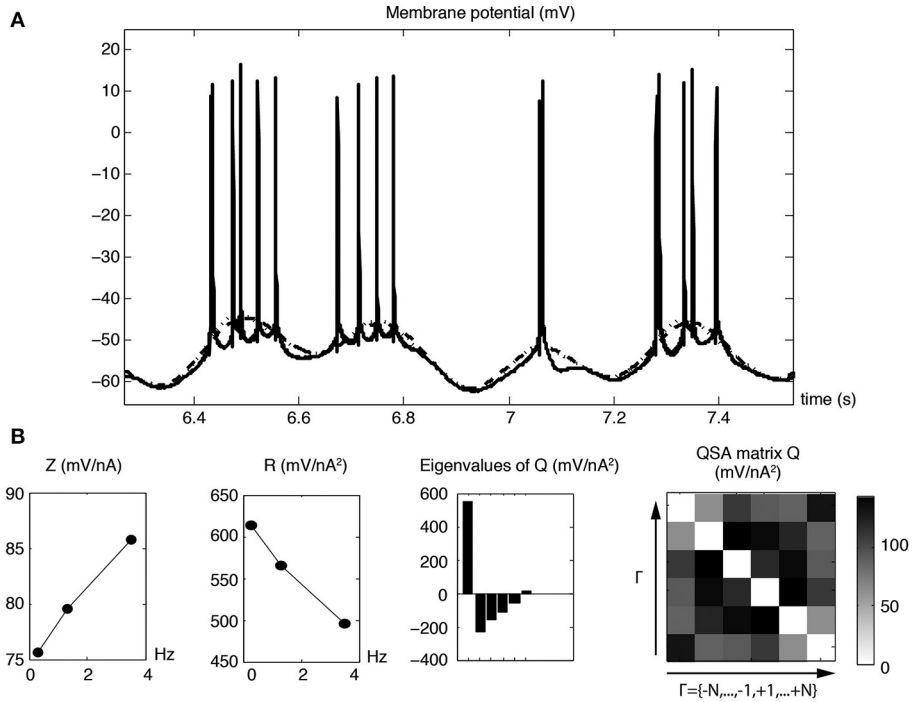

FIGURE 11 | Linear and quadratic membrane potential responses for pre-resonance stimulation frequencies ($f_1 = 0.3$, $f_2 = 1.3$ and $f_3 = 3.5$ Hz). **(A)** Membrane potential responses (solid line) with modulated action potential responses. The dashed and dotted curves show the linear and quadratic responses of the underlying membrane potential for the three stimulating frequencies. **(B)** Linear and quadratic analyses for a subthreshold response displaced by 0.5 mV without action potentials. The corresponding reconstructed time domain analyses are almost identical to those shown in the first row.

QSA matrix and the R function indicate that both low and higher frequencies near the harmonics have the greater interactive responses, which are also chararactized by a dominant eigenvalue.

The time instants of each action potential of **Figure 11A** were converted to unit impulses (UI), as illustrated in **Figure 12A**. The dashed and dotted traces show the linear and quadratic analyses computed from the Fourier transform of the unit impulses. **Figure 12A** shows the waveforms of both the linear and quadratic analyses of the unit impulses, which are similar to those of the membrane potential of **Figure 11A**. The QSA matrix and the R functions are slightly different, showing a greater amplitude for the highest frequency interactions, mainly the highest harmonic frequencies $2f_3 = 7$ Hz. It is evident from **Figure 12A** that, when the frequency of spiking modulation is high, namely the dotted quadratic response has a much greater amplitude than the dashed linear line. Also, both the membrane potential and unit impulses analyses have a dominant eigenvalue, which suggests that they have features in common for their nonlinear behavior.

Since the Fourier analysis of a spike train contains many high frequency components unrelated to the lower modulated spiking frequencies, it is useful to construct an instantaneous frequency (IF) curve from the spike times. A slightly Gaussian filtered IF curve is shown in **Figure 12C** as a solid trace for the same time range illustrated for the unit impulses in **Figure 12A**. The dashed linear and dotted quadratic traces are the reconstructed responses of the solid trace. The linear and quadratic analyses are shown in **Figure 12D** and are similar to the analysis of the unit impulses in **Figure 12B** except for the details of the QSA matrix. The QSA matrix of unit impulses shows high frequency interactions at sums $f_i + f_j$ and harmonics $2f_i$. The QSA matrix of instantaneous frequency curve has increased amplitudes of high frequency interactions at differences $|f_i - f_j|$. These various effects are also reflected in the time domain of the reconstructed responses (first row compared to third).

Figure 13 illustrates linear and quadratic analyses of the membrane potential (**Figure 13A**) measured without action potentials compared to unit impulses (**Figure 13B**), for a stimulation based on four frequencies ($f_1 = 4, f_2 = 6.4, f_3 = 8.7$ and $f_4 = 12.1$ Hz) that encompass the resonance of a stellate neuron. It is apparent that both the linear and nonlinear behaviors are quite comparable in this frequency range. The quadratic responses associated with the middle two frequencies are enhanced for both the membrane potential and unit impulses analyses. In general, the QSA matrix of unit impulses shows a more restricted set of intermediate frequency interactions than observed for the QSA matrix of the membrane potential, as can be observed on **Figure 13**. Nevertheless, the similarity of the linear and quadratic analyses of the subthreshold membrane potential and unit impulses are striking. This suggests that the suprathreshold modulated spiking behavior is reasonably well approximated by the subthreshold membrane potential nonlinearity, just below threshold. As threshold is approached, the subthreshold responses take on a more nonlinear character, which finally determines the actual

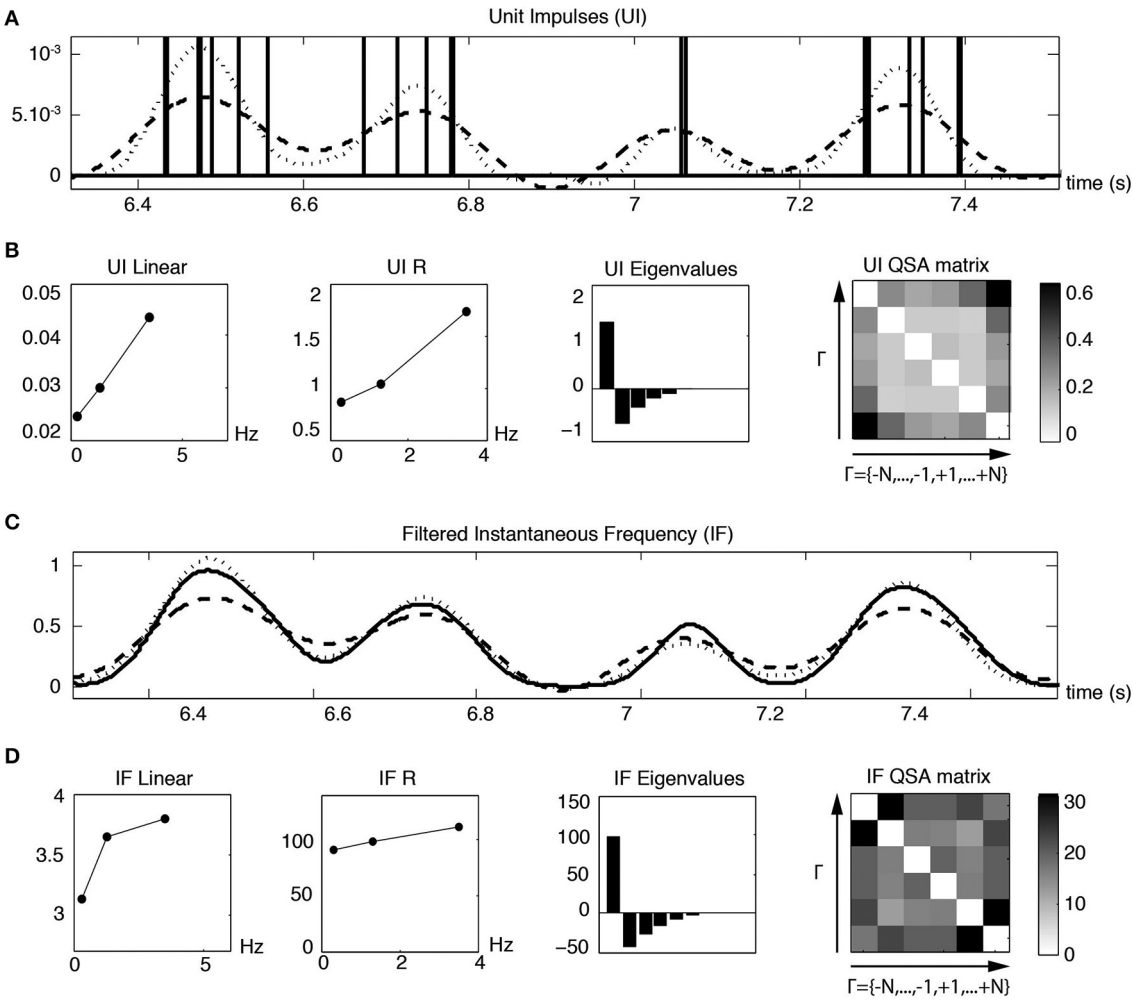

FIGURE 12 | Linear and quadratic responses of unit impulses (UI) to pre-resonance stimulation frequencies ($f_1 = 0.3$, $f_2 = 1.3$ and $f_3 = 3.5$ Hz). (A) Unit impulses corresponding to each action potential event of **Figure 11**. The dashed and dotted lines are the reconstructed linear and quadratic components based on the analysis of the second row. **(B)** Linear and quadratic analyses computed from the Fourier transform of the unit impulses. **(C)** The solid line is a slightly Gaussian filtered instantaneous frequency (IF) trace constructed from the spike times. The dashed and solid lines are the reconstructed linear and quadratic components based on the analysis of the fourth row. The Gaussian filter is sufficient to remove peaks related to spike times. The analysis of less filtered IF curves (not shown), such that distorted spike events are visible, is very similar to scaled unit impulses analyses. **(D)** Linear and quadratic analyses computed from the Fourier transform of the filtered instantaneous frequency.

unit impulses behavior, albeit in combination with the linear behavior.

4. DISCUSSION

The firing properties of the MEC stellate cells play a critical role in their function as part of the grid cell network. These neurons show oscillatory and nonlinear properties that are likely to be involved in the operation of networks involved in spatial awareness. We have used a novel theory, quadratic sinsoidal analysis (QSA), to rigorously determine the nonlinearity of SCs (stellate cells) near threshold for a direct comparison with linear behavior. This multi-sinusoidal frequency probing not only provides a quantitative measurement of these properties through the QSA matrix, but also an algebraic characterization of the quadratic function as a Hermitian operator. The nature of the quadratic responses are significantly different than subthreshold linear behavior and gives an indication of the distinctive differences between sub- and suprathreshold responses in SC neurons (Haas et al., 2007). We have shown that at physiological levels of stimulation, neurons and their models generate significant responses at harmonic and interactive frequencies that are not present in the input signal. Thus, the quadratic responses contain more frequencies over a wider frequency band than the input signal. As a consequence, they provide significant amplification at dynamically changing membrane potentials.

Previous studies have shown that the nonlinear responses measured in neurons appears to be dominated by the dendrites (Magnani and Moore, 2011), which receive the bulk of the synaptic input. It is likely that the principal source of nonlinearity in stellate neurons near threshold is the persistent stochastic

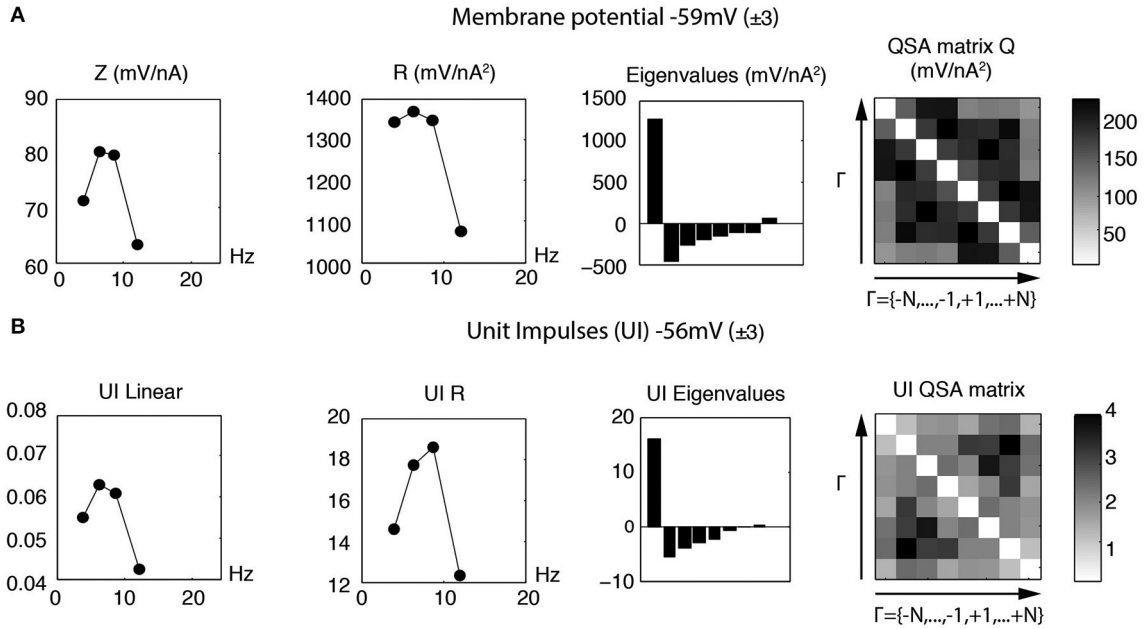

FIGURE 13 | Linear and quadratic analyses of membrane potential and unit impulses for stimulation frequencies near the resonance ($f_1 = 4$, $f_2 = 6.4$, $f_3 = 8.7$ and $f_4 = 12.1$ Hz). (A) Analysis of subthreshold membrane potential. **(B)** Analysis of suprathreshold unit impulses. The linear and quadratic behaviors for the subthreshold and suprathreshold responses have similar form for these resonance frequencies.

sodium conductance (g_{NaP}), which has been shown to be the primary source of channel noise in these neurons (Dorval and White, 2005). Thus, dendritic processing plays an important role in the firing behavior of stellate neurons in a number of ways (Zhuchkova et al., 2013). For example, the inherent filter properties of cable structures in combination with their active voltage dependent channels alter the profile of the stimulation reaching the soma. We have shown that dendritic filtering greatly alters the nonlinear membrane potential response at the soma, which will depend on both the spatial location and frequency content of the stimulation. Finally, we have demonstrated that quadratic analysis of modulated spiking behavior has significant similarities to membrane potential nonlinearities when the membrane potential is just below threshold.

In conclusion, this analysis indicates that subthreshold linear and nonlinear responses are similar to suprathreshold firing behavior. Thus, the combined linear and nonlinear behaviors near threshold of the membrane potential are reasonable estimates of suprathreshold behavior given by spike frequency modulation. Linear and nonlinear behaviors a few millivolts below the threshold membrane potential are quite different with the nonlinear component being significantly reduced. The linear components of stellate neurons, such as resonance, are present at membrane potentials hyperpolarized to threshold despite the diminishing nonlinearities. In these membrane potential ranges, the linear resonance behavior is essentially due to the H current (Giocomo and Hasselmo, 2009). There is also a nonlinear component of the H conductance that can be measured at hyperpolarized values, however it is much smaller than nonlinear effects of the sodium conductances near threshold (Magnani et al., 2013). An additional effect of H conductances could occur if they are present in the dendritic tree. In this case, distal inputs could show bandpass resonance characteristics that would propagate to the soma involving both active and passive dendritic filtering, and further increase a nonlinear soma response.

AUTHOR CONTRIBUTIONS

Christophe Magnani and Lee E. Moore developed the QSA theory and implemented the analysis in MATLAB. Christophe Magnani, Lee E. Moore, John A. White, and Michael N. Economo designed the experiments. Michael N. Economo did the whole cell patch clamp experiments. Lee E. Moore, Christophe Magnani, John A. White, and Michael N. Economo interpreted the results of the experiments. Lee E. Moore and Christophe Magnani did the model simulations, analyzed data and drafted the manuscript. Lee E. Moore, Christophe Magnani, John A. White, and Michael N. Economo edited and revised manuscript.

ACKNOWLEDGMENTS

Research reported in this paper was supported by the National Institutes of Health under award numbers NIH R01 EB016407 and NIH R01 MH085074. We wish to thank Dr. Lyle Graham for helpful comments.

REFERENCES

Boyd, S., Tang, Y., and Chua, L. (1983). Measuring volterra kernels. *IEEE Trans. Circ. Syst.* 30, 571–577. doi: 10.1109/TCS.1983.1085391

Burgalossi, A., and Brecht, M. (2014). Cellular, columnar and modular organization of spatial representations in medial entorhinal cortex. *Curr. Opin. Neurobiol.* 24, 47–54. doi: 10.1016/j.conb.2013.08.011

Dodson, P. D., Pastoll, H., and Nolan, M. F. (2011). Dorsal-ventral organization of theta-like activity intrinsic to entorhinal stellate neurons is mediated by differences in stochastic current fluctuations. *J. Physiol.* 589(Pt 12), 2993–3008. doi: 10.1113/jphysiol.2011.205021

Dorval, A. D. J., and White, J. A. (2005). Channel noise is essential for perithreshold oscillations in entorhinal stellate neurons. *J. Neurosci.* 25, 10025–10028. doi: 10.1523/JNEUROSCI.3557-05.2005

Engel, T. A., Schimansky-Geier, L., Herz, A. V. M., Schreiber, S., and Erchova, I. (2008). Subthreshold membrane-potential resonances shape spike-train patterns in the entorhinal cortex. *J. Neurophysiol.* 100, 1576–1589. doi: 10.1152/jn.01282.2007

Erchova, I., Kreck, G., Heinemann, U., and Herz, A. V. M. (2004). Dynamics of rat entorhinal cortex layer II and III cells: characteristics of membrane potential resonance at rest predict oscillation properties near threshold. *J. Physiol.* 560(Pt 1), 89–110. doi: 10.1113/jphysiol.2004.069930

Fernandez, F. R., Malerba, P., Bressloff, P. C., and White, J. A. (2013). Entorhinal stellate cells show preferred spike phase-locking to theta inputs that is enhanced by correlations in synaptic activity. *J. Neurosci.* 33, 6027–6040. doi: 10.1523/JNEUROSCI.3892-12.2013

Fernandez, F. R., and White, J. A. (2008). Artificial synaptic conductances reduce subthreshold oscillations and periodic firing in stellate cells of the entorhinal cortex. *J. Neurosci.* 28, 3790–3803. doi: 10.1523/JNEUROSCI.5658-07.2008

Giocomo, L. M., and Hasselmo, M. E. (2008). Time constants of h current in layer ii stellate cells differ along the dorsal to ventral axis of medial entorhinal cortex. *J. Neurosci.* 28, 9414–9425. doi: 10.1523/JNEUROSCI.3196-08.2008

Giocomo, L. M., and Hasselmo, M. E. (2009). Knock-out of HCN1 subunit flattens dorsal-ventral frequency gradient of medial entorhinal neurons in adult mice. *J. Neurosci.* 29, 7625–7630. doi: 10.1523/JNEUROSCI.0609-09.2009

Haas, J. S., Dorval, A. D. N., and White, J. A. (2007). Contributions of ih to feature selectivity in layer II stellate cells of the entorhinal cortex. *J. Comput. Neurosci.* 22, 161–171. doi: 10.1007/s10827-006-0005-7

Haas, J. S., and White, J. A. (2002). Frequency selectivity of layer II stellate cells in the medial entorhinal cortex. *J. Neurophysiol.* 88, 2422–2429. doi: 10.1152/jn.00598.2002

Idoux, E., Eugne, D., Chambaz, A., Magnani, C., White, J. A., and Moore, L. E. (2008). Control of neuronal persistent activity by voltage-dependent dendritic properties. *J. Neurophysiol.* 100, 1278–1286. doi: 10.1152/jn.90559.2008

Magnani, C., Eugne, D., Idoux, E., and Moore, L. E. (2013). Vestibular integrator neurons have quadratic functions due to voltage dependent conductances. *J. Comput. Neurosci.* 35, 243–259. doi: 10.1007/s10827-013-0451-y

Magnani, C., and Moore, L. E. (2011). Quadratic sinusoidal analysis of voltage clamped neurons. *J. Comput. Neurosci.* 31, 595–607. doi: 10.1007/s10827-011-0325-0

Pastoll, H., Ramsden, H. L., and Nolan, M. F. (2012). Intrinsic electrophysiological properties of entorhinal cortex stellate cells and their contribution to gridcell firing fields. *Front. Neural. Circuits* 6:17. doi: 10.3389/fncir.2012.00017

Ray, S., Naumann, R., Burgalossi, A., Tang, Q., Schmidt, H., and Brecht, M. (2014). Grid-layout and theta-modulation of layer 2 pyramidal neurons in medial entorhinal cortex. *Science* 343, 891–896. doi: 10.1126/science.1243028

Schreiber, S., Erchova, I., Heinemann, U., and Herz, A. V. M. (2004). Subthreshold resonance explains the frequency-dependent integration of periodic as well as random stimuli in the entorhinal cortex. *J. Neurophysiol.* 92, 408–415. doi: 10.1152/jn.01116.2003

Shay, C. F., Boardman, I. S., James, N. M., and Hasselmo, M. E. (2012). Voltage dependence of subthreshold resonance frequency in layer II of medial entorhinal cortex. *Hippocampus* 22, 1733–1749. doi: 10.1002/hipo.22008

Victor, J., and Shapley, R. (1980). A method of nonlinear analysis in the frequency domain. *Biophys. J.* 29, 459–483. doi: 10.1016/S0006-3495(80)85146-0

Yoshida, M., Giocomo, L. M., Boardman, I., and Hasselmo, M. E. (2011). Frequency of subthreshold oscillations at different membrane potential voltages in neurons at different anatomical positions on the dorsoventral axis in the rat medial entorhinal cortex. *J. Neurosci.* 31, 12683–12694. doi: 10.1523/JNEUROSCI.1654-11.2011

Zhuchkova, E., Remme, M. W. H., and Schreiber, S. (2013). Somatic versus dendritic resonance: differential filtering of inputs through non-uniform distributions of active conductances. *PLoS ONE* 8:e78908. doi: 10.1371/journal.pone.0078908

Conflict of Interest Statement: The authors declare that the research was conducted in the absence of any commercial or financial relationships that could be construed as a potential conflict of interest. The reviewer Michael E. Hasselmo declares that, despite having collaborated with co-author John A. White, the review process was handled objectively.

Received: 19 June 2014; paper pending published: 13 July 2014; accepted: 29 July 2014; published online: 19 August 2014.

Citation: Magnani C, Economo MN, White JA and Moore LE (2014) Nonlinear properties of medial entorhinal cortex neurons reveal frequency selectivity during multi-sinusoidal stimulation. Front. Cell. Neurosci. ***8****:239. doi: 10.3389/fncel.2014.00239*

This article was submitted to the journal Frontiers in Cellular Neuroscience.

frontiers in
CELLULAR NEUROSCIENCE

ORIGINAL RESEARCH ARTICLE
published: 16 September 2014
doi: 10.3389/fncel.2014.00287

A simulation study on the effects of dendritic morphology on layer V prefrontal pyramidal cell firing behavior

Maria Psarrou[1,2,3†], Stefanos S. Stefanou[1,4†], Athanasia Papoutsi[1], Alexandra Tzilivaki[1,4], Vassilis Cutsuridis[1] and Panayiota Poirazi[1]*

[1] *Institute of Molecular Biology and Biotechnology, Foundation for Research and Technology–Hellas, Heraklion, Greece*
[2] *Centre for Computer Science and Informatics Research, Science and Technology Institute, University of Hertfordshire, Hatfield, UK*
[3] *School of Computer Science, University of Hertfordshire, Hatfield, UK*
[4] *Department of Biology, University of Crete, Heraklion, Greece*

Edited by:
Sergey M. Korogod, National Academy of Sciences of Ukraine, Ukraine

Reviewed by:
Annalisa Scimemi, SUNY Albany, USA
Elena Emilianovna Saftenku, Bogomoletz Institute of Physiology, Ukraine

****Correspondence:***
Panayiota Poirazi, Computational Biology Lab, Institute of Molecular Biology and Biotechnology, Foundation for Research and Technolog–Hellas, Vassilika Vouton, Heraklion 71110, Crete, Greece
e-mail: poirazi@imbb.forth.gr

† These authors have contributed equally to this work.

Pyramidal cells, the most abundant neurons in neocortex, exhibit significant structural variability across different brain areas and layers in different species. Moreover, in response to a somatic step current, these cells display a range of firing behaviors, the most common being (1) repetitive action potentials (Regular Spiking—RS), and (2) an initial cluster of 2–5 action potentials with short interspike interval (ISIs) followed by single spikes (Intrinsic Bursting—IB). A correlation between firing behavior and dendritic morphology has recently been reported. In this work we use computational modeling to investigate quantitatively the effects of the basal dendritic tree morphology on the firing behavior of 112 three-dimensional reconstructions of layer V PFC rat pyramidal cells. Particularly, we focus on how different morphological (diameter, total length, volume, and branch number) and passive [Mean Electrotonic Path length (MEP)] features of basal dendritic trees shape somatic firing when the spatial distribution of ionic mechanisms in the basal dendritic trees is uniform or non-uniform. Our results suggest that total length, volume and branch number are the best morphological parameters to discriminate the cells as RS or IB, regardless of the distribution of ionic mechanisms in basal trees. The discriminatory power of total length, volume, and branch number remains high in the presence of different apical dendrites. These results suggest that morphological variations in the basal dendritic trees of layer V pyramidal neurons in the PFC influence their firing patterns in a predictive manner and may in turn influence the information processing capabilities of these neurons.

Keywords: dendrites, PFC, morphology, pyramidal cell, single neuron modeling, firing pattern, layer V

INTRODUCTION

Cortical neurons exhibit a wide range of firing behaviors (Connors and Gutnick, 1990). Pyramidal cells in particular, the most abundant cortical excitatory neurons, have been shown to fire in at least three different patterns: (a) repetitive action potentials with or without adaptation (Regular Spiking—RS), (b) an initial doublet followed by single spikes (Intrinsic Bursting—IB), or (c) repetitive bursts (2–5 action potentials with inter-spike-intervals of less than 10 ms) (Repetitive Oscillatory Bursting—ROB) (Yang et al., 1996; Dégenètais et al., 2002; Wang et al., 2006; Chang and Luebke, 2007; Van Aerde and Feldmeyer, 2013).

The abovementioned firing patterns are likely to serve distinct functions within the network and contribute differentially to its behavior. Experimental studies have shown that bursts improve the signal-to-noise ratio of neuronal responses and convey specific stimulus-related information (Eggermont and Smith, 1996; Martinez-Conde et al., 2002). In synapses with short-term facilitation, bursts are transmitted more reliably than isolated spikes (Lisman, 1997). Other studies have shown a link between neuronal sub-types, their outputs and their target areas. IB neurons in layer V of the auditory cortex send signals to higher-order thalamic nuclei as well as midbrain and brainstem nuclei, whereas RS neurons send signals to the ipsilateral and contralateral cortex (Sun et al., 2013). Similarly, IB and RS neurons in the prefrontal cortex (PFC) project to the pons (cortico-pontine) or the striatum but no IB neurons project to the contralateral cortex (cortico-cortical) (Morishima and Kawaguchi, 2006). IB neurons in the distal parts of the subiculum project primarily to the medial enthorhinal cortex but not the amygdala (Kim and Spruston, 2012). This segregation seen across several brain areas is likely to be associated with some form of functional specialization of RS and IB neurons. Therefore, it is important to understand what features of their morphology, connectivity and/or biophysics may determine the firing pattern of cortical pyramidal neurons.

Studies have shown that sources of firing pattern variability may be the distribution and density of active mechanisms within a cell (Jensen et al., 1994; Andreasen and Lambert, 1995; Migliore et al., 1995; Jensen and Yaari, 1997; Schwindt and Crill, 1999), synaptic connectivity (Williams and Johnston, 1989; Weisskopf et al., 1994; Nicoll and Malenka, 1995; Maccaferri et al., 1998; Yeckel and Berger, 1998; Sidiropoulou and Poirazi,

2012; Sun et al., 2013), morphological diversity (Bilkey and Schwartzkroin, 1990; Chagnac-Amitai et al., 1990; Mason and Larkman, 1990; Mainen and Sejnowski, 1996; Yang et al., 1996; Krichmar et al., 2002; Van Ooyen et al., 2002; Van Elburg and van Ooyen, 2010), and inhibition on soma and/or dendrites of the cell (Lovett-Barron et al., 2012; Royer et al., 2012).

Neuronal firing behavior depends strongly on the distribution and density of ionic currents. Neurophysiological studies have shown that RS pyramidal cells can generate bursts if the extracellular K^+ concentration is increased (Jensen et al., 1994; Andreasen and Lambert, 1995; Jensen and Yaari, 1997; Schwindt and Crill, 1999). Similarly, a modeling study showed that the CA3 pyramidal cell's firing characteristics can be changed from non-bursting to bursting by modifying the Ca^{2+}-independent K^+ conductance 100 μm from the soma (Migliore et al., 1995). Along the same line, the modeling study of Sidiropoulou and Poirazi (2012) showed that doubling the Na^+ and Ca^{2+} conductances turns an RS LV PFC cell into an IB one. Combination of neurophysiology with computational modeling has suggested that pyramidal cell bursting may be due to the interplay of somatic and dendritic voltage-gated Na^+ and K^+ conductances (Krahe and Gabbiani, 2004). These conductances promote propagation of action potentials from the soma into the dendrites, causing the dendrites to be depolarized when, at the end of a somatic spike, the soma is hyperpolarized, leading to a rebound current from the dendrites to the soma. This rebound current causes a depolarizing after-potential at the soma, which, if strong enough, may lead to another somatic spike. This whole process has been described as a "ping-pong" interaction between the soma and the dendritic tree (Wang, 1999).

In addition to intrinsic mechanisms, changes in the strength, timing or connectivity of synaptic input can alter the firing behavior of a neuron. Studies have shown that long-term potentiation of mossy fibers to CA3 pyramidal cell synapses may cause postsynaptic pyramidal cells to burst (Williams and Johnston, 1989; Weisskopf et al., 1994; Nicoll and Malenka, 1995; Maccaferri et al., 1998; Yeckel and Berger, 1998). Pissadaki et al. (2010) investigated how timing and spatial variations in synaptic inputs to the distal and proximal dendritic layers of a CA1 pyramidal cell model influenced the cell's firing pattern. Introduction of a temporal delay in the activation of the two layers acted as a switch between excitability modes: short delays induced bursting, while long delays caused low frequency RS. Such activity-induced changes in neuronal firing patterns suggest a key role of these patterns in information processing in the brain.

Apart from ionic and synaptic effects, dendritic morphology has also been suggested to influence the firing behavior of neocortical and hippocampal pyramidal neurons (Bilkey and Schwartzkroin, 1990; Chagnac-Amitai et al., 1990; Mason and Larkman, 1990; Yang et al., 1996). Previous studies reported that IB neurons are characterized by large cell bodies, long and extensive apical dendritic trees, and axons that tend to ramify in subcortical and brainstem nuclei (Kelly and Wong, 1981; Games and Winer, 1988; Ojima et al., 1992). RS neurons on the other hand have smaller cell bodies, smaller dendritic arborizations with fewer oblique branches that end without terminal tufts, and their axons project via callosal connections to sensory cortices in the other hemisphere and to corticostriatal projections (Games and Winer, 1988; Rüttgers et al., 1990; Ojima et al., 1992; Winer and Prieto, 2001; Hattox and Nelson, 2007). Such differences in anatomical features have been associated to the different firing patterns in previous computational modeling studies (Mainen and Sejnowski, 1996; Krichmar et al., 2002; Van Ooyen et al., 2002). However, these earlier studies were qualitative and limited in the sense that they focused exclusively on the apical trees of morphologically very distinct cell classes (Mainen and Sejnowski, 1996; Krichmar et al., 2002).

Here, we use a modeling approach to investigate in a quantitative manner the effects of neuronal morphology (dendritic size and dendritic topology) on the firing behavior of 112 three-dimensional reconstructions of layer V PFC pyramidal cells. By systematically varying the basal and/or apical dendritic trees of these neurons as well as the distribution of ionic mechanisms along their dendritic trees, we predict which of the morphological parameters (diameter, total length, volume, branch number) and/or passive properties (Mean Electrotonic Path length—MEP) can best discriminate between IB and RS neurons. Considering that dendritic morphology alterations may lead to many pathological conditions, such as Alzheimer's disease and epilepsy (Yamada et al., 1988; Moolman et al., 2004; Teskey et al., 2006), the results of our modeling study are instrumental in uncovering, in a systematic way, the underlying mechanisms by which dendritic morphology and its alterations affect neuronal firing behavior.

MATERIALS AND METHODS

MORPHOLOGICAL DATA

Three-dimensional morphological data of 112 layer V pyramidal cells (PC) from the rat PFC were obtained from the NeuroMorpho database (http://neuromorpho.org) (see Supplementary Tables S1, S2 for morphological features of basal and apical dendritic trees of all 112 pyramidal cells). These neurons were previously reconstructed in the Smith lab from the brains of adult Long-Evans rats at 2–4 months of age (Bergstrom et al., 2008). No data regarding the size, shape and distribution of spines in the estimation of the dendritic surface area were provided. Images of three of these 112 cells are shown in **Figure 1**. The images of the remaining cells are available at the abovementioned web site.

The digitized cell reconstructions were acquired in SWC format (Ascoli, 1999). All SWC files were checked for any morphological reconstruction inconsistencies before being converted into the HOC format and loaded into the NEURON neural simulator (Hines and Carnevale, 1997).

PYRAMIDAL CELL MODEL

For all model cells, unless mentioned otherwise, we assumed a uniform membrane resistance of $R_m = 30\,k\Omega\ cm^2$ in the soma and the axon. In the basal dendrites, the membrane resistance decreased sigmoidally up to half of the somatic value, according to the function $R_m(x) = 30 - \frac{15}{1+e^{\frac{10-x}{5}}}$. Similarly, the membrane resistance in the apical dendrites decreased sigmoidally up to half of the somatic value according to the formula $R_m(x) = 30 - \frac{15}{1+e^{\frac{300-x}{50}}}$ (Stuart and Spruston, 1998). A uniform intracellular

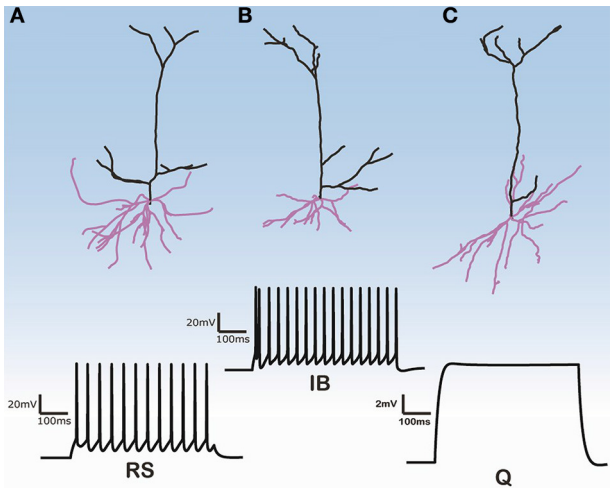

FIGURE 1 | Morphologies of three model cells and their responses to a somatic depolarization of 0.35 nA multiplied by the normalization factor for the input resistance. Upper panel: The somatic compartment is the same in all model cells but apical and dendritic trees are taken from three distinct reconstructed morphologies. Lower panel: Cells either display regular spiking with no adaptation **(A)**, are intrinsic bursting **(B)**, that is an initial burst (1–2 spikes) followed by a regular spiking or are silent **(C)**.

resistivity $R_a = 210\,\Omega$ cm and a specific membrane capacitance (C_m) of $1.2\,\mu F\ cm^{-2}$ were used in the soma, axon, apical and basal dendrites. The resting membrane potential was set at −66 mV.

Active mechanisms included two types of Hodgkin–Huxley-type Na^+ currents (transient: I_{Naf}; persistent I_{Nap};), three voltage-dependent K^+ currents (I_{Kdr}; I_A; I_D), a fast Ca^{2+} and voltage-dependent K^+ current, I_{fAHP}; a slow Ca^{2+}-dependent K^+ current, I_{sAHP}; a hyperpolarization-activated non-specific cation current (I_h); a low-voltage activated calcium current I_{CaT} and three types of Ca^{2+}- and voltage-dependent calcium currents (I_{caN}; I_{caR}; I_{caL}). In all cells, the conductance of I_{Naf} was highest in the axon, and increased in the soma and apical dendrites compared to basal dendrites (González-Burgos and Barrionuevo, 2001). The conductance of all three different K^+ currents was decreased in the apical dendrites compared to the soma (Korngreen and Sakmann, 2000; Schaefer et al., 2007). Both fast and slow AHP currents were present in the soma and much less in the apical dendrites (Lorenzon and Foehring, 1992). The h-current conductance increased sigmoidally, in the apical tree, reaching a maximum value that was10 times greater than the somatic value (Day et al., 2005; Kole et al., 2006). This increase was not implemented in the basal dendrites (Nevian et al., 2007). The mathematical formalism of the pyramidal neuron model used in this study was based on the model of Sidiropoulou and Poirazi (2012) and can be found in the Supporting Online Material (SOM). The parameter values of all active mechanisms are reported in Supplementary Table S3 in the SOM.

SIMULATIONS SETUP

Cell "C3_5" (as referred in the NeuroMorpho database) was selected as the control morphology because it was previously used and extensively validated with respect to passive and active membrane properties as well as apical and basal dendritic responses against experimental data by Sidiropoulou and Poirazi (2012) (see Supplementary Figure S1 in Sidiropoulou and Poirazi, 2012 study). To investigate the effects of dendritic tree variability on firing behavior, we kept the soma of cell "C3_5" and varied the apical and basal trees attached to this soma using the 112 PFC layer V PCs previously described in Section "Morphological Data." Which apical and/or basal tree(s) were attached depended on the specific experiment (see "Results" section for details). The input resistances of all simulated cells were calculated by measuring the steady-state voltage change in response to a 500 ms hyperpolarizing current pulse (0.1 nA). Previous studies (Washington et al., 2000; Krichmar et al., 2002) have shown that dendritic morphology has a strong effect on input resistance. In order to ensure equivalent depolarization in each model cell and eliminate the influence of the input resistance on the electrophysiological response to current injections, the current injections were scaled by the ratio of the cell's input resistance to that of the control cell (cell "C3_5") multiplied by a constant factor of 0.35 (i.e., the current 0.35 nA), where cell "C3_5" first spiked). Thus, simulations consisted of depolarizing the PFC pyramidal cell model's soma with a normalized injection current, such that the initial instantaneous depolarization was equivalent for all cells, and recording the membrane potential at the soma.

MORPHOLOGICAL PARAMETERS

Morphological parameters were obtained directly from the three-dimensional neuroanatomical description and included the dendritic size (median diameter, total length, volume, and branch number). The MEP for each apical and basal dendritic tree was also derived. To estimate the median diameter, we first calculated the diameter of each cylindrical section of the dendritic tree (basal or apical) of each cell (112 cells in total) and then took the median value. To estimate the total length we summed the length of all sections of each tree (basal or apical) for all cells. To estimate the branch number, we calculated the branch number of each tree (basal or apical) for all cells.

The volume was estimated using the following equation:

$$V = \sum_{i=1}^{N} \pi \cdot L_i \cdot (D_i/2)^2 \tag{1}$$

where for every cylindrical section i of each tree, L_i is the length and D_i is the diameter. We estimated MEP as in Van Elburg and van Ooyen (2010). More specifically, to obtain the MEP of a dendritic tree, we first normalized the length l_i of each terminal, intermediate or root section i with respect to its electrotonic length constants λ_i, yielding a dimensionless electrotonic length $\Lambda_i = l_i/\lambda_i$, in which λ_i was defined as:

$$\lambda_i = \sqrt{\frac{b_i \cdot r_m}{2 \cdot r_a}} \tag{2}$$

where b_i was the radius of dendritic section i, and r_m and r_a were constants denoting the specific membrane resistance and the

intracellular resistivity, respectively. The MEP of a dendritic tree with N terminal sections was then given by:

$$MEP = \frac{1}{N}\sum_{j=1}^{N} P_j \quad (3)$$

where P_j was the sum of the electrotonic lengths Λ_i of all dendritic sections in the path from the tip of terminal section j to the soma.

DATA ANALYSIS

We used two types of active mechanism distributions in the basal dendritic trees of cells: (1) uniform (i.e., the conductance of an active mechanism does not depend on the distance from the soma), and (2) non-uniform (distance dependent) (see Table S3). For each distribution of active mechanisms, the firing behaviors of the model cells were classified into two categories: (1) RS, and (2) IB. A model cell was considered as IB if the interspike interval (ISI) of the first two spikes in its spike train was smaller than 20 ms. Otherwise, the cell was considered as RS. For each firing behavior category (RS or IB), we estimated the median diameter, volume, MEP, branch number, and the total length of the basal or apical tree. A non-parametric statistical Mann–Whitney U-test was performed to test if these features were significantly different between the two categories.

In addition to detecting statistical differences, features such as the diameter, total length, MEP, volume, or branch number were used to classify each model cell as an RS or an IB via the use of a probabilistic Bayesian classifier. Probability distributions for the two categories ("training") were estimated using 80% of the total number of cells ($N_{RS} + N_{IB}$) and the classifier's classification accuracy was measured on the remaining 20% of cells ("testing"). This procedure was repeated 10 times, using different randomly selected training/test sets of the same size. The performance accuracy reported here was evaluated solely on the 10 test sets, namely the 20% of the samples that were not used for training. The performance reported is the average over the 10 different trials. If the sizes of the RS (N_{RS}) and IB (N_{IB}) samples were unequal (e.g., $N_{RS} > N_{IB}$), then we set the size of the larger sample equal to the size of the smaller one, and used the 80% of each sample for training and the remaining 20% for testing. Classification performance was assessed using the sensitivity, specificity and accuracy metrics. Given a two class problem with Negative and Positive examples, sensitivity refers to the percentage of true Positives that are correctly identified, whereas specificity refers to the percentage of true Negatives that are correctly identified as such. Accuracy measures the proportion of true Positives and true Negatives correctly identified. The larger the sensitivity, specificity, and accuracy values, the better the classification.

IMPLEMENTATION

The simulations were run in the NEURON simulation environment (Hines and Carnevale, 1997) and simulations were executed on a parallel cluster (8 core Intel Xeon processors). Data analysis was performed using MATLAB (The MathWorks Inc., Natick, Massachusetts) and was adapted from the Cuntz et al. (2010) work. The source code of the model is available upon request to the corresponding author at poirazi@imbb.forth.gr. The source code of the original model by Sidiropoulou and Poirazi (2012) can be found on ModelDB (accession number: 144089).

RESULTS

The firing behavior of the 112 simulated PFC layer V pyramidal cells in response to simulated somatic depolarization varied greatly. Model cells were either quiescent, i.e., with no spike response, displayed RS with no adaptation, or IB, that is an initial burst followed by RS. **Figure 1** shows the responses of the two cell categories investigated in this simulation study, namely RS and IB, plus the quiescent state (Q) seen in just a few model cells. Images of the reconstructed cellular morphologies are superimposed (**Figure 1**, upper panel). Note that spiking activity was measured in response to a somatic depolarization of 0.35 nA multiplied by the normalization factor of the input resistance (see Materials and Methods). Indicative voltage traces before this normalization are shown in Supplementary Figure S1. For small currents (0.2 nA) IB cells displayed a characteristic fast afterdepolarization (fADP) that generated the burst profile for larger currents (0.35 nA, Supplementary Figure S1). Since the channel distribution, Ca^{2+} concentration, soma volume and depolarization levels were the same across all cells, the firing behavior variation can be attributed to differences in the apical and basal dendritic morphology of the neurons.

To isolate the effect of basal dendritic morphology variations from those of the apical dendritic tree, on the firing behavior of layer V PFC pyramidal cells, we created two additional models. As before, the soma of both of these models corresponded to the soma of cell "C3_5" and their apical dendritic trees were taken from cells "30-3a" (hereby termed "complex apical model") and "31-3" (hereby termed "simple apical model") in our neuron pool (**Figure 2A**). These two apical trees were selected because they represented a simple and a complex morphology (Supplementary Table S1), in an effort to approximate the two extreme cases where the morphology of the apical tree may influence responses. The 112 different basal trees were subsequently attached to both of these models and the resulting somatic responses to the normalized somatic current injection were measured (**Figure 2**). We observed that in the complex apical model, the distribution of firing patterns in the 112 cells with different basal trees was 70% RS, 29% IB, and 1% quiescent (**Figure 2C**). In the simple apical model however, these proportions were reversed. We measured 23% RS, 76% IB, and 1% quiescent responses (**Figure 2C**). These results are in agreement with previous findings regarding the significant effect of the apical morphology on neuronal firing patterns (Chang and Luebke, 2007).

Importantly, while the apical tree morphology introduces a bias in neuronal output (seen in the different distributions of RS vs. IB model cells in **Figure 2C**), given the same apical dendrite (complex or simple) the different firing patterns observed are solely due to the different basal morphologies. As shown in **Figure 2B**, the total length, the volume and the branch number of the basal dendritic tree were statistically different (p-value < 0.001) between the RS and IB spiking profiles, irrespectively of the apical tree used. In fact these features could also be used to predict the model cell's firing pattern via a probabilistic classifier (see Supplementary Figure S2). This suggests that, apart

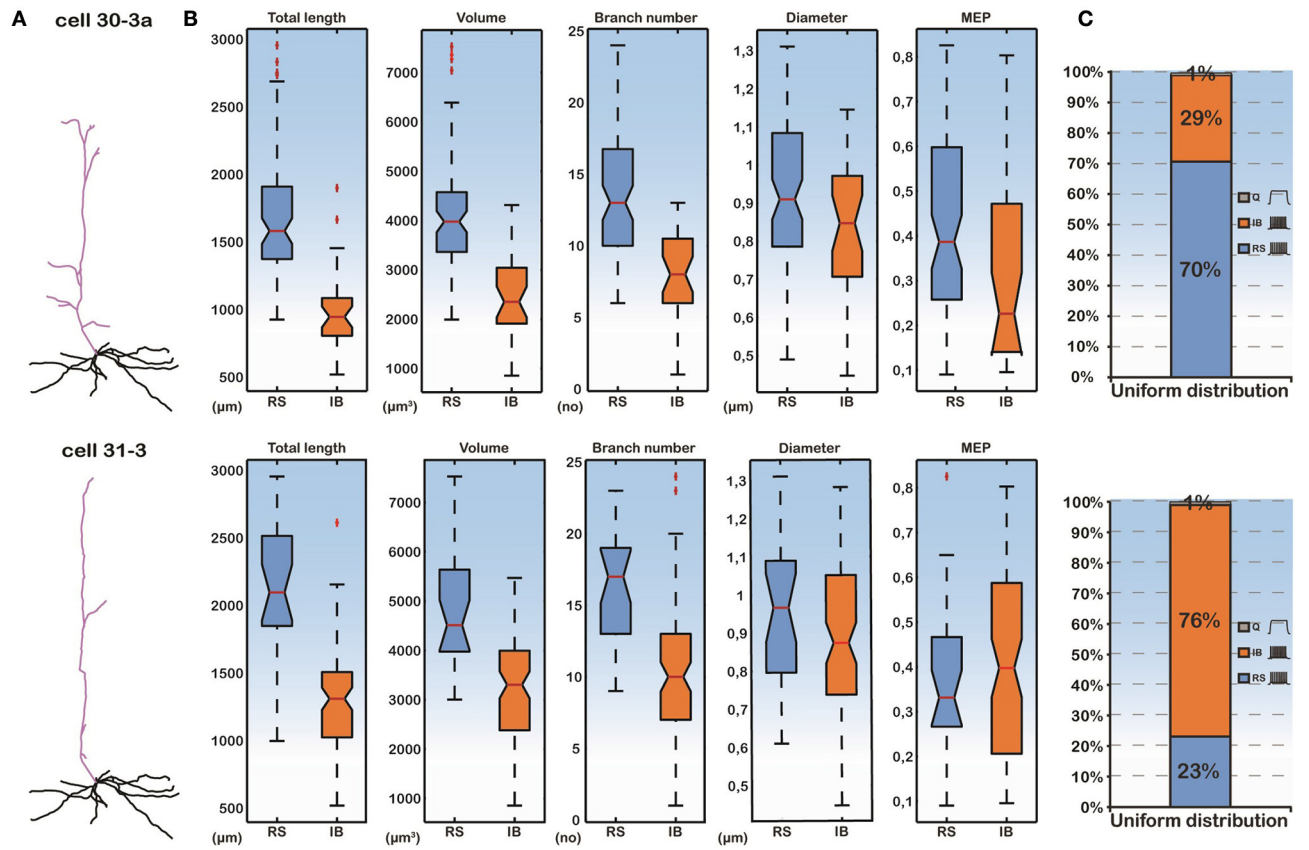

FIGURE 2 | (A) Categorization of model cell firing patterns when using two different apical dendrites (a complex "30-3a" and a simple "31-3") and 112 different basal dendrites. Ionic mechanisms are distributed uniformly along the basal tree. **(B)** Box plots of all morphological features of the basal trees and the MEP for the RS and IB categories. Differences in the features are statistically significant between the two categories. **(C)** Proportions of RS, IB, and Q cells are significantly different in the "30-3a" and "31-3" model cell cases.

from the morphology of the apical tree, basal tree morphology also contributes to the spiking profile of layer V PFC pyramidal neurons.

Thus, we sought to thoroughly examine how basal dendritic tree variability may influence the firing behavior of layer V PFC pyramidal cells, irrespectively of the apical tree morphology. Toward this goal, we again used the soma of cell "C3_5," but this time varied both its basal and apical dendritic trees, thus generating 112 × 112 morphological combinations (**Figure 3A**). For each of the 112 basal trees, 112 different apical trees were attached and somatic response patterns to normalized current injection were recorded as detailed previously. As shown in **Figure 3A**, utilization of different basal trees (y-axis) greatly influenced the percentage of RS vs. IB firing patterns produced for each apical tree attached (x-axis). To somehow average the effect of apical tree morphology on the firing pattern of a model cell with a given basal tree we applied the following approach: for each basal dendritic morphology (row in **Figure 3A**), if more than half of the 112 model cells produced a RS response, then this basal dendritic morphology was considered an RS (that is it has the "tendency" to produce an RS profile, irrespectively of the apical tree used). Otherwise, the basal dendritic morphology was considered an IB. Out of the 112 basal trees used, 54 (48%) were assigned an RS profile and 58 (52%) were assigned an IB profile (**Figure 3B**). Since in all these experiments the distribution of ionic mechanisms along the basal tree was uniform, we investigated the robustness of our findings in the presence of a non-uniform mechanism distribution (i.e., distance-dependent, see also Supplementary Table S3). The results were very similar: 46% of the basal trees were assigned an RS profile and 54% were considered IB (**Figure 3B**).

A detailed analysis of the model cells that exhibited an RS or an IB profile showed that the basal trees of RS cells had a median diameter of 0.97 μm, a total length of 1739.2 μm, a volume of 4349.1 μm^3, a MEP of 0.34 and a branch number of 15. The basal trees of IB model cells on the other hand, had a median diameter of 0.837 μm, a total length of 1152.3 μm, a volume of 2924.6 μm^3, a MEP of 0.39 and a branch number of 10. A Mann–Whitney U-test showed a statistically significant difference ($p < 0.01$) for the total length, volume, and branch number between the RS and IB model cells, for both uniform and non-uniform distributions of the ionic mechanisms along the basal tree (see **Table 1** for details). Box-plots of RS and IB median diameter, total length, MEP, volume, and branch number in the uniform and non-uniform distribution cases are depicted in **Figure 4**. It is clearly

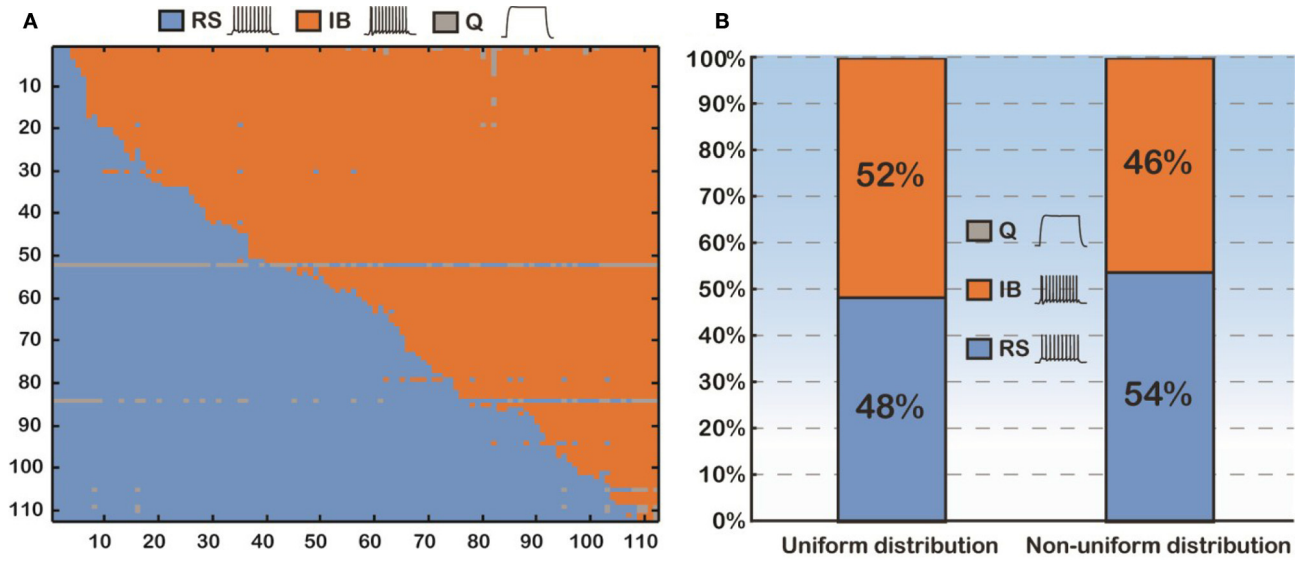

FIGURE 3 | (A) Confusion matrix of 12544 (112 × 112) combinations of dendritic trees (basal and apical) sorted according to the firing pattern of the model cells. **(B)** Proportions of the model cells' firing behavior (RS vs. IB). Uniform distribution means that the conductance of an active mechanism is not dependent on the distance from the soma. Non-uniform distribution means the conductance of an active mechanism is distance-dependent.

Table 1 | Median diameter, total length, MEP, volume, and branch number values for both RS and IB in the uniform and non-uniform cases.

	Diameter (μm)	Total length (μm)	MEP	Volume (μm^3)	Branch number
UNIFORM					
RS	0.967	1739.2	0.3391	4349.1	15
IB	0.837	1152.3	0.3921	2924.6	10
p-value	0.0061	3.37E-13	0.7532	1.50E-10	5.65E-09
NON-UNIFORM					
RS	0.963	1699.2	0.385	4322.3	14
IB	0.8375	1128.8	0.4528	2722.9	9
p-value	0.012	1.30E-12	0.9117	7.13E-12	3.71E-08

A Mann–Whitney U-test showed a statistically significant difference ($p < 0.01$, alpha level = 0.05) for the total length, volume, and branch number between the RS and IB cells regardless of the distribution of ionic mechanisms.

evident that in both cases the total length, volume and branch number are the parameters that differ the most between model cells exhibiting an RS vs. an IB firing behavior.

In light of these statistical differences in anatomical features of RS vs. IB model cells, we next questioned whether the morphology of the basal tree has a determinant role in shaping the resulting response patterns, irrespectively of the apical tree. Toward this goal, we used a probabilistic classifier. Specifically, we employed a Bayes classifier (see Materials and Methods) and used the diameter, total length, MEP, volume, or branch number of basal trees to test whether these features can correctly predict the firing pattern (RS or IB) of the respective model cell. Prediction accuracy was evaluated using the sensitivity, specificity, and classification accuracy metrics. We found that the best discriminatory parameters (i.e., the parameters with the highest sensitivity, specificity, and accuracy values) were the total length, volume and branch number, for both uniform and non-uniform distributions of ionic mechanism (**Figure 5**). Given that the accuracy achieved when using, for example, the total length of the basal tree is very high (>80%), these results suggest that anatomical features of the basal tree determine to a very large extent the firing pattern of the resulting model cell.

Since total length, volume and branch number of the basal tree were the morphological parameters that determined the electrophysiological profile, we also performed correlation analysis of these features. As expected, the volume and branch number correlate strongly with the total length in both uniform and non-uniform cases (**Figure 6**). These results explain why these three features have a high discriminatory power: any of them is sufficient to predict with high confidence the firing pattern of a model cell with a particular basal tree.

DISCUSSION

GENERAL ISSUES

A biophysically realistic model of a layer V PFC pyramidal cell was extended to quantitatively investigate the effects of dendritic morphology and distribution of ionic mechanisms (uniform vs. non-uniform) along its basal dendrites on its firing behavior. The model cell was extensively validated in a previous study (Sidiropoulou and Poirazi, 2012) from our group against a wealth of experimental data (Haj-Dahmane and Andrade, 1998, 1999; Fowler et al., 2007; Milojkovic et al., 2007; Nevian et al., 2007; Wang et al., 2008; Sidiropoulou et al., 2009) casting it as a faithful representation of a biologically realistic layer V PFC pyramidal cell. Using this experimentally validated model we systematically varied its basal and apical dendritic trees as well as its ionic mechanism distribution along the basal dendritic trees

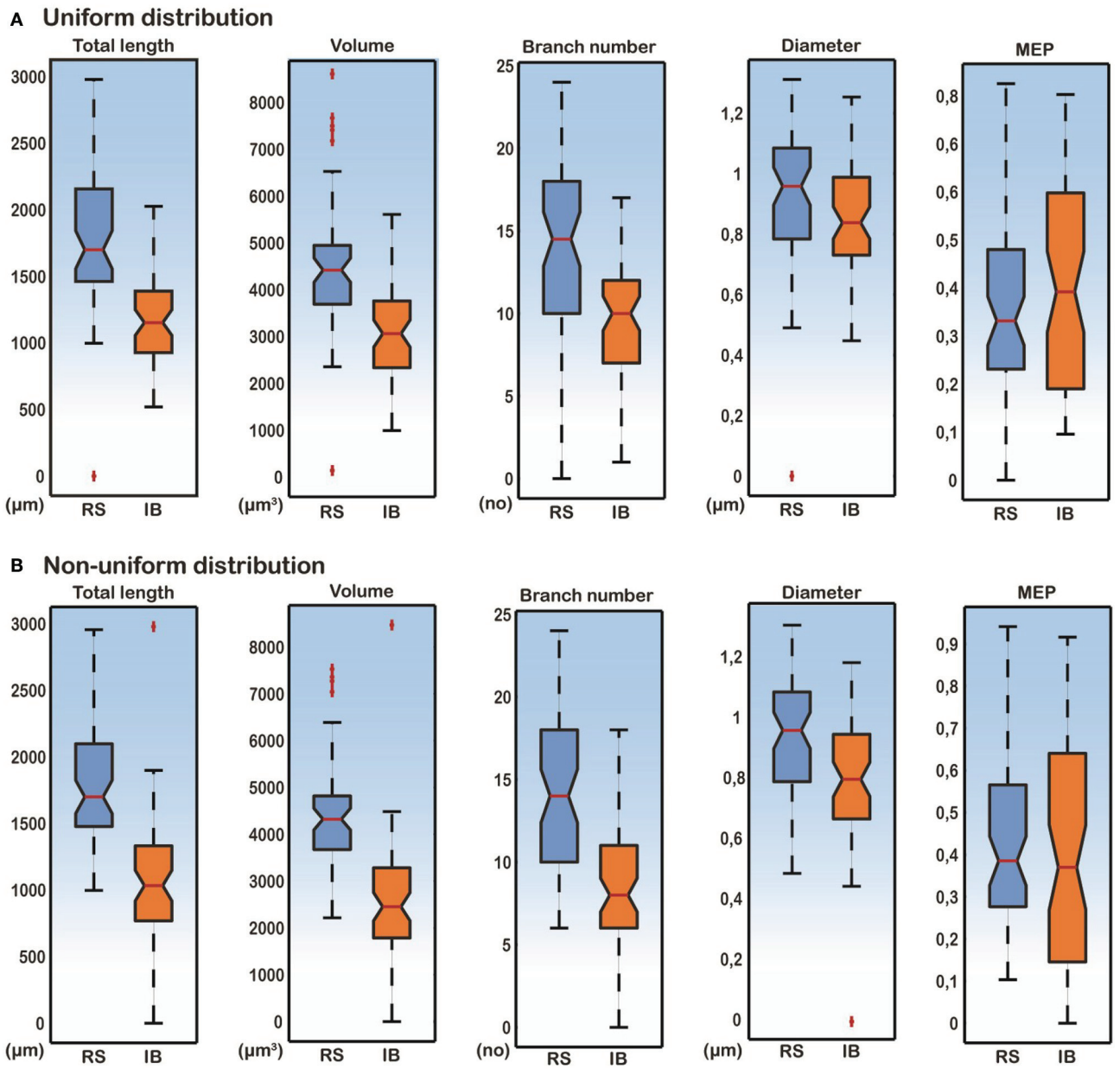

FIGURE 4 | Box-plots of total length, volume, branch number, median diameter, and MEP features for RS and IB model cells, under conditions of both uniform and non-uniform ionic mechanism distributions. Total length, volume and branch number are the best discriminatory parameters of the RS and IB firing behavior for both uniform **(A)** and non-uniform **(B)** distributions.

to parametrically investigate which morphological parameters (diameter, total length, volume, and basal number) and passive properties (MEP) discriminated the cell's firing behavior as an RS or an IB when it was stimulated with a somatic current injection. Our simulation study has quantitatively showed that total length, volume and branch number of the basal dendritic tree are the best morphological parameters to discriminate the cell as an RS or an IB regardless of what is the distribution of ionic mechanisms along the basal trees and irrespectively of the apical tree. Varying combinations of the basal and the apical dendritic tree plexuses and their ionic mechanism distribution produced different cell type percentages indicating that the morphology of apical and basal trees has a strong effect on firing behavior. It should be noted ionic conductance changes are also likely to have an effect on firing patterns. However, the goal of this work was to dissect the effect of morphology from that of biophysics, therefore we chose the use of a model whose ionic mechanisms have been extensively validated against experimental data, to ensure that our analysis is within realistic bounds for these mechanisms. Under such realistic conditions, this work shows in a quantitative

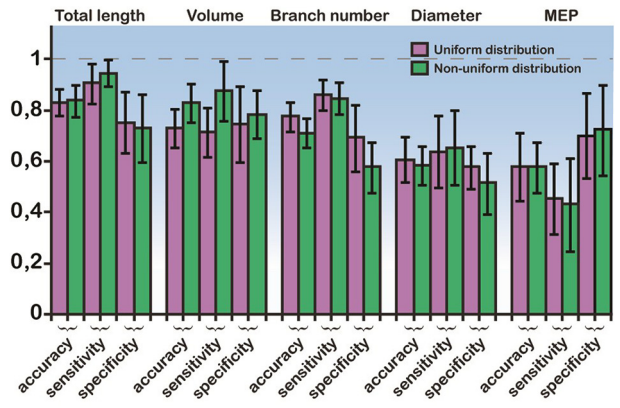

FIGURE 5 | Bayes classifier performance. Sensitivity, specificity, and accuracy values for the classification when using a single feature: the mean diameter, the total length, the MEP, the volume, and the branch number of basal trees. Performance is shown for both uniform and non-uniform ionic mechanism distributions. The error bars are also depicted (black lines). Total length, volume, and branch number are the best discriminatory features for predicting whether a model cell will express an RS or an IB firing behavior.

manner that specific anatomical features of basal trees in layer V PFC pyramidal neurons are largely determinant of the cells' firing pattern.

WHAT HAVE WE LEARNED FROM THIS MODEL?

The major finding of our simulation study was that the morphological parameters that best discriminated our cells as RS and IB were the total length, volume, and branch number of the basal dendritic tree. This finding was independent of the distribution of ionic mechanisms (uniform vs. non-uniform) along the basal tree (see **Table 1** and **Figures 2**, **4**, **5**), and insensitive to the use of specific apical trees (**Figure 2** and Supplementary Figure S2). The total length of the basal dendritic tree of the RS cells was found to be significantly larger than the total length of the basal dendritic tree of the IB cells. That means that the basal dendritic trees of RS cells are more extensive than the basal trees of IB cells. This result is in line with recent experimental evidence (Chang and Luebke, 2007) and supported by our finding that the branch number in RS model cells is significantly larger than that of IB model cells (Chang and Luebke, 2007). Chang and Luebke (2007) have also reported that the total length and branch number of RS cells in layer V of PFC are greater than that of IB cells in the same layer. On the other hand, another experimental study has shown that IB cells in layer V of the somatosensory neocortex in rats have extensive basal dendritic trees, and their axons tend to ramify in infragranular layers, while RS cells in same layer have smaller dendritic arborizations and their axons ramify to supragranular layers (Chagnac-Amitai and Connors, 1989; Connors and Long, 2004). Yang et al. (1996) showed in layers V-VI of the PFC that RS' proximal, but not basal, dendritic trees bifurcated less profusely than those of IB cells. We think that these variations are region dependent. The basal total length and branch numbers in layer V basal trees of RS pyramidal cells are greater than those of layer V IB pyramidal cells only in the PFC (Chang and Luebke, 2007).

In addition, our simulation study showed that the volume of the basal dendritic trees of RS cells is significantly greater than the volume of IB cells (**Figure 4**). A larger volume would mean a greater attenuation of the current flowing through the basal tree making the cell less excitable. A larger value of the total length and branch number of the basal tree would also contribute significantly to the reduced cell excitability. In our study, the diameter and the MEP of the basal trees were not the best discriminatory parameters of the cell's firing behavior. This result is contrary to the one reported by Van Elburg and van Ooyen (2010), where MEP was the best discriminatory parameter of the cell's output. One potential explanation for this discrepancy is that dendritic tree size and topological structure was altered without changing the total dendritic length to induce RS or IB firing in that study.

The percentages of RS and IB cells in our simulation study varied greatly, depending on the morphology of the apical tree used and the distribution of ionic mechanisms. In the complex model cell case with a uniform mechanism distribution 70% of the cells were RS, 29% were IB and 1% were quiescent. Use of a simpler apical tree reversed these percentages, resulting in 23% RS vs. 76% IB cells (**Figure 2**). On average however, across all possible apical trees, the percentages of RS and IB cells were 52% and 48%, respectively, for a uniform mechanism distribution. Changing the distribution into a non-uniform only slightly affected these numbers: 46% IB vs. 54% RS cells. Experimental studies (Yang et al., 1996) have reported similar percentages of IB cells in the layer V PFC (64% IB). The percentages of RS cells though were significantly smaller than ours (19% RS cells in Yang et al., 1996). We think this is due to the fact that in our study we only had two classes of cells (RS and IB), whereas in theirs the cells were classified into four types [RS, IB, ROB, and IM (intermediate)]. Also, in the Yang et al. (1996) although the cells studied were from the prelimbic area of the rat PFC as in ours, nevertheless their sample was an under-representative one of PFC neurons projecting to nucleus accumbens (NAc). In fact almost 80% of their PFC → NAc cells were bursting (IB and ROB) ones.

WHAT IS NEXT?

Several extensions to the basic idea deserve further consideration. One such idea is to thoroughly investigate how dendritic morphology affects the somatic firing behavior of a layer V PFC pyramidal cell when the cell's dendritic trees are driven by excitatory synaptic inputs. For example, nonlinear dendritic integration of spatially segregated inputs or spatially clustered synapses may have a much larger impact on the firing behavior of our model cells. Cortical and subcortical excitatory inputs drive PFC pyramidal cell's apical, proximal and basal dendrites, respectively. Each input may convey different information to the pyramidal cell. An experimental study (Schwindt and Crill, 1999) investigated the mechanisms underlying burst and RS evoked by dendritic depolarization in layer V pyramidal neurons in the rat somatosensory cortex. They reported that small dendritic depolarizations evoked spikes consisting of repetitive bursts of action potentials. Larger dendritic depolarizations evoked regular spikes. Burst firing was due to the interplay of Na^+ and Ca^{2+} spikes. Somatic depolarizations evoked only RS in almost all recorded cells. A

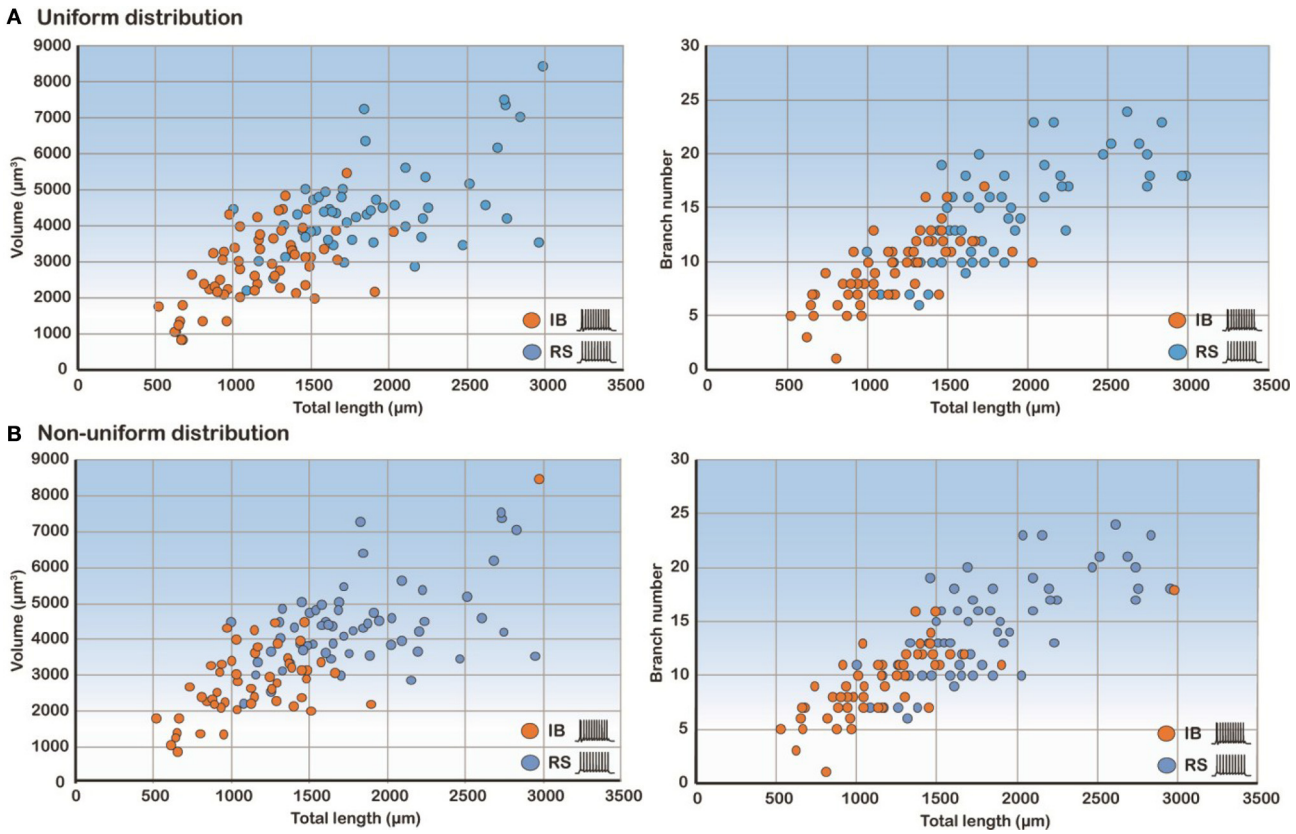

FIGURE 6 | Correlation analysis of the three most predictive features. Scatter plots of volume and branch number as a function of the total length in the uniform **(A)** and non-uniform **(B)** distribution cases show that these features are highly correlated.

recent simulation study investigated the impact of the cell's dendritic morphology on the ping-pong mechanism of burst firing reported earlier, under either somatic current injection or synaptic stimulation of the apical dendritic tree of a layer V pyramidal cell of a cat visual cortex (Van Elburg and van Ooyen, 2010). They reported that burst firing is heavily dependent on the branching structure of the tree. However, none of these studies investigated explicitly the effects of synaptic stimulation of the basal dendritic trees of layer V pyramidal cells on their firing behavior.

Another idea is to investigate the role of basal and apical dendritic inhibition on the firing behavior of PFC pyramidal cells with varying dendritic morphologies. Recent optogenetic studies in the hippocampus have shown that dendritic inhibition can modulate the pyramidal cell somatic output more efficiently than somatic inhibition (Lovett-Barron et al., 2012). Silencing of dendritic inhibition allows NMDA dendritic spikes to turn the PCs from regular spikers to bursters (Lovett-Barron et al., 2012). A recent experimentally based theoretical study (Gidon and Segev, 2012) offered new insights into how dendritic inhibition controls dendritic excitability and affects the firing behavior of a neuron. They showed that distal "off-path" rather than proximal "on-path" inhibition effectively dampens proximal excitable dendritic hotspots, as it operates as a global threshold mechanism that powerfully controls the neuron's output. Varying the morphological parameters (diameter, total length, volume, MEP, etc.) of the dendritic segments at which inhibition impinges onto may uncover a different role of inhibition, perhaps that of a local as opposed to a global threshold setter.

CONCLUDING REMARKS

In summary, our computational work provides quantitative evidence that there is strong correlation between the firing behavior of pyramidal cells in layer V of the PFC and their dendritic morphology variations. We predict that, under realistic conditions for ionic mechanisms, irrespectively of their distribution along the basal tree, the total length, volume and branch number of basal dendritic trees determine to a large extent whether the firing pattern of the cell will be an RS or an IB. When both basal and apical dendritic trees varied, then the percentages of cells in the two categories did not change. These findings are likely to have serious implications in the information processing capabilities of pyramidal cells in layer V of the PFC in both normal and pathological conditions.

AUTHOR CONTRIBUTIONS

Maria Psarrou, Stefanos S. Stefanou, and Athanasia Papoutsi designed experiments, run the simulations, analyzed the data, prepared the figures and helped with writing the manuscript. Alexandra Tzilivaki performed some simulations. Vassilis Cutsuridis helped with writing the manuscript and

advised on certain experiments. Panayiota Poirazi designed the experiments, wrote/edited the manuscript and supervised the work.

ACKNOWLEDGMENTS

This work was supported by the ERC Starting Grant "dEMORY" (ERC-2012-StG-311435) awarded to Dr. Panayiota Poirazi and the European Social Fund and the BIOSYS research project, Action KRIPIS, project No MIS-448301 (2013SE01380036) that was funded by the General Secretariat for Research and Technology, Ministry of Education, Greece and the European Regional Development Fund (Sectoral Operational Programme: Competitiveness and Entrepreneurship, NSRF 2007-2013)/European Commission.

SUPPLEMENTARY MATERIAL

The Supplementary Material for this article can be found online at: http://www.frontiersin.org/journal/10.3389/fncel.2014.00287/abstract

REFERENCES

Andreasen, M., and Lambert, J. D. C. (1995). The excitability of CA1 pyramidal cell dendrites Is modulated by a local Ca2+-dependent K+-conductance. *Brain Res.* 698, 193–203. doi: 10.1016/0006-8993(95)00910-I

Ascoli, G. A. (1999). Progress and perspectives in computational neuroanatomy. *Anat. Rec.* 257, 195–207.

Bergstrom, H. C., McDonald, C. G., French, H. T., and Smith, R. F. (2008). Continuous nicotine administration produces selective, age-dependent structural alteration of pyramidal neurons from prelimbic cortex. *Synapse* 39, 31–39. doi: 10.1002/syn.20467

Bilkey, D. K., and Schwartzkroin, P. A. (1990). Variation in electrophysiology and morphology of hippocampal CA3 pyramidal cells. *Brain Res.* 514, 77–83. doi: 10.1016/0006-8993(90)90437-G

Chagnac-Amitai, Y., and Connors, B. W. (1989). Horizontal spread of synchronized activity in neocortex and its control by GABA-mediated inhibition. *J. Neurophysiol.* 61, 747–758.

Chagnac-Amitai, Y., Luhmann, H. J., and Prince, D. A. (1990). Burst generating and regular spiking layer 5 pyramidal neurons of rat neocortex have different morphological features. *J. Comp. Neurol.* 296, 598–613.

Chang, Y. M., and Luebke, J. I. (2007). Electrophysiological diversity of layer 5 pyramidal cells in the prefrontal cortex of the rhesus monkey: *in vitro* slice studies. *J. Neurophysiol.* 98, 2622–2632. doi: 10.1152/jn.00585.2007

Connors, B. W., and Gutnick, M. J. (1990). Intrinsic firing patterns of diverse neocortical neurons. *Trends Neurosci.* 13, 99–104. doi: 10.1016/0166-2236(90)90185-D

Connors, B. W., and Long, M. A. (2004). Electrical synapses in the mammalian brain. *Annu. Rev. Neurosci.* 27, 393–418. doi: 10.1146/annurev.neuro.26.041002.131128

Cuntz, H., Forstner, F., Borst, A., and Häusser, M. (2010). One rule to grow them all: a general theory of neuronal branching and its practical application. *PLoS Comput. Biol.* 6:e1000877. doi: 10.1371/journal.pcbi.1000877

Day, M., Carr, D. B., Ulrich, S., Ilijic, E., Tkatch, T., and Surmeier, D. J. (2005). Dendritic excitability of mouse frontal cortex pyramidal neurons is shaped by the interaction among HCN, Kir2, and kleak channels. *J. Neurosci.* 25, 8776–8787. doi: 10.1523/JNEUROSCI.2650-05.2005

Dégenètais, E., Thierry, A. M., Glowinski, J., and Gioanni, Y. (2002). Electrophysiological properties of pyramidal neurons in the rat prefrontal cortex: an *in vivo* intracellular recording study. *Cereb. Cortex* 12, 1–16. doi: 10.1093/cercor/12.1.1

Eggermont, J. J., and Smith, G. M. (1996). Burst-firing sharpens frequency-tuning in primary auditory cortex. *Neuroreport* 7, 753–757.

Fowler, M. A., Sidiropoulou, K., Ozkan, E. D., Phillips, C. W., and Cooper, D. C. (2007). Corticolimbic expression of TRPC4 and TRPC5 channels in the rodent brain. Edited by Brian McCabe. *PLoS ONE* 2:e573. doi: 10.1371/journal.pone.0000573

Games, K. D., and Winer, J. A. (1988). Layer V in rat auditory cortex: projections to the inferior colliculus and contralateral cortex. *Hear. Res.* 34, 1–25. doi: 10.1016/0378-5955(88)90047-0

Gidon, A., and Segev, I. (2012). Principles governing the operation of synaptic inhibition in dendrites. *Neuron* 75, 330–341. doi: 10.1016/j.neuron.2012.05.015

González-Burgos, G., and Barrionuevo, G. (2001). Voltage-gated sodium channels shape subthreshold epsps in layer 5 pyramidal neurons from rat prefrontal cortex. *J. Neurophysiol.* 86, 1671–1684.

Haj-Dahmane, S., and Andrade, R. (1998). Ionic mechanism of the slow afterdepolarization induced by muscarinic receptor activation in rat prefrontal cortex. *J. Neurophysiol.* 80, 1197–1210.

Haj-Dahmane, S., and Andrade, R. (1999). Muscarinic receptors regulate two different calcium-dependent non-selective cation currents in rat prefrontal cortex. *Eur. J. Neurosci.* 11, 1973–1980.

Hattox, A. M., and Nelson, S. B. (2007). Layer V neurons in mouse cortex projecting to different targets have distinct physiological properties. *J. Neurophysiol.* 98, 3330–3340. doi: 10.1152/jn.00397.2007

Hines, M. L., and Carnevale, N. T. (1997). The NEURON simulation environment. *Neural Comput.* 9, 1179–1209.

Jensen, M. S., Azouz, R., and Yaari, Y. (1994). Variant firing patterns in rat hippocampal pyramidal cells modulated by extracellular potassium. *J. Neurophysiol.* 71, 831–839.

Jensen, M. S., and Yaari, Y. (1997). Role of intrinsic burst firing, potassium accumulation, and electrical coupling in the elevated potassium model of hippocampal epilepsy. *J. Neurophysiol.* 77, 1224–1233.

Kelly, J. P., and Wong, D. (1981). Laminar connections of the cat's auditory cortex. *Brain Res.* 212, 1–15. doi: 10.1016/0006-8993(81)90027-5

Kim, Y., and Spruston, N. (2012). Target-specific output patterns are predicted by the distribution of regular-spiking and bursting pyramidal neurons in the subiculum. *Hippocampus* 22, 693–706. doi: 10.1002/hipo.20931

Kole, M. H., Hallermann, S., and Stuart, G. J. (2006). Single ih channels in pyramidal neuron dendrites: properties, distribution, and impact on action potential output. *J. Neurosci.* 26, 1677–1687. doi: 10.1523/JNEUROSCI.3664-05.2006

Korngreen, A., and Sakmann, B. (2000). Voltage-gated K+ channels in layer 5 neocortical pyramidal neurones from young rats: subtypes and gradients. *J. Physiol.* 525, 621–639. doi: 10.1111/j.1469-7793.2000.00621.x

Krahe, R., and Gabbiani, F. (2004). Burst firing in sensory systems. *Nat. Rev. Neurosci.* 5, 13–23. doi: 10.1038/nrn1296

Krichmar, J. L., Nasuto, S. J., and Scorcioni, R. (2002). Effects of dendritic morphology on ca3 pyramidal cell electrophysiology: a simulation study. *Brain Res.* 941, 11–28. doi: 10.1016/S0006-8993(02)02488-5

Lisman, J. E. (1997). Bursts as a unit of neural information: making unreliable synapses reliable. *Trends Neurosci.* 20, 38–43. doi: 10.1016/S0166-2236(96)10070-9

Lorenzon, N. M., and Foehring, R. C. (1992). Relationship between repetitive firing and afterhyperpolarizations in human neocortical neurons. *J. Neurophysiol.* 67, 350–363.

Lovett-Barron, M., Turi, G. F., Kaifosh, P., Lee, P. H., Bolze, F., Sun, X. H., et al. (2012). Regulation of neuronal input transformations by tunable dendritic inhibition. *Nat. Neurosci.* 15, 423–430, S1–S3. doi: 10.1038/nn.3024

Maccaferri, G., Tóth, K., and McBain, C. J. (1998). Target-specific expression of presynaptic mossy fiber plasticity. *Science* 279, 1368–1371.

Mainen, Z. F., and Sejnowski, T. J. (1996). Influence of dendritic structure on firing pattern in model neocortical neurons. *Nature* 382, 363–366.

Martinez-Conde, S., Macknik, S. L., and Hubel, D. H. (2002). The function of bursts of spikes during visual fixation in the awake primate lateral geniculate nucleus and primary visual cortex. *Proc. Natl. Acad. Sci. U.S.A.* 99, 13920–13925. doi: 10.1073/pnas.212500599

Mason, A., and Larkman, A. (1990). Correlations between morphology and electrophysiology of pyramidal neurons in slices of rat visual cortex. II. electrophysiology. *J. Neurosci.* 10, 1415–1428.

Migliore, M., Cook, E. P., Jaffe, D. B., Turner, D. A., and Johnston, D. (1995). Computer simulations of morphologically reconstructed CA3 hippocampal neurons. *J. Neurophysiol.* 73, 1157–1168.

Milojkovic, B. A., Zhou, W. L., and Antic, S. D. (2007). Voltage and calcium transients in basal dendrites of the rat prefrontal cortex. *J. Physiol.* 585(pt 2), 447–468. doi: 10.1113/jphysiol.2007.142315

Moolman, D. L., Vitolo, O. V., Vonsattel, J. P., and Shelanski, M. L. (2004). Dendrite and dendritic spine alterations in alzheimer models. *J. Neurocytol.* 33, 377–387. doi: 10.1023/B:NEUR.0000044197.83514.64

Morishima, M., and Kawaguchi, Y. (2006). Recurrent connection patterns of corticostriatal pyramidal cells in frontal cortex. *J. Neurosci.* 26, 4394–4405. doi: 10.1523/JNEUROSCI.0252-06.2006

Nevian, T., Larkum, M. E., Polsky, A., and Schiller, J. (2007). Properties of basal dendrites of layer 5 pyramidal neurons: a direct patch-clamp recording study. *Nat. Neurosci.* 10, 206–214. doi: 10.1038/nn1826

Nicoll, R. A., and Malenka, R. C., (1995). Contrasting properties of two forms of long-term potentiation in the hippocampus. *Nature* 377, 115–118.

Ojima, H., Honda, C. N., and Jones, E. G. (1992). Characteristics of intracellularly injected infragranular pyramidal neurons in cat primary auditory cortex. *Cereb. Cortex* 2, 197–216. doi: 10.1093/cercor/2.3.197

Pissadaki, E. K., Sidiropoulou, K., Reczko, M., and Poirazi, P. (2010). Encoding of spatio-temporal input characteristics by a CA1 pyramidal neuron model. *PLoS Comput. Biol.* 6:e1001038. doi: 10.1371/journal.pcbi.1001038

Royer, S., Zemelman, B. V., Losonczy, A., Kim, J., Chance, F., Magee, J. C., et al. (2012). Control of timing, rate and bursts of hippocampal place cells by dendritic and somatic inhibition. *Nat. Neurosci.* 15, 769–775. doi: 10.1038/nn.3077

Rüttgers, K., Aschoff, A., and Friauf, E. (1990). Commissural connections between the auditory cortices of the rat. *Brain Res.* 509, 71–79. doi: 10.1016/0006-8993(90)90310-8

Schaefer, A. T., Helmstaedter, M., Schmitt, A. C., Bar-Yehuda, D., Almog, M., Ben-Porat, H., et al. (2007). Dendritic voltage-gated k+ conductance gradient in pyramidal neurones of neocortical layer 5b from rats. *J. Physiol.* 579(pt 3), 737–752. doi: 10.1113/jphysiol.2006.122564

Schwindt, P., and Crill, W. (1999). Mechanisms underlying burst and regular spiking evoked by dendritic depolarization in layer 5 cortical pyramidal neurons. *J. Neurophysiol.* 81, 1341–1354.

Sidiropoulou, K., Lu, F. M., Fowler, M. A., Xiao, R., Phillips, C., Ozkan, E. D., et al. (2009). Dopamine modulates an mGluR5-mediated depolarization underlying prefrontal persistent activity. *Nat. Neurosci.* 12, 190–199. doi: 10.1038/nn.2245

Sidiropoulou, K., and Poirazi, P. (2012). Predictive features of persistent activity emergence in regular spiking and intrinsic bursting model neurons. *PLoS Comput. Biol.* 8:e1002489. doi: 10.1371/journal.pcbi.1002489

Stuart, G., and Spruston, N. (1998). Determinants of voltage attenuation in neocortical pyramidal neuron dendrites. *J. Neurosci.* 18, 3501–3510.

Sun, Y. J., Kim, Y. J., Ibrahim, L. A., Tao, H. W., and Zhang, L. I. (2013). Synaptic mechanisms underlying functional dichotomy between intrinsic-bursting and regular-spiking neurons in auditory cortical layer 5. *J. Neurosci.* 33, 5326–5339. doi: 10.1523/JNEUROSCI.4810-12.2013

Teskey, G. C., Monfils, M. H., Silasi, G., and Kolb, B. (2006). Neocortical kindling is associated with opposing alterations in dendritic morphology in neocortical layer v and striatum from neocortical layer III. *Synapse* 59, 1–9. doi: 10.1002/syn.20215

Van Aerde, K. I., and Feldmeyer, D. (2013). Morphological and physiological characterization of pyramidal neuron subtypes in rat medial prefrontal cortex. *Cereb. Cortex*. doi: 10.1093/cercor/bht278. Available online at: http://cercor.oxfordjournals.org/papfaq

Van Elburg, R. A. J., and van Ooyen, A. (2010). Impact of dendritic size and dendritic topology on burst firing in pyramidal cells. *PLoS Comput. Biol.* 6:e1000781. doi: 10.1371/journal.pcbi.1000781

Van Ooyen, A., Duijnhouwer, J., Remme, M. W., and van Pelt, J. (2002). The effect of dendritic topology on firing patterns in model neurons. *Network* 13, 311–325. doi: 10.1088/0954-898X/13/3/304

Wang, H. X., Stradtman, G. G., Wang, X. J., and Gao, W. J. (2008). A specialized NMDA receptor function in layer 5 recurrent microcircuitry of the adult rat prefrontal cortex. *Proc. Natl. Acad. Sci. U.S.A.* 105, 16791–16796. doi: 10.1073/pnas.0804318105

Wang, X.-J. (1999). Fast burst firing and short-term synaptic plasticity: a model of neocortical chattering neurons. *Neuroscience* 89, 347–362. doi: 10.1016/S0306-4522(98)00315-7

Wang, Y., Markram, H., Goodman, P. H., Berger, T. K., Ma, J., and Goldman-Rakic, P. S. (2006). Heterogeneity in the pyramidal network of the medial prefrontal cortex. *Nat. Neurosci.* 9, 534–542. doi: 10.1038/nn1670

Washington, S. D., Ascoli, G. A., and Krichmar, J. L. (2000). A statistical analysis of dendritic morphology's effect on neuron electrophysiology of ca3 pyramidal cells. *Neurocomputing* 32–33, 261–269. doi: 10.1016/S0925-2312(00)00173-9

Weisskopf, M. G., Castillo, P. E., Zalutsky, R. A., and Nicoll, R. A. (1994). Mediation of hippocampal mossy fiber long-term potentiation by cyclic AMP. *Science* 265, 1878–1882. doi: 10.1126/science.7916482

Williams, S., and Johnston, D. (1989). Long-term potentiation of hippocampal mossy fiber synapses is blocked by postsynaptic injection of calcium chelators. *Neuron* 3, 583–588. doi: 10.1016/0896-6273(89)90268-7

Winer, J. A., and Prieto, J. J. (2001). Layer V in cat primary auditory cortex (ai): cellular architecture and identification of projection neurons. *J. Comp. Neurol.* 434, 379–412. doi: 10.1002/cne.1183

Yamada, M., Wada, Y., Tsukagoshi, H., Otomo, E., and Hayakawa, M. (1988). A quantitative golgi study of basal dendrites of hippocampal ca1 pyramidal cells in senile dementia of alzheimer type. *J. Neurol. Neurosurg. Psychiatry* 51, 1088–1090.

Yang, C. R., Seamans, J. K., and Gorelova, N. (1996). Electrophysiological and morphological properties of layers v-vi principal pyramidal cells in rat prefrontal cortex *in vitro*. *J. Neurosci.* 16, 1904–1921.

Yeckel, M. F., and Berger, T. W. (1998). Spatial distribution of potentiated synapses in hippocampus: dependence on cellular mechanisms and network properties. *J. Neurosci.* 18, 438–450.

Conflict of Interest Statement: The authors declare that the research was conducted in the absence of any commercial or financial relationships that could be construed as a potential conflict of interest.

Received: 14 April 2014; accepted: 29 August 2014; published online: 16 September 2014.

*Citation: Psarrou M, Stefanou SS, Papoutsi A, Tzilivaki A, Cutsuridis V and Poirazi P (2014) A simulation study on the effects of dendritic morphology on layer V prefrontal pyramidal cell firing behavior. Front. Cell. Neurosci. **8**:287. doi: 10.3389/fncel.2014.00287*

This article was submitted to the journal Frontiers in Cellular Neuroscience.

frontiers in
CELLULAR NEUROSCIENCE

HYPOTHESIS AND THEORY ARTICLE
published: 17 September 2014
doi: 10.3389/fncel.2014.00292

Spiny neurons of amygdala, striatum, and cortex use dendritic plateau potentials to detect network UP states

Katerina D. Oikonomou, Mandakini B. Singh, Enas V. Sterjanaj and Srdjan D. Antic*

Department of Neuroscience, University of Connecticut Health Center, Farmington, CT, USA

Edited by:
Sergey M. Korogod, National Academy of Sciences of Ukraine, Ukraine

Reviewed by:
Marco Capogna, Medical Research Council, UK
Daniela Gandolfi, University of Pavia, Italy

***Correspondence:**
Srdjan D. Antic, Department of Neuroscience, University of Connecticut Health Center, Room L-4054, 263 Farmington Avenue, Farmington, CT 06030, USA
e-mail: antic@neuron.uchc.edu

Spiny neurons of amygdala, striatum, and cerebral cortex share four interesting features: (1) they are the most abundant cell type within their respective brain area, (2) covered by thousands of thorny protrusions (dendritic spines), (3) possess high levels of dendritic NMDA conductances, and (4) experience sustained somatic depolarizations *in vivo* and *in vitro* (UP states). In all spiny neurons of the forebrain, adequate glutamatergic inputs generate dendritic plateau potentials ("dendritic UP states") characterized by (i) fast rise, (ii) plateau phase lasting several hundred milliseconds, and (iii) abrupt decline at the end of the plateau phase. The dendritic plateau potential propagates toward the cell body decrementally to induce a long-lasting (longer than 100 ms, most often 200–800 ms) steady depolarization (~20 mV amplitude), which resembles a neuronal UP state. Based on voltage-sensitive dye imaging, the plateau depolarization in the soma is precisely time-locked to the regenerative plateau potential taking place in the dendrite. The somatic plateau rises after the onset of the dendritic voltage transient and collapses with the breakdown of the dendritic plateau depolarization. We hypothesize that neuronal UP states *in vivo* reflect the occurrence of dendritic plateau potentials (dendritic UP states). We propose that the somatic voltage waveform during a neuronal UP state is determined by dendritic plateau potentials. A mammalian spiny neuron uses dendritic plateau potentials to detect and transform coherent network activity into a ubiquitous neuronal UP state. The biophysical properties of dendritic plateau potentials allow neurons to quickly attune to the ongoing network activity, as well as secure the stable amplitudes of successive UP states.

Keywords: NMDA spike, dendritic plateau potentials, dendritic spike, voltage-sensitive dye imaging, UP states, amygdala, striatum

INTRODUCTION

NEURONAL UP STATES

The binding theory

The dynamic structure composed of synchronously activated neurons engaged in the same task is termed "neural ensemble" (Hebb, 1949; Eichenbaum, 1993; Engel and Singer, 2001). Individual members of a "neural ensemble" are widely distributed across different areas of the brain (**Figure 1A**), each specialized in signaling a different attribute of the object or different element within the scene (Perrett et al., 1982; Mountcastle, 1997; Singer, 1999; Yu and Ferster, 2010). Proper representation of a physical or mental "object" during sensory perception requires the "binding" together of many attributes into a single experience. "Binding" is simply a synchronization of electrical activity of large populations of neurons on a definite temporal scale (**Figure 1B**).

Dynamic ensembles

The dynamic feature of information processing in the brain is reflected in the fact that at one instant of time any given neuron is a member of one ensemble, while in the next instant of time the same neuron participates meaningfully in the function of another neuronal ensemble (Desimone et al., 1984; Eichenbaum, 1993; Wilson and McNaughton, 1993; Engel and Singer, 2001). This "time-sharing" feature of the ensemble-organization principle assures virtually an infinite number of neuronal ensembles in the mammalian brain that can be assigned to an infinite number of specific objects, including perceptual and mental objects.

Neural synchronization

Synchronized spiking activity has been found in different species and different cortical areas (Bair, 1999; Salinas and Sejnowski, 2001; Buzsaki and Silva, 2012). For the same level of firing, a synchronous input is more effective on postsynaptic neurons than asynchronous input (Schneidman et al., 1998; London et al., 2002). Large-scale models predict that synchrony occurs due to the reciprocal connectivity and loops between clumps of neurons (Tononi et al., 1992; Durstewitz et al., 2000; Compte et al., 2003). It is tempting to state that oscillatory activity and phase alignment between distant groups of neurons is the preferred mechanism of the "*Binding theory*" (Engel and Singer, 2001; Tononi and Koch, 2008; Ainsworth et al., 2012). Oscillatory activity, even when subthreshold, could facilitate synchronous interactions by biasing neurons to discharge within the same time frame (Engel et al., 2001; Yu and Ferster, 2010; Petersson and Fransen, 2012). The main effect of the oscillatory modulation of neuronal membrane potential is that it constrains the time interval during which nerve cells are susceptible to excitatory input and can reliably emit bursts of action potentials (**Figure 1B**). In this paper we will argue that glutamate-mediated dendritic plateau potentials provide such time intervals.

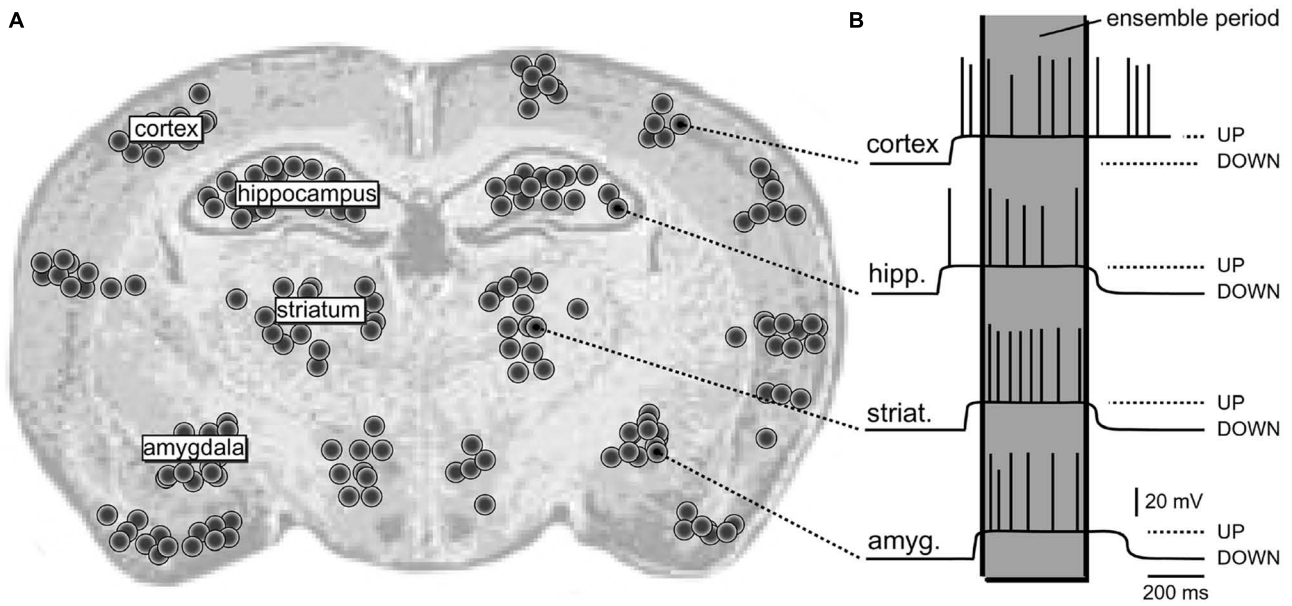

FIGURE 1 | Schematic depiction of a neural ensemble (hypothetical). **(A)** Coronal section of a rat brain. One hypothetical neural ensemble is comprised of neurons synchronously experiencing suprathreshold depolarizations. These neurons are distributed unevenly across several brain regions, including cortical layers 2–6, neostriatum, hippocampus, and amygdala. Each black dot denotes 50 neurons. **(B)** Intracellular recordings show a plateau depolarization (UP state) crowned by action potentials (APs). Note that neurons do not fire APs in the DOWN state. Also, the onsets and offsets of UP states are not perfectly synchronized. However, in one brief period of time (marked by the gray column – "ensemble period") all relevant neurons are in the UP state; they all joined the dynamic neural ensemble.

Time window 200–500 ms

The majority of brain processes related to the feeling of awareness require that neural activity lasts for 200–500 ms (Libet et al., 1979). This window of time is perhaps a minimum amount of time needed to guarantee interactions among multiple brain regions. The 200–500 ms of sustained firing triggers the awareness of a stimulus either directly by producing significant glutamatergic output in target brain areas, or indirectly by allowing the feedforward stream from thalamus to interact appropriately with feedback stream from higher cortical areas (Cauller, 1995; Lamme and Roelfsema, 2000; Engel et al., 2001; Ro et al., 2003; Larkum, 2012). The 200–500 ms time window of sustained neuronal depolarization may be the consequence of reverberant activity closing the loop between past and present features of a moving object, or by closing the loop between long-term memory traces and the current sensory percept (reviewed in Tononi and Koch, 2008). Interestingly, the duration of synaptically evoked dendritic plateau potentials is also in the range of 200–500 ms (Milojkovic et al., 2004; Oikonomou et al., 2012).

Spiny neurons

The distribution of neurons involved in one functional neural ensemble is not restricted to the cerebral neocortex, but it is likely to include subcortical gray matter (**Figure 1A**; Brecht et al., 1998; Ziaei et al., 2013). In brain regions strongly implicated in cognition and memory formation (neocortex, thalamus, neostriatum, ventral striatum, amygdala, and hippocampus), the principle and/or most numerous neurons are those that have protoplasmatic protrusions termed "dendritic spines" (Nimchinsky et al., 2002). During non-REM slow-wave sleep, spiny neurons experience 1 Hz fluctuations in membrane potential (UP and DOWN states), as documented by *in vivo* intracellular recordings (Volgushev et al., 2006). The spontaneous plateau depolarizations (UP states) are ∼20 mV in amplitude and several 100 ms in duration. The UP states may or may not be accompanied by action potential firing (O'Donnell and Grace, 1995; Branchereau et al., 1996; Contreras et al., 1996; Wilson, 2008). *In vivo* intracellular recordings have documented UP and DOWN transitions in cortical L5 pyramidal neurons, cortical L4 stellate cells, striatal medium spiny neurons and spiny neurons of the amygdala (Wilson and Kawaguchi, 1996; Steriade et al., 2001; Brecht and Sakmann, 2002; Volgushev et al., 2006; Padival et al., 2013). These four neuron types differ in many respects including their fine morphology, developmental origin, wiring, and immunohistochemical markers. However, viewed from a purely biophysical aspect, all four aforementioned neuron subtypes exhibit identical plan of organization, except for the addition of one apical dendrite to the pyramidal neurons (**Figure 2**). It can be said that the basilar dendritic tree is a common feature of all spiny neurons (**Figure 2**). Benucci et al. (2004) manipulated the gross morphological structure of cortical pyramidal and neostriatal MSNs cells in realistic multicompartmental models. Benucci et al. (2004) kept the morphology of the basal dendritic tree unchanged, but reduced the apical part of a pyramidal neuron to a single equivalent compartment. Despite of this drastic morphological modification, the qualitative aspects of the bimodal intracellular dynamics (UP and DOWN states) were preserved (Benucci et al., 2004). Benucci et al. (2004) concluded that an intact basal dendritic tree is the minimal

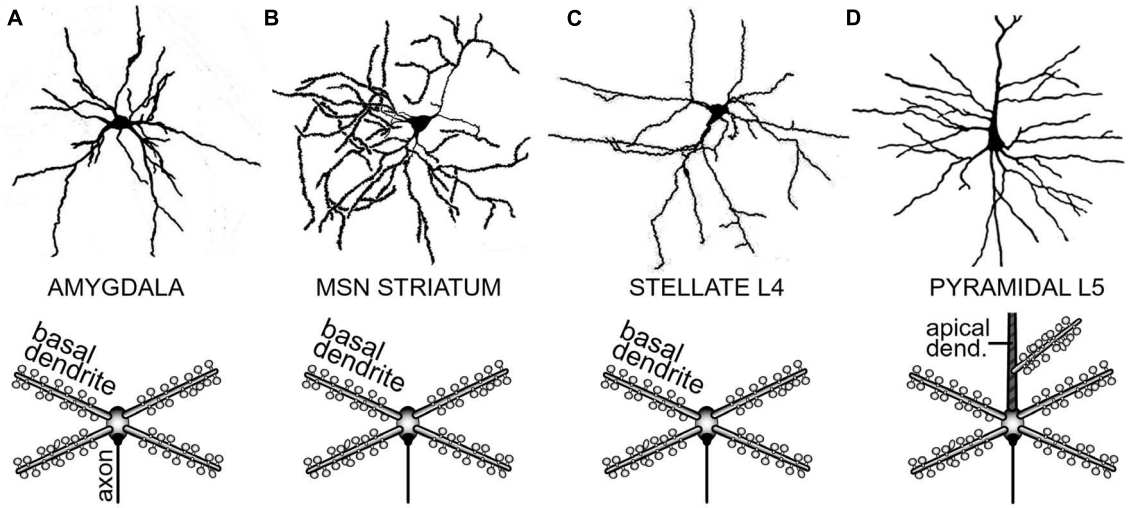

FIGURE 2 | Determinants of dendritic morphology in spiny neurons of the forebrain. (A) Spiny neuron in the amygdaloid complex. In this and all the remaining panels, upper image is a camera lucida drawing, while the lower image is a conceptual representation of the dendritic tree. Upper image adopted from (Shaikh and Shaikh, 1982). **(B)** Medium spiny neuron (MSN) of the neostriatum. Upper image adopted from (Klapstein et al., 2001). **(C)** Spiny stellate cell in cortical layer 4. Upper image adopted from (Andjelic et al., 2009). **(D)** Cortical layer 5 pyramidal neuron. Upper image adopted from Gray's Anatomy, p. 722. Major morphological distinction of L5 pyramidal neurons is the presence of an apical dendrite (striped area). Basilar dendrites are the common feature of all spiny neurons.

condition necessary for the emergence of UP and DOWN states. In support of this conclusion, *in vitro* electrophysiological experiments performed in cortical pyramidal cells showed that brief (5 ms) glutamate pulses delivered on a single basal branch produce long-lasting somatic plateau depolarizations, which resemble neuronal UP states *in vivo* (**Figure 3**; Branchereau et al., 1996; Wilson, 2008).

Spiny CNS neurons (pyramidal and MSN neurons) rarely fire action potentials from a DOWN state (**Figure 3A**). A successful synchronization of the firing activity among neurons would require that members of a neuronal ensemble enter UP state at the same moment of time (**Figure 1B**). To become eligible for inclusion into a functional neuronal ensemble, a spiny neuron must quickly, and reliably switch from a DOWN to an UP state, remain in the depolarized UP state as long as necessary, and quickly abort the UP state when a percept is formed or expired. Although the focus of this manuscript is on glutamatergic transmission, one should not ignore that the great majority of GABAergic inputs impinge directly on the dendrites of cortical and sub-cortical principal neurons and may profoundly influence the dendritic processing of glutamatergic inputs (Gidon and Segev, 2012), which in turn may impact the onset and offset of neuronal UP states (Shu et al., 2003; Windels et al., 2010).

Cellular bases of UP states

Several competing theories aim to explain the cellular bases of UP and DOWN states. The first hypothesis stated that spontaneous transmitter release occurring during a DOWN state occasionally depolarizes certain cells to the firing threshold, thus initiating an active state in the network (Timofeev et al., 2000; Bazhenov et al., 2002). The "spontaneous release" hypothesis predicts that cells receiving largest excitatory convergence will have the highest probability of being activated before other cells in the network (Chauvette et al., 2010). Note that spiny neurons are cells with the largest excitatory convergence in any given network. The second hypothesis suggests that UP states are mediated by intrinsic oscillations of layer 5 pyramidal neurons. The "intrinsic oscillation" hypothesis predicts that once initiated by layer 5 neurons, activity then propagates to other cortical layers (Sanchez-Vives and McCormick, 2000). The third hypothesis attributes transitions from silent to active states to the selective synchronization of neuronal ensembles involving a small number of "pacemaker" cells grouped in a cluster. The "pacemaker cluster" hypothesis predicts a very stereotyped spatiotemporal dynamics of UP state triggering (Cossart et al., 2003). In this paper we propose that dendritic plateau potentials occur in principal neurons during network UP states and are responsible for voltage waveforms regularly observed in the cell body using intracellular *in vivo* recordings (Timofeev et al., 2000; Chauvette et al., 2010). The relation between dendritic plateau potentials and UP states can be both causal and correlative. In the causal relation, a dendritic plateau potential triggers an UP state in one neuron, which in turn recruits other neurons to form a local network UP state. In the correlative relation, dendritic plateau potentials are caused by network UP states, given that the network UP states provide sufficient glutamatergic drives congregated onto one dendritic segment. In either case, causative or correlative, dendritic plateau potentials produce characteristic sustained depolarizations of the neuronal cell body during the UP states (Milojkovic et al., 2007; Augustinaite et al., 2014).

DENDRITIC PLATEAU POTENTIALS

Glutamate-mediated dendritic spike

The voltage waveforms of glutamate-mediated dendritic spikes (Schiller et al., 2000) were characterized using voltage-sensitive

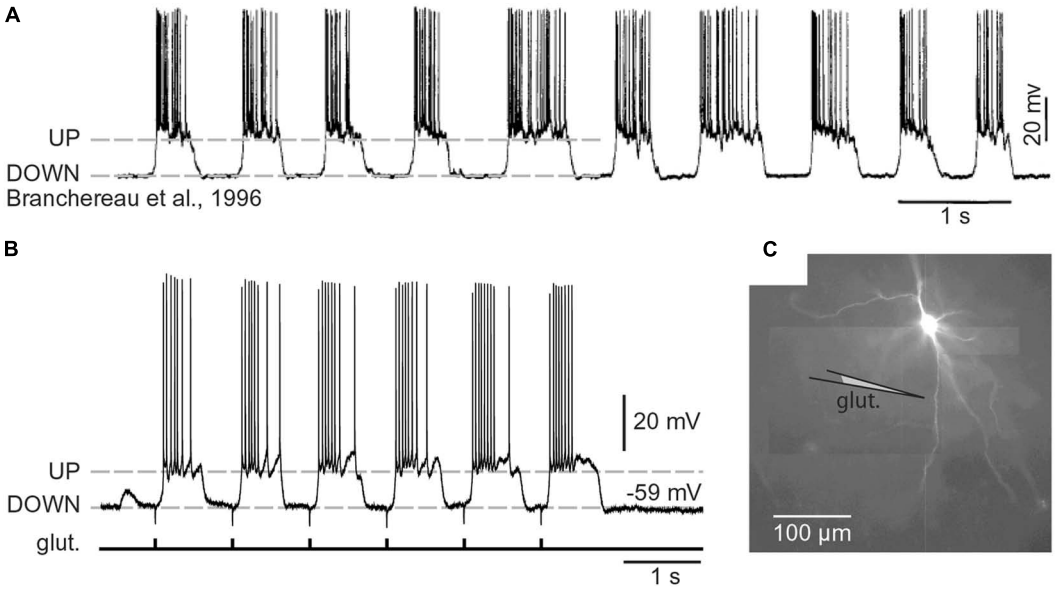

FIGURE 3 | Cortical UP and DOWN states. (A) *In vivo* intracellular recording from a pyramidal neuron in the rat medial prefrontal cortex. Adapted from Branchereau et al. (1996). **(B)** *In vitro* whole-cell recording from a pyramidal neuron in the rat medial prefrontal cortex (brain slice). Glutamate pulses (duration 5 ms) were delivered every second on a basal dendritic branch, at a distance of 105 µm from the cell body. Dashed line marks the resting potential (−59 mV). Note that the slow component of somatic depolarization alternates between depolarized (UP) and hyperpolarized (DOWN) level. **(C)** Composite microphotograph of a rhodamine-filled neuron. Schematic drawing marks the position of the glutamate stimulation pipette on a basal dendrite. Adapted from Antic et al. (2007).

dye imaging (Milojkovic et al., 2004, 2005a,b) and dendritic patch (Nevian et al., 2007; Larkum et al., 2009). Dendritic voltage-sensitive dye imaging revealed that the somatic plateau rises a few milliseconds after the onset of the dendritic voltage transient and collapses with the breakdown of the dendritic plateau depolarization (Milojkovic et al., 2005a). The slow component of the somatic depolarization accurately mirrors the glutamate-evoked dendritic plateau potential (dendritic UP state). This observation is most apparent in experiments in which a gradually increasing intensity of glutamatergic input was delivered onto a basilar dendritic branch. At subthreshold glutamate input intensities the dendritic and somatic depolarizations are both subthreshold. As soon as the dendritic membrane develops a regenerative dendritic plateau potential (Milojkovic et al., 2004, 2005a), the somatic compartment of this neuron reports a neuronal UP state (Oikonomou et al., 2012, their Figure 3). In summary, the relation between dendritic plateau potential and somatic UP state is uniquely reliable and faithful (Milojkovic et al., 2004, 2005a,b, 2007).

Dendritic NMDA spikes versus dendritic plateau potentials – differences

Glutamate-mediated dendritic plateau potentials can be distinguished from classic dendritic NMDA spikes based on:

Duration. The half-widths (durations) of NMDA spikes are in the range of 15–50 ms. The half-widths of plateau potentials are greater than 100 ms, often in the range 200–500 ms. Notably, the dendrite will stay in the plateau phase as long as glutamate is present in the extracellular space (Milojkovic et al., 2005a; Oikonomou et al., 2012). Glutamate remains bound to the NMDA receptors because there is a surplus of glutamate in the extracellular space (**Figure 9**, glutamate pond).

Amplitude. The somatic amplitude of a dendritic NMDA spike is not sufficient to trigger AP firing in healthy neurons at rest (Schiller et al., 2000; Polsky et al., 2004, 2009; Chalifoux and Carter, 2011; Oikonomou et al., 2012). Whereas the somatic amplitude of the dendritic plateau potential is a successful trigger of neuronal AP firing in ∼90% of trials (Milojkovic et al., 2004, 2005a,b; Major et al., 2008).

Ca^{2+} Map. During an NMDA spike the dendritic calcium influx is highly restricted to the excitatory input site (Schiller et al., 2000). During a glutamate-mediated dendritic-plateau potential the calcium flux engulfs the entire length of the respective dendritic branch (Milojkovic et al., 2007). While the influx of calcium at glutamate input site is solely due to the opening of NMDA receptor channels (Schiller et al., 2000), the influx of calcium in dendritic segments away from the glutamate input site is due to the propagation of plateau potential along dendritic cable, resulting in the activation (opening) of voltage gated calcium channels (**Figure 8**; Milojkovic et al., 2007).

Synaptic Requirement. Synaptic stimulation (synaptic shock) is a standard procedure in cellular neuroscience used to evoke release of neurotransmitters from axon terminals by applying a brief (0.1 ms) current pulse via a stimulation electrode positioned near the afferent axons (**Figures 5A1,B1**). The major practical distinction between NMDA spikes and dendritic UP states (plateau

potentials) lies primarily in the fact that NMDA spikes can readily be triggered by two synaptic shocks (Polsky et al., 2004; Chalifoux and Carter, 2011) and sometimes even one synaptic shock is sufficient (Milojkovic et al., 2004, their Figure 7). Dendritic plateau potentials, on the other hand, require repetitive synaptic stimulation; more than two synaptic shocks (Milojkovic et al., 2004; Oikonomou et al., 2012).

In summary, these four parameters (duration, amplitude, spatial distribution of calcium signal, and dependence on more than two consecutive excitatory inputs) can be used to distinguish between dendritic NMDA spike and glutamate-mediated plateau potential (Oikonomou et al., 2012, their Figure 2).

Dendritic NMDA spikes and dendritic plateau potentials – similarities

Dendritic NMDA spikes and Dendritic Plateau Potentials share several properties, such as:

Ionic Composition. Both NMDA spikes and dendritic plateau potentials strongly depend on dendritic NMDA current (Schiller et al., 2000; Milojkovic et al., 2005a; Major et al., 2013; Augustinaite et al., 2014). Dendritic plateau potentials initially start as NMDA spikes, but their dynamics/waveform change significantly upon stronger (or repetitive) synaptic stimulation (Milojkovic et al., 2004, 2005a; Major et al., 2008).

Somatic Depolarization. Both types of dendritic potentials produce somatic depolarizations significantly greater in amplitude than the conventional EPSPs. However, upon conversion from NMDA spike to dendritic plateau potential, the somatic voltage waveform is no longer like a large, pointy EPSP (Polsky et al., 2004, 2009; Oikonomou et al., 2012; Brandalise and Gerber, 2014); it becomes a more sustained depolarization event, reminiscent of a cortical UP state (Milojkovic et al., 2004, 2005a).

Calcium Influx. Both types of dendritic potentials produce strong calcium accumulation at the glutamate input site. However, upon conversion from NMDA spike to dendritic plateau potential, the dendritic calcium signal switches from a highly localized calcium transient characteristic of NMDA spikes (Schiller et al., 2000; Holthoff et al., 2004; Chalifoux and Carter, 2011; Katona et al., 2011) to a robust calcium flux that engulfs the entire dendritic branch (Milojkovic et al., 2007; Major et al., 2008).

Synaptic Requirement. Generation of NMDA spikes and glutamate-mediated dendritic plateau potentials can be achieved by any type of stimulation which brings substantial quantities of glutamate to synaptic and extrasynaptic NMDA receptors at the same time. Both NMDA spikes and plateau potentials can be triggered by repetitive synaptic stimulation (Milojkovic et al., 2004; Polsky et al., 2004; Oikonomou et al., 2012) or focal application of exogenous glutamate (Schiller et al., 2000; Milojkovic et al., 2005a; Losonczy et al., 2008; Chalifoux and Carter, 2011).

Neuron types supporting NMDA spikes and glutamate-mediated dendritic plateau potentials. Both NMDA spikes and plateau potentials can be triggered in thin spiny dendrites of pyramidal neurons (basal, tuft, oblique), and not so successfully in aspiny segments of the thick apical dendrite (Schiller and Schiller, 2001; Larkum et al., 2009). This is probably due to the fact that the presence of dendritic spines (**Figure 4**) effectively increases two important factors: (a) the number of presynaptic glutamatergic terminals impinging on the dendritic segment; and (b) the number of postsynaptic glutamate receptors exposed to synaptic and extrasynaptic glutamate (Rusakov and Kullmann, 1998; Chalifoux and Carter, 2011; Oikonomou et al., 2012). Because NMDA spikes strongly depend on the density of NMDA receptor channels on spine heads, spine necks and dendritic shafts between dendritic spines (**Figure 4**), the ability of a dendrite to support an NMDA spike is a tell-tale sign of the ability of that dendrite to also generate dendritic UP states (plateau potentials). We searched for NMDA spikes in four neuron subtypes including spiny neurons of the amygdala ($n = 24$ neurons), striatal medium spiny neurons ($n = 12$ neurons), stellate cells in cortical layer 4 ($n = 11$ neurons), and pyramidal neurons in cortical layer 5 ($n = 30$ neurons).

Neurons were filled with calcium sensitive dye Oregon Green Bapta-1 (OGB-1) and synaptic stimulation electrodes were positioned in the middle portion of a thin (basilar) dendritic branch 70–90 μm away from the soma. Synaptic stimulation consisted of two shocks (pulse duration = 0.1 ms, interval = 20 ms, **Figure 5A1**, syn.). In each neuron type, we readily obtained characteristic voltage waveform of an NMDA spike (**Figures 5A2,A3**, soma). When synaptic stimulation electrodes were replaced by glutamate iontophoresis (**Figure 5B1**, pulse duration = 5 ms), each neuron type produced characteristic sustained plateau depolarizations crowned by AP firing (**Figure 5B2**, soma).

Regenerative properties of glutamate-evoked dendritic plateau potentials were revealed when a series of gradually increasing glutamatergic stimuli was applied on the same dendrite (**Figure 6A1**). The transition from subthreshold to suprathreshold response (**Figure 6A2**, red trace) is attributed to the negative slope conductance in the current–voltage profile of the dendritic NMDA conductance (Schiller et al., 2000; Korogod et al., 2002; Rhodes, 2006; Major et al., 2013; Bressloff and Newby, 2014). It has been also postulated that cessation or reversal of the glutamate transport from extracellular spaces into glial processes may contribute to the abrupt transitions from subthreshold to suprathreshold response (Oikonomou et al., 2012). Regardless of the exact mechanism, the nonlinear membrane responses (abrupt transitions) were regularly observed in all four neuron subtypes during focal glutamate applications (**Figure 6B**, transition from green trace to red trace). We concluded that (1) spiny neurons of the amygdala, (2) medium spiny neurons of striatum, (3) cortical layer 4 stellate cells, and (4) cortical layer 5 pyramidal neurons process afferent glutamatergic inputs using one unified basic principle. Each neuron subtype is equipped with relatively short primary dendrites (basilar), directly attached to the soma (**Figure 2**). This morphology allows for an efficient transfer of depolarizing currents from mid dendritic segments to the soma resulting in ∼20 mV somatic depolarizations (Oakley et al., 2001; Milojkovic et al., 2004, 2005a). The primary (basilar) dendrites of spiny neurons carry high density of dendritic spines, which yields to a high density of AMPA and NMDA receptors (**Figure 4**). The density of dendritic glutamatergic receptors in

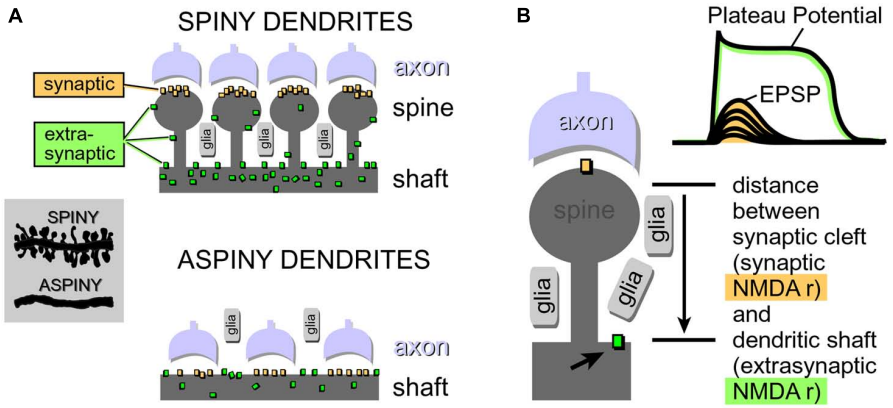

FIGURE 4 | Physical aspects of glutamatergic transmission in spiny and aspiny neurons. (A) Dendritic spines increase the receptive area for impinging axons, resulting in a greater density of synaptic contacts in spiny neurons compared to aspiny neurons. For the same reason (increased receptive area), the total number of NMDA receptors per unit length is also greater in spiny neurons. Synaptic NMDA receptors are activated during all modes of synaptic transmission. Extrasynaptic NMDA receptors, on the other hand, are mostly activated by glutamate spillover during barrages of (repetitive) synaptic inputs. **(B)** If glutamate breaches the distance between synaptic cleft (synaptic) and the surface of the dendritic shaft (extrasynaptic), then subthreshold potential (EPSP) converts into a suprathreshold potential (Plateau Potential). Arrow points to an extrasynaptic NMDA receptor.

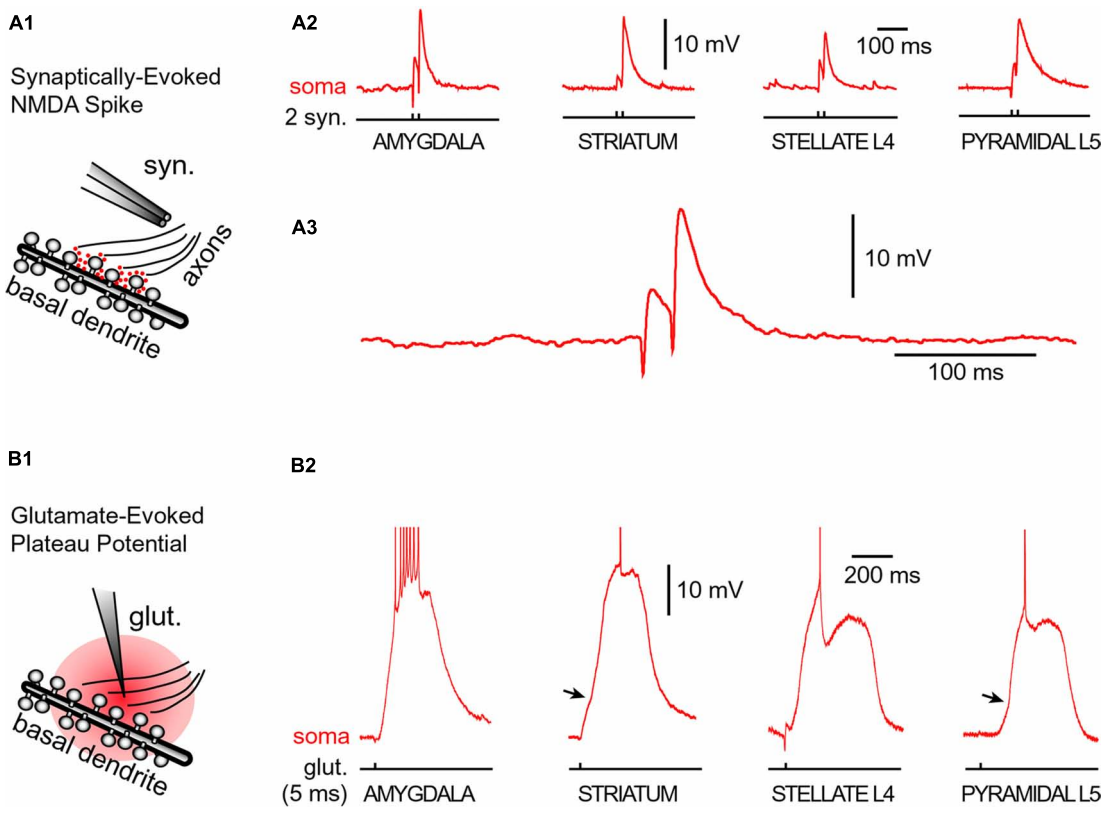

FIGURE 5 | Glutamate-mediated dendritic spikes and plateaus in spiny neurons. (A1) Drawing depicts an experimental outline. Syn. – synaptic stimulation electrode. Red dots depict glutamate in synaptic and extrasynaptic spaces. **(A2)** Two consecutive synaptic shocks trigger classic NMDA spikes in all four types of spiny neurons. **(A3)** Amygdala NMDA spike on expanded time scale. **(B1)** Drawing depicts focal microiontophoresis of glutamate. Dendritic segment is engulfed in exogenous glutamate (red). **(B2)** Individual glutamate pulses (pulse duration = 5 ms), when delivered on spiny dendrites, produced sustained somatic depolarizations accompanied by action potential firing. APs are truncated for display. See also **Figure 3B**. Infliction points on the somatic voltage waveforms (arrows) testify to dendritic spike initiation, as determined by simultaneous dendritic voltage imaging and somatic whole-cell recordings (Milojkovic et al., 2005b).

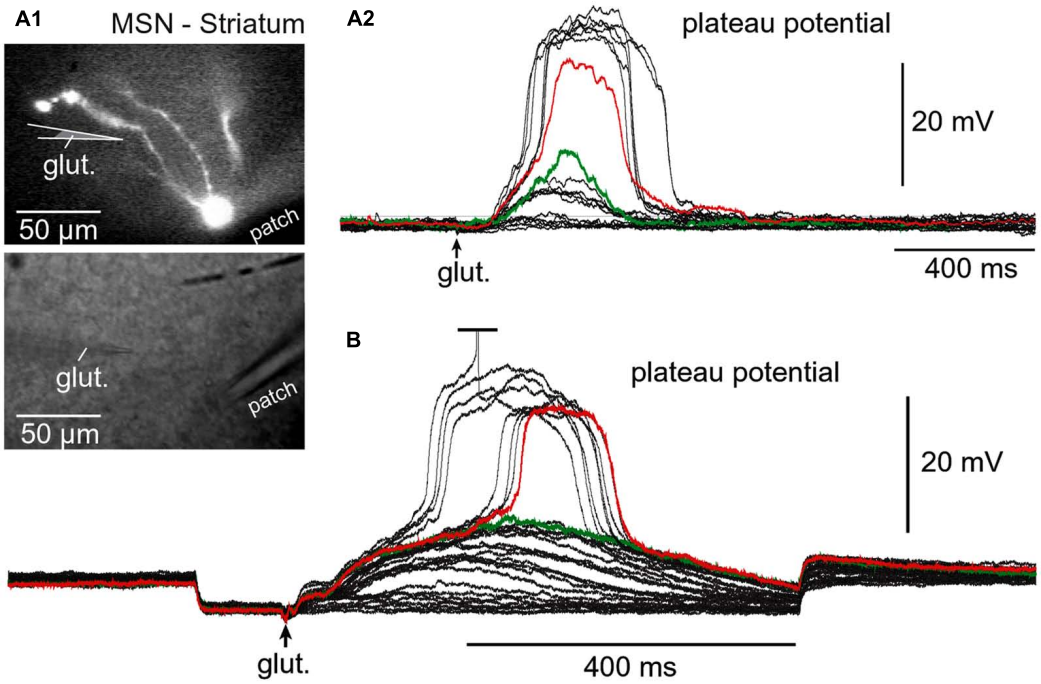

FIGURE 6 | Regenerative property of glutamate-evoked dendritic plateau potentials in neostriatum. (A) Upper image: Neostriatal medium spiny neuron filled with OGB-1 and AF-594. Lower image: Two glass electrodes used for stimulation (glut.) and whole-cell recording (patch). **(A2)** Gradually increasing levels of the glutamate iontophoresis current produced a nonlinear membrane response (sudden jump). **(B)** Same as in **(A2)** except different cell and negative current was injected into the cell body to block action potential firing. Green indicates subthreshold and red indicates threshold responses.

all spiny neurons is sufficient to support dendritic NMDA spikes (**Figure 5A**) and glutamate-mediated dendritic plateau potentials (**Figures 5B** and **6**).

DENDRITIC UP STATES

Dendritic UP state in one dendrite

We do not know what causes cortical and striatal networks to turn ON and OFF on a definite temporal scale, resulting in alternating periods of high glutamatergic supply (UP state) followed by the absence of glutamatergic input (DOWN state; Wilson and Groves, 1981; Volgushev et al., 2006; Wilson, 2008). Although we do not know what causes cortical and striatal UP states (network UP states), we might be able to explain the neuronal processes which occur in dendrites of cortical and striatal neurons during such states. Here we propose that somatic voltage waveforms in spiny neurons (**Figure 3A**) are determined by dendritic UP states. The neuronal cell body shifts from a DOWN to UP state after the generation of the dendritic plateau potential (Milojkovic et al., 2004). The cell body stays in the UP state as long as the dendritic plateau lasts. The voltage waveform (sustained somatic depolarization) collapses in the cell body after the collapse of the dendritic plateau potential (Milojkovic et al., 2005a). In this way, the slow component of the somatic signal during each UP state is just a mere reflection of a flamboyant integration process occurring somewhere in the dendritic tree (Milojkovic et al., 2005a; Antic et al., 2010). This "flamboyant" integration process (dendritic plateau potential) needs to take place in only one basal branch to be a successful driver of the neuronal UP state (Milojkovic et al., 2004, 2005a, 2007).

Dendritic UP states occurring simultaneously in two dendrites

With thousands of synaptic contacts distributed on the basilar dendritic tree of cortical and striatal spiny neurons (Larkman, 1991; Benavides-Piccione et al., 2006; Elston et al., 2009; Garcia et al., 2010), it is likely that two or more primary (basilar) dendrites may experience glutamate-mediated plateau potentials at the same moment of time. The likelihood of coincident UP states in two and more dendrites belonging to the same neuron is high during a vigorous network activity, during elevated levels of attention or motivation, or in the face of an intense computational task. A very potent glutamatergic drive is achieved during slow wave sleep, at each "UP" phase (**Figure 3**).

Experiments performed with two glutamate iontophoresis pipettes positioned on two basal dendrites were used to model dendritic spikes occurring in two basal branches at the same moment of time (Oikonomou et al., 2012). Each glutamatergic stimulus (intensity, duration) was set to trigger a dendritic plateau potential in its respective branch (**Figure 7A**). The experimental paradigm consisted of three successive steps: blue dendrite alone, red dendrite alone and both dendrites at the same time (**Figure 7B**). All traces shown in **Figures 7B–D**, represent somatic voltage waveforms. Based on the amplitude of the slow component of the somatic voltage waveform, an observer cannot readily distinguish if dendritic UP state occurred in one branch (blue or red) versus two branches simultaneously (yellow).

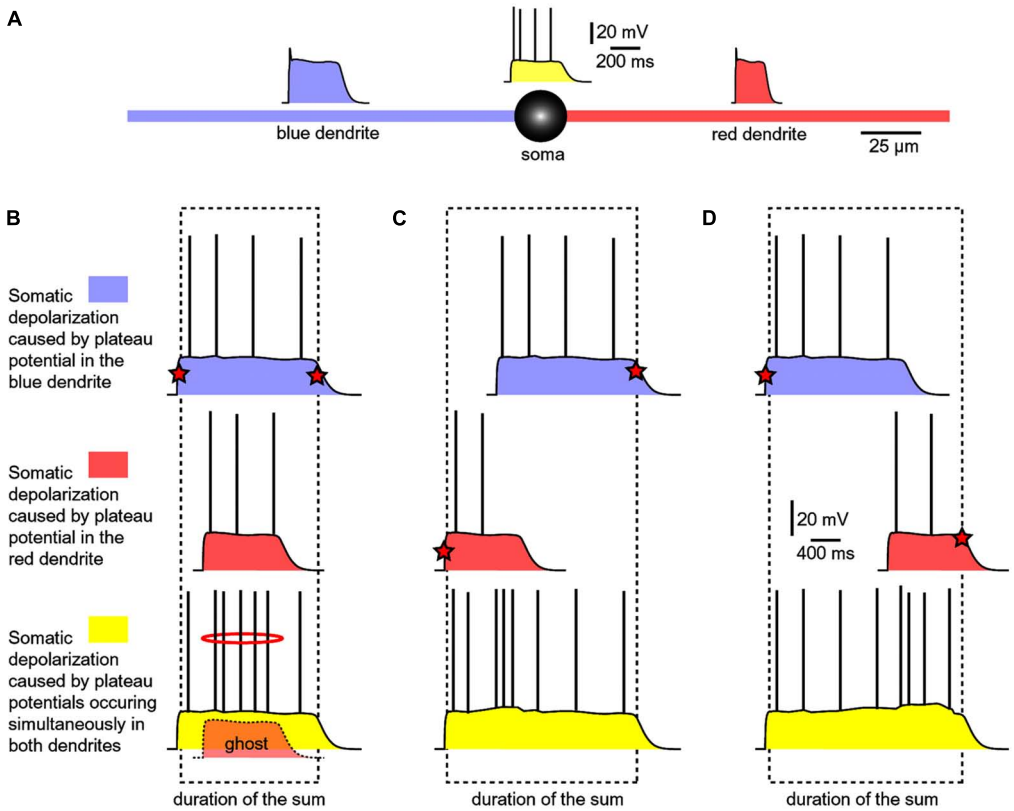

FIGURE 7 | Summation of dendritic plateau potentials on the soma. **(A)** Schematic diagram of a spiny neuron representing membrane potential transients occurring simultaneously on two basal dendrites and soma. Each column/panel **(B–D)** represents one experimental sequence. Each experimental sequence has three steps. In the first step, only blue dendrite received glut. stimulus (top trace). In the second step, only red dendrite received glut. stimulus (middle trace). In the third step, both dendrites received glut. stimuli (bottom trace). Dashed rectangle marks the beginning and the end of the somatic plateau potential in the bottom trace. Red star marks the summand which contributes to the leading edge or finishing edge of the sum (yellow trace). **(B)** The red plateau starts and finishes during the plateau phase of the blue plateau. "Ghost" potential is a copy of the red trace superimposed on the bottom trace with preserved timing. The red plateau is completely "eclipsed" by the longer blue plateau, as indicated by the "ghost" potential. **(C)** The red plateau starts before the blue plateau. Duration of the sum is determined by the onset of red and the collapse of blue plateau. **(D)** The blue plateau finishes before the red plateau phase is over. Duration of the sum is thus determined by the onset of blue and the collapse of red plateau.

If a shorter dendritic plateau potential (**Figure 7B**, red) was set to occur within the plateau phase of a longer plateau potential (blue), then the shorter event would completely be "eclipsed" by the longer event upon summation (yellow). Because the amplitude of the somatic voltage waveform (slow component) was the same before (blue and red) and after summation (yellow), the only clue about the occurrence of the shorter dendritic spike (**Figure 7B**, ghost) comes from a moderate increase in AP firing (**Figure 7B**, red ring). In respect to the somatic depolarization envelope, the shorter plateau potential (red) is, in a sense, "eclipsed" by a longer dendritic plateau (blue).

In order to become a "visible" component of the sum (yellow), the red dendritic UP state must occur before the onset of the blue dendritic UP state (**Figure 7C**), or after the collapse of the blue dendritic UP state (**Figure 7D**). As long as two dendritic UP states partially overlap in time, the resulting waveform (the sum) appears as one continuous UP state in the soma (**Figures 7C,D**, yellow). One important conclusion of experiments performed with two glutamate releasing electrodes on two basal branches (**Figure 7**) is that during a neuronal UP state, the slow component of the somatic voltage waveform does not reveal the number of basal dendrites experiencing glutamate-mediated plateau potentials (Oikonomou et al., 2012). Only when these potentials are separated (shifted) in time, so that their profiles (plateau phases) no longer overlap, the cell body can "experience" two dendritic plateau potentials arriving from two basal dendrites as two separate events (Oikonomou et al., 2012, their Figure 9).

DETECTORS OF STRONG NETWORK ACTIVITY

A successful synchronization of the firing activity among neurons would require that members of a neuronal ensemble enter UP state at the same moment of time (**Figure 1B**). To become eligible for inclusion into a functional neuronal ensemble, a spiny neuron must quickly, and reliably switch from a DOWN to an UP state, remain in the depolarized UP state as long as necessary, and quickly abandon the UP state when a percept is formed or expired. Several lines of evidence listed below (Sections Efficient Depolarization of the Cell Body, Dependence

on the Surplus Glutamate, Duration of Sustained Depolarization, and Dendritic Spines and Glial Processes) suggest that glutamate-mediated dendritic plateau potentials may serve as detectors of significant or meaningful network activity, and may underlie the neuronal voltage waveforms recorded *in vivo* (**Figure 3A**).

Efficient depolarization of the cell body

A glutamate-mediated dendritic plateau potential (dendritic UP state) produces enough depolarizing current to drive the cell body into a sustained depolarized state (neuronal UP state; Milojkovic et al., 2004; Augustinaite et al., 2014). The amplitude of the slow component (plateau phase) at the dendritic initiation site (**Figure 8**, input site) located in the middle of a basal dendrite (100–150 μm away from the cell body) is ∼2/3 of the backpropagating AP at the same location (Milojkovic et al., 2004). The amplitude of the backpropagating AP at 100–150 μm away from the cell body is ∼60 mV (Antic, 2003; Acker and Antic, 2009). Therefore, the amplitude of the dendritic plateau potential is ∼40 mV. The amplitude of the dendritic plateau potential decreases gradually as dendritic voltage transient spreads passively into the cell body (**Figure 8A**, centripetal direction of propagation), resulting in a ∼20 mV somatic depolarization (Milojkovic et al., 2004, 2005a,b, 2007; Major et al., 2008). The amplitude of the sustained somatic depolarization (neuronal UP state) depends on the physical location of the input site. It is lessened if its glutamatergic input is moved more distally, away from the cell body (Milojkovic et al., 2004, their Figure 1; Major et al., 2008; Augustinaite et al., 2014; Jadi et al., 2014).

Dependence on the surplus glutamate

Cortical or striatal UP and DOWN states are caused by the alternating presence and absence of activity in excitatory neuronal network (Wilson and Kawaguchi, 1996; Sanchez-Vives and McCormick, 2000; Fellin et al., 2004; Poskanzer and Yuste, 2011). During periods of greater network activity, a significant glutamatergic input impinges on individual neurons, causing these neurons to enter the UP state. Transitions to the UP state are robust phenomena that accurately reflect the underlying structure of consistent increases in afferent input over a limited time period. There are no transitions back to the DOWN state until the excitatory glutamatergic input is reduced (Wolf et al., 2005). Similarly to

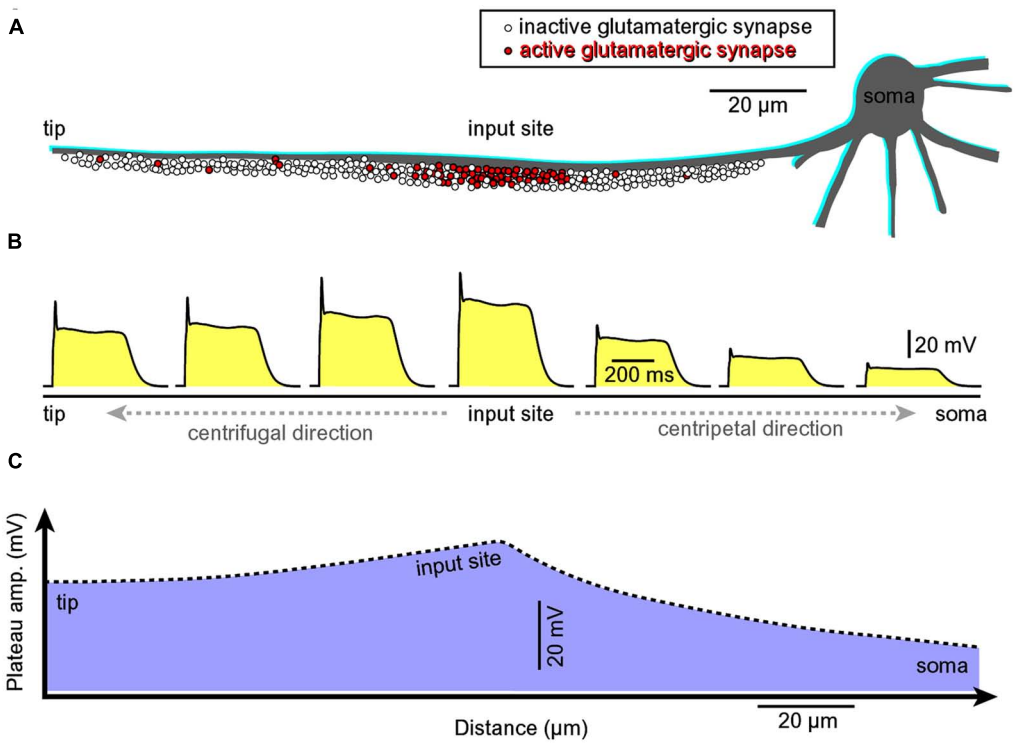

FIGURE 8 | Asymmetric propagation of dendritic plateau potential. **(A)** Schematic drawing of a spiny basal dendrite. Red dots denote glutamatergic afferents actively releasing glutamate at this moment of time. **(B)** Voltage waveform of the glutamate-induced plateau potential simultaneously viewed at seven different sites along the spiny dendrite (Milojkovic et al., 2004, 2005a, 2007). **(C)** The amplitude of the slow component (plateau phase) attenuates as dendritic potential spreads passively toward the cell body (centripetal direction, Milojkovic et al., 2004; their Figures 3 and 4). However, the duration remains the same across the entire dendritic branch. The grade of attenuation is less in centrifugal direction (from the initiation site toward the dendritic tip) than in the centripetal direction. Regardless of direction (centripetal or centrifugal), the propagating plateau potentials successively open voltage-gated Ca^{2+} channels in dendritic segments, which explains why the entire dendritic branch experiences significant calcium influx during a glutamate-evoked dendritic plateau potential (even though synaptic glutamate receptor channels are activated at the input site only). This interplay between dendritic membrane potential and dendritic calcium influx in space and time was revealed by combining voltage-sensitive and calcium-sensitive multi-site recordings along the same dendritic branch (Milojkovic et al., 2007).

UP states, dendritic plateau potentials occur only if dendritic shafts and associated extrasynaptic NMDA receptors are surrounded by a surplus of glutamate ions/molecules (Suzuki et al., 2008; Chalifoux and Carter, 2011; Oikonomou et al., 2012). In summary, a surplus of glutamate (spillover) occurs during network UP states (Lambe and Aghajanian, 2006; Poskanzer and Yuste, 2011). A surplus of glutamate in the extrasynaptic space triggers dendritic plateau potential (Suzuki et al., 2008; Chalifoux and Carter, 2011; Oikonomou et al., 2012).

Duration of sustained depolarization

There is a strong similarity between UP states and dendritic plateau potentials regarding the duration of sustained depolarization. Both network UP states and glutamate-mediated dendritic plateau potentials last several hundred milliseconds (**Figures 3** and **5**). We think that a continued presence of glutamate molecules bound to NMDA receptors in synaptic and more importantly in extrasynaptic spaces is critical for the maintenance of the UP state. Unlike a classic sodium spike which is terminated by the inactivation of Na^+ and strong activation of K^+ currents, the glutamate-mediated dendritic plateau potential is terminated by unbinding of glutamate and weak activation of K^+ currents (Cai et al., 2004). Glutamate unbinding from dendritic NMDA receptor channels is a slower process because it takes place inside the glutamate pond created by repetitive synaptic stimulation (Oikonomou et al., 2012), hence explaining the prolonged plateau phases of these dendritic events (Milojkovic et al., 2004, 2005a, 2007).

Dendritic spines and glial processes

CNS spiny neurons possess an inherent mechanism for generation of dendritic UP states, which is based on anatomical and functional relations between dendritic spines and glial processes interposed between dendritic spines. The growth of dendritic spines endows spiny neurons with four cardinal features:

High density of impinging glutamate-releasing axon terminals (Figure 4). Note that an ample supply of glutamate is essential for dendritic plateau potentials. The amount of glutamate required to drive a plateau potential can only be obtained by repetitive synaptic stimulation or glutamate iontophoresis (Milojkovic et al., 2004; Major et al., 2008; Suzuki et al., 2008; Augustinaite et al., 2014). However, sequential glutamate uncaging on 10 dendritic spines cannot supply enough glutamate to create a glutamate pond (Losonczy et al., 2008; Remy et al., 2009; Branco and Hausser, 2011), and this may be the reason why these experiments did not yield glutamate-mediated dendritic plateau potentials lasting hundreds of milliseconds.

High density of NMDA receptor-channels. High density of dendritic NMDA conductance is essential for the generation of glutamate-mediated dendritic regenerative potentials (Schiller et al., 2000; Rhodes, 2006; Major et al., 2013). Without any doubt, dendritic spines increase the surface area for the insertion of synaptic and extrasynaptic NMDA receptors resulting in a significantly greater NMDA conductance per dendritic branch (**Figure 4**), thus providing the critical requirement for dendritic NMDA spike initiation (Schiller et al., 2000; Rhodes, 2006; Major et al., 2013).

High density of glial processes surrounding dendritic branch. Growth of spines creates space for glial processes to grow in between dendritic spines (**Figure 4A**, glia). Strategic positioning of glial processes between the populations of synaptic and extrasynaptic NMDA receptors (**Figure 4B**), provides astrocytes with a mechanism to gate neuronal transitions from DOWN to UP state (Lambe and Aghajanian, 2006; Poskanzer and Yuste, 2011).

Spine necks provide for the separation between two principal modes of synaptic transmission. (a) Subthreshold (dendritic EPSP) and (b) suprathreshold dendritic response (plateau potential). Dendritic spines create a physical separation between synaptic and extrasynaptic NMDA receptor-channels (**Figure 4A**). The length of the spine neck represents a physical distance that spillover glutamate has to travel in order to reach extrasynaptic NMDA receptors located on the dendritic shaft (**Figure 4B**). If glutamate molecules "survive" the trip from the releasing axons to the surface of the dendritic shaft (**Figure 4A**), then a subthreshold dendritic potential (**Figure 4B**, EPSP) is converted into a suprathreshold membrane response termed "dendritic plateau potential" (**Figure 4B**).

The presence of glutamate molecules is not simply a permissive factor for the initiation of a glutamate-mediated dendritic plateau potential (dendritic UP state). Instead, a nonlinear buildup of glutamate is probably the primary mechanism of the observed voltage jump from subthreshold voltage transient to a full-blown spike (**Figure 6B**), see also (Schiller et al., 2000; Milojkovic et al., 2004, 2005a; Oikonomou et al., 2012). It can be said that dendritic plateau potentials have a "glutamate threshold" (Milojkovic et al., 2005b; Major et al., 2008; Polsky et al., 2009).

Nonlinear build-up of glutamate in the extracellular space ("glutamate threshold"). During intense network activity, many converging glutamatergic preterminals (**Figure 4**, axon) are activated repetitively by bursts of action potentials traveling through axonal lines of communication (Lisman, 1997). Repetitive synaptic input is a key requirement for the dendritic UP state (Milojkovic et al., 2004; Oikonomou et al., 2012). At some point during repetitive synaptic stimulation, an ensuing glutamatergic drive overwhelms the ability of glial processes to absorb the spilled glutamate. The "glutamate threshold" is reached when glia is no longer able to cope with repetitive glutamatergic inputs arriving in a confined space at the same moment of time (**Figure 9**). For a brief period of time the dendritic segment is surrounded by a surplus of glutamate (**Figure 9**, "glutamate pond"). During such an overwhelming glutamatergic stimulus, the dendritic spike cannot be perturbed by negative voltage pulses (Oikonomou et al., 2012; their Figure 5).

Repetitive inputs. In the process of dendritic spike initiation, the primary role of the repetitive glutamatergic input is not a local depolarization needed to cross the voltage threshold (Polsky et al., 2009), but instead multiple shocks are necessary to reverse glial function from glutamate uptake to glutamate release (Parpura et al., 1994). In glutamate uncaging experiments, the NMDA spike is initiated only when experimenters select neighboring dendritic spines (Losonczy et al., 2008; Remy et al., 2009; Branco and Hausser, 2011). The reason for this is contained in the spatial

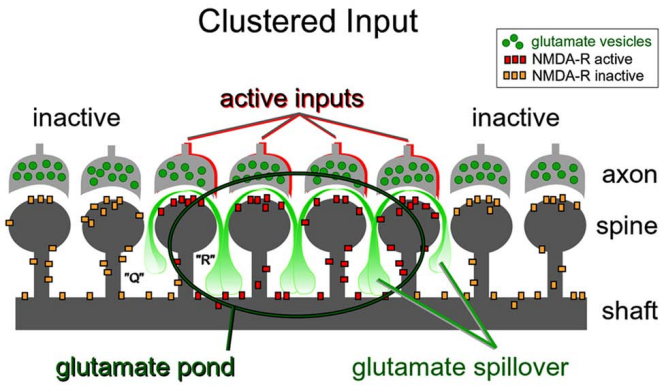

FIGURE 9 | Dendritic plateau potentials improve the efficacy of the conversion of excitatory inputs into sustained somatic depolarizations. Active glutamatergic inputs are spatiotemporally "clustered" onto a dendritic segment. Glutamate spillover is more efficient between two neighboring active inputs (space "R") than between an active and inactive input (space "Q"). Glutamate spillover may overwhelm glial processes located between neighboring active inputs causing a local accumulation of glutamate in the extracellular space (glutamate pond). Inside the glutamate pond, both synaptic and extrasynaptic NMDA receptors are fully activated, thus creating favorable conditions for firing of a glutamate-mediated dendritic plateau potential.

arrangement of the participating ultrastructures. Glial processes interposed between two active dendritic spines (**Figure 9**, space "R") are more likely to reverse glial function from glutamate uptake to glutamate release (Parpura et al., 1994), than the glial processes interposed in between active and inactive spines (**Figure 9**, space "Q"). In summary, the new evidence (Major et al., 2008; Polsky et al., 2009; Oikonomou et al., 2012) supports the notion that dendritic spikes in glutamate uncaging experiments do not arise from summation of voltage alone, but rather from summation of three glutamate sources: (1) uncaged glutamate; (2) synaptically released glutamate triggered by the presence of uncaged glutamate; and (3) glutamate released from glia stimulated by the uncaged glutamate (Min and Nevian, 2012).

CONCLUDING REMARKS

Although a diffuse glutamatergic input distributed across an entire dendritic tree may be used by neurons for the detection of strong network activity and conversion of such activity into a sustained plateau depolarization (UP state; Shu et al., 2003), a more effective mechanism is the mechanism based on the convergence of synaptic inputs onto one dendritic branch (Mel, 1993) and induction of a long-lasting glutamate-mediated regenerative dendritic potential (Milojkovic et al., 2004). Excitatory glutamatergic inputs confined to a single dendrite can profoundly influence the neuronal output of layer 5 pyramidal neurons in brain slices (**Figure 3**). "A common preconception about central nervous system neurons is that thousands of small postsynaptic potentials sum across the entire dendritic tree to generate substantial firing rates" (Milojkovic et al., 2004). Contrary to this common presumption, a brief glutamatergic stimulation delivered in a restricted part of the basilar dendritic tree invariably produces sustained plateau depolarizations of the cell body, accompanied by bursts of action potentials (Milojkovic et al., 2004, 2005a). Glutamatergic inputs converging on a narrow segment of a single dendritic branch is sufficient input for generation of a somatic depolarization, which strongly resembles neuronal UP state (Milojkovic et al., 2004, 2005a; Antic et al., 2007, 2010). Plotkin et al. (2011), arrived at an identical conclusion studying striatal medium spiny neurons.

All spiny neurons of the mammalian telencephalon, including pyramidal layers 2–6 and stellate layer 4 neurons of the cerebral cortex, medium spiny neurons of the neostriatum, amygdala, and nucleus accumbens are well positioned to detect multiple patterns of highly selected inputs, perhaps as few as 50–100 inputs from each afferent structure. Spiny neurons integrate inputs over a relatively large time window and are probably detecting the co-occurrence of signature patterns of afferent inputs relating context, emotion, and working memory (Bar-Gad et al., 2003; Wolf et al., 2005). Glutamate-mediated dendritic plateau potentials are ideally built to provide neurons with a relatively large integration window lasting several hundred milliseconds (Milojkovic et al., 2004, 2005a). This temporal window is a critical determinant of the "ensemble period" as depicted in **Figure 1**. The size (number of cell-members) and power (ability to drive the organism toward a distinct behavior) of a neuronal ensemble both depend on the ability of each cell-member to remain in a sustained depolarized state. The amount of time each neuron spends in a sustained depolarized UP state is the product of the duration of a dendritic plateau potential and the number of dendritic branches experiencing plateau potentials overlapping in time (**Figure 7**, *duration of the sum*).

Initially, *in vivo* recordings were unable to provide evidence that dendritic NMDA spikes or plateau potentials occur in living animals (Waters and Helmchen, 2006; Waters, 2007; Varga et al., 2011). However, recent advancements in technology have produced experimental evidence in favor of dendritic spikes in anesthetized and behaving animals (Lavzin et al., 2012; Smith et al., 2013). What's more, a recent study has found NMDA-dependent dendritic calcium signals locked to neuronal UP states (Hill et al., 2013). All in all, experimental studies reporting the occurrence on dendritic NMDA spikes *in vivo* may accumulate with time (Grienberger et al., 2014; Palmer et al., 2014).

Whether spiny neurons have evolved a dendritic mechanism for detecting activity of neuronal ensembles (**Figure 1**) and joining the active ensemble (transition to UP state) remains to be further investigated *in vivo*. Nevertheless, there is little doubt that in all telencephalic neurons with dendritic spines (spiny neurons), dendritic NMDA spikes and glutamate-mediated dendritic plateau potentials represent the dominant forms of dendritic integration.

REFERENCES

Acker, C. D., and Antic, S. D. (2009). Quantitative assessment of the distributions of membrane conductances involved in action potential backpropagation along basal dendrites. *J. Neurophysiol.* 101, 1524–1541. doi: 10.1152/jn.00651.2007

Ainsworth, M., Lee, S., Cunningham, M. O., Traub, R. D., Kopell, N. J., and Whittington, M. A. (2012). Rates and rhythms: a synergistic view of frequency and temporal coding in neuronal networks. *Neuron* 75, 572–583. doi: 10.1016/j.neuron.2012.08.004

Andjelic, S., Gallopin, T., Cauli, B., Hill, E. L., Roux, L., Badr, S., et al. (2009). Glutamatergic nonpyramidal neurons from neocortical layer VI and their comparison with pyramidal and spiny stellate neurons. *J. Neurophysiol.* 101, 641–654. doi: 10.1152/jn.91094.2008

Antic, S. D. (2003). Action potentials in basal and oblique dendrites of rat neocortical pyramidal neurons. *J. Physiol.* 550, 35–50. doi: 10.1113/jphysiol.2002.033746

Antic, S. D., Acker, C. D., Zhou, W. L., Moore, A. R., and Milojkovic, B. A. (2007) "The role of dendrites in the maintenance of the UP state," in *Mechanisms of Spontaneous Active States in the Neocortex*, ed. I. Timofeev (Kerala: Research Signpost), 45–72.

Antic, S. D., Zhou, W. L., Moore, A. R., Short, S. M., and Ikonomu, K. D. (2010). The decade of the dendritic NMDA spike. *J. Neurosci. Res.* 88, 2991–3001. doi: 10.1002/jnr.22444

Augustinaite, S., Kuhn, B., Helm, P. J., and Heggelund, P. (2014). NMDA spike/plateau potentials in dendrites of thalamocortical neurons. *J. Neurosci.* 34, 10892–10905. doi: 10.1523/JNEUROSCI.1205-13.2014

Bair, W. (1999). Spike timing in the mammalian visual system. *Curr. Opin. Neurobiol.* 9, 447–453. doi: 10.1016/S0959-4388(99)80067-1

Bar-Gad, I., Heimer, G., Ritov, Y., and Bergman, H. (2003). Functional correlations between neighboring neurons in the primate globus pallidus are weak or nonexistent. *J. Neurosci.* 23, 4012–4016.

Bazhenov, M., Timofeev, I., Steriade, M., and Sejnowski, T. J. (2002). Model of thalamocortical slow-wave sleep oscillations and transitions to activated states. *J. Neurosci.* 22, 8691–8704.

Benavides-Piccione, R., Hamzei-Sichani, F., Ballesteros-Yanez, I., DeFelipe, J., and Yuste, R. (2006). Dendritic size of pyramidal neurons differs among mouse cortical regions. *Cereb. Cortex* 16, 990–1001. doi: 10.1093/cercor/bhj041

Benucci, A., Verschure, P. F., and Konig, P. (2004). Two-state membrane potential fluctuations driven by weak pairwise correlations. *Neural Comput.* 16, 2351–2378. doi: 10.1162/0899766041941871

Branchereau, P., Van Bockstaele, E. J., Chan, J., and Pickel, V. M. (1996). Pyramidal neurons in rat prefrontal cortex show a complex synaptic response to single electrical stimulation of the locus coeruleus region: evidence for antidromic activation and GABAergic inhibition using in vivo intracellular recording and electron microscopy. *Synapse* 22, 313–331. doi: 10.1002/(SICI)1098-2396(199604)22:4<313::AID-SYN3>3.0.CO;2-E

Branco, T., and Hausser, M. (2011). Synaptic integration gradients in single cortical pyramidal cell dendrites. *Neuron* 69, 885–892. doi: 10.1016/j.neuron.2011.02.006

Brandalise, F., and Gerber, U. (2014). Mossy fiber-evoked subthreshold responses induce timing-dependent plasticity at hippocampal CA3 recurrent synapses. *Proc. Natl. Acad. Sci. U.S.A.* 111, 4303–4308. doi: 10.1073/pnas.1317667111

Brecht, M., and Sakmann, B. (2002). Dynamic representation of whisker deflection by synaptic potentials in spiny stellate and pyramidal cells in the barrels and septa of layer 4 rat somatosensory cortex. *J. Physiol.* 543, 49–70. doi: 10.1113/jphysiol.2002.018465

Brecht, M., Singer, W., and Engel, A. K. (1998). Correlation analysis of corticotectal interactions in the cat visual system. *J. Neurophysiol.* 79, 2394–2407.

Bressloff, P. C., and Newby, J. M. (2014). Stochastic hybrid model of spontaneous dendritic NMDA spikes. *Phys. Biol.* 11:016006. doi: 10.1088/1478-3975/11/1/016006

Buzsaki, G., and Silva, F. L. (2012). High frequency oscillations in the intact brain. *Prog. Neurobiol.* 98, 241–249. doi: 10.1016/j.pneurobio.2012.02.004

Cai, X., Liang, C. W., Muralidharan, S., Kao, J. P., Tang, C. M., and Thompson, S. M. (2004). Unique roles of SK and Kv4.2 potassium channels in dendritic integration. *Neuron* 44, 351–364. doi: 10.1016/j.neuron.2004.09.026

Cauller, L. (1995). Layer I of primary sensory neocortex: where top-down converges upon bottom-up. *Behav. Brain Res.* 71, 163–170. doi: 10.1016/0166-4328(95)00032-1

Chalifoux, J. R., and Carter, A. G. (2011). Glutamate spillover promotes the generation of NMDA spikes. *J. Neurosci.* 31, 16435–16446. doi: 10.1523/JNEUROSCI.2777-11.2011

Chauvette, S., Volgushev, M., and Timofeev, I. (2010). Origin of active states in local neocortical networks during slow sleep oscillation. *Cereb. Cortex* 20, 2660–2674. doi: 10.1093/cercor/bhq009

Compte, A., Sanchez-Vives, M. V., McCormick, D. A., and Wang, X. J. (2003). Cellular and network mechanisms of slow oscillatory activity (<1 Hz) and wave propagations in a cortical network model. *J. Neurophysiol.* 89, 2707–2725. doi: 10.1152/jn.00845.2002

Contreras, D., Timofeev, I., and Steriade, M. (1996). Mechanisms of long-lasting hyperpolarizations underlying slow sleep oscillations in cat corticothalamic networks. *J. Physiol.* 494(Pt 1), 251–264.

Cossart, R., Aronov, D., and Yuste, R. (2003). Attractor dynamics of network UP states in the neocortex. *Nature* 423, 283–288. doi: 10.1038/nature01614

Desimone, R., Albright, T. D., Gross, C. G., and Bruce, C. (1984). Stimulus-selective properties of inferior temporal neurons in the macaque. *J. Neurosci.* 4, 2051–2062.

Durstewitz, D., Seamans, J. K., and Sejnowski, T. J. (2000). Neurocomputational models of working memory. *Nat. Neurosci.* 3, 1184–1191. doi: 10.1038/81460

Eichenbaum, H. (1993). Thinking about brain cell assemblies. *Science* 261, 993–994. doi: 10.1126/science.8351525

Elston, G. N., Oga, T., and Fujita, I. (2009). Spinogenesis and pruning scales across functional hierarchies. *J. Neurosci.* 29, 3271–3275. doi: 10.1523/JNEUROSCI.5216-08.2009

Engel, A. K., Fries, P., and Singer, W. (2001). Dynamic predictions: oscillations and synchrony in top-down processing. *Nat. Rev. Neurosci.* 2, 704–716. doi: 10.1038/35094565

Engel, A. K., and Singer, W. (2001). Temporal binding and the neural correlates of sensory awareness. *Trends Cogn. Sci.* 5, 16–25. doi: 10.1016/S1364-6613(00)01568-0

Fellin, T., Pascual, O., Gobbo, S., Pozzan, T., Haydon, P. G., and Carmignoto, G. (2004). Neuronal synchrony mediated by astrocytic glutamate through activation of extrasynaptic NMDA receptors. *Neuron* 43, 729–743. doi: 10.1016/j.neuron.2004.08.011

Garcia, B. G., Neely, M. D., and Deutch, A. Y. (2010). Cortical regulation of striatal medium spiny neuron dendritic remodeling in parkinsonism: modulation of glutamate release reverses dopamine depletion-induced dendritic spine loss. *Cereb. Cortex* 20, 2423–2432. doi: 10.1093/cercor/bhp317

Gidon, A., and Segev, I. (2012). Principles governing the operation of synaptic inhibition in dendrites. *Neuron* 75, 330–341. doi: 10.1016/j.neuron.2012.05.015

Grienberger, C., Chen, X., and Konnerth, A. (2014). NMDA receptor-dependent multidendrite Ca^{2+} spikes required for hippocampal burst firing in vivo. *Neuron* 81, 1274–1281. doi: 10.1016/j.neuron.2014.01.014

Hebb, D. O. (1949). *The Organisation of Behaviour*: *A Neuropsychological Theory*. New York: Wiley.

Hill, D. N., Varga, Z., Jia, H., Sakmann, B., and Konnerth, A. (2013). Multibranch activity in basal and tuft dendrites during firing of layer 5 cortical neurons in vivo. *Proc. Natl. Acad. Sci. U.S.A.* 110, 13618–13623. doi: 10.1073/pnas.1312599110

Holthoff, K., Kovalchuk, Y., Yuste, R., and Konnerth, A. (2004). Single-shock LTD by local dendritic spikes in pyramidal neurons of mouse visual cortex. *J. Physiol.* 560, 27–36. doi: 10.1113/jphysiol.2004.072678

Jadi, M., Behabadi, B. F., Poleg-Polsky, A., Schiller, J., and Mel, B. W. (2014). An augmented 2-layer model captures nonlinear analog spatial integration effects in pyramidal neuron dendrites. *Conf. Proc. IEEE Eng. Med. Biol. Soc.* 102, 782–798. doi: 10.1109/JPROC.2014.2312617

Katona, G., Kaszas, A., Turi, G. F., Hajos, N., Tamas, G., Vizi, E. S., et al. (2011). Roller coaster scanning reveals spontaneous triggering of dendritic spikes in CA1 interneurons. *Proc. Natl. Acad. Sci. U.S.A.* 108, 2148–2153. doi: 10.1073/pnas.1009270108

Klapstein, G. J., Fisher, R. S., Zanjani, H., Cepeda, C., Jokel, E. S., Chesselet, M. F., et al. (2001). Electrophysiological and morphological changes in striatal spiny neurons in R6/2 Huntington's disease transgenic mice. *J. Neurophysiol.* 86, 2667–2677.

Korogod, S. M., Kulagina, I. B., Kukushka, V. I., Gogan, P., and Tyc-Dumont, S. (2002). Spatial reconfiguration of charge transfer effectiveness in active bistable dendritic arborizations. *Eur. J. Neurosci.* 16, 2260–2270. doi: 10.1046/j.1460-9568.2002.02312.x

Lambe, E. K., and Aghajanian, G. K. (2006). Hallucinogen-induced UP states in the brain slice of rat prefrontal cortex: role of glutamate spillover and NR2B-NMDA receptors. *Neuropsychopharmacology* 31, 1682–1689. doi: 10.1038/sj.npp.1300944

Lamme, V. A., and Roelfsema, P. R. (2000). The distinct modes of vision offered by feedforward and recurrent processing. *Trends Neurosci.* 23, 571–579. doi: 10.1016/S0166-2236(00)01657-X

Larkman, A. U. (1991). Dendritic morphology of pyramidal neurones of the visual cortex of the rat: III. Spine distributions. *J. Comp. Neurol.* 306, 332–343. doi: 10.1002/cne.903060209

Larkum, M. (2012). A cellular mechanism for cortical associations: an organizing principle for the cerebral cortex. *Trends Neurosci.* 36, 141–151. doi: 10.1016/j.tins.2012.11.006

Larkum, M. E., Nevian, T., Sandler, M., Polsky, A., and Schiller, J. (2009). Synaptic integration in tuft dendrites of layer 5 pyramidal neurons: a new unifying principle. *Science* 325, 756–760. doi: 10.1126/science.1171958

Lavzin, M., Rapoport, S., Polsky, A., Garion, L., and Schiller, J. (2012). Nonlinear dendritic processing determines angular tuning of barrel cortex neurons in vivo. *Nature* 490, 397–401. doi: 10.1038/nature11451

Libet, B., Wright, E. W. Jr., Feinstein, B., and Pearl, D. K. (1979). Subjective referral of the timing for a conscious sensory experience: a functional role for the somatosensory specific projection system in man. *Brain* 102, 193–224. doi: 10.1093/brain/102.1.193

Lisman, J. E. (1997). Bursts as a unit of neural information: making unreliable synapses reliable. *Trends Neurosci.* 20, 38–43. doi: 10.1016/S0166-2236(96)10070-9

London, M., Schreibman, A., Hausser, M., Larkum, M. E., and Segev, I. (2002). The information efficacy of a synapse. *Nat. Neurosci.* 5, 332–340. doi: 10.1038/nn826

Losonczy, A., Makara, J. K., and Magee, J. C. (2008). Compartmentalized dendritic plasticity and input feature storage in neurons. *Nature* 452, 436–441. doi: 10.1038/nature06725

Major, G., Larkum, M. E., and Schiller, J. (2013). Active properties of neocortical pyramidal neuron dendrites. *Annu. Rev. Neurosci.* 36, 1–24. doi: 10.1146/annurev-neuro-062111-150343

Major, G., Polsky, A., Denk, W., Schiller, J., and Tank, D. W. (2008). Spatiotemporally graded NMDA spike/plateau potentials in basal dendrites of neocortical pyramidal neurons. *J. Neurophysiol.* 99, 2584–2601. doi: 10.1152/jn.00011.2008

Mel, B. W. (1993). Synaptic integration in an excitable dendritic tree. *J. Neurophysiol.* 70, 1086–1101.

Milojkovic, B. A., Radojicic, M. S., and Antic, S. D. (2005a). A strict correlation between dendritic and somatic plateau depolarizations in the rat prefrontal cortex pyramidal neurons. *J. Neurosci.* 25, 3940–3951. doi: 10.1523/JNEUROSCI.5314-04.2005

Milojkovic, B. A., Wuskell, J. P., Loew, L. M., and Antic, S. D. (2005b). Initiation of sodium spikelets in basal dendrites of neocortical pyramidal neurons. *J. Membr. Biol.* 208, 155–169. doi: 10.1007/s00232-005-0827-7

Milojkovic, B. A., Radojicic, M. S., Goldman-Rakic, P. S., and Antic, S. D. (2004). Burst generation in rat pyramidal neurones by regenerative potentials elicited in a restricted part of the basilar dendritic tree. *J. Physiol.* 558, 193–211. doi: 10.1113/jphysiol.2004.061416

Milojkovic, B. A., Zhou, W. L., and Antic, S. D. (2007). Voltage and calcium transients in basal dendrites of the rat prefrontal cortex. *J. Physiol.* 585, 447–468. doi: 10.1113/jphysiol.2007.142315

Min, R., and Nevian, T. (2012). Astrocyte signaling controls spike timing-dependent depression at neocortical synapses. *Nat. Neurosci.* 15, 746–753. doi: 10.1038/nn.3075

Mountcastle, V. B. (1997). The columnar organization of the neocortex. *Brain* 120(Pt 4), 701–722. doi: 10.1093/brain/120.4.701

Nevian, T., Larkum, M. E., Polsky, A., and Schiller, J. (2007). Properties of basal dendrites of layer 5 pyramidal neurons: a direct patch-clamp recording study. *Nat. Neurosci.* 10, 206–214. doi: 10.1038/nn1826

Nimchinsky, E. A., Sabatini, B. L., and Svoboda, K. (2002). Structure and function of dendritic spines. *Annu. Rev. Physiol.* 64, 313–353. doi: 10.1146/annurev.physiol.64.081501.160008

O'Donnell, P., and Grace, A. A. (1995). Synaptic interactions among excitatory afferents to nucleus accumbens neurons: hippocampal gating of prefrontal cortical input. *J. Neurosci.* 15, 3622–3639.

Oakley, J. C., Schwindt, P. C., and Crill, W. E. (2001). Dendritic calcium spikes in layer 5 pyramidal neurons amplify and limit transmission of ligand-gated dendritic current to soma. *J. Neurophysiol.* 86, 514–527.

Oikonomou, K. D., Short, S. M., Rich, M. T., and Antic, S. D. (2012). Extrasynaptic glutamate receptor activation as cellular bases for dynamic range compression in pyramidal neurons. *Front. Physiol.* 3:334. doi: 10.3389/fphys.2012.00334

Padival, M., Quinette, D., and Rosenkranz, J. A. (2013). Effects of repeated stress on excitatory drive of basal amygdala neurons in vivo. *Neuropsychopharmacology* 38, 1748–1762. doi: 10.1038/npp.2013.74

Palmer, L. M., Shai, A. S., Reeve, J. E., Anderson, H. L., Paulsen, O., and Larkum, M. E. (2014). NMDA spikes enhance action potential generation during sensory input. *Nat. Neurosci.* 17, 383–390. doi: 10.1038/nn.3646

Parpura, V., Basarsky, T. A., Liu, F., Jeftinija, K., Jeftinija, S., and Haydon, P. G. (1994). Glutamate-mediated astrocyte-neuron signalling. *Nature* 369, 744–747. doi: 10.1038/369744a0

Perrett, D. I., Rolls, E. T., and Caan, W. (1982). Visual neurones responsive to faces in the monkey temporal cortex. *Exp. Brain Res.* 47, 329–342. doi: 10.1007/BF00239352

Petersson, M. E., and Fransen, E. (2012). Long-lasting small-amplitude TRP-mediated dendritic depolarizations in CA1 pyramidal neurons are intrinsically stable and originate from distal tuft regions. *Eur. J. Neurosci.* 36, 2917–2925. doi: 10.1111/j.1460-9568.2012.08199.x

Plotkin, J. L., Day, M., and Surmeier, D. J. (2011). Synaptically driven state transitions in distal dendrites of striatal spiny neurons. *Nat. Neurosci.* 14, 881–888. doi: 10.1038/nn.2848

Polsky, A., Mel, B., and Schiller, J. (2009). Encoding and decoding bursts by NMDA spikes in basal dendrites of layer 5 pyramidal neurons. *J. Neurosci.* 29, 11891–11903. doi: 10.1523/JNEUROSCI.5250-08.2009

Polsky, A., Mel, B. W., and Schiller, J. (2004). Computational subunits in thin dendrites of pyramidal cells. *Nat. Neurosci.* 7, 621–627. doi: 10.1038/nn1253

Poskanzer, K. E., and Yuste, R. (2011). Astrocytic regulation of cortical UP states. *Proc. Natl. Acad. Sci. U.S.A.* 108, 18453–18458. doi: 10.1073/pnas.1112378108

Remy, S., Csicsvari, J., and Beck, H. (2009). Activity-dependent control of neuronal output by local and global dendritic spike attenuation. *Neuron* 61, 906–916. doi: 10.1016/j.neuron.2009.01.032

Rhodes, P. (2006). The properties and implications of NMDA spikes in neocortical pyramidal cells. *J. Neurosci.* 26, 6704–6715. doi: 10.1523/JNEUROSCI.3791-05.2006

Ro, T., Breitmeyer, B., Burton, P., Singhal, N. S., and Lane, D. (2003). Feedback contributions to visual awareness in human occipital cortex. *Curr. Biol.* 13, 1038–1041. doi: 10.1016/S0960-9822(03)00337-3

Rusakov, D. A., and Kullmann, D. M. (1998). Extrasynaptic glutamate diffusion in the hippocampus: ultrastructural constraints, uptake, and receptor activation. *J. Neurosci.* 18, 3158–3170.

Salinas, E., and Sejnowski, T. J. (2001). Correlated neuronal activity and the flow of neural information. *Nat. Rev. Neurosci.* 2, 539–550. doi: 10.1038/35086012

Sanchez-Vives, M. V., and McCormick, D. A. (2000). Cellular and network mechanisms of rhythmic recurrent activity in neocortex. *Nat. Neurosci.* 3, 1027–1034. doi: 10.1038/79848

Schiller, J., Major, G., Koester, H. J., and Schiller, Y. (2000). NMDA spikes in basal dendrites of cortical pyramidal neurons. *Nature* 404, 285–289. doi: 10.1038/35005094

Schiller, J., and Schiller, Y. (2001). NMDA receptor-mediated dendritic spikes and coincident signal amplification. *Curr. Opin. Neurobiol.* 11, 343–348. doi: 10.1016/S0959-4388(00)00217-8

Schneidman, E., Freedman, B., and Segev, I. (1998). Ion channel stochasticity may be critical in determining the reliability and precision of spike timing. *Neural Comput.* 10, 1679–1703. doi: 10.1162/089976698300017089

Shaikh, M. B., and Shaikh, A. B. (1982). Degenerative and compensatory changes in the basal amygdaloid neurons under cortical disorders. *J. Pak. Med. Assoc.* 32, 56–65.

Shu, Y. S., Hasenstaub, A., and McCormick, D. A. (2003). Turning on and off recurrent balanced cortical activity. *Nature* 423, 288–293. doi: 10.1038/nature01616

Singer, W. (1999). Neuronal synchrony: a versatile code for the definition of relations? *Neuron* 24, 49–65, 111–125. doi: 10.1016/S0896-6273(00)80821-1

Smith, S. L., Smith, I. T., Branco, T., and Hausser, M. (2013). Dendritic spikes enhance stimulus selectivity in cortical neurons in vivo. *Nature* 503, 115–120. doi: 10.1038/nature12600

Steriade, M., Timofeev, I., and Grenier, F. (2001). Natural waking and sleep states: a view from inside neocortical neurons. *J. Neurophysiol.* 85, 1969–1985.

Suzuki, T., Kodama, S., Hoshino, C., Izumi, T., and Miyakawa, H. (2008). A plateau potential mediated by the activation of extrasynaptic NMDA receptors in rat hippocampal CA1 pyramidal neurons. *Eur. J. Neurosci.* 28, 521–534. doi: 10.1111/j.1460-9568.2008.06324.x

Timofeev, I., Grenier, F., Bazhenov, M., Sejnowski, T. J., and Steriade, M. (2000). Origin of slow cortical oscillations in deafferented cortical slabs. *Cereb. Cortex* 10, 1185–1199. doi: 10.1093/cercor/10.12.1185

Tononi, G., and Koch, C. (2008). The neural correlates of consciousness: an update. *Ann. N. Y. Acad. Sci.* 1124, 239–261. doi: 10.1196/annals.1440.004

Tononi, G., Sporns, O., and Edelman, G. M. (1992). Reentry and the problem of integrating multiple cortical areas: simulation of dynamic integration in the visual system. *Cereb. Cortex* 2, 310–335. doi: 10.1093/cercor/2.4.310

Varga, Z., Jia, H., Sakmann, B., and Konnerth, A. (2011). Dendritic coding of multiple sensory inputs in single cortical neurons in vivo. *Proc. Natl. Acad. Sci. U.S.A.* 108, 15420–15425. doi: 10.1073/pnas.1112355108

Volgushev, M., Chauvette, S., Mukovski, M., and Timofeev, I. (2006). Precise long-range synchronization of activity and silence in neocortical neurons during slow-wave sleep. *J. Neurosci.* 26, 5665–5672. doi: 10.1523/JNEUROSCI.0279-06.2006

Waters, J. (2007). Back to basals: do basal dendrites link plateau potentials and up states? *J. Physiol.* 585:317. doi: 10.1113/jphysiol.2007.146977

Waters, J., and Helmchen, F. (2006). Background synaptic activity is sparse in neocortex. *J. Neurosci.* 26, 8267–8277. doi: 10.1523/JNEUROSCI.2152-06.2006

Wilson, C. J. (2008). Up and down states. *Scholarpedia J.* 3:1410. doi: 10.4249/scholarpedia.1410

Wilson, C. J., and Groves, P. M. (1981). Spontaneous firing patterns of identified spiny neurons in the rat neostriatum. *Brain Res.* 220, 67–80. doi: 10.1016/0006-8993(81)90211-0

Wilson, C. J., and Kawaguchi, Y. (1996). The origins of two-state spontaneous membrane potential fluctuations of neostriatal spiny neurons. *J. Neurosci.* 16, 2397–2410.

Wilson, M. A., and McNaughton, B. L. (1993). Dynamics of the hippocampal ensemble code for space. *Science* 261, 1055–1058. doi: 10.1126/science.8351520

Windels, F., Crane, J. W., and Sah, P. (2010). Inhibition dominates the early phase of up-states in the basolateral amygdala. *J. Neurophysiol.* 104, 3433–3438. doi: 10.1152/jn.00531.2010

Wolf, J. A., Moyer, J. T., Lazarewicz, M. T., Contreras, D., Benoit-Marand, M., O'Donnell, P., et al. (2005). NMDA/AMPA ratio impacts state transitions and entrainment to oscillations in a computational model of the nucleus accumbens medium spiny projection neuron. *J. Neurosci.* 25, 9080–9095. doi: 10.1523/JNEUROSCI.2220-05.2005

Yu, J., and Ferster, D. (2010). Membrane potential synchrony in primary visual cortex during sensory stimulation. *Neuron* 68, 1187–1201. doi: 10.1016/j.neuron.2010.11.027

Ziaei, M., Peira, N., and Persson, J. (2013). Brain systems underlying attentional control and emotional distraction during working memory encoding. *Neuroimage* 87, 276–286. doi: 10.1016/j.neuroimage.2013.10.048

Conflict of Interest Statement: The authors declare that the research was conducted in the absence of any commercial or financial relationships that could be construed as a potential conflict of interest.

Received: 17 June 2014; accepted: 01 September 2014; published online: 17 September 2014.

Citation: Oikonomou KD, Singh MB, Sterjanaj EV and Antic SD (2014) Spiny neurons of amygdala, striatum, and cortex use dendritic plateau potentials to detect network UP states. Front. Cell. Neurosci. ***8****:292. doi: 10.3389/fncel.2014.00292*

This article was submitted to the journal Frontiers in Cellular Neuroscience.

frontiers in
CELLULAR NEUROSCIENCE

REVIEW ARTICLE
published: 18 September 2014
doi: 10.3389/fncel.2014.00290

A synaptic mechanism for network synchrony

Simon T. Alford* and Michael H. Alpert

Department of Biological Sciences, University of Illinois at Chicago, Chicago, IL, USA

Edited by:
Sergey M. Korogod, National Academy of Sciences of Ukraine, Ukraine

Reviewed by:
Patrik Krieger, Ruhr University Bochum, Germany
Stefano Taverna, Italian Institute of Technology, Italy

****Correspondence:***
Simon T. Alford, Department of Biological Sciences, University of Illinois at Chicago, M/C 068, Rm 4285, 840 West Taylor Street, Chicago, IL 60607, USA
e-mail: sta@uic.edu

Within neural networks, synchronization of activity is dependent upon the synaptic connectivity of embedded microcircuits and the intrinsic membrane properties of their constituent neurons. Synaptic integration, dendritic Ca^{2+} signaling, and non-linear interactions are crucial cellular attributes that dictate single neuron computation, but their roles promoting synchrony and the generation of network oscillations are not well understood, especially within the context of a defined behavior. In this regard, the lamprey spinal central pattern generator (CPG) stands out as a well-characterized, conserved vertebrate model of a neural network (Smith et al., 2013a), which produces synchronized oscillations in which neural elements from the systems to cellular level that control rhythmic locomotion have been determined. We review the current evidence for the synaptic basis of oscillation generation with a particular emphasis on the linkage between synaptic communication and its cellular coupling to membrane processes that control oscillatory behavior of neurons within the locomotor network. We seek to relate dendritic function found in many vertebrate systems to the accessible lamprey central nervous system in which the relationship between neural network activity and behavior is well understood. This enables us to address how Ca^{2+} signaling in spinal neuron dendrites orchestrate oscillations that drive network behavior.

Keywords: lamprey, oscillation, SK2, $K_{Ca}2$, NMDA, locomotion, calcium, dendrites

INTRODUCTION

Orchestration of neuronal activity within networks is integral to correct execution of behavior. Synchronization between groups of neurons is an organizational feature of many neural networks found in the central nervous systems of invertebrates (Wehr and Laurent, 1996; Riffell et al., 2009) to vertebrates (Womelsdorf et al., 2014) alike, and between microcircuits. Large-scale synchrony between neurons is particularly evident in the spinal (Grillner, 2003; Goulding, 2009) and brainstem networks (Koshiya and Smith, 1999) controlling rhythmic movement, but are also common to hippocampal and neocortical networks (Buzsáki and Draguhn, 2004; Grillner et al., 2005; Yuste et al., 2005). Synchronously active microcircuits, like the neurons that comprise the lamprey spinal central pattern generator (CPG), are driven through the synaptic connectivity of excitatory and inhibitory neurons combined with intrinsic burst-terminating electrical properties (Wallén and Grillner, 1987; Buchanan, 1993). However, little is known about the electrical and integrative properties of the complex dendritic architecture of lamprey spinal neurons where synaptic- and voltage-dependent conductances shape potentials arriving at the soma. In contrast, the integrative properties of cortical pyramidal neuron dendrites and their synaptic inputs have been extensively characterized (Spruston, 2008), while less is known about how these intrinsic properties generate rhythmic network activity, and ultimately the behaviors they are thought to subserve. To understand how neural networks generate complex patterns of activity underlying behaviors, it will be necessary to understand both the specific patterns of connectivity between neurons and how individual neurons respond to the inputs that they receive. Thus, this review seeks to merge disparate fields of research—dendritic integration and spinal central pattern generation. In doing so, we hypothesize that the ionic mechanisms driven through two rhythm-generating conductances, namely the synaptic interaction between ensembles of NMDA receptors (NMDARs) and Ca^{2+}-dependent K^+ channels, may have general implications for the synchronization of spinal to cortical networks. Thus, to explore the idea that active dendritic properties are at the core of this behavior, we examine in detail the lamprey spinal network and draw from other areas of dendritic research to enhance our understanding of what occurs at the level of the dendritic synapse to generate behavior.

SUPRASPINAL NETWORKS IN THE BRAINSTEM INITIATE AND MAINTAIN LOCOMOTOR DRIVE

Vertebrate locomotion is initiated and maintained by evolutionarily conserved serial pathways originating in the forebrain (Ericsson et al., 2013; Grillner et al., 2013), projecting to the mesencephalic locomotor region (MLR; Dubuc et al., 2008) and then to command neurons of the reticulospinal (RS) system, which innervates the entire rostro-caudal extent of the spinal cord, including cervical and lumbar centers in mammals (Goulding, 2009), and all segmental levels in fish as well as lamprey (Buchanan et al., 1987). However, following their

activation by the brainstem, it is the circuits and neurons of the spinal CPG (Buchanan and Cohen, 1982) that create the complex synergy that rhythmically activates the locomotor musculature (Grillner et al., 2008). The structure of descending commands to spinal CPGs and the synaptic connectivity of the spinal network itself provides an opportunity to understand how dendritic activation within behaviorally relevant circuits underlies the astonishing complexity of vertebrate behavioral patterns. The circuitry of the lamprey CPG is well understood (Grillner et al., 2000, 2008) including the identities of the key neurons (Rovainen, 1974; Buchanan and Cohen, 1982), their neuronal targets, and neuropharmacology (Alford et al., 2003). However, in common with most neurons, these circuit components possess a complex dendritic morphology (**Figure 1**), yet we understand little of the spatiotemporal profile of dendritic activation within these neurons and the role that such patterns of activation might play in the physiological activity of the neurons during behavior. This lack of understanding is true for simple inputs, but particularly during goal-directed locomotion. This is partly because tracing the spatial distribution of physiological targets of neurons is challenging, but also because most studies of CPGs, whether in simple systems like the lamprey, or in more complex systems such as mammals, use isolated spinal cords and activate the networks pharmacologically (Sigvardt et al., 1985; Rossignol et al., 1998; Kyriakatos et al., 2011). This undoubtedly obscures the precise physiologically relevant spatiotemporal activation patterns of dendritic synapses that would otherwise drive these behaviors *in vivo*. In studies of spinal motor activity this has been largely overlooked perhaps due to the strong resemblance of electrophysiological output (i.e., fictive locomotion), or even actual movement, to observed locomoting animals. Despite this similarity, it is crucial to understand how physiological patterns of synaptic input and intrinsic membrane electrodynamics generate rhythmic behaviors.

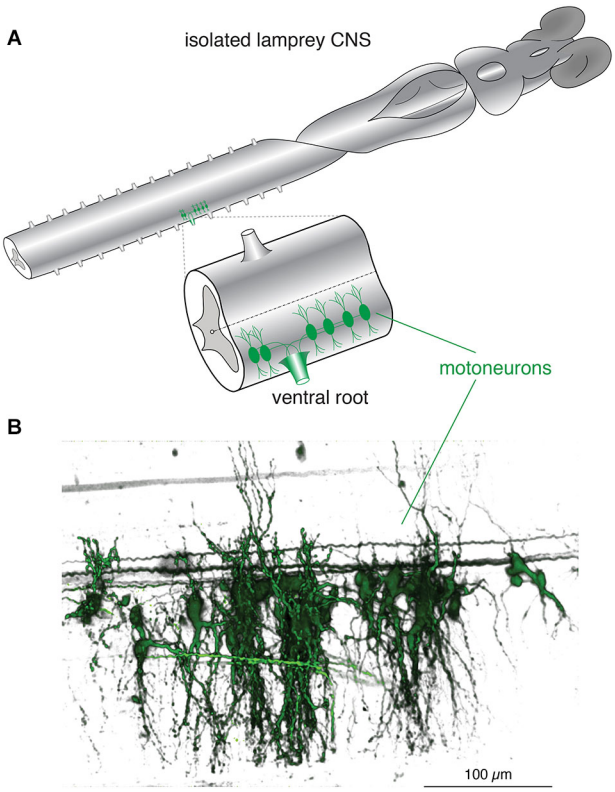

FIGURE 1 | Lamprey spinal motoneurons have a complex dendritic architecture. (A) Schematic representation of an isolated lamprey brain and spinal cord. Spinal motoneurons and their complete dendritic architecture can be retrogradely labeled through an intramuscular injection of a dextran-conjugated fluorescent dye. Labeling (green) is visible on the side and segment of injection through axons converging into ventral roots (VRs) and to their respective neurons. Expansion shows a single spinal segment with multiple motoneurons labeled as in **(B)**. **(B)** A 3D reconstruction of motoneurons labeled from one spinal ventral root to emphasize the complexity of their structure and dendritic trees. Neurons were labeled by injecting the muscle wall of an animal with 5 μL of 5 mM Oregon Green 488 BAPTA1 Dextran. After 24 h the animal was sacrificed and the spinal cord fixed and cleared. A confocal stack was imaged to generate the full extent of the motoneurons in one spinal segment (Viana di Prisco and Alford, 2004).

THE SYNAPTIC CONNECTIVITY OF THE SPINAL CPG NETWORK DRIVES RHYTHMIC NETWORK OSCILLATIONS

The very fluid, controlled nature of lamprey locomotion is produced after RS axons activate the local circuit neurons within the spinal ventral horn (**Figure 2**). Among these neurons, collectively referred to as ventral horn neurons (VHNs), the best characterized neurons responsible for pattern generation are excitatory interneurons (EINs) that provide ipsilateral, glutamatergic excitation (Buchanan and Grillner, 1987; Buchanan et al., 1989), while crossed caudally projecting interneurons (CCINs) provide contralateral, glycinergic inhibition (Grillner and Wallén, 1980; Alford and Williams, 1989). Motor neurons are the final common output neuron of each segment, which bundle into ventral roots (VRs) as they leave the spinal cord, before synapsing directly onto myotomal cells of the trunk musculature (Buchanan and Cohen, 1982). The precise, synaptic connectivity of the VHNs within and between individual segments serves to ipsilaterally excite (i.e., EINs), while simultaneously delivering contralateral inhibition (i.e., CCINs; Buchanan and Grillner, 1987). This reciprocally inhibited network ensures that within each segment, when one side of the trunk musculature contracts, the contralateral side is inhibited. Lateral interneurons, which project ipsilaterally to inhibit CCINs, facilitate the relief of reciprocal inhibition (Buchanan, 1982). However, the importance of lateral interneurons in maintaining network rhythmicity has been less emphasized because alternating, rhythmic bursting can persist in their absence as demonstrated by computer simulation (Wallén et al., 1992).

Work in lamprey (Grillner et al., 1981; Brodin et al., 1985, 1988; Brodin and Grillner, 1985; Buchanan and Grillner, 1987), *Xenopus* tadpoles (Dale and Roberts, 1984; Roberts and Alford, 1986), rats (Kudo and Yamada, 1987), and cats (Douglas et al., 1993) demonstrates that spinal glutamate receptor-mediated transmission activates and maintains locomotion. These data are supported by recordings of excitatory postsynaptic potentials (EPSPs) onto motoneurons and premotor interneurons

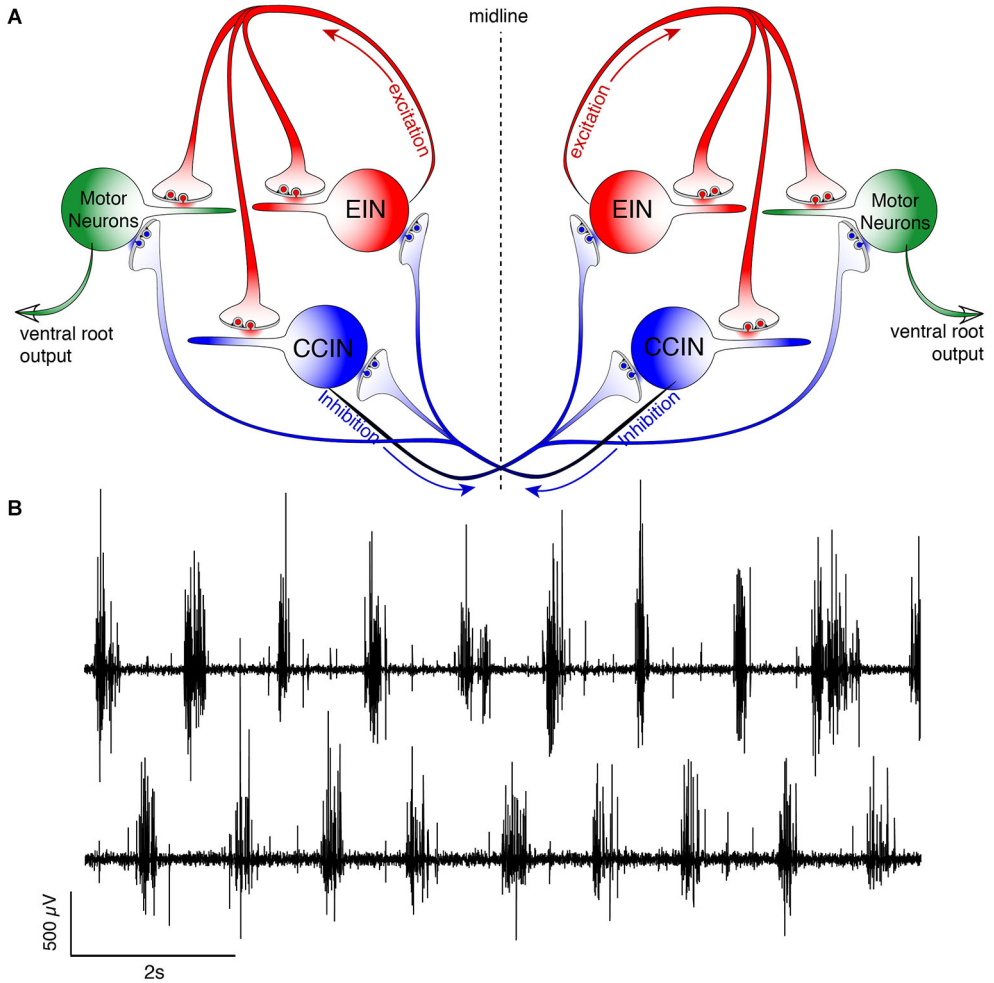

FIGURE 2 | Schematic representation of the lamprey spinal central pattern generator. (A) Spinal CPG neurons receive both ipsilateral glutamatergic (red) input from excitatory interneurons (EINs, red) and contralaterally projecting glycinergic inhibition (blue) from reciprocally inhibiting, crossed glycinergic interneurons (CCINs, blue). Output of the CPG occurs from motoneurons (green), which directly synapse onto myotomal cells of the trunk musculature to cause muscle contraction producing rhythmic locomotion. **(B)** Output pattern recorded using glass suction electrodes from paired, contralateral (top vs. bottom traces) VRs showing alternating bursting of the spinal network during rhythmic locomotion. The reciprocally connected network described in **(A)** prevents excitation of the contralateral spinal cord when the ipsilateral side is bursting for each cycle (burst-to-burst), leading each side of the spinal cord to be precisely 180° out-of-phase from the other (Alford et al., 2003).

(Dale and Roberts, 1985; Brodin et al., 1988; Noga et al., 2003) and pharmacological manipulation of the resultant behaviors (Brodin and Grillner, 1985; Dale and Roberts, 1985; Cazalets et al., 1992; Chau et al., 2002; Rybak et al., 2006). This neurotransmission both directly excites neurons of the CPG, and also activates complex non-linear membrane interactions, or oscillations, in these neurons mediated by NMDAR voltage-dependency and Ca^{2+} permeability coupled to the activation of Ca^{2+}-dependent currents. The cellular processes underlying such oscillations are believed to be central to the coordination of locomotor behavior. In lampreys the identity of the descending glutamatergic RS command neurons is well-defined (Dubuc et al., 2008) and similarly spinal neurons that release glutamate locally within the spinal ventral horn (i.e., EINs) have been identified (Buchanan et al., 1989; Buchanan, 1993) as has their network role (Wallén et al., 1992).

One prominent feature of the spinal network is that it transforms unpatterned, exogenous glutamatergic input into a patterned, rhythmic output. The details of synaptic connectivity responsible for this phenomenon have been substantially explored in the lamprey (Wallén and Grillner, 1987; Grillner et al., 2001; Grillner, 2006) and the *Xenopus* embryo (Dale and Roberts, 1984, 1985). More recently, work in higher vertebrates (Masino et al., 2012) has emphasized how well conserved this network motif is throughout the vertebrate subphylum including lampreys, fishes, amphibians, chelonids and mammals (Dale and Roberts, 1984; Sigvardt et al., 1985; Kudo and Yamada, 1987; Hernandez et al., 1991; Guertin and Hounsgaard, 1998; Gabriel et al., 2009; Masino et al., 2012). After complete

spinal transection (Cohen and Wallén, 1980; Brodin et al., 1985), the lamprey swimming network can still generate the electrophysiological correlates of swimming. While recording output from pairs of contralateral VRs using glass suction electrodes, excitatory amino acid (EAA) receptor agonists, such as kainate, *D*-glutamate, or *N*-methyl-*D*-aspartic acid (NMDA; Brodin et al., 1985; Brodin and Grillner, 1985; Wallén and Grillner, 1987), bath-applied to an isolated spinal cord (devoid of muscle or any other surrounding tissue) generates antiphasic bursts of activity across the spinal midline—the phase relationship across sides of the spinal cord is enforced by glycinergic inhibition (Cohen and Wallén, 1980; Alford and Williams, 1989)—and the same rostro-caudal phase lag as seen in intact behavior (Wallén and Williams, 1984). This network behavior, termed "fictive locomotion", refers to the electrical output of the spinal CPG. Thus, the network acts as a CPG, a term that refers collectively to centrally located, local circuit spinal neurons that provide precise rhythmic output from spinal motoneurons. The spinal CPG operates in the absence of both sensory feedback from the spinal dorsal roots or descending networks and is found in all vertebrates (Kahn and Roberts, 1978; Forssberg et al., 1980; Roberts et al., 1981; Sholomenko and Steeves, 1987; Delvolvé et al., 1997; Field and Stein, 1997; Masino and Fetcho, 2005). Thus, the ability to generate rhythmic output via network oscillations is inherent to the spinal network itself and does not require supraspinal control.

SINGLE NEURONS ARE INTRINSICALLY RHYTHMIC

The study of spinal neurons offers a unique insight into how properties of neural networks emerge from membrane activity at the cellular level and provides a straightforward behavioral context—locomotion—in which to place this activity. EAA agonists, like NMDA, cause the membrane potential (V_m) of individual VHNs in isolated spinal cords to undergo repetitive oscillations that are in-phase with the ipsilateral VR of the corresponding hemisegment (Sigvardt et al., 1985; Wallén and Grillner, 1987). During the depolarized phase, the cells can fire multiple action potentials (APs) before the cell is repolarized. This finding demonstrates how electrical properties of single cells within a network scale to direct the behavior of the network at large. Most VHNs oscillate in NMDA driven by phase-appropriate synaptic excitation from EINs and subsequent hyperpolarization from CCINs (Buchanan and Cohen, 1982). However, when tetrodotoxin (TTX) is applied, spiking is abolished, while the underlying V_m oscillation persists (Wallén and Grillner, 1987). Since TTX pharmacologically isolates the recorded neuron by preventing synaptic communication within the network, the cell then oscillates with tonic exposure to NMDA. This phenomenon, termed NMDA-dependent, TTX-resistant oscillations (NMDA-TTX oscillations), is seen in most lamprey VHNs. This demonstrates that spinal neurons show intrinsic membrane properties that are capable of hyperpolarizing the cell during constant depolarizing challenge from an agonist. The net effect is to produce V_m oscillations. Removal of Mg^{2+} from the perfusing Ringer's solution abolishes the oscillation and causes the neurons to remain at depolarized potentials because Mg^{2+} confers voltage-sensitivity to the NMDAR (Wallén and Grillner, 1987). Thus, the intrinsic membrane property of spinal neurons that causes oscillations is subject to the voltage-dependency of Mg^{2+} block of the NMDAR.

More generally within the nervous system, NMDARs have been well characterized as non-specific cation channels permeable to Na^+, K^+, and Ca^{2+} (MacDermott et al., 1986; Ascher and Nowak, 1988). More recently, NMDAR-dependent Ca^{2+} entry has been demonstrated to be integral to dendritic computation (Branco et al., 2010) through regenerative "NMDA spikes" in pyramidal neurons (Schiller and Schiller, 2001; Larkum et al., 2009) with roles spanning from the induction of synaptic plasticity (Alford et al., 1993) to behavior (Smith et al., 2013b). In lamprey VHNs, removal of Ca^{2+} from the ringer and replacement with Ba^{2+} (an equivalent divalent cation which can also permeate Ca^{2+} ionophores) during NMDA-TTX oscillations causes the cell to become similarly trapped at a depolarized V_m. Thus, Ca^{2+} is necessary to hyperpolarize the cell from the depolarized state. Ca^{2+} activates myriad Ca^{2+}-dependent proteins. In particular, VHNs contain Ca^{2+}-dependent K^+ channels (El Manira et al., 1994; Wall and Dale, 1995; Han et al., 2007; Li and Bennett, 2007), which upon binding Ca^{2+}, rapidly open a K^+ channel that hyperpolarizes the cell. This "excitation-inhibition coupling" is a mechanism that effectively allows the cell to "turn off" autonomously following activation.

The Ca^{2+}-dependent K^+ channel of the $K_{Ca}2$ subtype (formerly SK2 (Wei et al., 2005)) participates in two distinct processes in lamprey VHNs both of which are integral to the behavioral locomotor output of the spinal cord. Its most well-described role follows the AP when depolarization activates N- and P/Q-type (Wikström and El Manira, 1998) voltage-gated Ca^{2+} channels (VGCCs) and the entering Ca^{2+} activates $K_{Ca}2$ channels to cause an afterhyperpolarization (AHP; **Figure 3;** Hill et al., 1992; Meer and Buchanan, 1992). The AHP can be divided into fast, medium and slow subcomponents, of which the medium AHP (mAHP) is mediated by $K_{Ca}2$ channels (Bond et al., 2004). Due to slow kinetics (decay time constant of ∼200 ms), the mAHP mediates spike frequency adaptation, the reduction in spike frequency from repeated spiking, by raising the relative threshold for subsequent AP generation due to an increase in K^+ conductance. Blockade of $K_{Ca}2$ channels with the selective antagonist, apamin, increases spike frequency from intracellular current pulses (Meer and Buchanan, 1992; Díaz-Ríos et al., 2007; Jones and Stuart, 2013). $K_{Ca}2$ channels are extremely important for regulating neuronal firing, conserved among different species and cell types (Meer and Buchanan, 1992; Sah and Bekkers, 1996; Marrion and Tavalin, 1998; Wikström and El Manira, 1998; Faber and Sah, 2002; Bloodgood and Sabatini, 2007; Jones and Stuart, 2013).

The second role for $K_{Ca}2$ lies in the plateau termination and membrane repolarization during NMDA-TTX oscillations (**Figure 3**). The ionic mechanism driving V_m oscillations is well-characterized and is hypothesized to proceed as: (1) NMDAR activation depolarizes VHNs; (2) increasing NMDAR conductance by ejecting Mg^{2+} from the pore; (3) causing further depolarization and Ca^{2+} entry via the NMDAR as the V_m plateaus; (4) which activates $K_{Ca}2$ channels to hyperpolarize the cell; and (5) ending the depolarized plateau to repolarize the cell where it can repeat the cycle (Wallén and Grillner,

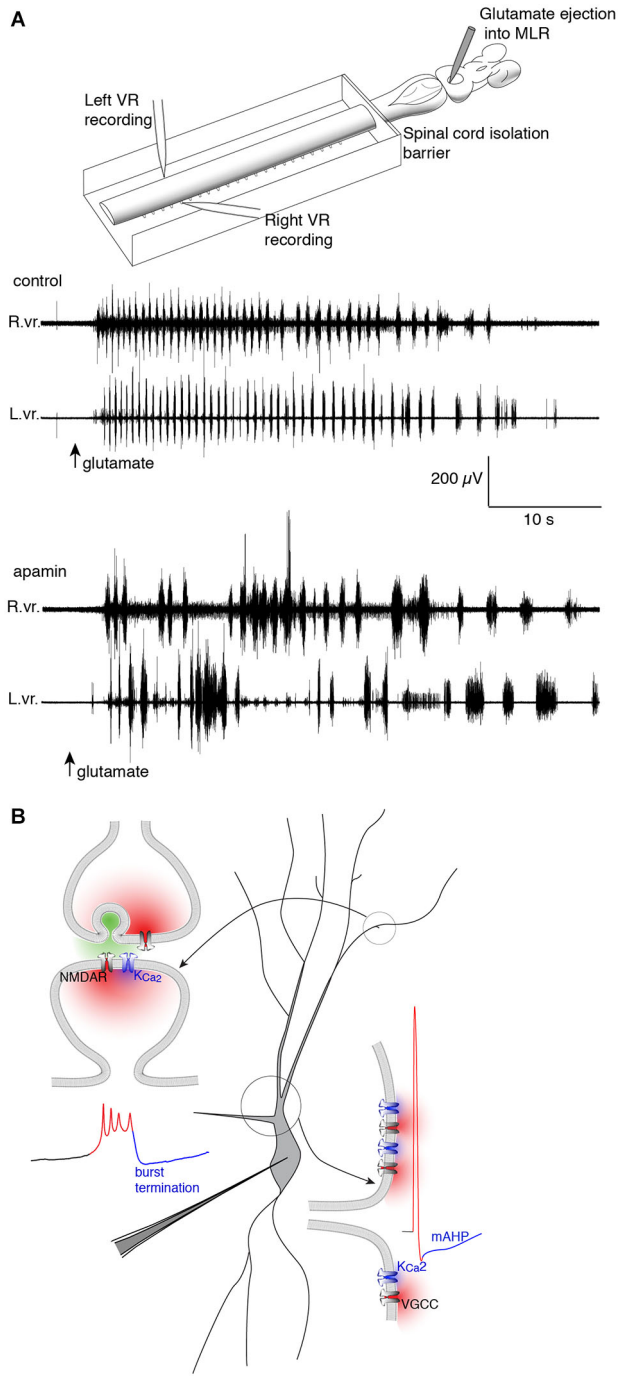

FIGURE 3 | Repolarizing $K_{Ca}2$ channels are spatially segregated in lamprey spinal VHNs according to their function and mechanism of activation. (A) Top: An isolated lamprey CNS can be used to study the brain and spinal circuits controlling locomotion. Pressure-ejection of L-glutamate into the lamprey mesencephalic locomotor region (MLR) induces short episodes of fictive locomotion, the electrophysiological correlate of locomotion. Using a dual-pool recording chamber, pharmacological agents can be selectively applied to the spinal cord, without interfering with descending commands originating in the brainstem that initiate and maintain locomotion. Locomotor bursts are recorded directly from left and right VRs. Bottom: A long locomotor episode with regular, alternating bursts (control) follows after a puff of glutamate into the MLR (arrow, glutamate). Blockade of $K_{Ca}2$ channels with the selective antagonist, apamin, decreases the burst frequency and disrupts the alternating locomotor rhythm. This demonstrates the necessity of $K_{Ca}2$ channels for correct alternation and regularity of the locomotor rhythm (Nanou et al., 2013). **(B)** The effect of $K_{Ca}2$ channel blockade on locomotion can be explained by the role the channel plays at the cellular level. Within VHNs, $K_{Ca}2$ currents may be evoked either at synapses (top left) whereby synaptic release of glutamate activates NMDAR-mediated Ca^{2+} entry and thereby closely located $K_{Ca}2$ channels. It is this $K_{Ca}2$-mediated current that is critical for the termination of NMDA-TTX oscillations (blue portion of trace) shown below recorded from somatic microelectrode recordings. $K_{Ca}2$-mediated currents are also responsible for the mAHP seen following action potential firing shown at bottom left. However, this current is activated following Ca^{2+} entry from VGCCs.

1987). Selective blockade of $K_{Ca}2$ channels with apamin (El Manira et al., 1994) or UCL 1684 (Alpert and Alford, 2013) prolongs the oscillation, and can even abolish the oscillation completely. The cell becomes trapped in a depolarized state, similar to extracellular Ca^{2+} removal, the substitution of Ca^{2+} for Ba^{2+}, or non-specific blockade of K^+ channels (Grillner and Wallén, 1985; Grillner et al., 2001). Thus, $K_{Ca}2$ channels are necessary for rhythmogenesis (**Figure 3**) in lamprey VHNs by supplying a cell-autonomous repolarization, or "off signal", without the need of network inhibition (Nanou et al., 2013).

DENDRITIC Ca^{2+} SIGNALING IS DYNAMIC AND DETERMINED BY CELLULAR AND MICROCIRCUIT PROPERTIES

$K_{Ca}2$ channels within a single neuron have more than one distinct computational role. Two have been identified in lamprey VHNs, both subject to intracellular Ca^{2+} dynamics. Such a functional sub-specialization may be explained both by distinct spatial locations of channel expression and the adequate spatial and functional coupling to distinct sources of Ca^{2+} contributing to $K_{Ca}2$ activation (**Figure 3**). Indeed, N- and P/Q-type (Wikström and El Manira, 1998) VGCCs are activated during the AP in lamprey, triggering Ca^{2+} entry that activates $K_{Ca}2$ channels underlying the mAHP. However, the mAHP activated by somatic current injection is unaffected by NMDA application (Hill et al., 1989). This distinct separation between mAHP activation and NMDA-TTX oscillation repolarization can be explained by NMDAR-generated Ca^{2+} entry occurring in spatially distinct cellular sub-regions from VGCC-generated Ca^{2+} entry during the AP. Across different species and neuron types, the precise subtypes of VGCCs can differ, but to mediate the mAHP, $K_{Ca}2$ channels must be sufficiently close to VGCCs to be activated by their Ca^{2+} permeation. Similarly, $K_{Ca}2$ channels mediating repolarization during NMDA-TTX oscillations should be coupled to a distinct Ca^{2+} source, or a Ca^{2+} source in a distinct subcellular location. The two likely candidates for the latter are NMDARs and VGCCs (Wallén and Grillner, 1987)—located separately from those responsible for the mAHP (Hill et al., 1989)—while Ca^{2+} released from internal stores might also contribute. NMDAR activation is necessary to initiate oscillations, but as they lead to membrane depolarization, this may subsequently activate VGCCs. However, release from

internal stores likely contributes little because their depletion has no effect on NMDA-induced swimming (Krieger et al., 2000)—a behavior to which NMDAR-dependent intrinsic oscillations contribute. The subcellular location of $K_{Ca}2$ channels responsible for the repolarization may also be critical because physiological NMDAR activation requires the presynaptic release of glutamate, which occurs only at synapses. Determining the route of Ca^{2+} entry for repolarization of the oscillation is important for understanding how distinct Ca^{2+} domains and their coupling to $K_{Ca}2$ channels impacts computation both within individual neurons and between synaptically connected neurons.

The spatial and temporal patterning over which dendritic Ca^{2+} signaling occurs in spinal motor system VHNs during locomotion in lamprey (or in other vertebrate systems) is unknown. Do many dendrites receive synchronous input from their various synaptic partners? Does input occur in discrete spatial locations? The location and timing of synaptic input is crucial for the transmission of potentials arriving at the soma, which will greatly influence neuronal output (Larkum et al., 1999; Stuart and Häusser, 2001; Jarsky et al., 2005). Indeed, dendritic mechanisms that are location-dependent and rely on clustered NMDAR-dependent input generate plateau potentials and can change the mode of cell firing (Major et al., 2008; Augustinaite et al., 2014; Grienberger et al., 2014). Elucidating this pattern within lamprey spinal neurons will inform how the location and timing of Ca^{2+} entry leads to $K_{Ca}2$ channel activation, and furthermore, how synaptic activity distributed across a dendritic tree is integrated to produce cell rhythmicity. This, in turn, will facilitate our understanding of how intrinsic membrane properties combined with synaptic input causes synchronization between neurons of the CPG. Neuronal Ca^{2+} signaling can have distinct spatial components, easily identifiable using Ca^{2+} imaging. APs will lead to Ca^{2+} entry wherever VGCCs are driven above threshold, and can cause many regions of a cell (e.g., soma and proximal dendrites) to show synchronized increases in intracellular Ca^{2+} ($Ca^{2+}{}_i$). In contrast, local Ca^{2+} signaling domains (i.e., micro- and nano-domains) in dendrites can occur following neurotransmitter receptor activation (e.g., NMDAR), but also from VGCCs following depolarization from local synaptic potentials (Augustine et al., 2003). Synaptic signals are remarkably localized, confined to individual dendritic spines or discrete areas in dendritic shafts. For this reason, Ca^{2+} imaging can directly identify active synapses. Each type of Ca^{2+} signaling domain may be considered to be a distinct processing unit within a neuron because Ca^{2+} signals can regulate local Ca^{2+}-dependent processes precisely where free Ca^{2+} levels transiently escape local buffering. However, Ca^{2+} signals exceeding this local threshold are transient—Ca^{2+} is rapidly buffered by Ca^{2+}-binding proteins, and then extruded via membrane pumps, or sequestered in intracellular stores (Augustine et al., 2003; Berridge, 2006). This places temporal and spatial restrictions on diffusion of Ca^{2+} within neurons and is an important consideration when assessing the degree of localization. Dendritic morphology, like the presence of spines (~1 μm in length), is a large determinant for the extent of spread of Ca^{2+} because diffusion is restricted at the spine neck (Nimchinsky et al., 2002). Lamprey spinal neuron dendrites lack spines, but still posses fine compartments along dendritic shafts (~10 μm, see **Figure 1;** Viana di Prisco and Alford, 2004; Alpert and Alford, 2013) that may theoretically serve a similar purpose—the local restriction of the flow of ions and intracellular messengers (Svoboda et al., 1996). Thus, morphology and the intrinsic properties of the dendritic membrane impacts Ca^{2+} dynamics and the integration of electrical and chemical signals.

The functional distinction between global and local Ca^{2+} signals and their associated topography is integral to single neuron computation necessary to generate rhythmic activity. The synaptic localization of Ca^{2+} signals may represent the encoding of distinct presynaptic information. Global, synchronized Ca^{2+} signals can be generated by back-propagating action potential (bAP)-driven VGCC activation in dendrites (Schiller et al., 1997; Stuart et al., 1997; Svoboda et al., 1997). When $Ca^{2+}{}_i$ is elevated during these events, the number of parallel computations being performed by the dendritic arbor is effectively reduced. In contrast, local and spatially distributed NMDAR-dependent synaptic Ca^{2+} signals reflect multiple discrete, simultaneous computations (Chen et al., 2011). Each synapse can thus be understood to be its own computational unit, capable of being selectively tuned to support distinct information arriving within a network.

Multiple, distinct routes can lead to Ca^{2+} entry. In behaving neurons within some networks, these mechanisms may work in concert, leading to nonlinear interactions between ion channels and Ca^{2+} sources when occurring simultaneously. For instance, following presynaptic release of glutamate, AMPA receptors (AMPARs), NMDARs and metabotropic glutamate receptors (mGluRs) may be activated in the postsynaptic compartment. AMPARs are responsible for fast depolarization, and can locally activate nearby VGCCs to cause Ca^{2+} entry. Local depolarization, or depolarization induced from bAPs can alleviate Mg^{2+} block of the NMDAR, facilitating Ca^{2+} influx during concurrent and subsequent release of glutamate at that synapse (Yuste and Denk, 1995; Nevian and Sakmann, 2004; Bloodgood and Sabatini, 2007). During bAPs, layer 5 pyramidal neurons have been shown to require tight spatial coupling between Ca^{2+} entry through R-type channels and $K_{Ca}2$ channels in proximal dendrites and spines (Jones and Stuart, 2013). Group I mGluR activation can lead to the release of Ca^{2+} from internal stores (Frenguelli et al., 1993; Kettunen et al., 2002; Larkum et al., 2003; Topolnik et al., 2009; Plotkin et al., 2013). Release from internal stores has been shown to activate Ca^{2+}-dependent K^+ channels in many neurons and species (Kawai and Watanabe, 1989; Akita and Kuba, 2000; Yamada et al., 2004; Faber, 2010; Nakamura and Yokotani, 2010). It is unknown if such combinatory mechanisms are present in lamprey spinal neurons, but lamprey neurons do possess all the necessary components. Indeed, specific agonists and antagonists acting on discrete components have well-described cellular and network effects (Alford et al., 2003). Any modulation of Ca^{2+} entry, either increasing or decreasing, within close proximity to $K_{Ca}2$ channels, could impact subsequent channel activation and particular effects on the locomotor behavior. For example, an enhancement of Ca^{2+} could lead to early burst termination—an effect that, if it were to occur within many neurons simultaneously, would scale to the behavioral level to terminate muscle contraction earlier within the locomotor cycle. Upon repeated enhancements in Ca^{2+}, during rhythmic activity, this could

facilitate a fast swimming rhythm. Defining their roles while acting in concert is necessary to delineate how Ca^{2+} entry and $K_{Ca}2$ activations drives oscillation generation.

The location of Ca^{2+} entry and the distance to its secondary effectors determines the efficacy with which Ca^{2+} will reach its target (Marrion and Tavalin, 1998). If the site of Ca^{2+} entry is located far from $K_{Ca}2$ channels, then the probability of Ca^{2+} binding to a $K_{Ca}2$ channel is diminished compared to its binding to other endogenous buffers that are located more proximally or are cytosolic and diffusible. Thus, a larger Ca^{2+} signal will be necessary to outcompete endogenous buffers. Conversely, if $K_{Ca}2$ channels are located close to the site of Ca^{2+} entry, then depolarization will be quickly and locally counteracted by K^+ activation. For $K_{Ca}2$ channels to generate the mAHP, they must be sufficiently close to the site of Ca^{2+} entry generated by AP-driven VGCC activation. This functional coupling has been demonstrated in numerous species and cell types (Sah and Bekkers, 1996; Marrion and Tavalin, 1998; Wikström and El Manira, 1998; Faber and Sah, 2002; Bloodgood and Sabatini, 2007; Jones and Stuart, 2013). At present, the distance between the site of Ca^{2+} entry and $K_{Ca}2$ channels can only be estimated based on differences between BAPTA and EGTA-mediated occlusion of $K_{Ca}2$ activation in lamprey spinal VHNs. The range has been estimated to be between 20 and >200 nm in multiple CNS neuron types depending on the target's affinity for Ca^{2+} (Fakler and Adelman, 2008). A recent measurement has suggested that $K_{Ca}2$ channels activated following APs exhibit weak coupling to VGCCs, as they are occluded by EGTA, the slow Ca^{2+} buffer ($K_{forward}$ = 1.5 × 10^6 $M^{-1}s^{-1}$) (Roberts, 1993), placing the separation at greater than ∼100 nm in neocortical pyramidal neurons (Jones and Stuart, 2013). Occlusion of $K_{Ca}2$ channel activation from NMDAR-dependent Ca^{2+} entry using BAPTA, the fast Ca^{2+} buffer ($K_{forward}$ = 6 × 10^8 $M^{-1}s^{-1}$) (Roberts, 1993), demonstrates a narrow range of 20–50 nm (Ngo-Anh et al., 2005), with experiments in lamprey suggesting similar degree of coupling (Alpert and Alford, 2013; Nanou et al., 2013).

For $K_{Ca}2$ channels to repolarize NMDA-TTX V_m oscillations, they must be activated by NMDAR-dependent Ca^{2+} entry. The subcellular expression of ion channels, including $K_{Ca}2$ channels, is unknown in lamprey, while some spatial information has been detailed for mammalian hippocampal neurons. $K_{Ca}2$ channel immunoreactivity demonstrates channel expression on dendritic spines in CA1 pyramidal neurons (Sailer et al., 2004; Ballesteros-Merino et al., 2012) in addition to shafts and soma in cultured mice hippocampal neurons (Ngo-Anh et al., 2005). Recently, however, using single-molecule atomic force microscopy with unprecedented spatial resolution (<10 nm (Müller et al., 2009)), $K_{Ca}2$ channels were shown to be in high concentration in the dendrites relative to the soma of live, cultured hippocampal neurons (Maciaszek et al., 2012). Functional evidence for complexes of NMDARs and $K_{Ca}2$ channels has been demonstrated in many species and cell types. NMDAR-mediated field potentials are potentiated by apamin in CA1 hippocampal pyramidal neurons (Gu et al., 2008). Direct NMDA application leads to an inward current followed by an apamin-dependent outward current (Shah and Haylett, 2002; Nanou et al., 2013). Apamin potentiates both synaptically evoked NMDAR EPSPs on CA1 dendrites, while also potentiating apical spine Ca^{2+} transients (Ngo-Anh et al., 2005). However, it was later demonstrated using 2-photon glutamate uncaging that Ca^{2+} entry via R-type VGCCs is necessary and directly coupled to $K_{Ca}2$ channels at these spine synapses, whereas NMDAR-dependent Ca^{2+} is insufficient to activate $K_{Ca}2$ channels (Bloodgood and Sabatini, 2007). This discrepancy was recently reconciled with experiments demonstrating that $K_v4.2$-containing channels and NMDARs are differentially coupled to R-type VGCCs and NMDARs, respectively (Wang et al., 2014b). Furthermore, $K_{Ca}2$ channel activation by NMDAR-induced spine Ca^{2+} transients is also occluded by BAPTA, but not by EGTA, indicating a very close physical coupling of the route of Ca^{2+} entry and the $K_{Ca}2$ channel (Ngo-Anh et al., 2005)—a similar role for NMDARs and $K_{Ca}2$ channel is also demonstrated in the lateral amygdala (Faber et al., 2005) and in layer 5 neocortical pyramidal neurons (Faber, 2010). Furthermore, overexpression of $K_{Ca}2$ channels depresses synaptically evoked glutamatergic EPSPs (Hammond et al., 2006). Due to the role of NMDAR-dependent Ca^{2+} entry in synaptic plasticity, blockade of $K_{Ca}2$ channels facilitates the induction of LTP (Stackman et al., 2002) because this, in turn, facilitates Ca^{2+} entry through NMDARs, presumably by augmenting depolarization. Similarly, downregulation of $K_{Ca}2$ channels is necessary for amplification of dendritic responses in a compartment- (Ohtsuki et al., 2012) or synapse-specific (Lin et al., 2008) manner, partially explaining the subsequent potentiation of current.

Thus, the very precise subcellular targeting of $K_{Ca}2$ channels to ion channels responsible for Ca^{2+} transients (demonstrated by sensitivity to rapid Ca^{2+} binding by BAPTA) will profoundly impact cell firing rates, dendritic integration, and processing both in real-time during individual cycles of locomotor activity, but also in the long-term. The molecular complexing of Ca^{2+} sources to secondary effector proteins, like $K_{Ca}2$ in lamprey, will consequently impact spike-timing through activation of the mAHP (Buchanan and Grillner, 1987; Wallén and Grillner, 1987; Alford and Williams, 1989; Wallén et al., 1989; Hill et al., 1992; Hochman et al., 1994; Wall and Dale, 1995; Buchanan, 2001; Harris-Warrick, 2002; Wang, 2010) in addition to burst termination (El Manira et al., 1994; Alpert and Alford, 2013; Nanou et al., 2013) during NMDAR-dependent rhythmic activity. These intrinsic membrane properties have direct consequences on spinal neuron output, and hence the locomotor pattern generation of the spinal network.

EVIDENCE FOR A DENDRITIC MECHANISM OF INTRINSIC OSCILLATIONS IN THE CNS

In lamprey VHNs filled with a Ca^{2+}-sensitive dye, $Ca^{2+}{}_i$ oscillates in-phase with VR bursts and V_m oscillations, varying with different NMDA-induced swimming speeds (Bacskai et al., 1995; Viana di Prisco and Alford, 2004). In contrast, during activity that was subthreshold to action potential firing, the soma showed no Ca^{2+} fluctuations, while the dendritic fluorescence oscillated in-phase with the V_m, with the largest oscillations in $Ca^{2+}{}_i$ found in the distal dendrites. When spiking, the somatic Ca^{2+} then showed spike-dependent activity, which is in-phase

with V_m, oscillations because spiking occurs at the depolarized phase of activity. However, despite spikes also elevating dendritic Ca^{2+} signals, the largest increases in fluorescence occurred in the soma, likely reflecting somatically localized VGCC activation (Viana di Prisco and Alford, 2004). The elevated dendritic signals could be due to dendritic VGCC activation, enhanced NMDAR conductance due to local depolarization from bAPs, or both. The phase relationships of the Ca^{2+} oscillations in dendrites relative to V_m oscillations suggest that these Ca^{2+} signals are responsible for $K_{Ca}2$ activation, and hence repolarization of the membrane. This result along with experiments discussed earlier (Grillner and Wallén, 1985; Wallén and Grillner, 1987) provide substantial evidence that NMDAR-dependent Ca^{2+} entry underlies the repolarization of V_m oscillations.

Results from experiments in which the spinal CPG is activated by application of exogenous NMDA also imply that rhythmic V_m oscillations are driven by phasic Ca^{2+} oscillations that are synchronized across large regions, if not all, of the dendritic tree (**Figure 4**). However, during bath-application of NMDA, both synaptic and extrasynaptic NMDARs are activated and thus the dendritic Ca^{2+} signals are likely to be much less spatially and temporally constrained than signals driven during physiologically evoked locomotion. This forces the concerted activation of all NMDARs when the dendritic membrane is depolarized, which would consequently synchronize all parts of the neuron. Thus, it is unclear if during NMDA-evoked locomotion whether network synchrony is driven by synchronized presynaptic activity caused directly by bath-applied NMDA, or if rhythmicity emerges from more physiologically derived synaptic integration of distributed input and is then transformed into well-defined V_m oscillations. Similarly, the spatiotemporal profile of dendritic activation and Ca^{2+} signaling underlying membrane potential oscillations during locomotion remains unknown. This profile will, however, be particularly important for understanding how membrane properties drive the activity of the network.

Synchronized oscillations are widespread in the CNS. While critical for the generation of motor rhythms, they are key components of many neural systems. In the neocortex and hippocampus, oscillations at the cellular level are correlated with synchrony at the network level (Contreras and Steriade, 1995) and are thought to underlie cognitive processes such as working memory (Llinás, 1988), spatial navigation, and memory encoding (Buzsáki and Moser, 2013). Both theoretical approaches and experimental evidence suggest that the cellular basis for working memory relies upon persistent firing of networks generated by recurrent synaptic excitation of NMDARs due to its slow kinetics and voltage-dependency (Lisman et al., 1998; Wang, 2001) conferring bistability (Durstewitz et al., 2000). NMDA-TTX oscillations are also found in midbrain dopamine neurons (Johnson et al., 1992; Deister et al., 2009) cat neocortical pyramidal neurons (Flatman et al., 1986), rat inferior olivary neurons (Placantonakis and Welsh, 2001), *Xenopus* RS neurons (Li et al., 2010), guineau pig and rat trigeminal motor neurons (Kim and Chandler, 1995; Hsiao et al., 2002), and rat and cat thalamocortical neurons (Leresche et al., 1991), demonstrating a similar intrinsic oscillatory mechanism to lamprey spinal neurons.

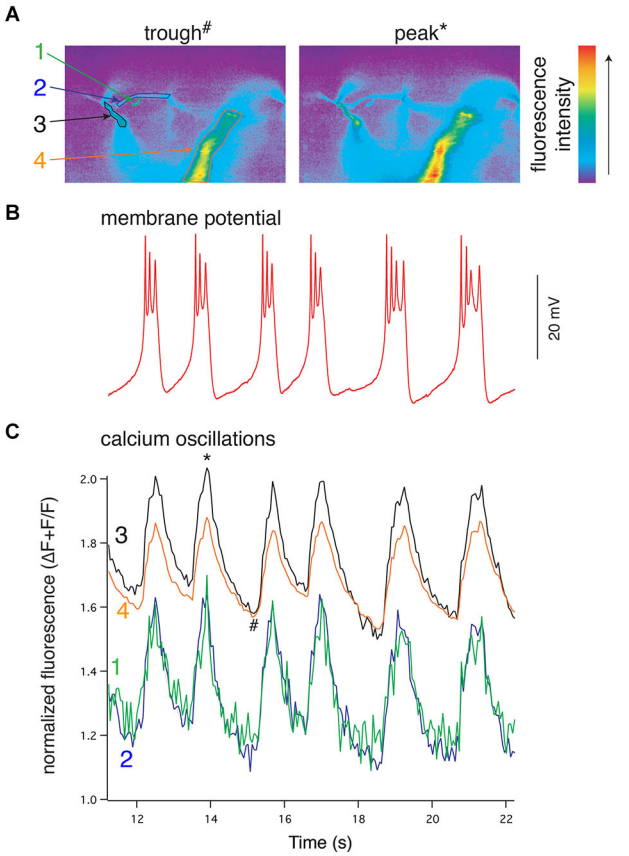

FIGURE 4 | NMDA-evoked, TTX-resistant oscillations in lamprey VHNs show simultaneous oscillations in Ca^{2+} throughout the dendritic tree. **(A)** VHN neurons were labeled with the Ca^{2+}-sensitive dye, Oregon Green 488 BAPTA1, by pressure injection from a recording microelectrode and recorded during oscillations evoked by application of NMDA (100 μM) in TTX (1 μM). Pseudocolored, raw images are shown from the trough of the hyperpolarization (left, denoted by # in **(C)**) and the peak of depolarization (right, denoted by * in **(C)**). Colored numbers and arrows point to discrete regions of interest whose fluorescence measurements are shown in **(C)**. Fluorescence intensity scale shown to the right. **(B)** Current clamp recording of the membrane potential oscillations. **(C)** Simultaneous to the membrane potential oscillations in **(B)**, Ca^{2+} recorded using the fluorescent dye Oregon Green 488 BAPTA1 shows transient increases in concentration in the dendrites. In the proximal dendrites, the oscillations are above a higher baseline Ca^{2+} evoked by NMDA application than that recorded in the distal dendrites, however, all recorded regions of the dendrites exhibit these Ca^{2+} oscillations. All Ca^{2+} fluorescence is normalized to the fluorescence at rest prior to the application of NMDA. The regions recorded are indicated by colored numbers in **(A)** and **(C)** (Alford et al., 2003).

Although arrangements involving NMDARs and $K_{Ca}2$ channels have been shown in many other systems and synapses, their functions have not been expressly linked to specific behaviors or to rhythm generation, but rather have been proposed to serve a more generalized mechanism for tempering synaptic potentials and synaptic plasticity (Shah and Haylett, 2002; Stackman et al., 2002; Maher and Westbrook, 2005; Ngo-Anh et al., 2005; Gu et al., 2008; Lin et al., 2008; Faber, 2010; Harvey-Girard and Maler, 2013). Apamin or intracellular dialysis with BAPTA prolongs glutamate-induced plateau potentials and Ca^{2+} transients

in CA1 pyramidal neuron distal apical dendrites (Wei et al., 2001; Cai et al., 2004), but these plateau potentials are produced through a combination of R-type VGCCs, NMDARs and bAPs (Takahashi and Magee, 2009), and thus does not explicitly link Ca^{2+} entry via NMDARs to $K_{Ca}2$ activation. NMDAR-dependent activation of $K_{Ca}2$ channels at layer 5 pyramidal neuron synapses (Faber, 2010) indicates the necessary components are present, but the mechanism of dendritic oscillation generation has yet to be explored. Recently, a dendritic mechanism for synchronizing spatially disparate synaptic input has been described in CA1 pyramidal neurons, which has implications in the synchronization of hippocampal networks (Vaidya and Johnston, 2013). In lamprey spinal neurons, the nonlinear dynamics of the NMDAR combined with its spatial coupling to $K_{Ca}2$ channels confers V_m bistability, enabling these neurons to be oscillators to synchronize spinal networks for rhythmic locomotion.

EVIDENCE FOR CLOSE COUPLING OF NMDARs AND $K_{Ca}2$ CHANNELS

If NMDARs are the primary route of Ca^{2+} entry necessary for repolarization, then synaptically activated NMDARs will evoke highly localized Ca^{2+} entry within spinal neuron dendrites, and this Ca^{2+} must be located sufficiently close to $K_{Ca}2$ channels to activate an outward current. EIN stimulation causes localized, NMDAR-dependent Ca^{2+} entry in VHN dendrites (Alpert and Alford, 2013). NMDAR EPSCs are sufficient to activate K^+ currents, which are blocked by the $K_{Ca}2$ blockers, apamin and UCL 1684, or following whole cell dialysis with BAPTA. In contrast, EGTA dialysis is ineffective at preventing $K_{Ca}2$ activation (Nanou et al., 2013). Furthermore, BAPTA also prevents repolarization from depolarized plateaus in oscillating neurons induced by NMDA in TTX, whereas those dialyzed with EGTA are able to repeatedly repolarize (Alpert and Alford, 2013). Since BAPTA, but not EGTA, occludes the binding of Ca^{2+} to secondary effectors, presumably $K_{Ca}2$, the channel must be located physically close to the site of Ca^{2+} entry (Marrion and Tavalin, 1998; Ngo-Anh et al., 2005; Fakler and Adelman, 2008).

Any possible role for VGCCs in directly providing Ca^{2+} to drive the repolarization is somewhat limited by the voltage threshold of activation relative to the V_m oscillation range. Lamprey VHNs contain multiple subtypes of VGCCs including N-, P/Q-, and L-type channels with varying contributions to depolarization-evoked whole-cell currents1 (El Manira and Bussières, 1997) and presumably distinct cellular localizations (Llinás and Yarom, 1981; Llinás, 1988; Westenbroek et al., 1990, 1992; Mills et al., 1994; Isope et al., 2012). In cultured lamprey spinal neurons, N- and P/Q-type channels account for ∼75% of the total whole cell VGCC current, while L-type current contributes ∼15% with the residual Ca^{2+} current uncharacterized, but sensitive to Cd^{2+}, the non-specific VGCC blocker (El Manira and Bussières, 1997). However, these values are likely impacted by reduced dendritic arbors in culture and space clamp issues common to somatic recordings. Cd^{2+} abolishes whole-cell current *in situ*, yet NMDA-TTX oscillations persist in Cd^{2+} (Alpert and Alford, 2013), while simultaneous $Ca^{2+}{}_i$ oscillations are insensitive to selective blockade of N- and P/Q-type VGCCs. L-type channels couple to $K_{Ca}2$ channels in hippocampal pyramidal neurons (Marrion and Tavalin, 1998), while Ca^{2+} imaging suggests that this coupling may exist in a subset of dendritic loci in lamprey (Wang et al., 2013) because modulation of L-type channels impacts Ca^{2+} oscillations and the V_m oscillation waveform (Wang et al., 2014a). The current-voltage (I-V) relationship of VGCCs in VHNs shows minimal activation at −60 mV, with significant activation occurring between −40 mV and −30 mV, peaking between −10 and 0 mV (El Manira and Bussières, 1997; Alpert and Alford, 2013). Interestingly, the same V_m where VGCCs become activated, −40 mV, is also the peak plateau potential reached during membrane potential oscillations in NMDA (Alpert and Alford, 2013). Thus, for the majority of VHNs, the neurons oscillate subthreshold to the VGCC activation thresholds except for the initial transient peak of the oscillation amplitude. Indeed, NMDA application reveals a depolarizing step-evoked inward current that occurs within the V_m oscillation range at substantially more hyperpolarized V_ms than currents mediated by VGCCs in these neurons. Similarly, Ca^{2+}-imaging indicates that Ca^{2+} entry within the oscillation range is robustly potentiated and dominated by NMDAR-dependent Ca^{2+} entry (Alpert and Alford, 2013). During voltage steps in NMDA, biphasic currents are generated. This NMDA-induced inward current followed by an outward current is present within the oscillation range (i.e., below −40 mV) and blocked by BAPTA, but not EGTA, again reflecting a close functional coupling between NMDAR current and presumably $K_{Ca}2$ channel activation leading to the outward current. Therefore, both V_m and $Ca^{2+}{}_i$ oscillations are driven through a dendritic mechanism requiring closely apposed ensembles of NMDARs and $K_{Ca}2$ channels and little contribution of Ca^{2+} from VGCCs.

DENDRITIC STRUCTURE AND SYNAPTIC INTEGRATION OF PRESYNAPTIC MICROCIRCUITRY OF VENTRAL HORN NEURONS

In general, the origin of presynaptic input, synapse location within the dendritic tree, and electrotonic distance to soma informs the computation performed by the postsynaptic neuron. Spatially and anatomically compartmentalized dendritic targeting by presynaptic axons is found in many vertebrate neural circuits including the tectum (Bollmann and Engert, 2009), hippocampus (Pouille and Scanziani, 2004; Jarsky et al., 2005), neocortex (Weiler et al., 2008; Anderson et al., 2010), and cerebellum (Ito, 2006; Gao et al., 2012). Variability in presynaptic activity can lead to variation of the topology of Ca^{2+} signaling postsynaptically where it may be encoded predictably onto distinct dendritic compartments (Bollmann and Engert, 2009; Xu et al., 2012). In other instances, Ca^{2+} signaling is unpredictably encoded and may demonstrate extremely heterogeneous expression of activity, even at neighboring synapses (Chen et al., 2011). Global Ca^{2+} signals generated by AP-induced VGCC activation may appear qualitatively similar to those generated from convergent presynaptic activation leading to a global rise in Ca^{2+}. However, the computation performed by a neuron is distinct, depending on the modality of Ca^{2+} signaling. Somatic signals provide intrinsic information about cell firing, while local, synaptic

signals inform about the spatial and functional connectivity of the network and its activation state. Indeed, the computational ability of a neuron's dendrites is intimately tied to and ultimately informed by presynaptic inputs, whose activity leads to discernable behavioral functions postsynaptically (Jia et al., 2010). In hippocampal and neocortical pyramidal neurons, neighboring dendritic synapses are more likely to be activated synchronously than synapses spaced further apart (Kleindienst et al., 2011; Takahashi et al., 2012). This functional clustering is NMDAR-dependent and likely due to synchronized and convergent targeting of multiple presynaptic axons projecting to the recorded neurons, rather than a single presynaptic axon making multiple contacts. Such functional clustering may be important for circuit orchestration during development (Kleindienst et al., 2011) and experience-dependent synaptic plasticity (Makino and Malinow, 2011). Furthermore, NMDAR activation is essential for nonlinear boosting of temporally and spatially integrated synaptic potentials (Polsky et al., 2004). Synaptic potentials arriving at the soma from discrete synaptic events can vary according to degree of clustering (Losonczy and Magee, 2006) and the direction and velocity of synaptic input along single dendritic branches (Branco et al., 2010). The patterning of synaptic input has profound consequences on $Ca^{2+}{}_i$ and this "within dendritic branch" form of computation is NMDAR-dependent. Furthermore, synaptic plasticity—the Ca^{2+}-dependent change in strength of a synapse—can occur selectively at a single synapse (Matsuzaki et al., 2004; Enoki et al., 2009; Makino and Malinow, 2011). Thus, postsynaptic responses to Ca^{2+}, and hence dendritic computational capacity (Poirazi and Mel, 2001), are highly dynamic and depend on presynaptic input and subsequent post-synaptic Ca^{2+} signals as well as the function of the circuit in which the neuron is embedded.

Discrete targeting provides neurons with more processing power (Häusser and Mel, 2003; Polsky et al., 2004) by integrating origin-specific, segregated streams of presynaptic information. This is further enhanced as the location and expression of various voltage-gated ion channels and synaptic receptors varies between different types of neurons but also subcellularly, between different regions of a single neuron (Migliore and Shepherd, 2002; Williams and Stuart, 2003; Jones et al., 2014). Such circuit and dendrite dynamics may also be present in spinal networks controlling movement. A well-defined topographic map of spinal motoneuron recruitment in larval zebrafish proceeds from the ventral to dorsal spinal cord as swimming frequency increases (McLean et al., 2007) and neurons are recruited functionally according to intrinsic rhythm-generating capabilities and requirement for presynaptic oscillatory synaptic drive (Menelaou and McLean, 2012). However, the interneurons that drive motoneuron recruitment demonstrate more complex activation patterns (McLean et al., 2008). The spatial targeting of motoneuron or interneuron dendrites and the integration of synaptic inputs conferring rhythmicity have yet to be defined, but dendritic filopodial activity follows a topographic pattern that maps (Kishore and Fetcho, 2013) onto their recruitment order (McLean et al., 2007) and subsequent electrical activity level, delineating behavioral function to dendrites located in discrete regions along the dorsoventral axis. Thus, the location and targeting of specific dendritic subregions by spatially defined presynaptic neurons may suggest a functional role for individual dendritic branches (Wei et al., 2001; Poirazi et al., 2003; Branco and Häusser, 2010), or perhaps even synapses (Jia et al., 2010), in the output of a given motor neuron.

Dendrite distribution has been shown to differ for motoneurons innervating distinct muscles in the chick spinal cord (Okado et al., 1990). Mice motoneuron dendrites are genetically oriented to particular spinal territories, which influence the connectivity patterns of their proprioceptive afferent inputs (Vrieseling and Arber, 2006). The targeting of dendrites into specific lamina provides distinct opportunities for different classes of presynaptic excitatory and inhibitory interneurons to also target different dendritic regions (Kosugi et al., 2013). *Drosophila* motoneuron dendrites are topographically organized whereby individual neurons genetically target their dendrites to precise anatomical territories centrally, representing their muscle distribution peripherally (Landgraf et al., 2003; Brierley et al., 2009). Within a single dendritic tree there can be a heterogeneous patterning of excitatory synapses (Mauss et al., 2009) and, furthermore, distinct dendritic subtrees can target discrete regions of the neuropil (Vonhoff and Duch, 2010). Therefore, organizational principles orchestrating spinal circuits controlling locomotion are subject to genetic, developmental, and activity-dependent specificity, but determining the function of distinct subcellular targeting requires further investigation.

SYNAPSE-SPECIFICITY OF $K_{Ca}2$ CHANNELS IS BEHAVIORALLY RELEVANT

The precise coupling of synaptically activated receptors and secondarily activated ion channels may complement anatomical specificity of excitatory connections. The behavioral importance of this coupling becomes evident when considering how descending brainstem RS neuron drive interacts with the spinal cord CPG. In vertebrates, RS neurons receive feedback modulation from the spinal CPG that causes them to fire in-phase with the rostral spinal segments (Kasicki et al., 1989; Sirota et al., 2000; Dubuc et al., 2008). This phenomenon creates a paradox with respect to RS innervation of the spinal CPG. In lamprey, each VHN receives input from both local circuit interneurons (glutamatergic and glycinergic) (Buchanan, 1982; Buchanan and Grillner, 1987) and descending RS axons (glutamatergic) (Buchanan et al., 1987; Brodin et al., 1988). Thus, a single VHN may receive two distinct types of glutamatergic contacts. Since the animal creates a rostro-caudal phase lag of 360° from head to tail (Wallén and Williams, 1984), substantial regions of the spinal cord are necessarily out-of-phase with RS neuron firing. Furthermore, as the fish swims, RS axon APs are initiated in the brainstem and project throughout the length of the spinal cord where they excite local CPGs. The AP propagation rate is faster than the speed of the mechanical wave driven by the propagation of neural excitation by segmental CPGs (~10 Hz traveling wave). Thus, there are two traveling waves, RS axon-generated AP propagation and CPG neural waves, which are out-of-phase across substantial rostro-caudal regions of the spinal cord and whose phase mismatch varies with locomotor frequency (**Figure 5**). This phase mismatch precludes RS axons from being phase-locked

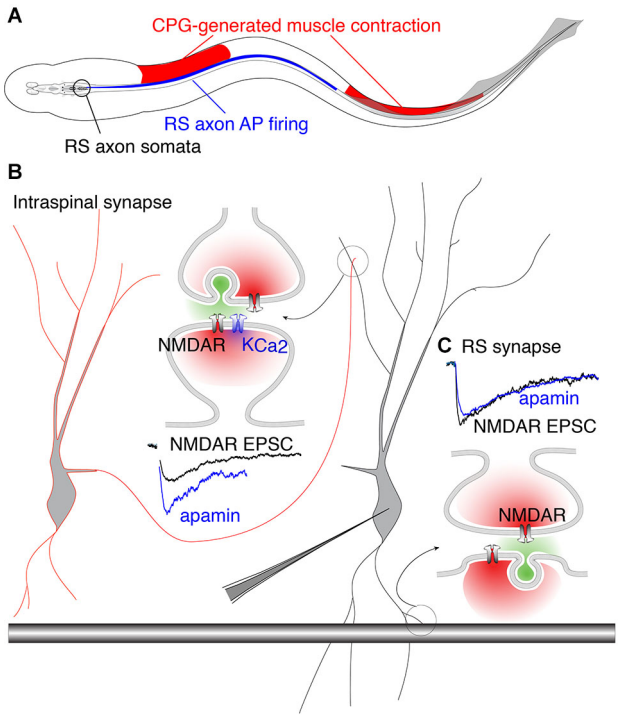

FIGURE 5 | Phase-matched and phase-mismatched excitatory synapses in the spinal cord of lamprey. (A) As the lamprey swims it generates a traveling wave from head to tail. The sinusoidal body curvature illustrated here represents a single moment in body movement during a bout of swimming. During swimming, command excitation is continually provided by RS axons whose somata in the brainstem (encircled in black) fire (blue) in phase with the rostral spinal CPG neurons. This is illustrated by the rostro-caudal overlap of red and blue. It is the output of spinal segments that causes ipsilateral muscle contraction (red). Due to the speed at which the action potential (AP) propagates along RS axons, the AP invades more caudal areas of the spinal cord whose associated muscles do not undergo contraction because the CPG wave (responsible for contraction) travels at a delay relative to the AP. This leads to regions along the spinal cord where AP firing overlaps with inhibited musculature (illustrated by overlap of blue and white regions in the middle). This would predictably lead VHN excitation at inappropriate times during the swim cycle. This phase mismatch between RS axons and CPG neurons may be avoided by synapse-specific $K_{Ca}2$ channel activation. **(B)** Circuit model in which excitation from EINs (red outlined cell) projects to other VHNs (black outlined cell) locally within the spinal cord. NMDAR currents from these neurons (black trace, NMDAR EPSC) are enhanced by the addition of apamin, the specific $K_{Ca}2$ channel antagonist, to block $K_{Ca}2$ currents (blue trace). **(C)** RS synapses from large descending axons (black shaded bar) which project throughout the spinal cord, show NMDAR currents (black trace, NMDAR EPSC) that are unaffected by apamin (blue trace) (Alpert and Alford, 2013).

with VHNs, thus removing the need for pre- and postsynaptic synchronization conferred by coupling of NMDARs and $K_{Ca}2$ channel activation.

Accordingly, it may be considered problematic for RS synapses expressing NMDARs to be coupled to $K_{Ca}2$ channels, which would instill a strict phase-relationship between the pre- and post-synaptic neuron via excitation-inhibition coupling. In contrast, spinal EINs are appropriately phase-locked to their targets because the extent of their spinal projections are limited (Buchanan et al., 1989). This hypothesis is supported by experiments utilizing paired recordings between RS axons and VHNs, demonstrating that postsynaptic NMDAR-mediated responses are insensitive to apamin (Cangiano et al., 2002; Alpert and Alford, 2013). In contrast, glutamatergic synapses between EINs and other VHNs within the spinal cord exhibit strong NMDAR coupling to $K_{Ca}2$ channels (Alpert and Alford, 2013; Nanou et al., 2013), conferring excitation-inhibition coupling and phase-locking as the CPG waves propagate between segments. Such synapse-specificity emphasizes the highly localized nature of dendritic Ca^{2+} signals and the profound importance for restricting Ca^{2+} entry within local domains (**Figure 5**). Within this framework, the synapse-specificity of $K_{Ca}2$ channel activation is crucial for creating synchrony between neurons of the spinal network. Thus, the synaptic localization of the $K_{Ca}2$ channel coupled to NMDARs is not just important for opposing depolarization, but together with the precise function of the presynaptic neuron, establish the foundation for generating network rhythmicity.

NEUROMODULATION OF $K_{Ca}2$ CHANNELS MEDIATING LOCOMOTION

Locomotion is also activated and modulated by monoaminergic systems. Bath-applied serotonin (5-HT), alone or within a cocktail of monoamines, can activate locomotion and fictive locomotion in many preparations (Cazalets et al., 1992; Rossignol et al., 2002). Like glutamate, spinal release of 5-HT originates from both intraspinal (Schotland et al., 1995, 1996; Zhang and Grillner, 2000) and brainstem neurons (Zhang et al., 1996; Abalo et al., 2007; Antri et al., 2008; Barreiro-Iglesias et al., 2008). In lampreys, bath-applied 5-HT has a well-defined modulatory effect on the CPG—it slows ventral root bursting during both spinal exogenous agonist-evoked (Wikström et al., 1995) and brainstem-evoked locomotion (Gerachshenko et al., 2009). 5-HT mediates its effects both pre- and post-synaptically through mechanistically distinct but behaviorally convergent effects. Postsynaptically, 5-HT modifies the activation of $K_{Ca}2$ channels. This postsynaptic effect is mediated at two distinct subcellular sites. 5-HT suppresses burst termination during fictive locomotion induced by NMDA (Harris-Warrick and Cohen, 1985), an effect present during NMDA-TTX driven intrinsic oscillations (Wallén et al., 1989) and which is analogous to blockade of $K_{Ca}2$ channels with apamin (El Manira et al., 1994) or UCL 1684 (Alpert and Alford, 2013). This prolongation of the oscillation may be mediated by direct interaction of 5-HT receptors on $K_{Ca}2$ channels, or alternatively, via an indirect inhibition of NMDARs (Schotland and Grillner, 1993) or VGCCs (Wang et al., 2014a) supplying Ca^{2+} for $K_{Ca}2$ channels responsible for the repolarization. Interestingly, the effects of 5-HT are absent when the network is activated by kainate, which will not activate NMDARs directly. This suggests that NMDAR-dependent Ca^{2+} entry contributing to burst termination (Alpert and Alford, 2013; Nanou et al., 2013) is necessary for 5-HT to modulate the oscillation and that 5-HT receptors inhibit $K_{Ca}2$ channels activated directly by NMDAR-mediated Ca^{2+} permeation.

In addition to effects of 5-HT directly on NMDAR-mediated oscillations, 5-HT_{1A} receptors (Wikström et al., 1995) inhibit N-type VGCCs (Hill et al., 2003), reducing Ca^{2+} necessary for

$K_{Ca}2$ channel activation involved in mAHP (Wikström and El Manira, 1998). This effect is accordingly limited to individual neurons that spike repetitively during locomotion (or fictive locomotion). Thus, 5-HT interactions with $K_{Ca}2$ channels are important in controlling firing rates in lamprey (Wallén et al., 1989; Hill et al., 1992; Meer and Buchanan, 1992) as well as other systems, but are also integral to the ionic mechanism contributing to NMDAR-dependent oscillatory properties (Harris-Warrick and Cohen, 1985; El Manira et al., 1994; Alpert and Alford, 2013; Nanou et al., 2013).

Presynaptically, 5-HT modulates glutamate release from intraspinal connections (e.g., EIN-VHN synapses) as well as from RS command neurons (Buchanan and Grillner, 1991; Blackmer et al., 2001, 2005). This effect mediated by 5-HT_{1B} receptors acts synergistically with the effects on $K_{Ca}2$ channels. It also lengthens the locomotor burst duration during agonist- and (Schwartz et al., 2005) brainstem-evoked locomotion (Gerachshenko et al., 2009) by blocking synaptotagmin/SNARE complex interactions (Blackmer et al., 2005). This reduces cleft glutamate concentration, which leads to a selective reduction of AMPAR activation because NMDARs respond to low glutamate cleft concentrations more readily than do AMPARs (Patneau and Mayer, 1990; Choi et al., 2000; Schwartz et al., 2007). Sustained NMDAR activation combined with reduced AMPAR activation slows bursting recorded during fictive locomotion. This is similar to pharmacologically induced locomotion, which shows slower burst rates in NMDA compared to AMPA or kainate (Brodin et al., 1985; Alford and Grillner, 1990). It may in part be attributed to the slow and fast kinetics of NMDARs and AMPARs, respectively (Alford and Grillner, 1990), but is also a function of the spinal network in which repetitive activation that causes augmenting synaptic responses as seen in 5-HT favors slower rates of fictive locomotion (Kozlov et al., 2001; Svensson et al., 2001). Therefore, the complement of excitation of different glutamate receptors on VHN dendrites and the subsequent integration of those inputs, in conjunction with $K_{Ca}2$ channels, is subject to serotonergic modulation of both synaptic transmission and intrinsic membrane properties. These very different effects of modulators impacting synaptic function and $K_{Ca}2$ converge to influence the output of single neurons that scale to alter motor output.

Thus, the serotonergic system in the spinal cord plays a crucial role in modulating the output of the spinal network. While these results, whether mediated by pre- (Schwartz et al., 2005; Gerachshenko et al., 2009) or postsynaptic (Harris-Warrick and Cohen, 1985; Wallén et al., 1989; Wikström et al., 1995) 5-HT receptors explain effects of exogenous 5-HT, pharmacological application obscures crucial information regarding the spatiotemporal pattern of 5-HT release during swimming. Nevertheless, it is clear that 5-HT has profound effects on neural patterns and phase relationships within the spinal cord during locomotion and that this effect is substantially mediated through effects on $K_{Ca}2$ channel activation.

IMPORTANCE OF STUDYING DENDRITIC PROPERTIES WITHIN A BEHAVING NETWORK

In all vertebrates, 5-HT and glutamate applied exogenously can initiate and influence locomotor-like activity. While it is remarkable that systemic drug application can reliably produce ethologically relevant locomotor patterns in lamprey (Sigvardt et al., 1985) and in other model systems (Rossignol et al., 1998; Kyriakatos et al., 2011), NMDARs *in vivo* are not physiologically activated by a tonic and diffuse release of glutamate. Instead, the release of neurotransmitter and subsequent receptor binding is exquisitely targeted to discrete postsynaptic loci with temporal precision. The physiological activation of NMDARs in any circuit is almost entirely mediated by the synaptic release of glutamate. This will only occur at synapses, and only following presynaptic release of glutamate at those synapses. This constrains the activation of NMDARs spatially and temporally, as well as the $K_{Ca}2$ channels that are subsequently activated.

While pharmacological activation of the spinal network is presumably far from physiological, it has remained to be demonstrated just how distinct this artificial induction is from supraspinal control of descending command neurons and subsequent spinal CPG activation. It is important to note that generating rhythmic activity and appropriate phase coupling has many theoretical solutions (Wallén et al., 1992; Williams, 1992). In the spinal network that generates swimming, there can be multiple pathways which achieve a similar behavioral mode (Menelaou and McLean, 2012), an idea that emerged from the study of invertebrate CPGs (Marder and Bucher, 2007). In *Xenopus* larval tadpoles, there may be little specificity in anatomical connections early in development (Li et al., 2007) suggesting that precise dendritic targeting is not necessary for functional circuit formation. Instead, a very basic scaffolding of neuronal connections is sufficient to construct early behaviors (Roberts et al., 2014). However, the specificity of microcircuit connectivity is subject to change. Synapses are plastic as is the dendritic architecture (Kishore and Fetcho, 2013). Nevertheless, synaptic connectivity and subsequent location-dependent dendritic integration is paramount to neural computation within microcircuits controlling behavior.

Furthermore, our understanding of how monoamines in general and 5-HT in particular act *in vivo* is even less certain than glutamate because exogenous application of these modulators over an artificially and pharmacologically activated network merely compounds errors and cannot match physiological release. Indeed, monoamine cocktails with glutamate agonists evoke spinal network activity (Rossignol et al., 1998; Masino et al., 2012) and when applied individually to active networks, monoamines modulate network activity (Barbeau and Rossignol, 1990; Rossignol et al., 1998). To develop a comprehensive understanding of the true pattern of synaptic drive to spinal neurons and microcircuits requires a more physiological method of activation of these spinal circuits than has previously been employed (Issberner and Sillar, 2007; Dubuc et al., 2008; McLean et al., 2008; Kyriakatos et al., 2011), while retaining the capacity to study them directly from the subcellular to systems level.

Bath-applied NMDA leads to a large increase in baseline $Ca^{2+}{}_i$ while Ca^{2+} oscillations are synchronized throughout the dendrites of a single neuron (Bacskai et al., 1995; Viana di Prisco and Alford, 2004). In this context, all NMDARs will

become active and are independent of presynaptic release of glutamate. Under these conditions, the precise relationship between activated routes of Ca^{2+} entry, whether NMDARs or VGCCs, may become obscured. This may allow $K_{Ca}2$ channels to couple to Ca^{2+} microdomains as opposed to nanodomains implied by their physiological BAPTA sensitivity. Indeed, in VHNs dialyzed with EGTA, oscillation plateau progressively lengthen immediately following whole-cell access, on a time course equivalent to the diffusion of dyes to the most distal dendrites (Alpert and Alford, 2013). This may be interpreted as a progressive increase in EGTA-mediated Ca^{2+} buffering into the distal dendrites where Ca^{2+} oscillations are largest (Viana di Prisco and Alford, 2004), preventing some Ca^{2+} from binding $K_{Ca}2$ channels to cause the repolarization (Alpert and Alford, 2013). This effect suggests that Ca^{2+} diffusing greater distances from its site of entry can, under certain circumstances, activate $K_{Ca}2$ channels, which then contribute to the repolarization. Nevertheless, even under these non-physiological conditions of bath applied NMDA, cells dialyzed with BAPTA displayed immediate, severely impaired repolarization (Alpert and Alford, 2013).

The ability of NMDAR-induced Ca^{2+} entry to bind $K_{Ca}2$ channels in Ca^{2+} microdomains may be an artifact of bath-applied NMDA and the robust increase in intracellular Ca^{2+}, which may also cause Ca^{2+}-induced Ca^{2+} release from internal stores. However, it was recently demonstrated that this $K_{Ca}2$ channel conductance is physiologically activated by synaptically driven NMDAR-mediated Ca^{2+} entry (Alpert and Alford, 2013) and is vital for the proper functioning of the network during brain-evoked locomotion (Nanou et al., 2013). If the spatially and temporally precise synaptic activation of glutamate receptors during locomotion is sensitive to blockade of $K_{Ca}2$ channels, then it should follow that there is complementary patterning dendritic Ca^{2+} entry which drives the activation of $K_{Ca}2$ channels important for rhythm generation. However, we know very little about the spatiotemporal pattern of dendrite activation during behavior and how synaptic input is integrated in real time to impact cell output.

Several recent advances have made it possible to begin to assess how dendrites integrate incoming synaptic information within an active, behaving network. Dendritic spatiotemporal Ca^{2+} dynamics in active networks are crucial to understanding how physiological patterns of synaptic input are integrated in real time to shape the cellular output and have only recently been investigated. With new advances in genetically encoded Ca^{2+} indicators (Muto et al., 2011) and *in vivo* 2-photon microscopy, it is now becoming possible to "watch dendrites in action" and correlate their activity to sensory input and behavioral output (Dombeck et al., 2010; Xu et al., 2012; Smith et al., 2013b; Grienberger et al., 2014). However, particularly in the lamprey model system, but presumably in other systems like zebrafish, there is a distinct advantage in imaging dendritic behavior-the activity of spinal motoneuron and interneuronal dendrites and the subsequent electrical output of individual cells can be precisely correlated to the real time network output, whose role in generating behavior is well characterized and directly measureable. Such multilevel analyses will undoubtedly enhance our understanding of how nervous systems generate behavior from subcellular to systems level with unprecedented detail.

REFERENCES

Abalo, X. M., Villar-Cheda, B., Meléndez-Ferro, M., Pérez-Costas, E., Anadón, R., and Rodicio, M. C. (2007). Development of the serotonergic system in the central nervous system of the sea lamprey. *J. Chem. Neuroanat.* 34, 29–46. doi: 10.1016/j.jchemneu.2007.03.010

Akita, T., and Kuba, K. (2000). Functional triads consisting of ryanodine receptors, Ca(2+) channels and Ca(2+)-activated K(+) channels in bullfrog sympathetic neurons. Plastic modulation of action potential. *J. Gen. Physiol.* 116, 697–720. doi: 10.1085/jgp.116.5.697

Alford, S., Frenguelli, B. G., Schofield, J. G., and Collingridge, G. L. (1993). Characterization of Ca2+ signals induced in hippocampal CA1 neurones by the synaptic activation of NMDA receptors. *J. Physiol.* 469, 693–716.

Alford, S., and Grillner, S. (1990). CNQX and DNQX block non-NMDA synaptic transmission but not NMDA-evoked locomotion in lamprey spinal cord. *Brain Res.* 506, 297–302. doi: 10.1016/0006-8993(90)91266-j

Alford, S., Schwartz, E., and Viana di Prisco, G. (2003). The pharmacology of vertebrate spinal central pattern generators. *Neuroscientist* 9, 217–228. doi: 10.1177/1073858403009003014

Alford, S., and Williams, T. L. (1989). Endogenous activation of glycine and NMDA receptors in lamprey spinal cord during fictive locomotion. *J. Neurosci.* 9, 2792–2800.

Alpert, M. H., and Alford, S. (2013). Synaptic NMDA receptor-dependent Ca^{2+} entry drives membrane potential and Ca^{2+} oscillations in spinal ventral horn neurons. *PLoS One* 8:e63154. doi: 10.1371/journal.pone.0063154

Anderson, C. T., Sheets, P. L., Kiritani, T., and Shepherd, G. M. G. (2010). Sublayer-specific microcircuits of corticospinal and corticostriatal neurons in motor cortex. *Nat. Neurosci.* 13, 739–744. doi: 10.1038/nn.2538

Antri, M., Auclair, F., Albrecht, J., Djeudjang, N., and Dubuc, R. (2008). Serotoninergic modulation of sensory transmission to brainstem reticulospinal cells. *Eur. J. Neurosci.* 28, 655–667. doi: 10.1111/j.1460-9568.2008.06368.x

Ascher, P., and Nowak, L. (1988). The role of divalent cations in the N-methyl-D-aspartate responses of mouse central neurones in culture. *J. Physiol.* 399, 247–266.

Augustinaite, S., Kuhn, B., Helm, P. J., and Heggelund, P. (2014). NMDA spike/plateau potentials in dendrites of thalamocortical neurons. *J. Neurosci.* 34, 10892–10905. doi: 10.1523/JNEUROSCI.1205-13.2014

Augustine, G. J., Santamaria, F., and Tanaka, K. (2003). Local calcium signaling in neurons. *Neuron* 40, 331–346. doi: 10.1016/s0896-6273(03)00639-1

Bacskai, B. J., Wallén, P., Lev-Ram, V., Grillner, S., and Tsien, R. Y. (1995). Activity-related calcium dynamics in lamprey motoneurons as revealed by video-rate confocal microscopy. *Neuron* 14, 19–28. doi: 10.1016/0896-6273(95)90237-6

Ballesteros-Merino, C., Lin, M., Wu, W. W., Ferrandiz-Huertas, C., Cabañero, M. J., Watanabe, M., et al. (2012). Developmental profile of SK2 channel expression and function in CA1 neurons. *Hippocampus* 22, 1467–1480. doi: 10.1002/hipo.20986

Barbeau, H., and Rossignol, S. (1990). The effects of serotonergic drugs on the locomotor pattern and on cutaneous reflexes of the adult chronic spinal cat. *Brain Res.* 514, 55–67. doi: 10.1016/0006-8993(90)90435-e

Barreiro-Iglesias, A., Villar-Cerviño, V., Anadón, R., and Rodicio, M. C. (2008). Development and organization of the descending serotonergic brainstem-spinal projections in the sea lamprey. *J. Chem. Neuroanat.* 36, 77–84. doi: 10.1016/j.jchemneu.2008.06.001

Berridge, M. J. (2006). Calcium microdomains: organization and function. *Cell Calcium* 40, 405–412. doi: 10.1016/j.ceca.2006.09.002

Blackmer, T., Larsen, E. C., Bartleson, C., Kowalchyk, J. A., Yoon, E.-J., Preininger, A. M., et al. (2005). G protein betagamma directly regulates SNARE protein fusion machinery for secretory granule exocytosis. *Nat. Neurosci.* 8, 421–425. doi: 10.1038/nn1423

Blackmer, T., Larsen, E. C., Takahashi, M., Martin, T. F., Alford, S., and Hamm, H. E. (2001). G protein betagamma subunit-mediated presynaptic inhibition: regulation of exocytotic fusion downstream of Ca2+ entry. *Science* 292, 293–297. doi: 10.1126/science.1058803

Bloodgood, B. L., and Sabatini, B. L. (2007). Nonlinear regulation of unitary synaptic signals by CaV(2.3) voltage-sensitive calcium channels located in dendritic spines. *Neuron* 53, 249–260. doi: 10.1016/j.neuron.2006.12.017

Bollmann, J. H., and Engert, F. (2009). Subcellular topography of visually driven dendritic activity in the vertebrate visual system. *Neuron* 61, 895–905. doi: 10.1016/j.neuron.2009.01.018

Bond, C. T., Herson, P. S., Strassmaier, T., Hammond, R., Stackman, R., Maylie, J., et al. (2004). Small conductance Ca2+-activated K+ channel knock-out mice reveal the identity of calcium-dependent afterhyperpolarization currents. *J. Neurosci.* 24, 5301–5306. doi: 10.1523/jneurosci.0182-04.2004

Branco, T., Clark, B. A., and Häusser, M. (2010). Dendritic discrimination of temporal input sequences in cortical neurons. *Science* 329, 1671–1675. doi: 10.1126/science.1189664

Branco, T., and Häusser, M. (2010). The single dendritic branch as a fundamental functional unit in the nervous system. *Curr. Opin. Neurobiol.* 20, 494–502. doi: 10.1016/j.conb.2010.07.009

Brierley, D. J., Blanc, E., Reddy, O. V., VijayRaghavan, K., and Williams, D. W. (2009). Dendritic targeting in the leg neuropil of Drosophila: the role of midline signalling molecules in generating a myotopic map. *PLoS Biol.* 7:e1000199. doi: 10.1371/journal.pbio.1000199

Brodin, L., and Grillner, S. (1985). The role of putative excitatory amino acid neurotransmitters in the initiation of locomotion in the lamprey spinal cord. I. The effects of excitatory amino acid antagonists. *Brain Res.* 360, 139–148. doi: 10.1016/0006-8993(85)91229-6

Brodin, L., Grillner, S., Dubuc, R., Ohta, Y., Kasicki, S., and Hökfelt, T. (1988). Reticulospinal neurons in lamprey: transmitters, synaptic interactions and their role during locomotion. *Arch. Ital. Biol.* 126, 317–345.

Brodin, L., Grillner, S., and Rovainen, C. M. (1985). N-Methyl-D-Aspartate (NMDA), kainate and quisqualate receptors and the generation of fictive locomotion in the lamprey spinal cord. *Brain Res.* 325, 302–306. doi: 10.1016/0006-8993(85)90328-2

Buchanan, J. T. (1982). Identification of interneurons with contralateral, caudal axons in the lamprey spinal cord: synaptic interactions and morphology. *J. Neurophysiol.* 47, 961–975.

Buchanan, J. T. (1993). Electrophysiological properties of identified classes of lamprey spinal neurons. *J. Neurophysiol.* 70, 2313–2325.

Buchanan, J. T. (2001). Contributions of identifiable neurons and neuron classes to lamprey vertebrate neurobiology. *Prog. Neurobiol.* 63, 441–466. doi: 10.1016/s0301-0082(00)00050-2

Buchanan, J. T., Brodin, L., Dale, N., and Grillner, S. (1987). Reticulospinal neurones activate excitatory amino acid receptors. *Brain Res.* 408, 321–325. doi: 10.1016/0006-8993(87)90397-0

Buchanan, J. T., and Cohen, A. H. (1982). Activities of identified interneurons, motoneurons and muscle fibers during fictive swimming in the lamprey and effects of reticulospinal and dorsal cell stimulation. *J. Neurophysiol.* 47, 948–960. Available online at: http://jn.physiology.org/content/47/5/948.abstract.

Buchanan, J. T., and Grillner, S. (1987). Newly identified 'glutamate interneurons' and their role in locomotion in the lamprey spinal cord. *Science* 236, 312–314. doi: 10.1126/science.3563512

Buchanan, J. T., and Grillner, S. (1991). 5-Hydroxytryptamine depresses reticulospinal excitatory postsynaptic potentials in motoneurons of the lamprey. *Neurosci. Lett.* 122, 71–74. doi: 10.1016/0304-3940(91)90196-z

Buchanan, J. T., Grillner, S., Cullheim, S., and Risling, M. (1989). Identification of excitatory interneurons contributing to generation of locomotion in lamprey: structure, pharmacology and function. *J. Neurophysiol.* 62, 59–69.

Buzsáki, G., and Draguhn, A. (2004). Neuronal oscillations in cortical networks. *Science* 304, 1926–1929. doi: 10.1126/science.1099745

Buzsáki, G., and Moser, E. I. (2013). Memory, navigation and theta rhythm in the hippocampal-entorhinal system. *Nat. Neurosci.* 16, 130–138. doi: 10.1038/nn.3304

Cai, X., Liang, C. W., Muralidharan, S., Kao, J. P. Y., Tang, C.-M., and Thompson, S. M. (2004). Unique roles of SK and Kv4.2 potassium channels in dendritic integration. *Neuron* 44, 351–364. doi: 10.1016/j.neuron.2004.09.026

Cangiano, L., Wallén, P., and Grillner, S. (2002). Role of apamin-sensitive k(ca) channels for reticulospinal synaptic transmission to motoneuron and for the afterhyperpolarization. *J. Neurophysiol.* 88, 289–299.

Cazalets, J. R., Sqalli-Houssaini, Y., and Clarac, F. (1992). Activation of the central pattern generators for locomotion by serotonin and excitatory amino acids in neonatal rat. *J. Physiol.* 455, 187–204.

Chau, C., Giroux, N., Barbeau, H., Jordan, L., and Rossignol, S. (2002). Effects of intrathecal glutamatergic drugs on locomotion I. NMDA in short-term spinal cats. *J. Neurophysiol.* 88, 3032–3045. doi: 10.1152/jn.00138.2002

Chen, X., Leischner, U., Rochefort, N. L., Nelken, I., and Konnerth, A. (2011). Functional mapping of single spines in cortical neurons in vivo. *Nature* 475, 501–505. doi: 10.1038/nature10193

Choi, S., Klingauf, J., and Tsien, R. W. (2000). Postfusional regulation of cleft glutamate concentration during LTP at 'silent synapses'. *Nat. Neurosci.* 3, 330–336. doi: 10.1038/73895

Cohen, A. H., and Wallén, P. (1980). The neuronal correlate of locomotion in fish. *Exp. Brain Res.* 41, 11–18. doi: 10.1007/bf00236674

Contreras, D., and Steriade, M. (1995). Cellular basis of EEG slow rhythms: a study of dynamic corticothalamic relationships. *J. Neurosci.* 15, 604–622.

Dale, N., and Roberts, A. (1984). Excitatory amino acid receptors in Xenopus embryo spinal cord and their role in the activation of swimming. *J. Physiol.* 348, 527–543.

Dale, N., and Roberts, A. (1985). Dual-component amino-acid-mediated synaptic potentials: excitatory drive for swimming in Xenopus embryos. *J. Physiol.* 363, 35–59.

Deister, C. A., Teagarden, M. A., Wilson, C. J., and Paladini, C. A. (2009). An intrinsic neuronal oscillator underlies dopaminergic neuron bursting. *J. Neurosci.* 29, 15888–15897. doi: 10.1523/JNEUROSCI.4053-09.2009

Delvolvé, I., Bem, T., and Cabelguen, J. M. (1997). Epaxial and limb muscle activity during swimming and terrestrial stepping in the adult newt, Pleurodeles waltl. *J. Neurophysiol.* 78, 638–650.

Díaz-Ríos, M., Dombeck, D. A., Webb, W. W., and Harris-Warrick, R. M. (2007). Serotonin modulates dendritic calcium influx in commissural interneurons in the mouse spinal locomotor network. *J. Neurophysiol.* 98, 2157–2167. doi: 10.1152/jn.00430.2007

Dombeck, D. A., Harvey, C. D., Tian, L., Looger, L. L., and Tank, D. W. (2010). Functional imaging of hippocampal place cells at cellular resolution during virtual navigation. *Nat. Neurosci.* 13, 1433–1440. doi: 10.1038/nn.2648

Douglas, J. R., Noga, B. R., Dai, X., and Jordan, L. M. (1993). The effects of intrathecal administration of excitatory amino acid agonists and antagonists on the initiation of locomotion in the adult cat. *J. Neurosci.* 13, 990–1000.

Dubuc, R., Brocard, F., Antri, M., Fénelon, K., Gariépy, J.-F., Smetana, R., et al. (2008). Initiation of locomotion in lampreys. *Brain Res. Rev.* 57, 172–182. doi: 10.1016/j.brainresrev.2007.07.016

Durstewitz, D., Seamans, J. K., and Sejnowski, T. J. (2000). Neurocomputational models of working memory. *Nat. Neurosci.* 3(Suppl.), 1184–1191. doi: 10.1038/81460

El Manira, A., and Bussières, N. (1997). Calcium channel subtypes in lamprey sensory and motor neurons. *J. Neurophysiol.* 78, 1334–1340.

El Manira, A., Tegnér, J., and Grillner, S. (1994). Calcium-dependent potassium channels play a critical role for burst termination in the locomotor network in lamprey. *J. Neurophysiol.* 72, 1852–1861.

Enoki, R., Hu, Y.-L., Hamilton, D., and Fine, A. (2009). Expression of long-term plasticity at individual synapses in hippocampus is graded, bidirectional and mainly presynaptic: optical quantal analysis. *Neuron* 62, 242–253. doi: 10.1016/j.neuron.2009.02.026

Ericsson, J., Stephenson-Jones, M., Pérez-Fernández, J., Robertson, B., Silberberg, G., and Grillner, S. (2013). Dopamine differentially modulates the excitability of striatal neurons of the direct and indirect pathways in lamprey. *J. Neurosci.* 33, 8045–8054. doi: 10.1523/JNEUROSCI.5881-12.2013

Faber, E. S. L. (2010). Functional interplay between NMDA receptors, SK channels and voltage-gated Ca2+ channels regulates synaptic excitability in the medial prefrontal cortex. *J. Physiol.* 588, 1281–1292. doi: 10.1113/jphysiol.2009.185645

Faber, E. S. L., Delaney, A. J., and Sah, P. (2005). SK channels regulate excitatory synaptic transmission and plasticity in the lateral amygdala. *Nat. Neurosci.* 8, 635–641. doi: 10.1038/nn1450

Faber, E. S. L., and Sah, P. (2002). Physiological role of calcium-activated potassium currents in the rat lateral amygdala. *J. Neurosci.* 22, 1618–1628.

Fakler, B., and Adelman, J. P. (2008). Control of K(Ca) channels by calcium nano/microdomains. *Neuron* 59, 873–881. doi: 10.1016/j.neuron.2008.09.001

Field, E. C., and Stein, P. S. (1997). Spinal cord coordination of hindlimb movements in the turtle: intralimb temporal relationships during scratching and swimming. *J. Neurophysiol.* 78, 1394–1403.

Flatman, J. A., Schwindt, P. C., and Crill, W. E. (1986). The induction and modification of voltage-sensitive responses in cat neocortical nuerons by N-methyl-D-aspartate. *Brain Res.* 363, 62–77. doi: 10.1016/0006-8993(86)90659-1

Forssberg, H., Grillner, S., Halbertsma, J., and Rossignol, S. (1980). The locomotion of the low spinal cat. II. Interlimb coordination. *Acta Physiol. Scand.* 108, 283–295. doi: 10.1111/j.1748-1716.1980.tb06534.x

Frenguelli, B. G., Potier, B., Slater, N. T., Alford, S., and Collingridge, G. L. (1993). Metabotropic glutamate receptors and calcium signalling in dendrites of hippocampal CA1 neurones. *Neuropharmacology* 32, 1229–1237. doi: 10.1016/0028-3908(93)90017-w

Gabriel, J. P., Mahmood, R., Kyriakatos, A., Söll, I., Hauptmann, G., Calabrese, R. L., et al. (2009). Serotonergic modulation of locomotion in zebrafish: endogenous release and synaptic mechanisms. *J. Neurosci.* 29, 10387–10395. doi: 10.1523/JNEUROSCI.1978-09.2009

Gao, Z., van Beugen, B. J., and De Zeeuw, C. I. (2012). Distributed synergistic plasticity and cerebellar learning. *Nat. Rev. Neurosci.* 13, 619–635. doi: 10.1038/nrn3391

Gerachshenko, T., Schwartz, E., Bleckert, A., Photowala, H., Seymour, A., and Alford, S. (2009). Presynaptic G-protein-coupled receptors dynamically modify vesicle fusion, synaptic cleft glutamate concentrations and motor behavior. *J. Neurosci.* 29, 10221–10233. doi: 10.1523/JNEUROSCI.1404-09.2009

Goulding, M. (2009). Circuits controlling vertebrate locomotion: moving in a new direction. *Nat. Rev. Neurosci.* 10, 507–518. doi: 10.1038/nrn2608

Grienberger, C., Chen, X., and Konnerth, A. (2014). NMDA receptor-dependent multidendrite Ca2+ spikes required for hippocampal burst firing in vivo. *Neuron* 81, 1274–1281. doi: 10.1016/j.neuron.2014.01.014

Grillner, S. (2003). The motor infrastructure: from ion channels to neuronal networks. *Nat. Rev. Neurosci.* 4, 573–586. doi: 10.1038/nrn1137

Grillner, S. (2006). Biological pattern generation: the cellular and computational logic of networks in motion. *Neuron* 52, 751–766. doi: 10.1016/j.neuron.2006.11.008

Grillner, S., Cangiano, L., Hu, G., Thompson, R., Hill, R., and Wallén, P. (2000). The intrinsic function of a motor system—from ion channels to networks and behavior. *Brain Res.* 886, 224–236. doi: 10.1016/s0006-8993(00)03088-2

Grillner, S., Markram, H., De Schutter, E., Silberberg, G., and LeBeau, F. E. N. (2005). Microcircuits in action—from CPGs to neocortex. *Trends Neurosci.* 28, 525–533. doi: 10.1016/j.tins.2005.08.003

Grillner, S., McClellan, A., Sigvardt, K., Wallén, P., and Wilén, M. (1981). Activation of NMDA-receptors elicits "fictive locomotion" in lamprey spinal cord in vitro. *Acta Physiol. Scand.* 113, 549–551. doi: 10.1111/j.1748-1716.1981.tb06937.x

Grillner, S., Robertson, B., and Stephenson-Jones, M. (2013). The evolutionary origin of the vertebrate basal ganglia and its role in action-selection. *J. Physiol.* 591, 5425–5431. doi: 10.1113/jphysiol.2012.246660

Grillner, S., and Wallén, P. (1980). Does the central pattern generation for locomotion in lamprey depend on glycine inhibition? *Acta Physiol. Scand.* 110, 103–105. doi: 10.1111/j.1748-1716.1980.tb06637.x

Grillner, S., and Wallén, P. (1985). The ionic mechanisms underlying N-methyl-D-aspartate receptor-induced, tetrodotoxin-resistant membrane potential oscillations in lamprey neurons active during locomotion. *Neurosci. Lett.* 60, 289–294. doi: 10.1016/0304-3940(85)90592-0

Grillner, S., Wallén, P., Hill, R., Cangiano, L., and El Manira, A. (2001). Ion channels of importance for the locomotor pattern generation in the lamprey brainstem-spinal cord. *J. Physiol.* 533, 23–30. doi: 10.1111/j.1469-7793.2001.0023b.x

Grillner, S., Wallén, P., Saitoh, K., Kozlov, A., and Robertson, B. (2008). Neural bases of goal-directed locomotion in vertebrates—an overview. *Brain Res. Rev.* 57, 2–12. doi: 10.1016/j.brainresrev.2007.06.027

Gu, N., Hu, H., Vervaeke, K., and Storm, J. F. (2008). SK (KCa2) channels do not control somatic excitability in CA1 pyramidal neurons but can be activated by dendritic excitatory synapses and regulate their impact. *J. Neurophysiol.* 100, 2589–2604. doi: 10.1152/jn.90433.2008

Guertin, P. A., and Hounsgaard, J. (1998). NMDA-Induced intrinsic voltage oscillations depend on L-type calcium channels in spinal motoneurons of adult turtles. *J. Neurophysiol.* 80, 3380–3382.

Hammond, R. S., Bond, C. T., Strassmaier, T., Ngo-Anh, T. J., Adelman, J. P., Maylie, J., et al. (2006). Small-conductance Ca2+-activated K+ channel type 2 (SK2) modulates hippocampal learning, memory and synaptic plasticity. *J. Neurosci.* 26, 1844–1853. doi: 10.1523/jneurosci.4106-05.2006

Han, P., Nakanishi, S. T., Tran, M. A., and Whelan, P. J. (2007). Dopaminergic modulation of spinal neuronal excitability. *J. Neurosci.* 27, 13192–13204. doi: 10.1523/jneurosci.1279-07.2007

Harris-Warrick, R. M. (2002). Voltage-sensitive ion channels in rhythmic motor systems. *Curr. Opin. Neurobiol.* 12, 646–651. doi: 10.1016/s0959-4388(02)00377-x

Harris-Warrick, R. M., and Cohen, A. H. (1985). Serotonin modulates the central pattern generator for locomotion in the isolated lamprey spinal cord. *J. Exp. Biol.* 116, 27–46.

Harvey-Girard, E., and Maler, L. (2013). Dendritic SK channels convert NMDA-R-dependent LTD to burst timing-dependent plasticity. *J. Neurophysiol.* 110, 2689–2703. doi: 10.1152/jn.00506.2013

Häusser, M., and Mel, B. (2003). Dendrites: bug or feature? *Curr. Opin. Neurobiol.* 13, 372–383. doi: 10.1016/s0959-4388(03)00075-8

Hernandez, P., Elbert, K., and Droge, M. H. (1991). Spontaneous and NMDA evoked motor rhythms in the neonatal mouse spinal cord: an in vitro study with comparisons to in situ activity. *Exp. Brain Res.* 85, 66–74. doi: 10.1007/bf00229987

Hill, R. H., Brodin, L., and Grillner, S. (1989). Activation of N-methyl-D-aspartate (NMDA) receptors augments repolarizing responses in lamprey spinal neurons. *Brain Res.* 499, 388–392. doi: 10.1016/0006-8993(89)90790-7

Hill, R., Matsushima, T., Schotland, J., and Grillner, S. (1992). Apamin blocks the slow AHP in lamprey and delays termination of locomotor bursts. *Neuroreport* 3, 943–945. doi: 10.1097/00001756-199210000-00032

Hill, R. H., Svensson, E., Dewael, Y., and Grillner, S. (2003). 5-HT inhibits N-type but not L-type Ca(2+) channels via 5-HT1A receptors in lamprey spinal neurons. *Eur. J. Neurosci.* 18, 2919–2924. doi: 10.1111/j.1460-9568.2003.03051.x

Hochman, S., Jordan, L. M., and Schmidt, B. J. (1994). TTX-resistant NMDA receptor-mediated voltage oscillations in mammalian lumbar motoneurons. *J. Neurophysiol.* 72, 2559–2562.

Hsiao, C.-F., Wu, N., Levine, M. S., and Chandler, S. H. (2002). Development and serotonergic modulation of NMDA bursting in rat trigeminal motoneurons. *J. Neurophysiol.* 87, 1318–1328.

Isope, P., Hildebrand, M. E., and Snutch, T. P. (2012). Contributions of T-type voltage-gated calcium channels to postsynaptic calcium signaling within Purkinje neurons. *Cerebellum* 11, 651–665. doi: 10.1007/s12311-010-0195-4

Issberner, J. P., and Sillar, K. T. (2007). The contribution of the NMDA receptor glycine site to rhythm generation during fictive swimming in Xenopus laevis tadpoles. *Eur. J. Neurosci.* 26, 2556–2564. doi: 10.1111/j.1460-9568.2007.05892.x

Ito, M. (2006). Cerebellar circuitry as a neuronal machine. *Prog. Neurobiol.* 78, 272–303. doi: 10.1016/j.pneurobio.2006.02.006

Jarsky, T., Roxin, A., Kath, W. L., and Spruston, N. (2005). Conditional dendritic spike propagation following distal synaptic activation of hippocampal CA1 pyramidal neurons. *Nat. Neurosci.* 8, 1667–1676. doi: 10.1038/nn1599

Jia, H., Rochefort, N. L., Chen, X., and Konnerth, A. (2010). Dendritic organization of sensory input to cortical neurons in vivo. *Nature* 464, 1307–1312. doi: 10.1038/nature08947

Johnson, S. W., Seutin, V., and North, R. A. (1992). Burst firing in dopamine neurons induced by N-methyl-D-aspartate: role of electrogenic sodium pump. *Science* 258, 665–667. doi: 10.1126/science.1329209

Jones, R. S., Pedisich, M., Carroll, R. C., and Nawy, S. (2014). Spatial organization of AMPAR subtypes in ON RGCs. *J. Neurosci.* 34, 656–661. doi: 10.1523/JNEUROSCI.1140-13.2014

Jones, S. L., and Stuart, G. J. (2013). Different calcium sources control somatic versus dendritic SK channel activation during action potentials. *J. Neurosci.* 33, 19396–19405. doi: 10.1523/JNEUROSCI.2073-13.2013

Kahn, J. A., and Roberts, A. (1978). The central nervous generation of the swimming rhythm in an amphibian embryo [proceedings]. *J. Physiol.* 277, 20P–21P.

Kasicki, S., Grillner, S., Ohta, Y., Dubuc, R., and Brodin, L. (1989). Phasic modulation of reticulospinal neurones during fictive locomotion and other types of spinal motor activity in lamprey. *Brain Res.* 484, 203–216. doi: 10.1016/0006-8993(89)90363-6

Kawai, T., and Watanabe, M. (1989). Effects of ryanodine on the spike after-hyperpolarization in sympathetic neurones of the rat superior cervical ganglion. *Pflugers Arch.* 413, 470–475. doi: 10.1007/bf00594175

Kettunen, P., Krieger, P., Hess, D., and El Manira, A. (2002). Signaling mechanisms of metabotropic glutamate receptor 5 subtype and its endogenous role in a locomotor network. *J. Neurosci.* 22, 1868–1873.

Kim, Y. I., and Chandler, S. H. (1995). NMDA-induced burst discharge in guinea pig trigeminal motoneurons in vitro. *J. Neurophysiol.* 74, 334–346.

Kishore, S., and Fetcho, J. R. (2013). Homeostatic regulation of dendritic dynamics in a motor map in vivo. *Nat. Commun.* 4:2086. doi: 10.1038/ncomms3086

Kleindienst, T., Winnubst, J., Roth-Alpermann, C., Bonhoeffer, T., and Lohmann, C. (2011). Activity-dependent clustering of functional synaptic inputs on developing hippocampal dendrites. *Neuron* 72, 1012–1024. doi: 10.1016/j.neuron.2011.10.015

Koshiya, N., and Smith, J. C. (1999). Neuronal pacemaker for breathing visualized in vitro. *Nature* 400, 360–363. doi: 10.1038/22540

Kosugi, M., Kato, G., Lukashov, S., Pendse, G., Puskar, Z., Kozsurek, M., et al. (2013). Subpopulation-specific patterns of intrinsic connectivity in mouse superficial dorsal horn as revealed by laser scanning photostimulation. *J. Physiol.* 591, 1935–1949. doi: 10.1113/jphysiol.2012.244210

Kozlov, A., Kotaleski, J. H., Aurell, E., Grillner, S., and Lansner, A. (2001). Modeling of substance P and 5-HT induced synaptic plasticity in the lamprey spinal CPG: consequences for network pattern generation. *J. Comput. Neurosci.* 11, 183–200. doi: 10.1023/A:1012806018730

Krieger, P., Hellgren-Kotaleski, J., Kettunen, P., and El Manira, A. J. (2000). Interaction between metabotropic and ionotropic glutamate receptors regulates neuronal network activity. *J. Neurosci.* 20, 5382–5391.

Kudo, N., and Yamada, T. (1987). N-methyl-D,L-aspartate-induced locomotor activity in a spinal cord-hindlimb muscles preparation of the newborn rat studied in vitro. *Neurosci. Lett.* 75, 43–48. doi: 10.1016/0304-3940(87)90072-3

Kyriakatos, A., Mahmood, R., Ausborn, J., Porres, C. P., Büschges, A., and El Manira, A. (2011). Initiation of locomotion in adult zebrafish. *J. Neurosci.* 31, 8422–8431. doi: 10.1523/JNEUROSCI.1012-11.2011

Landgraf, M., Jeffrey, V., Fujioka, M., Jaynes, J. B., and Bate, M. (2003). Embryonic origins of a motor system: motor dendrites form a myotopic map in Drosophila. *PLoS Biol.* 1:E41. doi: 10.1371/journal.pbio.0000041

Larkum, M. E., Nevian, T., Sandler, M., Polsky, A., and Schiller, J. (2009). Synaptic integration in tuft dendrites of layer 5 pyramidal neurons: a new unifying principle. *Science* 325, 756–760. doi: 10.1126/science.1171958

Larkum, M. E., Watanabe, S., Nakamura, T., Lasser-Ross, N., and Ross, W. N. (2003). Synaptically activated Ca2+ waves in layer 2/3 and layer 5 rat neocortical pyramidal neurons. *J. Physiol.* 549, 471–488. doi: 10.1113/jphysiol.2002.037614

Larkum, M. E., Zhu, J. J., and Sakmann, B. (1999). A new cellular mechanism for coupling inputs arriving at different cortical layers. *Nature* 398, 338–341. doi: 10.1038/18686

Leresche, N., Lightowler, S., Soltesz, I., Jassik-Gerschenfeld, D., and Crunelli, V. (1991). Low-frequency oscillatory activities intrinsic to rat and cat thalamocortical cells. *J. Physiol.* 441, 155–174.

Li, X., and Bennett, D. J. (2007). Apamin-sensitive calcium-activated potassium currents (SK) are activated by persistent calcium currents in rat motoneurons. *J. Neurophysiol.* 97, 3314–3330. doi: 10.1152/jn.01068.2006

Li, W.-C., Cooke, T., Sautois, B., Soffe, S. R., Borisyuk, R., and Roberts, A. (2007). Axon and dendrite geography predict the specificity of synaptic connections in a functioning spinal cord network. *Neural Dev.* 2:17. doi: 10.1186/1749-8104-2-17

Li, W.-C., Roberts, A., and Soffe, S. R. (2010). Specific brainstem neurons switch each other into pacemaker mode to drive movement by activating NMDA receptors. *J. Neurosci.* 30, 16609–16620. doi: 10.1523/JNEUROSCI.3695-10.2010

Lin, M. T., Luján, R., Watanabe, M., Adelman, J. P., and Maylie, J. (2008). SK2 channel plasticity contributes to LTP at Schaffer collateral-CA1 synapses. *Nat. Neurosci.* 11, 170–177. doi: 10.1038/nn2041

Lisman, J. E., Fellous, J. M., and Wang, X. J. (1998). A role for NMDA-receptor channels in working memory. *Nat. Neurosci.* 1, 273–275. doi: 10.1038/1086

Llinás, R. (1988). The intrinsic electrophysiological properties of mammalian neurons: insights into central nervous system function. *Science* 242, 1654–1664. doi: 10.1126/science.3059497

Llinás, R., and Yarom, Y. (1981). Properties and distribution of ionic conductances generating electroresponsiveness of mammalian inferior olivary neurones in vitro. *J. Physiol.* 315, 569–584.

Losonczy, A., and Magee, J. C. (2006). Integrative properties of radial oblique dendrites in hippocampal CA1 pyramidal neurons. *Neuron* 50, 291–307. doi: 10.1016/j.neuron.2006.03.016

MacDermott, A. B., Mayer, M. L., Westbrook, G. L., Smith, S. J., and Barker, J. L. (1986). NMDA-receptor activation increases cytoplasmic calcium concentration in cultured spinal cord neurones. *Nature* 321, 519–522. doi: 10.1038/321519a0

Maciaszek, J. L., Soh, H., Walikonis, R. S., Tzingounis, A. V., and Lykotrafitis, G. (2012). Topography of native SK channels revealed by force nanoscopy in living neurons. *J. Neurosci.* 32, 11435–11440. doi: 10.1523/JNEUROSCI.1785-12.2012

Maher, B. J., and Westbrook, G. L. (2005). SK channel regulation of dendritic excitability and dendrodendritic inhibition in the olfactory bulb. *J. Neurophysiol.* 94, 3743–3750. doi: 10.1152/jn.00797.2005

Major, G., Polsky, A., Denk, W., Schiller, J., and Tank, D. W. (2008). Spatiotemporally graded NMDA spike/plateau potentials in basal dendrites of neocortical pyramidal neurons. *J. Neurophysiol.* 99, 2584–2601. doi: 10.1152/jn.00011.2008

Makino, H., and Malinow, R. (2011). Compartmentalized versus global synaptic plasticity on dendrites controlled by experience. *Neuron* 72, 1001–1011. doi: 10.1016/j.neuron.2011.09.036

Marder, E., and Bucher, D. (2007). Understanding circuit dynamics using the stomatogastric nervous system of lobsters and crabs. *Annu. Rev. Physiol.* 69, 291–316. doi: 10.1146/annurev.physiol.69.031905.161516

Marrion, N. V., and Tavalin, S. J. (1998). Selective activation of Ca2+-activated K+ channels by co-localized Ca2+ channels in hippocampal neurons. *Nature* 395, 900–905. doi: 10.1038/27674

Masino, M. A., Abbinanti, M. D., Eian, J., and Harris-Warrick, R. M. (2012). TTX-resistant NMDA receptor-mediated membrane potential oscillations in neonatal mouse Hb9 interneurons. *PLoS One* 7:e47940. doi: 10.1371/journal.pone.0047940

Masino, M. A., and Fetcho, J. R. (2005). Fictive swimming motor patterns in wild type and mutant larval zebrafish. *J. Neurophysiol.* 93, 3177–3188. doi: 10.1152/jn.01248.2004

Matsuzaki, M., Honkura, N., Ellis-Davies, G. C. R., and Kasai, H. (2004). Structural basis of long-term potentiation in single dendritic spines. *Nature* 429, 761–766. doi: 10.1038/nature02617

Mauss, A., Tripodi, M., Evers, J. F., and Landgraf, M. (2009). Midline signalling systems direct the formation of a neural map by dendritic targeting in the Drosophila motor system. *PLoS Biol.* 7:e1000200. doi: 10.1371/journal.pbio.1000200

McLean, D. L., Fan, J., Higashijima, S.-I., Hale, M. E., and Fetcho, J. R. (2007). A topographic map of recruitment in spinal cord. *Nature* 446, 71–75. doi: 10.1038/nature05588

McLean, D. L., Masino, M. A., Koh, I. Y., Lindquist, W. B., and Fetcho, J. R. (2008). Continuous shifts in the active set of spinal interneurons during changes in locomotor speed. *Nature* 11, 1419–1429. doi: 10.1038/nn.2225

Meer, D. P., and Buchanan, J. T. (1992). Apamin reduces the late afterhyperpolarization of lamprey spinal neurons, with little effect on fictive swimming. *Neurosci. Lett.* 143, 1–4. doi: 10.1016/0304-3940(92)90219-w

Menelaou, E., and McLean, D. L. (2012). A gradient in endogenous rhythmicity and oscillatory drive matches recruitment order in an axial motor pool. *J. Neurosci.* 32, 10925–10939. doi: 10.1523/JNEUROSCI.1809-12.2012

Migliore, M., and Shepherd, G. M. (2002). Emerging rules for the distributions of active dendritic conductances. *Nat. Rev. Neurosci.* 3, 362–370. doi: 10.1038/nrn810

Mills, L. R., Niesen, C. E., So, A. P., Carlen, P. L., Spigelman, I., and Jones, O. T. (1994). N-type Ca2+ channels are located on somata, dendrites and a subpopulation of dendritic spines on live hippocampal pyramidal neurons. *J. Neurosci.* 14, 6815–6824.

Müller, D. J., Helenius, J., Alsteens, D., and Dufrêne, Y. F. (2009). Force probing surfaces of living cells to molecular resolution. *Nat. Chem. Biol.* 5, 383–390. doi: 10.1038/nchembio.181

Muto, A., Ohkura, M., Kotani, T., Higashijima, S.-I., Nakai, J., and Kawakami, K. (2011). Genetic visualization with an improved GCaMP calcium indicator reveals spatiotemporal activation of the spinal motor neurons in zebrafish. *Proc. Natl. Acad. Sci. U S A* 108, 5425–5430. doi: 10.1073/pnas.1000887108

Nakamura, K., and Yokotani, K. (2010). Presynaptic BK type Ca2+-activated K+ channels are involved in prostanoid TP receptor-mediated inhibition of

noradrenaline release from the rat gastric sympathetic nerves. *Eur. J. Pharmacol.* 629, 111–117. doi: 10.1016/j.ejphar.2009.11.056

Nanou, E., Alpert, M. H., Alford, S., and El Manira, A. (2013). Differential regulation of synaptic transmission by pre- and postsynaptic SK channels in the spinal locomotor network. *J. Neurophysiol.* 109, 3051–3059. doi: 10.1152/jn.00067.2013

Nevian, T., and Sakmann, B. (2004). Single spine Ca2+ signals evoked by coincident EPSPs and backpropagating action potentials in spiny stellate cells of layer 4 in the juvenile rat somatosensory barrel cortex. *J. Neurosci.* 24, 1689–1699. doi: 10.1523/jneurosci.3332-03.2004

Ngo-Anh, T. J., Bloodgood, B. L., Lin, M., Sabatini, B. L., Maylie, J., and Adelman, J. P. (2005). SK channels and NMDA receptors form a Ca2+-mediated feedback loop in dendritic spines. *Nat. Neurosci.* 8, 642–649. doi: 10.1038/nn1449

Nimchinsky, E. A., Sabatini, B. L., and Svoboda, K. (2002). Structure and function of dendritic spines. *Annu. Rev. Physiol.* 64, 313–353. doi: 10.1146/annurev.physiol.64.081501.160008

Noga, B. R., Kriellaars, D. J., Brownstone, R. M., and Jordan, L. M. (2003). Mechanism for activation of locomotor centers in the spinal cord by stimulation of the mesencephalic locomotor region. *J. Neurophysiol.* 90, 1464–1478. doi: 10.1152/jn.00034.2003

Ohtsuki, G., Piochon, C., Adelman, J. P., and Hansel, C. (2012). SK2 channel modulation contributes to compartment-specific dendritic plasticity in cerebellar purkinje cells. *Neuron* 75, 108–120. doi: 10.1016/j.neuron.2012.05.025

Okado, N., Homma, S., Ishihara, R., and Kohno, K. (1990). Distribution patterns of dendrites in motor neuron pools of lumbosacral spinal cord of the chicken. *Anat. Embryol. (Berl)* 182, 113–121. doi: 10.1007/bf00174012

Patneau, D. K., and Mayer, M. L. (1990). Structure-activity relationships for amino acid transmitter candidates acting at N-methyl-D-aspartate and quisqualate receptors. *J. Neurosci.* 10, 2385–2399.

Placantonakis, D. G., and Welsh, J. P. (2001). Two distinct oscillatory states determined by the NMDA receptor in rat inferior olive. *J. Physiol.* 534, 123–140. doi: 10.1111/j.1469-7793.2001.t01-1-00123.x

Plotkin, J. L., Shen, W., Rafalovich, I., Sebel, L. E., Day, M., Chan, C. S., et al. (2013). Regulation of dendritic calcium release in striatal spiny projection neurons. *J. Neurophysiol.* 110, 2325–2336. doi: 10.1152/jn.00422.2013

Poirazi, P., Brannon, T., and Mel, B. W. (2003). Pyramidal neuron as two-layer neural network. *Neuron* 37, 989–999. doi: 10.1016/s0896-6273(03)00149-1

Poirazi, P., and Mel, B. W. (2001). Impact of active dendrites and structural plasticity on the memory capacity of neural tissue. *Neuron* 29, 779–796. doi: 10.1016/s0896-6273(01)00252-5

Polsky, A., Mel, B. W., and Schiller, J. (2004). Computational subunits in thin dendrites of pyramidal cells. *Nat. Neurosci.* 7, 621–627. doi: 10.1038/nn1253

Pouille, F., and Scanziani, M. (2004). Routing of spike series by dynamic circuits in the hippocampus. *Nature* 429, 717–723. doi: 10.1038/nature02615

Riffell, J. A., Lei, H., and Hildebrand, J. G. (2009). Neural correlates of behavior in the moth Manduca sexta in response to complex odors. *Proc. Natl. Acad. Sci. U S A* 106, 19219–19226. doi: 10.1073/pnas.0910592106

Roberts, W. M. (1993). Spatial calcium buffering in saccular hair cells. *Curr. Opin. Neurobiol.* 363, 74–76. doi: 10.1038/363074a0

Roberts, A., and Alford, S. T. (1986). Descending projections and excitation during fictive swimming in Xenopus embryos: neuroanatomy and lesion experiments. *J. Comp. Neurol.* 250, 253–261. doi: 10.1002/cne.902500212

Roberts, A., Conte, D., Hull, M., Merrison-Hort, R., al Azad, A. K., Buhl, E., et al. (2014). Can simple rules control development of a pioneer vertebrate neuronal network generating behavior? *J. Neurosci.* 34, 608–621. doi: 10.1523/JNEUROSCI.3248-13.2014

Roberts, A., Kahn, J. A., Soffe, S. R., and Clarke, J. D. (1981). Neural control of swimming in a vertebrate. *Science* 213, 1032–1034. doi: 10.1126/science.7196599

Rossignol, S., Bouyer, L., Barthélemy, D., Langlet, C., and Leblond, H. (2002). Recovery of locomotion in the cat following spinal cord lesions. *Brain Res. Brain Res. Rev.* 40, 257–266. doi: 10.1016/s0165-0173(02)00208-4

Rossignol, S., Chau, C., Brustein, E., Giroux, N., Bouyer, L., Barbeau, H., et al. (1998). Pharmacological activation and modulation of the central pattern generator for locomotion in the cat. *Ann. N Y Acad. Sci.* 860, 346–359. doi: 10.1111/j.1749-6632.1998.tb09061.x

Rovainen, C. M. (1974). Synaptic interactions of identified nerve cells in the spinal cord of the sea lamprey. *J. Comp. Neurol.* 154, 189–206. doi: 10.1002/cne.901540206

Rybak, I. A., Shevtsova, N. A., Lafreniere-Roula, M., and McCrea, D. A. (2006). Modelling spinal circuitry involved in locomotor pattern generation: insights from deletions during fictive locomotion. *J. Physiol.* 577, 617–639. doi: 10.1113/jphysiol.2006.118703

Sah, P., and Bekkers, J. M. (1996). Apical dendritic location of slow afterhyperpolarization current in hippocampal pyramidal neurons: implications for the integration of long-term potentiation. *J. Neurosci.* 16, 4537–4542.

Sailer, C. A., Kaufmann, W. A., Marksteiner, J., and Knaus, H.-G. (2004). Comparative immunohistochemical distribution of three small-conductance Ca2+-activated potassium channel subunits, SK1, SK2 and SK3 in mouse brain. *Mol. Cell. Neurosci.* 26, 458–469. doi: 10.1016/j.mcn.2004.03.002

Schiller, J., and Schiller, Y. (2001). NMDA receptor-mediated dendritic spikes and coincident signal amplification. *Curr. Opin. Neurobiol.* 11, 343–348. doi: 10.1016/s0959-4388(00)00217-8

Schiller, J., Schiller, Y., Stuart, G., and Sakmann, B. (1997). Calcium action potentials restricted to distal apical dendrites of rat neocortical pyramidal neurons. *J. Physiol.* 505(Pt. 3), 605–616. doi: 10.1111/j.1469-7793.1997.605ba.x

Schotland, J., and Grillner, S. (1993). Effects of serotonin on fictive locomotion coordinated by a neural network deprived of NMDA receptor-mediated cellular properties. *Exp. Brain Res.* 93, 391–398. doi: 10.1007/bf00229355

Schotland, J. L., Shupliakov, O., Grillner, S., and Brodin, L. (1996). Synaptic and nonsynaptic monoaminergic neuron systems in the lamprey spinal cord. *J. Comp. Neurol.* 372, 229–244. doi: 10.1002/(sici)1096-9861(19960819)372:2<229::aid-cne6>3.3.co;2-j

Schotland, J., Shupliakov, O., Wikström, M., Brodin, L., Srinivasan, M., You, Z. B., et al. (1995). Control of lamprey locomotor neurons by colocalized monoamine transmitters. *Nature* 374, 266–268. doi: 10.1038/374266a0

Schwartz, E. J., Blackmer, T., Gerachshenko, T., and Alford, S. (2007). Presynaptic G-protein-coupled receptors regulate synaptic cleft glutamate via transient vesicle fusion. *J. Neurosci.* 27, 5857–5868. doi: 10.1523/jneurosci.1160-07.2007

Schwartz, E. J., Gerachshenko, T., and Alford, S. (2005). 5-HT prolongs ventral root bursting via presynaptic inhibition of synaptic activity during fictive locomotion in lamprey. *J. Neurophysiol.* 93, 980–988. doi: 10.1152/jn.00669.2004

Shah, M. M., and Haylett, D. G. (2002). K+ currents generated by NMDA receptor activation in rat hippocampal pyramidal neurons. *J. Neurophysiol.* 87, 2983–2989.

Sholomenko, G. N., and Steeves, J. D. (1987). Effects of selective spinal cord lesions on hind limb locomotion in birds. *Exp. Neurol.* 95, 403–418. doi: 10.1016/0014-4886(87)90148-8

Sigvardt, K. A., Grillner, S., Wallén, P., and Van Dongen, P. A. (1985). Activation of NMDA receptors elicits fictive locomotion and bistable membrane properties in the lamprey spinal cord. *Brain Res.* 336, 390–395. doi: 10.1016/0006-8993(85)90676-6

Sirota, M. G., Di Prisco, G. V., and Dubuc, R. (2000). Stimulation of the mesencephalic locomotor region elicits controlled swimming in semi-intact lampreys. *Eur. J. Neurosci.* 12, 4081–4092. doi: 10.1046/j.1460-9568.2000.00301.x

Smith, J. J., Kuraku, S., Holt, C., Sauka-Spengler, T., Jiang, N., Campbell, M. S., et al. (2013a). Sequencing of the sea lamprey (Petromyzon marinus) genome provides insights into vertebrate evolution. *Nat. Genet.* 45, 415–421, 421e1–421e2. doi: 10.1038/ng.2568

Smith, S. L., Smith, I. T., Branco, T., and Häusser, M. (2013b). Dendritic spikes enhance stimulus selectivity in cortical neurons in vivo. *Nature* 503, 115–120. doi: 10.1038/nature12600

Spruston, N. (2008). Pyramidal neurons: dendritic structure and synaptic integration. *Nat. Rev. Neurosci.* 9, 206–221. doi: 10.1038/nrn2286

Stackman, R. W., Hammond, R. S., Linardatos, E., Gerlach, A., Maylie, J., Adelman, J. P., et al. (2002). Small conductance Ca2+-activated K+ channels modulate synaptic plasticity and memory encoding. *J. Neurosci.* 22, 10163–10171.

Stuart, G. J., and Häusser, M. (2001). Dendritic coincidence detection of EPSPs and action potentials. *Nat. Neurosci.* 4, 63–71. doi: 10.1038/82910

Stuart, G., Spruston, N., Sakmann, B., and Häusser, M. (1997). Action potential initiation and backpropagation in neurons of the mammalian CNS. *Trends Neurosci.* 20, 125–131. doi: 10.1016/s0166-2236(96)10075-8

Svensson, E., Grillner, S., and Parker, D. (2001). Gating and braking of short- and long-term modulatory effects by interactions between colocalized neuromodulators. *J. Neurosci.* 21, 5984–5992.

Svoboda, K., Denk, W., Kleinfeld, D., and Tank, D. W. (1997). In vivo dendritic calcium dynamics in neocortical pyramidal neurons. *Nature* 385, 161–165. doi: 10.1038/385161a0

Svoboda, K., Tank, D. W., and Denk, W. (1996). Direct measurement of coupling between dendritic spines and shafts. *Science* 272, 716–719. doi: 10.1126/science.272.5262.716

Takahashi, N., Kitamura, K., Matsuo, N., Mayford, M., Kano, M., Matsuki, N., et al. (2012). Locally synchronized synaptic inputs. *Science* 335, 353–356. doi: 10.1126/science.1210362

Takahashi, H., and Magee, J. C. (2009). Pathway interactions and synaptic plasticity in the dendritic tuft regions of CA1 pyramidal neurons. *Neuron* 62, 102–111. doi: 10.1016/j.neuron.2009.03.007

Topolnik, L., Chamberland, S., Pelletier, J.-G., Ran, I., and Lacaille, J.-C. (2009). Activity-dependent compartmentalized regulation of dendritic Ca2+ signaling in hippocampal interneurons. *J. Neurosci.* 29, 4658–4663. doi: 10.1523/jneurosci.0493-09.2009

Vaidya, S. P., and Johnston, D. (2013). Temporal synchrony and gamma-to-theta power conversion in the dendrites of CA1 pyramidal neurons. *Nat. Neurosci.* 16, 1812–1820. doi: 10.1038/nn.3562

Viana di Prisco, G., and Alford, S. (2004). Quantitative investigation of calcium signals for locomotor pattern generation in the lamprey spinal cord. *J. Neurophysiol.* 92, 1796–1806. doi: 10.1152/jn.00138.2004

Vonhoff, F., and Duch, C. (2010). Tiling among stereotyped dendritic branches in an identified Drosophila motoneuron. *J. Comp. Neurol.* 518, 2169–2185. doi: 10.1002/cne.22380

Vrieseling, E., and Arber, S. (2006). Target-induced transcriptional control of dendritic patterning and connectivity in motor neurons by the ETS gene Pea3. *Cell* 127, 1439–1452. doi: 10.1016/j.cell.2006.10.042

Wall, M. J., and Dale, N. (1995). A slowly activating Ca(2+)-dependent K+ current that plays a role in termination of swimming in Xenopus embryos. *J. Physiol.* 487(Pt. 3), 557–572.

Wallén, P., Buchanan, J. T., Grillner, S., Hill, R. H., Christenson, J., and Hökfelt, T. (1989). Effects of 5-hydroxytryptamine on the afterhyperpolarization, spike frequency regulation and oscillatory membrane properties in lamprey spinal cord neurons. *J. Neurophysiol.* 61, 759–768.

Wallén, P., Ekeberg, O., Lansner, A., Brodin, L., Tråvén, H., and Grillner, S. (1992). A computer-based model for realistic simulations of neural networks. II. The segmental network generating locomotor rhythmicity in the lamprey. *J. Neurophysiol.* 68, 1939–1950.

Wallén, P., and Grillner, S. (1987). N-methyl-D-aspartate receptor-induced, inherent oscillatory activity in neurons active during fictive locomotion in the lamprey. *J. Neurosci.* 7, 2745–2755.

Wallén, P., and Williams, T. L. (1984). Fictive locomotion in the lamprey spinal cord in vitro compared with swimming in the intact and spinal animal. *J. Physiol.* 347, 225–239.

Wang, X. J. (2001). Synaptic reverberation underlying mnemonic persistent activity. *Trends Neurosci.* 24, 455–463. doi: 10.1016/s0166-2236(00)01868-3

Wang, X.-J. (2010). Neurophysiological and computational principles of cortical rhythms in cognition. *Physiol. Rev.* 90, 1195–1268. doi: 10.1152/physrev.00035.2008

Wang, D., Grillner, S., and Wallén, P. (2013). Calcium dynamics during NMDA-induced membrane potential oscillations in lamprey spinal neurons—contribution of L-type calcium channels (CaV1.3). *J. Physiol.* 591, 2509–2521. doi: 10.1113/jphysiol.2012.248526

Wang, D., Grillner, S., and Wallén, P. (2014a). Endogenous release of 5-HT modulates the plateau phase of NMDA-induced membrane potential oscillations in lamprey spinal neurons. *J. Neurophysiol.* 112, 30–38. doi: 10.1152/jn.00582.2013

Wang, K., Lin, M. T., Adelman, J. P., and Maylie, J. (2014b). Distinct Ca2+ sources in dendritic spines of hippocampal CA1 neurons couple to SK and Kv4 channels. *Neuron* 81, 379–387. doi: 10.1016/j.neuron.2013.11.004

Wehr, M., and Laurent, G. (1996). Odour encoding by temporal sequences of firing in oscillating neural assemblies. *Nature* 384, 162–166. doi: 10.1038/384162a0

Wei, A. D., Gutman, G. A., Aldrich, R., Chandy, K. G., Grissmer, S., and Wulff, H. (2005). International Union of pharmacology. LII. Nomenclature and molecular relationships of calcium-activated potassium channels. *Pharmacol. Rev.* 57, 463–472. doi: 10.1124/pr.57.4.9

Wei, D. S., Mei, Y. A., Bagal, A., Kao, J. P., Thompson, S. M., and Tang, C. M. (2001). Compartmentalized and binary behavior of terminal dendrites in hippocampal pyramidal neurons. *Science* 293, 2272–2275. doi: 10.1126/science.1061198

Weiler, N., Wood, L., Yu, J., Solla, S. A., and Shepherd, G. M. G. (2008). Top-down laminar organization of the excitatory network in motor cortex. *Nat. Neurosci.* 11, 360–366. doi: 10.1038/nn2049

Westenbroek, R. E., Ahlijanian, M. K., and Catterall, W. A. (1990). Clustering of L-type Ca2+ channels at the base of major dendrites in hippocampal pyramidal neurons. *Nature* 347, 281–284. doi: 10.1038/347281a0

Westenbroek, R. E., Hell, J. W., Warner, C., Dubel, S. J., Snutch, T. P., and Catterall, W. A. (1992). Biochemical properties and subcellular distribution of an N-type calcium channel alpha 1 subunit. *Neuron* 9, 1099–1115. doi: 10.1016/0896-6273(92)90069-p

Wikström, M., Hill, R., Hellgren, J., and Grillner, S. (1995). The action of 5-HT on calcium-dependent potassium channels and on the spinal locomotor network in lamprey is mediated by 5-HT1A-like receptors. *Brain Res.* 678, 191–199. doi: 10.1016/0006-8993(95)00183-q

Wikström, M. A., and El Manira, A. (1998). Calcium influx through N- and P/Q-type channels activate apamin-sensitive calcium-dependent potassium channels generating the late afterhyperpolarization in lamprey spinal neurons. *Eur. J. Neurosci.* 10, 1528–1532. doi: 10.1046/j.1460-9568.1998.00194.x

Williams, T. L. (1992). Phase coupling by synaptic spread in chains of coupled neuronal oscillators. *Science* 258, 662–665. doi: 10.1126/science.1411575

Williams, S. R., and Stuart, G. J. (2003). Role of dendritic synapse location in the control of action potential output. *Trends Neurosci.* 26, 147–154. doi: 10.1016/s0166-2236(03)00035-3

Womelsdorf, T., Valiante, T. A., Sahin, N. T., Miller, K. J., and Tiesinga, P. (2014). Dynamic circuit motifs underlying rhythmic gain control, gating and integration. *Nat. Neurosci.* 17, 1031–1039. doi: 10.1038/nn.3764

Xu, N.-L., Harnett, M. T., Williams, S. R., Huber, D., O'Connor, D. H., Svoboda, K., et al. (2012). Nonlinear dendritic integration of sensory and motor input during an active sensing task. *Nature* 492, 247–251. doi: 10.1038/nature11601

Yamada, S.-I., Takechi, H., Kanchiku, I., Kita, T., and Kato, N. (2004). Small-conductance Ca2+-dependent K+ channels are the target of spike-induced Ca2+ release in a feedback regulation of pyramidal cell excitability. *J. Neurophysiol.* 91, 2322–2329. doi: 10.1152/jn.01049.2003

Yuste, R., and Denk, W. (1995). Dendritic spines as basic functional units of neuronal integration. *Nature* 375, 682–684. doi: 10.1038/375682a0

Yuste, R., MacLean, J. N., Smith, J., and Lansner, A. (2005). The cortex as a central pattern generator. *Nat. Rev. Neurosci.* 6, 477–483. doi: 10.1038/nrn1686

Zhang, W., and Grillner, S. (2000). The spinal 5-HT system contributes to the generation of fictive locomotion in lamprey. *Brain Res.* 879, 188–192. doi: 10.1016/s0006-8993(00)02747-5

Zhang, W., Pombal, M. A., El Manira, A., and Grillner, S. (1996). Rostrocaudal distribution of 5-HT innervation in the lamprey spinal cord and differential effects of 5-HT on fictive locomotion. *J. Comp. Neurol.* 374, 278–290. doi: 10.1002/(sici)1096-9861(19961014)374:2<278::aid-cne9>3.0.co;2-#

Conflict of Interest Statement: The authors declare that the research was conducted in the absence of any commercial or financial relationships that could be construed as a potential conflict of interest.

Received: 30 June 2014; accepted: 31 August 2014; published online: 18 September 2014.

Citation: Alford ST and Alpert MH (2014) A synaptic mechanism for network synchrony. Front. Cell. Neurosci. ***8****:290. doi: 10.3389/fncel.2014.00290*

This article was submitted to the journal Frontiers in Cellular Neuroscience.

frontiers in Cellular Neuroscience

REVIEW
published: 24 March 2015
doi: 10.3389/fncel.2015.00067

Contribution of sublinear and supralinear dendritic integration to neuronal computations

*Alexandra Tran-Van-Minh[1], Romain D. Cazé[2,3], Therése Abrahamsson[1,4], Laurence Cathala[5], Boris S. Gutkin[2,6] and David A. DiGregorio[1]**

[1] Unit of Dynamic Neuronal Imaging, Department of Neuroscience, CNRS UMR 3571, Institut Pasteur, Paris, France, [2] Group for Neural Theory, LNC INSERM U960, Institut d'Etude de la Cognition de l'Ecole normale supérieure, Ecole normale supérieure, Paris, France, [3] Department of Bioengineering, Imperial College London, London, UK, [4] Center for Research in Neuroscience, Department of Neurology and Neurosurgery, The Research Institute of the McGill University Health Centre, Montreal General Hospital, Montreal, QC, Canada, [5] Sorbonne Universités, UPMC Univ Paris 6, UMR 8256 B2A, Team Brain Development, Repair and Aging, Paris, France, [6] Federal Research University Higher School of Economics, Moscow, Russia

Nonlinear dendritic integration is thought to increase the computational ability of neurons. Most studies focus on how supralinear summation of excitatory synaptic responses arising from clustered inputs within single dendrites result in the enhancement of neuronal firing, enabling simple computations such as feature detection. Recent reports have shown that sublinear summation is also a prominent dendritic operation, extending the range of subthreshold input-output (sI/O) transformations conferred by dendrites. Like supralinear operations, sublinear dendritic operations also increase the repertoire of neuronal computations, but feature extraction requires different synaptic connectivity strategies for each of these operations. In this article we will review the experimental and theoretical findings describing the biophysical determinants of the three primary classes of dendritic operations: linear, sublinear, and supralinear. We then review a Boolean algebra-based analysis of simplified neuron models, which provides insight into how dendritic operations influence neuronal computations. We highlight how neuronal computations are critically dependent on the interplay of dendritic properties (morphology and voltage-gated channel expression), spiking threshold and distribution of synaptic inputs carrying particular sensory features. Finally, we describe how global (scattered) and local (clustered) integration strategies permit the implementation of similar classes of computations, one example being the object feature binding problem.

Keywords: dendrites, neural computation, nonlinear transformations, Boolean analysis, binary neruons, uncaging, input-output transformation, votlage activated channels

OPEN ACCESS

Edited by:
Sergey M. Korogod, International Center for Molecular Physiology, National Academy of Sciences of Ukraine, Ukraine

Reviewed by:
Kenji Morita, The University of Tokyo, Japan
Alain Destexhe, Unité de Neurosciences, Information and Complexité Centre National de la Recherche Scientifique, France

****Correspondence:***
David A. DiGregorio, Unit of Dynamic Neuronal Imaging, Department of Neuroscience, CNRS UMR 3571, Institut Pasteur, 25 rue du Dr Roux, 75724 Paris Cedex 15, France
david.digregorio@pasteur.fr

Received: *15 October 2014*
Accepted: *13 February 2015*
Published: *24 March 2015*

Citation:
Tran-Van-Minh A, Cazé RD, Abrahamsson T, Cathala L, Gutkin BS and DiGregorio DA (2015) Contribution of sublinear and supralinear dendritic integration to neuronal computations. Front. Cell. Neurosci. 9:67. doi: 10.3389/fncel.2015.00067

Introduction

In order to control behavior, the brain relies on the ability of its neuronal networks to process information arising from external and internal sources. How single neurons decode combinations of sensory features and transform them into a spiking output is still unknown, and represents a subject of intense study. The complexity of the single neuronal coding problem can be illustrated by the paradoxical finding that neurons exhibiting narrowly tuned receptive fields often appear to be driven by synaptic inputs that themselves are broadly tuned (Chadderton et al., 2014). One hypothesis is that nonlinear dendritic transformations are critical for such neuronal computations.

Decades of experimental and modeling studies on dendrites have led to the consensus that active properties of dendrites are primarily responsible for nonlinear integration, in particular **supralinear** operations (Mel, 1994; Spruston and Kath, 2004; Johnston and Narayanan, 2008). Nonetheless other findings indicate that **sublinear** integration of synaptic inputs is possible in multiple neuron types, and results from either active (Cash and Yuste, 1998; Hu et al., 2010) or passive dendritic properties (Abrahamsson et al., 2012; Vervaeke et al., 2012).

What is the evidence that nonlinear dendritic properties contribute to neuronal computations? Numerical simulations suggest that supralinear dendritic operations are essential for translation-invariant orientation tuning (Mel et al., 1998) and binocular disparity tuning (Archie and Mel, 2000), while sublinear dendritic operations contribute to coincidence detection of auditory stimuli (Agmon-Snir et al., 1998). Recently, state-of-the-art *in vivo* recordings have shown that dendritic supralinearities are associated with various other neuronal computations: formation of hippocampal place fields (Lee et al., 2012), detection of multi-modal sensory stimuli (Xu et al., 2012), angular tuning of barrel cortex pyramidal neurons (Lavzin et al., 2012), and enhancement of orientation tuning (Smith et al., 2013). Sublinear operations have also been shown to underlie orientation selectivity of binocular neurons in visual cortex *in vivo* (Longordo et al., 2013).

Nevertheless, a direct link between the dendritic transformations and the associated neuronal computations is still lacking. Analytical methods implementing mathematical approximations of measured dendritic operations can be used to make estimates of the possible number and type of neuronal computations. For example, binary neuron models were used to quantify what was previously shown with biophysical models (Mel, 1994), namely that nonlinear dendrites support a larger number of neuronal computations (Poirazi and Mel, 2001; Cazé et al., 2013). Such simplifications can provide analytical insight and make testable predictions as to which computations are made possible by dendritic operations. Moreover, analytical methods show under which conditions the expanded computational capacities are generic, i.e., not tied to the specific example parameters of the biophysical model.

Here we review the biophysical determinants of different classes of dendritic operations (linear, sublinear and supralinear), how they are measured experimentally, and finally, using a recently published Boolean-based analysis of equivalent dendritic trees (Cazé et al., 2012, 2013, 2014), we review how these operations combine with other cellular properties to determine neuronal computations.

Dendritic Integration

Neurons integrate synaptic inputs arriving primarily on dendritic trees carrying information from presynaptic neurons, by transforming them into synaptic potentials using a variety of cell-specific synaptic and cellular mechanisms. During synaptic transmission, the activation of neurotransmitter-gated conductances results in either a transient depolarization or hyperpolarization of the postsynaptic membrane potential. When the net depolarization resulting from **synaptic integration** of multiple synaptic inputs is greater than the spike threshold potential, the neuron generates an **action potential** (AP), or **spike**. Synaptic integration is a critical determinant of **neuronal computations**, the process by which a postsynaptic neuron transforms presynaptic information (coded in input activation patterns) into an output signal (encoded in a firing pattern) (Häusser and Mel, 2003; London and Häusser, 2005; Silver, 2010; Larkum, 2013; Chadderton et al., 2014). This review will focus primarily on the integration of excitatory post-synaptic potentials (EPSPs) mediated by ionotropic glutamate receptors.

Dendritic integration can be quantified by comparing the **observed** depolarization resulting from the simultaneous activation of the same synaptic inputs (**Figure 1B**), also called a compound EPSP, and the arithmetic sum of individual EPSPs (**expected** membrane depolarization) (**Figure 1C**). The dendritic subthreshold input-output (sI/O) relationship is easily described by plotting observed vs. expected depolarizations for different numbers of co-activated synapses (**Figure 1**). Mathematical functions can be used to describe the **operation** performed. The sI/O relationships fall into three categories of dendritic operations: (1) **linear**, where the observed depolarization equals the expected depolarization; (2) **supralinear**, where the observed depolarization exceeds the expected depolarization (above the linear line; **Figure 1D**, left); and (3) **sublinear**, where the observed depolarization is less than the expected depolarization (below the linear line; **Figure 1D**, right). Much of the experimental evidence of nonlinear integration suggests dendrites perform **supralinear** operations, resulting from the contribution of active dendritic conductances (Mel, 1994; Johnston and Narayanan, 2008; Spruston, 2008). Recent studies suggest that **sublinear** operations could be mediated solely by passive properties (Abrahamsson et al., 2012; Vervaeke et al., 2012), while other studies have shown that activation of potassium channels can produce sublinear summation (Cash and Yuste, 1999; Hu et al., 2010). The detailed biophysical mechanisms determining specific dendritic operations are discussed in depth below.

The type of **dendritic operation** strongly contributes to the nature of the resultant **neuronal computation**. For example, co-activation of synapses within a single electrical compartment that exhibits supralinear integration will produce dendritic voltage signals that are larger than expected due to amplification by activation of voltage-sensitive channels. This large depolarization is thereby more likely to drive the neuron to spike threshold. The resulting sI/O will reflect a neuronal computation that is **cluster sensitive** (**Figures 1E,F**, left, θ_1). For a neuron with sublinear dendrites, clustered synaptic activity will be less efficient at triggering a spike than if the same inputs were distributed in different compartments, thus promoting computations that are **scatter sensitive** (**Figures 1E,F**, right, θ_1; Cazé et al., 2013). Such neuronal computations enable the discrimination of patterns of synaptic activation with different levels of spatial and temporal correlations, which could not be otherwise performed by linear dendrites (Mel, 1992). Nevertheless, it should be noted that the dendritic operation is insufficient to define the computation, synaptic placement and spike threshold also influence the final

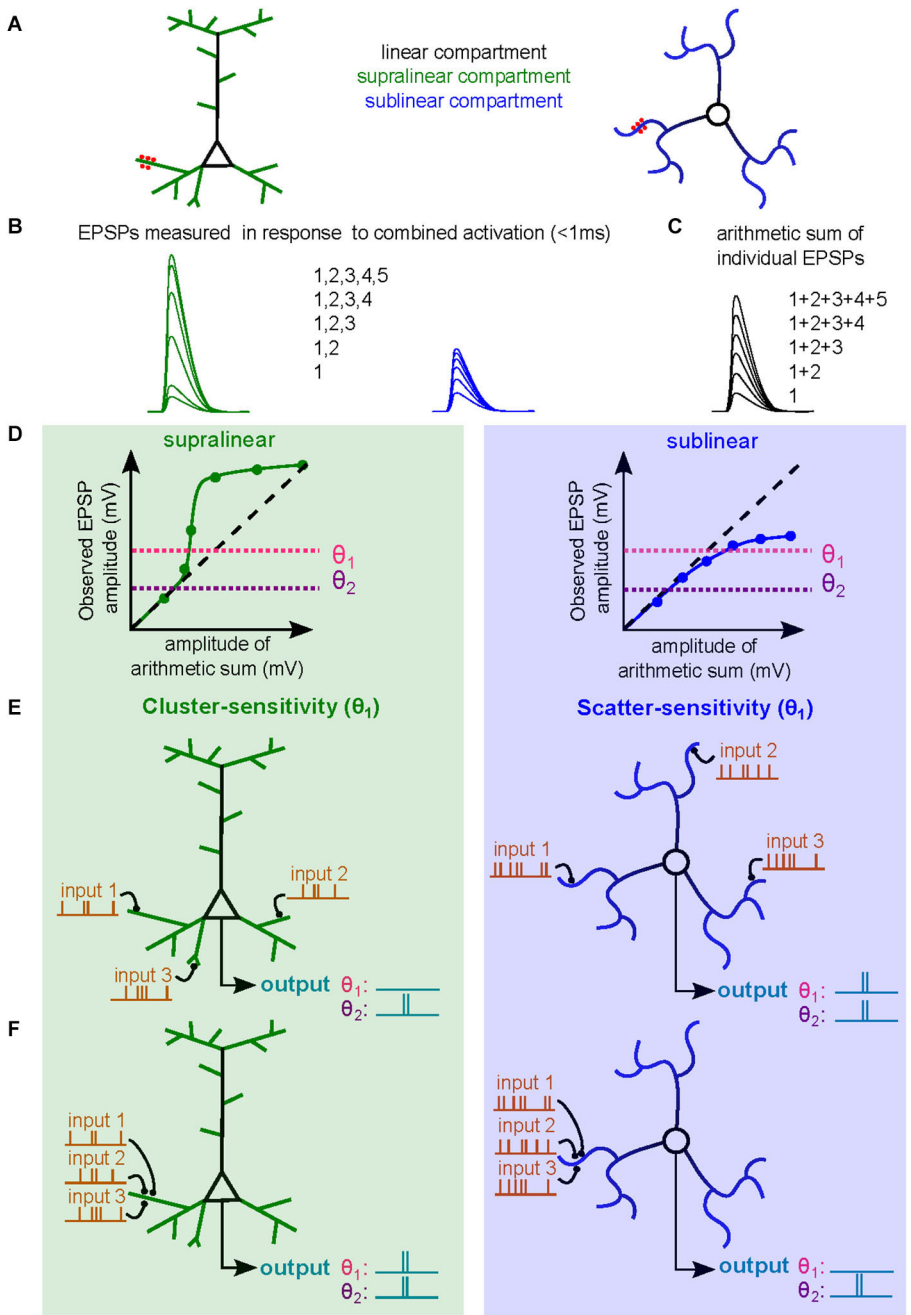

FIGURE 1 | Dendritic operations and their influence on neuronal firing. **(A)** Schematic diagram of a subthreshold synaptic input-output experiment in a neuron with supralinear dendritic compartments (*left*, supralinear compartments in green, linear compartments in black) or in a neuron with sublinear dendritic compartments (*right*, sublinear compartments in blue). The red spots are sites of synaptic activation or sites of glutamate uncaging. **(B)** Somatic voltage responses evoked by simultaneous synaptic activation or uncaging. Green curves are responses evoked with increasing number of synapses activated within a supralinear dendrites. Blue traces are similarly obtained within a sublinear dendrite. **(C)** Arithmetic sum of individual responses to synaptic activation or uncaging. **(D)** Subthreshold input/output relationships (sI/O) used to quantify dendritic operations. The dashed line represents a linear releationship. Two horizontal dotted lines indicate two example somatic spike thresholds (θ_1 and θ_2). **(E,F)** Example of synaptic integration of three synaptic inputs distributed across the dendritic tree **(E)** or clustered on a single dendritic branch **(F)** of a neuron with supralinear dendritic compartments (*left*) or sublinear compartments (*right*). The output spike train, and hence neuronal computation, differs depending on the threshold. The more depolarized threshold value (θ_1) allows the neuron with supralinear dendrites to exhibit a cluster-sensitive neuronal computation (fires only when three inputs are activated in the same compartment). The θ_1 threshold also allows a neuron with sublinear dendrites to exhibit scatter-sensitive neuronal computations. The lower threshold (θ_2) imparts a different neuronal computation based on simple linear summation and is not sensitive to activated synapse location.

neuronal computation. In **Figures 1D–F** we show that lowering the spike threshold (θ_2) would restrict the access to only the linear regime of the subthreshold dendritic operation. Finally, ongoing synaptic activity can occur in the presence of AP firing, and thus constitutes supra-threshold synaptic integration (Silver, 2010), which we will not address in this review.

Biophysical Mechanisms Influencing Synaptic Integration

Effect of Passive Membrane Properties on EPSPs Summation

Because neurons communicate with each other using electrical signals, the analysis of their signaling properties is generally performed using principles of electrical circuits. A **single compartment** equivalent circuit describes well the electrical behavior of a cell without any dendrite or active properties. Four parameters determine the amplitude and time course of the EPSP: a transient synaptic conductance (G_{syn}), the electromotive force of its ion flux (driving force), the membrane resistance (specific membrane resistance; R_m), and the specific membrane capacitance (C_m). The difference between the membrane potential and the reversal potential for G_{syn} sets the driving force ($V_m - E_{rev}$; **Figure 2A**), thus as G_{syn} increases, I_{syn} increases, and V_m becomes more depolarized. For large conductances, V_m approaches E_{rev} and the driving force is reduced, resulting in decreased current flow for the same G_{syn} (**Figure 2A**). This results in a sublinear relationship between G_{syn} and EPSP size. Since quantal synaptic conductances are generally small, it is when multiple synapses are activated simultaneously that the driving force decreases sufficiently to produce sublinear integration (**Figure 2C**). Therefore, for passive single compartment model cells, synaptic summation is already essentially sublinear, which was first demonstrated at the neuromuscular junction (Martin, 1955).

More complex, but also more realistic, equivalent circuit models take into account neuronal morphology, such as dendritic arborizations. Wilfrid Rall pioneered the use of such multi-compartmental equivalent circuit models in order to study synaptic integration in neurons with **passive** dendrites. His primary advance was to consider dendrites as electrical cables (Rall, 1967) that contained an additional parameter, the axial resistance (r_a), which electrically couples multiple elementary single compartment models (**Figure 2B**). Because each elementary compartment will allow current to leak across the membrane, the current injected in the next compartment (across r_a) decreases progressively as it travels along the cable or dendrite, which results in an attenuation of the local EPSP amplitude and a slowing of its time course. Such **dendritic filtering** accounts for why local EPSPs in dendrites tend to be larger and faster than those recorded in the soma. It therefore follows that more distal synaptic inputs (for a given G_{syn}) would result in a progressively smaller somatic depolarization and thus a smaller influence on the firing output of a neuron (Rinzel and Rall, 1974; Magee and Cook, 2000; Spruston, 2008). Also in dendrites the **local input resistance (R_D) or impedance (Z_D**; to account for the effect of capacitance on fast time-varying inputs) increases with increasing distance from the soma due to a diminished shunt effect of the soma and the high resistance of the sealed cable (Rinzel and Rall, 1974). We will henceforth refer to Z_D, since it is the more general form that accounts for the capacitive current dependance on synaptic conductance time course. It should be noted that at steady state $Z_D = R_D$. This distance-dependent increase in Z_D results progressively larger local EPSPs, which in some morphologies, can combine with an efficient passive propagation of EPSPs to the soma (transfer impedance), thereby counteracting the distance-dependance reduction in the somatic EPSP amplitude due to cable filtering (Jaffe and Carnevale, 1999; Nevian et al., 2007; Schmidt-Hieber et al., 2007). This location independence of EPSP amplitude is also referred to as passive normalization (Jaffe and Carnevale, 1999). Distance-dependent increases in Z_D are also thought to be important to increase the probability of evoking a local dendritic spike at distal inputs of basal dendrites of pyramidal neurons, which can then propagate to the soma (Rudolph and Destexhe, 2003).

Rall provided a simple parameter that describes cable filtering: the space constant (λ), derived from the steady state (λ_{DC}) or frequency-dependent (λ_{AC}) solution to the cable equations. It represents the distance along a cable where the membrane potential is 63% of the maximal at the site of current injection. Therefore if the dendrite length is longer than λ, significant cable filtering can be expected; similarly, if the dendritic length is much shorter than λ then EPSPs propagating to the soma are filtered very little. A critical morphological parameter determining λ is the dendritic **diameter**, to which λ is proportional (**Figure 2B**); meaning a larger diameter produces a longer λ (**Figure 3A**, left). For fast synaptic conductances (rise and decay $<$2 ms), the capacitive current acts as a frequency-dependent shunt and can dramatically alter λ. In cerebellar molecular layer interneurons, for example, the frequency-dependent length constant (λ_{AC}) can be over a factor of 5 shorter than λ_{DC}. Their thin ($\sim$0.4 μm diameter), 100 μm long dendrites are electrically compact for steady-state depolarizations (with total length 3 times shorter than λ_{DC}, 300 μm). But for rapid synaptic conductances λ_{AC} is 50 μm (half the dendritic length), resulting in significant dendritic filtering of EPSPs for distances greater than 20 μm (Abrahamsson et al., 2012). **Dendritic branching** tends to shorten the space constant, since it effectively decreases the membrane resistance (acting like a shunt for current flow (**Figure 3A**; right; Abrahamsson et al., 2012). It is also worth noting that λ also serves as a rough indicator of the size of effective dendritic compartments. Synapses located within a distance of λ are more likely to interact than non-neighboring synapses (**Figure 2C**; Abrahamsson et al., 2012).

The Influence of Passive Dendrites on sI/Os

As described above, sublinear summation of simultaneously occurring EPSPs within an electrical compartment is a natural consequence of the loss of driving force for synaptic currents. Dendritic compartments with narrow diameters are particularly sensitive to this due to a high Z_D. Therefore when multiple dendritic synapses are activated simultaneously within a close proximity ($<\lambda$), the local depolarization resulting from the

activation of a given synaptic input will be large, thus decreasing the local driving force, resulting in a sublinear sI/O (**Figures 1D**, **2B**). As the **diameter** of the passive dendrite decreases, Z_D will increase and the local EPSPs will be even larger (Abrahamsson et al., 2012). One can use the equation for input resistance of an infinite cable to appreciate the influence of dendritic diameter (**Figure 2B**, equation 3). The larger Z_D causes a larger depolarization, thus the sublinear summation of synaptic inputs will be more prominent with fewer active inputs (**Figure 3A**, left; see also Rinzel and Rall, 1974). If the **distance of the synapse from the soma** increases, the current sink of the soma, the end effect of the dendrite and/or dendritic tapering will contribute to a distance-dependent increase in Z_D, together resulting in more pronounced sublinear sI/O curves particularly for more distal dendritic compartments (**Figure 3A**, middle). Finally, the number of dendritic branch points, despite increasing dendritic filtering, tends to decrease the local Z_D by adding a current sink, thus favoring a more linear sI/O (**Figure 3A**, right). Gap junctions have also been shown to reduce sublinear summation by providing a current sink (Vervaeke et al., 2012).

Although passive membrane properties are sufficient to produce sublinear dendritic operations, experimental evidence of such a mechanism has only recently been described (Abrahamsson et al., 2012; Vervaeke et al., 2012). The authors concluded that the combination of thin dendrites and low levels of expression of voltage-gated channels favors sublinear dendritic operations. In these neurons, sublinear summation is apparent even for as few as two active synapses

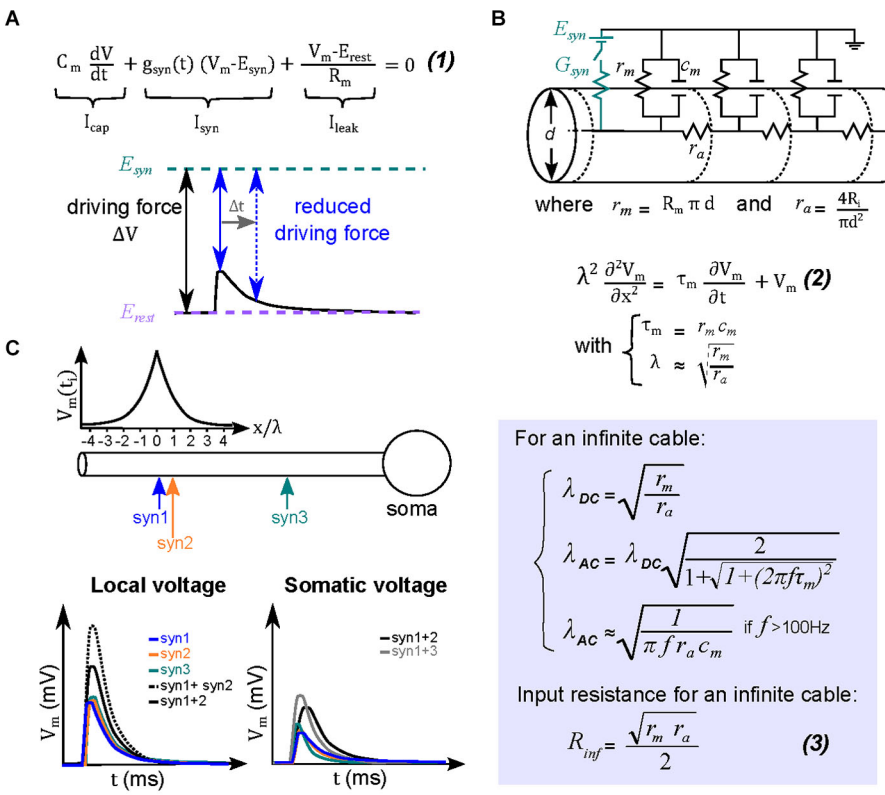

FIGURE 2 | Theoretical basis for sublinear summation within passive dendrites. (A) Equation (1) describes the different current components underlying an EPSP in a single electrical compartment. Integration of this equation describes the variation of the membrane voltage over time. The transient change in driving force ($\Delta V = V_m - E_{syn}$) is determined by the amplitude and time course of the local dendritic EPSP (black trace). At the peak of the EPSP (solid blue arrow) the driving force is maximally reduced, and then recovers back to that at resting membrane potentials during the EPSP decay (dotted blue arrow). The reduced driving force decreases the synaptic current, and hence the net depolarization, creating a sublinear relationship between EPSP and its underlying conductance. **(B)** Equivalent circuit for dendritic cables, where g_m and c_m are the membrane conductance and capacitance, respectively, and r_a is the axial resistance of a unit of cable. A synapse is represented in the circuit (by the synaptic conductance G_{syn} and the synaptic reversal potential E_{syn}). For an infinite cable, the spatio-temporal distribution of voltage is described by the relation (2), where τ_m is the membrane time constant, and λ is the length constant. The length constant relationships are derived from solving the cable equation (2) for step changes in membrane voltage (λ_{DC}) or for a sinusoidal membrane potential change (λ_{AC}). The latter is helpful to understand the dendritic filtering of transient EPSPs. Equation (3) is the relation for the input resistance R_D for an infinite cable. **(C)** *Top*, ball-and-stick model of a neuron with colored arrows indicating the location of three synapses (Syn 1–3). The graph above the diagram represents the peak amplitude of a dendritic EPSP as a function of distance. *Bottom*, the two graphs describe respectively the dendritic and somatic depolarizations in response to individual (colored lines) or combined synaptic inputs (black lines). Concomitant activation of two neighboring synaptic inputs (within $\sim \lambda_{AC}$) will therefore mutually reduce their driving force and sum sublinearly (for example synapses 1 and 2, solid black trace for the EPSP observed in response to their simultaneous activation, dashed black trace for the arithmetic sum of the individual EPSPs). More separated synapses will, however, sum more linearly (synapses 1 and 3, gray trace).

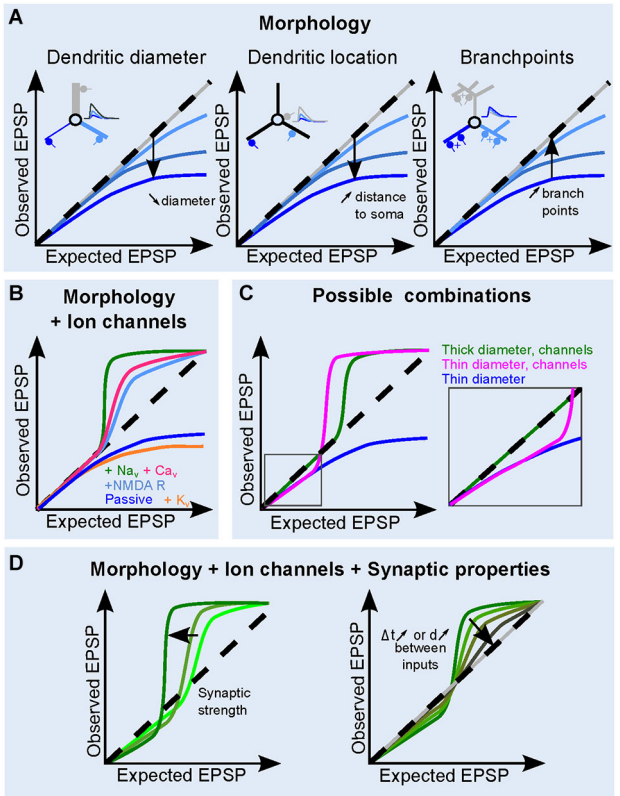

FIGURE 3 | Contribution of dendritic and synaptic properties to EPSP summation. (A) Influence of morphological parameters dendritic: diameter (*left*), increasing distance to soma (*middle*) and increasing dendritic branching (*right*) on the dendritic sI/O. The inserts illustrate the effect of morphology on somatic EPSPs under the different conditions. Synapse location and traces are color coded. Dashed line shows a linear I/O for reference. **(B)** The role of ion channels on the shape of the sI/O, for a given morphology. Either K^+ channels, (*orange*), Na^+ channels (*green*), VGCC (*pink*), or NMDA receptors (*sky blue*) are added to a passive dendrite (blue). **(C)** Example of sI/O in three realistic combinations: thick (>2 μm) dendrites with active conductances (blue curve, as in Branco and Häusser, 2011), thinner dendrites with active conductances (brown curve, <1 μm, Losonczy and Magee, 2006), or thin dendrites with only passive properties (blue curve, Abrahamsson et al., 2012). **(D)** Influence of synaptic properties on the sI/O for a given morphology and ion channel combination. An increase in synaptic strength makes the sI/O diverge from linearity both in the sublinear and the supralinear regime, whereas increasing the interval or the distance between synaptic inputs tends to linearize the curve (*right*).

(Abrahamsson et al., 2012). Synapses activated on separate dendrites summed linearly, supporting a **scatter sensitive** neuronal computation (Abrahamsson et al., 2012), that was confirmed in a realistic active model (Cazé et al., 2013).

The Influence of Active Dendrites on sI/Os

The large local synaptic depolarizations produced in dendrites can also recruit the activation of voltage-dependent channels (NMDARs, Na^+, Ca^{2+}, K^+ and HCN channels, see Johnston and Narayanan, 2008; **Figure 3B**). The number of activated synaptic inputs needed to engage active conductances is determined, in part, by the passive properties of the dendrite, the amplitude and kinetics of the synaptic conductance, the voltage-dependance of channel gating, and the channel density and distribution along the somato-dendritic axis. Active conductances can either enhance (Williams and Stuart, 2000; Migliore and Shepherd, 2002) or dampen (Cash and Yuste, 1999; Hu et al., 2010) local dendritic depolarizations, depending on whether the channels mediate inward (depolarizing) or outward (hyperpolarizing) currents, respectively. Distance-dependent increases in I_h currents have been shown to compensate for the temporal slowing caused by dendritic filtering (Magee and Cook, 2000; Williams and Stuart, 2002). Differential expression of HCN channels across mitral cells has also been shown to increase the membrane noise and lower the rheobase, thus facilitating AP generation (Angelo and Margrie, 2011). Because of the presence of NMDARs at many glutamatergic synapses, most studies find that NMDARs activate other voltage-dependent channels by boosting local synaptic depolarization (Schiller et al., 2000; Losonczy and Magee, 2006; Nevian et al., 2007; Makara et al., 2009; Branco and Häusser, 2011; Katona et al., 2011; Krueppel et al., 2011). The resulting dendritic operation is determined by the concurrence of a passively determined sublinear (Losonczy and Magee, 2006; Krueppel et al., 2011; Chiovini et al., 2014) or linear operation (Branco and Häusser, 2011), and a supralinear operation.

In some cases, the voltage activation of conductances results not only in EPSP boosting, but in a threshold-dependent, all-or-none regenerative response, often called a dendritic spike. This regenerative behavior is characterized by a steep change in the sI/O followed by a plateau (**Figures 1D**, **3B**; Polsky et al., 2004; Losonczy and Magee, 2006; Larkum, 2013). Locally-generated dendritic spikes can be mediated by either Na^+ channels, Ca^{2+} channels or NMDA receptors (NMDARs). Na^+-spikes are triggered by high-amplitude local depolarization, are relatively brief, and can be accompanied by entry of Ca^{2+} through VGCC or NMDARs. In pyramidal cells, these dendritic Na^+ spikes can be generated in most regions of the dendritic tree, propagate throughout the dendritic tree, albeit with some attenuation, but can still trigger somatic spiking (Golding and Spruston, 1998; Rudolph and Destexhe, 2003; Nevian et al., 2007). Recent findings have also shown Na^+-channel dependent spikes in dendrites of dentate gyrus granule cells (Chiovini et al., 2014). On the other hand, Ca^{2+} and NMDA spikes are longer, plateau-like events, that are thought to be generated in particular regions of the dendritic tree, and require the synchronous activation of many clustered synapses. The biophysical mechanisms of the NMDA spikes and their functional consequences have been described in detail in a recent review (Major et al., 2013). In cortical pyramidal neurons, the Ca^{2+} spike is likely to propagate actively from the primary apical dendrite to the soma, thereby representing a more global dendritic operation, whereas NMDA spikes are locally restricted to dendritic compartments such as tufts or basal dendrites (Larkum, 2013). In contrast, simulations of *in vivo* spontaneous synaptic activity allow glutamate-bound NMDARs to act as global nonlinearities providing an entirely different computation than those initiated in single dendrites (Farinella et al., 2014). Nevertheless, several recent *in vivo* studies have reported the involvement of local NMDA spikes during sensory processing, across all layers of the cortex (Lavzin

et al., 2012; Xu et al., 2012; Smith et al., 2013; Gambino et al., 2014; Palmer et al., 2014). It should also be noted that Polsky et al. (Polsky et al., 2004) pointed out that a Ca^{2+}-spike exhibits saturation of the voltage response and thus can also be considered sublinear for very high stimulation strengths.

In summary, the modus operandi of supralinear dendritic compartments is comprised of a continuum of voltage-dependent operations from simple boosting of synaptic depolarization to regenerative spikes. Considering the biophysical underpinnings of this range of operations, it follows that the interplay of the active and passive properties of dendrites ultimately determines the shape of the sI/O (**Figure 3C**). For example, sI/Os of thick dendrites, which have a low Z_D, do not suffer from driving force losses, thus sum linearly for low numbers of activated synapses, then transition into supralinear summation (Makara and Magee, 2013). Thin dendrites on the other hand may exhibit sublinear sI/O relationships for only a few inputs, but then easily engage NMDAR and Ca^{2+} channels (Losonczy and Magee, 2006; Chiovini et al., 2014) with fewer synaptic inputs than in larger dendrites (**Figure 3C**). Due to tapering of dendritic width, which increases the Z_D along the dendrite with increasing distance to the soma, the dendritic operations can be altered as a function of distance from the soma (Branco and Häusser, 2010, 2011).

The Influence of the Size, Time Course and Location of the Synaptic Conductance on sI/Os

The strength of synaptic conductance varies from synapse to synapse across neuron types, but also within neurons. The **synaptic strength** not only serves to bias the output of a neuron to particular inputs (Ko et al., 2011), but it can also be tuned to compensate for dendritic attenuation by passive dendritic properties (Magee, 2000). Synaptic strength influences dendritic operations by modulating the gain (slope) and shape of the sI/O, which is achieved by engaging sub- and supralinear transformations with different numbers of synaptic inputs (**Figure 3D**). Larger synaptic conductances will lead to larger dendritic depolarizations, and in turn either a larger reduction in driving force or increased activation of voltage-gated conductances. Depending on the intrinsic membrane properties and synaptic conductance amplitude the "linear regime" may be more or less prominent in the sI/O relationship.

The **temporal window** for synaptic interactions depends ultimately on the time course of local EPSPs, which is itself shaped by the local passive dendritic properties and the time course of the synaptic conductance (Jonas, 2000). Although the local dendritic EPSPs are larger than those at the soma, it is important to note that their time course is generally much faster, due to charge redistribution down the dendrite (Schmidt-Hieber et al., 2007). The degree to which nonlinear mechanisms are engaged during EPSP summation also depends on the temporal summation of local EPSPs (Losonczy and Magee, 2006; Abrahamsson et al., 2012; Makara and Magee, 2013). Simultaneous synaptic activation enables the largest degree of nonlinear summation, which will progressively decrease as the time difference between synaptic events increases (**Figures 2A, 3D**). Thus, combined with the synaptic strength, the temporal coincidence between co-activated synapses within a single dendritic compartment will determine gain of the dendritic operations (Gómez González et al., 2011; Abrahamsson et al., 2012; Makara and Magee, 2013).

The location of synapses carrying similar information (e.g., a single sensory feature) determines which dendritic mechanism is recruited. For example, if features of an object are always clustered on a single dendritic compartment, then nonlinear summation will be the prominent operation influencing integration. Below we will use a mathematical formalism to provide insight into how **synaptic placement** and dendritic operations influence neuronal computations.

Experimental Strategies for Studying Dendritic Integration

How do researchers study the biophysical properties of dendrites and their influence on excitatory synaptic integration? Classical electrophysiology methods such as sharp electrode- or patch-clamp-based recordings of somatic membrane potential provided insight into the intrinsic passive electrical properties of neurons by measuring the input resistance and the membrane time constant ($\tau = R_m{}^*C_m$) (Spruston and Johnston, 1992). When combined with multi-compartmental dendritic models, with either simplified morphologies (equivalent cylinder approximation) or full anatomical reconstructions (Clements and Redman, 1989; Major et al., 1994), the passive electrotonic properties of dendrites can be estimated from model parameters that predict the membrane potential decay from somatic current injections (Rall et al., 1992). These constrained models are then used to examine dendritic transformations of EPSPs as they propagate to the soma.

Unfortunately, single electrode recordings at the soma do not provide sufficient information about dendritic properties to constrain complex morphological models. With the advent of dendritic patch recordings (Stuart et al., 1993), at least for large diameter dendrites ($\geq 1\ \mu m$), cable model predictions could be directly verified. This powerful recording method allows estimations of the critical parameters influencing dendritic filtering, such as internal resistivity (R_i; Stuart et al., 1993; Stuart and Spruston, 1998; Roth and Häusser, 2001; Nevian et al., 2007; Schmidt-Hieber et al., 2007; Hu et al., 2010), R_m and voltage-gated channel properties and density along the somato-dendritic axis (Magee and Johnston, 1995; Stuart and Spruston, 1998; Hu et al., 2010). Dendritic recordings also enabled the measurement of local EPSPs and EPSCs, which allowed the authors to conclude that dendritic filtering can be compensated by a distance-dependent increase in synaptic conductance in certain neuron types (Magee and Cook, 2000).

More recently, fluorescence imaging techniques have greatly increased the toolkit for studying dendritic integration, particularly in those dendrites with narrow diameters ($<1\ \mu m$). Ca^{2+} indicators are one of the most popular class of fluorescence probes, which are used to indirectly study dendritic nonlinearities resulting from activation of voltage-dependent ion channels, provided at least one type of Ca^{2+} conductance

was activated (Markram et al., 1995; Schiller et al., 1995, 1997, 2000). Ca^{2+} indicators have also been used to monitor synaptic activity because of the prevalence of NMDAR activation in single spines and Ca^{2+}-permeable AMPARs at synapses in interneurons (Soler-Llavina and Sabatini, 2006). *In vivo* two-photon Ca^{2+} imaging experiments provided the first insights into the spatial and temporal distribution of sensory-evoked synaptic signaling within dendrites (Varga et al., 2011; Lavzin et al., 2012; Smith et al., 2013; Jia et al., 2014; Palmer et al., 2014). The contribution of *in vivo* Ca^{2+} imaging studies to understanding dendritic function has been recently reviewed by Grienberger et al (Grienberger et al., 2015). However, a limitation of using Ca^{2+} imaging to study synaptic integration is that it does not report the true dendritic voltage, a parameter critically influencing dendritic operations. Also, the slow nature of the whole-cell averaged $[Ca^{2+}]$ and the use of high affinity Ca^{2+} indicators limits the temporal resolution of this method (Farinella et al., 2014; Fernández-Alfonso et al., 2014). Voltage-sensitive dyes are, in principle, an ideal alternative for direct measurement of dendritic integration. Whereas voltage-sensitive dye recordings have provided unprecedented optical reports of the spatial and temporal distribution of APs in axons (Foust et al., 2010; Popovic et al., 2011) and dendrites (Acker and Antic, 2009; Casale and McCormick, 2011), their use to monitor EPSPs in dendrites has been less successful due to poor signal-to-noise ratio, typically requiring hundreds of trials of averaging (Palmer and Stuart, 2009). However, inhibitory post-synaptic potentials (IPSPs) have been detected (Canepari et al., 2008) and a recent study reports good signal-to-noise ratios sufficient to detect spine EPSPs (Popovic et al., 2014). The advances in genetically-encoded voltage indicators are also rapidly maturing (Hochbaum et al., 2014; St-Pierre et al., 2014; Zou et al., 2014), and could eventually provide a powerful tool for studying dendritic integration *in vivo*.

Another widely-used *in vitro* technique to characterize the integration properties of dendrites is to directly activate postsynaptic receptors using photolysis of caged-neurotransmitter (i.e., caged-glutamate) within the diffraction-limited focal volume of the microscope (Gasparini and Magee, 2006; Losonczy and Magee, 2006). Using galvanometer-driven mirrors, the type regularly used in scanning confocal microscopy, the focal illumination volume can be rapidly moved (within 0.1–1 ms) and positioned at multiple locations. The uncaging light pulse is then rapidly gated at each location to focally release glutamate. This allows for the near simultaneous activation of many postsynaptic sites. The somatic depolarization is then recorded using standard whole-cell patch-clamp methods. The observed response to uncaging at multiple synaptic locations (typically within 1 ms) is compared to the arithmetic sum of the uncaging-evoked responses at individual sites. The resulting plot is identical to the sI/O plots described in **Figures 1**, **3**, provided that the uncaging responses are similar to synaptic activation. Using light, rather than presynaptic vesicular release, to activate neurotransmitter receptors provides a more flexible strategy to systematically vary the number, pattern, and timing of synapse activation. Electrical stimulation does not permit a precise identification of the synapses being activated, nor precise control of the number of synapses activated. Holographic illumination provides an alternative strategy for true simultaneous glutamate uncaging at multiple sites within the dendrites and is more amenable to multibranch activation (Lutz et al., 2008; Yang et al., 2014, 2011). The only potential drawback of uncaging is the difficulty in some preparations to accurately reproduce very fast synaptic conductances due to the large volume of diffraction-limited focal spots relative to the point source nature of neurotransmitter release from synaptic vesicles (DiGregorio et al., 2007), as well as a tendency to partially block GABARs (Fino et al., 2009). Nevertheless, neurotransmitter uncaging is an essential tool for quantifying the biophysical properties underlying dendritic operations.

Linking Dendritic Operations to Neuronal Computations Using Mathematical Models

Because experimental evidence of a direct link between the dendritic operations and the associated neuronal computations is still lacking, a parallel strategy is to use analytical models to make testable predictions (Poirazi and Mel, 2001; Legenstein and Maass, 2011; Cazé et al., 2013). These methods take advantage of mathematical approximations of measured dendritic operations to make estimates of the possible number and type of neuronal computations. Biophysical models, in contrast, although explicit, do not easily provide insight into the classes of possible computations because of the large parameter space. There is no doubt that such models have provided deep insights into neuronal computations that involve nonlinear dendritic operations. They have been used to show that neurons with supralinear dendrites are **cluster-sensitive** (Mel, 1993) and neurons with sublinear dendrites are **scatter-sensitive** (Koch et al., 1983; Cazé et al., 2013). Yet it was not clear whether either type of nonlinearity provides similar computational advantages. To examine the difference between supralinear and sublinear operations of binary neuron models Cazé et al. (2013) used a Boolean-based analysis. Here we review how this Boolean framework can be used to argue that either supralinear or sublinear summation is sufficient to endow neurons with a new class of computations.

Within this analytical framework, neurons are modeled as having binary inputs (x_i), which can be weighted and integrated, resulting in binary outputs (y). In this context the input-output relation is described by a unique truth table, corresponding to a Boolean function. In **Figure 4A**, the truth table describes three simple Boolean functions: OR, AND and XOR. This well-known mathematical framework (Wegener, 1987; Crama and Hammer, 2011), which deals with binary classifications of binary words, allows us to analytically determine what type of classifications are possible with nonlinear dendrites and which are otherwise impossible.

The simplest binary neuron model is called the threshold linear unit, also known as the point neuron model as described first by McCulloch and Pitts (**Figure 4B**; McCulloch and Pitts, 1943). Synapses are assigned a binary value of 0 or 1, for inactive or active states, which is then multiplied by a positive synaptic

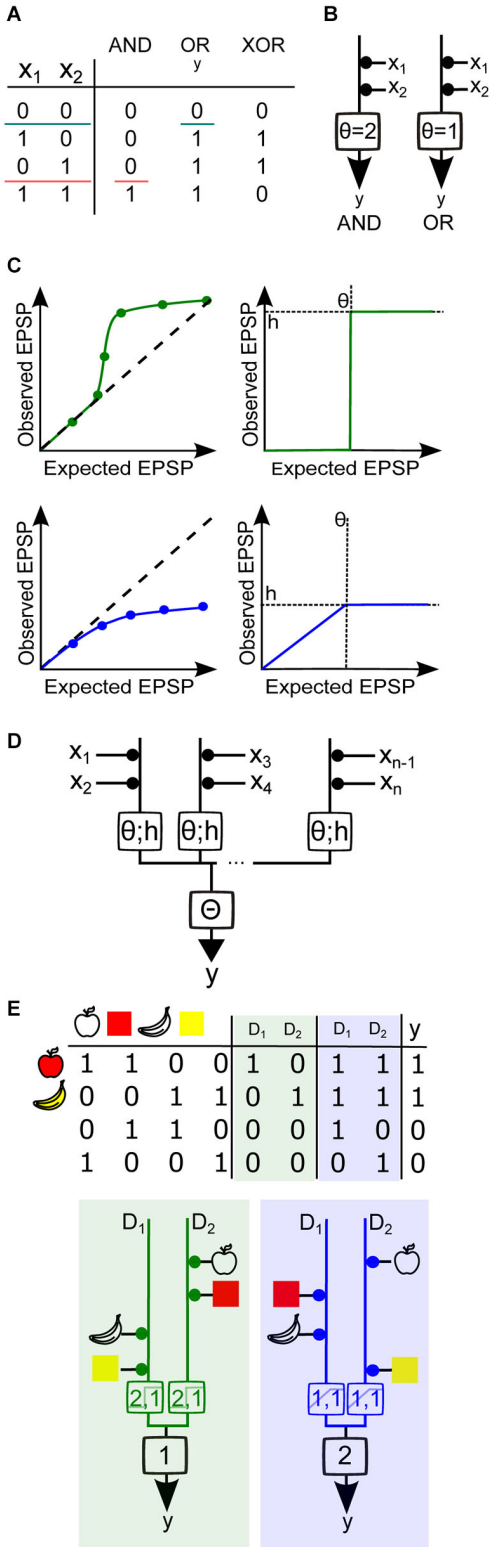

FIGURE 4 | Using Boolean algebra to analyze binary neuron models with dendritic nonlinearities. (A) Truth tables for the Boolean functions AND, OR and XOR for two synaptic inputs (x_1 and x_2). The two colored horizontal lines illustrate how the AND and OR functions are linearly separable, (*Continued*)

FIGURE 4 | Continued
i.e., a single line divides all inputs between two groups, one group having an output of 0 and the other group having an output of 1. Neuron output binary value is denoted as *y*. **(B)** Threshold linear unit model neuron with two inputs. The weight of each input is represented by the area of the black disc drawn between the input and the model neuron. Here all weights are equal to 1. A spiking threshold (θ) of 2 allows the model neuron to compute the AND function (*left*), whereas if θ =1 the neuron computes the OR function (*right*). **(C)** *Top*, Simplified representations of a supralinear sI/O (*left*) and its mathematical approximation by a Heaviside function (*right*) with a height h and a threshold θ. *Bottom*, simplified representation of a sublinear sI/O and its mathematical approximation by a piecewise linear, then saturating function. **(D)** Generalized diagram representing a two-layer integration model neuron with several compartments and n inputs. Each branch represents a dendritic compartment, and the integration operation performed by this compartment is represented by the box on the branch. The threshold θ and the output value h of the nonlinearity are indicated within the box. The result from the integration from each branch is then linearly summed and compared to the somatic spike threshold Θ. **(E)** Implementation of the (partial) feature binding problem (pFBP) by binary neurons with two dendritic compartments D_1 and D_2, either supralinear or sublinear. *Top*, truth table describing various input feature combinations, the response of each dendritic compartment, D (0:inactive/1:active), and the final neuronal output, *y*. Columns with green shading are the outputs of dendrites exhibiting supralinear operations, while columns shaded in blue contain outputs of dendrites that exhibit sublinear operations. *Bottom*, Model neuron with equivalent dendrite representation that can implement the pFBP using supralinear (*left*) or sublinear dendritic compartments (*right*), with θ and h values indicated in the box. If dendritic integration is supralinear, two groups of inputs are needed to activate a compartment, and a single compartment can trigger a spike. If dendritic integration is sublinear, a single input can activate the dendritic compartment and the two compartments must be active to trigger a spike.

weight for excitatory synapses. The sum of the active weighted inputs is then compared to a somatic spike threshold Θ. If this weighted sum is greater than the threshold, the output is assigned a value of 1, and otherwise zero. If one considers a neuron with linearly summing excitatory inputs, adjustment of the threshold allows it to either perform a Boolean AND or OR (**Figure 4B**). However, it is not possible to find a threshold value and positive synaptic weight that allows the computation of the XOR, the function corresponding to a binary neuron that would fire only when one synapse is active, but not otherwise. This illustrates well the fact that the threshold linear unit can only perform functions that are linearly separable, i.e., there is a set of weights and a spike threshold that categorizes the inputs into two distinct groups, which differ by their output values (**Figure 4A**). The XOR does not meet this criterion and is therefore a part of the class of functions that are linearly non-separable. To solve this problem we must either invoke a non-monotone function to combine synaptic values (Zador et al., 1992) or consider synaptic inhibition by using negative weights (Mel, 1994; Cazé et al., 2014). Because the former has not been described experimentally, and the latter requires specific wiring within the network, we will focus here on linearly non-separable functions that can be implemented with only excitatory synapses and monotone dendritic operations. These functions are known as positive Boolean functions (Cazé et al., 2013).

Linearly–separable functions represent only a small fraction of all the possible computations (Cazé et al., 2013). However, a

neuron with nonlinear dendritic compartments can implement the set of linearly non-separable functions, which encompasses a much larger fraction of all computations (Cazé et al., 2013). Thus both supralinear and sublinear compartments unlock the access to all the possible computations (Mel and Koch, 1990; Mel, 1991). This formal result is true for an infinite number of dendritic compartments (Poirazi and Mel, 2001). This is clearly impossible in practice. So what can a neuron compute with a finite number of dendritic compartments?

To address this question we can construct a two-layer binary model with nonlinear dendritic compartments. We first approximated the dendritic sI/O with functions each having a characteristic dendritic threshold **θ**, which represents the threshold of the dendritic nonlinearity, and **h**, which represents the maximal value of the dendritic nonlinearity. To approximate supralinear compartments we used a Heaviside function, and for sublinear functions we used a piecewise linear saturating function (**Figure 4C**). The output of the dendritic compartments is then linearly summed and compared with spike threshold (**Figure 4D**). If we vary synaptic weights, the thresholds, and the nonlinear dendritic operations, we can use Boolean analysis to examine the different functions this model can implement. A functionally salient neuronal computation that requires dendritic nonlinearities is the association (or binding) of two features of an object (for example, their shape and color). This is known as the feature binding problem (FBP). If we suppose that that different features of objects are encoded by different groups of pre synaptic neurons impinging on the same post synaptic neuron, then it is obvious that by allowing the features of an object to target the same supralinear dendrite, the coincidence of those features can be easily detected when co-active (i.e., "red" + "apple shape"; **Figure 4E**). It can also be shown that a sublinear operation can bind features if the inputs that encode object features are distributed onto different dendritic subunits (and the spiking threshold increased). From these simple binary models it is again clear that supralinear operations favor cluster sensitivity and sublinear operations favor scatter sensitivity. However, a keen eye may notice that the sublinear model will also produce a spike if the apple shape and banana shape are both activated. This therefore constitutes a partial FBP. Below we will describe a neuron model with equivalent dendrites that can implement the complete FBP.

Because neurons are known to have both linear and nonlinear compartments, we considered how more realistic dendritic trees could be represented using our simple binary model, by creating a neuron model with equivalent dendrites (**Figures 5A,B**). All linear regions of the dendritic tree (typically, the perisomatic compartment or the large diameter primary dendrites) were collapsed to a single equivalent "linear" compartment (black regions of schematic neuron and left branch of the model neuron). The nonlinear dendritic compartments receiving more than one synaptic input were represented as a second equivalent dendritic branch. This then generalizes to an equivalent dendritic branch for each nonlinear electrical compartment (**Figure 4D**). The presence of a linear compartment is important, since inputs contacting two separate nonlinear dendrites will sum linearly (**Figure 5A**). Also, even inputs contacting the same nonlinear dendrite, provided they are not in the same electrical compartment, will sum linearly.

Legenstein et al. demonstrated that a model neuron with supralinear dendritic integration is capable of learning and computing the FBP (Legenstein and Maass, 2011). This function detects any correct combination of features for an object, but not incorrect combinations. In the Boolean framework this would be the truth table corresponding to ("red" + "apple shape") or ("yellow" + "banana shape"). In **Figure 4** we showed that two supralinear dendrites are sufficient to solve the FBP for two objects made of two features each. In **Figure 5**, a neuron displaying at least one supralinear compartment and a linear compartment can also solve the FBP for four inputs. In this case, inputs encoding the features of one object are assigned to the supralinear compartment, and the features corresponding to the other object are assigned to the linear compartment (**Figure 5C**). Because the features of the object must "cluster" on the same compartment we refer to this model as using a **local strategy** of computation. Interestingly, it is also possible to implement the same computation using a **global strategy**, meaning that the features corresponding to one object need to be "scattered" onto both the nonlinear and the linear compartment (**Figure 5D**), provided that appropriate changes in the synaptic weights and threshold values are also implemented. As shown by Cazé et al. (2013), a model with a linear and sublinear compartment requires the global strategy to perform the FBP (**Figure 5E**). The synaptic weights and threshold will also be different than in the case of a model neuron with a supralinear compartment. The fact that the FBP can be implemented using a global strategy contrasts with the notion that recognition of an object required the clustering of the inputs carrying its features onto a same dendritic branch (Legenstein and Maass, 2011), and the assumption that two-layer integration models require independent branch-specific operations (Behabadi and Mel, 2014). Using a biophysical model with a model stellate cell morphology, Cazé et al. showed the predictions are robust, since only passive thin dendrites were necessary to convey a scatter sensitivity of output firing, even in the presence of synaptic noise (Cazé et al., 2013).

How might simplified Boolean models be modified for more features and/or more objects? For objects represented by more than two features, clustered strategies would simply require more synaptic inputs, such that the number of the number of inputs per subunit (dendritic compartment) equals the number features. A change in threshold would also be required. The requirements for neuronal computations using sublinear dendrites, however, depend on the type of computation and are less straightforward to determine explicitly. The necessary number of nonlinear subunits also varies given the implementation strategy, the number of objects, the type of nonlinear subunits and the number of features. To solve the FBP with more objects using supralinear operations, each object will require at least one subunit (Cazé et al., 2012). For computations with sublinear operations, Cazé et al. showed that using binary weights, the FBP requires a maximum of 2^n

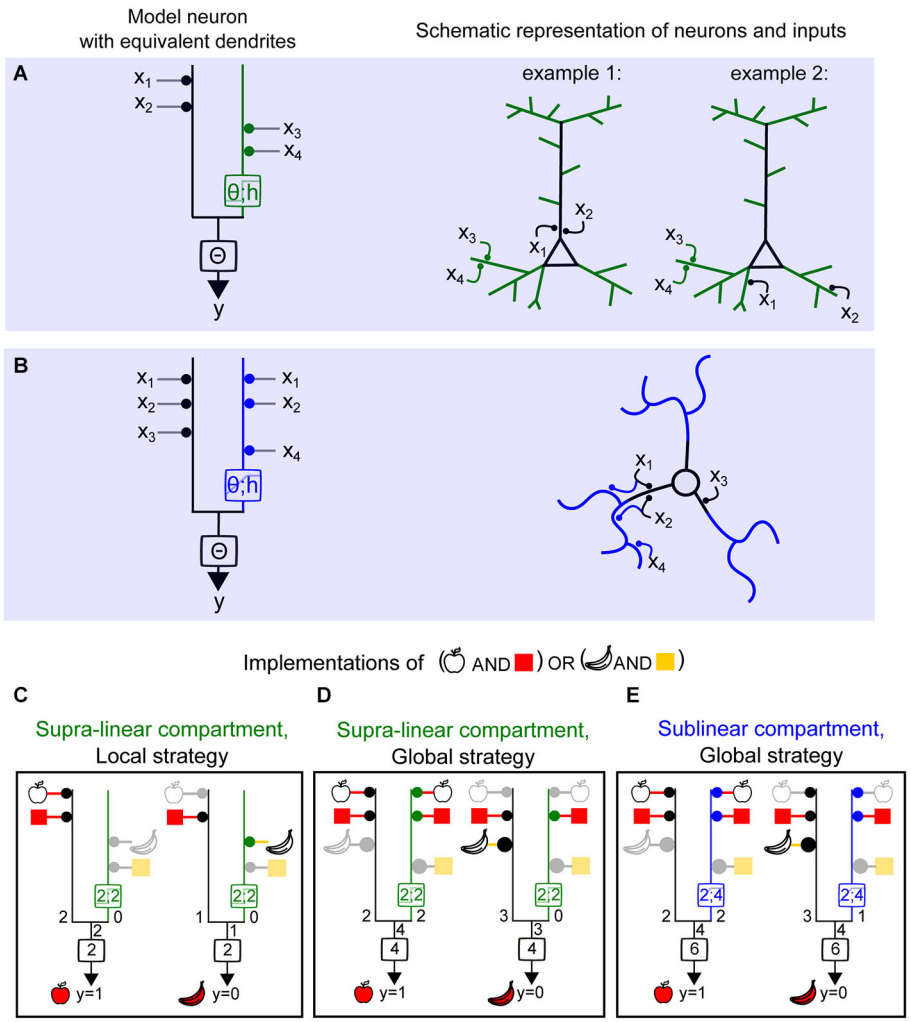

FIGURE 5 | Computing a linearly non-separable function (full FBP) with supralinear and sublinear dendrites and using local vs. global synaptic wiring strategies. **(A)** *Left*, model neuron with equivalent dendrite representation of two compartments, linear (black) and supralinear (green), and a clustered distribution of object features (object 1 : ×1, ×2 and object 2 : ×3, x4) (local strategy). *Right*, schematic representations of synaptic placements equivalent to the model on the left. **(B)** *Left*, model neuron with equivalent dendrite representation of two compartments, linear (black) and sublinear (blue), and a distributed placement of inputs carrying object features. **(C–E)** Implementation of the full FBP (y = 1; "apple shape and red" or "banana shape and yellow"). **(C)**, implementation of the full FBP using a model with a supralinear compartment and a local wiring strategy. Inactive inputs are represented in light gray and the corresponding feature in lighter color. **(D)** Implementation of the full FBP using a model with a supralinear compartment and a global wiring strategy. The area of the disc adjacent to a compartment next to each object feature represents the relative weight of this feature. Here the relative weights used are of 1 and 2. **(E)** Implementation of the full FBP using a model with sublinear compartment and a global wiring strategy.

subunits (Cazé et al., 2012). Considering non-binary weights then reduces the number of subunits needed, but this number is still higher than the number of necessary supralinear subunits ($n_{\text{subunits}} = n_{\text{objects}}$).

In summary, neurons with sublinear dendrites are capable of solving linearly non-separable functions, but require using a distributed strategy of synaptic placement (**Figure 5E**). These neurons will be scatter sensitive. On the other hand, neurons with supralinear dendrites can also access the same class of computations either by using this strategy (**Figure 5C**) or by clustering functionally relevant inputs onto the same compartment (**Figure 5C**). Hence they can be either scatter or cluster sensitive. Thus, the final neuronal computations depend not only on the type of dendritic operation and the dendritic and axosomatic thresholds, but also the *global* mapping of input features throughout the dendritic tree.

Open Questions

To understand how a neuron integrates its synaptic inputs we need precise knowledge of the morphology, ion channel distribution along the tree, strength and time course of

synaptic conductances carrying particular information features, the output spike threshold, and the spatio-temporal pattern of activation of the synapses carrying these features. Although we can determine most of these parameters, as we reviewed above, the most challenging experiments are those designed to estimate the spatio-temporal distribution of all synapses carrying relevant sensory features (i.e., a functional connectivity map). Strategies using injection of viral-based retrograde tracers (Marshel et al., 2010) are powerful for the identification of connected presynaptic cells, but these methods lack information about features conveyed by the inputs. Using *in vivo* Ca^{2+} imaging, researchers have begun the herculean task of estimating how sensory features are mapped onto dendritic trees by examining how single synapses and dendrites respond to behavioral stimuli. It is not clear whether such feature mapping can be performed on the entire dendritic tree, but initial results provide hints as to whether there may be general mapping rules. Some studies argue that features are clustered in single dendrites within the somato-sensory cortex (Takahashi et al., 2012), consistent with a **local computation strategy**, while other studies have shown that neighboring synapses onto layer 2/3 pyramidal neurons of the visual and auditory cortex respond maximally for activation of inputs carrying different sensory features (Jia et al., 2010; Chen et al., 2011), consistent with a **global strategy**. In light of the conclusions described here, both computation strategies are capable of performing linearly non-separable functions.

Why might neurons use different dendritic operations and wiring strategies? It is conceivable that differences in timing of sensory development or optimal local circuit wiring may constrain wiring strategies for particular neurons. Thus to perform the same computation, different wiring and dendritic strategies are needed. Global wiring strategies are more amenable to "random wiring," in contrast to the specific connectivity required for engaging local strategies. We speculate that different dendritic operations may be implemented by neurons given certain biological constraints, such as limitations in the number and location of synapses carrying a particular feature, or spike threshold. For example when both principal neurons and interneurons receive a common set of input features along relatively fixed axonal projections, but are required to perform different computations, they may engage different dendritic operations. In the cerebellum interneurons have been shown to exhibit sublinear dendritic operations (Abrahamsson et al., 2012; Vervaeke et al., 2012) on their parallel fiber inputs, while Purkinje cells are thought to receive the same or similar features from the same set of input fibers, yet display supralinear dendritic operations (Rancz and Häusser, 2006). One could speculate that the different nonlinearities and synaptic placement strategies of Purkinje neurons and interneurons may enable them to implement complementary computations, which ultimately could result in a microcircuit that is highly selective for specific input patterns.

What are the wiring rules? Three possible wiring strategies are (1) predetermined connectivity (genetically encoded); (2) random connectivity; and (3) activity-dependent pruning and stabilization of connections. Although the exact contribution of each mechanism is yet to be determined, synaptic plasticity has been shown to modify and ultimately determine the functional connectivity. For example computational modeling showed that a local wiring strategy, in which synapses carrying features of objects are clustered, can be learned using simple plasticity rules (Legenstein and Maass, 2011). Experimental evidence supports this theoretical work, suggesting that activity-dependent, branch-specific plasticity strengthens clustered synaptic inputs and their compartmentalization (Makara et al., 2009; Makino and Malinow, 2011; Takahashi et al., 2012). On the other hand, synaptic plasticity could also reinforce global computational strategies. In cerebellar stellate cells, high-frequency firing of clustered inputs has been described to induce profound presynaptic short- and long-term synaptic depression (Beierlein and Regehr, 2006; Soler-Llavina and Sabatini, 2006). Such plasticity mechanisms would reinforce the neuron's **scatter sensitivity**, and thus tend to optimize the output firing for specific spatially and temporally sparse synaptic activity patterns (Abrahamsson et al., 2012; Cazé et al., 2013).

Synchronized neuronal activity is known to cause oscillations of the dendritic voltage, which would inevitably reinforce electrical interactions between dendrites and thus alter the effective number of isolated dendritic subunits that contribute to the neuronal computation. For example, Remme et al. (2009) showed theoretically that input-dependent synchronization of intrinsic dendritic voltage oscillations can facilitate global voltage propagation, even throughout highly distributed dendritic trees. It will be important to examine how local and global dendritic integration strategies might be influenced by brain oscillations, thus ultimately altering neuronal and even circuit computations.

Since many types of interneurons are known to contact specific locations within the dendritic tree, inhibition will undoubtedly influence integration properties and information processing by neuronal circuits (as reviewed by Palmer et al., 2012). Nevertheless, the experimental challenge is to determine not only the timing and location of inhibition within the dendrite, in order to determine their alteration of dendritic operations, but also whether particular features are conveyed similarly or differently by excitatory and inhibitory inputs. Although complex, the problem is critical to understanding brain function as the balance of excitation and inhibition is well known to be tightly regulated, with alterations being implicated in disease (Yizhar et al., 2011). Using the Boolean analysis of equivalent dendrites, one can deduce that negative weight associated with inhibition is capable of performing the Boolean NOT function. Such a function would enable a simple implementation of XOR computations, further expanding the number of computable linearly non-separable functions.

Summary

In this review we described categories of biophysical and cellular mechanisms that influence dendritic operations: passive and active membrane properties of the dendritic tree, the time course and amplitude of synaptic activation, the output spike threshold, and finally the location and pattern of the activation of synaptic inputs. We discussed how each of these

parameters shapes and tunes the sI/O. We briefly discussed techniques for the characterization of dendritic operations, including electrode-based methods to stimulate and/or record from dendrites, optical techniques to image dendritic activity or uncage neurotransmitter, and biophysical modeling. In order to understand how the major classes of dendritic operations (linear, sublinear and supralinear) link to neuronal computations, we reviewed the use of binary models associated with Boolean analysis. This analysis provides insight into the types of computable neuronal functions, such as the object feature binding problem. We also reviewed how such functions can be implemented with either supralinear or sublinear dendrites depending on the spatial mapping of those features within the dendritic tree. Because the synaptic activity pattern ultimately determines the neuronal computations, we propose that the elemental computational unit is the neuron rather than the dendrite (Cazé et al., 2014). Although there are cases (local strategies) where dendritic operations can dictate the neuronal computation, dendritic operations must be studied and understood in the context of the knowledge of the wiring of specific features onto the dendritic tree.

Acknowledgments

We thank members of the DiGregorio lab for helpful discussions and comments on the manuscript. ATVM and DD were supported by the French National Agency for Research (ANR-2010-BLANC-1411 and ANR-13-BSV4-0016) and the Fondation de Recherche Medicale (Team grant). ATVM was also supported by the Ecole des Neurosciences de Paris, a EMBO Long-Term Fellowship 1582-2011, a Roux-Howard-Cantarini post-doctoral fellowship and a Marie Curie Individual Fellowship 301362 within the 7th European Community Framework Program (FP7-PEOPLE-2011-IEF). RC was supported by the EC Marie Curie Initial Training Network 289146 "NETT".

References

Abrahamsson, T., Cathala, L., Matsui, K., Shigemoto, R., and Digregorio, D. A. (2012). Thin dendrites of cerebellar interneurons confer sublinear synaptic integration and a gradient of short-term plasticity. *Neuron* 73, 1159–1172. doi: 10.1016/j.neuron.2012.01.027

Acker, C. D., and Antic, S. D. (2009). Quantitative assessment of the distributions of membrane conductances involved in action potential backpropagation along basal dendrites. *J. Neurophysiol.* 101, 1524–1541. doi: 10.1152/jn.00651.2007

Agmon-Snir, H., Carr, C., and Rinzel, J. (1998). The role of dendrites in auditory coincidence detection. *Nature* 393, 268–272. doi: 10.1038/30505

Angelo, K., and Margrie, T. W. (2011). Population diversity and function of hyperpolarization-activated current in olfactory bulb mitral cells. *Sci. Rep.* 1:50. doi: 10.1038/srep00050

Archie, K. A., and Mel, B. W. (2000). A model for intradendritic computation of binocular disparity. *Nat. Neurosci.* 3, 54–63. doi: 10.1038/71125

Behabadi, B. F., and Mel, B. W. (2014). Mechanisms underlying subunit independence in pyramidal neuron dendrites. *Proc. Natl. Acad. Sci. U S A* 111, 498–503. doi: 10.1073/pnas.1217645111

Beierlein, M., and Regehr, W. G. (2006). Local interneurons regulate synaptic strength by retrograde release of endocannabinoids. *J. Neurosci.* 26, 9935–9943. doi: 10.1523/jneurosci.0958-06.2006

Branco, T., and Häusser, M. (2010). The single dendritic branch as a fundamental functional unit in the nervous system. *Curr. Opin. Neurobiol.* 20, 494–502. doi: 10.1016/j.conb.2010.07.009

Branco, T., and Häusser, M. (2011). Synaptic integration gradients in single cortical pyramidal cell dendrites. *Neuron* 69, 885–892. doi: 10.1016/j.neuron.2011.02.006

Canepari, M., Vogt, K., and Zecevic, D. (2008). Combining voltage and calcium imaging from neuronal dendrites. *Cell. Mol. Neurobiol.* 28, 1079–1093. doi: 10.1007/s10571-008-9285-y

Casale, A. E., and McCormick, D. A. (2011). Active action potential propagation but not initiation in thalamic interneuron dendrites. *J. Neurosci.* 31, 18289–18302. doi: 10.1523/JNEUROSCI.4417-11.2011

Cash, S., and Yuste, R. (1998). Input summation by cultured pyramidal neurons is linear and position-independent. *J. Neurosci.* 18, 10–15.

Cash, S., and Yuste, R. (1999). Linear summation of excitatory inputs by CA1 pyramidal neurons. *Neuron* 22, 383–394. doi: 10.1016/s0896-6273(00)81098-3

Cazé, R. D., Humphries, M. D., and Gutkin, B. S. (2012). Spiking and saturating dendrites differentially expand single neuron computation capacity. *Adv. Neural Inf. Process. Syst.* 25, 1–9.

Cazé, R. D., Humphries, M., and Gutkin, B. (2013). Passive dendrites enable single neurons to compute linearly non-separable functions. *PLoS Comput. Biol.* 9:e1002867. doi: 10.1371/journal.pcbi.1002867

Cazé, R. D., Humphries, M. D., and Gutkin, B. S. (2014). "Dendrites enhance both single neuron and network computation," in *The Computing Dendrite: From Structure to Function*, eds H. Cuntz, M. W. H. Remme and B. Torben-Nielsen (New York: Springer), 365–380.

Chadderton, P., Schaefer, A. T., Williams, S. R., and Margrie, T. W. (2014). Sensory-evoked synaptic integration in cerebellar and cerebral cortical neurons. *Nat. Rev. Neurosci.* 15, 71–83. doi: 10.1038/nrn3648

Chen, X., Leischner, U., Rochefort, N. L., Nelken, I., and Konnerth, A. (2011). Functional mapping of single spines in cortical neurons in vivo. *Nature* 475, 501–505. doi: 10.1038/nature10193

Chiovini, B., Turi, G. F., Katona, G., Kaszás, A., Pálfi, D., Maák, P., et al. (2014). Dendritic spikes induce ripples in parvalbumin interneurons during hippocampal sharp waves. *Neuron* 82, 908–924. doi: 10.1016/j.neuron.2014.04.004

Clements, J. D., and Redman, S. J. (1989). Cable properties of cat spinal motoneurones measured by combining voltage clamp, current clamp and intracellular staining. *J. Physiol.* 409, 63–87. doi: 10.1113/jphysiol.1989.sp017485

Crama, Y., and Hammer, P. L. (2011). *Boolean Functions. Theory, Algorithms and Applications.* New York: Cambridge University Press.

DiGregorio, D. A., Rothman, J. S., Nielsen, T. A., and Silver, R. A. (2007). Desensitization properties of AMPA receptors at the cerebellar mossy fiber granule cell synapse. *J. Neurosci.* 27, 8344–8357. doi: 10.1523/jneurosci.2399-07.2007

Farinella, M., Ruedt, D. T., Gleeson, P., Lanore, F., and Silver, R. A. (2014). Glutamate-bound NMDARs arising from in vivo-like network activity extend spatio-temporal integration in a L5 cortical pyramidal cell model. *PLoS Comput. Biol.* 10:e1003590. doi: 10.1371/journal.pcbi.1003590

Fernández-Alfonso, T., Nadella, K. M., Iacaruso, M. F., Pichler, B., Roš, H., Kirkby, P. A., et al. (2014). Monitoring synaptic and neuronal activity in 3D with synthetic and genetic indicators using a compact acousto-optic lens two-photon microscope. *J. Neurosci. Methods* 222, 69–81. doi: 10.1016/j.jneumeth.2013.10.021

Fino, E., Araya, R., Peterka, D. S., Saliemo, S., Etchenique, R., and Yuste, R. (2009). RuBi-Glutamate: two-photon and visible-light photoactivation of neurons and dendritic spines. *Front. Neural Circuits* 3:2. doi: 10.3389/neuro.04.002.2009

Foust, A., Popovic, M., Zecevic, D., and McCormick, D. A. (2010). Action potentials initiate in the axon initial segment and propagate through axon collaterals reliably in cerebellar Purkinje neurons. *J. Neurosci.* 30, 6891–6902. doi: 10.1523/JNEUROSCI.0552-10.2010

Gambino, F., Pagès, S., Kehayas, V., Baptista, D., Tatti, R., Carleton, A., et al. (2014). Sensory-evoked LTP driven by dendritic plateau potentials in vivo. *Nature* 515, 116–119. doi: 10.1038/nature13664

Gasparini, S., and Magee, J. C. (2006). State-dependent dendritic computation in hippocampal CA1 pyramidal neurons. *J. Neurosci.* 26, 2088–2100. doi: 10.1523/jneurosci.4428-05.2006

Golding, N. L., and Spruston, N. (1998). Dendritic sodium spikes are variable triggers of axonal action potentials in hippocampal CA1 pyramidal neurons. *Neuron* 21, 1189–1200. doi: 10.1016/s0896-6273(00)80635-2

Gómez González, J., Mel, B. W., and Poirazi, P. (2011). Distinguishing linear vs. Non-linear integration in CA1 radial oblique dendrites: it's about time. *Front. Comput. Neurosci.* 5:44. doi: 10.3389/fncom.2011.00044

Grienberger, C., Chen, X., and Konnerth, A. (2015). Dendritic function in vivo. *Trends Neurosci.* 38, 45–54. doi: 10.1016/j.tins.2014.11.002

Häusser, M., and Mel, B. (2003). Dendrites: bug or feature? *Curr. Opin. Neurobiol.* 13, 372–383. doi: 10.1016/s0959-4388(03)00075-8

Hochbaum, D. R., Zhao, Y., Farhi, S. L., Klapoetke, N., Werley, C. A., Kapoor, V., et al. (2014). All-optical electrophysiology in mammalian neurons using engineered microbial rhodopsins. *Nat. Methods* 11, 825–833. doi: 10.1038/nmeth.3000

Hu, H., Martina, M., and Jonas, P. (2010). Dendritic mechanisms underlying rapid synaptic activation of fast-spiking hippocampal interneurons. *Science* 327, 52–58. doi: 10.1126/science.1177876

Jaffe, D. B., and Carnevale, N. T. (1999). Passive normalization of synaptic integration influenced by dendritic architecture. *J. Neurophysiol.* 82, 3268–3285.

Jia, H., Rochefort, N. L., Chen, X., and Konnerth, A. (2010). Dendritic organization of sensory input to cortical neurons in vivo. *Nature* 464, 1307–1312. doi: 10.1038/nature08947

Jia, H., Varga, Z., Sakmann, B., and Konnerth, A. (2014). Linear integration of spine Ca2+ signals in layer 4 cortical neurons in vivo. *Proc. Natl. Acad. Sci. U S A* 111, 9277–9282. doi: 10.1073/pnas.1408525111

Johnston, D., and Narayanan, R. (2008). Active dendrites: colorful wings of the mysterious butterflies. *Trends Neurosci.* 31, 309–316. doi: 10.1016/j.tins.2008.03.004

Jonas, P. (2000). The time course of signaling at central glutamatergic synapses. *News Physiol. Sci.* 15, 83–89.

Katona, G., Kaszás, A., Turi, G. F., Hájos, N., Tamás, G., Vizi, E. S., et al. (2011). Roller Coaster Scanning reveals spontaneous triggering of dendritic spikes in CA1 interneurons. *Proc. Natl. Acad. Sci. U S A* 108, 2148–2153. doi: 10.1073/pnas.1009270108

Ko, H., Hofer, S. B., Pichler, B., Buchanan, K. A., Sjöström, P. J., and Mrsic-Flogel, T. D. (2011). Functional specificity of local synaptic connections in neocortical networks. *Nature* 473, 87–91. doi: 10.1038/nature09880

Koch, C., Poggio, T., and Torre, V. (1983). Nonlinear interactions in a dendritic tree: localization, timing and role in information processing. *Proc. Natl. Acad. Sci. U S A* 80, 2799–2802. doi: 10.1073/pnas.80.9.2799

Krueppel, R., Remy, S., and Beck, H. (2011). Dendritic integration in hippocampal dentate granule cells. *Neuron* 71, 512–528. doi: 10.1016/j.neuron.2011.05.043

Larkum, M. (2013). A cellular mechanism for cortical associations: an organizing principle for the cerebral cortex. *Trends Neurosci.* 36, 141–151. doi: 10.1016/j.tins.2012.11.006

Lavzin, M., Rapoport, S., Polsky, A., Garion, L., and Schiller, J. (2012). Nonlinear dendritic processing determines angular tuning of barrel cortex neurons in vivo. *Nature* 490, 397–401. doi: 10.1038/nature11451

Lee, D., Lin, B. J., and Lee, A. K. (2012). Hippocampal place fields emerge upon single-cell manipulation of excitability during behavior. *Science* 337, 849–853. doi: 10.1126/science.1221489

Legenstein, R., and Maass, W. (2011). Branch-specific plasticity enables self-organization of nonlinear computation in single neurons. *J. Neurosci.* 31, 10787–10802. doi: 10.1523/JNEUROSCI.5684-10.2011

London, M., and Häusser, M. (2005). Dendritic computation. *Annu. Rev. Neurosci.* 28, 503–532. doi: 10.1146/annurev.neuro.28.061604.135703

Longordo, F., To, M.-S., Ikeda, K., and Stuart, G. J. (2013). Sublinear integration underlies binocular processing in primary visual cortex. *Nat. Neurosci.* 16, 714–723. doi: 10.1038/nn.3394

Losonczy, A., and Magee, J. C. (2006). Integrative properties of radial oblique dendrites in hippocampal CA1 pyramidal neurons. *Neuron* 50, 291–307. doi: 10.1016/j.neuron.2006.03.016

Lutz, C., Otis, T. S., DeSars, V., Charpak, S., DiGregorio, D. A., and Emiliani, V. (2008). Holographic photolysis of caged neurotransmitters. *Nat. Methods* 5, 821–827. doi: 10.1038/nmeth.1241

Magee, J. C. (2000). Dendritic integration of excitatory synaptic input. *Nat. Rev. Neurosci.* 1, 181–190. doi: 10.1038/35044552

Magee, J. C., and Cook, E. P. (2000). Somatic EPSP amplitude is independent of synapse location in hippocampal pyramidal neurons. *Nat. Neurosci.* 3, 895–903. doi: 10.1038/78800

Magee, J. C., and Johnston, D. (1995). Characterization of single voltage-gated Na+ and Ca2+ channels in apical dendrites of rat CA1 pyramidal neurons. *J. Physiol.* 487(Pt. 1), 67–90. doi: 10.1113/jphysiol.1995.sp020862

Major, G., Larkman, A. U., Jonas, P., Sakmann, B., and Jack, J. J. (1994). Detailed passive cable models of whole-cell recorded CA3 pyramidal neurons in rat hippocampal slices. *J. Neurosci.* 14, 4613–4638.

Major, G., Larkum, M. E., and Schiller, J. (2013). Active properties of neocortical pyramidal neuron dendrites. *Annu. Rev. Neurosci.* 36, 1–24. doi: 10.1146/annurev-neuro-062111-150343

Makara, J. K., Losonczy, A., Wen, Q., and Magee, J. C. (2009). Experience-dependent compartmentalized dendritic plasticity in rat hippocampal CA1 pyramidal neurons. *Nat. Neurosci.* 12, 1485–1487. doi: 10.1038/nn.2428

Makara, J. K., and Magee, J. C. (2013). Variable dendritic integration in hippocampal CA3 pyramidal neurons. *Neuron* 80, 1438–1450. doi: 10.1016/j.neuron.2013.10.033

Makino, H., and Malinow, R. (2011). Compartmentalized versus global synaptic plasticity on dendrites controlled by experience. *Neuron* 72, 1001–1011. doi: 10.1016/j.neuron.2011.09.036

Markram, H., Helm, P. J., and Sakmann, B. (1995). Dendritic calcium transients evoked by single back-propagating action potentials in rat neocortical pyramidal neurons. *J. Physiol.* 485(Pt. 1), 1–20. doi: 10.1113/jphysiol.1995.sp020708

Marshel, J. H., Mori, T., Nielsen, K. J., and Callaway, E. M. (2010). Targeting single neuronal networks for gene expression and cell labeling in vivo. *Neuron* 67, 562–574. doi: 10.1016/j.neuron.2010.08.001

Martin, A. R. (1955). A further study of the statistical composition on the end-plate potential. *J. Physiol.* 130, 114–122. doi: 10.1113/jphysiol.1955.sp005397

McCulloch, W. S., and Pitts, W. (1943). A logical calculus of the ideas immanent in nervous activity. *Bull. Math. Biol.* 5, 115–133. doi: 10.1007/bf02478259

Mel, B. W. (1991). A connectionist model may shed light on neural mechanisms for visually guided reaching. *J. Cogn. Neurosci.* 3, 273–292. doi: 10.1162/jocn.1991.3.3.273

Mel, B. W. (1992). NMDA-based pattern discrimination in a modeled cortical neuron. *Neural Comput.* 4, 502–517. doi: 10.1162/neco.1992.4.4.502

Mel, B. W. (1993). Synaptic integration in an excitable dendritic tree. *J. Neurophysiol.* 70, 1086–1101.

Mel, B. W. (1994). Information processing in dendritic trees. *Neural Comput.* 6, 1031–1085. doi: 10.1162/neco.1994.6.6.1031

Mel, B. W., and Koch, C. (1990). "Sigma-pi learning: on radial basis functions and cortical associative learning," in *Advances in Neural Information Processing Systems*, ed D. S. Touretzky (San Mateo, CA: Morgan Kaufmann), 474–481.

Mel, B. W., Ruderman, D. L., and Archie, K. A. (1998). Translation-invariant orientation tuning in visual "complex" cells could derive from intradendritic computations. *J. Neurosci.* 18, 4325–4334.

Migliore, M., and Shepherd, G. M. (2002). Emerging rules for the distributions of active dendritic conductances. *Nat. Rev. Neurosci.* 3, 362–370. doi: 10.1038/nrn810

Nevian, T., Larkum, M. E., Polsky, A., and Schiller, J. (2007). Properties of basal dendrites of layer 5 pyramidal neurons: a direct patch-clamp recording study. *Nat. Neurosci.* 10, 206–214. doi: 10.1038/nn1826

Palmer, L., Murayama, M., and Larkum, M. (2012). Inhibitory regulation of dendritic activity in vivo. *Front. Neural Circuits* 6:26. doi: 10.3389/fncir.2012.00026

Palmer, L. M., Shai, A. S., Reeve, J. E., Anderson, H. L., Paulsen, O., and Larkum, M. E. (2014). NMDA spikes enhance action potential generation during sensory input. *Nat. Neurosci.* 17, 383–390. doi: 10.1038/nn.3646

Palmer, L. M., and Stuart, G. J. (2009). Membrane potential changes in dendritic spines during action potentials and synaptic input. *J. Neurosci.* 29, 6897–6903. doi: 10.1523/JNEUROSCI.5847-08.2009

Poirazi, P., and Mel, B. W. (2001). Impact of active dendrites and structural plasticity on the memory capacity of neural tissue. *Neuron* 29, 779–796. doi: 10.1016/s0896-6273(01)00252-5

Polsky, A., Mel, B. W., and Schiller, J. (2004). Computational subunits in thin dendrites of pyramidal cells. *Nat. Neurosci.* 7, 621–627. doi: 10.1038/nn1253

Popovic, M. A., Foust, A. J., McCormick, D. A., and Zecevic, D. (2011). The spatio-temporal characteristics of action potential initiation in layer 5 pyramidal neurons: a voltage imaging study. *J. Physiol.* 589, 4167–4187. doi: 10.1113/jphysiol.2011.209015

Popovic, M. A., Gao, X., Carnevale, N. T., and Zecevic, D. (2014). Cortical dendritic spine heads are not electrically isolated by the spine neck from membrane potential signals in parent dendrites. *Cereb. Cortex* 24, 385–395. doi: 10.1093/cercor/bhs320

Rall, W. (1967). Distinguishing theoretical synaptic potentials computed for different soma-dendritic distributions of synaptic input. *J. Neurophysiol.* 30, 1138–1168.

Rall, W., Burke, R. E., Holmes, W. R., Jack, J. J., Redman, S. J., and Segev, I. (1992). Matching dendritic neuron models to experimental data. *Physiol. Rev.* 72, S159–S186.

Rancz, E. A., and Häusser, M. (2006). Dendritic calcium spikes are tunable triggers of cannabinoid release and short-term synaptic plasticity in cerebellar Purkinje neurons. *J. Neurosci.* 26, 5428–5437. doi: 10.1523/jneurosci.5284-05.2006

Remme, M. W. H., Lengyel, M., and Gutkin, B. S. (2009). The role of ongoing dendritic oscillations in single-neuron dynamics. *PLoS Comput. Biol.* 5:e1000493. doi: 10.1371/journal.pcbi.1000493

Rinzel, J., and Rall, W. (1974). Transient response in a dendritic neuron model for current injected at one branch. *Biophys. J.* 14, 759–790. doi: 10.1016/s0006-3495(74)85948-5

Roth, A., and Häusser, M. (2001). Compartmental models of rat cerebellar Purkinje cells based on simultaneous somatic and dendritic patch-clamp recordings. *J. Physiol.* 535, 445–472. doi: 10.1111/j.1469-7793.2001.00445.x

Rudolph, M., and Destexhe, A. (2003). A fast-conducting, stochastic integrative mode for neocortical neurons in vivo. *J. Neurosci.* 23, 2466–2476.

Schiller, J., Helmchen, F., and Sakmann, B. (1995). Spatial profile of dendritic calcium transients evoked by action potentials in rat neocortical pyramidal neurones. *J. Physiol.* 487(Pt. 3), 583–600. doi: 10.1113/jphysiol.1995.sp020902

Schiller, J., Major, G., Koester, H. J., and Schiller, Y. (2000). NMDA spikes in basal dendrites of cortical pyramidal neurons. *Nature* 404, 285–289. doi: 10.1038/35005094

Schiller, J., Schiller, Y., Stuart, G., and Sakmann, B. (1997). Calcium action potentials restricted to distal apical dendrites of rat neocortical pyramidal neurons. *J. Physiol.* 505(Pt. 3), 605–616. doi: 10.1111/j.1469-7793.1997.605ba.x

Schmidt-Hieber, C., Jonas, P., and Bischofberger, J. (2007). Subthreshold dendritic signal processing and coincidence detection in dentate gyrus granule cells. *J. Neurosci.* 27, 8430–8441. doi: 10.1523/jneurosci.1787-07.2007

Silver, R. A. (2010). Neuronal arithmetic. *Nat. Rev. Neurosci.* 11, 474–489. doi: 10.1038/nrn2864

Smith, S. L., Smith, I. T., Branco, T., and Häusser, M. (2013). Dendritic spikes enhance stimulus selectivity in cortical neurons in vivo. *Nature* 503, 115–120. doi: 10.1038/nature12600

Soler-Llavina, G. J., and Sabatini, B. L. (2006). Synapse-specific plasticity and compartmentalized signaling in cerebellar stellate cells. *Nat. Neurosci.* 9, 798–806. doi: 10.1038/nn1698

Spruston, N. (2008). Pyramidal neurons: dendritic structure and synaptic integration. *Nat. Rev. Neurosci.* 9, 206–221. doi: 10.1038/nrn2286

Spruston, N., and Johnston, D. (1992). Perforated patch-clamp analysis of the passive membrane properties of three classes of hippocampal neurons. *J. Neurophysiol.* 67, 508–529.

Spruston, N., and Kath, W. L. (2004). Dendritic arithmetic. *Nat. Neurosci.* 7, 567–569. doi: 10.1038/nn0604-567

St-Pierre, F., Marshall, J. D., Yang, Y., Gong, Y., Schnitzer, M. J., and Lin, M. Z. (2014). High-fidelity optical reporting of neuronal electrical activity with an ultrafast fluorescent voltage sensor. *Nat. Neurosci.* 17, 884–889. doi: 10.1038/nn.3709

Stuart, G. J., Dodt, H. U., and Sakmann, B. (1993). Patch-clamp recordings from the soma and dendrites of neurons in brain slices using infrared video microscopy. *Pflugers Arch.* 423, 511–518. doi: 10.1007/bf00374949

Stuart, G., and Spruston, N. (1998). Determinants of voltage attenuation in neocortical pyramidal neuron dendrites. *J. Neurosci.* 18, 3501–3510.

Takahashi, N., Kitamura, K., Matsuo, N., Mayford, M., Kano, M., Matsuki, N., et al. (2012). Locally synchronized synaptic inputs. *Science* 335, 353–356. doi: 10.1126/science.1210362

Varga, Z., Jia, H., Sakmann, B., and Konnerth, A. (2011). Dendritic coding of multiple sensory inputs in single cortical neurons in vivo. *Proc. Natl. Acad. Sci. U S A* 108, 15420–15425. doi: 10.1073/pnas.1112355108

Vervaeke, K., Lorincz, A., Nusser, Z., and Silver, R. A. (2012). Gap junctions compensate for sublinear dendritic integration in an inhibitory network. *Science* 335, 1624–1628. doi: 10.1126/science.1215101

Wegener, I. (1987). *The Complexity of Boolean Functions*. New York, NY: John Wiley & Sons, Inc.

Williams, S. R., and Stuart, G. J. (2000). Site independence of EPSP time course is mediated by dendritic I(h) in neocortical pyramidal neurons. *J. Neurophysiol.* 83, 3177–3182.

Williams, S. R., and Stuart, G. J. (2002). Dependence of EPSP efficacy on synapse location in neocortical pyramidal neurons. *Science* 295, 1907–1910. doi: 10.1126/science.1067903

Xu, N.-L., Harnett, M. T., Williams, S. R., Huber, D., O'Connor, D. H., Svoboda, K., et al. (2012). Nonlinear dendritic integration of sensory and motor input during an active sensing task. *Nature* 492, 247–251. doi: 10.1038/nature11601

Yang, S., Emiliani, V., and Tang, C. M. (2014). The kinetics of multibranch integration on the dendritic arbor of CA1 pyramidal neurons. *Front. Cell Neurosci.* 8:127. doi: 10.3389/fncel.2014.00127

Yang, S., Papagiakoumou, E., Guillon, M., de Sars, V., Tang, C. M., and Emiliani, V. (2011). Three-dimensional holographic photostimulation of the dendritic arbor. *J. Neural Eng.* 8:046002. doi: 10.1088/1741-2560/8/4/046002

Yizhar, O., Fenno, L. E., Prigge, M., Schneider, F., Davidson, T. J., O'Shea, D. J., et al. (2011). Neocortical excitation/inhibition balance in information processing and social dysfunction. *Nature* 477, 171–178. doi: 10.1038/nature10360

Zador, A. M., Claiborne, B. J., and Brown, T. J. (1992). "Nonlinear pattern separation in single hippocampal neurons with active dendritic membrane," in *Advances in Neural Information Processing Systems*, eds J. Moody, S. Hanson and R. Lippman (Cambridge, MA: Morgan Kaufmann).

Zou, P., Zhao, Y., Douglass, A. D., Hochbaum, D. R., Brinks, D., Werley, C. A., et al. (2014). Bright and fast multicoloured voltage reporters via electrochromic FRET. *Nat. Commun.* 5:4625. doi: 10.1038/ncomms5625

Conflict of Interest Statement: The authors declare that the research was conducted in the absence of any commercial or financial relationships that could be construed as a potential conflict of interest.

frontiers in
CELLULAR NEUROSCIENCE

ORIGINAL RESEARCH ARTICLE
published: 12 January 2015
doi: 10.3389/fncel.2014.00456

Dendritic atrophy constricts functional maps in resonance and impedance properties of hippocampal model neurons

Neha Dhupia[1,2], Rahul K. Rathour[1] and Rishikesh Narayanan[1]*

[1] *Cellular Neurophysiology Laboratory, Indian Institute of Science, Bangalore, India*
[2] *Centre for Converging Technologies, University of Rajasthan, Jaipur, India*

Edited by:
Sergey M. Korogod, National Academy of Sciences of Ukraine, Ukraine

Reviewed by:
Benjamin Torben-Nielsen, Okinawa Institute of Science and Technology Graduate University, Japan
Peter Jedlicka, Goethe University, Germany

***Correspondence:**
Rishikesh Narayanan, Cellular Neurophysiology Laboratory, Indian Institute of Science, Molecular Biophysics Unit, Bangalore 560012, India
e-mail: rishi@mbu.iisc.ernet.in

A gradient in the density of hyperpolarization-activated cyclic-nucleotide gated (HCN) channels is necessary for the emergence of several functional maps within hippocampal pyramidal neurons. Here, we systematically analyzed the impact of dendritic atrophy on nine such functional maps, related to input resistance and local/transfer impedance properties, using conductance-based models of hippocampal pyramidal neurons. We introduced progressive dendritic atrophy in a CA1 pyramidal neuron reconstruction through a pruning algorithm, measured all functional maps in each pruned reconstruction, and arrived at functional forms for the dependence of underlying measurements on dendritic length. We found that, across frequencies, atrophied neurons responded with higher efficiency to incoming inputs, and the transfer of signals across the dendritic tree was more effective in an atrophied reconstruction. Importantly, despite the presence of identical HCN-channel density gradients, spatial gradients in input resistance, local/transfer resonance frequencies and impedance profiles were significantly constricted in reconstructions with dendritic atrophy, where these physiological measurements across dendritic locations converged to similar values. These results revealed that, in atrophied dendritic structures, the presence of an ion channel density gradient alone was insufficient to sustain homologous functional maps along the same neuronal topograph. We assessed the biophysical basis for these conclusions and found that this atrophy-induced constriction of functional maps was mediated by an enhanced spatial spread of the influence of an HCN-channel cluster in atrophied trees. These results demonstrated that the influence fields of ion channel conductances need to be localized for channel gradients to express themselves as homologous functional maps, suggesting that ion channel gradients are necessary but not sufficient for the emergence of functional maps within single neurons.

Keywords: dendritic morphology, functional maps, HCN channel, impedance, resonance

INTRODUCTION

Hippocampal pyramidal neurons exhibit tremendous morphological variability. These variations in morphology could be simple baseline variability (Bannister and Larkman, 1995; Ishizuka et al., 1995; Dougherty et al., 2012), or be a consequence of structural plasticity that is associated with several physiological and pathophysiological conditions (Leuner and Gould, 2010). Specifically, structural plasticity in the CA1 subregion has shown to be associated with development (Pokorny and Yamamoto, 1981), aging (Lolova, 1989; Kadar et al., 1994; Markham et al., 2005; Mora et al., 2007), reproductive experience (Pawluski and Galea, 2006), enriched environment (Faherty et al., 2003; Leggio et al., 2005) and with pathological conditions that include Alzheimer's disease (Hanks and Flood, 1991; De Leon et al., 1997; Elgh et al., 2006; Kerchner et al., 2012), various forms of chronic stress (Lambert et al., 1998; McEwen, 1999; Bartesaghi et al., 2003; Isgor et al., 2004; Brunson et al., 2005; Pinto et al., 2014) and depression (Sheline et al., 1996; Campbell and Macqueen, 2004). What are the functional consequences of such innate and remodeling-dependent changes in pyramidal neuron morphology? Primarily, it has been shown that changes in dendritic arborization could alter synaptic and neuronal excitability, somatodendritic coupling, firing properties and firing patterns (Mainen and Sejnowski, 1996; Krichmar et al., 2002; Van Ooyen et al., 2002; Sjöström et al., 2008; Narayanan and Chattarji, 2010; Torben-Nielsen and Stiefel, 2010; Van Elburg and Van Ooyen, 2010; Ferrante et al., 2013; Platschek et al., 2013), and modulate forward/back-propagation of electrical potentials (Vetter et al., 2001; Sjöström et al., 2008; Narayanan and Chattarji, 2010; Ferrante et al., 2013) and coincidence detection (Schaefer et al., 2003). Although the modulation of these physiological measurements emphasize an important role for neuronal morphology in action potential firing and in the response of a neuron to a single or an array of synaptic inputs, these studies do not address the role of neuronal morphology on frequency-dependent response properties of neurons. Such analyses are critical because hippocampal neurons reside in an oscillating network where inputs arrive at specific frequency bands (Buzsaki, 2002, 2006; Wang, 2010),

and their responses are tuned to optimally respond to these frequency bands (Gimbarzevsky et al., 1984; Hutcheon and Yarom, 2000; Pike et al., 2000; Hu et al., 2002; Narayanan and Johnston, 2007). In an effort to fill this lacuna, in this study, we quantitatively assessed the role of neuronal morphology on location- and frequency-dependent response properties of hippocampal pyramidal neurons and their dendrites.

Hippocampal pyramidal neurons typically respond to afferent oscillatory inputs with spikes at specific oscillatory phases of these inputs (O'keefe and Recce, 1993; Buzsaki, 2002, 2006; Wang, 2010). In doing so, they recruit several voltage-gated ion channels (VGIC) in tuning their frequency-dependent response properties in a stratified manner enabling location-dependent input processing. A classic and extremely useful measure of frequency-dependent neuronal responses is electrical impedance, which is simply defined as the ratio of voltage response to the current input at various input frequencies (Cole, 1932, 1968; Cole and Baker, 1941). Impedance measurements from hippocampal pyramidal neurons have shown that they exhibit a maximal response at a particular frequency (known as the resonance frequency) in the theta-frequency range (4–10 Hz), and that the impedance phase is positive (inductive) in this theta-frequency range (Gimbarzevsky et al., 1984; Pike et al., 2000; Hu et al., 2002, 2009; Narayanan and Johnston, 2007, 2008; Vaidya and Johnston, 2013). Several ion channels with specific constraints on their kinetics and voltage-dependent properties could elicit such resonance, and these resonance properties could be dependent on dendritic location based on several mechanisms (Gimbarzevsky et al., 1984; Hutcheon and Yarom, 2000; Pike et al., 2000; Hu et al., 2002, 2009; Narayanan and Johnston, 2007, 2008; Vaidya and Johnston, 2013; Zhuchkova et al., 2013; Laudanski et al., 2014).

In hippocampal pyramidal neurons, impedance-dependent properties have been shown to be location-dependent, with both resonance frequency and inductive phase varying with distance from the cell body. Specifically, two forms of resonance have been reported to express in hippocampal pyramidal neurons, with complementary location-dependent profiles. The hyperpolarization-activated cyclic-nucleotide gated (HCN) channels mediate resonance at more hyperpolarized voltages, and the *M*-type K^+ channels mediate resonance at relatively depolarized voltages. Furthermore, resonance frequency measured at hyperpolarized voltages increases with distance from the cell body whereas that at depolarized voltage ranges decreases with distance from the cell body, thereby complementing each other both as functions of voltage range as well as somatodendritic location (Pike et al., 2000; Hu et al., 2002, 2009; Narayanan and Johnston, 2007, 2008, 2012).

What mediates these resonance frequency maps in hippocampal pyramidal neurons? Several lines of experimental and modeling evidence suggest that these topographic functional maps are *actively* mediated by ion channel localization profiles. First, HCN channels express at higher densities in the distal dendrites of hippocampal pyramidal neurons (Magee, 1998; Lorincz et al., 2002), *M*-type K^+ channels are largely perisomatic (Hu et al., 2007). In conjunction with the monotonic relationship between resonating conductance density and resonance frequency (Hutcheon et al., 1996; Narayanan and Johnston, 2007), this suggests that the resonance frequency maps reflect the respective conductance gradient. Second, pharmacological blockade of these channels in hippocampal pyramidal neurons clearly demonstrates that the associated resonance frequency maps are exclusively dependent on the specific ion channels. Specifically, at hyperpolarized voltages, blockade of HCN channels rendered the somatodendritic structure to be simple low-pass structures with the abolishment of resonance and phase lead in the voltage response, across dendritic locations (Narayanan and Johnston, 2007, 2008; Hu et al., 2009; Vaidya and Johnston, 2013). On the other hand, at depolarized voltages, blocking *M*-type K^+ channels eliminated band-pass characteristics of somatodendritic response properties (Hu et al., 2002, 2007). Third, if resonance were merely reflective of passive gradients in the neuronal topograph, maintaining two spatial gradients with opposing signs would be infeasible. However, in a hippocampal pyramidal neuron, two distinct complementary location-dependent gradients of resonance and impedance profiles express on the *same* neuronal topograph and reflect the corresponding channel localization profiles. Fourth, and importantly, input resistance and impedance properties are rendered largely location-independent when HCN channels are blocked (Narayanan and Johnston, 2007, 2008), implying that resistance and impedance gradients at hyperpolarized voltages express only in the presence of HCN channels. Therefore, it is imperative that the presence of a gradient in HCN channels is essential in mediating these *coexisting* functional maps of input resistance and local/transfer impedance properties (Narayanan and Johnston, 2007, 2008, 2012; Vaidya and Johnston, 2013). Finally, modeling studies performed in the presence of these important experimental constraints have clearly demonstrated that a constant density of HCN channels or a shallow gradient in their density is insufficient to elicit these coexistent maps of input resistance and local/transfer resonance properties (Hu et al., 2002, 2009; Narayanan and Johnston, 2007, 2008; Vaidya and Johnston, 2013).

Together, these experimental and modeling studies on hippocampal pyramidal neurons demonstrate that a somatodendritic gradient in the density of a resonating conductance is *necessary* for the expression of the functional maps in input resistance, resonance frequency and other impedance properties (Narayanan and Johnston, 2007, 2008, 2012). In other words, in a hippocampal pyramidal neuron, in the absence of the gradient in the density of the resonating conductance, the specific functional map ceases to exist. Is a gradient in the density of a resonating conductance *sufficient* to impose these functional maps on a neuronal topograph? What is the impact of dendritic structure on how neurons respond to time-varying inputs under conditions where the neuron is passive? How does such impact change when the same neurons express gradients in ion channel properties/densities? Do functional maps of impedance-related and resonance measurements depend on dendritic arborization? To answer these questions, and motivated to assess the role of dendritic morphology on neuronal intrinsic response dynamics, we analyzed several well-established functional maps mediated by HCN channels in conductance-based neuronal models with different morphological complexities.

We found that, in the passive structure or in a neuronal model endowed with a HCN-channel gradient, dendritic atrophy induced a frequency-nonspecific increase in neuronal excitability across dendritic locations and significantly enhanced somatodendritic coupling. Further, assessing local and transfer resonance frequencies in a model endowed with an HCN-channel gradient, we found that the presence of this gradient was not sufficient to impose a map in resonance frequencies in an atrophied neuron. This conclusion was consistent across several other measurements, suggesting that ion channel gradients along a dendritic topograph alone are insufficient to introduce gradients in physiological measurements along the same topograph. Finally, we explored the biophysical basis for these conclusions, and found that our results were a direct consequence of an atrophy-induced increase in the spatial influence of a local channel cluster on several physiological measurements. Our results have important implications for structure-function relationships, especially with reference to neuronal excitability, induction of synaptic plasticity, rate and temporal coding of place fields, channelostasis and targeting of specific ion channels, propagation of electrical and biochemical signals along the dendritic arbor and neuronal spike initiation dynamics, both from physiological and pathophysiological standpoints.

MATERIALS AND METHODS

In this study, we employed conductance-based multicompartmental models built upon a three-dimensional reconstruction of a hippocampal CA1 pyramidal neuron for understanding the impact of dendritic remodeling on neuronal impedance properties. Progressive dendritic atrophy of this reconstruction was achieved through a pruning algorithm designed to elicit uniform pruning across all dendritic *strata* (Narayanan et al., 2005). The pruning algorithm was employed to create 16 different pruned morphologies, with the difference between successive morphologies set at around 1 mm atrophy of total dendritic length (see **Figure 1A** for representative examples of pruned morphologies). In what follows, the unpruned morphology will be referred to as the base model, and the other models will be referred by their total dendritic length in mm (**Figure 1A**). We employed this approach of systematically altering a single base dendritic morphological structure for our study owing to its advantages in comparison to a correlative approach of using different morphological structures and obtaining physiological measurements from them (Narayanan et al., 2005; Narayanan and Chattarji, 2010):

(1) The algorithm allows us to induce specific structural changes in a given neuron and examine its functional consequences in the same neuron, thereby enabling us to establish a *causal* link between dendritic remodeling and its biophysical effects.
(2) The use of multiple neurons to arrive at the relationship between structure and function of neurons has the potential pitfall that biologically observed statistical variability across neurons might cause a non-atrophied neuron to elicit functional responses similar to an atrophied neuron. Our algorithm uses a single neuron to causally construct the structure–function relationship, thereby precluding the effects of intrinsic variability across morphologies from specific dendritic remodeling.
(3) The algorithm provides us with trees with varying percentages of atrophy of the original dendritic tree. This enables us to analyze the functional form of the relationship between various biophysical parameters and the total dendritic length.
(4) Comparison of the neuronal responses to stimulation with multiple frequencies at the *same* dendritic point in different trees is made possible because atrophied trees are subtrees of the base reconstruction. This implies that the branching structure remains the same, thereby ensuring that the analysis is not confounded by the impact of branching patterns on the propagation of information along the dendritic tree (Vetter et al., 2001; Ferrante et al., 2013). This is especially necessary in our analysis of local and transfer impedance properties with varying gradients in passive and active properties, where maintaining the same location across trees becomes crucial.

MULTICOMPARTMENTAL MODEL: PASSIVE PROPERTIES

A three-dimensional reconstruction of a hippocampal CA1 pyramidal neuron (*n123*), obtained from NeuroMorpho.Org (Ascoli et al., 2007), originally reconstructed by Pyapali et al. (1998) was used as the base morphology for all multicompartmental simulations. Passive electrical parameters were tuned in a manner such that the local input resistance (R_{in}) remained constant (~120 MΩ) throughout the trunk (Narayanan and Johnston, 2007). The specific membrane capacitance was set as 1 μF/cm^2. Specific membrane resistivity R_m and intracellular resistivity R_a, for compartments along the somatodendritic compartments as functions of radial distance from the soma, x, were set as:

$$R_m(x) = R_m^{som} + \frac{\left(R_m^{end} - R_m^{som}\right)}{1 + \exp\left(\frac{250-x}{50}\right)} \text{k}\Omega.\text{cm}^2 \quad (1)$$

$$R_a(x) = R_a^{som} + \frac{\left(R_a^{end} - R_a^{som}\right)}{1 + \exp\left(\frac{250-x}{50}\right)} \Omega.\text{cm} \quad (2)$$

where $R_m^{som} = 55\,\text{k}\Omega.\text{cm}^2$ and $R_a^{som} = 70\,\Omega.\text{cm}$ were the values at soma, $R_m^{end} = 20\,\text{k}\Omega.\text{cm}^2$ and $R_a^{end} = 30\,\Omega.\text{cm}$ were values at distal end of the apical trunk (which was ~450 μm distance from the soma for the reconstruction). The basal dendrites have similar R_m and R_a as somatic compartments. This model was compartmentalized using the d_λ rule (Carnevale and Hines, 2006), ensuring that each compartment was smaller than $0.1\lambda_{100}$, where λ_{100} constitutes the space constant computed at 100 Hz.

CHANNEL KINETICS AND DISTRIBUTION

The kinetics and voltage-dependent properties of the hyperpolarization activated cyclic nucleotide gated (HCN or simply *h*) channel was derived from Magee (1998) and Poolos et al. (2002). In simulations where an *h*-channel gradient was included, the maximal conductance value for the *h* conductance for compartments all over somato-apical arbor, as a function of radial distance from soma, x was set as:

$$\bar{g}_h(x) = 50\left(1 + \frac{25}{1 + \exp\left(-(x - 350)/15\right)}\right) \mu\text{S/cm}^2 \quad (3)$$

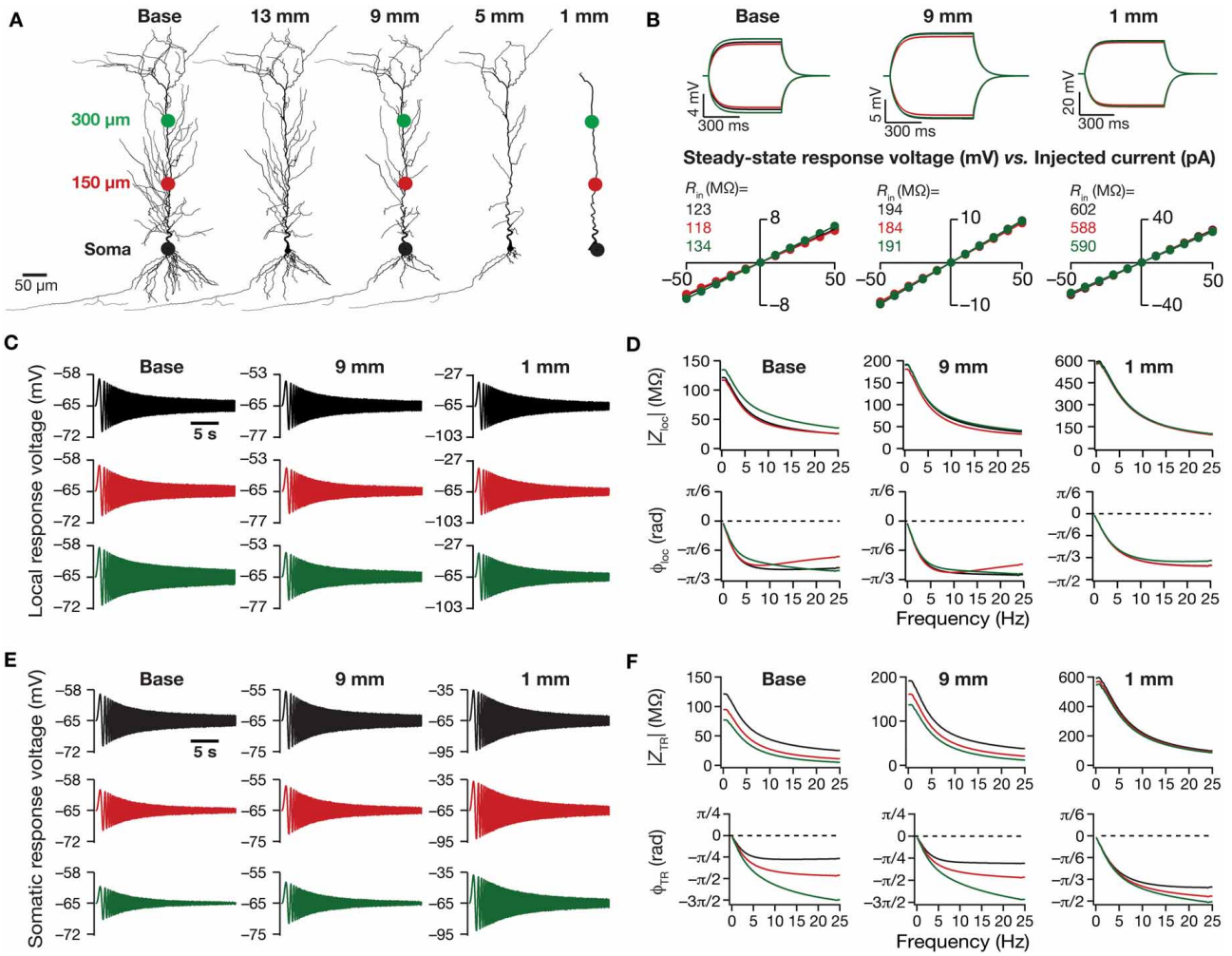

FIGURE 1 | Traces and measurements related to neuronal intrinsic response dynamics revealed significant somatodendritic changes with dendritic atrophy in a passive neuronal model. (A) Baseline and a subset of pruned morphologies employed in this study. Base: two-dimensional projection of a CA1 pyramidal neuron reconstruction. The total dendritic length of the neuron was 17.5, 13, 9, 5, and 1 mm are the labels provided for atrophied dendritic reconstruction, and correspond to the total dendritic length of these pruned morphologies. The three colored dots along the trunk marked at the soma (black), and at ∼150 µm (red) and ∼300 µm (green) away from soma depict the color-coded locations corresponding to the traces and plots shown across all figures of the manuscript. The markings are shown only on dendritic trees where traces/analyses are elaborated in **(B–F)**. **(B)** Local voltage traces (top) and steady-state *V–I* plots (bottom) fitted with straight lines obtained in response of depolarizing and hyperpolarizing current pulses injected at three identical locations on three different morphological reconstructions. **(C)** Local voltage traces obtained in response to a chirp stimulus (a sinusoidal current wave of constant amplitude with frequency linearly increasing from 0 to 25 Hz in 25 s) injected at three identical locations on three different morphological reconstructions. **(D)** Local impedance amplitude (top) and phase (bottom) profiles obtained from traces shown in **(C)** and plotted as functions of frequency for various somatodendritic locations and levels of atrophy. **(E)** Somatic voltage traces obtained in response of a chirp stimulus injected at three identical locations on three different morphological reconstructions. **(F)** Transfer impedance amplitude (top) and phase (bottom) profiles obtained from traces shown in **(E)** and plotted as functions of frequency for various somatodendritic locations and levels of atrophy.

The basal dendrites had the same $\bar{g}_h$ as the somatic compartments. The values in Equation (3) were tuned in a manner such that the R_{in} reduced from ∼75 to 40 MΩ along the somatoapical trunk of the base model, with a corresponding increase in resonance frequency (f_R) from 3 to 11 Hz, measured at −65 mV (Narayanan and Johnston, 2007).

MEASUREMENTS

All physiological relevant measurements were computed employing procedures listed in previous studies (Narayanan and Johnston, 2007, 2008; Rathour and Narayanan, 2012a, 2014; Das and Narayanan, 2014). Specifically, R_{in} was measured as the slope of the *V–I* plot, with *V* representing the local steady-state voltage response to depolarizing and hyperpolarizing current pulses of amplitude *I*, ranging from −50 pA to 50 pA, in steps of 10 pA, for 300 ms, at specific locations along the somatodendritic arbor. In certain cases, to minimize the overall voltage deflections, the current range was reduced to −25 pA to 25 pA in steps of 5 pA.

The stimulus used for computing the impedance was a chirp stimulus, a sinusoidal current wave with constant amplitude

(50 pA), with frequency linearly increasing from 0 to 25 Hz in 25 s. For models endowed with HCN channels, the amplitude of the chirp stimulus waveform was normalized with respect to input resistance of somatic compartment such that peak-to-peak amplitude of voltage response was similar across various pruned morphologies. Two types of impedance measurements were performed: local and transfer. For local measurements, the voltage response was recorded at the same location where the chirp stimulus was injected. For transfer impedance measurements, on the other hand, the chirp stimulus was injected at different somatodendritic locations, but the voltage response was always recorded at the soma. $Z_{loc}(f)$ and $Z_{TR}(f)$ were used to represent local and transfer impedance, respectively. When impedance properties were represented as functions of distance, the distance corresponded to the location of chirp injection.

The magnitude of the ratio of the Fourier transform of voltage response to the Fourier transform of the chirp stimulus formed the impedance amplitude profile (ZAP). The impedance magnitude for a given impedance $Z(f)$ was calculated using following equation:

$$\left|Z(f)\right| = \sqrt{\left(Re(Z(f))\right)^2 + \left(Im(Z(f))\right)^2} \tag{4}$$

where $\mathrm{Im}\left(Z(f)\right)$ and $\mathrm{Re}\left(Z(f)\right)$ were the imaginary and real parts of the impedance $Z(f)$, respectively.

The frequency at which the $Z_{\mathrm{loc}}(f)$ and $Z_{\mathrm{TR}}(f)$ reached their maximum was considered as the local (f_{R}) and transfer (f_{TR}) resonance frequency, respectively (Hutcheon and Yarom, 2000; Hu et al., 2002, 2009; Narayanan and Johnston, 2007; Vaidya and Johnston, 2013). $|Z_{\mathrm{loc}}|_{\max}$ and $|Z_{\mathrm{TR}}|_{\max}$ represented the maximum values of the local and transfer ZAP, which as per definition equal $|Z_{\mathrm{loc}}(f_{\mathrm{R}})|$ and $|Z_{\mathrm{TR}}(f_{\mathrm{TR}})|$, respectively. Local resonance strength (Q) was measured as the ratio of $|Z_{\mathrm{loc}}(f_{\mathrm{R}})|$ to $|Z_{\mathrm{loc}}(0.5)|$ and transfer resonance strength (Q_{TR}) was measured as the ratio of $|Z_{\mathrm{TR}}(f_{\mathrm{TR}})|$ to $|Z_{\mathrm{TR}}(0.5)|$(Hu et al., 2002; Das and Narayanan, 2014).

Impedance phase profile (ZPP) for a given impedance $Z(f)$ was calculated as:

$$\phi(f) = \tan^{-1}\frac{Im\left(Z(f)\right)}{Re\left(Z(f)\right)} \tag{5}$$

where $\phi_{\mathrm{loc}}(f)$ and $\phi_{\mathrm{TR}}(f)$, computed respectively from $Z_{\mathrm{loc}}(f)$ and $Z_{\mathrm{TR}}(f)$ using Equation (5), represented local and transfer ZPPs, respectively. The total inductive phase was computed as the area under the inductive part of the corresponding ZPP (Narayanan and Johnston, 2008; Rathour and Narayanan, 2014):

$$\Phi_L(f) = \int_{\phi(f)>0} \phi(f)df \tag{6}$$

$\Phi_L(f)$ and $\Phi_L^{TR}(f)$, computed respectively from $\phi_{\mathrm{loc}}\ (f)$ and $\phi_{\mathrm{TR}}(f)$ using Equation (6), represented the total inductive phase for local and transfer ZPPs, respectively.

INFLUENCE FIELD QUANTIFICATION

The influence field for an ion channel cluster inserted at location x_i, for measurement M, was calculated through the normalized influence factor, $\Lambda_M\ (x; x_i)$ as follows (Rathour and Narayanan, 2012b):

$$\Lambda_M\ (x; x_i) = \frac{\mathrm{IF_M}(x; x_i)}{\max \mathrm{IF_M}(x; x_i)} \tag{7}$$

where x stands for location along trunk length and $\mathrm{IF_M}\ (x;\ x_i)$ is the unnormalized influence factor, calculated as:

$$\mathrm{IF_M}(x; x_i) = \frac{\left|M_{\mathrm{org}}(x) - M_{\mathrm{new}}(x; x_i)\right|}{M_{\mathrm{org}}(x)} \tag{8}$$

where M_{org} represented the measurement obtained in absence of the ion channel cluster at location x_i and M_{new} was obtained after inserting channel cluster at location x_i. For example, for measuring the influence field of an HCN-channel cluster on R_{in}, $R_{\mathrm{org}}\ (x)$ and $R_{\mathrm{new}}\ (x;\ x_i)$ were calculated in the absence and in the presence of the channel cluster located at x_i, respectively. Unless otherwise stated, the HCN-channel cluster was located at a dendritic path distance of $x_i = \sim$450 μm away from soma (around the center of the apical trunk).

For quantitative analyses of the influence field, we employed the area under the influence field plot as a measure of the extent of influence of a single ion channel cluster located at x_i:

$$\text{AUC of } \Lambda_M = \int_0^{L_d} \Lambda_M(x; x_i)dx \tag{9}$$

where L_d is the total path length of the apical trunk. Whereas $\Lambda_M\ (x; x_i)$ was employed for computing the area under the curve (AUC) of the normalized influence field, for computing the AUC of the unnormalized influence field, we employed $\mathrm{IF}_M\ (x; x_i)$ (Equation 8).

COMPUTATIONAL DETAILS

All simulations were performed using the NEURON simulation environment (Carnevale and Hines, 2006). Simulations were performed with the membrane potential set at −65 mV. The temperature was set at 34°C, and ion channel kinetics were adjusted appropriately to account for their experimentally determined Q_{10} factors. The default integration time step for the simulations was set at 25 μs. Computation of physiologically-relevant measurements from simulation traces and quantification of influence fields were performed with custom-built software written within the IGOR Pro (Wavemetrics) programming environment.

RESULTS

How does dendritic morphology alter intrinsic response dynamics in a passive neuronal model? To address this question, we employed a 3D reconstructed CA1 pyramidal neuron as our base morphology and adjusted its passive properties to match with experimental measurements (Narayanan and Johnston, 2007). We then applied an iterative pruning algorithm (Narayanan et al., 2005) on this base morphology to obtain 17 different morphologies, each successively pruned by ∼1 mm (from the ∼17.5 mm of

total dendritic length of the base morphology to ∼1 mm of total dendritic length of the most pruned morphology; **Figure 1A**). We employed these pruned reconstructions, imposed identical passive properties on each of them and analyzed the impact of dendritic atrophy on somatodendritic excitability in passive neuronal models.

DENDRITIC ATROPHY INCREASED LOCAL AND TRANSFER IMPEDANCE AMPLITUDES ACROSS LOCATIONS

We computed R_{in} at different locations along the dendritic arbor (**Figure 1B**), and found that R_{in} increased across the dendritic arbor with atrophy (**Figures 2A,B**). This should be expected because a reduction in total surface area and branching directly translates into an increase in the input resistance of the compartment (Rall, 1977; Mainen and Sejnowski, 1996; Krichmar et al., 2002; Van Ooyen et al., 2002; Narayanan and Chattarji, 2010; Van Elburg and Van Ooyen, 2010). Whereas this steady-state neuronal response property showed an expected outcome, how does the frequency-dependent response of a neuron vary with dendritic remodeling? To address this question, we computed the local impedance amplitude and phase using the chirp stimulus (**Figures 1C,D**). As our model contained only passive components, the voltage response to a chirp stimulus behaved like a low pass filter, with higher responses at lower frequencies and lower responses at higher frequencies (**Figure 1D**). Dendritic atrophy did not significantly alter the shape of this low-pass filter (**Figure 1D**), but changed only the actual response amplitude (**Figure 1D**). The impedance phase profile always stayed negative across all frequencies (**Figure 1D**), suggesting that the voltage response lagged the current input at all measured frequencies. This should be expected in a passive system, which behaves similar to an RC circuit, thereby eliciting only negative phases (Cole, 1932, 1968; Cole and Baker, 1941; Narayanan and Johnston, 2008). The shape of the phase response also did not show any significant change with dendritic atrophy across the three measured locations (**Figure 1D**).

Do conclusions on atrophy-induced increases in the maximal local impedance amplitude at these three locations extend to other locations of the dendritic tree? To address this, we measured $|Z_{loc}|_{max}$ associated with the local impedance of various locations along the somatoapical trunk, and plotted it for various levels of dendritic atrophy. We found that the maximal local impedance

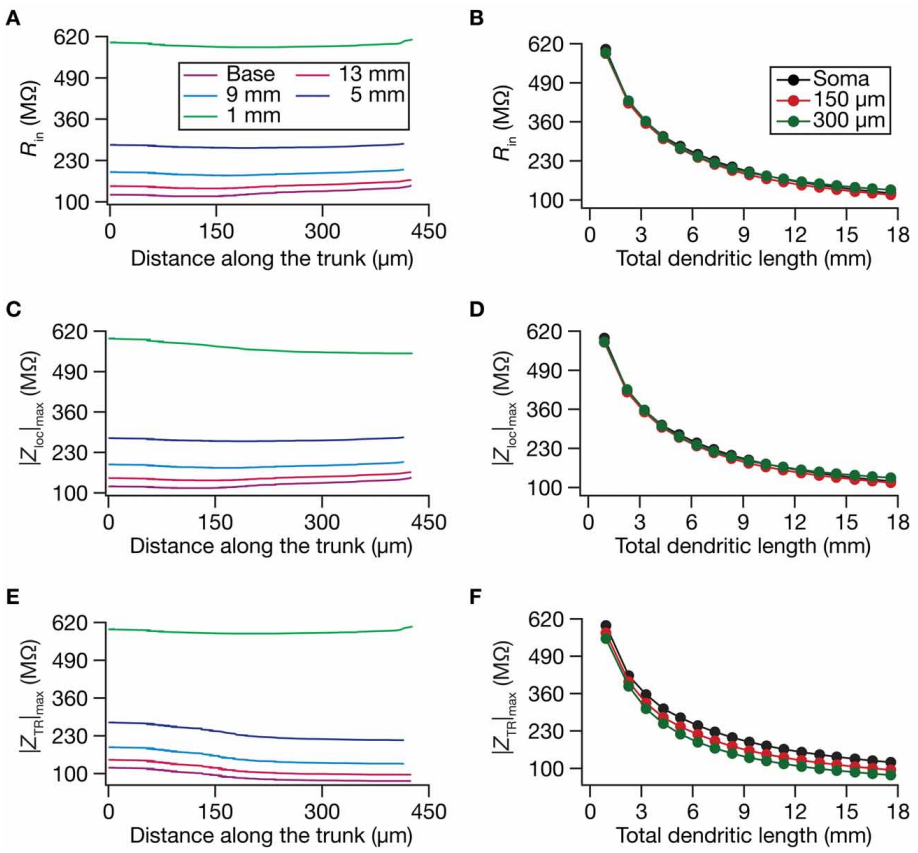

FIGURE 2 | Steady-state and frequency-dependent measures of excitability increased with dendritic atrophy across somatodendritic locations of a passive neuronal model. (A,B) Input resistance (R_{in}) plotted as functions of somatodendritic location (**A**; for 5 different pruned morphologies, **Figure 1A**) and total dendritic length (**B**; for 3 distinct somatodendritic locations, **Figure 1A**). **(C,D)** Maximal local impedance amplitude ($|Z_{loc}|_{max}$) plotted as functions of somatodendritic location **(C)** and dendritic length **(D)**. **(E,F)** Maximal transfer impedance amplitude ($|Z_{TR}|_{max}$) plotted as functions of somatodendritic location **(E)** and total dendritic length **(F)**. The legends for all graphs on the left and right are given in **(A,B)**, respectively.

amplitude, measured at several locations along the somatoapical trunk, increased with atrophy (**Figures 2C,D**).

Information arriving at a dendritic location undergoes a two-step filtering process before integration occurs at the soma. The first is governed by the local frequency response of the dendritic branch, and the second depends on the propagation of this signal along the dendritic tree. A quantitative manner to study the latter is through transfer impedance properties, which may be evaluated by recording the voltage response to a chirp current injected at a somatodendritic location (Ulrich, 2002; Hu et al., 2009; Vaidya and Johnston, 2013). For passive neurons, this transfer impedance profile is expected to be low-pass in nature given the resistor-capacitor electrical structure of a passive neuron (**Figures 1E,F**). Although the passive nature of the transfer impedance amplitude and phase profiles did not change with dendritic atrophy, atrophy introduced quantitative differences in these profiles (**Figure 1F**). To quantify this, we computed the transfer impedance amplitude, $|Z_{TR}|_{max}$, at various locations along the somatoapical trunk, and found that $|Z_{TR}|_{max}$ shifted to higher values with dendritic atrophy across the entire somatoapical trunk (**Figures 2E,F**). The pattern of evolution of the transfer impedance amplitude was very similar to the evolution of local impedance amplitude, with a monotonic increase with dendritic atrophy (**Figures 2C–F**). These, together, implied that atrophied neurons responded with higher efficiency to incoming inputs, and that the transfer of signals across the dendritic tree was more effective in an atrophied tree across frequencies.

DENDRITIC ATROPHY CONSTRICTED HCN-CHANNEL MEDIATED SPATIAL MAPS OF LOCAL AND TRANSFER IMPEDANCES

Although the input resistance values are flat with low-pass frequency response profiles in the absence of HCN channels, native

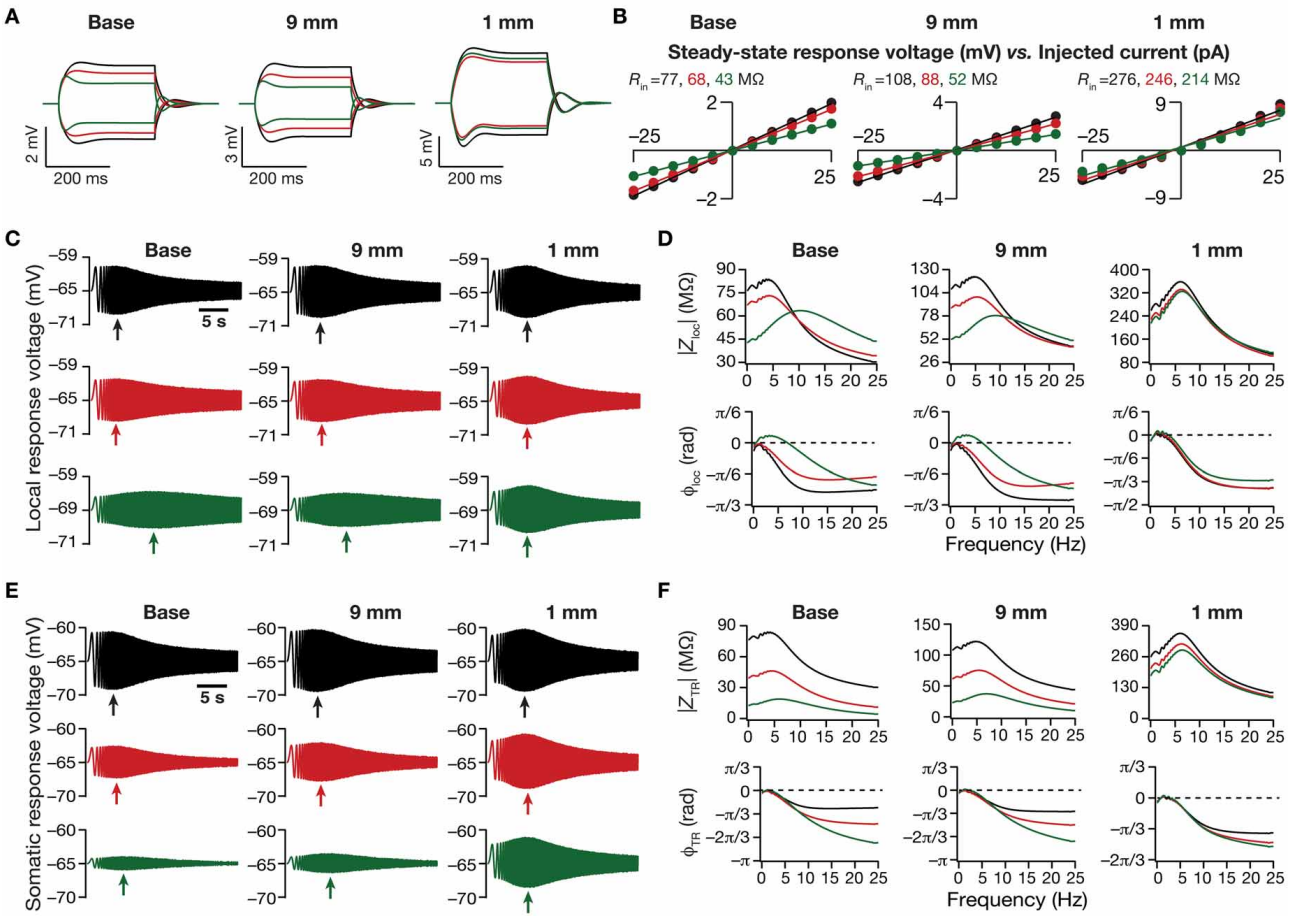

FIGURE 3 | Dendritic atrophy in the presence of a physiologically constrained HCN-channel gradient introduced significant somatodendritic changes in neuronal intrinsic response dynamics. (A,B) Local voltage traces **(A)** and steady-state *V–I* plots **(B)** fitted with straight lines obtained in response of depolarizing and hyperpolarizing current pulses injected at three identical locations on three different morphological reconstructions. **(C)** Local voltage traces obtained in response of a chirp stimulus injected at three identical locations on three different morphological reconstructions. **(D)** Local impedance amplitude (top) and phase (bottom) profiles obtained from traces shown in **(C)** and plotted as functions of frequency for various somatodendritic locations and levels of atrophy. **(E)** Somatic voltage traces obtained in response of a chirp stimulus injected at three identical locations on three different morphological reconstructions. **(F)** Transfer impedance amplitude (top) and phase (bottom) profiles obtained from traces shown in **(E)** and plotted as functions of frequency for various somatodendritic locations and levels of atrophy. Arrows in **(C,E)** refer to the location of maximal response on those specific traces. See **Figure 1A** for the morphologies and locations referred here.

hippocampal dendrites are endowed with a HCN-channel gradient that mediates a functional gradient of input resistance, and bestows band-pass characteristics on the location-dependent impedance profiles (Magee, 1998; Lorincz et al., 2002; Narayanan and Johnston, 2007; Hu et al., 2009; Vaidya and Johnston, 2013). In hippocampal pyramidal neurons, whereas R_{in} stays at almost ∼120 MΩ throughout the somatoapical trunk in the absence of the HCN channels, in their presence, R_{in} reduces from around 70 MΩ at the soma to around 20–30 MΩ at the distal dendritic locations (Narayanan and Johnston, 2007). To understand the impact of dendritic remodeling on R_{in} in the presence of HCN channels, we introduced a density gradient of HCN channels into our morphologies. We imposed the same HCN gradient and passive properties on all the 17 morphologies, and asked if this input resistance map altered with dendritic atrophy. Consistent with our results with passive models (**Figures 1**, **2**), we found that R_{in} increased with atrophy (**Figures 3A,B**). Importantly, we also found that the R_{in} map became more uniform in an atrophied neuron, compared to the base morphology (**Figures 4A,B**). Specifically, whereas there was a reduction in R_{in} with distance in the base morphology, with atrophy, the ratio between somatic and dendritic R_{in} values was lesser in the pruned dendritic tree compared to its control counterpart (**Figures 4A,B**). Therefore, in atrophied dendritic trees, the gradient in HCN channels was insufficient to maintain a gradient in R_{in}.

Next, we turned our attention to intrinsic response dynamics associated with time-varying inputs and assessed the impact of dendritic atrophy on impedance profiles in the presence of a HCN channel gradient. In the absence of an inductive element, the local and the transfer impedance profiles are low pass in nature and reflect an RC circuit. However, in the presence of HCN channels, which act as inductive elements, the local (**Figures 3C,D**) and the transfer (**Figures 3E,F**) filters resemble band-pass structures with the resonance frequency in the theta frequency range (Hutcheon and Yarom, 2000; Hu et al., 2002, 2009; Ulrich, 2002; Narayanan and Johnston, 2007; Rathour and Narayanan, 2012a; Vaidya and Johnston, 2013). Consistent with the inductive role for HCN channels and their higher densities at distal locations, we also noted that the local impedance phase profile showed significant positive phases for distal dendritic locations, especially in the theta frequency ranges (**Figure 3D**).

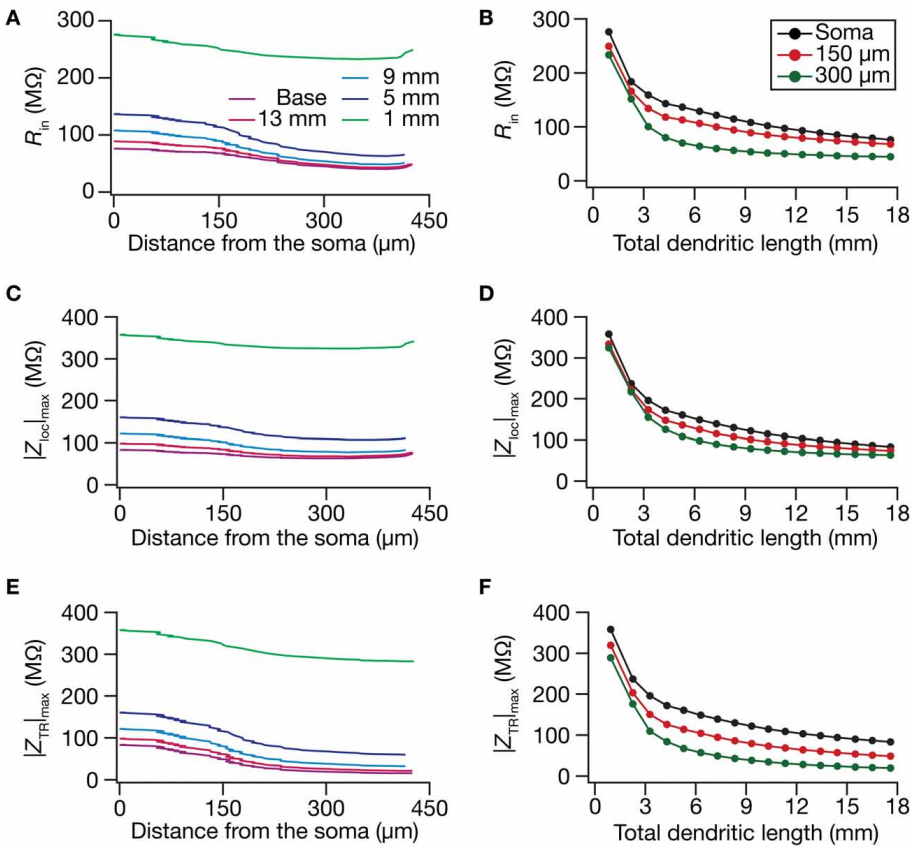

FIGURE 4 | In the presence of a somatodendritic HCN-channel gradient, steady-state and frequency-dependent measures of excitability increased with dendritic atrophy across somatodendritic locations. (A,B) Input resistance (R_{in}) plotted as functions of somatodendritic location (**A**; for 5 different pruned morphologies, **Figure 1A**) and total dendritic length (**B**; for 3 distinct somatodendritic locations, **Figure 1A**). **(C,D)** Maximal local impedance amplitude ($|Z_{loc}|_{max}$) plotted as functions of somatodendritic location **(C)** and total dendritic length **(D)**. **(E,F)** Maximal transfer impedance amplitude ($|Z_{TR}|_{max}$) plotted as functions of somatodendritic location **(E)** and dendritic length **(F)**. The legends for all graphs on the left and right are given in **(A,B)**, respectively.

Upon dendritic atrophy, although the band-pass structures of the local and transfer impedance profiles were retained, there were signficant quantitative differences in the amplitude of the responses and their gradients along the somatodendritic axis. Specifically, dendritic atrophy translated into a monotonic increase in local as well as transfer impedance amplitudes (**Figures 3C–F**, **4C–F**). Whereas the atrophy-induced increase in local impedance amplitude could be attributed to a reduction in overall surface area of the neuron, the corresponding increase in transfer impedance amplitude is a direct consequence of the improved somatodendritic coupling in trees with lesser dendritic length and dendritic branch points. Specifically, in the base tree, owing to distance-dependent dendritic filtering, distal inputs were attenuated more compared to proximal inputs, resulting in a progressively lower values for the transfer impedance amplitude with increase in distance (**Figures 3E,F**, **4E**). However, with dendritic atrophy, the somatodendritic coupling was higher owing to the loss of dendritic branches through which information flow could otherwise have been channeled and resulted in an increase in transfer impedance amplitude (**Figures 3E,F**, **4E**). Furthermore, and similar to our observations with R_{in}, the ZAP profiles across locations were very similar to each other in the atrophied tree (**Figures 3D,F**), resulting in an atrophy-induced constriction of the somatoapical maps in both local and transfer impedance amplitudes (**Figures 4C–F**). We also noted that the location-dependent differences in impedance phase plots were significantly reduced with increasing levels of dendritic atrophy (**Figures 3D,F**).

Together, consistent with our earlier conclusions with passive trees, these results in the presence of a HCN-channel gradient suggested that atrophied neurons responded with higher efficiency to incoming inputs, and that the transfer of signals across the dendritic tree was more effective in an atrophied arborization across frequencies. Importantly, despite the presence of identical HCN-channel density gradients, spatial gradients in input resistance and in local/transfer impedance amplitudes were significantly diminished in neuronal models with dendritic atrophy.

THE SOMATODENDRITIC LOCAL AND TRANSFER RESONANCE FREQUENCY MAPS WERE CONSTRICTED BY DENDRITIC ATROPHY

How do local and transfer resonance properties and their spatial maps depend on dendritic atrophy? To address this, we first computed the local resonance frequency at several locations along the somatoapical trunk of all pruned reconstructions and plotted it as functions of distance from the soma (**Figure 5A**) and of dendritic length (**Figure 5B**). With the insertion of the HCN-channel gradient in the base model, the resonance frequency along the somatodendritic trunk compartments increased ∼3-fold with distance from the soma (**Figure 5A**; Base model), in a manner that was consistent with experimental observations (Narayanan and Johnston, 2007). With atrophy, however, this topographic map of resonance frequency was severely constricted, whereby the distal and proximal resonance frequency values became progressively similar with increasing levels of atrophy (**Figures 5A,B**). These results suggest that the mere presence of a gradient in HCN channels is insufficient to sustain the resonance frequency map in neurons with lower dendritic length and lesser branches. Apart from the local resonance frequency map, we also computed the maps for total inductive phase (**Figures 5C,D**) and resonance strength (**Figures 5E,F**) and found that these conclusions extended to these measurements as well. In conjunction with our conclusions on the input resistance and local impedance amplitude maps (**Figure 4**), these results suggested that a gradient in HCN-channel density was insufficient to sustain a gradient in several HCN-channel dependent local physiological measurements in an atrophied tree.

What was the impact of dendritic atrophy on spectral selectivity in the transfer impedance amplitude profile? To address this, we quantified resonance frequency (**Figures 6A,B**), total inductive phase (**Figures 6C,D**), and resonance strength (**Figures 6E,F**) on transfer impedance profiles computed at different locations on different morphologies. We found that in an atrophied tree, the transfer impedance-related measurements were nearly identical across the somatodendritic axis despite the presence of an underlying HCN-channel gradient. Together these results suggested that the presence of identical HCN-channel density gradient was insufficient to sustain functional maps in input resistance and in local/transfer impedance properties in neuronal models with dendritic atrophy. Specifically, in an atrophied dendritic tree endowed with identical somatodendritic channel gradients as an unatrophied one, several functional maps fail to express and the entire length of the dendrite converges to similar intrinsic response dynamics (**Figures 3–6**).

ATROPHY-INDUCED CONSTRICTION OF FUNCTIONAL MAPS WAS MEDIATED BY ENHANCED SPATIAL SPREAD OF THE INFLUENCE OF A HCN-CHANNEL CLUSTER IN ATROPHIED TREES

Thus far, employing models with a somatodendritic HCN-channel gradient, we had demonstrated that the presence of a somatodendritic gradient in an ion channel density alone was insufficient to establish a functional gradient in a given physiological measurement. What is the biophysical basis for such constricted functional gradients? Why was an identical channel gradient inadequate in sustaining functional maps on atrophied trees? In answering these questions, we reasoned that, in a dendritic tree with heavy arborization, the influence of a point conductance located at any given compartment would be spatially localized owing to the branching and the higher surface area (Williams, 2004; Rathour and Narayanan, 2012b). However, in a dendritic tree with lesser arborization and lower surface area, as a consequence of higher coupling across the compartments (**Figures 4E,F**), the spread of influence of an ion channel cluster would be enhanced. Together, we hypothesized that this large increase in the influence field of any point conductance would ensure that the impact of this gradient on functional properties is minimized, even in the presence of an ion channel density gradient. In other words, the impact of a dendritically expressed channel is not confined only to the dendritic location, but spreads to a larger extent, thereby altering even somatic properties. This loss of compartmentalization of dendritic conductances, in conjunction with a reciprocally widespread influence of somatic ion channels on dendritic measurements, would ensure that ion channel gradients do not necessarily translate to functional map gradients.

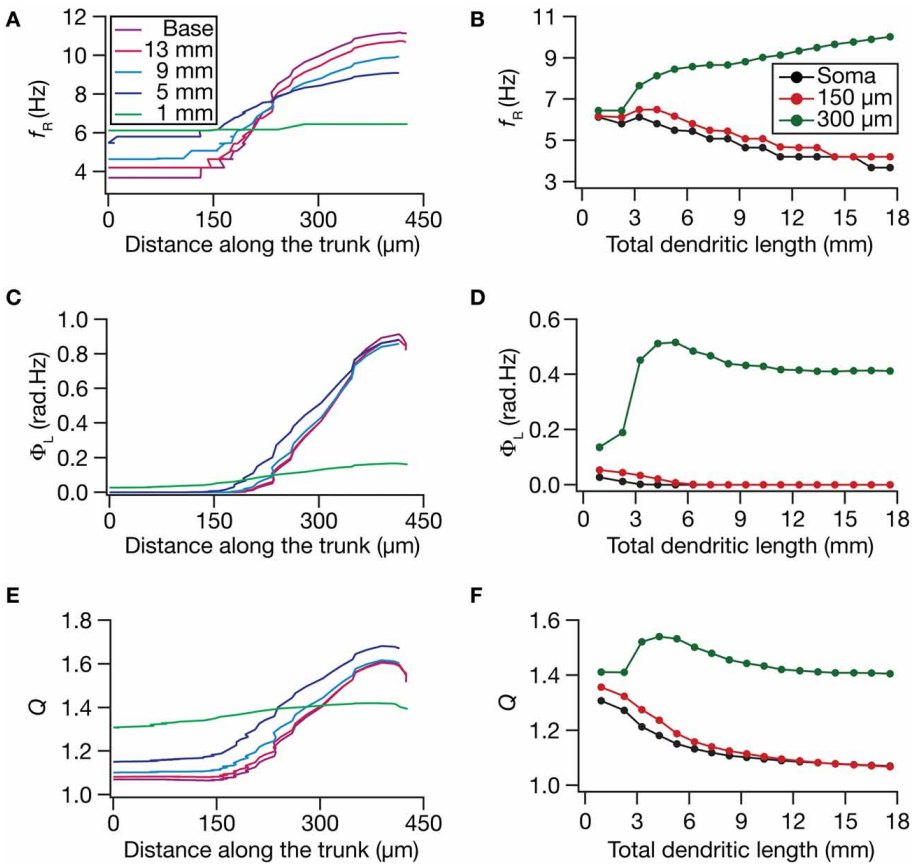

FIGURE 5 | Functional maps of several HCN-channel-dependent local impedance measurements were critically regulated by dendritic atrophy. (A,B) Local resonance frequency (f_R) plotted as functions of distance from the soma (**A**; for 5 different pruned morphologies, **Figure 1A**) and total dendritic length (**B**; for 3 distinct somatodendritic locations, **Figure 1A**). **(C,D)** Total inductive phase of the local impedance phase profile (Φ_L) plotted as functions of distance from the soma **(C)** and total dendritic length **(D)**. **(E,F)** Local resonance strength (Q) plotted as functions of distance from the soma **(E)** and total dendritic length **(F)**.

To test this hypothesis, we employed the recently developed quantification on "influence fields" to assess the spread of influence of a single ion channel cluster on any given measurement (Rathour and Narayanan, 2012b). We picked the two prominent measurements that are sensitive to HCN channels,—input resistance (**Figure 4**) and resonance frequency (**Figure 5**)—and asked if the spread of influence of a single HCN-conductance cluster was altered in an atrophied dendritic tree. Specifically, we placed a HCN-conductance cluster (normalized by the specific surface area of the compartment under consideration) at around the center of the somatoapical trunk and quantified the influence field of that cluster (Rathour and Narayanan, 2012b) on input resistance (**Figures 7**, **8**) and resonance frequency (**Figure 9**). We performed this analysis on either the passive model (**Figures 7**, **9**; where the only active component was this added HCN-conductance cluster) or on the active model (**Figures 8**, **9**; where the baseline HCN-channel gradient was already present, and an additional HCN conductance cluster was appended to it at one location). We employed two different measures to quantify the influence field of the ion channel cluster on the measurements: the area under the curve of the normalized and unnormalized influence fields under these parametric variations.

Employing these two measurements for assessing the influence field of HCN-channel clusters on R_{in} and f_R on the 17 different morphologies, each with two different background conductance profiles (passive vs. HCN-channel gradient), we found that the influence field of an ion-channel cluster increased with dendritic atrophy (**Figures 7–9**). This increase in influence field was not just restricted to the somatoapical trunk (**Figures 7–9**), but extended to even the obliques (**Figures 7E**, **8E**), and was common for both measurements (**Figures 7**, **8** for R_{in}; **Figure 9** for f_R) and for both cases of background conductances (**Figures 7**, **9** for passive and **Figures 8**, **9** for models with the baseline HCN-channel gradient). These results indicated that the influence fields of ion channel conductances need to be localized for channel gradients to express themselves as functional maps. In the absence of such compartmentalization, such as the case observed in atrophied dendrites, gradients in ion channel properties do not translate into maps in functional properties along the specified neuronal topograph. In other words, HCN-channel gradients are necessary but not sufficient for the emergence of functional maps of input

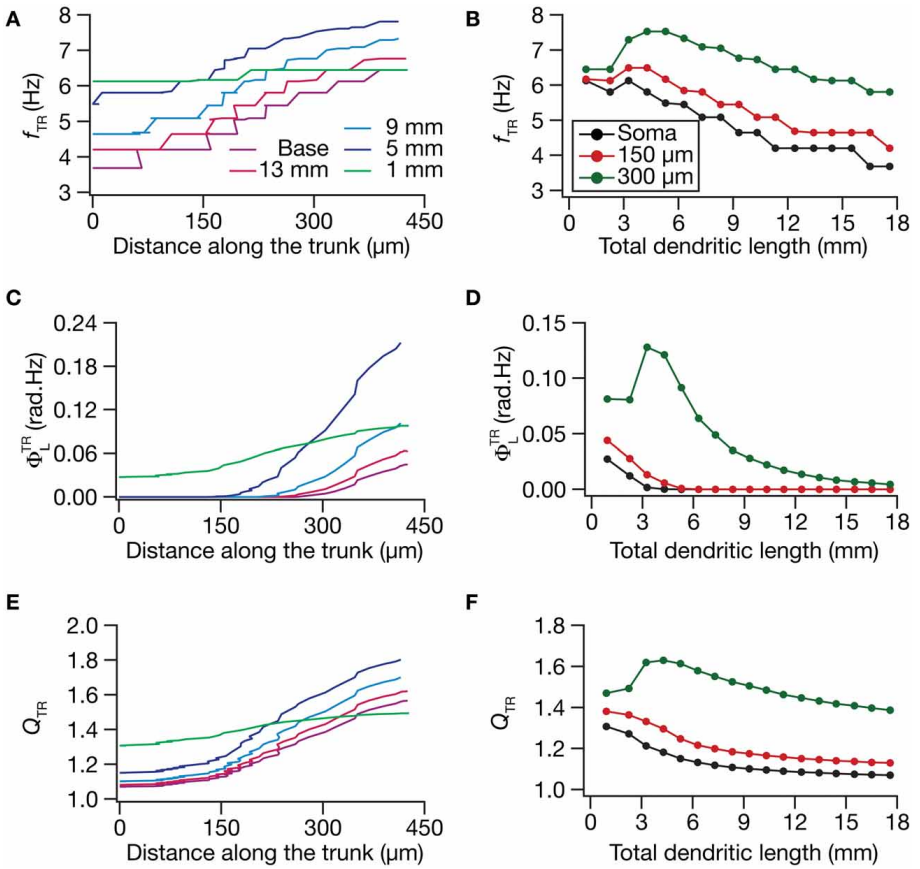

FIGURE 6 | Functional maps of several HCN-channel-dependent transfer impedance measurements were critically regulated by dendritic atrophy. (A,B) Transfer resonance frequency (f_{TR}) plotted as functions of distance from the soma (**A**; for 5 different pruned morphologies, **Figure 1A**) and total dendritic length (**B**; for 3 distinct somatodendritic locations, **Figure 1A**). **(C,D)** Total inductive phase of the transfer impedance phase profile (Φ_L^{TR}) plotted as functions of distance from the soma **(C)** and total dendritic length **(D)**. **(E,F)** Transfer resonance strength (Q_{TR}) plotted as functions of distance from the soma **(E)** and total dendritic length **(F)**.

resistance, resonance frequency and impedance properties within single hippocampal pyramidal neurons.

DISCUSSION

The principal finding of this study is that dendritic morphology critically regulates impedance-related functional maps, with the primary implication that the presence of ion channel gradient alone is not sufficient to impose a continuous gradient of an associated physiological measurement along a neuronal topograph. We arrived at this conclusion using systematically pruned dendritic morphologies, and assessing five local (input resistance, resonance frequency, maximal impedance amplitude, total inductive phase, resonance strength) and four transfer (resonance frequency, maximal impedance amplitude, total inductive phase and resonance strength) measurements on these morphologies. Given that our approach was to prune a specific tree and assess these measurements, we were able to arrive at functional forms for the dependence of each of these measurements on dendritic length. These results clearly show that despite the presence of a gradient in HCN-conductance density along a neuronal topograph, the corresponding physiological measurements do not form a topographic map in atrophied trees. We assessed the biophysical mechanisms behind these observations using the "influence field" framework, and found that these were consequent to an atrophy-induced increase in the spread of influence of an ion channel cluster on these physiological measurements. Apart from these, our study also provides further evidence for a direct relationship between increased excitability and dendritic atrophy, even in frequency-dependent measures of excitability. Further, our results point to an increase in coupling across compartments in an atrophied dendritic tree, ensuring an effective transfer of signals across the somatodendritic axis of an atrophied dendritic tree. These conclusions about morphology-dependent changes in excitability and in functional gradients have direct implications for physiological variability in dendritic length and branching of neurons across different brain regions and for pathophysiological changes in dendritic trees and their branching patterns.

IMPLICATIONS FOR ATROPHY-INDUCED ENHANCEMENT IN NEURONAL EXCITABILITY AND SOMATODENDRITIC COUPLING

The dependence of synaptic and intrinsic neuronal excitability as well as somatodendritic coupling on dendritic arborization

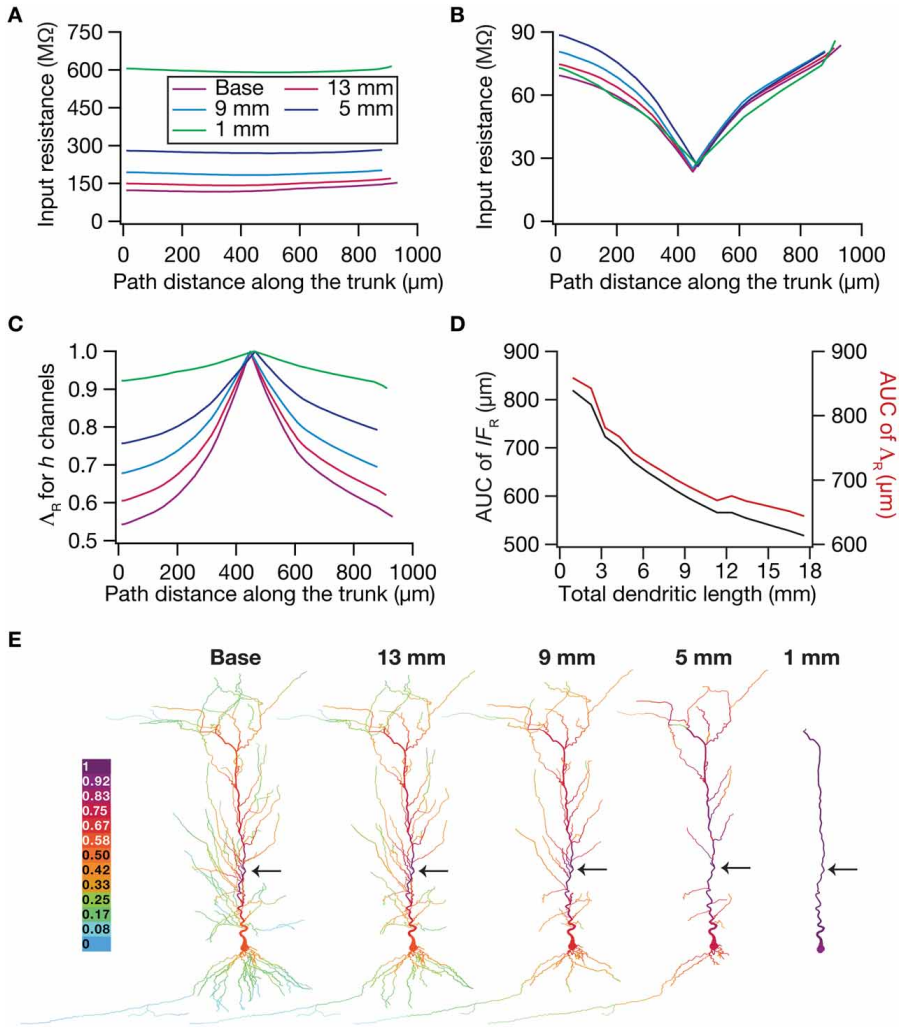

FIGURE 7 | Dendritic atrophy enhanced the influence of an HCN-conductance cluster on input resistance in a passive model. (A) Input resistance (R_{in}) measured along the somato-apical trunk for different morphologies. **(B)** R_{in}, in different morphologies, measured in the presence of a single HCN-channel cluster, incorporated at ∼450 µm (path distance) location away from soma. **(C)** Λ_R, the normalized influence field for R_{in}, along the somato-apical trunk for different morphologies. **(D)** Area under curve (AUC) for unnormalized (black) and normalized (red) influence field, plotted as functions of dendritic length of the neuronal morphology under consideration. **(E)** Color-coded influence field across the entire dendritic arbor showing the effect of a single HCN-channel cluster located (black arrow) at ∼450 µm from the soma on R_{in} for various morphologies.

is clearly established (Mainen and Sejnowski, 1996; Vetter et al., 2001; Krichmar et al., 2002; Van Ooyen et al., 2002; Schaefer et al., 2003; Kole et al., 2007; Sjöström et al., 2008; Narayanan and Chattarji, 2010; Van Elburg and Van Ooyen, 2010; Ferrante et al., 2013; Platschek et al., 2013). By analyzing local and transfer impedances as functions of input frequency, our results add additional lines of evidence to these conclusions by extending the analyses beyond pulse-current- and firing rate-based measurements of neuronal excitability (Narayanan and Johnston, 2008). Specifically, we show that dendritic atrophy increased both the local and transfer impedance amplitudes across all analyzed frequencies and across all locations along the dendritic arbor. These conclusions also extended to the case where an HCN-channel gradient was present across the somatodendritic gradient, where the local and transfer impedance amplitude profiles were band-pass in structure. These conclusions are especially important in the context of the hippocampus residing in an oscillatory environment where oscillations of different frequencies impinge on the somatodendritic arbor, and mediate various forms of rate, temporal and phase coding (O'keefe and Dostrovsky, 1971; O'keefe and Recce, 1993; Buzsaki, 2002, 2006; Wang, 2010; Lisman and Jensen, 2013). Such widespread increases in frequency-independent excitability, and the tighter somatodendritic coupling inferred from higher transfer impedance amplitudes would together imply that atrophied neurons generate higher number of spikes even for smaller inputs. Further, spike generation in an atrophied dendritic tree would also be expected to be earlier within the theta frequency oscillations. Given this, future studies should focus on the impact of dendritic atrophy on various forms of rate, temporal and phase coding in the hippocampus,

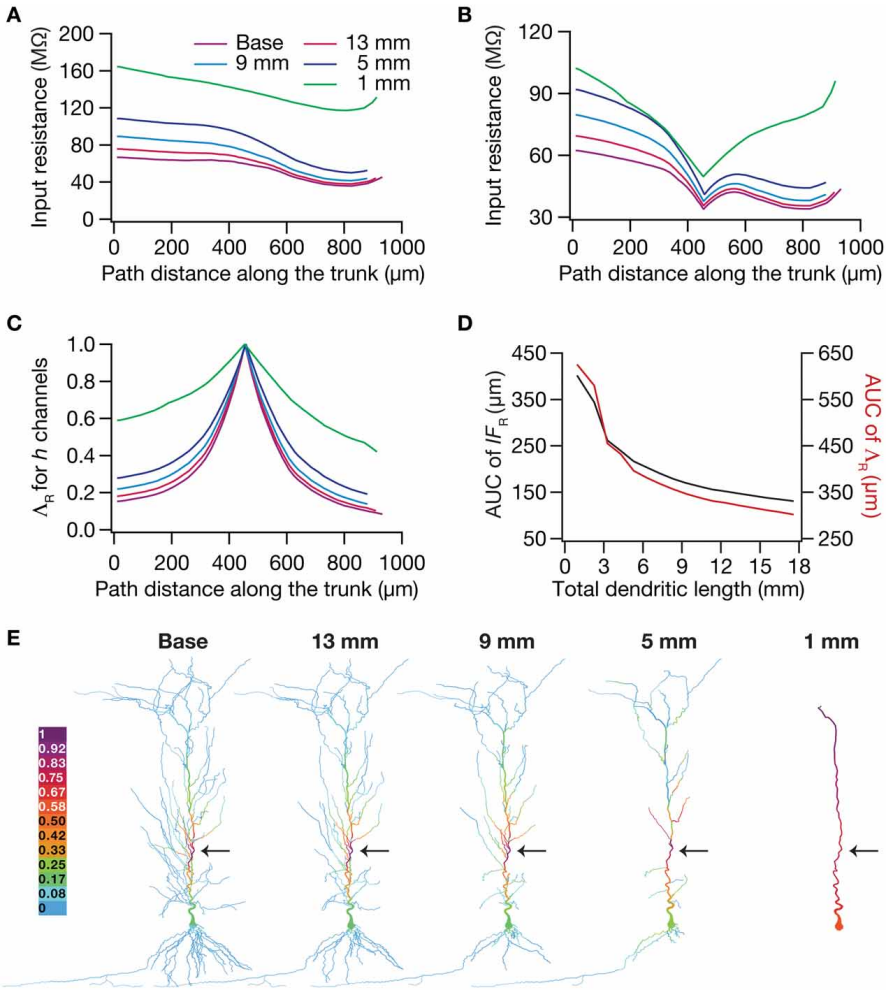

FIGURE 8 | Dendritic atrophy enhanced the influence of an HCN-conductance cluster on input resistance in a model endowed with a somatodendritic HCN-conductance gradient. (A) Input resistance measured along the somato-apical trunk for different morphologies. **(B)** R_{in}, in different morphologies, measured in the presence of an HCN-channel cluster, incorporated at ∼450 μm (path distance) location away from soma. **(C)** Λ_R, the normalized influence field for R_{in}, along the somato-apical trunk for different morphologies. **(D)** Area under curve (AUC) for unnormalized (black) and normalized (red) influence field, plotted as functions of dendritic length of the neuronal morphology under consideration. **(E)** Color-coded influence field across the entire dendritic arbor showing the effect of a single HCN-channel cluster located (black arrow) at ∼450 μm from soma on R_{in} for various morphologies.

including possible expansion in place-cell firing fields and potential saturation in phase precession that is observed in CA1 place cells.

The critical importance of dendritic morphology and surface-area-to-volume ratio in reaction-diffusion systems that regulate biochemical signal transduction (Sabatini et al., 2002; Frick et al., 2003; Neves et al., 2008; Neves and Iyengar, 2009; Kotaleski and Blackwell, 2010; Ross, 2012; Ashhad and Narayanan, 2013) and the vital role that excitability plays in regulating calcium propagation and plasticity rules (Johnston et al., 2003; Schaefer et al., 2003; Sjöström et al., 2008; Narayanan and Johnston, 2010; Ashhad and Narayanan, 2013; Sehgal et al., 2013) are well established. Given these, we postulate that dendritic atrophy and consequent increase in neuron-wide excitability would regulate the amplitudes and propagation of calcium transients, thereby significantly altering the rules for plasticity induction and the spread of signaling components (Narayanan and Chattarji, 2010). If these atrophy-induced changes in excitability were to be nullified for the maintenance of homeostasis in activity, signal propagation and plasticity, then concurrent homeostatic mechanisms should be activated through changes in synaptic and/or intrinsic properties of the neuron (Kole et al., 2004; Turrigiano and Nelson, 2004; Narayanan and Chattarji, 2010; Turrigiano, 2011; Honnuraiah and Narayanan, 2013). Therefore, future studies should recognize morphology as an important additional variable for neurons to adjust local and global neuronal excitability and coupling strengths across compartments, and assess its roles in either maintaining or hampering homeostasis of several neuronal functions.

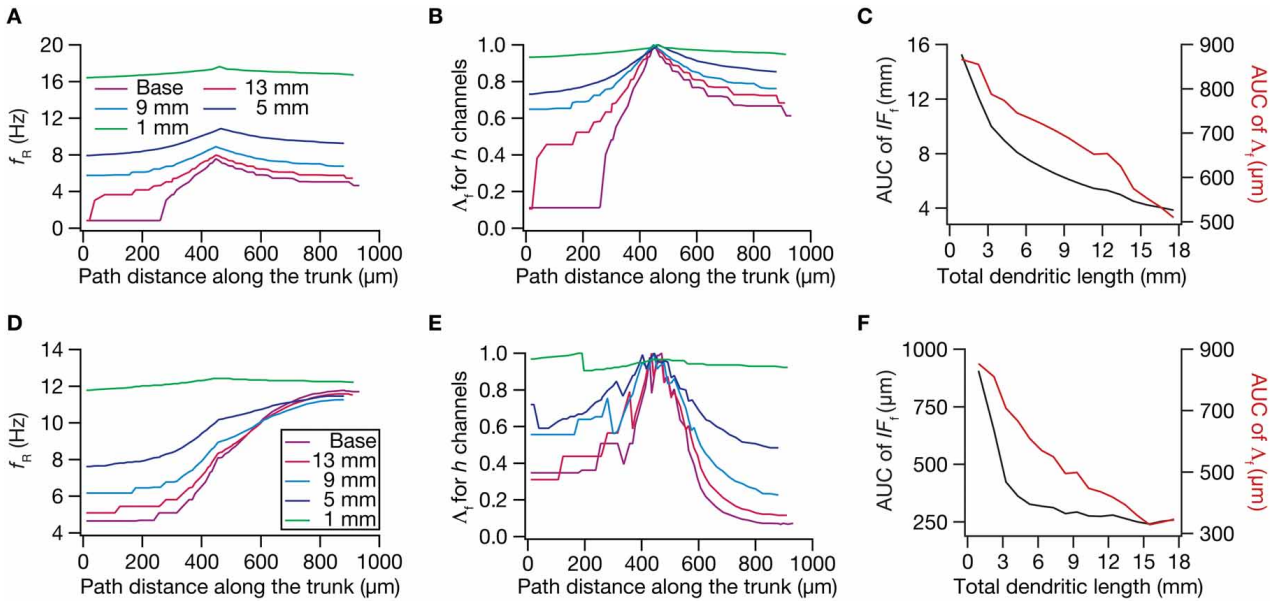

FIGURE 9 | Dendritic atrophy broadened the influence of a HCN conductance cluster on resonance frequency. The analyses presented in panels **(A–C)** correspond to passive neuronal models, and those presented in **(D–F)** correspond to models endowed with a physiologically relevant somatodendritic HCN-channel gradient. **(A)** Resonance frequency (f_R), in different morphologies, measured in the presence of an HCN-channel cluster, incorporated at ∼450 μm (path distance) location away from soma. **(B)** Λ_f, the normalized influence field for f_R, along the somato-apical trunk for different morphologies. **(C)** Area under curve (AUC) for unnormalized (black) and normalized (red) influence field, plotted as functions of dendritic length of the neuronal morphology under consideration. **(D)** f_R, in different morphologies, measured in the presence of an additional HCN-channel cluster, incorporated at ∼450 μm location away from soma. The baseline values of f_R, in the absence of this additional HCN-channel cluster, were the same as the plots shown in **Figure 5A**. **(E)** Λ_f, the normalized influence field of the additional HCN-channel cluster for f_R, along the somato-apical trunk for different morphologies. **(F)** Area under curve (AUC) for unnormalized (black) and normalized (red) influence field of the additional HCN-channel cluster, plotted as functions of dendritic length of the neuronal morphology under consideration.

IMPLICATIONS FOR THE REGULATION OF FUNCTIONAL MAPS BY DENDRITIC ATROPHY

Our study clearly elucidates the critical role of neuronal morphology in the emergence of several functional maps in input resistance and in local/transfer impedance properties. From the perspective of intraneuronal maps (Narayanan and Johnston, 2012), it should be noted that the maps of local EPSP amplitude and backpropagating action potentials (bAP) have already been shown to be dependent on dendritic remodeling (Vetter et al., 2001; Narayanan and Chattarji, 2010). Together with this, our study establishes that dendritic atrophy plays a significant role in the emergence of functional maps, especially constricting several of these maps despite the presence of ion channel gradients. Physiologically, this implies that the distance-dependent processing capabilities that are enabled by the presence of ion channel gradients would cease to exist under dendritic atrophy or in neurons with severely limited branching profiles. Specifically, the presence of channel gradients introduce location-dependent processing capabilities that regulate the location dependence of spike initiation dynamics, bAP amplitude coincidence detection and frequency-dependent input processing, apart from normalizing temporal summation and input phase of the transfer impedance profiles (Magee, 1998, 1999, 2000; Hausser et al., 2000; Vetter et al., 2001; Schaefer et al., 2003; Narayanan and Johnston, 2007, 2008; Vaidya and Johnston, 2013; Das and Narayanan, 2014). Under pathologically induced or developmentally observed reduction in dendritic arborization, neurons lose their ability to process their inputs differentially based on their inputs, translating to errors in rate or temporal coding that are dependent on the presence of these functional maps (Magee, 2000; London and Hausser, 2005; Spruston, 2008; Wang, 2010; Narayanan and Johnston, 2012), unless concurrent homeostatic mechanisms are invoked to maintain functional map homeostasis in these neuronal structures (O'leary et al., 2014; Rathour and Narayanan, 2014). Therefore, future studies could focus on the role of dendritic atrophy in altering stratified input processing, and their implications for neural coding and homeostasis in hippocampal and cortical neuronal structures.

In addition to these, our results also outline the importance of dendritic morphology in the regulation of channelostasis in particular, and proteostasis in general. Specifically, it is well established that the localization, targeting and turnover of individual channel and protein molecules at specific dendritic locations in neurons with complex arborization is an extremely complex puzzle (Lai and Jan, 2006; Vacher et al., 2008; Nusser, 2012; Hanus and Schuman, 2013; Rathour and Narayanan, 2014). If dendritic morphology plays a critical role in the emergence of functional maps, it stands to reason that maintenance of homeostasis in these functional maps in the face of changes in dendritic arborization (baseline or pathologically or developmentally regulated changes) would have to follow different regimes of channelostasis for channels that mediate these functional maps. Thus, baseline or

remodeling-induced variability in pyramidal neuron morphology needs to be systematically analyzed for their specific contributions to the proteostatic mechanisms behind functional map homeostasis. Additionally, the differences in pyramidal neuron morphology across the dorsal and ventral CA1 subregions are well established. Given this, it is important to address questions on the specific contributions of branching patterns in the observed differences in somatodendritic physiology and functional maps of dorsal vs. ventral CA1 pyramidal neurons (Dougherty et al., 2012, 2013; Marcelin et al., 2012a,b).

Finally, our results also pose the question on whether ion channel gradients are necessary and therefore express only in neurons with large dendritic arborizations. Specifically, let us consider that the premise for the presence of gradients in channel densities of active dendrites is to provide for somatodendritic normalization of certain physiological properties or to bestow location-dependent processing with reference to stratified incoming stimulus (Magee, 2000; Johnston and Narayanan, 2008; Sjöström et al., 2008; Spruston, 2008; Narayanan and Johnston, 2012; Nusser, 2012). Such normalization is necessary and stratified processing is feasible only in neurons that have large dendritic arborization, that translate to higher electrotonic lengths and compartmentalized influence fields of ion channels. However, if neurons possess minimal arborization and are electrotonically compact (Rall, 1977), the aforementioned purpose for the expression of channel gradients would be defeated. This is because several physiological properties would already be normalized owing to the compact structure, and gradients in ion channels would not translate to stratified processing of input stimulus as a result of constricted functional maps. Therefore, the analyses of proteostasis in complex dendrites (Lai and Jan, 2006; Vacher et al., 2008; Nusser, 2012; Hanus and Schuman, 2013; Rathour and Narayanan, 2014) should account for the morophological complexity and the electrotonic compactness of the neuronal structure (Vetter et al., 2001; Sjöström et al., 2008; Zhuchkova et al., 2013) in assessing the necessity for specific targeting of ion channels in achieving certain functional goals.

ACKNOWLEDGMENTS

The authors thank members of the cellular neurophysiology laboratory for helpful discussions and for critical comments on a draft of this manuscript. This work was supported by the International Human Frontier Science Program (HFSP) Organization (Rishikesh Narayanan), the Indian Institute of Science (Rishikesh Narayanan & Rahul K. Rathour) and the University Grants Commission (Rahul K. Rathour).

REFERENCES

Ascoli, G. A., Donohue, D. E., and Halavi, M. (2007). NeuroMorpho.Org: a central resource for neuronal morphologies. *J. Neurosci.* 27, 9247–9251. doi: 10.1523/JNEUROSCI.2055-07.2007

Ashhad, S., and Narayanan, R. (2013). Quantitative interactions between the A-type K^+ current and inositol trisphosphate receptors regulate intraneuronal Ca^{2+} waves and synaptic plasticity. *J. Physiol.* 591, 1645–1669. doi: 10.1113/jphysiol.2012.245688

Bannister, N. J., and Larkman, A. U. (1995). Dendritic morphology of CA1 pyramidal neurones from the rat hippocampus: I. Branching patterns. *J. Comp. Neurol.* 360, 150–160. doi: 10.1002/cne.903600111

Bartesaghi, R., Severi, S., and Guidi, S. (2003). Effects of early environment on pyramidal neuron morphology in field CA1 of the guinea-pig. *Neuroscience* 116, 715–732. doi: 10.1016/S0306-4522(02)00753-4

Brunson, K. L., Kramar, E., Lin, B., Chen, Y., Colgin, L. L., Yanagihara, T. K., et al. (2005). Mechanisms of late-onset cognitive decline after early-life stress. *J. Neurosci.* 25, 9328–9338. doi: 10.1523/JNEUROSCI.2281-05.2005

Buzsaki, G. (2002). Theta oscillations in the hippocampus. *Neuron* 33, 325–340. doi: 10.1016/S0896-6273(02)00586-X

Buzsaki, G. (2006). *Rhythms of the Brain.* New York, NY: Oxford University Press. doi: 10.1093/acprof:oso/9780195301069.001.0001

Campbell, S., and Macqueen, G. (2004). The role of the hippocampus in the pathophysiology of major depression. *J. Psychiatry Neurosci.* 29, 417–426.

Carnevale, N. T., and Hines, M. L. (2006). *The Neuron Book.* Cambridge: Cambridge University Press. doi: 10.1017/CBO9780511541612

Cole, K. S. (1932). Electrical phase angle of cell membranes. *J. Gen. Physiol.* 15, 641–649. doi: 10.1085/jgp.15.6.641

Cole, K. S. (1968). *Membranes, Ions and Impulses: A Chapter of Classical Biophysics.* Berkeley, CA: University of California, Berkeley Press.

Cole, K. S., and Baker, R. F. (1941). Longitudinal impedance of the squid giant axon. *J. Gen. Physiol.* 24, 771–788. doi: 10.1085/jgp.24.6.771

Das, A., and Narayanan, R. (2014). Active dendrites regulate spectral selectivity in location-dependent spike initiation dynamics of hippocampal model neurons. *J. Neurosci.* 34, 1195–1211. doi: 10.1523/JNEUROSCI.3203-13.2014

De Leon, M. J., George, A. E., Golomb, J., Tarshish, C., Convit, A., Kluger, A., et al. (1997). Frequency of hippocampal formation atrophy in normal aging and Alzheimer's disease. *Neurobiol. Aging* 18, 1–11. doi: 10.1016/S0197-4580(96)00213-8

Dougherty, K. A., Islam, T., and Johnston, D. (2012). Intrinsic excitability of CA1 pyramidal neurones from the rat dorsal and ventral hippocampus. *J. Physiol.* 590, 5707–5722. doi: 10.1113/jphysiol.2012.242693

Dougherty, K. A., Nicholson, D. A., Diaz, L., Buss, E. W., Neuman, K. M., Chetkovich, D. M., et al. (2013). Differential expression of HCN subunits alters voltage-dependent gating of h-channels in CA1 pyramidal neurons from dorsal and ventral hippocampus. *J. Neurophysiol.* 109, 1940–1953. doi: 10.1152/jn.00010.2013

Elgh, E., Lindqvist Astot, A., Fagerlund, M., Eriksson, S., Olsson, T., and Nasman, B. (2006). Cognitive dysfunction, hippocampal atrophy and glucocorticoid feedback in Alzheimer's disease. *Biol. Psychiatry* 59, 155–161. doi: 10.1016/j.biopsych.2005.06.017

Faherty, C. J., Kerley, D., and Smeyne, R. J. (2003). A Golgi-Cox morphological analysis of neuronal changes induced by environmental enrichment. *Brain Res. Dev. Brain Res.* 141, 55–61. doi: 10.1016/S0165-3806(02)00642-9

Ferrante, M., Migliore, M., and Ascoli, G. A. (2013). Functional impact of dendritic branch-point morphology. *J. Neurosci.* 33, 2156–2165. doi: 10.1523/JNEUROSCI.3495-12.2013

Frick, A., Magee, J., Koester, H. J., Migliore, M., and Johnston, D. (2003). Normalization of Ca^{2+} signals by small oblique dendrites of CA1 pyramidal neurons. *J. Neurosci.* 23, 3243–3250.

Gimbarzevsky, B., Miura, R. M., and Puil, E. (1984). Impedance profiles of peripheral and central neurons. *Can. J. Physiol. Pharmacol.* 62, 460–462. doi: 10.1139/y84-074

Hanks, S. D., and Flood, D. G. (1991). Region-specific stability of dendritic extent in normal human aging and regression in Alzheimer's disease. I. CA1 of hippocampus. *Brain Res.* 540, 63–82. doi: 10.1016/0006-8993(91)90493-F

Hanus, C., and Schuman, E. M. (2013). Proteostasis in complex dendrites. *Nat. Rev. Neurosci.* 14, 638–648. doi: 10.1038/nrn3546

Hausser, M., Spruston, N., and Stuart, G. J. (2000). Diversity and dynamics of dendritic signaling. *Science* 290, 739–744. doi: 10.1126/science.290.5492.739

Honnuraiah, S., and Narayanan, R. (2013). A calcium-dependent plasticity rule for HCN channels maintains activity homeostasis and stable synaptic learning. *PLoS ONE* 8:e55590. doi: 10.1371/journal.pone.0055590

Hu, H., Vervaeke, K., Graham, L. J., and Storm, J. F. (2009). Complementary theta resonance filtering by two spatially segregated mechanisms in CA1 hippocampal pyramidal neurons. *J. Neurosci.* 29, 14472–14483. doi: 10.1523/JNEUROSCI.0187-09.2009

Hu, H., Vervaeke, K., and Storm, J. F. (2002). Two forms of electrical resonance at theta frequencies, generated by M-current, h-current and persistent Na^+ current in rat hippocampal pyramidal cells. *J. Physiol.* 545, 783–805. doi: 10.1113/jphysiol.2002.029249

Hu, H., Vervaeke, K., and Storm, J. F. (2007). M-channels (Kv7/KCNQ channels) that regulate synaptic integration, excitability, and spike pattern of CA1 pyramidal cells are located in the perisomatic region. *J. Neurosci.* 27, 1853–1867. doi: 10.1523/JNEUROSCI.4463-06.2007

Hutcheon, B., Miura, R. M., and Puil, E. (1996). Models of subthreshold membrane resonance in neocortical neurons. *J. Neurophysiol.* 76, 698–714.

Hutcheon, B., and Yarom, Y. (2000). Resonance, oscillation and the intrinsic frequency preferences of neurons. *Trends Neurosci.* 23, 216–222. doi: 10.1016/S0166-2236(00)01547-2

Isgor, C., Kabbaj, M., Akil, H., and Watson, S. J. (2004). Delayed effects of chronic variable stress during peripubertal-juvenile period on hippocampal morphology and on cognitive and stress axis functions in rats. *Hippocampus* 14, 636–648. doi: 10.1002/hipo.10207

Ishizuka, N., Cowan, W. M., and Amaral, D. G. (1995). A quantitative analysis of the dendritic organization of pyramidal cells in the rat hippocampus. *J. Comp. Neurol.* 362, 17–45. doi: 10.1002/cne.903620103

Johnston, D., Christie, B. R., Frick, A., Gray, R., Hoffman, D. A., Schexnayder, L. K., et al. (2003). Active dendrites, potassium channels and synaptic plasticity. *Philos. Trans. R. Soc. Lond. B. Biol. Sci.* 358, 667–674. doi: 10.1098/rstb.2002.1248

Johnston, D., and Narayanan, R. (2008). Active dendrites: colorful wings of the mysterious butterflies. *Trends Neurosci.* 31, 309–316. doi: 10.1016/j.tins.2008.03.004

Kadar, T., Arbel, I., Silbermann, M., and Levy, A. (1994). Morphological hippocampal changes during normal aging and their relation to cognitive deterioration. *J. Neural Transm. Suppl.* 44, 133–143.

Kerchner, G. A., Deutsch, G. K., Zeineh, M., Dougherty, R. F., Saranathan, M., and Rutt, B. K. (2012). Hippocampal CA1 apical neuropil atrophy and memory performance in Alzheimer's disease. *Neuroimage* 63, 194–202. doi: 10.1016/j.neuroimage.2012.06.048

Kole, M. H., Brauer, A. U., and Stuart, G. J. (2007). Inherited cortical HCN1 channel loss amplifies dendritic calcium electrogenesis and burst firing in a rat absence epilepsy model. *J. Physiol.* 578, 507–525. doi: 10.1113/jphysiol.2006.122028

Kole, M. H., Czeh, B., and Fuchs, E. (2004). Homeostatic maintenance in excitability of tree shrew hippocampal CA3 pyramidal neurons after chronic stress. *Hippocampus* 14, 742–751. doi: 10.1002/hipo.10212

Kotaleski, J. H., and Blackwell, K. T. (2010). Modelling the molecular mechanisms of synaptic plasticity using systems biology approaches. *Nat. Rev. Neurosci.* 11, 239–251. doi: 10.1038/nrn2807

Krichmar, J. L., Nasuto, S. J., Scorcioni, R., Washington, S. D., and Ascoli, G. A. (2002). Effects of dendritic morphology on CA3 pyramidal cell electrophysiology: a simulation study. *Brain Res.* 941, 11–28. doi: 10.1016/S0006-8993(02)02488-5

Lai, H. C., and Jan, L. Y. (2006). The distribution and targeting of neuronal voltage-gated ion channels. *Nat. Rev. Neurosci.* 7, 548–562. doi: 10.1038/nrn1938

Lambert, K. G., Buckelew, S. K., Staffiso-Sandoz, G., Gaffga, S., Carpenter, W., Fisher, J., et al. (1998). Activity-stress induces atrophy of apical dendrites of hippocampal pyramidal neurons in male rats. *Physiol. Behav.* 65, 43–49. doi: 10.1016/S0031-9384(98)00114-0

Laudanski, J., Torben-Nielsen, B., Segev, I., and Shamma, S. (2014). Spatially distributed dendritic resonance selectively filters synaptic input. *PLoS Comput. Biol.* 10:e1003775. doi: 10.1371/journal.pcbi.1003775

Leggio, M. G., Mandolesi, L., Federico, F., Spirito, F., Ricci, B., Gelfo, F., et al. (2005). Environmental enrichment promotes improved spatial abilities and enhanced dendritic growth in the rat. *Behav. Brain Res.* 163, 78–90. doi: 10.1016/j.bbr.2005.04.009

Leuner, B., and Gould, E. (2010). Structural plasticity and hippocampal function. *Annu. Rev. Psychol.* 61, 111–140, C111–113. doi: 10.1146/annurev.psych.093008.100359

Lisman, J. E., and Jensen, O. (2013). The theta-gamma neural code. *Neuron* 77, 1002–1016. doi: 10.1016/j.neuron.2013.03.007

Lolova, I. (1989). Dendritic changes in the hippocampus of aged rats. *Acta Morphol. Hung.* 37, 3–10.

London, M., and Hausser, M. (2005). Dendritic computation. *Annu. Rev. Neurosci.* 28, 503–532. doi: 10.1146/annurev.neuro.28.061604.135703

Lorincz, A., Notomi, T., Tamas, G., Shigemoto, R., and Nusser, Z. (2002). Polarized and compartment-dependent distribution of HCN1 in pyramidal cell dendrites. *Nat. Neurosci.* 5, 1185–1193. doi: 10.1038/nn962

Magee, J. C. (1998). Dendritic hyperpolarization-activated currents modify the integrative properties of hippocampal CA1 pyramidal neurons. *J. Neurosci.* 18, 7613–7624.

Magee, J. C. (1999). Dendritic lh normalizes temporal summation in hippocampal CA1 neurons. *Nat. Neurosci.* 2, 508–514. doi: 10.1038/9158

Magee, J. C. (2000). Dendritic integration of excitatory synaptic input. *Nat. Rev. Neurosci.* 1, 181–190. doi: 10.1038/35044552

Mainen, Z. F., and Sejnowski, T. J. (1996). Influence of dendritic structure on firing pattern in model neocortical neurons. *Nature* 382, 363–366. doi: 10.1038/382363a0

Marcelin, B., Liu, Z., Chen, Y., Lewis, A. S., Becker, A., McClelland, S., et al. (2012a). Dorsoventral differences in intrinsic properties in developing CA1 pyramidal cells. *J. Neurosci.* 32, 3736–3747. doi: 10.1523/JNEUROSCI.5870-11.2012

Marcelin, B., Lugo, J. N., Brewster, A. L., Liu, Z., Lewis, A. S., McClelland, S., et al. (2012b). Differential dorso-ventral distributions of Kv4.2 and HCN proteins confer distinct integrative properties to hippocampal CA1 pyramidal cell distal dendrites. *J. Biol. Chem.* 287, 17656–17661. doi: 10.1074/jbc.C112.367110

Markham, J. A., McKian, K. P., Stroup, T. S., and Juraska, J. M. (2005). Sexually dimorphic aging of dendritic morphology in CA1 of hippocampus. *Hippocampus* 15, 97–103. doi: 10.1002/hipo.20034

McEwen, B. S. (1999). Stress and hippocampal plasticity. *Annu. Rev. Neurosci.* 22, 105–122. doi: 10.1146/annurev.neuro.22.1.105

Mora, F., Segovia, G., and Del Arco, A. (2007). Aging, plasticity and environmental enrichment: structural changes and neurotransmitter dynamics in several areas of the brain. *Brain Res. Rev.* 55, 78–88. doi: 10.1016/j.brainresrev.2007.03.011

Narayanan, R., and Chattarji, S. (2010). Computational analysis of the impact of chronic stress on intrinsic and synaptic excitability in the hippocampus. *J. Neurophysiol.* 103, 3070–3083. doi: 10.1152/jn.00913.2009

Narayanan, R., and Johnston, D. (2007). Long-term potentiation in rat hippocampal neurons is accompanied by spatially widespread changes in intrinsic oscillatory dynamics and excitability. *Neuron* 56, 1061–1075. doi: 10.1016/j.neuron.2007.10.033

Narayanan, R., and Johnston, D. (2008). The h channel mediates location dependence and plasticity of intrinsic phase response in rat hippocampal neurons. *J. Neurosci.* 28, 5846–5860. doi: 10.1523/JNEUROSCI.0835-08.2008

Narayanan, R., and Johnston, D. (2010). The h current is a candidate mechanism for regulating the sliding modification threshold in a BCM-like synaptic learning rule. *J. Neurophysiol.* 104, 1020–1033. doi: 10.1152/jn.01129.2009

Narayanan, R., and Johnston, D. (2012). Functional maps within a single neuron. *J. Neurophysiol.* 108, 2343–2351. doi: 10.1152/jn.00530.2012

Narayanan, R., Narayan, A., and Chattarji, S. (2005). A probabilistic framework for region-specific remodeling of dendrites in three-dimensional neuronal reconstructions. *Neural Comput.* 17, 75–96. doi: 10.1162/0899766052530811

Neves, G., Cooke, S. F., and Bliss, T. V. (2008). Synaptic plasticity, memory and the hippocampus: a neural network approach to causality. *Nat. Rev. Neurosci.* 9, 65–75. doi: 10.1038/nrn2303

Neves, S. R., and Iyengar, R. (2009). Models of spatially restricted biochemical reaction systems. *J. Biol. Chem.* 284, 5445–5449. doi: 10.1074/jbc.R800058200

Nusser, Z. (2012). Differential subcellular distribution of ion channels and the diversity of neuronal function. *Curr. Opin. Neurobiol.* 22, 366–371. doi: 10.1016/j.conb.2011.10.006

O'keefe, J., and Dostrovsky, J. (1971). The hippocampus as a spatial map. Preliminary evidence from unit activity in the freely-moving rat. *Brain Res.* 34, 171–175. doi: 10.1016/0006-8993(71)90358-1

O'keefe, J., and Recce, M. L. (1993). Phase relationship between hippocampal place units and the EEG theta rhythm. *Hippocampus* 3, 317–330. doi: 10.1002/hipo.450030307

O'leary, T., Williams, A. H., Franci, A., and Marder, E. (2014). Cell types, network homeostasis, and pathological compensation from a biologically plausible ion channel expression model. *Neuron* 82, 809–821. doi: 10.1016/j.neuron.2014.04.002

Pawluski, J. L., and Galea, L. A. (2006). Hippocampal morphology is differentially affected by reproductive experience in the mother. *J. Neurobiol.* 66, 71–81. doi: 10.1002/neu.20194

Pike, F. G., Goddard, R. S., Suckling, J. M., Ganter, P., Kasthuri, N., and Paulsen, O. (2000). Distinct frequency preferences of different types of rat hippocampal neurones in response to oscillatory input currents. *J. Physiol.* 529 (Pt 1), 205–213. doi: 10.1111/j.1469-7793.2000.00205.x

Pinto, V., Costa, J. C., Morgado, P., Mota, C., Miranda, A., Bravo, F. V., et al. (2014). Differential impact of chronic stress along the hippocampal dorsal-ventral axis. *Brain Struct. Funct.* doi: 10.1007/s00429-014-0713-0. [Epub ahead of print].

Platschek, S., Cuntz, H., Vuksic, M., Deller, T., and Jedlicka, P. (2013). Denervation-induced dendritic reorganization leads to changes in the electrotonic architecture of model dentate granule cells. *BMC Neurosci.* 14(Suppl. 1):P191. doi: 10.1186/1471-2202-14-S1-P191

Pokorny, J., and Yamamoto, T. (1981). Postnatal ontogenesis of hippocampal CA1 area in rats. I. Development of dendritic arborisation in pyramidal neurons. *Brain Res. Bull.* 7, 113–120. doi: 10.1016/0361-9230(81)90075-7

Poolos, N. P., Migliore, M., and Johnston, D. (2002). Pharmacological upregulation of h-channels reduces the excitability of pyramidal neuron dendrites. *Nat. Neurosci.* 5, 767–774. doi: 10.1038/nn891

Pyapali, G. K., Sik, A., Penttonen, M., Buzsaki, G., and Turner, D. A. (1998). Dendritic properties of hippocampal CA1 pyramidal neurons in the rat: intracellular staining *in vivo* and *in vitro*. *J. Comp. Neurol.* 391, 335–352.

Rall, W. (1977). "Core conductor theory and cable properties of neurons," in *Handbook of physiology. The Nervous System. Cellular Biology of Neurons*, ed E. R. Kandel (Bethesda, MD: American Physiological Society), 39–97.

Rathour, R. K., and Narayanan, R. (2012a). Inactivating ion channels augment robustness of subthreshold intrinsic response dynamics to parametric variability in hippocampal model neurons. *J. Physiol.* 590, 5629–5652. doi: 10.1113/jphysiol.2012.239418

Rathour, R. K., and Narayanan, R. (2012b). Influence fields: a quantitative framework for representation and analysis of active dendrites. *J. Neurophysiol.* 107, 2313–2334. doi: 10.1152/jn.00846.2011

Rathour, R. K., and Narayanan, R. (2014). Homeostasis of functional maps in active dendrites emerges in the absence of individual channelostasis. *Proc. Natl. Acad. Sci. U.S.A.* 111, E1787–E1796. doi: 10.1073/pnas.1316599111

Ross, W. N. (2012). Understanding calcium waves and sparks in central neurons. *Nat. Rev. Neurosci.* 13, 157–168. doi: 10.1038/nrn3168

Sabatini, B. L., Oertner, T. G., and Svoboda, K. (2002). The life cycle of $Ca^{(2+)}$ ions in dendritic spines. *Neuron* 33, 439–452. doi: 10.1016/S0896-6273(02)00573-1

Schaefer, A. T., Larkum, M. E., Sakmann, B., and Roth, A. (2003). Coincidence detection in pyramidal neurons is tuned by their dendritic branching pattern. *J. Neurophysiol.* 89, 3143–3154. doi: 10.1152/jn.00046.2003

Sehgal, M., Song, C., Ehlers, V. L., and Moyer, J. R. Jr. (2013). Learning to learn—intrinsic plasticity as a metaplasticity mechanism for memory formation. *Neurobiol. Learn. Mem.* 105, 186–199. doi: 10.1016/j.nlm.2013.07.008

Sheline, Y. I., Wang, P. W., Gado, M. H., Csernansky, J. G., and Vannier, M. W. (1996). Hippocampal atrophy in recurrent major depression. *Proc. Natl. Acad. Sci. U.S.A.* 93, 3908–3913. doi: 10.1073/pnas.93.9.3908

Sjöström, P. J., Rancz, E. A., Roth, A., and Häusser, M. (2008). Dendritic excitability and synaptic plasticity. *Physiol. Rev.* 88, 769–840. doi: 10.1152/physrev.00016.2007

Spruston, N. (2008). Pyramidal neurons: dendritic structure and synaptic integration. *Nat. Rev. Neurosci.* 9, 206–221. doi: 10.1038/nrn2286

Torben-Nielsen, B., and Stiefel, K. M. (2010). An inverse approach for elucidating dendritic function. *Front. Comput. Neurosci.* 4:128. doi: 10.3389/fncom.2010.00128

Turrigiano, G. (2011). Too many cooks? Intrinsic and synaptic homeostatic mechanisms in cortical circuit refinement. *Annu. Rev. Neurosci.* 34, 89–103. doi: 10.1146/annurev-neuro-060909-153238

Turrigiano, G. G., and Nelson, S. B. (2004). Homeostatic plasticity in the developing nervous system. *Nat. Rev. Neurosci.* 5, 97–107. doi: 10.1038/nrn1327

Ulrich, D. (2002). Dendritic resonance in rat neocortical pyramidal cells. *J. Neurophysiol.* 87, 2753–2759. doi: 10.1152/jn.01000.2001

Vacher, H., Mohapatra, D. P., and Trimmer, J. S. (2008). Localization and targeting of voltage-dependent ion channels in mammalian central neurons. *Physiol. Rev.* 88, 1407–1447. doi: 10.1152/physrev.00002.2008

Vaidya, S. P., and Johnston, D. (2013). Temporal synchrony and gamma-to-theta power conversion in the dendrites of CA1 pyramidal neurons. *Nat. Neurosci.* 16, 1812–1820. doi: 10.1038/nn.3562

Van Elburg, R. A., and Van Ooyen, A. (2010). Impact of dendritic size and dendritic topology on burst firing in pyramidal cells. *PLoS Comput. Biol.* 6:e1000781. doi: 10.1371/journal.pcbi.1000781

Van Ooyen, A., Duijnhouwer, J., Remme, M. W., and Van Pelt, J. (2002). The effect of dendritic topology on firing patterns in model neurons. *Network* 13, 311–325. doi: 10.1088/0954-898X/13/3/304

Vetter, P., Roth, A., and Häusser, M. (2001). Propagation of action potentials in dendrites depends on dendritic morphology. *J. Neurophysiol.* 85, 926–937.

Wang, X. J. (2010). Neurophysiological and computational principles of cortical rhythms in cognition. *Physiol. Rev.* 90, 1195–1268. doi: 10.1152/physrev.00035.2008

Williams, S. R. (2004). Spatial compartmentalization and functional impact of conductance in pyramidal neurons. *Nat. Neurosci.* 7, 961–967. doi: 10.1038/nn1305

Zhuchkova, E., Remme, M. W., and Schreiber, S. (2013). Somatic versus dendritic resonance: differential filtering of inputs through non-uniform distributions of active conductances. *PLoS ONE* 8:e78908. doi: 10.1371/journal.pone.0078908

Conflict of Interest Statement: The authors declare that the research was conducted in the absence of any commercial or financial relationships that could be construed as a potential conflict of interest.

Received: 07 September 2014; accepted: 16 December 2014; published online: 12 January 2015.

Citation: Dhupia N, Rathour RK and Narayanan R (2015) Dendritic atrophy constricts functional maps in resonance and impedance properties of hippocampal model neurons. Front. Cell. Neurosci. ***8****:456. doi: 10.3389/fncel.2014.00456*

This article was submitted to the journal Frontiers in Cellular Neuroscience.

frontiers in Cellular Neuroscience

ORIGINAL RESEARCH
published: 02 September 2015
doi: 10.3389/fncel.2015.00349

Developing electrical properties of postnatal mouse lumbar motoneurons

Jacques Durand[1], Anton Filipchuk[1†], Arnaud Pambo-Pambo[1†], Julien Amendola[1†], Iryna Borisovna Kulagina[2] and Jean-Patrick Guéritaud[1]*

[1] Institut de Neurosciences de la Timone, Aix Marseille Université – CNRS, UMR 7289, Marseille, France, [2] International Center for Molecular Physiology, Kiev, Ukraine

OPEN ACCESS

Edited by:
Alessandro Tozzi,
University of Perugia, Italy

Reviewed by:
Michele Nutini,
Fondazione Santa Lucia, Italy
Randall Keith Powers,
University of Washington, USA

***Correspondence:**
Jacques Durand,
Institut de Neurosciences de la Timone, Aix Marseille Université – CNRS, UMR 7289, 27 Bd Jean Moulin, 13397 Marseille Cedex 20, France
jacques.durand@univ-amu.fr

† Present address:
Anton Filipchuk,
Laboratory of Cellular and Molecular Mechanisms of Brain Wiring, Guillermina López-Bendito Lab, Alicante, Spain;
Arnaud Pambo-Pambo,
Faculté des Sciences, Franceville, Gabon;
Julien Amendola,
Inserm UMR 1072, Faculté de Médecine Secteur Nord, Université de la Méditerranée, Marseille, France

Received: 05 June 2015
Accepted: 20 August 2015
Published: 02 September 2015

Citation:
Durand J, Filipchuk A, Pambo-Pambo A, Amendola J, Kulagina IB and Guéritaud J-P (2015) Developing electrical properties of postnatal mouse lumbar motoneurons.
Front. Cell. Neurosci. 9:349.
doi: 10.3389/fncel.2015.00349

We studied the rapid changes in electrical properties of lumbar motoneurons between postnatal days 3 and 9 just before mice weight-bear and walk. The input conductance and rheobase significantly increased up to P8. A negative correlation exists between the input resistance (Rin) and rheobase. Both parameters are significantly correlated with the total dendritic surface area of motoneurons, the largest motoneurons having the lowest Rin and the highest rheobase. We classified the motoneurons into three groups according to their discharge firing patterns during current pulse injection (transient, delayed onset, sustained). The delayed onset firing type has the highest rheobase and the fastest action potential (AP) whereas the transient firing group has the lowest rheobase and the less mature AP. We found 32 and 10% of motoneurons with a transient firing at P3–P5 and P8, respectively. About 20% of motoneurons with delayed onset firing were detected at P8. At P9, all motoneurons exhibit a sustained firing. We defined five groups of motoneurons according to their discharge firing patterns in response to ascending and descending current ramps. In addition to the four classical types, we defined a fifth type called transient for the quasi-absence of discharge during the descending phase of the ramp. This transient type represents about 40% between P3–P5 and tends to disappear with age. Types 1 and 2 (linear and clockwise hysteresis) are the most preponderant at P6–P7. Types 3 and 4 (prolonged sustained and counter clockwise hysteresis) emerge at P8–P9. The emergence of types 3 and 4 probably depends on the maturation of L type calcium channels in the dendrites of motoneurons. No correlation was found between groups defined by step or triangular ramp of currents with the exception of transient firing patterns. Our data support the idea that a switch in the electrical properties of lumbar motoneurons might exist in the second postnatal week of life in mice.

Keywords: spinal, discharge firing pattern, dendritic arborization, calcium

Introduction

Electrical properties of developing spinal motoneurons have been studied in several species and at different embryonic and postnatal stages (Ziskind-Conhaim, 1988; Navarrette and Vrbová, 1993; Perrier and Hounsgaard, 2000; Vinay et al., 2000a,b, 2002; Carrascal et al., 2005; Kanning et al., 2010). Only a few studies deal with developing mouse spinal motoneurons

(Mynlieff and Beam, 1992a,b; Nakanishi and Whelan, 2010; Quinlan et al., 2011). A new interest to study the development of electrical properties in mouse motoneurons came with the discovery that spinal motoneuron pathology starts during the postnatal period in superoxide dismutase 1 (SOD1) transgenic mice, a standard model of amyotrophic lateral sclerosis (ALS; Amendola et al., 2004, 2007; Durand et al., 2006; Bories et al., 2007; Amendola and Durand, 2008; Pambo-Pambo et al., 2009; Quinlan et al., 2011; Filipchuk and Durand, 2012; Saxena et al., 2013).

The functional differentiation into fast and slow-twitch muscle fibers takes place late in embryonic and early in postnatal life and depends on the properties of the motoneuron (Buchthal and Schmalbruch, 1980; Navarrette and Vrbová, 1993; Kanning et al., 2010). Poly-innervation and gap junctions are present at that time period when motoneurons are still competing at the periphery (Navarrette and Vrbová, 1993; Kopp et al., 2000; Vinay et al., 2000b; Pun et al., 2002) precluding a functional identification of motor units *in situ*. For example, 64% of neuromuscular junctions mouse soleus muscle are multiply innervated by P7 whereas about 43% of the junctions are still innervated by two or more axons at P9 (Kopp et al., 2000). At that time, the firing patterns of soleus motor units are "quite phasic" (Navarrette and Vrbová, 1993; Kopp et al., 2000; Personius and Balice-Gordon, 2002).

During the early postnatal period, three patterns of discharge firing (single, transient and sustained) following current pulse stimulation have been well documented in rat spinal motoneurons (Vinay et al., 2000a,b, 2002; Mentis et al., 2007). In addition, a delayed onset firing type was recently described in mouse spinal motoneurons (Pambo-Pambo et al., 2009; Leroy et al., 2014). This delayed onset firing is due to transient outward potassium currents (Takahashi, 1990; Russier et al., 2003; Pambo-Pambo et al., 2009). It was observed in postnatal abducens motoneurons during a precise postnatal period between P4 and P9 (Russier et al., 2003). In this study we investigated whether the different patterns are present in mouse lumbar motoneurons at the same age and we focused on the postnatal period P3–P9 when pathological signs have been observed in the spinal cord of SOD1 mice (Bories et al., 2007; Amendola and Durand, 2008; Filipchuk and Durand, 2012; Saxena et al., 2013). We also analysed the development of the delayed onset firing type in spinal motoneurons to determine whether it disappears in the second postnatal week as in the case of abducens motoneurons.

Correlation between rheobase and input resistance (Rin) of motoneurons has been found in the neonate rat (Seebach and Mendell, 1996). Indeed, we investigated the correlations between the size of motoneurons and both parameters (rheobase and Rin) using our database on mouse lumbar motoneurons that have been intracellularly recorded and stained with Neurobiotin at both ages P3–P4 and P8–P9. We also compared several parameters at two different postnatal ranges (P3–P5 and P8–P9) to detect rapid changes during this period and to supplement previous studies on mouse lumbar motoneurons (Nakanishi and Whelan, 2010; Quinlan et al., 2011). Finally, we investigated the development of repetitive firing and the electrical properties of mouse lumbar motoneurons in the different groups sorted by their firing patterns. We found three types of discharge firing patterns using current step stimulation. Surprisingly in a recent study, only two patterns of discharge firing were described in mouse lumbar motoneurons in postnatal mouse (Leroy et al., 2014). Four firing patterns were previously found with ascending and descending current ramp stimulation (Amendola et al., 2007; Pambo-Pambo et al., 2009). In this study we defined a fifth type (transient firing) and we determined the ratio of motoneurons in the different types.

Part of this work has been published in abstract form (Durand et al., 2013).

Materials and Methods

Experiments were carried out on C57BL/6J mice aged from postnatal day 3 (P3) to 9 (P9), P0 being the first postnatal day. All surgical and experimental procedures are conformed to the European Communities council directive (86/609/EEC) and approved by our ethics committee (Comité National de Réflexion Ethique sur l'Expérimentation Animale n° 71). Most of the experimental procedures were described previously (Bories et al., 2007; Amendola and Durand, 2008).

Electrophysiological Experiments

P3–9 pups were anesthetized by hypothermia, decapitated, eviscerated and pinned down onto a Petri dish and immersed in cold (4°C) artificial cerebrospinal fluid (ACSF). Then, a laminectomy was performed and the spinal cord and brainstem were removed, taking care to preserve sufficient length of L5 ventral root, placed in a recording chamber and superfused with ACSF containing (in mM): NaCl, 130; KCl, 4; $MgCl_2$, 1.2; $CaCl_2$, 2; NaH_2PO_4, 1; $NaHCO_3$, 25; D-glucose, 30; bubbled with a 95% O_2/5% CO_2 mixture, adjusted to pH 7.4 at 24–25°C. Monopolar stainless steel electrodes were placed in contact with the L5 ventral root and insulated with petroleum jelly for recordings and simulations.

To allow for microelectrode penetration in the spinal cord, the pia was carefully removed medially to L5 ventral root entry, using very fine forceps under binocular control. Fine tip micropipettes for intracellular recordings were made from 1.2 mm filamented glass tubes (Clark Instruments) using a pipette puller (model P-97; Sutter Instruments). Electrodes were filled with 2 M potassium acetate, and their resistances ranged between 60 and 110 MΩ. The microelectrode was positioned to penetrate the L5 spinal segment with an angle of 30–45° above the horizontal and advanced in the tissue using a Narishige^{TM} three-dimensional hydraulic microdrive. Motoneurons were impaled at a depth of 150–450 μm from the spinal cord surface corresponding to the fifth lumbar segment. Motoneurons were identified by their antidromic action potential (anti AP) evoked following electrical stimulation of the ventral root L5. Intracellular recordings were made either in bridge mode with an output bandwidth of 3.0 kHz or in Discontinuous Current Clamp (DCC) mode, using an Axoclamp 2B amplifier (Axon instruments). Electrode resistance and

capacitance were compensated before intracellular recordings. Signals were digitized at 10 kHz by an A/D converter (Digidata 1322 Axon Instruments) and saved on a computer using Clampex 9.2 (Axon instruments).

Data Analysis

Rin was measured by computing the voltage deflections derived from series of hyperpolarizing and depolarizing constant current pulses (350 ms; −0.4 nA to +0.4 nA) injected into the motoneurons. Measurements were made from the averaged voltage over 50 ms taken from the steady state membrane potential at the end of the pulses. Retained values were the averages of three sets of measurements.

Spike potentials were analyzed using the Event Detection/Threshold Search module of Clampfit 9.2. Firing behavior was studied as described previously (Bories et al., 2007). Briefly, we used intracellular injection of series of depolarizing constant current pulses of increasing amplitude, 800 ms to 1 s in duration. Frequency/current relationship was determined as the slope of the regression line fitted to the F-I curve in the steady state (last 500 ms). A second protocol using triangular current injection was performed to study the firing pattern, instantaneous frequency and F-I relationship following ascending and descending ramps of current (Amendola et al., 2007). The triangular current stimulation consisted in an ascending followed by a descending current command. Both ramps were symmetric and series of ramps were performed every 30 s each with a speed between 0.25 nA/s to 0.95 nA/s. The different types of F-I patterns depend upon comparing the F-I curve when current is increasing to that obtained when current is decreasing (Hounsgaard et al., 1988).

Statistical significance was assessed with the non-parametric Permutation with General Score Exact Test for independent or paired samples or the Fisher exact test (StatXact7. Cytel software). The correlation between two sets of data was evaluated by using Pearson's correlation test or Spearman's correlation test (Graphpad Prism 6 or StatXact 7). Two groups of data were considered statistically different (*) if $p < 0.05$, the difference being highly significant (**) if $p < 0.01$ or (***) if $p < 0.005$. Results were expressed as means ± SEM or medians with interquartile range when indicated. Graphical representations were obtained using Origin 7.5 (Origin Lab Corporation), Graph pad Prism 6.0 and Corel Draw 12 (Vector Capital, San Francisco, CA, USA).

Labeling of Motoneurons

All the procedures for morphological studies were described previously (Amendola and Durand, 2008; Filipchuk and Durand, 2012). Labeling of recorded motoneurons was done by intracellular injection of 2% Neurobiotin following recording sessions. The motoneurons were stained using depolarizing current pulses (duration 150 ms, 1–4 nA) applied at 3.3 Hz for 10–20 min. After Neurobiotin injection, the spinal cord was maintained in the recording chamber for 1–2 h to allow for diffusion of marker into distal dendrites. The spinal cord was then immersed in 4% Paraformaldehyde fixative at 4°C overnight, rinsed in PBS (pH 7.4), blocked and cut transversally at 75 μm on a vibratome (Microm HM 650V). Neurobiotin was revealed using the standard avidin-HRP-diaminobenzidin staining procedure. Serial sections were mounted on gelatin covered glass slides, air dried overnight and coversliped.

Quantitative Morphometric Analysis

The labeled motoneurons were reconstructed from serial sections (75 μm thick) on Nikon microscope equipped with a computer interfaced motorized stage and *z*-axis optical encoder using Neurolucida^{TM} software. The Nikon microscope was equipped with ×20 dry objective and a numerical zoom ×3 (final magnification ×60).

A single motoneuron was described by up to 18.000 data points, which were stored in a database together with fiducial marks (boundaries of transverse spinal cord sections and central canal) in ASCII format files. Reconstructed cells were visualized and three-dimensionally analyzed using Neurolucida^{TM}. Our own database of intracellularly recorded and stained motoneurons with Neurobiotin comprises more than 50 postnatal mouse lumbar motoneurons at different ages between P3 and P10. Among them, 32 motoneurons were fully reconstructed in 3D with Neurolucida^{TM}. In the present work we used 14 motoneurons at both ages (P3–P4, $n = 3$ and P8–P9, $n = 11$).

Results

The data base for the electrophysiological study comprises 103 motoneurons from mice aged between P3 and P9. Only neurons displaying a stable membrane potential more negative than −50 mV with overshooting APs during the whole test procedure were kept for analysis. All the motoneurons were identified by recording either the anti AP evoked by the ventral root stimulation (**Figure 1A**, two superposed traces) or the orthodromic AP in the ventral root (**Figure 1B**, VR lower trace) evoked by direct intracellular stimulation (**Figure 1B**, upper trace). Among them, 12 motoneurons intracellularly recorded and stained were taken from our library of 3D reconstructed lumbar mouse motoneurons to link the electrical parameters (rheobase, Rin) and the morphology of individual lumbar motoneurons (see below and graphs; **Figures 2E,F**).

Morphological Changes Between P3 and P9

Most of the results on morphological data were published elsewhere for 9 out of 12 motoneurons (Amendola et al., 2007; Amendola and Durand, 2008; Elbasiouny et al., 2010a; Filipchuk and Durand, 2012). The dendritic arborizations elongated between P3 and P9 without increasing their number of branches (Filipchuk and Durand, 2012). The soma size significantly increases with age (P3–4: 1864 ± 120 μm^2, $n = 3$; P8–9: 3212 ± 314 μm^2, $n = 9$; $p = 0.04$) as well as the mean diameter of primary dendrites (P3–4: 3.56 ± 0.32 μm^2, $n = 3$; P8–9: 5.07 ± 0.31 μm^2, $n = 9$; $p = 0.03$). The total dendritic length increases from P3 to P9 by 22% (P3–4: 13622 ± 2468 μm; P8–9: 16658 ± 1625 μm; non-significant difference, ns) and the total dendritic

surface area by 20% (Filipchuk and Durand, 2012). Depending on the soma location in the ventro-lateral part of the spinal cord, distal dendrites reached different distal zones. When the soma was located centrally and dorsally in the ventro-lateral region, the dendrites projecting medially reach a region close to the central canal known to contain premotor interneurons (**Figure 1C**). On the contrary the dendritic extension of motoneurons was restricted when the soma was situated in close proximity to the ventral horn boundaries (**Figure 1D**). The full 3D reconstructions of the whole dendritic arborizations include the rostro-caudal extensions (between 450 and 750 μm) and illustrate the relative complexity of the single trees at both ages P3 and P8 (see also Figure 3 in Amendola and Durand, 2008).

Electrical Properties of Mouse Lumbar Motoneurons: Correlations with Size

In this series of experiments, a number of parameters of electrical properties was analyzed in two populations of lumbar motoneurons of different ages (P3–P5, n = 19) and P8–P9 (n = 34). The anti AP has comparable amplitude in the two populations (77.9 ± 1.71 mV vs. 82.98 ± 2 mV; ns) as well as the resting membrane potential (Em; **Table 1**). The latency of the anti AP was significantly reduced in older motoneurons (2.40 ± 0.29 ms vs. 1.18 ± 0.13 ms; p = 0.0008) due to ongoing motor axon myelination during this postnatal period.

As expected, the mean Rin was lower in the oldest motoneurons (16.2 ± 0.82 MΩ, n = 34, P8–P9) compared to the mean Rin in the P3–P5 population (19.36 ± 1.42 MΩ; n = 19, p = 0.023). However, the Rin stabilizes between P8 and P9 (**Figure 2A**). At the same time, the rheobase (minimum current to elicit an AP) increases two times in motoneurons from 0.87 ± 0.11 nA (n = 19) to 1.76 ± 0.2 nA (n= 31) between P3 and P8 (**Table 1**; **Figure 1B**, p = 0.009). The mean rheobase is significantly higher at P6/P7 (1.53 ± 0.19 nA, n = 20; p = 0.0036) compared to that in P3–P5. Indeed, a significant and negative correlation exists between the rheobase and the Rin (**Figure 2C**; r = 0.16, p = 0.023, Pearson's correlation test) but no significant correlation was found between the gain and the Rin (**Figure 2D**; R^2 = 0.09, p > 0.05). The mean rheobase was significantly lower at P9 (1.19 ± 0.2, n = 12) compared to that at P8 (2.12 ± 0.25, n = 19). Thus the progression of the rheobase stopped between P8 and P9 in lumbar motoneurons.

In twelve motoneurons intracellularly stained and fully reconstructed, significant correlations were found between the Rin and the total dendritic surface area (**Figure 2E**, r = −0.67; p = 0.016; Pearson's correlation test) and between the rheobase and the total dendritic surface area (**Figure 2F**, r = 0.63; p = 0.028; Pearson's correlation test) confirming that the largest motoneurons in the lumbar cord have the lowest Rin and the highest rheobase also during postnatal development. However, we noticed that some motoneurons with similar total dendritic surface area (40,000 μm^2) may have different Rin ranging from 10 to almost 30 MΩ (**Figure 2E**). Others motoneurons with an Rin around 10–15 MΩ also display different dendritic surface areas (30,000–60,000 μm^2).

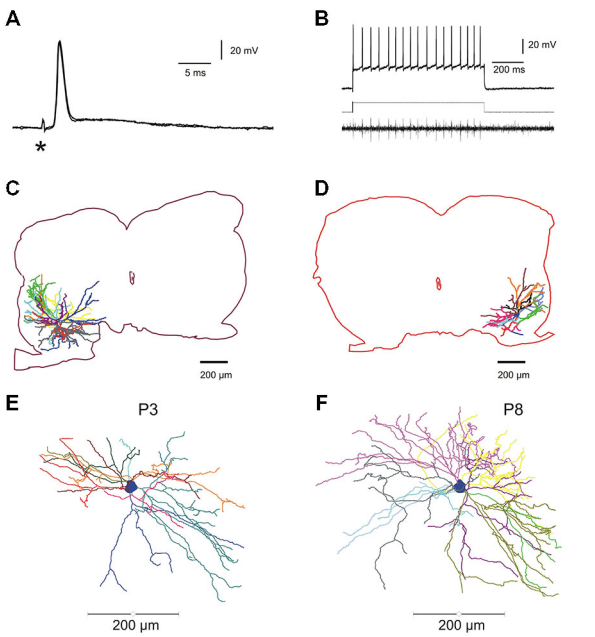

FIGURE 1 | Electrophysiological identification and intracellular staining of lumbar motoneurons in the developing mouse spinal cord. (A) Electrical stimulation of the fifth lumbar (L5) ventral root evoked an anti AP. Asterisk indicates the stimulus artifact. **(B)** Direct intracellular stimulation of L5 motoneuron giving rise to a train of action potentials (APs; sustained discharge) recorded intracellularly (upper trace) and the propagated spikes in the ventral root (lower trace); rectangular injected current: 1.2 nA (middle trace). **(C,D)**, two fully reconstructed lumbar motoneurons recorded from P8–P9 mice. Depending on the location of the soma in the ventro-lateral part of the spinal cord, dendritic arborisations extended either in all rostro-caudal directions and medially near the central canal **(C)** or confined in a restricted area into the latero-ventral part of the spinal cord **(D)**. **(E,F)** Digitized full reconstructions of two motoneurons at postnatal days 3 and 8 (P3 and P8) in the transverse plane. During this period, the total dendritic length increases by 22%, only. Each dendrite is represented by a specific color.

Changes in AP Shape

As summarized on **Table 1**, significant differences on the AP shape were found between the two groups of ages. Peak amplitude of the AP was increased from 62.08 ± 1.68 mV to 68.11 ± 1.76 mV (p = 0.028) together with the maximum depolarizing speed which was accelerated from 123 ± 8.69 $mV.ms^{-1}$ to 149 ± 7.38 $mV.ms^{-1}$ with age (p < 0.01). Thus younger motoneurons have spikes with lower amplitude and slower time course. No changes with age were seen in AHP amplitude and total AHP duration between P3 and P9. However, AHP half-duration was shorter and half decay time faster in the P8–P9 group (**Table 1**). Others parameters did not change during this short period of time such as spike threshold and the gain of motoneurons measured in the steady state of the discharge frequency.

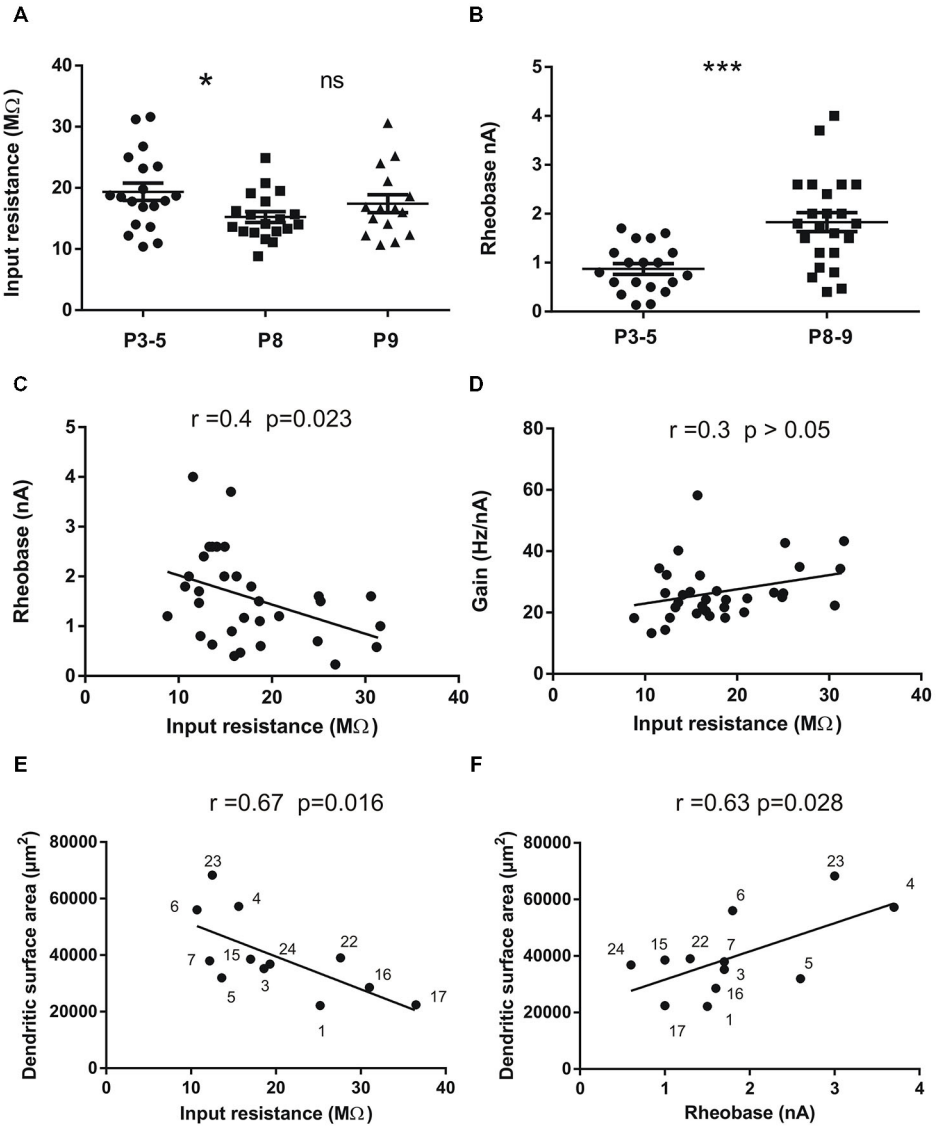

FIGURE 2 | Input resistance (Rin) and rheobase of mouse lumbar motoneurons (n = 53) at different postnatal ages (P3 to P9) and correlations with total dendritic surface area in 12 motoneurons stained with neurobiotin. (A) Mean Rin significantly decreases between the groups P3–5 and P8 (p = 0.028, n = 19 in each group) and then stabilizes at P9 (n = 15). **(B)** the mean rheobase (minimum current injected into a neuron to elicit an AP in 50% of cases) increases in the same period of time (p = 0.0033, n = 19 for P3–5 and n = 31 for P8–9). **(C)** significant negative correlation exists between rheobase and Rin in the whole population (n = 32); **(D)** no significant correlation was found between the Rin and the gain of the motoneurons (n = 32). The gain is the slope of the F-I curves measured in the steady state of the discharge firing elicited during rectangular pulses of currents. **(E,F)** significant correlations between Rin **(E)** rheobase **(F)** and the total dendritic surface area measured using 3D reconstructed motoneurons with neurolucida. Each motoneuron is numbered so that it can be identified from previous publications Amendola and Durand (2008) for Mn n° 1–7 and Filipchuk and Durand (2012) for Mn n° 15, 16, 17. The morphologies of motoneurons n° 22, 23 and 24 were not previously published. The largest motoneurons tend to have the lowest Rin and the highest rheobase. Horizontal bars indicated mean ± sem in the scatter plots of A and B. For statistical significance nonparametric permutation or mann-whitney exact tests and Pearson's correlation test were used. *p < 0.05; **p < 0.01; ***p < 0.005. Non-significant (ns) p > 0.05.

Discharge Properties

During the development of spinal motoneurons, different patterns of discharge have been previously described (Vinay et al., 2000a; Mentis et al., 2007; Pambo-Pambo et al., 2009; Leroy et al., 2014). Only recently a delayed onset firing pattern was detected in lumbar motoneurons in slice preparation (Pambo-Pambo et al., 2009; Leroy et al., 2014). We then used intracellular injection of depolarizing constant current pulses (pulse protocols, see methods) to analyze in details the discharge firing pattern of the motoneurons in the whole brainstem-spinal cord preparation. Three different firing patterns were clearly identified during this period of maturation (P3–P9)

TABLE 1 | Changes of electrical properties of lumbar motoneurons with age in postnatal mice.

	P3–P5	P8–P9	
Em (mV)	−68.89 ± 1.02 (19)	−70.03 ± 1.23 (34)	ns
Rin (MΩ)	19.36 ± 1.42 (19)	16.2 ± 0.82 (34)	*
Anti AP latency (ms)	2.40 ± 0.29 (13)	1.18 ± 0.13 (24)	***
Anti AP amplitude (mV)	77.9 ± 1.71 (13)	82.98 ± 2 (24)	ns
Anti AP time to Peak (ms)	1.39 ± 0.13	1.25 ± 0.06 (24)	ns
Anti AP half-width (ms)	1.37 ± 0.08	1.08 ± 0.04 (24)	**
Rheobase (nA)	0.87 ± 0.11 (19)	1.76 ± 0.2 (31)	**
AP threshold (mV)	−50.2 ± 1.73 (9)	−47.88 ± 1.24 (26)	ns
AP amplitude (mV)	62.08 ± 1.68 (12)	68.11 ± 1.76 (11)	*
Time to peak (ms)	1.19 ± 0.07 (12)	0.99 ± 0.05 (11)	ns
Half-width (ms)	1.28 ± 0.11 (12)	0.97 ± 0.03 (11)	**
AP Max depol slope (mV/ms)	123 ± 8.69 (12)	149 ± 7.38 (11)	*
AP Max repol slope (mV/ms)	−54.81 ± 5.34 (12)	−72.12 ± 2.90 (11)	**
Gain (Hz/nA)	23.80 ± 2.05 (13)	25.63 ± 1.60 (11)	ns
AHP duration (ms)	93.27 ± 7.40 (8)	96.63 ± 6.61 (11)	ns
AHP amplitude (mV)	5.01 ± 0.72 (8)	5.26 ± 0.50 (11)	ns
AHP time max amplitude (ms)	13.90 ± 1.94 (8)	10.00 ± 1.37 (11)	ns
AHP 1/2 duration (ms)	47.10 ± 4.33 (8)	36.78 ± 3.01 (11)	*
AHP decay time (ms)	79.61 ± 8.27 (8)	82.74 ± 5.40 (11)	ns
AHP 1/2 decay time (ms)	34.16 ± 3.50 (8)	27.78 ± 2.01 (11)	*

*P3–P5, postnatal days 3–5; P8–P9, postnatal days 8 and 9; Em, resting membrane potential; Rin, Input resistance, anti AP, antidromic action potential, latency, latency of AP elicited by electrical stimulation of the L5 ventral root; Time to peak, time needed for potential to rise from spike threshold to maximum value. Half width, time spent by the potential >50% of the maximum amplitude of action potential; Rheobase, lowest intensity of current injected through the electrode to elicit an action potential; AP threshold, voltage threshold measured at the foot of the action potential evoked by intracellular current injection; AP amplitude, amplitude of action potential measured between the foot and the peak; time to peak, measured as the time needed for the potential to reach the peak; Max depol slope, maximum slope of the depolarizing phase of action potential; Max repol slope, maximum slope of the repolarizing phase of action potential; Gain, slope of the steady state frequency-intensity curves measured during injection of long-duration pulse currents (800 ms to 1 s. AHP, Afterhyperpolarization, half duration of AHP is significantly shortened with age as well as half decay time. All values are means ± sem. The number of motoneurons is indicated between brackets after each mean value and sem. ns, non-significant difference; *p < 0.05, **p < 0.01; ***p < 0.005. Nonparametric permutation exact test.*

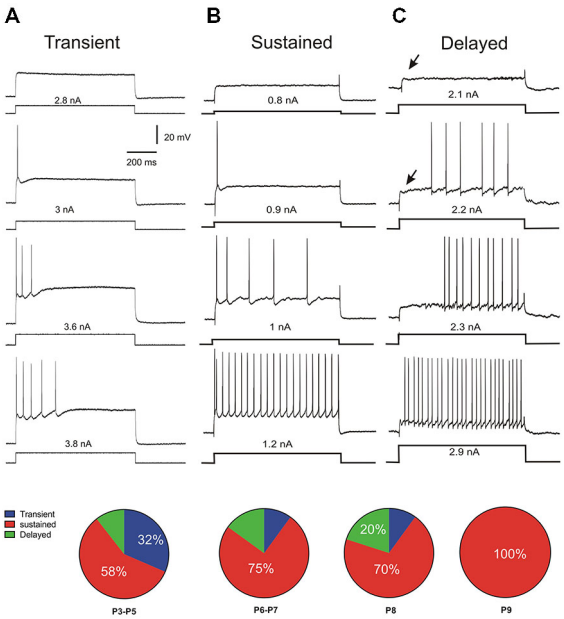

FIGURE 3 | Discharge firing patterns and distributions with age. Three different types of discharge firing patterns were found in lumbar motoneurons (n = 70) at different postnatal ages in response to rectangular current injection. The transient discharge **(A)** is characterized by a short burst of spike. The sustained pattern **(B)** starts by an early spiking followed by a burst and discharge firing maintained during the whole pulse. The third pattern is called delayed onset discharge firing **(C)** the arrow indicating a late depolarization. At P3–P5, one third of motoneurons still present a transient discharge and the motoneuron is not able to fire APs up to the end of the pulse as illustrated in **(A)** (see pie chart). In older animals the number of motoneurons presenting this pattern decreases up to P9. At that age, there is no more transient firing but all motoneurons exhibit a sustained discharge firing pattern **(B)**. Between P3 and P8 a fraction of motoneurons has a delayed onset firing pattern which disappears at P9.

according to the mode of discharge firing which was transient (**Figure 3A**), sustained (**Figure 3B**) or delayed (**Figure 3C**) in the different motoneurons. **Figure 3A** illustrates the typical pattern of discharge of transient firing cells. The motoneuron fired a single spike or a burst of spikes and the discharge firing did not last during the entire pulse but a few hundreds of ms, only. This transient firing was recorded in 32% of motoneurons at P3–P5 (pie chart in **Figure 3**). This ratio is in agreement with previous report on extensor motoneurons in the neonate rat (Vinay et al., 2000a). The transient firing pattern was not observed in motoneurons from animals older than P8 (see pie chart). The second group called sustained firing also displayed an early AP at rheobase and then several APs appeared with increasing current intensities (**Figure 3B**). The instantaneous discharge frequency progressively increased and the motoneuron was able to fire continuously up to the end of the pulse (**Figure 3B**; 1.2 nA). A third group is composed of motoneurons that display a delayed onset firing. The delayed onset firing (**Figure 3C**) corresponds to the late bursting motoneurons previously described in spinal motoneurons (Pambo-Pambo et al., 2009). As illustrated on **Figure 3C**, they were characterized by a delayed trigger of the AP. At potentials below spike threshold, an initial transient small overshoot in voltage response to the current pulse was observed (arrow on **Figure 3C**, upper traces). It was followed by a slow rising, late depolarization. This delayed onset firing was seen in 20% of motoneurons in our sample at P8 but was not detected at P9 (n = 12). The distribution of the different firing patterns is illustrated in pie charts in **Figure 3**. Most motoneurons exhibit an early and sustained discharge (as in 3B) at all postnatal ages.

We then analysed the electrical properties of the subgroups. We focused on the three patterns of discharge firing in motoneurons from P6–P9 animals. We analyzed 14 passive and active electrical properties (**Figure 4**). The motoneurons with delayed onset firing pattern have the highest rheobase, input conductance and time constant (**Figures 4A–C**) suggesting that they are the largest motoneurons. Others parameters show significant differences between the three groups such as

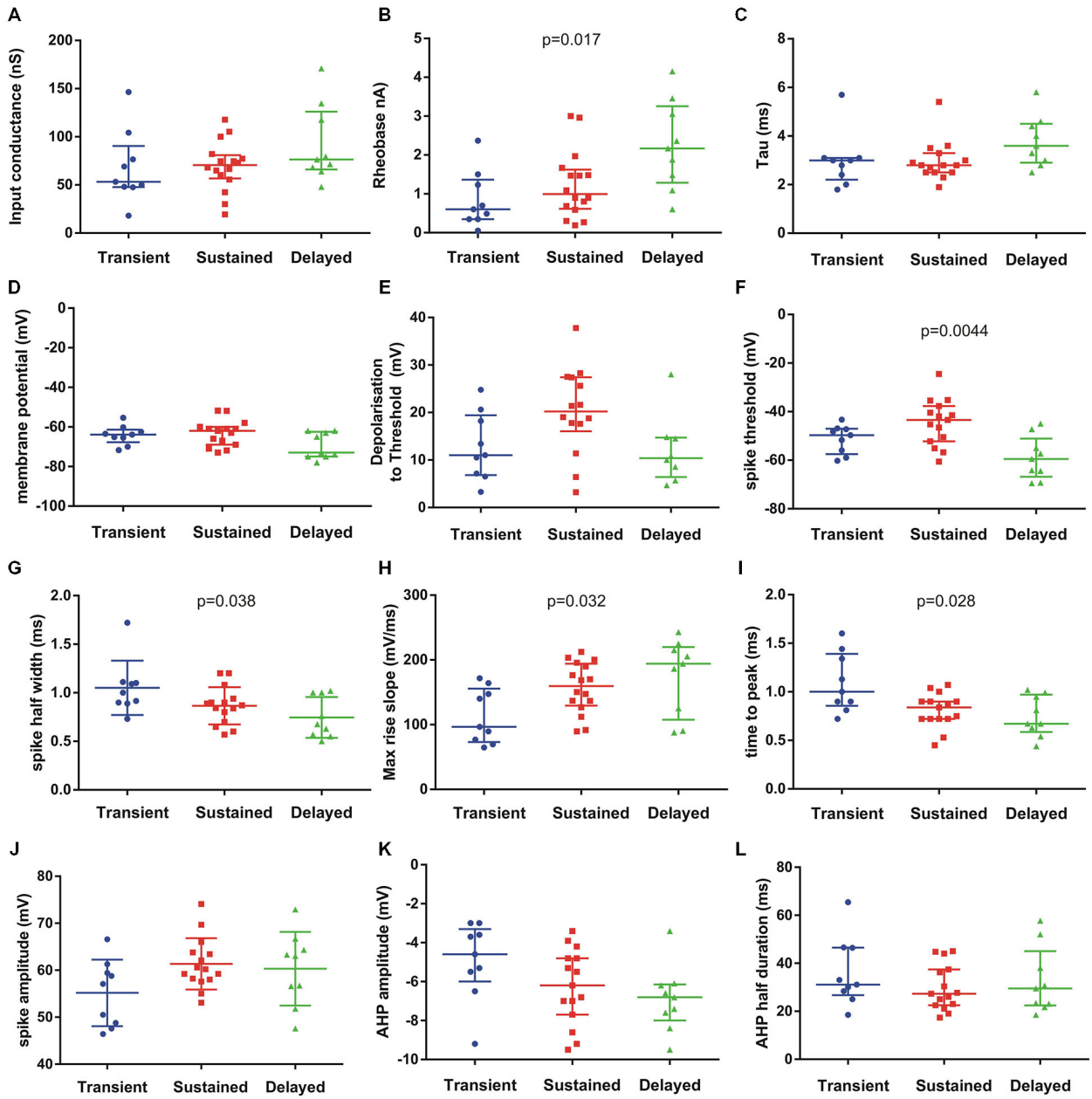

FIGURE 4 | Passive and active electrical properties of postnatal mouse lumbar motoneurons (*n* = 33) in three subgroups defined by their discharge firing pattern. Fourteen electrical properties were compared (12 illustrated). Among them, several electrical properties show significant differences in the medians as indicated on each graph (Kruskal–Wallis test). The delayed subgroup has the highest conductance **(A)** rheobase **(B)** and time constant **(C)** suggesting they represent the largest motoneurons. The resting membrane potential (Em) **(D)** was hyperpolarized in this subgroup (delayed) but the spike voltage threshold was the lowest **(F)**. The spike voltage threshold and the depolarization to threshold were the highest in the sustained subgroup **(E,F)**. The AP was the shortest in the delayed population (half width in **G**) and the fastest **(H,I)** compared to the two others groups. The AP amplitude was similar in sustained and delayed subgroups but lower in the transient group **(J)**. The AHP amplitude was smaller in the transient subgroup and larger in the delayed subgroup **(K)** whereas the medians of AHP half durations were comparable in the three subgroups **(L)**. Bars indicate median and quartile. Statistical significance for three populations: Kruskal–Wallis exact test.

the spike threshold (p = 0.0044, Kruskall–Wallis test), spike half width (p = 0.038, Kruskall–Wallis test), max rise slope (p = 0.032, Kruskall–Wallis test) and time to peak (p = 0.028, Kruskall–Wallis test) of the AP. The maximum decay slope also shows statistically significant difference between the three groups (not illustrated). All spike parameters (time to peak, max rise slope) indicate that the delayed firing type do have the fastest AP. The AHP parameters did not show significant differences

although there is a tendency in the AHP amplitude to be larger in the delayed group (**Figures 4K,L**). The gain of the motoneurons measured at the steady state firing frequency (in the last 500 ms of the current pulse) was also higher in the delayed onset firing group compared with the gain in the sustained firing group (delayed : 37.2 ± 2.5 Hz/nA, $n = 9$; sustained : 27.7 ± 3.4 Hz/nA, $n = 15$; $p = 0.024$; non parametric permutation exact test).

Firing Behavior on Slow Triangular Current Ramps

Firing pattern was further characterized using increasing and decreasing (triangular) slow current ramps as described previously (Hounsgaard et al., 1988; Amendola et al., 2007; Pambo-Pambo et al., 2009). The F-I plots revealed differences in discharge patterns which could be classified in five types according to the frequency response on up and down going ramps. The four classical types already described in motoneurons from adult (Bennett et al., 2001) or neonate (Amendola et al., 2007) rodents are illustrated as followed: linear (**Figure 5A**), clockwise hysteresis (**Figure 5B**), prolonged sustained (**Figure 5C**) and counterclockwise hysteresis (**Figure 5D**). A fifth type was defined by the lack or the quasi-absence of discharge firing during the descending phase of the ramp at early postnatal ages (**Figure 5E**). This fifth type was present in 40% of motoneurons at P3–P5, in 25% of motoneurons at P6–P7 and in less than 10% at P8–P9 (**Figure 5F**). At an early postnatal age, type 1 (linear) and type 2 (clockwise) were predominant whereas the number of motoneurons exhibiting type 3 and type 4 markedly increases at P8–P9. Type 3 and type 4 discharge patterns, displaying a sustained firing during the down going ramp and a counter-clockwise hysteresis, respectively, was observed in 50% of motoneurons in older animals whereas the number of motoneurons exhibiting a non-linear electrical behavior during ramp current injection was <20% before P8. The emergence of types 3 and 4 discharge patterns correspond with the period of maturation of L-type calcium channels in mouse motoneurons (Carlin et al., 2000).

We found no correlation between the different groups of motoneurons defined by step of current and those defined by triangular ramp of currents with the exception of the transient firing patterns. In other words, the delayed onset firing group and the sustained firing group both contain motoneurons of different types 1–4 in the Bennett's classification following ascending descending ramps of current (Bennett et al., 2001).

Discussion

In this work, we show rapid changes in electrical properties of postnatal mouse lumbar motoneurons. We defined three different groups of lumbar motoneurons according to their discharge firing patterns and differences in several electrical properties. The delayed onset firing type has the characteristics of the largest motoneurons whereas the transient type is the less mature group of motoneurons and contains mainly small motoneurons with low rheobase and slow APs. We found that 32% of motoneurons still discharged transiently at an early age (P3–P5) whereas some motoneurons exhibit a delayed onset firing pattern up to the second postnatal week. A majority of motoneurons have a sustained firing at all ages between P3 and P9. The sustained firing is present in all motoneurons at P9. The results also show that a counter clockwise hysteresis and/or a prolonged sustained firing in response to current ramp (types 3 and 4) emerge at P8–P9 corresponding to the maturation of L type calcium channels in dendrites of mouse motoneurons. Dendrites of postnatal motoneurons mainly elongated during this short period of time. Although most morphological parameters were not significantly different between P3 and P9 (Filipchuk and Durand, 2012), a significant correlation exists between the size of the dendritic arborizations and the Rin or the rheobase of motoneurons (**Figures 2E,F**).

Postnatal Changes in Electrical Properties of Lumbar Motoneurons

The electrical properties of spinal motoneurons have been well documented in the neonate rat (Seebach and Mendell, 1996; Vinay et al., 2000a, 2002) but only two studies concern neonate mouse spinal motoneurons and the evolution of several passive and active properties (Nakanishi and Whelan, 2010; Quinlan et al., 2011). We show that rheobase, Rin, spike half-width and spike depolarization speed changed significantly in mouse spinal motoneurons between postnatal days 3 and 9. The AP and half decay AHP are found to shorten significantly in duration (**Table 1**). The shape of AP is modified with a higher speed of depolarization in older animals probably linked with the density of sodium channels (García et al., 1998; Carlin et al., 2008) and a faster repolarization indicating potassium channels maturation (McLarnon, 1995; Gao and Ziskind-Conhaim, 1998; Nakanishi and Whelan, 2010). During the same time, some parameters of electrical properties remain constant such as the membrane potential, AP threshold and amplitude, gain at steady state and after hyperpolarization duration and amplitude (**Table 1**).

Our results are comparable to those obtained previously in rodents (Fulton and Walton, 1986; Seebach and Mendell, 1996; Vinay et al., 2000a,b; Mentis et al., 2007; Nakanishi and Whelan, 2010; Quinlan et al., 2011).

A few exceptions concerns some parameters such as membrane potentials and Rin (Nakanishi and Whelan, 2010; Quinlan et al., 2011). In the study by Quinlan et al. (2011) membrane potentials were significantly different probably because the younger population of motoneurons started from P0 where motoneurons have more depolarized potentials whereas in our study the younger group was aged between P3 and P5. Surprisingly the mean Rin were not different between the younger and older groups of motoneurons in the study by Nakanishi and Whelan (2010). The slicing procedure and the visual selection of neurons cannot fully explain this result since those by Quinlan et al. (2011) have been also obtained in slice. All other developmental changes in electrical parameters have been described in many other species (Kellerth et al., 1971; Hammarberg and Kellerth, 1975; Navarrette and Vrbová, 1993; Perrier and Hounsgaard, 2000; Vinay et al., 2000b) including human spinal motoneurons derived from embryonic stem cells (Takazawa et al., 2012).

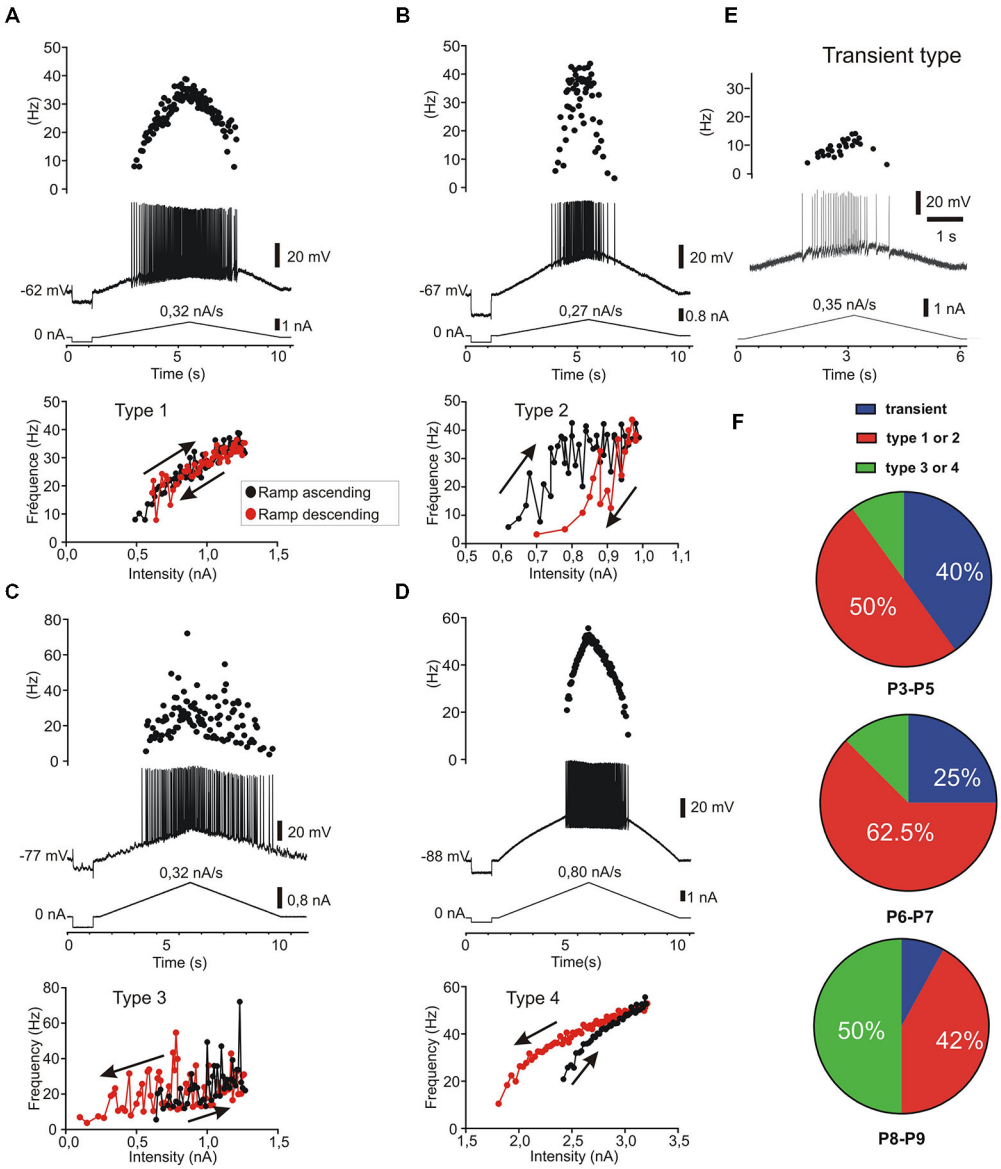

FIGURE 5 | Five patterns of discharge recorded in response to current ramp stimulation in postnatal lumbar motoneurons (*n* = 38). The four classical types **(A–D)** as described in adult motoneurons (Bennett et al., 2001) are present and a fifth type called transient, since no discharge firing, or only a few spikes (<5), could be evoked during the descending phase **(E)**. **(A)** type 1: linear F-I relationship where the firing frequency curves overlapped on the ascending and descending phases. **(B)** type 2: clockwise hysteresis pattern where the instantaneous frequency is lower in the descending phase for the same current intensity. **(C)** type 3: Linear F-I relationship with sustained firing in the descending phase. **(D)** type 4: Counter clockwise hysteresis where the frequency is higher during the descending phase; **(E)** type 5: transient discharge during the ascending phase with usually no discharge or only a few spikes in the descending phase. In this case which is frequent before P5 (40%), it was not possible to plot an F-I curve during the descending ramp. **(F)** distribution of the five discharge patterns according to the postnatal ages. Note that types 1 and 2 are the predominant types before P8 (*n* = 15/26) whereas the types 3 and 4 are most frequent at P8–P9 (*n* = 6/12) but rare before P8 (*n* = 3/26).

The rheobase current significantly increased during this short time period between P3 and P8 and stabilized between P8 and P9 precisely when the Rin stops decreasing. As already described in neonate rats (Seebach and Mendell, 1996), a significant correlation exists between Rin and rheobase in our sample of developing mouse motoneurons (see **Figure 2**). We also found a positive correlation between the size of the dendritic arborizations and the rheobase of developing motoneurons (**Figure 2**). The size of motoneurons (both soma and dendritic arborizations) increases with age although the dendritic arborizations did not increase in complexity during this postnatal period in mice (Li et al., 2005; Filipchuk and Durand,

2012). In fact this is a time for rapid changes in active electrical properties whereas the morphology of motoneurons with their dendritic arborizations growth in a slow and progressive manner.

Different Patterns of Discharge Firing

In this study, we found 20% of motoneurons with a delayed onset firing pattern. In another set of motoneurons, a maximal proportion of 27% of such delayed firing was reached at an age between P6 and P8 (not shown). This proportion is rather low compared to that (65%) observed in lumbar motoneurons recorded in slice (Pambo-Pambo et al., 2009; Leroy et al., 2014). The delayed onset firing pattern is due to transient outward potassium currents as shown by blockade with apamin and TEA (Takahashi, 1990; Russier et al., 2003; Pambo-Pambo et al., 2009). Thus the major difference between both ratios obtained in the different spinal cord preparations might be linked to modulation by supraspinal descending pathways controlling potassium conductances and the absence of such control in slice preparations (McLarnon, 1995; Perrier and Hounsgaard, 2000). The number of motoneurons with such firing pattern might not have been under evaluated due to short current pulse (which are used in most studies) as suggested in recent work (Leroy et al., 2014) since comparable current pulses (1 s) were applied in our study in slice preparation (Pambo-Pambo et al., 2009) and in the present study. The delayed onset firing was not seen in spinal motoneurons from neonate rat probably due to the level of the brainstem section and/or the age of the animals. We found a transient expression of the delayed onset firing type between P3 and P8 (**Figure 3**) which is rather close to results obtained in rat abducens motoneurons (Russier et al., 2003) and neonate oculomotor (Nieto-Gonzalez et al., 2007). Although we did not investigate younger animals than P3, it is noteworthy that the delayed onset firing type was never seen in large studies performed at P0–P2 in neonate rat (Vinay et al., 2000a,b, 2002). In most work performed on older animals (>P8), the delayed onset firing pattern was not described in spinal motoneurons (Miles et al., 2005; Delestrée et al., 2014) but see Zhu et al. (2012). The delayed onset firing pattern is also present in adult rat facial motoneurons (Nishimura et al., 1989) but not in adult abducens and oculomotor motoneurons (Durand, 1989a,b).

The differences of several parameters in the electrical properties of the three groups of motoneurons likely reflect differences in maturation as suggested by APs parameters (**Figure 4**). Indeed our results show that the motoneurons with transient firing pattern are populations of immature cells whose properties will change after P8. The transient firing pattern was present in most brainstem and spinal motoneurons in neonate animals (Vinay et al., 2000b; Nieto-Gonzalez et al., 2007) but see Leroy et al. (2014). The transient firing type was seen in more than half of extensor motoneurons at P0–P2 and in 30% at P3–P5, whereas the sustained firing type represents 70% in extensor and 100% in flexor motoneurons at P3–P5 (Vinay et al., 2000a). The reason why the transient firing was not found in some studies might be due to recording of a majority of flexor motoneurons.

We can notice that a transient firing type is still present in adult brainstem motoneurons (Durand, 1989a; Nishimura et al., 1989; Nieto-Gonzalez et al., 2007) and in adult zebrafish (Ampatzis et al., 2013) but not in mammalian spinal motoneurons (Delestrée et al., 2014).

It is difficult to speculate on the presence of these discharge patterns in the different types of motoneurons and species. Our study shows that both delayed and transient firing patterns disappear at P9 in mouse lumbar motoneurons. At that age there is still gap junctions between motoneurons as shown by multiple staining after a single intracellular injection (Amendola and Durand, 2008). Gap junctions between motoneurons and polyinnervation of muscular fibers disappear between the second and the third postnatal week (Navarrette and Vrbová, 1993; Kopp et al., 2000; Mentis et al., 2002; Vinay et al., 2002). The complementarity of the delayed and transient discharges might insure an asynchronous firing in the same pool promoting synapse elimination (Buffelli et al., 2002, 2004). The transient and the delayed onset types might represent the last motoneurons innervating common muscle fibers. We speculate that the large motoneurons with delayed onset type will prefer fast twitch fibers whereas the motoneurons with transient type will win the innervation of slow muscle fibers. If motoneurons are recruited together, it may also represent a protection for the muscular fibers against strong activation by two motoneurons. On the other hand, the different discharge pattern might contribute to enhance the phenotypic differences among fast and slow muscle fiber types by differentially regulating transcription in a use dependent manner (Rana et al., 2009).

Persistent Inward Current and Ramp in Motoneurons

Using ramp of current we found an increase with age in the number of motoneurons with non-linear behaviors (types 3 and 4). They represent up to 50% of motoneurons at P8–P9 but only 10% at P3–P5 (**Figure 5**). We found no correlation between the different types of motoneurons based on their firing properties defined by pulse steps or triangular current stimulations except for transient types. Mouse spinal motoneurons are endowed with functionally mature calcium channels in the second postnatal week (Carlin et al., 2000).

The non-linear behavior may originate from sodium and/or calcium persistent inward currents (Schwindt and Crill, 1980; Perrier and Hounsgaard, 2000; Heckman et al., 2008). Recently, it was found that bistable behaviors are unmasked 1 week after birth in 80% of motoneurons when the temperature was raised >30°C (Bouhadfane et al., 2013). However all our experiments have been performed at a lower temperature (24–25°C). Our results are compatible with those describing the development of L type calcium channels in the mouse (Jiang et al., 1999b). This also parallels the maturation of functional behaviors in rodents (Vinay et al., 2005), mice begin to weight-bear and walk at P9–P10 (Fox, 1965; Jiang et al., 1999a; Amendola et al., 2004).

Importance of Our Findings for Future Studies on ALS

Our results show that the rheobase, input conductance and gain of motoneurons are the highest in the delayed firing group. These results are in agreement with those suggesting

that motoneurons with delayed onset firing pattern correspond to the fast motoneurons (Leroy et al., 2014). Indeed it is tempting to speculate that these motoneurons will be part of the future population of fast motoneurons in older animals since a proportion of 30% motoneurons expressing Dlk1, a biophysical marker for fast motoneurons, was recently found (Muller et al., 2014). In addition the delayed onset firing type motoneurons present the more hyperpolarized membrane potential (**Figure 4D**). Recently, Hadzipasic et al. (2014) identified four types of spinal motoneurons in the adult mice and showed that the fastest firing motoneuron type was lost in a $SOD1^{G85R}$ transgenic mouse model of ALS at 3–4 months of age. Furthermore they found that this population of motoneurons that disappears in SOD1 adult mice was greatly hyperpolarized, which would favour hypoexcitability. We previously showed that lumbar motoneurons from $SOD1^{G85R}$ mice were hypoexcitable very early during the postnatal period having a higher rheobase and lower gain (Bories et al., 2007). It would be important to determine whether the population of motoneurons which degenerate first in adult SOD1 mice corresponds to the hypoexcitable cells detected in the postnatal period. Therefore, it remains to be determined whether the delayed onset firing type is affected in SOD1 postnatal mice. It seems not to be the case in the study by Leroy et al. (2014). However this latter study used the high expressor strain of $SOD1^{G93A}$ mice in which an accelerated maturation of lumbar motoneurons might lead to a different time course in the ALS pathology (Quinlan et al., 2011, 2015). Further longitudinal studies from low expressor strains of $SOD1^{G85R}$ or $SOD1^{G93A}$ mice are needed to elucidate this question.

Conclusions

We found rapid changes in the progression of electrical properties of mouse lumbar motoneurons between P3 and P9 whereas the morphology of dendritic arborization evolves slowly. A change of rheobase and Rin progressions occurs, with the disappearance of transient and delayed onset firing types following direct current pulse stimulation, and the emergence of types 3 and 4 discharge patterns following direct ramp current stimulation. We conclude that a switch might exist in the electrical properties of mouse lumbar motoneurons around P8–P9 during the maturation of motor behaviors.

Acknowledgments

This work was supported by The Thierry Latran Fundation (OHEX project). Julien Amendola was supported by a PhD fellowship from Association Française contre les myopathies (AFM). Anton Filipchuk was funded by the French Ministry of Foreign Affairs. Arnaud Pambo-Pambo received financial support by Gabon Government. This work was partly supported by the international program of the French-Ukrainian joint grant n° 21360 the Centre National de la Recherche Scientifique and the Association pour la recherche sur la sclérose latérale amyotrophique. We thank Anne Duhoux for taking care of the animals. We also thank all our colleagues and members of the P3M team for invaluable discussions with special thoughts to its head for more than 10 years, the late Dr Laurent Vinay.

References

Amendola, J., and Durand, J. (2008). Morphological differences between wild-type and transgenic superoxide dismutase 1 lumbar motoneurons in postnatal mice. *J. Comp. Neurol.* 511, 329–341. doi: 10.1002/cne.21818

Amendola, J., Gueritaud, J. P., Lamotte D'incamps, B., Bories, C., Liabeuf, S., Allene, C., et al. (2007). Postnatal electrical and morphological abnormalities in lumbar motoneurons from transgenic mouse models of amyotrophic lateral sclerosis. *Arch. Ital. Biol.* 145, 311–323.

Amendola, J., Verrier, B., Roubertoux, P., and Durand, J. (2004). Altered sensorimotor development in a transgenic mouse model of amyotrophic lateral sclerosis. *Eur. J. Neurosci.* 20, 2822–2826. doi: 10.1111/j.1460-9568.2004.03745.x

Ampatzis, K., Song, J., Ausborn, J., and El Manira, A. (2013). Pattern of innervation and recruitment of different classes of motoneurons in adult zebrafish. *J. Neurosci.* 33, 10875–10886. doi: 10.1523/JNEUROSCI.0896-13.2013

Bennett, D. J., Li, Y., and Siu, M. (2001). Plateau potentials in sacrocaudal motoneurons of chronic spinal rats, recorded *in vitro*. *J. Neurophysiol.* 86, 1955–1971.

Bories, C., Amendola, J., Lamotte d'incamps, B., and Durand, J. (2007). Early electrophysiological abnormalities in lumbar motoneurons in a transgenic mouse model of amyotrophic lateral sclerosis. *Eur. J. Neurosci.* 25, 451–459. doi: 10.1111/j.1460-9568.2007.05306.x

Bouhadfane, M., Tazerart, S., Moqrich, A., Vinay, L., and Brocard, F. (2013). Sodium-mediated plateau potentials in lumbar motoneurons of neonatal rats. *J. Neurosci.* 33, 15626–15641. doi: 10.1523/JNEUROSCI.1483-13.2013

Buchthal, F., and Schmalbruch, H. (1980). Motor unit of mammalian muscle. *Physiol. Rev.* 60, 90–142.

Buffelli, M., Busetto, G., Bidoia, C., Favero, M., and Cangiano, A. (2004). Activity-dependent synaptic competition at mammalian neuromuscular junctions. *News Physiol. Sci.* 19, 85–91. doi: 10.1152/nips.01464.2003

Buffelli, M., Busetto, G., Cangiano, L., and Cangiano, A. (2002). Perinatal switch from synchronous to asynchronous activity of motoneurons: link with synapse elimination. *Proc. Natl. Acad. Sci. U S A* 99, 13200–13205. doi: 10.1073/pnas.202471199

Carlin, K. P., Jiang, Z., and Brownstone, R. M. (2000). Characterization of calcium currents in functionally mature mouse spinal motoneurons. *Eur. J. Neurosci.* 12, 1624–1634. doi: 10.1046/j.1460-9568.2000.00050.x

Carlin, K. P., Liu, J., and Jordan, L. M. (2008). Postnatal changes in the inactivation properties of voltage-gated sodium channels contribute to the mature firing pattern of spinal motoneurons. *J. Neurophysiol.* 99, 2864–2876. doi: 10.1152/jn.00059.2008

Carrascal, L., Nieto-Gonzalez, J. L., Cameron, W. E., Torres, B., and Nunez-Abades, P. A. (2005). Changes during the postnatal development in physiological and anatomical characteristics of rat motoneurons studied *in vitro*. *Brain Res. Brain Res. Rev.* 49, 377–387. doi: 10.1016/j.brainresrev.2005.02.003

Delestrée, N., Manuel, M., Iglesias, C., Elbasiouny, S. M., Heckman, C. J., and Zytnicki, D. (2014). Adult spinal motoneurones are not hyperexcitable in a mouse model of inherited amyotrophic lateral sclerosis. *J. Physiol.* 592, 1687–1703. doi: 10.1113/jphysiol.2013.265843

Durand, J., Filipchuk, A., Pambo-Pambo, A., Liabeuf, S., Brocard C., Kulagina, I. B., et al. (2013). Low-excitable lumbar motoneurons are selectively affected in the spinal cord of postnatal transgenic SOD1–G93A mice. Abstract à la Société Française des Neurosciences, Lyon, France, June 2013.

Durand, J. (1989a). Electrophysiological and morphological properties of rat abducens motoneurones. *Exp. Brain Res.* 76, 141–152. doi: 10.1007/bf00253631

Durand, J. (1989b). Intracellular study of oculomotor neurons in the rat. *Neuroscience* 30, 639–649. doi: 10.1016/0306-4522(89)90157-7

Durand, J., Amendola, J., Bories, C., and Lamotte d'incamps, B. (2006). Early abnormalities in transgenic mouse models of amyotrophic lateral sclerosis. *J. Physiol. Paris* 99, 211–220. doi: 10.1016/j.jphysparis.2005.12.014

Elbasiouny, S. M., Amendola, J., Durand, J., and Heckman, C. J. (2010a). Evidence from computer simulations for alterations in the membrane biophysical properties and dendritic processing of synaptic inputs in mutant superoxide dismutase-1 motoneurons. *J. Neurosci.* 30, 5544–5558. doi: 10.1523/JNEUROSCI.0434-10.2010

Filipchuk, A. A., and Durand, J. (2012). Postnatal dendritic development in lumbar motoneurons in mutant superoxide dismutase 1 mouse model of amyotrophic lateral sclerosis. *Neuroscience* 209, 144–154. doi: 10.1016/j.neuroscience.2012.01.046

Fox, W. M. (1965). Reflex-ontogeny and behavioural development of the mouse. *Anim. Behav.* 13, 234–241. doi: 10.1016/0003-3472(65)90041-2

Fulton, B. P., and Walton, K. (1986). Electrophysiological properties of neonatal rat motoneurones studied *in vitro*. *J. Physiol.* 370, 651–678. doi: 10.1113/jphysiol.1986.sp015956

Gao, B. X., and Ziskind-Conhaim, L. (1998). Development of ionic currents underlying changes in action potential waveforms in rat spinal motoneurons. *J. Neurophysiol.* 80, 3047–3061.

García, K. D., Sprunger, L. K., Meisler, M. H., and Beam, K. G. (1998). The sodium channel Scn8a is the major contributor to the postnatal developmental increase of sodium current density in spinal motoneurons. *J. Neurosci.* 18, 5234–5239.

Hadzipasic, M., Tahvildari, B., Nagy, M., Bian, M., Horwich, A. L., and McCormick, D. A. (2014). Selective degeneration of a physiological subtype of spinal motor neuron in mice with SOD1-linked ALS. *Proc. Natl. Acad. Sci. U S A* 111, 16883–16888. doi: 10.1073/pnas.1419497111

Hammarberg, C., and Kellerth, J. O. (1975). The postnatal development of some twitch and fatigue properties of single motor units in the ankle muscles of the kitten. *Acta Physiol. Scand.* 95, 243–257. doi: 10.1111/j.1748-1716.1975.tb10048.x

Heckman, C. J., Johnson, M., Mottram, C., and Schuster, J. (2008). Persistent inward currents in spinal motoneurons and their influence on human motoneuron firing patterns. *Neuroscientist* 14, 264–275. doi: 10.1177/1073858408314986

Hounsgaard, J., Hultborn, H., Jespersen, B., and Kiehn, O. (1988). Bistability of alpha-motoneurones in the decerebrate cat and in the acute spinal cat after intravenous 5-hydroxytryptophan. *J. Physiol.* 405, 345–367. doi: 10.1113/jphysiol.1988.sp017336

Jiang, Z., Carlin, K. P., and Brownstone, R. M. (1999a). An *in vitro* functionally mature mouse spinal cord preparation for the study of spinal motor networks. *Brain Res.* 816, 493–499. doi: 10.1016/s0006-8993(98)01199-8

Jiang, Z., Rempel, J., Li, J., Sawchuk, M. A., Carlin, K. P., and Brownstone, R. M. (1999b). Development of L-type calcium channels and a nifedipine-sensitive motor activity in the postnatal mouse spinal cord. *Eur. J. Neurosci.* 11, 3481–3487. doi: 10.1046/j.1460-9568.1999.00765.x

Kanning, K. C., Kaplan, A., and Henderson, C. E. (2010). Motor neuron diversity in development and disease. *Annu. Rev. Neurosci.* 33, 409–440. doi: 10.1146/annurev.neuro.051508.135722

Kellerth, J. O., Mellström, A., and Skoglund, S. (1971). Postnatal excitability changes of kitten motoneurones. *Acta Physiol. Scand.* 83, 31–41. doi: 10.1111/j.1748-1716.1971.tb05048.x

Kopp, D. M., Perkel, D. J., and Balice-Gordon, R. J. (2000). Disparity in neurotransmitter release probability among competing inputs during neuromuscular synapse elimination. *J. Neurosci.* 20, 8771–8779.

Leroy, F., Lamotte d'incamps, B., Imhoff-Manuel, R. D., and Zytnicki, D. (2014). Early intrinsic hyperexcitability does not contribute to motoneuron degeneration in amyotrophic lateral sclerosis. *Elife* 3. doi: 10.7554/elife.04046

Li, Y., Brewer, D., Burke, R. E., and Ascoli, G. A. (2005). Developmental changes in spinal motoneuron dendrites in neonatal mice. *J. Comp. Neurol.* 483, 304–317. doi: 10.1002/cne.20438

McLarnon, J. G. (1995). Potassium currents in motoneurones. *Prog. Neurobiol.* 47, 513–531. doi: 10.1016/0301-0082(95)00032-1

Mentis, G. Z., Díaz, E., Moran, L. B., and Navarrete, R. (2002). Increased incidence of gap junctional coupling between spinal motoneurones following transient blockade of NMDA receptors in neonatal rats. *J. Physiol.* 544, 757–764. doi: 10.1113/jphysiol.2002.028159

Mentis, G. Z., Díaz, E., Moran, L. B., and Navarrete, R. (2007). Early alterations in the electrophysiological properties of rat spinal motoneurones following neonatal axotomy. *J. Physiol.* 582, 1141–1161. doi: 10.1113/jphysiol.2007.133488

Miles, G. B., Dai, Y., and Brownstone, R. M. (2005). Mechanisms underlying the early phase of spike frequency adaptation in mouse spinal motoneurones. *J. Physiol.* 566, 519–532. doi: 10.1113/jphysiol.2005.086033

Muller, D., Cherukuri, P., Henningfeld, K., Poh, C. H., Wittler, L., Grote, P., et al. (2014). Dlk1 promotes a fast motor neuron biophysical signature required for peak force execution. *Science* 343, 1264–1266. doi: 10.1126/science.1246448

Mynlieff, M., and Beam, K. G. (1992a). Characterization of voltage-dependent calcium currents in mouse motoneurons. *J. Neurophysiol.* 68, 85–92.

Mynlieff, M., and Beam, K. G. (1992b). Developmental expression of voltage-dependent calcium currents in identified mouse motoneurons. *Dev. Biol.* 152, 407–410. doi: 10.1016/0012-1606(92)90148-a

Nakanishi, S. T., and Whelan, P. J. (2010). Diversification of intrinsic motoneuron electrical properties during normal development and botulinum toxin-induced muscle paralysis in early postnatal mice. *J. Neurophysiol.* 103, 2833–2845. doi: 10.1152/jn.00022.2010

Navarrette, R., and Vrbová, G. (1993). Activity-dependent interactions between motoneurones and muscles: their role in the development of the motor unit. *Prog. Neurobiol.* 41, 93–124. doi: 10.1016/0301-0082(93)90041-p

Nieto-Gonzalez, J. L., Carrascal, L., Nunez-Abades, P., and Torres, B. (2007). Phasic and tonic firing properties in rat oculomotor nucleus motoneurons, studied *in vitro*. *Eur. J. Neurosci.* 25, 2682–2696. doi: 10.1111/j.1460-9568.2007.05516.x

Nishimura, Y., Schwindt, P. C., and Crill, W. E. (1989). Electrical properties of facial motoneurons in brainstem slices from guinea pig. *Brain Res.* 502, 127–142. doi: 10.1016/0006-8993(89)90468-x

Pambo-Pambo, A., Durand, J., and Gueritaud, J. P. (2009). Early excitability changes in lumbar motoneurons of transgenic SOD1G85R and SOD1G(93A-Low) mice. *J. Neurophysiol.* 102, 3627–3642. doi: 10.1152/jn.00482.2009

Perrier, J. F., and Hounsgaard, J. (2000). Development and regulation of response properties in spinal cord motoneurons. *Brain Res. Bull.* 53, 529–535. doi: 10.1016/s0361-9230(00)00386-5

Personius, K. E., and Balice-Gordon, R. J. (2002). Activity-dependent synaptic plasticity: insights from neuromuscular junctions. *Neuroscientist* 8, 414–422. doi: 10.1177/107385802236970

Pun, S., Sigrist, M., Santos, A. F., Ruegg, M. A., Sanes, J. R., Jessell, T. M., et al. (2002). An intrinsic distinction in neuromuscular junction assembly and maintenance in different skeletal muscles. *Neuron* 34, 357–370. doi: 10.1016/s0896-6273(02)00670-0

Quinlan, K. A., Lamano, J. B., Samuels, J., and Heckman, C. J. (2015). Comparison of dendritic calcium transients in juvenile wild type and SOD1(G93A) mouse lumbar motoneurons. *Front. Cell. Neurosci.* 9:139. doi: 10.3389/fncel.2015.00139

Quinlan, K. A., Schuster, J. E., Fu, R., Siddique, T., and Heckman, C. J. (2011). Altered postnatal maturation of electrical properties in spinal motoneurons in a mouse model of amyotrophic lateral sclerosis. *J. Physiol.* 589, 2245–2260. doi: 10.1113/jphysiol.2010.200659

Rana, Z. A., Gundersen, K., and Buonanno, A. (2009). The ups and downs of gene regulation by electrical activity in skeletal muscles. *J. Muscle Res. Cell Motil.* 30, 255–260. doi: 10.1007/s10974-010-9200-2

Russier, M., Carlier, E., Ankri, N., Fronzaroli, L., and Debanne, D. (2003). A-, T- and H-type currents shape intrinsic firing of developing rat abducens motoneurons. *J. Physiol.* 549, 21–36. doi: 10.1113/jphysiol.2002.037069

Saxena, S., Roselli, F., Singh, K., Leptien, K., Julien, J. P., Gros-Louis, F., et al. (2013). Neuroprotection through excitability and mTOR required in ALS motoneurons to delay disease and extend survival. *Neuron* 80, 80–96. doi: 10.1016/j.neuron.2013.07.027

Schwindt, P. C., and Crill, W. E. (1980). Properties of a persistent inward current in normal and TEA-injected motoneurons. *J. Neurophysiol.* 43, 1700–1724.

Seebach, B. S., and Mendell, L. M. (1996). Maturation in properties of motoneurons and their segmental input in the neonatal rat. *J. Neurophysiol.* 76, 3875–3885.

Takahashi, T. (1990). Membrane currents in visually identified motoneurones of neonatal rat spinal cord. *J. Physiol.* 423, 27–46. doi: 10.1113/jphysiol.1990.sp018009

Takazawa, T., Croft, G. F., Amoroso, M. W., Studer, L., Wichterle, H., and Macdermott, A. B. (2012). Maturation of spinal motor neurons derived from human embryonic stem cells. *PLoS One* 7:e40154. doi: 10.1371/journal.pone.0040154

Vinay, L., Ben-Mabrouk, F., Brocard, F., Clarac, F., Jean-Xavier, C., Pearlstein, E., et al. (2005). Perinatal development of the motor systems involved in postural control. *Neural Plast.* 12, 131–139. doi: 10.1155/np.2005.131

Vinay, L., Brocard, F., and Clarac, F. (2000a). Differential maturation of motoneurons innervating ankle flexor and extensor muscles in the neonatal rat. *Eur. J. Neurosci.* 12, 4562–4566. doi: 10.1046/j.0953-816x.2000.01321.x

Vinay, L., Brocard, F., Clarac, F., Norreel, J. C., Pearlstein, E., and Pflieger, J. F. (2002). Development of posture and locomotion: an interplay of endogenously generated activities and neurotrophic actions by descending pathways. *Brain Res. Brain Res. Rev.* 40, 118–129. doi: 10.1016/s0165-0173(02)00195-9

Vinay, L., Brocard, F., Pflieger, J. F., Simeoni-Alias, J., and Clarac, F. (2000b). Perinatal development of lumbar motoneurons and their inputs in the rat. *Brain Res. Bull.* 53, 635–647. doi: 10.1016/s0361-9230(00)00397-x

Zhu, J., Feng, F., Ni, K., Zheng, Y., and Zhang, J. (2012). Four subtypes of motor neurons exhibiting mutually exclusive firing patterns in the spinal ventral horn. *Neurosci. Lett.* 525, 163–167. doi: 10.1016/j.neulet.2012.07.062

Ziskind-Conhaim, L. (1988). Electrical properties of motoneurons in the spinal cord of rat embryos. *Dev. Biol.* 128, 21–29. doi: 10.1016/0012-1606(88)90262-x

Conflict of Interest Statement: The authors declare that the research was conducted in the absence of any commercial or financial relationships that could be construed as a potential conflict of interest.

frontiers in
COMPUTATIONAL NEUROSCIENCE

ORIGINAL RESEARCH ARTICLE
published: 27 January 2014
doi: 10.3389/fncom.2014.00004

The dendritic location of the L-type current and its deactivation by the somatic AHP current both contribute to firing bistability in motoneurons

Marin Manuel, Daniel Zytnicki and Claude Meunier*

Laboratoire de Neurophysique et Physiologie, CNRS UMR 8119, Institut des Neurosciences et de la Cognition, Université Paris Descartes, Paris, France

Edited by:
Sergey M. Korogod, International Center for Molecular Physiology, Ukraine

Reviewed by:
David Golomb, Ben Gurion University of the Negev, Israel
Ervin Wolf, University of Debrecen, Hungary

***Correspondence:**
Claude Meunier, Laboratoire de Neurophysique et Physiologie, CNRS UMR 8119, Institut des Neurosciences et de la Cognition, Université Paris Descartes, 45 rue des Saints-Pères, 75270 Paris Cedex 06, France
e-mail: claude.meunier@parisdescartes.fr

Spinal motoneurons may display a variety of firing patterns including bistability between repetitive firing and quiescence and, more rarely, bistability between two firing states of different frequencies. It was suggested in the past that firing bistability required that the persistent L-type calcium current be segregated in distal dendrites, far away from the spike generating currents. However, this is not supported by more recent data. Using a two compartment model of motoneuron, we show that the different firing patterns may also result from the competition between the more proximal dendritic component of the dendritic L-type conductance and the calcium sensitive potassium conductance responsible for afterhypolarization (AHP). Further emphasizing this point, firing bistability may be also achieved when the L-type current is put in the somatic compartment. However, this requires that the calcium-sensitive potassium conductance be triggered solely by the high threshold calcium currents activated during spikes and not by calcium influx through the L-type current. This prediction was validated by dynamic clamp experiments *in vivo* in lumbar motoneurons of deeply anesthetized cats in which an artificial L-type current was added at the soma. Altogether, our results suggest that the dynamical interaction between the L-type and afterhyperpolarization currents is as fundamental as the segregation of the calcium L-type current in dendrites for controlling the discharge of motoneurons.

Keywords: bistability, persistent calcium current, afterhyperpolarization, modeling, dynamic clamp

INTRODUCTION

The discovery of a L-type calcium current in the dendrites of motoneurons (Schwindt and Crill, 1984; Hounsgaard and Kiehn, 1985) greatly changed our vision of their excitability properties. The steep secondary range of the current-frequency curve was ascribed to its activation (Li et al., 2004), and this persistent calcium current may also trigger dendritic plateau potentials and induce bistability (Hounsgaard and Mintz, 1988; Hounsgaard and Kiehn, 1989), which is defined as the existence of two stable output states for the same input. When bistability occurs between quiescence and firing, motoneurons keep on firing after a depolarizing current pulse instead of going back to rest. Firing bistability, where two stable firing states coexist, was first demonstrated in decerebrate cats in which descending monoaminergic pathways were tonically active (Hounsgaard et al., 1988). When a depolarizing pulse was superimposed on a bias current, the motoneurons fired at higher frequency after the pulse than before.

Plateau potentials and bistability were initially thought to arise from a L-type calcium current located rather distally in dendrites. The presence of a hysteresis in the current-voltage curve in voltage-clamp experiments and the voltage threshold for initiating plateau potentials suggested that the inward current resided in the unclamped portions of the dendritic tree (Lee and Heckman, 1998b). Accordingly, Booth et al. (1997) introduced a model (BRK model hereafter) with two weakly coupled compartments, a spike initiation region and a distal dendritic compartment where the calcium L-type current could initiate a plateau potential, to account for firing bistability. Passive voltage attenuation from soma to dendrites reaches 70% in this model, which would correspond to a distance from the soma of 1.2 times the space constant λ in an equivalent cable. This does not fit with later immunocytochemical and modeling studies (Simon et al., 2003; Elbasiouny et al., 2005, 2006; Ballou et al., 2006; Bui et al., 2006; Zhang et al., 2006; Grande et al., 2007; Zhang et al., 2008), which suggest that the L-type current is closer to the soma ($0.6 \pm 0.2\ \lambda$) and also displays a smaller somatic component. This more proximal location allows the somatic afterhyperpolarization (AHP) following spikes to deactivate the L-type current. Elbasiouny et al. (2006) pointed out that the AHP could enable graded activation of that current in response to synaptic excitation of the dendrites.

This raises the question of the mechanisms underlying motoneuron bistability, and notably firing bistability. Are the same mechanisms at work for the proximal and distal components of the L-type current? Under what conditions is firing bistability achieved? Is some spatial segregation of currents necessary, or can it occur even when the two currents are colocalized? Does the interaction between the L-type and AHP currents play a major role in controlling the firing pattern? We address these issues using a BRK-like model with a stronger coupling between compartments that better matches the location of the bulk of

the L-type current in dendrites and allows it to interact with the somatic AHP current. We demonstrate that the dynamical interaction between these currents conditions the firing pattern. To emphasize this point, we show that a somatic L-type current may also lead to firing bistability. However, this requires that the AHP conductance be solely activated by the high-voltage-activated calcium conductances turned on during action potentials. Using dynamic clamp, we mimicked experimentally that condition in motoneurons of anesthetized cats and validated our theoretical prediction. Altogether, our study indicates that, in addition to the spatial segregation of most of the calcium L-type current in the dendrites, the competition between the somatic AHP current and the L-type current largely determines the firing pattern. In particular, firing bistability is achieved when a large AHP current counterbalances a strong L-type calcium current. The spatial segregation acts by increasing the hysteresis of the current-frequency (*F-I*) curve and the firing bistability that are created by the dynamical interaction between the somatic AHP current and the L-type current.

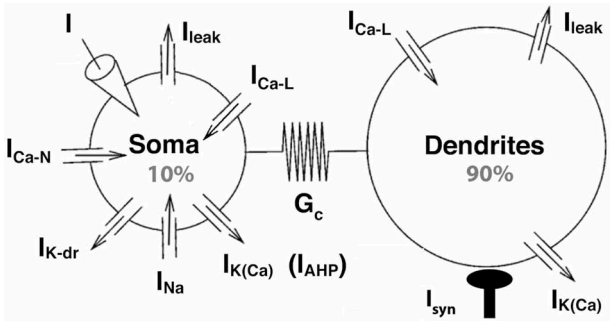

FIGURE 1 | The strong coupling model. The two compartments have similar passive properties, and they are coupled via a symmetrical conductance ten times larger than in the BRK model. The soma is endowed with spike generating currents and an AHP current. A L-type calcium current is present in the soma (somatic variant of the model) or in the dendrites (dendritic variant). The dendritic component of the N-type calcium current was eliminated from the BRK model, and the activation curve of the somatic component is steeper (see text). Dendrites are endowed with a calcium sensitive potassium conductance. Input consists in either a current injected in the soma or synaptic excitation of the dendrites.

MATERIALS AND METHODS

MODEL

Our model has the same bi-compartmental structure as the BRK model and the same complement of currents (see **Figure 1**). Briefly, the membrane areas of the somatic and dendritic compartments represent $p = 10\%$ and $1 - p = 90\%$ of the total membrane surface S, respectively. They are electrically coupled via the passive conductance $G_c S$. We set the coupling conductance G_c to 1.0 mS/cm^2, one order of magnitude larger than in the BRK model. We adopted a symmetrical coupling, i.e., the same coupling conductance G_c from soma to dendrites and from dendrites to soma, and assumed that soma and dendrites had the same specific leak conductance G_{leak}, as in the BRK model.

The somatic compartment of our model is endowed with transient sodium and delayed rectifier potassium currents, responsible for the generation of action potentials. A fast activating and slowly inactivating N-type current allows calcium to enter the soma during action potentials as in the BRK model. A non-inactivating L-type calcium current $I_{Ca-L} = G_{Ca-L} m_{Ca-L} (V_{Ca} - V_S)$ is added to the soma in the second part of our study. Here, V_S is the somatic current, V_{Ca} the reversal potential of the calcium currents, G_{Ca-L} the maximal conductance of the L-type current and m_{Ca-L} its activation variable of the current. Elevation of the calcium concentration in the soma triggers the calcium-sensitive potassium current $I_{\text{AHP}} = G_{\text{AHP}}[Ca^{2+}]/([Ca^{2+}] + K_{Ca})(V_K - V_S)$, of maximum conductance G_{AHP}, reversal potential V_K and half-activation calcium concentration K_{Ca}. This current is responsible for the AHP following spikes (hence the "AHP" subscript that allows to distinguish this current from the dendritic calcium-activated potassium current). We steepened the activation curve of the somatic N-type calcium current compared to the BRK model (1 mV width vs. 5 mV) so that this AHP conductance is not activated before firing onset.

In the first part of our study, dendrites, whose voltage is denoted by V_D, are endowed with a L-type calcium current, the activation of which can trigger plateau potentials, and a calcium sensitive potassium current $I_{K(Ca)} = G_{K(Ca)}[Ca^{2+}]/([Ca^{2+}] + K_{Ca})(V_K - V_D)$. We removed the dendritic N-type calcium current of the BRK model as it was not activated enough to affect significantly the behavior of the model. Finally, we hyperpolarized the reversal potential of the leak current from −60 to −70 mV in both soma and dendrites. The value of −60 mV was required in the original BRK model to allow the current injected in the soma to depolarize substantially the dendrites in spite of the weak coupling. In contrast, they are too easily depolarized in our strongly coupled model if V_{leak} is set at −60 mV. That is why we adopted a more hyperpolarized value. All differences with the BRK model are summarized in **Table 1**. All other parameters are the same as in Booth et al. (1997).

Except for these differences, the gating variables of the voltage-dependent currents follow the same first order kinetic equations as in Booth et al. (1997). The evolution of the calcium concentration in a compartment is modeled by the phenomenological equation $\tau_{Ca} d[Ca^{2+}]/dt = \alpha_N I_{Ca-N} + \alpha_L I_{Ca-L} - [Ca^{2+}]$ where calcium ions influx through the L- and N-type conductances, quantified by α_L and α_N respectively, is counterbalanced by buffering (Booth et al., 1997). The differential equations describing the model are solved using a standard fourth order Runge-Kutta algorithm.

Our model does not incoporate all the ionic currents known to exist in motoneurons. As in the BRK model, no hyperpolarization-activated I_h current was added, because this current would contribute little to the repetitive discharge. Similarly, we did not introduce a persistent sodium current (Kuo et al., 2006) since robust repetitive firing was elicited in the model without it. Finally, we decided to not incorporate voltage-dependent potassium conductances in dendrites after checking that they counterbalanced the calcium L-type in the same way as calcium-sensitive potassium channels. These deviations from

Table 1 | Differences between the BRK model and our model.

	BRK model	Our model
Coupling conductance	0.1 mS/cm^2	1.0 mS/cm^2
Leak reversal potential	−60 mV	−70 mV
Dendritic N-type conductance	0.3 mS/cm^2	None
Activation of somatic N-type current	$1/(1+\exp(-(V+30)/5))$, V in mV	$1/(1+\exp(-(V+30)))$
Dendritic potassium conductance	Always 0.7 mS/cm^2	Set to 0 or 0.7 mS/cm^2

We set the dendritic potassium conductance $G_{K(Ca)}$ to 0 in most of our study and accordingly decreased G_{Ca-L}.

realism are of limited significance as our emphasis is on the interplay between calcium and calcium-sensitive potassium currents. We also note that the Cav1 channels underlying the L-type current may display facilitation properties, as demonstrated by Moritz et al. (2007) in rat hypoglossal motoneurons, which might have some impact on hysteretical properties of motoneurons. They are not incorporated in the present model.

We investigated the response of the model (current-frequency curve, conductance-frequency curve, activation of the L-type current) to triangular ramps of current injected in the soma and ramps of tonic synaptic excitation of the dendrites. Tonic synaptic excitation of dendrites was modeled by a current $I_D(t) = G_{\text{syn}}(t)(V_{\text{syn}} - V_D(t))$ with slowly varying conductance $G_{\text{syn}}(t)$ and reversal potential $V_{\text{syn}} = 0$ mV. The model behavior was strongly affected by the ramp velocity. We had to use very slow ramps (velocity of 0.01–0.1 nA/cm^2.s) to be sure that the hysteresis of the F-I curve did not arise from memory effects.

Finally, we note that Kim et al. (2009) showed, using two-ports circuit theory (Jaffe and Carnevale, 1999), that a two compartments model could account for the bi-directional voltage attenuation between the soma and some given location in dendrites, if the coupling between compartments was assymetrical or if the two compartments had different specific conductance. However, these two compartments do not map to the soma and the denditic tree. Therefore, such models are unsuitable for our purpose that is to study how active currents located in the soma and in the dendrites interact.

DYNAMIC CLAMP EXPERIMENTS

Experiments were carried out on four adult cats (3.9–4.4 kg) deeply anesthetized with sodium pentobarbitone (Pentobarbital, Sanofi). In accordance with French legislation, the investigators had a valid license to perform experiments on live vertebrates delivered by the Direction des Services Vétérinaires (Préfecture de Police, Paris). The animal house and the experimental room had received the agreement of the same authority. Anesthesia was induced with an intraperitoneal injection (45 mg·kg^{-1}), supplemented whenever necessary (usually every 2 h) by intravenous injections (3–6 mg·kg^{-1}). Animals were paralyzed with Pancuronium Bromide (Pavulon, Organon SA) at a rate of 0.4 mg·h^{-1} and artificially ventilated (end tidal pCO_2 maintained around 4%). A bilateral pneumothorax prevented movements of the rib cage. The adequacy of anesthesia was assessed on myotic pupils and on the stability of blood pressure (measured in the carotid) and of heart rate. At the onset of experiment, amoxicillin (500 mg; Clamoxyl, Merieux) and methylprenidsolone (5 mg; Solu-Medrol, Pharmacia) were given subcutaneously to prevent the risk of infection and edema, respectively. The central temperature was kept at 38°C. Blood pressure was maintained above 90 mmHg by perfusion of a 4% glucose solution containing $NaHCO_3$ (1%) and gelatin (14%; Plasmagel, Roger Bellon) at a rate of 3–12 ml·h^{-1}. A catheter allowed evacuation of urine from the bladder. At the end of the experiments, animals were killed with a lethal intravenous injection of pentobarbitone (250 mg).

The following nerves were cut, dissected and mounted on a pair of stimulating electrodes to identify recorded motoneurons: anterior biceps and semi-membranosus taken together (ABSm), the gastrocnemius medialis together with gastrocnemius lateralis and soleus nerves (Triceps surae, TS), the remaining part of the tibialis nerve (Tib), the common peroneal nerve (CP), and the posterior biceps and semitendinosus taken together (PBSt). The lumbosacral spinal segments were exposed by laminectomy, and the tissues in hind limb and spinal cord were covered with pools of mineral oil kept at 38°C.

Intracellular recordings of motoneurons were made using micropipettes (tip diameter 2.0–2.5 μm) filled with KCl 3 M (resistance 2–4 MΩ) and an Axoclamp 2B amplifier (Molecular Devices, Sunnyvale, USA) connected to a Power1401 interface using the Spike2 software (CED, Cambridge, UK). After impalement, identification of motoneurons rested on the observation of antidromic action potentials in response to the electrical stimulation of their axon in a peripheral nerve. All motoneurons retained for analysis had a resting membrane potential more hyperpolarized than 50 mV, which varied by less than 5 mV over the recording session. The axonal conduction velocity was computed from the latency of the antidromic action potentials.

Dynamic clamp recordings were done using the Discontinuous Current Clamp mode (7–9 kHz) of the amplifier because it allows for reliable measurements of the membrane potential, even when large currents are injected (Brizzi et al., 2004 see also Prinz et al., 2004). A dynamic clamp current $I_{DC} = G_{DC}m_{DC}(V_{DC} - V_S)$ of maximum conductance G_{DC}, activation variable m_{DC} and reversal potential V_{DC}, mimicking a L-type calcium current, was injected into the motoneuron soma through the recording micropipette. The activation variable evolved according to $\tau_{DC}dm_{DC}/dt = m_\infty(V_S) - m_{DC}$ where the steady-state activation function is $m_\infty(V_S) = 1/(1+\exp((V-\theta_{DC})/k_{DC}))$, τ_{DC} is the activation time constant, θ_{DC} is the half activation voltage and k_{DC} determines the slope of the activation curve. This artificial L-type current was computed at a speed of 10 kHz by a PC running the real time RTLinux kernel and the dynamic clamp software MRCI (software MRCI, Raikov et al., 2004).

RESULTS

INCREASING THE COUPLING SUPPRESSES THE FIRING BISTABILITY OF THE BRK MODEL

The (somatic) input conductance $G_{in} = (G_S/p)(G_C + p(1-p)G_{leak})/(G_C + (1-p)G_{leak})$ of our model is 7.8 times the conductance $G_S = G_{leak}pS$ of the soma itself, thrice more than in the BRK model (2.6). This is more in keeping with the ratio of dendritic dominance of motoneurons, i.e., the ratio of the input conductance at the soma to the soma conductance, which is typically of the order of 10 (Fleshman et al., 1988). Passive steady-state voltage attenuation from the soma to the dendrites $G_{leak}/(G_{leak} + G_C/(1-p))$ is 35%, which corresponds to a distance of 0.43 λ from the soma on an equivalent cable and fits better with the location of the L-type current in dendrites than in the BRK model. This is because the dendritic compartment represents only the distal part of dendrites in the BRK model, all the proximal part being modeled by the low coupling conductance between the two compartments.

The firing bistability observed in the BRK model for standard parameters (dendritic $G_{Ga-L} = 0.33\,mS/cm^2$, dendritic $G_{K(Ca)} = 0.7\,mS/cm^2$, $G_{AHP} = 3.14\,mS/cm^2$) disappears when the coupling conductance G_c is increased to $1\,mS/cm^2$. A slow triangular ramp of current injected in the soma (from 0 to $70\,\mu A/cm^2$ and back with a velocity of $10^{-4}\,\mu A/cm^2.s$) elicits a symmetrical discharge, as shown in **Figure 2A**. The *F-I* curve is graded, the firing rate linearly increasing from 5 Hz at recruitment to 100 Hz for an injected current of $75\,\mu A/cm^2$ (see **Figure 2C**) and then progressively saturates.

When the L-type current is increased to compensate for the larger input conductance, quiescence/firing bistability is achieved, but firing bistability cannot be recovered. This is illustrated in **Figure 2B** for $G_{Ca-L} = 0.45\,mS/cm^2$. The discharge becomes asymmetrical and exhibits a large domain of bistability between quiescence and firing, as shown by the *F-I* curve (**Figure 2C**, right trace). On the ascending ramp, firing starts at high frequency (175 Hz). On the descending ramp, the discharge persists well below the recruitment current.

Only these two firing regimes are observed. No firing bistability occurs for intermediate values of G_{Ca-L}. We also note that decreasing the potassium conductance in dendrites has the same effect as increasing the L-type current, as illustrated in **Figure 2C** (dashed line). $G_{K(Ca)}$ can even be set to 0 provided that the L-type current is appropriately decreased.

Increasing G_{Ca-L} has the same effect on firing when the drive is provided by synaptic excitation of dendrites, as shown in **Figure 2D**. For $G_{Ca-L} = 0.1\,mS/cm^2$ and no

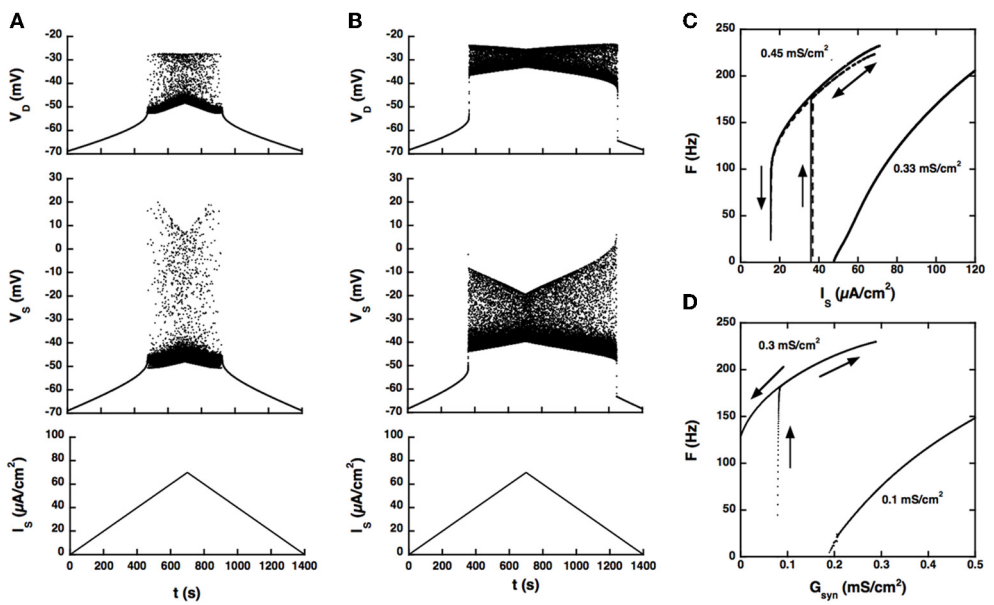

FIGURE 2 | Response of the strong coupling model ($G_c = 1\,mS/cm^2$) to excitatory input. (A) Voltage response to a triangular current ramp. Dendritic G_{Ca-L} is 0.33 mS/cm² as in the BRK model. From bottom to top: current injected in the soma, soma voltage and dendritic voltage. The discharge is symmetrical, the recruitment current on the ascending ramp and the derecruitment current on the descending ramp differing by less than 1.5% (50.2 and 49.4 mV, respectively). **(B)** Same as A but G_{Ca-L} increased to 0.45 mS/cm². The discharge is clearly asymmetrical. A dendritic plateau potential of 16 mV sets in at firing onset ($I_S = 38\,\mu A/cm^2$). On the descending ramp, firing persists down to $20\,\mu A/cm^2$. **(C)** *F-I* curves. Current ramp from 0 to $120\,\mu A/cm^2$ and back. *F-I* curves (solid lines) are displayed for $G_{Ca-L} = 0.33$ (right), and 0.45 mS/cm² (left). For this latter value,firing stops when the injected current reaches $70\,\mu A/cm^2$ because of spike blockade. Decreasing the dendritic $G_{K(Ca)}$ from 0.7 to 0.25 mS/cm² (with G_{Ca-L} kept at 0.33 mS/cm², dashed line) has the same effect as increasing G_{Ca-L} from 0.33 to 0.45 mS/cm² [with $G_{K(Ca)}$ kept at 0.7 mS/cm²]. **(D)** Synaptic excitation of dendrites. *F-*G_{syn} curves are shown for $G_{Ca-L} = 0.1$ (right) and 0.3 mS/cm² (left). No dendritic potassium conductance $G_{K(Ca)}$. Triangular conductance ramp from 0 to 0.5 mS/cm² (i.e., equal to the leak conductance of dendrites) and back, velocity of 0.01 mS/cm²/s. Note that frequency plateaus are present near firing onset for $G_{Ca-L} = 0.1$ mS/cm² as in the subprimary firing range of mouse motoneurons (Manuel et al., 2009). We showed that they are due to mixed mode oscillations in a previous paper (Iglesias et al., 2011). The ascending (upward pointing arrows) and descending branches (downward pointing arrows) of the hysteresis loops are indicated on panels **(C,D)** and on the following figures.

potassium conductance in dendrites, firing starts at 5 Hz and the conductance-frequency curve is graded. In contrast, for $G_{Ca-L} = 0.3\,\text{mS/cm}^2$, firing starts at 165 Hz and the F-G_{syn} curve displays a large range of bistability between quiescence (on the ascending ramp) and firing (on the descending ramp). No firing bistability is observed at any intermediate value of G_{Ca-L}.

FIRING BISTABILITY REQUIRES LARGE DENDRITIC G_{CA-L} AND SOMATIC $G_{K(CA)}$

Because the two compartments are strongly coupled, the AHP triggered by spikes at the soma may produce a sufficient hyperpolarization of dendrites to hinder activation of the L-type current, in line with the results of Elbasiouny et al. (2006). As a consequence, increasing the AHP prevents high frequency firing at discharge onset and suppresses quiescence/firing bistability, as shown in **Figure 3A** for $G_{Ca-L} = 0.2\,\text{mS/cm}^2$.

Increasing the somatic AHP conductance is not equivalent to increasing the dendritic $G_{K(Ca)}$ (or decreasing the L-type current). Because the AHP conductance is recruited only during spikes, following the activation of the N-type calcium current, the recruitment threshold is insensitive to G_{AHP} (see **Figure 3A**), whereas it considerably increases with $G_{K(Ca)}$. For the same reason, the AHP current has no impact on the current-voltage (I–V) curve in the subthreshold voltage range, as illustrated in **Figure 3B**. For $G_{Ca-L} = 0.2\,\text{mS/cm}^2$ the somatic I–V curve is slightly N-shaped in the absence of AHP. Adding an AHP conductance of $10\,\text{mS/cm}^2$ alters the curve only in the suprathreshold voltage range, so that it remains N-shaped. In contrast, adding a dendritic potassium conductance of $0.7\,\text{mS/cm}^2$ also modifies the I–V curve in the subthreshold range, and it becomes monotonic.

Although the I–V curve displays a negative slope region for $G_{AHP} = 10\,\text{mS/cm}^2$, the membrane voltage exhibits no plateau potential (not shown). Moreover, the synaptic conductance-frequency (F-G_{syn}) curve is graded and exhibits no hysteresis when the synaptic conductance is decreased back (see **Figure 3A**). This demonstrates that the disappearance of quiescence/firing bistability is not due a change of the I–V curve from N shaped to monotonic. It results from the dynamical interaction between the L-type current and the AHP current during firing.

Importantly, the interaction between the L-type and AHP conductances can elicit firing bistability when G_{Ca-L} is increased beyond $0.27\,\text{mS/cm}^2$. This is illustrated in **Figure 3C** for $G_{Ca-L} = 0.35\,\text{mS/cm}^2$. Quiescence/firing bistability is observed for G_{AHP} below $12\,\text{mS/cm}^2$ (upper curve, $G_{\text{AHP}} = 10\,\text{mS/cm}^2$). For G_{AHP} above $30\,\text{mS/cm}^2$ (bottom curve, $G_{\text{AHP}} = 40\,\text{mS/cm}^2$) the F-G_{syn} curve smoothly increases from a very low value (1.2 Hz). In between, for G_{AHP} ranging from 12 to $30\,\text{mS/cm}^2$, firing bistability is achieved. This is almost one order of magnitude larger than for the transition from quiescence/firing bistability to graded firing for $G_{Ca-L} = 0.2\,\text{mS/cm}^2$ (see **Figure 3A**).

Similar results are obtained for current injection in the soma, but the domain of firing bistability is wider than for synaptic excitation of dendrites. For instance, firing bistability is achieved for G_{AHP} between 5 and $40\,\text{mS/cm}^2$ when G_{Ca-L} is set at $0.35\,\text{mS/cm}^2$ (see **Figure 3D**), nearly twice more than for synaptic input. The counterclockwise hysteresis of the F-I reflects a genuine bistability between two different firing states. Indeed, we also checked that excitatory and inhibitory current pulses could switch the model from the low frequency firing state to the high frequency state and back (not illustrated).

Altogether our results demonstrate that bistability is controlled by the competition between the dendritic calcium L-type current and the somatic AHP current when the two compartments of the model are strongly coupled. This competition did not occur in the weakly coupled BRK model where the AHP was too attenuated in dendrites to deactivate the L-type current. This shows that the strong spatial segregation between the L-type current and the currents underlying the discharge (transient sodium, delayed rectifier and AHP currents) present in the BRK model is not necessary for achieving firing bistability.

A SOMATIC L-TYPE CALCIUM CURRENT MAY ELICIT FIRING BISTABILITY BY ITSELF

Our model suggests that the firing pattern of motoneurons is largely determined by the interaction between the AHP and L-type currents. To further test this hypothesis, we examined whether the competition between the AHP conductance and a somatic L-type current could also lead to bistability. Accordingly, we suppressed the dendritic component of the L-type current and incorporated instead a somatic L-type current in the model. As before, no potassium current was present in the dendrites. Dendrites were thus passive, all active conductances being confined to the axo-somatic compartment.

Firing bistability can be achieved in this somatic model (see **Figure 4A**) but this requires that three conditions be satisfied. Firstly, the L-type current must activate during the voltage ramp preceding spikes and deactivate substantially during the AHP. Accordingly, we decreased the half-activation voltage of the L-type current from −40 to −55 mV to make it lower than the spike voltage threshold (−47 mV at the onset of the discharge), and we steepened its steady-state activation curve by decreasing the mid-activation voltage from 7 to 2 mV. For $G_{\text{AHP}} = 20\,\text{mS/cm}^2$, the activation of the L-type current then reached 75% after the first spike for $G_{Ca-L} = 0.4\,\text{mS/cm}^2$ and decayed to 7% at the end of the first interspike interval. This deactivation of the L-type current is crucial to ensure a strong dynamical competition with the AHP current.

Secondly, and importantly, the AHP conductance must be very little activated by calcium ions influx through L-type calcium channels, i.e., α_L must be much smaller than α_N in the evolution equation of the calcium concentration (see Materials and Methods). Otherwise, the AHP conductance is tonically activated and the discharge pattern dramatically altered, as illustrated in **Figure 4B**.

Thirdly, the L-type current must be sufficiently large, here again, as illustrated in **Figure 4C** for $G_{Ca-L} = 0.5\,\text{mS/cm}^2$. In the example shown, no firing bistability is achieved whereas firing bistability was observed for $G_{Ca-L} = 1.0\,\text{mS/cm}^2$ (see **Figure 4A**). Firing bistability actually requires that G_{Ca-L} be larger than $0.7\,\text{mS/cm}^2$. For smaller G_{Ca-L}, a direct transition from graded response to quiescence/firing bistability occurs.

Our results demonstrate that firing bistability may still occur when the L-type current is located at the soma. It then results from the dynamical competition between the L-type and AHP

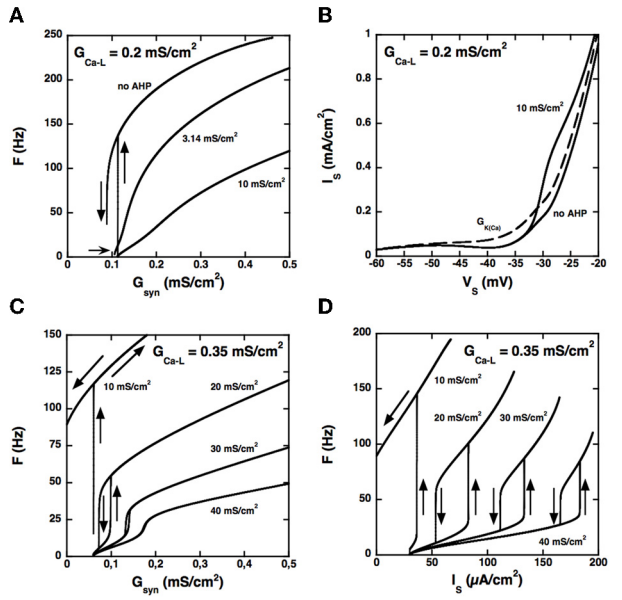

FIGURE 3 | Control of the firing pattern by the AHP conductance. **(A)** *F*-G_{syn} curves for $G_{Ca-L} = 0.2\,mS/cm^2$. Somatic AHP conductance $G_{AHP} = 0.0$, 3.14, and 10 mS/cm^2 (see labels) but no potassium conductance in dendrites. For $G_{AHP} = 3.14\,mS/cm^2$ (the same value as in the BRK model), the *F*-G_{syn} curve is graded and displays only a tiny range of bistability below recruitment (thin arrow). When the AHP is suppressed, firing starts at 137 Hz, and the size of the bistability range considerably increases. In contrast, bistability disappears when G_{AHP} is increased to $10\,mS/cm^2$. **(B)** Somatic I–V curves. Same conditions as in **(A)**. The curves obtained without AHP and for $G_{AHP} = 10\,mS/cm^2$ (solid lines, see labels) differ only above −33 mV. In contrast, increasing the dendritic $G_{K(Ca)}$ to $0.7\,mS/cm^2$ (in the absence of somatic AHP) suppresses the negative slope region of the I–V curve in the subthreshold voltage range [dashed line labeled $G_{K(Ca)}$]. The curves are not hysteretic because a dendritic compartment strongly coupled to the soma cannot account for the distal dendritic component of the L-type current. This departure from realism is of little significance as we focus here on the interaction between the proximal component of the L-type current and the somatic AHP. **(C)** *F*-G_{syn} curves for $G_{Ca-L} = 0.35\,mS/cm^2$. $G_{AHP} = 10$, 20, 30, and 40 mS/cm^2 (see labels). At variance with panel A, the *F*-G_{syn} curves display a primary range of firing when G_{AHP} is large enough to counterbalance the L-type current and has then a strong regulatory effect on the discharge. **(D)** *F-I* curves for $G_{Ca-L} = 0.35\,mS/cm^2$. Same as in D but current is injected in the soma. Note that the large AHPs at play create a wide primary firing range, in keeping with the traditional role of the AHP in firing rate control.

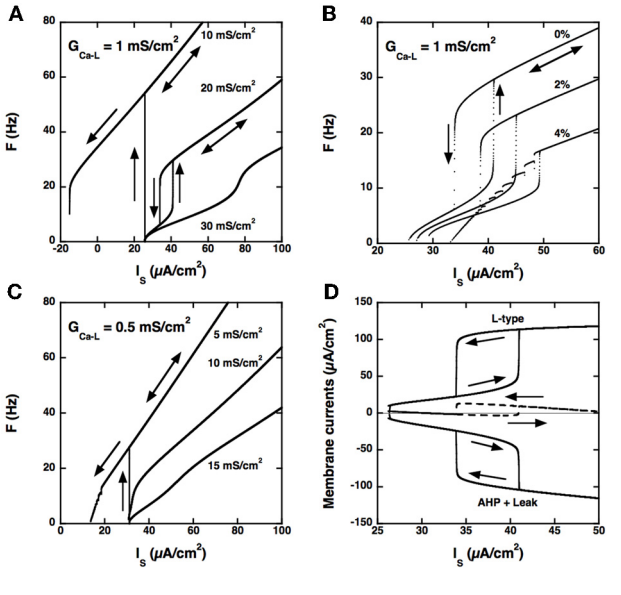

FIGURE 4 | Model with somatic L-type current and passive dendrites. **(A)** *F-I* curves for $G_{Ca-L} = 1.0\,mS/cm^2$. Triangular ramp of current injected in the soma from 0 to 100 $\mu A/cm^2$ and back (velocity: $10^{-4}\,\mu A/cm^2.s$). Increasing values of G_{AHP} from top to bottom, see labels). $\alpha_N = 0.0045$ mol/nA.cm as before, but α_L is set to 0. When $G_{AHP} = 10\,mS/cm^2$ (top curve), firing starts at 54 Hz at the recruitment threshold (32 $\mu A/cm^2$), and the *F-I* curve shows a large domain of quiescence/firing bistability, derecruitment occuring only for a negative current of $-15\,\mu A/cm^2$ on the descending ramp. Firing bistability is observed for between 15 and 25 (middle curve, $G_{AHP} = 20\,mS/cm^2$). When G_{AHP} is increased beyond $25\,mS/cm^2$, bistability disappears and the *F-I* curve becomes graded (bottom curve, $G_{AHP} = 30\,mS/cm^2$). Note that the recruitment threshold remains unchanged. **(B)** Effect of α_L on firing. *F-I* curves for $G_{Ca-L} = 1\,mS/cm^2$ and $G_{AHP} = 20\,mS/cm^2$ and $\alpha_N = 0.0045$ mol/nA.cm. Increasing values of α_L from top to bottom (see labels). The firing bistability displayed in A (top, α_L set to 0) persists when α_L is increased to 2% of α_N, but the firing frequency is strongly reduced. When α_L is doubled, to 4% of α_N, the abrupt transition to the low frequency state on the down ramp is replaced by a series of frequency plateaus reflecting mixed mode oscillations. **(C)** *F-I* curve for $G_{Ca-L} = 0.5\,mS/cm^2$. α_L set to 0 and $\alpha_N = 0.0045$ mol/nA.cm as in A. Increasing values of G_{AHP} (see labels). Quiescence/firing bistability occurs for G_{AHP} smaller than $10\,mS/cm^2$ (top), and the *F-I* curve is graded for larger G_{AHP}. No firing bistability takes place. **(D)** Membrane currents. $G_{Ca-L} = 1\,mS/cm^2$ and $G_{AHP} = 20\,mS/cm^2$ (regime of firing bistability, see **A**). Top: L-type current (positive); bottom: sum of the leak and AHP currents (negative); dashed line: sum of the three currents. All currents are time averaged over the interspike interval and plotted as a function of the current injected in the soma. The zero current line is displayed in gray. The ascending current ramp is indicated by rightward pointing arrows and the descending branch by leftward pointing arrows.

currents. This shows that segregation of the L-type current in the dendrites is not required for firing bistability. However, the dendritic location of the L-type current in motoneurons enhances firing bistability. In the somatic variant of our model, a large, and likely unrealistic, type-L conductance is needed to achieve firing bistability, and the hysteresis loop is distinctively smaller than in the dendritic variant studied in the preceding sections (compare **Figures 3**, **4**).

The L-type and AHP currents respectively produce positive and negative feedbacks on the discharge. **Figure 4D** shows how the balance between these currents changes with the injected current in our somatic model. On the ascending branch of the ramp, the depolarizing L-type current (top) and the hyperpolarizing current (bottom), obtained by summing the AHP and leak currents, both increase with the injected current. Below $40\,\mu A/cm^2$, the AHP current displays little saturation as the firing frequency increases and may successfully contain the activation of the L-type current. The L-type and hyperpolarizing currents remain approximately balanced, their sum never exceeding $3\,\mu A/cm^2$ (dashed), and the firing rate increases at a low rate with the injected current. This is no longer possible when the injected current exceeds $40\,\mu A/cm^2$. Then, the L-type current augments more

than the hyperpolarizing current, their sum abruptly increases by 13 $\mu A/cm^2$, and the model is pushed to the higher frequency state. On the descending branch of the ramp, the opposite scenario takes place. As long as the L-type current remains strongly activated, it maintains the discharge at an elevated frequency despite the negative feedback due to the AHP current. This happens until the injected current is decreased below 34 $\mu A/cm^2$. The sum of currents then drops from 13 to $-2\,\mu A/cm^2$, and the model is pushed back to the low frequency state.

We performed a complete bifurcation analysis of this model but did not include it here to avoid technicalities. The mathematically oriented reader is invited to contact the corresponding author for full details (including bifurcation diagrams) about the bifurcation structure that underlies quiescence/firing bistability and firing bistability.

Altogether, our results suggest that firing bistability may occur whether the L-type current is located in the soma or in the dendrites and that it stems from the dynamical competition between L-type and AHP currents. Firing bistability occurs when both currents are large and is enhanced when the L-type current is located in dendrites.

EXPERIMENTAL VALIDATION

We verified experimentally that bistability may indeed arise from the dynamical interaction between a somatic L-type current and the AHP current. Using dynamic clamp, an artificial L-type current was imposed through the recording microelectrode, which was, most likely, located at the soma. At variance with genuine L-type calcium currents, this artificial current provoked no calcium influx as the microelectrode was filled with KCl (see Methods). Therefore, it did not turn on the small conductance calcium-activated potassium channels (SK channels) responsible for the medium duration AHP. The AHP conductance was triggered only by calcium influx through high threshold calcium conductances during spikes, just like in our model. Thus, we turned limitations of the dynamic clamp methods (restriction to the soma, no calcium influx) to advantages.

We first checked whether the artificial L-type current could induce a hysteresis of the *F-I* curve in a sample of 14 motoneurons, mostly CP motoneurons. No hysteresis occurred in control condition in these cells as illustrated in **Figure 5A**, probably because the barbiturate used for anesthesia cats strongly depresses the natural calcium L-type current (Guertin and Hounsgaard, 1999). We recall that bistability has never been observed in anesthetized cats (Schwindt and Crill, 1982) but was shown to occur in decerebrate preparations where motoneurons were submitted to an intense monoaminergic neuromodulation (Hounsgaard et al., 1988; Lee and Heckman, 1998a,b, 1999). In contrast, when we added the artificial L-type current to the motoneuron of **Figure 5A**, we observed a clear counterclockwise hysteresis in the F-I relationship as shown in **Figure 5B**.

Altogether, the dynamic clamp current elicited a clear counterclockwise hysteresis in the *F-I* relationship of 8 motoneurons of our sample (7 CP, 1 Tib, 1 AbSm) but not in 6 others (5 CP and 1 Tib), at least in the range of parameters of the artificial current that we explored. The presence or absence of hysteresis is not a matter of motor pool. Indeed, most neurons recorded

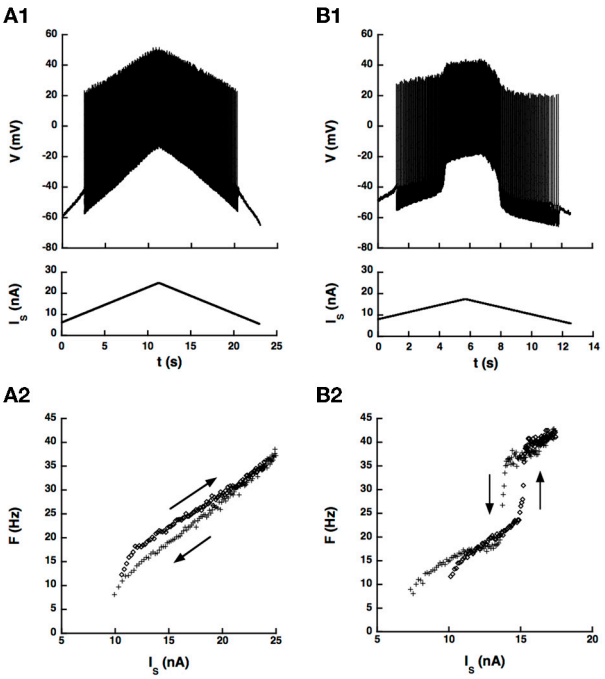

FIGURE 5 | An artificial L-type current injected in the soma can elicit a counterclockwise hysteresis in a spinal motoneuron. CP motoneuron (axonal conduction velocity: 80 m/s, input conductance: 0.5 μS). **(A)** No dynamic clamp current (control case). **(A1)** Ramp of current applied to the soma (bottom) and intracellular recording of soma voltage (top). **(A2)** F-I curve. The ascending branch (increasing current) is indicated by diamonds (upward arrow) and the descending branch (decreasing current) by crosses (downward arrow). **(B)** Same as A but a dynamic clamp current mimicking the L-type current was injected in the soma. Parameters of this current were the following. Conductance: 100 nS, half activation voltage: −35 mV, steepness of the activation curve: 2 mV, activation time constant: 50 ms, reversal potential: 80 mV.

(86%) were CP motoneurons, 58% of which exhibited a hysteresis and 42% did not. In addition, hysteretic behavior was achieved only if the L-type current was large enough (conductance between 100 and 500 nS) and activated in the subthreshold voltage range traversed during the AHP after the first spike. This required that the half activation voltage of the L-type current be a few millivolts below the threshold for action potential generation (-4.5 ± 3 mV [-1 − -10 mV]), the most stringent condition to meet, and also that the steady-state activation curve was steep enough (k_{DC} between 0.5 and 4.0 mV). Under these conditions, similar to those of our somatic model, the artificial L-type current was strongly modulated during the AHP, and a hysteresis was obtained over a wide range of activation time constant of the artificial L-type current, from 5 to 500 ms.

The observation of a hysteresis of the *F-I* curve in our experimental conditions is not sufficient to conclude that the recorded motoneurons exhibit genuine bistability. Indeed, the finite velocity (here, 2–5 nA /s depending on the motoneuron) of the current ramps enlarges the hysteresis loops and transforms the abrupt transitions from one firing state to the other into steep secondary ranges. Moreover, we cannot distinguish between

long lasting up states (partial bistability over several seconds, see Lee and Heckman, 1998a,b) and genuinely stable up states (full bistability).

Therefore, we investigated whether current pulses elicited transitions between states in 5 of the 14 recorded motoneurons (4 CP and 1 ABSm). We used an artificial L-type current slower than the AHP by one order of magnitude, which induced bistability more easily. We provoked transitions between quiescence and firing in the ABSm motoneuron and in 2 CP motoneurons tested, as illustrated in **Figure 6A**, and we successfully triggered transitions between two different firing states in one of those two CP motoneurons, as illustrated in **Figure 6B**.

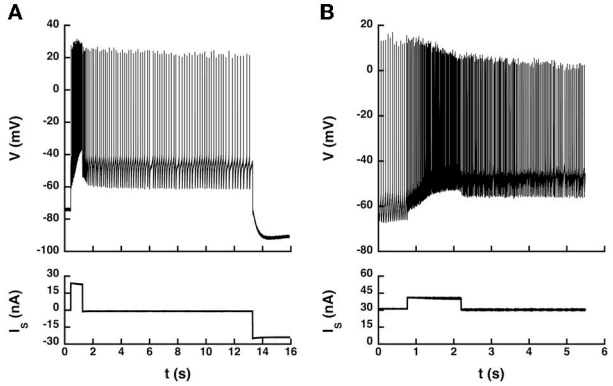

FIGURE 6 | Transitions between states elicited by current pulses. (A) Quiescence/firing bistability. CP motoneuron (axonal conduction velocity: 90 m/s, input conductance: 1.0 μS). The current pulse (24 nA , 1 s) elicited an accelerating discharge that started with a frequency of 14 Hz and reached 50 Hz at the end of the pulse. After the pulse, the motoneuron kept firing at a lower frequency (5 Hz) instead of going back to rest. A hyperpolarizing current pulse (−24 nA) terminated firing. Artificial L-type current conductance: 350 nS, half-activation voltage: −50 mV, steepness of the activation curve: 2 mV, activation time constant: 400 ms. **(B)** Firing bistability. CP motoneuron (axonal conduction velocity: 90 m/s, input conductance: 1.1 μS). A 31 nA bias current was applied, which made the neuron steadily discharge at the mean frequency of 19 Hz. A pulse of 10 nA lasting 1.5 s was then superimposed to shift the motoneuron toward its up state (57 Hz, three times more than before the pulse). After the pulse, the motoneuron kept firing at a mean frequency of 30 Hz, about half more than the before the pulse. Two different firing states were thus obtained for the same injected current. The discharge in the up state (during and after the pulse) was more irregular than in the down state (before the pulse). L-type conductance: 820 nS, half-activation: −58 mV, steepness: 1 mV, activation time constant: 400 ms, reversal potential: 20 mV.

DISCUSSION

SUMMARY OF RESULTS

We studied a model of motoneuron where the somatic and the dendritic compartments are 10 times more strongly coupled than in the BRK model. This is more in keeping with the location of the bulk of the L-type current in the dendrites of motoneurons. We demonstrated that the dynamical competition between the dendritic calcium L-type current and the somatic AHP current may lead to graded firing, quiescence/firing bistability below recruitment, or firing bistability, depending on the balance between these two currents. Firing bistability is achieved only for large intensities of the L-type current and when the AHP current also is sufficiently large to oppose the L-type current. In contrast, dendritic potassium currents play no other role than to decrease or suppress the negative slope region of the dendritic I–V curve.

Similar results were obtained when the L-type current was localized at the soma. In particular, firing bistability could still be achieved for large L-type current. However, this required that the AHP conductance be decoupled from the calcium L-type current, i.e., that it be triggered only by calcium ions influx through High Voltage Activated (HVA) conductances. This condition was naturally fulfilled in the dynamic clamp experiments in anesthetized cats that we performed to verify our theoretical predictions. Altogether, our results show that the dynamical interaction between the L-type current and AHP can create the couterclockwise hysteresis of the *F-I* curve. However, the spatial segregation that results from the different locations of the two currents in motoneurons (the L-type current mostly in dendrites and the AHP current in the soma) enhances that hysteresis.

SOMATIC AND DENDRITIC COMPONENTS OF THE L-TYPE CURRENTS

Most of the L-type current is found in the dendrites of motoneurons. Initially, the L-type current was thought to be located in distal dendrites, which explained the counterclockwise hysteresis of the I–V curve of motoneurons in response to a triangular voltage ramp in voltage clamp experiments. However, more recent studies suggest that the bulk of the L-type current is closer to the soma (0.6 ± 0.2 λ and spreads over a region where most synapses impinge (Elbasiouny et al., 2005, 2006; Bui et al., 2006; Grande et al., 2007). Booth et al. (1997) focused on the distal dendritic component of the L-type current and showed that firing bistability could emerge from the weak coupling between the distal dendrites and the axo-somatic region where spikes are initiated. In contrast, we focused in our two compartment model on the more proximal component of the L-type current, and we showed that firing bistability may result from the dynamical competition between the L-type current and the AHP current. In real motoneurons, there is of course no clear-cut separation between proximal and distal dendrites. Both scenarios likely contribute to bistability: the more proximal the L-type conductance is, the more it is coupled to the soma and the more its activation is controlled by the AHP.

Ballou et al. (2006) also showed that the calcium L-type current, although mostly dendritic, also displays a somatic component. We demonstrate that a somatic L-type current may also elicit quiescence/firing bistability and firing bistability in our model, provided it is large enough. This is not directly relevant for motoneurons, in which most of the L-type current is dendritic, but it indicates that the dynamical interaction of the L-type and AHP-currents *per se* is sufficient to produce firing bistability. This theoretical result was validated by dynamic clamp experiments.

Importantly, the control of the firing pattern by the interaction of the L-type and AHP currents requires in our model that somatic SK channels be mostly opened following the activation of the N-type calcium conductance. In contrast, dendritic potassium channels are essentially activated by calcium influx through L-type channels, HVA calcium channels being barely sensitive to the attenuated spikes that propagate back to the

dendritic compartment. Our model thus suggests that motoneurons present two complements of SK channels, in the soma and in the dendrites, respectively activated by HVA and L-type calcium currents. Li and Bennett (2007) provided experimental evidence for that distinction. These authors indeed showed that the medium AHP was suppressed by the HVA calcium channel blocker ω-conotoxin but not by the L-type channel blocker nimodipine. In contrast, the dendritic calcium-sensitive potassium current that opposed the L-type current was eliminated by nimodipine.

CONDITIONS FOR FIRING BISTABILITY

Bistability between two firing states has been more rarely observed in motoneurons than between quiescence and firing. We suggest an explanation for that. In our model, firing bistability occurs when the following conditions are satisfied (i) the L-type current is large enough to elicit high frequency firing in the absence of AHP, (ii) the AHP current is also large and would create a wide primary firing range in the absence of L-type current, (iii) these two opposing currents are approximately balanced. Monaminergic neuromodulation of motoneurons increases the intensity of the L-type current (Hultborn and Kiehn, 1992). However, it also increases the overall excitability of motoneurons by reducing the AHP current. This is unfavorable to the balanced competition between the two currents required for firing bistability.

Firing bistability has been experimentally observed in motoneurons stimulated by a current injected in the soma. Elbasiouny et al. (2006) argued that firing bistability occurred only in that condition, whereas synaptic excitation of the dendrites led to secondary range firing at discharge onset. In our model, both current injection and synaptic excitation may elicit firing bistability when G_{Ca-L} is large enough, but the appropriate G_{AHP} range is narrower than for somatic current injection. Altogether, we may conclude that synaptic input to dendrites is indeed less favorable to firing bistability than somatic current injection.

DIFFERENCES WITH THE BRK MODEL

In the BRK model, spikes are attenuated by 96% in the dendrites because of the filtering by the small coupling conductance (0.1 mS/cm^2) and the AHP is too small in dendrites (0.5 mV typically) to have a substantial impact on the activation of the L-type current. Increasing G_{AHP} extends the primary firing range (lower branch of the F-I curve), in keeping with the known role of the AHP (Kernell, 1968; Ermentrout, 1998; Manuel et al., 2006), but does not suppress firing bistability. As the current flowing from the soma is little modulated in time, the discharge properties can be deduced from the dendritic I–V curve. When the I–V curve is monotonic, the *F-I* curve is graded. In contrast, plateau potentials and bistability are observed when the I–V curve is N-shaped. When the I–V curve intersects only once the zero current axis, a high frequency discharge occurs right from firing onset, and quiescence/firing bistability is achieved below recruitment. When there are three intersections, firing bistability is observed in response to a triangular current ramp, alone or together with quiescence/firing bistability.

In our model, where the two compartments are more strongly coupled (1 mS/cm^2), the AHP is barely reduced in the dendrites and may deactivate the L-type current. Increasing sufficiently the AHP leads to graded firing. This cannot be explained by a change in the I–V curve. Indeed, increasing G_{AHP} does alter the I–V curve in the suprathreshold voltage range but does not eliminate the negative slope region created by the L-type current below threshold. The interaction between the L-type and AHP currents is a dynamical effect that occurs during firing and controls the firing pattern. It could not be grasped by the BRK model, in which the L-type current was located distally in dendrites in a region unaffected by the AHP and bistability emerged from the plateau properties of the dendritic compartment.

At variance with the BRK model, our model does not incorporate a distal L-type current, which is why the somatic I–V curve displays no counterclockwise hysteresis. As a result, the L-type current is larger in our model than was estimated in motoneurons of decerebrate cats (see, for instance, Lee and Heckman, 1998a,b). This is particularly true of the somatic component. It is likely that the introduction of a distal component of the L-type current, in addition to the proximal component considered in our study, would allow bistable behavior for weaker L-type current.

THE INTERACTION BETWEEN THE L-TYPE AND AHP CURRENTS IS CRUCIAL FOR THE CONTROL OF MOTONEURON DISCHARGE

Motoneurons exhibit a large AHP that plays a fundamental role in controlling their firing pattern. It is well established that the AHP limits the frequency and the variability of their discharge (Kernell, 1999; Powers and Binder, 2000; Manuel et al., 2006). The AHP also affects excitability by interacting with inward currents. For instance, we recently showed that the AHP suppressed the mixed mode oscillations associated with subprimary range firing in mouse motoneurons (Iglesias et al., 2011) by deinactivating the sodium current, thus increasing membrane excitability. In the present study, the AHP decreases the excitability by deactivating the L-type current, which is in line with the modeling study of Elbasiouny et al. (2006). This did not occur in the BRK model because the coupling was too weak to allow the AHP to interact with the distal dendritic L-type current. Altogether, the firing properties of motoneurons appear to be largely regulated by the interaction between the AHP and L-type currents.

ACKNOWLEDGMENTS

Financial support provided by the Association Française conter les Myopathies (MNM2 2006) and Agence Nationale de la Recherche (Projet ANR 2010 BLAN 1429) is gratefully acknowledged. Dr. M. Manuel was a research fellow of Délégation Générale pour l'Armement when the experiments were performed. We are indebted to Prof. CJ Heckman and Dr. Hojeong Kim for careful reading of the manuscript and useful comments.

REFERENCES

Ballou, E. W., Smith, W. B., Anelli, R., and Heckman, C. J. (2006). Measuring dendritic distribution of membrane proteins. *J. Neurosci. Methods*. 156, 257–266. doi: 10.1016/j.jneumeth.2006.03.014

Booth, V., Rinzel, J., and Kiehn, O. (1997). Compartmental model of vertebrate motoneurons for Ca2+-dependent spiking and plateau potentials under pharmacological treatment. *J. Neurophysiol.* 78, 3371–3385.

Brizzi, L., Meunier, C., Zytnicki, D., Donnet, M., Hansel, D., Lamotte d'Incamps, B., et al. (2004). How shunting inhibition affects the discharge of lumbar motoneurones: a dynamic clamp study in anaesthetized cats. *J. Physiol.* 558(Pt 2), 671–683. doi: 10.1113/jphysiol.2003.059964

Bui, T. V., Ter-Mikaelian, M., Bedrossian, D., and Rose, P. K. (2006). Computational estimation of the distribution of L-type Ca(2+) channels in motoneurons based on variable threshold of activation of persistent inward currents. *J. Neurophysiol.* 95, 225–241. doi: 10.1152/jn.00646.2005

Elbasiouny, S. M., Bennett, D. J., and Mushahwar, V. K. (2005). Simulation of dendritic CaV1.3 channels in cat lumbar motoneurons: spatial distribution. *J. Neurophysiol.* 94, 3961–3974. doi: 10.1152/jn.00391.2005

Elbasiouny, S. M., Bennett, D. J., and Mushahwar, V. K. (2006). Simulation of Ca2+ persistent inward currents in spinal motoneurones: mode of activation and integration of synaptic inputs. *J. Physiol.* 570, 355–374. doi: 10.1113/jphysiol.2005.099119

Ermentrout, B. (1998). Linearization of F-I curves by adaptation. *Neural Comput.* 10, 1721–1729. doi: 10.1162/089976698300017106

Fleshman, J. W., Segev, I., and Burke, R. B. (1988). Electrotonic architecture of type-identified alpha-motoneurons in the cat spinal cord. *J. Neurophysiol.* 60, 60–85.

Grande, G., Bui, T. V., and Rose, P. K. (2007). Estimates of the location of L-type Ca2+ channels in motoneurons of different sizes: a computational study. *J. Neurophysiol.* 97, 4023–4035. doi: 10.1152/jn.00044.2007

Guertin, P. A., and Hounsgaard, J. (1999). Non-volatile general anaesthetics reduce spinal activity by suppressing plateau potentials. *Neuroscience* 88, 353–358. doi: 10.1016/S0306-4522(98)00371-6

Hounsgaard, J., Hultborn, H., Jespersen, B., and Kiehn, O. (1988). Bistability of α-motoneurones in the decerebrate cat and in the acute spinal cat after intravenous 5-hydroxytryptophan. *J. Physiol.* 405, 345–367.

Hounsgaard, J., and Kiehn, O. (1985). Ca^{++} dependent bistability induced by serotonin in spinal motoneurons. *Exp. Bain Res.* 57, 422–425. doi: 10.1007/BF00236551

Hounsgaard, J., and Kiehn, O. (1989). Serotonin-induced bistability of turtle motoneurones caused by a nifedipine-sensitive calcium plateau potential. *J. Physiol.* 414, 265–282.

Hounsgaard, J., and Mintz, I. (1988). Calcium conductance and firing properties of spinal motoneurones in the turtle. *J. Physiol.* 398, 591–603.

Hultborn, H., and Kiehn, O. (1992). Neuromodulation of vertebrate motor neuron membrane properties. *Curr. Opin. Neurobiol.* 2, 770–775. doi: 10.1016/0959-4388(92)90132-5

Iglesias, C., Meunier, C., Manuel, M., Timofeeva, Y., Delestrée, N., and Zytnicki, D. (2011). Mixed mode oscillations in mouse spinal motoneurons arise from a low excitability state. *J. Neurosci.* 31, 5829–5840. doi: 10.1523/JNEUROSCI.6363-10.2011

Jaffe, D., and Carnevale, N. (1999). Passive normalization of synaptic integration influenced by dendritic architecture. *J. Neurophysiol.* 82, 3268–3285.

Kernell, D. (1968) The repetitive impulse discharge of a simple neurone model compared to that of spinal motoneurones. *Brain Res.* 11, 685–687. doi: 10.1016/0006-8993(68)90157-1

Kernell, D. (1999). Repetitive impulse firing in motoneurons: facts and perspectives. *Prog. Brain Res.* 123, 31–37. doi: 10.1016/S0079-6123(08)62841-1

Kim, H., Major, L., and Jones, K. (2009). Derivation of cable parameters for a reduced model that retains asymmetric voltage attenuation of reconstructed spinal motor neuron dendrites. *J. Comput. Neurosci.* 27, 321–336. doi: 10.1007/s10827-009-0145-7

Kuo, J. J., Lee, R. H., Zhang, L., and Heckman, C. J. (2006). Essential role of the persistent sodium current in spike initiation during slowly rising inputs in mouse spinal neurones. *J. Physiol.* 574(Pt 3), 819–834. doi: 10.1113/jphysiol.2006.107094

Lee, R. H., and Heckman, C. J. (1998a). Bistability in spinal motoneurons *in vivo*: systematic variations in rhythmic firing patterns. *J. Neurophysiol.* 80, 572–582.

Lee, R. H., and Heckman, C. J. (1998b). Bistability in spinal motoneurons *in vivo*: systematic variations in persistent inward currents. *J. Neurophysiol.* 81, 2164–2174.

Lee, R. H., and Heckman, C. J. (1999). Enhancement of bistability in spinal motoneurons *in vivo* by the noradrenergic alpha1 agonist methoxamine. *J. Neurophysiol.* 80, 583–593.

Li, X., and Bennett, D. J. (2007). Apamin-sensitive calcium-activated potassium currents (SK) are activated by persistent calcium currents in rat motoneurons. *J. Neurophysiol.* 97, 3314–3330. doi: 10.1152/jn.01068.2006

Li, Y., Gorassini, M. A., and Bennett, D. J. (2004). Role of persistent sodium and calcium currents in rat motoneuron firing and spasticity in chronic spinal rats. *J. Neurophysiol.* 91, 767–783. doi: 10.1152/jn.00788.2003

Manuel, M., Iglesias, C., Donnet, M., Leroy, F., Heckman, C. J., and Zytnicki, D. (2009). Fast kinetics, high-frequency oscillations, and subprimary firing range in adult mouse spinal motoneurons. *J. Neurosci.* 29, 11246–11256. doi: 10.1523/JNEUROSCI.3260-09.2009

Manuel, M., Meunier, C., Donnet, M., and Zytnicki, D. (2006). The afterhyperpolarization conductance exerts the same control over the gain and variability of motoneurone firing in anaesthetized cats. *J. Physiol.* 576(Pt 3), 873–886. doi: 10.1113/jphysiol.2006.117002

Moritz, A. T., Newkirk, G., Powers, R. K., and Binder, M. D. (2007). Facilitation of somatic calcium channels can evoke prolonged tail currents in rat hypoglossal motoneurons. *J. Neurophysiol.* 98, 1042–1047. doi: 10.1152/jn.01294.2006

Powers, R. K., and Binder, M. D. (2000). Relationship between the time course of the afterhyperpolarization and discharge variability in cat spinal motoneurones. *J. Physiol.* 528, 131–150. doi: 10.1111/j.1469-7793.2000.t01-1-00131.x

Prinz, A. A., Abbott, L. F., and Marder, E. (2004). The dynamic clamp comes of age. *Trends Neurosci.* 27, 218–224. doi: 10.1016/j.tins.2004.02.004

Raikov, I., Preyer, A., and Butera, R. J. (2004). MRCI: a flexible real-time dynamic clamp system for electrophysiology experiments. *J. Neurosci. Methods* 132, 109–123. doi: 10.1016/j.jneumeth.2003.08.002

Schwindt, P. C., and Crill, W. E. (1982). Factors influencing rhythmic firing: results fromm a voltage-clamp study. *J. Neurophysiol.* 48, 875–890.

Schwindt, P. C., and Crill, W. E. (1984). "Membrane properties of cat spinal motoneurons," in *Handbook of the Spinal Cord*, ed R. Davidoff (New York, NY: Dekker), 199–242.

Simon, M., Perrier, J. F., and Hounsgaard, J. (2003). Subcellular distribution of L-type Ca2+ channels responsible for plateau potentials in motoneurons from the lumbar spinal cord of the turtle. *Eur. J. Neurosci.* 18, 258–266. doi: 10.1046/j.1460-9568.2003.02783.x

Zhang, M., Møller, M., Broman, J., Sukiasyan, N., Wienecke, J., and Hultborn, H. (2008). Expression of calcium channel CaV1.3 in cat spinal cord: light and electron microscopic immunohistochemical study. *J. Comp. Neurol.* 507, 1109–1127. doi: 10.1002/cne.21595

Zhang, M., Sukiasyan, N., Møller, M., Bezprozvanny, I., Zhang, H., Wienecke, J., et al. (2006). Localization of L-type calcium channel Ca(V)1.3 in cat lumbar spinal cord with emphasis on motoneurons. *Neurosci. Lett.* 407, 42–47. doi: 10.1016/j.neulet.2006.07.073

Conflict of Interest Statement: The authors declare that the research was conducted in the absence of any commercial or financial relationships that could be construed as a potential conflict of interest.

Received: 12 November 2013; accepted: 08 January 2014; published online: 27 January 2014.

Citation: Manuel M, Zytnicki D and Meunier C (2014) The dendritic location of the L-type current and its deactivation by the somatic AHP current both contribute to firing bistability in motoneurons. Front. Comput. Neurosci. ***8****:4. doi: 10.3389/fncom.2014.00004*

This article was submitted to the journal Frontiers in Computational Neuroscience.

frontiers in
CELLULAR NEUROSCIENCE

ORIGINAL RESEARCH ARTICLE
published: 13 May 2014
doi: 10.3389/fncel.2014.00127

The kinetics of multibranch integration on the dendritic arbor of CA1 pyramidal neurons

Sunggu Yang[1], Valentina Emiliani[2] and Cha-Min Tang[1,3]*

[1] *Department of Neurology, University of Maryland School of Medicine, Baltimore, MD, USA*
[2] *Wavefront-engineering Microscopy Group, Neurophotonics Laboratory, CNRS UMR 8250, Paris Descartes University, Paris, France*
[3] *Baltimore Veterans Adminstration Medical Center, Baltimore, MD, USA*

Edited by:
Sergey M. Korogod, International Center for Molecular Physiology, National Academy of Sciences of Ukraine, Ukraine

Reviewed by:
Valentin Nägerl, Université de Bordeaux, France
Guido C. Faas, University of California, Los Angeles, USA

***Correspondence:**
Cha-Min Tang, Department of Neurology, University of Maryland School of Medicine, Rm 12-029, 655 West Baltimore Street, Baltimore, MD 21201, USA
e-mail: CTang@som.umaryland.edu

The process by which synaptic inputs separated in time and space are integrated by the dendritic arbor to produce a sequence of action potentials is among the most fundamental signal transformations that takes place within the central nervous system. Some aspects of this complex process, such as integration at the level of individual dendritic branches, have been extensively studied. But other aspects, such as how inputs from multiple branches are combined, and the kinetics of that integration have not been systematically examined. Using a 3D digital holographic photolysis technique to overcome the challenges posed by the complexities of the 3D anatomy of the dendritic arbor of CA1 pyramidal neurons for conventional photolysis, we show that integration on a single dendrite is fundamentally different from that on multiple dendrites. Multibranch integration occurring at oblique and basal dendrites allows somatic action potential firing of the cell to faithfully follow the driving stimuli over a significantly wider frequency range than what is possible with single branch integration. However, multibranch integration requires greater input strength to drive the somatic action potentials. This tradeoff between sensitivity and temporal precision may explain the puzzling report of the predominance of multibranch, rather than single branch, integration from in vivo recordings during presentation of visual stimuli.

Keywords: multibranch integration, 3D digital holography

INTRODUCTION

Individual thin dendritic branches are fundamental functional units in the nervous system (Branco and Hausser, 2011). Experimental data support the concept that they can operate as quasi-independent processing and signaling units capable of non-linear behavior (Mel, 1993; Wei et al., 2001). In combination with their parent dendritic branches, these thin distal dendrites can function in two distinct modes (Gasparini and Magee, 2006; Katz et al., 2009). If distributed synaptic inputs arrive on multiple distal branches, the depolarization on each branch may be below the threshold for recruiting local active conductances in a regenerative manner and yet be sufficient to trigger a somatic sodium spike. This is sometimes referred to as the traditional "integrate and fire" model (Abbott, 1999), the "synaptic democracy" model (Yuste, 2011), and the "global" model of integration. Alternatively, if synaptic inputs arrive in a clustered pattern on a single or a few distal dendrites, the focused inputs could initiate a non-linear response on the distal dendrite which is then relayed to and summed linearly in the more proximal compartment. This is referred to as either the "two-layer" or the "compartmentalization" model of integration (Mel, 1993; Golding and Spruston, 1998; Häusser and Mel, 2003; Poirazi et al., 2003a,b; Polsky et al., 2004; Larkum and Nevian, 2008; Winnubst and Lohmann, 2012). The advantages of the two-layer model of integration are well understood. It is more efficient in evoking somatic action potentials and can do so at the lowest synaptic strengths. By placing amplification close to the input optimal signal-to-noise performance can be achieved. This is analogous to the mechanism in a two-stage electronic amplification system, such as the preamplifier-power amplifier system typically used in electrophysiology; the amplification is entirely carried out in the preamplifier. Two-stage integration can also greatly increase the computational power of the neuron over that of global integration because it increases the number of non-linear operations that a single neuron can possess (Mel, 1993; Häusser and Mel, 2003). In the two-stage mode of integration it is the dendritic branch, rather than the synapse, that is the elementary unit of signaling. The tradeoffs associated with these two modes of integration have not been adequately examined, and doing so may lend insights into the controversy regarding the functional impacts of global and two-layer integration.

Whether integration on pyramidal neuron follows a global or a two-stage model is difficult to address because it depends on the spatial-temporal pattern of the inputs which is an in vivo phenomenon that may change with different physiological stimuli. Investigators from Konnerth's group addressed this challenge using calcium imaging in an in vivo study of pyramidal neurons in the visual cortex in response to directionally selective visual

inputs (Jia et al., 2010). They found that orientation-selective synaptic inputs were widely distributed throughout the dendritic field rather than being clustered on individual dendrites. This finding is more consistent with the global model of integration. The extent to which this conclusion can be applied to other pyramidal neurons in response to different physiological stimuli is not known. For example, Takahashi et al. (2012) reported that in layer 2/3 pyramidal neurons of the barrel cortex, related inputs frequently arrived synchronously on neighboring synapses, creating the possibility of local non-linear integration, which is more consistent with the two-stage model (Takahashi et al., 2012). In this study we take another approach towards addressing the global vs. two-stage controversy. We compared the property of single- and multibranch integration in response to photolysis as a surrogate for two-stage and global integration, respectively. The critical parameters differentiating the global and two-stage mode of integration are the precise location of non-linear integration within the dendritic arbor and the active conductances expressed at that location. Precise photolytic stimulation with complex 3D digital holographic-generated patterns allowed us to systematically examine this issue. Single- and multibranch integration was used to simulate clustered and distributed synaptic inputs that have different thresholds for non-linear integration. We found that the dendritic arbor of CA1 pyramidal neurons can support both the global and the two-stage modes of integration. The global mode of integration is less sensitive to low strength stimuli, but allows for accurate response following over a greater frequency range, while the two-stage mode of integration has high sensitivity but allows for accurate response following only at low frequencies.

MATERIALS AND METHODS

BRAIN SLICE PREPARATION

All procedures were approved by the Institutional Animal Care and Use Committee at the University of Maryland School of Medicine. Sprague-Dawley rats (postnatal age: 3–6 weeks) were deeply anesthetized with halothane. The brains were quickly removed and placed into chilled (4°C), oxygenated (5% CO_2 and 95% O_2) slicing medium containing (in mM): 4 KCl, 1.23 NaH_2PO_4, 10 $MgSO_4$, 0.5 CaCl2, 26 $NaHCO_3$, 10 glucose, and 212.7 sucrose. Hippocampal slices (300 mm thickness) were cut using a vibrating tissue slicer and transferred to a holding chamber containing oxygenated physiological saline that contained (in mM): 124 NaCl, 4 KCl, 1.23 NaH_2PO_4, 1.5 $MgCl_2$, 2.5 $CaCl_2$, 26 $NaHCO_3$, and 10 glucose. Individual slices were then transferred to a recording chamber and oxygenated physiological saline was continuously superfused at a rate of 0.7 ml/min. Certain experiments were carried out at 32°C (those illustrated in **Figures 1**, **2**, **3**, **4**, **7**, and **8**) and the remaining experiments at room temperature.

BRAIN SLICE RECORDING

Whole-cell patch recordings were obtained using an Axon instruments Axoclamp 700B Amplifier (Molecular Devices), and pClamp Version 10.2 software was used for data acquisition. Recording pipettes had tip resistances of 3–7 MΩ when filled with a solution containing (in mM): 135 K-gluconate, 5 KCl, 1 $MgCl_2$, 0.02 $CaCl_2$, 0.2 EGTA, 10 HEPES, 4 Na_2-ATP, and 0.3 Na-GTP. The pH and osmolarity of intracellular solution were adjusted to 7.3 and 290 mOsm, respectively. Alexa 594 (50 μM) was included in the internal solution for visualization of dendrites. Recordings were done in "current-clamp" configuration and cells were held at −65 mV. For electrical stimulation experiment, synaptic responses were evoked with 15–60 μA, 0.4 ms current pulses delivered through a concentric bipolar stimulating electrode (FHC, 100 μm o.d.).

3D DIGITAL HOLOGRAPHY

The procedures for digital holographic photolysis were explained in detail in an earlier methods paper (Lutz et al., 2008; Yang et al., 2011). Briefly, the holographic beam was brought into the optical axis of an upright fluorescence microscope (Olympus BX51) below the epi-fluorescence unit, with a longpass dichroic mirror (**Figure 1**). The output beam of a 150 mW, 405 nm diode laser (CNI Laser) is expanded by a beam expander (BE) (3X) to fill the short axis of a reflective spatial light modulator (SLM) (LCOS Hamamatsu, model X10468-05). The SLM plane is projected onto the back aperture of the microscope objective through a telescope (L1, f_1 = 500 mm; L2, f_2 = 200 mm). The magnification of the telescope is chosen in order to match the SLM short axis with the diameter of the objective's back aperture (Olympus, 60x, W 0.9NA). The undiffracted component of the hologram (zero order spot) is removed by placing a small (<0.5 mm) anodized metal plate on antireflective coated glass plate at the focal plane of L1 (spatial filter (SF)). This plane is conjugate to the image plane of the microscope. In order to change the total number of spots of excitation without changing the intensity of the remaining spots, spots that were not needed for excitation were steered onto the same small SF for blocking the zero order beam. The algorithm for the phase hologram calculation and calibration of the temporal spatial resolution were previously described (Yang et al., 2011).

PHARMACOLOGICAL AGENTS

Concentrated stock solutions of various pharmacological agents were initially prepared and diluted in physiological saline to a final concentration before use. For uncaging experiments, MNI-caged-L-glutamate (Tocris, Ellisville, MO) or and MNI-L-glutamate trifluoro acetate (Femtonics, Hungary) were prepared each day at final concentration in physiological solution. All agonists and antagonists were purchased from Sigma (St. Louis, MO) or Tocris (Ellisville, MO). The presence or absence of tetrodotoxin (TTX) is provided for each experiment.

RESULTS

3D DIGITAL HOLOGRAPHIC PHOTOLYSIS

This study was made possible by 3D digital holographic photolysis (Anselmi et al., 2011; Yang et al., 2011; Go et al., 2012), therefore it is useful to describe its strengths and potential weaknesses. A schematic of the optical system is illustrated in **Figure 1A**. 3D digital holography has three characteristics important to experimental investigation of dendritic integration: (1) the ability to efficiently deliver light to diffraction limited spots and photorelease glutamate in a way that mimics normal synaptic transmission (Nikolenko et al., 2008; Yang et al., 2011); (2) the

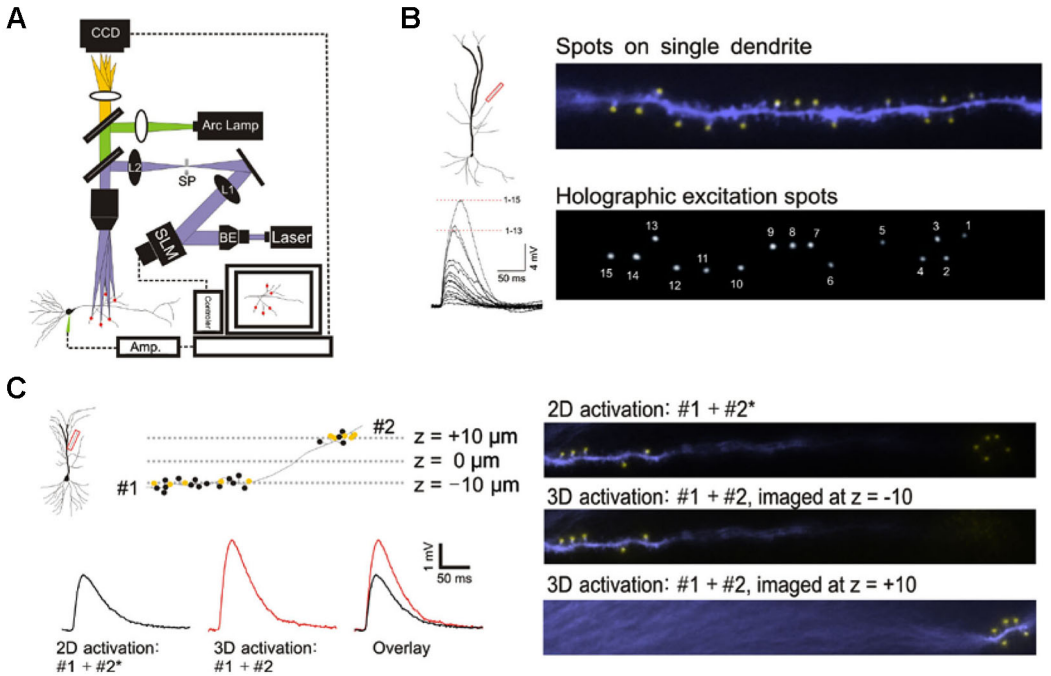

FIGURE 1 | 3D digital holographic photolysis of oblique spines. (A) Schematic of the 3D digital holographic setup. The locations of the sites to be stimulated are first identified and their 3D coordinates determined from fluorescence imaging of the dendrite. An in-house algorithm is then used to generate a digital holographic pattern of those coordinates which is project by a phase modulating spatial light modulator (SLM). The output of a 150 mW, 405 nm diode laser is expanded by a beam expander (BE) to fill the aperture of the SLM. The beam is then telescoped by two lenses (L1 and L2) to fill the back aperture of the microscope objective. A spatial filter (SF) is used to block the zero-order beam of the hologram from reaching the specimen. **(B)** Simultaneous photostimulation at multiple spines. The distal oblique of CA1 neuron was photostimulated. The yellow spot indicate sites of simultaneous uncaging on multiple spines (*upper panel*). Spot size is similar to that of spine (*compare with lower panel*). The spatially summed response (*lower left*) demonstrate non linear integration on single oblique dendrite. **(C)** Simultaneous photostimulation in two planes. Dendritic spines located at two imaging planes (#1 and #2) along a single dendrite are targeted. The yellow spots represent spines that are stimulated and the black spots represent those that are not stimulated. 2D stimulation of #1 and #2* (*x*, *y*-coordinates of #2 but with the *z*-coordinate set at -10) produces a lower amplitude (black trace) compared to simultaneous 3D activation (#1 + #2) (red trace).

ability to stimulate simultaneously; at a large number of locations in arbitrary, user defined, temporal-spatial patterns, (**Figure 1B**); and (3) the ability to stimulate in 3D space such as is traversed by multiple dendrites oriented in different directions (**Figure 1C**).

The holographic system used in this study utilizes single photon excitation, whereas other studies have utilized two-photon excitation. It is reasonable to question whether the novel observations of this study could be accounted for by differences in the ability of single- and two-photon photolytic methods to focus the light. This issue was addressed by three independent methods: direct visualization of the illumination pattern and spot size on the target dendrite in the hippocampal slice, comparison of the kinetics of the photolytic responses produced by single- and two-photon holographic photolysis at individual target sites, and comparison of responses to branch wide stimulation with single- and two-photon photolysis. If no significant differences could be observed under these three conditions, there would be little reason to expect greater light scattering of single photon excitation to account for unexpected findings associated with multibranch integration. **Figure 1B** shows the area of illumination when the holographic pattern was directed on a dendrite that had been dialyzed with an intracellular fluorescent dye. The spatial resolution under experimental conditions is consistent with the previously measured optical resolution for this system of 0.4 and 2 µm in the transverse and axial directions, respectively (Yang et al., 2011). This degree of spatial resolution is not unexpected when studying those structures <60 µm from the slice surface. We had previously shown that the kinetics of the voltage clamped holographically induced response are comparable to a fast EPSC (Yang et al., 2011). Most importantly, the single branch response to single-photon holographic stimulation (**Figures 1B, 2A, 3C, 3D, 4C, 4D**) is indistinguishable from what has been reported for two-photon stimulation (Branco and Hausser, 2011). Since multibranch integration is the sum of single branch integration, anomalous behavior of multibranch integration should not be dismissed as artifacts of single photon excitation.

DIFFERENCES BETWEEN SINGLE- AND MULTIBRANCH INTEGRATION

Whole cell patch recordings were made on CA1 neurons in transverse hippocampal slices. Alexa594 was placed in the patch electrode and was allowed to dialyze into the dendritic arbor. Once the fluorescence signal of the oblique dendrites became visible, the 3D coordinates of the photolysis sites on the spines

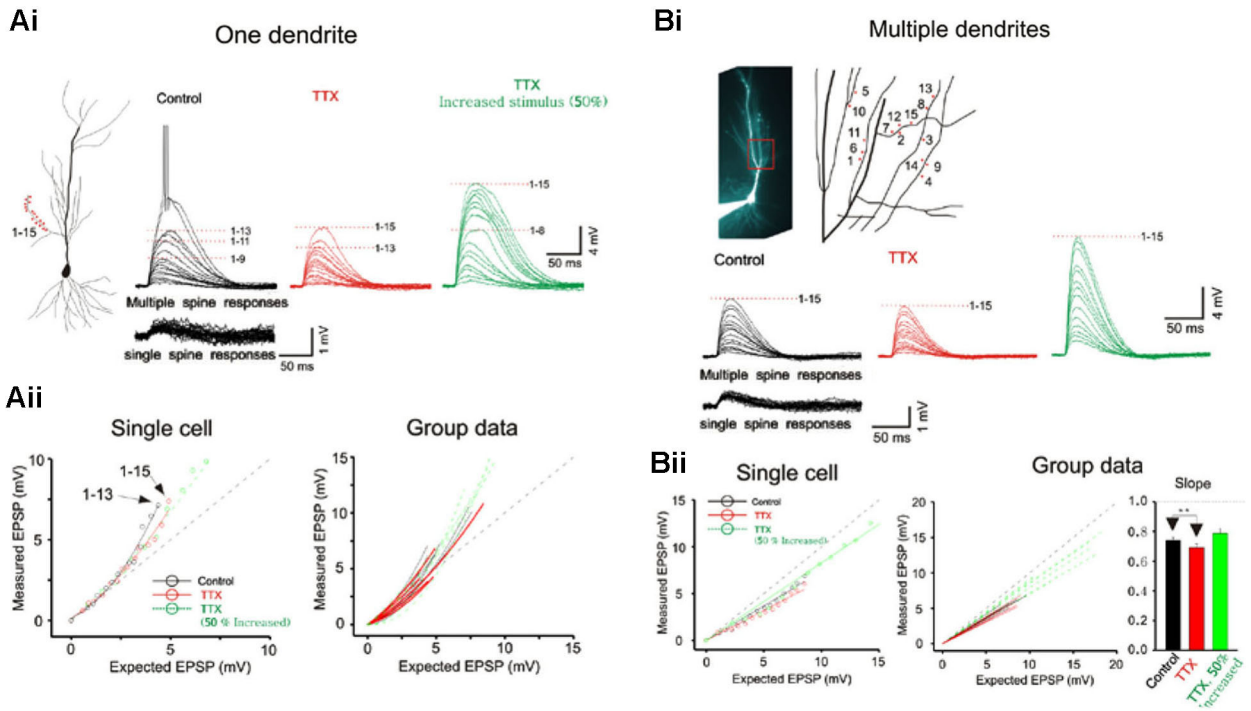

FIGURE 2 | Integration on spines. (A) The photostimulation is distributed over 15 spines along a single dendrite without TTX. The somatic voltage responses to stimulation of individual spines (lower panels) and the responses to increasing number of simultaneous spines (upper panels) are shown in *black*. In presence of TTX, the responses are shown in *red*. The responses to increased laser stimulation are shown in *green*. The cell responses are plotted to examine the linearity of summation (expected vs. measured voltage response). Group data is obtained without TTX (n = 7), with TTX (n = 5) and with increased stimulation in TTX (n = 5). Supralinear summation is observed with single branch integration. **(B)** Photostimulation for the 15 spines along multiple branches. Two or four spines are stimulated per dendrite. The responses of the cell are plotted to examine the linearity of summation (expected vs. measured voltage response). Sublinear summation is observed with multibranch integration. Group data is obtained without TTX (n = 7), with TTX (n = 7) and with increased stimulation in TTX (n = 7). Error bars represent SE. ** $p < 0.05$.

were identified. Individual spots first stimulated individual spines (lower panels **Figure 2A**) and were then sequentially combined (upper panels). In the presence of TTX the supralinearity of single branch integration was decreased (red vs. black exponentially fitted lines in **Figure 2A**). The average depolarization immediately before the onset of the sodium spike occurred was about 7.8 mV at an expected response of 5.3 mV (group data in **Figure 2Aii**). The non-linearity for this group data was 1.47 in the absence of TTX (n = 7) and 1.27 with TTX (n = 5; $p > 0.05$, t-test). The responses of single oblique dendrites to holographic photolysis are nearly identical to that previously reported for synaptic stimulation (Polsky et al., 2004) and 2P photostimulation (Branco and Hausser, 2011). After validating the reliability of the stimulating technique at the level of individual spines, the same holographic technique was then employed to stimulate five separate oblique dendrites. The responses in this case were significantly sublinear (**Figure 2B**). The slope of multibranch sublinearity was 0.74 ± 0.02 (n = 7) without TTX (black traces) and was 0.69 ± 0.03 (n = 7) with TTX (red traces). Voltage-gated sodium channels have a relatively small but statistically significant influences on the sublinearity of multibranch integration ($p > 0.05$, paired t-test). Such contrasting tendencies of single vs. multibranch integration were not altered by increasing stimulating power to activate spine and shaft together (**Figure 2** *green*).

Next, photolysis was directed at 5 to 7 spots distributed over ∼100 μm length of the mid portion of a single oblique dendrite and TTX (1 μM) was added to permit observation of synaptic responses over a wider range of intensity (**Figures 3A** and left panel, **3B**). Integration was linear at low stimulus intensities (<3–5 mV), supralinear at moderate intensities (3–10 mV), and trending towards saturation at high intensities (>5–10 mV) (**Figures 3C** and **D**). The supralinear integration is NMDAR-mediated (**Figure 3E**).

The same procedures were then repeated for multibranch stimulation in the same cells. Stimuli delivered to each of the five dendrites were distributed between at least two separate spots of photolysis in the mid-dendritic region (right panel, **Figure 3B**). The average degree of linearity observed here from 14 cells is 0.68 (**Figures 3C** and **D**), was substantially more sublinear than previously revealed from summation of two branches (Cash and Yuste, 1999; Polsky et al., 2004). The group data also show that multibranch integration is also more sublinear than single branch integration over the same stimulus intensity range (**Figure 3D**). The nearly identical behavior illustrated in

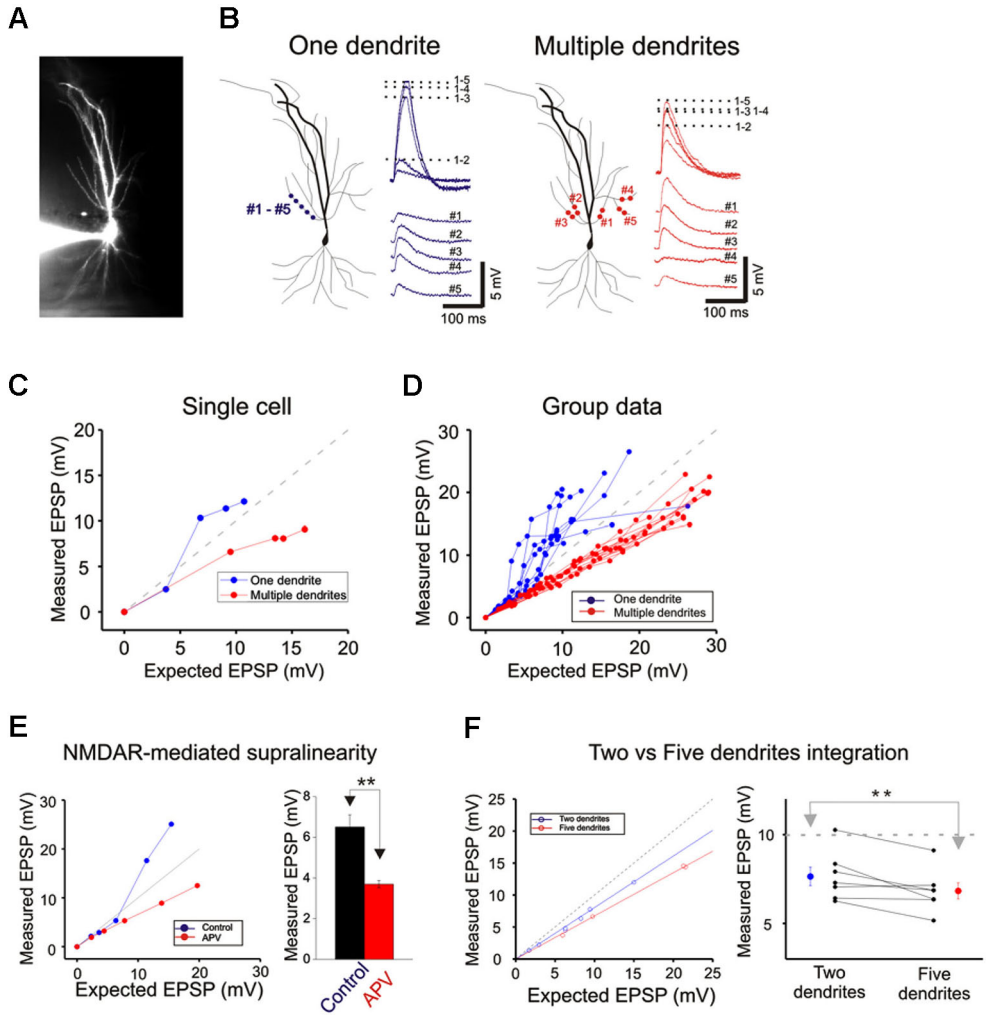

FIGURE 3 | Integration on a single dendrite is fundamentally different from that on multiple dendrites. (A) Wide field image of a CA1 pyramidal neuron filled with Alexa 594. **(B)** Locations of focal photolysis of caged glutamate directed on a single oblique dendrite are labeled in blue. The stimulation is distributed over 5–7 spots spread out over an 80–100 micron length of an individual dendrite. Locations of photolysis for the multibranch stimulation are directed on five separate oblique dendrites in the same cell (labeled in red). Two sites located in the mid dendritic region are stimulated per dendrite. The somatic voltage responses to stimulation of individual spots or dendrites are shown in the lower panels. The responses to an increasing number of simultaneous spots or dendrites are shown in the upper panels. For example the trace labeled 1–5 in the one dendrite panel represents the response to simultaneous stimulation of all five blue spots. **(C)** The responses of the cell shown in panel (B) are plotted to examine the linearity of summation (expected vs. measured voltage response). Sublinear summation is observed with multibranch integration, whereas an abrupt transition to supralinear summation is observed when the expected voltage reached ~5 mV with single dendrite summation. **(D)** The finding shown in **C** was obtained from 13 recordings of single dendrites and 14 recordings from multiple dendrites. The average slope of the multibranch summation is 0.68. **(E)** NMDAR-mediated dendritic spikes. The supralinear dendritic spike ($n = 5$, 6.5 ± 0.6) is blocked by APV (100 μM; $n = 5$; 3.7 ± 0.17, $p < 0.05$, paired t-test). Error bars represent SE. ** $p < 0.05$. **(F)** Magnitude of sublinear multi-branch integration increases with the number of branches. The linearity of summation between two branches and five branches is compared within the same cell (left). The measured EPSP for an expected EPSP of 10 mV is plotted for 7 cells (right). Error bars represent SE. ** $p < 0.05$.

Figures 2 and **3** also suggests that spine stimulation does not influence the fundamental nature of single- and multibranch integration.

We examined the effect of varying the number of branches involved in integration between two and five in the same cell. The degree of sublinearity lessened with a decrease in numbers of branches that were involved (**Figure 3F**). The measured EPSP for an expected EPSP of 10 mV is 7.65 ± 0.52 mV for two branches and 6.84 ± 0.45 mV for five branches ($n = 7$, $p < 0.05$, paired-t test). These findings suggest that multibranch integration may recruit additional conductances in addition to those involved in single branch integration, and that these are expressed near the locus where the branches converge. With increasing numbers of stimulated branches, these conductances are recruited at a rate that exceeds the more linearly summated depolarizing signal.

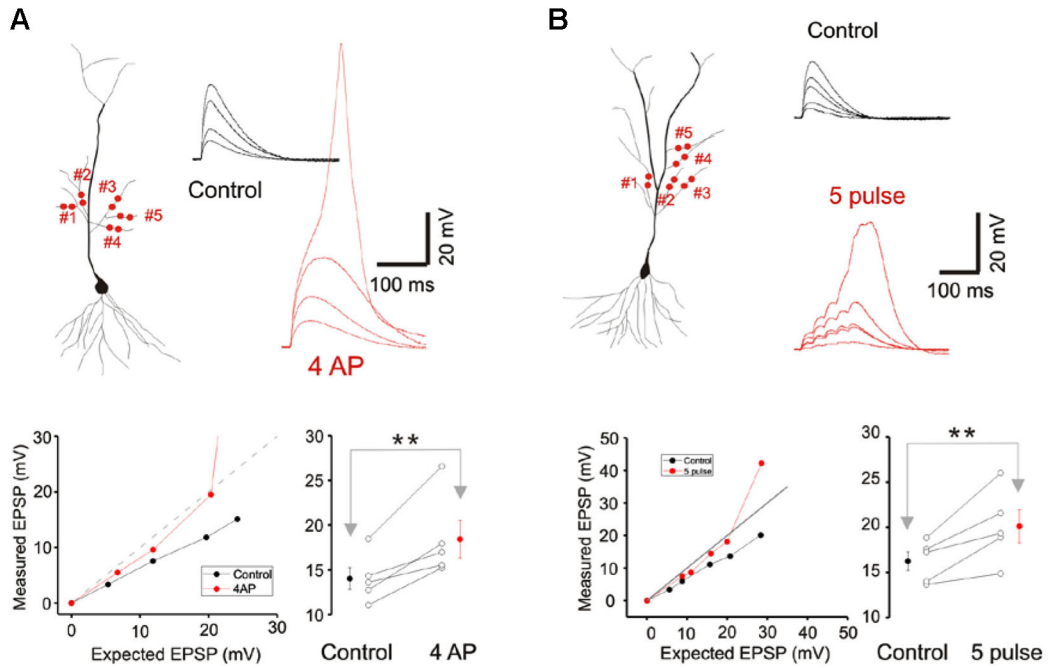

FIGURE 4 | A-type potassium conductance contributes to sublinear integration. (A) Blockade of the A-type potassium conductance by the addition of 4AP removes the sublinear multi-branch summation at the oblique dendrites. It also uncovers the latent NMDA conductance and lowers the threshold for calcium spikes. Group data ($n = 5$) for the observed EPSP to a stimulus with an expected EPSP of 20 mV is shown to the lower right. Error bars represent SE. ** $p < 0.05$. **(B)** Sublinear multi-branch integration is abolished during burst stimulation (50 Hz). Instantaneous multibranch summation (black traces) is compared with summation to a burst of inputs (red traces). Summation is less sublinear with the burst stimulus. Group data ($n = 5$) for the observed EPSP to a stimulus with an expected EPSP of 25 mV is to the lower right. Error bars represent SE. ** $p < 0.05$.

Cash and Yuste (1999) had suggested that the A-type potassium conductance (I_A) could act as a counterbalancing force to the recruitment of NMDA conductance during branch point summation and linearize integration. We investigated whether I_A serves a more prominent role in multibranch integration. Indeed, applying the A-type potassium channel antagonist, 4AP (3 mM), reversed the sublinearity (**Figure 4A**; Control: 14.04 ± 1.23 mV, 4AP: 18.43 ± 2.09 mV, $n = 5$, $p < 0.05$, paired t-test). To circumvent the poor target selectivity of 4AP, we examined whether sublinear summation could be attenuated during a burst stimulus, a condition that promotes inactivation of I_A. Indeed, sublinear summation is eliminated during burst stimulation (**Figure 4B**; Control: 16.25 ± 1.03 mV, burst: 20.12 ± 1.82 mV, $n = 5$, $p < 0.05$, paired t-test). Taken together, these findings suggest that the difference between single- and multibranch integration of the oblique dendrites could be accounted for by the recruitment of additional A-type potassium conductance at the locus where distal oblique branches converge.

We next examined single- and multibranch summation on the basal dendrites. Qualitatively, single- and multibranch summation of the basal dendrites was similar to that of the oblique dendrites (**Figure 5**). The opposing tendencies of single- and multibranch summation of basal dendrites suggest that basal dendrites are functionally similar to oblique dendrites.

DOMAIN SPECIFIC MULTIBRANCH INTEGRATION

We next compared single- and multibranch integration in the distal apical tuft dendrites to test the idea that the mode of integration can vary in different domains of the dendritic arbor. Because the tuft receive inputs that are distinct from those of oblique and basal dendrites, it would not be surprising to find domain-specific differences. Integration on individual tuft dendrites, as was in the case of oblique dendrites, is linear at weak intensities, followed by supralinear summation at moderate intensities, and finally trending to sublinear summation at high intensities (*Blue* **Figures 6A, B** and **C**). But in contrast to the case at the oblique dendrites, multibranch integration of the tuft is not sublinear at low or moderate stimulation intensities (*red* **Figures 6A, B** and **C**). The base of the apical tuft where signals from distal tuft dendrites converge and pass through to reach the soma, is thought to express high levels of voltage gated calcium conductances (Larkum et al., 1999, 2009). In support of this proposed mechanism, we found the application of nickel (50–100 μM) which preferentially blocks the T/R-type calcium channels, partially attenuated the multibranch supralinear summation at the apical tuft (**Figure 6D**; Control: 17.50 ± 1.43 mV, Ni^{2+}: 13.68 ± 1.19 mV, $n = 5$, $p < 0.05$, paired t-test). The remainder of the supralinear component could be eliminated with application of AP5 (100 μM; Ni^{2+} + AP5: 11.28 ± 0.87 mV, $n = 6$, $p < 0.05$, paired t-test with Ni^{2+} group). In contrast, the supralinear summation

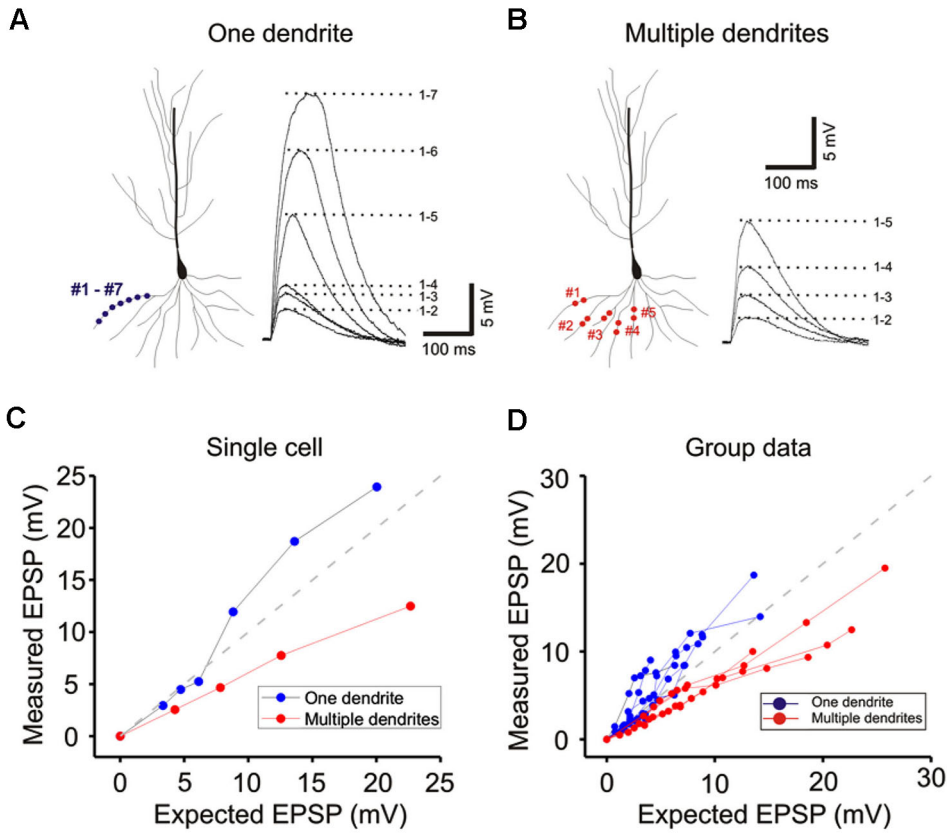

FIGURE 5 | Basal dendrites integration is qualitatively similar to integration on oblique dendrites. (A) Response of a single basal dendrite to progressive increasing strength of stimulation distributed over 7 sites. **(B)** Response of the same cell to stimulation on five separate branches. **(C)** Responses shown in A and B are plotted and compared for linearity. **(D)** Group data from 8 cells.

of single branches in the tuft was not blocked by Ni^{2+} (**Figure 6E**; Control: 12.59 ± 0.61 mV, Ni^{2+}: 12.28 ± 0.56 mV, $n = 5$, $p < 0.05$, paired t-test) but it was blocked by AP5 (100 μM; Ni^{2+} + AP5: 7.66 ± 0.35 mV, $n = 5$, $p < 0.05$, paired t-test with Ni^{2+} group).

The focus of most studies on dendritic integration has been on the linearity of integration and the efficiency with which inputs can generate a somatic action potential. Efficiency is defined in terms of the amount of synaptic excitation required to produce a somatic action potential. The two-layer model of integration achieves greater efficiency by allowing supralinear summation to occur on the distal dendritic compartment. We confirm this prediction of the two-layer model of integration by demonstrating that there is a lower threshold for evoking a somatic action potential when excitation is directed on a single dendrite than when it is directed towards multiple dendrites (**Figure 7A**; AP threshold for Oblique: multiple = 5.4 ± 0.09 μJ, single = 3.84 ± 0.08 μJ, $n = 8$, $P < 0.05$, paired t-test). Interestingly, there is little difference in terms of the action potential threshold at the tuft (**Figure 7B**; AP threshold for Tuft: single = 8.04 ± 0.18 μJ, multiple = 8.82 ± 0.09 μJ, $n = 5$, $P > 0.1$, paired t-test).

We next examined and compared the kinetics of the responses to single- and multibranch excitation at each of the three domains of the pyramidal neuron (**Figure 8A**). Studies were first carried out on individual branches from the three dendritic domains of the same cell (left, **Figure 8A**). For photolytically induced depolarizations at the tuft that were >5–10 mV the durations of the responses at half maximum were largely >100 ms for both single- and multi-branch excitation (**Figures 6–8**). In contrast to the results at the tuft, the duration of depolarizations at the oblique and basal dendrites to strong stimuli were typically longer for single branch excitation (right, **Figure 8A**; **Figures 2** and **5**). Thus, at stimulus evoked depolarizations above the expected threshold for evoking a somatic action potential, the onset and duration of the multibranch oblique and basal responses remained fast and brief. Because of variable activation of repolarizing conductances a more reliable measure of response kinetics is the time to peak depolarization (**Figure 8A**, right panel; One oblique: 50.81 ± 3.37 ms, $n = 20$; One basal: 54.69 +/− 4.9 ms, $n = 9$; One tuft: 66.24 ± 4.24 ms, $n = 13$; Multiple oblique: 23.69 ± 1.27 ms, $n = 15$; Multiple basal: 25.96 ± 3.36 ms, $n = 5$; Multiple tuft: 50.09 ± 3.30 ms, $n = 10$).

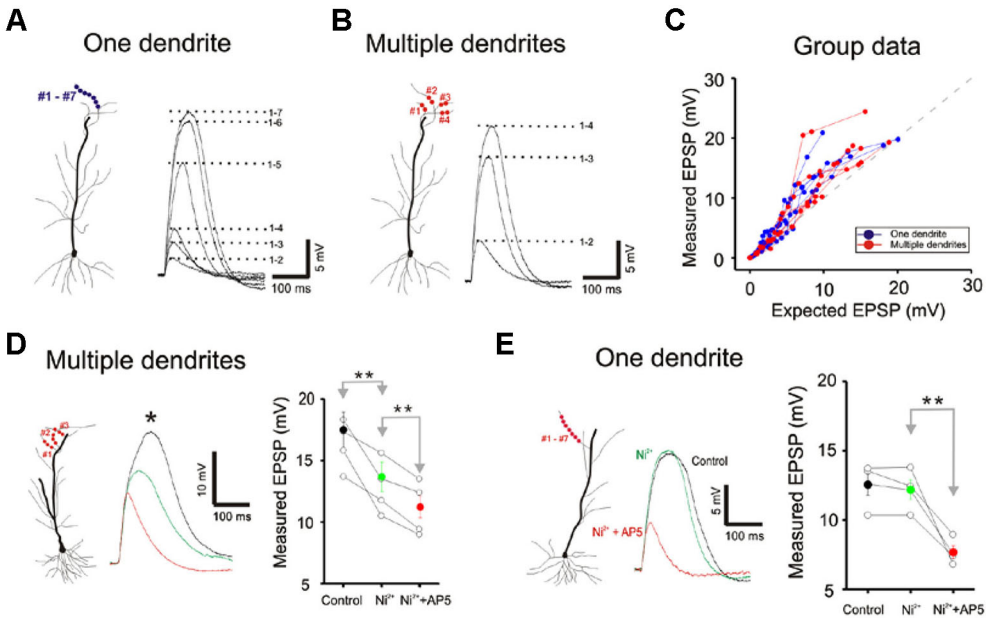

FIGURE 6 | Little difference is apparent between single and multibranch summation in the distal apical tuft. (A) Response of a single distal apical dendrite to progressively increasing number of stimulation spots. **(B)** Response of the same cell to stimulation on multiple dendritic branches. **(C)** Group data from 8 cells. Responses to very strong stimulation levels are not displayed. **(D)** Conductances that contribute to non-linear multibranch integration of tuft. Nickel sensitive calcium conductances contribute partially to the supralinear summation at the multiple tuft dendrites. The remaining component is eliminated with application of AP5. Error bars represent SE. ** $p < 0.05$. **(E)** Conductances that contribute to non-linear single branch integration of tuft. Blockade of the T/R-type calcium channel by the addition of nickel does not affect the supralinear summation at the single tuft dendrites. However, NMDA receptor blocker, AP5 (100 μM) completely eliminate the supralinearity. Error bars represent SE. ** $p < 0.05$.

FUNCTIONAL ADVANTAGE OF MULTIBRANCH INTEGRATION

The tradeoff between response efficiency and kinetics for oblique dendrites predicts that multibranch integration of the oblique dendrites could enable precise entrainment at higher frequencies. In addition, the absence of fast multibranch integration at the tuft suggests that the tuft would not be able to support entrainment at similar high frequencies. We first tested these predictions in the absence of TTX by directing trains of five stimuli at different frequencies at tufts (**Figure 8B**). The stimulus intensity was set at a level that reliably elicits an action potential. The five stimuli were then given at progressively faster frequencies. The highest frequency at which the somatic action potential could still precisely follow the dendritic input (entrainment) was recorded (low trace of each pair of traces in **Figure 8B**). For multiple oblique inputs the entrainment frequency was significantly higher than for tuft inputs (16.7 ± 3.8 vs. 5.7 ± 1.3 Hz, respectively; paired *t*-test, $p < 0.05$). Precise entrainment by multibranch oblique integration was also significantly faster than for single branch integration (16.7 ± 3.8 vs. 2.8 ± 0.4 Hz, $p < 0.05$). We next tested these predictions using electrical stimulation of their respective excitatory pathways in the presence of $GABA_A$ and $GABA_B$ receptor antagonists (10 μM SR 95531 and 10 μM CGP 35348 respectively). Electrical stimulation at intensities strong enough to reliably evoke action potentials it is likely to activate multiple dendritic branches. Consistent with the photostimulation responses, multibranch electrical stimulation of the oblique dendrites led to precise entrainment over a wider frequency range than tuft entrainment. (**Figure 8C**; SC stimulation: 4.9 ± 0.7 Hz; PP stimulation: 2.6 ± 0.5 Hz; paired *t*-test, $n = 6$, $p < 0.05$).

DISCUSSION

This study compared the properties of single- and multibranch integration to complex patterns of photostimulation as a means to probe and compare the global and the two-stage model of dendritic integration. This strategy provided the means to implement non-linear and linear integration at precise locations using clustered and distributed inputs. Non-linear integration is an integral part of both modes of integration. The critical difference lies in their loci of non-linear integration and the active conductances that are recruited at those loci. The results suggest that both global and two-stage integration can drive somatic outputs. Novel findings reported here include the significant differences in the kinetics of dendritic integration response between single- and multibranch integration at the oblique and basal dendrites. Single branch integration possesses a low threshold for evoking a fast sodium- and slow NMDAR-mediated local dendritic spike compared to multibranch integration. But this increased sensitivity is achieved at a cost of response kinetics. This tradeoff between sensitivity and integration kinetics is further confirmed by the finding of significant differences in spike entrainment. Indeed, multibranch integration can precisely entrain somatic action potentials 6-fold faster than single branch integration. It is important to note that the maximal entrainment frequency described here is not the same as the maximal frequency.

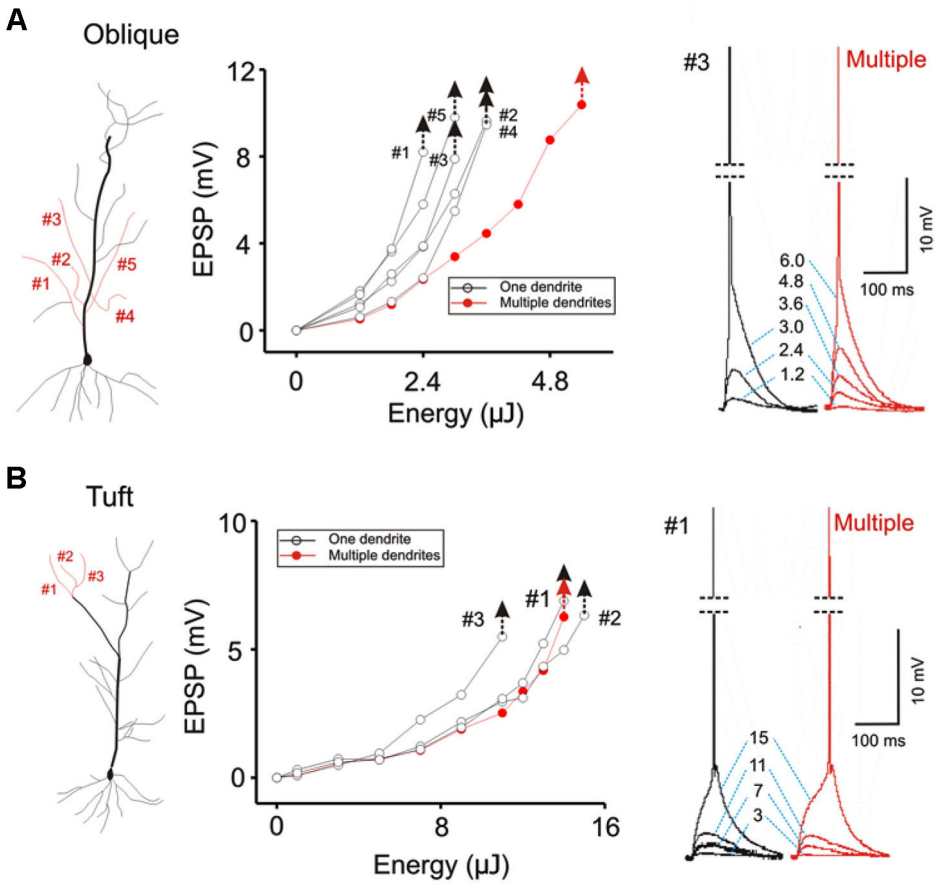

FIGURE 7 | Contrasting modes of integration translates into different thresholds for eliciting action potentials. (A) The threshold for evoking somatic action potential is compared for five oblique dendrites when they are stimulated individually (black hollow circles) and simultaneously (solid red circles). Individual responses for each stimulus intensity are shown on the right. The threshold for single-branch stimulation is about half of that for multi-branch stimulation. The latency between stimulation and the spike is brief. **(B)** The same procedure is repeated for apical tuft dendrites. The threshold for single- and multi-branch stimulation is not significantly different at the tuft. The latency between stimulation and spike is slower.

In fact, the low entrainment frequency to single branch integration is due to the production of additional spikes. It is as if single branch integration is better suited for eliciting bursting responses. This would not be surprising since the degree of recruitment of voltage gated calcium conductances responsible for burst firing increases with the duration of depolarization (Kay and Wong, 1987). Why is this finding significant? It is relevant for an ongoing controversy on a fundamental issue in neuroscience, what is the format of the information that is transmitted in the brain. Is the information being transmitted through "spike timing" or "spike rate" (or the number of spikes)? The findings here suggest that multibranch integration would better preserve the information in spike timing transmission, whereas single branch integration would best optimize information being transmitted via spike rate. Single branch integration provides the input-output transfer function with high dynamic range. The latter would also be well suited for initiating burst firing modes. Our findings do not weigh in on the spike timing vs. spike rate controversy. But they suggest that dendrites of pyramidal neurons have the capacity to support both mode of signal transmission.

A second consistent observation from this study is that the behavior of multibranch integration is domain-specific. Multibranch integration of oblique dendrites is sublinear, whereas multibranch integration of tuft dendrites is supralinear at moderate stimulation intensities. This dichotomy exists even though the response of individual tuft and oblique dendrites are qualitatively indistinguishable. Furthermore, this dichotomy extends to their ability for precise spike entrainment. These observations are not simply a phenomena related to the photolysis technique, since the differences in entrainment were also apparent to synaptic stimulation. The mechanistic basis for the domain specific integration is likely to lie in the expression of different voltage-dependent conductances at the differing loci where distal dendrites converge. At the base of the tuft where the distal tuft branches converge, voltage gated calcium channels are expressed in high densities (Larkum et al., 1999, 2009). The sublinear summation observed for multibranch oblique integration suggests that the recruitment of the A-type potassium conductance at the proximal apical trunk outweighs the recruitment of voltage-gated calcium and NMDA conductances. The preferential recruitment of the

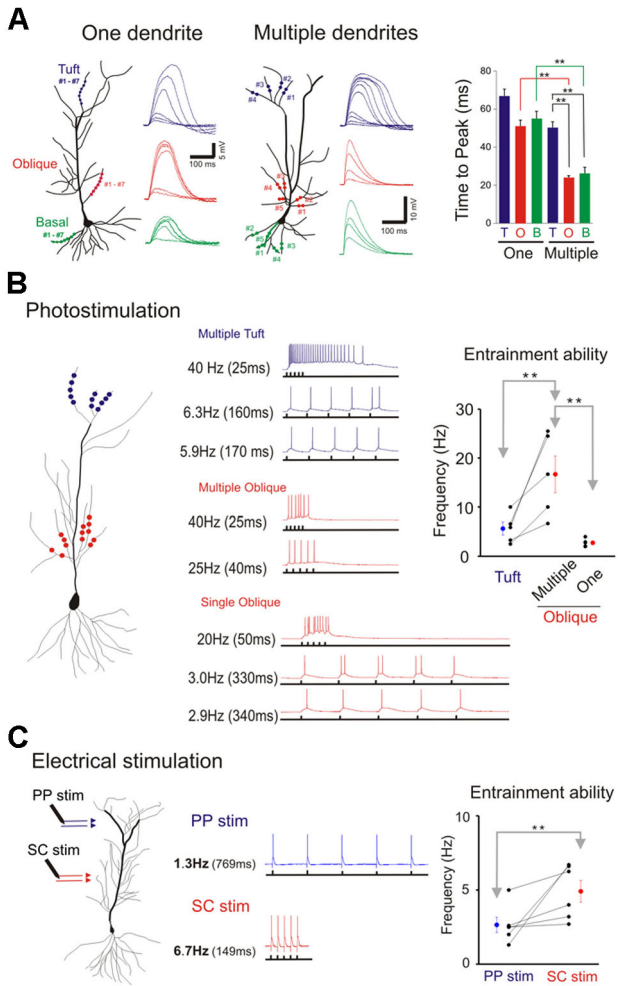

FIGURE 8 | Domain specific response kinetics. (A) Differential response kinetics between single- and multi-branch integration and between different dendritic domains. In the presence of TTX time to peak is significantly slower for single branch integration compared to that for multibranch integration of oblique and basal dendrites (right panel). Error bars represent SE. ** $p < 0.05$. Time to peak is also significantly slow for multibranch integration of the tuft compared to that of oblique and basal dendrites. **(B)** Entrainment properties of tuft vs. oblique dendrites and single vs. multiple dendrites. The five stimuli were given at different frequencies. The highest frequency at which the somatic action potential can still precisely follow the dendritic input (entrainment) is recorded. Multibranch oblique integration had faster entrainment ability than either single branch oblique or multibranch tuft integration. Error bars represent SE. ** $p < 0.05$. **(C)** The differential frequency response between PP (blue) and SC (red) pathway. The highest frequency at which the somatic action potential can still precisely follow the dendritic input (entrainment) is recorded. SC pathway had better entrainment ability than PP pathway. Error bars represent SE. ** $p < 0.05$.

potassium conductance with multibranch oblique integration can be explained simply by the fact that NMDA receptors in the region of dendritic convergence on the apical trunk are not exposed to glutamate, yet the A-type potassium conductances can be activated by distant excitation. This study does not compare the relative expression the A-type conductance on the main apical trunk and on the thin oblique dendrites. On the distal dendrites NMDA and the A-type potassium conductances may be well counter-balanced (Cash and Yuste, 1999; Gasparini and Magee, 2006; Losonczy and Magee, 2006; Losonczy et al., 2008). The differential expression of conductances at the base of the tuft and the proximal apical trunk suggests that the tuft and the oblique dendrites may employ different temporal coding strategies. However, predicting in vivo behavior from in vitro observations must always be done with caution since it is difficult to account for the many presynaptic factors such as feedforward and feedback inhibition that contribute to in vivo behavior.

This study provides an experimental demonstration of a widely held belief that the dendritic arbor can support non-linear integration at multiple locations (Mel, 1993; Schiller et al., 2000; Wei et al., 2001; Polsky et al., 2004; Gasparini and Magee, 2006; Losonczy and Magee, 2006; Johnston and Narayanan, 2008; Major et al., 2008; Larkum et al., 2009; Branco and Hausser, 2011). However, this is the first study to systematically examine the kinetic consequences of supralinear integration at different locations on the dendritic arbor and to demonstrate the tradeoffs between temporal precision and signal amplification. There is no single mode of integration with optimal performance. But the ability to switch between different loci of non-linear integration would provide the flexibility to optimize response to a specific condition. The findings here may be relevant to the controversy on whether information is transmitted in the form of spike timing or spike rate and the contributory role of dendritic integration.

REFERENCES

Abbott, L. F. (1999). Lapicque's introduction of the integrate-and-fire model neuron (1907). *Brain Res. Bull.* 50, 303–304. doi: 10.1016/S0361-9230(99)00161-6

Anselmi, F., Ventalon, C., Begue, A., Ogden, D., and Emiliani, V. (2011). Three-dimensional imaging and photostimulation by remote-focusing and holographic light patterning. *Proc. Natl. Acad. Sci. U S A* 108, 19504–19509. doi: 10.1073/pnas.1109111108

Branco, T., and Hausser, M. (2011). Synaptic integration gradients in single cortical pyramidal cell dendrites. *Neuron* 69, 885–892. doi: 10.1016/j.neuron.2011.02.006

Cash, S., and Yuste, R. (1999). Linear summation of excitatory inputs by CA1 pyramidal neurons. *Neuron* 22, 383–394. doi: 10.1016/s0896-6273(00)81098-3

Gasparini, S., and Magee, J. C. (2006). State-dependent dendritic computation in hippocampal CA1 pyramidal neurons. *J. Neurosci.* 26, 2088–2100. doi: 10.1523/jneurosci.4428-05.2006

Go, M. A., Stricker, C., Redman, S., Bachor, H. A., and Daria, V. R. (2012). Simultaneous multi-site two-photon photostimulation in three dimensions. *J. Biophotonics* 5, 745–753. doi: 10.1002/jbio.201100101

Golding, N. L., and Spruston, N. (1998). Dendritic sodium spikes are variable triggers of axonal action potentials in hippocampal CA1 pyramidal neurons. *Neuron* 21, 1189–1200. doi: 10.1016/s0896-6273(00)80635-2

Häusser, M., and Mel, B. (2003). Dendrites: bug or feature? *Curr. Opin. Neurobiol.* 13, 372–383. doi: 10.1016/s0959-4388(03)00075-8

Jia, H., Rochefort, N. L., Chen, X., and Konnerth, A. (2010). Dendritic organization of sensory input to cortical neurons in vivo. *Nature* 464, 1307–1312. doi: 10.1038/nature08947

Johnston, D., and Narayanan, R. (2008). Active dendrites: colorful wings of the mysterious butterflies. *Trends Neurosci.* 31, 309–316. doi: 10.1016/j.tins.2008.03.004

Katz, Y., Menon, V., Nicholson, D. A., Geinisman, Y., Kath, W. L., and Spruston, N. (2009). Synapse distribution suggests a two-stage model of dendritic integration in CA1 pyramidal neurons. *Neuron* 63, 171–177. doi: 10.1016/j.neuron.2009.06.023

Kay, A. R., and Wong, R. K. (1987). Calcium current activation kinetics in isolated pyramidal neurones of the Ca1 region of the mature guinea-pig hippocampus. *J. Physiol.* 392, 603–616.

Larkum, M. E., Kaiser, K. M., and Sakmann, B. (1999). Calcium electrogenesis in distal apical dendrites of layer 5 pyramidal cells at a critical frequency of back-propagating action potentials. *Proc. Natl. Acad. Sci. U S A* 96, 14600–14604. doi: 10.1073/pnas.96.25.14600

Larkum, M. E., Nevian, T., Sandler, M., Polsky, A., and Schiller, J. (2009). Synaptic integration in tuft dendrites of layer 5 pyramidal neurons: a new unifying principle. *Science* 325, 756–760. doi: 10.1126/science.1171958

Larkum, M. E., and Nevian, T. (2008). Synaptic clustering by dendritic signalling mechanisms. *Curr. Opin. Neurobiol.* 18, 321–331. doi: 10.1016/j.conb.2008.08.013

Losonczy, A., and Magee, J. C. (2006). Integrative properties of radial oblique dendrites in hippocampal CA1 pyramidal neurons. *Neuron* 50, 291–307. doi: 10.1016/j.neuron.2006.03.016

Losonczy, A., Makara, J. K., and Magee, J. C. (2008). Compartmentalized dendritic plasticity and input feature storage in neurons. *Nature* 452, 436–441. doi: 10.1038/nature06725

Lutz, C., Otis, T. S., DeSars, V., Charpak, S., DiGregorio, D. A., and Emiliani, V. (2008). Holographic photolysis of caged neurotransmitters. *Nat. Methods* 5, 821–827. doi: 10.1038/nmeth.1241

Major, G., Polsky, A., Denk, W., Schiller, J., and Tank, D. W. (2008). Spatiotemporally graded NMDA spike/plateau potentials in basal dendrites of neocortical pyramidal neurons. *J. Neurophysiol.* 99, 2584–2601. doi: 10.1152/jn.00011.2008

Mel, B. W. (1993). Synaptic integration in an excitable dendritic tree. *J. Neurophysiol.* 70, 1086–1101.

Nikolenko, V., Watson, B. O., Araya, R., Woodruff, A., Peterka, D. S., and Yuste, R. (2008). SLM microscopy: scanless two-photon imaging and photostimulation with spatial light modulators. *Front. Neural Circuits* 2:5. doi: 10.3389/neuro.04.005.2008

Poirazi, P., Brannon, T., and Mel, B. W. (2003a). Arithmetic of subthreshold synaptic summation in a model CA1 pyramidal cell. *Neuron* 37, 977–987. doi: 10.1016/s0896-6273(03)00148-x

Poirazi, P., Brannon, T., and Mel, B. W. (2003b). Pyramidal neuron as two-layer neural network. *Neuron* 37, 989–999. doi: 10.1016/s0896-6273(03)00149-1

Polsky, A., Mel, B. W., and Schiller, J. (2004). Computational subunits in thin dendrites of pyramidal cells. *Nat. Neurosci.* 7, 621–627. doi: 10.1038/nn1253

Schiller, J., Major, G., Koester, H. J., and Schiller, Y. (2000). NMDA spikes in basal dendrites of cortical pyramidal neurons. *Nature* 404, 285–289. doi: 10.1038/35005094

Takahashi, N., Kitamura, K., Matsuo, N., Mayford, M., Kano, M., Matsuki, N., et al. (2012). Locally synchronized synaptic inputs. *Science* 335, 353–356. doi: 10.1126/science.1210362

Wei, D. S., Mei, Y. A., Bagal, A., Kao, J. P., Thompson, S. M., and Tang, C. M. (2001). Compartmentalized and binary behavior of terminal dendrites in hippocampal pyramidal neurons. *Science* 293, 2272–2275. doi: 10.1126/science.1061198

Winnubst, J., and Lohmann, C. (2012). Synaptic clustering during development and learning: the why, when and how. *Front. Mol. Neurosci.* 5:70. doi: 10.3389/fnmol.2012.00070

Yang, S., Papagiakoumou, E., Guillon, M., de Sars, V., Tang, C. M., and Emiliani, V. (2011). Three-dimensional holographic photostimulation of the dendritic arbor. *J. Neural. Eng.* 8:046002. doi: 10.1088/1741-2560/8/4/046002

Yuste, R. (2011). Dendritic spines and distributed circuits. *Neuron* 71, 772–781. doi: 10.1016/j.neuron.2011.07.024

Conflict of Interest Statement: The authors declare that the research was conducted in the absence of any commercial or financial relationships that could be construed as a potential conflict of interest.

Received: 20 December 2013; accepted: 22 April 2014; published online: 13 May 2014.
Citation: Yang S, Emiliani V and Tang C-M (2014) The kinetics of multibranch integration on the dendritic arbor of CA1 pyramidal neurons. Front. Cell. Neurosci. ***8****:127. doi: 10.3389/fncel.2014.00127*
This article was submitted to the journal Frontiers in Cellular Neuroscience.

frontiers in
COMPUTATIONAL NEUROSCIENCE

ORIGINAL RESEARCH ARTICLE
published: 09 September 2014
doi: 10.3389/fncom.2014.00110

Neuromodulation impact on nonlinear firing behavior of a reduced model motoneuron with the active dendrite

Hojeong Kim*[1,2] *and C. J. Heckman*[2,3,4]

[1] *Division of Robotics Research, Daegu Gyeongbuk Institute of Science and Technology, Daegu, South Korea*
[2] *Department of Physiology, Northwestern University, Chicago, IL, USA*
[3] *Department of Physical Medicine and Rehabilitation, Northwestern University, Chicago, IL, USA*
[4] *Department of Physical Therapy and Human Movement Science, Northwestern University, Chicago, IL, USA*

Edited by:
Sergey M. Korogod, National Academy of Sciences of Ukraine, Ukraine

Reviewed by:
Gennady Cymbalyuk, Georgia State University, USA
Maria Piotrkiewicz, Polish Academy of Sciences, Poland

***Correspondence:**
Hojeong Kim, Division of Robotics Research, Daegu Gyeongbuk Institute of Science and Technology, 50-1, Sang, Daegu 711-873, South Korea
e-mail: hojeong.kim03@gmail.com

Neuromodulatory inputs from brainstem systems modulate the normal function of spinal motoneurons by altering the activation properties of persistent inward currents (PICs) in their dendrites. However, the effect of the PIC on firing outputs also depends on its location in the dendritic tree. To investigate the interaction between PIC neuromodulation and PIC location dependence, we used a two-compartment model that was biologically realistic in that it retains directional and frequency-dependent electrical coupling between the soma and the dendrites, as seen in multi-compartment models based on full anatomical reconstructions of motoneurons. Our two-compartment approach allowed us to systematically vary the coupling parameters between the soma and the dendrite to accurately reproduce the effect of location of the dendritic PIC on the generation of nonlinear (hysteretic) motoneuron firing patterns. Our results show that as a single parameter value for PIC activation was either increased or decreased by 20% from its default value, the solution space of the coupling parameter values for nonlinear firing outputs was drastically reduced by approximately 80%. As a result, the model tended to fire only in a linear mode at the majority of dendritic PIC sites. The same results were obtained when all parameters for the PIC activation simultaneously changed only by approximately ±10%. Our results suggest the democratization effect of neuromodulation: the neuromodulation by the brainstem systems may play a role in switching the motoneurons with PICs at different dendritic locations to a similar mode of firing by reducing the effect of the dendritic location of PICs on the firing behavior.

Keywords: neuromodulation, motoneurons, nonlinear firing, persistent inward current, reduced modeling, computer simulation

INTRODUCTION

Spinal motoneurons have large, highly branched dendrites and voltage-gated ion channels that generate strong persistent inward currents (PICs) (Schwindt and Crill, 1980). Over the past 30 years, the impact of PICs on the firing output of the motoneurons has been extensively investigated in various species, including turtles (Hounsgaard and Kiehn, 1985, 1989), rats (Bennett et al., 2001; Li and Bennett, 2003), mice (Carlin et al., 2000; Meehan et al., 2010) and cats (Lee and Heckman, 1998, 1999). There has been a consensus in the motoneuron physiology community that in the presence of monoamines (i.e., norepinephrine and serotonin), the activation of the L-type Ca^{2+} PIC channels is facilitated, producing a long-lasting membrane depolarization (i.e., plateau potential) (reviewed in Powers and Binder, 2001; Heckman et al., 2008). The spatiotemporal interaction between the spike-generating channels at the soma and the plateau-generating PIC channels at the dendrites, may be the mechanism underlying the nonlinear (e.g., bistable) firing of the motoneurons.

The firing patterns of the motoneurons have been characterized experimentally using slowly rising and falling current stimulation to the soma. Four types of firing have been identified during this triangular current clamp, characterized by the relationship between their frequency and current intensity (F-I) (Bennett et al., 2001; Button et al., 2006; Cotel et al., 2009): Type I, a linearly overlapped F-I curve; Type II, lower firing rates during the falling phase than during the rising phase of the stimulation, showing clockwise hysteresis for the F-I curve; Type III, a linearly overlapped F-I curve with sustained firing on the descending phase of the stimulation below the threshold for spike initiation; and Type IV, higher firing rates during the falling phase than during the rising phase of the stimulation, showing counterclockwise hysteresis for the F-I curve, with sustained firing behavior. Type IV firing has also been referred to as "fully bistable" firing, whereas when the plateau potential is deactivated at a higher current level during the descending stimulation phase than the threshold for spike initiation, Type IV firing has been called "partially bistable" (Lee and Heckman, 1998). In particular, the Type III and IV firing patterns have been associated with the activation of plateau potentials mediated by the PIC channels in the dendrites. In the present study, the terms "fully hysteretic" and "partially hysteretic" were used for

Type IV firing instead of "fully bistable" and "partially bistable" due to their compound meaning from a dynamic systems perspective.

The location of the PIC channels is a crucial factor for generating nonlinear (i.e., fully hysteretic Type IV) firing in motoneurons. Many experimental and computational studies have suggested that the PIC channels must not be uniformly distributed but rather clustered near the middle (i.e., 300–600 μm from the soma) of the dendrites for fully hysteretic, Type IV firing patterns (Hounsgaard and Kiehn, 1993; Carlin et al., 2000, 2009; Elbasiouny et al., 2005; Ballou et al., 2006; Bui et al., 2006). In our recent computational studies (Kim and Jones, 2011, 2012; we have further demonstrated 1) that the types of firing patterns (I–IV) can be generated by simply changing the dendritic location of a constant amplitude PIC and 2) that these location-dependent effects of firing depend on the attenuation of voltage along the dendrites and that both the dendrite-to-soma and soma-to-dendrite attenuation behaviors are important.

Another factor that may play a critical role in determining the firing output is the neuromodulatory inputs (in particular monoamines) from the brainstem to the motoneurons. The primary effect of neuromodulation is a profound facilitation of PIC activation, presumably via G-protein-mediated signaling pathways (Hille, 2001), which leads to an increase in the intrinsic excitability of the motoneuron dendrites. However, it remains unclear how the interplay between the neuromodulation effect and the PIC location influences the firing dynamics of the motoneurons. In this study, we used our recently developed reduced modeling approach, which allowed us to explicitly manipulate these two key factors determining the nonlinear dynamics of the motoneurons: *location* and *neuromodulation effect on the PIC*.

MATERIALS AND METHODS

THE CONDUCTANCE-BASED, REDUCED NEURON MODEL

The structure of the neuron model used in this study is similar to the conventional two-compartment model, which consists of the somatic and dendritic compartments, coupled by electrotonic coupling. Each compartment can be characterized separately by its specific membrane conductance ($G_{m,S}$ and $G_{m,D}$) and capacitance ($C_{m,S}$ and $C_{m,D}$), and connected together via a coupling conductance (G_C). The major difference from the conventional reduced modeling approach is that five passive parameters ($G_{m,S}$, $G_{m,D}$, $C_{m,S}$, $C_{m,D}$, and G_C) of our reduced model can be analytically determined to retain five system properties obtained from the anatomically reconstructed motoneuron: input resistance (R_N), membrane time constant (τ_m) and three voltage attenuation (VA) factors between the soma and the dendrites:

- VA_{SD}^{DC} is the ratio ($V_{dendrite}/V_{soma}$) of voltage at the dendrites to voltage at the soma for DC input at the soma.
- VA_{SD}^{AC} is the ratio ($V_{dendrite}/V_{soma}$) of voltage at the dendrites to voltage at the soma for AC input at the soma.
- VA_{DS}^{DC} is the ratio ($V_{soma}/V_{dendrite}$) of voltage at the dendrites to voltage at the soma for DC input at the dendrites.

The five system properties are related analytically to the five cable parameters of the reduced model as follows,

$$G_{m,S} = \frac{1 - VA_{DS}^{DC}}{r_N(1 - VA_{SD}^{DC}VA_{DS}^{DC})}$$

$$G_{m,D} = \frac{pVA_{DS}^{DC}(1 - VA_{SD}^{DC})}{(1-p)r_N VA_{SD}^{DC}(1 - VA_{SD}^{DC}VA_{DS}^{DC})}$$

$$G_C = \frac{pVA_{DS}^{DC}}{r_N(1 - VA_{SD}^{DC}VA_{DS}^{DC})}$$

$$C_{m,D} = \frac{1}{\omega(1-p)}\sqrt{\frac{G_C^2}{\left(VA_{SD}^{AC}\right)^2} - \left\{G_C + G_{m,D}(1-p)\right\}^2}$$

$$C_{m,S} = \frac{\tau_m\left\{p\left(1-p\right)\tau_m G_{m,S}G_{m,D} + pG_{m,S}\left(\tau_m G_C - C_{m,D}\right) + p^2 G_{m,S}C_{m,D} + \left(1-p\right)\left(\tau_m G_C G_{m,D} - G_C C_{m,D}\right)\right\}}{p\left\{\left(1-p\right)\left(\tau_m G_{m,D} - C_{m,D}\right) + \tau_m G_C\right\}}$$

where r_N is the input resistance (R_N) normalized with the surface area of the somatic compartment; ω is the maximum frequency component in an action potential; p is the ratio of somatic to total surface area of the reduced model. In the present study, the values of r_N (0.198), τ_m (10.4), p (0.168). and ω ($2\pi \times 250$) were calculated based on the experimental data and set to be constant for simulations (Kim and Jones, 2012).

The calculation of the system properties from the anatomical model and the derivation of inverse equations for the cable parameters of the reduced model were fully presented in our previous studies (Kim et al., 2009; Kim and Jones, 2012). The Morris-Lecar type of membrane excitability was added to the soma to generate the spikes mediated by lumped inward current (represents fast Na^+) and outward current (represents delayed rectified K^+) and to the dendrite to produce the plateau potentials mediated by the L-type Ca^{2+} and K^+ currents.

The somatic (V_S) and dendritic (V_D) membrane potential responses to the somatically injected current (I_S) were governed by the following current-balance equation at the somatic compartment,

$$C_{m,S}\dot{V_S} = -G_{m,S}(V_S - E_{Leak}) - \frac{G_C}{p}(V_S - V_D) - G_{Na} m_{S\infty}(V_S - E_{Na}) - G_{K,S}n_S(V_S - E_K) + I_S \quad (1)$$

$$m_{S\infty}(V_S) = 0.5\left(1 + \tanh\frac{V_S + 0.01}{0.15}\right) \quad (2)$$

$$\dot{n_S} = 0.2\left(\frac{n_{S\infty}(V_S) - n_S}{\tau_S(V_S)}\right) \text{ where}$$

$$n_{S\infty}(V_S) = 0.5\left(1 + \tanh\frac{V_S + 0.04}{0.1}\right),$$

$$\tau_S(V_S) = \left(\cosh\frac{V_S + 0.04}{0.1}\right)^{-1} \quad (3)$$

and the dendritic compartment,

$$C_{m,D}\dot{V_D} = -G_{m,D}(V_D - E_{Leak}) - \frac{G_C}{1-p}(V_D - V_S) - G_{Ca}m_D(V_D - E_{Ca}) - G_{K,D}n_D(V_D - E_K) \quad (4)$$

$$\dot{m_D} = 0.2\left(\frac{m_{D\infty}(V_D) - m_D}{\tau_{mD}(V_D)}\right) \text{ where}$$

$$m_{D\infty}(V_D) = 0.5\left(1 + \tanh\frac{V_D - V_{1D}}{V_{2D}}\right),$$

$$\tau_{mD}(V_D) = \left(\cosh\frac{V_D - 0.07}{0.1}\right)^{-1} \quad (5)$$

$$\dot{n_D} = 0.2\left(\frac{n_{D\infty}(V_D) - n_D}{\tau_{nD}(V_D)}\right) \text{ where}$$

$$n_{D\infty}(V_D) = 0.5\left(1 + \tanh\frac{V_D}{0.1}\right),$$

$$\tau_{nD}(V_D) = \left(\cosh\frac{V_D}{0.1}\right)^{-1} \quad (6)$$

where the subscripts S and D indicate the soma and dendrite; The initial values for maximum conductances of active currents were $G_{Na} = 11.0$, $G_{K,S} = 14.0$, $G_{Ca} = 0.89$, and $G_{K,D} = 0.44$; m and n are activation functions for inward and outward active currents; The reversal potentials for individual ions were $E_{Na} = 1.0$, $E_K = -0.7$, $E_{Ca} = 1.0$, and $E_{Leak} = -0.5$; The initial values for the half-activation voltage and one over the slope of the activation curve for the voltage-gated Ca^{2+} current at the dendrite were current at the dendrite were $V_{1D} = 0.07$ and $V_{2D} = 0.1$. All parameter values were adopted from our previous model that produced fully hysteretic, Type IV firing. The numbers are dimensionless, unless otherwise stated (see the dimensionless analysis in Rinzel and Ermentrout, 1998).

SIMULATIONS

The firing behavior of the reduced model was simulated by applying the triangular current stimulation (peak of 2.5 with a duration of 3000) to the soma. The simulation was performed while varying individual VA factors independently over a full range (0∼1). To facilitate the process of identifying the firing types (i.e., Type I–IV) during simulations, three characteristic indices (CIs) were defined based on spike trains and firing frequency (see the bottom panel in **Figure 1A** for graphical explanation):

- Time To onset of Plateau potential (TTP): this index measures the latency between the first somatic action potential and the onset of the dendritic plateau potential. If this value is positive, the onset of the plateau potential follows the first somatic spike. If the value is negative, the plateau potential precedes somatic spiking.
- Time to End of somatic Spiking (TES): this index measures the duration of spiking during the downward phase of current stimulation relative to the current threshold from the upward phase. If this value is positive, somatic spiking persists past the spiking threshold on the upward phase. If the value is negative, spiking stops before reaching the threshold determined on the upward phase of stimulation.
- Difference in Spiking Frequency (DSF): this index measures the difference in instantaneous spiking frequency at the current threshold determined on the upward phase of stimulation. If this value is positive, the firing frequency is greater on the downward phase and indicates counter-clockwise frequency hysteresis. If this value is negative, spiking frequency on the downward phase is less or repetitive spiking has ceased.

The signs of individual CIs were operationally evaluated to determine the firing type while varying individual VA factors. For instance, the Type I–III firing behavior could be detected when [TTP = 0, DSF = 0, TES = 0], [TTP = 0, DSF < 0, TES = 0] and [TTP = 0, DSF = 0, TES > 0], respectively. Notably, the Type IV firing of particular interest displayed all positive CIs.

All of the sets of VA factor values that produced the same firing type with the reduced model were plotted as points in the three-dimensional (3D) VA space defined as x = VA_{DS}^{DC}, y = VA_{SD}^{DS}, and z = VA_{SD}^{AC}. To map the VA space on the physical locations of the dendritic trees, five type-identified motoneurons were fully reconstructed in the NEURON environment. The physiological data for each VA factor were measured as a function of the distance (D_{path}) from the soma of the anatomical motoneuron models and fitted to a single exponential function [i.e., $\exp(-D_{path}/\eta)$] to represent the spatial profile of the voltage attenuation with the single parameter (η). Using the fitting functions (η = {2680.6, 3059.5, 2758, 1941, 2145.8} for VA_{SD}^{DC}, {224.2, 144.7, 119.5, 143.9, 190.8} for VA_{DS}^{DC}, and {420.1, 437.1, 402.3, 373.1, 464.7} for VA_{SD}^{AC}), the mean for individual VA factors (VA_{SD}^{DC}, VA_{DS}^{DC}, VA_{SD}^{AC}) was investigated as a function of D_{path} for the VA data. The physiological VA data were represented by plotting their mean values in the 3D VA space with assumption of normal distribution of physiological VA values at a specific distance from the soma (see thick solid lines, **Figures 2**, **4**). All details about the anatomical model reconstruction and VA analysis were fully addressed in our previous studies (Kim et al., 2009; Kim and Jones, 2012). The dendritic locations of PIC channels for generating the Type IV (fully hysteretic) firing were estimated by superimposing the physiological VA data associated with the distance on the solution VA space for the Type IV firing in the 3D VA space.

The facilitating effect of monoaminergic neuromodulation on the activation of the PIC in the dendrites was simulated by varying either individual or all three activation parameters [i.e., G_{Ca} V_{1D}, V_{2D}, and in Equations (4) and (5)] of CaPIC channels in the dendrite from −100 to 100% of their standard values. Given the activation parameter values for the CaPIC channel, all sets of VA factor values that produced positive values for the three CIs were plotted in the VA space. The variation in the dendritic locations of the PIC channels for the Type IV firing under neuromodulatory effects was evaluated recognizing the intersection area between the theoretical VA solution and the physiological VA data in the VA space.

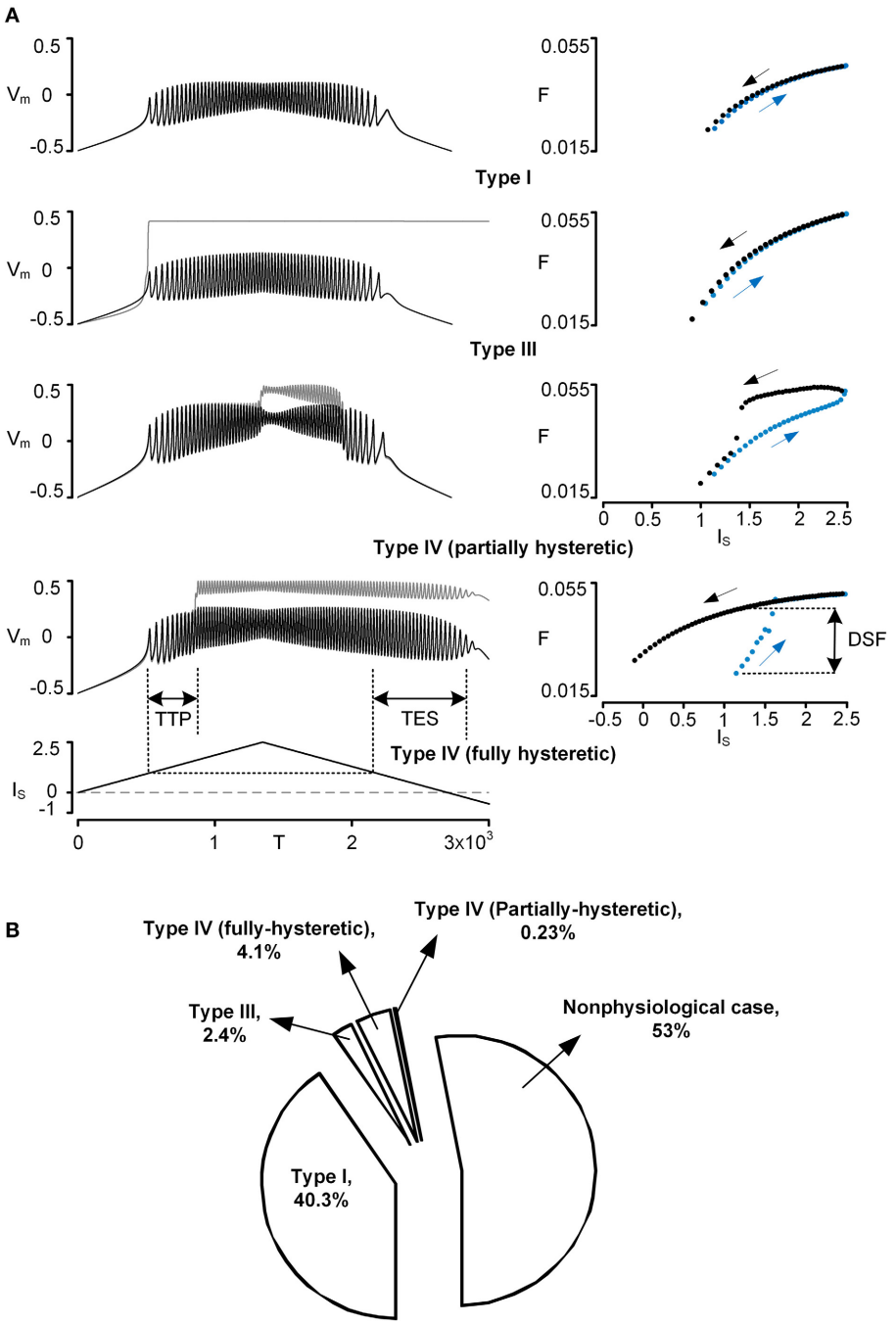

FIGURE 1 | Physiological firing patterns of a reduced motoneuron model. Firing patterns were simulated while systematically varying three VA factors over a whole range of values (0–1). **(A)** Four examples of physiological firing types (Types I–IV): time courses of voltage responses (V_m) of the soma (black solid lines) and the dendrite (gray solid lines) to the triangular current stimulation (I_S) to the soma (left column) and the corresponding frequency-current (F–I_S) curves (blue and black dots for ascending and descending phase of the current stimulation, right column). To automatically process the detection of firing types during simulations, the three characteristic indexes (TTP, TES, DSF) were defined based on both V_m–I_S and F–I_S responses; TTP, TES, and DSF indicate time to onset of plateau potential, time to end of somatic spiking, and difference in spiking frequency, respectively. For instance, Type I firing was detected when all characteristic indexes were zero, whereas Type IV firing (fully hysteretic) was detected when all characteristic indexes were positive. Note that V_m, I_S, T, and F are dimensionless. The values of VA factors (VA_{SD}^{DC}, VA_{DS}^{DC}, VA_{SD}^{AC}) and cable parameters ($G_{m,S}$, $G_{m,D}$, G_C, $C_{m,S}$, $C_{m,D}$) for the reduced models are (0.97, 0.63, 0.84) and (4.805, 0.051, 1.375, 49.499, 0.626) for Type I firing, (0.65, 0.003, 0.08) and (5.045, 0.002, 0.003, 52.425, 0.024) for Type III firing, (0.96, 0.57, 0.81) and (4.796, 0.054, 1.068, 49.952, 0.542) for Type IV (partially hysteretic) firing, and (0.94, 0.38, 0.69) and (4.871, 0.039, 0.502, 50.772, 0.378) for Type IV (fully hysteretic) firing. **(B)** Pie chart: the size of the individual pieces corresponds to the number of points in the VA space at which the model produces the specific firing types. Nonphysiological case indicates when there is no real solution for the model parameter values or no spiking at all (see Kim and Jones, 2012, for the full description).

RESULTS

PIC LOCATION DEPENDENCY OF PHYSIOLOGICAL FIRING PATTERNS IN THE REDUCED MODEL

Firing patterns of the reduced model were simulated with triangular current stimulation to the soma while varying individual voltage attenuation (VA) factors (i.e., VA_{SD}^{DC}, VA_{DS}^{DC}, and VA_{SD}^{AC}). We first evaluated the capability of the reduced model to produce physiological firing patterns that have been observed experimentally from spinal motoneurons. Based on the results from the VA analysis, the locations of the persistent inward current (PIC) for individual firing patterns were then estimated as a function of the path length from the soma by comparing the VA factor values with those measured from the anatomically reconstructed motoneuron models.

Model capability for generating physiological firing patterns

Four types of five physiologically observed firing patterns [i.e., Type I–III and IV (fully and partially hysteretic) except Type II] could be explicitly reproduced by the reduced model during the computer simulations (**Figure 1A**). When the PIC in the dendrite was not activated during the stimulation, the reduced model produced Type I firing with a linearly overlapped F-I relation and without sustained firing in the descending phase of the current stimulation below the rheobase for spike initiation. When the dendritic PIC was activated near the current threshold for spike initiation in the ascending stimulation phase, the reduced model displayed Type III firing, giving a linearly overlapped F-I relation with sustained firing in the descending phase. The Type IV (fully hysteretic) firing, with a counter-clockwise F-I relation with sustained firing, was detected when the onset and offset of the PIC was delayed relative to the spike initiation during the ascending and descending stimulation phase. At a limited range of the voltage attenuation factors near their default values, the PIC during the ascending stimulation phase was deactivated in the descending phase prior to reaching the current threshold for the initiation of action potentials, showing a partially hysteretic Type IV firing pattern. The reduced model rarely produced Type II firing (characterized with the strong clockwise frequency-current relationship without sustained firing) while varying only the voltage attenuation properties between the soma and the dendrite. This result suggests that the location of the PIC channels in the dendrites may not be a main factor of generating Type II firing, supporting the idea that a slow adaptation of firing rate, mediated by active currents at the soma, could be the main mechanism underlying Type II firing (Iglesias et al., 2011).

Overall, the firing patterns produced by the reduced model during the variation of the VA factors were categorized as 40.3% Type I, 2.4% Type III, 4.1% fully hysteretic Type IV, 0.23% partially hysteretic Type IV firing, and 53% nonphysiological (**Figure 1B**). The distribution of the VA factor values associated with individual firing types in the 3D VA space was graphically presented along with the physiological VA data in the next section. Briefly, Type I firing tended to be generated as the VA_{SD}^{DC} decreased, the VA_{DS}^{DC} increased, and the VA_{SD}^{AC} decreased from their default values. Type III firing was found where the VA_{SD}^{DC} and VA_{SD}^{AC} were much greater than the VA_{DS}^{DC}. Type IV firing, characterized at the default values of three voltage attenuation factors, was much more sensitive to variation of the VA_{SD}^{DC} than the other voltage attenuation factors.

Spatial relationship of the firing types

In physiological conditions, the three VA factors characterized between the soma and all individual points of the dendrites are not free parameters to be independently varied but are tightly constrained by the path length from the soma of the cell (Hausser et al., 2000; Bui et al., 2003; Kim and Jones, 2012). For instance, all three VA factors of motoneurons have the same value of 1 at the soma and exponentially decay with increasing distance toward the dendritic terminals depending on the propagation direction and frequency of the signal. To infer the physical locations of the CaPIC channels at which the reduced model generated one of the four firing types, we superimposed the VA factors measured from five anatomically reconstructed motoneurons on the 3D VA space in which each point represented a set of the three VA factor values (**Figure 2**).

Figure 2 shows that the reduced motoneuron model is capable of producing all four firing types shown in **Figure 1** within the physiological range of the VA factors, depending on the location of the PIC. The physiological VA data obtained from the anatomically reconstructed motoneuron models were superimposed over the VA space where the reduced model produces fully hysteretic Type IV firing (**Figure 2A**). Based on the spatial relationship of the physiological VA factors with the distance from the soma, the fully hysteretic Type IV (i.e., counterclockwise F-I curve with sustained firing) was found to be generated in the intermediate range between 88 μm and 685 μm as reported previously (Elbasiouny et al., 2005; Ballou et al., 2006; Bui et al., 2006). Similarly, the overlap of the physiological VA data on the VA spaces for Type I, III, and IV (partially hysteretic) firing indicated the spatial relationship between the individual firing types and the location of PIC channels in the dendrites (**Figure 2B**). The partially hysteretic Type IV was evoked at the very limited range of the distance, which was just around the lower bound of the distance range for the fully hysteretic Type IV firing. The Type I (i.e., linearly overlapped F-I curve) firing tended to occur when the PIC channels were placed at proximal sites (<88 μm) to the soma, whereas the Type III (i.e., linearly overlapped F-I curve with sustained firing) was produced at distal sites (>685 μm) to the soma.

In addition, the tendency of the Type I firing (without PIC activation) at the region proximal to the soma and the Type III firing (with PIC activation) at the distal area of the dendrites indicates that the excitability of the dendrites increases as the PIC channel moves toward dendritic terminals from the soma. The increasing excitability of the dendrites with increasing distance may be attributed to the increasing input resistance of the dendrites with the distance (Kim et al., 2009).

The shape of the nonlinear firing pattern was potentially adjustable depending on the PIC location in the dendrites. For instance, the extent of the counterclockwise hysteresis of the Type IV firing was maximized at the proximal distance of 88 μm, whereas it was minimized at the distal distance of 685 μm to the soma (see Figure 6 in Kim and Jones, 2012). All these results emphasize the importance of PIC channel location over the dendritic trees in determining the firing patterns of the motoneurons.

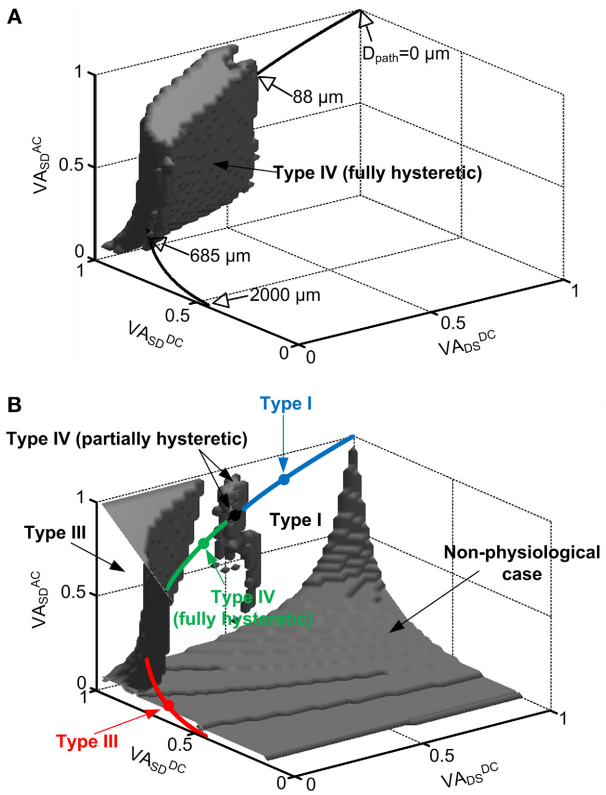

FIGURE 2 | Location dependent firing patterns of a reduced motoneuron model. The gray volumes in the 3D VA space indicate the values of the VA factors with which the reduced model generated: fully hysteretic Type IV firing **(A)** showing all positive characteristic indexes, Type III firing in the upper-left corner **(B)**, partially hysteretic Type IV firing in the upper-middle region **(B)**, and nonphysiological case in the lower-right corner **(B)** where cable parameters are negative or somatic capacitance to produce system time constant does not exist. The rest space outside the gray volumes represents the VA values for Type I firing. In both **(A,B)**, the physiological VA factors obtained at all distances (D_{path}) from the soma of the anatomical motoneuron models were mapped on the same VA space by statistically plotting their mean values (thick solid lines). The open arrows indicate the physical locations (D_{path}) of the CaPIC channel in the 3D VA space, whereas the close arrows indicate the firing types that the reduced model can produce with the physiological values of the VA factors. The four closed circles (blue, black, green, red) on the line for the mean of physiological VA data indicate the points where the reduced model produces Type I, IV (partially hysteretic), IV (fully hysteretic) and III firing shown in **Figure 1A**. The blue, green and red sold line show the region of physiological VA factors for Type I, IV (fully hysteretic) and III firing, respectively. Note that in the physiological case, all three VA factors are 1 at the soma ($D_{path} = 0$) and decrease approaching the dendritic terminals ($D_{path} = 2000\,\mu m$).

NEUROMODULATION EFFECTS ON PIC LOCATION DEPENDENCE OF THE FIRING PATTERNS

Because the molecular mechanisms underlying the neuromodulatory facilitation of PIC activation are still unclear, we first evaluated how individual activation properties of the CaPIC channel in the dendrite influence the PIC characteristics that have been experimentally measured at the soma. Then, the spatial relation of the firing behavior (i.e., Type I–IV) to the PIC locations was reevaluated while varying the activation properties of the CaPIC channel.

Dependence of PIC characteristics on CaPIC activation properties

The effects of monoaminergic neuromodulation on the PIC (I_{PIC}) characterized at the soma were simulated by modulating three activation parameters (i.e., G_{Ca}, V_{1D}, and V_{2D}) that govern the dynamics of the L-type Ca^{2+} channel in the dendrite of the reduced model (**Figure 3**). The activation parameters were varied by ±20% from their initial values when they were considered individually or by ±10% when all of the parameter values were changed at the same time. The percentage of variation in the activation parameter values was determined to match the physiological variation of the I_{PIC} peak that has been observed experimentally (approximately 31% increased at an enhanced level of neuromodulation and 41% decreased at a reduced level, compared with a moderate level of neuromodulation) (Lee and Heckman, 2000). As expected, an increase in G_{Ca} (maximum conductance of the L-type Ca^{2+} channel) and V_{2D} (one over the slope of the activation curve for the L-type Ca^{2+} channel) produced excitatory effects lowering the voltage threshold for the PIC activation and increasing the PIC amplitude (bottom panel of **Figures 3A,C**), whereas an increase in V_{1D} (half activation voltage of the activation curve for the L-type Ca^{2+} channel) caused inhibitory effects increasing the voltage threshold for the activation of the dendritic PIC and lowering the PIC amplitude (**Figure 3B**). Similar results were obtained when these three activation parameters were varied simultaneously to produce the same effect on the activation of the PIC (**Figure 3D**). Prior to its activation at the reduced level of neuromodulation, a positive I_{PIC} was found in all four cases (**Figures 3A–D**), indicating an increase in the net outward current due to the decrease in PIC by downgraded neuromodulation. At each level of neuromodulation, no significant difference was found in the onset timing and amplitude of the I_{PIC} during the rising phase of the stimulation between the four manipulations (i.e., change in G_{Ca}, V_{1D}, V_{2D} or all). This result indicates that varying the individual activation parameters of the CaPIC channel in the same inhibitory or excitatory direction has similar effects on the activation of the PIC, when measured at the soma.

Influence of neuromodulation on the spatial relationship of the firing types

Figure 4 demonstrates how varying the PIC activation parameters influences the range of PIC locations over which the reduced motoneuron model can produce distinctive firing types. Overall, the VA space (i.e., gray area in **Figure 2**), where the reduced model produced the nonlinear firing (i.e., fully hysteretic Type IV) at a moderate level of neuromodulation, dramatically shrank and shifted along the VA_{SD}^{DC} axis in the 3D VA domain, depending on the inhibitory or excitatory effect of the CaPIC parameter variation on the I_{PIC}.

When neuromodulation was decreased by decreasing the PIC's V_{1D} (**Figure 4A2**) or increasing its V_{2D} (**Figure 4B1**) by 20%, the solution space for Type IV firing on the 3D VA plot was significantly reduced and moved downward along the VA_{SD}^{DC} axis.

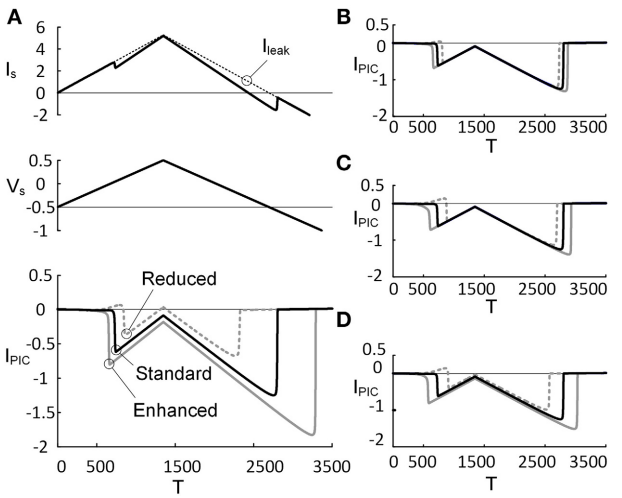

FIGURE 3 | PIC characteristics depending on PIC activation property. Three activation parameters (G_{Ca}, V_{1D}, and V_{2D}) underlying the CaPIC activation were varied individually **(A–C)** or all together **(D)** at three different levels (reduced, standard, enhanced) of neuromodulation. **(A)** A triangular voltage clamp (V_s, middle) was applied at the soma and measured the total current (I_S, top) injected to follow up the voltage command (V_s). PIC (I_{PIC}, bottom) was calculated by subtracting I_S (solid line, top) from the leak current (I_{leak}, dotted line, top). The gray dotted, black solid, and gray solid lines indicate PICs with G_{Ca} reduced by 20%, default value and increased by 20%, respectively. **(B–D)** The same simulation protocol for A was applied for other parameters: V_{1D} **(B)**, V_{2D} **(C)**, and all three parameters **(D)**. Note that at the third case, the individual parameters were varied by 10% in the same direction (inhibiting or facilitating the PIC activation).

Consequently, the reduced model was only capable of generating Type III firing patterns at most dendritic locations of PIC channels. In contrast, an increase in neuromodulation by increasing V_{1D} (**Figure 4A1**) or by decreasing V_{2D} (**Figure 4B2**) by 20% caused the solution space for the Type IV firing to move upward along the VA_{SD}^{DC} axis, leading to a significant reduction in the range of the PIC location for Type IV firing of 66 or 74%, relative to the default values. In this case, the reduced model could produce Type I firing only at the distances from the soma outside the reduced range of the PIC location for Type IV firing.

Varying G_{Ca} showed a larger impact on the size and location of the VA region for the Type IV firing of the reduced model. The CaPIC channel locations for Type IV firing almost disappeared when the value of G_{Ca} was either increased (**Figure 4C1**) or decreased (**Figure 4C2**) by 20%. Consequently, the reduced model could display only two firing modes, Type I or Type III, depending on the modulation level (reduced or enhanced) regardless of PIC channel positions in the dendrites.

Furthermore, when all PIC activation parameters were simultaneously modulated by 10% to either increase (**Figure 4D1**) or decrease (**Figure 4D2**) the excitability of the PIC in the dendrites, the location and the size of the Type IV firing space was shifted further away from the physiological voltage attenuation data and decreased more severely than for the case where individual PIC activation parameters were changed independently.

All simulation results suggest that any variation of neuromodulation, either enhancement or reduction, may lead to a significant reduction in the dendritic sites of the CaPIC for Type IV firing, indicating an alleviation of the PIC location effect on the firing behavior.

THE ROBUSTNESS OF THE REDUCED MODEL FOR THE NONLINEAR FIRING UNDER NEUROMODULATORY CONTROL

Having shown the effects of neuromodulation on the nonlinear firing behavior of the reduced model, within the physiological range of the variation in the I_{PIC}, we further extended the VA analysis to a broader range of activation parameter values (±100% from default values) to evaluate how robustly the reduced model can produce the nonlinear firing behavior. The robustness of the reduced model for the nonlinear firing was indirectly evaluated by counting the number of points in the VA space where the reduced model produced Type IV firing patterns.

Figure 5 shows that the robustness of the reduced model for the Type IV firing is sharply reduced when the excitability of the dendrites is increased or decreased. In general, the reduced robustness of the model was more severe when the activation parameters varied in the inhibitory direction. Whether individual parameter values decreased or increased by 20%, the model robustness for Type IV firing decreased minimally by 70% in the case of V_{1D} and maximally by 97% in the case of G_{Ca}. When the activation parameter values were simultaneously changed by 10% in the same direction (such that all three parameters similarly increased or decreased dendritic excitability), the robustness was decreased by 97% in the inhibitory direction and 85% in the excitatory direction.

The dramatic reduction in the model's robustness for Type IV firing, in response to a relatively small change in the neuromodulation level, supports the idea that neuromodulation may control the firing mode of the motoneurons by modulating the influence of the PIC locations on the firing behavior.

DISCUSSION

Using a realistic two-compartment model, we theoretically investigated the neuromodulatory control of the firing behavior in motoneurons. The physiological firing patterns of the reduced model strongly related to the location of PIC channels in the dendrites. However, when the level of neuromodulation was either reduced or enhanced, the PIC locations estimated for the nonlinear (i.e., Type IV) firing behavior were almost abolished, and the whole solution space for Type IV firing in the 3D VA domain dramatically shrank. Consequently, neuromodulation could switch the reduced model between distinct firing modes (i.e., Type I and III), regardless of the PIC locations over the majority of the dendritic area. This result suggests that neuromodulation might play a role in controlling the firing mode of motoneurons by modulating the location dependency of PIC activation in the dendrites.

DEMOCRATIZATION OF PIC IMPACT ON FIRING BEHAVIOR THROUGH NEUROMODULATION

The concept of democracy in the dendrites has been suggested both theoretically (Rumsey and Abbott, 2006) and experimentally (Magee and Cook, 2000; Hausser, 2001). That is, the contribution of individual synaptic inputs at different dendritic sites to

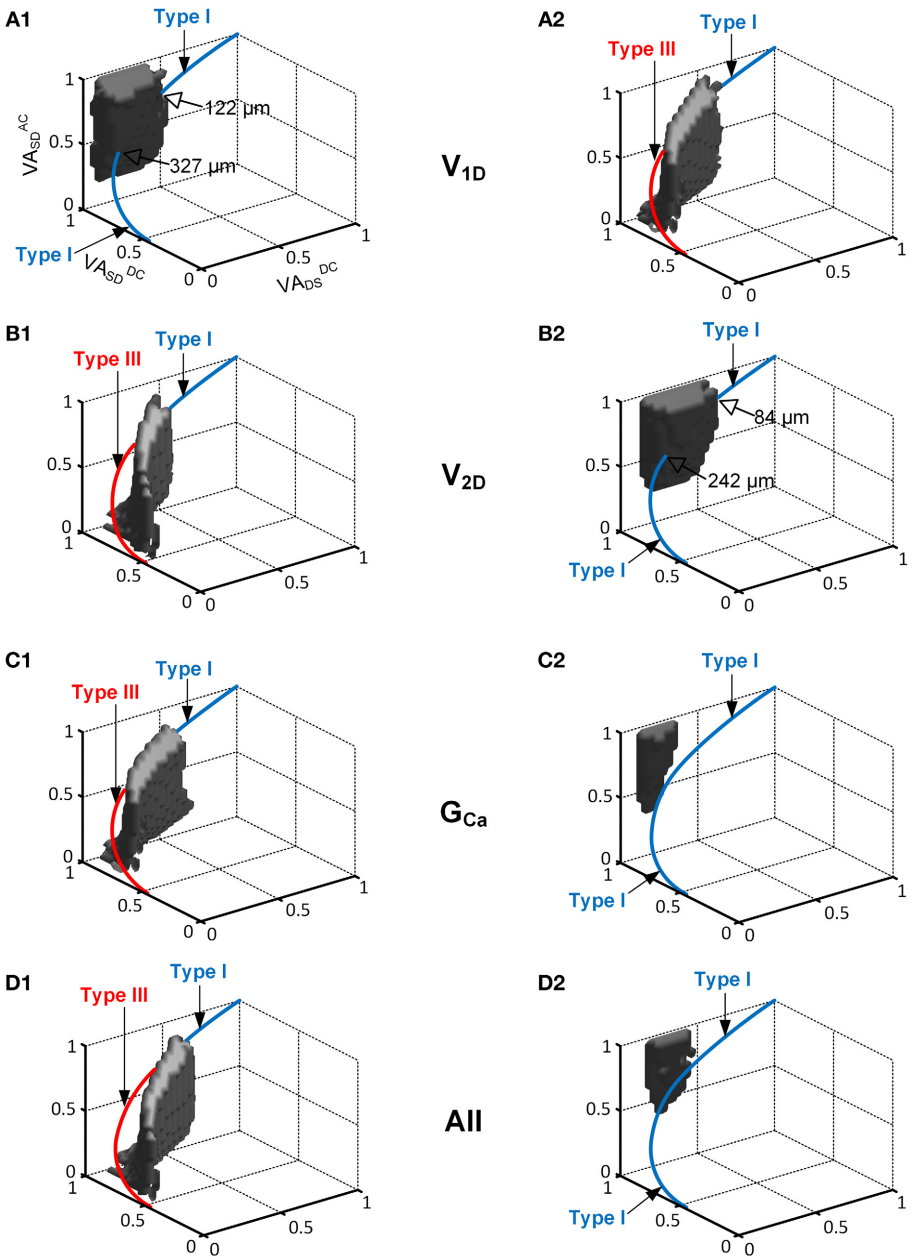

FIGURE 4 | The interaction of the location and activation properties of PIC channels on the firing patterns. The same simulation performed in **Figure 2** was conducted while varying the individual activation properties (V_{1D}, V_{2D}, and G_{Ca}) of the CaPIC channel. **(A1,B1,C1)** show the simulation results with 20% increments of V_{1D}, V_{2D}, and G_{Ca}, whereas **(A2,B2,C2)** show the results for 20% decreases from their standard values. **(D1,D2)** show the simulation results from a simultaneous change in all of the activation parameter values at the same time, where **(D1)** shows a 10% increase in V_{2D} and G_{Ca}, and 10% decrease in V_{1D} whereas **(D2)** shows the opposite.

the postsynaptic potentials at the soma could be normalized (or equalized), not only by the structure of the dendrites but also by passive and active membrane properties. A similar democratic phenomenon was found during the current study regarding PIC activation at different dendritic sites. In this study, the synaptic input and active current (i.e., PIC) in the dendrites were considered as extrinsic and intrinsic signals that may control the firing output at the soma. Similar to the synaptic input case, the firing output was investigated under neuromodulation while varying the location of PIC along the path of the dendrites from the soma. For this investigation, we used our recently developed reduced modeling approach for two reasons: (1) our

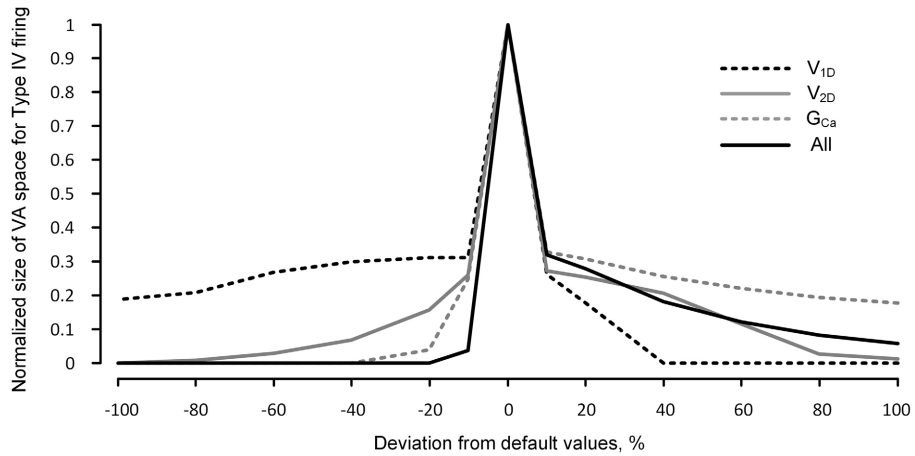

FIGURE 5 | Robustness of the reduced model for nonlinear firing under neuromodulation. The same simulation for **Figure 4** was performed for a broader range (from −100 to 100%) of change in the values of the individual and all activation parameters (V_{1D}, V_{2D}, and G_{Ca}) of the CaPIC channel. The y-axis indicates the normalized number of the points in the 3D VA space where the reduced model produced the fully hysteretic Type IV firing (see the gray VA space in **Figure 2** as an example with default values of the VA factors).

reduced modeling approach provides the framework where the dendritic compartment can retain the dendritic excitability (i.e., input resistance) of the anatomically reconstructed models as a function of the distance by reflecting the voltage attenuation properties between the soma and the dendrites, and (2) the values for the cable parameters of the reduced model are analytically determined from the system properties (input resistance, time constant and three voltage attenuation factors) which is well suited for the generality of the simulation covering a full range of the voltage attenuation properties of the dendrites. Our simulation results showed that the effects of PIC channels' location on firing behavior could be normalized in a "democratic" manner under neuromodulatory control (**Figure 4**). For instance, when neuromodulation was reduced, the reduced model displayed only Type I firing without PIC activation, independent of the PIC location in the dendrites. However, when neuromodulation was enhanced, Type III firing with PIC activation at the initiation of firing was produced for PIC channels over most of the dendritic sites. This result suggests that neuromodulatory control might act as an extrinsic mechanism for democratizing the activation of the active channels over the dendritic trees.

ROBUSTNESS OF TYPE IV FIRING DURING NORMAL BEHAVIOR

Typically, when neuromodulation levels are fixed, the Type IV (fully hysteretic) firing pattern showing strong counter-clockwise hysteresis has been characterized to demonstrate the influence of PIC activation at the dendrites on firing behavior in spinal motoneurons. In the present study, the capability of the reduced motoneuron model to produce the Type IV firing was found to be highly sensitive to variations in the level of neuromodulation (**Figure 5**). That is, as neuromodulation increased, Type III firing became predominant for the PIC located over the majority of the dendritic area. This result might explain recent experimental observations both in animals and humans during normal behavior, which have demonstrated that the PICs tend to be activated almost simultaneously at the initiation of firing by synaptic inputs to the motoneurons, leading to a linear F-I relationship with sustained firing (i.e., Type III firing) (Gorassini et al., 2002a,b; Li et al., 2004). Taken together, these theoretical and experimental results suggest that the fully hysteretic, Type IV firing behavior might not be functionally important for normal movements, during which the neuromodulation level continuously varies in response to physical and emotional states.

LIMITATIONS OF THE CURRENT MODELING

The only firing type that was difficult to produce with this reduced model while varying the VA factors was Type II firing: a clockwise F-I relationship without sustained firing behavior (**Figure 1**). This result indicates that Type II firing does not seem to be related to the locations of the PIC in the dendrites. The underlying mechanisms for the firing adaptation during the falling phase of the triangular stimulation may be related to both passive and active membrane properties. A recent study of anesthetized hindlimb rat motoneurons has shown that the motoneurons with less input resistance tend to display the Type II pattern (Hamm et al., 2010; Turkin et al., 2010). Indeed, decreased input resistance in the reduced model led to the characteristics of Type II firing while blocking plateau-generating channels in the dendrite (not shown). For the active mechanisms, the slow kinetics of the voltage-gated Na^+ and K^+ (M-like) currents involved in shaping action potentials may be a factor contributing to the Type II firing pattern in mouse preparations (Iglesias et al., 2011). The K^+ currents responsible for after hyperpolarization (AHP) may also affect the degree of the adaptation in the Type II firing of the reduced model. Both the input resistance and AHP property have been associated with motoneuron types (Zengel et al., 1985) and influenced by neuromodulation (Powers and Binder, 2001). Thus, further work will be needed to clarify if Type II firing is controlled by the neuromodulation in a type-specific manner in a pool of

motoneurons. Other limitations to the modeling approach used in this study were addressed in detail in our previous studies (Kim and Jones, 2011, 2012). Briefly, the details of active currents involved in generating action potentials at the soma and plateau potentials at the dendrites have been collapsed into an inward and outward current at each compartment of the reduced model for the theoretical purpose of the present study. In addition, the current modeling approach may not be appropriate for the case where the PIC channels are located at multiple branches of the dendrites.

Detailed cellular mechanisms for the monoaminergic neuromodulation that facilitates PICs in spinal motoneurons are not yet clear (Heckman et al., 2009). The effects of monoamines on motoneuron excitability have been simulated by varying the peak conductance of K^+ currents in the dendrites (Booth et al., 1997). In the current study, we varied three parameters (i.e., peak conductance, half activation voltage and slope of activation curve) that govern the activation of L-type Ca^{2+} channels in the dendrite of the reduced model to simulate neuromodulatory effects (**Figure 3**). We have found that both simulation approaches are comparable in that the excitability of the dendrite increases. However, what we found interesting in the current study was that changes in individual activation parameters had almost same effect on the PIC facilitation at different levels of monoamines. This result suggests that the monoamines might have compound effects on PIC activation in the dendrites, not only increasing the PIC amplitude but also varying the kinetic properties of the PIC. Furthermore, the activation properties of other voltage-gated inward and outward currents might also be varied under neuromodulation. Further systematic works would be needed to investigate whether or not and how the activation properties of non-PIC channels interact on the PIC location-dependent firing patterns under neuromodulation.

In the present study, individual firing types (i.e., Type I–IV) were identified based on temporal characteristics of the model response to a triangular current stimulation to the soma. Thus, one might concern that the firing types might depend on the kinetics of the triangular stimulation. With regard to this issue, we have shown in our previous studies (Kim and Jones, 2011, 2012) that Type I, III, and IV (fully hysteretic) firing could be defined mechanistically via steady-state bifurcation analysis. In addition, we could not find any significant difference in the firing types [Type I, III, and IV (fully hysteretic)] during simulations with a very slow (e.g., 10 time less steep) ramp stimulation (not shown).

Our intention of introducing the fully and partially hysteretic Type IV firing was to show the ability of the model to generate the two types of Type IV firing that have been experimentally observed in motoneurons. The main difference in the partially compared to fully hysteretic Type IV firings is the phenomenon of gradually deactivating plateau potential after the dendritic PICs are activated. In contrast to the fully hysteretic Type IV firing, the partially hysteretic Type IV firing was found to be sensitive to the kinetics of the ramp stimulation. Due to this reason, we have focused on Type I, III, and IV (fully hysteretic) firing for the theoretical purpose of the present study.

FUNCTIONAL ROLE OF NEUROMODULATORY CONTROL

Functional implications of the Type IV firing mediated by dendritic PICs have been suggested, not only for normal (i.e., gain and postural control) but also for pathological (i.e., spasticity) movement control (Kiehn and Eken, 1997; Lee and Heckman, 2000; Li and Bennett, 2003). Furthermore, it has also been reported that neuromodulatory control is likely to be predominant during physiological responses to external stimuli such as fight-or-flight-or-freeze behavior (Marder and Bucher, 2007; Inagaki et al., 2012; Suver et al., 2012). In all above cases, many motoneurons might need to fire together in a similar mode to ensure the strength and speed of muscle contraction required to generate those abrupt movements. This idea might be supported by our simulation results that the reduced models could be switched between distinct firing modes in a collective manner by varying the neuromodulation level, overriding the influence of PIC location on firing patterns (**Figures 4**, **5**). Overall, neuromodulation might play a pivotal role in controlling the firing mode of motoneurons at the population level, instead of individually.

In conclusion, the monoaminergic inputs descending from brainstem nuclei to the motoneurons may differ depending on motor demands during normal behaviors. Variation of the neuromodulatory drive could adjust the influence of PIC location on the firing behavior in the reduced motoneuron models. Our simulation results suggest the hypothesis that neuromodulation may have a role in encoding the demanding motor states by switching the heterogeneous input-output properties of a population of motoneurons to a uniform operation mode.

AUTHOR CONTRIBUTIONS

Conceived and designed the simulations: Hojeong Kim and C. J. Heckman. Performed the simulations: Hojeong Kim. Analyzed the data: Hojeong Kim and C. J. Heckman. Wrote the paper: Hojeong Kim and C. J. Heckman.

ACKNOWLEDGMENTS

The authors thank Dr. Kelvin Jones for his advice on the previous draft of this manuscript. This work was supported by National Institutes of Health Grant R01 NS071951, NS62200, and the DGIST R&D Program of the Ministry of Science, ICT and Future Planning of Korea (13-01-HRSS-03 and 14-RS-02).

REFERENCES

Ballou, E. W., Smith, W. B., Anelli, R., and Heckman, C. J. (2006). Measuring dendritic distribution of membrane proteins. *J. Neurosci. Methods* 156, 257–266. doi: 10.1016/j.jneumeth.2006.03.014

Bennett, D. J., Li, Y., and Siu, M. (2001). Plateau potentials in sacrocaudal motoneurons of chronic spinal rats, recorded *in vitro*. *J. Neurophysiol.* 86, 1955–1971.

Booth, V., Rinzel, J., and Kiehn, O. (1997). Compartmental model of vertebrate motoneurons for Ca^{2+}-dependent spiking and plateau potentials under pharmacological treatment. *J. Neurophysiol.* 78, 3371–3385.

Bui, T. V., Cushing, S., Dewey, D., Fyffe, R. E., and Rose, P. K. (2003). Comparison of the morphological and electrotonic properties of Renshaw cells, Ia inhibitory interneurons, and motoneurons in the cat. *J. Neurophysiol.* 90, 2900–2918. doi: 10.1152/jn.00533.2003

Bui, T. V., Ter-Mikaelian, M., Bedrossian, D., and Rose, P. K. (2006). Computational estimation of the distribution of L-type Ca(2+) channels in motoneurons based on variable threshold of activation of persistent inward currents. *J. Neurophysiol.* 95, 225–241. doi: 10.1152/jn.00646.2005

Button, D. C., Gardiner, K., Marqueste, T., and Gardiner, P. F. (2006). Frequency-current relationships of rat hindlimb alpha-motoneurones. *J. Physiol.* 573, 663–677. doi: 10.1113/jphysiol.2006.107292

Carlin, K. P., Bui, T. V., Dai, Y., and Brownstone, R. M. (2009). Staircase currents in motoneurons: insight into the spatial arrangement of calcium channels in the dendritic tree. *J. Neurosci.* 29, 5343–5353. doi: 10.1523/JNEUROSCI.5458-08.2009

Carlin, K. P., Jones, K. E., Jiang, Z., Jordan, L. M., and Brownstone, R. M. (2000). Dendritic L-type calcium currents in mouse spinal motoneurons: implications for bistability. *Eur. J. Neurosci.* 12, 1635–1646. doi: 10.1046/j.1460-9568.2000.00055.x

Cotel, F., Antri, M., Barthe, J. Y., and Orsal, D. (2009). Identified ankle extensor and flexor motoneurons display different firing profiles in the neonatal rat. *J. Neurosci.* 29, 2748–2753. doi: 10.1523/JNEUROSCI.3462-08.2009

Elbasiouny, S. M., Bennett, D. J., and Mushahwar, V. K. (2005). Simulation of dendritic CaV1.3 channels in cat lumbar motoneurons: spatial distribution. *J. Neurophysiol.* 94, 3961–3974. doi: 10.1152/jn.00391.2005

Gorassini, M., Yang, J. F., Siu, M., and Bennett, D. J. (2002a). Intrinsic activation of human motoneurons: possible contribution to motor unit excitation. *J. Neurophysiol.* 87, 1850–1858. doi: 10.1152/jn.00024.2001

Gorassini, M., Yang, J. F., Siu, M., and Bennett, D. J. (2002b). Intrinsic activation of human motoneurons: reduction of motor unit recruitment thresholds by repeated contractions. *J. Neurophysiol.* 87, 1859–1866. doi: 10.1152/jn.00025.2001.

Hamm, T. M., Turkin, V. V., Bandekar, N. K., O'Neill, D., and Jung, R. (2010). Persistent currents and discharge patterns in rat hindlimb motoneurons. *J. Neurophysiol.* 104, 1566–1577. doi: 10.1152/jn.00380.2010

Hausser, M. (2001). Synaptic function: dendritic democracy. *Curr. Biol.* 11, R10–R12. doi: 10.1016/S0960-9822(00)00034-8

Hausser, M., Spruston, N., and Stuart, G. J. (2000). Diversity and dynamics of dendritic signaling. *Science* 290, 739–744. doi: 10.1126/science.290.5492.739

Heckman, C. J., Johnson, M., Mottram, C., and Schuster, J. (2008). Persistent inward currents in spinal motoneurons and their influence on human motoneuron firing patterns. *Neuroscientist* 14, 264–275. doi: 10.1177/1073858408314986

Heckman, C. J., Mottram, C., Quinlan, K., Theiss, R., and Schuster, J. (2009). Motoneuron excitability: the importance of neuromodulatory inputs. *Clin. Neurophysiol.* 120, 2040–2054. doi: 10.1016/j.clinph.2009.08.009

Hille, B. (2001). *Ion Channels of Excitable Membranes.* Sunderland, MA: Sinauer.

Hounsgaard, J., and Kiehn, O. (1985). Ca^{++} dependent bistability induced by serotonin in spinal motoneurons. *Exp. Brain Res.* 57, 422–425.

Hounsgaard, J., and Kiehn, O. (1989). Serotonin-induced bistability of turtle motoneurones caused by a nifedipine-sensitive calcium plateau potential. *J. Physiol.* 414, 265–282.

Hounsgaard, J., and Kiehn, O. (1993). Calcium spikes and calcium plateaux evoked by differential polarization in dendrites of turtle motoneurones *in vitro*. *J. Physiol.* 468, 245–259.

Iglesias, C., Meunier, C., Manuel, M., Timofeeva, Y., Delestree, N., and Zytnicki, D. (2011). Mixed mode oscillations in mouse spinal motoneurons arise from a low excitability state. *J. Neurosci.* 31, 5829–5840. doi: 10.1523/JNEUROSCI.6363-10.2011

Inagaki, H. K., Ben-Tabou De-Leon, S., Wong, A. M., Jagadish, S., Ishimoto, H., Barnea, G., et al. (2012). Visualizing neuromodulation *in vivo*: TANGO-mapping of dopamine signaling reveals appetite control of sugar sensing. *Cell* 148, 583–595. doi: 10.1016/j.cell.2011.12.022

Kiehn, O., and Eken, T. (1997). Prolonged firing in motor units: evidence of plateau potentials in human motoneurons? *J. Neurophysiol.* 78, 3061–3068.

Kim, H., and Jones, K. E. (2011). Asymmetric electrotonic coupling between the soma and dendrites alters the bistable firing behaviour of reduced models. *J. Comput. Neurosci.* 30, 659–674. doi: 10.1007/s10827-010-0284-x

Kim, H., and Jones, K. E. (2012). The retrograde frequency response of passive dendritic trees constrains the nonlinear firing behaviour of a reduced neuron model. *PLoS ONE* 7:e43654. doi: 10.1371/journal.pone.0043654

Kim, H., Major, L. A., and Jones, K. E. (2009). Derivation of cable parameters for a reduced model that retains asymmetric voltage attenuation of reconstructed spinal motor neuron dendrites. *J. Comput. Neurosci.* 27, 321–336. doi: 10.1007/s10827-009-0145-7

Lee, R. H., and Heckman, C. J. (1998). Bistability in spinal motoneurons *in vivo*: systematic variations in persistent inward currents. *J. Neurophysiol.* 80, 583–593.

Lee, R. H., and Heckman, C. J. (1999). Enhancement of bistability in spinal motoneurons *in vivo* by the noradrenergic alpha1 agonist methoxamine. *J. Neurophysiol.* 81, 2164–2174.

Lee, R. H., and Heckman, C. J. (2000). Adjustable amplification of synaptic input in the dendrites of spinal motoneurons *in vivo*. *J. Neurosci.* 20, 6734–6740.

Li, Y., and Bennett, D. J. (2003). Persistent sodium and calcium currents cause plateau potentials in motoneurons of chronic spinal rats. *J. Neurophysiol.* 90, 857–869. doi: 10.1152/jn.00236.2003

Li, Y., Gorassini, M. A., and Bennett, D. J. (2004). Role of persistent sodium and calcium currents in motoneuron firing and spasticity in chronic spinal rats. *J. Neurophysiol.* 91, 767–783. doi: 10.1152/jn.00788.2003

Magee, J. C., and Cook, E. P. (2000). Somatic EPSP amplitude is independent of synapse location in hippocampal pyramidal neurons. *Nat. Neurosci.* 3, 895–903. doi: 10.1038/78800

Marder, E., and Bucher, D. (2007). Understanding circuit dynamics using the stomatogastric nervous system of lobsters and crabs. *Annu. Rev. Physiol.* 69, 291–316. doi: 10.1146/annurev.physiol.69.031905.161516

Meehan, C. F., Sukiasyan, N., Zhang, M., Nielsen, J. B., and Hultborn, H. (2010). Intrinsic properties of mouse lumbar motoneurons revealed by intracellular recording *in vivo*. *J. Neurophysiol.* 103, 2599–2610. doi: 10.1152/jn.00668.2009

Powers, R. K., and Binder, M. D. (2001). Input-output functions of mammalian motoneurons. *Rev. Physiol. Biochem. Pharmacol.* 143, 137–263. doi: 10.1007/BFb0115594

Rinzel, J., and Ermentrout, B. (1998). "Analysis of neural excitability and oscillations," in *Methods in Neuronal Modeling: From Ions to Networks*, eds C. Koch and I. Segev (Cambridge, MA, MIT Press), 251–291.

Rumsey, C. C., and Abbott, L. F. (2006). Synaptic democracy in active dendrites. *J. Neurophysiol.* 96, 2307–2318. doi: 10.1152/jn.00149.2006

Schwindt, P. C., and Crill, W. E. (1980). Properties of a persistent inward current in normal and TEA-injected motoneurons. *J. Neurophysiol.* 43, 1700–1724.

Suver, M. P., Mamiya, A., and Dickinson, M. H. (2012). Octopamine neurons mediate flight-induced modulation of visual processing in Drosophila. *Curr. Biol.* 22, 2294–2302. doi: 10.1016/j.cub.2012.10.034

Turkin, V. V., O'Neill, D., Jung, R., Iarkov, A., and Hamm, T. M. (2010). Characteristics and organization of discharge properties in rat hindlimb motoneurons. *J. Neurophysiol.* 104, 1549–1565. doi: 10.1152/jn.00379.2010

Zengel, J. E., Reid, S. A., Sypert, G. W., and Munson, J. B. (1985). Membrane electrical properties and prediction of motor-unit type of medial gastrocnemius motoneurons in the cat. *J. Neurophysiol.* 53, 1323–1344.

Conflict of Interest Statement: The authors declare that the research was conducted in the absence of any commercial or financial relationships that could be construed as a potential conflict of interest.

Received: 01 May 2014; accepted: 23 August 2014; published online: 09 September 2014.

Citation: Kim H and Heckman CJ (2014) Neuromodulation impact on nonlinear firing behavior of a reduced model motoneuron with the active dendrite. Front. Comput. Neurosci. ***8****:110. doi: 10.3389/fncom.2014.00110*

This article was submitted to the journal Frontiers in Computational Neuroscience.

frontiers in
COMPUTATIONAL NEUROSCIENCE

ORIGINAL RESEARCH ARTICLE
published: 13 October 2014
doi: 10.3389/fncom.2014.00128

Electrical responses of three classes of granule cells of the olfactory bulb to synaptic inputs in different dendritic locations

Fábio M. Simões-de-Souza[1,2]*, Gabriela Antunes[1] and Antonio C. Roque[3]

[1] *Laboratory of Neural Systems (SisNE), Department of Psychology, Faculdade de Filosofia Ciencias e Letras de Ribeirão Preto, Universidade de São Paulo, Ribeirão Preto, Brazil*

[2] *Center for Mathematics, Computation and Cognition, Federal University of ABC, São Bernardo do Campo, Brazil*

[3] *Laboratory of Neural Systems (SisNE), Department of Physics, Faculdade de Filosofia Ciencias e Letras de Ribeirão Preto, Universidade de São Paulo, Ribeirão Preto, Brazil*

Edited by:
Sergey M. Korogod, National Academy of Sciences of Ukraine, Ukraine

Reviewed by:
Upinder S. Bhalla, National Center for Biological Sciences, India
Ricardo C. Araneda, University of Maryland, USA

****Correspondence:***
Fábio M. Simões-de-Souza, Center for Mathematics, Computation and Cognition, Federal University of ABC, Rua Arcturus, 03, Room 250D, Jardim Antares, São Bernardo do Campo, São Paulo 09606-0709, Brazil
e-mail: fabio.souza@ufabc.edu.br

This work consists of a computational study of the electrical responses of three classes of granule cells of the olfactory bulb to synaptic activation in different dendritic locations. The constructed models were based on morphologically detailed compartmental reconstructions of three granule cell classes of the olfactory bulb with active dendrites described by Bhalla and Bower (1993, pp. 1948–1965) and dendritic spine distributions described by Woolf et al. (1991, pp. 1837–1854). The computational studies with the model neurons showed that different quantities of spines have to be activated in each dendritic region to induce an action potential, which always was originated in the active terminal dendrites, independently of the location of the stimuli, and the morphology of the dendritic tree. These model predictions might have important computational implications in the context of olfactory bulb circuits.

Keywords: granule cells, olfactory bulb, active dendrites, spikes, dendrodendritic synapses

INTRODUCTION

Computational models of the olfactory system have produced several important contributions about the functioning of this system, which has been considered a model system for computational neuroscience (Davis and Eichenbaum, 1991; Cleland and Linster, 2005; Simões-de-Souza and Antunes, 2007). But, despite the large number of computational models of olfactory bulb networks using neurons with simplified dendritic trees of granule cells (Davison et al., 2003; Simões de Souza and Roque, 2004; Yu et al., 2013; Kaplan and Lansner, 2014; Migliore et al., 2014), little has been done to investigate the outcome of the complex morphology of the different classes of granule cells of the olfactory bulb with active dendrites in the integration of their synaptic inputs.

Granule cells are the most numerous inhibitory interneurons present in the olfactory bulb, which has a proportion of 100–200 granule cells to each mitral and tufted cell (Saghatelyan et al., 2003; Shepherd et al., 2007). New granule cells develop constantly in the olfactory bulb through a process of neurogenesis and cell migration that is implied with synaptic plasticity and memory (Nissant et al., 2009; Sakamoto et al., 2014). In the olfactory bulb, granule cells play a key role in the information processing of the olfactory system (Shepherd et al., 2007; Labarrera et al., 2013).

The terminal dendrites of the granule cells have active membrane properties that can boost the excitability of the neurons to excitatory synaptic inputs impinging in different dendritic locations (Pinato and Midtgaard, 2005; Balu et al., 2007). These terminal dendrites make dendrodendritic synapses with the lateral dendrites of the mitral and tufted cells, which are the principal neurons of the olfactory bulb. Glutamate is released from the dendrites of the mitral/tufted cells that excite glutamatergic receptors in the spines of the granule cells. Presumably, the stimulation of AMPA, and NMDA type synapses lead to calcium inflow mainly through NMDA receptor channels in the spines of the granule cells (Schoppa et al., 1998), which induces the release of GABA in the synaptic cleft promoting the inhibition of the secondary dendrites of the mitral/tufted cells (Rall et al., 1966; Rall and Shepherd, 1968). Thus, the spines of the granule cells produce dendrodendritic recurrent inhibition of the mitral/tufted cells and lateral inhibition between mitral/tufted cells (Rall et al., 1966; Yokoi et al., 1995). Moreover, the dendritic trunk and deep dendrites of the granule cells can receive centrifugal fiber (CF) inputs from several brain regions that modulate the activity of the olfactory bulb (Laaris et al., 2007; Whitman and Greer, 2007; O'Connor and Jacob, 2008; Doucette et al., 2011).

Accordingly with morphological criteria there are three classes of granule cells in the olfactory bulb termed type I, II, and III (Mori et al., 1983; Woolf et al., 1991; Shepherd et al., 2007). The type I granule cell has terminal dendrites that branches and has spines present throughout the external plexiform layer. The type II granule neuron has branching patterns that are confined to the lower one-half to one-third of the external plexiform layer.

The type III granule cell arbors extensively only in the upper one-half to one-third of the external plexiform layer. Despite the morphological differences among different classes of granule cells that have been long recognized, it remains unclear whether the presence of active dendrites in each one of them induce different electrical responses to the same pattern of synaptic inputs. To investigate this aspect, we developed a computational model of three classes of granule cells with distinct distributions of dendritic spines along the active dendrites to investigate how each class integrate their its synaptic inputs.

MATERIALS AND METHODS

The computational models used to simulate the granule neurons were based on Bhalla and Bower detailed compartmental reconstructions of the three granule neuron classes of the olfactory bulb with active properties (Bhalla and Bower, 1993). Bhalla and Bower models are the most detailed reconstructed compartmental models with conductance based active dendrites available in the literature, and the reader is referred to the original paper to obtain more information about their development (Bhalla and Bower, 1993). The original model neurons were modified to include distinct distributions of dendritic spines (Woolf et al., 1991) that receive glutamatergic excitatory synapses on their dendritic spines containing NMDA and AMPA receptors.

The source code of the computational model is available at: https://senselab.med.yale.edu/modeldb/ShowModel.asp?model=156828, password=1416.

GRANULE CELLS

To investigate the effect of active dendrites on the integration of synaptic inputs in the three classes of granule cells, we kept the original compartmental composition and number of active channels of the type I, II, and II granule cells unchanged (Bhalla and Bower, 1993), which include the rat brain sodium, potassium, anomalous rectifier potassium and non-inactivating muscarinic potassium currents (Bhalla and Bower, 1993). Then, we modified the distributions of the spines in the terminal dendrites, dendritic trunk, and deep dendrites of the model cells to reproduce the detailed location, number and type of spines of a representative granule neuron of each class reconstructed in camera lucida (Woolf et al., 1991).

There are 194 pedunculated spines in the type I experimentally reconstruct granule neuron, 118 pedunculated spines in the type II granule neuron, and 114 spines in the type III granule neuron. The type I and II have more pedunculated spines near the soma than the type III (Woolf et al., 1991). Each spine was simulated as two compartments representing the neck and the head. We included one spine per granule cell compartment. Because the number of compartments was smaller than the number of peduculated spines observed experimentally, the membrane area of these missing spines was taken in consideration by increasing the membrane area of the cell with the area of the missing spines, considered as $3.37\,\mu m^2$ per missing spine. According to morphological data, the type III granule cell was simulated with no spines in the proximal trunk and deep dendrite (Woolf et al., 1991). The final constructed model for the type I granule neuron has 112 compartments and 112 simulated spines, the type II granule cell has 114 compartments and 114 simulated spines, the type III granule cell has 89 compartments and 61 simulated spines (**Figure 1A**, Supplementary Table 1).

The curves of spike frequency per injected current in the soma of the three simulated granule cells are shown in **Figure 1B**, which is a standard procedure to characterize computational model of single cells. The curves were very similar in the three model cells, in particular the firing threshold of the type I and II model cells is 0.04 nA, and the threshold of the type II is 0.03 nA.

A resting membrane potential of −65 mV was adopted for all granule cells, which is inside a range of values obtained with *in vivo* whole-cell recording in the rat olfactory bulb (Cang and Isaacson, 2003).

DENDRITIC SPINES

Each simulated spine has two cylindrical compartments, one representing the spine neck with a diameter of 0.23 μm and length 1.9 μm and another representing the spine head with a diameter of 0.8 μm and a length of 0.8 μm (Woolf et al., 1991). The spines were simulated containning both AMPA and NMDA receptor channels and a thin shell model immediatelly beneath the membrane that receive the calcium that flows through the activated NMDAR channels. The parameters used to simulate of these channels were based mainly in the Davison's model (Davison et al., 2003), which were obtained from the experimental works of Schoppa et al. (1998).

The AMPAR channel was simulated according to Equation (1):

$$G_{AMPAR}(V,t) = \frac{g_{AMPAR}\left(e^{\left(-t/\tau_1\right)} - e^{\left(-t/\tau_2\right)}\right)}{\tau_1 - \tau_2} \quad (1)$$

where G_{AMPAR} is the calculated AMPA conductance, $g_{AMPAR} = 1$ nS is the maximal conductance of the channel, and $\tau_1 = 2$ ms, and $\tau_2 = 5.5$ ms are the rising and decaying time constants, respectively (Davison et al., 2003).

The NMDA receptor model was based on Equation (2) (Zador et al., 1990):

$$G_{NMDAR}(V,t) = g_{NMDAR}\left(\frac{e^{-t/\tau_1} - e^{-t/\tau_2}}{1 + \eta[Mg^{2+}]e^{-\gamma V}}\right) \quad (2)$$

which considers the voltage-dependent blocking of the channel by the ion magnesium. G_{NMDAR} is the calculated NMDAR conductance, $g_{NMDAR} = 0.593$ nS is the maximal conductance of the channel, $\tau_1 = 52$ ms and $\tau_2 = 343$ ms are the rising and decaying time constants, respectively (Davison et al., 2003), $[Mg^{2+}] = 1.2$ mM is the ion magnesium concentration, $\eta = 0.2801$ and $\gamma = 62$.

The current through the channels was calculated by Equation (3),

$$I(t) = G(t)\,(E_K - V_m) \quad (3)$$

where I is the calculated current, G is the calculated channel conductance (G_{NMDAR} or G_{AMPAR}), V_m is the compartmental membrane potential and E_K is the reversal potential of the channel, considered zero for the AMPA receptor channels.

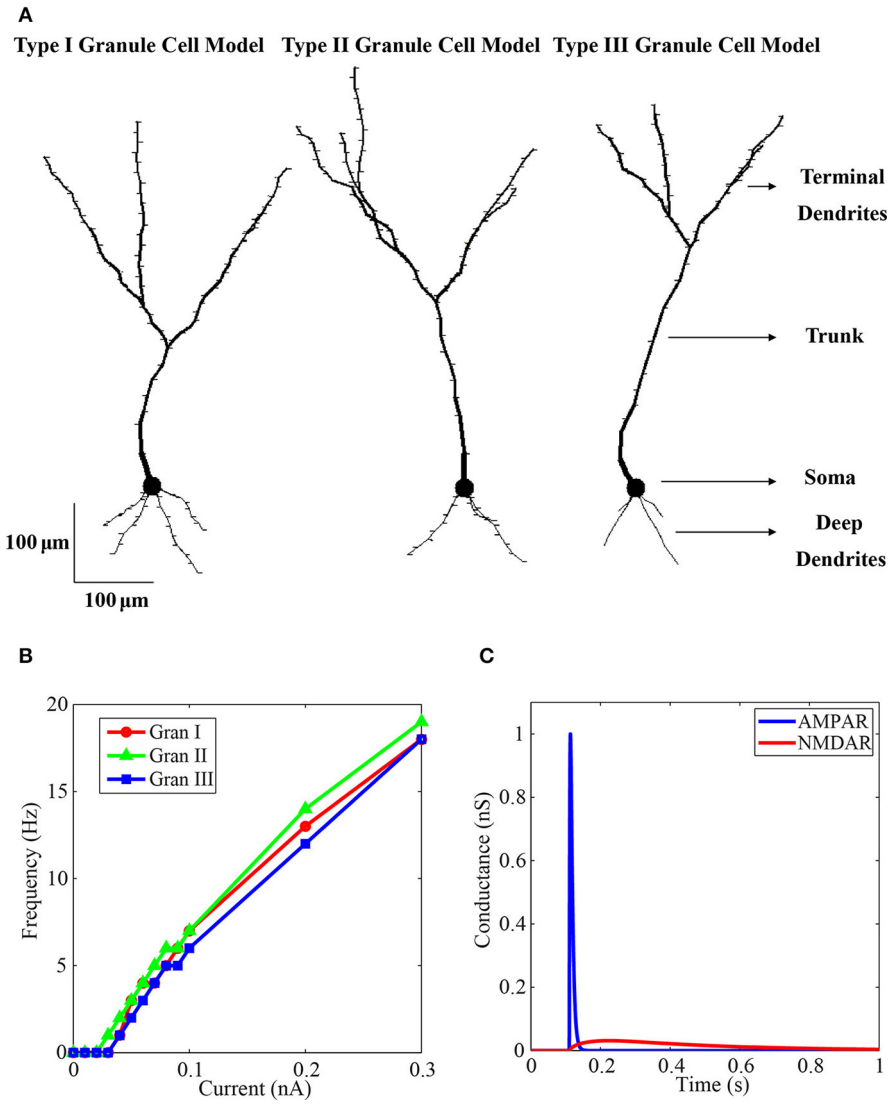

FIGURE 1 | Granule neuron model. (A) Morphology of the final model neurons with the dendritic spines. At left is the type I granule neuron model with 112 compartments and 112 spines, in the middle is the type II granule neuron with 114 compartments and 114 spines, and at right is the type III granule neuron with 89 compartments and 61 spines. Each model neuron has a soma, a trunk, the deep dendrites and the terminal dendrites. **(B)** Curves of injected current in the soma vs. spike frequency of the three simulated granule neurons. The markers are the simulated points. There are more points to the weak currents to determine the spike threshold of the neurons. The red line shows the firing rate of the type I granule neuron, the green line shows the firing rate of the type II granule neuron, and the blue line shows the firing rate of the type III granule neuron. **(C)** Activation of the model AMPA (blue line) and NMDA (red line) receptor channel conductances by glutamate. The concentration of ion magnesium was 1.2 mM.

An example of the time variations of the AMPA and NMDA receptor channel conductances of the model in response to glutamate activation is shown in **Figure 1C**. The maximum AMPAR conductance is 1 nS. There is a fast rising and fast decaying time in the variation of the AMPAR conductance (**Figure 1C**, blue) when compared with the NMDAR conductance that has very slow rising and decaying time constants (**Figure 1C**, red). Because of the blocking of the NMDAR by 1.2 mM of ion magnesium the maximum conductance of this channel, which is 0.593 nS, was not reached. The shell used to simulate the calcium dynamics was based on Equation (4) (Traub et al., 1991; Bower and Beeman, 2007):

$$\frac{d[Ca^{2+}]}{dt} = BI_{Ca} - r\mathrm{Ca}^{2+} \tag{4}$$

where the parameters were calculated for the spine dimensions considered here. $B = 5.2 \cdot 10^{-6}/(a \cdot L)$ is the ion calcium diffusion rate constant of the shell, where the spine head area is $a = 2\,\mu\mathrm{m}^2$ and the shell thickness is $L = 0.1\,\mu\mathrm{m}$. Because of buffering factors $B = B/10$, then $B = 26 \cdot 10^{11}$. $[\mathrm{Ca}^{2+}]$ is the calculated ion calcium concentration on the shell, I_{Ca} is the inward ion calcium current coming from NMDAR channel, $r = 870\ \mathrm{s}^{-1}$ is the extrusion rate of ion calcium (Egger and Stroh, 2009). The resting intracellular ion calcium is 0.05 µM (Egger and Stroh, 2009).

The fractional calcium concentration (P_f) through NMDAR channels followed the Equation (5) (Schneggenburger, 1996):

$$P_f = \frac{[Ca^{2+}]_o}{[Ca^{2+}]_o + \left(\frac{PM}{PCa^{2+}}\right)^{-1} \frac{[M]}{4}\left(1 - e^{\left(2V\frac{F}{RT}\right)}\right)} \quad (5)$$

where $[Ca^{2+}]_o$ is the extracellular free Ca^{2+} concentration (2 mM), V is the membrane potential in the spine head, F is the Faraday constant (96,485 C·mol^{-1}), R is the gas constant (8.314 J·K^{-1}·mol^{-1}), T is the temperature in degree Kelvin (298.15 K), M is the monovalent ion concentration (155 mM), and PCa^{2+}/PM is the permeability ratio of Ca^{2+} over monovalent ions (3.6). $P_f = 15\%$ at the membrane resting potential.

The reversal potential ($V_r = 2.18$ mV) for the NMDAR channel was obtained from the extended Goldman-Hodgkin-Katz (GHK) Equation (6) (Jan and Jan, 1976; Schneggenburger, 1996):

$$V_r = \frac{RT}{F} \ln \frac{\left(4[M]\left([M] + 4\frac{PCa^{2+}}{PM}[Ca^{2+}]_o\right)\right)^{1/2}}{2[M]} \quad (6)$$

SIMULATIONS

The simulations were performed on the GENESIS simulator (Bower and Beeman, 2007). We utilized the Crank–Nicolson implicit numerical method to solve the differential equations and all the simulated data were saved in files and processed using the MATLAB package (Mathworks Inc.)

Three series of simulations were performed with the granule cell models. The first series of simulations was used to test the model of dendritic spines implemented with its synaptic channels and calcium shell. The second series of simulations was used to investigate the effect of synaptic activation in different locations of the dendritic tree of each simulated cell on the generation of excitatory post synaptic potentials (EPSPs) and action potentials in the soma. The third series of simulations was performed to determine the origin of the generation of action potentials by simultaneous measurements in the terminal location of the dendritic trunk and in the soma during synaptic stimulation in different positions of the dendritic tree.

RESULTS

DENDRITIC SPINE MODEL

The electrical response of the type I granule neuron to a glutamatergic activation of only one spine at the tip of a terminal dendrite to different values of $[Mg^{2+}]$ was simulated to test the dendritic spine model (**Figure 2A**). The results obtained demonstrate that the conductance of the channels increase gradually with the reduction of the $[Mg^{2+}]$. The somatic EPSP during different $[Mg^{2+}]$ is shown in **Figure 2B**. The head of the spine was voltage clamped at different levels to verify the intracellular concentration of calcium ions resulting from the NMDAR currents (**Figures 2C,D**), This is a typical curve for the voltage dependence of the NMDAR current (**Figure 2D**) and the voltage dependence of the Ca^{2+} flux through NMDAR channels (**Figure 2C**) (Garaschuk et al., 1996).

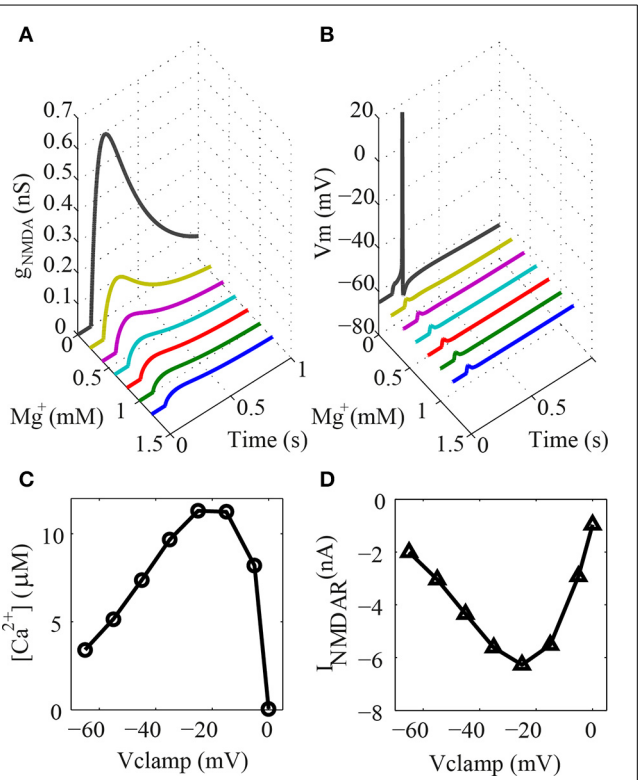

FIGURE 2 | Dendritic spine model. (A) NMDA conductance on the dendritic spine with varying concentrations of ion magnesium during a synaptic activation. Note that the reference level of ion magnesium is 1.2 mM **(B)** Somatic EPSP to the same situation described in **(A)**. **(C)** Concentration of ion calcium in the spine shell voltage-clamped at different potentials during synaptic activation. **(D)** Voltage dependence of the NMDAR current to the same situation described in **(C)**.

The simulation of the dendritic spine model showed that both the NMDAR and AMPAR conductances and the influx of ion calcium into the spine head shell is working as expected after synaptic activation (Supplementary Figure 1). In particular, the model simulated the crucial role of the ion magnesium blocking on the NMDA receptors. Since the ion calcium influx in the spines mediates the GABA release of the reciprocal synapses of the olfactory bulb (Chen et al., 2000), the present model can be used to simulate the dendrodendritic interactions between the granule neurons and mitral/tufted cells.

EFFECTS OF THE SYNAPTIC INPUTS IN DIFFERENT LOCATIONS OF THE DENDRITIC TREE

The results of the study of the impact of the synaptic activation in different locations of the dendritic tree in the generation of EPSPs and action potentials for three classes of granule cells are presented in **Figure 3**. The stimuli consist in the synaptic activation of NMDA and AMPA receptors in the spines located at the tip of the terminal dendrites, in the dendritic trunk or in the tip of the deep dendrites. We varied the number of activated spines for each of these three locations. We stimulated spines from different dendritic branches but located in the same horizontal plane of the

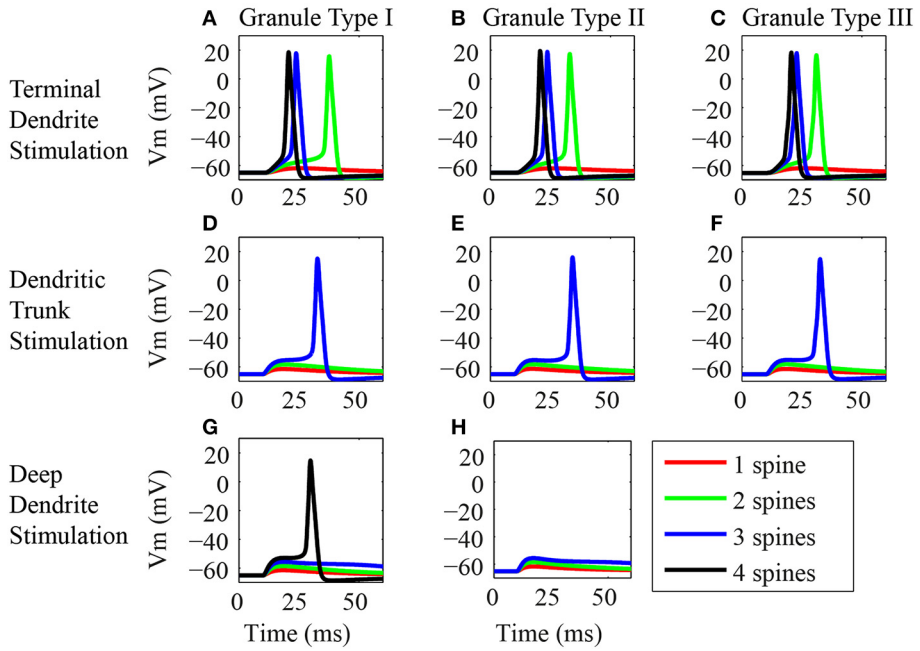

FIGURE 3 | Synaptic inputs in different dendritic locations. (A–H) Somatic EPSP or action potential responses of the three classes of granule neuron models to synaptic activation in different locations of the dendritic tree. In the left column **(A,D,G)** are the panels showing the responses of the type I granule neuron model, in the middle **(B,E,H)** are the responses of the type II granule neuron model, and in the right **(C,F)** are the responses of the type III granule neuron model. The top row **(A–C)** shows the responses to stimulations of the spines located in the terminal dendrite. The middle row **(D–F)** shows the responses to stimulations of the spines located in the trunk. The bottom row **(G,H)** shows the responses to stimulations of the dendrites located in the deep dendrite. Only the type III granule neuron models have no spines in the deep dendrites. Note that several spines were stimulated in each location, where red, green, blue, and black traces are respectively, the responses of the granule neuron models to stimulation of one, two, three, and four dendritic spines. The stimulus consists of the synaptic activation of NMDA and AMPA receptors by glutamate in the dendritic spines. The black line is absent in some panels because the stimulation of up to three spines in the dendritic trunk was sufficient to generate an action potential. In addition, type II granule cells have only three deep dendrites and therefore only three spines were stimulated in the deep dendrites of these cells.

terminal and deep dendrites. In the trunk, we increased the number of activated spines from the nearest spine to the soma to the next.

The responses of the three classes of granule cells to the stimulation of the spines located in the terminal dendrites were very similar (**Figures 3A–C**). The stimulation of only one spine in this location produced a slight depolarization of the postsynaptic membrane (red trace), however, the stimulation of more than one spine induced action potentials in all three cells (green, blue and black traces). The higher the number of activated spines, the lower was the latency for the occurrence of the spikes.

The electrical responses of the three classes of granule cells to stimulation of the spines on the dendritic trunk were again very similar (**Figures 3D–F**). The stimulation of only one or two spines produced a small depolarization of the membrane potential (red and green traces), however, the stimulation of three spines induced action potentials in all three cells (blue traces). The amplitude of the EPSP increased with the number of activated spines (read and green traces). Although the type III granule cell has no spines on proximal dendritic trunk, the stimulation of the spines located in the distal dendritic trunk produced similar responses to the ones obtained by stimulating the proximal spines of the type I and II granule cells (**Figures 3D–F**, blue traces).

The types I and II granule cells show equivalent electrical responses to stimulation of the spines in the deep dendrites (**Figures 3G,H**). Since the type III granule cell model has no spines in the deep dendrites, it was not stimulated. The stimulation of one to three spines in this location produced only an EPSP in the types I and II granule cells. The EPSP response increases with the number of activated spines (red, green, and blue traces). The stimulation of four spines in the type I granule cell induced an action potential (black trace). Note that the type I granule cell had four branches of deep dendrites and the type II granule cell had only three branches of deep dendrites (**Figure 1A**).

The study of the effect of the synaptic activation in different positions of the dendritic arbor of the three classes of granule cells did not find strong differences between the cells. However, it showed significant differences in the response of each type of granule cell to the activation of the spines in different locations of the dendritic tree. In particular, the minimum number of activated spines required to generate an action potential in these cells was at least two spines in the terminal dendrite, three in the trunk and four in the deep dendrites.

DETERMINATION OF THE ORIGIN OF THE ACTION POTENTIALS

We performed simulations to determine whether the action potentials initiate first in the soma or in the active dendrites in

response to synaptic inputs (**Figure 4**). The stimuli consist of the synaptic activation of NMDA and AMPA receptors on all the spines located in the tip of the terminal dendrites, on the three spines located in the trunk or on all spines located in the tip of the deep dendrites. In each of these three locations the number of activated spines followed the number of dendritic branches of each type of granule cell. The action potentials were recorded simultaneously in soma and in the terminal region of the trunk to determine whether it was generated first in the soma or in the terminal dendrites.

Similar responses were obtained to the stimulation of all the spines in the tip of the terminal dendrites for all classes of granule cells (**Figures 4A–C**) (Supplementary Figures 2–4). EPSP begins first in the terminal dendrite that reaches the threshold and generates an action potential in the trunk (blue traces) followed by an action potential in the soma (red traces). Equivalent responses occurred to the stimulation of the spines located in the dendritic trunk of all three granule cell types (**Figures 4D–F**). The action potential was generated first in the trunk (blue trace) followed by an action potential in the soma (red trace).

The stimulation of the spines on the deep dendrites of the type I granule cell (**Figure 4G**) generated an EPSP that reached a higher value first in the soma (red trace), but the trunk reached the threshold earlier and the action potential was generated first in the dendrite (blue trace) followed by an action potential in the soma (red trace). The type II granule cell did not generate action potentials (**Figure 4H**), and the EPSP reached a higher value first in the soma (red trace) followed by a higher amplitude in the dendrite (blue trace). Because the type III granule cell model has no spines in the deep dendrites, it was not stimulated in this region.

The secondary dendrites of the mitral and tufted cells are tangentially oriented in the external plexiform layer, where the granule cell dendrites are located. The radial orientation of the granule cell processes imply that a given mitral/tufted cell may make synapses only to a small number of spines on any given granule cell (Woolf et al., 1991), depending of the location of the contact of the mitral/tufted secondary dendrites on the terminal dendrites of the granule cells. All spines aligned along a transversal line passing through the terminal dendrites of the granule cells were activated to simulate this tangential orientation of the mitral/tufted secondary dendrites on the terminal dendrites of the type I granule cell. Thus, one line crossed the tip of the terminal dendrites, other line crossed the middle of the terminal dendrites, and another the beginning of the terminal dendrites. Because of the dendritic branching, the tip has four branches, the middle has three branches and the beginning has two branches. Therefore, the dendritic tip had four stimulated spines, the middle had three and the beginning had two stimulated spines. The responses of the type I granule cell to these patterns of stimulation are shown in **Figure 5**.

The action potentials occurred only when at least three spines were activated (**Figures 5A,C**). Note that both the EPSPs and action potentials were generated first in the trunk (blue trace) and after in the soma (red trace). The latency of the action potential

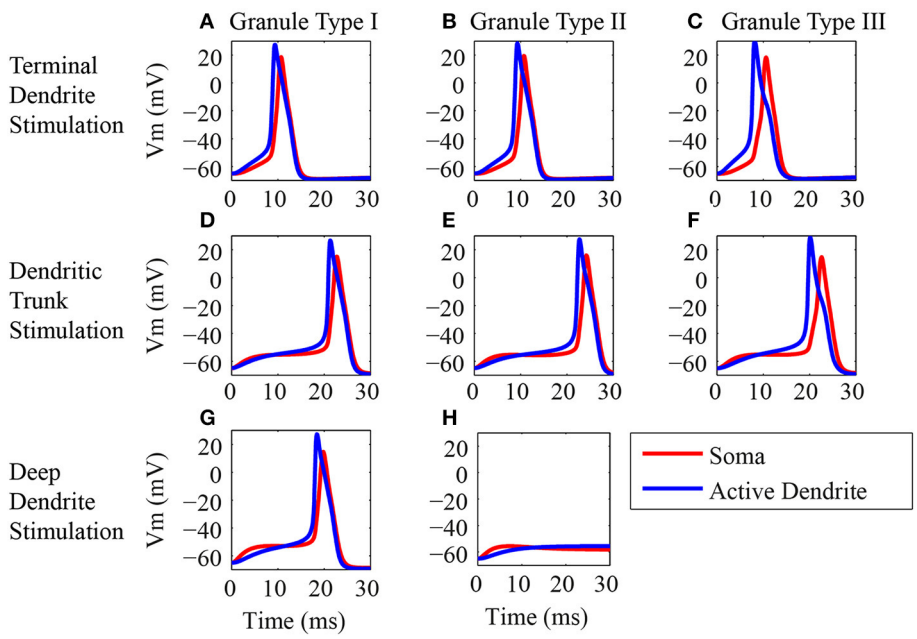

FIGURE 4 | Origin of the action potentials. (A–H) Generation of action potentials in the dendritic trunk (blue line) and soma (red line) of the three classes of granule neuron models in response to synaptic activation in different locations of the dendritic tree. The left column **(A,D,G)** shows the responses of the type I granule neuron model, the middle column **(B,E,H)** shows the responses of the type II granule neuron model, and the right column shows the responses of the type III granule neuron model **(C,F)**. The top row shows the responses to stimulations of the spines located in the terminal dendrite **(A–C)**. The middle row **(D–F)** shows the responses to stimulations of the spines located in the dendritic trunk. The bottom row shows the responses to stimulations of the spines located in the deep dendrite. Note that the type III granule neuron model has no spines in the dendrite. The stimulus consists in the synaptic activation of NMDA and AMPA receptors by glutamate in the dendritic spines.

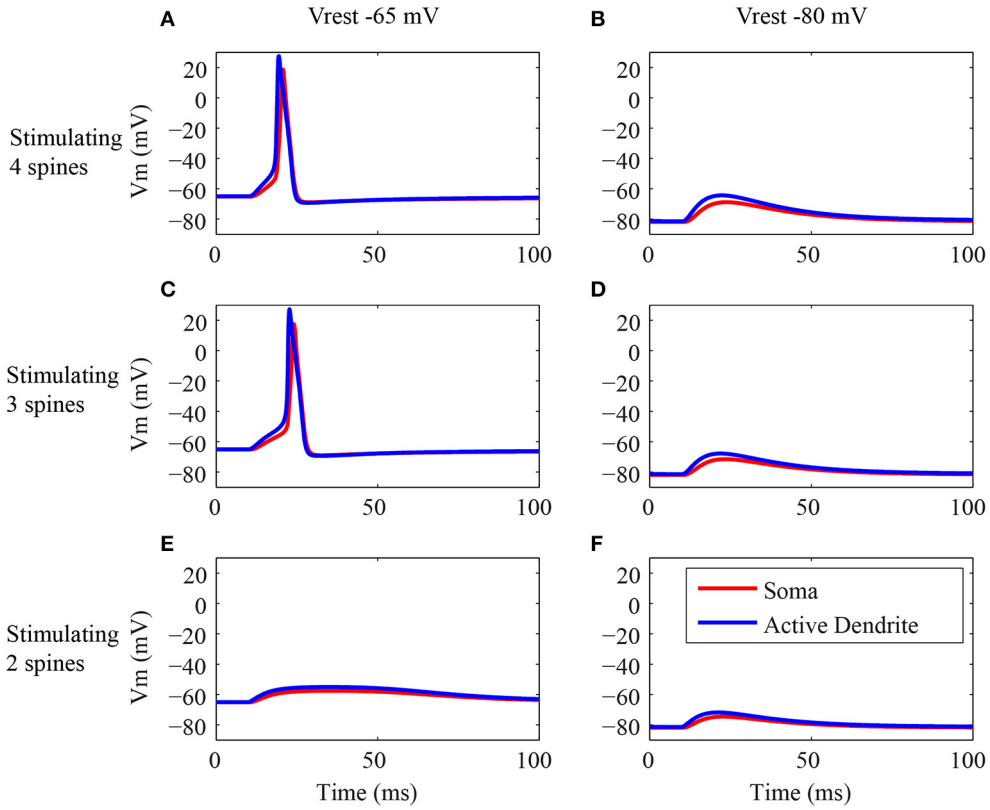

FIGURE 5 | Electrical responses in the active dendrite and soma. (A–F) EPSP and action potential generation in the dendritic trunk (blue line) and soma (red line) of the type I granule neuron model in response to synaptic activation of the terminal dendrite. The first row shows the responses of the type I granule neuron model to stimulation of four spines at the tip of the terminal dendrite **(A,B)**. The second row shows the responses of the same cell model to stimulation of three spines **(C,D)**, and the third row shows the responses to stimulation of two spines at the tip of the terminal dendrite **(E,F)**. Note that the left column **(A,C,E)** shows the simulation results for the regular resting membrane potential of −65 mV, and the right column **(B,D,F)** shows the results for the same stimulus pattern, but during the injection of a hyperpolarizing current of −0.1 nA in the soma leading to a resting membrane potential of −80 mV to avoid the generation of action potentials. The stimulus consists in the synaptic activation of NMDA and AMPA receptors by glutamate in the dendritic spines.

in response to the activation of four spines (**Figure 5A**) was lower than the latency in response to the activation of three spines (**Figure 5C**). The activation of two spines (**Figure 5E**) generated an EPSP stronger in the dendrite (blue trace) in comparison to the soma (red trace).

The same conditions described above were simulated with a hyperpolarizing current injected in soma to avoid the generation of action potentials (**Figures 5B,D,F**). These simulations confirmed that always the EPSPs had a higher amplitude in the dendrite (blue trace) and lower amplitudes in the soma (red trace). Also, the higher is the number of acivated spines the higher is the amplitude of the depolarization (**Figures 5B,D,F**).

DISCUSSION

This computational study characterized the synaptic inputs in the dendritic spines of three classes of granule cells, and verified the impact of the synaptic activation in different regions of these cells in the generation of EPSPs and action potentials. The type I granule cell model was used to study the impact of the mitral/tufted contacts in three different locations of the terminal dendrites of this cell.

The model results predicted that different numbers of spines should be activated in each different dendritic region to induce action potentials in the granule cells. Woolf and colleagues suggested that mitral/tufted cells can connect only to few spines in the granule cell terminal dendrites with an average number estimated near one (Woolf et al., 1991). If this estimate is correct, the present results predict that probably more than one mitral/tufted cell should connect simultaneously to the same granule cell to induce an action potential in this cell. Moreover, because the recurrent axon connections of the mitral/tufted cells in the granule cell occur mainly in the trunk and deep dendrites, the model results predict that the minimum number of recurrent synapses to produce an action should be of at least three in the trunk and four in the deep dendrites. Although the deep dendrites are shorter than the dendritic trunk, deep dendrites are passive compartments, and more spines are required to elicit an action potential. This higher threshold to fire action potentials in response to synaptic inputs in the deep dendrites of the granule cells suggests that they are less sensitive to modulatory inputs of the CFs coming from different brain regions than to synaptic inputs coming from lateral dendrites of the mitral/tufted cells.

All the spikes occurred first in the terminal dendrites rather than in the soma of the three classes of granule cells, even when the stimulation was delivered in the deep dendrites. If this prediction is correct, the recurrent mitral/tufted cell axon connections in the granule cells should induce action potentials first in the terminal dendrites, which could produce more effective reciprocal inhibition in the mitral/tufted cells.

The study of the activation of the spines in different locations of the terminal dendrites suggested that as far from the soma are the mitral/tufted secondary dendrites connections in the granule cell terminal dendrites as stronger are the induced depolarizations in these cells. It probably should occur because the secondary dendrites of the mitral and tufted cells are tangentially oriented in the external plexiform layer, which imply that depending of the location of the contacts of the mitral/tufted secondary dendrites on the granule terminal dendritic branches, different numbers of spines will be activated. The tip of the terminal dendrites has four branches, the middle has three branches, and the beginning has two branches, which imply that mitral/tufted secondary dendrites passing through these regions can connect to four spines, three spines or two spines, respectively.

The small differences in the responses of the three classes of granule neurons could be justified because the type II and type III granule cell models were adaptations of the type I granule cell model (Bhalla and Bower, 1993). The differential distributions of the spines on the dendrites of the three model cells did not induce strong differences in the electrical responses of these cells, and the three model neurons have a very strong tendency to produce spikes first in the active terminal dendrites rather than in the soma.

There are several canonic computational studies and experimental works in literature showing the origin of the generated action potentials in the different regions of the mitral cells (Bischofberger and Jonas, 1997; Chen et al., 1997, 2002; Shen et al., 1999; O'Connor et al., 2012; Migliore et al., 2014). These computational models and experimental evidence have shown that different intensities of the current or synaptic activation of the dendritic tufts of the mitral cells can shift the origin of the action potentials from the terminal dendrites to the soma. However, computational studies utilizing detailed compartmental models of granule cells with spines were performed only in passive models until now (Woolf et al., 1991). The present work is the first to consider the responses of compartmental granule cell models with active properties to synaptic activation in different dendritic locations. Although the models did not present shifts in the origin of the generated action potentials, they predicted that different quantities of spines should be activated in each region of the dendritic tree to induce action potential in the cells, which have important computational implications in the context of the olfactory bulb circuitry.

Electrophysiological evidence demonstrate that mitral and middle tufted cells differ in the decoding manner of odors in the rat olfactory bulb (Nagayama et al., 2004) and have distinct patterns of axonal projection to the olfactory cortex (Haberly and Price, 1977; Scott et al., 1980; Schoenfeld and Macrides, 1984; Nagayama et al., 2010). Because different types of granule cells connect with distinct classes of mitral and tufted cells (Mori et al., 1983), the diverse odor decoding strategies could be at least in part a property of the different types of granule cells that are renewed constantly in the olfactory bulb by the process of adult neurogenesis (Gheusi et al., 2013; Sakamoto et al., 2014). However, because of the similar responses of the three types of granule cell models to several patterns of synaptic activation, the present study favors the hypothesis that the different coding strategies could be both intrinsic properties of the mitral and tufted cells or emergent properties of the olfactory bulb circuitry. More experimental studies and computational models should be developed to test all these possibilities.

Furthermore, recent evidence have shown the expression of transient receptor potential (TRP) channels in mitral and granule cells of the olfactory bulb (Dong et al., 2012; Stroh et al., 2012). The activation of cationic TRP channels in the granule cells is dependent of NMDARs and affects the calcium dynamics required for release of neurotransmitters from the granule cell spines (Egger, 2008; Stroh et al., 2012). In this way, TRP channels that are absent in the present model may play an important role in the reciprocal synapses between mitral and granule cell with active dendrites, and deserve to be investigated in future modeling studies.

ACKNOWLEDGMENTS

The research leading to these results has received funding from the Programa Nacional de Pós-Doutorado (PNPD)/Coordenação de Aperfeiçoamento de Pessoal de Nível Superior (CAPES). Antonio C. Roque is the recipient of a Conselho Nacional de Desenvolvimento Científico e Tecnológico (CNPq) research grant.

SUPPLEMENTARY MATERIAL

The Supplementary Material for this article can be found online at: http://www.frontiersin.org/journal/10.3389/fncom.2014.00128/abstract

REFERENCES

Balu, R., Pressler, R. T., and Strowbridge, B. W. (2007). Multiple modes of synaptic excitation of olfactory bulb granule cells. *J. Neurosci.* 27, 5621–5632. doi: 10.1523/JNEUROSCI.4630-06.2007

Bhalla, U. S., and Bower, J. M. (1993). Exploring parameter space in detailed single neuron models: simulations of the mitral and granule cells of the olfactory bulb. *J. Neurophysiol.* 69, 1948–1965.

Bischofberger, J., and Jonas, P. (1997). Action potential propagation into the presynaptic dendrites of rat mitral cells. *J. Physiol.* 504(Pt 2), 359–365. doi: 10.1111/j.1469-7793.1997.359be.x

Bower, J. M., and Beeman, D. (2007). Constructing realistic neural simulations with GENESIS. *Methods Mol. Biol.* 401, 103–125. doi: 10.1007/978-1-59745-520-6_7

Cang, J., and Isaacson, J. S. (2003). *In vivo* whole-cell recording of odor-evoked synaptic transmission in the rat olfactory bulb. *J. Neurosci.* 23, 4108–4116.

Chen, W. R., Midtgaard, J., and Shepherd, G. M. (1997). Forward and backward propagation of dendritic impulses and their synaptic control in mitral cells. *Science* 278, 463–467. doi: 10.1126/science.278.5337.463

Chen, W. R., Shen, G. Y., Shepherd, G. M., Hines, M. L., and Midtgaard, J. (2002). Multiple modes of action potential initiation and propagation in mitral

cell primary dendrite. *J. Neurophysiol.* 88, 2755–2764. doi: 10.1152/jn.00057.2002

Chen, W. R., Xiong, W., and Shepherd, G. M. (2000). Analysis of relations between NMDA receptors and GABA release at olfactory bulb reciprocal synapses. *Neuron* 25, 625–633. doi: 10.1016/S0896-6273(00)81065-X

Cleland, T. A., and Linster, C. (2005). Computation in the olfactory system. *Chem. Senses* 30, 801–813. doi: 10.1093/chemse/bji072

Davis, J. L., and Eichenbaum, H. (eds.). (1991). *Olfaction : A Model System for Computational Neuroscience*. Cambridge, MA: MIT Press.

Davison, A. P., Feng, J., and Brown, D. (2003). Dendrodendritic inhibition and simulated odor responses in a detailed olfactory bulb network model. *J. Neurophysiol.* 90, 1921–1935. doi: 10.1152/jn.00623.2002

Dong, H. W., Davis, J. C., Ding, S., Nai, Q., Zhou, F. M., and Ennis, M. (2012). Expression of transient receptor potential (TRP) channel mRNAs in the mouse olfactory bulb. *Neurosci. Lett.* 524, 49–54. doi: 10.1016/j.neulet.2012.07.013

Doucette, W., Gire, D. H., Whitesell, J., Carmean, V., Lucero, M. T., and Restrepo, D. (2011). Associative cortex features in the first olfactory brain relay station. *Neuron* 69, 1176–1187. doi: 10.1016/j.neuron.2011.02.024

Egger, V. (2008). Synaptic sodium spikes trigger long-lasting depolarizations and slow calcium entry in rat olfactory bulb granule cells. *Eur. J. Neurosci.* 27, 2066–2075. doi: 10.1111/j.1460-9568.2008.06170.x

Egger, V., and Stroh, O. (2009). Calcium buffering in rodent olfactory bulb granule cells and mitral cells. *J. Physiol.* 587, 4467–4479. doi: 10.1113/jphysiol.2009.174540

Garaschuk, O., Schneggenburger, R., Schirra, C., Tempia, F., and Konnerth, A. (1996). Fractional Ca2+ currents through somatic and dendritic glutamate receptor channels of rat hippocampal CA1 pyramidal neurones. *J. Physiol.* 491(Pt 3), 757–772.

Gheusi, G., Lepousez, G., and Lledo, P. M. (2013). Adult-born neurons in the olfactory bulb: integration and functional consequences. *Curr. Top. Behav. Neurosci.* 15, 49–72. doi: 10.1007/7854_2012_228

Haberly, L. B., and Price, J. L. (1977). The axonal projection patterns of the mitral and tufted cells of the olfactory bulb in the rat. *Brain Res.* 129, 152–157. doi: 10.1016/0006-8993(77)90978-7

Jan, L. Y., and Jan, Y. N. (1976). L-glutamate as an excitatory transmitter at the Drosophila larval neuromuscular junction. *J. Physiol.* 262, 215–236.

Kaplan, B. A., and Lansner, A. (2014). A spiking neural network model of self-organized pattern recognition in the early mammalian olfactory system. *Front. Neural Circuits* 8:5. doi: 10.3389/fncir.2014.00005

Laaris, N., Puche, A., and Ennis, M. (2007). Complementary postsynaptic activity patterns elicited in olfactory bulb by stimulation of mitral/tufted and centrifugal fiber inputs to granule cells. *J. Neurophysiol.* 97, 296–306. doi: 10.1152/jn.00823.2006

Labarrera, C., London, M., and Angelo, K. (2013). Tonic inhibition sets the state of excitability in olfactory bulb granule cells. *J. Physiol.* 591, 1841–1850. doi: 10.1113/jphysiol.2012.241851

Migliore, M., Cavarretta, F., Hines, M. L., and Shepherd, G. M. (2014). Distributed organization of a brain microcircuit analyzed by three-dimensional modeling: the olfactory bulb. *Front. Comput. Neurosci.* 8:50. doi: 10.3389/fncom.2014.00050

Mori, K., Kishi, K., and Ojima, H. (1983). Distribution of dendrites of mitral, displaced mitral, tufted, and granule cells in the rabbit olfactory bulb. *J. Comp. Neurol.* 219, 339–355. doi: 10.1002/cne.902190308

Nagayama, S., Enerva, A., Fletcher, M. L., Masurkar, A. V., Igarashi, K. M., Mori, K., et al. (2010). Differential axonal projection of mitral and tufted cells in the mouse main olfactory system. *Front. Neural Circuits* 4:120. doi: 10.3389/fncir.2010.00120

Nagayama, S., Takahashi, Y. K., Yoshihara, Y., and Mori, K. (2004). Mitral and tufted cells differ in the decoding manner of odor maps in the rat olfactory bulb. *J. Neurophysiol.* 91, 2532–2540. doi: 10.1152/jn.01266.2003

Nissant, A., Bardy, C., Katagiri, H., Murray, K., and Lledo, P. M. (2009). Adult neurogenesis promotes synaptic plasticity in the olfactory bulb. *Nat. Neurosci.* 12, 728–730. doi: 10.1038/nn.2298

O'Connor, S., Angelo, K., and Jacob, T. J. (2012). Burst firing versus synchrony in a gap junction connected olfactory bulb mitral cell network model. *Front. Comput. Neurosci.* 6:75. doi: 10.3389/fncom.2012.00075

O'Connor, S., and Jacob, T. J. (2008). Neuropharmacology of the olfactory bulb. *Curr. Mol. Pharmacol.* 1, 181–190. doi: 10.2174/1874467210801030181

Pinato, G., and Midtgaard, J. (2005). Dendritic sodium spikelets and low-threshold calcium spikes in turtle olfactory bulb granule cells. *J. Neurophysiol.* 93, 1285–1294. doi: 10.1152/jn.00807.2004

Rall, W., and Shepherd, G. M. (1968). Theoretical reconstruction of field potentials and dendrodendritic synaptic interactions in olfactory bulb. *J. Neurophysiol.* 31, 884–915.

Rall, W., Shepherd, G. M., Reese, T. S., and Brightman, M. W. (1966). Dendrodendritic synaptic pathway for inhibition in the olfactory bulb. *Exp. Neurol.* 14, 44–56. doi: 10.1016/0014-4886(66)90023-9

Saghatelyan, A., Carleton, A., Lagier, S., de Chevigny, A., and Lledo, P. M. (2003). Local neurons play key roles in the mammalian olfactory bulb. *J. Physiol. Paris* 97, 517–528. doi: 10.1016/j.jphysparis.2004.01.009

Sakamoto, M., Kageyama, R., and Imayoshi, I. (2014). The functional significance of newly born neurons integrated into olfactory bulb circuits. *Front. Neurosci.* 8:121. doi: 10.3389/fnins.2014.00121

Schneggenburger, R. (1996). Simultaneous measurement of Ca2+ influx and reversal potentials in recombinant N-methyl-D-aspartate receptor channels. *Biophys. J.* 70, 2165–2174. doi: 10.1016/S0006-3495(96)79782-5

Schoenfeld, T. A., and Macrides, F. (1984). Topographic organization of connections between the main olfactory bulb and pars externa of the anterior olfactory nucleus in the hamster. *J. Comp. Neurol.* 227, 121–135. doi: 10.1002/cne.902270113

Schoppa, N. E., Kinzie, J. M., Sahara, Y., Segerson, T. P., and Westbrook, G. L. (1998). Dendrodendritic inhibition in the olfactory bulb is driven by NMDA receptors. *J. Neurosci.* 18, 6790–6802.

Scott, J. W., McBride, R. L., and Schneider, S. P. (1980). The organization of projections from the olfactory bulb to the piriform cortex and olfactory tubercle in the rat. *J. Comp. Neurol.* 194, 519–534. doi: 10.1002/cne.901940304

Shen, G. Y., Chen, W. R., Midtgaard, J., Shepherd, G. M., and Hines, M. L. (1999). Computational analysis of action potential initiation in mitral cell soma and dendrites based on dual patch recordings. *J. Neurophysiol.* 82, 3006–3020.

Shepherd, G. M., Chen, W. R., Willhite, D., Migliore, M., and Greer, C. A. (2007). The olfactory granule cell: from classical enigma to central role in olfactory processing. *Brain Res. Rev.* 55, 373–382. doi: 10.1016/j.brainresrev.2007.03.005

Simões-de-Souza, F. M., and Antunes, G. (2007). Biophysics of olfaction. *Rep. Prog. Phys.* 70, 451–491. doi: 10.1088/0034-4885/70/3/R04

Simões de Souza, F. M., and Roque, A. C. (2004). A biophysical model of vertebrate olfactory epithelium and bulb exhibiting gap junction dependent odor-evoked spatiotemporal patterns of activity. *Biosystems* 73, 25–43. doi: 10.1016/j.biosystems.2003.08.002

Stroh, O., Freichel, M., Kretz, O., Birnbaumer, L., Hartmann, J., and Egger, V. (2012). NMDA receptor-dependent synaptic activation of TRPC channels in olfactory bulb granule cells. *J. Neurosci.* 32, 5737–5746. doi: 10.1523/JNEUROSCI.3753-11.2012

Traub, R. D., Wong, R. K., Miles, R., and Michelson, H. (1991). A model of a CA3 hippocampal pyramidal neuron incorporating voltage-clamp data on intrinsic conductances. *J. Neurophysiol.* 66, 635–650.

Whitman, M. C., and Greer, C. A. (2007). Synaptic integration of adult-generated olfactory bulb granule cells: basal axodendritic centrifugal input precedes apical dendrodendritic local circuits. *J. Neurosci.* 27, 9951–9961. doi: 10.1523/JNEUROSCI.1633-07.2007

Woolf, T. B., Shepherd, G. M., and Greer, C. A. (1991). Local information processing in dendritic trees: subsets of spines in granule cells of the mammalian olfactory bulb. *J. Neurosci.* 11, 1837–1854.

Yokoi, M., Mori, K., and Nakanishi, S. (1995). Refinement of odor molecule tuning by dendrodendritic synaptic inhibition in the olfactory bulb. *Proc. Natl. Acad. Sci. U.S.A.* 92, 3371–3375. doi: 10.1073/pnas.92.8.3371

Yu, Y., McTavish, T. S., Hines, M. L., Shepherd, G. M., Valenti, C., and Migliore, M. (2013). Sparse distributed representation of odors in a large-scale olfactory bulb circuit. *PLoS Comput. Biol.* 9:e1003014. doi: 10.1371/journal.pcbi.1003014

Zador, A., Koch, C., and Brown, T. H. (1990). Biophysical model of a Hebbian synapse. *Proc. Natl. Acad. Sci. U.S.A.* 87, 6718–6722. doi: 10.1073/pnas.87.17.6718

Conflict of Interest Statement: The authors declare that the research was conducted in the absence of any commercial or financial relationships that could be construed as a potential conflict of interest.

Received: 30 June 2014; accepted: 25 September 2014; published online: 13 October 2014.

Citation: Simões-de-Souza FM, Antunes G and Roque AC (2014) Electrical responses of three classes of granule cells of the olfactory bulb to synaptic inputs in different dendritic locations. Front. Comput. Neurosci. ***8****:128. doi: 10.3389/fncom.2014.00128*
This article was submitted to the journal Frontiers in Computational Neuroscience.

frontiers in Cellular Neuroscience

ORIGINAL RESEARCH
published: 05 November 2015
doi: 10.3389/fncel.2015.00439

Distinct and synergistic feedforward inhibition of pyramidal cells by basket and bistratified interneurons

Michele Ferrante[1]* *and Giorgio A. Ascoli*[2]*

[1] Computational Neurophysiology Laboratory, Center for Memory and Brain, Psychology Department, Boston University, Boston, MA, USA, [2] Krasnow Institute for Advanced Study, George Mason University, Fairfax, VA, USA

Feedforward inhibition (FFI) enables pyramidal cells in area CA1 of the hippocampus (CA1PCs) to remain easily excitable while faithfully representing a broad range of excitatory inputs without quickly saturating. Despite the cortical ubiquity of FFI, its specific function is not completely understood. FFI in CA1PCs is mediated by two physiologically and morphologically distinct GABAergic interneurons: fast-spiking, perisomatic-targeting basket cells and regular-spiking, dendritic-targeting bistratified cells. These two FFI pathways might create layer-specific computational sub-domains within the same CA1PC, but teasing apart their specific contributions remains experimentally challenging. We implemented a biophysically realistic model of CA1PCs using 40 digitally reconstructed morphologies and constraining synaptic numbers, locations, amplitude, and kinetics with available experimental data. First, we validated the model by reproducing the known combined basket and bistratified FFI of CA1PCs at the population level. We then analyzed how the two interneuron types independently affected the CA1PC spike probability and timing as a function of inhibitory strength. Separate FFI by basket and bistratified respectively modulated CA1PC threshold and gain. Concomitant FFI by both interneuron types synergistically extended the dynamic range of CA1PCs by buffering their spiking response to excitatory stimulation. These results suggest testable hypotheses on the precise effects of GABAergic diversity on cortical computation.

Keywords: feedforward inhibiton, bistratified, basket, interneurons, CA1 pyramidal cells, neuronal connectivity, hippocampus, input-output transformation

OPEN ACCESS

Edited by:
Sergey M. Korogod, National Academy of Sciences of Ukraine, Ukraine

Reviewed by:
Dirk Feldmeyer, RWTH Aachen University, Germany
Corette J. Wierenga, Utrecht University, Netherlands

***Correspondence:**
Michele Ferrante
mferr133@bu.edu;
Giorgio A. Ascoli
ascoli@gmu.edu

Received: *11 August 2015*
Accepted: *22 October 2015*
Published: *05 November 2015*

Citation:
Ferrante M and Ascoli GA (2015) Distinct and synergistic feedforward inhibition of pyramidal cells by basket and bistratified interneurons. Front. Cell. Neurosci. 9:439. doi: 10.3389/fncel.2015.00439

INTRODUCTION

CA1 Pyramidal Cells (CA1PCs) constitute the output of the hippocampal tri-synaptic circuit, relaying the information processed by area CA3 onto the subiculum and the deep layers of the entorhinal cortex. CA1PCs activity encodes spatial (O'Keefe and Dostrovsky, 1971) and temporal (MacDonald et al., 2011) features of episodic memories. This representation is mediated by the integration of excitatory and inhibitory inputs from ~30,000 glutamatergic and ~1700 GABAergic synapses, respectively (Megías et al., 2001). CA1PCs receive widely divergent and

Abbreviations: FFI, Feedforward inhibition; CA1PCs, Pyramidal cells in area CA1 of the hippocampus; EPSP, Excitatory post-synaptic potential; IPSP, Inhibitory post-synaptic potential; sp, stratum pyramidale; sl-m, stratum lacunosum-moleculare; so, stratum oriens; sr, stratum radiatum.

convergent stimulations from the ipsilateral and contralateral Schaffer collaterals. Without inhibitory control, even minimal alterations in the number of activated pre-synaptic neurons could result in all-or-none recruitment of the whole CA1PC population (Shadlen and Newsome, 1998). To counteract the substantial activity fluctuations of CA3 pyramidal cells (Wilson and McNaughton, 1993; Csicsvari et al., 2000), CA1PCs use feedforward inhibition (FFI) to expand the dynamic range of stimulus strengths over which they faithfully respond (Pouille et al., 2009). FFI is a ubiquitous connectivity motif in hippocampus and neocortex in which an axonal pathway (e.g., Schaffer collateral from CA3) excites both the principal cells in an area (CA1PCs) and a group of GABAergic interneurons that contact the same target (Buzsáki, 1984). FFI also allows CA1PC dendrites to sum incoming activity over broader time windows while enforcing precise coincidence detection in the soma (Pouille and Scanziani, 2001). This mechanism increases the temporal fidelity of the circuit by reducing spike onset jitter.

Synaptic contacts in CA1PCs are organized in orderly spatial sub-domains along complex dendritic trees enriched with diverse sets of active properties. In particular, two physiologically, biochemically, and morphologically distinct interneuron classes can inhibit CA1PCs in a feedforward manner (Buhl et al., 1996; Halasy et al., 1996; Klausberger, 2009; Tricoire et al., 2011): basket cells are fast-spiking, express parvalbumin, and target CA1PCs perisomatically in stratum pyramidale; bistratified cells are regular-spiking, express 5HT3R, NPY, SOM, and Coup-TFII (all of which are absent in basket cells), and target CA1PCs on the basal dendrites in stratum oriens and on the apical dendrites in stratum radiatum[1] (Wheeler et al., 2015). Therefore, these two FFI pathways can in principle form distinct layer-specific computational sub-domains within the same CA1PC. Basket and bistratified cells in the CA1 area are activated by the same (CA3 Schaffer collateral) axons in a feedforward manner, but the EPSP dynamics and kinetics in these two cell types are different (Buhl et al., 1996). Moreover, basket and bistratified interneurons exhibit clearly distinct intrinsic and computational properties. For instance, compared to basket cells, bistratified interneurons have a more hyperpolarized resting membrane potential (−64.5 vs. −69.2 mV) and a nearly double input resistance (31.3 vs. 60.2 MΩ).

Due to their differences in intrinsic excitability and network connectivity, basket and bistratified cells might differentially affect CA1PCs activity. Moreover, their combined action might produce non-trivial synergistic effects on the computational properties of CA1PCs. Despite ongoing efforts to quantitatively characterize the CA1 circuit (Bezaire and Soltesz, 2013), the distinct functional contributions of different interneuron types on CA1PCs remain technically challenging to tease apart in the wet lab. The present study investigates the specific effects of basket and bistratified FFI on CA1PC using biophysically and morphologically detailed computational simulations constrained by and validated against experimental data. Specifically, we analyzed the CA1PC population activity as well as the single neuron spike probability and onset in four conditions: FFI by both basket and bistratified cells; FFI by basket cells alone; FFI by bistratified cells alone; and pure excitation. Furthermore, we investigated how modulating the synaptic strength of the two interneuron populations may regulate CA1PC firing.

MATERIALS AND METHODS

A biophysically realistic model of FFI in CA1PCs (**Figure 1A**) was designed based on previous work (Li and Ascoli, 2006; Ferrante et al., 2009). Model and simulations were implemented in NEURON (Hines and Carnevale, 1997) v7.3 using variable time step on a 32-bit Pentium quad-core Dell precision T3500 running Windows 7. The model is publicly available under the ModelDB section of SenseLab[2].

Neuronal Morphologies and Membrane Properties

The model included 40 digitally reconstructed CA1PC morphologies downloaded from the Korte (Michaelsen et al., 2010), Claiborne (Carnevale et al., 1997), Amaral (Ishizuka et al., 1995), Turner (Pyapali et al., 1998), Larkman (Bannister and Larkman, 1995), Gulyás (Megías et al., 2001), and Spruston (Golding et al., 2005) archives of NeuroMorpho.Org (Ascoli et al., 2007). CVAPP (Cannon et al., 1998) was used to differentially tag oblique dendrites (in stratum radiatum) from the main apical trunk and distal branches (in stratum lacunosum-moleculare). Basal dendrites (in stratum oriens) were already pre-tagged in NeuroMorpho.Org.

Active (I_{Na}, I_{Kdr}, I_{KA}, I_h) and passive properties (τ_m = 28 ms, R_m = 28 kΩ · cm^2, R_a = 50 Ω · cm) were the same for each neuronal morphology and have been previously described and experimentally validated for CA1PCs (Migliore et al., 2004, 2005; Ferrante et al., 2013). Briefly, I_{Na} and I_{Kdr} were uniformly distributed throughout the neuronal membrane (g_{Na} = 0.25 nS/μm^2; g_{Kdr} = 0.1 nS/μm^2), while I_{KA} and I_h increased linearly with the distance from the soma as in previously reported experiments (Hoffman et al., 1997; Magee, 1998), namely $g_{KA} = 0.3 \cdot (1 + \text{dist}/100)$ and $g_h = 0.0005 \cdot (1 + 3 \cdot \text{dist}/100)$.

As it can be appreciated from publicly available morphological tracings in NeuroMorpho.Org (Ascoli et al., 2007), the axons of the bistratified interneurons (NMO_ID: 02343, 02344, 02346, 02349 from Cossart et al., 2006) tend to selectively target stratum oriens and stratum radiatum, avoiding stratum pyramidale. In contrast, axons from basket cells (NMO_ID: 07323, 07326, 07338, 07339 from Glickfeld and Scanziani, 2006) tend to preferentially target the perisomatic region of CA1PCs (i.e., stratum pyramidale). This is consistent with seminal summaries clearly describing the morphologies and synaptic connectivity from bistratified (Somogyi and Klausberger, 2005) and basket (Buhl et al., 1994) cells to CA1PCs.

[1] Hippocampome.Org

[2] senselab.med.yale.edu

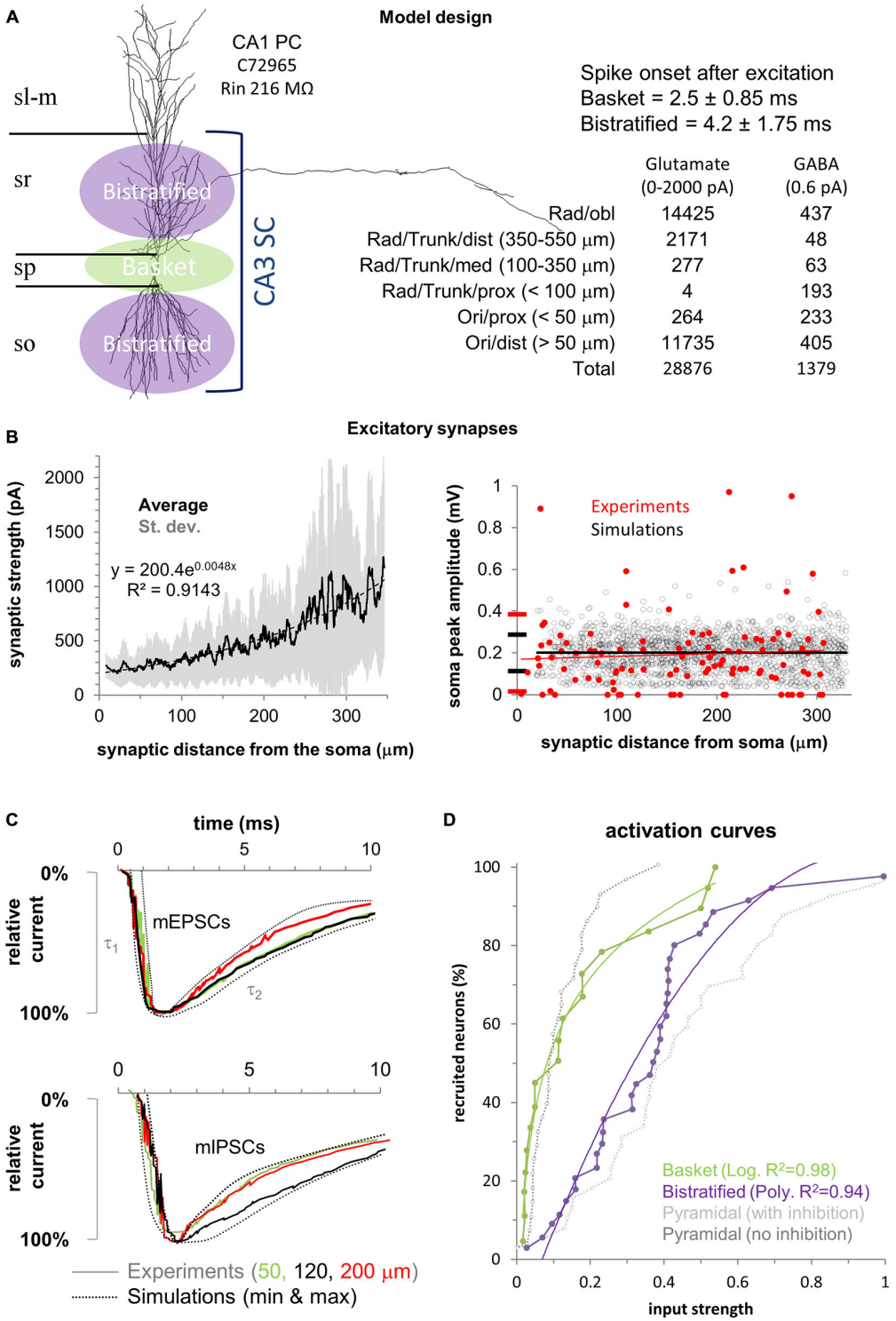

FIGURE 1 | Model design and experimental validation. (A) *Left*: Schematic of the feedforward inhibition (FFI) model in a CA1 pyramidal cell (CA1PC) illustrated with one of the 40 3D morphologies used. Basket cells synapse on the CA1PC perisomatic region (green) while bistratified cells synapse on the apical and basal dendrites (purple). *Right*: Temporal activation of the two interneuron populations and number of excitatory and inhibitory synapses with their respective spatial distributions. Stratum lacunosum-moleculare (sl-m), stratum radiatum (sr), stratum pyramidale (sp), and stratum oriens (so). **(B)** *Left*: Synaptic current increase (synaptic scaling) along the proximal-to-distal axis in the 40 neuronal morphologies. Solid black line shows the average synaptic strength for all synapses, with standard deviation in gray. Black dotted line is the exponential fit (equation on the chart). *Right*: Synaptic normalization at the soma compared to available

(*Continued*)

FIGURE 1 | Continued
experimental measurements (in red). **(C)** The model (dotted lines) replicates the experimental (solid traces) rise (τ_1), and decay (τ_2) time constants for mEPSCs (top panel) and mIPSCs (bottom panel) at different distances from the soma (color coded). **(D)** Fitting used in the model for the activation curves of the two interneuron populations (data from Pouille et al., 2009). Experimental activation curves for CA1PCs with (gray) and without (black) inhibition are provided for reference (respectively "control" and "gabazine" conditions from Pouille et al., 2009).

Synaptic Properties

A realistic number (Megías et al., 2001) of excitatory (n = 28,876) and inhibitory (n = 1379) synapses were randomly redistributed in each simulation within spatial boundaries (**Figure 1**) defined to emulate available experimental data (Megías et al., 2001). The model assumes that all excitatory synapses from CA3 Schaffer collaterals are located in strata oriens and radiatum, while inhibitory synapses from basket and bistratified interneurons are spatially non-overlapping: basket cells synapse on the soma, proximal basal dendrites (<50 μm from the soma), and proximal apical dendrites (<100 μm from the soma). Bistratified cells target the dendrites more distally on both the basal (>50 μm from the soma) and apical arbors (>100 μm and up to 550 μm from the soma). The numbers and dendritic distributions of excitatory and inhibitory synapses allocated in each simulation are reported in **Figure 1A**.

In agreement with experimental results (Magee and Cook, 2000), the weight of each excitatory synapse was adjusted so as to yield an average somatic depolarization of 0.2 mV in all CA1PCs (**Figure 1B**). To achieve this, we placed an excitatory synapse in each compartment of the main trunk of every neuron (up to 320 μm from the soma, as in the experiments). The synaptic weights varied with the distance from the soma according to the same formula for all neurons: $Syn\ weight = (A^*dist^2) + B$. We then adjusted the parameters (A and B) so that the average somatic depolarization was 0.2 mV and did not depend on the synaptic distance from the soma (Li and Ascoli, 2006). Experimental data suggest that each CA1PC receives on average 11 synaptic contacts from both basket and bistratified cells (Bezaire and Soltesz, 2013) and their compound effect ranges between 5 and 25 pA (Andrásfalvy and Mody, 2006). The conductance of all inhibitory synapses was accordingly set to 0.6 pA.

The kinetics and reversal potentials for both excitatory and inhibitory synaptic currents (**Figure 1C**) were modeled by fitting double-exponential functions (*Exp2Syn*) to experimental voltage data (Andrásfalvy and Mody, 2006). For the excitatory synapses, rise and decay times were 0.5 and 5.5 ms, respectively, and the reversal potential was 0 mV. Local mIPSCs recordings (Andrásfalvy and Mody, 2006) reveal no variation of kinetics with distance from the soma. Thus, the fitted synaptic properties were identical for basket and bistratified cells: rise time 0.73 ms, decay 6.5 ms, and reversal potential -80 mV.

Synapses were activated asynchronously and each synapse was only activated once per simulation. The activation time for excitatory synapses was sampled from a Gaussian distribution with mean equal 5 ms and standard deviation equal to 2.34 ms. The model assumes that, due to the local nature of basket and bistratified inhibition, the spike transmission through the short axons adds a negligible temporal delay to synaptic onset relative the somatic firing of the presynaptic interneurons. Accordingly, in agreement with experimental evidence (Pouille et al., 2009), basket cell synapses were activated on average 2.5 ms after stimulation (standard deviation 0.92 ms) and bistratified synapses 4.2 ms after excitation (standard deviation 1.32 ms).

Stimulation Protocol

To simulate varying stimulus strength, we increased the number of activated excitatory synapses one at the time, starting from 1. The outcome of every simulation for a given CA1PC was either a spike or not. For each given number of synapses, we run 50 simulations with every CA1PC. A CA1PC is considered to be "recruited" if it spikes in at least half of the simulations (≥25/50). In order to most meaningfully compare simulation with experimental data, we define a unitary input strength (following Pouille et al., 2009) as the number of activated excitatory synapses sufficient to recruit 95% of the CA1PCs (38 out of 40) in the presence of basket and bistratified FFI ("control" condition in Pouille et al., 2009). The activity of the two populations of interneurons in response to stimulation (that is, the proportion of activated inhibitory synapses) was simulated by using mathematical fitting (**Figure 1D**) that closely replicated ($R^2 > 0.94$) the experimental data (Pouille et al., 2009). For each neuron, we stopped increasing the stimulus strength and ended the simulations when a spike was observed in all 50 stimulations (100% spike probability) for the last three numbers of activated synapses.

RESULTS

Model Validation and CA1PC Population

Despite identical distributions of active and passive properties, the natural diversity of CA1PC morphologies results in clear differences in excitability as evidenced by the input/output curves of two representative neurons (**Figure 2A**), and reflecting a similar variability in the experimental data (Pouille et al., 2009). The number of synapses necessary to recruit a CA1PC (that is, to make it spike in at least half of 50 simulations) in the absence of inhibition varied from less than 20 to more than 100. At the population level, the activation curves of our simulations closely matched experimental data both with inhibition (control condition in Pouille et al., 2009) and without (GABA blocked or "gabazine" conditions in Pouille et al., 2009), reproducing the experimentally observed extension of the CA1PC dynamic range through FFI (**Figure 2B**). The Schaffer collateral input strength that recruited 95% of CA1PC with no inhibition was 0.27 relative to the same with "control" FFI, well matching the experimental value of 0.26 in the presence of gabazine (Pouille et al., 2009).

What are the distinct contributions of basket and bistratified cells to the CA1PC dynamic range extension? When only activating bistratified synapses while selectively blocking basket synapses in the simulation, FFI mostly affects the recruitment of

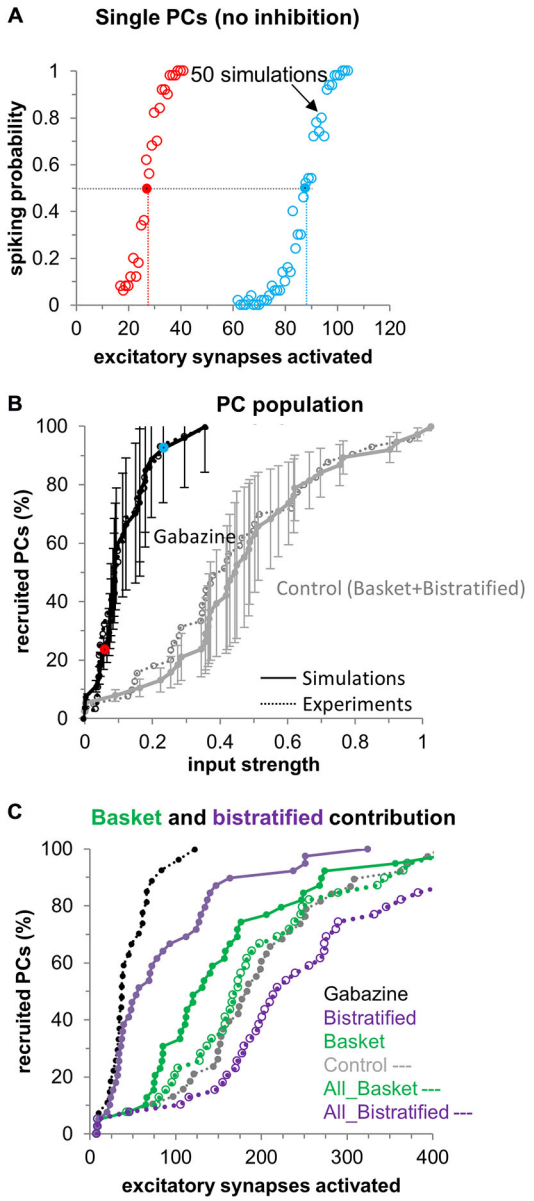

FIGURE 2 | CA1PC input/output curves: distinct FFI by basket and bistratified interneurons. (A) CA1PC input/output curves for two representative neurons in the absence of inhibition. Each dot represents the spiking probability over 50 simulations each with random redistribution of the synaptic spatial location. The dotted lines indicate the number of synapses necessary to "recruit" the cell (i.e., passing the 50% spiking probability). **(B)** Activation curve of the CA1PC population (n = 40 cells). Simulations (solid lines with error bars) closely match experiments (dotted lines, from Pouille et al., 2009) for the control (black) and gabazine conditions (gray). Red and blue dots represent the cells shown in **(A)**. **(C)** Distinct contribution of basket (solid green line) and bistratified (solid purple line) interneurons to the CA1PC activation curve, and predicted effect if all the existent inhibitory synapses belonged to basket (dotted green line) or bistratified (dotted purple line) cells.

relatively less excitable CA1PCs, i.e., those requiring activation of more excitatory synapses to fire (**Figure 2C**). In this context we define as "easily excitable" any CA1PC recruited by 30 excitatory synapses or less in absence of any inhibitory inputs. Correspondingly, CA1PCs requiring more than 30 synapses to be recruited are considered "less excitable". The activation curve in the Gabazine condition (**Figure 2C**) suggests a continuum of CA1PCs excitability without sharp separation between two groups. In general, less excitable cells tended to possess lower input resistance, but other factors may also play a role, such as the total number of branches or the specific branching patterns in each neuronal morphology.

In contrast, FFI by basket synapses without bistratified synapses affected the whole CA1PC population, more closely resembling the effect of the control condition (i.e., combined basket and bistratified). Hence, taken as individual neuronal populations, basket cells play a larger role in regulating the CA1PC dynamic range by FFI compared to bistratified cells. What features of basket cells enable them to regulate the CA1PC dynamic range more efficiently? Aside from their spike timing and activation curves, basket and bistratified cells also differ in the number and spatial distribution of their synapses onto CA1PCs. Although in our model the synaptic domains of basket and bistratified synapses are completely segregated on CA1 PC somato-dendritic domains, some degree of spatial overlap between these interneurons may indeed exist in real biological systems. To ascertain the effects of partial overlaps, we ran simulations corresponding to the extreme case in which all synapses (disregarding their spatial location on the dendritic tree) were set with basket-like (or bistratified-like) activation (**Figure 2C**). Specifically, to differentiate the effects of spike timing and of the activation curves in basket and bistratified cells from the number and spatial location of their synapses, we left the number and spatial distribution of all synapses intact, but we adopted for all synapses the spike timing and activation curve of one of the two interneuron types (**Figure 2C** dotted lines). In these conditions, the ability of bistratified cells to extend the dynamic range of CA1PCs increased dramatically, becoming more pronounced than that of basket cells or of the control condition (basket and bistratified combined). This result suggests that the differential FFI regulation of CA1PC activity by distinct GABAergic interneurons results from a combination of their specific biophysical and morphological properties. However, when the microcircuit details are computationally equalized, the spike timing and activation characteristics of bistratified cells are more conducive to extending the CA1PC dynamic range than those of basket cells.

These results shed light on the possible properties of the basket and bistratified interneurons responsible for the changes in the CA1pc I/O curve. Specifically, the activation curves of the two interneurons play a major role (empty blue and green symbols in **Figure 2C**). At the same time, the spatial distribution of the synapses also seems to significantly contribute to this effect: when the synapses of bistratified cells are moved perisomatically their effect changes from rather small (purple symbols) to highly prominent.

Single CA1PCs Input/Output Curves

Next we examined the effects of different levels of FFI on individual CA1PCs. Although pharmacological treatments allow

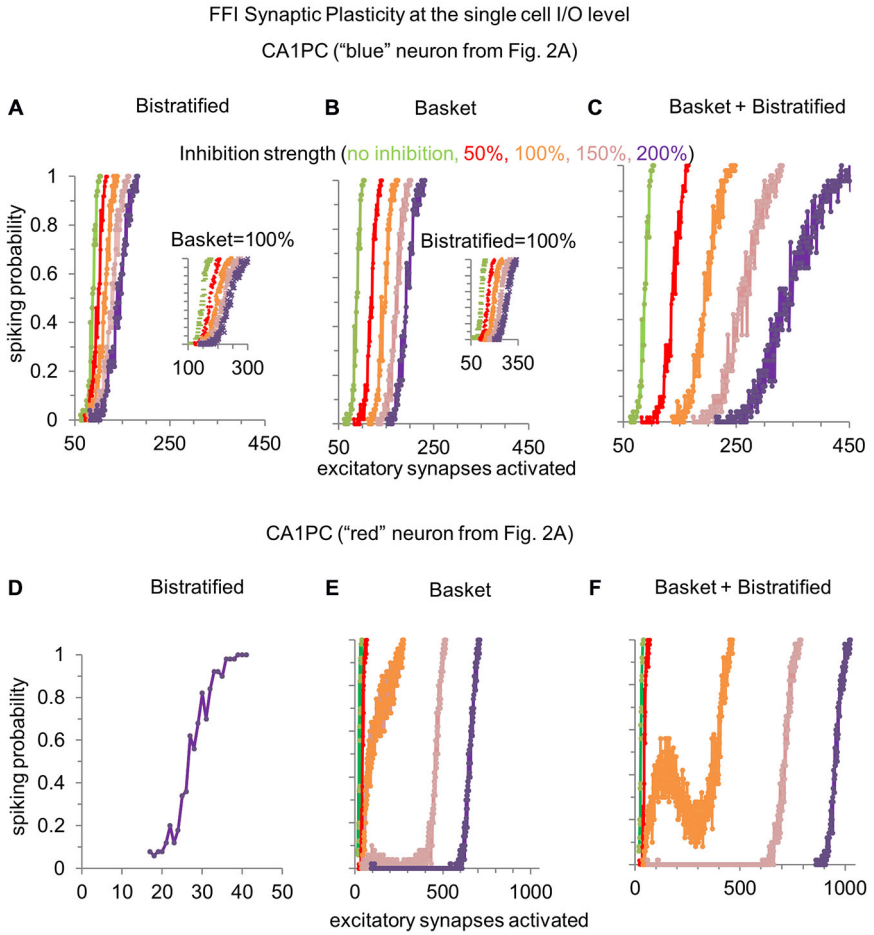

FIGURE 3 | Modulating the synaptic strength of basket and bistratified interneurons onto relatively less or more excitable CA1PCs. (A) Increasing the strength of FFI by bistratified interneurons on a single CA1PC recruited by a high number of excitatory synapses progressively reduces the response gain. When compared to the no inhibition condition (in green), the computational operation performed by bistratified cells can be reduced to a division of the CA1PC I/O curve. Inset shows the same effect when basket cell synapses are activated. **(B)** Modulating the synaptic strength of basket interneurons on the same CA1PC increases the response threshold. When compared to the no inhibition condition (in green), the computational operation performed by basket cells can be reduced to a subtraction of the CA1PC I/O curve. Inset shows the same effect when bistratified cell synapses are activated. **(C)** Simultaneously increasing the strength of basket and bistratified FFI changes both the gain and threshold of CA1PC response to stimulation. **(D–F)** Same as **(A–C)** but on a CA1PC recruited by a low number of excitatory synapses. Note the emergence of a buffering effect with baseline inhibitory strength of combined basket and bistratified FFI (orange curve of **F**).

to increase or decrease the overall post-synaptic consequences of GABAergic transmission (Ferrante et al., 2008), computational simulations enable the selective manipulation of individual interneuron types. Thus, we modeled the progressive increase (150% and 200%) and decrease (50% and 0%) of FFI by bistratified cells alone, basket cell alone, and basket and bistratified combined (**Figure 3**), illustrating the results on CA1PC input/output curves using the same neurons singled out in **Figure 2A**.

Modulating the synaptic strength of bistratified interneurons alone onto a relatively less excitable CA1PC (one requiring more excitatory synapses to spike) changed the slope of its input/output curve (**Figure 3A**). This corresponds to a reduction of response gain with increasing FFI. In other words, bistratified cells enable CA1PCs to perform a divisive operation on their I/O curve. In contrast, altering the synaptic strength of basket cells regulated the intercept of the CA1PC input/output. This corresponds to a rise of the response threshold with increasing FFI (**Figure 3B**). Functionally, this translates in basket cells enabling CA1PCs to perform a subtractive operation on their I/O relationship. These complementary effects of bistratified and basket cells on CA1PCs remained present when the other interneuron class was also activated at its baseline strength (insets in **Figures 3A,B**). The two effects could be combined by varying at the same time the synaptic strength of both basket and bistratified cells (**Figure 3C**), controlling simultaneously slope and intercept.

When instead considering a relatively more excitable CA1PC, bistratified interneurons alone displayed no effect whatsoever on the input/output curve (**Figure 3D**). This result is explained by the stronger input required to activate

bistratified cells (**Figure 1D**). The modulation of basket cell synaptic strength onto easily excitable CA1PCs led to the emergence of a plateau in the input/output curve, corresponding to a signal processing buffer (Ferrante et al., 2009). When basket and bistratified cells acted together, their combined effect synergistically enhanced the buffering effect, occasionally producing a "reversal" input/output zone (**Figure 3F**), even though bistratified interneurons alone did not alter CA1PC activity (**Figure 3D**).

FFI Buffering of the CA1PC Input-Output Relation

To quantify the distinct contributions of different FFI pathways to the input/output buffering of CA1PCs, we measured the buffering range (BR) of activated excitatory synapses within which the response remains constant or decreases (Ferrante et al., 2009). This is achieved by fitting the computed spiking probability with three lines (the second of which of zero slope) by minimizing the squared distance from all data points in the 50 simulations (**Figure 4A**; simulation noise is due to the spatial redistribution of activated synapses along the dendritic tree). In the gabazine (**Figure 4B**; no inhibition) condition most (56%) CA1PCs do not exhibit input/output buffering, and the few exceptions (due to synaptic redistribution noise) are confined to limited buffering ranges (<8 synapses). Basket and bistratified FFI, each taken in isolation, produced modest to moderate buffering effect, with e.g., ~10–20% of CA1PC buffered for more than eight activated excitatory synapses. In contrast, the combined FFI by both basket and bistratified interneurons produced substantial buffering, with the vast majority of CA1PCs showing a buffering range of 10–100 activated excitatory synapses. This result suggests that FFI buffering of CA1PCs synergistically produces the greatest computational impact through the interaction of diverse interneuron populations.

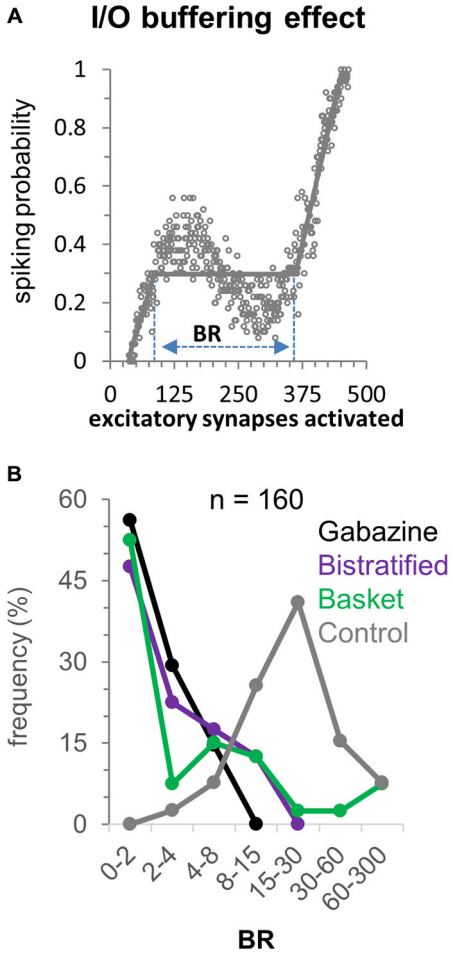

FIGURE 4 | Buffering effect of FFI on the CA1PC input/output relationship. (A) Computation of the buffering range (BR) following the definition of Ferrante et al., 2009. **(B)** Frequency of BR values over the 40 CA1PC morphologies with no inhibition, basket alone, bistratified alone, and combined basket and bistratified FFI (all at baseline range). The synergistic FFI effect of basket and bistratified interneurons generates BR values between 15 and 30 synapses in approximately half of the neurons.

Distinct and Synergistic Effects of FFI on CA1PC Spike Timing

How does the modulation of FFI in basket and bistratified interneurons, alone or combined, affect the spike onset of CA1PCs? In the absence of inhibition (gabazine condition), activation of larger numbers of excitatory synapses generally reduces the CA1PC spike onset. Progressively increasing the synaptic strength of bistratified interneurons alone (**Figure 5A**), while requiring a correspondingly growing number of activated excitatory synapses to elicit a spike, also reduced the spread in the spike onset of CA1PCs across the entire stimulation range. Specifically, bistratified FFI nearly halved the spike onset differential from 13 ms with no inhibition (26.3 ms at 76 EPSPs minus 13.3 ms at 109 EPSPs), to 7.1 ms at 200% inhibitory strength (18.7 ms at 116 EPSPs minus 11.6 ms at 182 EPSPs). Modulating the synaptic strength of basket cells produced a slightly greater reduction of the spike onset differential relative to bistratified interneurons, down to 5.2 ms (17.2 ms at 156 EPSPs minus 12 ms at 226 EPSPs), but also created a sharper separation in the number of activated excitatory synapses required to spike (**Figure 5B**). The combination of basket and bistratified interneurons reduced the CA1PC spike onset differential similarly to the basket cells alone (5.7 ms), but synergistically produced the largest increase in the number of activated excitatory synapses necessary to fire a spike (**Figure 5C**). Overall, the effect of FFI on CA1PC firing is to reduce sensitivity (increase the number of required inputs) while reducing temporal delay and jitter. As a consequence, potentiating FFI synapses may allow CA1PCs to respond to heightened excitation with improved temporal fidelity.

DISCUSSION

Seminal experiments have demonstrated a fundamental role of FFI on CA1PCs in enforcing temporal fidelity (Pouille and Scanziani, 2001) and in expanding the dynamic range, in terms of both spiking probability of single neurons and

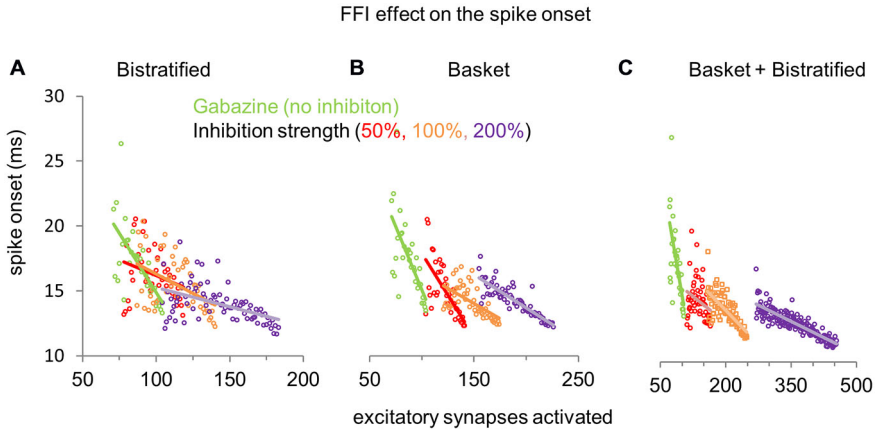

FIGURE 5 | Effect of FFI on CA1PC spike onset. (A) Modulation of CA1PC spike onset by increasing synaptic strength of bistratified interneurons alone. **(B)** Same as **(A)**, but altering the synaptic strength of basket interneurons alone. **(C)** Same as **(A,B)**, except simultaneously modifying the synaptic strengths of both basket and bistratified interneurons. The gabazine data (green dots and line: no inhibition) are the same for all conditions and are repeated across panels for reference.

fraction of recruited cells at the population level (Pouille et al., 2009). However, it has so far remained challenging to distinguish experimentally the specific contributions of distinct FFI pathways across the diversity of GABAergic interneurons. In addition to providing insights on possible circuit mechanisms, quantifying the separate effect of multiple FFI pathways is important in light of the state-dependent rhythmic change in CA1PCs excitability due to the temporal redistribution of inhibition over perisomatic and dendritic domains (Somogyi et al., 2013).

Furthermore, previous experimental studies only compared CA1PC activity with and without inhibition, and could not investigate the consequence of gradually modulating or potentiating FFI. This effect could be important because inhibitory synaptic plasticity regulates CA1PCs spiking (Saraga et al., 2008) and feedforward disinhibition mediates hippocampal long-term potentiation in CA1PCs (Ormond and Woodin, 2009). In order to bypass existing experimental limitations, we pursued a computational modeling strategy to explore a broader range of possible mechanisms regarding the interaction between fast-spiking basket cells, regular-spiking bistratified cells, and CA1PCs.

Our simulation analyses suggest that basket cells are overall more effective than bistratified cells in expanding the dynamic range of CA1PCs (**Figure 2C**). This differential influence is likely due to the number and distributions of the respective synapses, since adopting the timing and activation response of bistratified cells for all synapses augmented the effect of FFI. Furthermore, when activated alone, bistratified interneurons mostly affect less excitable CA1PCs, i.e., those recruited by a high number of excitatory synapses. However, when basket cells are also activated, the bistratified FFI exercises a clear effect on more excitable CA1PCs as well.

The ability to gradually and independently alter the synaptic strength of basket and bistratified cells while keeping the other interneuron type constant or silent also revealed a double-dissociation of the effects of these two FFI pathways on the response properties of CA1PCs. Specifically, regulating basket cell synapses affected the input/output intercept or spiking threshold of CA1PCs, while altering bistratified cell synapses modulated the CA1PC input/output slope or spiking probability gain. This result is important because it suggests that basket and bistratified cells perform two functionally distinct operations into the I/O of CA1PCs: basket cells subtract, while bistratified divide the sigmoidal I/O of CA1PCs. The ability of simulations to isolate the independent effects of the interneuron activation curves, axonal distributions, and synaptic properties may in future work help determine the biophysical determinants of these complementary transformations.

We previously showed that FFI in the dentate gyrus buffered the input/output curve of principal (granule) cells, with the buffering range and buffered firing rate modulated by the number and weight of incoming excitatory synapses on the inhibitory interneuron (Ferrante et al., 2009). Recent experimental evidence lends support to this mechanism (cf. red curve of Figure 9D in Sun et al., 2014), and direct experimental testing in the same neuronal circuit now appears feasible (Li et al., 2013). Similarly, in this study, FFI buffering was observed when the CA1PC activation curve overlapped substantially with those of the inhibitory interneurons, most notably when both basket and bistratified cells were activated at their baseline level. Why, in these same conditions, was CA1PC input/output buffering not observed by Pouille et al., 2009? The most likely reason is that the input strength was not finely controlled at the single cell level in that study: for each set of recordings in every CA1PC, only one or two data points were acquired in the range of input strengths across which the spike probability went from 0 and 1 (i.e., where the plateaus or response reversal would be found), preventing the detection of any possible buffering effect. Synaptic input strength (Perez-Rosello et al., 2011) and its temporal summation

(Migliore et al., 2004) can be highly regulated/shaped by intrinsic neuronal properties. It would be interesting to test how intrinsic cellular differences affect the dividing, subtracting, and buffering I/O operations performed by the different types of FFIs in CA1PCs.

Our spike onset results suggest that, notwithstanding specific differences between basket and bistratified interneurons, potentiating FFI synapses could maintain CA1PC spike timing constant for larger input strength. This might be considered as an additional and complementary aspect of the broad phenomena related to homeostatic plasticity (Turrigiano, 1999). These interactions are also likely to influence network dynamics over time through multiple parallel mechanisms. For example, $GABA_A$-mediated FFI modulates hippocampal spike timing-dependent plasticity (Jang and Kwag, 2012). FFI also underlies the propagation into CA1 of cholinergically induced gamma oscillations intrinsically generated in CA3 (Zemankovics et al., 2013), but not the intrinsic generation of faster gamma oscillations in CA1 (Craig and McBain, 2015). Interestingly, recent *in vitro* and *in vivo* results (Shay et al., 2015; Tsuno et al., 2015) suggest that in neurons with strong I_h conductances, inhibitory synaptic inputs may enable post-inhibitory APs in restricted phases of theta oscillations. This alternative role of FFI could provide a possible mechanism to encode spatial navigation (Hasselmo, 2013). Such I_h-dependent post-inhibitory rebound spiking could be dynamically unmasked by plastic regulation of I_{KA} (Ascoli et al., 2010).

Despite the electrophysiological and morphological realism of our computational model, it is impractical if not impossible to capture the full range of variability observed in nature. For instance, experiments tend to be noisier (i.e., displaying larger variability) when compared to simulations (**Figure 1B**), probably due to cellular differences in biophysical properties not implemented in our model. It would be interesting to investigate how intrinsic differences in ionic channels and other membrane characteristics affect the FFI modulation of CA1PC input/output properties. Our model accounts for all excitatory synapses (Megías et al., 2001), thus including recurrent local feed-forward excitation by CA1 pyramidal cells. Possible biophysical differences between these recurrent CA1 synapses and the main input from CA3, including the ∼2 ms delay due to di-synaptic activation, were not simulated. However, only ∼10% of the excitatory synapses are from CA1 recurrent axons, thus these differential effects can be assume to be minimal.

In addition, this study focused on a specific sub-circuit of the CA1 network, namely, the FFI interaction of basket and bistratified cells onto CA1PCs. Nonetheless, the same interneurons also provide inhibitory feedback to CA1PCs (Ali et al., 1998), possibly enhancing FFI buffering during sustained CA1PC activity. More generally, a number of other GABAergic interneurons may also participate in the complex regulation of CA1PC response to CA3 pyramidal neuron input (Somogyi, 2010), including ivy cells, axo-axonic cells, trilaminar cells, quadrilaminar cells, Schaffer collateral-associated cells, apical-targeting cells, and oriens-alveus cells among others (see also Hippocampome.org). Furthermore, the parallel, converging, and diverging interaction of these pathways can be coordinated by a diverse family of interneuron-specific interneurons (Francavilla et al., 2015). Given such complex circuitry, neurobiologically plausible models and detailed compartmental simulations can play an essential role in the elucidation of the computational mechanisms at play.

AUTHOR CONTRIBUTIONS

MF implemented the model, run the simulations, and analyzed the data. MF and GAA conceived the research design, interpreted the data, and wrote the manuscript.

ACKNOWLEDGMENTS

The authors would like to thank Drs. Michele Migliore and Michael Hasselmo for invaluable feedback. This work was supported in part by National Institutes of Health grant R01 NS39600, Office of Naval Research grant MURI N00014-10-1-0198, and National Science Foundation grant RI IIS-1302256 to GAA. Publication of this article was funded in part by the George Mason University Libraries Open Access Publishing Fund.

REFERENCES

Ali, A. B., Deuchars, J., Pawelzik, H., and Thomson, A. M. (1998). CA1 pyramidal to basket and bistratified cell EPSPs: dual intracellular recordings in rat hippocampal slices. *J. Physiol.* 507, 201–217. doi: 10.1111/j.1469-7793.1998.201bu.x

Andrásfalvy, B. K., and Mody, I. (2006). Differences between the scaling of miniature IPSCs and EPSCs recorded in the dendrites of CA1 mouse pyramidal neurons. *J. Physiol.* 576, 191–196. doi: 10.1113/jphysiol.2006.115428

Ascoli, G. A., Donohue, D. E., and Halavi, M. (2007). NeuroMorpho.Org: a central resource for neuronal morphologies. *J. Neurosci.* 27, 9247–9251. doi: 10.1523/jneurosci.2055-07.2007

Ascoli, G. A., Gasparini, S., Medinilla, V., and Migliore, M. (2010). Local control of postinhibitory rebound spiking in CA1 pyramidal neuron dendrites. *J. Neurosci.* 30, 6434–6442. doi: 10.1523/jneurosci.4066-09.2010

Bannister, N. J., and Larkman, A. U. (1995). Dendritic morphology of CA1 pyramidal neurones from the rat hippocampus: I. Branching patterns. *J. Comp. Neurol.* 360, 150–160. doi: 10.1002/cne.903600111

Bezaire, M. J., and Soltesz, I. (2013). Quantitative assessment of CA1 local circuits: knowledge base for interneuron-pyramidal cell connectivity. *Hippocampus* 23, 751–785. doi: 10.1002/hipo.22141

Buhl, E. H., Halasy, K., and Somogyi, P. (1994). Diverse sources of hippocampal unitary inhibitory postsynaptic potentials and the number of synaptic release sites. *Nature* 368, 823–828. doi: 10.1038/368823a0

Buhl, E. H., Szilágyi, T., Halasy, K., and Somogyi, P. (1996). Physiological properties of anatomically identified basket and bistratified cells in the CA1 area of the rat hippocampus *in vitro*. *Hippocampus* 6, 294–305. doi: 10.1002/(sici)1098-1063(1996)6:3<294:aid-hipo7>3.0.co;2-n

Buzsáki, G. (1984). Feed-forward inhibition in the hippocampal formation. *Prog. Neurobiol.* 22, 131–153. doi: 10.1016/0301-0082(84)90023-6

Cannon, R. C., Turner, D. A., Pyapali, G. K., and Wheal, H. V. (1998). An on-line archive of reconstructed hippocampal neurons. *J. Neurosci. Methods* 84, 49–54. doi: 10.1016/s0165-0270(98)00091-0

Carnevale, N. T., Tsai, K. Y., Claiborne, B. J., and Brown, T. H. (1997). Comparative electrotonic analysis of three classes of rat hippocampal neurons. *J. Neurophysiol.* 78, 703–720.

Cossart, R., Petanjek, Z., Dumitriu, D., Hirsch, J. C., Ben-Ari, Y., Esclapez, M., et al. (2006). Interneurons targeting similar layers receive synaptic inputs with similar kinetics. *Hippocampus* 16, 408–420. doi: 10.1002/hipo.20169

Craig, M. T., and McBain, C. J. (2015). Fast gamma oscillations are generated intrinsically in CA1 without the involvement of fast-spiking basket cells. *J. Neurosci.* 35, 3616–3624. doi: 10.1523/JNEUROSCI.4166-14.2015

Csicsvari, J., Hirase, H., Mamiya, A., and Buzsáki, G. (2000). Ensemble patterns of hippocampal CA3-CA1 neurons during sharp wave-associated population events. *Neuron* 28, 585–594. doi: 10.1016/s0896-6273(00)00135-5

Ferrante, M., Blackwell, K. T., Migliore, M., and Ascoli, G. A. (2008). Computational models of neuronal biophysics and the characterization of potential neuropharmacological targets. *Curr. Med. Chem.* 15, 2456–2471. doi: 10.2174/092986708785909094

Ferrante, M., Migliore, M., and Ascoli, G. A. (2009). Feed-forward inhibition as a buffer of the neuronal input-output relation. *Proc. Natl. Acad. Sci. U S A* 106, 18004–18009. doi: 10.1073/pnas.0904784106

Ferrante, M., Migliore, M., and Ascoli, G. A. (2013). Functional impact of dendritic branch-point morphology. *J. Neurosci.* 33, 2156–2165. doi: 10.1523/JNEUROSCI.3495-12.2013

Francavilla, R., Luo, X., Magnin, E., Tyan, L., and Topolnik, L. (2015). Coordination of dendritic inhibition through local disinhibitory circuits. *Front. Synaptic Neurosci.* 7:5. doi: 10.3389/fnsyn.2015.00005

Glickfeld, L. L., and Scanziani, M. (2006). Distinct timing in the activity of cannabinoid-sensitive and cannabinoid-insensitive basket cells. *Nat. Neurosci.* 9, 807–815. doi: 10.1038/nn1688

Golding, N. L., Mickus, T. J., Katz, Y., Kath, W. L., and Spruston, N. (2005). Factors mediating powerful voltage attenuation along CA1 pyramidal neuron dendrites. *J. Physiol.* 568, 69–82. doi: 10.1113/jphysiol.2005.086793

Halasy, K., Buhl, E. H., Lörinczi, Z., Tamás, G., and Somogyi, P. (1996). Synaptic target selectivity and input of GABAergic basket and bistratified interneurons in the CA1 area of the rat hippocampus. *Hippocampus* 6, 306–329. doi: 10.1002/(sici)1098-1063(1996)6:3<306::aid-hipo8>3.0.co;2-k

Hasselmo, M. E. (2013). Neuronal rebound spiking, resonance frequency and theta cycle skipping may contribute to grid cell firing in medial entorhinal cortex. *Philos. Trans. R. Soc. Lond. B Biol. Sci.* 369:20120523. doi: 10.1098/rstb.2012.0523

Hines, M. L., and Carnevale, N. T. (1997). The NEURON simulation environment. *Neural Comput.* 9, 1179–1209. doi: 10.1162/neco.1997.9.6.1179

Hoffman, D. A., Magee, J. C., Colbert, C. M., and Johnston, D. (1997). K+ channel regulation of signal propagation in dendrites of hippocampal pyramidal neurons. *Nature* 387, 869–875. doi: 10.1038/43119

Ishizuka, N., Cowan, W. M., and Amaral, D. G. (1995). A quantitative analysis of the dendritic organization of pyramidal cells in the rat hippocampus. *J. Comp. Neurol.* 362, 17–45. doi: 10.1002/cne.903620103

Jang, H. J., and Kwag, J. (2012). GABAA receptor-mediated feedforward and feedback inhibition differentially modulate hippocampal spike timing-dependent plasticity. *Biochem. Biophys. Res. Commun.* 427, 466–472. doi: 10.1016/j.bbrc.2012.08.081

Klausberger, T. (2009). GABAergic interneurons targeting dendrites of pyramidal cells in the CA1 area of the hippocampus. *Eur. J. Neurosci.* 30, 947–957. doi: 10.1111/j.1460-9568.2009.06913.x

Li, X., and Ascoli, G. A. (2006). Computational simulation of the input-output relationship in hippocampal pyramidal cells. *J. Comput. Neurosci.* 21, 191–209. doi: 10.1007/s10827-006-8797-z

Li, Y., Stam, F. J., Aimone, J. B., Goulding, M., Callaway, E. M., and Gage, F. H. (2013). Molecular layer perforant path-associated cells contribute to feed-forward inhibition in the adult dentate gyrus. *Proc. Natl. Acad. Sci. U S A* 110, 9106–9111. doi: 10.1073/pnas.1306912110

MacDonald, C. J., Lepage, K. Q., Eden, U. T., and Eichenbaum, H. (2011). Hippocampal "time cells" bridge the gap in memory for discontiguous events. *Neuron* 71, 737–749. doi: 10.1016/j.neuron.2011.07.012

Magee, J. C. (1998). Dendritic hyperpolarization-activated currents modify the integrative properties of hippocampal CA1 pyramidal neurons. *J. Neurosci.* 18, 7613–7624.

Magee, J. C., and Cook, E. P. (2000). Somatic EPSP amplitude is independent of synapse location in hippocampal pyramidal neurons. *Nat. Neurosci.* 3, 895–903. doi: 10.1038/78800

Megías, M., Emri, Z., Freund, T. F., and Gulyás, A. I. (2001). Total number and distribution of inhibitory and excitatory synapses on hippocampal CA1 pyramidal cells. *Neuroscience* 102, 527–540. doi: 10.1016/s0306-4522(00)00496-6

Michaelsen, K., Murk, K., Zagrebelsky, M., Dreznjak, A., Jockusch, B. M., Rothkegel, M., et al. (2010). Fine-tuning of neuronal architecture requires two profilin isoforms. *Proc. Natl. Acad. Sci. U S A* 107, 15780–15785. doi: 10.1073/pnas.1004406107

Migliore, M., Ferrante, M., and Ascoli, G. A. (2005). Signal propagation in oblique dendrites of CA1 pyramidal cells. *J. Neurophysiol.* 94, 4145–4155. doi: 10.1152/jn.00521.2005

Migliore, M., Messineo, L., and Ferrante, M. (2004). Dendritic Ih selectively blocks temporal summation of unsynchronized distal inputs in CA1 pyramidal neurons. *J. Comput. Neurosci.* 16, 5–13. doi: 10.1023/b:jcns.0000004837.81595.b0

O'Keefe, J., and Dostrovsky, J. (1971). The hippocampus as a spatial map. Preliminary evidence from unit activity in the freely-moving rat. *Brain Res.* 34, 171–175. doi: 10.1016/0006-8993(71)90358-1

Ormond, J., and Woodin, M. A. (2009). Disinhibition mediates a form of hippocampal long-term potentiation in area CA1. *PLoS One* 4:e7224. doi: 10.1371/journal.pone.0007224

Perez-Rosello, T., Baker, J. L., Ferrante, M., Iyengar, S., Ascoli, G. A., and Barrionuevo, G. (2011). Passive and active shaping of unitary responses from associational/commissural and perforant path synapses in hippocampal CA3 pyramidal cells. *J. Comput. Neurosci.* 31, 159–182. doi: 10.1007/s10827-010-0303-y

Pouille, F., Marin-Burgin, A., Adesnik, H., Atallah, B. V., and Scanziani, M. (2009). Input normalization by global feedforward inhibition expands cortical dynamic range. *Nat. Neurosci.* 12, 1577–1585. doi: 10.1038/nn.2441

Pouille, F., and Scanziani, M. (2001). Enforcement of temporal fidelity in pyramidal cells by somatic feed-forward inhibition. *Science* 293, 1159–1163. doi: 10.1126/science.1060342

Pyapali, G. K., Sik, A., Penttonen, M., Buzsaki, G., and Turner, D. A. (1998). Dendritic properties of hippocampal CA1 pyramidal neurons in the rat: intracellular staining *in vivo* and *in vitro*. *J. Comp. Neurol.* 391, 335–352. doi: 10.1002/(sici)1096-9861(19980216)391:3<335::aid-cne4>3.0.co;2-2

Saraga, F., Balena, T., Wolansky, T., Dickson, C. T., and Woodin, M. A. (2008). Inhibitory synaptic plasticity regulates pyramidal neuron spiking in the rodent hippocampus. *Neuroscience* 155, 64–75. doi: 10.1016/j.neuroscience.2008.05.009

Shadlen, M. N., and Newsome, W. T. (1998). The variable discharge of cortical neurons: implications for connectivity, computation and information coding. *J. Neurosci.* 18, 3870–3896.

Shay, C. F., Ferrante, M., Chapman, G. W., IVth, and Hasselmo, M. E. (2015). Rebound spiking in layer II medial entorhinal cortex stellate cells: possible mechanism of grid cell function. *Neurobiol. Learn. Mem.* doi: 10.1016/j.nlm.2015.09.004 [Epub ahead of print].

Somogyi, P. (2010). "Hippocampus: intrinsic organization," in *Handbook of Brain Microcircuits*, ed. G. M. Shepherd and S. Grillner (New York: Oxford University Press), 148–164.

Somogyi, P., Katona, L., Klausberger, T., Lasztóczi, B., and Viney, T. J. (2013). Temporal redistribution of inhibition over neuronal subcellular domains underlies state-dependent rhythmic change of excitability in the hippocampus. *Philos. Trans. R. Soc. Lond. B Biol. Sci.* 369:20120518. doi: 10.1098/rstb.2012.0518

Somogyi, P., and Klausberger, T. (2005). Defined types of cortical interneurone structure space and spike timing in the hippocampus. *J. Physiol.* 562, 9–26. doi: 10.1113/jphysiol.2004.078915

Sun, Q., Srinivas, K. V., Sotayo, A., and Siegelbaum, S. A. (2014). Dendritic Na+ spikes enable cortical input to drive action potential output from hippocampal CA2 pyramidal neurons. *Elife* 3:e04551. doi: 10.7554/elife.04551

Tricoire, L., Pelkey, K. A., Erkkila, B. E., Jeffries, B. W., Yuan, X., and McBain, C. J. (2011). A blueprint for the spatiotemporal origins of mouse hippocampal interneuron diversity. *J. Neurosci.* 31, 10948–10970. doi: 10.1523/JNEUROSCI.0323-11.2011

Tsuno, Y., Chapman, G. W., and Hasselmo, M. E. (2015). Rebound spiking properties of mouse medial entorhinal cortex neurons *in vivo*. *Eur. J. Neurosci.* doi: 10.1111/ejn.13097 [Epub ahead of print].

Turrigiano, G. G. (1999). Homeostatic plasticity in neuronal networks: the more things change, the more they stay the same. *Trends Neurosci.* 22, 221–227. doi: 10.1016/s0166-2236(98)01341-1

Wheeler, D. W., White, C. M., Rees, C. L., Komendantov, A. O., Hamilton, D. J., and Ascoli, G. A. (2015). Hippocampome.org: a knowledge base of neuron types in the rodent hippocampus. *Elife* 4, 1–28. doi: 10.7554/elife.09960

Wilson, M. A., and McNaughton, B. L. (1993). Dynamics of the hippocampal ensemble code for space. *Science* 261, 1055–1058. doi: 10.1126/science.8351520

Zemankovics, R., Veres, J. M., Oren, I., and Hájos, N. (2013). Feedforward inhibition underlies the propagation of cholinergically induced gamma oscillations from hippocampal CA3 to CA1. *J. Neurosci.* 33, 12337–12351. doi: 10.1523/JNEUROSCI.3680-12.2013

Conflict of Interest Statement: The authors declare that the research was conducted in the absence of any commercial or financial relationships that could be construed as a potential conflict of interest.

frontiers in Computational Neuroscience

ORIGINAL RESEARCH
published: 09 June 2017
doi: 10.3389/fncom.2017.00042

Modulating STDP Balance Impacts the Dendritic Mosaic

Nicolangelo Iannella[1,2]* *and Thomas Launey*[3]*

[1] School of Mathematical Sciences, University of Nottingham, Nottingham, United Kingdom, [2] Computational and Theoretical Neuroscience Laboratory, Institute for Telecommunications Research, University of South Australia, Mawson Lakes, SA, Australia, [3] Laboratory for Synaptic Molecules of Memory Persistence, RIKEN, Brain Science Institute, Saitama, Japan

The ability for cortical neurons to adapt their input/output characteristics and information processing capabilities ultimately relies on the interplay between synaptic plasticity, synapse location, and the nonlinear properties of the dendrite. Collectively, they shape both the strengths and spatial arrangements of convergent afferent inputs to neuronal dendrites. Recent experimental and theoretical studies support a clustered plasticity model, a view that synaptic plasticity promotes the formation of clusters or hotspots of synapses sharing similar properties. We have previously shown that spike timing-dependent plasticity (STDP) can lead to synaptic efficacies being arranged into spatially segregated clusters. This effectively partitions the dendritic tree into a tessellated imprint which we have called a dendritic mosaic. Here, using a biophysically detailed neuron model of a reconstructed layer 2/3 pyramidal cell and STDP learning, we investigated the impact of altered STDP balance on forming such a spatial organization. We show that cluster formation and extend depend on several factors, including the balance between potentiation and depression, the afferents' mean firing rate and crucially on the dendritic morphology. We find that STDP balance has an important role to play for this emergent mode of spatial organization since any imbalances lead to severe degradation- and in some case even destruction- of the mosaic. Our model suggests that, over a broad range of of STDP parameters, synaptic plasticity shapes the spatial arrangement of synapses, favoring the formation of clustered efficacy engrams.

Keywords: STDP balance, dendritic efficacy mosaic, functional compartments, dendritic spike generation, mutual information index

OPEN ACCESS

Edited by:
Sergey M. Korogod, Bogomoletz Institute of Physiology, Ukraine

Reviewed by:
Petia D. Koprinkova-Hristova, Institute of Information and Communication Technologies, Bulgaria
Guy Elston, Centre for Cognitive Neuroscience, Australia

***Correspondence:**
Nicolangelo Iannella
nicolangelo.iannella@gmail.com
Thomas Launey
thomas.launey@riken.jp

Received: *30 September 2016*
Accepted: *12 May 2017*
Published: *09 June 2017*

Citation:
Iannella N and Launey T (2017) Modulating STDP Balance Impacts the Dendritic Mosaic. Front. Comput. Neurosci. 11:42. doi: 10.3389/fncom.2017.00042

INTRODUCTION

Activity-dependent changes in the firing properties of cortical neurons can arise from modifying the spatial arrangement of afferent fibers converging onto dendrites and their corresponding synaptic strengths (Poirazi et al., 2003a; De Roo et al., 2008; McBride et al., 2008). The pattern of activity conveyed by such afferents can either strengthen (Bliss and Gardner-Medwin, 1973; Bliss and Lomo, 1973) or weaken (Kirkwood and Bear, 1994) stimulated synapses. Such physiological changes are believed to represent a substrate for learning and memory; however the mechanisms responsible for the spatial arrangement have yet to be fully elucidated.

Experiments show that synaptic plasticity exhibits both associativity (McNaughton et al., 1978; Levy and Steward, 1979) and cooperativity (McNaughton et al., 1978) between synapses; where groups of stimulated synapses can collectively induce either LTP or LTD but are each individually incapable of inducing change. Experiments have also identified two additional properties. The first

is heterogeneity (nonuniformity) in the form, induction and location of expression of different types LTP and LTD. The second is temporal specificity where the temporal order and separation of pre-synaptic and post-synaptic firing determines whether a synapse is potentiated or depressed. The magnitude of change is characterized by a temporally asymmetric function of spike timing that describes a "critical window" for such alterations (Markram et al., 1997b; Bi and Poo, 1998; Debanne et al., 1994, 1998; Zhang et al., 1998).

This latter form of plasticity is typically called spike timing-dependent plasticity (STDP). The discovery of STDP has stimulated many experimental and theoretical studies on the role of action potential timing with respect to the development of cortical circuits. In particular, previous theoretical studies have typically used formulations of STDP that allows it to behave as a competitive learning rule (even though the weakly competitive version of multiplicative STDP has also been used), illustrating that the temporal asymmetric window allows the neuron to learn some temporal structure of its input, even under noisy conditions (Song et al., 2000; Song and Abbott, 2001; Gutig et al., 2003).

Historically, competitive learning rules have been important in explaining not just learning the temporal structure embedded in the afferent inputs to target neurons, but also the formation of the various types of cortical maps, most notably the development of orientation and ocular dominance columns (Kohonen, 1982; Tanaka, 1990; Miyashita and Tanaka, 1992; Miller, 1994; Erwin et al., 1995; Swindale, 1996; Young et al., 2007). This suggests potential link between competitive learning, functional map formation, and the segregation of independent input streams onto dendrites. This link has been recently discussed in Narayanan and Johnston (2012) where the authors have argued that various functional maps can be imprinted onto dendrites, each serving different roles.

There is growing interest in the nonlinear synergy between dendritic excitability and synaptic plasticity in spatially extended neuron models (Mel, 1992a; Zador et al., 1992; Poirazi et al., 2001) or STDP (Rumsey and Abbott, 2004, 2006; Iannella and Tanaka, 2006; Rabinowitch and Segev, 2006a,b; Gidon and Segev, 2009; Iannella et al., 2010). Notably, our previous studies have demonstrated that the synaptic strengths of axons from different functional streams of inputs organize themselves into spatially segregated clusters. This emergent property relies on an STDP rule admitting strong competition between synapses (Iannella and Tanaka, 2006; Iannella et al., 2010).

Here, we investigate these effects using spike timing-dependent plasticity (STDP) in a biophysically detailed model of a reconstructed layer 2/3 pyramidal cell. In this model, the neuron receives inputs independently from multiple yet equally sized groups of correlated fibers. We focus on the role of STDP (im)balance in altering the spatial representation of synapses in dendrites and especially in the emergence of spatially segregated clusters of synapse with similar properties and representing the different input streams. We conclude that dendritic mosaic robustly emerge over a wide range of dendrite morphology, mean input frequencies and degree of balance, in a nonlinear and unpredictable manner.

MATERIALS AND METHODS

Assessing Differences in Spatial Patterns

There are measures that can quantify the spatial differences or dissimilarity between the resulting spatial organization of synaptic efficacy from two respective groups for various levels of competition. One such measure is called the spatial dissimilarity index (SDI) (Duncan and Duncan, 1955; Traulsen and Claussen, 2004). This index measures of the dissimilarity or equivalently the overlap between two spatial patterns, where segregated or similar patterns give a value close to unity or zero, respectively. The SDI is formulated as:

$$\mathrm{SDI} = \frac{1}{2}\sum_{\mathrm{j}}\left|\frac{W_{\mathrm{j}}^{\mathrm{A}}}{W_{\mathrm{tot}}^{\mathrm{A}}} - \frac{W_{\mathrm{j}}^{\mathrm{B}}}{W_{\mathrm{tot}}^{\mathrm{B}}}\right|, \tag{1}$$

where $W_{\mathrm{j}}^{\mathrm{A,B}}$ are the total synaptic efficacies at dendritic position j contributed by groups A and B, respectively, and $W_{\mathrm{tot}}^{\mathrm{A,B}}$ are the total synaptic efficacies summed over all dendritic sites for each of these two groups.

To assess the spatial differences between multiple (more than two) spatial patterns, the above described index is replaced by one based upon mutual information. We have previously used the multigroup mutual information index (mMHI) (Iannella et al., 2010), defined as

$$\mathrm{mMHI} = \sum_{j}\frac{W_{\cdot\mathrm{j}}}{W_{\mathrm{tot}}}\sum_{m}\pi_{\mathrm{jm}}\ln\left(\frac{\pi_{\mathrm{jm}}}{\pi_{\mathrm{m}}}\right), \tag{2}$$

where subscripts j denotes dendritic location and m indexes the particular afferent group where:

$$W_{\cdot j} = \sum_{m} W_{mj} \quad \text{total synaptic efficacy at dendritic location } j.$$

$$W_{m\cdot} = \sum_{j} W_{mj} \quad \text{total of group } m\text{'s synaptic efficacies.}$$

$$W_{tot} = \sum_{m,j} W_{mj} \quad \text{total synaptic efficacy contributed by all groups.}$$

$$\pi_{m} = \frac{W_{m\cdot}}{W_{tot}} \quad \text{proportion of group } m \text{ synaptic weights.}$$

$$\pi_{jm} = \frac{W_{mj}}{W_{\cdot j}} \quad \text{proportion of group } m \text{ synaptic weights at } j.$$

To quantify the degree of spatial segregation between multiple spatial patterns.

The Layer 2/3 Pyramidal Cell Model

A biophysically detailed compartmental model of a reconstructed layer 2/3 pyramidal neuron receiving randomly timed excitatory and inhibitory synaptic inputs across the dendrite, was simulated using the NEURON simulation package (Hines and Carnevale, 2001). The model consisted of 119 sections with 263 segments, including a simplified myelinated axon, similar to those used in previous studies (Mainen et al., 1995; Iannella and Tanaka, 2006), consisting of a hillock, initial segment, five nodes and

five myelin internodes, respectively. The parameters and channel types used in the simplified axon were the same as those used in Iannella and Tanaka (2006). A variety of synaptic receptors, voltage and calcium dependent ion channels known to exist in real layer 2/3 pyramidal cells were incorporated into the model. These receptors included the α-Amino-3-hydroxy-5-methyl-4-isoxazolepropionic acid (AMPA) receptor, the calcium permeable N-methyl-D-aspartate (NMDA) receptor, the ionotropic and G-protein coupled gamma-aminobutyric acid receptors ($GABA_A$ and $GABA_B$), respectively. The included ion channel currents were a passive leak I_{leak}, the fast sodium I_{Na}, the delayed rectifier potassium I_{Kdr}, the hyperpolarization activated potassium I_h, the transient A-type potassium I_A, a muscarinic potassium I_M, the T-type calcium I_T, (high voltage activated) L-type calcium I_{HVA}, the calcium dependent potassium C-type I_C, the medium after hyperpolarization (AHP) I_{mAHP}; and the slow AHP I_{sAHP}. These channels were distributed throughout the dendrites, soma, and axon with densities according to published experimental data from the rat. In case when data was absent, both distributions and parameter values similar to those used in previous studies were used. Finally, passive properties used in our Layer 2/3 model neuron, were similar or adopted from previous investigations (Mainen et al., 1995; Iannella et al., 2004, 2010): the dendritic membrane capacitance was $C_m = 0.9\ \mu F/cm^2$, the resting potential was -80 mV, and the internal resistivity R_a was 200 Ωm.

A full description of the ion channels, their corresponding currents and distributions used in the simulations were similar or identical to those used in previous modeling studies (Rhodes and Gray, 1994; Mainen et al., 1995; Rhodes and Llinás, 2001; Traub et al., 2003; Iannella et al., 2004, 2010; Iannella and Tanaka, 2006). These descriptions are detailed in the Supplementary Materials.

Stimulation to the Layer 2/3 pyramidal cell was provided by a single inhibitory group consisting of 250 afferent fibers and either two of four groups of equally sized groups of correlated excitatory fibers. Here, when two groups were used there were 500 afferent fibers per excitatory group, while for stimulation originating from four groups there were 250 afferents per group. Furthermore, there were no or little correlation between the activity carried by any single afferent fiber from one group and those from any other group. Put simply, the activity within any single group was correlated, but the activity of afferents between different groups were not correlated with each other. Finally, the activity carried by excitatory and inhibitory fibers are also uncorrelated. These excitatory groups will be labeled alphabetically, i.e. for two groups they will be referred to as groups A and B, while for four, they will referred to as groups A, B, C, and D. Whether inhibitory or excitatory, each afferent fiber forms five synaptic contacts at randomly chosen locations throughout the dendrite of the model, as suggested by current anatomical data (Thomson et al., 1994, 2002; Markram et al., 1997a; Feldmeyer et al., 2002).

Each simulation began by allowing each excitatory afferent fiber to connect to five randomly selected positions across the dendrite. Similarly, each inhibitory afferent also made five synapses at locations randomly selected throughout the initial segment, hillock, soma, and dendrite. All synapses were activated at random times. Inhibitory fiber activity was modeled via a temporally homogeneous Poisson processes with a mean frequency of 10 Hz. Excitatory afferent activity was modeled as correlated Poisson processes where the activity of a particular group contains higher order statistics (correlations) (Kuhn et al., 2003). These correlations are mediated by coincident activity involving distinct subsets of fibers that only belong to a single group of afferents, while there is no correlation between the activity of any pair of input fibers that belong to different groups, i.e., the cross-correlation between these fibers is zero. The adopted within group correlation coefficient was set to $C = 0.05$, with a mean firing rate for all excitatory fibers of 40 Hz, accepted where otherwise stated.

STDP Learning Rule

The synaptic weights of AMPA conductances $w_j(t) \in [0, 1]$ were altered by STDP, (NMDA, $GABA_A$ and $GABA_B$ conductances remained fixed). Learning was implemented using a nonlinear STDP rule (Gutig et al., 2003). For clarity, this rule is described below.

Gutig Rule: Pair Based Nonlinear STDP

$$\Delta w_j = \begin{cases} A_+(1 - w_j)^\mu \exp(-|\Delta t|/\tau_+) & \text{if} \Delta t > 0 \\ -A_- w_j^\mu \exp(-|\Delta t|/\tau_-) & \text{if} \Delta t \leq 0 \end{cases} \quad (3)$$

where $\Delta t = t^{post} - t^{pre}$ denotes the timing difference between pre-synaptic and post-synaptic events. A_+ and A_- are positive constants scaling the magnitude of individual weight changes, and τ_+ and τ_- are time constants determining the size of the temporal learning window in which potentiation and depression occurs. The pre-synaptic event t^{pre} denotes the arrival time of pre-synaptic input to some specific dendritic location, while the post-synaptic event t^{post} typically denotes the time when a local dendritic spike was generated. When Δt is positive, synaptic efficacy is potentiated, and depressed otherwise; where individual changes in synaptic efficacy w_j are also weight dependent. This weight dependence has the form of a power law where the exponent μ is a positive constant. This STDP rule has a nonlinear weight dependence when changing the weights of AMPA receptors. One can't help to notice that the additive STDP rule is recovered when $\mu = 0$ and corresponds to changes in synaptic efficacy that are independent of the weight w_j; while the multiplicative rule is recovered when $\mu = 1$, corresponding to linearly dependent weight changes. The parameters used for potentiation and depression components of this learning rule were $A_+ = 0.0025$, $A_- = 0.001125$, $\tau_+ = 13.5$ ms and $\tau_- = 34.5$ ms, in agreement with previous experimental observations (Froemke and Dan, 2002; Froemke et al., 2005). Detection of post-synaptic events were recorded when the local membrane potential surpasses a pre-specified threshold of $\theta = -20$ mV.

RESULTS

Competition Dependent Emergence of Clustered Synaptic Efficacy Engrams

The formation of spatial patterns displaying a clustered organization typically emerge by balancing the requirements of co-operation and competition of some limited resource. In the

case of Gütig's nonlinear STDP (see Materials and Methods—STDP learning rules), synapses compete both spatially and temporally to control the timing of somatic and/or dendritic spike generation. This competition is believed to take the form of a spatio-temporal winner-take-all process that ultimately leads to the formation of synaptic efficacy clusters. A key feature of Gütig's nonlinear STDP rule is the presence of the exponent μ. This parameter controls the weight dependence of the rule and can be interpreted as a parameter that controls the degree of competition, since $\mu = 0$ corresponds to the additive STDP and exhibits strong competition (Song et al., 2000; Song and Abbott, 2001); while $\mu = 1$ recovers the multiplicative STDP rule, a rule known to display stable yet weak competition dynamics (van Rossum et al., 2000). For intermediate values of μ the weight dependence is nonlinear and can be interpreted as introducing some intermediate degree of strong and weak competition.

To assess spatial segregation and complementarity in the case of two independent stream of inputs, we used the spatial dissimilarity index (SDI) (Duncan and Duncan, 1955; Traulsen and Claussen, 2004) (see Section Materials and Methods). Note that two spatial patterns are considered to be complementary when they possess a reciprocal relationship in space so that one pattern can be considered the negative image of the other. This index provides a quantitative measure of the difference between two spatial patterns. Two patterns are similar if the SDI is close to zero, while values close to unity indicates that two patterns are spatially segregated.

The SDI varies over time, in a manner that depends on the exponent μ (**Figure 1**). Note that for each trial, a different random seed was used to initialize the simulation, assuring that both the pattern of afferent connectivity and the activity seen at any location in the dendrite are different between trials. There is an optimum value for μ maximizing the SDI; for which synaptic competition produced the largest degree of spatial complementarity. Above the optimum, high value of μ weakens synaptic competition, leading to an increase in the average size of the efficacy engram contributed by each respective group of excitatory fibers. Such increases in size increases the overlap between the clusters contributed by each respective group of excitatory afferent fibers, to the point where there is little difference between them. More surprisingly, too high competition also leads to cluster fragmentation and SDI decrease.

STDP Balance Modulates Spatial Segregation and Complementarity

Another important facet is to determine how altering the balance between potentiation and depression ($A_-\tau_-/A_+\tau_+$ ratio), impacts the formation of clustered synaptic efficacy engrams. Previous theoretical studies, using the simple integrate-and-fire model neuron, have shown that in order to avoid unphysiological increase of synaptic weights, this ratio is important for stable yet competitive learning (Song et al., 2000; Song and Abbott, 2001). However, for a spatial model neuron, the impact of such alterations was unknown. This issue was directly addressed here by increasing the maximal amplitude of the STDP learning window's depression component A_-. Again SDI was averaged from ten trials, each initialized using a different random seed.

The imbalance between depression and potentiation in STDP was increased from 1 to 6, for which synaptic depression is overwhelmingly dominant and results essentially in silencing the neuron. Furthermore, this avoided the situation where, irrespective of the afferent group, the total synaptic efficacy contributed by a single group at any location was zero, i.e., $W_{\text{tot}}^{\text{A}} = 0$ and/or $W_{\text{tot}}^{\text{B}} = 0$. Beyond these conditions (ratios > 6), numerical singularities prevented SDI calculation.

Figure 2 indicates that increasing the imbalance from 1.05 to 6 resulted in a strong non-monotonous effect on the emergence of synaptic clusters across the dendrite. Firstly, there is a clear maximum SDI value indicating that for that particular value of the ratio, the degree of spatial complementarity between the two patterns is greatest. Secondly, increasing the ratio to a value of 2.25 eventually leads to a minimum SDI value of ≈ 0.45, with no clear segregation of synaptic clusters. Finally, further increases in the balance ratio $A_-\tau_-/A_+\tau_+$ to 3.3 (**Figure 2B**)

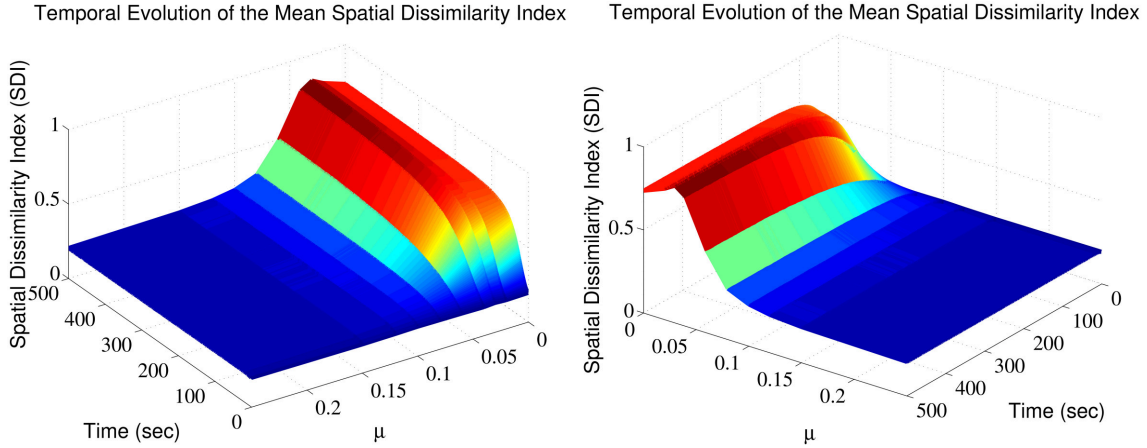

FIGURE 1 | Synaptic efficacy clusters and spatial complementarity depends upon synaptic competition. The mean SDI calculated over 10 randomly initialized trials, as a function of both μ and time. We jointly observe the temporal evolution and the effect of altering competition on the resulting SDI.

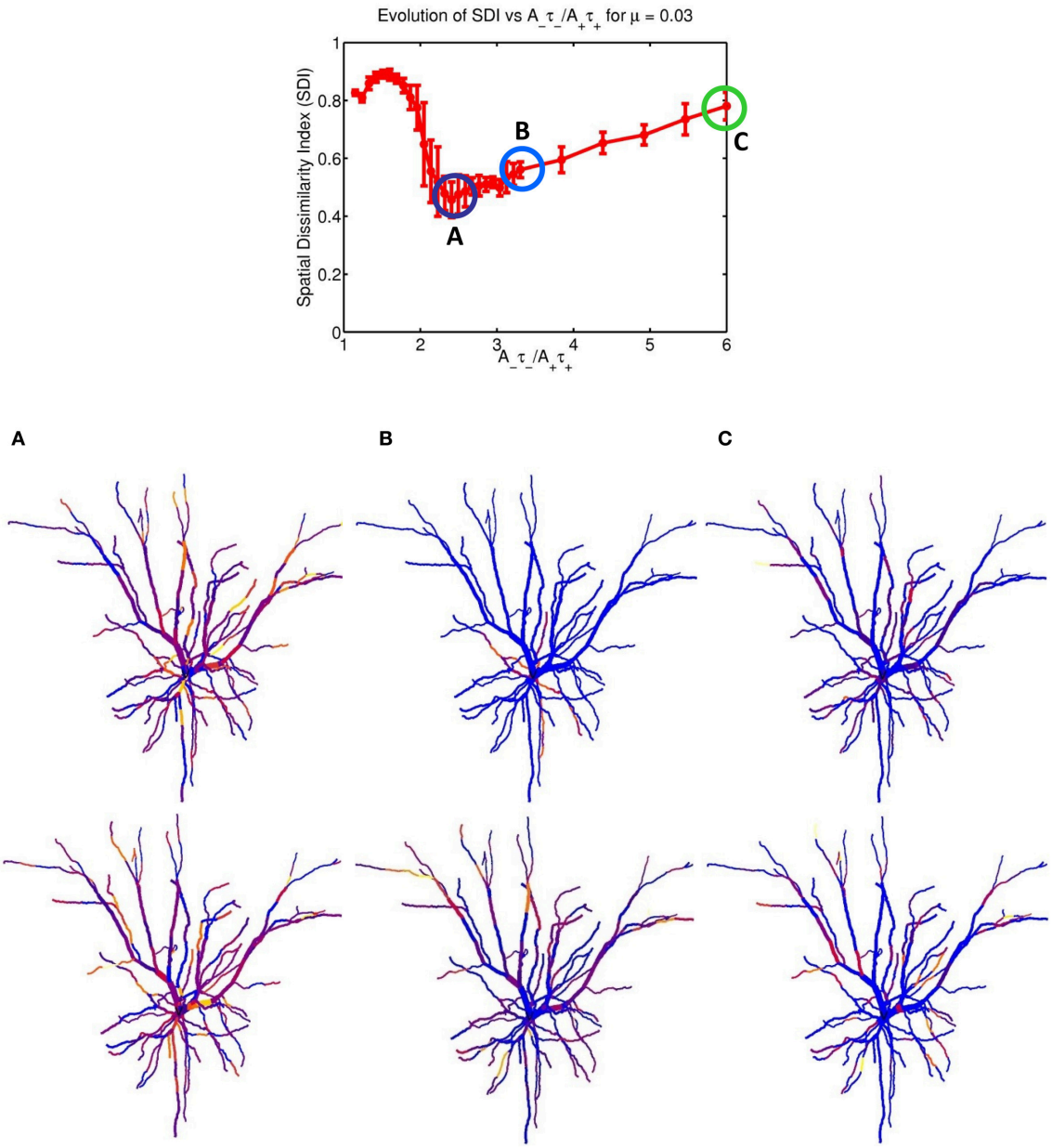

FIGURE 2 | STDP balance controls efficacy cluster formation. Each data point of the mean SDI was calculated using 10 randomly initialized trials, as a function of STDP balance ratio $A_{-}\tau_{-}/A_{+}\tau_{+}$. The balance was changed by systematically incrementing A_{-} by 0.0001 until a balance value of 3.3 then by 0.005 , up to a ratio of 6. Increasing the imbalance between depression and potentiation leads to initial degradation in the SDI, and further increases leads to a recovery of clustering. The spatial distribution of clusters is illustrated for the three balance ratio values of 2.25, 3.3 and 6 (column denoted by **A–C**, respectively), for each specific afferent group. The color coding indicate the synaptic strength for the two afferent group, for each compartment. For a ratio of 2.25 (lowest SDI) each branch receive essentially similar input strength from the two afferent groups while **(B,C)** show increasing segregation.

and to 6 (**Figure 2C**) leads to increased spatial segregation of synaptic efficacies across the dendrite, contributed by each afferent group (appearing in **Figures 2B,C**), and gives rise to a surprising recovery in the value of the SDI, where spatially segregated efficacy clusters (appearing to the right of the central plot) are still present in the dendrite. Intuitively, our expectation was that increasing the imbalance by favoring LTD, would lead to degradation of the clustering; surprisingly, the synaptic efficacy clusters were still present but at the cost of decreased spatial complementarity of the original tiling pattern. Here, complementarity is referred as the amount of spatial segregation and overlap between two patterns where one pattern can viewed as the "negative" of the other, and example is provided in **Figure 3** for an imbalance ratio of 1.5 where one group dominates regions in dendritic space where the second group does not. Interestingly, a very steep transition separates the SDI maxima and minima,

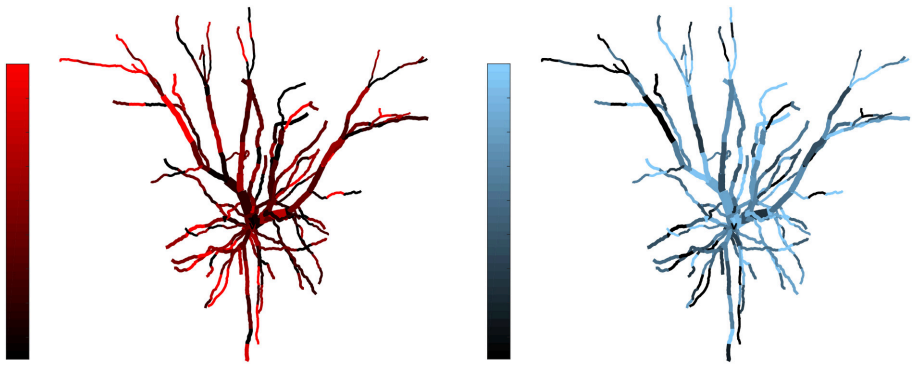

FIGURE 3 | Example of complementarity. Spatial distribution of synaptic efficacy after STDP learning for $\mu = 0.03$ and a balance ratio of 1.5 (the maximum of the SDI plot in **Figure 2**). The color coding represents the normalized weights for a each afferent group. Note that the patterns complement each other, with one afferent being strong where the other is weak, thus giving rise to a large SDI.

with an inflection point at 2. While the exact position of the inflection point is irrelevant (as it is probably multi-factorial), this reveals a high sensitivity of the model to LTP/LTD balance that may be detected experimentally.

STDP Balance Impacts the Formation of the Dendritic Mosaic

We have observed the formation of synaptic efficacy clusters when there are only two different groups of afferent axons. When more than two streams of inputs are simulated, altering the balance ratio $A_-\tau_-/A_+\tau_+$ admitted by the STDP rule also leads to changes in the formation of dendritic mosaic. To quantify clustering in these multi stream conditions, we have previously identified the multi-group Mutual Information Index (mMHI) to be a suitable metric (Iannella et al., 2010; see Materials and Methods section for details).

$$\text{mMHI} = \sum_j \frac{W_{\cdot j}}{W_{\text{tot}}} \sum_m \pi_{\text{jm}} \ln\left(\frac{\pi_{\text{jm}}}{\pi_{\text{m}}}\right), \tag{4}$$

Figure 4 shows how STDP imbalance impacts the mMHI for three values of $\mu = 0.03, 0.08, 0.15$, when the neuron is being stimulated by four groups of afferent fibers. Note that the same incremental changes to A_- used in **Figure 2** was adopted. The general shape of the relationship between mMHI and balance ratio is comparable to the one quantified by SDI for two groups of axons and is similar for all values of mu. This dependency is thus robust to change of clustering metric and to increase in the number of inputs, suggesting that this emergent properties could be characterized experimentally (see Section Discussion) .

Mean Input Frequencies and STDP Balance Jointly Influences the Dendritic Mosaic

We have shown above that both the degree of synaptic competition and LTP/LTD balance ultimately determines the emergence of the dendritic mosaic. Previously, we have shown that the mean firing frequency of afferent inputs also play an role in this emergence (Iannella et al., 2010).

We thus examined the interplay between firing frequency and STDP balance. **Figure 5**, illustrates how increasing the degree of imbalance affects the mMHI, for a mean input frequency of 10 Hz. Note that in contrast to **Figure 4**, the mMHI reaches a plateau (≤ 0.25) at high ratio rather than showing monotonous increase. Equally surprising is the apparent lack of correlation between the low mMHI and the pattern of synaptic efficacy clusters. For a balance ratio of 1.8 (**Figure 6**, Row B) corresponding to maximal mMHI, we observed intense clustering, with most dendritic compartments being dominated by a single input stream (bright color). Clearly, these inputs have been potentiated through STDP while the inputs from other streams have been depressed.

For lower (A) and higher (C) balance ratio, this pattern is degraded, with a decrease of the contrast between clusters and appearance of overlaps (regions where two or more stream remain strong, thus shown in black). For a balance ratio of 6 (**Figure 6C**) we even observed subsections of the dendritic tree where efficacy clusters were absent. These dendritic subsections had essentially become regions that do not respond to any group of afferent inputs.

Increasing both the mean input frequencies and the degree of imbalance induce non-trivial changes for the mMHI (**Figure 7**). Above 20 Hz, a local mMHI minimum replaces the steady decay seen at lower frequency. The value of the mMHI minimum is approximately independent of frequency but frequency determines the balance ratio at which the minimum occurs. The mMHI maximum remains at $1.8\,A_-\tau_-/A_+\tau_+$ for all frequencies. Note that already at 40Hz, the upward slope of the mMHI tend toward an asymptotic limit. Indeed no further change were observed at frequencies >40Hz. Thus, the mMHI in the $0 \sim 2.5$ $A_-\tau_-/A_+\tau_+$ range is similar for all input frequencies and below and in the $2.5 \sim 6$ range for input frequencies above 30 Hz. This suggests that the conditions required for the optimal tiling of synaptic clustering are robust for a wide range of parameters. The unexpected appearance of a local minimum at $\sim$2.5 may be linked to the degree of local excitability, the number of post-synaptic events generated by incoming inputs and where they

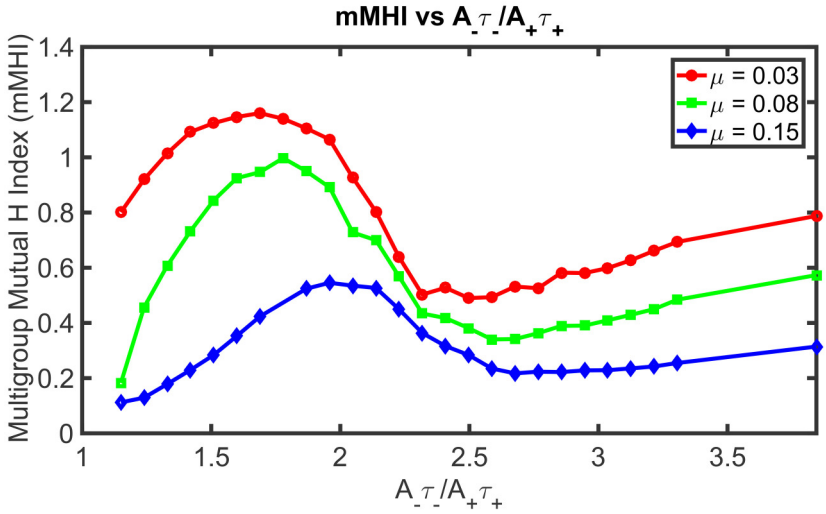

FIGURE 4 | STDP imbalance impacts the dendritic mosaic. Increasing the $A_-\tau_-/A_+\tau_+$ ratio leads to changes in the mMHI for three different values of the exponent μ appearing in the Gütig STDP model of synaptic competition. Note that we used here the same incremental increases in the value of A_- as in **Figure 2**, for the three different values of $\mu = 0.03,\ 0.08,\ 0.15$.

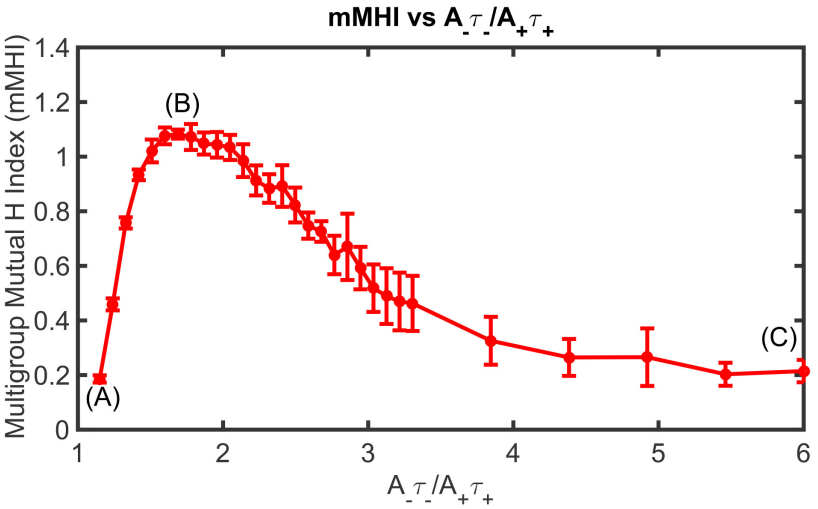

FIGURE 5 | Mean Input Frequency and STDP balance jointly affect the dendritic mosaic. At a given mean input frequency of 10 Hz and $\mu = 0.03$, stepwise increase of $A_-\tau_-/A_+\tau_+$ produces changes in the mMHI, with a maximum for a ratio of 1.8. Note that (A), (B), and (C) appearing in Figure correspond to balance ratio values of 1.1, 1.8, and 6, respectively.

occur in dendrites. The number of generated action potentials clearly follows a nonlinear relationship with the mean frequency of the inputs locally targeting the dendrite.

STDP Balance and Mean Input Frequencies Jointly Influence Local Spiking

In the previous section, we saw how the mean input frequencies and the degree of STDP balance affects the emergence of the dendritic mosaic. Here, we analyze the corresponding alterations to local neuronal response at the soma and several representative dendritic locations, as shown in **Figures 8A,B**. Firing rate at the soma (when subjected to inputs from all four afferent groups) dramatically decreases from 86 Hz to 0.2 Hz as the degree of imbalance (balance ratio) increases from 1.05 through to 1.8 (**Figure 8A**).

For larger degrees of imbalance (from 1.8 to 6) the neuronal firing rate remains relatively constant around 0.03 Hz. In contrast, the firing rate for the dendritic locations display maximal spikes rates at different values of the balance ratio (**Figure 8B**) and different level of activity, even when LTD is favored (high STDP imbalance ratio).

Influence of Morphology

In the realistic model presented above, we have measured how STDP balance and mean input frequency influence the

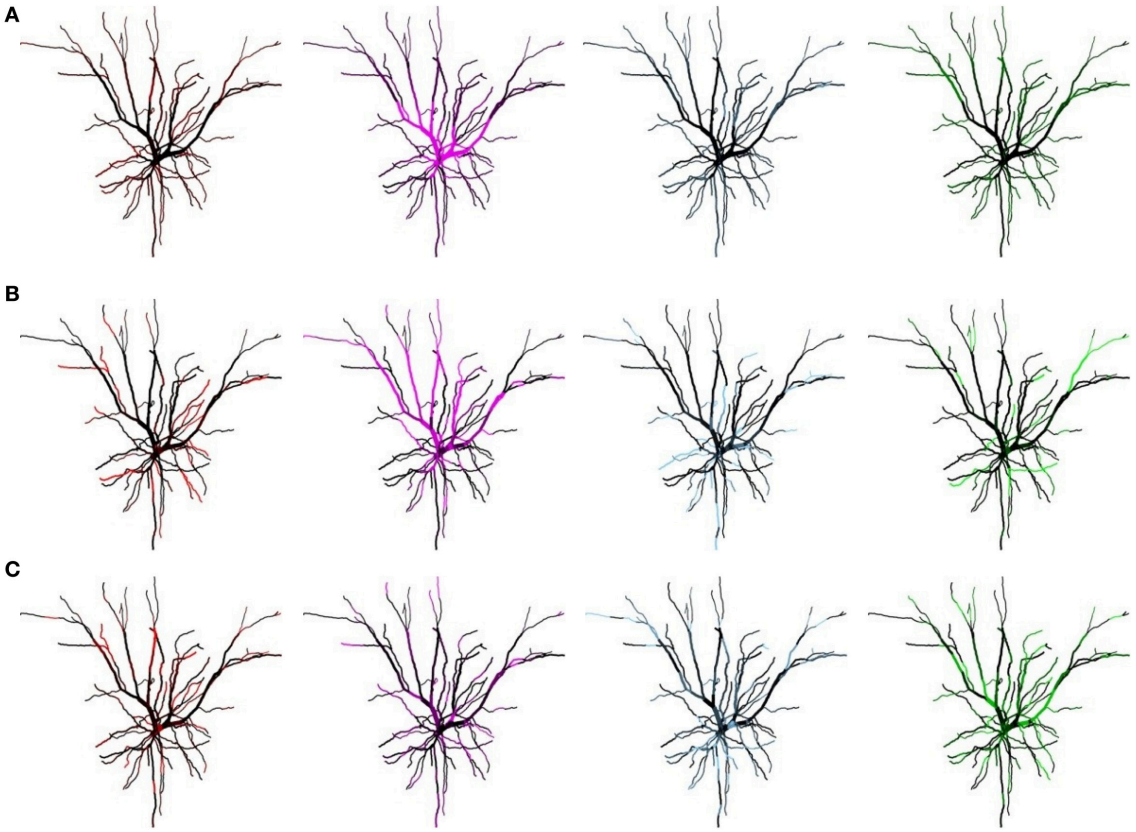

FIGURE 6 | Mean Input Frequency and STDP balance jointly affect the dendritic mosaic. Spatial organization pattern of synaptic efficacies associated with **Figure 5** for a balance ratio $A_-\tau_-/A_+\tau_+$, of 1.1 **(A)**, 1.8, **(B)**, and 6 **(C)**, for each of the four afferent groups. Increasing the balance ratio changes the patterning of synaptic efficacies. Note that while **(C)** corresponds to a low mMHI (**Figure 4**), the inputs are still clustered, albeit with lower complementarity (i.e., some dendrite segments still show similar synapse strength for different inputs streams after STDP plasticity).

emergence of efficacy clusters. Since clustering emerge from local interactions of synaptic inputs, we wondered to what extend dendritic morphology plays in the appearance and stability of the mosaic. Historically, Rall (1964) was the first to show how neural morphology can influence the firing properties of neurons, using simple compartmentalized ball-and-stick models (Rall, 1964). To directly investigate whether the morphology of the dendrites impacts the emergence of the dendritic mosaic, we chose to compare a realistic (reconstructed from tracing) neuron morphology to an extremely simplified simple cable equivalent. This extreme approach allowed us to preserve the active properties of the original cell with only simple transformations while reducing the morphology to an unbranched dendrite. We thus generated the simplified models using two published reduction methods that map complex dendritic morphologies to an unbranched cable structure while maintaining axial resistance and without altering the active properties used in the original model. An alternative approach could be to systematically change the lengths and diameters of dendritic branches, or to gradually merge branches together until significant mosaic alterations are detected. This approach has the double handicap of being both computationally intensive and not amenable to experimental testing. Instead, in a future study, we intend to compare mosaic formation in realistic but different morphologies such as CA1 pyramidal cell, Purkinje cell and spinal cord motoneurons and compare simulation data to physiological data.

The first of these methods relies upon a very simple construction yielding a simplified equivalent cable morphology of the original dendritic tree, consisting of only three identified regions but conserving the electrical properties, length and total surface area of the original cell (Iannella et al., 2004), as shown in **Figure 9**. The second method is based upon combining branches into an equivalent cylinder where the axial resistance of the original branches are not altered (Destexhe et al., 1998). This requires summing the cross sectional area of each contributing branch and results in an equivalent cylinder with a radius given by the square root of sum of all contributing radii squared, $r = \sqrt{\sum_i r_i^2}$. The length of the cable is taken to be the average length of contributing branches weighted by their respective radii r_i, in order to take different contributing branch lengths into account, $l = \sum_i l_i r_i / \sum_i r_i$. The resulting total surface area of the simplified model differs from the original, requiring correction of all conductances and the membrane capacitance

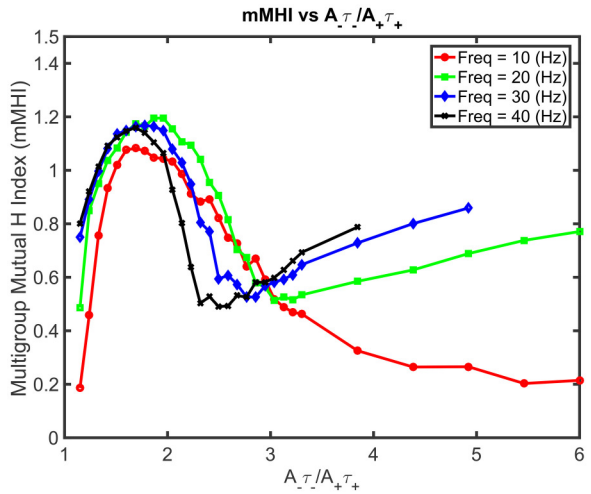

FIGURE 7 | Mean Input Frequency and STDP balance leads to nonlinear effects on mMHI. Increasing both the balance ratio $A_-\tau_-/A_+\tau_+$ (stepwise as in **Figure 2**) and the mean input frequency leads to nontrivial changes in the mMHI, with appearance of a local mMHI minimum for higher firing frequencies. Note that the balance ratio at which this minimum is observed seem to depend on the firing frequency.

by a multiplicative factor to maintain input resistance (see Destexhe et al., 1998 for more details). The Destexhe simplified morphology is presented in **Figure 9**.

Figure 10 presents the mMHI index as a function of STDP imbalance for both of these simplified models. Altering the morphology while keeping the same active properties alters the mMHI (Compare to **Figure 2**). Notably, for the first method, there is an initial sharp drop followed by a slower monotonic rise in the mMHI index while for the second method, mMHI is a monotonic function of balance. Both mMHI profiles are less complex than profile obtained for the complex model (**Figure 2**), showing that dendritic morphology plays an important role in the emergence of the dendritc mosaic and its constituent synaptic efficacy clusters.

Increasing the degree of imbalance (by increasing the balance ratio) leads to different quantitative effects on the resulting spatial patterning of synaptic efficacy for each simplified model. For the Iannella reduced model one clearly sees that for an initial balance ratio value of 1.15 there is a preference to form large spatial clusters that occupy distinct portions of the unbranched dendrite, thus indicating that for this balance ratio, STDP implements an underlying spatial winner-take-all process that allow large spatial clusters to emerge. The formation of large spatial clusters, however, is a transient occurrence since a small increase in the balance ratio from 1.15 to 1.33 leads to the emergence of smaller clusters spread throughout the dendrite that can overlap in space with other clusters contributed by other groups.

This is in stark contrast to the formation of large distinct clusters. The appearance of large spatial clusters usually indicates synergy between synapses however the transformation from large to small clusters signifies a sudden loss of spatial extent of co-operativity between synapses. Increasing the balance ratio further leads to small synaptic efficacy clusters that are sparsely distributed but can overlap with other efficacy clusters contributed by other afferent groups. In comparison, the Destexhe simplified model results in only small clusters that are spread out throughout the entire extent of the unbranched dendrite, but as the balance ratio is increased, this gives rise to small efficacy clusters that can spatially overlap with other clusters (contributed by other afferent groups) but are also freely distributed along the extent of the dendrite.

Inspecting the spatial organization of clusters that have emerged in both simplified models reveals some interesting common traits. For both simplified models, increasing the degree of imbalance leads to the formation of small localized synaptic efficacy clusters that are sparsely distributed in dendritic space. Notably, when balance ratio is large, there are spatial regions in the dendrite that are devoid of any input (see **Figure 11** these are indicated by black arrowheads), while in other regions there can be two or more localized clusters that overlap, potentially mutually augmenting their inputs (see **Figure 11** indicated by red arrows).

Since there is a drastic change of synaptic efficacy, we wondered about the concurrent alterations the neuron's input-output relationship in both the space and time domains. Samples of the membrane potential recorded from three different locations, the soma and two different dendritic locations respectively labeled as "S," "Pos 3," and "Pos 5" as indicated in **Figure 12** before and after STDP learning for both simplified models. **Figure 12** illustrates these membrane potential traces for each model at two different values of the balance ratio $\frac{A_-\tau_-}{A_+\tau_+} = 1.15$ and $\frac{A_-\tau_-}{A_+\tau_+} = 6.0$ denoted by $A1$ and $A4$, respectively. Here, when a balance ratio of 1.15 is used, one can observe small qualitative changes to the membrane potential at the above described locations after STDP. Conversely, a large balance ratio value leads to marked qualitative alterations to these membrane potential traces after STDP ($A4$). Specifically, the membrane potential tends to the resting state, with the occasional occurrence of spikes or burst of spikes, at the three specified locations.

DISCUSSION

In this study, we investigated how synaptic competition and STDP jointly determines the formation and stability of clustered synaptic efficacy engrams in a realistic biophysical model. Similar to our previous study (Iannella and Tanaka, 2006), when the model received inputs from two groups of correlated afferent fibers (with no inter-group correlation), STDP learning results in the formation of interdigitated regions of synaptic efficacy clusters, forming a spatially complementary pattern of synaptic strength for each respective group of afferents. With four groups of afferent fibers (again with intra-group correlation), we still observe the emergence of the dendritic mosaic as a result of STDP learning. Here we examined the relative contribution and influence of mean

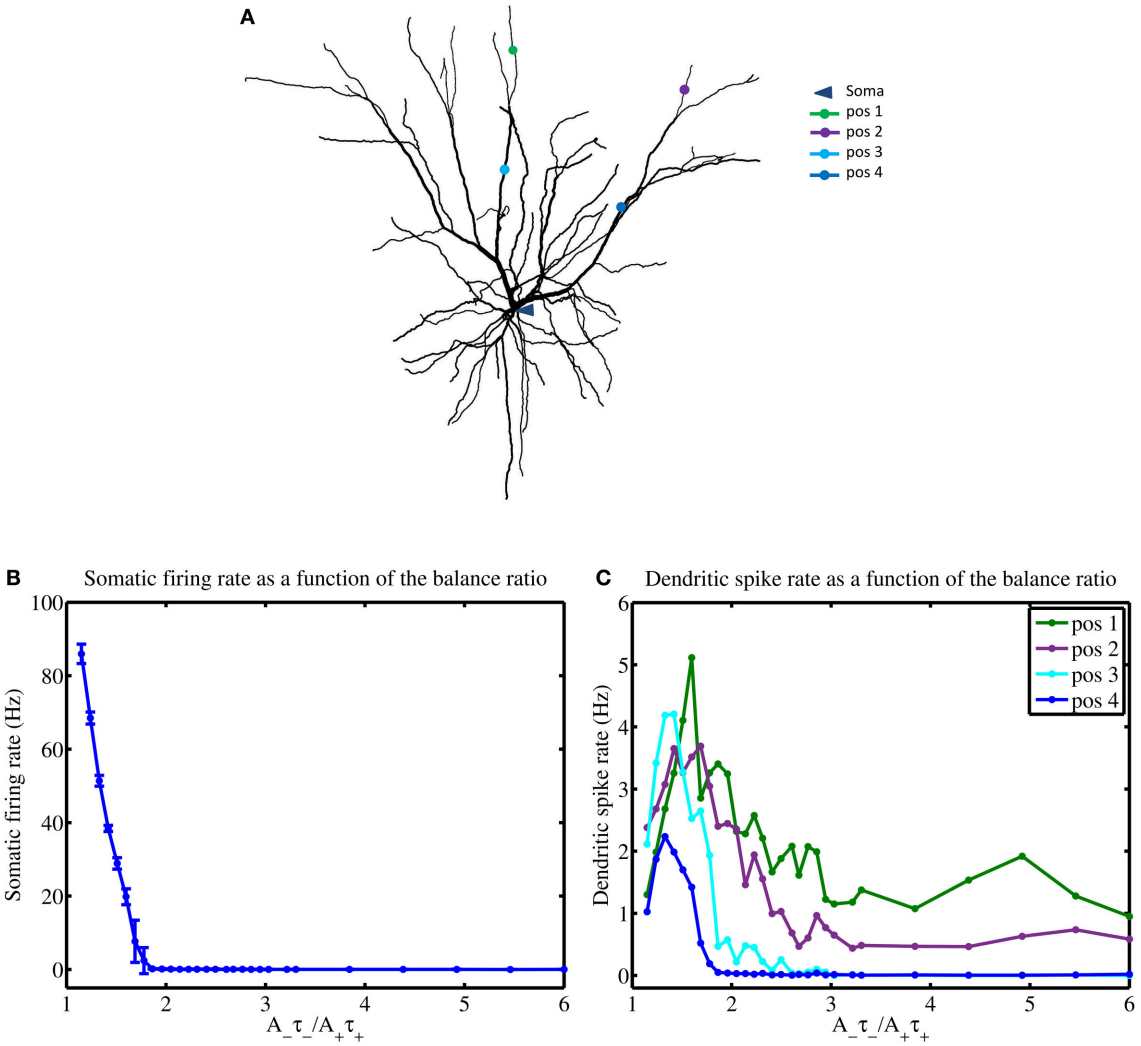

FIGURE 8 | STDP balance affects local spiking. **(A)** Layer 2/3 cell used in simulations indicating the locations of the soma and four distinct dendritic locations denoted by pos 1 through to pos 4, respectively. **(B)** Increasing the $A_-\tau_-/A_+\tau_+$ balance causes a rapid monotonous decrease of somatic firing rate **(B)** while dendrites show complex responses, measured at 4 different locations (pos 1–4) **(C)**, using a mean input stimulus frequency of 10 Hz. All four dendritic locations show a spiking maxima for the balance ratio resulting in maximal mMHI (1.8) but only approximately and with marked differences. Notably, for larger values of the balance ratio, the dendritic firing rates reduce to zero for positions 3 and 4, while the other two locations show sustained nonzero rate.

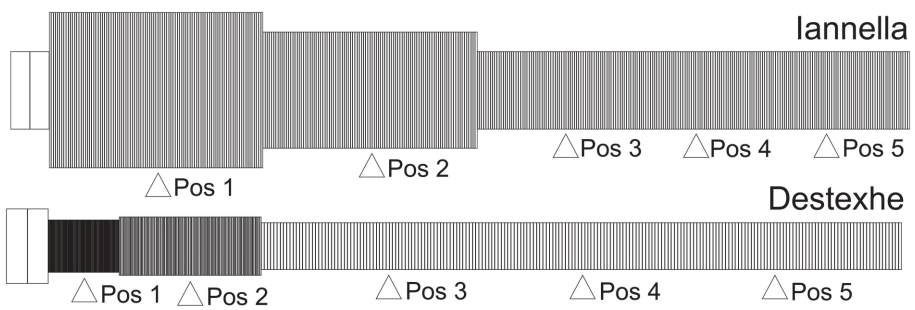

FIGURE 9 | Unbranched cable morphology. Application of the reduction schemes proposed by us (Iannella et al., 2004) and by Destexhe et al. (1998) to transform the original dendritic tree into an unbranched cable composed of three sections, each with different radii. Pos 1, 2, and 4 are at the middle of each section while Pos 3 and 5 are at 0.2 and 0.8 of the most distal section.

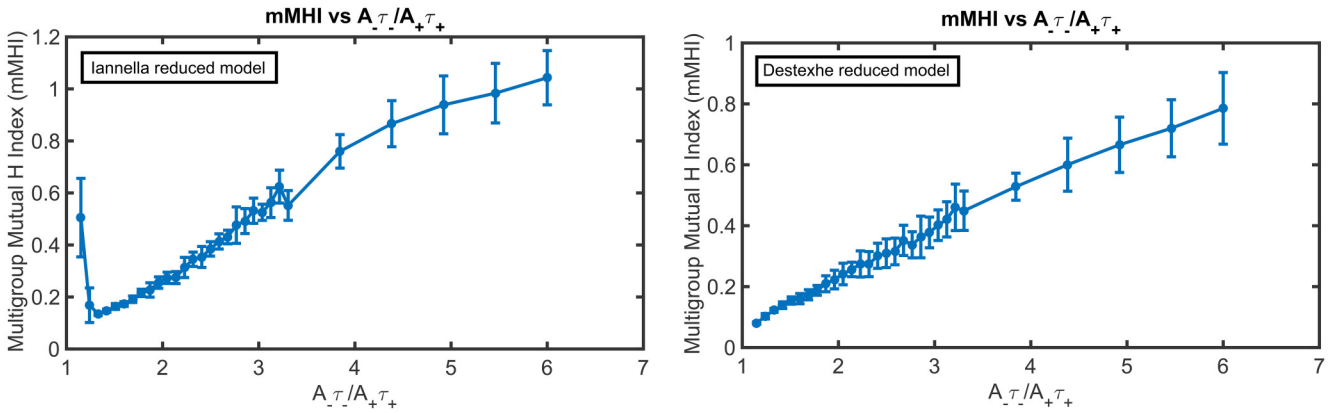

FIGURE 10 | The mMHI in reduced models. mMHI is computed for the balance ratio $A_-\tau_-/A_+\tau_+$ ranging from 1.15 to 6.0, using a mean input stimulus frequency of 40 Hz. Note that mMHI was more densely sampled for balance ratio between 1.15 to 3.3, as in **Figure 2**.

input frequency, the degree of synaptic competition, and the balance between potentiation and depression, in this phenomenon.

Considering the non-linear dynamic of the system under study (a spatially extended model with full complement of ion channels) and the stochasticity introduced through the random arrival times of the afferent inputs, analysis of parameters contributions to spatial pattern formation is not possible analytically. Here we addressed the issue by an exhaustive exploration of the parameter space through simulation, both in a complex model and in a model with simplified morphology but similar electrophysiological properties.

One of the key features used of the model is that it detects local dendritic spikes to convey post-synaptic timing information locally, as opposed to the global nature of the back propagating action potential (BPAP). Whether BPAPs can fulfill the role of telling every synapse in the dendrite when the neuron fired an action potential has come into question. Experiments have shown that the BPAP does not fully invade the dendrite due to voltage attenuation (Larkum et al., 2001; Stuart and Häusser, 2001) and that synaptic activity either reduce or block BPAP invasion into the dendrite completely (Paré et al., 1998; Mickus et al., 1999; Larkum et al., 2001). In addition, changes in synaptic efficacy can occur without the need of a BPAP (Schiller et al., 2000; Golding et al., 2002; Holthoff et al., 2004) and constant synaptic bombardment across the dendrite can cause spike generation in dendrites, which may also limit BPAP propagation (Paré et al., 1998; Larkum et al., 2001). Therefore, it seems unlikely that the BPAP could provide every synapse located within the dendritic tree with the necessary timing information of when postsynaptic firing occurred. Post-synaptic timing information carried by locally triggered dendritic spikes may provide a more robust signal. From a theoretical standpoint, the use of dendritic spikes may play an important computational role in permitting the neuron to develop functional compartments, allowing the neuron to perform complex computations or increase its memory storage capacity (Poirazi et al., 2001, 2003b; Polsky et al., 2004).

A defining feature of our model is the emergence under STDP of synaptic clusters forming a dendritic mosaic (tessellation). This was observed over a restricted region of the multidimensional parameter space defined by (1) the degree of synaptic competition, (2) mean input frequency, and (3) the amount of synaptic balance. In addition, we found that when STDP learning is dominated by depression, learning still gives rise to synaptic clusters despite the imbalance introduced between depression and potentiation components of the temporal learning window. Note however that the spatial organization of these clusters fail to form a continuous tiling pattern in some regions of the dendrites. This result in degraded dendritic mosaic, with areas essentially devoid of synaptic inputs. Functionally, this may correspond to regions of silent synapses or the synaptic cold-spot previously described experimentally (Zador et al., 1992). Finally, comparison with simple model derived from the realistic one shows degraded ability to form a mosaic, confirming the role of local non-linearities. Specifically, our model layer 2/3 pyramidal cell was compared to two equivalent cable models (whose reduction has been detailed elsewhere, Destexhe et al., 1998; Iannella et al., 2004) that conserve input resistance of the original neuron. Both full and reduced models used identical sets of ion channels. After STDP learning, analysis of the mutual information index and of the corresponding synaptic clusters shows an altered mosaic formation, for a wide range of STDP balance. These differences arise since altering the morphology of the dendrites ultimately changes how synaptic inputs interact with each other and with local channels in dendrites. This leads to non-linear inputs summation and local alteration of input resistance, thus altering the local conditions of STDP.

Our study provide new insight on the interplay between synapse location, active dendritic properties, morphology and synaptic plasticity in shaping the strengths and spatial arrangements of synapses. One strong prediction arising from this study is that "inputs clustering" may be the favored and natural outcome of synaptic plasticity when neurons receive

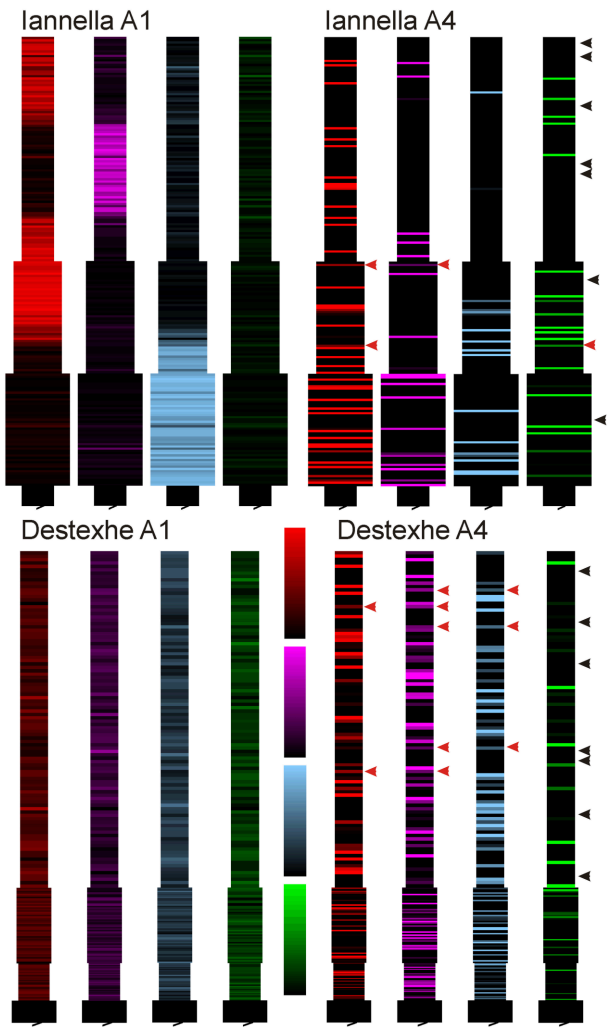

FIGURE 11 | Synaptic efficacy clusters in simplified model. Spatial organization pattern of synaptic efficacies associated with **Figure 10** for balance ratios $A_-\tau_-/A_+\tau_+$, of 1.15 (A1) and 6.0 (A4), for each of the four afferent groups. Increasing the balance ratio has qualitatively different effect on the two simplified models (compare A1), but high ratio yields clear local clustering for both models (A4). Note that at high ratio, some regions are essentially devoid of dominant input (black arrowheads) while some regions show mixed dominance by two or more inputs (red arrowheads).

different streams of correlated inputs, as often seen in sensory and associative brain areas. Indeed, in the visual and auditory systems (and probably other sensory systems), clustering functionally related inputs on different dendritic domains seem to play a role in tuning the neuron for contrasting stimuli in time and/or spac (McBride et al., 2008; Jia et al., 2010; Kleindienst et al., 2011; Podgorski et al., 2012). Our results indicate that maximum clustering -and thus the ability to discriminate stimuli- emerge and is only produced and maintained for a narrow band of input frequency. This implies that there is conflict between building the ability to discriminate between stimuli (through STDP) and the ability to encode stimuli intensity as spike rate. Indeed, our results predict that a neuron exhibiting mosaic clustering should exhibit approximately constant EPSP frequency when stimulus intensity varies widely. This limitation only exists however if STDP is maintained throughout life. If the mosaic is formed during a developmental critical period, before "crystallization" in the adult then the same neuron would exhibit both synaptic mosaic (input discrimination) and ability to integrate rat-coded signals. We predict that genetic or pharmacological manipulation of plasticity balance in the young, typically by changing the level of GABA inhibition (Hensch et al., 1998; Morales et al., 2002; Takesian and Hensch, 2013), homeostatic mechanisms (Turrigiano and Nelson, 2004), the activity of NMDA receptors (Medina et al., 1999; Quinlan et al., 1999; Krapivinsky et al., 2003; Bender et al., 2006; Nevian and Sakmann, 2006), should permanently impair formation of cluster, with the correlate that this would diminish the ability to detect contrast stimuli in the adult.

Comparing the profiles of somatic and dendritic firing rates (**Figure 8**) with the mMHI (**Figure 8**), it appears that the non-monotonic variations of mMHI with increased imbalance may result from the interplay between membrane excitability and the exposure to STDP. This results in a large reduction of the neuron's (somatic) firing rate after STDP learning, from 86 Hz to 0.2 Hz to 0.03 Hz. The reason is that STDP net effect is to reduce synaptic weights. Interestingly, an emergent feature in this context is the presence of dendritic regions that seem to resist being silenced (enduring the suppressive nature of STDP due to increasing balance ratios), and responding with higher rates of spike generation than those observed at the soma. This suggests that these particular regions of the dendrite essentially behave as functional subunits, providing the neuron with additional levels of processing (similar to what one expects from a neural network) before global integration and spike firing takes place in the soma (albeit at a diminished rate). Put simply, one observes the emergence (via STDP) of neuron that functionally behaves more as a two-layer (or more) distributed network rather than as a globally weighted summation device. This view is in agreement with the view that dendritic branches can potentially behave as independent functional units (computational subunits) and secondly, that they may promote functional compartmentalization of inputs in dendrites (Poirazi et al., 2003b; Losonczy and Magee, 2006; Harvey and Svoboda, 2007; De Roo et al., 2008; Larkum et al., 2009; Govindarajan et al., 2011; Kleindienst et al., 2011; Legenstein and Maass, 2011; Makino and Malinow, 2011; Harnett et al., 2012; Major et al., 2013; Sajikumar et al., 2014). It is important to note, however, that dendritic branches behaving as computational subunits tend to be dynamic in nature where the spatial and temporal patterning of inputs and the nonlinear nature of the dendritic membrane drives the functional properties of dendritic integration.

Furthermore, the firing profiles at different dendritic locations (**Figure 8**) are the result of generating dendritic spikes at different rates and depend on the nonlinear nature of the dendritic channels and local branching morphology. The clustering results in tuning various portions of the dendritic tree in an unsupervised manner. This self-organization process causes specific portion of the dendritic tree to become maximally

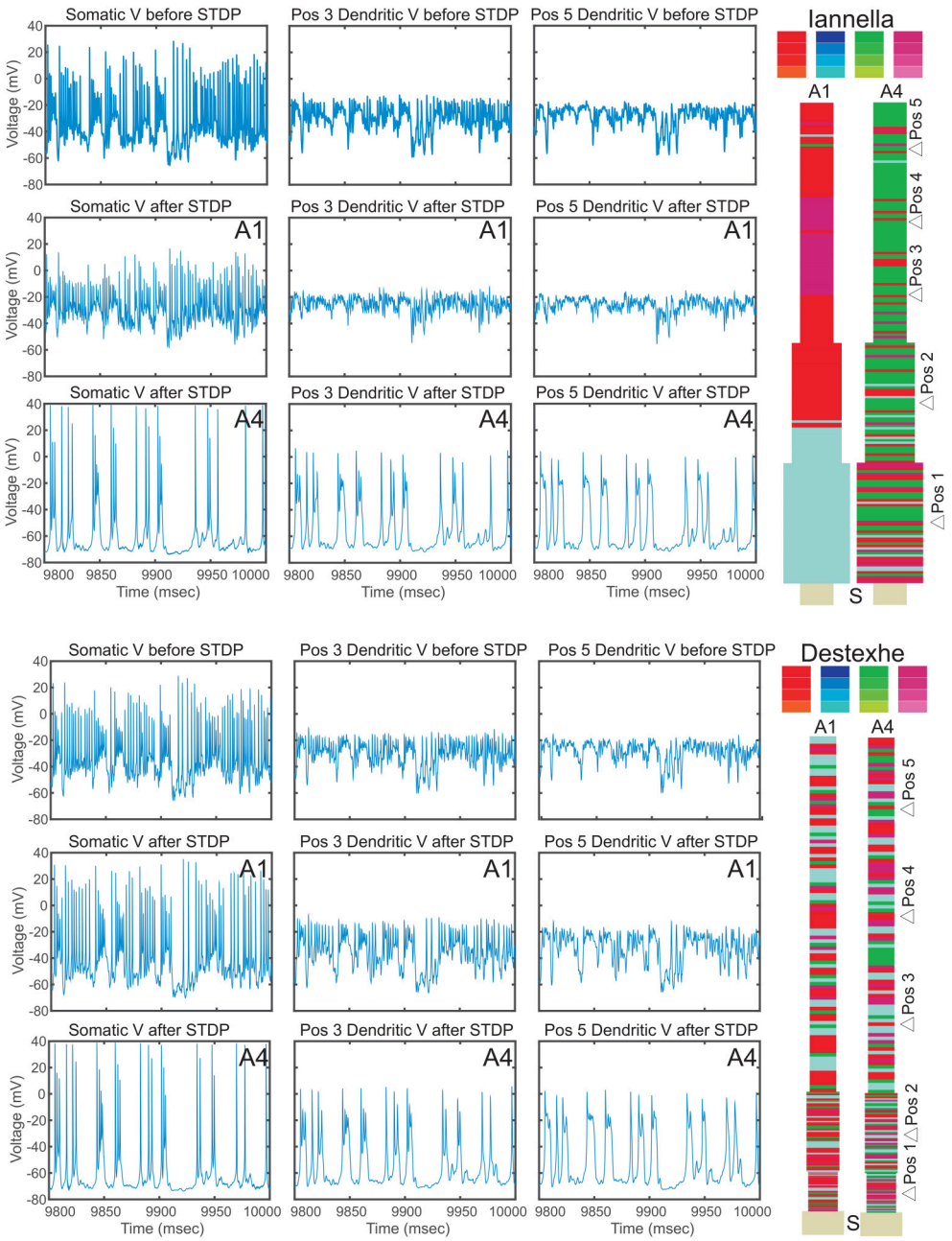

FIGURE 12 | Electrical activity before and after STDP. Traces of the membrane potential recorded from the soma and dendritic locations Pos 3 and Pos 5 before and after the of STDP, for two different values of STDP balance denoted by A1 = 1.15 and A4 = 6. After STDP, the membrane potential tends to the resting potential value, with spikes or spike bursts occurring irregularly. Note that the two simplified models converge to remarkably similar pattern of activity, despite the markedly different synaptic mosaic (see Supplementary Materials for other locations).

responsive to specific inputs. This is akin to the branch specific plasticity recently described by Losonczy et al. (2008), Kleindienst et al. (2011), Legenstein and Maass (2011), Makino and Malinow (2011), and Sajikumar et al. (2014). These results thus point to previously not fully unrecognized properties of dendrites, allowing different sections of the dendritic tree to be "selectively tuned" through synaptic plasticity processes that take into account the nonlinear nature of dendritic voltage depolarization and the statistical structure of the inputs. Such selective tuning may allow the dendrites to process inputs independently and to compartmentally store input features in a robust manner. This added complexity yield a more dynamic and nontrivial computational model of neuronal processing and input/output responses.

Relation to Other Models

There is renewed interest in investigating how synaptic plasticity applied to passive or active dendritic trees shapes the storage of input features via the formation of dendritic compartmentalization (Rabinowitch and Segev, 2006a,b). For example, Tamosiunaite et al. (2007) have reported a type of winner-take-all competition between dendritic branches. In contrast to our study and that of Legenstein and Maass (2011), they only considered the case where individual input groups were initially spatially segregated and would target single branches (Tamosiunaite et al., 2007). More realistically, Legenstein and Maass (2011) have directly implemented neuronal mechanisms where both functional compartmentalization of input features takes place and dendritic branches compete and behave as individual computational subunits. These authors have shown that when explicitly incorporating two levels of competition, one between dendritic branches and the other at the winning branch between locally situated synapses, correlated synaptic activity is strengthened while the efficacy of other synapses decays with time. This permits the features of single input pattern to be stored locally even in one single branch. This type of self-organization thus allows the storage of multiple input features by a single neuron in different non-overlapping regions of the dendrite.

Mechanisms Underlying Inhomogeneous Spatial Patterns of Clusters

The functional benefits of spatially organized synaptic inputs are well documented (Rall, 1964; Mel, 1992b). The precise biophysical mechanisms leading to this organization, allowing memory engram to be represented in "synaptic clusters" are thus of prime interest, both from biological and theoretical perspectives. Previous studies of neural networks self-organization into functional maps have shown that non-linear interaction of short-range excitation and longer-range inhibition are fundamental in the emergence of any type of clustered organization (Haken, 1977; Kohonen, 1982; Haken, 1983). This interaction is important since it sets up a winner-take-all mechanism which, under the appropriate conditions, ultimately leads to the development of the functional clusters thus forming the map. The interaction function is spatial in nature and usually balanced in the sense that positive and negative areas of the function are (nearly) equal and thus balance each other out. This type of interaction is also envisioned to occur in dendritic trees.

Limitations of the Study

Our study describes the conditions under which synaptic efficacy clusters may emerge to form a dendritic mosaic. We found that it is jointly determined by multiple factors, including mean input frequency, the degree of synaptic competition, synaptic balance and dendrite morphology. The region in this multidimensional parameter space where both synaptic efficacy clusters and the dendritic mosaic emerge as a result of STDP learning correspond to a physiological range (frequency) or range used by others. Future work may consider investigating the role of synaptic balance when both excitatory and inhibitory synapses undergo plastic change, to elucidate how balance and plastic inhibitory synapses jointly impact the spatial organization of both excitatory and inhibitory synaptic efficacies.

A novel extension may be to investigate other forms of morphological influences. Recent studies have pointed out additional influence of neuronal morphology on synaptic plasticity and on formation of cortical circuits. For example, important differences in the shape and distribution of dendritic spines along neuronal dendrites between pyramidal cells from different cortical areas, layers, and species have been observed (Murayama et al., 1997; Elston, 2003; Bianchi et al., 2013; Elston and Manger, 2014). In primates, for example, both the numbers, density, and distribution of dendritic spines differ for pyramidal neurons in different cortical areas, while in the mouse the spine density seems to be constant (Murayama et al., 1997; Elston, 2003; Ballesteros-Yáñez et al., 2006; Benavides-Piccione et al., 2006; Bianchi et al., 2013; Elston and Manger, 2014). Another aspect are dendritic spines, as these are the loci where the formation and refinement of cortical circuitry through processes of synaptic plasticity and (consequently) synaptic transmission takes place. In basal dendrites, it has been reported that the size of the spine head is proportional to the number of post-synaptic receptors and pre-synaptic docked vesicle, while the length of the spine neck seems to be associated with the calcium compartmentalization (Ballesteros-Yáñez et al., 2006). Taken together, all these point to the need to re-examine the role played by neuronal morphology in brain development, especially the impact of developmental morphological changes, synaptic plasticity, and synaptogenesis has on the formation of cortical circuits including the patterning of convergent afferent inputs to neurons. Although such a study would be highly valuable, care needs to be taken to incorporate biophysically meaningful processes that correctly capture the biochemical processes of activity-dependent synaptic plasticity, neuronal growth, and spine creation and elimination. The results of such a study will be presented in a future publication and is thus beyond the scope of this paper.

Another extension would be to base the STDP plasticity on an explicit biophysical model of calcium dynamics and biochemical signaling cascades involved in learning and memory. One candidate is the plasticity rule first introduced by Graupner and Brunel (2007). Using such a rule would allow to correlate the emergence of synaptic efficacy clusters with the underlying states of the biochemical signaling cascade, generating experimentally testable predictions. Other potential improvements are an explicit modeling of dendritic spines and of the underlying reaction-diffusion processes, along with Graupner's calcium-based plasticity rule (Graupner and Brunel, 2007). We expect that the spatially restricted calcium signals may allow the emergence of synaptic mosaic for more streams of correlated inputs, beyond the two and four groups tested in the current model.

CONCLUSIONS

This current study illustrates how the level of synaptic balance, admitted by STDP, impacts the formation of synaptic efficacy clusters in dendrites. We believe that the current study

provides useful insights for the interplay between synapse location, synaptic plasticity, and the active properties of the membrane not only shapes the strengths and spatial arrangements of synapses but highlights the emergence of a functional compartmentalization from STDP. Furthermore, we also illustrated that cellular morphology can play a significant role in the emergence of efficacy clusters. In particular our results hint that dendritic branches, under the right conditions, can act as (near) independent functional units, in agreement with other authors (Losonczy et al., 2008; Kleindienst et al., 2011; Legenstein and Maass, 2011; Makino and Malinow, 2011). This permits a novel subdivision of dendritic space and paves the way for the formation of selectively responsive regions of the dendrite and further suggests that the distributed storage of information is the natural mode of information storage in neural circuits. Finally, we are considering further extensions to the current research, such as the inclusion of more detailed biochemistry, dendritic spines, and reaction diffusion processes. These extensions would permit a deeper understanding, at the subcellular level, into how the interplay between synapse location, calcium based biochemistry, and synaptic plasticity in neuronal dendrites shapes dendritic information storage within neural circuits.

AUTHOR CONTRIBUTIONS

Conceived the simulations, analyzed the data, and wrote the manuscript: TL and NI. Performed the simulations: NI.

ACKNOWLEDGMENTS

The authors (NI and TL) wish to thank the support of the RIKEN, Brain Science Institute and the Advanced Center for Computing and Communication (ACCC) for their supercomputing facilities. NI was supported by the People Programme (Marie Curie Actions) of the European Unions Seventh Framework Programme (FP7/2007-2013) under REA grant agreement no. PCOFUND-GA-2012-600181. We also acknowledge the fruitful discussion with Dr. S.M. Korogod during the revision of this manuscript.

SUPPLEMENTARY MATERIAL

The Supplementary Material for this article can be found online at: http://journal.frontiersin.org/article/10.3389/fncom.2017.00042/full#supplementary-material

REFERENCES

Ballesteros-Yáñez, I., Benavides-Piccione, R., Elston, G., Yuste, R., and DeFelipe, J. (2006). Density and morphology of dendritic spines in mouse neocortex. *Neuroscience* 138, 403–409. doi: 10.1016/j.neuroscience.2005.11.038

Benavides-Piccione, R., Hamzei-Sichani, F., Ballesteros-Yáñez, I., DeFelipe, J., and Yuste, R. (2006). Dendritic size of pyramidal neurons differs among mouse cortical regions. *Cereb. Cortex* 16, 990–1001. doi: 10.1093/cercor/bhj041

Bender, V. A., Bender, K. J., Brasier, D. J., and Felsman, D. E. (2006). Two coincidence detectors for spike timing-dependent plasticity in somatosensory cortex. *J. Neurosci.* 26, 4166–4177. doi: 10.1523/JNEUROSCI.0176-06.2006

Bi, G.-Q., and Poo, M.-M. (1998). Synaptic modifications in cultured hippocampal neurons: dependence on spike timing, synaptic strength, and postsynaptic cell type. *J. Neurosci.* 18, 10464–10472.

Bianchi, S., Stimpson, C. D., Duka, T., Larsen, M. D., Janssen, W. G., Collins, Z., et al. (2013), Synaptogenesis and development of pyramidal neuron dendritic morphology in the chimpanzee neocortex resembles humans. *Proc. Natl. Acad. Sci. U.S.A.* 110(Suppl. 2), 10395–10401. doi: 10.1073/pnas.1301224110

Bliss, T. V., and Gardner-Medwin, A. R. (1973). Long-lasting potentiation of synaptic transmission in the dentate area of the unanaestetized rabbit following stimulation of the perforant path. *J. Physiol.* 232, 357–374. doi: 10.1113/jphysiol.1973.sp010274

Bliss, T. V., and Lomo, T. (1973). Long-lasting potentiation of synaptic transmission in the dentate area of the anaesthetized rabbit following stimulation of the perforant path. *J. Physiol.* 232, 331–356. doi: 10.1113/jphysiol.1973.sp010273

Debanne, D., Gahwiler, B. H., and Thompson, S. M. (1994). Asynchronous pre- and postsynaptic activity induces associative long-term depression in area CA1 of the rat hippocampus *in vitro*. *Proc. Natl. Acad. Sci. U.S.A.* 91, 1148–1152. doi: 10.1073/pnas.91.3.1148

Debanne, D., Gähwiler, B. H., and Thompson, S. M. (1998). Long-term synaptic plasticity between pairs of individual ca3 pyramidal cells in rat hippocampal slice cultures. *J. Physiol.* 507, 237–247. doi: 10.1111/j.1469-7793.1998.237bu.x

Destexhe, A., Neubig, M., Ulrich, D., and Huguenard, J. (1998). Dendritic low-threshold calcium currents in thalamic relay cells. *J. Neurosci.* 18, 3574–3588.

De Roo, M., Klauser, P., and Muller, D. (2008). LTP promotes a selective long-term stabilization and clustering of dendritic spines. *PLoS Biol.* 6, 1850–1860. doi: 10.1371/journal.pbio.0060219

Duncan, O., and Duncan, B. (1955). A methodological analysis of segregation indexes. *Am. Soc. Rev.* 20, 210–217. doi: 10.2307/2088328

Elston, G. and Manger, P. (2014), Pyramidal cells in v1 of african rodents are bigger, more branched and more spiny than those in primates. *Front. Neuroanat.* 8:4. doi: 10.3389/fnana.2014.00004

Elston, G. N. (2003), Cortex, cognition and the cell: new insights into the pyramidal neuron and prefrontal function. *Cereb. Cortex* 13, 11, 1124–1138. doi: 10.1093/cercor/bhg093

Erwin, E., Obermayer, K., and Schulten, K. (1995). Models of orientation and ocular dominance columns in the visual cortex: a critical comparison. *Neural Comput.* 7, 425–468. doi: 10.1162/neco.1995.7.3.425

Feldmeyer, D., Lubke, J., Silver, R. A., and Sakmann, B. (2002). Synaptic connections between layer 4 spiny neurone-layer 2/3 pyramidal cell pairs in juvenile rat barrel cortex: physiology and anatomy of interlaminar signalling within a cortical column. *J. Physiol.* 538.3, 803–822. doi: 10.1113/jphysiol.2001.012959

Froemke, R. C., and Dan, Y. (2002). Spike-timing dependent synaptic modification induced by natural spike trains. *Nature* 416, 433–438. doi: 10.1038/416433a

Froemke, R. C., Poo, M.-M., and Dan, Y. (2005). Spike-timing-dependent synaptic plasticity depends on dendritic location. *Nature* 434, 221–225. doi: 10.1038/nature03366

Gidon, A., and Segev, I. (2009). Spike-timing-dependent synaptic plasticity and synaptic democracy in dendrites. *J. Neurophysiol.* 101, 3226–3234. doi: 10.1152/jn.91349.2008

Golding, N. L., Staff, N. P., and Spruston, N. (2002). Dendritic spikes as a mechanism for cooperative long-term potentiation. *Nature* 418, 326–331. doi: 10.1038/nature00854

Govindarajan, A., Israely, I., Huang, S.-Y., and Tonegawa, S. (2011). The dendritic branch is the preferred integrative unit for protein synthesis-dependent ltp. *Neuron* 69, 132–146. doi: 10.1016/j.neuron.2010.12.008

Graupner, M., and Brunel, N. (2007). STDP in a bistable synapse model based on CaMKII and associated signaling pathways. *PLoS Comp. Biol.* 3, 2299–2323. doi: 10.1371/journal.pcbi.0030221

Gutig, R., Aharonov, R., Rotter, S., and Sompolinsky, H. (2003). Learning input correlations through nonlinear temporally asymmetric hebbian plasticity. *J. Neurosci.* 23, 3697–3714.

Haken, H. (1977). *Synergetics. An Introduction*. Berlin; Heidelberg; New York, NY: Springer-Verlag.

Haken, H. (1983). *Advanced Synergetics. Instabilities of Self-Organizing Systems and Devices*. Berlin; Heidelberg; New York, NY; Tokyo: Springer-Verlag.

Harnett, M. T., Makara, J. K., Spruston, N., Kath, W. L., and Magee, J. C. (2012). Synaptic amplification by dendritic spines enhances input cooperativity. *Nature* 491, 599–602. doi: 10.1038/nature11554

Harvey, C. D., and Svoboda, K. (2007). Locally dynamic synaptic learning rules in pyramidal neuron dendrites. *Nature* 450, 1195–1202. doi: 10.1038/nature06416

Hensch, T. K., Fagiolini, M., Mataga, N., Stryker, M. P., Baekkeskov, S., and Kash, S. F. (1998). Local gaba circuit control of experience-dependent plasticity in developing visual cortex. *Science* 282, 1504–1508. doi: 10.1126/science.282.5393.1504

Hines, M. L., and Carnevale, N. T. (2001). NEURON: A tool for neuroscientists. *Neuroscientist* 7, 123–135. doi: 10.1177/107385840100700207

Holthoff, K., Kovalchuk, Y., Yuste, R., and Konnerth, A. (2004). Single-shock LTD by local dendritic spikes. *J. Physiol.* 560, 27–36. doi: 10.1113/jphysiol.2004.072678

Iannella, N., and Tanaka, S. (2006). Synaptic efficacy cluster formation across the dendrite via STDP. *Neurosci. Lett.* 403, 24–29. doi: 10.1016/j.neulet.2006.03.079

Iannella, N., Tuckwell, H., and Tanaka, S. (2004). Firing properties of a stochastic PDE model of a rat sensory cortex layer 2/3 pyramidal cell. *Math. Biosci.* 188, 117–132. doi: 10.1016/j.mbs.2003.10.002

Iannella, N. L., Launey, T., and Tanaka, S. (2010). Spike timing-dependent plasticity as the origin of the formation of clustered synaptic efficacy engrams. *Front. Comput. Neurosci.* 4:21. doi: 10.3389/fncom.2010.00021

Jia, H., Rochefort, N. L., Chen, X., and Konnerth, A. (2010). Dendritic organization of sensory input to cortical neurons *in vivo*. *Nature* 464, 1307–1312. doi: 10.1038/nature08947

Kirkwood, A., and Bear, M. F. (1994). Homosynaptic long-term depression in the visual cortex. *J. Neurosci.* 14, 3404–3412.

Kleindienst, T., Winnubst, J., Roth-Alpermann, C., Bonhoeffer, T., and Lohmann, C. (2011). Activity-dependent clustering of functional synaptic inputs on developing hippocampal dendrites. *Neuron* 72, 1012–1024. doi: 10.1016/j.neuron.2011.10.015

Kohonen, T. (1982). Self-organized formation of topologically correct feature maps. *Biol, Cybern.* 43, 59–69. doi: 10.1007/BF00337288

Krapivinsky, G., Krapivinsky, L., Manasian, Y., Ivanov, A., Tyzio, R., Pellegrino, C., et al. (2003). The nmda receptor is coupled to the erk pathway by a direct interaction between nr2b and rasgrf1. *Neuron* 40, 775–784. doi: 10.1016/S0896-6273(03)00645-7

Kuhn, A., Aertsen, A., and Rotter, S. (2003). Higher-order statistics of input ensembles and the response of simple model neurons. *Neural Comput.* 15, 67–101. doi: 10.1162/089976603321043702

Larkum, M. E., Kaiser, K. M. M., and Sakmann, B. (2001). Dendritic mechanisms underlying the coupling of the dendritic with the axonal action potential initiation zone of adult layer 5 pyramidal neurons. *J. Physiol.* 533, 447–466. doi: 10.1111/j.1469-7793.2001.0447a.x

Larkum, M. E., Nevian, T., Sandler, M., Polsky, A., and Schiller, J. (2009). Synaptic integration in tuft dendrites of layer 5 pyramidal neurons: a new unifying principle. *Science* 325, 756–760. doi: 10.1126/science.1171958

Legenstein, R., and Maass, W. (2011). Branch-specific plasticity enables self-organization of nonlinear computation in single neurons. *J. Neurosci.* 31, 10787–10802. doi: 10.1523/JNEUROSCI.5684-10.2011

Levy, W. B., and Steward, O. (1979). Synapses as associative memory elements in the hippocampal formation. *Brain Res.* 175, 233–245. doi: 10.1016/0006-8993(79)91003-5

Losonczy, A., and Magee, J. C. (2006). Integrative properties of radial oblique dendrites in hippocampal CA1 pyramidal neurons. *Neuron* 50, 291–307. doi: 10.1016/j.neuron.2006.03.016

Losonczy, A., Makara, J. K., and Magee, J. C. (2008). Compartmentalized dendritic plasticity and input feature storage in neurons. *Nature* 452, 436–441. doi: 10.1038/nature06725

Mainen, Z. F., Joerges, J., Huguenard, J. R., and Sejnowski, T. J. (1995). A model of spike initiation in neocortical pyramidal cells. *Neuron* 15, 1427–1439. doi: 10.1016/0896-6273(95)90020-9

Major, G., Larkum, M. E., and Schiller, J. (2013). Active properties of neocortical pyramidal neuron dendrites. *Ann. Rev. Neurosci.* 36, 1–24. doi: 10.1146/annurev-neuro-062111-150343

Makino, H., and Malinow, R. (2011). Compartmentalized versus global synaptic plasticity on dendrites controlled by experience. *Neuron* 72, 1001–1011. doi: 10.1016/j.neuron.2011.09.036

Markram, H., Lubke, J., Frotscher, M., Roth, A., and Sakmann, B. (1997a). Physiology and anatomy of synaptic connections between thick tufted pyramidal neurones in the developing rat neocortex. *J. Physiol.* 500.2, 409–440. doi: 10.1113/jphysiol.1997.sp022031

Markram, H., Lübke, J., Frotscher, M., and Sakmann, B. (1997b). Regulation of synapic efficacy by coincidence of postsynaptic AP and EPSP. *Science* 275, 213–215. doi: 10.1126/science.275.5297.213

McBride, T. J., Rodriguez-Contreras, A., Trinh, A., Bailey, R., and DeBello, W. M. (2008). Learning drives differential clustering of axodendritic contacts in the barn owl auditory system. *J. Neurosci.* 28, 6960–6973. doi: 10.1523/JNEUROSCI.1352-08.2008

McNaughton, B. L., Douglas, R. M., and Goddard, G. V. (1978). Synaptic enhancement in fascia dentata: cooperativity among coactive afferents. *Brain Res.* 157, 277–293. doi: 10.1016/0006-8993(78)90030-6

Medina, I., Leinekugel, X., and Ben-Ari, Y. (1999). Calcium-dependent inactivation of the monosynaptic nmda epscs in rat hippocampal neurons in culture. *Euro. J. Neurosci.* 11, 2422–2430. doi: 10.1046/j.1460-9568.1999.00664.x

Mel, B. W. (1992a). "The clusteron: toward a simple abstraction for a complex neuron," in *Advances in Neural Information Processing Systems*, Vol. 4., eds J. Moody, S. Hanson, and R. Lippmann (San Mateo, CA: Morgan Kaufmann), 35–42.

Mel, B. W. (1992b). NMDA-based pattern discrimination in a modeled cortical neuron. *Neural Computat.* 4, 502–517. doi: 10.1162/neco.1992.4.4.502

Mickus, T., Jung, H.-Y., and Spruston, N. (1999). Properties of slow, cumulative sodium channel inactivation in rat hippocampal CA1 pyramidal cells. *Biophys. J.* 76, 846–860. doi: 10.1016/S0006-3495(99)77248-6

Miller, K. D. (1994). A model for the development of simple cell receptive fields and the ordered arrangement of orientation columns through activity-dependent competition between on- and off-center inputs. *J. Neurosci.* 14, 409–441.

Miyashita, M., and Tanaka, S. (1992). A mathematical model for the self-organization of orientation columns in visual cortex. *Neuroreport* 3, 69–72. doi: 10.1097/00001756-199201000-00018

Morales, B., Choi, S.-Y., and Kirkwood, A. (2002). Dark rearing alters the development of gabaergic transmission in visual cortex. *J. Neurosci.* 22, 8084–8090.

Murayama, Y., Fujita, I., and Kato, M. (1997). Contrasting forms of synaptic plasticity in monkey inferotemporal and primary visual cortices. *Neuroreport* 8, 1503–1507. doi: 10.1097/00001756-199704140-00036

Narayanan, R., and Johnston, D. (2012). Functional maps within a single neuron. *J. Neurophysiol.* 108, 2343–2351. doi: 10.1152/jn.00530.2012

Nevian, T., and Sakmann, B. (2006). Spine ca^{2+} signaling in spike-timing-dependent plasticity. *J. Neurosci.* 26, 11001–11013. doi: 10.1523/JNEUROSCI.1749-06.2006

Paré, D., Shink, E., Gaudreau, H., Destexhe, A., and Lang, E. J. (1998). Impact of spontaneous synaptic activity on the resting properties of cat neocortical pyramidal neurons *in vivo*. *J. Neurophysiol.* 79, 1450–1460.

Podgorski, K., Dunfield, D., and Haas, K. (2012). Functional clustering drives encoding improvement in a developing brain network during awake visual learning. *PLoS Biol.* 10:e1001236. doi: 10.1371/journal.pbio.1001236

Poirazi, P., Brannon, T., and Mel, B. W. (2001). Impact of active dendrites and structural plasticity on the memory capacity of neural tissue. *Neuron* 29, 779–796. doi: 10.1016/S0896-6273(01)00252-5

Poirazi, P., Brannon, T., and Mel, B. W. (2003a). Arithmetic of subthreshold synaptic summation in a model CA1 pyramidal cell. *Neuron* 37, 977–987. doi: 10.1016/S0896-6273(03)00148-X

Poirazi, P., Brannon, T., and Mel, B. W. (2003b). Pyramidal neuron as a two-layer neural network. *Neuron* 37, 989–999. doi: 10.1016/S0896-6273(03)00149-1

Polsky, A., Mel, B. W., and Schiller, J. (2004). Computational subunits in thin dendrites of pyramidal cells. *Nat. Neurosci.* 7, 621–627. doi: 10.1038/nn1253

Quinlan, E. M., Olstein, D. H., and Bear, M. F. (1999). Bidirectional, experience-dependent regulation of n-methyl-d-aspartate receptor subunit composition in the rat visual cortex during postnatal development. *Proc. Natl. Acad. Sci. U.S.A.* 96, 12876–12880. doi: 10.1073/pnas.96.22.12876

Rabinowitch, I., and Segev, I. (2006a). The endurance and selectivity of spatial patterns of long-term potentiation/depression in dendrites under homeostatic synaptic plasticity. *J. Neurosci.* 26, 13474–13484. doi: 10.1523/JNEUROSCI.4333-06.2006

Rabinowitch, I., and Segev, I. (2006b). The interplay between homeostatic synaptic plasticity and functional dendritic compartments. *J. Neurophysiol.* 96, 276–283. doi: 10.1152/jn.00074.2006

Rall, W. (1964). "Theoretical significance of dendritic trees for neuronal input-output relations," in *Neural Theory and Modeling*, Chapter 4, ed R. Riess, (Stanford, CA: Stanford University Press), 73–97.

Rhodes, P. A., and Gray, C. M. (1994). Simulations of intrinsically bursting neocortical pyramidal neurons. *Neural Comput.* 6, 1086–1110. doi: 10.1162/neco.1994.6.6.1086

Rhodes, P. A., and Llinás, R. R. (2001). Apical tuft input efficacy in layer 5 pyramidal cells from rat visual cortex. *J. Physiol.* 6, 1086–1110. doi: 10.1111/j.1469-7793.2001.00167.x

Rumsey, C. C., and Abbott, L. F. (2004). Equalization of synaptic efficacy by activity and timing-dependent synaptic plasticity. *J. Neurophysiol.* 91, 2273–2280. doi: 10.1152/jn.00900.2003

Rumsey, C. C., and Abbott, L. F. (2006). Synaptic democracy in active dendrites. *J. Neurophysiol.* 96, 2307–2318. doi: 10.1152/jn.00149.2006

Sajikumar, S., Morris, R. G., and Korte, M. (2014). Competition between recently potentiated synaptic inputs reveals a winner-take-all phase of synaptic tagging and capture. *Proc. Natl. Acad. Sci. U.S.A.* 111, 12217–12221. doi: 10.1073/pnas.1403643111

Schiller, J., Major, G., Koester, H. J., and Schiller, Y. (2000). NMDA spikes in basal dendrites of cortical pyramidal cells. *Nature* 404, 285–289. doi: 10.1038/35005094

Song, S., and Abbott, L. F. (2001). Cortical development and remapping through spike timing-dependent plasticity. *Neuron* 32, 339–350. doi: 10.1016/S0896-6273(01)00451-2

Song, S., Miller, K. D., and Abbott, L. F. (2000). Competitive hebbian learning through spike-timing-dependent synaptic plasticity. *Nat. Neurosci.* 3, 919–926. doi: 10.1038/78829

Stuart, G. J., and Häusser, M. (2001). Dendritic coincidence detection of EPSPs and action potentials. *Nat. Neurosci.* 4, 63–71. doi: 10.1038/82910

Swindale, N. (1996). The development of topography in the visual cortex: a review of models. *Netw. Comput. Neural Syst.* 7, 161–247. doi: 10.1088/0954-898X_7_2_002

Takesian, A. E., and Hensch, T. K. (2013). Balancing plasticity/stability across brain development. *Prog. Brain Res.* 207, 3–34. doi: 10.1016/B978-0-444-63327-9.00001-1

Tamosiunaite, M., Porr, B., and Wörgötter, F. (2007). Self-influencing synaptic plasticity: Recurrent changes of synaptic weights can lead to specific functional properties. *J. Comput. Neurosci.* 23, 113–127. doi: 10.1007/s10827-007-0021-2

Tanaka, S. (1990). Theory of self-organization of cortical maps: mathematical framework. *Neural Netw.* 3, 625–640. doi: 10.1016/0893-6080(90)90053-N

Thomson, A. M., Deuchars, J., and West, D. C. (1994). Relationships between morphology and physiology of pyramid-pyramid single axon connections in rat neocortex *in vitro*. *J. Physiol.* 478.3, 423–435. doi: 10.1113/jphysiol.1994.sp020262

Thomson, A. M., West, D. C., Wang, Y., and Bannister, A. P. (2002). Synaptic connections and small circuits involving excitatory and inhibitory neurons in layers 2-5 of adult rat and cat neocortex:triple intracellular recordings and biocytin labelling *in vitro*. *Cereb. Cortex* 12, 936–953. doi: 10.1113/jphysiol.1994.sp020262

Traub, R. D., Buhl, E. H., Gloveli, T., and Whittington, M. A. (2003). Fast rhythmic bursting can be induced in a layer 2/3 cortical neurons by enhancing persistent Na^+ conductance or by blocking bk channels. *J. Neurophysiol.* 89, 909–921. doi: 10.1152/jn.00573.2002

Traulsen, A., and Claussen, J. C. (2004). Similarity-based cooperation and spatial segregation. *Phys. Rev. E.* 70:046128. doi: 10.1103/PhysRevE.70.046128

Turrigiano, G. G., and Nelson, S. B. (2004). Homeostatic plasticity in the developing nervous system. *Nat. Rev. Neurosci.* 5, 97–107. doi: 10.1038/nrn1327

van Rossum, M. C. W., Bi, G.-Q., and Turrigiano, G. G. (2000). Stable hebbian learning from spike timing-dependent plasticity. *J. Neurosci.* 20, 8812–8821.

Young, J. M., Waleszczyk, W. J., Wang, C., Calford, M. B., Dreher, B., and Obermayer, K. (2007). Cortical reorganization consistent with spike timing-dependent but not correlation-dependent plasticity. *Nat. Neurosci.* 10, 887–895. doi: 10.1038/nn1913

Zador, A. M., Claiborne, B. J., and Brown, T. H. (1992). "Nonlinear pattern separation in single hippocampal neurons with active dendritic membrane," in *Advances in Neural Information Processing Systems*, eds. J. E. Moody, S. J. Hanson, and R. P. Lippmann (Burlington, MA: Morgan-Kaufmann), 51–58.

Zhang, L. I., Tao, H. W., Holt, C. E., Harris, W. A., and Poo, M.-M. (1998). A critical window for cooperation and competition among developing retinotectal synapses. *Nature* 395, 37–44. doi: 10.1038/25665

Conflict of Interest Statement: The authors declare that the research was conducted in the absence of any commercial or financial relationships that could be construed as a potential conflict of interest.

frontiers in
CELLULAR NEUROSCIENCE

ORIGINAL RESEARCH ARTICLE
published: 02 October 2014
doi: 10.3389/fncel.2014.00303

Maximum likelihood estimation of biophysical parameters of synaptic receptors from macroscopic currents

***Andrey Stepanyuk*[1,2]*, *Anya Borisyuk*[1,2] *and Pavel Belan*[1,2]**

[1] *Laboratory of Molecular Biophysics, Bogomoletz Institute of Physiology, Kiev, Ukraine*
[2] *State Key Laboratory of Molecular and Cellular Biology, Bogomoletz Institute of Physiology, Kiev, Ukraine*

Edited by:
Sergey M. Korogod, National Academy of Sciences of Ukraine, Ukraine

Reviewed by:
Sergio Solinas, Fondazione "Istituto Neurologico Nazionale C. Mondino," Italy
Thierry Ralph Nieus, Istituto Italiano di Tecnologia, Italy

***Correspondence:**
Andrey Stepanyuk, Bogomoletz Institute of Physiology, Bogomoletz Street 4, Kiev 01024, Ukraine
e-mail: standrey@biph.kiev.ua

Dendritic integration and neuronal firing patterns strongly depend on biophysical properties of synaptic ligand-gated channels. However, precise estimation of biophysical parameters of these channels in their intrinsic environment is complicated and still unresolved problem. Here we describe a novel method based on a maximum likelihood approach that allows to estimate not only the unitary current of synaptic receptor channels but also their multiple conductance levels, kinetic constants, the number of receptors bound with a neurotransmitter, and the peak open probability from experimentally feasible number of postsynaptic currents. The new method also improves the accuracy of evaluation of unitary current as compared to the peak-scaled non-stationary fluctuation analysis, leading to a possibility to precisely estimate this important parameter from a few postsynaptic currents recorded in steady-state conditions. Estimation of unitary current with this method is robust even if postsynaptic currents are generated by receptors having different kinetic parameters, the case when peak-scaled non-stationary fluctuation analysis is not applicable. Thus, with the new method, routinely recorded postsynaptic currents could be used to study the properties of synaptic receptors in their native biochemical environment.

Keywords: unitary current, synaptic currents, peak-scaled non-stationary fluctuation analysis, maximum likelihood, semiseparable matrix, kinetic model, Markov chain Monte Carlo

INTRODUCTION

Intrinsic biophysical properties of synaptic receptor channels are important for determining of both efficacy of synaptic transmission and activation of dendritic voltage-gated channels underlying active properties of dendrites. For example, synaptic NMDA receptors directly contribute to non-linear depolarizing drive in dendrites and control dendritic firing patterns and local dendritic Ca^{2+} concentration transients (Major et al., 2013). Changes in the postsynaptic receptor number, unitary conductance, and kinetics may affect dendritic integration (Magee, 2000) and lead to alteration in synaptic strength and memory function (Li and Tsien, 2009) in normal (Benke et al., 1998) and pathological states (Kittler et al., 2004). Thus, precise estimation of these parameters is important for a better understanding of synaptic transmission and dendritic excitability.

However, postsynaptic receptors in their native environment are hardly accessible experimentally, and this limitation has rendered their biophysical properties notoriously difficult to study. In order to cope with this problem, postsynaptic receptors are heterologously expressed and studied using single channel recording in small membrane patches by means of fast application of respective neurotransmitters. At the same time it has been claimed using proteomic approaches that postsynaptic receptors can interact with dozens of intracellular proteins (Husi et al., 2000) that results in modulation of their functioning. Besides, many extracellular factors such as, e.g., ions, certainly affect synaptic receptor function (Paoletti et al., 1997; Low et al., 2000). Altogether it makes it almost impossible to directly apply receptor biophysical parameters obtained in a heterologous system to the analysis of postsynaptic receptors under physiological conditions.

The peak-scaled non-stationary fluctuation analysis (PS NSFA) (Traynelis et al., 1993) is a most commonly used indirect method by which unitary current of synaptic receptors can be extracted from the macroscopic synaptic currents. This continuation of the conventional non-stationary noise analysis (Sigworth, 1980) overcomes impact of the quantal variability of postsynaptic currents on the accuracy of unitary current estimation by scaling the mean postsynaptic current waveform to the peak amplitude of each individual postsynaptic current. The two waveforms are then subtracted to isolate fluctuations arising from the synaptic channel gating. However, by using PS NSFA information about the total number of synaptic receptors bound or exposed to a neurotransmitter is lost and only the average number of receptors open at the peak of the postsynaptic current can be estimated (Traynelis et al., 1993; Silver et al., 1996). Activation, inactivation, and desensitization, key features of synaptic receptor behavior, which are determined by receptor kinetic parameters, also could not be evaluated by PS NSFA. Although many attempts have been performed to estimate the kinetic constants of ion channels from fluctuations of postsynaptic macroscopic currents (Neher and Stevens, 1977; Traynelis and Jaramillo, 1998; Milescu et al., 2005; Moffatt, 2007) all of them do not get over the quantal variability of postsynaptic currents or could not be easily applied to the analysis of these currents because of restricted accuracy and efficiency.

By overcoming computational complexity that emerges due to quantal variability of postsynaptic currents, a maximum likelihood non-stationary fluctuation analysis (ML NSFA) suggested in this work makes it possible to estimate unitary currents, number of channels bound with a neurotransmitter, peak open probability, and some kinetic constants for synaptic channels in their native biochemical environment from the experimentally feasible number of macroscopic postsynaptic currents.

MATERIALS AND METHODS

KINETIC MODEL

In this work we consider simulated macroscopic synaptic currents generated by a varying number of synaptic receptor channels. The channels are assumed to be independent and identical. We assume that the synaptic channel gating is a Markov process and p_{ij} is the probability of channel transition from state j to state i at time Δt. The rate matrix is an $N_s \times N_s$ matrix $\mathbf{Q}: q_{ij} = \lim_{\Delta t \to 0} \frac{p_{ij}}{\Delta t}$, N_s is the number of states of the synaptic channel model. Each element of the matrix $\mathbf{Q}$ gives the rate constant of transition $j \to i$ if the transition is allowed by the model and otherwise $q_{ij} = 0$. The diagonal elements, q_{ii}, are set to $-\sum_j q_{ij}$, so the sum over each column is zero. Synaptic release of neurotransmitter is modeled as a step pulse of its concentration in the synaptic cleft, which leads to instantaneous change of concentration-dependent transition probabilities, p_{ij}.

We assume that the kinetic matrix topology (i.e., a set of allowed transitions) and the number of conducting states are known. The required model parameters were arranged into the parameter vector $\theta = [q, i_{ch}, N_{ch}]$ and they were: rate constants, $q_{ij} = \lim_{\Delta t \to 0} \frac{p_{ij}}{\Delta t}$, $i \neq j$, unitary currents, i_{ch}, and the number of postsynaptic receptors bound with a neurotransmitter right after the concentration transient, N_{ch}.

THE LOG-LIKELIHOOD FUNCTION

The likelihood function, $L_{\boldsymbol{\theta}}$, that is to be maximized by ML NSFA in order to find the most likely set of parameters is defined as the conditional probability to observe N macroscopic current traces $\boldsymbol{c}_i$, $i = 1:N$, sampled at time points $t = [1 \ldots N_T]$ given the model parameters $\boldsymbol{\theta}$ (Colquhoun and Hawkes, 1977; Celentano and Hawkes, 2004; Milescu et al., 2005; Stepanyuk et al., 2011):

$$L_\theta \equiv P(\mathbf{c}|\boldsymbol{\theta}) \underset{N_{ch} \longrightarrow \infty}{\longrightarrow} \frac{1}{(2\pi)^{NN_T/2} \prod_{i=1}^{N} |\mathbf{c}_{m1} N_{chi}|^{1/2}} \exp\left\{-\frac{1}{2}\sum_{i=1}^{N} (\boldsymbol{c}_i - \boldsymbol{\mu} N_{chi})^T \frac{\mathbf{c}_{m1}^{-1}}{N_{chi}} (\boldsymbol{c}_i - \boldsymbol{\mu} N_{chi})\right\} \quad (1)$$

Here N is the number of synaptic macroscopic current traces $\boldsymbol{c}_i$ (sample size) and N_T is the number of points in each trace; N_{chi} is a number of channels exposed to neurotransmitter in each current $\boldsymbol{c}_i$; $\boldsymbol{\mu}$, an $N_T \times 1$ vector and $\mathbf{c}_{m1}$, an $N_T \times N_T$ matrix with elements $\{\mathbf{c}_{m1}\}_{t,t'}$, and denote mean and covariance of single channel current, respectively, and they both are the functions of $\boldsymbol{\theta}$. $\mathbf{c}_{m1}$ is related to the covariance matrix, $\mathbf{c}_m$, of a macroscopic synaptic current $\boldsymbol{c}_i$ by the following expression: $\mathbf{c}_m = \mathbf{c}_{m1} N_{chi}$. Mean and covariance follow equations (Colquhoun and Hawkes, 1977)

$$\begin{aligned} \boldsymbol{\mu} &= \boldsymbol{i}^T e^{\mathbf{Q}t} \boldsymbol{p}(0) \\ \{\mathbf{c}_{m1}\}_{t,t'} &= \left(\boldsymbol{i}^T e^{\mathbf{Q}t} \boldsymbol{p}(0)\, e^{\mathbf{Q}(t'-t)} \boldsymbol{i} - \left(\boldsymbol{i}^T e^{\mathbf{Q}t'} \boldsymbol{p}(0)\right)\left(\boldsymbol{i}^T e^{\mathbf{Q}t} \boldsymbol{p}(0)\right)\right) \end{aligned} \quad (2)$$

Here $\mathbf{Q}$ is a rate matrix (Colquhoun and Hawkes, 1977; Celentano and Hawkes, 2004) and $\boldsymbol{p}(0)$ is an initial state vector. The elements of $\boldsymbol{p}(0)$ can be calculated as the equilibrium probabilities determined by the initial experimental conditions, which are assumed to last for sufficiently long time T to allow the channels reach equilibrium

$$\boldsymbol{p}(0) = \prod_j e^{\mathbf{Q}_j \Delta t_j} \boldsymbol{p}(-T) \quad (3)$$

It is generally accepted to maximize the logarithm of the likelihood function $\log L_\theta$ instead of the likelihood function L_θ itself. Therefore, our objective was to find the most likely model parameter set, $\boldsymbol{\theta}_{ML}$, i.e., the parameter set that maximized the log-likelihood

$$\boldsymbol{\theta}_{ML} = \underset{\theta}{\operatorname{argmax}} \left(\log L_\theta\right) \quad (4)$$

The log-likelihood function $\log L_\theta$ can be efficiently estimated using the fact that $\mathbf{c}_{m1}$ has a specific structure of semiseparable matrix (DeWilde and van der Veen, 1998; Stepanyuk et al., 2011).

EFFICIENT ESTIMATION OF THE LOG-LIKELIHOOD FUNCTION FOR SYNAPTIC CURRENTS WITH NOISE

Efficient log-likelihood estimation used in this article is based on our previously described method (Stepanyuk et al., 2011). Briefly, the method was based on the fact that the covariance matrix $\mathbf{c}_{m1}$, has a specific structure of semiseparable matrix, namely $\mathbf{c}_{m1}$ can be represented as Stepanyuk et al. (2011).

$$\begin{aligned} \{\mathbf{c}_{m1}\}_{ij} &= \sum_{k=1}^{N_S+1} A_{ik} B_{kj}, \mathrm{i} \geq \mathrm{j} \\ \{\mathbf{c}_{m1}\}_{ji} &= \{\mathbf{c}_{m1}\}_{ij}, \mathrm{i} \geq \mathrm{j} \end{aligned} \quad (5)$$

where

$$\begin{aligned} A_{ik} &= e^{\lambda_k t_i} \sum_{o=1}^{N_O} i_o U(o,k), 1 \leq k \leq N_S \\ A_{ik} &= \mu_{t_j}, k = N_S + 1 \end{aligned} \quad (6)$$

and

$$\begin{aligned} B_{kj} &= e^{\lambda_k (T_{s(j)} - t_j)} \left(\sum_{o'=1}^{N_O} U^{-1}(k,o')\, p_{o'}(t_j)\, i_{o'}\right), 1 \leq k \leq N_S \\ B_{kj} &= -\mu_{t_j}, k = N_S + 1 \end{aligned} \quad (7)$$

where $\mathbf{U}$: $e^{\mathbf{Q}t} = \mathbf{U} e^{\mathbf{D}t} \mathbf{U}^{-1}$ is $N_s \times N_s$ matrix of the eigenvectors of $\mathbf{Q}$, and $\mathbf{D}$ is a diagonal form of $\mathbf{Q}$ provided all the eigenvalues of $\mathbf{Q}$, λ, are different; N_o is a number of open states in the channel model. Efficient linear algebra algorithms for semiseparable matrices (Vandebril et al., 2007; Eidelman and

Gohberg, 2008) allowed us to compute the log-likelihood and provided almost linear scaling of its computational cost with the number of states in a kinetic model for the case of sufficiently large number of currents, ensuring fast, and accurate estimation of model parameters. The number of synaptic channels exposed to neurotransmitter was assumed to be the same for all currents. However, in the case of synaptic currents this number could vary between trials due to quantal variability. As a result, $\log L_\theta$ must be estimated separately for each current, and then summed up, thus increasing the number of operations in N times at least. However, calculations could be substantially simplified if the majority of receptors, which will participate in the current, are found in one particular state immediately after the neurotransmitter concentration transient, as it is expected for the synaptic receptors. To compute $\log L_\theta$ in this case, let denote noisy macroscopic synaptic current with an $N_T \times 1$ vector $\boldsymbol{c_i}$ and let denote by $\boldsymbol{n_i}$ an $N_T \times 1$ vector of noise imposed on the i-th current. Then $-\log L_\theta$ of the set of parameters $\boldsymbol{\theta}$ given macroscopic synaptic currents without noise imposed on them is (we omit here the constant term $NN_T \log(2\pi)/2$)

$$-\log L_\theta(\mathbf{c}-\mathbf{n}) = \frac{1}{2}\sum_{i=1}^{N}\left(\boldsymbol{c}_i - \boldsymbol{n}_i - \boldsymbol{\mu}N_{ch_i}\right)^T \frac{\mathbf{c_{m1}^{-1}}}{N_{ch_i}} (\boldsymbol{c}_i - \boldsymbol{n}_i - \boldsymbol{\mu}N_{chi}) + \frac{1}{2}\sum_{i=1}^{N}\left(\log|\mathbf{c}_{m1}N_{chi}|\right) \quad (8)$$

where $\boldsymbol{\mu}$ is an expectation of synaptic current without noise and $\log L_\theta(\mathbf{c}-\mathbf{n})$ denotes the required log-likelihood given the set of macroscopic synaptic currents without noise. Equation (8) can be rewritten as

$$-\log L_\theta(\mathbf{c}-\mathbf{n}) = -\log L_\theta(\mathbf{c}) - \frac{1}{2}\sum_{i=1}^{N}\boldsymbol{n}_i^T\mathbf{c}_{m1}^{-1}\boldsymbol{n}_i\frac{1}{N_{ch_i}} - \sum_{i=1}^{N}\boldsymbol{n}_i^T\frac{\mathbf{c}_{m1}^{-1}}{N_{ch_i}}\left(\boldsymbol{c}_i - \boldsymbol{n}_i - \boldsymbol{\mu}N_{ch_i}\right) \quad (9)$$

Since the background noise and the macroscopic current are uncorrelated the last term in Equation (9) can be neglected without loss in accuracy given the number of currents, N, is large enough. Therefore, we have

$$-\log L_\theta(\mathbf{c}-\mathbf{n}) = -\log L_\theta(\mathbf{c}) - \frac{1}{2}\sum_{i=1}^{N}\boldsymbol{n}_i^T\mathbf{c}_{m1}^{-1}\boldsymbol{n}_i\frac{1}{N_{ch_i}} \quad (10)$$

To quickly evaluate the last term in Equation (10), let us approximate $\sum_{i=1}^{N}\frac{(\boldsymbol{n}_i^T)_k(\boldsymbol{n}_i)_j}{N_{ch_i}}$ by $\{\mathbf{c_{noise}}\}_{kj}N\left\langle\frac{1}{N_{ch}}\right\rangle$. Hence,

$$\sum_{i=1}^{N}\boldsymbol{n}_i^T\mathbf{c}_{m1}^{-1}\boldsymbol{n}_i\frac{1}{N_{ch_i}} = \sum_{k=1}^{N_T}\sum_{j=1}^{N_T}\left\{\mathbf{c}_{m1}^{-1}\right\}_{kj}\sum_{i=1}^{N}\left(\boldsymbol{n}_i^T\right)_k(\boldsymbol{n}_i)_j\frac{1}{N_{ch_i}} = \sum_{k=1}^{N_T}\sum_{j=1}^{N_T}\left\{\mathbf{c}_{m1}^{-1}\right\}_{kj}\{\mathbf{c}_{noise}\}_{kj}N\left\langle\frac{1}{N_{ch}}\right\rangle \quad (11)$$

Finally, from Equation (11) we obtain

$$\sum_{i=1}^{N}\boldsymbol{n}_i^T\mathbf{c}_{m1}^{-1}\boldsymbol{n}_i\frac{1}{N_{ch_i}} = \sum\sum\left(\mathbf{c}_{m1}^{-1}\circ\mathbf{c}_{noise}\right)N\left\langle\frac{1}{N_{ch}}\right\rangle \quad (12)$$

where $\circ$ denote Hadamard multiplication.

Keeping in mind that $\sum\sum\mathbf{c_{m1}^{-1}}\circ\mathbf{c_{noise}} = \mathrm{tr}\left(\mathbf{c_{m1}^{-1}c_{noise}}\right)$, we rewrite Equation (10) for $\log L_\theta(\mathbf{c}-\mathbf{n})$ as

$$-\log L_\theta(\mathbf{c}-\mathbf{n}) = -\log L_\theta(\mathbf{c}) - \frac{1}{2}\mathrm{tr}\left(\mathbf{c}_{m1}^{-1}\mathbf{c}_{noise}\right)N\left\langle\frac{1}{N_{ch}}\right\rangle, \quad (13)$$

where

$$\log L_\theta(\mathbf{c}) = -\frac{1}{2}\sum_{i=1}^{N}\left\{\left(\boldsymbol{c}_i - \boldsymbol{\mu}N_{ch_i}\right)^T\frac{\mathbf{c_{m1}^{-1}}}{N_{ch_i}}\left(\boldsymbol{c}_i - \boldsymbol{\mu}N_{ch_i}\right) + N_T\log N_{ch_i}\right\} - \frac{N}{2}\log|\mathbf{c}_{m1}| \quad (14)$$

is the log-likelihood function of macroscopic synaptic currents with noise.

To quickly evaluate $\mathrm{tr}\left(\mathbf{c}_{m1}^{-1}\mathbf{c}_{noise}\right)$ we note that matrices $\mathbf{c}_{m1}^{-1}$ and $\mathbf{c_{noise}}$ are quasiseparable (as an inverse of semiseparable matrix, Vandebril et al., 2007) and semiseparable matrice, respectively. Semiseparability of noise covariance matrix, $\mathbf{c_{noise}}$, follows from the fact that experimental background noise can be well approximated by a stationary Gaussian process, and the covariance matrix of such process is semiseparable (DeWilde and van der Veen, 1998). Then, the computation of trace of the product of such matrices can be accelerated by representing it as $\mathrm{tr}(\mathbf{F}\cdot\mathbf{C}) = 2\mathrm{tr}(\mathbf{H}\cdot\mathbf{B}) + \sum_{k=1}^{N_T}\mathbf{F_{kk}d_k}$, where $\mathbf{H}$ is $(N_T-1)\times N_S$ matrix, $\mathbf{F}$ is symmetric $N_T \times N_T$ semiseparable or quasiseparable matrix and $\mathbf{B}$ is defined by Equation (7) (see also Equations A1.26–A1.35 from Text S1 in Appendix in Stepanyuk et al., 2011).

ESTIMATION OF THE NUMBER OF CHANNELS AND PEAK OPEN PROBABILITY

To estimate the number of channels N_{ch_i} (see Results for further definition), we re-write Equation (8) for a single macroscopic synaptic current:

$$-\log L_\theta(\boldsymbol{c}_i - \boldsymbol{n}_i) = \frac{1}{2}\left(\frac{\boldsymbol{c}_i^T\mathbf{c}_{m1}^{-1}\boldsymbol{c}_i}{N_{chi}} + \boldsymbol{\mu}^T\mathbf{c}_{m1}^{-1}\boldsymbol{\mu}N_{chi} - 2\frac{(\boldsymbol{c}_i - \boldsymbol{n}_i - \boldsymbol{\mu}N_{chi})^T\mathbf{c}_{m1}^{-1}\boldsymbol{n}_i}{N_{chi}} - \frac{\boldsymbol{n}_i^T\mathbf{c}_{m1}^{-1}\boldsymbol{n}_i}{N_{chi}} - 2\boldsymbol{\mu}^T\mathbf{c}_{m1}^{-1}\boldsymbol{c}_i\right) + \frac{N_T}{2}\log N_{chi} + \frac{1}{2}\log|\mathbf{c}_{m1}| \quad (15)$$

In the last expression we neglect the 3-d term, as it was done in Equation (9), and the 5-th and the last terms does not depend

on N_{ch_i} at all. Leaving terms that depend on N_{chi} only we obtain log-likelihood as a function of the number of channels:

$$-\log L_\theta(\boldsymbol{c}_i-\boldsymbol{n}_i)=\frac{1}{2}\left(\frac{\boldsymbol{c}_i^{\mathrm{T}}\mathbf{c}_{m1}^{-1}\boldsymbol{c}_i-\boldsymbol{n}_i^{\mathrm{T}}\mathbf{c}_{m1}^{-1}\boldsymbol{n}_i}{N_{chi}}+\boldsymbol{\mu}^{\mathrm{T}}\mathbf{c}_{m1}^{-1}\boldsymbol{\mu}N_{chi}\right)+\frac{N_T}{2}\log N_{chi} \quad (16)$$

The number of channels, N_{chi}, can be approximated for each macroscopic synaptic current $\boldsymbol{c}_i$ as a number that gives maximum of the likelihood function when being substituted into Equation (16). Therefore, after differentiation of Equation (16) with respect to N_{ch}

$$\frac{\partial \log L_\theta(\boldsymbol{c}_i-\boldsymbol{n}_i)}{\partial N_{chi}}=0=\frac{1}{2N_{chi}^2}(\boldsymbol{c}_i-\boldsymbol{n}_i)^{\mathrm{T}}\mathbf{c}_{m1}^{-1}(\boldsymbol{c}_i-\boldsymbol{n}_i)-\frac{N_T}{2N_{chi}}-\frac{1}{2}\boldsymbol{\mu}^{\mathrm{T}}\mathbf{c}_{m1}^{-1}\boldsymbol{\mu}\Rightarrow N_{chi}^2\boldsymbol{\mu}^{\mathrm{T}}\mathbf{c}_{m1}^{-1}\boldsymbol{\mu}+N_{chi}N_T-(\boldsymbol{c}_i-\boldsymbol{n}_i)^{\mathrm{T}}\mathbf{c}_{m1}^{-1}(\boldsymbol{c}_i-\boldsymbol{n}_i)=0 \quad (17)$$

we find an approximation for the number of channels, N_{chi}, for each macroscopic synaptic current

$$N_{ch_i}=\frac{-N_T+\sqrt{N_T^2+4\boldsymbol{c}_i^{\mathrm{T}}\mathbf{c}_{m1}^{-1}\boldsymbol{c}_i\cdot\boldsymbol{\mu}^{\mathrm{T}}\mathbf{c}_{m1}^{-1}\boldsymbol{\mu}}}{2\boldsymbol{\mu}^{\mathrm{T}}\mathbf{c}_{m1}^{-1}\boldsymbol{\mu}} \quad (18)$$

Here $\boldsymbol{c}_i$ is not the whole decaying phase of each current but only those part where signal-to-noise ratio is high and therefore noise term can be neglected (usually from peak of the current to 0.1–0.5 of the peak). Therefore, before calculating the log-likelihood, we first estimate N_{chi} for each macroscopic synaptic current, $\boldsymbol{c}_i$, then substitute N_{chi} into Equations (13) and (14) and calculate the log-likelihood of the set of parameters θ given the set of simulated macroscopic synaptic currents. Accordingly, N_{ch} is estimated automatically when the maximization is finished.

The peak open probability, $P(o,\ peak)$, was defined as a probability that a channel is opened at the peak of the macroscopic current given that this channel was bound with a neurotransmitter immediately after the end of concentration transient, which was assumed to be sufficiently short (0.1–0.2 ms) with respect to the time interval (1–4 ms) from the moment of stimulation to the starting point of the analyzed fragment of current. $P(o,\ peak)$ can be expressed as a function of rate constants: $P(o,\ peak)=\max\left(e^{\mathbf{Q}t}\boldsymbol{p}(0)\right)$, where $\boldsymbol{p}(0)$ is an initial state probability vector assumed to be zero for all states except for the RG2 state in the case when currents were simulated with 7-state $GABA_AR$ scheme or RL state in the case when currents were simulated with simple 3-state kinetic scheme (see descriptions of both schemes below).

Summing up, ML NSFA can be used for the fast estimation of rate constants, unitary current of synaptic ion channel, the number of synaptic channels bound with a neurotransmitter right after the concentration transient for each synaptic current and peak open probability from the set of macroscopic synaptic currents under Gaussian colored background noise.

THE LOG-LIKELIHOOD MAXIMIZATION PROCEDURE

We search for the log-likelihood global maximum to obtain the required model parameters from a set of macroscopic synaptic currents. In order to do this, we minimize the negative log-likelihood with a variant of graduated optimization technique using SQP algorithm embedded in *fmincon* function in MATLAB Optimization toolbox. Initial estimates of each parameter were chosen randomly and uniformly from the logarithmic scale interval, $[\theta_0/10, \theta_0\cdot 10]$, where θ_0 is a vector composed of the true values of each parameter (rate constants and unitary current), i.e., of values utilized by the macroscopic current generator (see below). During the search of a minimum, all parameters were bounded within the interval $[\theta_0/50, \theta_0\cdot 50]$.

In our version of graduated optimization technique, the whole minimization procedure was divided into sequential minimization steps. On the first step the negative log-likelihood was minimized given the first 2 or 3 currents regularly sampled at 50 points each. On each consequent minimization step the number of points and the number of currents was increased. The parameter estimates, θ_{ML}, obtained on each previous step were taken as initial parameters θ_0 for each next minimization step. For all calculations in this work each minimization was rerun 5 (3-state scheme) or 10 (7-state scheme) times, each time starting from the different initial parameter set.

SIMULATION OF MACROSCOPIC SYNAPTIC CURRENTS

First series of simulations of macroscopic synaptic currents were based on experimentally derived 7-state kinetic scheme for $GABA_A$ receptor that had one unliganded state, R, two liganded closed states (RG, singly-liganded and RG2, doubly-liganded) and the respective open (O1 and O2) and desensitized (D1 and D2) states (Mozrzymas et al., 2003). The following rate constants were adapted from Mozrzymas et al. (2003): $k_{off}=0.13\,ms^{-1}$, $d_1=0.14\,ms^{-1}$, $d_2=1.5\,ms^{-1}$, $r_1=0.02\,ms^{-1}$, $r_2=0.12\,ms^{-1}$, $a_1=1.5\,ms^{-1}$, $a_2=1\,ms^{-1}$, $b_1=0.15\,ms^{-1}$, $b_2=8\,ms^{-1}$; $k_{on1}=4\,ms^{-1}\ mM^{-1}$, $k_{on2}=8\,ms^{-1}\ mM^{-1}$; Unitary current was the same for singly- and doubly-liganded states and was set to 1 pA. Variability in the amplitude of macroscopic postsynaptic responses was achieved by trail-to-trial Gaussian variation of the number of available synaptic channels (mean = 250; $SD=50$). Simulation time step was $\Delta t=0.2$ ms. Synaptic vesicle release was modeled as a square pulse of saturating agonist concentration with a duration equal to the single simulation time-step ($\Delta t=0.2$ ms), which caused transition of all available channels from R to RG2 state. A total of 1000 macroscopic synaptic currents were simulated and colored noise that resembled baseline noise of experimentally recorded IPSCs was added to each current. Colored noise ($SD=3$ pA) was modeled as a sum of 4 AR(1) processes (Qin et al., 2000; Venkataramanan and Sigworth, 2002):

$$noise_t=\sum_{k=1}^{N_{noise}}noise_{t,k},\ noise_{t,k}=\varphi_k noise_{(\tau-1),k}+\sigma_k w_{t,k},\ w_{t,k}\sim N(0,1) \quad (19)$$

with parameters $\varphi = [0.0067, 0.61, 0.96, 0.999]$ and $\boldsymbol{\sigma} = [0.32, 1.0, 1.42, 0.72]$, pA that were obtained from the approximation of autocorrelation function of experimentally recorded (whole-cell patch clamp) background noise by the sum of 4 exponentials (see Equations 23, 24 in Stepanyuk et al., 2011). The decaying phases of the responses (starting in 1 ms after the end of stimulation pulse) were taken for the consequent log-likelihood maximization.

In a second series of simulations we have used simple 3-state kinetic scheme of an abstract synaptic receptor. The scheme consisted of unliganded state, R, singly-liganded state, RL, and open state, O and had the following rate constants: binding rate, $k_{on} = 6\,\mathrm{mM}^{-1}\mathrm{ms}^{-1}$, unbinding rate, $k_{off} = 0.025\,\mathrm{ms}^{-1}$, opening rate, $b = 0.25\,\mathrm{ms}^{-1}$. The closing rate constant, a, was $2.5\,\mathrm{ms}^{-1}$ for Model R and Model N and $1.25\,\mathrm{ms}^{-1}$ for Model A (see Section ML NSFA Distinguishes Between Changes in the Channel Gating and Changes in the Number of Receptors Bound with a Neurotransmitter in Results). Unitary current was set to 1 pA. Variability in the amplitude of macroscopic postsynaptic responses was achieved by trail-to-trial Gaussian variation of the number of available synaptic channels (mean = 400; $SD = 50$ for Models R and A; mean = 800; $SD = 71$ for Model N). Simulation time step was $\Delta t = 0.1$ ms. Synaptic vesicle release was modeled as a square pulse of saturating agonist concentration with a duration equal to two simulation time-steps (0.2 ms), which caused transition of all channels from R to RL state.

ACCURACY OF THE ESTIMATES

Accuracy of kinetic rates, unitary current, number of liganded channels, and peak open probability estimates was estimated using bootstrap. To this end, $N = 5$, 10, 20, 30, 40, or 100 currents were randomly sampled with replacement from the initially generated set of 1000 macroscopic current traces. This procedure was repeated until that 30–40 bootstrap samples were generated. For each bootstrap sample we rerun likelihood maximization $m = 5$ or 10 times (for currents generated with 3- or 7-state scheme, respectively), starting m-1 times from different randomly generated initial parameter sets (see Section The Log-Likelihood Maximization Procedure above) and mth start was done from θ_0. The estimated model parameters, $\boldsymbol{\theta_{ML}}$, were obtained from a maximization trial that resulted in the best log-likelihood, which was considered to be a global maximum. The accuracy of estimated model parameters was assessed as a deviation of these parameters (θ_{ML}) from those (θ_0) used for the generation of the currents, $\frac{\sqrt{(\theta_{ML}-\theta_0)^2}}{\theta_0}$ (hereinafter relative error). The algorithm was implemented in MATLAB.

PEAK-SCALED NON-STATIONARY FLUCTUATION ANALYSIS

Accuracy of single-channel current estimates obtained with ML NSFA method presented here was compared to those obtained by PS NSFA. In PS NSFA, variance in currents arising from the stochastic gating of the ion channel is isolated from variance arising from sources such as quantal variability by scaling the mean simulated current waveform to the peak amplitude of each individual simulated current and then subtracting the two waveforms (Traynelis et al., 1993).

$$I_i^{peak-scaled} = I_i - \langle I \rangle \frac{\max(I_i)}{\max\langle I \rangle} \tag{20}$$

To estimate the accuracy of unitary current estimates with PS NSFA, it was applied to $n = 1000$ bootstrap samples each of which contained either $N = 5$, 10, 20, 30, 40, or 100 currents simulated with a 7-state $GABA_A$ receptor scheme (see Section Simulation of Macroscopic Synaptic Currents above). For each bootstrap sample the ensemble variance, σ^2, was plotted against the ensemble mean, $\langle I \rangle$, and then fitted with parabola:

$$\sigma^2\left(I^{peak-scaled}\right) = i_{ch}\langle I \rangle - \frac{\langle I \rangle^2}{\langle N_{ch} \rangle} + \sigma_0^2 \tag{21}$$

where σ_0^2 is the variance of the background noise. Accuracy of unitary current estimates was calculated as described above, and was then compared with the accuracy of estimates obtained with ML NSFA. To ensure the best accuracy possible with PS NSFA, the ensemble mean current $\langle I \rangle$ and variance, σ^2, were calculated for each data point and the rising phase of variance *vs.* mean curve was fitted with parabola using weighted (with weights $\omega_i = 1/\mathrm{var}\left(\sigma_i^2\right)$) least squares method.

ESTIMATION OF UNITARY CURRENT FROM A SINGLE MACROSCOPIC CURRENT

Sampling from a likelihood distribution of model parameters that were estimated from a single macroscopic synaptic current was done by the slice sampling Markov chain Monte Carlo algorithm (Neal, 2003), implemented in "MCMC Methods for MLP and GP and Stuff" toolbox by Toni Auranen and Aki Vehtari (available at http://www.lce.hut.fi/research/compinf/mcmcstuff/).

RESULTS

ML NSFA APPLICABILITY TO ESTIMATION OF UNITARY CURRENT AND KINETIC CONSTANTS OF POSTSYNAPTIC RECEPTOR CHANNELS

Postsynaptic architecture restricts direct electrophysiological access to individual receptors in native synaptic environments, with only occasional exceptions when channel openings and closings can be resolved on the very tail of postsynaptic currents (Silver et al., 1992). Both these exceptions and application of PS NSFA (Traynelis et al., 1993) do not allow estimating any parameters of synaptic receptors except their unitary conductance and the number of receptors open at the peak of synaptic current (Hartveit and Veruki, 2006).

In this part of the work we tested how ML NSFA estimates the unitary current and kinetic constants of $GABA_A$ receptors from stochastically simulated macroscopic currents having a trial-to-trial Gaussian variation in the number of available receptors ($N_{ch} = 250 \pm 50$). Currents were simulated with a 7-state model of this receptor (Mozrzymas et al., 2003, see Methods) having one unbound, two liganded closed, two open and two desensitized states (**Figure 1A**). Synaptic release of GABA was modeled as a brief (0.2 ms) step of saturating GABA concentration resembling GABA release in real synaptic connections (Perrais and Ropert, 1999, 2000; Hájos et al., 2000; Nusser et al., 2001; Biró et al.,

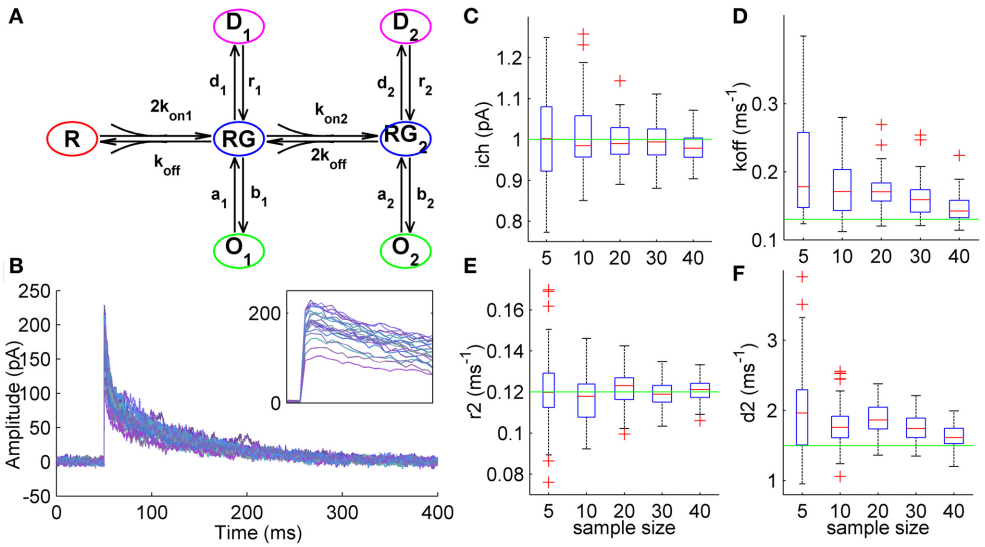

FIGURE 1 | Estimation of unitary current and kinetic constants from simulated GABAergic synaptic currents. (A) 7-state kinetic scheme of $GABA_A$ receptor that was used to simulate macroscopic synaptic currents (Mozrzymas et al., 2003, see Section Simulation of Macroscopic Synaptic Currents in Methods). The scheme has one unbound state, R, two liganded states (single-liganded, RG, and double-liganded, RG2,) and related open (O1 and O2) and desensitized (D1 and D2) states. Rate constants were adapted from Mozrzymas et al. (2003) and were as follows: $k_{off} = 0.13\,ms^{-1}$, $d_1 = 0.14\,ms^{-1}$, $d_2 = 1.5\,ms^{-1}$, $r_1 = 0.02\,ms^{-1}$, $r_2 = 0.12\,ms^{-1}$, $a_1 = 1.5\,ms^{-1}$, $a_2 = 1\,ms^{-1}$, $b_1 = 0.15\,ms^{-1}$, $b_2 = 8\,ms^{-1}$; $k_{on1} = 4\,mM^{-1}\,ms^{-1}$, $k_{on2} = 8\,mM^{-1}\,ms^{-1}$. Unitary currents for the states O1 and O2 were equal and were set to $i_1 = i_2 = 1$ pA. The number of channels exposed to GABA varied from trial to trail ($N_{ch} = 250$, $SD = 50$; Gaussian variation). Colored noise ($SD = 3$ pA) was added to the simulated currents (see Section Simulation of Macroscopic Synaptic Currents in Methods). **(B)** Synaptic currents simulated using the kinetic scheme shown in **(A)**. The currents demostrate high trial-to-trial variability resembling one observed in experimental electrophysiological recordings (inset). **(C)** Statistical plots demonstrating accuracy of unitary current estimates obtained by ML NSFA. On each plot, the central mark (red) is the median, the edges of the box are the 25th and 75th percentiles, the whiskers extend to the most extreme data points not considered outliers, and outliers are plotted individually by red crosses. Green line indicates true value of unitary current (1 pA). Note high accuracy of unitary current estimates obtained by ML NSFA even if a few (5–20) currents were used. **(D–F)** Statistical plots of estimates of some kinetic constants obtained by ML NSFA. Colors are the same as in **(C)**.

2006; Scimemi and Beato, 2009). 1000 macroscopic currents generated in response to this stimulation had the mean amplitude of 184 ± 35 pA and decay kinetics of 43.4 ± 3.6 ms (**Figure 1B**) and resembled postsynaptic currents routinely recorded in cortical GABAergic synapses (Nadkarni et al., 2010). Background colored noise ($SD = 3$ pA, see Section Simulation of Macroscopic Synaptic Currents in Methods) was added to the simulated currents.

Samples consisting of $N = 5$, 10, 20, 30, or 40 macroscopic currents were randomly chosen from initially generated set of 1000 currents and analyzed using ML NSFA. In order to assess the accuracy of estimates for the unitary current and kinetic rates, parameter search was performed for 60 samples obtained in such a way and log-likelihood maximization was run 10 times for each sample in order to achieve the global maximum (see Section Accuracy of the Estimates in Methods). For each run, the initial parameter values were chosen randomly and uniformly in the logarithmic scale from the range $[\theta_0/10, \theta_0 \cdot 10]$, where θ_0 denotes true parameter values, i.e., those used for simulation of currents.

The unitary current was estimated with good accuracy even from samples consisting of only 10 simulated postsynaptic currents (**Figure 1C**, 8.1% relative error) whereas it was estimated with almost 2-fold better accuracy when the number of currents in the sample was increased from 10 to 40 (4.3% relative error). Three rate constants: unbinding rate (k_{off}), desensitization (d_2) and resensitization (r_2) rate from double-liganded state could also be estimated (**Figures 1D–F**). For samples consisting of 10 and 40 currents the relative errors of estimates were: k_{off} —49.0% and 19.1%; d_2—28.3 and 14.6%; r_2—8.9 and 4.7%, respectively. Some of rate constants associated with single-liganded states were estimated in order of magnitude (a_1) or bounded from below (b_1, d_1).

Thus, we demonstrate that ML NSFA could reliably estimate the unitary current of synaptic receptor channel and several kinetic constants of synaptic receptor model from the very limited number of postsynaptic currents (5–40). These results indicate that ML NSFA may allow analysis of kinetic models of synaptic receptors in their native biochemical environment using routinely recorded macroscopic postsynaptic currents.

ML NSFA ACCURACY IN ESTIMATION OF UNITARY CURRENT COMPARED TO PS NSFA

The number of currents necessary for a particular algorithm to secure a given accuracy of unitary current estimate is an important practical issue. With many hundreds or even thousands of simulated macroscopic currents accuracy of PS NSFA in estimating the unitary current is fairly good (Markova et al., 2005; Hartveit and Veruki, 2006). At the same time it is hard to collect more than about 100 of evoked postsynaptic currents in steady-state conditions in routine electrophysiological experiments.

Thus, to see whether ML NSFA gives any advantage with respect to the number of required traces we calculated a relative error of unitary current estimates obtained with ML NSFA from the above described samples of different sizes (5, 10, 20, 30, 40, and 100 currents; 60 samples were analyzed in each case to estimate the error) and compared this error with one estimated with PS NSFA applied to 1000 samples of similar sizes.

Figure 2A demonstrates that the error of unitary current estimates obtained with both methods decreases with the number of currents taken for the analysis. However, the unitary current can be estimated with as low as 10.8, 8.1, and 4.9% relative error from only 5, 10, and 20 simulated synaptic currents, respectively, whereas PS NSFA resulted in about 2-fold lower accuracy (23.0, 14.7, and 10.4 relative error, respectively). The estimates obtained with ML NSFA from the analysis of samples of 30 and 40 currents had relative error of 4.6 and 4.3%, whereas PS NSFA gave 8.6 and 7.2% error for these cases. At last, accuracies of unitary current estimates obtained from 100 simulated currents were high for both methods and were comparable (Errors: 2.9% for ML NSFA vs. 4.5% for PS-NSFA; **Figure 2A**).

Thus, for some complex models ML NSFA allows evaluation of the unitary current with good accuracy using experimentally realistic number of macroscopic currents and substantially outperforms PS NSFA in terms of accuracy when only a few (5–30) postsynaptic currents are available for estimating the unitary current.

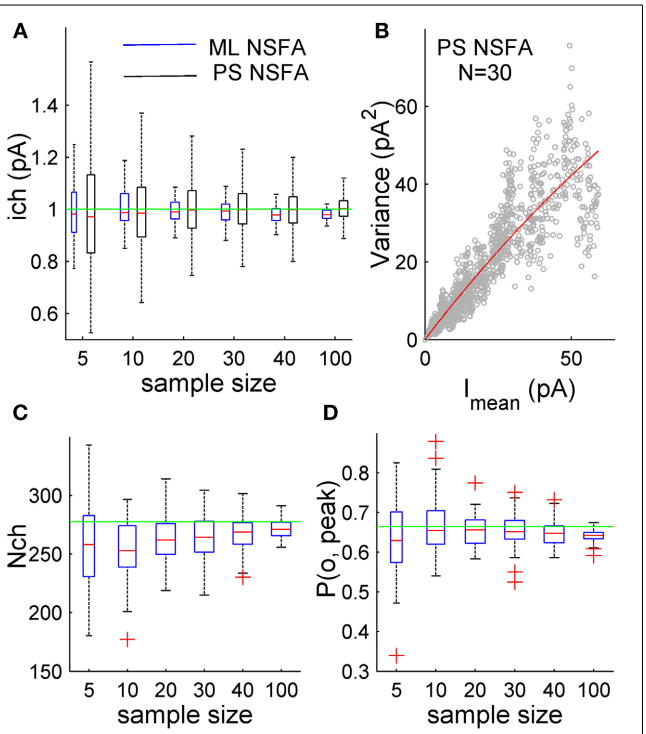

FIGURE 2 | ML NSFA is more accurate than PS NSFA in estimating of unitary current. Estimation of the number of receptors bound with a neurotransmitter and peak open probability with ML NSFA. **(A)** Statistical plots demonstrating accuracy of unitary current estimates obtained with ML NSFA (blue boxes) and PS NSFA (black boxes) from simulated macroscopic synaptic currents with trial-to-trial Gaussian variation in the number of receptors ($N_{ch} = 250$, $SD = 50$; see kinetic scheme in **Figure 1A**). On each plot, the central mark (red) is the median, the edges of the box are the 25th and 75th percentiles, the whiskers extend to the most extreme data points not considered outliers, and outliers are plotted individually by red crosses. Green line indicates a true value of unitary current. ML NSFA and PS NSFA were performed using $n = 60$ and $n = 1000$ samples consisting of $N = 5$, 10, 20, 30, 40 or 100 simulated currents, respectively. Note that the accuracy of estimates obtained with ML NSFA using a few (5–20) currents was 2-times better than one obtained with PS NSFA. **(B)** An example of variance *vs.* mean plot (gray dots) obtained with PS NSFA for $N = 30$ simulated macroscopic currents having trial-to-trial Gaussian variation in the number of receptors ($N_{ch} = 250$, $SD = 50$) and a parabolic fit of its rising phase (red). Note that variance-mean relationship (gray dots) is skewed rather than parabolic and therefore the number of receptors could not be estimated with PS NSFA. **(C,D)** Statistical plots for the estimates of the number of channels bound with a neurotransmitter right after the concentration transient, N_{ch}, and peak open probability, P(o, peak) obtained with ML NSFA. Green line in **C** indicated the true value of the number of channels estimated as mean peak current amplitude (averaged over $N = 1000$ currents) divided by the true value of P(o, Peak) and by the true value of unitary current (1 pA) and in **D** green line indicates the true value of P(o, Peak) estimated as $P(o) = e^{Qt}p_0$. Other colors and notations are the same as in **Figure 1C**.

ML NSFA ESTIMATES THE NUMBER OF SYNAPTIC RECEPTORS BOUND WITH NEUROTRANSMITTER AND PEAK OPEN PROBABILITY

PS NSFA was specifically designed to be independent of variations in the number of postsynaptic receptors exposed to neurotransmitter and peak open probability for the sake of more accurate estimation of a unitary current (Silver et al., 1996) from postsynaptic current fluctuations. Unfortunately, this method could not be used for the estimation of the total number of receptors in the synapse. To the contrary, ML NSFA presented here allows estimation of the number of receptors bound with neurotransmitter by the end of neurotransmitter concentration transient in each macroscopic current (liganded channels, N_{ch}). It is assumed that this transient time course is known or sufficiently brief, meaning that it could be approximated by delta function in the latter case. Indeed, GABA concentration in the synaptic cleft decreases by a factor of 10 during less than 0.1 ms after synaptic vesicle release (Scimemi and Beato, 2009) resulting in almost instantaneous concentration transient. For such a brief concentration transient and for a given GABA receptor model (**Figure 1A**) ML NSFA would estimate the number of receptors bound with two GABA molecules by the end of concentration transient in all synapses of particular synaptic connection independently upon receptor saturation in the case when most of the current is mediated by the receptors in double-liganded states.

The open probability P(o) at any given time is determined as a mean current divided by a product $i_{ch}N_{ch}$, and it is a function of rate constants: $P(o) = e^{\mathbf{Q}t}\boldsymbol{p}(0)$ (see Section Estimation of the Number of Channels and Peak Open Probability in Methods). Thus, P(o) as a function of time is automatically estimated at the end of log-likelihood maximization procedure. The peak open probability is simply a maximum of this function, $P(o,\ peak) = \max\left(e^{\mathbf{Q}t}\boldsymbol{p}(0)\right)$. Peak open probability estimated by ML NSFA is, thus far, a ratio of the number of receptors open at the peak of postsynaptic current to the number of double-liganded receptors by the end of neurotransmitter concentration transient.

Figures 2C,D demonstrate that the error of N_{ch} and $P(o,\ peak)$ estimates obtained with ML NSFA decreases with the number of currents taken for the analysis. The number of liganded receptor channels, N_{ch}, was calculated as an average over all currents in the sample and was estimated with 24.5 and 12.4% relative error from samples consisting of only 5 and 10 simulated macroscopic synaptic currents, respectively. The respective estimates of accuracy for the peak open probability, $P(o,\ peak)$, had 14.4 and 9.8% relative error, respectively. Both N_{ch} and $P(o,\ peak)$ were estimated with even better accuracy from samples consisting of 100 simulated currents (10.0 and 4.3% relative error, respectively).

At the same time PS NSFA applied to the same samples resulted in a variance vs. mean curve that was profoundly skewed (**Figure 2B**, gray dots) and, therefore, could not give an estimate of the number of liganded channels, N_{ch}.

ESTIMATION OF UNITARY CURRENT AND KINETIC CONSTANTS OF RECEPTORS HAVING MULTIPLE CONDUCTANCE LEVELS

Most ligand-gated channels are described by kinetic schemes with multiple, non-identical open states often having different conductance levels (Jin et al., 2003; Mozrzymas et al., 2003; Robert and Howe, 2003; Wyllie et al., 2006; Keramidas and Harrison, 2010; Mortensen et al., 2010). In practice some open states should be considered rare and excluded from the fitting of experimental results in order to estimate at least some parameters of receptor kinetic schemes (Mortensen et al., 2010). Unfortunately, PS NSFA is also not applicable to examination of receptors having multiple conductance levels giving values of unitary current and channel number having no obvious physical interpretation (Hartveit and Veruki, 2006). Thus, at the present moment single-channel recordings are virtually the only approach that allows identifying multiple conductance levels of ligand-gated receptors and this approach is also not applicable for studying of synaptic receptors.

We next wanted to investigate if ML NSFA suggested in this work is applicable to analysis of ion channels and ligand-gated receptors with multiple conductance levels, described by kinetic schemes with non-identical open states. 7-state kinetic model of $GABA_A$ receptor (Mozrzymas et al., 2003) having two open states O1 and O2 with identical unitary current ($i_1 = i_2$, see **Figure 1A**) was modified to have the unitary current $i_1 = 2$ pA and $i_2 = 1$ pA for the states O1 and O2, respectively (**Figure 3**). Rate constants of the model were modified in such a way that the contribution of single- and double-liganded open states to the total macroscopic current became comparable. Modified constants were (in ms^{-1}): $b_2 = 4,\ b_1 = 1.2,\ d_1 = 1,\ r_1 = 1,\ d_2 = 0.15,\ r_2 = 1$. Colored

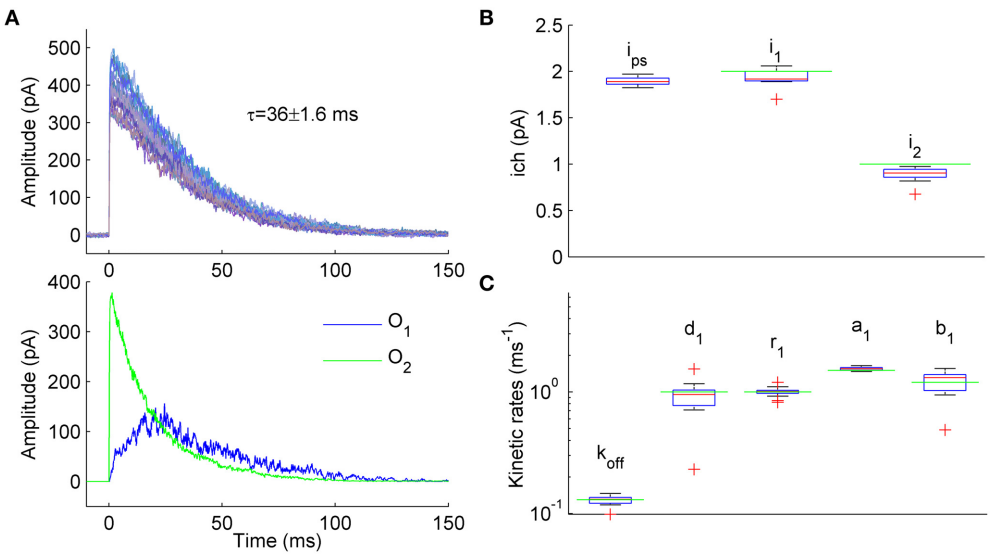

FIGURE 3 | Estimation of unitary currents and kinetic constants of receptors having two open states with different conductance levels. (A) *Upper panel.* Example of 50 synaptic currents simulated with a 7-state kinetic scheme of $GABA_A$ receptor having two open states (**Figure 1A**, some rate constants were modified: $b_2 = 4$, $b_1 = 1.2$, $d_1 = 1$, $r_1 = 1$, $d_2 = 0.15$, $r_2 = 1\ ms^{-1}$). Unitary currents were set to $i_1 = 2$ pA and $i_2 = 1$ pA for open states O1 and O2, respectively. The number of channels varied from trial to trail ($N_{ch} = 500 \pm 50$; Gaussian variation). *Lower panel.* Representative example of single simulated macroscopic current components mediated by single-liganded open state O1 (blue trace) and double-liganded open state O2 (green trace) demonstrating comparable contribution of O1 and O2 to the total macroscopic current. **(B)** Statistical plots for the estimates of unitary currents obtained with PS NSFA (leftmost bar, $i = 1.86 \pm 0.03$ pA) and ML NSFA (two bars on the right, $i_1 = 2.0 \pm 0.11$ pA and $i_2 = 0.89 \pm 0.08$ pA, i_1 and i_2 are unitary currents associated with open states O1 and O2, respectively. Both PS NSFA and ML NSFA were applied to samples of 50 macroscopic currents ($n = 15$ and $n = 250$ bootstrap samples for MS NSFA and PS NSFA, respectively) simulated as described in **(A)** and having true values of $i_{1(0)} = 2$ pA and $i_{2(0)} = 1$ pA, respectively (indicated by green lines). On each plot, the central mark (red) is the median, the edges of the box are the 25th and 75th percentiles, the whiskers extend to the most extreme data points not considered outliers, and outliers are plotted individually by red crosses. Note that ML NSFA accurately distinguishes both unitary current levels, whereas PS NSFA gave some value of the unitary current that was close to $i_{1(0)}$. **(C)** Statistical plot for the estimates of kinetic rates of transitions from and to a single-liganded state obtained by ML NSFA (in ms^{-1}: unbinding rate, $k_{off} = 0.13 \pm 0.01$, desensitization rate, $d_1 = 0.89 \pm 0.34$, resensitization rate $r_1 = 1.02 \pm 0.08$, closing rate, $a_1 = 1.55 \pm 0.05$, opening rate, $b_1 = 1.17 \pm 0.24$; $N = 50$ currents simulated as described in **(A)**. The estimates were in good agreement with their true values (green lines). See a legend to panel **(B)** for further description.

background noise with $SD = 3$ pA was added to the simulated currents (**Figure 3A**, upper panel).

Representative examples of the simulated current components associated with either state O1 or state O2 are shown in **Figure 3A**, lower panel, by blue and green lines, respectively. When 250 samples consisting of $N = 50$ simulated currents (**Figure 3A**, upper panel) were analyzed by PS NSFA the unitary current estimates were close to the unitary current of single-liganded open state O1 (1.86 ± 0.03 pA *vs* $i_1 = 2$ pA for the state O1). At the same time, ML NSFA gave reasonable estimates for both conductance levels (Mean $\pm$ *SE* $i_1 = 2.00 \pm 0.11$ pA and $i_2 = 0.89 \pm 0.08$ pA; $n = 15$ samples of $N = 50$ simulated currents; **Figure 3B**). ML NSFA also reliably estimated kinetic rates for single-liganded state transitions ($k_{off} = 0.13 \pm 0.01$, $d_1 = 0.89 \pm 0.34$, $r_1 = 1.02 \pm 0.08$, $a_1 = 1.55 \pm 0.05$, $b_1 = 1.17 \pm 0.24\,ms^{-1}$, **Figure 3C**) and the mean number of liganded channels ($N_{ch} = 557 \pm 53$ vs. 500 ± 50 used in simulation).

Thus, contrary to PS NSFA, ML NSFA can reliably estimate kinetic schemes with several open states having different conductance levels and gives precise values of unitary currents, some kinetic rates, and the mean number of liganded receptors in a given synaptic connection.

ML NSFA DISTINGUISHES BETWEEN CHANGES IN THE CHANNEL GATING AND CHANGES IN THE NUMBER OF RECEPTORS BOUND WITH A NEUROTRANSMITTER

We next attempted to explore ML NSFA capability to identify which postsynaptic parameters were changed in the case when mean amplitude of simulated currents was increased without changes in macroscopic current waveform and unitary current.

To this end three distinct groups of 1000 macroscopic currents were generated using a simple 3-state scheme of synaptic channel (**Figure 4A**, see Section Simulation of Macroscopic Synaptic Currents in Methods). A similar increase in mean current amplitude was achieved by changes in either receptor gating or receptor number. A reference kinetic scheme (Model R; **Figure 4A**, red) had the closing rate, $a = 2.5\,ms^{-1}$ and the total number of channels $N_{ch} = 400 \pm 50$ and was used to generate a group of macroscopic currents before putative remodeling of synaptic connection (**Figure 4B**). In the second kinetic scheme (Model A; **Figure 4A**, blue) mimicking remodeling of receptor gating the closing rate, a, was changed from $2.5\,ms^{-1}$ to $1.25\,ms^{-1}$ resulting in almost 2-fold increase of average current amplitude (**Figure 4C**, blue) without substantial changes in current waveform (**Figure 4D**, blue vs. red). Conversely, in the third model (Model N; **Figure 4A**, black) the number of available channels, N_{ch}, was increased from 400 ± 50 to 800 ± 71 without any changes in the kinetic constants, which led to similar changes in current amplitude (**Figure 4C**, black) as for Model A without any changes in current waveform (**Figure 4D**, black vs. red). Therefore, currents generated with Models A and N had similar amplitudes and when normalized, appeared to have the same waveforms as reference currents generated by Model R (**Figures 4B–D**).

ML NSFA was run with $n = 20$ bootstrap samples consisting of $N = 100$ currents (see Section Accuracy of the Estimates in Methods) for each of the 3 groups of simulated currents in order to evaluate the receptor model parameters and the respective errors. Log-likelihood maximization was run 5 times for each bootstrap sample in order to achieve the global maximum. When the parameter estimates obtained from currents generated with Model R were compared to those obtained from currents generated with Model A (**Figure 4E**, red vs. blue boxes) the difference, Δ_{RA}, between mean values of each parameter estimates except the closing rate, a, and peak open probability, P(o, peak), was small and was within the standard error (*SE*) range of the respective estimates: k_{off}: $\Delta_{RA} = 1.7\%$ ($SE = 2.2\%$), b: 8.5% (13.0%), i_{ch}: 0.6%(2.4%), N_{ch}: 8.8% (14.0%). At the same time, Δ_{RA} was 49.7% for the closing rate, a and 70.1% for the peak open probability, P(o, peak) and did not fall within the narrow ranges of the respective *SE*'s (2.4% and 14.1%, respectively). The mean values of the respective estimates were $a = 2.51 \pm 0.04$ for Model R and 1.26 ± 0.03 for Model A, P(o, peak) $= 0.08 \pm 0.01$ for Model R and 0.14 ± 0.02 for Model A. Therefore, we could infer that these were the parameters that altered. These results directly indicate that ML NSFA may reliably determine changes in receptor gating, which leads to an increase in peak open probability.

When estimates obtained from currents generated with Model R and Model N were compared, we observed insufficient differences, Δ_{RN}, between mean values of all parameter estimates except the number of receptors, N_{ch}, which was changed from 419 ± 62 for Model R to 942 ± 228 for Model N (**Figure 4E**, compare red vs black boxes). Δ_{RN} for N_{ch} was 124.9% and did not fall within the range of its SE (24.2%). At the same time, Δ_{RN} for other parameters fell within the respective standard error (*SE*) range: k_{off}: $\Delta_{RN} = 0.3\%$ ($SE = 1.7\%$), a: 1.3% (1.7%), b: 7.1% (18.0%), i_{ch}: 0.8%(1.6%), P(o, peak): 8.3% (18.9%) and it was possible to conclude that the number of receptors was the only altered parameter in this case.

Thus, with ML NSFA it becomes possible to distinguish between alteration in receptor channel gating and receptor number, which nonetheless resulted in visually indistinguishable postsynaptic currents.

ESTIMATION OF UNITARY CURRENT FROM MACROSCOPIC CURRENTS GENERATED BY RECEPTORS HAVING DIFFERENT KINETIC SCHEMES

The key assumption of the PS NSFA is that all receptors in a particular synaptic connection under study have identical kinetic properties (Silver et al., 1996). As a result, all variance in the currents could be attributed to the stochastic nature of the channel gating rather than to the variability in their kinetics. In fact, this assumption could be violated since receptors in the synaptic connection could have different subunit composition or could be differentially modulated (Popescu and Auerbach, 2003) and a set of receptors contributing to each postsynaptic current could vary from trial to trial. In this case PS NSFA overestimates the unitary current and this overestimation could be quite significant even if the difference between receptor kinetic rates is so small that it could be hardly noticed from the observation of synaptic currents (see **Figure 5A** and below).

Using likelihood approximation it is possible in principle to estimate unitary current and other parameters independently for each individual synaptic current. To test this possibility we

have conducted a series of computational experiments. A group of 1000 synaptic currents was simulated using 7-state kinetic scheme of $GABA_A$ receptor channel (Mozrzymas et al., 2003, see scheme in **Figure 1A**) and the other 1000 currents were simulated using similar scheme in which several parameters (closing rate, k_{off}, desensitization rate, d_2 and resensitization rate, r_2) varied between trials randomly and uniformly in the range of ±20% of parameter values that were used to generate the first group of currents. In both cases the unitary current was set at 1 pA and colored background noise ($SD = 3$ pA) was added to the simulated currents (see Section Simulation of Macroscopic Synaptic Currents in Methods for details). **Figure 5A** demonstrates that both groups of currents had similar waveforms and their decay times were almost identical although variability of decay times in the second group was slightly higher (Mean ± *SD*: 43.6 ± 3.7 ms vs. 43.9 ± 6.1 ms, $N = 1000$ currents). Nevertheless, variance vs. mean curves for these two groups of currents differed significantly (**Figure 5B**) and for the second group unitary current appeared to be 1.9-fold overestimated by PS NSFA (Mean ± *SE* was 1.01 ± 0.03 pA for the group of currents without variation of parameters vs 1.92 ± 0.05 pA for the group of currents with variation of k_{off}, d_2, and r_2; $N = 250$ currents; true value was 1 pA).

To the contrary, when ML NSFA was applied to the group of currents with varying rate constants and log-likelihood of each

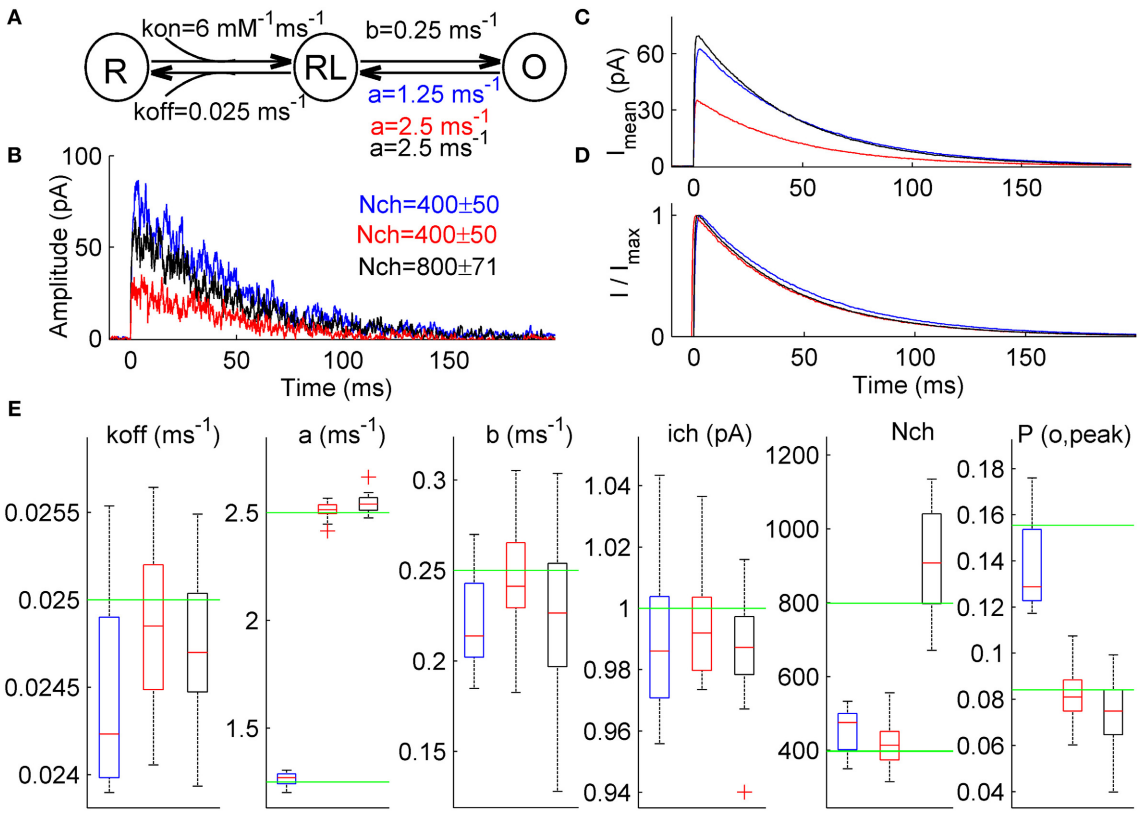

FIGURE 4 | ML NSFA distinguishes between changes in the receptor gating and the number of receptors in case when both unitary current and macroscopic current waveform are not changed. (A) Simple 3-state kinetic scheme of synaptic receptor channel. The scheme consists of one unbound state, R, one single-liganded state, RL, and one open state, O. Rate constants are shown below the respective transitions and were as follows: $k_{on} = 6\,mM^{-1}\ ms^{-1}$, $k_{off} = 0.025\,ms^{-1}$, $b = 0.25\,ms^{-1}$. Three different models were constructed based on this scheme and were used to simulate 3 sets of macroscopic currents. A closing rate constant, *a*, was set to $2.5\,ms^{-1}$ for Model R (red) and Model N (black) and $1.25\,ms^{-1}$ for Model A (blue). **(B)** An example of 3 macroscopic currents simulated using Model R (red), Model A (blue), and Model N (black) shown in **(A)**. The number of channels used for simulations is indicated in a respective color in the top-right corner (400 ± 50 for Models R and A and 800 ± 71 for Model N). **(C)** Mean simulated currents for each Model ($N = 1000$). Note that amplitudes of mean currents obtained with Model A and Model N (blue and black) are almost equal and almost twice larger than the mean current amplitude obtained with a reference Model R (red). **(D)** The same mean currents as in **(C)** but normalized. Note that all 3 waveforms almost coincide. **(E)** Statistical plots for the estimates of kinetic rates, unitary current, number of channels bound with a neurotransmitter, N_{ch}, and peak open probability, P(o, peak), obtained with ML NSFA ($N = 100$ currents; $n = 20$ bootstrap samples). On each plot, the central mark (red) is the median, the edges of the box are the 25th and 75th percentiles, the whiskers extend to the most extreme data points not considered outliers and outliers are plotted individually by red crosses. Green line indicates true value of parameter. Blue, red, and black boxes correspond to results of ML NSFA applied to macroscopic currents generated with Model A, R, and N, respectively. Note that estimates for the closing rate, *a*, and peak open probability, P(o, peak), obtained from currents generated with Model A (blue boxes) are close to their true values and do not coincide within SE's with the respective estimates obtained for reference Model R (red boxes). At the same time, estimate for the number of channels, N_{ch}, obtained from currents generated with Model N is close to its true value and differs from the respective value obtained from currents generated with reference Model R.

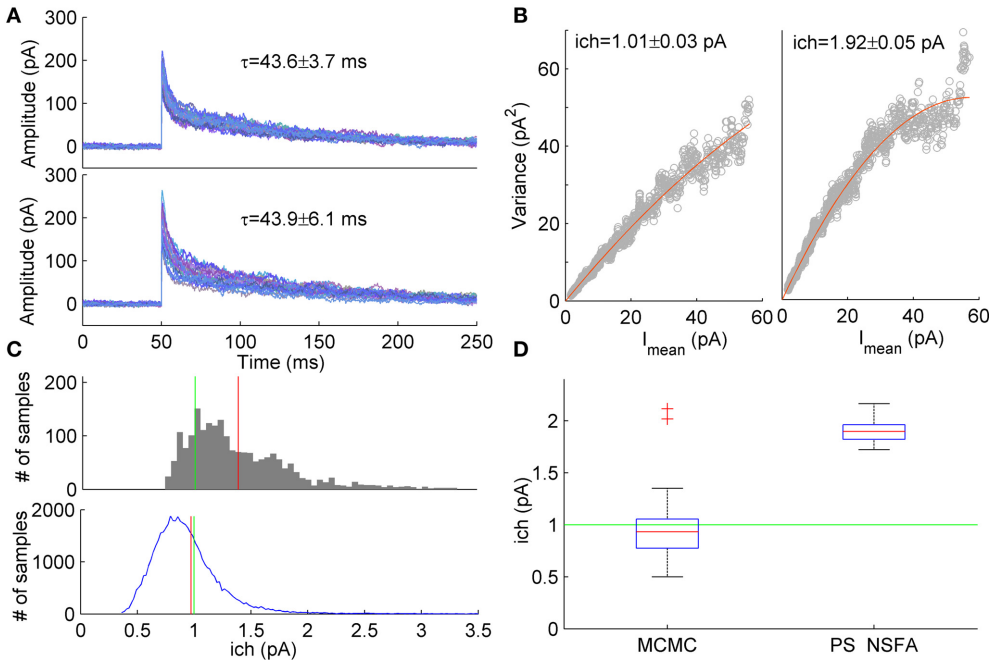

FIGURE 5 | Estimation of unitary current from macroscopic currents generated by receptors having different kinetic parameters. (A) *Upper panel.* An example of 20 currents generated with a 7-state kinetic scheme of $GABA_A$ receptor (see **Figure 1A**). *Lower panel.* Second group of 20 currents generated with similar model in which several parameters (k_{off}, d_2, r_2) were varied randomly from current to current (uniformly in ± 20% neighborhood of their standard values, see Methods and **Figure 1A**). The unitary current in both groups of currents was the same, $i_{ch} = 1$ pA. Mean ± *SD* of decay time calculated over 1000 currents was 43.6 ± 3.7 ms and 43.9 ± 6.1 ms for the first and second group of currents, respectively and is shown above the traces. **(B)** Variance *vs* mean dependencies for 250 peak-scaled currents generated with (right) and without (left) variation of the channel kinetic model parameters (gray dots), and their approximation by the quadratic function (red line). **(C)** *Upper panel.* Sampling distribution of unitary current estimates obtained by MCMC sampling from the likelihood distribution of single synaptic current. *Lower panel.* Sampling distribution aggregated over 50 single current likelihood distributions. Mean of the sampling distributions and true value of unitary current are shown by red and green line, respectively. **(D)** Box plots show the statistics of the mean unitary current estimates obtained with MCMC sampling from the likelihood distributions for the group of 50 currents with varying rate constants (left) in comparison with the statistics of PS NSFA estimates obtained from the group of 250 currents with varying rate constants (right). On each box plot, the central mark is the median, the edges of the box are the 25th and 75th percentiles, the whiskers extend to the most extreme data points not considered outliers, and outliers are plotted individually by red crosses.

current in the group was optimized independently, a reasonably accurate estimate of unitary current was obtained (Mean ± $SD = 0.89 \pm 0.23$ pA, $N = 50$ currents). Standard error of mean unitary current estimate was very low ($SE = 0.033$ pA), but bias from the true value (1 pA) was significant. We have noticed that the cause of this bias is the skewed shape of the likelihood distribution of a single simulated synaptic current, which means that for the case of single current the maximum likelihood value of unitary current is not the most common value. An example of the typical distribution of unitary current obtained by sampling from the likelihood distribution for a single simulated macroscopic current using the slice sampling Markov chain Monte Carlo method (MCMC, 2000 samples) is shown in **Figure 5C** (upper panel). It can be seen that the distribution maximum significantly differs from the distribution mean (red vertical line). Therefore, in order to obtain "typical" values of unitary current, mean values of unitary current were also estimated by slice sampling from the likelihood distributions obtained for individual synaptic currents (1000 MCMC samples for each current) from the same group of 50 currents. The resulting distribution of unitary current estimates obtained by accumulation of all 50 distributions for individual currents is represented in **Figure 5C** (lower panel). The final estimate of unitary current was obtained by averaging over $N = 50$ mean unitary currents and was in perfect agreement with its true value (Mean ± $SD = 0.97 \pm 0.39$ pA, red vertical line in **Figure 5C**, lower panel; $SE = 0.056$ pA). **Figure 5D** shows statistics of the mean unitary current estimates obtained with MCMC applied to likelihood distributions of individual currents (left box, $N = 50$) in comparison with the same statistics obtained with PS NSFA applied to individual currents as described above (right box, $N = 250$, $n = 50$ bootstraps). It is clearly seen that, contrary to MCMC, PS NSFA significantly overestimates unitary current (green line indicates true value, 1 pA). Among the other model parameters only the number of liganded channels, N_{ch}, and the resensitization rate, r_2, were estimated with MCMC with relatively high accuracy. The desensitization rate, d_2, and GABA unbinding rate, k_{off}, were estimated in order of magnitude. The median of the absolute difference between estimates of model parameters and their true values for k_{off}, d_2, r_2, i_{ch}, and N_{ch} was 191, 188, 22, 31, and 35% of their true values, respectively.

We conclude that the mean values for several parameters of the synaptic receptor model, such as the unitary current, the number

of channels and the peak open probability, can be estimated with a reasonable accuracy using ML NSFA or MCMC sampling from the likelihood distribution of each individual current in the group of currents even if these currents were mediated by receptors having different kinetic models.

DISCUSSION

In this study we have further developed a new maximum likelihood method that we suggested earlier (Stepanyuk et al., 2011) and applied it to analysis of simulated macroscopic currents, in which the number of receptors exposed to a neurotransmitter varied from trial to trial. In the newly developed method, ML NSFA, the number of liganded receptors was first optimized for each macroscopic current and then these estimates were used to maximize the log-likelihood in order to obtain a set of kinetic model parameters as it was described earlier (Stepanyuk et al., 2011).

We explored the performance of ML NSFA with several different kinetic schemes of varying complexity and varying conditions relevant for real synaptic transmission. It was shown that contrary to PS NSFA (Traynelis et al., 1993) ML NSFA could estimate not only the unitary current of synaptic receptor channel but also multiple conductance levels, the number of liganded receptors, peak open probability and some kinetic constants from the experimentally realistic number of simulated postsynaptic currents. We have also evaluated the accuracy of ML NSFA compared to PS NSFA with respect to estimating the unitary current and found it 2-fold more accurate for a few (5–30) macroscopic currents. ML NSFA estimation of the unitary current was robust even when currents were generated by receptors having different kinetic parameters, the case when PS NSFA is not applicable. Thus, our results demonstrate that ML NSFA that takes into account correlations between different time points of a macroscopic currents and computationally scales linearly with the number of channel states (Stepanyuk et al., 2011) quantitatively and qualitatively outperforms currently available approaches for analysis of kinetic schemes of synaptic receptors.

ML NSFA APPLICABILITY TO ANALYSIS OF SYNAPTIC RECEPTOR PROPERTIES

Noise analysis of macroscopic currents remains a useful tool for determining the properties of different ligand- and voltage-operated channels (Traynelis and Jaramillo, 1998). Moreover, PS NSFA, the most frequently used noise analysis approach, is the only approach that can be applied to analysis of channels with an unusually low unitary conductance (Swanson et al., 1997) and receptor channels localized at synapses (Traynelis and Jaramillo, 1998). At the same time the unitary current is virtually the only parameter that can be reliably obtained from this type of analysis (Traynelis et al., 1993; Silver et al., 1996). To the best of our knowledge, kinetic rates have never been estimated for any synaptic receptors in their intrinsic environment. Peak open probability of receptors and the number of receptors bound with a neurotransmitter could not be also directly analyzed by any current approach. Possibility to estimate the unitary current and some kinetic rates using a few simulated postsynaptic currents demonstrated in this study allows for the first time to follow a time course of receptor remodeling in one and the same synaptic connection. Having in mind that estimation of some receptor parameters with accuracy of 10% can be obtained from 10 macroscopic currents (**Figures 1**, **2**), which can be collected in routine electrophysiological experiments for about 30 s, dynamics of receptor remodeling can be followed with a time course of several measurements per minute. It can be, for example, used for studying of modal gating, which refers to low probability rearrangements in receptor structure producing a substantial change in the overall pattern of channel opening (Popescu, 2012). Modal switches can be observed in single channel recordings of most ionotropic ligand-gated channels (Popescu, 2012) but it has never been directly demonstrated for synaptic receptors located in their intrinsic environment in a response to synaptic release of neurotransmitter. Modal gating may result not only in the different unitary conductance of receptors but also in changes in their gating and peak open probability (Popescu, 2005; Lema and Auerbach, 2006; Zhang et al., 2008; Poon et al., 2010; Prieto and Wollmuth, 2010). Moreover, in many cases, especially for the instance of NMDA receptors, substantial changes in gating, and peak open probability is observed without changes in the unitary conductance (Popescu, 2005; Zhang et al., 2008). Thus, such remodeling of synaptic receptors cannot be, in general, revealed by PS NSFA, while ML NSFA should certainly uncover it due to intrinsic ability to estimate some kinetic constants and peak open probability (**Figures 1**, **2**). The modal gating is slow (Popescu, 2005; Zhang et al., 2008; >5 min) and agonist- and stimulus-sensitive (Armstrong and Gouaux, 2000; Poon et al., 2010). Thus, it looks potentially plausible to synchronize synaptic receptor switching between different modes for a set of synaptic receptors in a given synaptic connection and to study the modal gating of synaptic receptors in their intrinsic environment by means of ML NSFA. For example, multiple conductance levels observed in modal gating of GluA2 AMPA receptors (Prieto and Wollmuth, 2010) or different open channel probabilities found for the type 2A isoform of NMDA receptors (Popescu and Auerbach, 2003) can be resolved from the respective postsynaptic currents (**Figures 2–4**).

Moreover, different types of AMPA receptor regulation that occur during LTP or LTD expression, such as changes in receptor trafficking (Huganir and Nicoll, 2013), in interaction of AMPARs with auxiliary subunits (Khodosevich et al., 2014) or adapter proteins that could lead to changes in receptor kinetics (Studniarczyk et al., 2013), phosphorylation-evoked changes in unitary current and peak open probability (Traynelis and Wahl, 1997; Derkach, 2003) could be potentially resolved with ML NSFA applied to the respective postsynaptic currents. Studies of developmental, pathological, plastic, and tissue specific modifications of synaptic receptors (Kittler et al., 2004; Lüthi et al., 2004; Palmer, 2006; Stubblefield and Benke, 2010) including changes in receptor subunit composition and trafficking (Ruiz et al., 2005; Patten and Ali, 2007) that have been earlier analyzed by PS NSFA may now also obtain a second wind due to a possibility to evaluate many parameters of the respective synaptic receptors.

Conclusions about mechanisms of synaptic receptors modulation that are based solely on the analysis of the amplitude of postsynaptic currents or unitary current might be misleading.

Indeed, stable unitary conductance might be accompanied by changes in receptor gating that may lead to an increase in the total charge transferred via a single synaptic receptor (**Figure 4**). At the level of macroscopic current it would result in an increase of current amplitude without substantial changes of its waveform (**Figure 4**). Together with absence of changes in the unitary conductance reported by PS NSFA it would be interpreted as presynaptic modification or an increase in the number of postsynaptic receptors. At the same time ML NSFA would certainly reveal changes in postsynaptic receptor gating.

The new approach also allows separate estimation of kinetic parameters of synaptic and extrasynaptic receptors expressed in the same neuron. For that, a set of postsynaptic currents necessary for evaluation of synaptic receptor model parameters must be initially recorded. Then strong presynaptic stimulation that can activate the whole set of synaptic terminals innervating the neuron under study should be performed in the presence of an irreversible use-dependent inhibitor of the respective synaptic receptors (e.g., picrotoxin for $GABA_A$ (Olsen, 2006) or MK-801 for NMDA (McAllister and Stevens, 2000) receptors, respectively). Next, several different agonist concentrations should be sequentially applied to the preparation in order to activate the extrasynaptic receptors and to record the respective transmembrane currents. Analysis of these macroscopic currents by ML NSFA or some of previously developed approaches (Milescu et al., 2005; Moffatt, 2007; Stepanyuk et al., 2011) would give kinetic parameters of extrasynaptic receptors.

ML NSFA APPLICABILITY TO ANALYSIS OF SYNAPTIC RECEPTOR NUMBER AND PEAK OPEN PROBABILITY

PS NSFA provides only an estimate of unitary current (Traynelis et al., 1993). In spite of this, estimation of N_{ch} and P(o, peak) was performed for single mossy fiber synapses of hippocampal granule cells having saturating glutamate concentration induced by synaptic vesicles release (Silver et al., 1996). In this case variance due to quantal variability is negligible and conventional NSFA can estimate these parameters. Although saturation of postsynaptic receptors is not rare in central synapses (Auger and Marty, 1997; Perrais and Ropert, 1999, 2000; Hájos et al., 2000; Nusser et al., 2001; Biró et al., 2006) estimation of N_{ch} and P(o, peak) could not be performed for the synaptic connections with multiple release sites by conventional NSFA due to trial-to-trial variability in the number of released vesicles and, as a result, in the number of receptors exposed to neurotransmitter. Moreover, in most of the central synapses neurotransmitter does not saturate postsynaptic receptors making all current methods void in determining N_{ch} and P(o, peak). On the other hand ML NSFA suggested in this study can directly evaluate the number of receptors, N_{ch}, bound with neurotransmitter by the end of fast transient of neurotransmitter concentration in a synaptic cleft and P(o, peak) defined as a fraction of liganded receptors N_{ch}, opened at the peak of macroscopic current (**Figure 2**). Moreover, N_{ch} could be separately evaluated for each postsynaptic current (Equation 18) and open probability as a function of time, which, in particular, includes P(o, peak) (**Figure 2**) could be obtained from estimated kinetic rate constants (**Figures 1**, **3**, **5**). Assumptions underlying ML NSFA suggest that estimations of kinetic rates as well as N_{ch} and P(o, peak) are correct if all synaptic receptors are subjected to the same and fast neurotransmitter profile or if the receptors are saturated. For some kinetic schemes (**Figure 1A**) saturation or the same concentration profile for all receptors are not obligatory and fast (compared to some kinetic rates) neurotransmitter profile is the only necessary assumption for ML NSFA applicability.

ML NSFA might be generally applicable to studies of synaptic and extrasynaptic NMDA receptors, glutamate receptors that directly contribute to active properties of dendrites. In the case of synaptic AMPA and NMDA receptors the ability of ML NSFA to analyze currents with variable kinetics could be important due to significant variability of glutamate transients in the excitatory synapses, low saturation levels of both receptor types (McAllister and Stevens, 2000) and complexity of their kinetic schemes (Popescu and Auerbach, 2004).

In conclusion we would like to note that more accurate estimation of unitary current compared to PS NSFA together with possibilities to distinguish multiple conductance levels and evaluate the number of liganded receptors, peak open probability and some kinetic constants position ML NSFA as a powerful tool to study synaptic receptor properties in their native environment using experimentally recorded postsynaptic macroscopic currents.

ACKNOWLEDGMENTS

This work was supported by NASU Biotechnology and Functional Genomics and Metabolomics Grants and DFFD F46.2/001 and F47/066 Grants.

REFERENCES

Armstrong, N., and Gouaux, E. (2000). Mechanisms for activation and antagonism of an AMPA-sensitive glutamate receptor: crystal structures of the GluR2 ligand binding core. *Neuron* 28, 165–181. doi: 10.1016/S0896-6273(00)00094-5

Auger, C., and Marty, A. (1997). Heterogeneity of functional synaptic parameters among single release sites. *Neuron* 19, 139–150. doi: 10.1016/S0896-6273(00)80354-2

Benke, T. A., Lüthi, A., Isaac, J. T., and Collingridge, G. L. (1998). Modulation of AMPA receptor unitary conductance by synaptic activity. *Nature* 393, 793–797. doi: 10.1038/31709

Biró, A. A., Holderith, N. B., and Nusser, Z. (2006). Release probability-dependent scaling of the postsynaptic responses at single hippocampal GABAergic synapses. *J. Neurosci.* 26, 12487–12496. doi: 10.1523/JNEUROSCI.3106-06.2006

Celentano, J. J., and Hawkes, A. G. (2004). Use of the covariance matrix in directly fitting kinetic parameters: application to GABAA receptors. *Biophys. J.* 87, 276–294. doi: 10.1529/biophysj.103.036632

Colquhoun, D., and Hawkes, A. G. (1977). Relaxation and fluctuations of membrane currents that flow through drug-operated channels. *Proc. R. Soc. Lond. B. Biol. Sci.* 199, 231–262. doi: 10.1098/rspb.1977.0137

Derkach, V. A. (2003). Silence analysis of AMPA receptor mutated at the CaM-kinase II phosphorylation site. *Biophys. J.* 84, 1701–1708. doi: 10.1016/S0006-3495(03)74978-9

DeWilde, P., and van der Veen, A.-J. (1998). *Time-Varying Systems and Computations*. (Boston, MA: Kluwer Academic Publishers).

Eidelman, Y., and Gohberg, I. (2008). Out-of-band quasiseparable matrices. *Linear Algebra Appl.* 429, 266–289. doi: 10.1016/j.laa.2008.02.026

Hájos, N., Nusser, Z., Rancz, E. A., Freund, T. F., and Mody, I. (2000). Cell type- and synapse-specific variability in synaptic GABAA receptor occupancy. *Eur. J. Neurosci.* 12, 810–818. doi: 10.1046/j.1460-9568.2000.00964.x

Hartveit, E., and Veruki, M. L. (2006). Studying properties of neurotransmitter receptors by non-stationary noise analysis of spontaneous synaptic currents. *J. Physiol.* 574, 751–785. doi: 10.1113/jphysiol.2006.111856

Huganir, R. L., and Nicoll, R. A. (2013). AMPARs and synaptic plasticity: the last 25 years. *Neuron* 80, 704–717. doi: 10.1016/j.neuron.2013.10.025

Husi, H., Ward, M. A., Choudhary, J. S., Blackstock, W. P., and Grant, S. G. (2000). Proteomic analysis of NMDA receptor-adhesion protein signaling complexes. *Nat. Neurosci.* 3, 661–669. doi: 10.1038/76615

Jin, R., Banke, T. G., Mayer, M. L., Traynelis, S. F., and Gouaux, E. (2003). Structural basis for partial agonist action at ionotropic glutamate receptors. *Nat. Neurosci.* 6, 803–810. doi: 10.1038/nn1091

Keramidas, A., and Harrison, N. L. (2010). The activation mechanism of alpha1beta2gamma2S and alpha3beta3gamma2S GABAA receptors. *J. Gen. Physiol.* 135, 59–75. doi: 10.1085/jgp.200910317

Khodosevich, K., Jacobi, E., Farrow, P., Schulmann, A., Rusu, A., Zhang, L., et al. (2014). Coexpressed auxiliary subunits exhibit distinct modulatory profiles on AMPA receptor function. *Neuron* 83, 601–615. doi: 10.1016/j.neuron.2014.07.004.

Kittler, J. T., Thomas, P., Tretter, V., Bogdanov, Y. D., Haucke, V., Smart, T. G., et al. (2004). Huntingtin-associated protein 1 regulates inhibitory synaptic transmission by modulating gamma-aminobutyric acid type A receptor membrane trafficking. *Proc. Natl. Acad. Sci. U.S.A.* 101, 12736–12741. doi: 10.1073/pnas.0401860101

Lema, G. M. C., and Auerbach, A. (2006). Modes and models of GABA(A) receptor gating. *J. Physiol.* 572, 183–200. doi: 10.1113/jphysiol.2005.099093

Li, F., and Tsien, J. Z. (2009). Memory and the NMDA receptors. *N. Engl. J. Med.* 361, 302–303. doi: 10.1056/NEJMcibr0902052

Low, C. M., Zheng, F., Lyuboslavsky, P., and Traynelis, S. F. (2000). Molecular determinants of coordinated proton and zinc inhibition of N-methyl-D-aspartate NR1/NR2A receptors. *Proc. Natl. Acad. Sci. U.S.A.* 97, 11062–11067. doi: 10.1073/pnas.180307497

Lüthi, A., Wikström, M. A., Palmer, M. J., Matthews, P., Benke, T. A., Isaac, J. T. R., et al. (2004). Bi-directional modulation of AMPA receptor unitary conductance by synaptic activity. *BMC Neurosci.* 5:44. doi: 10.1186/1471-2202-5-44

Magee, J. C. (2000). Dendritic integration of excitatory synaptic input. *Nat. Rev. Neurosci.* 1, 181–190. doi: 10.1038/35044552

Major, G., Larkum, M. E., and Schiller, J. (2013). Active properties of neocortical pyramidal neuron dendrites. *Annu. Rev. Neurosci.* 36, 1–24. doi: 10.1146/annurev-neuro-062111-150343

Markova, O., Stepanyuk, A., Tsugorka, T., Drebot, Y., Cherkas, V., and Belan, P. (2005). Applicability of peak-scaled nonstationary fluctuation analysis to the study of inhibitory synaptic transmission in hippocampal cultures. *Neurophysiology* 37, 333–343. doi: 10.1007/s11062-006-0008-z

McAllister, A. K., and Stevens, C. F. (2000). Nonsaturation of AMPA and NMDA receptors at hippocampal synapses. *Proc. Natl. Acad. Sci. U.S.A.* 97, 6173–6178. doi: 10.1073/pnas.100126497

Milescu, L. S., Akk, G., and Sachs, F. (2005). Maximum likelihood estimation of ion channel kinetics from macroscopic currents. *Biophys. J.* 88, 2494–2515. doi: 10.1529/biophysj.104.053256

Moffatt, L. (2007). Estimation of ion channel kinetics from fluctuations of macroscopic currents. *Biophys. J.* 93, 74–91. doi: 10.1529/biophysj.106.101212

Mortensen, M., Ebert, B., Wafford, K., and Smart, T. G. (2010). Distinct activities of GABA agonists at synaptic- and extrasynaptic-type GABAA receptors. *J. Physiol.* 588, 1251–1268. doi: 10.1113/jphysiol.2009.182444

Mozrzymas, J. W., Barberis, A., Mercik, K., and Zarnowska, E. D. (2003). Binding sites, singly bound states, and conformation coupling shape GABA-evoked currents. *J. Neurophysiol.* 89, 871–883. doi: 10.1152/jn.00951.2002

Nadkarni, S., Bartol, T. M., Sejnowski, T. J., and Levine, H. (2010). Modelling vesicular release at hippocampal synapses. *PLoS Comput. Biol.* 6:e1000983. doi: 10.1371/journal.pcbi.1000983

Neal, R. M. (2003). Slice sampling. *Ann. Stat.* 31, 705–767. doi: 10.1214/aos/1056562461

Neher, E., and Stevens, C. F. (1977). Conductance fluctuations and ionic pores in membranes. *Annu. Rev. Biophys. Bioeng.* 6, 345–381. doi: 10.1146/annurev.bb.06.060177.002021

Nusser, Z., Naylor, D., and Mody, I. (2001). Synapse-specific contribution of the variation of transmitter concentration to the decay of inhibitory postsynaptic currents. *Biophys. J.* 80, 1251–1261. doi: 10.1016/S0006-3495(01)76101-2

Olsen, R. W. (2006). Picrotoxin-like channel blockers of GABAA receptors. *Proc. Natl. Acad. Sci. U.S.A.* 103, 6081–6082. doi: 10.1073/pnas.0601121103

Palmer, M. J. (2006). Functional segregation of synaptic GABAA and GABAC receptors in goldfish bipolar cell terminals. *J. Physiol.* 577, 45–53. doi: 10.1113/jphysiol.2006.119560

Paoletti, P., Ascher, P., and Neyton, J. (1997). High-affinity zinc inhibition of NMDA NR1-NR2A receptors. *J. Neurosci.* 17, 5711–5725.

Patten, S. A., and Ali, D. W. (2007). AMPA receptors associated with zebrafish Mauthner cells switch subunits during development. *J. Physiol.* 581(Pt 3), 1043–1056. doi: 10.1113/jphysiol.2007.129999

Perrais, D., and Ropert, N. (1999). Effect of zolpidem on miniature IPSCs and occupancy of postsynaptic GABAA receptors in central synapses. *J. Neurosci.* 19, 578–588.

Perrais, D., and Ropert, N. (2000). Altering the concentration of GABA in the synaptic cleft potentiates miniature IPSCs in rat occipital cortex. *Eur. J. Neurosci.* 12, 400–404. doi: 10.1046/j.1460-9568.2000.00957.x

Poon, K., Nowak, L. M., and Oswald, R. E. (2010). Characterizing single-channel behavior of GluA3 receptors. *Biophys. J.* 99, 1437–1446. doi: 10.1016/j.bpj.2010.06.058

Popescu, G. (2005). Mechanism-based targeting of NMDA receptor functions. *Cell. Mol. Life Sci.* 62, 2100–2111. doi: 10.1007/s00018-005-5227-8

Popescu, G., and Auerbach, A. (2003). Modal gating of NMDA receptors and the shape of their synaptic response. *Nat. Neurosci.* 6, 476–483. doi: 10.1038/nn1044

Popescu, G., and Auerbach, A. (2004). The NMDA receptor gating machine: lessons from single channels. *Neuroscientist* 10, 192–198. doi: 10.1177/1073858404263483

Popescu, G. K. (2012). Modes of glutamate receptor gating. *J. Physiol.* 590, 73–91. doi: 10.1113/jphysiol.2011.223750

Prieto, M. L., and Wollmuth, L. P. (2010). Gating modes in AMPA receptors. *J. Neurosci.* 30, 4449–4459. doi: 10.1523/JNEUROSCI.5613-09.2010

Qin, F., Auerbach, A., and Sachs, F. (2000). Hidden Markov modeling for single channel kinetics with filtering and correlated noise. *Biophys. J.* 79, 1928–1944. doi: 10.1016/S0006-3495(00)76442-3

Robert, A., and Howe, J. R. (2003). How AMPA receptor desensitization depends on receptor occupancy. *J. Neurosci.* 23, 847–858.

Ruiz, A., Sachidhanandam, S., Utvik, J. K., Coussen, F., and Mulle, C. (2005). Distinct subunits in heteromeric kainate receptors mediate ionotropic and metabotropic function at hippocampal mossy fiber synapses. *J. Neurosci.* 25, 11710–11718. doi: 10.1523/JNEUROSCI.4041-05.2005

Scimemi, A., and Beato, M. (2009). Determining the neurotransmitter concentration profile at active synapses. *Mol. Neurobiol.* 40, 289–306. doi: 10.1007/s12035-009-8087-7

Sigworth, F. J. (1980). The variance of sodium current fluctuations at the node of Ranvier. *J. Physiol.* 307, 97–129.

Silver, R. A., Cull-Candy, S. G., and Takahashi, T. (1996). Non-NMDA glutamate receptor occupancy and open probability at a rat cerebellar synapse with single and multiple release sites. *J. Physiol.* 494(Pt 1), 231–250.

Silver, R. A., Traynelis, S. F., and Cull-Candy, S. G. (1992). Rapid-time-course miniature and evoked excitatory currents at cerebellar synapses *in situ*. *Nature* 355, 163–166. doi: 10.1038/355163a0

Stepanyuk, A. R., Borisyuk, A. L., and Belan, P., V (2011). Efficient maximum likelihood estimation of kinetic rate constants from macroscopic currents. *PLoS ONE* 6:e29731. doi: 10.1371/journal.pone.0029731

Stubblefield, E. A., and Benke, T. A. (2010). Distinct AMPA-type glutamatergic synapses in developing rat CA1 hippocampus. *J. Neurophysiol.* 104, 1899–1912. doi: 10.1152/jn.00099.2010

Studniarczyk, D., Coombs, I., Cull-Candy, S. G., and Farrant, M. (2013). TARP γ-7 selectively enhances synaptic expression of calcium-permeable AMPARs. *Nat. Neurosci.* 16, 1266–1274. doi: 10.1038/nn.3473

Swanson, G. T., Kamboj, S. K., and Cull-Candy, S. G. (1997). Single-channel properties of recombinant AMPA receptors depend on RNA editing, splice variation, and subunit composition. *J. Neurosci.* 17, 58–69. Available online at: http://www.jneurosci.org/content/17/1/58.long

Traynelis, S. F., and Jaramillo, F. (1998). Getting the most out of noise in the central nervous system. *Trends Neurosci.* 21, 137–145. doi: 10.1016/S0166-2236(98)01238-7

Traynelis, S. F., Silver, R. A., and Cull-Candy, S. G. (1993). Estimated conductance of glutamate receptor channels activated during EPSCs at the cerebellar mossy fiber-granule cell synapse. *Neuron* 11, 279–289. doi: 10.1016/0896-6273(93)90184-S

Traynelis, S. F., and Wahl, P. (1997). Control of rat GluR6 glutamate receptor open probability by protein kinase A and calcineurin. *J. Physiol.* 503(Pt 3), 513–531.

Vandebril, R., Van Barel, M., and Mastronardi, N. (2007). *Matrix Computations and Semiseparable Matrices: Linear Systems.* (Baltimore, MD: JHU Press).

Venkataramanan, L., and Sigworth, F. J. (2002). Applying hidden Markov models to the analysis of single ion channel activity. *Biophys. J.* 82, 1930–1942. doi: 10.1016/S0006-3495(02)75542-2

Wyllie, D. J. A., Johnston, A. R., Lipscombe, D., and Chen, P. E. (2006). Single-channel analysis of a point mutation of a conserved serine residue in the S2 ligand-binding domain of the NR2A NMDA receptor subunit. *J. Physiol.* 574, 477–489. doi: 10.1113/jphysiol.2006.112193

Zhang, W., Howe, J. R., and Popescu, G. K. (2008). Distinct gating modes determine the biphasic relaxation of NMDA receptor currents. *Nat. Neurosci.* 11, 1373–1375. doi: 10.1038/nn.2214

Conflict of Interest Statement: The authors declare that the research was conducted in the absence of any commercial or financial relationships that could be construed as a potential conflict of interest.

Received: 30 June 2014; paper pending published: 10 August 2014; accepted: 09 September 2014; published online: 02 October 2014.

Citation: Stepanyuk A, Borisyuk A and Belan P (2014) Maximum likelihood estimation of biophysical parameters of synaptic receptors from macroscopic currents. Front. Cell. Neurosci. ***8****:303. doi: 10.3389/fncel.2014.00303*

This article was submitted to the journal Frontiers in Cellular Neuroscience.

frontiers in
COMPUTATIONAL NEUROSCIENCE

ORIGINAL RESEARCH ARTICLE
published: 16 December 2014
doi: 10.3389/fncom.2014.00164

Model reduction of strong-weak neurons

Bosen Du, Danny Sorensen and Steven J. Cox*

Department of Computational and Applied Mathematics, Rice University, Houston, TX, USA

Edited by:
Sergey M. Korogod, National Academy of Sciences of Ukraine, Ukraine

Reviewed by:
Bartlett W. Mel, University of Southern California, USA
Kresimir Josic, University of Houston, USA

****Correspondence:***
Steven J. Cox, Department of Computational and Applied Mathematics, Rice University, 6100 Main Street MS 134, Houston, TX 77005, USA
e-mail: cox@rice.edu

We consider neurons with large dendritic trees that are weakly excitable in the sense that back propagating action potentials are severly attenuated as they travel from the small, strongly excitable, spike initiation zone. In previous work we have shown that the computational size of weakly excitable cell models may be reduced by two or more orders of magnitude, and that the size of strongly excitable models may be reduced by at least one order of magnitude, without sacrificing the spatio–temporal nature of its inputs (in the sense we reproduce the cell's precise mapping of inputs to outputs). We combine the best of these two strategies via a predictor-corrector decomposition scheme and achieve a drastically reduced highly accurate model of a caricature of the neuron responsible for collision detection in the locust.

Keywords: LGMD, predictor-corrector, quasi-active, proper orthogonal decomposition, discrete empirical interpolation

1. INTRODUCTION

Since Hodgkin and Huxley the neuroscience community has built mathematical models of cells, junctions and circuits as means to both synthesize existing knowledge and to drive further experiments. The complexity of both individual neurons and the networks in which they function has posed serious challenges to those in search of minimal models. The goal of neuronal model reduction is to arrive at a compact description of the cell's "function" and an efficient means of computing its response to physiological stimuli. This is typically accomplished by discovering a smaller equivalent dynamical system and discerning from this a smaller equivalent electrical circuit. See Brunel et al. (2014), Jadi et al. (2014) and Hedrick and Cox (2014) for recent surveys.

We continue our focus, on reduced single cell models that preserve the spatio-temporal structure of their inputs, by providing a detailed synthesis of the active reduction strategy of Kellems et al. (2010) with the quasi-active reduction strategy of Hedrick and Cox (2013). The synthesis is achieved via an elegant method of Rempe and Chopp (2006) for decoupling portions of complex cells and is applied to a caricature of the Lobula Giant Movement Detector (LGMD), the neuron, Peron et al. (2009), responsible for collision detection in the locust. The LGMD has a large, non-spiking dendritic tree that integrates visual input in a retinotopic fashion and funnels this signal to a well defined Spike Initiation Zone (SIZ). Although the structural morphology of the LGMD, and its inputs, has been carefully mapped it is not yet understood what distribution of active and passive conductances permits the cell to discern threatening from, seemingly similar, innocuous visual stimuli. It is hoped that a reduced model will constrain the large parameter space and accelerate the search through this space, and that it will lead to a compact description of the complex task of collision detection as implemented by the full LGMD. For a thorough investigation of the notion of *weak excitability* in the context of hippocampal pryamidal cells see Golding et al. (2001).

We build and test a detailed (879 compartments) model of the LGMD in §2.1, decouple its branches in §2.2, reduce its active branch in §2.3 and then its quasi-active branches in §2.4. We recouple these two small (3 dimensional) systems in §2.5 and in §3 demonstrate that the drastically reduced system retains the full integrative qualities of the original 879-dimensional model while running 20 times faster.

2. MATERIALS AND METHODS

The caricature of the LGMD neuron raised by Peron et al. (2009) is the rake depicted in **Figure 1A**. We have numbered its 22 branches and marked its SIZ, in black, near the center of the handle (branch 21) and the joint, in red, where the deck (branch 22) meets the handle. We have chosen a compartment (spatial step) size of $dx_j = 10\,\mu m$ and so arrive at a base system with 879 compartments. These are illustrated in **Figure 1A** and their spatial dimensions are best seen in **Figure 1B**. We distribute standard sodium, potassium and chloride channels throughout the rake in such a fashion that the tines, branches 1 through 20, weakly integrate synaptic input, funnel it to the deck which then delivers it via the joint to a strongly excitable handle.

After specifying the full model we decompose it via a predictor-corrector scheme and then apply distinct reduction strategies to the strong and weak parts. Throughout we have used a time step of $dt = 0.005$ ms.

2.1. THE FULL MODEL

With regard to the rake depicted in **Figure 1A**, we suppose that the radius of the jth branch is $a_j = a_j(x)$, where x denotes distance along the branch, and that its associated transmembrane potential is $v_j = v_j(x, t)$. If the branch contains sodium, potassium and chloride ion channels and is subject to direct current stimulation then Kirchhoff's current law reads

$$C_m\partial_t v_j = \frac{1}{2a_jR_a}\partial_x(a_j^2\partial_x v_j) + I_{stim,j}/(2\pi a_j) - g_{Na,j}m_j^3h_j(v_j - E_{Na}) - g_{K,j}n_j^4(v_j - E_K) - g_{Cl,j}(v_j - E_{Cl})$$
$$\partial_t m_j = (m_\infty(v_j) - m_j)/\tau_m(v_j), \quad (1)$$

where similar gating equations hold for h_j and n_j. In addition, we solve Equation 1 subject to sealed ends, current balance at branch points and initial conditions $v_j(x, 0) = \bar{v}_j(x)$ and $w_j(x, 0) = w_\infty(\bar{v}_j(x))$ where $\bar{v}_j(x)$ is the associated rest potential, obtained by solving

$$(a_j^2(x)\bar{v}_j'(x))' = 2a_jR_a\Big\{g_{Na,j}(x)m_\infty^3(\bar{v}_j(x))h_\infty(\bar{v}_j(x))(\bar{v}_j(x) - E_{Na}) + g_{K,j}(x)n_\infty^4(\bar{v}_j(x))(\bar{v}_j(x) - E_K) + g_{Cl,j}(x)(\bar{v}_j(x) - E_{Cl})\Big\}, \quad (2)$$

again subject to sealed ends and current balance at branch points. We concentrate throughout on a single set of parameters. The choice

$$C_m = 1.5\,\mu F/cm^2, \quad R_a = 0.05\,k\Omega\,cm, \quad a_j = 5\,\mu m$$
$$E_{Na} = 56, \quad E_K = -77, \quad E_{Cl} = -68\,mV$$
$$g_{Na,j} = 2 \quad g_{K,j} = 3.6, \quad g_{Cl,j} = 0.9\,mS/cm^2 \quad (3)$$

will render the tines, branches 1–20, and the deck, branch 22, weakly excitable, while setting

$$g_{Na,21}(x) = \begin{cases} 216\,mS/cm^2, & 200 \le x < 260\,\mu m \\ 12\,mS/cm^2, & \text{otherwise.} \end{cases}$$
$$\text{and} \quad g_{Cl,21} = 0.3\,mS/cm^2 \quad (4)$$

will make the handle, branch 21, strongly excitable. We have illustrated the resulting rest potential, $\bar{v}$, in **Figure 1B**. We see that the non-uniformity in Equation 4 leads to a depolarized handle and a non-uniform rest potential throughout the remainder of the rake.

We will solve this full system, Equation 1, for two classes of inputs. For the first class, deemed coherent, we simulataneously inject 4 nano-Amperes of current at the midpoint of each tine for nine tenths of a millisecond. In symbols

$$I_{stim,j}(x, t) = 0.004\delta(x - 200)\chi_{[0.1,1]}(t), \quad 1 \le j \le 20, \quad (5)$$

where $\chi_{[a,b]}(t)$ equals one if $a \le t \le b$ and equals zero otherwise. For the second class, deemed random, we inject 4 nano-Amperes of current at a random location, and at a random time, on each tine for nine tenths of a millisecond. In symbols

$$I_{stim,j}(x, t) = 0.004\delta(x - x_j)\chi_{[t_j,t_j+0.9]}(t), \quad 1 \le j \le 20, \quad (6)$$

where the mean of x_j is 200 μm and the mean of t_j is 5 ms.

In response to coherent stimulus, Equation 5, we see in **Figure 1C** steady and significant $(20\,mV)$ depolarization at the joint (red trace) that is sufficient to drive the handle to spike (blue

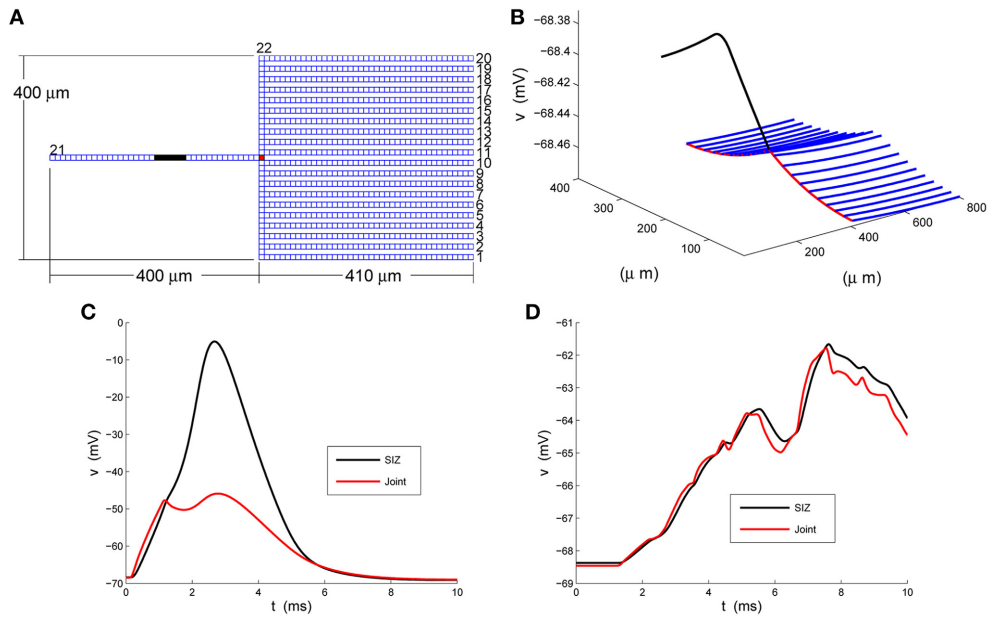

FIGURE 1 | A strong-weak neuron. (A) The layout of the rake with its 22 numbered branches, divided into compartments of length $dx_j = 10\,\mu m$. **(B)** The rest potential, $\bar{v}$, obtained by solving Equation 2 subject to the parameters specified in Equations 3 and 4. **(C)** The response of the full model, Equation 1, at the SIZ (left end of black region in **A**) and joint (red square in **A**) to the coherent synaptic input of Equation 5. **(D)** The response of the full model, Equation 1, at the SIZ (left end of black region in **A**) and joint (red square in **A**) to the random synaptic input of Equation 6.

trace at SIZ). This spike travels down the handle and leads to the second, smaller, depolarization at the joint. The random stimulus, Equation 6, delivers the same amount of current to the rake but spread over space and time. The response at the joint, red trace in **Figure 1D**, indicate $\approx 3\,mV$ depolarizations to individual current steps. These are not coherent enough to accumulate in a fashion sufficient to drive the handle to spike. Instead the response at the SIZ, blue trace in **Figure 1D**, is a filtered attenuated version of the joint trace.

2.2. BRANCH DECOMPOSITION

Rempe and Chopp (2006) introduced a rational scheme for decomposing large cells into smaller (typically single branch) regions. They were motivated by the fact that as an action potential travels through a cell, branches on either side of the action potential are relatively quiet and so need not be simulated/computed. As such they devised branch-wise activity measures, in both Rempe and Chopp (2006) and Rempe et al. (2008), that allowed them to build a spatially adaptive numerical scheme that focused resources solely on active branches. One significant advantage of their decomposition is that it permits simultaneous/parallel updating of the active branches. This feature has been successfully exploited by Kozloski and Wagner (2011). Our use of Rempe and Chopp (2006) is however, quite different. For we use their scheme to partition the cell into strong and weak zones that may then be reduced by strategies specific to the dynamics consistent with such zones.

Rempe and Chopp (2006) decompose the cell by giving special attention to those compartments, deemed **nodes**, at which branches meet. We have illustrated this decomposition on our rake in **Figure 2**. This spatial decomposition is only useful when coupled with a scheme for properly updating the components in time. Rempe and Chopp (2006) sketch a method that

(1) uses the present branch and node potentials to **predict** the future node potentials,
(2) updates the branch potentials based on the predicted node potentials,
(3) **corrects** the node potentials based on the updated branch potentials.

As the success of our method hinges on this predictor-corrector scheme we present it here in some detail.

We distinguish between branches 1 through 21, which are adjacent to a single node, and branch 22, which is adjacent to many. Given the branch, $v_j(k,\,t)$, and node, $w_j(t)$, potentials and gating variables at time t we advance the gating variables via the explicit in v implicit in m step

$$\begin{aligned} m_j(k,\,t+dt) &= \frac{m_j(k,\,t)\tau_m(v_j(k,\,t)) + m_\infty(v_j(k,\,t))dt}{dt+\tau_m(v_j(k,\,t))}, \\ &\qquad 1 \le k \le 39 \\ m_j(40,\,t+dt) &= \frac{m_j(40,\,t)\tau_m(w_j(t)) + m_\infty(w_j(t))dt}{dt+\tau_m(w_j(t))}, \\ &\qquad 1 \le j \le 21, \end{aligned} \tag{7}$$

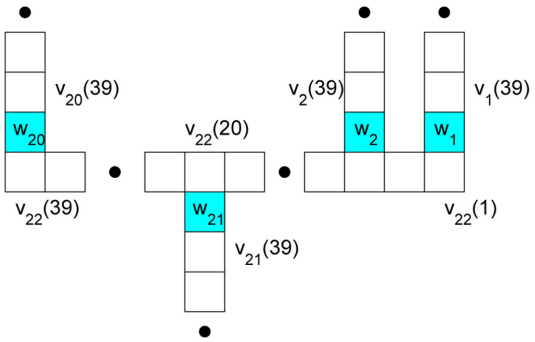

FIGURE 2 | Branch compartment and node labeling to facilitate decoupling via a predictor-corrector scheme. The nodes are colored blue and their potentials are w_1 through w_{21}. They occur at the ends of 21 respective branches. The potential in compartment k of branch j is denoted $v_j(k)$.

and collect these into

$$\begin{aligned} \Gamma_j(k,\,t+dt) &= g_{Na,j}(k)m_j^3(k,\,t+dt)h_j(k,\,t+dt) \\ &\quad + g_{K,j}(k)n_j^4(k,\,t+dt) + g_{Cl,j}(k) \\ \gamma_j(k,\,t+dt) &= g_{Na,j}(k)m_j^3(k,\,t+dt)h_j(k,\,t+dt)E_{Na} \\ &\quad + g_{K,j}(k)n_j^4(k,\,t+dt)E_K + g_{Cl,j}(k)E_{Cl}. \end{aligned}$$

We next use these to take a backward Euler step of the associated voltage equation, Equation 1,

$$\begin{aligned} &G_j(k-)v_j(k-1,\,t+dt) - (G_j(k-) + G_j(k+)) \\ &v_j(k,\,t+dt) + G_j(k+)v_j(k+1,\,t+dt) = \\ &\qquad \mu(v_j(k,\,t+dt) - v_j(k,\,t)) + \Gamma_j(k,\,t+dt)v_j(k,\,t+dt) \\ &\qquad - \gamma_j(k,\,t+dt) + I_{stim,j}(k,\,t+dt)/A_j(k) \end{aligned}$$

where

$$G_j(k\pm) = \frac{a_j(k)}{R_a dx_j^2}\frac{a_j^2(k\pm1)}{a_j^2(k)+a_j^2(k\pm1)}, \quad \mu = C_m/dt$$
$$\text{and} \quad A_j(k) = 2\pi a_j(k)dx_j.$$

While at the ends, $G_j(1-) = 0$ and

$$G_j(40-) \equiv G_{j-}^* = \frac{a_j(40)}{R_a dx_j^2}\frac{a_j^2(39)}{a_j^2(40)+a_j^2(39)}$$

$$G_j(40+) \equiv G_{j+}^* = \frac{a_j(40)}{2R_a dx_j}\frac{dx_{22}^2}{2a_j^2(40)dx_j + dx_{22}^2 a_{22}(p_j)}$$

$$\text{where} \quad p_j = \begin{cases} 2j-1, & 1 \le j \le 20 \\ 20, & j = 21. \end{cases}$$

With these we may now make sense of the node equation

$$\begin{aligned} &G^*_{j-}v_j(39,t+dt)-(G^*_{j-}+G^*_{j+}) \\ &w_j(t+dt)+G^*_{j+}v_{22}(p_j,t+dt)= \\ &\qquad \mu(w_j(t+dt)-w_j(t))+\Gamma_j(40,t+dt) \\ &\qquad w_j(t+dt)-\gamma_j(40,t+dt) \end{aligned} \tag{8}$$

Following Rempe and Chopp (2006) we decouple the node and branch equations in time by making a crude prediction of the nodal potentials by replacing the backward Euler step Equation 8 with the forward Euler step

$$\begin{aligned} &G^*_{j-}v_j(39,t)-(G^*_{j-}+G^*_{j+})w_j(t)+G^*_{j+}v_{22}(p_j,t)= \\ &\quad \mu(w^*_j(t)-w_j(t))+\Gamma_j(40,t+dt)w^*_j(t)-\gamma_j(40,t+dt) \end{aligned} \tag{9}$$

where $w^*_j(t)$ denotes our crude prediction of $w_j(t+dt)$. We note that Equation 9 may be solved explicitly for

$$\boxed{w^*_j(t)=\frac{\begin{array}{c}\mu w_j(t)+\gamma^*_j(t+dt)+G^*_{j-}v_j(39,t)\\ -(G^*_{j-}+G^*_{j+})w_j(t)+G^*_{j+}v_{22}(p_j,t)\end{array}}{\mu+\Gamma^*_j(t+dt)},} \tag{10}$$

where $\Gamma^*_j(t+dt)=\Gamma_j(40,t+dt)$ and $\gamma^*_j(t+dt)=\gamma_j(40,t+dt)$. We then use these predicted nodal potentials to drive the branch updates via

$$\boxed{\begin{aligned}&(\mu I+\mathrm{diag}(\Gamma_j(1:39,t+dt))-B_j)v_j(:,t+dt)= \\ &\mu v_j(:,t)+\gamma_j(1:39,t+dt)+I_{stim,j}(:,t+dt)+c_j(:,t),\end{aligned}} \tag{11}$$

where c_j is the node branch coupling vector and B_j is the branch tridiagonal matrix. For the branches adjacent to a single node, $j<22$, we find that c_j is zero at each compartment except for

$$c_j(39,t)=G^*_{j-}w^*_j(t), \tag{12}$$

while B_j is the tridiagonal matrix

$$\begin{aligned} B_j(1,1:2)&=[-G_j(1+)\quad G_j(1+)] \\ B_j(k,k-1:k+1)&=[G_j(k-)\quad -(G_j(k-)+G_j(k+)) \\ &\qquad G_j(k+)],\quad 1<k<39, \\ B_j(39,38:39)&=[G_j(39-)\quad -(G_j(39-) \\ &\qquad +G_j(39+))]. \end{aligned}$$

Turning to the deck, B_{22} is the tridiagonal matrix

$$\begin{aligned} B_{22}(1,1:2)&=[-(G_{22}(1+)+G^*_{1+})\quad G_j(1+)] \\ B_{22}(k,k-1:k+1)&=[G_{22}(k-)\quad -(G_{22}(k-) \\ &\qquad +G_{22}(k+))\quad G_{22}(k+)], \\ &\qquad 1<k<39,\quad k\neq p_j \\ B_{22}(k,k-1:k+1)&=[G_{22}(k-)\quad -(G_{22}(k-) \\ &\qquad +G_{22}(k+)+G^*_{j+})\quad G_{22}(k+)], \\ &\qquad 1<k<39,\quad k=p_j \\ B_{22}(39,38:39)&=[G_{22}(39-)\quad -(G_{22}(39-)+G^*_{20+})]. \end{aligned}$$

This differs from the previous B_j in the sense that it has no free ends (hence 2 terms on the end diagonals) and meets the 20 tines (and hence three terms on those diagonals). The associated coupling term is then zero except at

$$c_{22}(p_j,t)=G^*_{j+}w^*_j(t),\quad j=1,\ldots,21. \tag{13}$$

Upon updating all branches we may then return to correcting the nodal potentials, now via

$$\begin{aligned} &G^*_{j-}v_j(39,t+dt)-(G^*_{j-}+G^*_{j+}) \\ &w_j(t+dt)+G^*_{j+}v_p(p_j,t+dt)= \\ &\qquad \mu(w_j(t+dt)-w^*_j(t))+\Gamma^*_j(t+dt) \\ &\qquad w_j(t+dt)-\gamma^*_j(t+dt) \end{aligned} \tag{14}$$

which we solve explicitly for

$$\boxed{w_j(t+dt)=\frac{\begin{array}{c}\mu w_j(t)+\gamma^*_j(t+dt)+G^*_{j-}v_j(39,t+dt)\\ +G^*_{j+}v_p(p_j,t+dt)\end{array}}{\mu+\Gamma^*_j(t+dt)+G^*_{j-}+G^*_{j+}}.} \tag{15}$$

With this we may now offer a precise specification of the Predictor-Corrector Algorithm

[1] Given the branch potentials, node potentials and gating variables at time t update the gating variables per Equation 7.
[2] Predict the new values of the node potentials via Equation 10.
[3] Update the branch potentials via Equation 11.
[4] Correct the node potentials via Equation 15. Return to step [1].

2.3. REDUCTION OF THE STRONG PART

Following Kellems et al. (2010) we reduce the dynamics in the strong zone, $(v_{21}, m_{21}, h_{21}, n_{21})$ by the method of Proper Orthogonal Decomposition by collecting snapshots of the membrane potential and associated active current

$$\begin{aligned} &I_{act}(t)\equiv g_{Na,21}.m^3_{21}(t).h_{21}(t).(v_{21}(t)-E_{Na}) \\ &+g_{K,21}.n^4_{21}(t).(v_{21}(t)-E_K) \end{aligned}$$

in

$$V=[v_{21}(0)\ v_{21}(dt)\ \cdots\ v_{21}(T_{fin})]\quad \text{and}$$

$$F = [I_{act}(0)\, I_{act}(dt)\, \cdots\, I_{act}(T_{fin})]$$

under a stimulus regime that generates a spike on branch 21. The major features of spike generation and propagation are purportedly captured in the first few singular vectors of V and F. Accordingly we compute the respective singular value decompositions

$$V = U\Sigma A^T \quad \text{and} \quad F = W\Lambda C^T, \tag{16}$$

where the matrices of singular vectors, U, A, W and C, are orthonormal and the matrices of singular values, Σ and Λ, are diagonal – and ordered in a decreasing manner.

Our first stab at reduction is to suppose that v_{21} is well approximated by the first κ columns of U, i.e.,

$$v_{21}(t) \approx U_\kappa \hat{v}_{21}(t)$$

where U_κ denotes the first κ columns of U (from Equation 16) and so the reduced state $\hat{v}_{21}(t) \in \mathbb{R}^\kappa$. On placing this guess in the (spatially discretized version) of Equation 1 we find that the reduced state, $\hat{v}_{21}$, must obey

$$\begin{aligned} C_m\hat{v}'_{21} &= U_\kappa^T B_{21} U_\kappa \hat{v}_{21} - U_\kappa^T\{g_{Na,21}.m_{21}^3.h_{21}.(U_\kappa\hat{v}_{21} - E_{Na}) \\ &\quad + g_{K,21}.n_{21}^4.(U_\kappa\hat{v}_{21} - E_K) + g_{Cl,21}(U_\kappa\hat{v}_{21} - E_{Cl}) - c_{21}\} \\ m'_{21} &= (m_\infty(U_\kappa\hat{v}_{21}) - m_{21})./\tau_m(U_\kappa\hat{v}_{21}). \end{aligned} \tag{17}$$

This provides a clean reduction of the linear spatial coupling between compartments, in the sense that

$$\tilde{B}_{21} \equiv U_\kappa^T B_{21} U_\kappa$$

is merely κ-by-κ. The non-linearities however are still computed on the full dimensional vector $U_\kappa\hat{v}_{21}$. To address this we distil from W_κ, the first κ columns of W (from Equation 16), κ places along the handle at which it suffices to evaluate the non-linear gating functionals. These places are selected by Discrete Empirical Interpolation as those places at which the singular vectors of F have the greatest content. In particular,

$$\begin{aligned} &z_1 = \text{argmax}|W_\kappa(:,1)| \\ &P = e_{z_1} \\ &\text{for } i = 2:\kappa \\ &\quad s = (P^T W_\kappa(:,1:i-1))\backslash P^T W_\kappa(:,i) \\ &\quad r = W_\kappa(:,i) - W_\kappa(:,1:i-1)s \\ &\quad z_i = \text{argmax}|r| \\ &\quad P = [P\, e_{z_i}] \\ &\text{end} \end{aligned}$$

where e_k denotes the kth column of the identity matrix on $\mathbb{R}^{39}$. With these κ places, $z = [z_1, \ldots, z_\kappa]$ and their associated permutation matrix P we reduce the gating variables via

$$m_{21}(t) \approx P\hat{m}_{21}(t). \quad h_{21}(t) \approx P\hat{h}_{21}(t) \quad \text{and} \quad n_{21}(t) \approx P\hat{n}_{21}(t)$$

and so bring Equation 17 to

$$\begin{aligned} C_m\hat{v}'_{21} &= \tilde{B}_{21}\hat{v}_{21} - R\{g_{Na}(z).\hat{m}_{21}^3.\hat{h}_{21}.(Z\hat{v}_{21} - E_{Na}) \\ &\quad + g_K(z).\hat{n}_{21}^4.(Z\hat{v}_{21} - E_K)\} - U_\kappa^T g_{Cl,21}(U_\kappa\hat{v}_{21} - E_{Cl}) \\ &\quad + U_\kappa^T c_{21} \\ \hat{m}'_{21} &= (m_\infty(Z\hat{v}_{21}) - \hat{m}_{21})./\tau_m(Z\hat{v}_{21}) \end{aligned} \tag{18}$$

where $g_{Na}(z)$ denotes the evaluation of $g_{Na,21}$ at the compartments indexed by z. As both

$$R = U_\kappa^T W_\kappa (P^T W_\kappa)^{-1} \quad \text{and} \quad Z = P^T U_\kappa$$

are κ-by-κ we have arrived at a κ-dimesional reduction of the original 39-dimensional active handle. We solve Equation 18, subject to the initial conditions $\hat{v}_{21}(:,0) = U_\kappa^T\bar{v}$ and $\hat{m}_{21}(:,0) = m_\infty(Z\hat{v}_{21}(:,0))$, via the standard explicit-implicit Euler method

$$\boxed{\begin{aligned} \hat{m}_{21}(i,t+dt) &= \frac{m_\infty((Z\hat{v}_{21}(:,t))_i)dt + \tau_m((Z\hat{v}_{21}(:,t))_i)\hat{m}_{21}(i,t)}{dt + \tau_m((Z\hat{v}_{21}(:,t))_i)} \\ (\mu I - \tilde{B}_{21} + \Gamma_{21}) & \\ \hat{v}_{21}(:,t+dt) &= \mu\hat{v}_{21}(:,t) + \gamma_{21} + U_\kappa^T c_{21}(t) \end{aligned}} \tag{19}$$

where

$$\begin{aligned} \Gamma_{21} &= R\,\text{diag}(g_{Na}(z).\hat{m}_{21}^3(:,t+dt).\hat{h}_{21}(:,t+dt) \\ &\quad + g_K(z).\hat{n}_{21}^4(:,t+dt))Z + U_\kappa^T\text{diag}(g_{Cl,21})U_\kappa \\ \gamma_{21} &= R\,(g_{Na}(z).\hat{m}_{21}^3(:,t+dt).\hat{h}_{21}(:,t+dt)E_{Na} \\ &\quad + g_K(z).\hat{n}_{21}^4(:,t+dt)E_K) + E_{Cl}U_\kappa^T g_{Cl,21} \end{aligned}$$

The c_{21} term in Equation 19 remains the contribution from the nodal potential, w_{21}. Before specifying this we discuss how to reduce the remainder of the branches.

2.4. REDUCTION OF THE WEAK PART

In order to perform a single reduction on the remaining branches it is most convenient to gather the variables in the 800 tine compartments and 39 deck compartments into four long vectors v, m, h and n. The first step is then to linearize the full system, Equation 1, about its rest state. More precisely, assuming the stimulus to be order ε we develop the voltage and gating variables

$$\begin{aligned} v(x,t) &= \bar{v}(x) + \varepsilon\tilde{v}(x,t) + O(\varepsilon^2) \\ \text{and} \quad m(x,t) &= m_\infty(\bar{v}(x)) + \varepsilon\tilde{m}(x,t) + O(\varepsilon^2). \end{aligned} \tag{20}$$

On substituting Equation 20 into Equation 1 and identifying terms of order ε, we find that the so-called quasi-active variables, $\tilde{v}$, $\tilde{m}$, $\tilde{h}$ and $\tilde{n}$ must solve

$$\begin{aligned} C_m\partial_t\tilde{v} &= \frac{1}{2R_a a}\partial_x(a^2\partial_x\tilde{v}) - \big(g_{Na,j}m_\infty^3(\bar{v})h_\infty(\bar{v}) + g_{K,j}n_\infty^4(\bar{v}) \\ &\quad + g_{Cl,j}\,)\tilde{v} - 3g_{Na,j}m_\infty^2(\bar{v})h_\infty(\bar{v})(\bar{v} - E_{Na})\tilde{m} \end{aligned}$$

$$- g_{Na,j} m_\infty^3(\bar{v})(\bar{v} - E_{Na})\tilde{h} - 4g_{K,j} n_\infty^3(\bar{v})(\bar{v} - E_K)\tilde{n}$$
$$+ I_{stim}/(2\pi a)$$
$$\partial_t \tilde{m} = (m'_\infty(\bar{v}) - \tilde{m})/\tau_m(\bar{v}) \quad (21)$$

subject to current balance where the tines meet the deck and to the initial conditions $\tilde{v}(x, 0) = \tilde{m}(x, 0) = 0$. On stacking the quasi-active variables in

$$y = [\tilde{m}; \tilde{h}; \tilde{n}; \tilde{v}]$$

and the stimuli and coupling vector in

$$u = [I_{stim,1}; I_{stim,2}; \cdots; I_{stim,20}; c_{22}] \quad (22)$$

we may write Equation 21 as an $(839 \cdot 4)$–dimensional system for y,

$$y'(t) = Qy(t) + Bu(t), \quad y(0) = 0 \quad (23)$$

where the non-zero blocks of Q and B are

$$Q = \begin{pmatrix} D_{m,1} & & & D_{m,2} \\ & D_{h,1} & & D_{h,2} \\ & & D_{n,1} & D_{n,2} \\ D_{v,1} & D_{v,2} & D_{v,3} & H \end{pmatrix} \quad \text{and} \quad B = \begin{pmatrix} \\ \\ \\ I/C_m \end{pmatrix}.$$

See §9.4 of Gabbiani and Cox (2010) for the diagonal D matrices and the Hines matrix, H. Given the geometry of the rake we are really only interested in the potential at the joint (recall the red square in **Figure 1A**). As this is compartment number 820 in the natural ordering, out of the large system Equation 23 we ask only for a good approximation to the joint potential

$$J(t) = e_{839\cdot 3+820}^T y,$$

where e_n is the unit vector with a one in element n. Following Hedrick and Cox (2013) we suppose $y \approx \mathcal{X}\hat{y}$ and choose an $\mathcal{X}$, with only 4κ columns, that returns an accurate approximation of J. This is done by matching the first κ moments of the full and reduced transfer functions, or, equivalently, via the Arnoldi scheme

$$\begin{aligned} &x = H \backslash e_{820} \\ &X = x/\|x\| \\ &\text{for } \; i = 1 : \kappa - 1 \\ &\qquad x = H \backslash X(:, i) \\ &\qquad \text{for} \quad j = 1 : i \\ &\qquad\qquad x = x - (X(:, j)^T x) X(:, j) \\ &\qquad \text{end} \\ &\qquad X = [X \;\; x/\|x\|] \\ &\text{end} \end{aligned} \quad (24)$$

where, for simplicity, we have chosen our reduced dimension, κ, to agree with that used to reduce the cell's strong zone. We then arrive at the full reducer by tiling this X, i.e.,

$$\mathcal{X} = \begin{pmatrix} X & & & \\ & X & & \\ & & X & \\ & & & X \end{pmatrix}. \quad (25)$$

On inserting $y = \mathcal{X}\hat{y}$ into Equation 23 and using $\mathcal{X}^T\mathcal{X} = I$ we find that $\hat{y}$ must obeys

$$\hat{y}'(t) = \mathcal{X}^T Q \mathcal{X} \hat{y}(t) + \mathcal{X}^T B u(t), \quad \hat{y}(0) = 0.$$

This we solve by backward Euler

$$(I - dt\mathcal{X}^T Q \mathcal{X})\hat{y}(t + dt) = \hat{y}(t) + dt\mathcal{X}^T B u(t) \quad (26)$$

and then read off the approximate joint potential via $\hat{J}(t) = e_{839\cdot 3+820}^T \mathcal{X}\hat{y}(t)$.

2.5. THE REDUCED STRONG-WEAK NEURON

It remains only to specify the predictor and corrector updates of the single nodal potential, w_{21}, and to clarify their roles in the coupling vector c_{21} appearing in the strong reduction, Equation 19, and the coupling vector c_{22} in the weak reduction, Equation 26, via its presence in the u of Equation 22.

Regarding the expressions for w_{21}^* and w_{21} in Equation 10 and 15 we note that the required adjacent potentials are readily derived from our independent reductions,

$$v_{21}(39, t) \approx U_\kappa(39, :)\hat{v}(t) \quad \text{and} \quad v_{22}(20, t) \approx \bar{v}_{22}(20) + \hat{J}(t).$$

The coupling vector c_{21} is all zero except $c_{21}(39, t) = G_{21-}^* w_{21}^*(t)$, while the coupling vector c_{22} is all zero except $c_{22}(20, t) = G_{21+}^*(w_{21}^*(t) - \bar{v}_{22}(20))$.

3. RESULTS

We present in **Figure 3** structural components of the strong (A) and weak (B) reductions and in panels (C) and (D) contrast the responses of the full and reduced models, at SIZ and Joint, to the respective coherent and random stimuli used in **Figure 1**.

These results were robust to changes in the stimuli that generated the snapshots and to changes in the random stimuli, Equation 6. The reduced system consistently ran in less than $1/20^{th}$ of the time required by the original system. With $\kappa = 3$ the Discrete Empirical Interpolation method identified $z = [1, 21, 26]$ as the compartments along the handle at which to evaluate the gating variables. On comparison to the sodium channel distribution in Equation 4 we note that compartments 21 and 26 are the extent of the SIZ. Regarding **Figure 3B** we interpret the columns of X as the dendritic filter, seen at the joint, of the true inputs. For columns of X and biophysical interpretations of the elements of $\mathcal{X}^T Q \mathcal{X}$ see Hedrick and Cox (2013). The errors reported in **Figures 3C,D** are quite small relative to the original signals in **Figures 1C,D** and, regarding

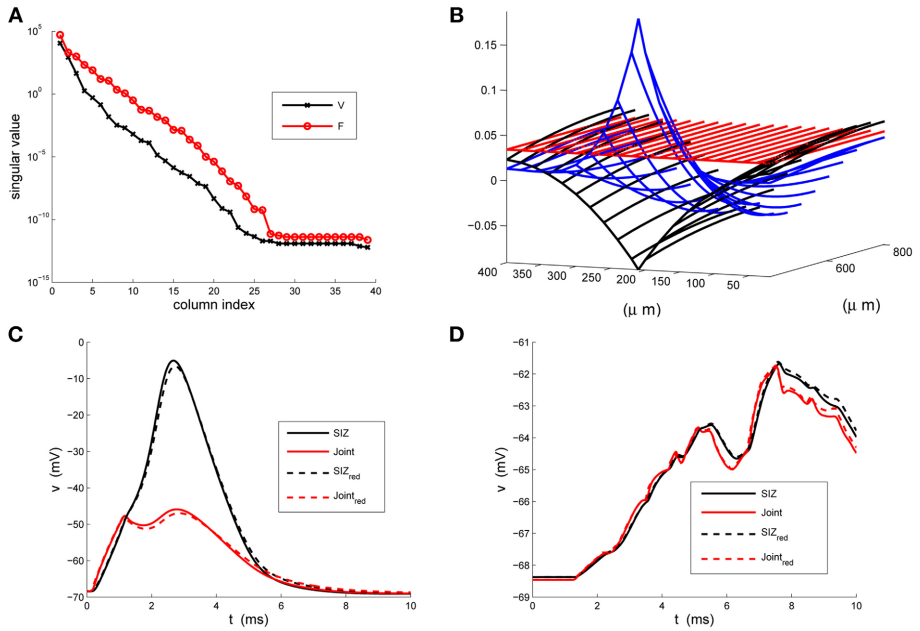

FIGURE 3 | The strong-weak reduction of the rake. (A) The singular values of the voltage (V) and active current (F) snapshots. We see that both have decreased by two orders of magnitude by their third index. **(B)** An illustration of the three columns of the reducer, X, computed in Equation 24, indicating how the reduced system processes the true inputs. **(C)** Contrasting the response of the full (solid) and reduced ($\kappa = 3$) models at the SIZ (black) and at the Joint (red) to identical coherent stimuli. **(D)** Contrasting the response of the full (solid) and reduced ($\kappa = 3$) models at the SIZ (black) and at the Joint (red) to identical random stimuli.

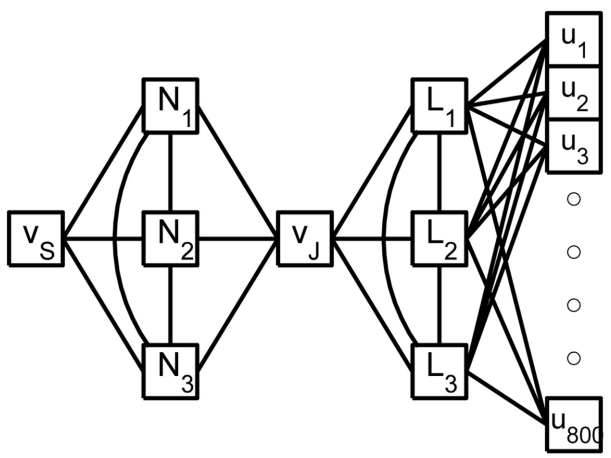

FIGURE 4 | A shematic of the reduced rake. The true inputs, u_i, into the 800 tine compartments are weighted by the columns of X and then summed as they enter the 3 linear nodes, L_i, of the reduced weak zone. The linear nodes are fully coupled and a linear combination of their responses contributes to the joint potential, v_J. The 3 fully coupled non-linear nodes, N_i, of the reduced strong zone contribute to both v_J and the SIZ potential v_S.

the timing of critical SIZ events, produce negligible (< 0.1 ms) errors. This then permits us to replace the complex 879 compartment model of **Figure 1A** with the 8 compartment model of **Figure 4**.

4. DISCUSSION

We have developed and demonstrated a strategy for the systematic reduction of models of strong-weak neurons. In particular, we have replaced a sensory neuron of dimension 879 with a 3-dimensional strong system coupled, via a single node, to a 3-dimensional weak system, **Figure 4**, and found negligible absolute differences in their voltage responses to complex spatio-temporal inputs while running 20 times faster than the original. We have achieved the strong-weak distinction through significant non-uniformity in the density of sodium channels. This was merely a matter of convenience. The effect can be achieved, see Golding et al. (2001) and Migliore and Shepherd (2002), by a large class of non-uniformities.

The critical assumption permitting our significant reduction is that the bulk of the neuron is weakly excitable - and this means that its response is well approximated by a quasi-active model. The delineation of such systems is of course wrapped up in the equally vexing questions of spike initiation and propagation. For neurons whose dendrites are not sufficiently weak to meet our definition we may apply our strong reduction to each branch and then invoke the activity measures of Rempe and Chopp (2006) and Rempe et al. (2008) to update these branches only when necessary. Regarding scope, our methods are equally suited to synaptic inputs modeled as conductance changes onto trees with arbitrary branching patterns and arbitrary non-uniform channel distributions, see Kellems et al. (2010) and Hedrick and Cox (2013), as well as to inputs via gap junctions, see Hedrick and Cox (2014). These methods can also be readily adapted to incorporate non-uniform distributions of spines and NMDA receptors

as well as interaction with the cell's calcium handling machinery of channels, buffers, receptors and pumps.

ACKNOWLEDGMENTS

This work was partially supported by NSF Grants DMS-1122455 and CCF-1320866 and AFOSR Grant FA9550-12-1-0155.

REFERENCES

Brunel, N., Hakim, V., and Richardson, M. J. E. (2014). Single neuron dynamics and computation. *Curr. Opin. Neurobiol.* 25, 149–155. doi: 10.1016/j.conb.2014.01.005

Gabbiani, F., and Cox, S. J. (2010). *Mathematics for Neuroscientists*. Amsterdam: Academic Press.

Golding, N. L., Kath, W. L., and Spruston, N. J. (2001). Dichotomy of action-potential backpropagation in CA1 pyramidal neuron dendrites. *Neurophysiology* 86, 2998-3010. Available on line at: http://jn.physiology.org/content/86/6/2998

Hedrick, K. R., and Cox, S. J. (2013). Structure-preserving model reduction of passive and quasi-active neurons. *J. Comput. Neurosci.* 34, 1–26. doi: 10.1007/s10827-012-0403-y

Hedrick, K. R., and Cox, S. J. (2014). "Morphological reduction of dendritic neurons," in *The Computing Dendrite*, eds H. Cuntz, M. Remme, and B. Torben-Nielsen (New York, NY: Springer), 483–506.

Jadi, M. P., Behabadi, B. F., Poleg-Polsky, A., Schiller, J., and Mel, B. W. (2014). An augmented two-layer model captures nonlinear analog spatial integration effects in pyramidal neuron dendrites. *Proc. IEEE* 102. 782–798. doi: 10.1109/JPROC.2014.2312671

Kellems, A. R., Chaturantabut, S., Sorensen, D. C., and Cox, S. J. (2010). Morphologically accurate reduced order modeling of spiking neurons. *J. Comput. Neurosci.* 28, 477–494. doi: 10.1007/s10827-010-0229-4

Kozloski, J., and Wagner, J., (2011). An ultrascalable solution to large-scale neural tissue simulation. Front. Neuroinform. 5, 1–21. doi: 10.3389/fninf.2011.00015

Migliore, M., and Shepherd, G. M. (2002). Emerging rules for the distributions of active dendritic conductances. *Nat. Rev. Neurosci.* 3, 362–370. doi: 10.1038/nrn810

Peron, S. P., Jones, P. W., and Gabbiani, F. (2009). Precise subcellular input retinotopy and its computational consequences in an identified visual interneuron. *Neuron* 63, 830–842. doi: 10.1016/j.neuron.2009.09.010

Rempe, M. J., and Chopp, D. L. (2006). A predictor–corrector algorithm for reaction-diffusion equations associated with neural activity on branched structures. *SIAM J. Sci. Comput.* 28, 2139–2161. doi: 10.1137/050643210

Rempe, M. J., Spruston, N., Kath, W. L., and Chopp, D. L. (2008). Compartmental neural simulations with spatial adaptivity. *J. Comput. Neurosci.* 25, 465–480. doi: 10.1007/s10827-008-0089-3

Conflict of Interest Statement: The authors declare that the research was conducted in the absence of any commercial or financial relationships that could be construed as a potential conflict of interest.

Received: 12 May 2014; accepted: 27 November 2014; published online: 16 December 2014.

Citation: Du B, Sorensen D and Cox SJ (2014) Model reduction of strong-weak neurons. Front. Comput. Neurosci. ***8****:164. doi: 10.3389/fncom.2014.00164*

This article was submitted to the journal Frontiers in Computational Neuroscience.

frontiers in Computational Neuroscience

HYPOTHESIS AND THEORY
published: 10 August 2015
doi: 10.3389/fncom.2015.00098

A simple transfer function for nonlinear dendritic integration

Matthew F. Singh[1,2]* *and David H. Zald*[1,3]*

[1] Department of Psychology, Vanderbilt University, Nashville, TN, USA, [2] Department of Psychiatry, Vanderbilt University, Nashville, TN, USA, [3] The Program in Neurosciences, Washington University School of Medicine in St. Louis, St. Louis, MO, USA

Relatively recent advances in patch clamp recordings and iontophoresis have enabled unprecedented study of neuronal post-synaptic integration ("dendritic integration"). Findings support a separate layer of integration in the dendritic branches before potentials reach the cell's soma. While integration between branches obeys previous linear assumptions, proximal inputs within a branch produce threshold nonlinearity, which some authors have likened to the sigmoid function. Here we show the implausibility of a sigmoidal relation and present a more realistic transfer function in both an elegant artificial form and a biophysically derived form that further considers input locations along the dendritic arbor. As the distance between input locations determines their ability to produce nonlinear interactions, models incorporating dendritic topology are essential to understanding the computational power afforded by these early stages of integration. We use the biophysical transfer function to emulate empirical data using biophysical parameters and describe the conditions under which the artificial and biophysically derived forms are equivalent.

Keywords: dendrite, transfer function, neural network, NMDA spike, pyramidal cell

OPEN ACCESS

Edited by:
Sergey M. Korogod, National Academy of Sciences of Ukraine, Ukraine

Reviewed by:
Benjamin Torben-Nielsen, Okinawa Institute of Science and Technology, Japan
Malte J. Rasch, Beijing Normal University, China

***Correspondence:**
Matthew F. Singh, The Program in Neurosciences, 660 S. Euclid Ave., St. Louis, MO 63110, USA
f.singh@wustl.edu;
David H. Zald, Department of Psychology, Vanderbilt University, PMB 407817, Nashville, TN 37240-7817, USA
david.zald@vanderbilt.edu

Received: *16 March 2015*
Accepted: *15 July 2015*
Published: *10 August 2015*

Citation:
Singh MF and Zald DH (2015) A simple transfer function for nonlinear dendritic integration. Front. Comput. Neurosci. 9:98. doi: 10.3389/fncom.2015.00098

Introduction

Over the past decade, increasing evidence indicates that dendritic architecture plays an active role in shaping somatic responses to synaptic input. Particularly in pyramidal neurons (e.g., Schiller et al., 2000; van Elburg and van Ooyen, 2010; Branco and Häusser, 2011), conceptualizations of the dendritic arbors have shifted from organizational topologies to primary units of computation with unique integration properties that challenge most network abstractions of biological neurons (Häusser and Mel, 2003; Spruston and Kath, 2004; Branco and Häusser, 2010, 2011). From the beginning of computational modeling, network neurons (or "nodes") have been described as non-linear integrators (often sigmoidal) of linear input. Most commonly, this translates into a nonlinear transform of the global sum of synaptically weighted input (inner-product of an input and weight vector). However, an increasing body of evidence suggests non-linear summation between relatively close inputs within a dendritic branch. For pyramidal neurons, these appear linear for weak inputs, highly super-linear for intermediate inputs and slightly sub-linear for strong inputs (Polsky et al., 2004; Branco and Häusser, 2011). Suggested bio-mechanisms focus upon regenerative branch spikes involving Na^+, Ca^+, and/or NMDA spikes (Schiller et al., 2000; Polsky et al., 2004; Antic et al., 2010). Fortunately, this effect becomes increasingly linear as the distance between inputs increases and when summation occurs between branches, suggesting a first layer of non-linear within-branch integration followed by a global integrator of their summed output (Polsky et al., 2004; Spruston and Kath, 2004). This framework has sometimes likened a single

neuron to a two or three-layer neural network with the outer (dendritic) layers all converging upon a single (somatic) node (Häusser and Mel, 2003; Polsky et al., 2004; Spruston and Kath, 2004). However, within this metaphor, the literature has consistently referred to sigmoidal dendritic integrators that do not fully match data. In fact, a sigmoidal function quickly generates implausible scenarios such as extremely limited ranges of inhibitory post-synaptic potentials (IPSP's). This is due to the fact that the sigmoid is anti-symmetric about its mid-point near a peak excitatory post-synaptic potential (EPSP) amplitude of 4 mV measured at the soma (Polsky et al., 2004). Moreover, the sigmoid's anti-symmetry implies both sides of the midpoint must be equally linear, which does not allow the observed sub-threshold linearity with extreme nonlinearity post-threshold (see **Figure 1A**). Rather, the data most resemble a monotonic "hook," which some have more accurately described as linear-nonlinear with the nonlinear segment concave (Jadi et al., 2014). Based upon current data of subthreshold linearity, it appears the sigmoid's resemblance is only due to oversampling the function's nonlinear upper half (specifically only positive inputs).

In contrast to the oft described "sigmoid," Poirazi et al. (2003) produced a two-layer model with a binomial-logistic hybrid function of synaptic activation count that resembles a "linear hook" within certain boundaries. This study provided some of the first evidence that a two-layer network (with a non-sigmoidal input layer) can approximate the firing frequency of a detailed model pyramidal cell (see **Figure 6B**). Importantly, Poirazi et al.'s (2003) model used the same linear-hook type function for each dendrite-to-soma transfer prior to a global sigmoidal transform. Results firmly established that simple linear-concave functions of binary input form an adequate input layer to describe firing rates (after a sigmoidal global transform). However, many applications involve continuous metrics of synaptic input or dynamic somatic compartments as in bursting behavior. These situations require information about membrane potentials rather than converting the number of glutamatergic synapses activated into firing rates. Here we use the separation principle of fast-slow dynamics (Genet and Delord, 2002; Wainrib et al., 2012) to derive simple, artificial and biophysical dendritic transfer functions for changes in somatic membrane potential. The biophysical transfer function is then compared to experimental data. Both versions of the transfer function are linear-sigmoid hybrids and hence computationally simple. This is notable because most current models use a single dendritic compartment (or none) for computational simplicity as individual branch models drastically increase processing time. However, the use of time-independent transfer functions removes this barrier as a single nodal compartment may then integrate the non-linear dendritic components. Rather than simulating each branch with a dynamical system of membrane potential, a suitable transfer function may directly convert dendritic input to the induced somatic potential.

Methods

General Transfer Function

We begin by characterizing the dendritic transfer function $T_D(V)$:

1. As the distance between input sites increases, T should become the linear sum.
2. At close distances, T is linear for weak inputs, super-linear for intermediate inputs, and slightly sub-linear for strong inputs.
3. Three currents must be accounted for: fast ionic currents (I_{fast}), leak current (I_{leak}), and a slow NMDAR-mediated current (I_{NMDA}).

Biophysical models have made use of the fast-slow dynamics of dendritic membrane to neglect relaxation times of fast channels, instead keeping them constant at equilibrium conductance (Genet and Delord, 2002). To remain time-independent (necessary for a transfer function), we model the net hyper/depolarization for a set of proximal inputs [$T_D(x_1, x_2, x_3,\ldots)$] using the distances between input sites as a proxy for time in determining an expectation for leak and NMDAR-mediated currents. The change in potential (relative to base) is then expressed as a bounded sum of linear inputs and nonlinear NMDAR-mediated currents.

As previously mentioned, the sigmoid function does not converge to the linear summation observed for inter-branch dendritic currents. Instead we make use of a juxtaposition of sigmoid integrals of the total polarization to form a locally linear function $G(V)$ with upper and lower bounds b_u, b_l.

$$0 < \alpha_{L,U},\ b_L < b_{U,}G(\mathrm{V}) = \int \frac{1}{1+e^{-\alpha_L(V-b_L)}} - \frac{1}{1+e^{-\alpha_U(V-b_U)}}dV$$

$$G(V) = ln\left(\frac{\left(1+e^{\alpha_L(V-b_L)}\right)^{\frac{1}{\alpha_L}}}{\left(1+e^{\alpha_U(V-b_U)}\right)^{\frac{1}{\alpha_U}}}\right) + b_L \quad (1)$$

Here α_L and α_U are the curvature of lower and upper boundaries respectively, while b_L and b_U are the lower and upper boundaries with the constant b_L added to center the function (**Figure 1B**). Throughout, all potentials are translated so that $E_{Leak} = 0$ for the leak potential. Using the multivariate logistic-sigmoid: $\sigma(X_D):R^n \rightarrow R = [1+\exp(-\Sigma\{X_i\})]^{-1}$ for input vector X_D we first describe a simple transfer function which, as can be seen in **Figure 1A**, qualitatively provides a superior fit relative to a simple sigmoid:

$$T_{Artificial}(X) = G\left(c_d\sigma\left(a_d\left[\hat{X}_D - b_d\right]\right) + \sum X_i\right) \quad (2)$$

This naïve form simply takes the boundary of the sum of linear and sigmoidally-nonlinear components from the dendritic input vector X with c_d the nonlinear maximum, a_d the curvature, and b_d the mid-point (related to threshold) of the nonlinear component (**Figure 1A**). Although not biophysical, this form bears substantial resemblance to empirical dendritic integration (e.g., Polsky et al., 2004) in its linear-hook appearance and is at least an improvement on linear-integration when few parameters are known. It must be noted that, the artificial transfer function does not consider the locations of input. However, we will now derive a biophysically-reasonable description of dendritic integration for which the naïve form becomes a specific case.

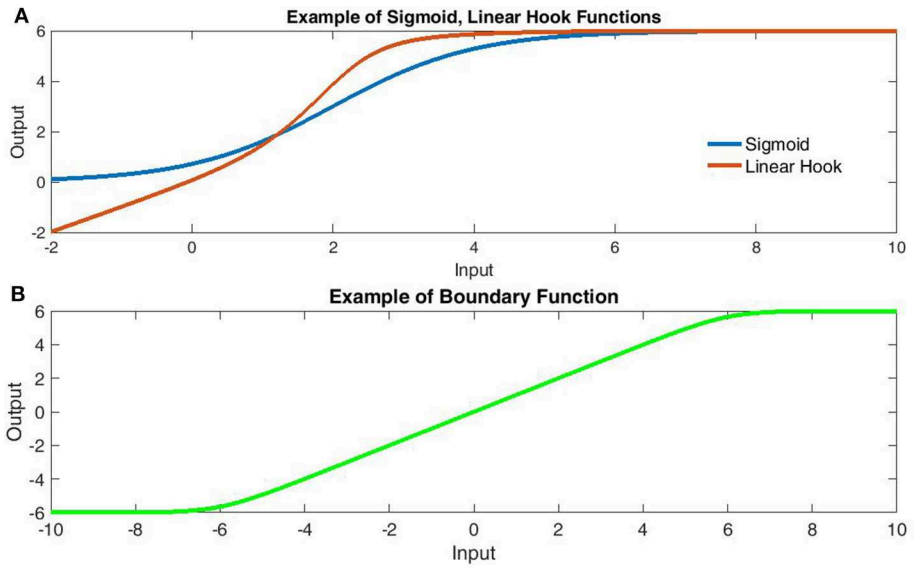

FIGURE 1 | Comparison of transfer function components. (A) Comparison of sigmoidal (Blue) and Linear Hook functions (Red). The linear hook is a bounded sum of linear and sigmoidal functions [Bound(x + σ(x))]. Note that the sigmoid function fails to capture the subthreshold linearity. **(B)** The linear-boundary function with limits at ±6. The linear boundary function applies soft edges to a linear component and is formed by taking the area under the difference of sigmoids.

Biophysical Transfer Function

To approximate peak EPSP amplitude as a function of input only, we make use of hierarchical dendritic time scales with the separation principle. In this approach, systems with slow and fast components are separated into a fast subsystem, in which the slow variables are held constant, and a slow subsystem contained in the fast nullcline. In the current case, the "linear" fast ionic currents stem from channels with substantially shorter opening times than NMDAR's, while the opening of NMDAR's and Mg^{2+} unblocking is many orders quicker than channel closing (Jahr and Stevens, 1990a,b). As such, we consider the peak EPSP a sum of passively propagating fast ionic currents and dynamically generated NMDA spikes, mirroring the experimental separation of "linear" (fast ionic) and "nonlinear" (spike) components (**Figure 2**). To remain time-independent, inputs are viewed in terms of the induced local depolarization (v_i) as in neurotransmission and brief current pulses. Throughout, vectors are ordered from the least to most distal dendritic segments and all potentials are translated for a resting potential of zero.

Spatial Decay

Because the fast ionic current is propagated passively, we consider it subject to spatial decay only. Decay is characterized by the functional length constant (λ), which is an empirical parameter derived by fitting attenuation data to a negative exponential of distance. Hence the attenuation from spatial decay, denoted $\varphi(x_{j\to i})$ is a negative exponential of the intervening distance:

$$\varphi\left(x_{j\to i}\right) = e^{-\frac{|x_j - x_i|}{\lambda}} \quad (3)$$

The functional length constant should not be confused with Rall's (1969) length constant for an infinite cable at steady state. In all simulations we used a length constant for arrival in spike generation half that of the length constant for reaching the soma. This method ensures that stimulus separation has more influence over dendritic spike threshold than passive somatic transients. Similarly, experimental findings demonstrate that increasing inter-electrode distance by a few tens of microns has enormous influence on the spike generation threshold (e.g., Polsky et al., 2004), while the changes in attenuation over that distance should be marginal.

Local Potential

For simplicity, we divide the NMDAR system into binary open and closed phases and take expectations based on open/close time distributions to transition between phases (**Figure 2**). While the duration prior to initial opening is considered based on single channel kinetics, the system's open period is defined by the resulting macroscopic current. This dissociation is based upon findings that single NMDAR activations may elicit cluster activation (Gibb and Colquhoun, 1991). Because NMDAR-mediated bursts and clustering determine the resulting macroscopic current dynamics, rather than isolated channels, we consider the NMDAR system's activation duration on the order of burst/cluster lengths as opposed to the brief openings of individual channels (Wyllie et al., 1998). Thus, the duration prior to NMDAR system activation is based on short single channel kinetics, while the period of activation is based on long macroscopic dynamics. Prior to NMDAR opening we consider two sources of depolarization: local and nonlocal input, both of which are subject to decay. Local inputs are subject only to

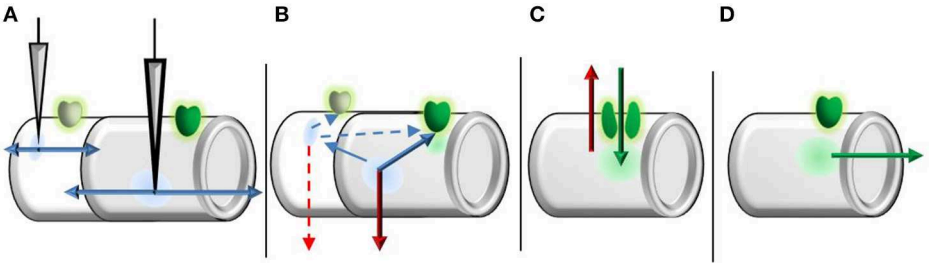

FIGURE 2 | Graphical representation of time-course separation used to derive the transfer function. (A) Fast ionic (linear) components exit the compartment near instantly and propagate bidirectionally. **(B)** Prior to NMDAR opening, local potentials (within a compartment) are subject to temporal decay (leak current). Starting potentials at channel opening are then formed by spatially decayed fast ionic currents from other compartments and temporally decayed potentials from the relevant compartment. The length of duration prior to opening is on the order of single channel kinetics, as a single channel is sufficient to trigger bursting/clustering behavior. **(C)** While the NMDAR system is active, only two currents are considered: leak current (red) and NMDAR current (green). The length of NMDAR system activation is on the much larger order of burst/cluster length to represent macroscopic currents, rather than the far shorter individual channel open durations. **(D)** After the NMDAR system inactivates, NMDAR currents propagate toward the soma under spatial decay.

temporal (leak) decay, while we only consider spatial decay for nonlocal inputs prior to channel opening. Letting the closed times (prior to opening) be multi-exponentially distributed (Gibb and Colquhoun, 1991, 1992; Wyllie et al., 1998), the expected leak constant at channel opening is then:

$$\varphi_i : \sum_{i=1}^{k} \theta_i \frac{R_m C}{\tau_i + R_m C} \tag{4}$$

Here C denotes membrane capacitance, τ_i are the time constants of each exponential, θ_i the associated amplitudes, and the product $R_m C$ gives the time constant of temporal decay. Repolarization due to leak current is represented in its usual linear differential equation, producing a solution proportional to the initial condition (as with spatial decay). Because Equations (3) and (4) represent constants of spatial and temporal decay each case requires only a single computation. Ordering segments from least to most distal, potentials at channel opening: $v(t_{ON})$, may then be represented with a computationally efficient linear matrix equation of the input vector $v(0)$:

$$v\left(t_{ON}\right) \sim \Phi v(0) \tag{5.1}$$

$$\Phi_{i,\,j} : = \begin{cases} \varphi(x_{j \to i}) & i \neq j \\ \varphi_i & i = j \end{cases} \tag{5.2}$$

This matrix is symmetric with diagonals corresponding to the constants of temporal decay while nondiagonals correspond to the constants of spatial decay when currents propagate from more distal locations($i<j$) and backpropagate ($i>j$). As backpropagation is generally considered more efficient we consider the possibility of differential length constants in Section Varying Distance, although both cases are exponential form of Equation (3). In computing NMDA spikes we use the following alternative notation for brevity in which temporal dynamics start at channel opening:

$$V\left(x_i, 0\right) : = V_0\left(x_i\right) : = \; v_i(t_{ON}) \tag{6}$$

NMDA Spikes

As stated previously, the NMDAR system may be separated into slow (closing/current flow) and fast (opening/Mg^{2+} gating) subcomponents. Because the fast subsystem rapidly converges to the steady state, the gate's nullcline is stable while the channel is open with nullcline:

$$B\left(V\right) = \frac{1}{1 + e^{-\left(\frac{V - V_s}{k_s}\right)}} \tag{7}$$

Due to the strong time separation, we follow the tradition of considering the gating function to be instantaneous, hence defined by the nullcline (Jahr and Stevens, 1990a,b). In contrast, the slow subsystem inherits the channel's long closing time scale and describes current flow for leak and NMDAR components. For simplicity we only consider the leak and NMDAR components:

$$C\frac{\partial V}{\partial t} = -\frac{V}{R_m} + gB\left(V\right)\left(E - V\right) \tag{8}$$

Here g denotes the max NMDAR conductance of the dendritic segment while E denotes the NMDAR reversal potential. As before, all potentials are translated for a resting potential of zero. In considering only NMDAR and leak current, it is necessary to increase the gating component's slope (decrease k_s), less this reduction lead to global stability while the channel is open. Global stability would compromise the voltage dependence of spike production as glutamate binding would always result in an NMDA spike. Depending on parametrization, Equation (9) may have up to three equilibria, enabling bistability. Equilibria correspond to solutions of the implicit equation:

$$V_{eq}(x) = \frac{gE}{g + {R_m}^{-1} B(V_{eq}(x))^{-1}} = \frac{\left(\frac{gE}{g+{R_m}^{-1}}\right)}{1 + \mathrm{Exp}\left[-\frac{(V_{eq}(x) - V_{mid} + k\ ln[gR_m + 1])}{k}\right]} \quad (9)$$

In the case of three equilibria, solutions possess locally stable lower (resting potential) and upper (saturation) equilibria. The middle equilibrium in this case is unstable leading to the "all or none" bifurcation in spikes. The single equilibrium case, in contrast, produces global stability, usually near the NMDAR reversal potential. As such, the single equilibrium case is pathological in the absence of other modulating voltage gated cation channels (VGC's) as glutamate binding would almost always produce an NMDA spike. However, in biological conditions, NMDA spikes still approach the NMDAR reversal potential, so the locally stable equilibria are roughly preserved. As long as three equilibria are maintained in the reduction to only leak and NMDAR dynamics, the locally stable equilibria remain accurate. To produce three equilibria, we simply modify the slope of Mg^{2+} blockade to compensate for the nonlinearity lost in removing other VGC's. However, it is important to note that full high-dimensional models include other equilibria due to Na^+-spikelet's and, in the apical dendrite, Ca^{2+} spikes (see Antic et al., 2010). Also, although the stable equilibria are unmodified in the bistable case, the point of bifurcation (unstable equilibrium) may be. Biological evidence suggests other VGC's mediate both the threshold and amplitude of NMDA spikes such as Na^+ (VGSC's) and Ca^+ channels (VGCC's) as revealed with application of Na^+ blocker TTX and Ca^{2+} blocker cadmium (Schiller et al., 2000). While the reduced dynamics still produce the correct amplitude for NMDA spikes, they may not produce the correct threshold in the absence of VGSC's/VGCC's. Hence, it may be necessary to additionally modify the midpoint of Mg^{2+} blockade. In the results section we describe when modification is and is not necessary due to the non-uniform distribution of spike thresholds (Major et al., 2008).

We make further reductions through the bifurcation of solutions. In assessing temporal dynamics after the initial channel opening, we consider the long time course of NMDAR bursts and clustering which give rise to macroscopic currents rather than the brief individual open durations Both decay and spiking occur on far shorter time scales than bursts, so states just prior to closing are almost binary and represent the nonlinear component of peak EPSP. As with the opening of individual channels, the population burst duration is considered multi-exponentially distributed (Gibb and Colquhoun, 1991, 1992; Wyllie et al., 1998) producing the expected value (V_{NMDA}):

$$V_{NMDA}(x) = \sum_{i=1}^{n} \frac{\omega_i}{a_i} \int e^{-\frac{t}{a_i}} V(x,t)\, dt = \sum_{i=1}^{n} \omega_i \left(\frac{R_m C}{R_m C + a_i}\right) \left[\frac{g}{C} \int e^{-\frac{t}{a_i}} B\left(V(x,t)\right) \left(E - V(x,t)\right) dt + V_0\right] \quad (10)$$

with ω_i the amplitude of the exponential component with slope a_i. In present form, however, both the local dynamics (Equation 8) and expected NMDA component (Equation 10) lack explicit solutions in terms of ordinary functions. Using the bifurcation, we approximate Equations (8) and (10) by making Mg^{2+} blockade constant, following channel opening. In a fully dynamic regime, this method would not be justified. However, because we are only interested in which equilibria solutions approach, rather than how they get there, this method has fair accuracy, provided the earlier condition that Equation (9) has three solutions. As the slope of Mg^{2+} blockade increases (as was done to ensure bistability), the bifurcation point approaches the midpoint of B(V) (Equation 8). At the same time B(V) approaches a step function. The result is that the Mg^{2+} blockade approaches invariance except for an increasingly small region about V_{mid}. Provided a sufficiently small k to ensure bistability, the Mg^{2+} blockade may then be approximated as invariant for initial points at channel opening sufficiently far from V_{mid}. Changing the dynamic B(V) to a constant function of potential at channel opening $B(V_0)$ produces the following solution to Equation (8):

$$V_{NMDA}(x,t) \sim V_0(x) + \left(\frac{gE}{g + {R_m}^{-1} B(V_0(x))^{-1}} - V_0(x)\right) \left(1 - Exp\left[-\left(\frac{gB\left(V_0(x)\right) + {R_m}^{-1}}{C}\right) t\right]\right) \quad (11)$$

Hence with Mg^{2+} blockade constant while the channels are open Equation (10) becomes linear, so all solutions exponentially approach an equilibrium determined by the Mg^{2+} blockade at channel opening. We stress that this approach is only valid in approximating the path toward an equilibrium for Equation (8), with bistability induced by increasing the Mg^{2+} blockade slope. Because the transfer function only considers peak EPSP, this approach is sufficient for the current purposes but is not a valid approximation for the time course of fully dynamic dendrites. As an exponential, this equation is readily combined with burst length distributions. For a given starting potential, the ending potential with an n-exponential burst length distribution is itself n-exponentially distributed following translation. The expected value used in computing peak EPSP is:

$$V_{NMDA}(x) \sim V_0(x) + \left(\frac{gE}{g + {R_m}^{-1} B(V_0(x))^{-1}} - V_0(x)\right) \left[1 - \sum_{i=1}^{n} \frac{\omega_i}{1 + a_i \left(\frac{gB(V_0(x)) + {R_m}^{-1}}{C}\right)}\right] \quad (12)$$

While we only present the case for multi-exponential closing distributions, the expected value is relatively insensitive to the type of distribution chosen as spiking and decay occur on much shorter time scales than the fall of NMDAR-mediated currents. When the NMDAR burst/cluster durations are considered sufficiently long, Equations (11) and (12) simplify

to a simple sigmoid as in the artificial transfer function's nonlinear component in Equation (2):

$$V_{NMDA}(x) \sim \frac{gE}{g + {R_m}^{-1} B(V_0(x))^{-1}} \quad (13.1)$$

$$= \left(\frac{gE}{g + {R_m}^{-1}}\right) \frac{1}{1 + \mathrm{Exp}\left[-\frac{(V_0(x) - V_{mid} + k\ ln[gR_m + 1])}{k}\right]} \quad (13.2)$$

The second Equation (13.2) results from substituting the Mg^{2+} blockade Equation (7) and is the same as the equilibria Equation (9) when the Mg^{2+} blockade is assumed invariant between initial depolarization and its limiting equilibrium (spike or rest). As discussed previously, the number of starting points (initial depolarizations) for which this assumption is justified increases with the slope of Equation (7) (inversely proportional to k_s). Hence, as Mg^{2+} blockade becomes increasingly binary, Equation (12) becomes an increasingly accurate description of NMDAR bistability. When the burst/cluster lengths are further assumed sufficiently long to approach limiting states (spike or rest), Equation (12) reduces to Equations (13). This reduction is greatly desirable as Equations (13) do not require explicit knowledge of burst length distributions.

Dendritic Integration

In generating a (time-independent) transfer function, we sacrifice some information concerning the interaction of nonlinear components (NMDAR currents) in separate dendritic segments. Regardless of the number of incoming spikes, for instance, the induced somatic voltage would not be expected to significantly exceed the NMDAR reversal potential. Due to the continuous distribution of NMDAR's along the path of propagation, surplus depolarization would leak back through NMDAR channels before ever reaching the soma. However, the time independence of a transfer function prohibits fully dynamical propagation. While no individual spike crosses the NMDAR reversal potential using the method described above, summation of multiple spikes may, necessitating a boundary function as in Equation (1) to mimic dendritic saturation. Although the function *G(V)* provides a soft boundary, all other components of the function are unchanged. Hence the final transfer function for a given dendrite is the bounded sum of linear (fast ionic currents) and nonlinear (NMDAR-mediated) components. The final dendritic transfer function, $T_{Bio}(\nu)$, may then be described explicitly in terms of the input vector ν and decay vector δ:

$$\delta_i := e^{\left(-\frac{x_i \to soma}{\lambda}\right)} \quad (14.1)$$

$$T_{Bio}(\nu) = G\left(\sum \delta_i \left[\nu_i + V_{NMDA}(x_i)\right]\right) \quad (14.2)$$

Here λ is the functional length constant as in Equation (3), $V_{NMDA}(x_i)$ is the nonlinear component for each input location, described by Equations (12) and (13) and *G(V)* is the linear-boundary function described in Equation (1). If desired, Equation (14.2) may be easily modified to allow differential spatial decay of spikes and subthreshold EPSP's. It is important to note that the boundary function to should be set to approach saturation with a single spike from the most proximal synapse, preventing the linear-summation of subthreshold EPSP's from applying to NMDA spikes in Equation (14.2). EPSP's between branches are allowed to sum linearly (Polsky et al., 2004) so the global transfer function is then the sum of individual dendritic transfer functions. For a single synapse with single-pulse stimulation, the use of an artificial boundary function is unnecessary as Equation (13.2) may be easily modified to the relative spike amplitude.

$$V_{Rel.Spike} = \left(\frac{gE}{g + {R_m}^{-1}} - \nu(0)\right) \frac{1}{1 + \mathrm{Exp}\left[-\frac{(V_0(x) - V_{mid} + k\ ln[gR_m + 1])}{k}\right]} \quad (15.1)$$

$$T_{Single} = \nu_0 + V_{Rel.Spike} \quad (15.2)$$

Here *ν(0)* is the initial local depolarization. For a single synapse the sum of fast ionic currents and the relative spike approximates the (bounded) maximal EPSP amplitude. However, the sum of spikes, each bounded near the NMDAR reversal potential, does not necessarily share that boundary so the artificial boundary function is necessary for all nontrivial applications to compensate for the sublinear summation of spikes (Polsky et al., 2004).

Parameterization

Throughout, parametrizations were generally that of Behabadi and Mel (2014): $R_m = 10\ \mathrm{K\Omega cm^2}$, $E_{Leak} = -70\ \mathrm{mV}$ (translated to 0 mV), $E_{NMDA} = 0\ \mathrm{mV}$ (translated to 70 mV), $g_{(NMDA)} =$ 3.9 nS. However, we used the conventional $C = 1\ \mu\mathrm{F/cm^2}$ as opposed to Behabadi and Mel's unusually large capacitance of twice that much. The mid potential for NMDAR's was $V_s = -23.7\ \mathrm{mV}$ (translated to 46.3 mV, Jadi et al., 2012). However, we only used 1/5 the typical value of k_s (2.5 vs. 12.5 mV, Major et al., 2008; Jadi et al., 2012), in order to compensate for the nonlinearity lost in computing expectations. This value was selected based upon the slope of target data (see **Figure 4**). To replicate double pulse data, the method of González et al. (2011) was utilized without modification. Durations prior to channel opening and burst/cluster lengths were based upon the multi-exponentials reported by Wyllie et al. (1998) for recombinant NR1a/NR2A after removing opening components less than 0.5 ms and burst/cluster length components less than 2 ms and reweighting. The filter on inter-opening times was to allow time for nonlocal inputs to reach the spike generation sites, while burst length distributions were filtered to place emphasis on the slower components which carry the vast majority of charge (Wyllie et al., 1998). NR1a/NR2A subunit was chosen due to its dominant role in spike generation (Polsky et al., 2009). Compartments for each input site had lengths of 10 μm and diameter 1 μm. To generate the observed small spike generation zone, the functional length constant for inter-compartmental contributions to spike generation was always half that of transients reaching the soma. Without this modification, the increasing threshold for spike generation with inter-electrode spacing would have to be on the same order as typical spatial decay which does not agree with the far greater effects observed empirically (see **Figure 4**).

Simulations

To test the biophysical transfer function, we performed two sets of simulations custom-coded in MatLab2015a (Mathworks Inc., Natick, MA). In the first set of simulations we used a 5-state kinetic model of NMDAR's (Destexhe et al., 1998) to test appropriateness of the earlier separation assumptions. This choice was based upon the 5-state model's high temporal accuracy in describing NMDAR conformation changes which serves as a suitable contrast to a temporally agnostic transfer function. Membrane potential was modeled similarly to Equation (8) with NMDAR current multiplied by the probability of the channel having an open conformation. Membrane potential parameterizations during the kinetic simulations were identical to those used in the transfer functions, except for NMDAR maximal conductance which was set to the original 0.6 nS for the kinetic model (Destexhe et al., 1998) and inversely weighted for peak opening ($\sim$1/3) in the transfer function. Because input was concentrated on a single site, we used the full inter-opening distribution described by Wyllie et al. (1998). The initial Glutamate concentration was 1 mMol in the synaptic cleft for a single input instance with stimulation length 10 ms during which membrane potential was held constant. We compared peak membrane potentials to those predicted by Equations (12) and (13). The upper bound was set equal to the transfer function's "spike" peak amplitude.

In the second set of simulations, we simulated conditions of the seminal paper by Polsky et al. (2004) which was among the first to examine the location dependence of NMDA spike generation. Using whole-cell patch clamp recordings, the authors focally stimulated basal dendrites of cortical pyramidal cells using a pair of electrodes with spacings ranging from 20 to 200 μm. EPSP's from separate dendritic branches seemed to sum linearly at the somatic recording site, while separate EPSP's generated within a dendritic branch produced threshold-nonlinear interactions (NMDA spikes). The relevant analyses focused on the relation between stimulating sites within a branch individually and simultaneously. The "arithmetic sum" or "expected" peak EPSP was defined as the sum of individually evoked EPSP peaks and was compared to the "actual" peak EPSP elicited with simultaneous stimuli (**Figure 4**). Stimulation of dendrites can occur both in isolation (single pulse) or in combination, such as paired-pulse stimulations which produce more robust EPSPs than responses to single pulses. When varying inter-electrode spacing, we largely relied on paired-pulse stimulation (20 ms ISI), while a separate analyses was performed to compare paired and single-pulse stimulation with a fixed inter-electrode spacing (30 μm; **Figure 5**). All code is available online or by emailing the corresponding author.

Results

Kinetic Model

Simulations with the 5-state kinetic NMDAR model generally supported the appropriateness of transfer function assumptions, provided a sufficiently large slope for Mg^{2+} blockade. As stated previously, NMDAR bistability relies on additional currents such as inward-rectifying K^+ (Shoemaker, 2011) in biological settings. Using the standard slope for Mg^{2+} blockade, a system composed solely of leak and NMDAR currents will possess a single equilibrium (**Figure 3D**) corresponding to a spike save in cases of extremely low NMDAR conductance (in the current case <150 pS; **Figure 3D**). As such, 5-state simulations used the same parametrization as the transfer functions (five times standard Mg^{2+} blockade slope). Simulations over a 50 ms period produced maximum peak EPSP's with the empirically observed "linear-hook" form described previously (**Figure 3A**). Three different transfer functions were simulated with all parameterizations identical except end time. The "Distribution Model" used the modified version of Wyllie et al. (1998) super-cluster lengths described previously. The "Long Distribution Model" used a single exponentially distributed (50 ms) burst/cluster length, while the "Simple Model" was as described in Equation (13) and only considers the limiting states (infinite burst/cluster duration). As should be expected, short burst/cluster lengths consistently over-predicted peak EPSP's as the local nonlinear currents did not have sufficient time to decay. The Simple Model, in contrast, only began to over-predict once approaching the Mg^{2+} midpoint near spike threshold. A simple and more accurate solution for the distributed closing time models would be use of a piecewise function making peak EPSP the maximum of linear (fast ionic) and nonlinear (NMDAR-mediated) components, rather than a bounded sum. Unfortunately, this approach is mathematically undesirable as it does not admit continuous derivatives of all orders. However, burst length distributions add little additional information due to the extremely short spike rise time (**Figure 3C**). As such, the Simple Model may also be more accurate in describing spike amplitude, particularly in subthreshold cases (**Figure 3B**). Overall, the rapid spike rise times (**Figure 3C**) and NMDAR bistability (**Figure 3B**) strongly support the time scale separations used in binary NMDAR open/shut states and bifurcations in Mg^{2+} blockade. In fact, results indicate that these factors may be exploited to an even greater extent, by further increasing the slope of Mg^{2+} blockade to approach the all-or-none spike threshold near Mg^{2+} blockade's midpoint (**Figure 3B**).

Varying Distance

To test the transfer function's accuracy, simulations were performed under the conditions of Polsky et al. (2004), described earlier. In all cases, we used a distance of 200 μm from the proximal input site to the soma, based upon the reported 80–250 μm range. While the proximal input site was fixed, distal input sites were varied to generate the 20, 60, and 200 μm inter-electrode spacings (Polsky et al., 2004). The boundary function was parameterized to match the observed boundaries ($b_U = 12$ mV, $b_L = -12$ mV, $\alpha_{L,U} = 0.5$).The simulation design included two cases of model type (Simple Model and Distribution-based) and both symmetric and asymmetric spatial decay. A functional length constant of 77 μm has been reported for spikes/plateaus in basal dendrites propagating toward the soma (Major et al., 2008) and asymmetric length constants

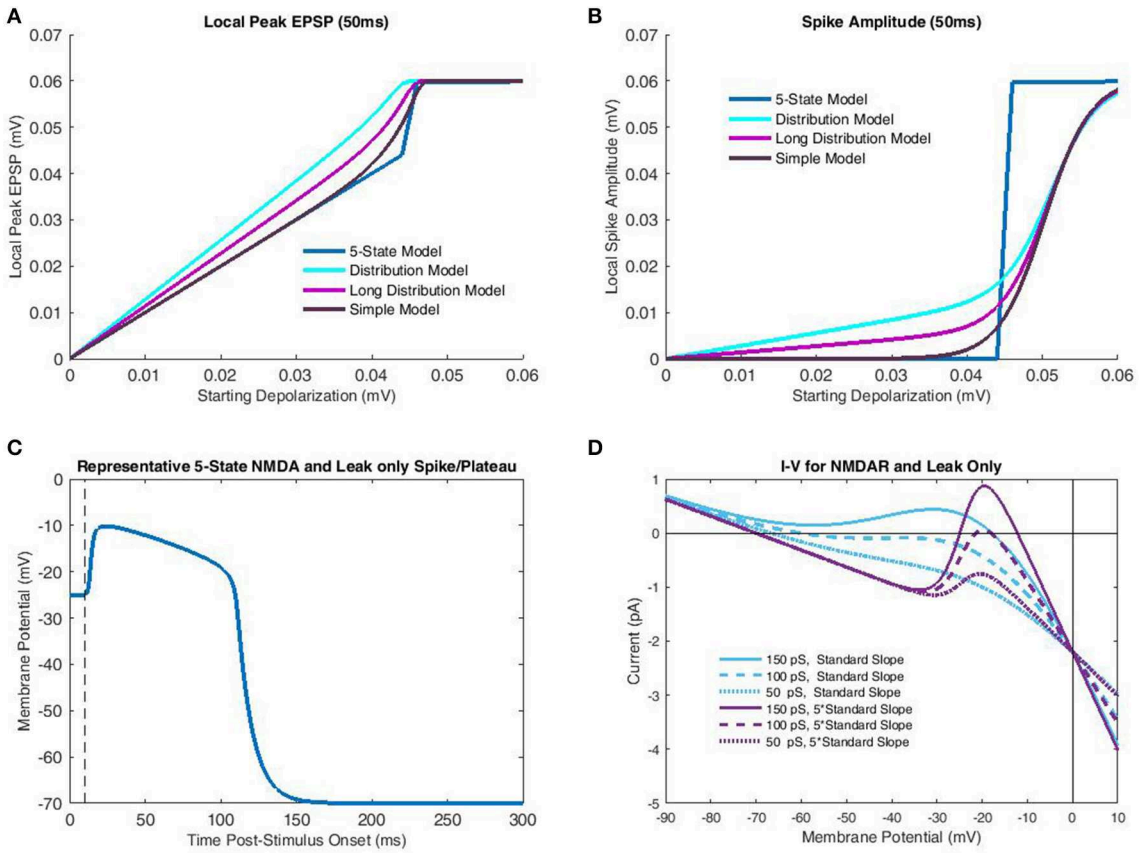

FIGURE 3 | Comparison of transfer functions with a 5-state kinetic model of NMDAR activation. In the kinetic-model simulations parameterization of the membrane potential was identical to that of the transfer functions, which included the increased slope of Mg^{2+} blockade necessary for bistability. Like the transfer function only leak and NMDAR currents were considered. **(A)** Peak local EPSP's predicted for each model (single-pulse) are plotted as a function of depolarization at time of glutamate release. The 5-state model, simulated over a 50 ms interval for each case, largely demonstrates binary behavior, with a linear subthreshold portion, and a constant (spike) peak EPSP post-threshold. The "Distribution Model" corresponds to the transfer function with empirical cluster length distributions, while the "Long Distribution Model" uses a 50 ms mono-exponential distribution. The "Simple Model" only considers limit states and so is equivalent to an infinite burst/cluster length. The greater semblance of "Long Distribution" and "Simple" models to the 5-state model is due to the decreased dependence on fast-components which do not allow sufficient time for temporal decay to dominate nonlinear components. **(B)** Spike amplitude is plotted against depolarization at the end of Glutamate release for the same models as **(A)**. In all cases, the "Simple Model" of limit states bears greatest semblance to the 5-state model, particularly subthreshold, in which shorter burst-length distributions do not allow adequate temporal decay. **(C)** A representative NMDA spike/plateau time course simulated by the 5-state model with −20 mV membrane potential just following Glutamate release. Note that despite the proximity to the spike generation threshold in **(B)**, the 5-state model still predicts a rapid approach to spiking behavior. **(D)** Net current is plotted as a function of membrane potential for various combinations of NMDAR conductance and Mg^{2+} blockade slope. To achieve bistability (crossing 0 pA three times) it is necessary to have sufficiently large NMDAR conductance, and Mg^{2+} slope. With increased slope, modest levels of macroscopic conductance permit bistability, while for the standard slope, bistability is not attained for any conductance value.

were tested using the spatial decay of back propagating action potentials (BAP; 138 μm; Nevian et al., 2007); (**Figures 4C,D**). Length constants for back-propagation were chosen based upon the BAP as the much larger length constants for unitary EPSP's could not allow the observed dependence on input spacing without additional spatial components (such as intracellular Ca^{2+} flow). As the distal ends of dendrites are "capped," there is substantially less attenuation for potentials spreading distally. In both cases, the length constant for contributing to spike generation was half that of the respective functional length constant. Simulated results for the Simple Model (**Figures 4A,C**) well matched empirical data for both symmetric and asymmetric (separate backpropagation) length constants, indicating that a transfer function which only considers limiting states is sufficient to reproduce location dependence of peak EPSP's. However, the increased length constant for backpropagation decreased input spacing dependence, as should be expected as additional factors such as intracellular Ca^{2+} likely mediate the relationship. The model based on the distribution for burst/cluster lengths was slightly better with asymmetric length constants, but still mediocre in both cases (**Figures 4B,D**). As with comparison to the 5-state model (**Figure 3**), results demonstrate the addition of burst/cluster length is not only unnecessary, but detrimental.

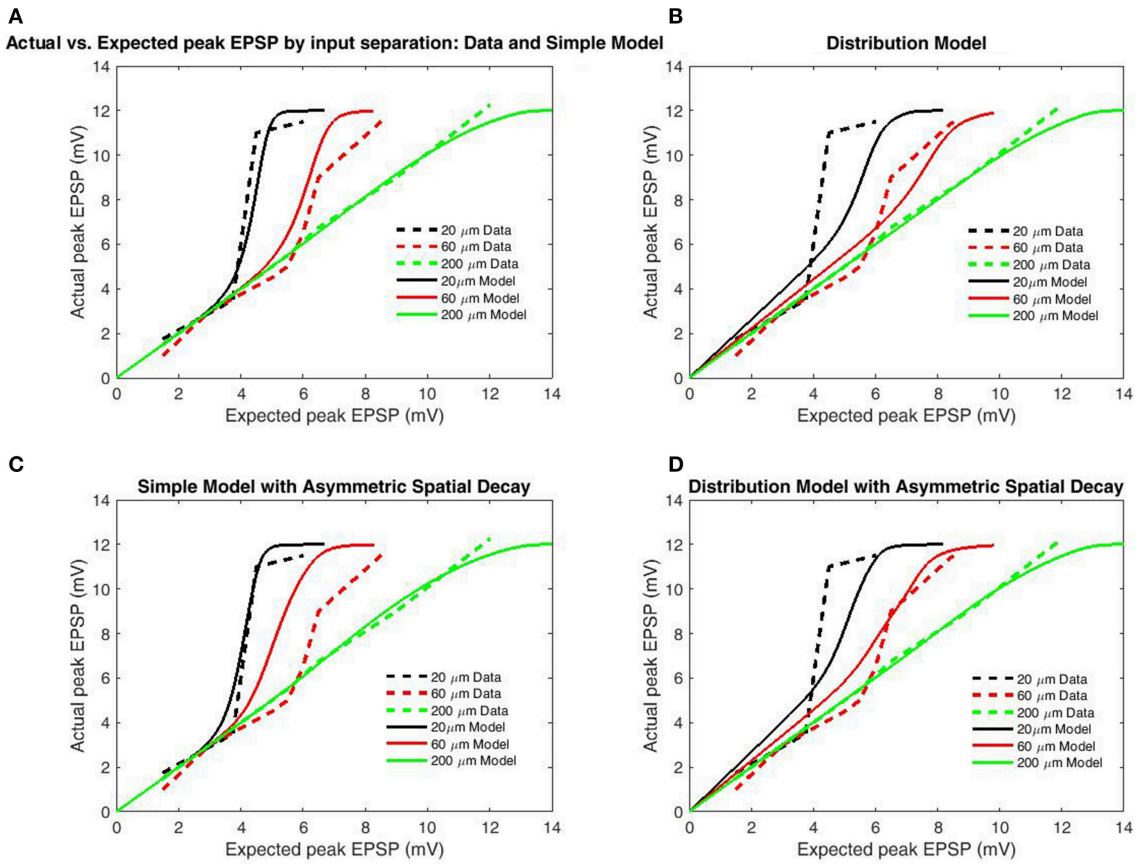

FIGURE 4 | Peak EPSP amplitudes for combined ("actual") input are plotted against the sum of their independent contributions ("expected") for varying distances between stimulation sites. Data is redrawn from Figure 5C in Polsky et al. (2004). **(A)** Model of limit states (infinite burst length) with identical length constants for forward and back-propagation. **(B)** Model using empirical burst length distributions. **(C)** Model of limit states with increased length constant for backpropagation. **(D)** Model with burst length distributions with increased length constant for backpropagation. Direction-independent spatial decay appears to produce slightly better fits, while the limit-state model produces far better fits than the distribution-based model. The superior fit of the limit-based model is expected as the majority of charge in NMDAR bursting is carried by the slower components, while expectations based solely on the distribution over-weight the fast components.

Paired Vs. Single-pulse

For a second analysis of transfer function accuracy, we compared simulated results for paired-pulse and single-pulse stimulation as by Polsky et al. (2004). Single-pulse protocols involve a single interval during which focal stimulation is delivered via an adjacent electrode, while paired-pulse protocols involve two stimulation intervals from the same electrode with very short ISI (in this case 20 ms). Paired-pulse stimulation is consistently superior in eliciting NMDAR-mediated currents, an effect known as paired-pulse facilitation (PPF) or NMDA priming. In accordance with the changed upper bound of data, boundary parameters were set as $b_U = 16.5\,\text{mV}$, $b_L = -16.5\,\text{mV}$. To further contrast PPF, synapses primed by the initial pulse are allowed, the previously removed fast components of the inter-opening distribution (the full distribution of Wyllie et al., 1998) which we term "non-uniform openings." Based upon the previous results (**Figure 4**) only the simple model was used and the modifications employed in modeling PPF were applied to the previous simulations to determine generality. From these modifications paired-pulse stimulation results in decreased spike threshold relative to the individual components for both symmetric (**Figure 5A**) and asymmetric spatial decay (**Figure 5B**). While these additions successfully replicate the paired-pulse/single-pulse relationship, they do not greatly affect the transfer functions ability to account for input spacing with symmetric spatial decay (**Figure 5C**) and thus the simpler simulations on inter-electrode spacing remain valid (**Figure 4**). In contrast, the previous effects of asymmetric spatial decay are accentuated resulting in a poor fit of the relation with input spacing (**Figure 5D**). In summary, results demonstrate that the transfer function is accurate when either spatial decay or opening times are symmetric (or both). However, the contrast with single-pulse stimulation requires non-uniform opening times to mimic priming of NMDAR's by pre-bound glutamate After these adjustments the transfer function appears accurate for both paired and single-pulse stimulation for a wide range of input/spacing combinations.

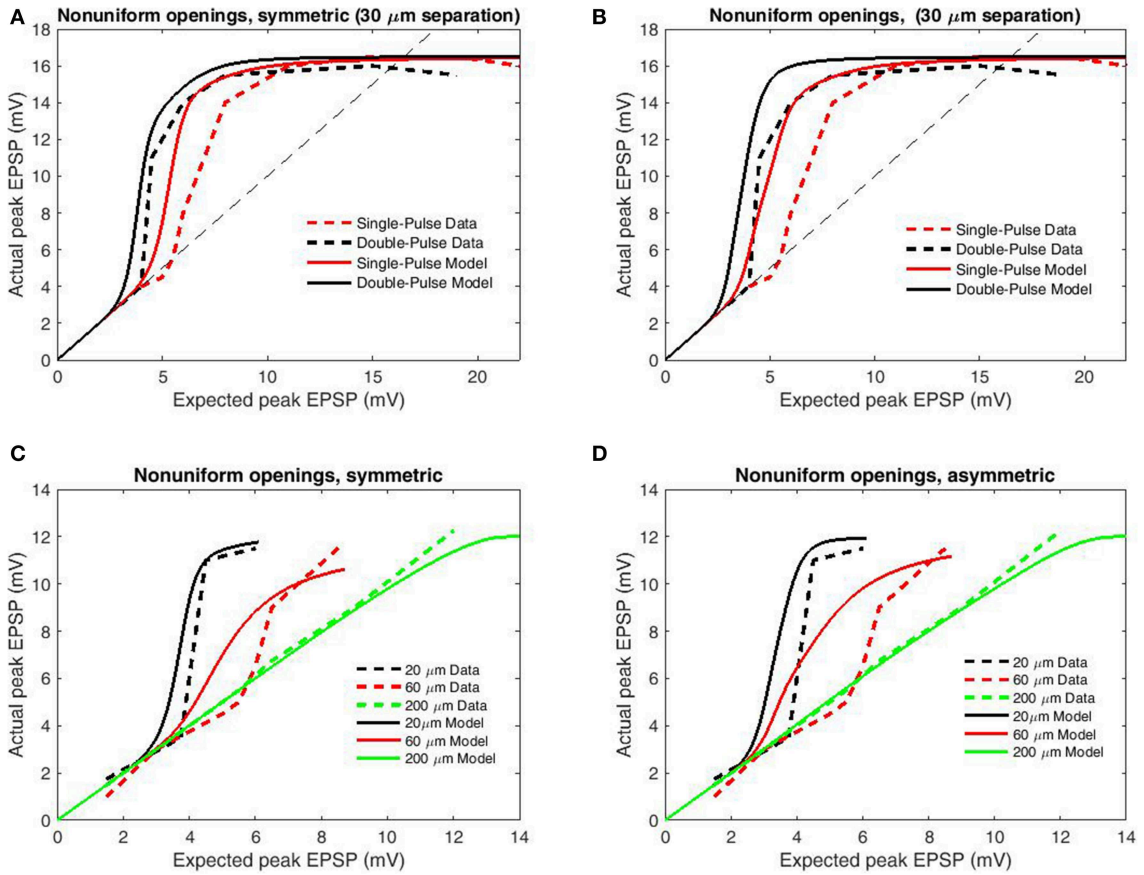

FIGURE 5 | Peak EPSP amplitudes for combined ("actual") input are plotted against the sum of their independent contributions ("expected") for paired-pulse and single-pulse stimulation methods at 30 μm inter-electrode distance. Data are redrawn from Figure 4C in Polsky et al. (2004). **(A)** Model permitting fast (empirical) opening components upon the second pulse for primed synapses, symmetric spatial decay. **(B)** Modifications of **(A)** applied to the conditions of **Figure 4A**. **(C)** Same as **(A)** but with increased length constant for backpropagation. **(D)** Same as **(B)** but with increased length constant for backpropagation. Note that the inclusion of faster opening components for primed synapses and differential spatial decay for general and spiking transients well replicates the relation between paired-pulse and single-pulse stimulation without greatly compromising the relation with input separation for symmetric spatial decay. In contrast, these modifications are significantly deleterious when combined with asymmetric spatial decay, indicative that the spacing dependence of nonlinear dendritic integration displays less directional dependence than does voltage attenuation.

Discussion

We have defined an artificial and a biophysical transfer function to model dendritic integration. Both functions are based upon sigmoidal opening dynamics of NMDA channels, however the biophysical function supports complex combinations of input, whereas the artificial function is agnostic to input location and simply considers a single nonlinear-component with each input equally weighted. Both transfer functions apply a bounded linear transform to the sum of linear and non-linear components to simulate saturation of the dendritic branch. Unlike many previous two-layer abstractions which describe sigmoidal components (**Figure 6A**) we implement a "linear hook" function to incorporate the observed subthreshold linearity (**Figure 6B**). In the current instantiation, the "linear hook" form results from two transformations akin to a "2-and-a-half layer" network (**Figure 6C**). In the first step, signals are split into a direct (passive) and indirect (active/spiking) pathway along the dendrite forming the "half layer." In the second step, dendritic saturation allows signals within a band to pass unmodified, while those outside are greatly attenuated corresponding to the function $G(x)$. The result is a "linear hook" function as in **Figure 6B** with subthreshold linearity, extreme concavity post threshold and fairly hard boundaries.

Due to the spatial decay of post-synaptic signals within a branch, the distance between sites of stimulation is critical for determining the nonlinear threshold. As in **Figure 4**, increasing the site distance by 20–40 μm under the current parameterization drastically changes the current reaching the site of integration. However, the location dependence is reduced with high synaptic conductances (Cook and Johnston, 1999; Williams, 2005). Empirical results support this condition for apical dendrites of pyramidal cells (Williams, 2005). Hence, with high synaptic

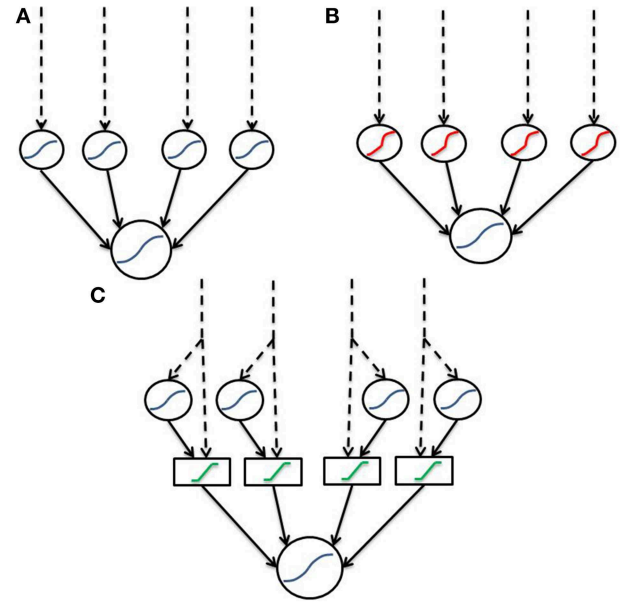

FIGURE 6 | Dendritic abstractions as neural networks. Dashed lines indicate input, while solid lines indicate connections between layers. Blue functions are sigmoids, red are the previously described "linear hook" and green functions are boundary functions for saturation. **(A)** Standard two-layer model consisting solely of sigmoids. Contrary to data, the sigmoidal two-layer model does not include subthreshold linearity. **(B)** Two-layer with a "linear hook" type function which does contain subthreshold linearity. **(C)** "Two-and-a-half" layer decomposition of **(B)**. "Linear hook" type functions are decomposed into a linear (passive) and nonlinear (spiking) signal. These signals are then fed through a boundary function for dendritic saturation.

and low membrane conductances, the artificial transfer function increases in similarity to its biophysical counterpart. However, the biophysical function also uses the reversal potential of NMDA channels and hence contains its own dampening mechanism once local potentials pass this threshold. Due to the relatively high reversal potential of NMDA channels, the influence of this additional factor should be minimized when the evoked changes in potential are small, but near the dynamic range of the NMDA channel. The biophysical form also has a more complicated nonlinear component which includes products of differing sigmoidal function. When membrane capacitance is low or channel closing time is long, allowing the slow currents to quickly approach their equilibria, the biophysical nonlinear component again resembles the artificial sigmoid. As both the artificial and biophysical transfer functions saturate, they are trivially equivalent with extreme stimulation. From the view of computational complexity (hence processing time), the biophysical model requires significantly more computations than the artificial with many input locations within a branch. As each site is considered as a function of all other inputs as well as its own, the number of integration sites increases linearly with the number of inputs, and the number of computations per site similarly increases. Thus the biophysical transfer function offers the greatest advantage over its artificial counterpart when only a few inputs are considered. However, as stated before, both functions are computationally simple compared to time-dynamic models, so the difference in artificial and biophysical computation times is unsubstantial. It should be noted that that other reductions for dendrite-soma transfer exist for active dendrites with known conductance evolution (Wybo et al., 2013) as well as passive dendritic trees with specific geometries (e.g., van Pelt, 1992). In particular, the approach of Wybo et al. (2013) yields relatively low computation times compared with other models of dynamical dendrites with complexity characterized by a Fourier transform of a hyperbolic-trigonometric quotient. As with the current approach, use of transfer functions allow arbitrary dendritic morphology to be captured in the reduction of somatic voltage, in contrast to equivalent cable approaches (e.g., Ohme and Schierwagen, 1998). However, the current further reduction of approximating peak EPSP amplitude in terms of input, rather than the somatic-response kernel is orders of magnitude quicker (being explicit) which presents an alternative to point-node neurons without any increases in dimensionality or the presence of implicit relations which constrain mathematical analysis of the entire network (e.g. using methods of topological dynamics). As such, endowing a point-neuron with the current transfer function admits the same mathematical properties as the host somatic function, such as Poincaré-Bendixson properties for phase-plane analysis. Thus the current approach is particularly advantageous in adding dendritic morphologies to spiking neural networks which previously employed point-nodes. Problems in pattern recognition, for instance, admit a natural spatial hierarchy which may benefit from the addition of plausible dendritic morphology and input spacing to spiking nodes, without attempting full anatomical reconstruction.

Despite its simplicity, the biophysical transfer function is capable of replicating the sorts of non-linear interactions seen in pyramidal dendrites, which are typically expressed as systems of non-linear differential equations. Although some properties are lost in the use of a time-invariant function, such as capacitive membrane interactions, our replication of Polsky et al.'s findings (2004) greatly exceeds both the historical linear integration and the more recent model of sigmoidally integrative dendrites, particularly in the basal dendrites of pyramidal cells (Häusser and Mel, 2003; Polsky et al., 2004; Spruston and Kath, 2004). The focus upon fast components, naturally ignores dynamic changes in diffusion gradients, such as intracellular Ca^{2+} concentration, which lead to complex interactions in driving force between NMDA spikes and occur over variable time scales due to factors such as release from intracellular stores and pumping back into the extracellular fluid. However, based upon simulation results, the function appears well suited for its intended use in estimating peak somatic EPSP. Accurate modeling of dendritic integration takes on increasing importance as a growing body of evidence points to dendritic roles in areas of joint interest to biophysical and artificial neural network modelers, such as place fields and feature detection (Ujfalussy et al., 2009). Artificial networks may also benefit from replacing a layer of point neurons

converging upon a single node with an artificial dendritic tree (Jadi et al., 2014) to greatly reduce dimensionality. As such, we hope this function will ease the computational demands of biologically-plausible dendritic integration while bridging gaps between artificial and biophysical models by allowing a smooth transition between forms.

References

Antic, S. D., Zhou, W. L., Moore, A. R., Short, S. M., and Ikonomu, K. D. (2010). The decade of the dendritic NMDA spike. *J. Neurosci. Res.* 88, 2991–3001. doi: 10.1002/jnr.22444

Behabadi, B. F., and Mel, B. W. (2014). Mechanisms underlying subunit independence in pyramidal neuron dendrites. *Proc. Natl. Acad. Sci. U.S.A.* 111, 498–503. doi: 10.1073/pnas.1217645111

Branco, T., and Häusser, M. (2010). The single dendritic branch as a fundamental functional unit in the nervous system. *Curr. Opin. Neurobiol.* 20, 494–502. doi: 10.1016/j.conb.2010.07.009

Branco, T., and Häusser, M. (2011). Synaptic integration gradients in single cortical pyramidal cell dendrites. *Neuron* 69, 885–892. doi: 10.1016/j.neuron.2011.02.006

Cook, E. P., and Johnston, D. (1999). Voltage-dependent properties of dendrites that eliminate location-dependent variability of synaptic input. *J. Neurophysiol.* 81, 535–543.

Destexhe, A., Mainen, Z. F., and Sejnowski, T. J. (1998). "Kinetic models of synaptic transmission," in *Methods in Neuronal Modeling*, eds C. Koch and I. Segev (Cambridge, MA: MIT Press), 1–25.

Genet, S., and Delord, B. (2002). A biophysical model of nonlinear dynamics underlying plateau potentials and calcium spikes in Purkinje cell dendrites. *J. Neurophysiol.* 88, 2430–2444. doi: 10.1152/jn.00839.2001

Gibb, A. J., and Colquhoun, D. (1991). Glutamate activation of a single NMDA receptor-channel produces a cluster of channel openings. *Proc. R. Soc. Lond. Ser. B Biol. Sci.* 243, 39–45. doi: 10.1098/rspb.1991.0007

Gibb, A. J., and Colquhoun, D. (1992). Activation of N-methyl-D-aspartate receptors by L-glutamate in cells dissociated from adult rat hippocampus. *J. Physiol.* 456, 143–179. doi: 10.1113/jphysiol.1992.sp019331

Gómez González, J. F., Mel, B. W., and Poirazi, P. (2011). Distinguishing linear vs. non-linear integration in CA1 radial oblique dendrites: it's about time. *Front. Comput. Neurosci.* 5:44. doi: 10.3389/fncom.2011.00044

Häusser, M., and Mel, B. (2003). Dendrites: bug or feature? *Curr. Opin. Neurobiol.* 13, 372–383. doi: 10.1016/S0959-4388(03)00075-8

Jadi, M. P., Behabadi, B. F., Poleg-Polsky, A., Schiller, J., and Mel, B. W. (2014). An augmented two- layer model captures nonlinear analog spatial integration effects in pyramidal neuron dendrites. *Proc. IEEE Inst. Electr. Electron. Eng.* 102, 782–798. doi: 10.1109/JPROC.2014.2312671

Jadi, M. P., Polsky, A., Schiller, J., and Mel, B. W. (2012). Location-dependent effects of inhibition on local spiking in pyramidal neuron dendrites. *PLoS Comput. Biol.* 8:e1002550. doi: 10.1371/journal.pcbi.1002550

Jahr, C. E., and Stevens, C. P. (1990a). A quantitative description of NMDA receptor-channel kinetic behavior. *J. Neurosci.* 10, 1830–1837.

Jahr, C. E., and Stevens, C. P. (1990b). Voltage dependence of NMDA-activated macroscopic conductances predicted by single-channel kinetics. *J. Neurosci.* 10, 3178–3182.

Major, G., Polsky, A., Denk, W., Schiller, J., and Tank, D. W. (2008). Spatiotemporally graded NMDA spike/plateau potentials in basal dendrites of neocortical pyramidal neurons. *J. Neurophysiol.* 99, 2584–2601. doi: 10.1152/jn.00011.2008

Nevian, T., Larkum, M. E., Polsky, A., and Schiller, J. (2007). Properties of basal dendrites of layer 5 pyramidal neurons: a direct patch-clamp recording study. *Nat. Neurosci.* 10, 206–214. doi: 10.1038/nn1826

Ohme, M., and Schierwagen, A. (1998). An equivalent cable model for neuronal trees with active membrane. *Biol. Cybern.* 78, 227–243. doi: 10.1007/s004220050429

Poirazi, P., Brannon, T., and Mel, B. W. (2003). Pyramidal neuron as two-layer neural network. *Neuron* 37, 989–999. doi: 10.1016/S0896-6273(03)00149-1

Polsky, A., Mel, B., and Schiller, J. (2009). Encoding and decoding bursts by NMDA spikes in basal dendrites of layer 5 pyramidal neurons. *J. Neurosci.* 29, 11891–11903. doi: 10.1523/JNEUROSCI.5250-08.2009

Polsky, A., Mel, B. W., and Schiller, J. (2004). Computational subunits in thin dendrites of pyramidal cells. *Nat. Neurosci.* 7, 621–627. doi: 10.1038/nn1253

Rall, W. (1969). Time constants and electrotonic length of membrane cylinders and neurons. *Biophys. J.* 9, 1483–1508. doi: 10.1016/S0006-3495(69)86467-2

Schiller, J., Major, G., Koester, H. J., and Schiller, Y. (2000). NMDA spikes in basal dendrites of neocortical pyramidal neurons. *Nature* 404, 285–289. doi: 10.1038/35005094

Shoemaker, P. A. (2011). Neural bistability and amplification mediated by NMDA receptors: analysis of stationary equations. *Neurocomputing* 74, 3058–3071. doi: 10.1016/j.neucom.2011.04.018

Spruston, N., and Kath,.W. L. (2004). Dendritic arithmetic. *Nat. Neurosci.* 7, 567–569. doi: 10.1038/nn0604-567

Ujfalussy, B., Kiss, T., and Érdi, P. (2009). Parallel computational subunits in dentate granule cells generate multiple place fields. *PLoS Comput. Biol.* 5:e1000500. doi: 10.1371/journal.pcbi.1000500

van Elburg, R. A. J., and van Ooyen, A. (2010). Impact of dendritic size and dendritic topology on burst firing in pyramidal cells. *PLoS Comput. Biol.* 6:e1000781. doi: 10.1371/journal.pcbi.1000781

van Pelt, J. (1992). A simple vector implementation of the Laplace-transformed cable equations in passive dendritic trees. *Biol. Cybern.* 68, 15–21. doi: 10.1007/BF00203133

Wainrib, G., Thieullen, M., and Pakdaman, K. (2012). Reduction of stochastic conductance-based neuron models with time-scales separation. *J. Comput. Neurosci.* 32, 327–346. doi: 10.1007/s10827-011-0355-7

Williams, S. R. (2005). Encoding and decoding of dendritic excitation during active states in pyramidal neurons. *J. Neurosci.* 25, 5894–5902. doi: 10.1523/JNEUROSCI.0502-05.2005

Wybo, W. A. M., Stiefel, K. M., and Torben-Nielsen, B. (2013). The Green's function formalism as a bridge between single- and multi-compartmental modeling. *Biol. Cybern.* 107, 685–694. doi: 10.1007/s00422-013-0568-0

Wyllie, D. J. A., Béhé, P., and Colquhoun, D. (1998). Single-channel activations and concentration jumps: comparisons of recombinant NR1a/NR2A and NR1a/NR2D NMDA receptors. *J. Physiol.* 510, 1–18. doi: 10.1111/j.1469-7793.1998.001bz.x

Conflict of Interest Statement: The authors declare that the research was conducted in the absence of any commercial or financial relationships that could be construed as a potential conflict of interest.

frontiers in Cellular Neuroscience

METHODS
published: 27 October 2015
doi: 10.3389/fncel.2015.00429

Fast and reliable identification of axons, axon initial segments and dendrites with local field potential recording

*Anders V. Petersen, Emil Ø. Johansen and Jean-François Perrier**

Department of Neuroscience and Pharmacology, Faculty of Health and Medical Sciences, University of Copenhagen, Copenhagen, Denmark

The axon initial segment (AIS) is an essential neuronal compartment. It is usually where action potentials are initiated. Recent studies demonstrated that the AIS is a plastic structure that can be regulated by neuronal activity and by the activation of metabotropic receptors. Studying the AIS in live tissue can be difficult because its identification is not always reliable. Here we provide a new technique allowing a fast and reliable identification of the AIS in live brain slice preparations. By simultaneous recording of extracellular local field potentials and whole-cell patch-clamp recording of neurons, we can detect sinks caused by inward currents flowing across the membrane. We determine the location of the AIS by comparing the timing of these events with the action potential. We demonstrate that this method allows the unequivocal identification of the AIS of different types of neurons from the brain.

Keywords: axon initial segment, dendrite, modulation, spike triggered averaging, axon, plasticity

OPEN ACCESS

Edited by:
Sergey M. Korogod, National Academy of Sciences of Ukraine, Ukraine

Reviewed by:
Thomas Launey, RIKEN Brain Science Institute, Japan
George Mentis, Columbia University, USA

****Correspondence:***
Jean-François Perrier
perrier@sund.ku.dk

Received: *27 August 2015*
Accepted: *13 October 2015*
Published: *27 October 2015*

Citation:
Petersen AV, Johansen EØ and Perrier J-F (2015) Fast and reliable identification of axons, axon initial segments and dendrites with local field potential recording. Front. Cell. Neurosci. 9:429. doi: 10.3389/fncel.2015.00429

INTRODUCTION

The axon initial segment (AIS) is the gatekeeper of neurons. It is there that nerve impulses are initiated before propagating toward the terminal regions of the axon and back to the somato-dendritic compartments (Eccles, 1964; Stuart and Sakmann, 1994). During the past years, it has become evident that the AIS is not a rigid structure that only generates action potentials each time the membrane potential reaches a threshold value. The modulation of ion channels permeable for Na^+, K^+, or Ca^{2+} ions expressed in this compartment provide a high degree of plasticity. For example $K_V7.2$ and $K_V7.3$ ion channels produce a slowly activating persistent outward current at the AIS (Pan et al., 2006; Rasmussen et al., 2007). The activation of muscarinic receptors inhibits the current and thereby increases the firing frequency of neurons (Brown and Adams, 1980; Brown and Passmore, 2009). In cartwheel neurons in the dorsal cochlear nucleus, the activation of dopamine D_3 receptors at the AIS specifically inhibits T-type calcium channels and thereby spike initiation (Bender et al., 2010). In spinal motoneurons, the activation of serotonergic 5-HT_{1A} receptors at the AIS inhibits the Na^+ current responsible for the genesis of action potentials. This mechanism is responsible for the central component of motor fatigue occurring during prolonged efforts (Cotel et al., 2013; Perrier and Cotel, 2015).

Identifying the AIS during an experiment is therefore highly relevant for physiological studies. However, this problem is far from being trivial because most neurons have several dendrites with diameters comparable to the ones of axons. For that reason, the visual identification of

the axon during electrophysiological recordings can be equivocal (**Figure 1**). In addition, the axon sometimes derives from a first order dendrite rather from the soma (Ruigrok et al., 1984; Hounsgaard et al., 1988; Hausser et al., 1995; Thome et al., 2014). So far, the most reliable method for identifying axons requires multiple recordings with the patch-clamp technique. This has been successfully done for few types of neurons such as pyramidal cells from the neocortex (Stuart and Sakmann, 1994; Stuart et al., 1997). However, this procedure is difficult and only allows the recording of relatively thick or cut axons presenting a bleb (Kole et al., 2007). In cell cultures, it is possible to label the AIS of all neurons by means of GFP-tagged proteins specific for the AIS (Zhang and Bennett, 1998) or by means of a mouse monoclonal antibody recognizing an extracellular epitope of neurofascin (Schafer et al., 2009). However, this method has not been used in slices, probably due to the poor visibility of the tags. Another approach is to stain the axon by means of antibodies directed against specific markers such as ankyrin G (Hedstrom et al., 2008), tau protein (Binder et al., 1986), or sodium channels (Duflocq et al., 2008; Grubb and Burrone, 2010; Cotel et al., 2013). This method, being performed on fixed tissue after the end of the experiment, only allows testing if a given neurite was an axon or not, which is not optimal for studying the modulation of the AIS.

Here we provide a simple method based on extracellular field potential of neuronal processes combined with spike patch clamp recording of soma allowing fast and reliable identification of AIS in *in vitro* preparations.

MATERIALS AND METHODS

Slice Preparation

After decapitation, the brain of C57BL/6 mice (Taconic) from P12 to P14 was removed and placed in cold artificial cerebrospinal fluid containing *N*-Methyl-D-glucamine 125 mM, KCl 2.5 mM, NaHCO3 26 mM, $CaCl_2$ 2 mM, $MgCl_2$ 1 mM, NaH_2PO_4 1.25 mM, glucose 25 mM. Three hundred micrometer parasagittal slices from the brain were cut with a vibratome (VT1200; Leica Microsystems A/S, Germany). Slices were then incubated for and hour in a chamber containing oxygenated Ringer's solution: NaCl 125 mM, KCl 2.5 mM, NaHCO3 26 mM, $CaCl_2$ 2 mM, $MgCl_2$ 1 mM, NaH_2PO_4 1.25 mM, glucose 25 mM. Slices were then positioned in a recording chamber and continuously perfused with Ringer's solution carbogenated by gassing with 95% O_2 plus 5% CO_2. Experiments were performed at room temperature. The surgical procedures complied with Danish legislation. This study was carried out in accordance with the recommendations of Department of Experimental Medicine of the University of Copenhagen. The protocol was approved by the Department of Experimental Medicine of the University of Copenhagen.

Patch Clamp Recording

Visual guided patch clamp recording was performed with a Multiclamp 700B amplifier (Molecular Devices, USA). Neurons were visualized by means of a BW51WI microscope (Olympus, Japan) equipped with differential interference contrast. Patch-clamp electrodes were made of borosilicate glass pulled with a P-87 micropipette puller (Sutter Instruments; USA). They were filled with the following solution (in mM): 122 K-gluconate, 2.5 MgCl2, 0.0003 CaCl2, 5.6 Mg-gluconate, 5 K-HEPES, 5 H-HEPES, 5 Na2ATP, 1 EGTA, 2.5 biocytin, 0.01 Alexa 488 hydrazide, sodium salt (Life Technologies, USA), and KOH to adjust the pH to 7.4. Electrodes had a resistance ranging from 4 to 8 MΩ. Recordings were sampled at 100 kHz with a 16-bit analog-to-digital converter (DIGIDATA 1440; Molecular Devices, USA) and displayed by means of Clampex 10.2 software (Molecular Devices, USA). Neurons were isolated from their surrounding synaptic environment by blocking AMPA receptors with CNQX (20 μM, Tocris), NMDA receptors with AP5 (50 μM, Tocris) and $GABA_A$ receptors with Gabazine (10 μM, Tocris).

Local Field Potential Recording

Local field potential (LFP) electrodes were made with borosilicate capillaries pulled with a P-87 micropipette puller (Sutter Instruments; USA). They were filled with artificial cerebrospinal fluid of the same composition as detailed above. The LFP electrodes had a diameter of 1 μm and an input resistance of 4–7 MΩ. They were mounted on a 3-axis micromanipulator (Luigs and Neumann, Germany). The signal was recorded with a Multiclamp 700B amplifier (Molecular Devices, USA) and sampled at 100 KHz.

Spike Triggered Average

The LFP electrode was positioned near the membrane of the recorded neuron. The acquisition of the signal was synchronized on the ascending phase of action potentials recorded with the patch-clamp technique. When the neuron was not firing spontaneously, positive bias currents were injected intracellularly. Between 200 and 2000 action potentials were acquired. Both signals were then averaged.

The spike threshold was determined as the first positive peak present on the third derivative of the voltage trace (Henze and Buzsaki, 2001). Extracellular events were considered only if their amplitude was more than five times the standard deviation of the baseline.

Data Analysis

Data were analyzed by means of a custom program written in Matlab (Mathworks, Natick, USA) used to determine the time position of the spike threshold and to average extracellular recordings. The program is available at the following permalink: http://www.mathworks.com/matlabcentral/fileexchange/53161-axon-initial-segment-identifier.

RESULTS

We recorded twelve neurons from different brain regions including principal cells and interneurons from neocortex, midbrain and hippocampus. For some neurons, one neurite was an obvious candidate for being the axon. The neuron illustrated in **Figure 1A** is a pyramidal cell from the neocortex recorded

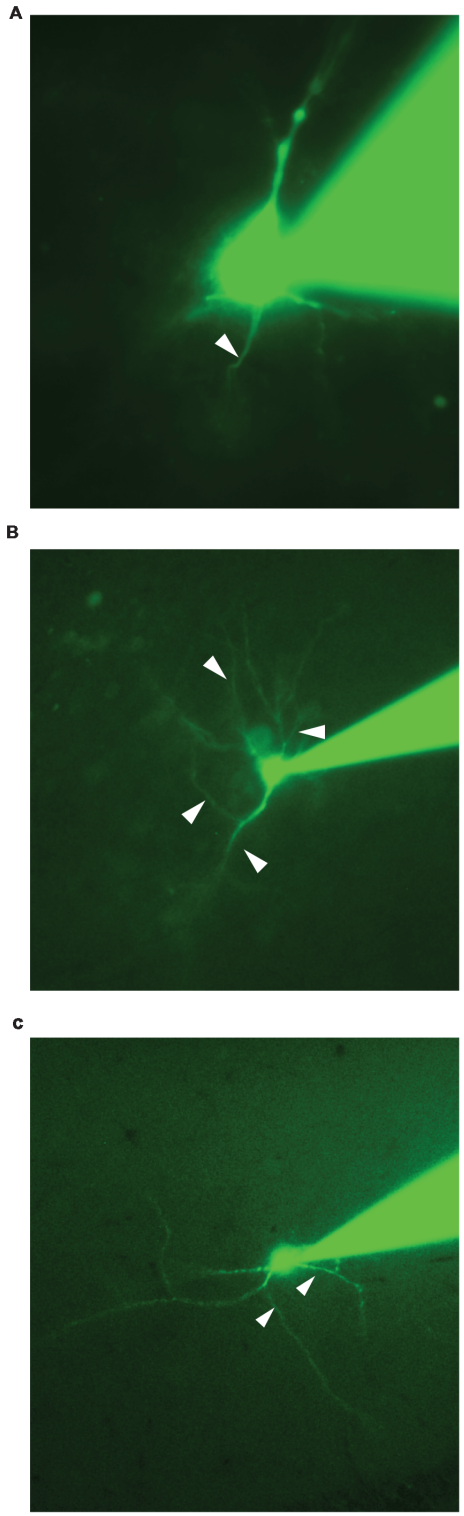

FIGURE 1 | Epifluorescence images of neurons obtained during their recordings. (A) Pyramidal neuron from the neocortex. In the example one neurite is very likely to be the axon (arrow). **(B)** Neuron from the hippocampus. At least two neurites could correspond to the axon (arrows). **(C)** Interneuron located in the *stratum radiatum* of the CA1 region of the hippocampus. At least two neurites could correspond to the axon (arrows).

in whole-cell configuration observed by means of fluorescence microscopy. In this example, the single neurite located between the basal dendrites is probably the axon (arrowhead). However, for other neurons, it was virtually impossible to determine which of the processes was the axon. In the example of **Figure 1B**, a pyramidal cell from the hippocampus has several processes leaving the soma in the basal region. One of them is probably an axon. However the similitude between diameters does not allow a clear distinction between the basal dendrites and the axon (arrowheads). Another example shows the morphology of an interneuron located in the *stratum radiatum* of the CA1 region of the hippocampus (**Figure 1C**). Here as well, it is difficult to know which of the processes corresponds to the axon. These examples demonstrate that the online identification of the AIS is far from being trivial. For that reason, we developed a method allowing a fast and reliable online identification of the AIS.

Theoretical Basis for the Identification of the Axon Initial Segment

Any current being absorbed from the extracellular medium into a neuronal element appears as a sink (Nicholson and Freeman, 1975). The resulting lack of positive charges on the extracellular side generates a local negative electrical field potential. This occurs outside the AIS when action potentials are initiated and in the vicinity of other neuronal compartments that carry active propagation of electric signals. By comparing the timing of such field potentials with the action potential of a neuron, it should be possible to distinguish the AIS from other compartments.

The first event that occurs during an action potential is the activation of Na^+ channels at the AIS (**Figure 2A**). This generates a negative field potential outside the AIS. The inward current then spreads passively in the cell, inducing a depolarization of the neighboring compartments. Because of the impedance mismatch, the resulting depolarization occurring in the soma is small (**Figure 2A**). Thus, the first component of an action potential recorded in the soma corresponds to the AIS spike (Eccles, 1964; Bean, 2007). This small depolarization, usually termed IS, is nevertheless sufficient to activate somatic Na^+ channels, ensuring a regeneration of the inward current and the back propagation of the action potential in the soma and then in dendrites (SD component; **Figure 2B**). An inflection point is sometimes visible on the depolarizing phase of an action potential. For that reason, one can distinguish the IS from the SD component by plotting the first derivative of the voltage trace (Eccles, 1964; Bean, 2007), (**Figure 2**). After reaching the soma, the current spreads out passively into the dendrites and outside the cell through leak conductances (**Figure 2B**). A local field potential electrode located near a dendrite can therefore detect an excess of positive charges, characterized by a positive deflection occurring during the late phase of the action potential (**Figure 2C**). In case of active dendrites, the subsequent activation of voltage gated ion channels produces a sink following the positive deflection (**Figure 2C**). Thus, by comparing the timing of local field potentials with the one of action potentials recorded intracellularly, it is theoretically possible to determine if a given neurite is an axon or a dendrite. In addition,

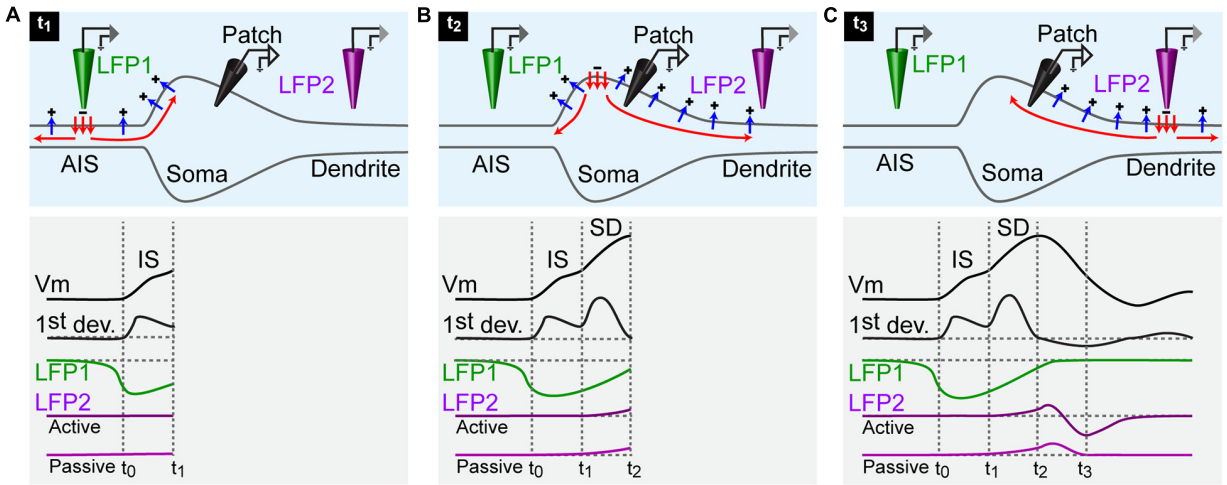

FIGURE 2 | Schematic representation of the currents responsible for an action potential. For all panels: upper row, current flowing across the membrane of a neuron; lower rows: black traces, membrane potential of a neuron recorded by an intracellular electrode positioned in the soma and first derivative of the membrane potential; green trace: local field potential recorded by an extracellular electrode positioned near the AIS (LFP1); purple traces: local field potential recorded by an extracellular electrode positioned near an active and a passive dendrite (LFP2). **(A)** An action potential is generated at time 0 (t_0). The inward current triggered by the activation of Na^+ channels at the AIS spreads actively in the axon (red arrows) and leaks out passively through the membrane (blue arrows). The intracellular electrode measures a depolarization of the soma at time 1 (t_1). The LFP electrode at the AIS detects a sink starting before the somatic depolarization. The dendritic LFP electrode does not record any change. **(B)** At time 2 (t_2), the active current has invaded the whole soma. The membrane potential reaches the peak of the action potential. The LFP recorded at the AIS terminates while the LFP recorded in dendrites starts. **(C)** At time 3 (t_3), the active current has reached the dendrite. The action potential recorded in the soma is finished. The dendritic LFP occurs as a positive deflection corresponding to the passive leakage of the current through the membrane. In case of an active dendrite, the positive event is immediately followed by a negative one caused by the presence of a sink.

it allows figuring out if a dendrite is active or purely passive.

Online Identification of the AIS

We recorded the electrical activity of principal cells and interneurons from the hippocampus, neocortex, and midbrain. We visualized the somatodendritic arborisation of neurons by means of epifluorescence microscopy. We observed local field potential electrodes with bright field illumination and positioned it in the vicinity of different neuronal compartments by alternating fluorescence and bright field (**Figure 3A**). This procedure allows sub-μm precision. The distance between the LFP electrode and the membrane of the neuron tested was typically 1–3 μm and always less than 5 μm. We evoked action potentials by injecting intracellular positive bias currents. We found that single action potentials were usually not sufficient to induce events detectable from the background electrical noise. For that reason, we used the spike-triggered average technique. It consists in triggering the recording of the local field potential electrode on the ascending phase of the action potential. Each time the voltage trace crosses a given value (e.g., 0 mV), the recording starts. In order to analyze what happens just before the spike, we used a pre-trigger of 40 ms. After averaging 200–2000 spikes, the signal of the LFP electrode displayed clear events (**Figure 3C**). To determine if the extracellular electrode was positioned near the AIS, we compared the timing of the LFP events relative to the spike threshold calculated as the first positive peak present on the third derivative of the voltage trace, which provides a reliable estimation (Henze and Buzsaki, 2001; lower trace of **Figure 3B**; vertical dashed line). A negative event starting before the threshold measured at the soma indicated that the electrode was positioned near the AIS. In the example of **Figure 3C** obtained from a pyramidal neuron from the hippocampus, the LFP trace at position 1 (green trace in **Figure 3C**) displayed a negative event starting 400 μs before the spike threshold, suggesting that this position corresponded to the AIS. In contrast, the events detected at other positions started after the beginning of the spike. At positions 2 and 3 (purple traces in **Figure 3C**), the recording displayed a positive event followed by a negative event occurring 360–400 μs after the spike threshold. Because the negative event started after the start of the spike we concluded that the electrode was positioned near a dendrite. In addition, the presence of a negative peak indicated that the passive propagation of the signal was followed by an active one. This suggests that the backpropagation of the action potential was amplified by voltage-gated conductances. We tested the method for other types of neurons. **Figures 3D–F** illustrates the results obtained with a midbrain neuron for which the axon could not be visually identified with certainty. Here again, the LFP electrode detected a sink starting before the action potential at one position identified as the AIS (LFP1 in **Figure 3F**), and sources followed by delayed sinks at other positions (LFP2/3 in **Figure 3F**). **Figures 4A–C** illustrates all the average LFP recordings obtained at various positions near the membrane of eleven neurons. For 9/11 neurons, we could unambiguously distinguish the AIS from dendrites, demonstrating that the technique provided reliable results.

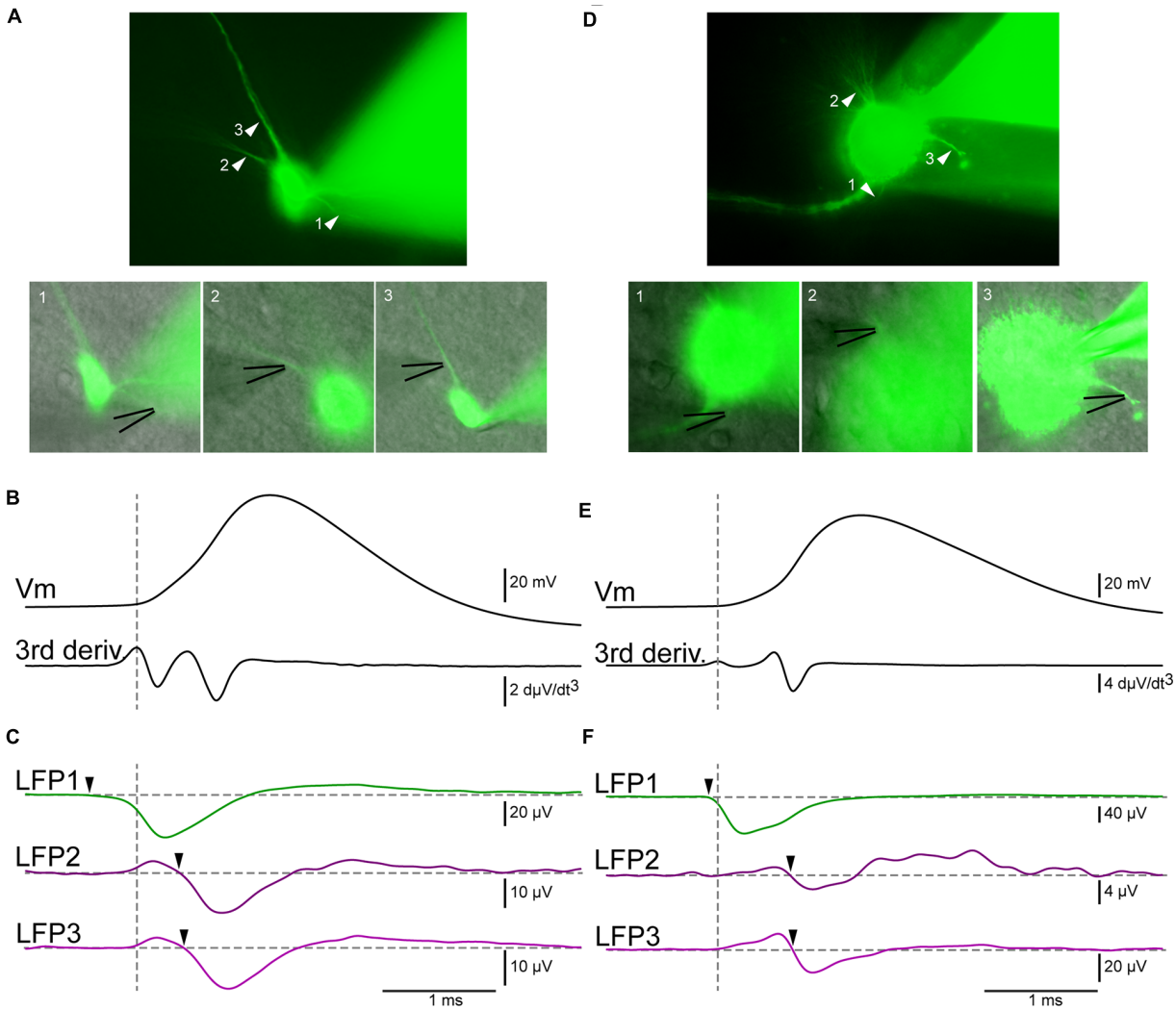

FIGURE 3 | LFP recordings allow the distinction of axon from dendrites. (A) Epifluorescent pictures of a pyramidal cell from the hippocampus. The black lines indicate the positions of the LFP electrodes **(B)** Upper trace: membrane potential recorded by a patch electrode located at the soma. Lower trace: third derivative of the membrane potential. The maximum of the first positive peak corresponds to the beginning of the action potential (vertical dashed line). **(C)** Green trace: average of the LFP obtained at position 1 (2095 sweeps). A negative event (arrowhead) started before the action potential, indicating that the electrode was positioned near the AIS. Upper purple trace: Average of the LFP obtained at position 2 (1002 sweeps). Lower purple trace: average of the LFP obtained at position 3 (1063 sweeps). In both cases the LFP consisted of a positive and then a negative deflection (arrowhead) occurring after the beginning of the spike, demonstrating that the electrode was located near an active dendrite. **(D–F)** Neuron from the midbrain. **(D)** Epifluorescent pictures of the neuron. **(E)** Membrane potential and third derivative of the membrane potential. **(F)** Green trace: Average of the LFP obtained at position 1 (1101 sweeps). A negative event started before the action potential (arrowhead), indicating that the electrode was positioned near the AIS. Upper purple trace: average of the LFP obtained at position 2 (1003 sweeps). Lower purple trace: average of the LFP obtained at position 3 (1188 sweeps). Here again, a negative deflection (arrowhead) occurring after the beginning of the spike shows that the electrode was located near an active dendrite.

We then tested if the initial segment could be localized more accurately along the axon by moving the electrode away from the soma. The LFP recording at the AIS should start earlier and have a bigger amplitude due to the higher density of voltage gated Na^+ channels in this compartment (Kole et al., 2008), (**Figure 5A**). By contrast, recordings obtained more distally along the axon should appear as a positive deflection caused to the passive current preceding the spike and followed by a delayed negative deflection reflecting the inward current carried by Na^+ ions (LFP3 in **Figure 5A**). In agreement, the LFP recorded along the axon of a cortical neuron was characterized by a negative event starting 50 μs before the spike threshold when positioned 15 μm from the soma of a cortical neuron (LFP2 in **Figure 5B**). When the LFP electrode was moved 5 μm closer to the soma, the negative event was detected 80 μs later (LFP1 in **Figure 5B**). When the extracellular electrode was moved 45 μm from the soma, along the axon, the LFP consisted of a positive event followed by a negative event starting 4 ms after the spike threshold (arrow in LFP3 in **Figure 5B**). It should be noticed that the amplitude of the recordings obtained at this position was one order of

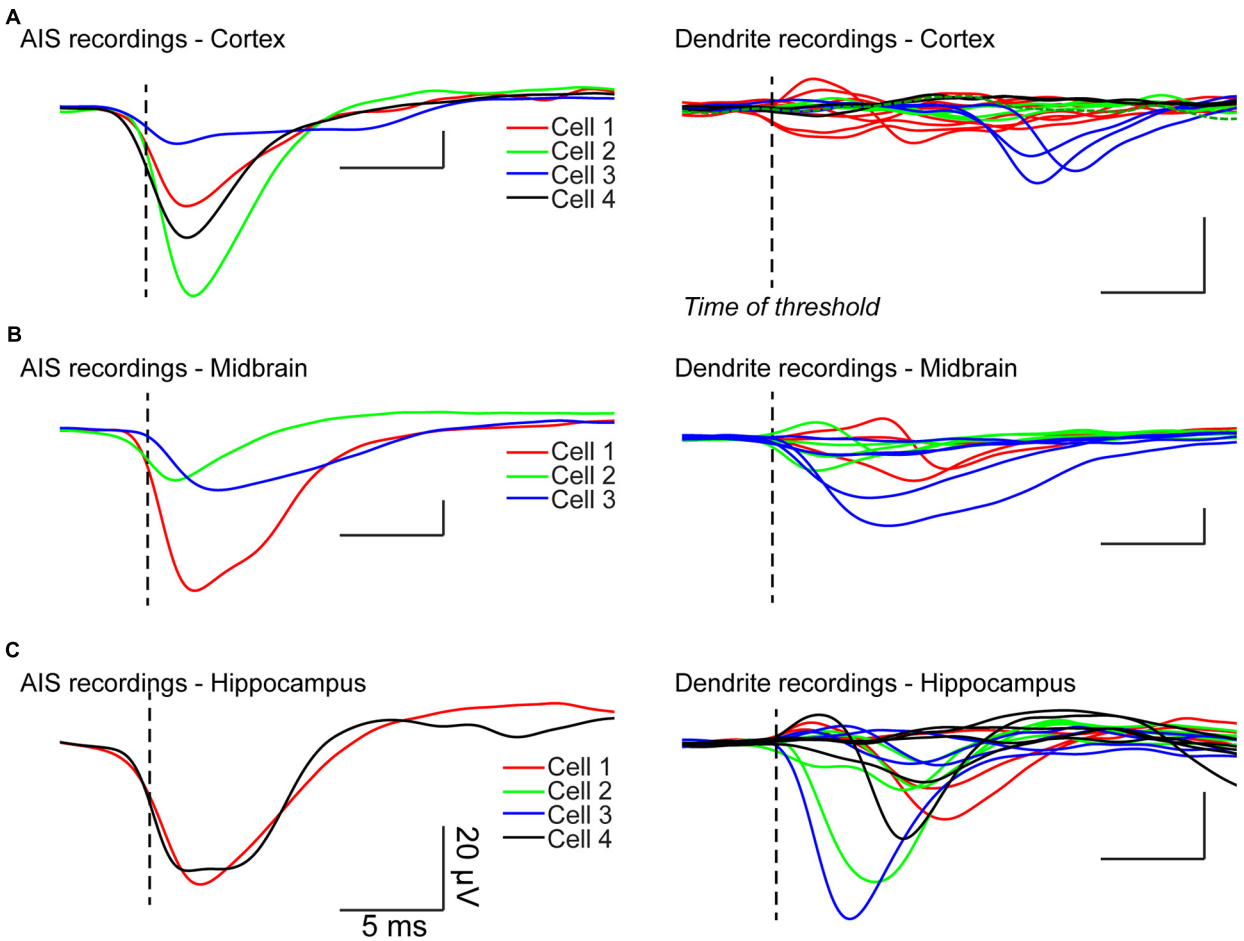

FIGURE 4 | LFP recordings from different neurons. Left: LFP recordings obtained near AIS. Right: dendritic LFP recordings. **(A)** Cortical neurons. A passive dendrite belonging to cell 2 was recorded (dashed green line). **(B)** Midbrain neurons. **(C)** Hippocampal neurons.

magnitude lower than the one obtained more proximally. These observations suggest that the spike was generated near position 2 (i.e., 15 µm from the soma). In agreement, position 2 was the only one identified as the AIS by our Matlab script (see Materials and Methods). Thus our technique does not only allow distinguishing dendrites from axon, but also permit determining the position of the AIS along an axon.

DISCUSSION

We have demonstrated a novel procedure allowing the online identification of the AIS during electrophysiological recording of neurons. Our method offers several advantages compared to others. First, it can be done in live tissue, while a neuron is recorded by means of the patch clamp technique. This facilitates the investigation of the physiological mechanisms involved in the modulation of the AIS. For example, one could focally apply agonists or antagonists by puffing or iontophoresing them from the LFP electrode, and determine if some receptors or ion channels are expressed at the AIS and if their activation has any impact on the excitability of the studied neuron (Perrier and Hounsgaard, 2003; Bender et al., 2010; Cotel et al., 2013). Second, the method is fast. The number of action potentials necessary for getting an acceptable signal to noise ratio with the LFP signal is about 200–1000. It is usually obtained within few minutes. By contrast, identifying the AIS by immunohistochemical staining with antibodies directed against proteins specific for the AIS requires several hours or days. Third, the technique is cheap. It only requires one extracellular recording electrode connected to an amplifier and does not necessitate any further investment. Fourth, the method is reliable provided that the patch recording is stable. It was possible to identify the axon for 10 of the 12 cells recorded in this study (i.e., more than 80%). Fifth, the method does not need any chemical that could potentially interfere with the physiological properties of the cell. Sixth, it is possible to determine the site of action potential initiation by mapping the LFP along the axon. Seventh, the size of the axon is not a limiting factor for the technique. Our approach allows the identification of the AIS of all neurons, independently of the diameter of the axon or of the presence of blebs caused by the slicing procedure.

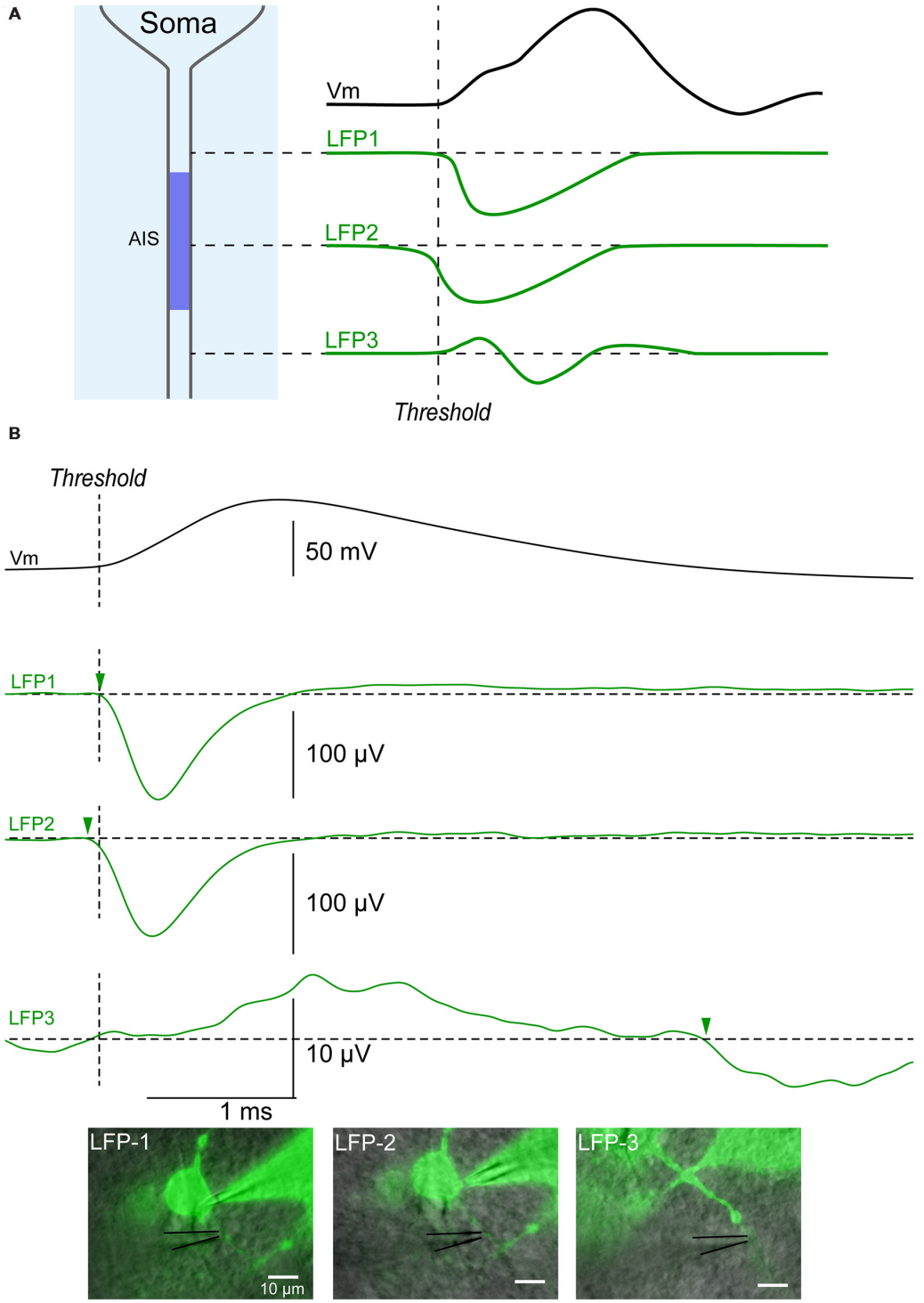

FIGURE 5 | Identification of the initial segment. (A) Upper trace (black): action potential recorded intracellularly. Green traces: theoretical LFPs recorded along an axon. The first LFP occurring is a negative potential caused by the sink occurring at the AIS where the spike is generated (LFP2). An LFP recorded more proximal to the soma should be characterized by sink starting slightly later (LFP1), while an LFP more distal on the axon should start with a source followed by a sink (LFP3). **(B)** Example of LFPs recorded along the axon of a cortical neuron. Black upper trace: action potential recorded intracellularly. Green traces: LFPs. LFP1: LFP recorded 10 µm from the soma (515 sweeps). LFP2: LFP recorded 15 µm from the soma (287 sweeps). The latency for the negative event was the shortest at this position (arrowhead), suggesting that the action potential was initiated in this area. LFP3: LFP recorded 45 µm from the soma (1149 sweeps). A positive event suggesting the presence of a source was followed by a negative event (arrowhead) starting 4 ms after the beginning of the somatic action potential. Note the small amplitude of the signal when compared to LFPs recorded at positions 1 and 2.

The method we developed also has limitations. The identification of the AIS requires a good visibility of the cell, which is usually not the case for cells deeper than 80 μm from the surface of the slice. The method is invasive and the AIS has to be accessible with the LFP electrode. If the axon leaves the soma from below, or if it is positioned under the patch electrode, the method cannot be used. This is probably why we failed to identify two of the 12 AIS from the neurons of our sample. In addition, if the LFP is positioned near two close processes, it can be difficult to ascribe the signal to a particular one. In case of myelination, the signal recorded near axons may be difficult to record if the LFP electrode is not located near a node of Ranvier. Finally and importantly, the identification of the AIS relies on the fact that the spike is initiated in this compartment. This is not always the case. In mitral cells from the olfactory bulb and in some instances in pyramidal cells from the neocortex, the action potential can have a dendritic origin (Stuart and Sakmann, 1994; Chen et al., 1997; Schiller et al., 2000).

Perspective

We believe that this new technique will prove useful for investigating the plasticity of the AIS. We tested our method in a slice preparation. It could also in principle be used *in vivo*, provided that one can visualize the whole somatodendritic arborisation of the investigated neuron, which would probably require multi-photon microscopy imaging techniques.

AUTHOR CONTRIBUTIONS

AP and J-FP, conception and design of research. AP, EJ and J-FP, performed experiments. AP analyzed data. AP and J-FP interpreted results of experiments. AP and J-FP wrote the manuscript. AP, EJ and J-FP approved final version of manuscript.

FUNDING

The project was funded by Inge Berthelsens legat Fonden (Dansk Epilepsiforening), the Owensenske Fond, Simon Fougner Hartmanns Familiefond, Agnes, and Poul Friis Fond, Novo Scholarship Programme and the Carlsberg Foundation.

ACKNOWLEDGMENT

We wish to thank Dr. Henrik Jahnsen and Dr. Florence Cotel for their precious comments.

REFERENCES

Bean, B. P. (2007). The action potential in mammalian central neurons. *Nat. Rev. Neurosci.* 8, 451–465. doi: 10.1038/nrn2148

Bender, K. J., Ford, C. P., and Trussell, L. O. (2010). Dopaminergic modulation of axon initial segment calcium channels regulates action potential initiation. *Neuron* 68, 500–511. doi: 10.1016/j.neuron.2010.09.026

Binder, L. I., Frankfurter, A., and Rebhun, L. I. (1986). Differential localization of MAP-2 and tau in mammalian neurons *in situ*. *Ann. N. Y. Acad. Sci.* 466, 145–166. doi: 10.1111/j.1749-6632.1986.tb38392.x

Brown, D. A., and Adams, P. R. (1980). Muscarinic suppression of a novel voltage-sensitive K+ current in a vertebrate neurone. *Nature* 283, 673–676. doi: 10.1038/283673a0

Brown, D. A., and Passmore, G. M. (2009). Neural KCNQ (Kv7) channels. *Br. J. Pharmacol.* 156, 1185–1195. doi: 10.1111/j.1476-5381.2009.00111.x

Chen, W. R., Midtgaard, J., and Shepherd, G. M. (1997). Forward and backward propagation of dendritic impulses and their synaptic control in mitral cells. *Science* 278, 463–467. doi: 10.1126/science.278.5337.463

Cotel, F., Exley, R., Cragg, S. J., and Perrier, J. F. (2013). Serotonin spillover onto the axon initial segment of motoneurons induces central fatigue by inhibiting action potential initiation. *Proc. Natl. Acad. Sci. U.S.A.* 110, 4774–4779. doi: 10.1073/pnas.1216150110

Duflocq, A., Le Bras, B., Bullier, E., Couraud, F., and Davenne, M. (2008). Nav1.1 is predominantly expressed in nodes of Ranvier and axon initial segments. *Mol. Cell. Neurosci.* 39, 180–192. doi: 10.1016/j.mcn.2008.06.008

Eccles, J. C. (1964). *The Physiology of Synapses*. Berlin: Springer-Verlag.

Grubb, M. S., and Burrone, J. (2010). Activity-dependent relocation of the axon initial segment fine-tunes neuronal excitability. *Nature* 465, 1070–1074. doi: 10.1038/nature09160

Hausser, M., Stuart, G., Racca, C., and Sakmann, B. (1995). Axonal initiation and active dendritic propagation of action potentials in substantia nigra neurons. *Neuron* 15, 637–647. doi: 10.1016/0896-6273(95)90152-3

Hedstrom, K. L., Ogawa, Y., and Rasband, M. N. (2008). AnkyrinG is required for maintenance of the axon initial segment and neuronal polarity. *J. Cell Biol.* 183, 635–640. doi: 10.1083/jcb.200806112

Henze, D. A., and Buzsaki, G. (2001). Action potential threshold of hippocampal pyramidal cells *in vivo* is increased by recent spiking activity. *Neuroscience* 105, 121–130. doi: 10.1016/S0306-4522(01)00167-1

Hounsgaard, J., Kiehn, O., and Mintz, I. (1988). Response properties of motoneurones in a slice preparation of the turtle spinal cord. *J. Physiol.* 398, 575–589. doi: 10.1113/jphysiol.1988.sp017058

Kole, M. H., Ilschner, S. U., Kampa, B. M., Williams, S. R., Ruben, P. C., and Stuart, G. J. (2008). Action potential generation requires a high sodium channel density in the axon initial segment. *Nat. Neurosci.* 11, 178–186. doi: 10.1038/nn2040

Kole, M. H., Letzkus, J. J., and Stuart, G. J. (2007). Axon initial segment Kv1 channels control axonal action potential waveform and synaptic efficacy. *Neuron* 55, 633–647. doi: 10.1016/j.neuron.2007.07.031

Nicholson, C., and Freeman, J. A. (1975). Theory of current source-density analysis and determination of conductivity tensor for anuran cerebellum. *J. Neurophysiol.* 38, 356–368.

Pan, Z., Kao, T., Horvath, Z., Lemos, J., Sul, J. Y., Cranstoun, S. D., et al. (2006). A common ankyrin-G-based mechanism retains KCNQ and NaV channels at electrically active domains of the axon. *J. Neurosci.* 26, 2599–2613. doi: 10.1523/JNEUROSCI.4314-05.2006

Perrier, J. F., and Cotel, F. (2015). Serotonergic modulation of spinal motor control. *Curr. Opin. Neurobiol.* 33, 1–7. doi: 10.1016/j.conb.2014.12.008

Perrier, J. F., and Hounsgaard, J. (2003). 5-HT2 receptors promote plateau potentials in turtle spinal motoneurons by facilitating an L-type calcium current. *J. Neurophysiol.* 89, 954–959. doi: 10.1152/jn.00753.2002

Rasmussen, H. B., Frokjaer-Jensen, C., Jensen, C. S., Jensen, H. S., Jorgensen, N. K., Misonou, H., et al. (2007). Requirement of subunit co-assembly and ankyrin-G for M-channel localization at the axon initial segment. *J. Cell Sci.* 120, 953–963. doi: 10.1242/jcs.03396

Ruigrok, T. J., Crowe, A., and Ten Donkelaar, H. J. (1984). Morphology of lumbar motoneurons innervating hindlimb muscles in the turtle Pseudemys scripta

elegans: an intracellular horseradish peroxidase study. *J. Comp. Neurol.* 230, 413–425. doi: 10.1002/cne.902300309

Schafer, D. P., Jha, S., Liu, F., Akella, T., Mccullough, L. D., and Rasband, M. N. (2009). Disruption of the axon initial segment cytoskeleton is a new mechanism for neuronal injury. *J. Neurosci.* 29, 13242–13254. doi: 10.1523/JNEUROSCI.3376-09.2009

Schiller, J., Major, G., Koester, H. J., and Schiller, Y. (2000). NMDA spikes in basal dendrites of cortical pyramidal neurons. *Nature* 404, 285–289. doi: 10.1038/35005094

Stuart, G., Schiller, J., and Sakmann, B. (1997). Action potential initiation and propagation in rat neocortical pyramidal neurons. *J. Physiol.* 505(Pt 3), 617–632. doi: 10.1111/j.1469-7793.1997.617ba.x

Stuart, G. J., and Sakmann, B. (1994). Active propagation of somatic action potentials into neocortical pyramidal cell dendrites. *Nature* 367, 69–72. doi: 10.1038/367069a0

Thome, C., Kelly, T., Yanez, A., Schultz, C., Engelhardt, M., Cambridge, S. B., et al. (2014). Axon-carrying dendrites convey privileged synaptic input in hippocampal neurons. *Neuron* 83, 1418–1430. doi: 10.1016/j.neuron.2014.08.013

Zhang, X., and Bennett, V. (1998). Restriction of 480/270-kD ankyrin G to axon proximal segments requires multiple ankyrin G-specific domains. *J. Cell Biol.* 142, 1571–1581. doi: 10.1083/jcb.142.6.1571

Conflict of Interest Statement: The authors declare that the research was conducted in the absence of any commercial or financial relationships that could be construed as a potential conflict of interest.

frontiers in Cellular Neuroscience

MINI REVIEW
published: 10 March 2015
doi: 10.3389/fncel.2015.00081

Physiological consequences of doublet discharges on motoneuronal firing and motor unit force

Włodzimierz Mrówczyński[1], Jan Celichowski[1], Rositsa Raikova[2] and Piotr Krutki[1]*

[1] Department of Neurobiology, University School of Physical Education, Poznań, Poland, [2] Institute of Biophysics and Biomedical Engineering, Bulgarian Academy of Sciences, Sofia, Bulgaria

The double discharges are observed at the onset of contractions of mammalian motor units (MUs), especially during their recruitment to strong or fast movements. Doublets lead to MU force increase and improve ability of muscles to maintain high force during prolonged contractions. In this review we discuss an ability to produce doublets by fast and slow motoneurons (MNs), their influence on the course of action potential afterhyperpolarization (AHP) as well as its role in modulation of the initial stage of the firing pattern of MNs. In conclusion, a generation of doublets is an important strategy of motor control, responsible for fitting the motoneuronal firing rate to the optimal for MUs at the start of their contraction, necessary for increment of muscle force.

Keywords: doublet, motoneuron, interspike interval, motor unit, force development

OPEN ACCESS

Edited by:
Sergey M. Korogod, International Center for Molecular Physiology, National Academy of Sciences of Ukraine, Ukraine

Reviewed by:
Oliver Röhrle, Universität Stuttgart, Germany
Alexander Kostyukov, A. A. Bogomoletz Institute of Physiology, Ukraine

****Correspondence:***
Włodzimierz Mrówczyński, Department of Neurobiology, University School of Physical Education, 27/39 Królowej Jadwigi St., 61-871 Poznań, Poland
mrowczynski@awf.poznan.pl

Received: *28 November 2014*
Accepted: *23 February 2015*
Published: *10 March 2015*

Citation:
Mrówczynski W, Celichowski J, Raikova R and Krutki P (2015) Physiological consequences of doublet discharges on motoneuronal firing and motor unit force. Front. Cell. Neurosci. 9:81. doi: 10.3389/fncel.2015.00081

Introduction

A pair of action potentials at short interspike intervals (ISIs, below 10 ms) called "doublet" (Simpson, 1969) has been frequently observed at the beginning of discharge pattern of motoneurons (MNs). Such initial doublets in trains of action potentials of motor units (MUs) have been recorded from numerous human muscles during different types of voluntary activity (Person and Kudina, 1972; Kudina, 1974; Bawa and Calancie, 1983; Kudina and Alexeeva, 1992; Garland and Griffin, 1999) or from animal muscles during locomotion (Zajac and Young, 1980b; Hennig and Lømo, 1985; Hoffer et al., 1987; Gorassini et al., 2000). Existence of doublets has also been confirmed in electrophysiological studies performed on MNs innervating inspiratory (Kirkwood and Munson, 1996) and locomotor muscles (Spielmann et al., 1993) of cat or hind limb muscles of rat (Mrówczyński et al., 2010; Bączyk et al., 2013) during their activation with intracellular current injection.

Many experiments on human muscles (Bawa and Calancie, 1983; Kirkwood and Munson, 1996; Van Cutsem et al., 1998; Garland and Griffin, 1999; Christie and Kamen, 2006) and MUs of various animal species (Zajac and Young, 1980a; Hennig and Lømo, 1987; Sandercock and Heckman, 1997) have suggested that doublets are responsible for considerable enhancement of muscle output force. From this reason, doublets are considered as a special strategy of the central nervous system, which improves efficiency of a motor task requiring large force especially at early stage of muscle contraction (Garland and Griffin, 1999; Kudina and Andreeva, 2013).

The occurrence of doublets is also an important mechanism of adaptation to increasing level of muscle activity. Binder-Macleod and Barker (1991) have demonstrated that effects of doublet in force enhancement are greater in fatigued than in unfatigued muscles. Furthermore, a substantial increase of a number of doublets in muscles of trained athletes during dynamic voluntary contractions have suggested their contribution to an increase in the speed of

contraction after the dynamic training (Griffin et al., 1998; Van Cutsem et al., 1998).

The paper aims to describe physiological consequences of the doublet occurrence for the afterhyperpolarization (AHP) parameters following the action potentials and consequently for initial ISIs in a pattern of motoneuronal discharges, which have not been described in previous reviews concerning the doublets (Garland and Griffin, 1999; Kudina and Andreeva, 2013). The consequences of the doublet discharges are discussed in relation to the MU force development.

The Incidence of Doublets in Motoneurones

Experimental data obtained in animal studies suggest that the ability to produce doublets is attributed rather to fast than to slow MNs (Gorassini et al., 2000). However, electrophysiological studies with the intracellular injection of depolarizing current into spinal MNs of cat (Spielmann et al., 1993) and rat (Mrówczyński et al., 2010; Bączyk et al., 2013) have shown that doublets were produced by both slow and fast MNs. Therefore, it is likely that specific organization of supraspinal pathways descending rather to fast than slow MNs is responsible for doublet discharges during strong contractions in natural conditions.

Some studies indicate that the occurrence of doublets in the pattern of motoneuronal discharges depends on motoneuronal excitability (Christie and Kamen, 2006) and on power of synaptic inputs to MNs (Gorassini et al., 2000). Experiments with intracellular injection of a depolarizing current to rat MNs have demonstrated that doublet discharges are generated at current intensity 2.1–2.4 and 2.1–3.24 times higher than the rheobase of fast and slow MNs, respectively (Mrówczyński et al., 2010; Bączyk et al., 2013). In electrophysiological experiments, the depolarizing current is considered as a physical equivalent of the total synaptic input (Baldissera et al., 1987; Binder and Powers, 1999). From this point of view, a rapid increase of postsynaptic activity evoked through descending drive in MNs seems to be a major factor enabling generation of doublets during strong movements.

Changes in the Firing Pattern and the After Hyperpolarization After the Doublet Discharge

The neuronal firing rate is regulated by several mechanisms. The spike frequency adaptation (SFA) is one of fundamental neuronal properties influencing their repetitive firing. It indicates a decrease in action potentials discharge rate over time (Miles et al., 2005). A period including the first few spikes of a motoneuronal firing has been determined as an "initial" phase of SFA and it is followed by an "early" (up to 250 ms) and "late" (from seconds to even minutes) adaptations (Granit et al., 1963; Kernell and Monster, 1982; Sawczuk et al., 1995; Powers et al., 1999). The initial high rate of motoneuronal firing is responsible for the increase of speed of force development at the onset of a MU contraction, and despite a decreased firing rate observed during the early and late adaptation phases MUs are still able maintain relatively steady level of force (Burke et al., 1976; Stein and Parmiggiani, 1979; Bigland-Ritchie et al., 1983).

The firing rate depends also on the excitation intensity. Studies with the intracellular injection of depolarization current into cat (Spielmann et al., 1993) or rat motoneurones (Mrówczyński et al., 2010) have demonstrated an increase of the overall firing frequency of a MN with increasing intensity of applied current (**Figure 1A**). However, after doublet, a prolongation of the following ISI is observed, causing a transient decrease of firing rate (compare a2 vs. a1 in **Figure 1A**). This reduction of the firing rate of MNs appears despite higher intensity of depolarization current applied. After all, direct comparison of discharge patterns without doublets (evoked at a lower intensity of intracellular depolarizing current or a weaker synaptic input to MNs) to those with doublets (evoked at a higher intensity of depolarizing current or a stronger synaptic input to MNs) seems insufficient to explain functional consequences of initial doublets.

A considerable variability of ISIs in motoneuronal firing evoked by stretching of a muscle and activation of proprioceptors has been observed (Kostyukov et al., 2009, 2011). According to these reports, this is related to non-linear processes of summation of consecutive AHPs, described earlier by Baldissera and Gustafsson (1974).

Studies on rat MNs stimulated antidromically by one pulse and by doublet of pulses at intervals from 5 to 10 ms have shown that doublet modulates the AHP duration and amplitude in both types of MNs (**Figure 1B**; Mrówczyński et al., 2007). In MNs antidromically stimulated with trains of stimuli, from one to five, applied at 5 ms ISIs, an evident increase of the AHP amplitude and a significant prolongation of the AHP duration have been demonstrated after a doublet or sometimes also after a triplet of stimuli (Mrówczyński et al., 2011; Krutki et al., 2014). The AHP duration has not been considerably modified by the following (4th and 5th) pulses in the train. The results indicate that at high stimulation frequency the second activation has the strongest effect on the AHP course.

Duration of the AHP is an important factor influencing a rate of neuronal discharges (Eccles et al., 1958). A considerable decrease of motoneuronal excitability during the AHP reduces the probability of occurrence of subsequent action potential (Kernell, 1965). From this reason the AHP duration is extremely important property of MNs, which controls their firing rate (Piotrkiewicz et al., 2007) and in addition can be used to differentiate fast (with short AHP) and slow MNs (with long AHP) (Gardiner, 1993).

The AHP is an effect of increased potassium conductance in a neuron following the action potential (Barrett et al., 1980). Therefore, it is supposed that the post-doublet prolongation of the AHP duration is an effect of increase in the potassium conductance. However, many studies on spinal MNs and ascending neurons (Kuno et al., 1970; Baldissera and Gustafsson, 1974; Baldissera et al., 1978; Gustafsson, 1984; Mrówczyński et al., 2008) have demonstrated a non-linear summation of the AHPs after the doublet activation. These results have

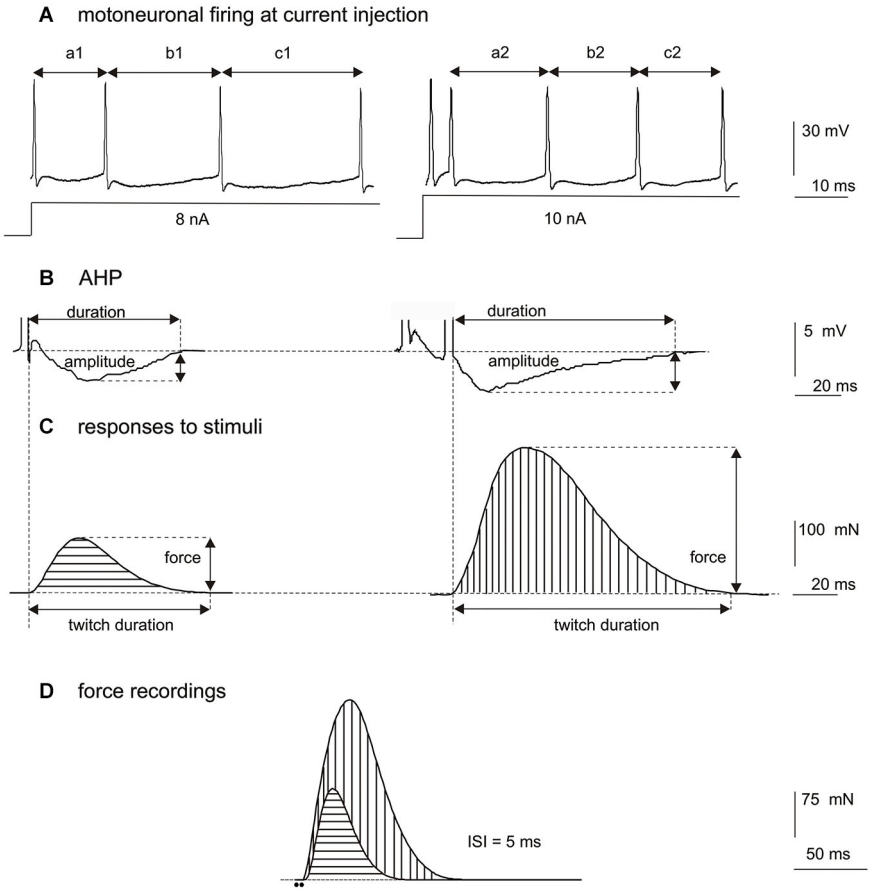

FIGURE 1 | (A) Comparison of discharge rates of a single hind-limb MN of rat under pentobarbital anesthesia, after intracellular injection of depolarizing current of 8 nA (left record, without a doublet) and 10 nA (right record, with a doublet at about 5 ms ISI). Note the increased firing frequency of the MN with increased depolarizing current (the mean of a1 + b1 + c1 is longer than the mean of a2 + b2 + c2), however, the ISI immediately following the doublet (a2) is longer than the ISI after a single pulse below the doublet threshold (a1), and is longer than mean ISI calculated for later discharges (b2 + c2). **(B)** Comparison of the afterhyperpolarization (AHP) amplitude and duration after a single pulse (left record) or a doublet of action potentials (right record), showing a prolongation of the AHP and an increase of the AHP amplitude following a doublet at 5 ms ISI. **(C)** Models of twitch-shape contractions mathematically subtracted from the contraction obtained by two consecutive pulses at 5 ms ISI, for a fast-type MU. On the left, the twitch record in response to a single stimulus, on the right the response to the second stimulus calculated as a difference between the two superimposed recordings in **(D)**. Note higher force and longer duration of twitch-shape response to the second stimulus. The beginning of each record corresponds to the appearance of a stimulus delivered to the axon. **(D)** Superimposed MU force records (the same MU as in **C**) obtained by application of one pulse (horizontal hatching) or by two consecutive pulses delivered at 5 ms ISI (vertical hatching). Note evidently increased MU force after the doublet. The time position of two stimuli at 5 ms ISI is indicated by dots below the record.

implied that additional ionic mechanisms are involved in prolongation of the AHP duration after the doublet than those responsible for the AHP following a single action potential. It is likely that activation of special types of potassium channels responding to increased intracellular concentration of sodium ions (K^{Na+} channels) may contribute to the increase of potassium conductance. Such channels have low sensitivity to normal cytoplasmatic concentration of sodium ions and are not involved in production of a single action potential. According to Safronov and Vogel (1996), a short train of stimuli delivered to the neuron can evoke an intracellular accumulation of sodium ions that is necessary to activate the K^{Na+} channels.

The increase of the AHP duration following the doublet seems to be responsible for a temporary reduction of motoneuronal firing rate, and therefore may be considered as important physiological mechanism fitting the motoneuronal firing rate to that optimal for MUs. Thus, this is an additional internal mechanism of motoneuronal firing rate reduction to previously described mechanisms related to the neuronal network activity, as reciprocal inhibition from the Renshaw cells, inhibition by Ib interneurons (from Golgi tendon organs) or inhibition from interneurons receiving information from descending pathways (Jankowska and Roberts, 1972; Hultborn et al., 1988; Jami, 1992).

The Influence of a Doublet on MU Force Development

The doublet of stimuli at the beginning of a train of pulses leads to an increase of the force output of contracting MU. Such effects have been frequently observed in experiments with doublets of pulses (in a range of 5–10 ms) on isolated fast or slow MUs of hind limb muscles of cat (Burke et al., 1976; Stein and Parmiggiani, 1979; Zajac and Young, 1980a) and rat (Hennig and Lømo, 1987; Celichowski and Grottel, 1998). A potentiation of MUs force in response to doublet has resulted from non-linear summation of twitch forces (Duchateau and Hainaut, 1986a) and could be twice to three times higher than the force of a twitch evoked by a single pulse (Parmiggiani and Stein, 1981; Kamavuako and Farina, 2010).

Simultaneous recording of the action potential from a single MN and the twitch of muscle fibers innervated by that neuron has revealed a positive correlation between the AHP duration and the twitch duration, and this correlation has been documented in several species, as cat (Zengel et al., 1985; Cope et al., 1986), rat (Gardiner and Kernell, 1990) or mouse (Meehan et al., 2010). All these studies have revealed that the activation with a single stimulus results in longer AHP and longer twitch of slow MUs in relation to fast ones. However, the amplitude and duration of both the AHP (Gustafsson, 1984; Mrówczyński et al., 2011) and twitch-shape responses (obtained by a mathematical decomposition of the recorded tetanus) to successive activations (Celichowski et al., 2008) are not constant. Recently, Krutki et al. (2014) have demonstrated in rat a parallelism in modification of the AHP as well as the contraction time and amplitude of the twitch-shape responses to individual stimuli. Parameters collected in one series of experiments with intracellular recordings of MNs (AHP amplitude and duration) (**Figure 1B**) have been compared to data from another series of experiments with the MU force recordings (**Figure 1D**) and to results of their mathematical decomposition (amplitude and duration of twitch-like responses to individual stimuli) (**Figure 1C**). In both series of experiments MNs as well as MUs were activated by trains of stimuli with the increasing numbers of pulses, from one to five, delivered at 5 ms ISIs. The most noticeable changes (the increase in the amplitude and the duration) have been observed in both the AHP and twitch-shape response parameters as an effect of activation with two stimuli (**Figures 1B,C**).

According to Krutki et al. (2014) an increase of twitch force in MUs after the doublet results rather from intracellular processes within muscle fibers than from electromechanical-coupling mechanisms. Duchateau and Hainaut (1986b) have suggested that an intensification of membrane processes in muscle fibers, leading to an increase of calcium concentration in the cell cytosol, is a cause of post-doublet twitch potentiation. Recently, Cheng et al. (2013) have pointed out that doublets evoked an increase of the Ca^{2+} release from sarcoplasmic reticulum, which is accompanied by greater force production in unfatigued muscle fibers of mouse. Thus, the increase of Ca^{2+} release enabling the phosphorylation of myosin light chain is responsible for facilitated formation of additional force-bearing cross bridges in the vicinity of already attached cross bridges leading to increase of MUs twitch force following the doublet (Sweeney et al., 1993; Abbate et al., 2002).

Functional Implications of Doublet

The initial doublet is a specific pattern of MN discharges described by Binder-Macleod (1995) as "high to low" strategy, with a transition from high to low discharge rate. Such patterns contain a strong initial dynamic component followed by the steady state activity. According to the hypothesis by Kostyukov and Korchak (1998), dynamic components in the efferent commands play a decisive role in coding the final position of limbs in real movements.

However, it should be stressed that during voluntary activity, a strong descending drive to MNs causes recruitment of many additional MUs (Aagaard, 2003). Some studies concerning human training have demonstrated that strong MUs may be included into the muscle contraction at an early stage of force development (Van Cutsem et al., 1998; Kamen and Knight, 2004; Vila-Chã et al., 2010). Therefore, although the recruitment is the main mechanism of force regulation, doublets add an extra force to the muscle contraction. However, Sandercock and Heckman (1997) have reported that muscle movement completely abolishes muscle potentiation evoked by doublet after about 0.4 s of eccentric or concentric contractions of cat soleus muscle. Such result suggests that the doublet can evoke an initial force increment, but this effect does not remain high throughout the movement (Garland and Griffin, 1999). Thus, the physiological meaning of doublets in the force increase could be less significant during voluntary activity than it appears from the traditional scheme based on comparison of linear summation of two isolated isometric twitches. Moreover, doublets are not unique components responsible for adding force at the beginning of MUs contraction. Gorassini et al. (2000) have noticed a variety of high-frequency firing patterns started with triplets in fast MUs during locomotion of rats. Thus, during natural activity different initial high-frequency trains of action potentials may lead to faster and stronger contractions.

In conclusion, the doublet at the beginning of motoneuronal activity can be observed in various mammals, and should be considered as a universal mechanism that enables rapid enhancement of force developed by muscles at the beginning of their activity, which lasts despite the passing after-doublet decrease of motoneuronal discharge frequency. Apart from this observation, the influence of doublets on further discharges in motoneuronal firing pattern, especially during voluntary movements, remains unclear.

References

Aagaard, P. (2003). Training-induced changes in neural function. *Exerc. Sport Sci. Rev.* 31, 61–67. doi: 10.1097/00003677-200304000-00002

Abbate, F., Bruton, J. D., De Haan, A., and Westerblad, H. (2002). Prolonged force increase following a high-frequency burst is not due to a sustained elevation of $[Ca^{2+}]$i. *Am. J. Physiol. Cell Physiol.* 283, C42–C47. doi: 10.1152/ajpcell.00416.2001

Bączyk, M., Hałuszka, A., Mrówczyński, W., Celichowski, J., and Krutki, P. (2013). The influence of a 5-wk whole body vibration on electrophysiological properties of rat hindlimb spinal motoneurons. *J. Neurophysiol.* 109, 2705–2711. doi: 10.1152/jn.00108.2013

Baldissera, F., Campadelli, P., and Piccinelli, L. (1987). The dynamic response of cat gastrocnemius motor units investigated by ramp-current injection into their motoneurones. *J. Physiol.* 387, 317–330. doi: 10.1113/jphysiol.1987.sp016575

Baldissera, F., and Gustafsson, B. (1974). Firing behaviour of a neurone model based on the afterhyperpolarization conductance time course and algebraical summation. Adaptation and steady state firing. *Acta Physiol. Scand.* 92, 27–47. doi: 10.1111/j.1748-1716.1974.tb05720.x

Baldissera, F., Gustafsson, B., and Parmiggiani, F. (1978). Saturating summation of the afterhyperpolarization conductance in spinal motoneurones: a mechanism for secondary range repetitive firing. *Brain Res.* 146, 69–82. doi: 10.1016/0006-8993(78)90218-4

Barrett, E. F., Barett, N. J., and Crill, W. E. (1980). Voltage-sensitive outward currents in cat motoneurones. *J. Physiol.* 304, 251–276. doi: 10.1113/jphysiol.1980.sp013323

Bawa, P., and Calancie, B. (1983). Repetitive doublets in human flexor carpi radialis muscle. *J. Physiol.* 339, 123–132. doi: 10.1113/jphysiol.1983.sp014707

Bigland-Ritchie, B., Johansson, R., Lippold, O. C., Smith, S., and Woods, J. J. (1983). Changes in motoneurone firing rates during sustained maximal voluntary contractions. *J. Physiol.* 340, 335–346. doi: 10.1113/jphysiol.1983.sp014765

Binder, M. D., and Powers, R. K. (1999). Synaptic integration in spinal motoneurones. *J. Physiol. Paris* 93, 71–79. doi: 10.1016/s0928-4257(99)80137-5

Binder-Macleod, S. A. (1995). Variable-frequency stimulation patterns for the optimization of force during muscle fatigue. Muscle wisdom and the catch-like property. *Adv. Exp. Med. Biol.* 384, 227–240. doi: 10.1007/978-1-4899-1016-5_18

Binder-Macleod, S. A., and Barker, C. B. (1991). Use of a catchlike property of human skeletal muscle to reduce fatigue. *Muscle Nerve* 14, 850–857. doi: 10.1002/mus.880140909

Burke, R. E., Rudomin, P., and Zajac, F. E. (1976). The effect of activation history on tension production by individual muscle units. *Brain Res.* 109, 515–529. doi: 10.1016/0006-8993(76)90031-7

Celichowski, J., and Grottel, K. (1998). The influence of a doublet of stimuli at the beginning of the tetanus on its time course. *Acta Neurobiol. Exp. (Wars)* 58, 47–53.

Celichowski, J., Raikova, R., Drzymała-Celichowska, H., Ciechanowicz-Kowalczyk, I., Krutki, P., and Rusev, R. (2008). Model-generated decomposition of unfused tetani of motor units evoked by random stimulation. *J. Biomech.* 41, 3448–3454. doi: 10.1016/j.jbiomech.2008.09.013

Cheng, A. J., Place, N., Bruton, J. D., Holmberg, H. C., and Westerblad, H. (2013). Doublet discharge stimulation increases sarcoplasmic reticulum Ca^{2+} release and improves performance during fatiguing contractions in mouse muscle fibres. *J. Physiol.* 591, 3739–3748. doi: 10.1113/jphysiol.2013.257188

Christie, A., and Kamen, G. (2006). Doublet discharges in motoneurons of young and older adults. *J. Neurophysiol.* 95, 2787–2795. doi: 10.1152/jn.00685.2005

Cope, T. C., Bodine, S. C., Fournier, M., and Edgerton, V. R. (1986). Soleus motor units in chronic spinal transected cats: physiological and morphological alterations. *J. Neurophysiol.* 55, 1202–1220.

Duchateau, J., and Hainaut, K. (1986a). Nonlinear summation of contractions in striated muscle. I. Twitch potentiation in human muscle. *J. Muscle Res. Cell Motil.* 7, 11–17. doi: 10.1007/bf01756197

Duchateau, J., and Hainaut, K. (1986b). Nonlinear summation of contractions in striated muscle. II. Potentiation of intracellular Ca^{2+} movements in single barnacle muscle fibres. *J. Muscle Res. Cell Motil.* 7, 18–24. doi: 10.1007/bf01756198

Eccles, J. C., Eccles, R. M., and Lundberg, A. (1958). The action potentials of the alpha motoneurones supplying fast and slow motor muscles. *J. Physiol.* 142, 275–291. doi: 10.1113/jphysiol.1958.sp006015

Gardiner, P. F. (1993). Physiological properties of motoneurons innervating different muscle unit types in rat gastrocnemius. *J. Neurophysiol.* 69, 1160–1170.

Gardiner, P. F., and Kernell, D. (1990). The "fastness" of rat motoneurones: time-course of afterhyperpolarization in relation to axonal conduction velocity and muscle unit contractile speed. *Pflugers Arch.* 415, 762–766. doi: 10.1007/bf02584018

Garland, S. J., and Griffin, L. (1999). Motor unit double discharges: statistical anomaly or functional entity? *Can. J. Appl. Physiol.* 24, 113–130. doi: 10.1139/h99-010

Gorassini, M., Eken, T., Bennett, D. J., Kiehn, O., and Hultborn, H. (2000). Activity of hindlimb motor units during locomotion in the conscious rat. *J. Neurophysiol.* 83, 2002–2011.

Granit, R., Kernell, D., and Shortess, G. K. (1963). Quantitative aspects of repetitive firing of mammalian motoneurones, caused by injected currents. *J. Physiol.* 168, 911–931. doi: 10.1113/jphysiol.1963.sp007230

Griffin, L., Garland, S. J., and Ivanova, T. (1998). Discharge patterns in human motor units during fatiguing arm movements. *J. Appl. Physiol. (1985)* 85, 1684–1692.

Gustafsson, B. (1984). Afterpotentials and transduction properties in different types of central neurones. *Arch. Ital. Biol.* 122, 17–30.

Hennig, R., and Lømo, T. (1985). Firing patterns of motor units in normal rats. *Nature* 314, 164–166. doi: 10.1038/314164a0

Hennig, R., and Lømo, T. (1987). Gradation of force output in normal fast and slow muscles of the rat. *Acta Physiol. Scand.* 130, 133–142. doi: 10.1111/j.1748--1716.1987.tb08119.x

Hoffer, J. A., Sugano, N., Loeb, G. E., Marks, W. B., O'Donovan, M. J., and Pratt, C. A. (1987). Cat hindlimb motoneurons during locomotion. II. Normal activity patterns. *J. Neurophysiol.* 57, 530–553.

Hultborn, H., Katz, R., and Mackel, R. (1988). Distribution of recurrent inhibition within a motor nucleus. II. Amount of recurrent inhibition in motoneurones to fast and slow units. *Acta Physiol. Scand.* 134, 363–374. doi: 10.1111/j.1748–1716.1988.tb08503.x

Jami, L. (1992). Golgi tendon organs in mammalian skeletal muscle: functional properties and central actions. *Physiol. Rev.* 73, 623–666.

Jankowska, E., and Roberts, W. J. (1972). Synaptic actions of single interneurones mediating reciprocal Ia inhibition of motoneurones. *J. Physiol.* 222, 623–642. doi: 10.1113/jphysiol.1972.sp009818

Kamavuako, E. N., and Farina, D. (2010). Time-dependent effects of pre-conditioning activation on muscle fiber conduction velocity and twitch torque. *Muscle Nerve* 42, 547–555. doi: 10.1002/mus.21726

Kamen, G., and Knight, C. A. (2004). Training-related adaptations in motor unit discharge rate in young and older adults. *J. Gerontol. A Biol. Sci. Med. Sci.* 59, 1334–1338. doi: 10.1093/gerona/59.12.1334

Kernell, D. (1965). The limits of firing frequency in cat lumbosacral motoneurones possessing different time course of afterhyperpolarization. *Acta Physiol. Scand.* 65, 87–100. doi: 10.1111/j.1748-1716.1965.tb04252.x

Kernell, D., and Monster, A. W. (1982). Time course and properties of late adaptation in spinal motoneurones of the cat. *Exp. Brain Res.* 46, 191–196. doi: 10.1007/bf00237176

Kirkwood, P. A., and Munson, J. B. (1996). The incidence of initial doublets in the discharges of motoneurones of two different inspiratory muscles in the cat. *J. Physiol.* 493, 577–587. doi: 10.1113/jphysiol.1996.sp021405

Kostyukov, A. I., and Korchak, O. E. (1998). Length changes of the cat soleus muscle under frequency-modulated distributed stimulation of efferents in isotony. *Neuroscience* 82, 943–955. doi: 10.1016/s0306-4522(97)00105-x

Kostyukov, A. I., Lytvynenko, S. V., Bulgakova, N. V., and Gorkovenko, A. V. (2009). Subthreshold activation of spinal motoneurones in the stretch reflex: experimental data and modeling. *Biol. Cybern.* 100, 307–318. doi: 10.1007/s00422-009-0303-z

Kostyukov, A. I., Lytvynenko, S. V., Bulgakova, N. V., and Gorkovenko, A. V. (2011). Changes in the threshold of generation of action potentials by spinal motoneurons under conditions of their natural activation. *Neurophysiology* 43, 182–191. doi: 10.1007/s11062-011-9201-9

Krutki, P., Mrówczyński, W., Raikova, R., and Celichowski, J. (2014). Concomitant changes in afterhyperpolarization and twitch following repetitive stimulation

of fast motoneurones and motor units. *Exp. Brain Res.* 232, 443–452. doi: 10.1007/s00221-013-3752-5

Kudina, L. P. (1974). Double discharges of human motor neurons. *Neirofiziologiia* 6, 152–160.

Kudina, L. P., and Alexeeva, N. L. (1992). Repetitive doublets of human motoneurones: analysis of interspike intervals and recruitment pattern. *Electroencephalogr. Clin. Neurophysiol.* 85, 243–247. doi: 10.1016/0168-5597(92)90112-o

Kudina, L. P., and Andreeva, R. E. (2013). Motoneuron double discharges: only one or two different entities? *Front. Cell. Neurosci.* 7:75. doi: 10.3389/fncel.2013.00075

Kuno, M., Miyahara, J. T., and Weakly, J. N. (1970). Post-tetanic hyperpolarization produced by an electrogenic pump in dorsal spinocerebellar tract neurones of the cat. *J. Physiol.* 210, 839–855. doi: 10.1113/jphysiol.1970.sp009245

Meehan, C. F., Sukiasyan, N., Zhang, M., Nielsen, J. B., and Hultborn, H. (2010). Intrinsic properties of mouse lumbar motoneurons revealed by intracellular recording in vivo. *J. Neurophysiol.* 103, 2599–25610. doi: 10.1152/jn.00668.2009

Miles, G. B., Dai, Y., and Brownstone, R. M. (2005). Mechanisms underlying the early phase of spike frequency adaptation in mouse spinal motoneurones. *J. Physiol.* 566, 519–532. doi: 10.1113/jphysiol.2005.086033

Mrówczyński, W., Krutki, P., and Celichowski, J. (2007). Double stimulation modulates afterhyperpolarization phase following action potentials evoked in rat motoneurones. *Acta Neurobiol. Exp. (Wars)* 67, 439–446.

Mrówczyński, W., Krutki, P., Chakarov, V., and Celichowski, J. (2008). Summation of afterhyperpolarization after a doublet in fast motoneurones of the rat spinal cord. *Arch. Ital. Biol.* 146, 63–73.

Mrówczyński, W., Krutki, P., Chakarov, V., and Celichowski, J. (2010). Doublet of action potentials evoked by intracellular injection of rectangular depolarization current into rat motoneurones. *Exp. Brain Res.* 205, 95–102. doi: 10.1007/s00221-010-2339-7

Mrówczyński, W., Krutki, P., Chakarov, V., and Celichowski, J. (2011). Modulation of afterhyperpolarization by various stimulation patterns in rat motoneurones. *J. Mot. Behav.* 43, 63–71. doi: 10.1080/00222895.2010.542507

Parmiggiani, F., and Stein, R. B. (1981). Nonlinear summation of contractions in cat muscles. II. Later facilitation and stiffness changes. *J. Gen. Physiol.* 78, 295–311. doi: 10.1085/jgp.78.3.295

Person, R. S., and Kudina, L. P. (1972). Discharge frequency and discharge pattern of human motor units during voluntary contraction of muscle. *Electroencephalogr. Clin. Neurophysiol.* 32, 471–483. doi: 10.1016/0013-4694(72)90058-2

Piotrkiewicz, M., Kudina, L., Mierzejewska, J., Jakubiec, M., and Hausmanowa-Petrusewicz, I. (2007). Age-related change in duration of afterhyperpolarization of human motoneurones. *J. Physiol.* 585, 483–490. doi: 10.1113/jphysiol.2007.142356

Powers, R. K., Sawczuk, A., Musick, J. R., and Binder, M. D. (1999). Multiple mechanisms of spike-frequency adaptation in motoneurones. *J. Physiol. Paris* 93, 101–114. doi: 10.1016/s0928-4257(99)80141-7

Safronov, B. V., and Vogel, W. (1996). Properties and functions of Na^+-activated K^+ channels in the soma of rat motoneurones. *J. Physiol.* 497, 727–734. doi: 10.1113/jphysiol.1996.sp021803

Sandercock, T. G., and Heckman, C. J. (1997). Doublet potentiation during eccentric and concentric contractions of cat soleus muscle. *J. Appl. Physiol. (1985)* 82, 1219–1228.

Sawczuk, A., Powers, R. K., and Binder, M. D. (1995). Spike frequency adaptation studied in hypoglossal motoneurons of the rat. *J. Neurophysiol.* 73, 1799–1810.

Simpson, J. A. (1969). Terminology of electromyogram. *Electroencephalogr. Clin. Neurophysiol.* 26, 224–226. doi: 10.1016/0013-4694(69)90217-x

Spielmann, J. M., Laouris, Y., Nordström, M. A., Robinson, G. A., Reinking, R. M., and Stuart, D. G. (1993). Adaptation of cat motoneurones to sustained and intermittent extracellular activation. *J. Physiol.* 464, 75–120. doi: 10.1113/jphysiol.1993.sp019625

Stein, R. B., and Parmiggiani, F. (1979). Optimal motor patterns for activating mammalian muscles. *Brain Res.* 175, 372–376. doi: 10.1016/0006-8993(79)91019-9

Sweeney, H. L., Bowman, B. F., and Stull, J. T. (1993). Myosin light chain phosphorylation in vertebrate striated muscle: regulation and function. *Am. J. Physiol.* 264, C1085–C1095.

Van Cutsem, M., Duchateau, J., and Hainaut, K. (1998). Changes in single motor unit behavior contribute to the increase in contraction speed after dynamic training in humans. *J. Physiol.* 513, 295–305. doi: 10.1111/j.1469-7793.1998.295by.x

Vila-Chã, C., Falla, D., and Farina, D. (2010). Motor unit behavior during submaximal contractions following six weeks of either endurance or strength training. *J. Appl. Physiol. (1985)* 109, 1455–1466. doi: 10.1152/japplphysiol.01213.2009

Zajac, E., and Young, J. L. (1980a). Properties of stimulus trains producing maximum tension-time area per pulse from single motor units in medial gastrocnemius muscle of the cat. *J. Neurophysiol.* 43, 1206–1220.

Zajac, F. E., and Young, J. L. (1980b). Discharge properties of hindlimb motoneurons in decerebrate cats during locomotion induced by mesencephalic stimulation. *J. Neurophysiol.* 43, 1221–1235.

Zengel, J. E., Reid, S. A., Sypert, G. W., and Munson, J. B. (1985). Membrane electrical properties and prediction of motor-unit type of medial gastrocnemius motoneurons in the cat. *J. Neurophysiol.* 53, 1323–1344.

Conflict of Interest Statement: The authors declare that the research was conducted in the absence of any commercial or financial relationships that could be construed as a potential conflict of interest.

frontiers in Cellular Neuroscience

ORIGINAL RESEARCH
published: 03 August 2016
doi: 10.3389/fncel.2016.00195

Firing Properties of Genetically Identified Dorsal Raphe Serotonergic Neurons in Brain Slices

Boris Mlinar[1], Alberto Montalbano[1], Lukasz Piszczek[2†], Cornelius Gross[2] and Renato Corradetti[1]*

[1] *Department of Neuroscience, Psychology, Drug Research and Children's Health, University of Florence, Florence, Italy,*
[2] *Mouse Biology Unit, European Molecular Biology Laboratory, Monterotondo, Italy*

Tonic spiking of serotonergic neurons establishes serotonin levels in the brain. Since the first observations, slow regular spiking has been considered as a defining feature of serotonergic neurons. Recent studies, however, have revealed the heterogeneity of serotonergic neurons at multiple levels, comprising their electrophysiological properties, suggesting the existence of functionally distinct cellular subpopulations. In order to examine in an unbiased manner whether serotonergic neurons of the dorsal raphe nucleus (DRN) are heterogeneous, we used a non-invasive loose-seal cell-attached method to record α1 adrenergic receptor-stimulated spiking of a large sample of neurons in brain slices obtained from transgenic mice lines that express fluorescent marker proteins under the control of serotonergic system-specific *Tph2* and *Pet-1* promoters. We found wide homogeneous distribution of firing rates, well fitted by a single Gaussian function ($r^2 = 0.93$) and independent of anatomical location ($P = 0.45$), suggesting that in terms of intrinsic firing properties, serotonergic neurons in the DRN represent a single cellular population. Characterization of the population in terms of spiking regularity was hindered by its dependence on the firing rate. For instance, the coefficient of variation of the interspike intervals (ISI), a common measure of spiking irregularity, is of limited usefulness since it correlates negatively with the firing rate ($r = -0.33$, $P < 0.0001$). Nevertheless, the majority of neurons exhibited regular, pacemaker-like activity, with coefficient of variance of the ISI lower than 0.5 in ∼97% of cases. Unexpectedly, a small percentage of neurons (∼1%) exhibited a particular spiking pattern, characterized by low frequency (∼0.02–0.1 Hz) oscillations in the firing rate. Transitions between regular and oscillatory firing were observed, suggesting that the oscillatory firing is an alternative firing pattern of serotonergic neurons.

Keywords: serotonergic neurons, neuronal population, pacemaker neurons, firing regularity, oscillatory firing

OPEN ACCESS

Edited by:
Sergey M. Korogod, National Academy of Sciences of Ukraine, Ukraine

Reviewed by:
Lynn G. Kirby, University of Pennsylvania, USA
Mariano Soiza-Reilly, French Institute of Health and Medical Research, France

****Correspondence:***
Boris Mlinar
bmlinar@unifi.it

†Present address:
Lukasz Piszczek, Research Institute of Molecular Pathology, Vienna, Austria

Received: *26 June 2016*
Accepted: *22 July 2016*
Published: *03 August 2016*

Citation:
Mlinar B, Montalbano A, Piszczek L, Gross C and Corradetti R (2016) Firing Properties of Genetically Identified Dorsal Raphe Serotonergic Neurons in Brain Slices. Front. Cell. Neurosci. 10:195. doi: 10.3389/fncel.2016.00195

INTRODUCTION

In mammals, the dorsal raphe nucleus (DRN) contains the largest population of serotonergic neurons, estimated to be ∼9000 in the mouse (Daszuta and Portalier, 1985; Ishimura et al., 1988), 11,500–15,000 in the rat (Descarries et al., 1982; Vertes and Crane, 1997) and ∼165,000 in humans (Baker et al., 1991). Early electrophysiological experiments carried

out in brain slices and in anesthetized animals have revealed that serotonergic neurons in DRN discharge with a slow (1–2 Hz), regular (clock-like) pattern, suggesting a homogeneous population of pacemaker neurons (Aghajanian et al., 1968; Mosko and Jacobs, 1974, 1976; Aghajanian and Vandermaelen, 1982). Studies in behaving animals further revealed that the firing rate of putative DRN serotonergic neurons is strongly linked to the sleep-wake cycle, showing strong positive correlation with the level of behavioral arousal (McGinty and Harper, 1976; Trulson and Jacobs, 1979; Jacobs and Fornal, 1991). In spite of uncertainty about neuron type identification, data drawn from a larger sample of putative DRN serotonergic neurons in awake animals revealed their heterogeneity with respect to the sleep-wake cycle and suggested the existence of atypical serotonergic neurons, exhibiting spiking activity different from the canonic clock-like pattern (Sakai and Crochet, 2001; Urbain et al., 2006; Sakai, 2011). In recordings from anesthetized animals, a subset of serotonergic neurons was found to discharge with a particular burst-like repetitive mode, characterized by doublets, or occasionally triplets, of closely separated spikes per cycle (Hajós et al., 1995, 1996; Hajós and Sharp, 1996).

By using a juxtacellular labeling method (Pinault, 1996), which greatly improved neuron type identification, it was confirmed that most DRN serotonergic neurons exhibit slow and regular spiking (Allers and Sharp, 2003) and that a subset discharges in burst-like repetitive mode (Hajós et al., 2007). Further studies using juxtacellular labeling revealed both a subset of fast-firing (>8 Hz) serotonergic neurons (Kocsis et al., 2006) and functional differences between single spike and burst firing serotonergic neurons (Schweimer and Ungless, 2010; Schweimer et al., 2011). Recent studies using optogenetic identification of serotonergic neurons have further strengthened the case for the heterogeneity of serotonergic neurons, as atypical, non-clock-like firing neurons have been observed (Cohen et al., 2015). Furthermore, different basal firing rates and reward-related tonic and phasic firing patterns have been reported (Liu et al., 2014; Li et al., 2016). The heterogeneity of DRN serotonergic neurons in behaving animal is at least in part consequential to differences in afferent connections (Warden et al., 2012; Weissbourd et al., 2014), but it could also be due to differences in intrinsic properties of serotonergic neurons. The results of some whole-cell patch clamp studies support this possibility, suggesting diverse subtypes of serotonergic neurons in the DRN (Lowry et al., 2000; Crawford et al., 2010; Calizo et al., 2011; Fernandez et al., 2016). However, evidence of intrinsically heterogeneous classes of serotonergic neurons is far from clear and the possibility that the diversity of serotonergic neurons represents only normal population variability of serotonergic neurons has been raised (Andrade and Haj-Dahmane, 2013).

In order to examine in an unbiased manner whether DRN serotonergic neurons are intrinsically heterogeneous we recorded the spiking activity in a large number of genetically identified serotonergic neurons by using a non-invasive loose-seal cell-attached method. Our data suggest that in terms of their intrinsic spiking properties, serotonergic neurons in the DRN can be considered as a single cellular population, characterized by a wide homogeneous distribution of firing rates and the regularity of spiking proportional to the rate.

MATERIALS AND METHODS

Transgenic Mice

All animal manipulations were performed according to the European Community guidelines for animal care (DL 116/92, application of the European Communities Council Directive 86/609/EEC) and were approved by the Committee for Animal Care and Experimental Use of the University of Florence. Animals were housed in groups of 3–5 per cage and maintained under standard laboratory conditions (food and water *ad libitum*, 12–12 h light-dark cycle with lights on from 08:00 to 20:00 h, ambient temperature 22 ± 1°C, relative humidity 40–50%). Three transgenic mouse lines with serotonergic system-specific fluorescent protein expression were used. The *Tph2*::SCFP (TSC) transgenic mouse line was produced by pronuclear injection in FVBxFVB embryos of a circular mouse BAC (RP23-112F24, Chori-BACPAC Resources, Oakland, CA, USA) containing 220 kb of the *Tph2* gene in which the Renilla luciferase (Rluc; psiCHECK^{TM}, Promega, Fitchburg, WI, USA), in-frame, with the T2A sequence (Holst et al., 2006), followed by super cyan fluorescent protein 3A (SCFP3A) coding sequence (from pSCFP3A-C1; Kremers et al., 2006), bovine growth hormone polyadenylation sequence and an FRT-flanked kanamycin resistance marker (FLP deleted in bacteria before DNA injection) had been inserted at the start codon of the *Tph2* gene (**Figure 1A**). Founders carrying the transgene were identified and genotyped by PCR. The *TSC* line had stable, high-level transgene expression as measured by Rluc expression (data not shown). Nearly all serotonergic neurons in the DRN were found to express SCFP (**Figure 1B**). Pet1-Cre::CAG.eGFP (PCG) line (Montalbano et al., 2015) was obtained by crossing Pet1-Cre mice, expressing Cre recombinase in 5-HT neurons by the *Pet1* promoter and enhancer (Dai et al., 2008) with CAG.eGFP reporter mice, carrying an inducible eGFP cassette (Nakamura et al., 2006). Pet1-Cre::Rosa26.YFP (PRY) was obtained by crossing Pet1-Cre mice with ROSA26-stop-YFP reporter mice (Srinivas et al., 2001). All lines were maintained in a pure C57BL/6 strain. Pet1-Cre and CAG.eGFP mice were kindly provided by Prof. K.P. Lesch (University of Würzburg, Würzburg, Germany). ROSA26-stop-YFP reporter mice were purchased from the Jackson Laboratory (Bar Harbor, ME, USA).

Immunofluorescence

Mice were anesthetized intraperitoneally with Avertin (Sigma-Aldrich, Milan, Italy) and perfused transcardially with 4% paraformaldehyde. Brains were post-fixed overnight at 4°C and sectioned into 70 μm thick slices with a vibratome (Leica Microsystems, Wetzlar, Germany). Free floating sections were stained with primary antibodies overnight at 4°C (1:400 mouse α-TPH, Sigma-Aldrich; 1:800 chicken α-GFP/CFP, Aves Labs, Tigard, OR, USA) and incubated with secondary antibodies for

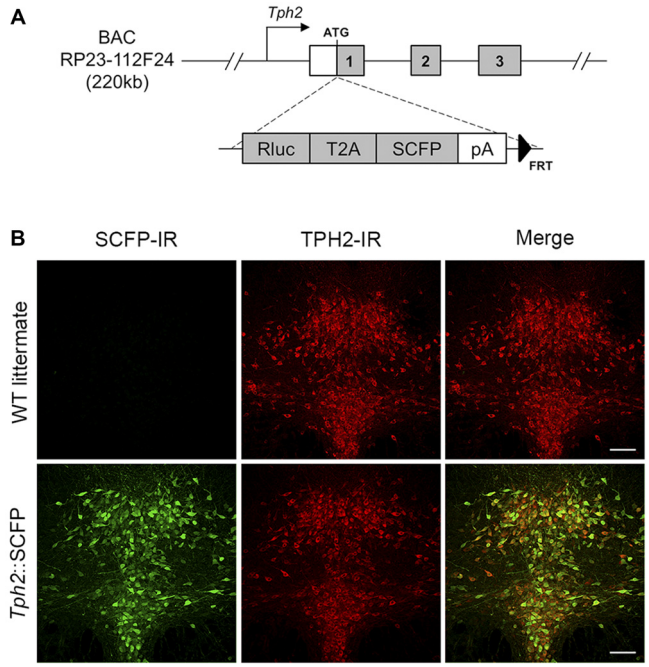

FIGURE 1 | Generation and characterization of *Tph2*::SCFP (TSC) transgenic mice. (A) Scheme of BAC construct used for generation of the *TSC* transgenic mouse line. The Rluc-T2A-SCFP cassette was inserted at the ATG site of the *Tph2* gene in an RP23-112F24 mouse BAC. The modified construct was used for creation of a transgenic mouse line, allowing super cyan fluorescent protein (SCFP) and *Renilla* luciferase expression under *Tph2* promoter. **(B)** Confocal images of SCFP and TPH2 immunoreactivity in 70 μm coronal sections of the dorsal raphe nucleus (DRN) in wild type littermates (upper panel) and *TSC* transgenic mice (lower panel). SCFP expression was detected in the DRN of *TSC* mice with an anti-GFP/CFP antibody (shown in green; left). No signal was seen in wild type littermates. TPH2 expression was detected with an anti-TPH2 antibody (red; middle). In *TSC* mice, the SCFP signal co-localizes with virtually all TPH2-positive neurons in the DRN (yellow in the sum of both channels; right). IR, immunoreactivity. Scale bar: 100 μm.

2 h at room temperature (IgG A488 or IgG A594, Molecular Probes/Thermo Fisher Scientific, Waltham, MA, USA). Confocal microscopy was performed with a TCS-SP5 Laser Scanning System (Leica Microsystems). The images were processed and analyzed using the ImageJ software (ImageJ, National Institutes of Health, Bethesda, MD, USA[1]).

Loose-Seal Cell-Attached Recordings

Mice (4–28 weeks of age) were anesthetized with isofluorane and decapitated. The brains were rapidly removed and dissected in ice-cold gassed (95% O_2 and 5% CO_2) ACSF composed of: 124 mM NaCl, 2.75 mM KCl, 1.25 mM NaH_2PO_4, 1.3 mM $MgCl_2$, 2 mM $CaCl_2$, 26 mM $NaHCO_3$, 11 mM D-glucose. The brainstem was sliced coronally into 200 μm thick slices with a vibratome (DSK, T1000, Dosaka, Japan). Slices were allowed to recover for at least 1 h at room temperature and then were individually transferred to a submersion type recording chamber and continuously superfused at a flow rate of 2 ml min^{-1} with oxygenated ACSF warmed to 37°C by a feedback-controlled in-line heater (TC-324B/SF-28, Warner Instruments, Hamden, CT, USA). Slices were allowed to equilibrate for 10–20 min before the beginning of the recording. To reproduce noradrenergic drive that facilitates serotonergic neuron firing during wakefulness (Baraban and Aghajanian, 1980; Levine and Jacobs, 1992), ACSF was supplemented with the natural agonist noradrenaline (NA; 30 μM) or with the α1 adrenergic receptor agonist phenylephrine (PE; 10 μM; Vandermaelen and Aghajanian, 1983). NA and PE were used at minimal concentrations sufficient to produce a full effect on firing (approximately 10 times higher than the respective EC_{50} values; **Figure 2**). An antioxidant, disodium metabisulfite ($Na_2S_2O_5$, 30 μM) was added to NA-supplemented ACSF to prevent NA oxidation. Recordings were done without the addition of synaptic blockers as we had previously established that under identical recording conditions, spiking of serotonergic neurons is not influenced by the antagonist application (Mlinar et al., 2015). Similarly, no

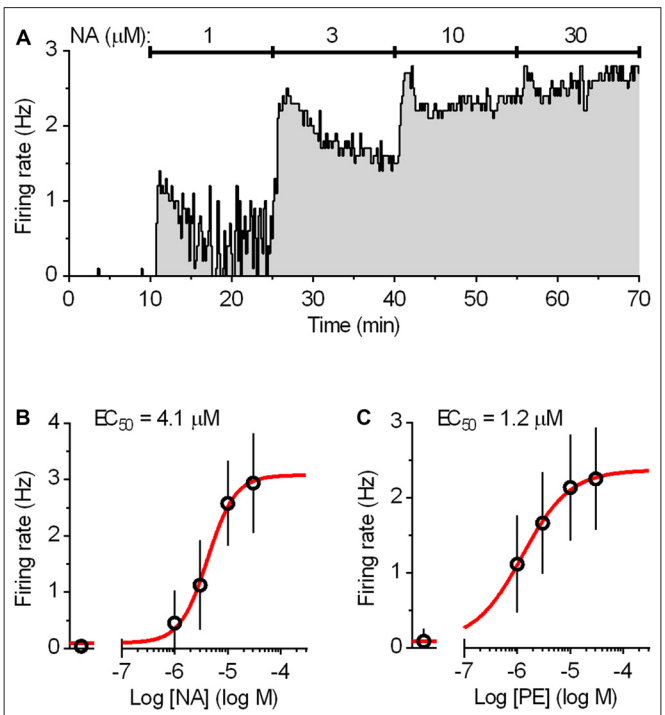

FIGURE 2 | Dose-response curves for the activation of the DRN serotonergic neurons by noradrenaline (NA) and phenylephrine (PE). (A) Integrated firing rate histogram (10 s bins) showing the effect of bath application of NA on the firing rate of a DRN serotonergic neuron. Increasing concentrations of NA (15 min each) were applied during the times indicated by solid lines. The firing rate during the last 3 min at each concentration was used for construction of the dose-response curve. **(B)** Average dose-response curve for NA. Symbols represent the mean of eight experiments. Error bars represent SD. Curve (red) represents the best least squares fit to four-parameter logistic equation. **(C)** Average dose-response curve for α1-adrenergic receptor agonist PE constructed in the same way as that of NA. Symbols represent the mean of nine experiments. Error bars represent SD. Curve (red) represents the best least squares fit to four-parameter logistic equation.

[1]https://imagej.nih.gov/ij/

5-HT1A receptor antagonist was applied since autoinhibition by endogenous 5-HT is insignificant under the conditions used (i.e., without supplementing ACSF with the 5-HT precursor Trp; Mlinar et al., 2005). Typically, recordings were done on four slices per animal, and 5–27 neurons were recorded per slice.

Neurons within DRN were visualized by infrared Dodt gradient contrast video microscopy, using a 40× water-immersion objective (N-Achroplan, numerical aperture 0.75, Zeiss, Göttingen, Germany) and a digital CCD camera (ORCA-ER C4742-80-12AG; Hamamatsu, Hamamatsu City, Japan) mounted on an upright microscope (Axio Examiner Z1; Zeiss) controlled by Axiovision software (Zeiss). Loose-seal cell-attached recordings were made from fluorescent protein-expressing neurons, visually identified by using Zeiss FilterSet 46 (eGFP and YFP, excitation BP 500/20, emission BP 535/30) or Zeiss FilterSet 47 (CFP, excitation BP 436/20, emission BP 480/40). Fluorescence was excited using a metal halide lamp (Zeiss HXP 120). Patch electrodes (3–6 MΩ) were pulled from thick-walled borosilicate capillaries (1.50 mm outer diameter, 0.86 mm inner diameter; Corning) on a P-97 Brown-Flaming puller (Sutter Instruments, Novato, CA, USA) and filled with solution containing (in mM): 125 NaCl, 10 HEPES, 2.75 KCl, 2 $CaCl_2$ and 1.3 $MgCl_2$, pH 7.4 with NaOH. Each pipette was used for several recordings (typically 5–10) and was replaced if tissue debris attached to the tip. When a new patch electrode was used, before touching the cell membrane, the positive pressure was released for several seconds to expose the pipette tip to slice tissue and thus prevent the development of giga-seal. After positioning the pipette in gentle contact with the cell membrane, development of loose seal was monitored by using a voltage-clamp protocol with holding potential of 0 mV and test pulse of 1 mV/100 ms, repeated every second. Weak positive pressure was released and gentle suction was slowly applied until detected spikes increased to 50–100 pA peak-to-peak amplitude. Corresponding seal resistance was in the 10–20 MΩ range. Following the sealing procedure, which lasted 10–30 s, the amplifier was switched to the track (slow voltage clamp) mode and spiking activity was continuously recorded for 2–3 min. Exceptionally, if the firing rate was very low or the spiking pattern appeared anomalous, recordings were prolonged for several minutes and/or the recorded neuron was repatched to confirm the observation. In a minority or recordings the loose seal was established at the beginning of the continuous recording in track mode and the seal resistance was verified at the end of the recording.

Recordings were made using an Axopatch 200B amplifier (Molecular Devices, Sunnyvale, CA, USA) controlled by Clampex 9.2 software (Molecular Devices). Signals were low-pass filtered with a cut-off frequency of 5 kHz (Bessel) and digitized with a sampling rate of 40 kHz (Digidata 1322A, Molecular Devices). After the recording, images of recorded neuron were acquired to document the expression of the fluorescent marker in the recorded neuron, as well as its anatomical location, size and shape.

Measures for Improving the Reliability of Loose-Seal Cell-Attached Recordings

Although loose-seal cell-attached recording under visual guidance is a conceptually simple procedure, reliable measurements of spiking activity rely on two critical factors: (I) the absence of interference of the patch pipette with the recorded neuron; and (II) the reliability that recordings are done on healthy cells. The interference of the pipette with the cell membrane, in particular mechanical stress, may compromise estimation of the neuronal firing rate by using cell-attached recordings (see Alcami et al., 2012 for a critical analysis). As we wanted to obtain reliable, artifact-free recordings from a large number of neurons, additional precautions were made in addition to the above described careful sealing procedure. Thus, the segment of the recording obtained during, and in some cases for up to 1 min following, the sealing procedure was not considered for analysis, because, in spite of our careful approach, spiking activity was transiently influenced by sealing in ∼30% of cases. In case of doubt that the mechanical stretch (exerted by the pipette pressing the plasma membrane and/or the applied suction stretching it) may have interfered with spiking activity, measurement reliability was verified at the end of the recording by application of an additional pulse of suction to the pipette (**Figures 3A–D**). In addition, recordings were interrupted and data discarded if the baseline current (i.e., segments between spikes), monitored online, showed any sign of instability, such as variable amplitude, irregular shape, inward current events, likely to be caused by opening of stretch-activated channels (Suchyna et al., 2009; Alcami et al., 2012).

Viability of preparation is the second crucial factor which may influence results obtained in brain slice recordings. We have previously observed that in unhealthy or aging slices serotonergic neurons fire at a lower rate and ultimately become silent. Under the experimental conditions used in this study, slices were typically viable for 8–10 h. Because our principal objective was to define firing characteristics of a population of neurons, we used several online and *post hoc* criteria to ensure that recordings were done from healthy neurons. First, the neurons selected for recordings were 30–60 μm distant from the slice surface, had an overall healthy appearance and clearly visible intact primary neurites. Second, no further recordings were done in slices in which fluctuations in baseline current or the presence of afterspike (tail) currents were detected more than once. We found that the appearance of afterspike current represents a particularly reliable symptom of decreased viability of brain slices, as it is absent in technically valid recordings from healthy neurons, but often gradually develops during recordings in aging slices. In extreme cases, spike shape can change from its normal form corresponding to the time derivative of action potential to an action potential-like shape, characterized by wider spike and the afterspike current with the time course corresponding to the after-hyperpolarization. We believe that such a deformation of spike shape reflects a decreased resistance of the membrane patch caused by compromised integrity of cell membrane in aging or unhealthy neurons. Third, the

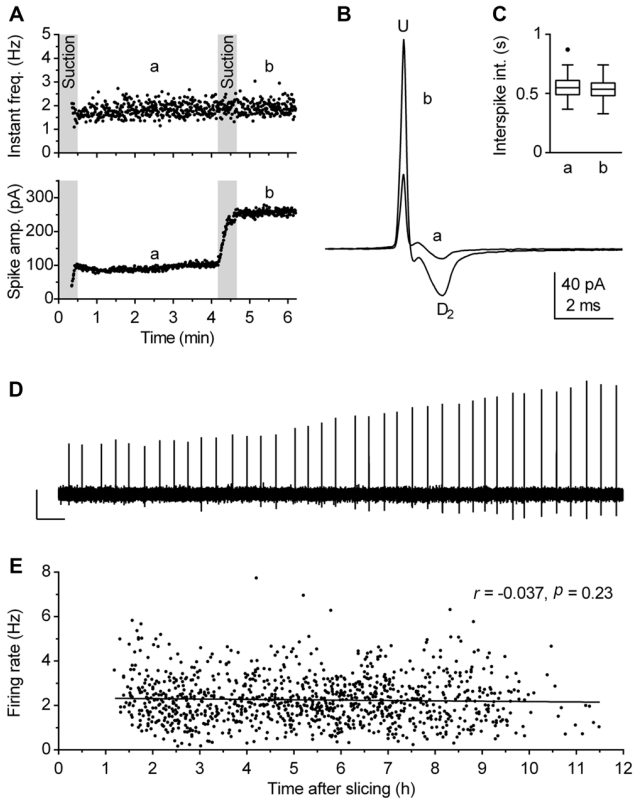

FIGURE 3 | Validity of firing rate measurement by use of loose-seal cell-attached recordings. (A–D) The procedure used to verify the lack of the pipette interference with the measurement. **(A)** Time-course of a recording illustrating the procedure. During the first 30 s, gentle suction was applied to the pipette to establish loose-seal cell-attached recording configuration. The pressure was then released and after 30 s, left to allow relaxation of the patched cell membrane, a 3-min-long segment (denoted a, from 1 to 4 min) was acquired for the measurement. Afterward, additional suction was slowly applied until the spike amplitude approximately doubled (lower panel) and the recording was prolonged for an additional 1.5 min (denoted b). Since the firing rate remained essentially the same after the test (second suction), the recording was considered reliable, i.e., free of pipette interference. **(B)** Superimposed average spikes of the same experiment. Spike duration, measured as the interval from the upstroke peak (U) to the second downstroke peak (D_2), was unchanged by the additional suction. **(C)** Box plot of the same experiments shows no changes in distribution of interspike intervals (ISI). Boxes represent median and the interquartile range (IQR). Whiskers denote 1.5 IQR. **(D)** Trace shows a segment (4:10–4:30 min) of the original recording during which additional (test) suction was applied. Scale bars: 50 pA, 1 s. **(E)** *Post hoc* analysis performed to verify that firing rate of recorded neurons was not influenced by the time passed between slicing and recording. Symbols represent individual neurons. Pearson correlation revealed no correlation between the time after slicing and the firing rate ($r = -0.037$, 95% CI −0.096 to 0.023, $r^2 = 0.0014$, $P = 0.23$). Lines represent linear regression (Slope −0.017 Hz h^{-1}).

reliability of recordings was additionally verified during analysis and several experiments in which there was an increase in spike width and/or the appearance of interspike current were excluded from further analysis. Finally, as a precaution, the order of recordings was scrambled on different days, both regarding slices in respect to their rostrocaudal position as well as regarding location of neurons in a given slice. The validity of these criteria were confirmed *post hoc* by lack of correlation between the firing rate of neurons accepted for analysis and the time interval between slicing and recording for each experimental day (not shown) as well as for the pooled data (**Figure 3E**).

Anatomical Location of Recorded Neurons

Location of recorded neurons in the slices were documented immediately after recording. In addition, for each slice, brightfield images (5× objective) and fluorescence images or stacks (10× objectives) were acquired and then stitched offline using ImageJ software to obtain composite images of an entire slice. For each animal, the rostrocaudal level of slices (distance from bregma) was first assigned based on comparisons with a mouse stereotaxic atlas (Paxinos and Franklin, 2001) and then used to reconstruct the stereotaxic coordinates of recorded neurons. The expected precision of the coordinates is ≤10 μm for the lateral axis and ≤50 μm for rostrocaudal and dorsoventral axes. Subdivisions of DRN are based on the observed distribution pattern of serotonergic neurons and the atlas (Paxinos and Franklin, 2001). Rostrocaudal divisions follow suggestions by Abrams et al. (2004).

Analysis

Spike detection was performed using the event detection routine of Clampfit 9.2 software. Spikes were inspected by eye to assure that there are no false or missed events. Spike duration (width) was determined from the shape of averaged spikes by measuring the interval between the spike upstroke and the second downstroke (see **Figure 3B**). It was determined only for spikes that had a well-defined second downstroke peak (D_2; ∼90% of neurons). The somatic surface area of recorded neurons was measured using the ImageJ freehand tracing tool. To characterize spiking characteristics, the following parameters were calculated for each recorded neuron: firing rate (number of spikes over time interval); SD of instantaneous frequency; COV of instantaneous frequency (SD of instantaneous frequency/mean instantaneous frequency); SD of interspike intervals (ISI); and COV of ISI (SD of ISI/mean ISI). Parametric tests were used for statistical analysis, i.e., ANOVA test with Tukey's multiple comparison *post hoc* test and unpaired *t*-test. Pearson's test and multivariate multiple regression were used to assess for correlation between variables. When appropriate, results of non-parametric tests were reported in addition to those of parametric tests. Data are reported as mean ± SD and median ± interquartile range (IQR). Statistical analysis was performed using Prism 6 software (GraphPad Software, San Diego, CA, USA) with the exception of multivariate multiple regression, which was done using STATA version 14 software (StataCorp LP, College Station, TX, USA).

RESULTS

Firing Rate

The α1 adrenergic receptor-driven spiking activity of fluorescent protein-marked DRN serotonergic neurons was examined in three transgenic mouse lines to reduce the likelihood of

peculiarities potentially caused by genetic modifications. In the PRY and PCG lines, serotonergic system-specific expression of YFP and eGFP, was achieved by Pet-1 promoter (Hendricks et al., 1999; Pfaar et al., 2002), while in the *TSC* line serotonergic system-specific expression of SCFP was achieved by Tph2 promoter. A comparison of data obtained by using all three lines showed that there were no significant differences across the lines in firing rate ($F_{(2,1084)} = 0.29$, $P = 0.75$, ANOVA; range: mean, 2.21–2.27 Hz; median, 2.03–2.18 Hz; **Figure 4A**), regularity of firing (SD of instantaneous frequency: $F_{(2,1084)} = 0.62$, $P = 0.54$, ANOVA; $P = 0.22$, Kruskal-Wallis; **Figure 4B**) and firing pattern (see below). Therefore, data obtained from all three lines will be considered as a uniform group. The activity of serotonergic neurons was examined in two conditions designed to fully facilitate their firing, i.e., in the presence of 30 μM NA (NA) and in the presence of 10 μM of the α1 receptor agonist PE (PE). As shown in **Figure 4C**, similar findings were found under both conditions. Serotonergic neurons exhibited an average firing rate of 2.17 ± 1.13 Hz in NA (mean ± SD, range 0.19–6.29 Hz, median = 2.01 Hz, $n = 358$) and 2.29 ± 1.02 Hz in PE (mean ± SD, range 0.18–7.74 Hz, median = 2.20 Hz, $n = 729$). Although the firing rate of serotonergic neurons was on average slightly lower in NA than in PE, the difference was non-significant ($P = 0.086$, *t* test with Welch's correction) and all subsequent analysis was done on pooled data.

The great majority of serotonergic neurons exhibited steady spiking, with the firing rate ranging from 0.30 to 5.81 Hz in 99% of recorded neurons (e.g., **Figures 4D,E**). In pooled data from all recordings, serotonergic neurons exhibited an average rate of 2.25 ± 1.06 Hz (mean ± SD, range 0.18–7.74 Hz, COV = 46.9%, median = 2.13 Hz, $n = 1087$). The frequency distribution of firing rates was well fit by a single Gaussian function (mean = 2.07 Hz, 95% CI 2.00–2.14 Hz; SD = 0.99 Hz, 95% CI 0.92–1.06 Hz; $r^2 = 0.93$, **Figure 4F**), whereas fitting with a sum of two Gaussians was ambiguous, suggesting that in terms of firing rate DRN serotonergic neurons represent a homogeneous population with a wide distribution of firing rates. Variability in firing rate of serotonergic neurons was evident in recordings from individual mice. For experimental days in which recordings were done from at least thirty serotonergic neurons from a single animal, the mean firing rate ranged from 1.75 to 2.73 Hz, with SD in 0.70–1.30 Hz range and COV in 29.2–63.3% range (**Figure 4G**). Similar findings were observed in individual slices and in sequences of recording from neighboring neurons (not shown). Additional *post hoc* analysis showed no significant difference in firing rate of serotonergic neurons with respect to animal age (range 27–195 days; $r = 0.040$, $P = 0.18$, Pearson) or sex ($P = 0.26$, *t* test; males, 2.24 ± 1.06 Hz, mean ± SD, $n = 843$; females, 2.32 ± 1.04 Hz, mean ± SD, $n = 244$).

Some recent studies have suggested different electrophysiological properties of DRN serotonergic neurons with respect to their anatomical location. To examine such differences, we reconstructed stereotaxic coordinates of almost all recorded neurons (1052 out of 1087; see "Materials and Methods" Section) and tested whether the firing rate depended on spatial location, as well as compared firing rates of neurons belonging to different subnuclei (**Figure 5**). Pearson's correlation revealed no significant difference along the rostrocaudal axis ($r = 0.012$, 95% CI −0.048 to 0.073, $P = 0.69$; **Figure 5B**) and dorsoventral axis ($r = 0.009$, 95% CI −0.052 to 0.069, $P = 0.78$; **Figure 5C**), while borderline significance was reached with respect to the lateral position from the midline ($r = -0.061$, 95% CI −0.122 to −0.0001, $P = 0.046$; **Figure 5D**). In addition, multivariate multiple regression revealed no significant correlation with respect to spatial location ($r = 0.05$, $P = 0.45$). Finally, no differences in firing rate were found among serotonergic neurons belonging to different dorsal raphe subnuclei ($F_{(5,1046)} = 0.56$, $P = 0.73$, ANOVA; **Figure 5E**). Together, these findings suggest a spatially homogeneous population of serotonergic neurons throughout the DRN.

Next, we examined the dependence of the firing rate on the size of neuron and spike duration. Analysis revealed no correlation between the somatic surface area and the firing rate (Pearson $r = 0.006$, $P = 0.84$; **Figure 6A**) and moderate negative correlation between the spike duration and firing rate (Pearson $r = -0.403$, 95% CI −0.455 to −0.348, $r^2 = 0.162$, $P < 0.0001$; **Figure 6B**). These findings indicate that pacemaker properties of serotonergic neurons do not significantly depend on neuron size and based on r^2 value, that only ∼16% of the variability in the firing rate can be explained by variation of spike duration. This suggests that variability in the expression and activity of voltage-gated ion channels determining spike duration, contributes only a small part to pacemaker properties of serotonergic neurons. Finally, the probability density function of spike duration of recorded neurons was found to follow a normal distribution ($r^2 = 0.94$; **Figure 6C**), further supporting the hypothesis that DRN serotonergic neurons constitute an electrophysiologically homogenous cell population.

Spiking Pattern

Clock-like regular spiking is considered one of the defining electrophysiological properties of serotonergic neurons. Consistently, the majority of recorded neurons exhibited a regular spiking pattern irrespective of firing rate (e.g., see **Figure 4D**). In order to define quantitatively the spiking regularity of serotonergic neurons, we first wanted to find a measure of regularity which is independent of the firing rate. For that, we run a correlation analysis of potential regularity measures, SD and COV of instantaneous frequency and ISI, vs. the firing rate (**Figure 7**). We found a weak positive correlation between the SD of instantaneous frequency and the firing rate ($r = 0.20$, $P < 0.0001$, Pearson; **Figure 7A**) and depending on the test used, a weak ($r = -0.35$, $P < 0.0001$, Pearson) or very strong ($r_s = -0.853$, $P < 0.0001$, Spearman) negative correlation between the SD of ISI and the firing rate (not shown). There was also a moderate negative correlation between COV of instantaneous frequency and the firing rate ($r = -0.49$, $P < 0.0001$, Pearson; **Figure 7B**) and between COV of ISI and the firing rate ($r = -0.33$, $P < 0.0001$, Pearson; **Figure 7C**). Similar values were obtained when correlations were run following exclusion of 1% of neurons with lowest and 1% with highest firing rate and/or neurons

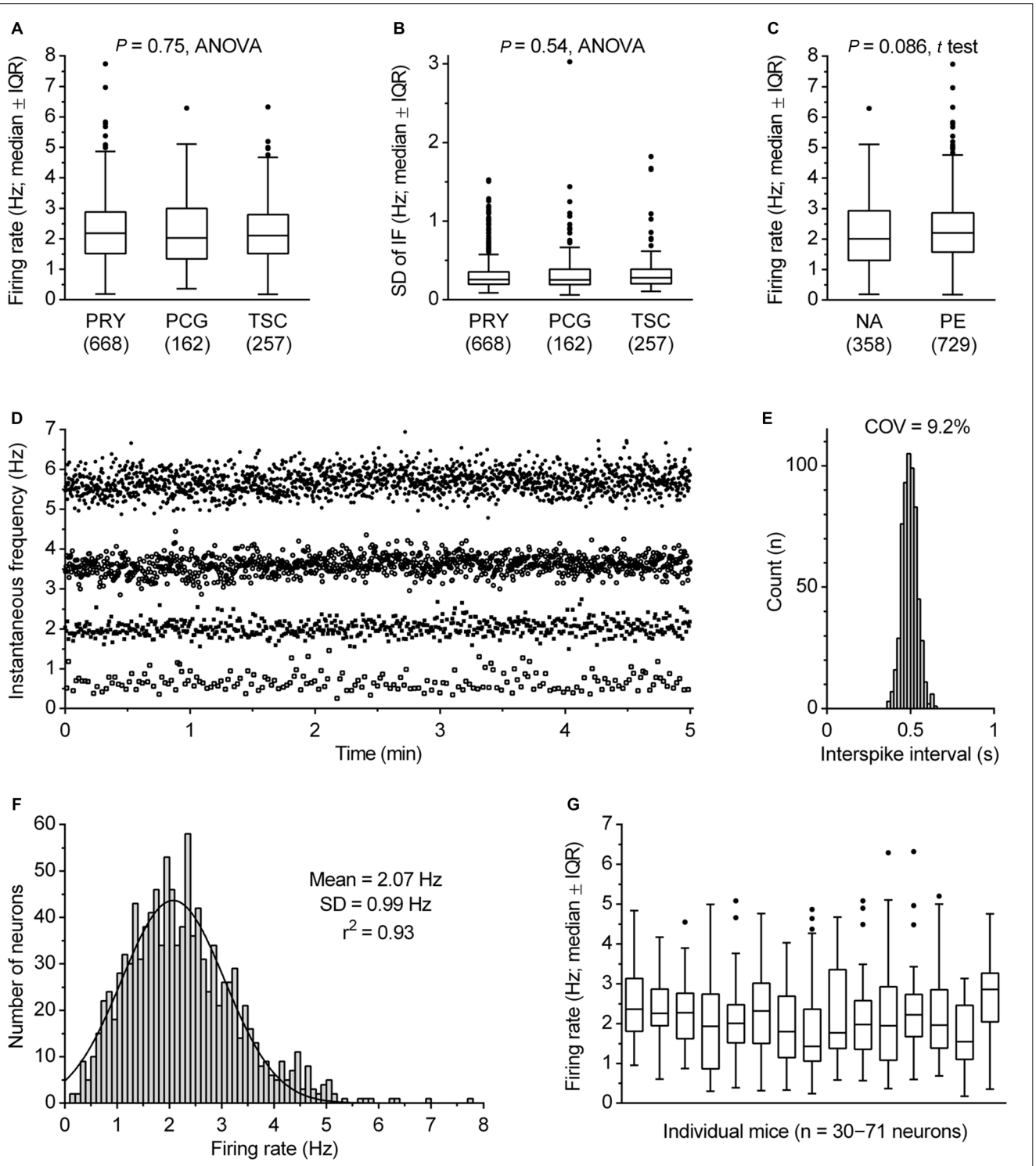

FIGURE 4 | Firing rate of serotonergic neuron population. (A) Comparison of firing rates in transgenic mice lines used in this study. Boxes represent medians and the IQR. Whiskers denote 1.5 IQR. PET1-CRE::ROSA26.YFP (PRY), PET1-CRE::CAG.EGFP (PCG) and TSC stay for PRY, PCG and Tph2-SCFP mouse line, respectively. The number of recorded neurons is indicated in parenthesis. **(B)** Comparison of SD of instantaneous firing (IF) in three mouse lines. **(C)** Comparison of firing rates obtained in the presence of 30 μM NA and 10 μM PE. Boxes represent medians and the IQR. Whiskers denote 1.5 IQR. **(D)** Superimposed time-course of four representative recordings covering firing rate range typical for DRN serotonergic neurons. In the examples shown, firing rates were 5.69, 3.59, 2.02 and 0.62 Hz, while SD of instantaneous frequency were 0.29, 0.22, 0.19 and 0.22 Hz, respectively. **(E)** ISI histogram of 2.02 Hz-firing neuron shown in **(C)**. COV denotes variation coefficients of ISI. **(F)** Firing rate histogram of DRN serotonergic neuron population. Curve represents best fit by single Gaussian function. **(G)** Box plot illustrating variability in firing rate of serotonergic neurons in individual animals. Boxes represent medians and the IQR. Whiskers denote 1.5 IQR.

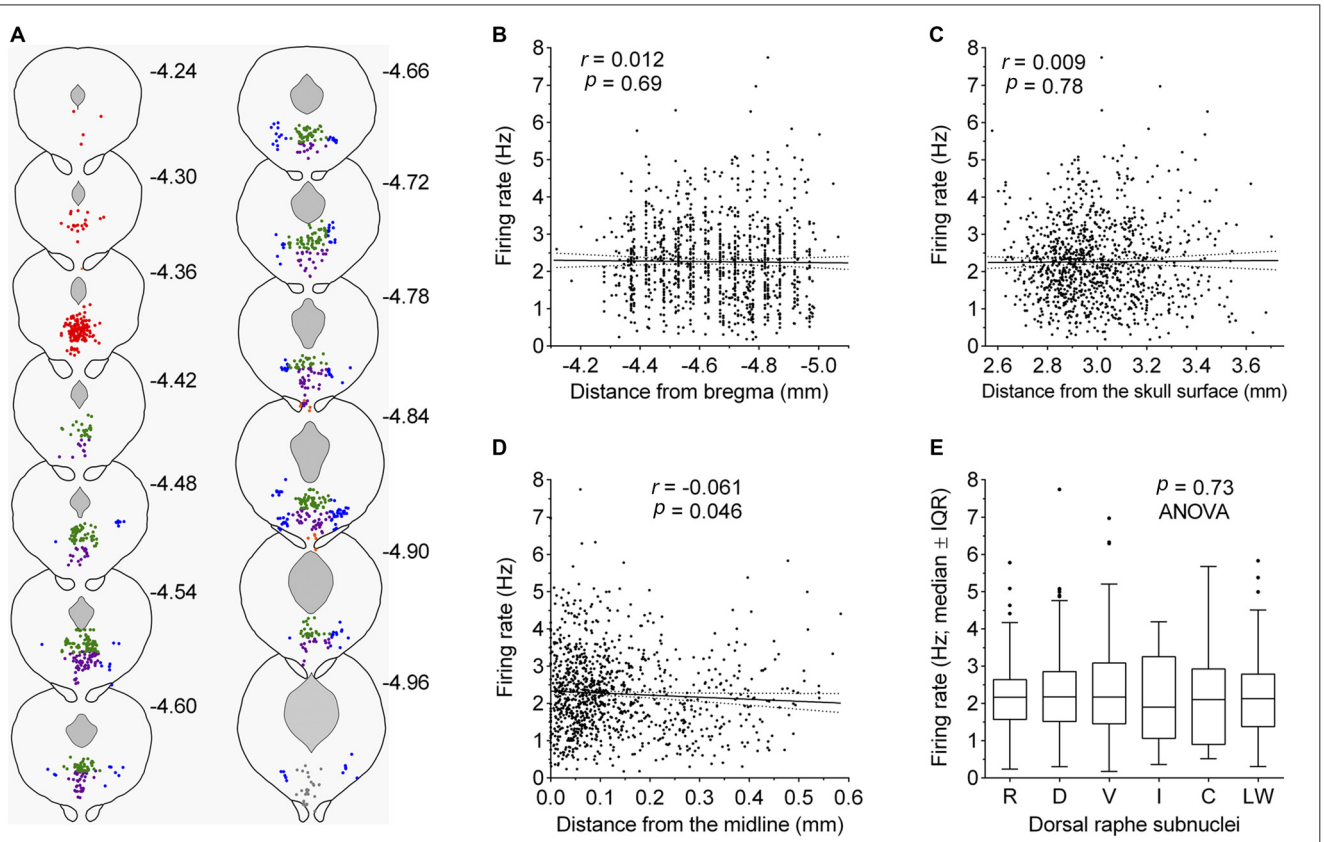

FIGURE 5 | Firing rate of serotonergic neuron is constant across the DRN. (A) Coronal sections showing the anatomical location of recorded serotonergic neurons; adaptations from Paxinos and Franklin (2001). Numbers indicate distance of the section from bregma. Symbols represent individual neurons. Colors indicate dorsal raphe subnuclei: red, rostral; green, dorsal; violet, ventral; orange, interfascicular; gray, caudal; blue, lateral wings. **(B–D)** Correlation between the firing rate and neuron location along the rostrocaudal axis **(B)**, the dorsoventral axis **(C)**, and the lateral distance from the midline **(D)**. In **(C)**, numbers on abscissa correspond to numbers on the right margin of coronal plates in mouse brain atlas (Paxinos and Franklin, 2001) and represent dorsoventral distance from the horizontal plane passing through bregma and lambda on the surface of the skull. Symbols represent individual neurons. Lines represent linear regression and 95% CI. *r* denotes Pearson's correlation coefficient. **(E)** Comparison of firing rates of neurons belonging to different dorsal raphe subnuclei. R, rostral; D, dorsal; V, ventral; I, interfascicular; C, caudal subnucleus; L, lateral wings. Median firing rates and number of recorded neurons per each subnucleus are: R, 2.16 Hz ($n = 165$); D, 2.18 Hz ($n = 440$); V, 2.17 Hz ($n = 290$); I, 1.90 Hz ($n = 11$); C, 2.11 Hz ($n = 27$), L, 2.13 Hz ($n = 119$).

showing slow oscillations in firing frequency (see below). These findings indicate an increased regularity of spiking in neurons firing at higher rates. As a consequence, there is no simple measure providing an adequate, rate-independent definition for firing regularity of serotonergic neurons. Importantly, ISI COV, the most commonly used measure of spike train irregularity, is of limited usefulness and although assumed to be rate-independent, shows a stronger correlation with the firing rate than SD of instantaneous frequency.

Regardless of the measure used to assess regularity, it was evident that not all neurons exhibited canonic clock-like spiking. For instance, if the ISI COV of less than 30% and more than 50% are used as a cutoff to classify highly regular and irregular neurons, respectively, then ~7% of recorded neurons could be considered as moderately regular and ~3% as irregular (**Figure 7D**). Not considering very slow-firing neurons (<0.6 Hz; 28 excluded), most of which would result as irregular according to ISI COV, but not according to instantaneous frequency SD, 1.4% of serotonergic neurons could still be considered as irregular. Most of moderately regular and irregular spiking neurons discharged at a relatively stable rate, but with higher variability in instantaneous frequency and wide positively skewed distribution of ISI. Representative examples of such neurons with firing rates in a range typical for serotonergic neurons (1.5–2.5 Hz) are shown in **Figure 8**. Irregular as well as moderately regular spiking neurons were located throughout the DRN, and were observed in slices obtained from all three transgenic lines and in both NA- and PE-containing ACSF. Irregular spiking persisted after re-patching the same neuron with a new pipette making it unlikely that it was caused by an interference of the pipette with the recorded neuron. Not different from typical serotonergic neurons, irregular spiking neurons stopped firing in response to a 5-HT1A receptor agonist (30 nM R(+)-8-hydroxy-2-(di-n-propylamino)tetralin, $n = 3$, not shown) and continued to discharge irregularly

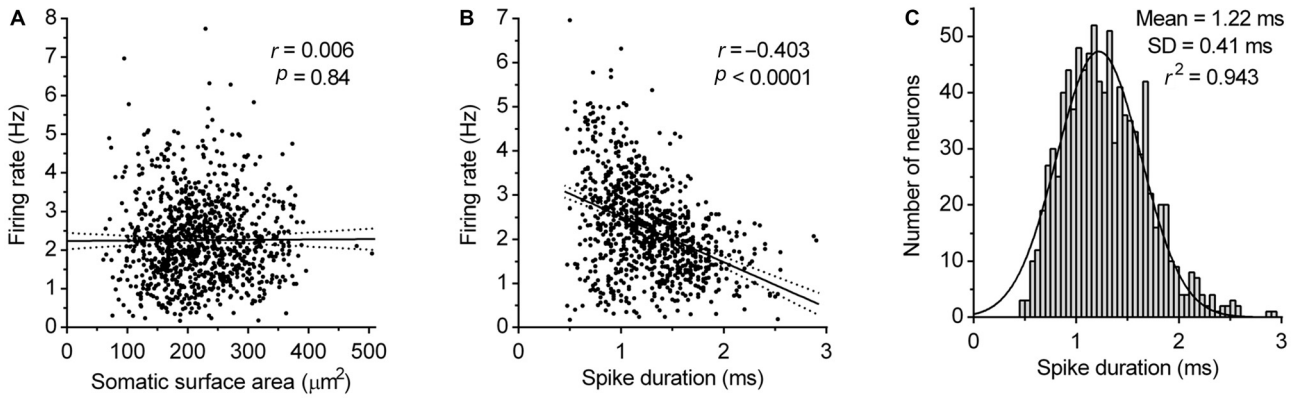

FIGURE 6 | Correlation of firing rate with neuron size and spike duration. (A) Correlation between the firing rate and somatic surface area. Symbols represent individual neurons. Lines represent linear regression and 95% CI. *r* denotes Pearson's correlation coefficient. **(B)** Correlation between the firing rate and spike duration. Symbols represent individual neurons. Lines represent linear regression and 95% CI. *r* denotes Pearson's correlation coefficient. **(C)** Spike duration histogram of DRN serotonergic neuron population. Curve represents best fit by single Gaussian function.

upon washout. Finally, moderately irregular-type firing was also observed in whole cell recordings in which firing was induced by constant current injection or by PE application (not shown). All together, moderately regular and irregular spiking neurons, apart from higher variability in instantaneous frequency, had properties indistinguishable from those of canonic firing serotonergic neurons.

In approximately one percent of cases ($n = 12$), serotonergic neurons exhibited a particular spiking pattern, characterized by low frequency oscillations (LFO) in firing rate with variable amplitude and the period of oscillation ranging from 10 s to almost a minute. Representative recordings covering the range of observed slow oscillatory behavior are shown in **Figure 9**. Compared with typical regular spiking serotonergic neurons, those exhibiting LFO had a similar firing rate (∼0.5–3 Hz), while their firing regularity was several-fold higher when assessed by SD of instantaneous frequency (∼0.7–1.5 Hz) and ∼10-fold higher when assessed by COV of ISI (∼80–300%). In extreme cases spiking was intermittent, with silent periods lasting up to 40 s ($n = 3$; e.g., **Figures 9K–O**). LFO-type neurons were observed in slices obtained from all three mouse lines and in both NA- and PE-containing ACSF. There were no obvious differences between regular spiking and LFO-type neurons with respect to size and shape of neurons, spike duration and anatomical location. LFO was also observed following repatching the same neuron (e.g., **Figure 9Q**), suggesting that it was not caused by pipette interference. In most cases in which LFO was detected, neurons continuously fired with an LFO pattern from the beginning of recording. As we often failed to recognize LFO during the recording, data were acquired for only 2–5 min, a period too short to examine the periodicity of LFO in greater detail. Nevertheless, spontaneous changes in firing pattern were occasionally detected in short recordings ($n = 2$). One such example, where spiking switched from regular to LFO mode is shown in **Figures 10A–E**. Finally, in one case where LFO was detected online, prolonged recording revealed multiple transitions between oscillatory and regular firing (**Figures 10F–H**) suggesting that neurons exhibiting LFO are not a separate subpopulation and that LFO is an alternative firing mode of serotonergic neurons.

DISCUSSION

The loose-seal cell-attached method, which allows recording of intact non-dialyzed neurons, was used to examine spiking activity in a large number of genetically identified DRN serotonergic neurons. This non-invasive recording method and a large sample size permitted us to characterize the spiking properties, which would have likely remained undetected by typical analysis of a lower sample size. The main conclusions of our study can be summarized as follows: (i) in terms of their spiking properties, serotonergic neurons in the DRN represent a homogeneous cellular population; (ii) their regularity of spiking is proportional to the rate of spiking; and (iii) in addition to regular spiking, serotonergic neurons in the DRN can exhibit LFO in firing rate.

In awake state, noradrenergic input exerts a maximal effect on serotonergic neuron firing (Levine and Jacobs, 1992) via activation of α1 receptors (Baraban and Aghajanian, 1980). In brain slice preparations, the noradrenergic input is severed off, but noradrenergic drive may be reinstated by pharmacological activation of α1 receptors (Vandermaelen and Aghajanian, 1983), such as that used in this study. Although α1 agonist-stimulated firing of serotonergic neurons in brain slices mimics an *in vivo* situation only to some extent and may be considered as pharmacologically induced rather than intrinsic, it is nevertheless well suited for assessment of electrophysiological properties of individual neurons because it reflects their intrinsic electrophysiological properties relevant for tonic firing in awake state. In this regard, it is noteworthy that firing rate of the DRN serotonergic neurons observed in this study (99% of neurons fired in 0.30–5.81 Hz range) corresponds fairly well with those

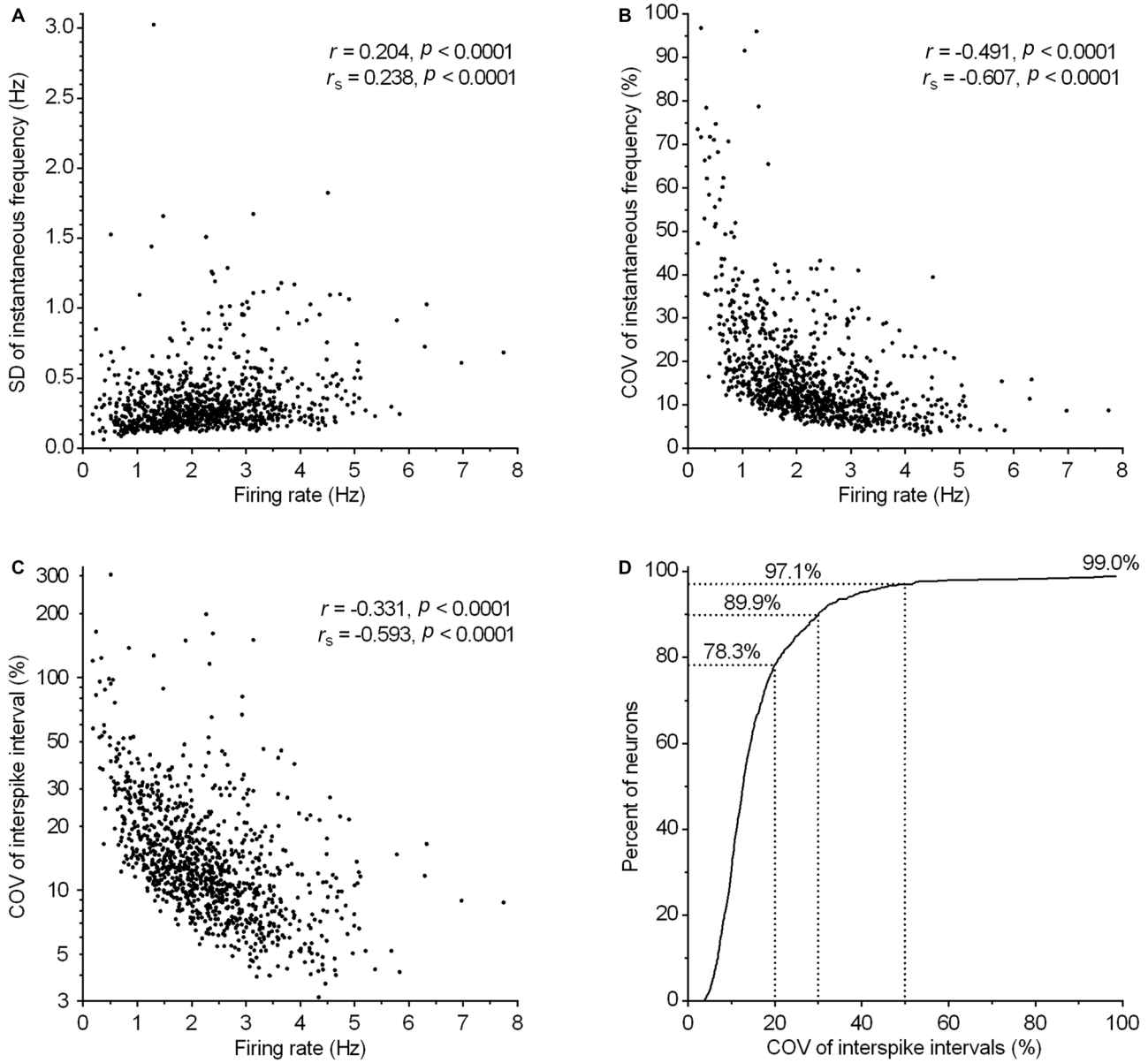

FIGURE 7 | Regularity of firing in serotonergic neuron population correlates with the firing rate. (A–C) Graphs show the correlation between various measures of firing regularity and the firing rate. Symbols represent individual neurons. *r* and r_s denote Pearson's and Spearman's correlation coefficients, respectively. **(A)** Correlation between SD of instantaneous frequency and the firing rate. **(B)** Correlation between COV of instantaneous frequency (SD of instantaneous frequency/mean instantaneous frequency) and the firing rate. **(C)** Correlation between COV of ISI (SD of ISI/mean ISI) and the firing rate. **(D)** Cumulative frequency distribution of COV of ISI for all recorded neurons. The curve reaches only ~99% because eleven neurons (~1%) having COV of ISI in the range between 116 and 304% are out of scale (for clarity).

reported in studies on awake mice. The mean and SD values of serotonergic neuron firing rate found here (2.25 ± 1.06 Hz) are similar to the basal firing rate of optogenetically-identified serotonergic neurons in freely moving mice (1.62 ± 1.70 Hz, $n = 80$; values provided by Li et al., 2016) and are somewhat lower than that of presumed serotonergic neurons during quiet waking (3.21 ± 1.47 Hz, $n = 194$) in head-restrained mice (Sakai, 2011). Furthermore, similar firing rate of the DRN serotonergic neurons (mean = 2.82 Hz) were observed during quiet waking in freely moving cats (Trulson and Jacobs, 1979; Jacobs and Fornal, 1991).

Approximately two thirds of neurons in the DRN are non-serotonergic (Descarries et al., 1982; Jacobs and Azmitia, 1992). Because serotonergic and non-serotonergic neurons are not easily distinguishable based on spike shape and firing properties (Allers and Sharp, 2003; Cohen et al., 2015; and references cited therein), characterization of serotonergic neurons, in particular of those exhibiting atypical spiking patterns, is

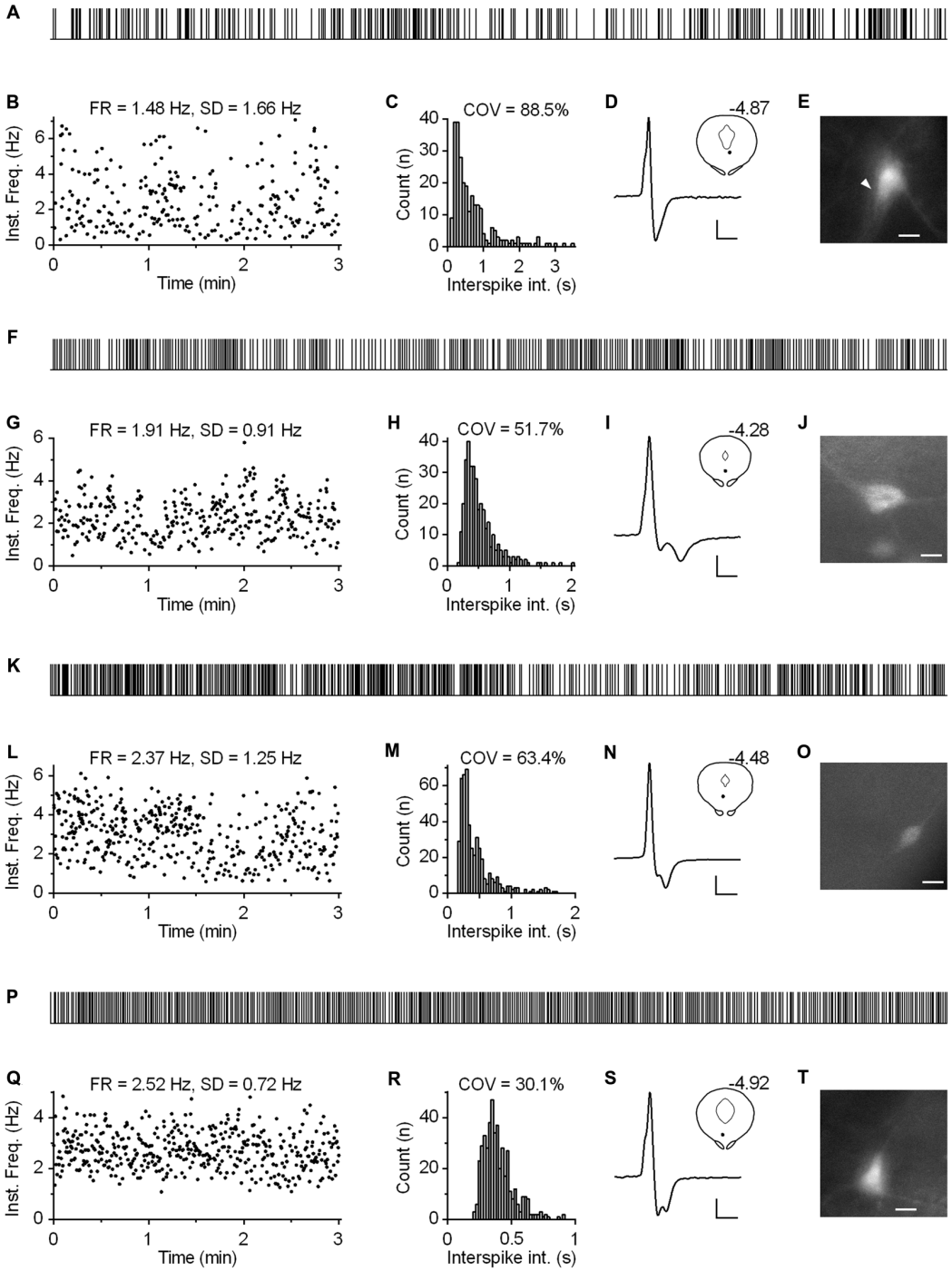

FIGURE 8 | Subset of serotonergic neurons exhibits somewhat irregular spiking. (A) 3-min-long spike train of an irregularly spiking serotonergic neuron. TSC mouse, PE-induced firing. **(B)** Time-course of instantaneous frequency of spike train shown in **(A)**. FR stands for the firing rate. SD stands for standard deviation of instantaneous frequency. **(C)** ISI histogram of the train shown in **(A)**. COV denotes variation coefficient of ISI. **(D)** Average spike of the same recording. Scale bars: 8 pA, 1 ms. Inset shows anatomical location of the neuron. Number indicates distance from bregma. **(E)** Fluorescence image of the recorded neuron. Scale bar: 10 μm. **(F–J)** Irregularly spiking serotonergic neuron in PRY mouse. NA-induced firing. **(F)** 3-min-long spike train. **(I)** Scale bars: 15 pA, 1 ms. Inset shows the anatomical location of the neuron. The number indicates distance from bregma. **(J)** Fluorescence image of the recorded neuron. Scale bar: 10 μm. **(K–O)** Irregularly spiking serotonergic neuron in PRY mouse. PE-induced firing. **(K)** 3-min-long spike train. **(N)** Scale bars: 15 pA, 1 ms. Inset shows anatomical location of the neuron. **(O)** Fluorescence image of the recorded neuron. Scale bar: 10 μm. **(P–T)** Moderately regularly spiking serotonergic neuron in PRY mouse. PE-induced firing. **(P)** 3-min-long spike train. **(S)** Scale bars: 15 pA, 1 ms. Inset shows the anatomical location of the neuron. The number indicates distance from bregma. **(T)** Fluorescence image of the recorded neuron. Scale bar: 10 μm.

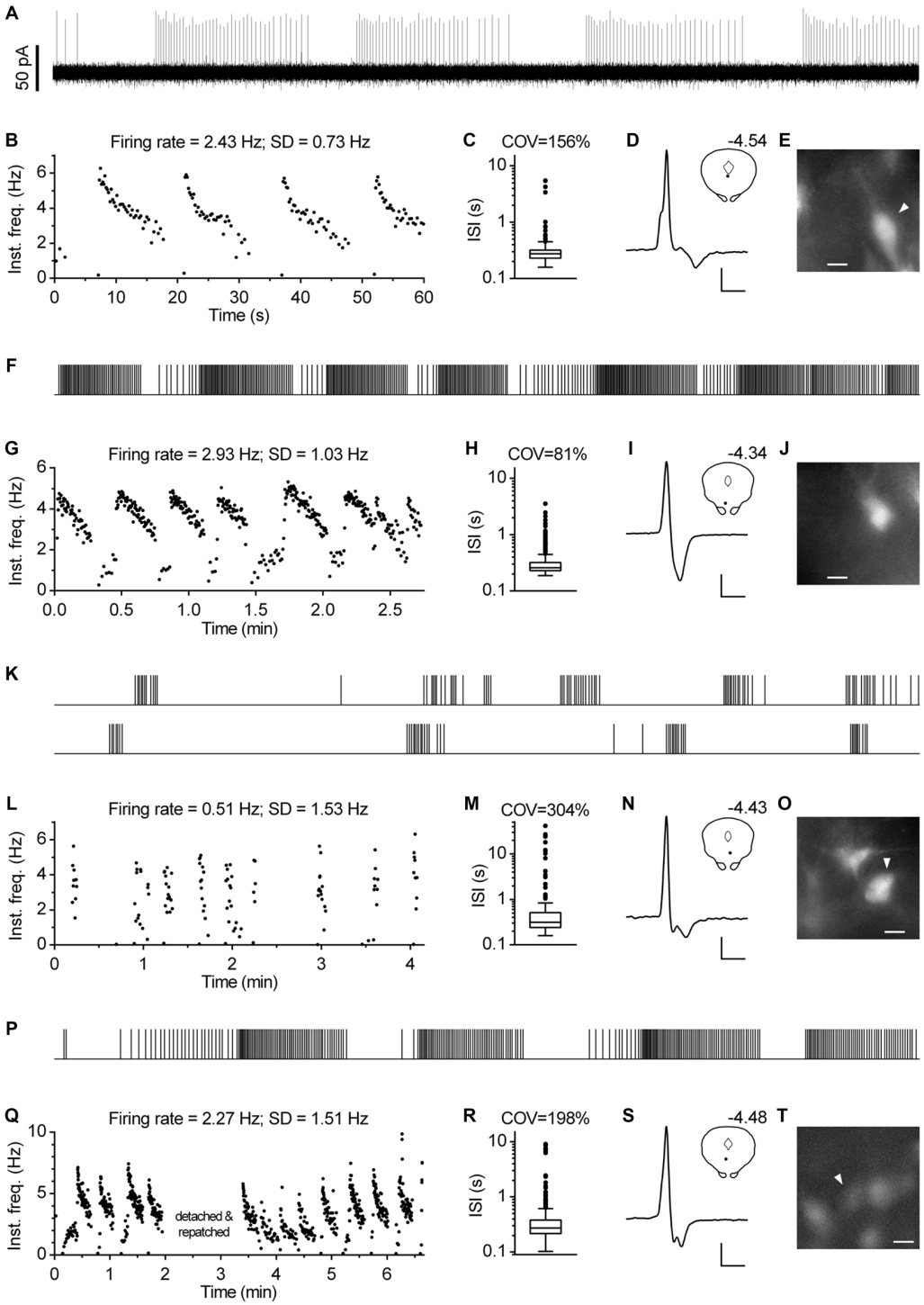

FIGURE 9 | Subset of serotonergic neurons exhibits low frequency oscillation in the firing rate. (A) 1-min-long segment of representative recording of serotonergic neuron exhibiting oscillations in firing rate. PCG mouse, PE-induced firing. **(B)** Time-course of instantaneous frequency of the recording shown in **(A)**. SD stands for standard deviation of instantaneous frequency. **(C)** Box plot shows distribution of ISI of the same recording. Log scale. Boxes represent medians and the IQR. Whiskers denote 1.5 IQR. COV denotes coefficient of variation of ISI. **(D)** Average spike of the same recording. Scale bars: 15 pA, 1 ms. Inset shows the anatomical location of the neuron. The number indicates distance from bregma. **(E)** Fluorescence image of the recorded neuron. Scale bar: 10 μm. **(F–J)** Representative recording of low-frequency oscillation in a serotonergic neuron of PRY mouse. NA-induced firing. **(F)** Spike train. Duration, 164 s. **(G)** Time-course of instantaneous frequency. **(H)** Distribution of ISI. Log scale. **(I)** Average spike. Scale bars: 20 pA and 1 ms. Inset shows the anatomical location of the neuron. The number indicates distance from bregma. **(J)** Fluorescence image of the recorded neuron. Scale bar: 10 μm. **(K–O)** Representative recording of

(*Continued*)

FIGURE 9 | Continued
serotonergic recording exhibiting intermittent firing with silent periods of up to 40 s. PRY mouse, NA-induced firing. **(K)** Spike train. The bottom part is a continuation of the upper one. Overall duration is 250 s. **(L)** Time-course of instantaneous frequency. **(M)** Distribution of ISI. Log scale. **(N)** Average spike. Scale bars: 15 pA and 1 ms. Inset shows the anatomical location of the neuron. The number indicates distance from bregma. **(O)** Fluorescence image of the recorded neuron. Scale bar: 10 μm. **(P–T)** Low-frequency oscillations persist following repatching of a neuron. PRY mouse, PE-induced firing. **(P)** Spike train of initial 117 s. **(Q)** Time-course of instantaneous frequency. **(R)** Distribution of ISI. Log scale. **(S)** Average spike. Scale bars: 12 pA, 1 ms. Inset shows the anatomical location of the neuron. The number indicates distance from bregma. **(T)** Fluorescence image of the recorded neuron. Scale bar: 10 μm.

crucially dependent on the precise identification of recorded neurons as serotonergic. For that, we relied on transgenic mice lines that express fluorescent marker proteins under the control of serotonergic system-specific *Tph2* and *Pet-1* promoters. TPH2 is necessary for serotonin synthesis in the brain and is specifically expressed in the serotonergic neurons of raphe nuclei (Gutknecht et al., 2009). Serotonergic neurons in the raphe can thus be precisely defined on the basis of TPH2 expression and *Tph2* promoter-driven expression of fluorescent reporter genes, such as that of SCFP in the TSC line, which is expected to unmistakably label serotonergic neurons. Pet-1 is an ETS-domain transcription factor whose expression in the brain is restricted to serotonergic neurons (Hendricks et al., 1999; Pfaar et al., 2002). Transgenic mouse lines in which the Cre recombinase expression is driven by the *Pet-1* promoter are well characterized and have been widely used to specifically label serotonergic neurons. There is a possibility, however, that the Pet1-Cre based method does not label all the serotonergic neurons in the DRN (Gaspar and Lillesaar, 2012; Hainer et al., 2015) and it has been shown that Pet1-driven Cre lines have lower specificity and recombination efficiency than Sert-driven Cre lines (Narboux-Nême et al., 2013). In addition, there is evidence suggesting that non-serotonergic neurons could be labeled in Pet1-driven Cre lines. In one Pet1-Cre mouse line it has been shown that Pet1 is expressed also in non-serotonergic neurons in raphe nuclei, with about 1% of Pet-1 expressing neurons being Tph2 negative (non-serotonergic) in the DRN and about 20% in the MRN (Pelosi et al., 2014). Therefore, it cannot be fully ruled out that in Pet1-Cre-based transgenic lines, such as in the PRY and PCG lines used here, some of the fluorescently labeled neurons are non-serotonergic. This possibility seems unlikely, however, because there was a close correspondence between findings obtained using Pet1-Cre based lines and *Tph2* promoter-based TSC line.

Perhaps the main conclusion of this study is that serotonergic neurons in the DRN can be considered as a homogeneous cellular population with respect to their spiking properties. This conclusion is supported by several findings: the probability density function of firing rates follows a normal distribution; multivariate multiple regression shows no correlation between the firing rate and spatial location; there is no difference in firing rate among serotonergic neurons belonging to different dorsal raphe subnuclei; the probability density function of spike durations also follows a normal distribution; and the vast majority of neurons exhibit regular spiking. These findings may seem surprising since there is convincing evidence of functionally distinct serotonergic neuron subtypes in raphe nuclei (Wylie et al., 2010; Calizo et al., 2011; Gaspar and Lillesaar, 2012; Brust et al., 2014; Okaty et al., 2015). Serotonergic neuron diversity is at least in part due to the differences in their developmental history, as different subgroups of serotonergic neurons in raphe nuclei derive from distinct rhombomeric sublineages (Jensen et al., 2008; Wylie et al., 2010; Okaty et al., 2015). Although the heterogeneity of DRN serotonergic neurons cannot be easily explained by diverse cellular origin, as the DRN derives *in toto* from rhombomere 1 (Jensen et al., 2008), recent evidence suggests the existence of distinct serotonergic neuron subtypes also in the DRN (Fernandez et al., 2016). In addition, it has been shown that afferent innervations of the DRN varies along the rostrocaudal axis (Commons, 2009; Soiza-Reilly and Commons, 2011) and that the caudal third of the DRN has afferent innervation more similar to the median raphe nucleus than to the rostral two-thirds of the DRN (Commons, 2015). Furthermore, it was found that a subset of serotonergic neurons do not express 5-HT1A autoreceptors (Kiyasova et al., 2013). Differences were found between serotonergic neurons in the ventromedian subnucleus and lateral wings with respect to electrophysiological properties (Crawford et al., 2010), connectivity and morphology (Crawford et al., 2011), and the expression of G-protein coupled receptors (Spaethling et al., 2014). In contrast to these studies which showed the heterogeneity of DRN serotonergic neurons at multiple levels, but consistent with their common developmental origin, our findings suggest that serotonergic neurons in the DRN represent a homogeneous cellular population with respect to their intrinsic spiking properties. In particular, the α1 receptor-driven firing activity of the DRN serotonergic neurons, which is physiologically important since it is one of the key parameters in determining the brain serotonergic tone, is considerably uniform in spite of the heterogeneity of individual neurons.

Consistent with previous studies, the majority of serotonergic neurons in the DRN exhibited moderately to highly regular spiking. Despite the fact that a quantitative description of spiking regularity was hindered by correlation of regularity measures with the firing rate, it can be concluded that the regularity of spiking of serotonergic neurons is to some extent proportional to their firing rate. This finding is not surprising as, in general, random fluctuations in membrane conductances are expected to introduce more irregularity during a longer-lasting depolarization phase of pacemaking cycle in slower spiking neurons. An additional finding, which was not the main objective of the study design, is that a small fraction of serotonergic neurons exhibit non-canonic firing patterns. Two different modes of atypical firing were observed: ∼1% of neurons discharged spikes with relatively high variability in instantaneous frequency (and ISI) while maintaining a fairly stable firing rate; and (an additional) ∼1% of neurons exhibited LFO in firing rate. Both atypical firing modes were observed in

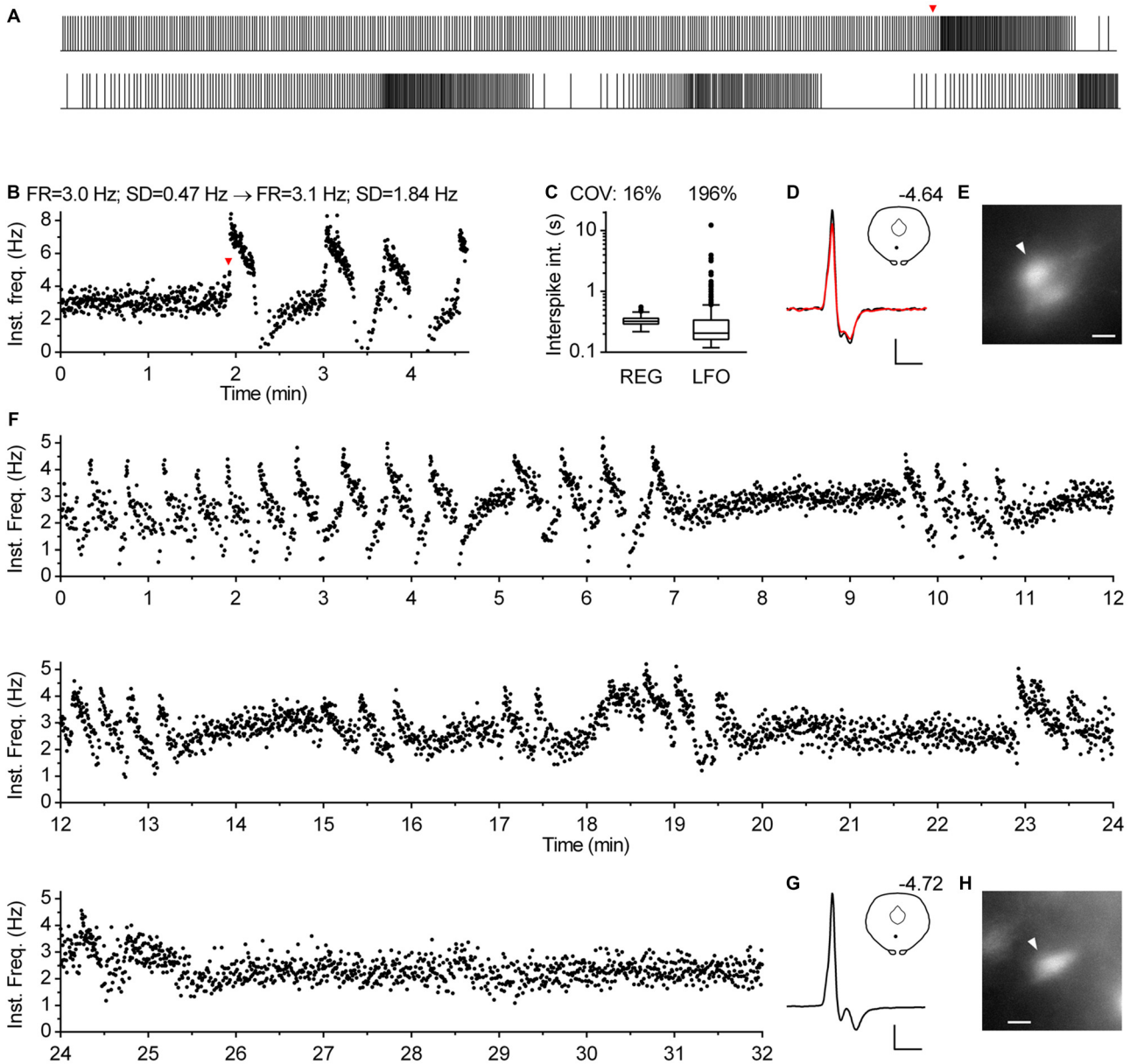

FIGURE 10 | Serotonergic neurons can spontaneously change spiking pattern. (A–E) Spontaneous transition from regular to oscillatory firing of a serotonergic neuron in TSC mouse. NA-induced firing. **(A)** Spike train. The bottom part is a continuation of the upper one. Overall duration is 278 s. Firing pattern changed from regular to oscillatory at 115 s (indicated by red arrowhead). **(B)** Time-course of instantaneous frequency of the train shown in **(A)**. Firing rate (FR) was similar during regular firing (0–115 s) and over the course of three full cycles of low-frequency oscillations (115–273 s), while standard deviation of instantaneous frequency (SD) notably increased. **(C)** Box plot shows distribution of ISI during regular firing segment (REG, 0–115 s) and during the segment of three cycles of low-frequency oscillations (LFO, 115–273 s). Log scale. Boxes represent median and the IQR. Whiskers denote 1.5 IQR. COV denotes coefficient of variation of ISI. **(D)** Superimposed average traces of spikes recorded during regular (black line) and oscillatory firing (red line). Scale bars: 15 pA, 1 ms. Inset shows the anatomical location of the neuron. The number indicates distance from bregma. **(E)** Fluorescence image of the recorded neuron. Scale bar: 10 μm. **(F–H)** Prolonged recording from a serotonergic neuron exhibiting LFO. PRY mouse, PE-induced firing. **(F)** Time-course of instantaneous frequency shows multiple transitions in firing pattern. **(G)** Average spike. Scale bars: 15 pA, 1 ms. Inset shows the anatomical location of the neuron. The number indicates distance from bregma. **(H)** Fluorescence image of the recorded neuron. Scale bar: 10 μm.

neurons which were otherwise indistinguishable from canonic-firing neurons and were observed in all three transgenic mouse lines, thus making it highly unlikely that these were "false positive fluorescently labeled" non-serotonergic neurons. In addition, as "high variability" firing can be considered just as an extreme of normal regular firing and since transitions between LFO mode and regular firing were observed, it seems reasonable to conclude that neurons which exhibited atypical firing modes

do not represent a separate subpopulation of serotonergic neurons.

Because LFO in firing rate was observed in quite a small percentage of DRN serotonergic neurons, we were surprised to find out that the same phenomenon had been previously observed. In a very first electrophysiological study of rat DRN neurons in brain slice preparations, Mosko and Jacobs (1976) reported that a subset of putative serotonergic neurons exhibits slow oscillation in firing rate. Moreover, the same authors observed the same firing pattern in recordings from chloral hydrate-anesthetized rats (Mosko and Jacobs, 1974). Interestingly, they found neurons exhibiting LFO specifically in the DRN, and not in the median raphe nucleus, and observed this type of spiking persisting for over 1 h. Although the identity of recorded neurons was unknown in these studies, on the basis of their morphology and anatomical location, as well as on the close resemblance of their spiking properties to our findings, at least some seem to be serotonergic. To the best of our knowledge, except for the pioneering studies by Mosko and Jacobs (1974, 1976), there seem to be no other studies reporting LFO-type serotonergic neurons in the DRN. The reason for this may lie in the fact that serotonergic neurons have been commonly identified on the basis of firing regularity and LFO-type neurons were considered irregular, especially if ISI COV was used as a regularity measure. Therefore, it seems likely that over the last 40 years the DRN serotonergic neurons exhibiting LFO spiking mode have been misidentified as non-serotonergic.

LFO is observed in a very small percentage of neurons. The proportion of neurons exhibiting LFO may result higher in recordings of longer duration. Although our recordings are too short for periodicity analysis, it seems that at least some of the moderately regular and irregular spiking neurons exhibited LFO-like spiking pattern. The fact that LFO-type neurons have been rarely observed does not preclude the possibility that *in vivo* a higher fraction, or even all serotonergic neurons in the DRN can discharge in LFO mode. In that respect an analogy can be drawn with spike doublets firing mode, which has not been observed *in vitro*, but has been observed in recordings from serotonergic neurons in anesthetized rats and mice (Hajós et al., 1995, 2007; Montalbano et al., 2015). The functional implications of LFO spiking mode are currently unclear. Further *in vivo* studies are needed to elucidate the relationship between LFO spiking mode and sleep/wake/arousal states as well as particular behaviors. At present, it can only be concluded that in terms of their intrinsic spiking properties, serotonergic neurons in the DRN are homogeneous and that, at least a subset of them, can discharge in LFO mode.

AUTHOR CONTRIBUTIONS

BM designed the study, analyzed data, and wrote the manuscript. AM performed and analyzed experiments. LP and CG designed and produced *TSC* mouse line. RC designed and coordinated the study.

FUNDING

This work was supported by grants from the University of Florence and Ente Cassa di Risparmio di Firenze (ECRF-2007-0758). AM was recipient of a fellowship from the Regione Toscana and Aziende Chimiche Riunite Angelini Francesco A.C.R.A.F. SpA (POR CRO FSE 2007-2013: 5-HT@DRUGeMOOD).

ACKNOWLEDGMENTS

We thank Prof. Andrea Nistri for valuable comments on the manuscript.

REFERENCES

Abrams, J. K., Johnson, P. L., Hollis, J. H., and Lowry, C. A. (2004). Anatomic and functional topography of the dorsal raphe nucleus. *Ann. N. Y. Acad. Sci.* 1018, 46–57. doi: 10.1196/annals.1296.005

Aghajanian, G. K., and Vandermaelen, C. P. (1982). Intracellular identification of central noradrenergic and serotonergic neurons by a new double labeling procedure. *J. Neurosci.* 2, 1786–1792.

Aghajanian, G. K., Foote, W. E., and Sheard, M. H. (1968). Lysergic acid diethylamide: sensitive neuronal units in the midbrain raphe. *Science* 161, 706–708. doi: 10.1126/science.161.3842.706

Alcami, P., Franconville, R., Llano, I., and Marty, A. (2012). Measuring the firing rate of high-resistance neurons with cell-attached recording. *J. Neurosci.* 32, 3118–3130. doi: 10.1523/JNEUROSCI.5371-11.2012

Allers, K. A., and Sharp, T. (2003). Neurochemical and anatomical identification of fast- and slow-firing neurones in the rat dorsal raphe nucleus using juxtacellular labelling methods *in vivo*. *Neuroscience* 122, 193–204. doi: 10.1016/s0306-4522(03)00518-9

Andrade, R., and Haj-Dahmane, S. (2013). Serotonin neuron diversity in the dorsal raphe. *ACS Chem. Neurosci.* 16, 22–25. doi: 10.1021/cn300224n

Baker, K. G., Halliday, G. M., Hornung, J. P., Geffen, L. B., Cotton, R. G., and Törk, I. (1991). Distribution, morphology and number of monoamine-synthesizing and substance P-containing neurons in the human dorsal raphe nucleus. *Neuroscience* 42, 757–775. doi: 10.1016/0306-4522(91)90043-n

Baraban, J. M., and Aghajanian, G. K. (1980). Suppression of firing activity of 5-HT neurons in the dorsal raphe by alpha-adrenoceptor antagonists. *Neuropharmacology* 19, 355–363. doi: 10.1016/0028-3908(80)90187-2

Brust, R. D., Corcoran, A. E., Richerson, G. B., Nattie, E., and Dymecki, S. M. (2014). Functional and developmental identification of a molecular subtype of brain serotonergic neuron specialized to regulate breathing dynamics. *Cell Rep.* 9, 2152–2165. doi: 10.1016/j.celrep.2014.11.027

Calizo, L. H., Akanwa, A., Ma, X., Pan, Y. Z., Lemos, J. C., Craige, C., et al. (2011). Raphe serotonin neurons are not homogenous: electrophysiological, morphological and neurochemical evidence. *Neuropharmacology* 61, 524–543. doi: 10.1016/j.neuropharm.2011.04.008

Cohen, J. Y., Amoroso, M. W., and Uchida, N. (2015). Serotonergic neurons signal reward and punishment on multiple timescales. *Elife* 4:e06346. doi: 10.7554/eLife.06346

Commons, K. G. (2009). Locally collateralizing glutamate neurons in the dorsal raphe nucleus responsive to substance P contain vesicular glutamate transporter 3 (VGLUT3). *J. Chem. Neuroanat.* 38, 273–281. doi: 10.1016/j.jchemneu.2009.05.005

Commons, K. G. (2015). Two major network domains in the dorsal raphe nucleus. *J. Comp. Neurol.* 523, 1488–1504. doi: 10.1002/cne.23748

Crawford, L. K., Craige, C. P., and Beck, S. G. (2010). Increased intrinsic excitability of lateral wing serotonin neurons of the dorsal raphe: a mechanism for selective activation in stress circuits. *J. Neurophysiol.* 103, 2652–2663. doi: 10.1152/jn.01132.2009

Crawford, L. K., Craige, C. P., and Beck, S. G. (2011). Glutamatergic input is selectively increased in dorsal raphe subfield 5-HT neurons: role of morphology, topography and selective innervation. *Eur. J. Neurosci.* 34, 1794–1806. doi: 10.1111/j.1460-9568.2011.07882.x

Dai, J. X., Han, H. L., Tian, M., Cao, J., Xiu, J. B., Song, N. N., et al. (2008). Enhanced contextual fear memory in central serotonin-deficient mice. *Proc. Natl. Acad. Sci. U S A* 105, 11981–11986. doi: 10.1073/pnas.0801329105

Daszuta, A., and Portalier, P. (1985). Distribution and quantification of 5-HT nerve cell bodies in the nucleus raphe dorsalis area of C57BL and BALBc mice. Relationship between anatomy and biochemistry. *Brain Res.* 360, 58–64. doi: 10.1016/0006-8993(85)91220-x

Descarries, L., Watkins, K. C., Garcia, S., and Beaudet, A. (1982). The serotonin neurons in nucleus raphe dorsalis of adult rat: a light and electron microscope radioautographic study. *J. Comp. Neurol.* 207, 239–254. doi: 10.1002/cne.902070305

Fernandez, S. P., Cauli, B., Cabezas, C., Muzerelle, A., Poncer, J. C., and Gaspar, P. (2016). Multiscale single-cell analysis reveals unique phenotypes of raphe 5-HT neurons projecting to the forebrain. *Brain Struct. Funct.* doi: 10.1007/s00429-015-1142-4 [Epub ahead of print].

Gaspar, P., and Lillesaar, C. (2012). Probing the diversity of serotonin neurons. *Philos. Trans. R. Soc. Lond. B Biol. Sci.* 367, 2382–2394. doi: 10.1098/rstb.2011.0378

Gutknecht, L., Kriegebaum, C., Waider, J., Schmitt, A., and Lesch, K. P. (2009). Spatiotemporal expression of tryptophan hydroxylase isoforms in murine and human brain: convergent data from Tph2 knockout mice. *Eur. Neuropsychopharmacol.* 19, 266–282. doi: 10.1016/j.euroneuro.2008.12.005

Hainer, C., Mosienko, V., Koutsikou, S., Crook, J. J., Gloss, B., Kasparov, S., et al. (2015). Beyond gene inactivation: evolution of tools for analysis of serotonergic circuitry. *ACS Chem. Neurosci.* 6, 1116–1129. doi: 10.1021/acschemneuro.5b00045

Hajós, M., Allers, K. A., Jennings, K., Sharp, T., Charette, G., Sík, A., et al. (2007). Neurochemical identification of stereotypic burst-firing neurons in the rat dorsal raphe nucleus using juxtacellular labelling methods. *Eur. J. Neurosci.* 25, 119–126. doi: 10.1111/j.1460-9568.2006.05276.x

Hajós, M., Gartside, S. E., Villa, A. E., and Sharp, T. (1995). Evidence for a repetitive (burst) firing pattern in a sub-population of 5-hydroxytryptamine neurons in the dorsal and median raphe nuclei of the rat. *Neuroscience* 69, 189–197. doi: 10.1016/0306-4522(95)00227-a

Hajós, M., and Sharp, T. (1996). A 5-hydroxytryptamine lesion markedly reduces the incidence of burst-firing dorsal raphe neurones in the rat. *Neurosci. Lett.* 204, 161–164. doi: 10.1016/0304-3940(96)12333-8

Hajós, M., Sharp, T., and Newberry, N. R. (1996). Intracellular recordings from burst-firing presumed serotonergic neurones in the rat dorsal raphe nucleus *in vivo*. *Brain Res.* 737, 308–312. doi: 10.1016/0006-8993(96)00936-5

Hendricks, T. J., Francis, N., Fyodorov, D. V., and Deneris, E. S. (1999). The ETS domain factor Pet-1 is an early and precise marker of central serotonin neurons and interacts with a conserved element in serotonergic genes. *J. Neurosci.* 19, 10348–10356.

Holst, J., Szymczak-Workman, A. L., Vignali, K. M., Burton, A. R., Workman, C. J., and Vignali, D. A. A. (2006). Generation of T-cell receptor retrogenic mice. *Nat. protoc.* 1, 406–417. doi: 10.1038/nprot.2006.61

Ishimura, K., Takeuchi, Y., Fujiwara, K., Tominaga, M., Yoshioka, H., and Sawada, T. (1988). Quantitative analysis of the distribution of serotonin-immunoreactive cell bodies in the mouse brain. *Neurosci. Lett.* 91, 265–270. doi: 10.1016/0304-3940(88)90691-x

Jacobs, B. L., and Azmitia, E. C. (1992). Structure and function of the brain serotonin system. *Physiol. Rev.* 72, 165–229.

Jacobs, B. L., and Fornal, C. A. (1991). Activity of brain serotonergic neurons in the behaving animal. *Pharmacol. Rev.* 43, 563–578.

Jensen, P., Farago, A. F., Awatramani, R. B., Scott, M. M., Deneris, E. S., and Dymecki, S. M. (2008). Redefining the serotonergic system by genetic lineage. *Nat. Neurosci.* 11, 417–419. doi: 10.1038/nn2050

Kiyasova, V., Bonnavion, P., Scotto-Lomassese, S., Fabre, V., Sahly, I., Tronche, F., et al. (2013). A subpopulation of serotonergic neurons that do not express the 5-HT1A autoreceptor. *ACS Chem. Neurosci.* 4, 89–95. doi: 10.1021/cn300157s

Kocsis, B., Varga, V., Dahan, L., and Sik, A. (2006). Serotonergic neuron diversity: identification of raphe neurons with discharges time-locked to the hippocampal theta rhythm. *Proc. Natl. Acad. Sci. U S A* 103, 1059–1064. doi: 10.1073/pnas.0508360103

Kremers, G. J., Goedhart, J., van Munster, E. B., and Gadella, T. W. Jr. (2006). Cyan and yellow super fluorescent proteins with improved brightness, protein folding and FRET Förster radius. *Biochemistry* 45, 6570–6580. doi: 10.1021/bi0516273

Levine, E. S., and Jacobs, B. L. (1992). Neurochemical afferents controlling the activity of serotonergic neurons in the dorsal raphe nucleus: microiontophoretic studies in the awake cat. *J. Neurosci.* 12, 4037–4044.

Li, Y., Zhong, W., Wang, D., Feng, Q., Liu, Z., Zhou, J., et al. (2016). Serotonin neurons in the dorsal raphe nucleus encode reward signals. *Nat. Commun.* 7:10503. doi: 10.1038/ncomms10503

Liu, Z., Zhou, J., Li, Y., Hu, F., Lu, Y., Ma, M., et al. (2014). Dorsal raphe neurons signal reward through 5-HT and glutamate. *Neuron* 81, 1360–1374. doi: 10.1016/j.neuron.2014.02.010

Lowry, C. A., Rodda, J. E., Lightman, S. L., and Ingram, C. D. (2000). Corticotropin-releasing factor increases *in vitro* firing rates of serotonergic neurons in the rat dorsal raphe nucleus: evidence for activation of a topographically organized mesolimbocortical serotonergic system. *J. Neurosci.* 20, 7728–7736.

McGinty, D. J., and Harper, R. M. (1976). Dorsal raphe neurons: depression of firing during sleep in cats. *Brain Res.* 101, 569–575. doi: 10.1016/0006-8993(76)90480-7

Mlinar, B., Montalbano, A., Baccini, G., Tatini, F., Berlinguer Palmini, R., and Corradetti, R. (2015). Nonexocytotic serotonin release tonically suppresses serotonergic neuron activity. *J. Gen. Physiol.* 145, 225–251. doi: 10.1085/jgp.201411330

Mlinar, B., Tatini, F., Ballini, C., Nencioni, S., Della Corte, L., and Corradetti, R. (2005). Differential autoinhibition of 5-hydroxytryptamine neurons by 5-hydroxytryptamine in the dorsal raphe nucleus. *Neuroreport* 16, 1351–1355. doi: 10.1097/01.wnr.0000175249.25535.bf

Montalbano, A., Waider, J., Barbieri, M., Baytas, O., Lesch, K. P., Corradetti, R., et al (2015). Cellular resilience: 5-HT neurons in Tph2$^{-/-}$ mice retain normal firing behavior despite the lack of brain 5-HT. *Eur. Neuropsychopharmacol.* 25, 2022–2035. doi: 10.1016/j.euroneuro.2015.08.021

Mosko, S. S., and Jacobs, B. L. (1974). Midbrain raphe neurons: spontaneous activity and response to light. *Physiol. Behav.* 13, 589–593. doi: 10.1016/0031-9384(74)90292-3

Mosko, S. S., and Jacobs, B. L. (1976). Recording of dorsal raphe unit activity *in vitro*. *Neurosci. Lett.* 2, 195–200. doi: 10.1016/0304-3940(76)90014-8

Nakamura, T., Colbert, M. C., and Robbins, J. (2006). Neural crest cells retain multipotential characteristics in the developing valves and label the cardiac conduction system. *Circ. Res.* 98, 1547–1554. doi: 10.1161/01.res.0000227505.19472.69

Narboux-Nême, N., Angenard, G., Mosienko, V., Klempin, F., Pitychoutis, P. M., Deneris, E., et al. (2013). Postnatal growth defects in mice with constitutive depletion of central serotonin. *ACS Chem. Neurosci.* 4, 171–181. doi: 10.1021/cn300165x

Okaty, B. W., Freret, M. E., Rood, B. D., Brust, R. D., Hennessy, M. L., deBairos, D., et al. (2015). Multi-Scale Molecular Deconstruction of the Serotonin Neuron System. *Neuron* 88, 774–791. doi: 10.1016/j.neuron.2015.10.007

Paxinos, G., and Franklin, K. B. J. (2001). *Sports Med.* 2nd edition. San DiegoPaxinos, CA: Academic Press

Pelosi, B., Migliarini, S., Pacini, G., Pratelli, M., and Pasqualetti, M. (2014). Generation of Pet1210-Cre transgenic mouse line reveals non-serotonergic expression domains of Pet1 both in CNS and periphery. *PLoS One* 9:e104318. doi: 10.1371/journal.pone.0104318

Pfaar, H., von Holst, A., Vogt Weisenhorn, D. M., Brodski, C., Guimera, J., and Wurst, W. (2002). mPet-1, a mouse ETS-domain transcription factor, is expressed in central serotonergic neurons. *Dev. Genes Evol.* 212, 43–46. doi: 10.1007/s00427-001-0208-x

Pinault, D. (1996). A novel single-cell staining procedure performed in vivo under electrophysiological control: morpho-functional features of juxtacellularly labeled thalamic cells and other central neurons with biocytin or neurobiotin. *J. Neurosci. Methods* 65, 113–136. doi: 10.1016/0165-0270(95)00144-1

Sakai, K. (2011). Sleep-waking discharge profiles of dorsal raphe nucleus neurons in mice. *Neuroscience* 197, 200–224. doi: 10.1016/j.neuroscience.2011.09.024

Sakai, K., and Crochet, S. (2001). Differentiation of presumed serotonergic dorsal raphe neurons in relation to behavior and wake-sleep states. *Neuroscience* 104, 1141–1155. doi: 10.1016/s0306-4522(01)00103-8

Schweimer, J. V., and Ungless, M. A. (2010). Phasic responses in dorsal raphe serotonin neurons to noxious stimuli. *Neuroscience* 171, 1209–1215. doi: 10.1016/j.neuroscience.2010.09.058

Schweimer, J. V., Mallet, N., Sharp, T., and Ungless, M. A. (2011). Spike-timing relationship of neurochemically-identified dorsal raphe neurons during cortical slow oscillations. *Neuroscience* 196, 115–123. doi: 10.1016/j.neuroscience.2011.08.072

Soiza-Reilly, M., and Commons, K. G. (2011). Glutamatergic drive of the dorsal raphe nucleus. *J. Chem. Neuroanat.* 41, 247–255. doi: 10.1016/j.jchemneu.2011.04.004

Spaethling, J. M., Piel, D., Dueck, H., Buckley, P. T., Morris, J. F., Fisher, S. A., et al. (2014). Serotonergic neuron regulation informed by *in vivo* single-cell transcriptomics. *FASEB J.* 28, 771–780. doi: 10.1096/fj.13-240267

Srinivas, S., Watanabe, T., Lin, C. S., William, C. M., Tanabe, Y., Jessell, T. M., et al. (2001). Cre reporter strains produced by targeted insertion of *EYFP* and *ECFP* into the *ROSA26* locus. *BMC Dev. Biol.* 1:4. doi: 10.1186/1471-213X-1-4

Suchyna, T. M., Markin, V. S., and Sachs, F. (2009). Biophysics and structure of the patch and the gigaseal. *Biophys. J.* 97, 738–747. doi: 10.1016/j.bpj.2009.05.018

Trulson, M. E., and Jacobs, B. L. (1979). Raphe unit activity in freely moving cats: correlation with level of behavioral arousal. *Brain Res.* 163, 135–150. doi: 10.1016/0006-8993(79)90157-4

Urbain, N., Creamer, K., and Debonnel, G. (2006). Electrophysiological diversity of the dorsal raphe cells across the sleep-wake cycle of the rat. *J. Physiol.* 573, 679–695. doi: 10.1113/jphysiol.2006.108514

Vandermaelen, C. P., and Aghajanian, G. K. (1983). Electrophysiological and pharmacological characterization of serotonergic dorsal raphe neurons recorded extracellularly and intracellularly in rat brain slices. *Brain Res.* 289, 109–119. doi: 10.1016/0006-8993(83)90011-2

Vertes, R. P., and Crane, A. M. (1997). Distribution, quantification and morphological characteristics of serotonin-immunoreactive cells of the supralemniscal nucleus (B9) and pontomesencephalic reticular formation in the rat. *J. Comp. Neurol.* 378, 411–424. doi: 10.1002/(SICI)1096-9861(19970217)378:3<411::AID-CNE8>3.0.CO;2-6

Warden, M. R., Selimbeyoglu, A., Mirzabekov, J. J., Lo, M., Thompson, K. R., Kim, S. Y., et al. (2012). A prefrontal cortex-brainstem neuronal projection that controls response to behavioural challenge. *Nature* 492, 428–432. doi: 10.1038/nature11617

Weissbourd, B., Ren, J., DeLoach, K. E., Guenthner, C. J., Miyamichi, K., and Luo, L. (2014). Presynaptic partners of dorsal raphe serotonergic and GABAergic neurons. *Neuron* 83, 645–662. doi: 10.1016/j.neuron.2014.06.024

Wylie, C. J., Hendricks, T. J., Zhang, B., Wang, L., Lu, P., Leahy, P., et al. (2010). Distinct transcriptomes define rostral and caudal serotonin neurons. *J. Neurosci.* 30, 670–684. doi: 10.1523/JNEUROSCI.4656-09.2010

Conflict of Interest Statement: The authors declare that the research was conducted in the absence of any commercial or financial relationships that could be construed as a potential conflict of interest.

frontiers in Computational Neuroscience

ORIGINAL RESEARCH
published: 18 November 2016
doi: 10.3389/fncom.2016.00118

Analysis of Nociceptive Information Encoded in the Temporal Discharge Patterns of Cutaneous C-Fibers

Kyeongwon Cho[1†], Jun Ho Jang[2†], Sung-Phil Kim[3†], Sang Hoon Lee[2], Soon-Cheol Chung[4], In Young Kim[1], Dong Pyo Jang[1] and Sung Jun Jung[2*]*

[1] Department of Biomedical Engineering, Hanyang University, Seoul, South Korea, [2] Department of Biomedical Science, Hanyang University, Seoul, South Korea, [3] Department of Human and Systems Engineering, Ulsan National Institute of Science and Technology, Ulsan, South Korea, [4] Department of Biomedical Engineering, College of Biomedical & Health Science, BK21+ Research Institute of Biomedical Engineering, Konkuk University, Chungju, South Korea

The generation of pain signals from primary afferent neurons is explained by a labeled-line code. However, this notion cannot apply in a simple way to cutaneous C-fibers, which carry signals from a variety of receptors that respond to various stimuli including agonist chemicals. To represent the discharge patterns of C-fibers according to different agonist chemicals, we have developed a quantitative approach using three consecutive spikes. By using this method, the generation of pain in response to chemical stimuli is shown to be dependent on the temporal aspect of the spike trains. Furthermore, under pathological conditions, gamma-aminobutyric acid resulted in pain behavior without change of spike number but with an altered discharge pattern. Our results suggest that information about the agonist chemicals may be encoded in specific temporal patterns of signals in C-fibers, and nociceptive sensation may be influenced by the extent of temporal summation originating from the temporal patterns.

Keywords: temporal decoding, temporal encoding, spike train analysis, discharge pattern, nociception

OPEN ACCESS

Edited by:
Sergey M. Korogod, National Academy of Sciences of Ukraine, Ukraine

Reviewed by:
Deolinda Lima, University of Porto, Portugal
Sangmin Lee, Inha University, South Korea

***Correspondence:**
Dong Pyo Jang
dongpjang@gmail.com
Sung Jun Jung
eurijj@hanyang.ac.kr

[†] These authors have contributed equally to this work.

Received: *03 May 2016*
Accepted: *04 November 2016*
Published: *18 November 2016*

Citation:
Cho K, Jang JH, Kim S-P, Lee SH, Chung S-C, Kim IY, Jang DP and Jung SJ (2016) Analysis of Nociceptive Information Encoded in the Temporal Discharge Patterns of Cutaneous C-Fibers. Front. Comput. Neurosci. 10:118. doi: 10.3389/fncom.2016.00118

INTRODUCTION

It is generally accepted that the activation of primary afferent C-fibers by noxious stimuli leads to a sensation of pain. However, some studies have reported the lack of a pain response to activation of C-fibers, whereas others have reported an increased pain response even without an increase in the discharge rate of the C-fibers (Van Hees and Gybels, 1981; Prescott et al., 2014). Taken together, these reports suggest that a more complex neural process may exist in C-fibers, rather than the simple one-to-one relationship between sensation and receptor type according to a labeled-line code, the key coding mechanism for stimuli (Johanek et al., 2008; Pereira and Alves, 2011; Wooten et al., 2014).

Nociceptive C-fibers typically express multiple types of ion channels that respond to each agonist chemicals (Bessou and Perl, 1969; Hanack et al., 2015). For example, certain chemical nociceptors express the transient receptor potential (TRP) cation channel subfamily A1 (TRPA1), which responds to cold and mustard oil, and the subfamily V1 (TRPV1) channel responding to heat and capsaicin (Bautista et al., 2005), and their activation evokes action potentials (APs) in a single C-fiber (Han et al., 2013). However, the difference in the discharge patterns generated by the different stimuli in the C-fibers (Wooten et al., 2014) cannot be explained by the labeled-line code alone. It is assumed, therefore, that the different types of stimuli may be encoded in the discharge patterns of the C-fibers. Today, almost all workers would agree that some degree of multiple function exists in the primary afferent fibers innervating the skin,

as many subpopulations have broad dynamic ranges (Kumazawa et al., 1996). Recent studies suggest that both specific function of each type of fiber, but also fiber's temporal encoding enable the generation of sensations (here, especially nociception) (Weber et al., 2013; Wooten et al., 2014). Accordingly we hypothesized that temporal encoding of spike trains from individual C-fibers may deliver key information together with combinational coding across multiple C-fibers. In a previous study, Sandkühler (1996) suggested that different responses before and after a nerve injury might be associated with the temporal patterns of spontaneous spikes, which vary according to inflammatory status. Here, we propose that activation of primary afferent C-fibers evokes nociceptive behaviors depending on temporal aspects of the spike trains, which are determined by the different chemical stimuli. Specific patterns of discharges are identified for different chemical stimuli that receptors are expressed commonly. We have analyzed these patterns by developing an analytic method that can characterize the distribution of inter-spike intervals (ISIs).

RESULTS

Activation of C-Fibers Does Not Always Result in Nociceptive Behavior

First, we investigated whether single C-fibers could be activated by three different chemicals: Potassium chloride (KCl), gamma-aminobutyric acid (GABA), and capsaicin; due to the high intracellular chloride concentration of peripheral neurons an excitatory effect of GABA is expected. Immunohistochemistry revealed the co-expression of TRPV1 and $GABA_A$ receptors in the some dorsal root ganglion (DRG) neurons (**Figure 1A**). Patch-clamp recording showed that GABA and capsaicin evoked inward currents in the same DRG neuron (**Figure 1B**) but that not all DRG neurons were responsive to both chemicals (7 of 28 total neurons responded for both GABA and capsaicin). In *ex vivo* recordings, 27 C-fibers were stimulated with the three chemicals in succession, with wash-out periods in between. Three fibers responded to all stimulants with identical AP shapes and sizes (**Figure 1C**, Supplementary Tables 1, 2).

It is known that C-fiber activation by KCl or capsaicin results in nociception. However, the sensation evoked by GABA is not reported despite the activation of C-fibers (Feltz and Rasminsky, 1974; Deschenes et al., 1976; Carlton et al., 1999). To test whether the application of GABA evoked a nociception, we performed behavioral tests for each chemical. Mouse hindpaw movements indicating pain, i.e., lifting/guarding, flinching/shaking, licking, and walking (Kawasaki-Yatsugi et al., 2012), significantly increased after subcutaneous injection of capsaicin or KCl ($Ps < 0.001$ vs. vehicle). On the other hand, GABA induced no significant increase ($P = 0.693$; **Figure 1D**), indicating that GABA could not induce nociception.

The Temporal Discharge Patterns of Single C-Fibers Characterize Different Chemicals

To further explore nociceptive information encoded in the activation of primary afferent C-fibers, *ex vivo* single-fiber recordings were conducted with each of the three chemicals separately (**Figure 2**). Analysis of the spike counts in *ex vivo* single-fiber recordings from the saphenous nerve showed that all three chemicals caused significant increases in the number of APs compared with control periods ($Ps < 0.001$; **Figures 2D–F**). In addition, there was no significant difference in the number of APs evoked by the three stimulants ($P = 0.925$; **Figure 2G**). Another measure of discharge rate is the instantaneous frequency (Lánský et al., 2004) and it is claimed that a discharge rate exceeding some threshold is associated with nociceptive behavior (Adriaensen et al., 1980). As shown in **Figures 2A–C**, the distribution of the instantaneous frequencies of GABA responses (mean: 1.72 Hz) did not differ from that of the KCl responses (mean: 1.25 Hz) while that of capsaicin responses (mean: 17.49 Hz) was much higher (**Figures 3A–D**).

As neither the number of APs nor the instantaneous frequencies could differentiate GABA responses from the other two responses, we considered the possibility that the differences might be temporally encoded in the spike trains. Visual inspection indicated that the most pronounced difference of GABA responses from the other responses lay in the repeated short bursts present in the GABA responses, we posited a fundamental unit of temporal discharge pattern to be three consecutive spikes (referred to as a spikelet hereafter), as this unit contained the minimum ISI pattern that could include both short ISIs within bursts and longer ISIs between bursts. In contrast to the results of spike counts or instantaneous frequency, GABA responses had a longer mean spikelet length (time elapsed from the first to the last spike in a spikelet) than those to the other chemicals (**Figures 3E–H**). The longer GABA spikelet lengths were primarily caused by a high frequency of relatively long spikelets (**Figure 3G**), which indicated that long and short ISIs were repeated in succession across bursts during a GABA response. To also measure asymmetry of two ISIs in a spikelet due to the intersection of long and short ISIs, we evaluated the distribution of absolute spikelet regularity (the ratio of difference between two consecutive ISIs to spikelet length) of each group and found that the regularity of GABA spikelets was significantly lower than those of KCl or capsaicin spikelets (**Figures 3I–L**). Both the length and the regularity of spikelets clearly distinguished the temporal pattern of GABA responses from the others, and this might be associated with the lack of nociceptive behavior from GABA.

We also analyzed the joint distribution of the two temporal features, the length and the regularity of spikelets and created a two-dimensional (2D) joint distribution map of spikelets for each group (**Figure 4**). The maps of each group could be distinguished from the others. KCl frequently generated temporal patterns with regular spikelets of a moderate length, whereas GABA tended to generate more irregular and longer spikelets. Capsaicin tended to generate short and regular spikelets (**Figures 4B–D**).

The three distribution patterns were clearly different, as the k-nearest neighbor classification scheme correctly discriminated between them with classification accuracy of 79.7% (55 of 69 C-fiber responses classified correctly), which was significantly higher than chance (binomial test, $P < 0.001$; Devroye et al., 1996). In addition, nine individual maps of the three C-fiber

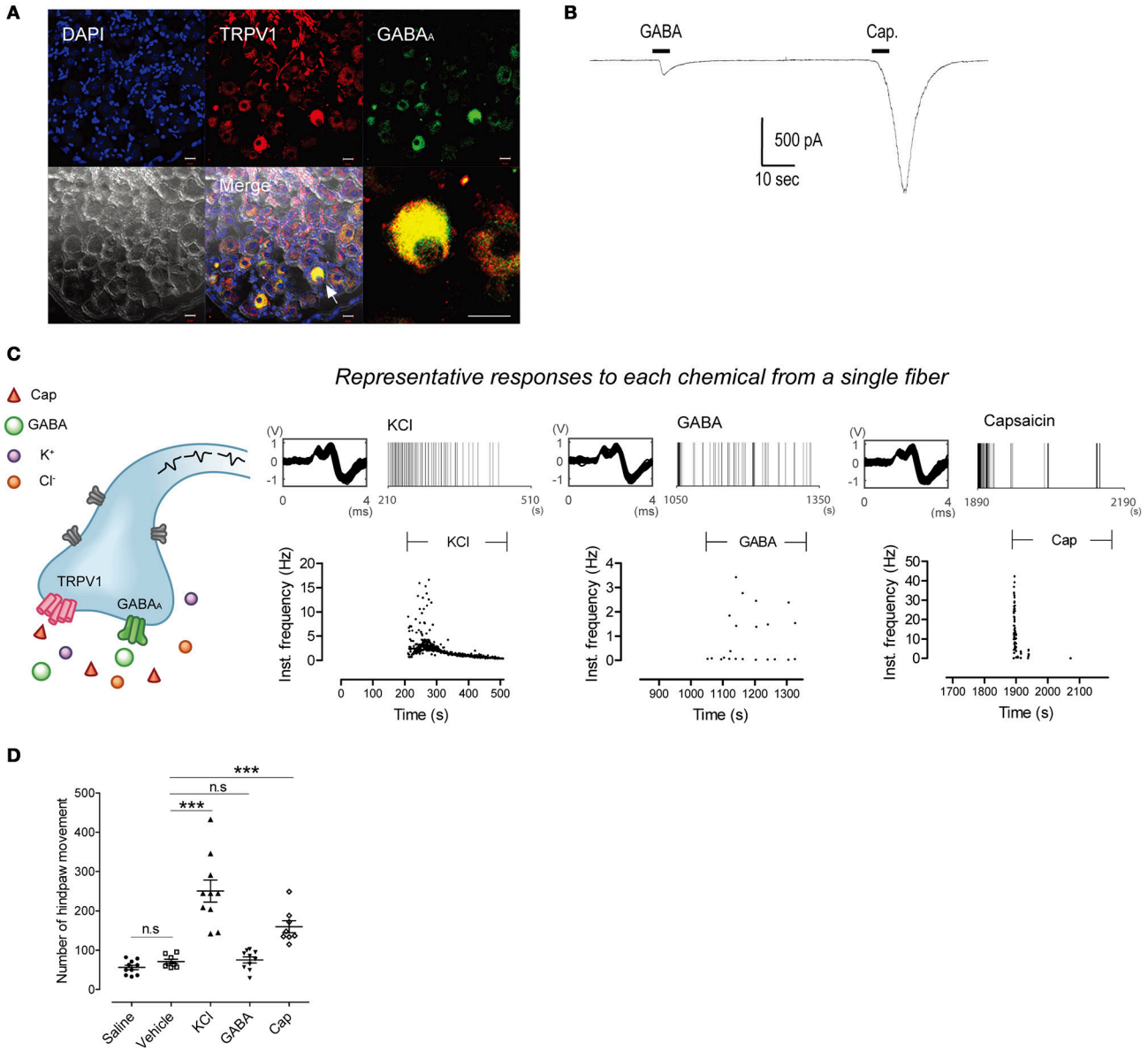

FIGURE 1 | Single fibers respond to all three chemical stimuli. (A) Immunohistochemistry showing co-expression of $GABA_A$ and TRPV1 in the same DRG neurons. Scale bar represents 20 μm. Arrow indicates $GABA_A$- and TRPV1-positive neurons. **(B)** Inward currents evoked by GABA (100 μM) and capsaicin (1 μM) in small DRG neurons. **(C)** Time stamp with instantaneous frequency of the response from a representative single C-fiber under application of KCl, GABA, and capsaicin in succession. It consisted of identically shaped action potentials. **(D)** Hindpaw movements after subcutaneous injection of saline ($n = 10$), vehicle ($n = 8$), KCl ($n = 10$), GABA ($n = 10$), and capsaicin ($n = 8$). (Mann–Whitney or *t*-test based on normality, $^{***}P < 0.001$. Error bars represent s.e.m.).

responses obtained from the successive chemical tests in the above section were also perfectly classified into KCl, GABA, and capsaicin using a classifier based on the set of three separate spike train datasets generated by the individual chemical stimuli (Supplementary Figure 1). This indicates that C-fibers may encode information concerning the specific receptors that have been stimulated by means of unique temporal patterns.

In an attempt to estimate the effect of the temporal summation of discharge patterns on the nociceptive level, a computational model was designed using the information of spikelet length and regularity. The model was applied to the C-fiber responses with over 20 spikes during the stimulation period to estimate the nociceptive level through the temporal summation of spikelet information. As a result, the detection rate of nociception by the model was 66.7% (14 of 21) for KCl, 17.4% (4 of 23) for GABA, and 88.9% (16 of 18) for capsaicin, respectively. This result indicated that the model could properly translate C-fiber spiking patterns, represented by spikelet length and regularity,

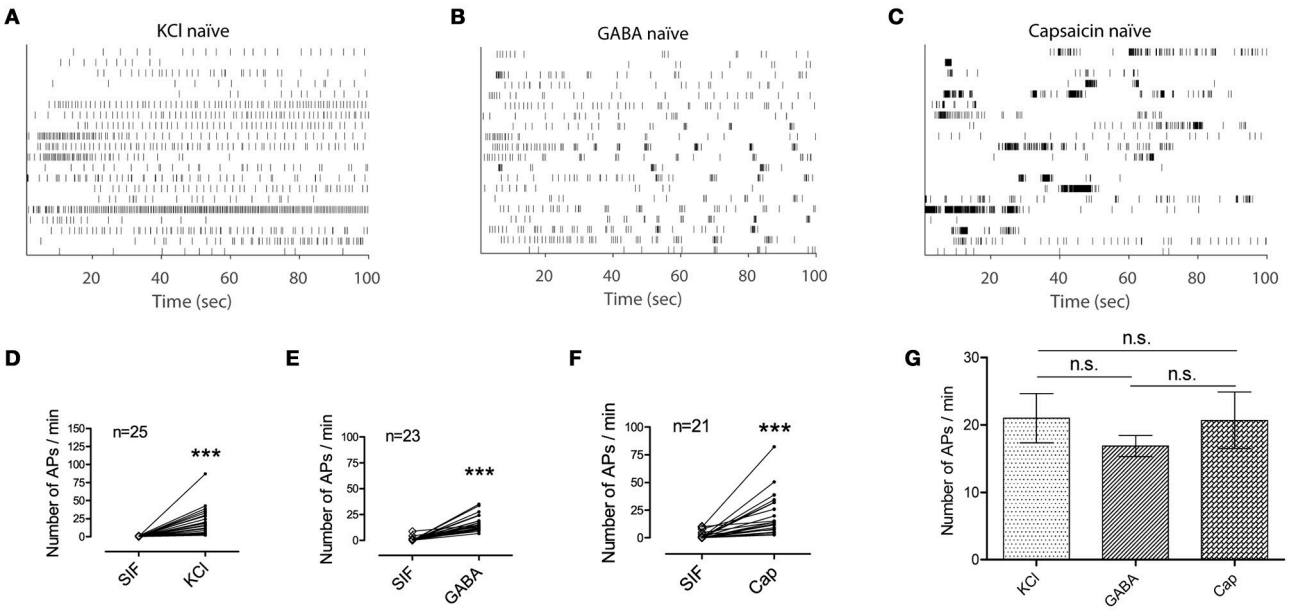

FIGURE 2 | Application of KCl, GABA, or capsaicin clearly activates primary afferents. (A–C) Time stamp of 20 randomly selected single fibers from each group of chemical responses i.e., KCl ($n = 25$) in **(A)**, GABA ($n = 23$) in **(B)**, capsaicin ($n = 21$) in **(C)**. **(D–F)** Spike counts from each single fiber during the control period of synthetic interstitial fluid (SIF) and the corresponding responsive period to a stimulant. (Wilcoxon signed rank test, $^{***}P < 0.001$) **(G)** Mean of the spike counts in the evoked responses for KCl, GABA, and capsaicin are compared. (Kruskal-Wallis one-way ANOVA, n.s., not significant. Error bars represent s.e.m.).

into the nociception level in response to different chemical stimuli.

Pathological Conditions Inducing Nociception Alter the Temporal Discharge Pattern in Response to GABA

We examined whether changes in pathological conditions could influence discharge patterns in C-fibers and subsequent nociceptive behavior (**Figure 5**). We conducted behavioral tests for GABA and capsaicin in mice subjected to chronic constriction injury (CCI; sciatic nerve cuffing). Compared with the controls, the number of hind paw movements were increased by both GABA and capsaicin ($P < 0.01$; **Figure 5A**), indicating that GABA induced a nociceptive behavior when exposed to a CCI.

The GABA and capsaicin discharge patterns were investigated using ex vivo single-fiber recordings from the sural nerves of CCI mice. First we found that the number of APs increased in response to GABA or capsaicin compared with control periods (**Figures 5D,E**) but there were no significant differences in the number of GABA- or capsaicin-induced APs in the CCI mice compared with the naïve mice (Supplementary Figure 2). The 2D joint distribution map for capsaicin in the CCI mice (**Figure 6B**) was closely akin to that in the naïve mice (**Figure 4D**). However, the GABA map in the CCI mice (**Figure 6A**) appeared to be dissimilar from that in naïve mice (**Figure 4C**). This suggested that the discharge pattern for a specific receptor in C-fibers could be influenced by the pathological conditions. Specifically, the short and regular spikelets, which were abundant in the capsaicin spike trains, became more frequent in the GABA spike trains of the CCI mice (**Figure 6C**). The abundance of the short and regular spikelets characterizing the capsaicin and CCI-induced GABA discharge patterns implied that the generation of pain might be related to the presence of high frequency continuous spikes in the afferent C-fibers. K-nearest neighbor classification analysis revealed that the binary classifier that had been trained using the GABA and capsaicin data from naïve mice had little difficulty in discriminating the novel GABA data from naïve mice but made many more errors (nearly 50% of the time) in discriminating the GABA data from the CCI mice, indicating that the GABA discharge patterns in the CCI mice were less distinguishable from the capsaicin discharge patterns (**Figure 6D**). Similarity analysis based on Kullback–Leibler (KL) divergence also revealed that the GABA pattern in the CCI mice was more similar to the capsaicin pattern (**Figure 6E**).

DISCUSSION

How are noxious stimuli encoded and processed to produce pain? Although the activation of C-fibers is related to nociceptive behaviors, the information may be encoded in the intervals between discharges as well as in discharge rates. Koltzenburg and Handwerker (1994) suggested that the magnitude of pain sensation is encoded by temporal summation of the nociceptive primary afferent discharge, compensating the concept of encoding by the number of APs. This study reported that the magnitude of pain increased when the repeated mechanical stimulus was more frequent, whereas the number of APs decreased. They concluded that a certain number of APs with

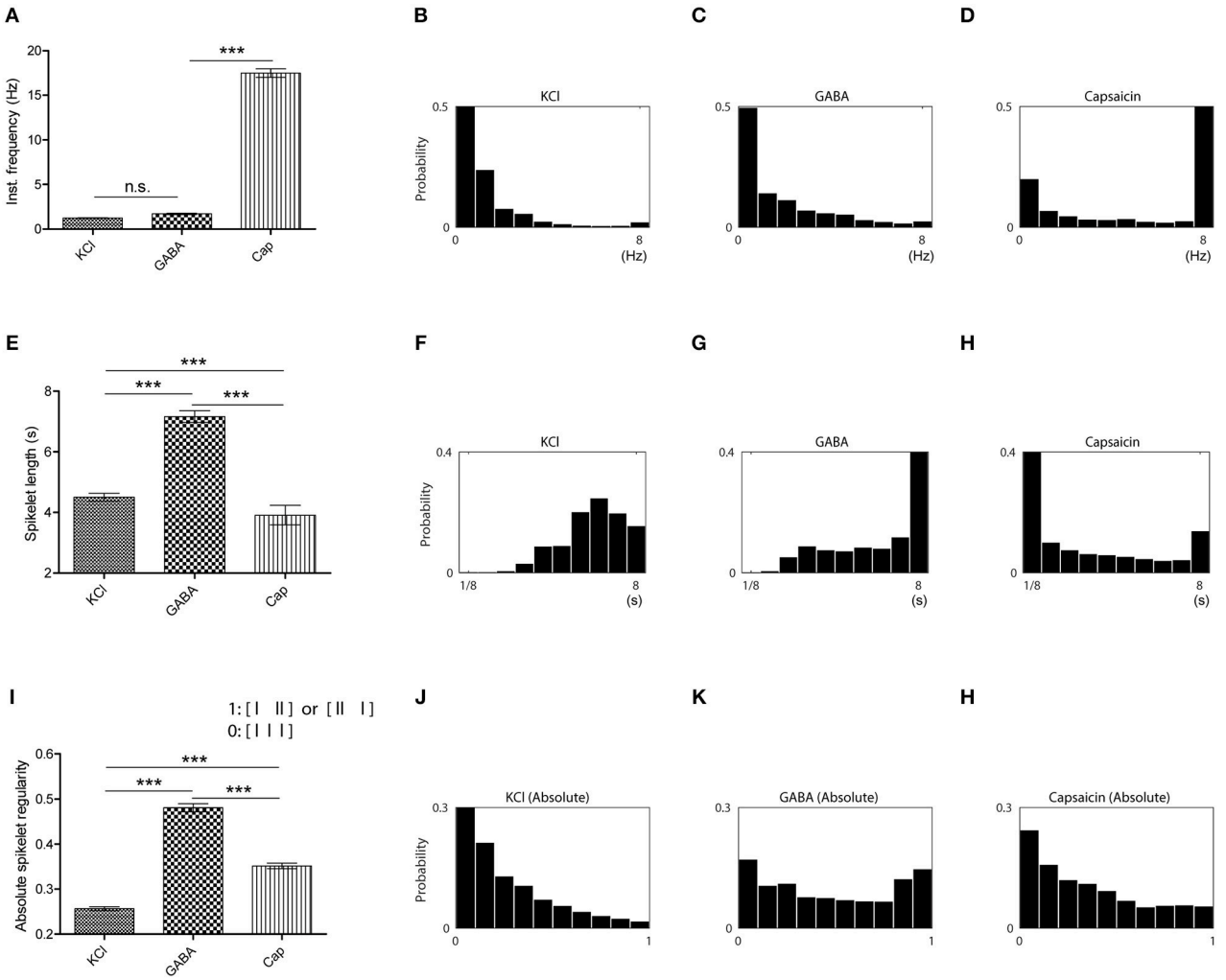

FIGURE 3 | Temporal characteristics of the different stimuli revealed in spikelet distributions. (A) Comparison of instantaneous frequencies for KCl, GABA, and capsaicin responses. (Kruskal-Wallis one-way ANOVA followed by Dunn's test for multiple comparisons, $^{***}P < 0.001$, n.s., not significant.) **(B–D)** Instantaneous frequency histograms for each chemical (KCl in **B**, GABA in **C** and capsaicin in **D**). **(E)** Comparison of spikelet lengths for KCl, GABA, and capsaicin responses. (Kruskal-Wallis one-way ANOVA followed by Dunn's test for multiple comparisons, $^{***}P < 0.001$) **(F–H)** Spikelet length histograms for each chemical (KCl in **F**, GABA in **G** and capsaicin in **H**). **(I)** Comparison of spikelet regularity for KCl, GABA, and capsaicin responses. (Kruskal-Wallis one-way ANOVA followed by Dunn's test for multiple comparisons, $^{***}P < 0.001$.) **(J–L)** Spikelet regularity histogram for each chemical (KCl in **J**, GABA in **K**, and capsaicin in **L**). All the error bars represent s.e.m.

discharge rates over the threshold is required for pain sensation. In our *ex vivo* data in naïve mice, however, spike numbers and instantaneous frequencies of spikes did not differ between the KCl and GABA groups (whereas instantaneous frequencies were significantly higher in the capsaicin group) (**Figures 2G**, **3A–D**), indicating that additional characteristics of the temporal discharge patterns had to be explored.

To explore the neural code for nociceptive information, we applied the idea of spikelets to the ISI data acquired from the chemical-induced discharge of C-fibers. As a large value for temporal summation is achieved only if consecutive spikes have short ISIs, we supposed that temporal summation could be described well by an analysis of consecutive ISIs such as spikelets as defined in our study. Sandkühler (1996) suggested a multidimensional analysis of ISI data that represented the temporal encoding (temporal aspect of ISIs) of spontaneous discharges in spinal neurons. In principle one could take advantage of this method to visualize temporal patterns of ISIs (Debus and Sandkühler, 1996). However, this is effective only for neural activity containing at least 2000 spikes. Because of the adaptation of neural afferent activity in C-fibers, there were not sufficient numbers of spikes in our data to use Sandkuhler's method directly. Taking consecutive spikes into account, we developed spikelet analysis (based on three consecutive spikes) to characterize the temporal characteristics of spiking responses evoked by different stimuli.

Our *ex vivo* data acquired from naïve mice could be categorized into specific discharge patterns for each chemical

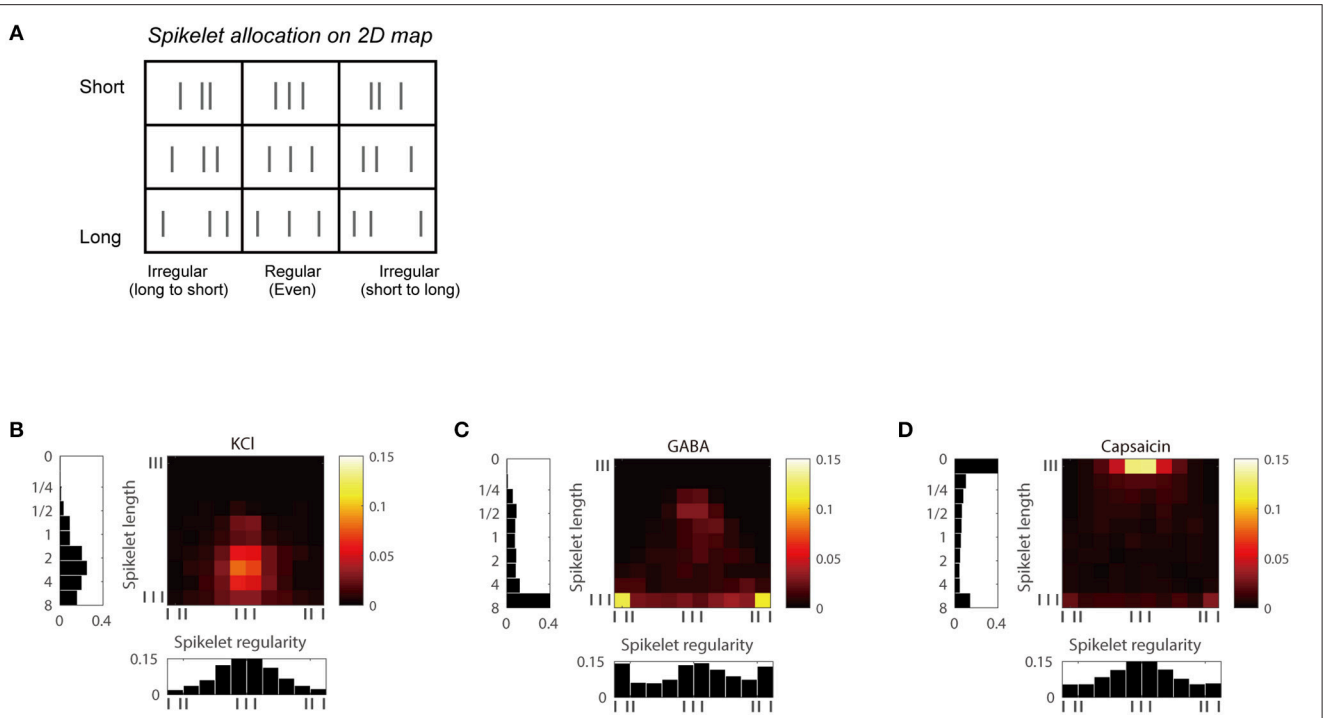

FIGURE 4 | Joint distribution maps of the length and the regularity of spikelet for each chemical. (A) Simple 3 × 3 bin-2D map of spikelets based on spikelet length and regularity. **(B)** 2D map of KCl responses based on spikelet length (vertical axis) and regularity (horizontal axis), including histograms for each. **(C,D)** Responses of GABA in **(C)**, and capsaicin in **(D)**.

(KCl: continuous firing; GABA: repeated short bursts or chattering; capsaicin: single or multiple bursts) using spikelet analysis. The spikelet analysis characterized the temporal patterns of the three groups by means of two parameters, namely spikelet length and regularity. Long and irregular spikelets in the GABA response developed from the start or the end of short bursts. The characteristic repeating short bursts in the GABA response that resulted in the repetition of long and short intervals might result in short temporal summation without evoking nociceptive behavior. On the other hand, short and regular spikelets were dominant in the capsaicin response and might generate longer temporal summation with pain. KCl had a greater proportion of longer spikelets than capsaicin but with little irregular ones (and long intervals), suggesting that a continuous and regular spiking pattern might be also associated with longer temporal summation resulting in nociceptive behavior (**Figure 3**).

GABA was not noxious in the naïve condition. However, the increase of hindpaw movement in CCI mice showed that nociceptive behavior was generated. Unlike the number of APs, the distribution of instantaneous frequencies of GABA responses was higher in CCI mice indicating an increase in the discharge rate (Supplementary Figure 3). As the spikelet length is the sum of two consecutive ISIs, the increased discharge rate is incorporated in the shorter spikelet length in **Figure 6C**. We measured the change of temporal components of the pattern in the CCI condition, i.e., spikelet length and regularity, and found differences in the temporal encoding of the transmitted information. According to the 2D joint distribution maps, the GABA responses in CCI mice were closer to those of capsaicin. The shift in GABA-induced temporal pattern reflected longer temporal summation, corresponding to the occurrence of pain behavior in the CCI mice.

Capsaicin-evoked responses consisted of several types of adaptation as described before (St Pierre et al., 2009). The underlying mechanism of adaptation was not considered in this study. Instead, we combined all the capsaicin responses and used them as a dataset for our analysis.

As the spikelet length and regularity revealed shorter temporal summation in GABA responses in naïve mice, the identity of a chemical stimulant can also be encoded by spikelets. Moreover, the 2D joint distribution maps of the spikelet parameters had clearly different characteristics in each condition of the fibers, indicating the possibility that a single C-fiber might encode specific biological conditions into temporal patterns. We demonstrated that nociceptive behavior was related to the temporal encoding of spike trains in primary afferent C-fibers, in which specific temporal patterns were generated according to the type of activated receptors. We also demonstrated the limitation of comparison using instantaneous frequency, and showed that nociceptive information was encoded in the temporal pattern evaluated by means of the minimum temporal unit, the spikelet. This suggests that there is a specific temporal pattern of encoding in C-fibers and the degree of temporal summation originating from the temporal patterns determines the behavioral differences.

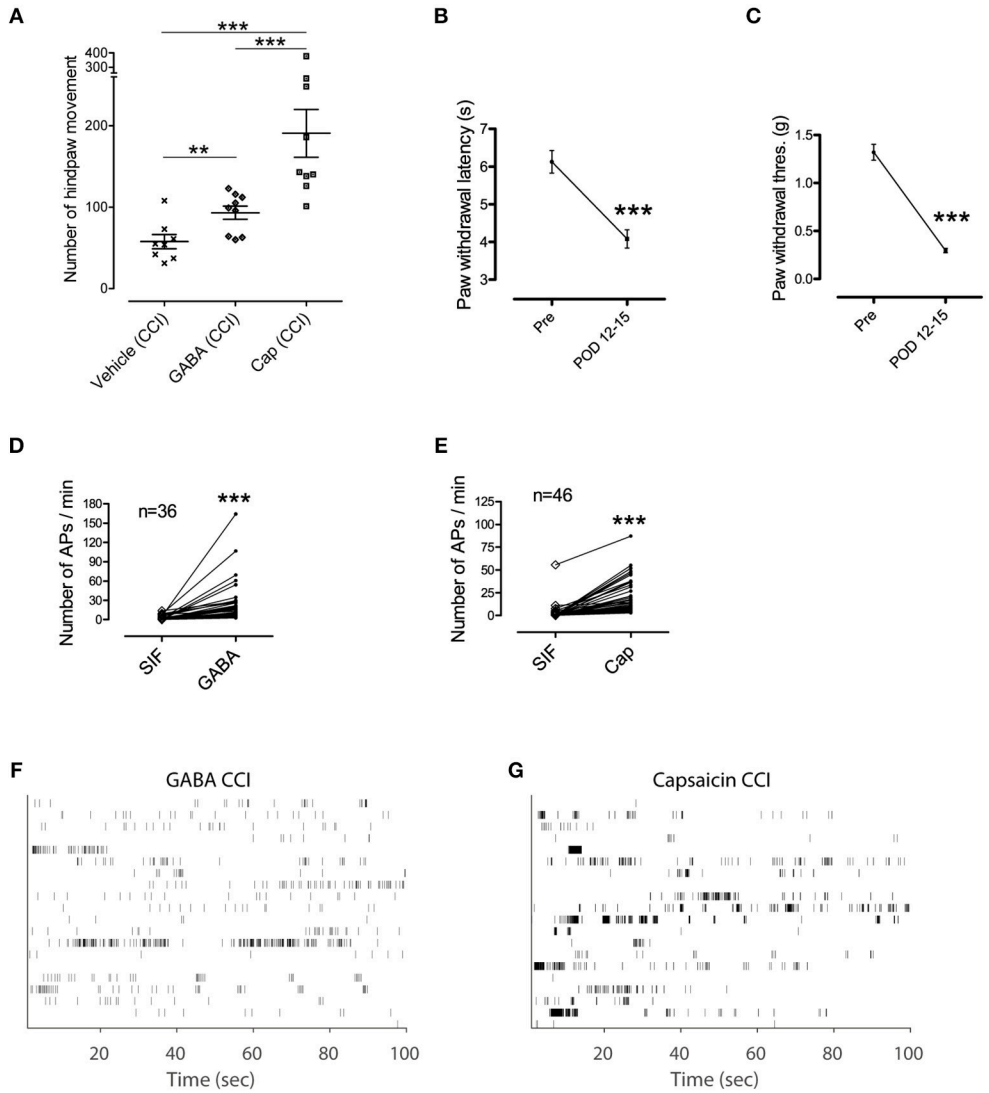

FIGURE 5 | GABA induced nociceptive behavior in pathological condition. (A) Hindpaw movements in CCI mice after injection of vehicle ($n = 8$), GABA ($n = 9$), and capsaicin ($n = 9$). Note, that GABA induced an increase in movement. **(B,C)** Paw withdrawal test to measure pain and hypersensitivity to heat and mechanical stimuli (Wilcoxon signed rank test). Error bars represent s.e.m. **(D,E)** Spike counts in each single fiber during the control period of SIF and the corresponding responsive period to a stimulant in CCI mice. $^{**}P < 0.01$, $^{***}P < 0.001$ **(F,G)** Time stamp of 20 randomly selected single fibers in each group of chemical responses in CCI mice i.e., GABA in **(F)** and capsaicin in **(G)**.

The computational model developed in the study also showed that the occurrence of nociception is estimated by discharge pattern based on spikelet. This finding corresponds to the previous studies reporting that the clustered spike trains (bursts) from the presynaptic neurons mediate the release of large dense-cored vesicles (containing neuropeptides) onto the postsynaptic membrane (Iverfeldt et al., 1989), consequently, the higher order neuron reaches the activation threshold potential. Even though the computational model does not represent an actual nociception level, it quantitatively evaluates temporal summation of spike trains that could be translated to a nociception level sensed by higher order neurons. The result of the model suggests that the nociception level might be estimated based on our spikelet analysis of discharge patterns.

In conclusion, we have expanded the concept of temporal encoding in evoked responses to sustained chemical stimuli. Our results may provide insight into the dependence of pain sensation on pathological conditions, in terms of changes in spiking patterns and receptor specificity based on a labeled-line code. The activity of multiple primary afferent C-fibers is the input for higher-order neurons (e.g., those in spinal cord); thus, the neural representation of a pain sensation may be encoded and mapped as a combination of temporal information and network processes of multiple C-fibers in a higher-order neural axis.

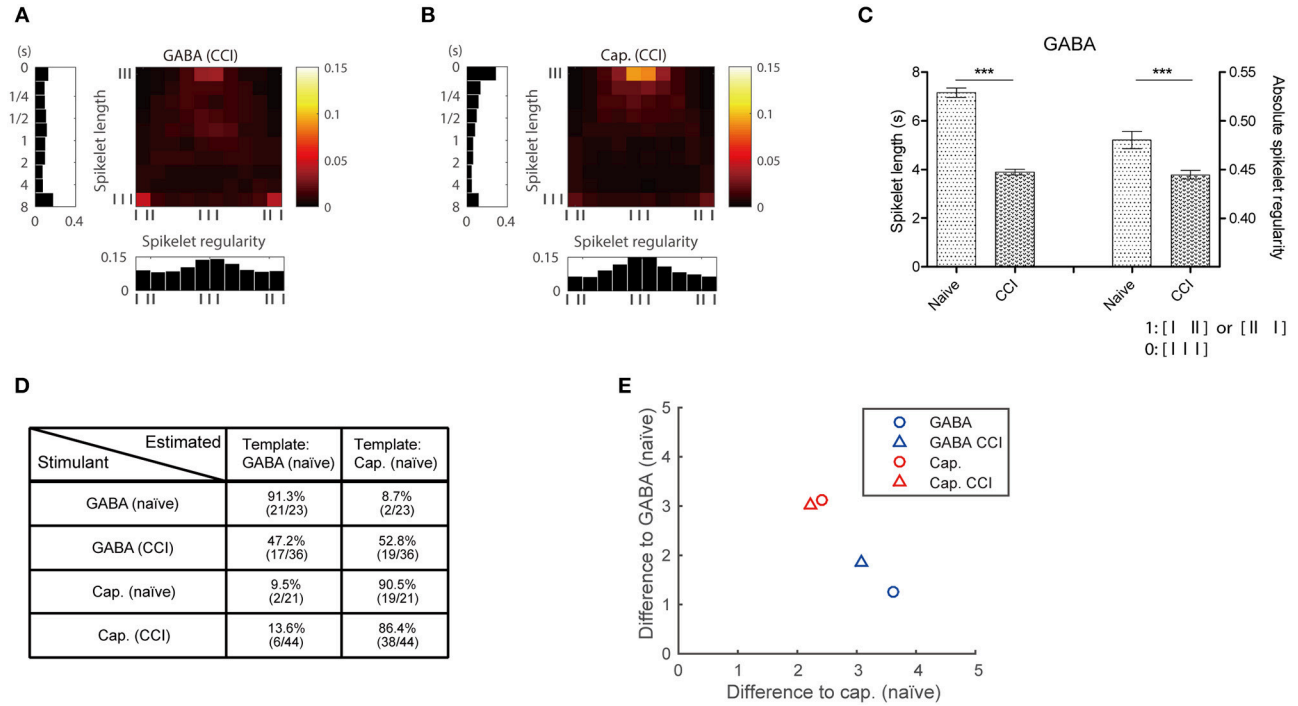

Stimulant \ Estimated	Template: GABA (naïve)	Template: Cap. (naïve)
GABA (naïve)	91.3% (21/23)	8.7% (2/23)
GABA (CCI)	47.2% (17/36)	52.8% (19/36)
Cap. (naïve)	9.5% (2/21)	90.5% (19/21)
Cap. (CCI)	13.6% (6/44)	86.4% (38/44)

FIGURE 6 | Temporal discharge patterns in pathological condition. (A,B) 2D map of responses in CCI mice to GABA and capsaicin, respectively. **(C)** Spikelets of GABA responses are shorter and more regular in CCI mice than naïve mice. (Mann–Whitney or *t*-test based on normality, ***$P < 0.001$) **(D)** Classification performance using KL divergence of the GABA and capsaicin patterns. **(E)** Mean differences from individual 2D maps to GABA and capsaicin 2D maps (**Figures 4C,D**).

MATERIALS AND METHODS

Overview of Animal Experiments

All experiments were conducted according to the guidelines of the Animal and Plant Quarantine Agency of Korea for the care and use of laboratory animals, and the study was approved by the Institutional Animal Care and Use Committee of Hanyang University (HY-IACUC-13-037A). Male C57BL/6 mice (8 weeks old) were used throughout the study.

First, the effect of the studied chemicals on nociceptive behavior was investigated. Behavioral changes were observed in 46 mice after subcutaneous injection of one or other of the chemical stimulants, KCl ($n = 10$), GABA ($n = 10$), or capsaicin ($n = 8$), or a control, saline ($n = 10$) or vehicle ($n = 8$).

Next, to examine the sensitivity of single C-fibers to multiple chemicals, *ex vivo* recordings were made with 14 fibers from another group of mice. Each fiber was tested by application of all three chemicals in succession, with a wash-out period between each application. The average conduction velocity of the fibers in the sensitivity test was 0.65 ± 0.17 m/s. In addition, the effects of the three chemicals (KCl, $n = 25$; GABA, $n = 23$; capsaicin, $n = 21$) on the neural response were tested separately, with each fiber exposed to only one of the chemical stimulants. To exclude extraneous effects, the mice used for the behavioral tests were not used for *ex vivo* recording. For a pathological model, 42 mice were subjected to CCI by sciatic nerve cuffing. Hypersensitivity to mechanical and heat stimuli was verified 12–15 days after surgery. Of the 42 CCI mice 26 were used for the behavioral test (response to vehicle, $n = 8$; GABA, $n = 9$; capsaicin, $n = 9$). Fibers for *ex vivo* recording (response to GABA, $n = 36$ or capsaicin, $n = 46$) were obtained from the remaining 16 mice (**Figure 7**).

Sciatic Nerve Cuffing Model

The CCI model was used for behavioral tests based on hindpaw movement (response to stimulus to the plantar surface of the foot) as well as *ex vivo* recording from the hairy skin under pathological conditions. Surgery was performed under brief isoflurane anesthesia. The main branch of the left sciatic nerve was exposed and a cuff of PE-20 polyethylene tubing (0.38 mm internal diameter, 1.09 mm external diameter; Harvard Apparatus) of standardized length (2 mm) was applied (Benbouzid et al., 2008). The shaved skin layer was closed using sutures. Compared with baseline, the mechanical and heat thresholds were significantly reduced following sciatic nerve cuffing on postoperative days 12–15 (Wilcoxon signed rank test, $Ps < 0.001$), indicating neuropathic pain. The left sural nerve, which was affected by the CCI, was used for *ex vivo* recording.

Behavioral Studies

Mice were acclimated to testing cages containing either a stainless steel mesh (for mechanical withdrawal responses) or a heat-tempered glass floor (for spontaneous pain behavior and heat withdrawal latency) for 2 h per day for at least 5 days before

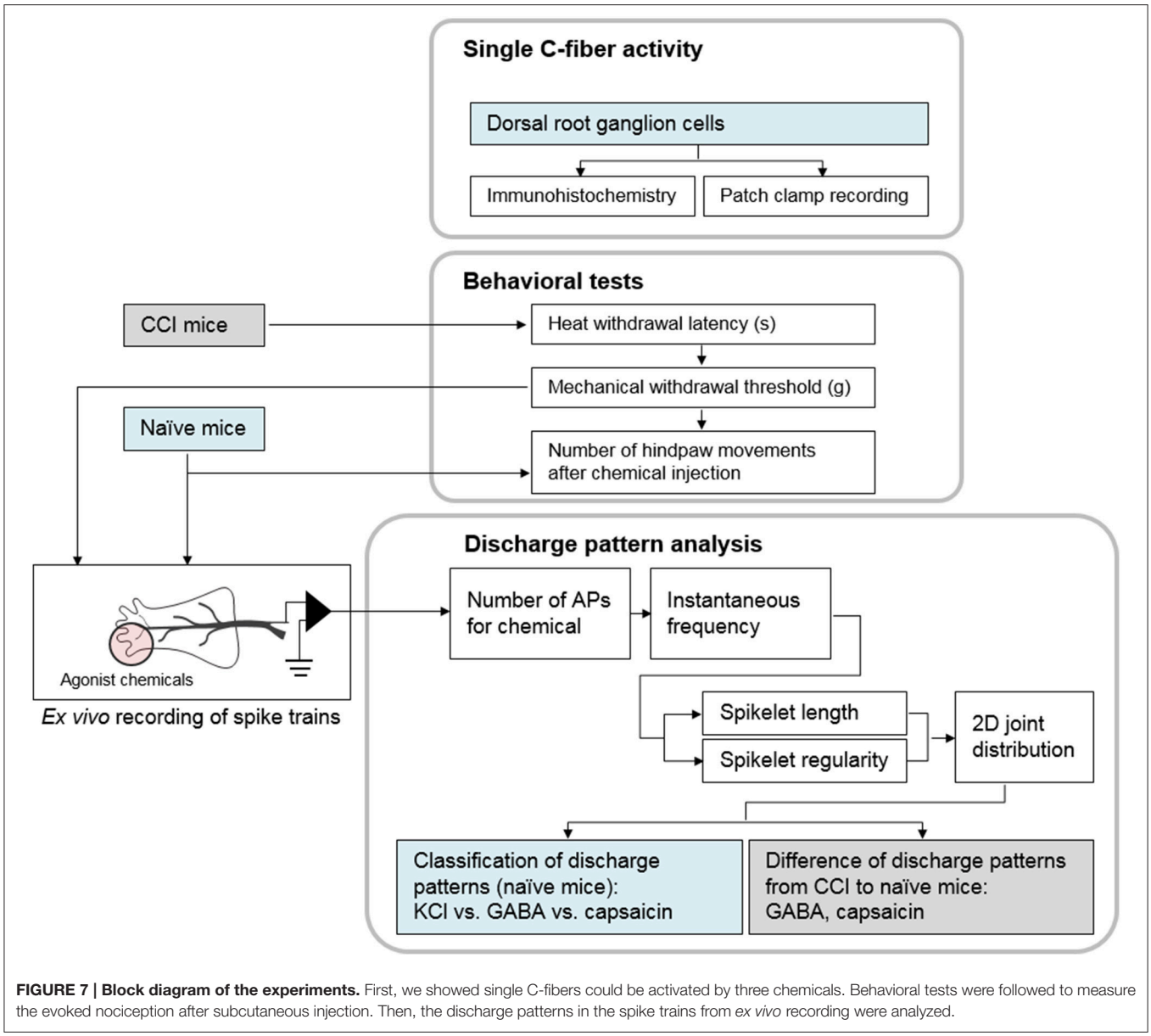

FIGURE 7 | Block diagram of the experiments. First, we showed single C-fibers could be activated by three chemicals. Behavioral tests were followed to measure the evoked nociception after subcutaneous injection. Then, the discharge patterns in the spike trains from *ex vivo* recording were analyzed.

testing. All behavioral tests were performed after at least 1 h acclimation on the day of the experiment.

Spontaneous Pain Behavior

Drugs were injected using gentle restraint without anesthesia. Fifty millimolars KCl, 3 mM GABA, 10 μM capsaicin, saline, or vehicle (98% synthetic interstitial fluid, SIF, mixed with 1% dimethyl sulfoxide and 1% saline) solution in a 20 μL volume was injected subcutaneously into the plantar surface of the hindpaw using an insulin syringe and a 30-gauge needle. Immediately after injection, mice were returned to the glass floor cage and 5 min video recordings were made. The number of movements of the injected limb, including lifting/guarding, flinching/shaking, licking, and walking, was determined by visual observation and considered as an indication of pain (Kawasaki-Yatsugi et al., 2012).

Heat Withdrawal Latency

The heat stimulus was a light from a projector lamp applied from underneath the glass floor onto the lateral part of the plantar surface (sural nerve territory). Before data collection, the intensity of the stimulus was adjusted so that mice withdrew after ~6 s. The latency in seconds before withdrawal was determined with a cutoff value of 12 s. The baseline values were obtained immediately before sciatic nerve injury.

Mechanical Withdrawal Responses

Von Frey filaments were applied to the lateral part of the plantar surface to estimate the 50% withdrawal threshold using the

SUDO up-down method (Bonin et al., 2014). The baseline values were obtained immediately before sciatic nerve injury.

Ex Vivo Single Fiber Recordings

Mice were killed using CO_2 inhalation and the hairy skin of the hindpaw innervated by the saphenous or sural nerve was dissected after the hair on the leg was clipped. For recording from the CCI model mice, only the left sural nerve, which was impacted by the cuffing of the left sciatic nerve, was used. Attached connective tissue, muscle, and tendon were removed. The organ bath consisted of two chambers separated by an acrylic-based wall. The larger perfusion chamber was continuously superfused with a SIF (107.8 mM NaCl, 3.5 mM KCl, 0.69 mM $MgSO_4{\cdot}7H_2O$, 26.2 mM $NaHCO_3$, 1.67 mM $NaH_2PO_4{\cdot}2H_2O$, 9.64 mM $C_6H_{11}NaO_7$, 5.55 mM glucose, 7.6 mM sucrose, 1.53 mM $CaCl_2{\cdot}2H_2O$) saturated with a mixture of 95% O_2 and 5% CO_2 (Bretag, 1969). The temperature of the bath solution was maintained at 31 ± 1°C. After dissection, the preparation was placed with the epidermal side down. The nerves attached to the skin were drawn through one small hole to the smaller second chamber, which was filled with paraffin oil. The nerve was placed on a fixed mirror, the sheath was removed, and nerve filaments repeatedly teased apart to allow single-fiber recordings to be made using gold electrodes, one for recording and the other for reference. The reference electrode was grounded to the perfusion chamber. Signals from single nociceptive afferent fibers were recorded extracellularly with a differential amplifier (DP 311; Warner instruments). Amplified signals were sent to an oscilloscope and an audio monitor and sampled at 33 kHz, then transferred to a computer by a data acquisition system (DAP5200a; Microstar Laboratories, Inc.). APs collected on the computer were analyzed off-line using the window discrimination feature of the software (Dapsys 8; Bethel University, http://dapsys.net/). Copper blocks were connected to common ground as a reservoir of current to prevent excessive noise. The entire setup was based on a study by Zimmermann et al. (2009). The conduction velocity of the axon was determined by monopolar electrical stimulation through a low impedance electrode (CBJPL75; FHC Inc.). The supramaximal square-wave pulses (0.2–2 ms duration, 0.5 Hz) were delivered at the mechanosensitive site of a receptive field using an electrical stimulator (SD9; Grass Technologies). The distance between the receptive field and the recording electrode (conduction distance) was divided by the latency of the AP. A single C-fiber was selected on the basis of the conduction velocity (slower than 1.2 m/s); fast conducting A-fibers were excluded. The primary search strategy was mechanical stimulation by a fire-polished glass rod targeting mechanosensitive fibers.

Temporal Pattern Analysis of Spike Trains

A histogram of instantaneous frequencies was constructed to show the empirical distribution of instantaneous frequencies for each chemical stimulus. For each chemical, all the instantaneous frequency values were divided into 10 equal-length (0.8 Hz) bins from 0–0.8 to 7.2–8 Hz. Frequency values >8 Hz were included in the last bin.

Given a spike train of N spikes, a spikelet s was defined as a set of three consecutive spikes,

$$s = (t_n, t_{n+1}, t_{n+2}), \tag{1}$$

where $n = 1, ..., N-2$. We characterized spikelets in terms of two simple and basic parameters: length and regularity. Spikelet length L was defined as the time elapsed from the first to the last spike,

$$L = (t_{n+2} - t_n). \tag{2}$$

Spikelet regularity was defined as the ratio of increment of two consecutive ISIs to spikelet length,

$$\Psi = 2(t_{n+2} - t_{n+1})/(t_{n+2} - t_n). \tag{3}$$

Note, that spikelet regularity ranges from 0 to 2. Finally, we identified every spikelet in the spike train, allowing overlapping of two spikes between successive spikelets and calculated the length and regularity of each (i.e., there are N–2 spikelets in a train of N spikes where $N > 2$).

Having measured spikelet length and regularity from the spike train generated in response to a particular chemical, we built histograms of each parameter. The values of spikelet length were divided into 10 bins in a logarithmic scale with base 2 from 0 to 8 s: 0–0.157 s, 0.157–0.250 s, 0.250–0.397 s, 0.397–0.630 s, 0.630–1.000 s, 1.000–1.587 s, 1.587–2.520 s, 2.520–4.000 s, 4.000–6.350 s, and 6.350 s to the maximum. The maximum length was set as 8 s in our analysis, and longer lengths were included in the last bin. The absolute values of spikelet regularity, $|\Psi|$, were divided into 10 equal-length bins from 0–0.1, 0.1–0.2, ..., 0.9–1.

A Modeling for the Estimation of Nociception Level

A computational model was developed to estimate a putative nociception level from the temporal integration of spikelets of an input spike train. Specifically, the model integrated the features of successive spikelets over time to estimate a nociception level and determined nociception when the estimated level exceeded a threshold. Given the n-th spikelet of an input spike train, our model first calculated the Gaussian radial basis function (RBF) kernels on the vector of spikelet length $[L(n)]$ and regularity $[R(n)]$ of the input spikelet and each of pre-determined template vectors. The template vectors included the mean vectors of spikelet length and regularity for KCl and capsaicin as well as two different vectors of spikelet length and regularity for GABA (**Figures 3E,I**). The two template vectors for GABA were made as either regular ($\Psi = 0$), and irregular ($\Psi = 1$) reflecting the characteristic of spikelet regularity histogram of GABA (**Figure 3K**). The RBF kernel width parameter, σ^2, was empirically set to 0.1. The RBF kernel outputs, $Z_1(n)$, $Z_2(n)$, $Z_3(n)$, and $Z_4(n)$, indicated the difference of the tested spikelet from the template vectors for KCl, capsaicin, regular ($\Psi = 0$), and irregular ($\Psi = 1$) GABA responses, respectively. These four outputs were then linearly combined and fed to a hyperbolic tangent sigmoid transfer function as:

$$z(n) = 2/(1 + e^{-2(Z1+Z2-Z3-Z4)}) - 1. \tag{4}$$

Note, that our model imposed positive weights (i.e., +1) on the RBF kernels for the nociceptive KCl and capsaicin [$Z_1(n)$ and $Z_2(n)$], while imposing negative weights (i.e., −1) on those for non-nociceptive GABA [$Z_3(n)$ and $Z_4(n)$], to estimate a nociception level. Finally, the model estimated a current nociception level, $y(n)$, by integrating the current transfer function output [$z(n)$] with the previous (n−1)-th estimate as:

$$y(n) = z(n) + \lambda^{L(n)} y(n-1). \quad (5)$$

A memory factor, λ, was set to a value in a range of (0, 1), describing the effect of temporal summation that would be diminished on the following spikelet. The power of λ was modeled as $L(n)$ to implement a condition that the previous estimate would affect less with a longer spikelet. Finally, the model deemed that nociception was evoked when $y(n) > \theta$, where θ was a threshold for the detection of nociceptive stimulations (Supplementary Figure 4).

Classification of Discharge Patterns

A joint distribution of spikelet length and regularity was created by building a 2D histogram (allocation of the spikelet to a bin on the 2D histogram map). We took into account both positive and negative values of spikelet regularity in building the 2D histogram by dividing the regularity values into 10 equal-length bins from −1 to 1 with a step of 0.2 in an ascending fashion. The counts in all the bins were divided by (N−2) to represent a probability distribution. We quantitatively assessed the similarity of the 2D joint distributions between different chemicals using the symmetrized KL divergence (Jeffreys, 1946). Given two probability distributions, P and Q, the KL divergence of Q from P was calculated as,

$$D(P||Q) = \Sigma_{i,j} P(i,j) \ln(P(i,j)/Q(i,j)) \quad (6)$$

with the sum over all the (i,j)-th bins, where i = 1st–10th bins for regularity and j = 1st–10th bins for length. The difference was then computed from the absolute value of the symmetrized KL divergence:

$$\Delta(P||Q) = (|D(P||Q)| + |D(Q||P)|)/2. \quad (7)$$

A larger value of Equation (7) indicated greater dissimilarity of the spikelet parameter distribution maps between chemicals. Spike trains were classified as a response to a particular chemical on the basis of the KL divergence. We first obtained a representative template of the 2D joint distribution map for each class from the training data (three classes each for KCl, GABA, and capsaicin, respectively). The representative template map was calculated by summing all bin counts per class over the 2D map followed by normalization. Next, when classifying a new spike train, we built the 2D map of the spikelet patterns and calculated the difference of it to each class template map. Lastly, the chemical of the class with the smallest difference was deemed to generate the spike train.

AUTHOR CONTRIBUTIONS

Performed the experiments and analyzed data: KC and JJ. Provided the analysis model and the classification: SK. Conducted patch clamp recording and immunohistochemistry: SL. Conceived the project and designed the study: SC and IK. Supervised the study and edited the manuscript: DJ and SJ.

ACKNOWLEDGMENTS

This work was supported by grants from the National Research Foundation of Korea (NRF) funded by the Korean government (MSIP) (2012M3A7B4035199, 2011-0027921, and 2016R1A2B4013332).

SUPPLEMENTARY MATERIAL

The Supplementary Material for this article can be found online at: http://journal.frontiersin.org/article/10.3389/fncom.2016.00118/full#supplementary-material

REFERENCES

Adriaensen, H., Gybels, J., Handwerker, H. O., and Van Hees, J. (1980). Latencies of chemically evoked discharges in human cutaneous nociceptors and of the concurrent subjective sensations. *Neurosci. Lett.* 20, 55–59. doi: 10.1016/0304-3940(80)90233-5

Bautista, D. M., Movahed, P., Hinman, A., Axelsson, H. E., Sterner, O., Högestätt, E. D., et al. (2005). Pungent products from garlic activate the sensory ion channel TRPA1. *Proc. Natl. Acad. Sci. U.S.A.* 102, 12248–12252. doi: 10.1073/pnas.0505356102

Benbouzid, M., Pallage, V., Rajalu, M., Waltisperger, E., Doridot, S., Poisbeau, P., et al. (2008). Sciatic nerve cuffing in mice: a model of sustained neuropathic pain. *Eur. J. Pain* 12, 591–599. doi: 10.1016/j.ejpain.2007.10.002

Bessou, P., and Perl, E. R. (1969). Response of cutaneous sensory units with unmyelinated fibers to noxious stimuli. *J. Neurophysiol.* 32, 1025–1043.

Bonin, R. P., Bories, C., and De Koninck, Y. (2014). A simplified up-down method (SUDO) for measuring mechanical nociception in rodents using von Frey filaments. *Mol. Pain.* 10:26. doi: 10.1186/1744-8069-10-26

Bretag, A. H. (1969). Synthetic interstial fluid for isolated mammalian tissue. *Life Sci.* 8(Pt 1), 319–329. doi: 10.1016/0024-3205(69)90283-5

Carlton, S. M., Zhou, S., and Coggeshall, R. E. (1999). Peripheral $GABA_A$ receptors: evidence for peripheral primary afferent depolarization. *Neuroscience* 93, 713–722. doi: 10.1016/S0306-4522(99)00101-3

Debus, S., and Sandkühler, J. (1996). Low dimensional attractors in discharges of sensory neurons of the rat spinal dorsal horn are maintained by supraspinal descending systems. *Neuroscience* 70, 191–200. doi: 10.1016/0306-4522(95)00344-I

Deschenes, M., Feltz, P., and Lamour, Y. (1976). A model for an estimate *in vivo* of the ionic basis of presynaptic inhibition: an intracellular analysis of the GABA-induced depolarization in rat dorsal root ganglia. *Brain Res.* 118, 486–493. doi: 10.1016/0006-8993(76)90318-8

Devroye, L., Gyorfi, L., and Lugosi, G. (1996). "Probabilistic theory of pattern recognition," in *Applications of Mathematics: Stochastic Modelling and Applied Probability*, eds I. Karatzas and M. A. Yor (New York, NY; Berlin; Heidelberg: Springer-Verlag), 27–28.

Feltz, P., and Rasminsky, M. (1974). A model for the mode of action of GABA on primary afferent terminals: depolarizing effects of GABA

applied iontophoretically to neurones of mammalian dorsal root ganglia. *Neuropharmacology* 13, 553–563. doi: 10.1016/0028-3908(74)90145-2

Han, L., Ma, C., Liu, Q., Weng, H. J., Cui, Y., Tang, Z., et al. (2013). A subpopulation of nociceptors specifically linked to itch. *Nat. Neurosci.* 16, 174–182. doi: 10.1038/nn.3289

Hanack, C., Moroni, M., Lima, W. C., Wende, H., Kirchner, M., Adelfinger, L., et al. (2015). GABA blocks pathological but not acute TRPV1 pain signals. *Cell* 160, 759–770. doi: 10.1016/j.cell.2015.01.022

Iverfeldt, K., Serfözö, P., Diaz-Arnesto, L., and Bartfai, T. (1989). Differential release of coexisting neurotransmitters; frequency dependence of the efflux of substance P, thyrotropin releasing hormone and [3H] serotonin from tissue slices of rat ventral spinal cord. *Acta Physiol. Scand.* 137, 63–71. doi: 10.1111/j.1748-1716.1989.tb08721.x

Jeffreys, H. (1946). An invariant form for the prior probability in estimation problems. *Proc. R. Soc. Lond.* 186, 453–461. doi: 10.1098/rspa.1946.0056

Johanek, L. M., Meyer, R. A., Friedman, R. M., Greenquist, K. W., Shim, B., Borzan, J., et al. (2008). A role for polymodal C-fiber afferents in nonhistaminergic itch. *J. Neurosci.* 28, 7659–7669. doi: 10.1523/JNEUROSCI.1760-08.2008

Kawasaki-Yatsugi, S., Nagakura, Y., Ogino, S., Sekizawa, T., Kiso, T., Takahashi, M., et al. (2012). Automated measurement of spontaneous pain-associated limb movement and drug efficacy evaluation in a rat model of neuropathic pain. *Eur. J. Pain* 16, 1426–1436. doi: 10.1002/j.1532-2149.2012.00142.x

Koltzenburg, M., and Handwerker, H. (1994). Differential ability of human cutaneous nociceptors to signal mechanical pain and to produce vasodilatation. *J. Neurosci.* 14, 1756–1765.

Kumazawa, T., Kruger, L., and Mizumura, K. (1996). *The Polymodal Receptor-A Gateway to Pathological Pain, Vol. 113.* Amsterdam; Lausanne; New York, NY; Oxford; Shannon; Tokyo: Elsevier.

Lánský, P., Rodriguez, R., and Sacerdote, L. (2004). Mean instantaneous firing frequency is always higher than the firing rate. *Neural Comput.* 16, 477–489. doi: 10.1162/089976604772744875

Pereira, J. C. Jr., and Alves, R. C. (2011). The labelled-lines principle of the somatosensory physiology might explain the phantom limb phenomenon. *Med. Hypotheses* 77, 853–856. doi: 10.1016/j.mehy.2011.07.054

Prescott, S. A., Ma, Q., and De Koninck, Y. (2014). Normal and abnormal coding of somatosensory stimuli causing pain. *Nat. Neurosci.* 17, 183–191. doi: 10.1038/nn.3629

Sandkühler, J. (1996). "Neurobiology of spinal nociception: new concepts," in *Progress in Brain Research*, Vol. 110, eds G. Carli, and M. Zimmermann (Amsterdam: Elsevier), 207–224.

St Pierre, M., Reeh, P. W., and Zimmermann, K. (2009). Differential effects of TRPV channel block on polymodal activation of rat cutaneous nociceptors *in vitro*. *Exp. Brain Res.* 196, 31–44. doi: 10.1007/s00221-009-1808-3

Van Hees, J., and Gybels, J. (1981). C nociceptor activity in human nerve during painful and non painful skin stimulation. *J. Neurol. Neurosurg. Psychiatr.* 44, 600–607. doi: 10.1136/jnnp.44.7.600

Weber, A. I., Saal, H. P., Lieber, J. D., Cheng, J. W., Manfredi, L. R., Dammann, J. F. III., et al. (2013). Spatial and temporal codes mediate the tactile perception of natural textures. *Proc. Natl. Acad. Sci. U.S.A.* 110, 17107–11012. doi: 10.1073/pnas.1305509110

Wooten, M., Weng, H. J., Hartke, T. V., Borzan, J., Klein, A. H., Turnquist, B., et al. (2014). Three functionally distinct classes of C-fibre nociceptors in primates. *Nat. Commun.* 5:4122. doi: 10.1038/ncomms5122

Zimmermann, K., Hein, A., Hager, U., Kaczmarek, J. S., Turnquist, B. P., Clapham, D. E., et al. (2009). Phenotyping sensory nerve endings *in vitro* in the mouse. *Nat. Protoc.* 4, 174–196. doi: 10.1038/nprot.2008.223

Conflict of Interest Statement: The authors declare that the research was conducted in the absence of any commercial or financial relationships that could be construed as a potential conflict of interest.

Advantages of publishing in Frontiers

OPEN ACCESS
Articles are free to read for greatest visibility and readership

FAST PUBLICATION
Around 90 days from submission to decision

HIGH QUALITY PEER-REVIEW
Rigorous, collaborative, and constructive peer-review

TRANSPARENT PEER-REVIEW
Editors and reviewers acknowledged by name on published articles

Frontiers
Avenue du Tribunal-Fédéral 34
1005 Lausanne | Switzerland

Visit us: www.frontiersin.org
Contact us: info@frontiersin.org | +41 21 510 17 00

REPRODUCIBILITY OF RESEARCH
Support open data and methods to enhance research reproducibility

DIGITAL PUBLISHING
Articles designed for optimal readership across devices

FOLLOW US
@frontiersin

IMPACT METRICS
Advanced article metrics track visibility across digital media

EXTENSIVE PROMOTION
Marketing and promotion of impactful research

LOOP RESEARCH NETWORK
Our network increases your article's readership